Available online at www.sciencedirect.com
SCIENCE DIRECT
Organic Electronics 7 (2006) 1–7
Organic Electronics
www.elsevier.com/locate/orgel

Study of the transient EL slow rise in single layer OLEDs

A. Rihani [a,*], L. Hassine [a,*], J.-L. Fave [b], H. Bouchriha [a]

[a] Laboratoire de Physique de la Matière Condensée, Département de Physique, Faculté des Sciences de Tunis, 1060 Campus Universitaire, Tunis, Tunisia

[b] Groupe de Physique des Solides, UMR 75-88 du CNRS, Universités Paris 6 et Paris 7, 2 Place de Jussieu 75251, Paris cedex 05, France

Available online 20 July 2005

Abstract

Study of the transient electroluminescence (EL) behavior at turn-on upon the application of a single voltage pulse is presented. Based on the continuity equations which describe the carrier dynamics, and on the recombination current which describe the EL output, we present a theoretical model to explain the slow rise of the EL associated to the electron packet motion in the bulk. The model enables us to determine, more than the mobility of majority carriers, the equilibrium density of free holes in the bulk. The dependence of free hole density (p_e) of the applied voltage shows that the unipolar current flow for holes in the bulk follows as expected, an SCLC regime characterized by a linear dependence of p_e with applied voltage. Our analysis allows us also to estimate the trap density (for holes) in the bulk of about 2×10^{15} cm^{-3}. Both experimental and theoretical results are compared to each other and to other works, and were found to be consistent with the proposed model. The device under investigation is the conventional ITO/MEH-PPV/Al OLED.

Keywords: Organic light emitting diodes (OLEDs); Transient EL; Free hole density; SCL current; Trap density

1. Introduction

Organic semiconductors has attracted extensive researches during the last decade because of their potential application in light-weight color flat panel displays [1,2]. The basic structure of an organic light emitting device (OLED) consists of a thin electroluminescent material sandwiched between tow electrodes. Electroluminescence (EL) is obtained by applying a forward bias to the device. The fundamental mechanisms involved are injection, transport, and radiative recombination of carriers in the bulk. In the injection mechanism charge carriers have to surmount or tunnel through a contact barrier at the metal–organic interface [3,4]. However, carrier transport in the bulk was found to be either injection limited [5], or bulk limited [6,7] dependent on the barrier heights at the interfaces [8]. Electroluminescence occurs via Langevin bimolecular electron–hole pair recombination [9] which leads to singlet and triplet excitons formation but only singlet can decay radiatively in MEH-PPV.

Further, transient EL has been attracting considerable interest for its potential application as a pulse light source [10,11], and for high resolution displays [12]. Upon the application of a rectangular voltage pulse to the OLED, one can study charge carrier

* Corresponding authors.
E-mail addresses: rihani_anis@yahoo.fr (A. Rihani), l_lotfi@yahoo.fr (L. Hassine).

1566-1199/$ - see front matter © 2005 Elsevier B.V. All rights reserved.
doi:10.1016/j.orgel.2005.06.004

kinetics, as well as estimate charge carrier mobility from the temporal response of the EL [13–16].

In our previous works [17,18], we are investigated bilayer structure in which charge densities, transient currents, as well as transient EL as function of applied voltage pulses has been modeled and compared to experimental data. This paper is focused on single layer devices and it is organized as follow: first we describe the device and we present the experimental setup, after we focus on the theoretical investigation based on rate equations, and finally we discuss and compare the experimental results to the theoretical ones.

2. Experimental setup

In this paper the device under investigation consists of an indium-tin oxide (ITO) coated glass substrate as the hole injecting electrode, followed by ~250 nm thick poly[2-methoxy-5-(2′-ethylhexyloxy)-*p*-phenylenevinylene] (MEH-PPV) as the emissive layer, and terminated with 250 nm thick aluminum (Al) as the electron injecting electrode: ITO/MEH-PPV/Al. The LED was manufactured by spin coating a solution of a commercial MEH-PPV onto commercially available ITO glass. The solution was formed by dissolving the polymer in the trichloro-1,1,2-ethane (~20 mg/ml) using an ultrasonic agitator during ~6 h at around 50 °C followed by filtration through a 10 μm filter. After solvent evaporation, the Al top contact was vapor deposed using a turbo pumped vacuum system at a pressure less than 10^{-6} mbar. All processes of fabrication of the diode were made in a white room without UV radiation. The sample after fabrication was conserved in a nitrogen glove box.

The LED was electrically excited by means of fast pulse generator Tektronix PG2012 which permitted accurate control of repetition rate, rise and decay times. Single pulses were varied in time between 100 and 400 μs, and in magnitude between 2 and 14 V. To avoid heating of the sample, all signals were with data cycle up to 50%. The EL response was detected using a PM Hamamatsu H5783 photomultiplier tube detector, and a 50 Ω external load resistance. Experimental setup for recording of the transient light, current, as well as the voltage across the sample, is shown in Fig. 1. For a simultaneous recording of the three quantities we have used a fast digital Tektronix TDS 5034 oscilloscope. All measurements were carried out at room temperature in vacuum and all data were averaged at variables rates. The overall RC time constant of the measurement system was estimated to be much lower than 1 μs.

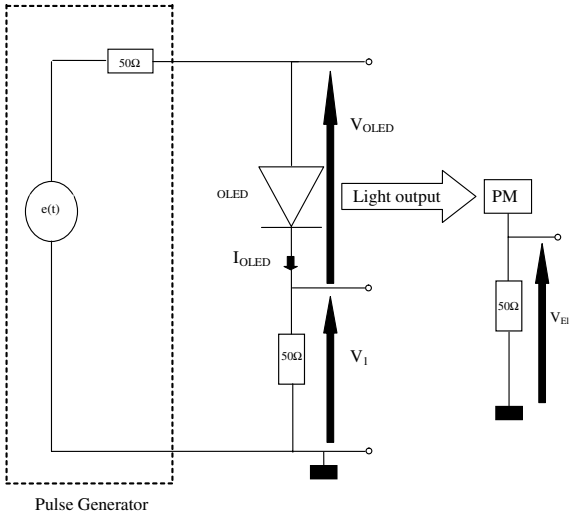

Fig. 1. Schematic view of the experimental setup for measuring transient EL, current and voltage across the device. The oscilloscope used allows a simultaneous visualisation of $e(t)$, V_{OLED}, V_1, and V_{EL}.

The EL spectrum of the device was measured with a Peltier cooled CCD camera coupled to a polychromator. Fig. 2 shows the EL spectrum of the device which is quite similar to any typical spectrum device based on the same material (MEH-PPV), and in Fig. 3 typical transient behaviors of EL and current in comparison with the applied rectangular voltage pulse (400 μs width and 9.75 V amplitude) are depicted.

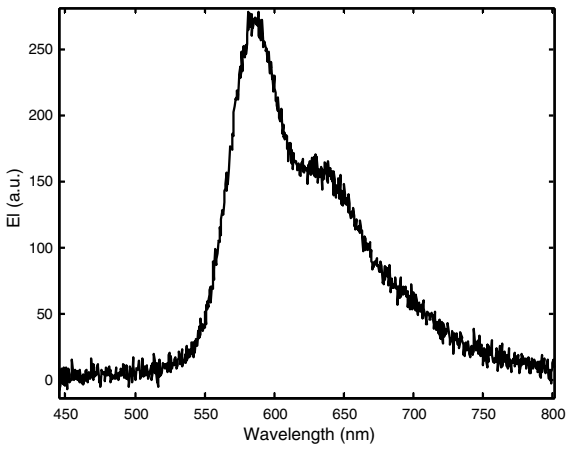

Fig. 2. Electroluminescence spectrum of the ITO/MEH-PPV/Al device.

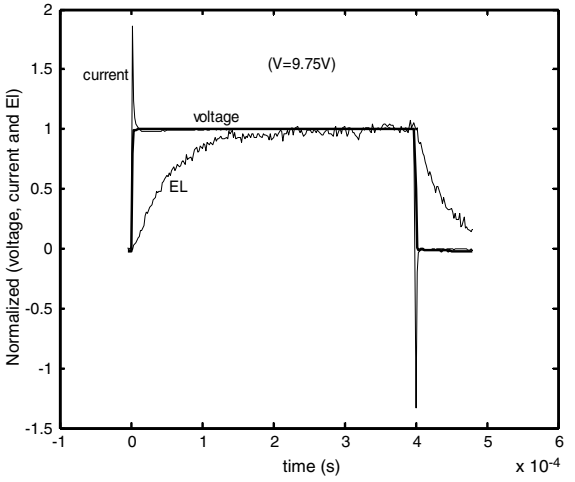

Fig. 3. Transient: voltage across the device after applying single voltage pulse with a duration of 400 μs and 9.75 V height, current density, and EL.

Our ITO/MEH-PPV/Al diode turned at around 8 V with a green emission peak at ~580 nm.

3. Analytical model for the slow rise of the EL

Typical transient behavior of the EL is obtained by addressing a rectangular voltage pulse to the device. In transient features the emission starts after a delay time t_d which is defined as the difference between the rising edge of the voltage pulse and the occurrence of the electroluminescence [13]. We focus on the transient features for $t > t_d$. It is well known and confirmed both experimentally [13,19–21] and by numerical simulations [21], that beyond t_d the electroluminescence signal in single layer OLEDs consists of two exponential components related to the transport of carriers in the bulk. The first starts at t_d and consists of a fast initial rise and corresponds to the hole dominated part. The second starts at a time t_1 and characterized by a slower rise which corresponds to the electron packet motion in the bulk. After EL turn-on and before t_1, the hole density gradually increase in the bulk yielding a fast initial EL rise. The density of electrons in this regime is very weak, and the latter can be associated to the hole dynamic and may be also to the mechanism of charge trapping within the device. However, this regime is very hard to be resolved experimentally because of the relatively high hole mobility and quenching effects, so t_1 can be approximated by t_d. Detailed study of t_1 can be found in Ref. [21]. Beyond t_1, it has been shown [21] that the hole density is at its steady state and only the electron density still moving in the bulk, than in this region the EL can be described only by the electron dynamic. In order to reproduce this feature, we consider the phenomenological model based on the following dynamic equations [8,22] for electrons and holes:

$$\frac{\partial n}{\partial t} = D_e \frac{\partial^2 n}{\partial x^2} + \mu_e \frac{\partial}{\partial x}(nE) - Rnp \tag{1a}$$

$$\frac{\partial p}{\partial t} = D_h \frac{\partial^2 p}{\partial x^2} - \mu_h \frac{\partial}{\partial x}(pE) - Rnp \tag{1b}$$

where μ_e and μ_h are the electron and hole mobilities (which next will be taken field independent), respectively, n and p are, respectively, the electron and hole concentrations in the bulk, D_e and D_h are, respectively, the diffusion constants for electrons and holes. E is the electric field and R is the Langevin recombination coefficient. These two equations should be completed by Poisson's equation:

$$\frac{\partial E}{\partial x} = \frac{q}{\varepsilon}(p + n_t - n - p_t) \tag{2}$$

where p_t and n_t denote trapped holes and electrons, respectively.

To our knowledge without any approximations the system of Eqs. (1), (2) cannot be resolved analytically. However, an analytic solution for the EL slow rise in the electron dominated region can be obtained taken into account of some approximations based on the above physical considerations: (i) for $t > t_d$, the hole density is independent of both time and space and it is not affected by the recombination; (ii) the hole density exceeds very much the electron one even at steady state (this can be achieved when the barrier for hole injection is small compared to the barrier for electron injection); (iii) in contrast to the EL decay mechanism after switching off the bias which is due to charge trapping at the polymer/metal interface and controlled by diffusion of the fastest carriers (holes) in the polymer [23,24], the EL slow rise is due to Langevin recombination of free independent carriers and its mechanism is controlled by the slow motion of electrons under the effect of the applied electric field. Furthermore, since the EL signal is obtained when the applied voltage become relatively high (in general $V > 2$ V), diffusion contribution to the current flow (first term in the second member of Eq. (1)) is negligible; (iv) finally, at the range of applied voltage when the EL is obtained we assume that the influence of traps is not important (all traps are filled).

Taken into account of these approximations one obtain the following equation which describes only the electron dynamic in the bulk:

$$\frac{\partial n}{\partial t} = \mu_e \frac{\partial}{\partial x}(nE) - Rnp_e \quad (t \geqslant t_d) \tag{3}$$

where p_e denote the steady state free hole density.

The EL output is directly proportional to the recombination current J_r given by [9]

$$J_r = q\int_0^L Rnp\,dx \tag{4}$$

Eq. (3) can be written as (taking into account that p_e is constant)

$$\frac{1}{Rp_e}\frac{\partial(qRp_e n)}{\partial t} = q\mu_e \frac{\partial}{\partial x}(nE) - qRp_e n \tag{5}$$

and the integration over the total device thickness and taken into account of Eq. (4), yields

$$\begin{aligned}\frac{1}{Rp_e}\frac{\partial J_r}{\partial t} &= q\mu_e \int_0^L \frac{\partial}{\partial x}(nE)\,dx - J_r \\ &= q\mu_e(n(L)E(L) - n(0)E(0)) - J_r\end{aligned} \tag{6}$$

Eq. (6) describes the time evolution of the recombination current. For $t > t_d$, $n(L)E(L) - n(0)E(0)$ is time independent since the external current reach its steady-state at a time much smaller. The time integration of Eq. (6) yields

$$J_r(t) = J_r(t \to \infty)\left(1 - \exp\left(-\frac{t}{\tau}\right)\right) \tag{7}$$

where $\tau^{-1} = Rp_e$, and the steady state recombination current is given by [25]

$$\begin{aligned}J_r(t \to \infty) &= q\mu_e(n(L)E(L) - n(0)E(0)) \\ &= J_n(L) - J_n(0) = J_p(0) - J_p(L)\end{aligned} \tag{8}$$

which is the difference between injection and external currents (the same for electrons as for holes). Hence, our assumptions express that the EL dynamic for $t > t_d$ is governed only by the slowest carriers (electrons) where the holes are approximated by their concentration at the equilibrium (p_e). Eq. (7) was used before [26] where τ and t_d are briefly studied in bilayer devices. Note that the above time dependent equation of the recombination current is independent of the nature of the current in the device. In the following section experimentally results will be modeled and compared in terms of the above analytic expression.

4. Results and discussion

Fig. 4 presents a set of transient light emission responses acquired by single voltage pulses of duration of 100 μs and with various pulse amplitudes. In this range of applied voltage the effective hole mobility (deduced from Eq. (9)) was found to be nearly field-independent.

Fig. 5 shows the magnitude of the logarithm of the normalized EL subtracted from its steady state value, i.e., $\ln[EL_N(t \to \infty) - EL_N(t)]$ (where the subscript N design normalized quantity), plotted vs. time for a constant voltage pulse amplitude of 8.85 V with a duration of 200 μs. It shows that the emission of light start after a delay time t_d (it is better seen in Fig. 5 rather than in Fig. 4) which is defined as the difference between the rising edge of the voltage pulse and the occurrence of the electroluminescence. t_d was found to be on the order of 6 μs. Since in the PPV (and majority organic materials) holes are the fastest injected carrier with a large mobility compared to the electron mobility [27], t_d will correspond to the time make by holes to reach and to recombine radiatively with the electrons waiting near the cathode. Than the hole mobility, neglecting an inhomogeneous field distribution in the bulk, can be estimated by the following expression [13]:

$$\mu_h = \frac{L^2}{Vt_d} \tag{9}$$

where V is the applied voltage (potential built-in is taken into account), and L is the device thickness

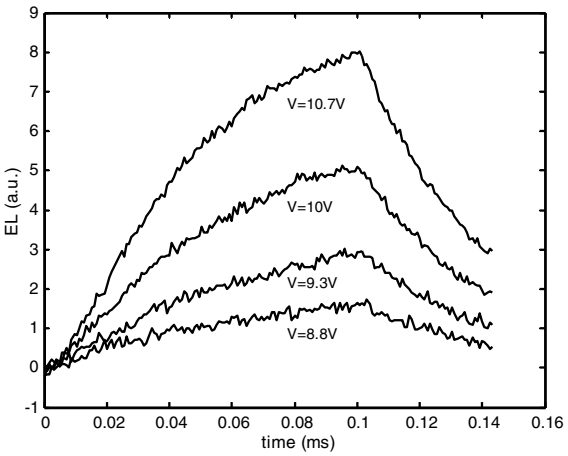

Fig. 4. Transient EL signals for different voltage pulse heights with a duration of 100 μs.

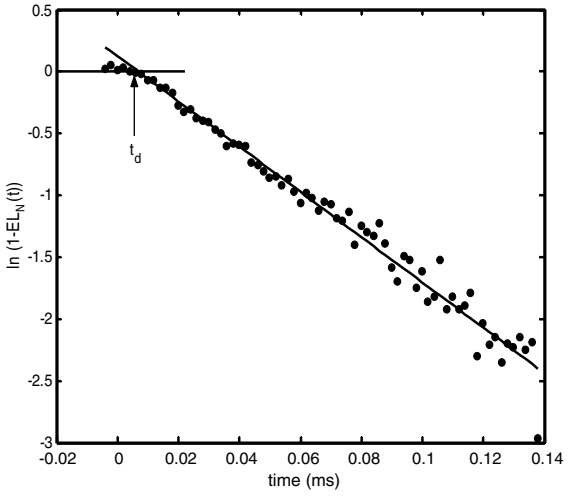

Fig. 5. Plot of $\ln[(EL(t\to\infty)-EL(t))/EL(t\to\infty)]$ $(=\ln[1-EL_N(t)])$ as a function of the time for a constant voltage pulse amplitude of 8.85 V with a duration of 200 μs. The solid circles are the experimental data and the solid line is a linear fit. The figure reveals clearly the expected linear dependence with a slope of the order of $2.2\times10^4\ s^{-1}$. From $\tau^{-1}=Rp_e$ (see the text), we derive a free hole density of the order of $3\times10^{15}\ cm^{-3}$.

(~250 nm). From Eq. (9) μ_h was found to be on the order of $1.2\times10^{-5}\ cm^2\ V^{-1}\ s^{-1}$, in agreement with other works [13,21]. In addition this plot clearly demonstrate as expected a linear behavior of $\ln[EL_N(t\to\infty)-EL_N(t)]$ for $t>t_d$. The fit between Eq. (7) and experimental data yields $\tau^{-1}\approx 2.2\times10^4\ s^{-1}$ for $V=8.85$ V. Using the above obtained hole mobility in the recombination coefficient which can be approximated by $R\approx q\mu_h/\varepsilon$, we derive $p_e\approx 3\times10^{15}\ cm^{-3}$. Hence, at an applied voltage of the order of 8.85 V we assume that the density of free holes in the bulk is about $3\times10^{15}\ cm^{-3}$, which is consistent with that found by simulations by Davids et al. [8] for the ITO/MEH-PPV/Al (10^{14}–$10^{15}\ cm^{-3}$). We can make a simple comparison considering an upper limit for the hole density in the bulk which can be estimated by a direct calculation of the holes injected through the ITO/MEH-PPV interface: assuming a barrier height (Δ) of the order of 0.3 eV [28] and a density of states (p_0) of the order of $10^{20}\ cm^{-3}$ [29], from $p_{inj}\sim p_0\exp(-\Delta/kT)$ one have $\sim10^{15}\ cm^{-3}$ of holes at the contact. Furthermore, we find that the experimental current density of the order of $3.3\ mA/cm^2$ at $(V-V_{bi})=8.85$ V is of the same order than its estimated value (from $J=q\mu_h p_e E$) $\sim2.5\ mA/cm^2$ at steady-state. In spite of some details (for instance: image force lowering, spatial inhomogenity of the electric field…) are not taken in account in these treatments, we can conclude that the above obtained value for p_e seems to be satisfactory. Thus we use the above expressions($\tau^{-1}=Rp_e$ and Eq. (7)) for the determination of p_e as a function of the applied voltage pulse amplitude. In Fig. 6 we show the variation of p_e vs. V. This plot clearly reveals a linear dependence with a slope of the order of $6\times10^{14}\ cm^{-3}\ V^{-1}$ (slight deviations are related to the mobility which is taken field independent). Indeed this behavior is not surprising and arises from the most commonly model of transport observed for holes in the PPV and its derivatives.

We start by noting that the observed transient current is due essentially to hole transport since bipolar transient current does not show any overshoot in single devices [30]. In addition since the barrier for hole injection at the ITO/MEH-PPV interface (~0.3 eV) is much lower than the barrier for electron injection at the MEH-PPV/AL interface (~1.2 eV), the current flow is carried mainly by holes which are in equilibrium state at a time close to t_d (the current density reach its equilibrium value at a time much smaller than the EL saturation see Fig. 3). Furthermore, if the contacts are non-ohmic we should observe an overshoot in the EL decay as discussed by Lupton et al. for MEH-PPV single layer devices [24]. For our device we do not observe any spike in the EL decay which suggests an ohmic contact at the ITO/MEH-PPV contact. This situation lead also to a space charge limited current

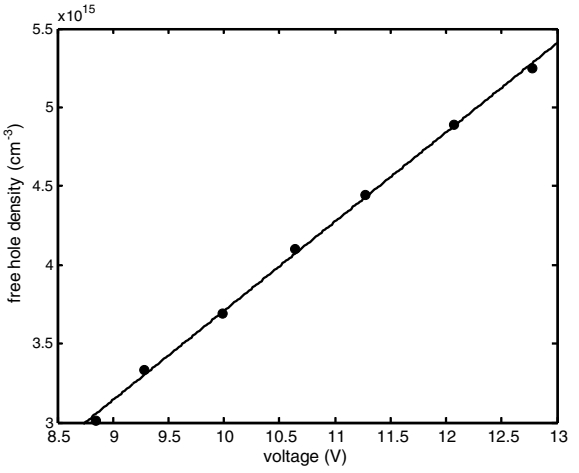

Fig. 6. Voltage dependence of free hole density in the bulk. The solid circles are the experimental data (derived from Eq. (7) and $\tau^{-1}=Rp_e$), and the solid line indicate the linear behavior with a slope of the order of $\sim6\times10^{14}\ cm^{-3}\ V^{-1}$.

(SCLC) for the transport of holes in the bulk. Regarding of these considerations and assuming a negligible influence of traps at the range of the applied voltage to the LED when the EL occurs (between 8 and 13 V) (we assume that the charge density stored in trap sites remain constant as the voltage is increased—all traps are filled—and this will be studied below), we write the following Mott–Gurney relation [31] for a pure SCL current for holes:

$$J_p = \frac{9}{8}\varepsilon\mu_h\frac{V^2}{L^3} \tag{10}$$

On the other hand, the concept of an SCL current is based on the following expression of the drift current (for holes):

$$J_p = q\mu_h p(x)E(x) \tag{11}$$

By replacing the electric field ($E(x)$) and the hole density ($p(x)$) by their mean values V/L and p_e, respectively, from Eqs. (10) and (11) we can derive the following linear relation for free hole density as function of the applied voltage:

$$p_e = \frac{9\varepsilon V}{8qL^2}, \tag{12}$$

We should note that Eq. (12) is an approximate expression where p_e and E are taken space independent (in the general case for a SCL current, pE in Eq. (11) is constant). In fact this assumption is usually used for the electric field. The calculated slope is of the order of $\sim 3\times 10^{15}\ \mathrm{cm^{-3}\ V^{-1}}$ which is in good agreement with its experimental value obtained above. This is moreover a direct evidence of an SCL unipolar hole current in the bulk.

Finally, until now we have neglected the influence of eventual traps in the bulk. By the extrapolation of the experimental curve for p_e vs. V to lower voltages, we find that the equilibrium density of free holes vanishes at a voltage value of $\approx$3.5 V. In fact, it has been demonstrated from impedance spectroscopy and current voltage characteristics [29,32,33], that at lower applied voltages the sample should be depleted and the injection is very weak which lead to smaller currents. At small voltages, filling of empty traps occurs and than reduce the free injected carriers in the bulk. As the voltage pulse is increased, the number of empty traps is reduced; consequently the number of free holes is increased. After filling of traps and when the depletion become small we assume that the density of free holes which is responsible of the current flow, starts to follow a linear behavior with the applied voltage (the unipolar hole current in the bulk become pure SCL). Hence, below $\sim$3.5 V all of injected holes are trapped and the amount of free holes in the bulk is negligible. This allows us to approximate a trap density for holes of the order of $2\times 10^{15}\ \mathrm{cm^{-3}}$ which is in good agreement with other works [21,29].

5. Conclusion

Summarizing, we have provided a simple model for the transient slow rise of the EL turn-on in a single layer organic device. The model is based on the continuity equations for carrier dynamics, as well as the expression of the recombination current. It provides a simple means for estimating the free hole density at the equilibrium in the bulk after EL turn-on. We found a linear dependence between the free hole density in the bulk and the applied voltage pulse with a slope of the order of $6\times 10^{14}\ \mathrm{cm^{-3}}$ comparable to its theoretical value ($\sim 3\times 10^{15}\ \mathrm{cm^{-3}}$) by assuming an SCL behavior for the current carried by holes. At low voltage pulses, we find from the p_e vs. V curve that p_e vanishes at around 3.5 V which suggest the presence of traps in the bulk. We have compared the model calculations with experimental results, and with other works, and the agreement is quite good. The model allows us also to estimate a trap density for holes of about $2\times 10^{15}\ \mathrm{cm^{-3}}$ in the device under investigation. Later, EL turn-off of this device will be investigated to more understand the physical mechanisms involved in OLEDs.

References

[1] J.R. Sheats, H. Antoniadis, M. Hueschen, W. Leonard, J. Miller, R. Moon, D. Roitman, A. Stocking, Science 273 (1996) 884.
[2] R.H. Friend, R.W. Gymer, A.B. Holmes, J.H. Burroughes, R.N. Marks, C. Taliani, D.D.C. Bardley, D.A. Dos Santos, J.L. Bredas, M. Logdlund, W.R. Salaneck, Nature 397 (1999) 121.
[3] I.H. Campbell, T.W. Hagler, D.L. Smith, Phys. Rev. Lett. 76 (1996) 1900.
[4] R.H. Fowler, L. Nordheim, Proc. R. Soc. A 119 (1928) 173.
[5] I.D. Parker, J. Appl. Phys. 75 (1994) 1656.
[6] P.W.M. Blom, M.J.M. de Jong, J.J.M. Vleggaar, Appl. Phys. Lett. 68 (1996) 3308.
[7] P.W.M. Blom, M.J.M. de Jong, M.G. Van Munster, Phys. Rev. B 55 (1997) R656.
[8] P.S. Davids, I.H. Campbell, D.L. Smith, J. Appl. Phys. 82 (1997) 6319.
[9] B.K. Crone, P.S. Davids, I.H. Campbell, D.L. Smith, J. Appl. Phys. 87 (2000) 1974.

[10] V. Savvateev, J.H. Friedl, L. Zou, J. Shinar, K. Christensen, W. Oldham, L.J. Rothberg, Z. Chen-Esterlit, R. Kopelman, Appl. Phys. Lett. 76 (2000) 1501.
[11] H. Kajii, T. Tsukagawa, T. Taneda, Y. Ohmori, J. Phys. D: Appl. Phys. 35 (2002) 1334.
[12] C. Hosokawa, M. Eida, M. Matsuura, K. Fukuoka, H. Nakamura, T. Kusumoto, Synth. Met. 91 (1997) 3.
[13] S. Karg, V. Dyakonov, M. Meir, W. Rieß, G. Paasch, Synth. Met. 67 (1994) 165.
[14] Y.H. Tak, H. Vestweber, H. Bässler, A. Bleyer, R. Stockmann, H.H. Hörhold, Chem. Phys. 212 (1996) 471.
[15] J. Rommens, A. Vaes, M. Van der Auweraer, F.C. De Schryver, H. Bässler, H. Vestweber, J. Pommerehne, J. Appl. Phys. 84 (1998) 4487.
[16] J.W. Jang, C.E. Lee, D.W. Lee, J.-I. Jin, Solid State Commun. 130 (2004) 265.
[17] L. Hassine, H. Bouchriha, J. Roussel, J.-L. Fave, Appl. Phys. Lett. 78 (2001) 1053.
[18] L. Hassine, H. Bouchriha, J. Roussel, J.-L. Fave, J. Appl. Phys. 91 (2002) 5170.
[19] A.R. Brown, N.C. Greenham, J.H. Burroughes, D.D.C. Bardley, R.H. Friend, Chem. Phys. Lett. 200 (1992) 46.
[20] J. Pommerehne, H. Vestweber, Y.H. Tak, H. Bässler, Synth. Met. 76 (1996) 67.
[21] D.J. Pinner, R.H. Friend, N. Tessler, J. Appl. Phys. 86 (1999) 5116.
[22] G.G. Malliaras, J.C. Scott, J. Appl. Phys. 83 (1998) 5399.
[23] K.O. Cheon, J. Shinar, Phys. Rev. B 69 (2004) 201306(R).
[24] J.M. Lupton, V.R. Nikitenko, I.D.W. Samuel, H. Bässler, J. Appl. Phys. 89 (2001) 311.
[25] B.K. Crone, I.H. Campbell, P.S. Davids, D.L. Smith, C.J. Neef, J.P. Ferraris, J. Appl. Phys. 86 (1999) 5767.
[26] V.V.N. Ravi Kishore, M.P. Patankar, N. Periasamy, K.L. Narasimhan, Synth. Met. 143 (2004) 295.
[27] M. Abkowitz, M. Stolka, Philos. Mag. Lett. 58 (1988) 239.
[28] D.D.C. Bardley, Synth. Met. 54 (1993) 401.
[29] A.J. Campbel, D.D.C. Bardley, D.G. Lidzey, J. Appl. Phys. 82 (1997) 6326.
[30] B. Ruhstaller, S.A. Carter, J. Appl. Phys. 89 (2001) 4575.
[31] M.A. Lampert, P. Mark, Current Injection in Solids, Academic Press, New York, 1970.
[32] I.H. Campbell, D.L. Smith, J.P. Ferraris, Appl. Phys. Lett. 66 (1995) 3030.
[33] M. Meir, S. Karg, W. Riess, J. Appl. Phys. 82 (1997) 1961.

Available online at www.sciencedirect.com
SCIENCE DIRECT®
Organic Electronics 7 (2006) 8–15
Organic Electronics
www.elsevier.com/locate/orgel

Efficient, color-stable fluorescent white organic light-emitting diodes with an effective exciton-confining device architecture

Jwo-Huei Jou *, Yung-Sheng Chiu *, Ren-Yang Wang, Huei-Ching Hu, Chung-Pei Wang, Hung-Wei Lin

Department of Materials Science and Engineering, National Tsing Hua University, 101, Section 2 Kuang Fu Road, Hsin-Chu 30013, Taiwan, Republic of China

Received 16 September 2005; received in revised form 14 October 2005; accepted 19 October 2005
Available online 18 November 2005

Abstract

Efficient, chromaticity-stable fluorescent white, including pure white, organic light-emitting diodes are fabricated by having an effective exciton-confining device architecture with a single emission layer via vapor-deposition of the solution-mixed targets of a blue light-emitting host doped with a trace amount of a red and/or a green dye. The used host is 1-butyl-9,10-naphthalene-anthracene. The red and green light-emitting dyes are 4-(dicyanomethylene)-2-methyl-6-(julolidin-4-yl-vinyl)-4H-pyran, and 2,3,6,7-tetrahydro-1,1,7,7-tetramethyl-1H,5H,11H-10-(2-benzothiazolyl) quinolizino[9,9*a*,1*gh*]coumarin, respectively. The employed electron-blocking effective hole-transporting material is *N*,*N*′-bis-(1-naphthy)-*N*,*N*′ diphenyl-1,1′-biphenyl-4-4′-diamine, and the hole-blocking effective electron-transporting material is 2-2′-2″-(1,3,5-benzinetriyl)tris(1-phenyl-1-H-benzimidazole). The best power efficiency of the resulting two-spectrum fluorescent devices is 7.5 lm/W (10.8 cd/A) at 11 cd/m^2 with Commission Internationale de l'Eclairage coordinates of (0.423, 0.426), or 6.5 lm/W (9.6 cd/A) at 12 cd/m^{2}with pure white light with coordinates of (0.346, 0.343). The best power efficiency of the three-spectrum counterparts is 6.7 lm/W (9.9 cd/A) at 15 cd/m^2 with a nearly pure white light with coordinates of (0.325, 0.374). All color variations are less than (0.007, 0.006) between 100 cd/m^2 to 10,000 cd/m^2.

PACS: 72.80.Le; 78.60.Fi

Keywords: White light; Organic light-emitting diodes; Efficient; Color-stable; Exciton confining

1. Introduction

White organic light-emitting diodes (WOLEDs) have attracted much interest for having great potential for use in high-quality flat-panel displays, plane illumination, liquid-crystal-display backlighting and opto-electronic applications [1–4]. The power

* Corresponding authors. Tel.: +886 3 5719524; fax: +886 3 5742617.
E-mail addresses: jjou@mx.nthu.edu.tw (J.-H. Jou), d907512@oz.nthu.edu.tw (Y.-S. Chiu).

1566-1199/$ - see front matter © 2005 Elsevier B.V. All rights reserved.
doi:10.1016/j.orgel.2005.10.001

efficiency and lifetime of WOLEDs are currently the primary concerns [5–7]. The emitting layer can be made of phosphorescent [8–10] and/or fluorescent [11–16] materials. Phosphorescent WOLEDs may be suitable for the future illumination for having shown very high luminance and power efficiency [4]. The best reported power efficiency of phosphorescent WOLEDs is 26 lm/W [10]. The best reported power efficiency, however, is 5.0 lm/W for three-spectrum fluorescent WOLEDs with pure white emission [11]. The efficiency is 5.35 lm/W with pure white emission, while 6.0 lm/W with a near pure white emission for two-spectrum fluorescent WOLEDs [12,13]. The power efficiency of fluorescent WOLEDs is comparatively low. Fluorescent WOLEDs with a much-improved efficiency are thus being pursued.

To increase luminous efficiency, the host must first exhibit efficient energy-transfer capability in triggering the emissions of the various dyes [17]. Second, the host is better coupled with appropriate electron- and hole-transporting materials to form low-energy barriers, thus enabling electrons and holes, respectively, to enter the emission layer easily. Third, electron- and hole-blocking functions are provided therein to effectively confine more electrons and holes having entered the desired emission zone to further increase the electron-hole recombination probability, and the corresponding efficiency [18–20].

This work reports the fabrication of efficient, color-stable, white and pure white fluorescent organic light-emitting diodes with an effective exciton-confining device architecture with a single emission layer by vapor-deposition of solution-mixed deposition targets. The best power efficiency of the resulting two-spectrum fluorescent devices is 7.5 lm/W (10.8 cd/A) at 11 cd/m^2 with Commission Internationale de l'Eclairage (CIE) coordinates of (0.423, 0.426), or 6.5 lm/W (9.6 cd/A) at 12 cd/m^2 with a pure white light of (0.346, 0.343). That of the three-spectrum counterparts is 6.7 lm/W (9.9 cd/A) at 15 cd/m^2 with a nearly pure white light of (0.325, 0.374). All color variations are less than (0.007, 0.006) between 100 cd/m^2 to 10,000 cd/m^2.

2. Experimental

Fig. 1 depicts the WOLED structure studied and the organic molecules used. The devices comprise a 125 nm indium tin oxide (ITO) anode, a 45 nm hole-transporting layer (HTL) of *N*,*N*′-bis-(1-naphthy)-*N*,*N*′ diphenyl-1,1′-biphenyl-4-4′-diamine (NPB), a 30 nm white emission layer, a 40 nm electron-transporting layer (ETL) of 2-2′-2″-(1,3,5-benzinetriyl)tris(1-phenyl-1-H-benzimidazole) (TPBi), a 0.5 nm electron-injecting layer of lithium fluoride and a 150 nm aluminum cathode. The white emission layer is formed by vapor-deposition of the solution-mixed deposition target composed of the blue host 1-butyl-9,10-naphthalene-anthracene (BANE) with a trace amount of red dye 4-(dicyanomethylene)-2-methyl-6-(julolidin-4-yl-vinyl)-4H-pyran (DCM2). To form three-spectrum white emission, an additional trace amount of green dye 2,3,6,7-tetrahydro-1,1,7,7-tetramethyl-1H,5H,11H-10-(2-benzothiazolyl)quinolizino[9,9*a*,1*gh*]coumarin (C545T) is added. Another blue host of 1,4-bis(2,2-diphenylvinyl)biphenyl (DPVBi) and two other ETLs of bathocuproine (BCP) and tris(8-hydroxylquinoline)aluminum (Alq_3) are studied for comparison.

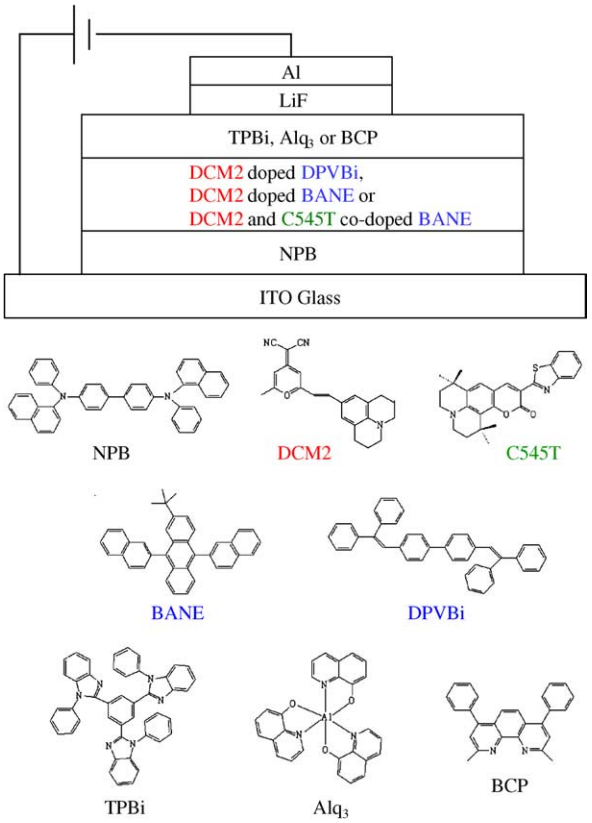

Fig. 1. Schematic illustrations of the structures of the two- or three-wavelength fluorescent WOLEDs and the organic molecules studied.

The deposition source of the white emission layer of two- or three-spectrum was prepared via solution-mixing [21] as followed. The composing dye(s) and host were first seperatively dissolved in an

organic solvent such as tetrahydrofuran or toluene. After complete dissolution, the resultant solutions were then mixed to form a host solution uniformly dispersed with the desired doping dye(s). Low doping concentrations were obtained by using the diluted dye solutions. The resulted dye-dispersed host solution was then vacuum-dried at 80 °C for 60 min prior to vapor-deposition.

The devices were fabricated by vapor-deposition using an ITO coated glass substrate (Merck Display Technologies, Ltd.) with a sheet resistance of 13 Ω/square. The substrate was cleaned in ultrasonic baths of detergent, de-ionized water, acetone and isopropyl alcohol in turn, and then treated with the boiling hydrogen peroxide. The substrate was then dried by purging nitrogen. The respective organic layers and the cathode layer were deposited at 2×10^{-5} Torr using resistively heated tantalum and tungsten boats. All the organic layers were deposited at rates ranging from 0.1 to 0.3 nm/s. The lithium fluoride and aluminum cathode were subsequently deposited at rates of 0.01 and 1 nm/s, respectively. The emission area of all the devices was 8 mm^2, and only the luminance in the forward direction was measured.

The luminance and Commission International de L'Eclairage (CIE) chromatic coordinates of the resulted OLEDs were measured by using Minolta CS-100 luminance-meter. The electroluminescence and photoluminescence spectra were measured using a Hitachi F-4500 fluorescence spectrophotometer. The ultraviolet visible (UV–VIS) absorption spectra of the DCM2 and C545T solutions were measured using a Hitachi U-3010 UV–VIS spectrophotometer. The highest occupied molecular orbital (HOMO) energy levels of the organic materials studied were calculated from their oxidation potentials measured by a cyclic voltammetry [22], while the corresponding lowest unoccupied molecular orbital (LUMO) energy levels were estimated based on their HOMO energy levels and the lowest-energy absorption edge of the UV–VIS absorption spectra. A Keithley 2400 electrometer was used to measure the current-voltage (*I–V*) characteristics. All the devices were characterized without packaging and all the measurements were carried out in the ambient condition.

3. Results and discussion

Fig. 2 shows the effect of the DCM2 concentration on the resultant electroluminescence spectra.

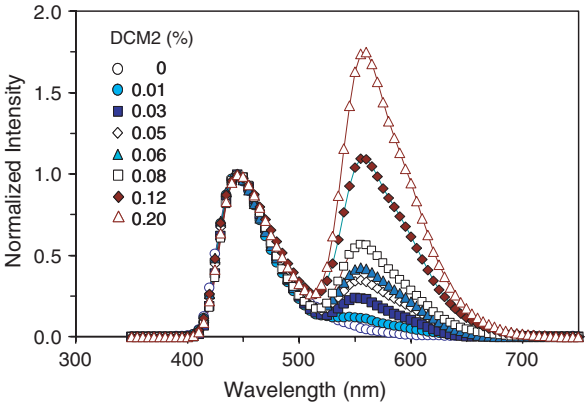

Fig. 2. Doping-concentration effects of the 'red' dye of DCM2 on the electro-luminescence spectra of the two-spectrum WOLEDs.

The spectra exhibit two major emission peaks at 450 nm from the blue host, BANE, and at 560 nm from the red-dopant, DCM2, respectively. The emission that yields pure DCM2 (100%) peaks at 630 nm is strongly blue-shifted when its doping-concentration becomes extremely low, ranging from 100 to 2000 ppm, which is due to a strong solid state solvation effect [23]. The marked blue-shift turned the DCM2, itself, from a so-called red dye to an orange one in these doping ranges.

Table 1 presents the effects of the concentration of the various light-emitting dopants on the resultant luminous characteristics. The resultant CIE coordinates change from that of blue light $(0.155, 0.122)$ to that of yellow light $(0.464, 0.457)$ as the DCM2 concentration increases from 0 to 2000 ppm. The changing path passes through the pure white light region, $(0.33 \pm 0.03, 0.33 \pm 0.03)$, indicating that pure white light can be obtained from these device systems if they are of proper composition. For example, the lower and upper limits are 300 and 1200 ppm, respectively, to emit white light, while only 500–600 ppm of red-dopant DCM2 can be presented to emit pure white light with emission between $(0.330, 0.322)$ and $(0.346, 0.343)$.

The maximum power efficiency, which is defined as the value obtained at a luminance of $\geqq 10$ cd/m^2, increases from 1.3 to 8.3 lm/W as the DCM2 concentration increases from 0 to 2000 ppm for devices A to H. Pure white emission of $(0.346, 0.343)$ with a power efficiency of 6.5 lm/W (9.6 cd/A) at 12 cd/m^2 is obtained by doping with 600 ppm of DCM2 (device E). A much higher power efficiency, 7.5 lm/W (10.8 cd/A) at 11 cd/m^2, is obtained by

Table 1
The effects of doping-concentration of the various light-emitting dopants on the luminous characteristics of the fluorescent WOLEDs having a single emission layer composing of the blue host of BANE doped with trace amounts of the 'red' dye of DCM2 and/or the green dye of C545T

No.	DCM2 (%)	C545T (%)	Max. luminance (cd/m^2)	Maximum power/current efficiency [a]		CIE1931 (x, y) chromatic coordinates at	
				(lm/W)	(cd/A)	100 cd/m^2	10,000 cd/m^2
A	–	–	6500	1.3	3.6	(0.155, 0.122)	–
B	0.01	–	9900	2.1	3.3	(0.192, 0.162)	(0.198, 0.169)
C	0.03	–	15,800	5.0	7.3	(0.280, 0.269)	(0.276, 0.263)
D	0.05	–	16,900	5.5	7.6	(0.330, 0.322)	(0.328, 0.317)
E	0.06	–	19,600	6.5	9.6	(0.346, 0.343)	(0.341, 0.337)
F	0.08	–	24,700	6.5	9.7	(0.382, 0.381)	(0.380, 0.380)
G	0.12	–	39,500	7.5	10.8	(0.423, 0.426)	(0.418, 0.420)
H	0.20	–	41,500	8.3	13.4	(0.464, 0.457)	(0.455, 0.452)
I	0.50	–	39,300	7.6	12.1	(0.479, 0.471)	(0.469, 0.466)
J	1.00	–	38,900	7.3	11.6	(0.485, 0.472)	(0.477, 0.469)
K	2.00	–	29,500	7.2	11.4	(0.505, 0.467)	(0.498, 0.467)
L	0.05	0.02	23,200	5.7	8.1	(0.320, 0.347)	(0.316, 0.342)
M	0.05	0.04	24,200	6.5	9.3	(0.325, 0.374)	(0.320, 0.370)
N	0.05	0.06	25,300	6.7	9.9	(0.324, 0.395)	(0.317, 0.389)
O	0.05	0.08	23,000	6.9	10.7	(0.316, 0.411)	(0.305, 0.401)
P	0.05	0.12	22,500	7.2	11.3	(0.321, 0.439)	(0.312, 0.432)

[a] The maximum power/current efficiency is defined as the value obtained at a luminance of $\geqq$10 cd/m^2.

raising DCM2 to 1200 ppm (device G). However, the corresponding color is not pure white, but is within the generally defined white emission region with CIE coordinates of (0.423, 0.426). These two devices exhibit the highest power efficiency of all reported two-spectrum fluorescent WOLEDs.

The power efficiency, however, decreases from 8.3 to 7.2 lm/W as the DCM2 concentration increases from 0.2% to 2% for devices H to K. This decreasing phenomenon may be attributed to the increasing formation of guest molecule aggregates [23] and low luminescent-efficiency excimers [24] at higher doping-concentrations. The combined effect of these two mechanisms would result in a lower luminous efficiency, which is typically known as concentration-quenching [25]. Moreover, carrier trapping frequently exists in the EL process of dye doped systems [26,27]. It would be more likely to occur when the doping-concentration is higher. This mechanism may also be taken into account for the aforementioned efficiency-decreasing phenomenon.

The chromaticity of emission from all resulting two-spectrum WOLEDs (devices C, D, E, F and G) changes slightly between 100 and 10,000 cd/m^2. The emission coordinates of the device E, for example, are (0.346, 0.343) at 100 cd/m^2 and (0.341, 0.337) at 10,000 cd/cm^2, respectively. The chromatic variation is as small as (0.005, 0.006), which is the least ever reported for pure white OLEDs. The chromaticity of all other devices varied less. Of these, device F, which contains 800 ppm DCM2 emits white light (0.382, 0.381), exhibits the least variation of (0.002, 0.001).

Three reasons may explain the relatively high color-stability of the WOLEDs. Importantly, the devices simply compose one emission layer [12,15,16]. The entering electrons/holes can be effectively confined and so recombine within the desired emission layer owing to the presence of two neighboring electron-blocking and hole-blocking layers. The recombination zone will hence barely shift as the applied voltage increases. Second, the guest molecules are uniformly dispersed throughout the entire thickness in the emission layer by employing the solution-mixing method in the preparation of the vapor-deposited target. A zone shift caused by applied-voltage-variation occurs mostly within the confined emission layer, explaining why the resulting colors are quite the same. Third, all the resulted WOLEDs employed comparatively low doping-concentrations. Less exciton quenching would have occurred and much less color variation was then observed as the current density increased [26].

Fig. 3 shows the effect of C545T concentration on the electroluminescence spectrum of the resultant three-spectrum WOLEDs. The spectra show three emission peaks at 450 nm from the blue host of BANE, at 495 nm from the green dopant of

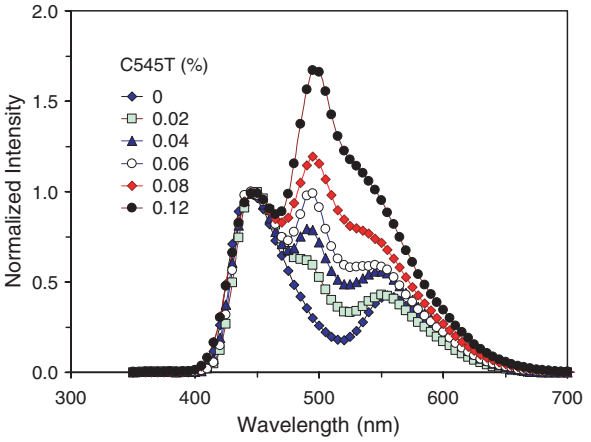

Fig. 3. Doping-concentration effects of the green dye of C545T on the electro-luminescence spectra of the three-spectrum WOLEDs.

C545T and at 560 nm from the red dopant of DCM2. The emission changes from a pure white light of (0.330, 0.322) to the upper boundary of white light with an emission of (0.324, 0.395) as the C545T concentration is increased from 0 to 600 ppm. Increasing the C545T concentration to 1200 ppm causes the emission to turn to green with chromatic coordinates of (0.321, 0.439).

The maximum power efficiency increases from 5.5 lm/W (7.6 cd/A) to 7.2 lm/W (11.3 cd/A) as the C545T concentration is increased from 0 to 1200 ppm. Device L, which contains 200 ppm of C545T, emits pure white light with a maximum power efficiency of 5.7 lm/W (8.1 cd/A) at 13 cd/m^2. A much higher power efficiency, 6.7 lm/W (9.9 cd/A) at 15 cd/m^2, is obtained by increasing the doping C545T to 600 ppm (device N). The corresponding emission remains white but no longer pure white. All the resulting three-spectrum WOLEDs exhibit very little change in color between 100 and 10,000 cd/m^2. For example, for devices L and N, the corresponding chromatic coordinates change from (0.320, 0.347) to (0.316, 0.342) and from (0.325, 0.374) to (0.320, 0.370), respectively. The corresponding chromatic variations are (0.004, 0.005) and (0.005, 0.004), respectively. The largest chromatic variation observed herein is (0.007, 0.006), i.e., smaller than those of all previously reported three-spectrum WOLEDs.

White emission can be obtained in both the two- and three-spectrum OLEDs. Taking the two-wavelength OLEDs for examples, the white emission is resulted from the mixing of the red, or more correctly orange, emission from the red dye and the blue emission from the blue light-emitting host. The concentration of DCM2 is so low that the coming carriers of hole and electron must have mostly gone through and recombined on the host molecules. The excited energy upon recombination has apparently transferred at least partly from the host to the guest of DCM2 to yield the observed orange emission, according to Förster energy transfer mechanism [28]. And, part of the excited energy is used to trigger its own blue emission as evidenced by the blue emission peak at 450 nm shown in Fig. 3. Similarly, the doping-concentration of green dye C545T is also very low and its green emission is triggered by the excited energy transferred from the host molecules via the same mechanism.

Fig. 4 shows the effect of host materials on the resultant luminous characteristics. The power efficiency is 6.7 lm/W at 0.05 mA/cm^2 for the BANE host, while 5.5 lm/W at 0.18 mA/cm^2 for the DPVBi host. Their respective CIE chromatic coordinates at 100 cd/m^2 are (0.330, 0.322) and (0.337, 0.349). The devices with these two different hosts yield almost, but not exactly, the same pure white emission. The minor difference is attributable to the difference between the colors originally emitted by the hosts, themselves. Pure BANE has chromatic coordinates of (0.155, 0.122) and pure DPVBi has ones of (0.170, 0.165). BANE is a host with a deeper blue color than DPVBi, so BANE is a more appropriate host for the 'red' dye, DCM2, to generate a pure white light.

Fig. 5 shows the photoluminescence spectra of the host molecules of BANE and DPVBi and the UV–VIS absorption spectra of the guest molecules

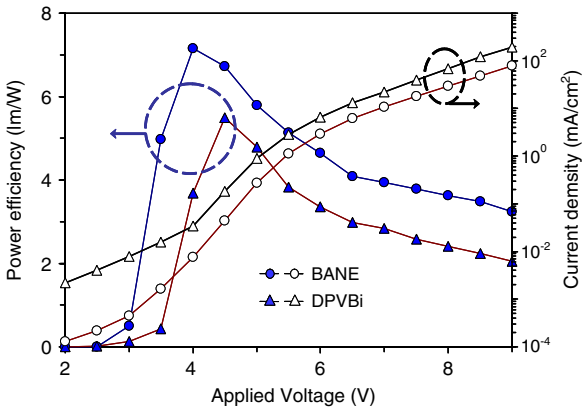

Fig. 4. The effects of the different hosts of BANE and DPVBi on the resulting power efficiency, current density of the WOLEDs using the two different hosts.

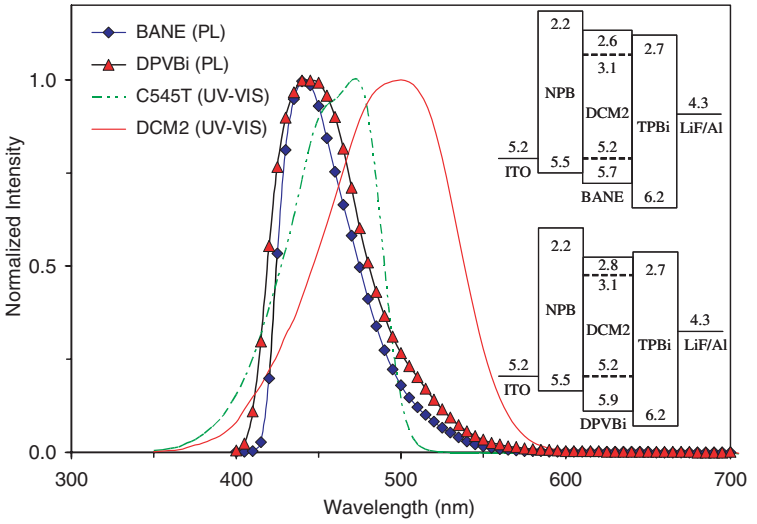

Fig. 5. The photoluminescence spectra of the host molecules of BANE and DPVBi, ultraviolet–visible absorption spectra of the guest molecules of DCM2 and C545T, and HOMO/LUMO energy-level alignments (inset) of the WOLEDs using the two different hosts.

of DCM2 and C545T. The spectral peak from the BANE host ranges from 415 to 580 nm, and that of DPVBi host ranges from 405 to 590 nm. The absorption peak of red-dopant DCM2 ranges from 380 to 585 nm, and that of green-dopant C545T from 370 to 515 nm. The photoluminescence spectra of both hosts overlap greatly with the UV–VIS absorption spectra of the two guest molecules, revealing the likeliness of high-efficiency energy-transfer [17]. Although the overlapping area of the host DPVBi is larger than that of the host BANE, the resulting efficiency is slightly lower than that of the BANE counterpart, revealing that other factors influence the overall efficiency of the device, as described below.

The electrons are initially injected from the cathode into the electron-transporting layer of TPBi, as shown by the energy-level alignment of the resultant device structure in the inset in Fig. 5. The LUMO of TPBi is 2.7 eV, and that of the emitting layer of BANE is 2.6 eV. An energy barrier of 0.1 eV must be overcome to transport the electrons from the TPBi layer into the BANE host. The LUMO of the other host, DPVBi, is 2.8 eV. The energy barrier is −0.1 eV, revealing that no barrier exists for the electrons to enter the host of DPVBi. These facts explain why the exhibited current density is obviously markedly higher for the device employing the DPVBi host (Fig. 4). Although possessing better electron-transporting characteristics, the device with a DPVBi host does not have a correspondingly higher luminous efficiency. This finding suggests yet another crucial factor affecting the resultant efficiency.

Also shown in the insert of Fig. 5, the holes are initially injected from the anode to the hole-transporting layer of NPB. The HOMO of NPB is 5.5 eV, while that of the BANE host is 5.7 eV. The energy barrier to the transport of holes from the NPB layer into the BANE host is 0.2 eV, whereas the barrier to entering the DPVBi host is 0.4 eV. Clearly, the holes can more easily enter the BANE host. Additionally, the energy barrier to the further transport of holes from the BANE host to the next layer, TPBi (HOMO = 6.2 eV), is 0.5 eV, whereas the barrier to transport from the DPVBi host is 0.3 eV. The higher energy barrier, 0.5 eV, would subsequently make it more difficult for the holes to leave the BANE host. More holes are then confined in the BANE host, increasing the electron-hole recombination probability and the luminous efficiency. These results explain why WOLEDs with a BANE host have a higher luminous efficiency.

Both energy transfer and carrier trapping exist simultaneously in the emission process [26,27]. The occurrence of carrier trapping on the dopants would reduce the total efficiency. Nevertheless, the above WOLEDs that employ BANE and DPVBi hosts both exhibit relatively high efficiency. This may be attributed to the comparatively low doping concentration used for the red dye of DCM2 since the occurrence of carrier trapping would be less [27].

Fig. 6 shows the effect of the electron-transporting material on the luminous characteristics. The

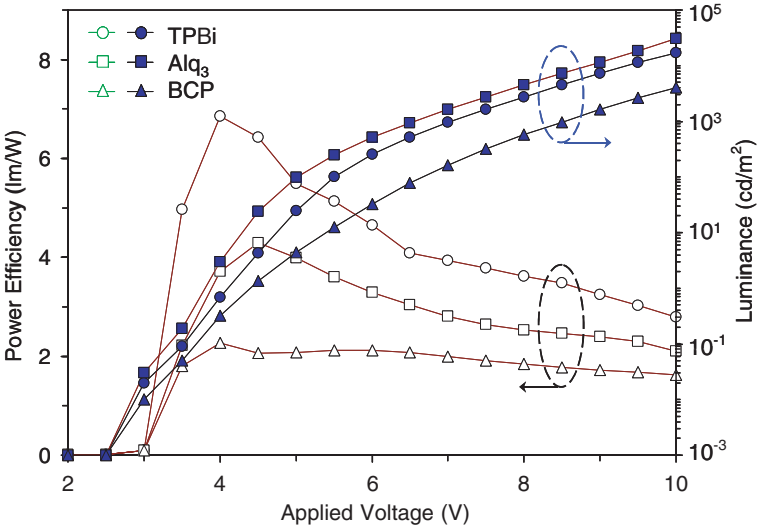

Fig. 6. The effects of the different electron-transporting materials of TPBi, BCP and Alq_3 on the resulting power efficiency and luminance of the two-spectrum WOLEDs.

maximum power efficiencies of WOLEDs with the electron-transporting layers of TPBi, Alq_3 and BCP are 6.8, 4.3 and 2.5 lm/W, respectively. Their corresponding luminances are 16,900, 30,700 and 4000 cd/m^2 at 10 V. The energy barrier to the transport of electrons from TPBi to the same BANE host is 0.1 eV, while the barrier to transport from Alq_3 (LUMO = 3.0 eV) is 0.4 eV and that from BCP is 0.6 eV (LUMO = 3.2 eV) as shown in Fig. 7. Consequently, the devices with a TPBi electron-transporting layer have the highest efficiency for having the lowest electron-injection barrier. Although BCP provides the best hole-blocking function, its huge electron-injection barrier, however, strongly hinders the entry of electrons into the emitting host.

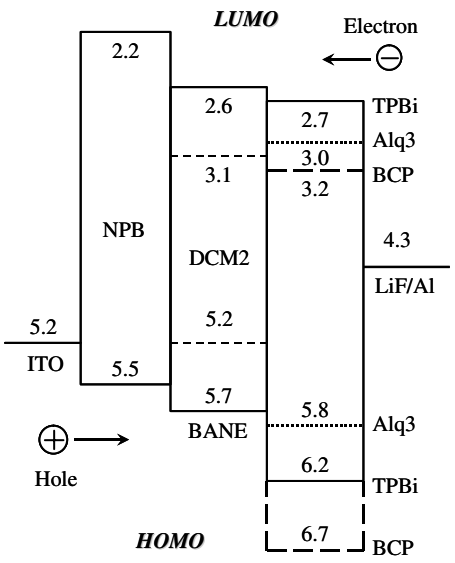

Fig. 7. The HOMO/LUMO energy-level alignment of the two-spectrum WOLEDs with the three different electron-transporting materials of TPBi, BCP and Alq_3.

The device using Alq_3 has yielded a poor efficiency for having as well a high electron-injection barrier. Nevertheless, its brightness is the greatest among all these devices. This may be attributed to its poorest hole-blocking effect that the unrecombined holes can easily enter the green light-emitting Alq_3 layer to recombine with the electrons injected from the cathode, substantially increasing the brightness, but changing the color to an undesired green.

4. Conclusion

In conclusion, we have presented the fabrication of efficient, color-stable, two- and three-spectrum white and pure white fluorescent organic light-emitting diodes with an effective exciton-confining device architecture with a single emission layer by vapor-deposition of the solution-mixed deposition targets of an efficient blue host of BANE doped with the red dye of DCM2 and/or green dye of C545T. The best power efficiency of the resulting two-spectrum fluorescent WOLEDs is as high as 7.5 lm/W (10.8 cd/A) at 11 cd/m^2 with chromatic

coordinates of (0.423, 0.426), or 6.5 lm/W (9.6 cd/A) at 12 cd/m^2 with a pure white light of (0.346, 0.343). The best power efficiency of the three-spectrum counterparts is 6.7 lm/W (9.9 cd/A) at 15 cd/m^2 with a nearly pure white light of (0.325, 0.374). All color variations are less than (0.007, 0.006) between 100 and 10,000 cd/m^2.

Acknowledgements

The authors thank the University System of Taiwan and National Science Council for their financially supporting in part this research under Grant nos. 92J0162J4 and NSC93-2216-E-007-018, respectively.

References

[1] Z. Shen, P.E. Burrows, V. Bulović, S.R. Forrest, M.E. Thompson, Science 276 (1997) 2009.
[2] S.R. Forrest, Org. Electron. 4 (2003) 45.
[3] A.R. Duggal, J.J. Shiang, C.M. Heller, D.F. Foust, Appl. Phys. Lett. 80 (2002) 3470.
[4] B.W. D'Andrade, S.R. Forrest, Adv. Mater. 16 (2004) 1585.
[5] O. Prache, Displays 22 (2001) 49.
[6] J.Y. Lee, J.H. Kwon, H.K. Chung, Org. Electron. 4 (2003) 143.
[7] M. Ricks, M. Boroson, J. Ludwicki, A. Arnold, Society for Information Display 2005, Boston, USA, 2005, p. 826.
[8] B.W. D'Andrade, M.E. Thompson, S.R. Forrest, Adv. Mater. 14 (2002) 147.
[9] S. Tokito, T. Iijima, T. Tsuzuki, F. Sato, Appl. Phys. Lett. 83 (2003) 2459.
[10] B.W. D'Andrade, R.J. Holmes, S.R. Forrest, Adv. Mater. 16 (2004) 624.
[11] Y.S. Huang, J.H. Jou, W.K. Weng, J.M. Liu, Appl. Phys. Lett. 80 (2002) 2782.
[12] C.H. Chuen, Y.T. Tao, F.I. Wu, C.F. Shu, Appl. Phys. Lett. 85 (2004) 4609.
[13] G. Li, J. Shinar, Appl. Phys. Lett. 83 (2003) 5359.
[14] R.S. Deshpande, V. Bulović, S.R. Forrest, Appl. Phys. Lett. 75 (1999) 888.
[15] C.H. Chuen, Y.T. Tao, Appl. Phys. Lett. 81 (2002) 4499.
[16] Y. Shao, Y. Yang, Appl. Phys. Lett. 86 (2005) 073510.
[17] M. Pope, C.E. Swenberg, Electronic Process in Organic Crystals and Polymers, second ed., Oxford University Press, New York, 1999.
[18] V.I. Adamovich, S.R. Cordero, P.I. Djurovich, A. Tamayo, M.E. Thompson, B.W. D'Andrade, S.R. Forrest, Organic Electron. 4 (2003) 45.
[19] R.C. Kwong, S. Lamansky, M.E. Thompson, Adv. Mater. 12 (2000) 1134.
[20] M. Ikai, S. Tokito, Y. Sakamoto, T. Suzuki, Y. Taga, Appl. Phys. Lett. 79 (2001) 156.
[21] J.H. Jou, Y.S. Chiu, C.P. Wang, R.Y. Wang, H.C. Hu, Efficient, color-stable fluorescent white organic light-emitting diodes with single emission layer by vapor-deposition from solvent premixed deposition targets, submitted for publication.
[22] S. Janietz, D.D.C. Bradley, M. Grell, C. Giebeler, M. Inbasekaran, E.P. Woo, Appl. Phys. Lett. 73 (1998) 2453.
[23] V. Bulović, R.S. Deshpande, M.E. Thompson, S.R. Forrest, Chem. Phys. Lett. 308 (1999) 317.
[24] V. Bulović, A. Shoustikov, M.A. Baldo, E. Bose, V.G. Kozlov, M.E. Thompson, S.R. Forrest, Chem. Phys. Lett. 287 (1998) 455.
[25] C.W. Tang, S.A. VanSlyke, C.H. Chen, J. Appl. Phys. 65 (1989) 3610.
[26] Y.T. Tao, C.W. Ko, E. Balasubramaniam, Thin Solid Films 417 (2002) 61.
[27] F. Nüesch, D. Berner, E. Tutiš, M. Schaer, C. Ma, X. Wang, B. Zhang, L. Zuppiroli, Adv. Funct. Mater. 15 (2005) 323.
[28] T. Förster, Ann. Phys. 6 (1948) 55.

Available online at www.sciencedirect.com
SCIENCE DIRECT®
Organic Electronics 7 (2006) 16–21
Organic Electronics
www.elsevier.com/locate/orgel

Gate induced leakage and drain current offset in organic thin film transistors

Huiping Jia, Gaurang K. Pant, Erich K. Gross, Robert M. Wallace, Bruce E. Gnade *

Department of Electrical Engineering, University of Texas at Dallas, Richardson, P.O. Box 830688 EC33, TX 75083, USA

Received 29 July 2005; received in revised form 21 October 2005; accepted 25 October 2005
Available online 28 November 2005

Abstract

Gate bias induced leakage current and drain current offset limit device performance in poly 3-hexylthiophene (P3HT) organic thin film transistors (OTFTs). The drain current offset distorts the drain current in the linear region of the transistor performance curve, making it difficult to extract device parameters. A higher drain current offset corresponds to higher leakage current, which contributes to poor drain current modulation. The drain current offset increases when the semiconductor doping density is higher or when the P3HT film is thicker. We propose that the most probable mechanism for the leakage and drain current offset is uncontrolled expansion of drain/source electrodes. Based on the proposed mechanisms, the drain current offset is dramatically reduced by patterning the active region to reduce non-channel leakage.

PACS: 73.61.Ph; 85.30.Tv

Keywords: Organic thin film transistor; Gate induced leakage; Drain current offset; Organic thin film patterning

1. Introduction

The first OTFT was made in 1983 by Ebisawa et al., even though organic semiconductors have been studied for more than 50 years [1,2]. Twenty years later, many researchers in both industry and academia are engaged in the research and development of OTFTs, because of the potential of low cost applications such as large area displays, disposable electronics, flexible electronics, etc. [3]. The performance of OTFTs has improved to the point where they are now comparable with amorphous-silicon thin film transistors [4–6]. Many fundamental issues need to be understood before commercial applications come to market. In this paper we examine the drain current offset (I_D offset) problem which is seen particularly in polymer-based OTFTs. I_D offset is defined as the drain current at different gate biases, when the drain–source bias (V_{DS}) is zero. Ideally when $V_{DS} = 0$ V, $I_D = 0$ A. In contrast, significant I_D offset is common in organic thin film transistors [7,8].

The I_D offset distorts the drain current response in the linear region of the transistor performance curve,

* Corresponding author. Tel.: +1 972 883 6636.
E-mail address: gnade@utdallas.edu (B.E. Gnade).

1566-1199/$ - see front matter
doi:10.1016/j.orgel.2005.10.003

making it difficult to evaluate the device characteristics and impossible for proper device performance in the linear region. The drain current offset leads to high leakage current, which in turn contributes to poor drain current modulation. We studied the possible sources of I_D offset experimentally, and propose possible mechanisms for the leakage current based on our experimental results. We have demonstrated that I_D offset is reduced by using a thinner active layer, lowering oxygen doping in the semiconductor by annealing, and by patterning the active layer.

2. Experimental details

The material for the active layer is the solution processable organic semiconductor poly 3-hexylthiophene (P3HT), which is purchased from Aldrich. The P3HT was used as-received. CMOS grade toluene (JT Baker) and HPLC grade chloroform (Aldrich) were used as the solvents for P3HT. A bottom contact configuration for the OTFTs was used in this work (Fig. 1). Highly doped (n or p-type, resistivity 0.01–0.02 Ω cm) silicon wafers with 100 nm thick thermal SiO_2 were used as the substrate. The back side of the wafer was etched with buffered oxide etchant (BOE) (JT Baker) and a gold layer of about 200 nm, deposited by either e-beam evaporation or sputtering, was used as the gate contact. Gold drain/source contacts were patterned by lift-off on the SiO_2 dielectric layer. The drain/source contacts have a thickness of 100 nm with a 3 nm chromium or titanium adhesion layer, deposited using the same method as the gate contact. The P3HT film was deposited by spin-coating the solution at 2000 rpm for 60 s. Prior to the P3HT solution coating, the substrates were cleaned using either O_2 plasma or UV O_3, followed by hexamethyldisilizane (HMDS) treatment. The deposited films were heated at 95 °C in an air oven for 1 h to remove the solvent. To pattern the P3HT film, a parylene capping layer 1 μm thick was evaporated over the P3HT layer, followed by photolithographic patterning and reactive ion etching (RIE) in an O_2 plasma etcher to remove the parylene and P3HT, except in the channel region. The etching time is approximately 7 min at 50 W and 200 mTorr. Thermal annealing of the OTFTs was done in vacuum at 90 °C and 5×10^{-5} Torr for 10 h. All data shown are for un-patterned and un-annealed samples unless specified. A Keithley 4200-SCS Semiconductor Characterization System was used to probe the devices, unless otherwise mentioned. The probe station is a Cascade Microtech Model Summit Microchamber with flowing N_2. All measurements were done at room temperature.

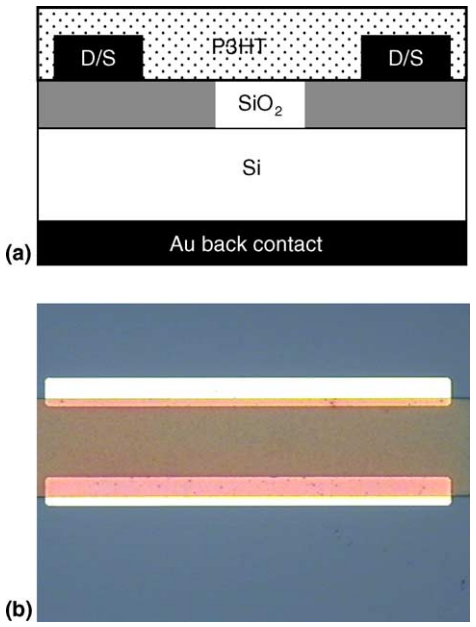

Fig. 1. The configuration of the P3HT OTFTs: (a) schematic view of the P3HT OTFTs, (b) a photograph (top view) of a P3HT patterned OTFT with P3HT in the channel area only.

3. Results and discussion

3.1. I_D offset and leakage

Fig. 2(a) shows the I–V characteristics of our standard P3HT device. The P3HT film is approximately 70 nm thick and was not patterned for these devices. The distortion of the I–V curves in the linear region because of the I_D offset can be clearly seen. The gate induced leakage (i.e. the gate current) (I_G) increases with gate bias and is much higher at lower V_{DS} and peaks at $V_{DS} = 0$ V (Fig. 2(b)). A plot of source current (I_S), drain current (I_D), and gate current (I_G) in Fig. 2(c) shows that at $V_{DS} = 0$ V, I_S and I_D are nearly equivalent and I_G is approximately twice as large as I_S or I_D. These results suggest that the I_D offset is closely related to I_G, and is a convenient indicator of gate induced leakage (I_G) in OTFTs.

3.2. Sources of I_D offset

In order to understand the origin of I_D offset, we consider the possibility of process related sources.

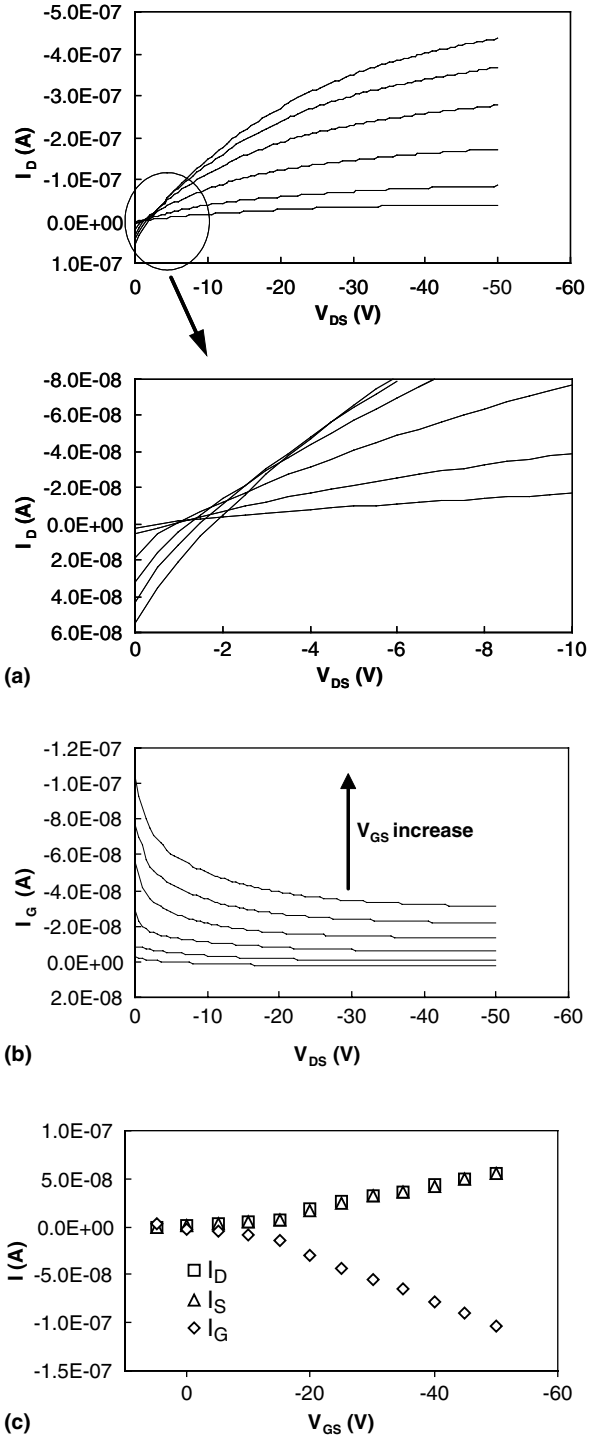

Fig. 2. The leakage current and I_D offset in a P3HT device. The data were obtained from an Agilent 4156B semiconductor parameter analyzer: (a) I–V curve and I_D offset, $W/L = 150/10$ μm, $V_{GS} = -5$ to -40 V, step $= -5$ V, (b) I_G changes with V_{GS} of the same device as in (a), and (c) I_S, I_D and I_G at $V_{DS} = 0$ V of the same device as in (a).

I_D offset exists in P3HT devices made from different solvents and different grades of solvents (HPLC chloroform and CMOS toluene for example), as well as for different batches of P3HT, indicating that I_D offset is not a function of the starting materials.

We also considered that the leakage current might be due to degradation of the gate dielectric caused by contamination from either the organic semiconductor or the solvents. To test this we removed the P3HT film from the devices by dissolving the organic film in chloroform and examined the I_D offset with no P3HT. The I_D offset after P3HT removal is the same as for samples that have never been exposed to the P3HT process. The SiO_2 dielectric layer remains intact. This result agrees with similar experiments of the leakage current observed in P3HT capacitors reported by Raja et al. [9].

I_D offset changes with the thickness of the P3HT films in OTFTs. Films of different thicknesses were made by changing the solution concentrations of P3HT for spin-coating. Higher concentrations result in thicker films for the same spin-coating conditions. As shown in Fig. 3, I_D offset increases when the P3HT film becomes thicker and does not change significantly below a thickness of about 4 nm, which is approximately two monolayers of P3HT [10,11]. The drain current of the transistors changes in a similar manner to that observed for I_D offset. Thicker films yield higher drain current at the same V_{GS} and V_{DS} because the channel conductance of the OTFTs is higher.

Additionally, we found that I_D offset after thermal annealing was reduced by >100× (Fig. 4). It is believed that P3HT films are de-doped during thermal annealing [12]. This de-doping can be clearly seen from the decreased drain current in Fig. 4. The drain current and the accumulation layer

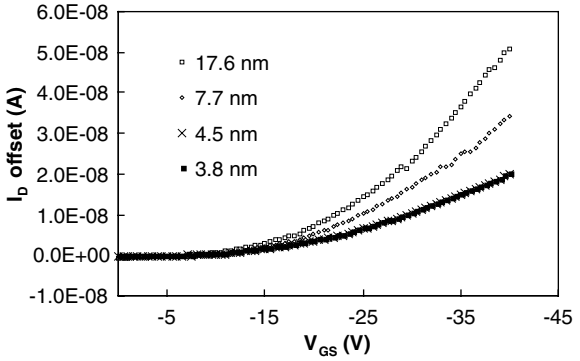

Fig. 3. I_D offset changes with P3HT film thicknesses, $W/L = 150/80$ μm.

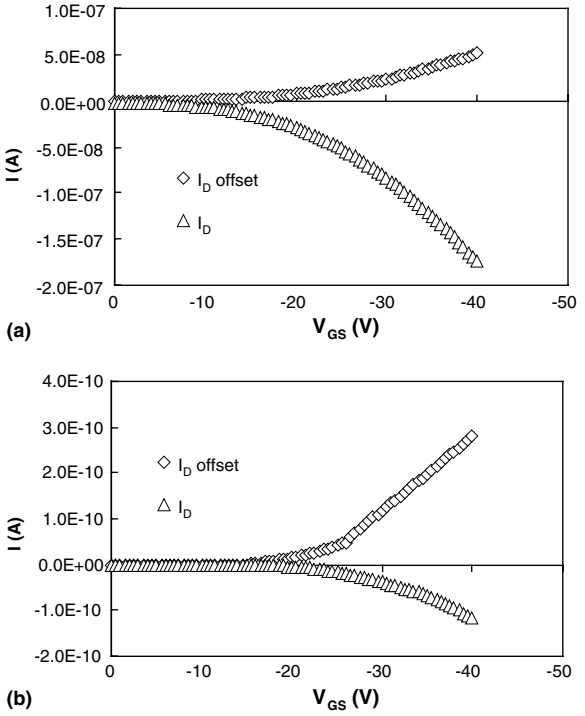

Fig. 4. Thermal annealing effect on I_D offset, $W/L = 150/80$ μm, $V_{DS} = -40$ V: (a) before thermal annealing, and (b) after thermal annealing in vacuum at 90 °C and 5×10^{-5} Torr for 10 h.

conductance, as a result, decreased by 1000×. This is further evidence that the P3HT film conductance impacts the I_D offset in agreement with the P3HT thickness measurements. Similar results were found by Raja et al., where the leakage current in Al_2O_3/P3HT capacitors increases with increased dopant concentration in P3HT films [9].

Finally, we studied the effect of patterning the P3HT on I_D offset. The leakage current through the SiO_2 dielectric is small (current density is 10^{-9} A/cm^2 at 40 V bias) when the only conduction path is from the source/drain contact through the SiO_2 to the back gate (Fig. 1(a)). While the leakage current density is small, when the P3HT is uniformly deposited, the semiconductor has the effect of enlarging the source/drain contacts. Since a common gate (the Si wafer) is used, when the gate bias is higher than the threshold voltage, there will be a hole accumulation layer covering the whole sample surface and making contacts with all of the drain/source contacts. Therefore, when the OTFTs are turned on, it is likely that the hole accumulation layer serves as an expansion of the drain/source contact electrodes. This is part of the source of the increased I_D offset after spin-coating the P3HT film. In addition, the higher the conductance of the conducting accumulation layer, the more the effective area of drain/source electrodes will expand and the higher the I_D offset will be, as we observed. After the OTFTs are on, the conductance of the hole accumulation layer of the P3HT film is controlled, as discussed previously, by the thickness and doping of the film. The thicker the film or the higher the doping density, the higher the conductance will be. As a result, the I_D offset is higher because of the larger expanded drain/source electrodes.

3.3. I_D offset reduction

As suggested in Section 3.2 the largest source of I_D offset is the expansion of the drain/source electrode. To reduce I_D offset it is necessary to eliminate the drain/source electrode expansion by confining the P3HT semiconductor layer within the active region. The P3HT film is lithographically patterned so the P3HT is only present in the channel area (Fig. 1(b)).

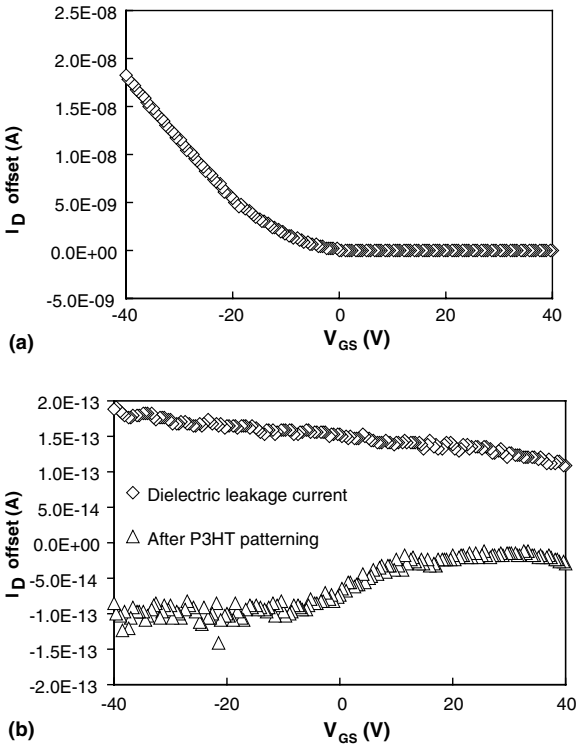

Fig. 5. I_D offset of P3HT OTFTs after patterning, $W/L = 500/5$ μm: (a) I_D offset before P3HT film patterning, and (b) comparable leakage current through the SiO_2 dielectric with no P3HT present and with patterned P3HT.

The I_D offsets of patterned and un-patterned P3HT OTFTs are shown in Fig. 5. The I_D offset of OTFTs after pattering reduced dramatically from 10^{-8} A (Fig. 5(a)) to 10^{-13} A (Fig. 5(b)). This reduced I_D offset is comparable to the leakage current through the SiO_2 dielectric only (Fig. 5(b)). Patterning the P3HT film effectively eliminated the I_D offset, eliminating the distortion of the linear region of the I–V curves (Fig. 6). The electrical characteristics of the patterned P3HT device represented in Fig. 6 show a p-channel OTFT with low gate induced leakage current. While the I_D offset is reduced significantly, the drive current for the transistor is comparable to the unpatterned devices.

While we suggest the drain/source electrode expansion as the major source of I_D offset, we cannot rule out other possible sources such as ion migration through the P3HT film as suggested by Raja et al. [9]. Lloyd et al. measured the leakage current of SiO_2/P3HT capacitors. In their results, the leakage current of the capacitor made from P3HT fractionated by solvent extraction is more than 10× higher than the unfractionated [13]. In the work by Kokubo et al., there is no significant difference in I_D offsets for OTFTs made of precipitation purified P3HT and unpurified P3HT, although the purified device has a drain current almost 10× higher than the unpurified material [14]. We are currently studying these potential sources of I_D offset.

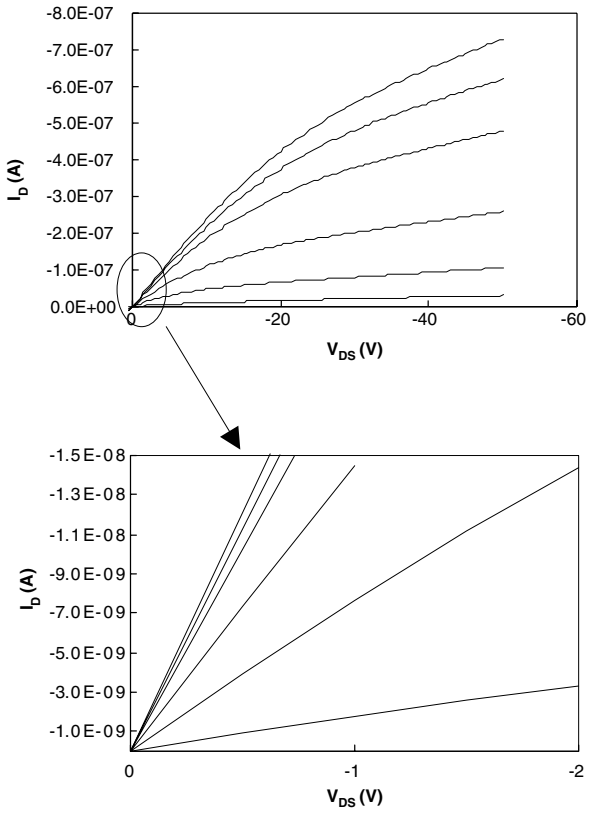

Fig. 6. I–V curves of a P3HT OTFT after patterning, $W/L = 500/5$ μm, $V_{GS} = 0$ to -50 V, step $= -10$ V.

4. Conclusion

In this paper, we studied the I_D offset in OTFTs with a bottom contact configuration. I_D offset is closely related to gate leakage and can be used to monitor the leakage of OTFTs. I_D offset changes with film thickness and doping density of P3HT films. Thicker films and higher doping densities result in higher I_D offset. We suggest that the major source of I_D offset is the effective expansion of drain/source electrodes from the conducting accumulation layer when unpatterned OTFTs are on. By patterning the P3HT film, I_D offset in OTFTs can be reduced to levels comparable to the leakage current of the SiO_2 dielectric. Patterning the P3HT film and limiting the film to the channel area eliminates a large source of I_D offset.

Acknowledgements

The authors would like to thank Dr. Isaac Trachtenberg for helpful discussions. This work was supported in part by the US Army Soldier Systems Center through contract numbers DAAD-16-00-9732 and DAAD-16-01-C-0026.

References

[1] F. Ebisawa, T. Kurokawa, S. Nara, J. Appl. Phys. 54 (1983) 3255.
[2] M. Pope, C.E. Swenberg, Electronic Processes in Organic Crystals and Polymers, second ed., Oxford University Press, New York, 1999.
[3] A. Dodabalapur, C. Dimitrakopoulos, Final Report for the National Science Foundation Workshop, January 16–17, Arlington, VA, 2003. Available online: <http://www.mrc.utexas.edu/NSFworkshop/finalreport.pdf>.
[4] C.D. Dimitrakopoulos, D.J. Mascaro, IBM J. Res. Dev. 45 (2001) 11.
[5] A.R. Brown, D.M. De Leeuw, M. Matters, C.P. Jarrett, Synth. Met. 88 (1997) 37.
[6] A. Lodha, R. Singh, IEEE Trans. Semiconduct. Manufact. 14 (2001) 281.
[7] W. Geens, S.E. Shaheen, B. Wessling, C.J. Brabec, J. Poortmans, N.S. Sariciftci, Org. Electron. 3 (2002) 105.
[8] S.H. Kim, Y.S. Yang, J.H. Lee, J.-I. Lee, H.Y. Chu, H. Lee, J. Oh, L.-M. Do, T. Zyung, Opt. Mater. 21 (2002) 439.

[9] M. Raja, G. Lloyd, N. Seghi, S.J. Higgins, W. Eccleston, Mater. Res. Soc. Symp. Proc. 725 (2002) P6.5.1.
[10] W. Luzny, M. Trznadel, A. Pron, Synth. Met. 81 (1996) 71.
[11] H.G.O. Sandberg, G.L. Frey, M.N. Shkunov, H. Sirringhaus, R.H. Friend, M. Meedom Nielsen, C. Kumpf, Langmuir 18 (2002) 10176.
[12] R.H.M. van de Leur, B. de Ruiter, J. Breen, Synth. Met. 54 (1993) 203.
[13] G. Lloyd, M. Raja, I. Sellers, N. Sedghi, R.D. Lucrezia, S. Higgins, B. Eccleston, Microelectron. Eng. 59 (2001) 323.
[14] H. Kokubo, T. Yamamoto, H. Kondo, Y. Akiyama, I. Fujimura, Jpn. J. Appl. Phys. 42 (Part 1, No. 10) (2003) 6627.

Available online at www.sciencedirect.com
SCIENCE DIRECT®
Organic Electronics 7 (2006) 22–28
Organic Electronics
www.elsevier.com/locate/orgel

Photolithographic patterning of organic electronic materials

John A. DeFranco [a], Bradley S. Schmidt [b], Michal Lipson [b], George G. Malliaras [a,*]

[a] Department of Materials Science and Engineering, Cornell University, 327 Bard Hall, Ithaca, NY 14853, USA
[b] School of Electrical and Computer Engineering, Cornell University, Ithaca, NY 14853, USA

Received 26 July 2005; received in revised form 22 October 2005; accepted 25 October 2005
Available online 18 November 2005

Abstract

The realization of organic electronic technologies requires the availability of patterning techniques that are compatible with chemically sensitive materials. We demonstrate an approach that allows the photolithographic patterning of organic films without their exposure to harmful solvents, and achieves micrometer resolution. Examples of additive and subtractive patterning of polymers as well as small molecules show this approach to be quite generic. The fabrication of a pentacene transistor with a 2 μm channel length and conducting polymer electrodes is demonstrated.

PACS: 81.16.−c; 85.30.−z

Keywords: Patterning; OTFTs

1. Introduction

The past two decades were characterized by tremendous progress in the performance of organic electronic devices such as light emitting diodes, thin film transistors, and photovoltaic cells [1–3]. The progress has been so remarkable, that the term ''organic electronics'' is now being used to describe the vision of an electronic technology using semiconductors, conductors and dielectrics based on organic materials [4]. A critical step for the realization of organic electronics is the availability of patterning techniques that are compatible with these materials. Although great strides have been achieved in our ability to pattern organics, the techniques used in the mature and entrenched industry of silicon processing have made little impact in this field. This is primarily due to incompatibilities between chemicals used in photolithography and the vast majority of organics. Overcoming these incompatibilities promises a breakthrough in the manufacturing of organic electronics since it would provide for massively parallel output along with process knowledge and equipment already available from a very successful industry. As a first step towards this goal, we report on a generic approach for the photolithographic patterning of organic

* Corresponding author. Tel.: +1 607 2551956; fax: +1 607 2551365.
E-mail addresses: ggm1@cornell.edu, george@ccmr.cornell.edu (G.G. Malliaras).

1566-1199/$ - see front matter © 2005 Elsevier B.V. All rights reserved.
doi:10.1016/j.orgel.2005.10.002

materials with micrometer resolution. We demonstrate the applicability of this approach to the additive and subtractive patterning of conducting polymers, as well as semiconducting small molecules. A pentacene transistor with 2 μm channel length and conducting polymer electrodes is fabricated as a proof-of-concept.

The particular challenge of patterning chemically-sensitive organic materials has stimulated much invention, and numerous approaches have been developed for making patterned structures with small features [5]. Particular attention has been paid in the patterning of semiconductors, used in organic light emitting diodes (OLEDs) and organic thin film transistors (OTFTs). Shadow masking has been the canonical technique for patterning low molecular weight materials, which are usually processed into films using vacuum deposition [6]. A stencil is placed either in contact with, or in close proximity to the substrate, and defines the areas that are coated with a film. Inkjet printing, on the other hand, is the technique of choice for polymeric materials, which are processed into films from solution [7]. It involves a modified inkjet or bubblejet printer that delivers small droplets of polymer solution to selected places on the substrate. Both of these techniques leave a lot to be desired. Large area stencils are hard to fabricate and need to be rigorously maintained to remove material that has been deposited on them. Inkjet printing, on the other hand, requires specially formulated inks and non-standard equipment, and it is a serial (hence low throughput) process. Certain recently developed techniques such as imprint lithography [8,9], microcontact printing [10], and organic vapor jet deposition [11] seem to overcome some of these limitations. Photolithography, however, which is the technique of choice for the patterning of inorganic electronic materials, remains the single most attractive thin film patterning technique to date. This is due to the host of advantages photolithography offers, which include straightforward scaling to large area substrates, availability of a broad basis of equipment and expertise, and the high throughput fabrication associated with its inherently parallel nature.

2. Subtractive patterning approach

In photolithography, the film to be patterned is coated with a polymeric photoresist, which is deposited by spin coating. The photoresist is then exposed to light through a photomask which carries the pattern to be transferred to the film. A developer (typically an alkaline solution) is used to remove the exposed parts in positive photoresists, or the unexposed parts in negative photoresists, replicating the mask pattern (or its reverse) on the photoresist film. Using the remaining photoresist as a contact mask, an etching step is then used to transfer the pattern to the underlying film. The etching can be dry (i.e. reactive ion etching), or wet (i.e. use of suitable solvent), depending on the nature of the film to be etched and the substrate. Finally, the photoresist is stripped off by an appropriate solvent. The incompatibility of organics with conventional lithography arises primarily due to the solvents used for the deposition, the development and the removal of the photoresist. The solvents used in these three steps have, with a few exceptions [12], detrimental

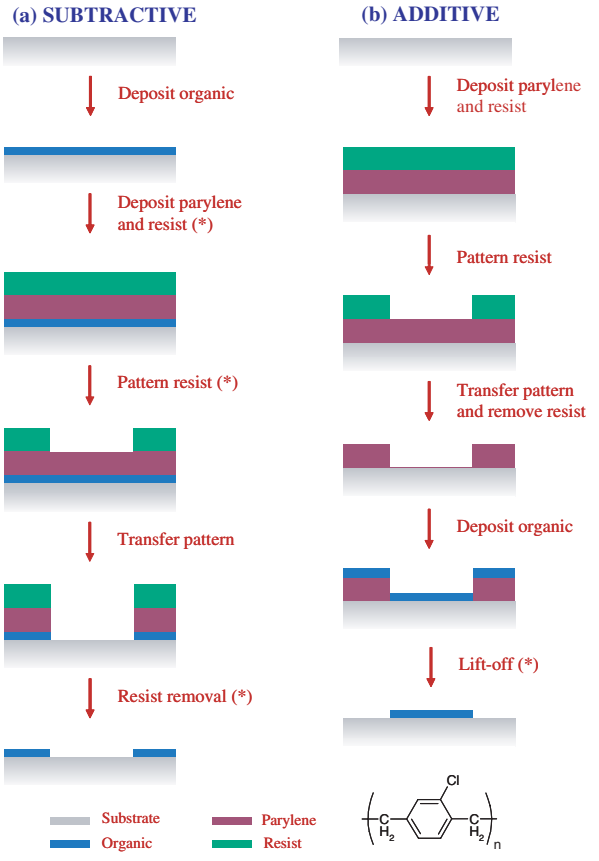

Fig. 1. Subtractive (a) and additive (b) photolithographic patterning approaches for organic films. The asterisks indicate the steps where the organics film would be damaged during conventional photolithography. The chemical structure of parylene-C is shown on the bottom.

effects on organic films, including dissolution, cracking, swelling, and delamination. Although chemical modification of conjugated polymers to include a photoactive element that allows their direct (without using a photoresist) patterning has been recently demonstrated [13], such a solution requires custom chemistry for each material used.

In Fig. 1a, an approach for carrying out the above photolithographic process on organic films is shown (experimental details are given at the end of this section, after the concept is described). The key to this approach is the use of parylene-C [poly (*para*-xylylene), Fig. 1, from now on referred to as parylene], to protect the organic film during the deposition and development of the photoresist, as well as to strip the photoresist in a dry (solvent-free) manner. Parylene is a chemical vapor deposited (CVD) polymer with a number of useful properties that endow it with applications as a barrier layer in electronic circuits and medical devices [14]. It is deposited near room temperature and gives rise to conformal coatings that can be applied on chemically sensitive materials (such as organics) without damaging them. The coatings are pinhole-free for films of sufficient thickness (typically >500 nm thick). Once deposited, parylene films are nearly inert; they resist solvents, strong acids and bases. As a result, conventional photolithography can be carried out on top of these films, as shown in Fig. 1a. Once developed, the photoresist (which is positive tone as indicated in Fig. 1a), serves as a mask for a dry etch step that is used to transfer the pattern to the parylene and the organic film below. In fact, Kymissis et al. have used photolithography to patterned a parylene layer, and selectively etch an underlying pentacene film [15].

In addition, and most importantly, parylene films show relatively weak adhesion to a number of organic films. Their adhesion is good enough for the parylene films to remain securely in place throughout all processing steps indicated in Fig. 1a, including deposition and development of the photoresist, plasma etching, and handling of the sample. Parylene films can, however, be peeled off from a variety of organic films, a process that can be assisted with adhesive tape. Peeling the parylene strips off the photoresist in a solvent free manner and leaves the patterned organic material on the substrate.

The patterning approach shown in Fig. 1a is subtractive and leads to organic films that are the reverse of the photomask when positive tone photoresist is used. Examples of organic films patterned using this approach are shown in Fig. 2. Fig. 2a shows 1 μm wide trenches, separated by 10 μm, etched in the conducting polymer poly(3,4-ethylene dioxythiophene):poly(styrene sulfonic acid)

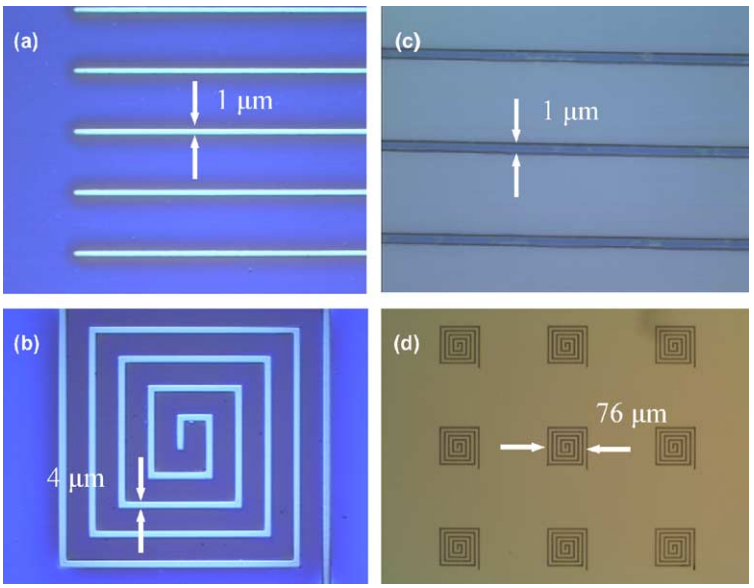

Fig. 2. Optical micrographs showing examples of organic electronic films patterned using the subtractive (a–b) and the additive (c–d) approaches: (a) 1 μm wide trenches etched in the conducting polymer poly(3,4-ethylene dioxythiophene):poly(styrene sulfonic acid) (PEDOT:PSS), (b) spiral shaped trenches in PEDOT:PSS. The width of the trenches is 4 μm, (c) 1 μm wide lines of PEDOT:PSS on a 10 μm pitch, and (d) spiral lines with a 4 μm width made from ruthenium tris-bipyridine, $[Ru(bpy_3)]^{2+}(PF_6^-)_2$.

(PEDOT:PSS). Such trenches can be used, for example, to define the channel in OTFTs [2]. Fig. 2b shows spiral shaped trenches in PEDOT:PSS. The width of the trenches is 4 μm, and the picture shows how well the parylene layer peels, even around tight corners.

The structures in Fig. 2 were fabricated as follows: The organic films were deposited on oxidized silicon wafers by spin coating. The parylene deposition took place in a PDS 2010 chamber from Specialty Coating Systems, in which the substrate was held at room temperature. The parylene layers were 1.5 μm thick. Shipley SPR220 3.0 positive photoresist was spun on the substrate and was baked in a convection oven (at sub-100 °C) to prevent damaging thermally sensitive organic layers. The patterns were exposed on a GCA 5X I-line stepper and developed with MIF300 developer. The process was optimized beforehand to yield near vertical sidewalls. The pattern formed in the photoresist during the photolithographic step was transferred to the parylene layer and the underlying organic film through an anisotropic oxygen plasma etch on a Plasma-Therm PT72. The etch rate was in the range of 120–160 nm/min. Peeling the parylene films was accomplished mechanically, and removal was sometimes assisted by attaching Scotch tape to the surface of the parylene before lift-off.

3. Additive patterning approach

A second popular way for patterning films using photolithography involves lift-off. In the lift-off process, the photoresist is used as a contact mask. It is deposited directly on the substrate, and it is exposed and developed to leave parts of the substrate bare. The film to be patterned is subsequently deposited and coats the bare parts of the substrate and the surface of the photoresist. An appropriate solvent is used to dissolve the remaining photoresist, removing the part of the film that was deposited on it. The problem with this process arises due to the incompatibility of organics with the solvent used for the removal of the photoresist.

Fig. 1b shows an approach for carrying out the above photolithographic process on organic films. Parylene is used here in the place of the photoresist to enable the dry lift-off of the organic. This approach, which relies on the limited adhesion of parylene to the substrate, was originally developed by Ilic and Craighead for patterning of biological materials such as proteins and cells [16]. The actual peeling process used a combination of Scotch tape and tweezers to peel the entire film from the substrate, starting from an edge. Once the edge is lifted, the film separates easily. The force required to peel parylene from various substrates has been investigated by Takeuchi et al. [17]. Examples of organic films patterned using this approach are shown in Fig. 2. These films are the direct image of the photomask when positive tone photoresist is used, and the overall process is additive. Fig. 2d shows 1 μm wide lines of PEDOT:PSS on a 10 μm pitch, and Fig. 2e shows spiral lines with a 4 μm width made from ruthenium tris-bipyridine, $[Ru(bpy_3)]^{2+}(PF_6^-)_2$, a material used in OLEDs [18]. Finally, Fig. 3a shows an array of square pixels with a 4 μm edge made from pentacene, an organic semiconductor used in OTFTs [2]. Such structures can be used, for example, to define pixels in OLED displays, or to define the p- and n-type regions in TFT circuits [2]. An AFM micrograph shown in

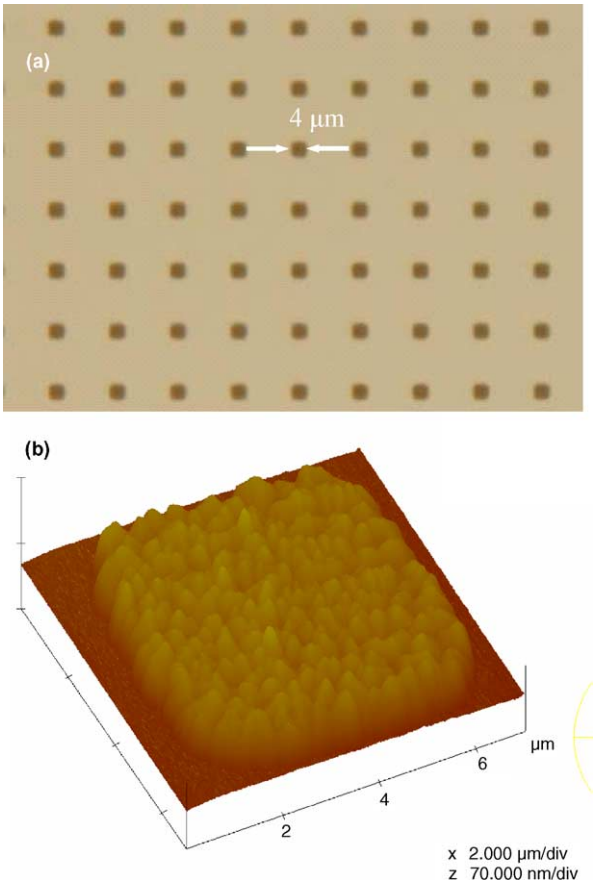

Fig. 3. Pentacene patterned using the additive approach: (a) optical micrograph of an array of square pixels with a 4 μm edge and (b) atomic force micrograph of a $4 \times 4\ \mu m^2$ pentacene pixel.

Fig. 3b reveals well-defined edges and uniform pentacene thickness.

The structures in Fig. 3 were fabricated as follows: Parylene was deposited on oxidized silicon wafers as described previously. Its patterning was also conducted in the same way as in the subtractive approach, but the photoresist was hard baked prior to exposure (it was found that heating at temperatures as high as 130 °C did not appear to affect the integrity of the parylene layer). After the parylene patterning, the residual photoresist was stripped off with an acetone/isopropanol bath before the deposition of the organic film and the wafer was treated in a UV/ozone cleaner. The organic material was subsequently deposited by spin coating (PEDOT:PSS and $[Ru(bpy_3)]^{2+}(PF_6^-)_2$), or vacuum sublimation (pentacene). The parylene layer was peeled off mechanically, as in the subtractive approach.

4. Discussion

The two approaches discussed here have some similarities as well as some differences. Both avoid exposure of the organic film to solvents used in photolithography, enabling a wide range of organics to be patterned without the need for custom synthesis. Both rely on the poor adhesion of parylene on a variety of substances. We found parylene films to peel easily from a variety of substrates used commonly in organic electronics, including freshly cleaned Au, indium tin oxide, and silicon oxide. Peeling of parylene films from glass substrates has also been reported in literature, as a way to fabricate dielectrics for OTFTs [19]. This makes the additive approach suitable to a variety of structures needed in organic electronics. Moreover, since the surface of the organic is left pristine, this approach is well-suited for applications where the quality of that organic surface is critical.

In the subtractive approach, the surface of the organic film comes in physical contact with parylene and runs the risk of getting damaged during the deposition and removal of the parylene film. In addition, successful peeling of the parylene requires stronger adhesion at the bottom (substrate/organic) than at the top (organic/parylene) interface. We found the success of this approach to be material dependent. Parylene peels easily from PEDOT:PSS and $[Ru(bpy_3)]^{2+}(PF_6^-)_2$ films deposited on a variety of substrates. Moreover, the conductivity of a 100 nm thick PEDOT:PSS film did not change upon deposition and removal of parylene, indicating that the process was benign. On the other hand, peeling parylene from pentacene and C_{60} films was not reproducible, and in certain cases the films would not peel at all. More detailed studies are necessary to understand the limitations of this technique. It should be stressed, however, that there is considerable latitude for tuning the properties of the organic/parylene interface, so that this patterning method becomes widely applicable. First, other derivatives of parylene, as well as other CVD films such as fluorocarbons [20] can be used to tune the properties of the top interface and strike the right balance between good adhesion and ease of delamination. Second, the peeling of the parylene films, which was carried out manually in this work, can be achieved, with better control, by a commercial delaminator. Third, CVD films that are soluble in supercritical CO_2 (which does not dissolve most organic films), offer an alternative to mechanical removal [21].

5. Demonstration of multi-level patterning

The photolithographic approaches described here can be used for the fabrication of organic electronic circuits, which require the patterning of more than one layers. This is demonstrated in Fig. 4, which shows a pentacene transistor with a 2 μm channel length and PEDOT:PSS electrodes. The transistor was fabricated by first applying the additive approach to pattern 1-mm long, 50-μm wide stripes of PEDOT:PSS (the PEDOT:PSS film was deposited on an oxidized p-type silicon wafer, which served as the gate electrode, with a 300 nm thick thermal oxide serving as the gate dielectric). A second additive step was then used to deposit a $2 \times 75\ \mu m^2$ island of pentacene, which was done by vacuum sublimation. The etching step that preceded the deposition of the pentacene partitioned the PEDOT:PSS stripe in the middle, defining the source and drain electrodes, separated by a 2 μm-long channel. This channel length was chosen for experimental convenience, and does not represent the limit of this technique (e-beam lithography can be used to define smaller channels).

The electrical characteristics of the transistor, which were measured under high vacuum in a probe station using Keithley 2400 source-meters, are shown in Fig. 4c. The transistor had a field effect mobility of $6.1 \times 10^{-3}\ cm^2/V\ s$. This is considerably lower than the mobility measured in pentacene transistors with polyaniline electrodes [22], indicating that further optimization of the patterning process

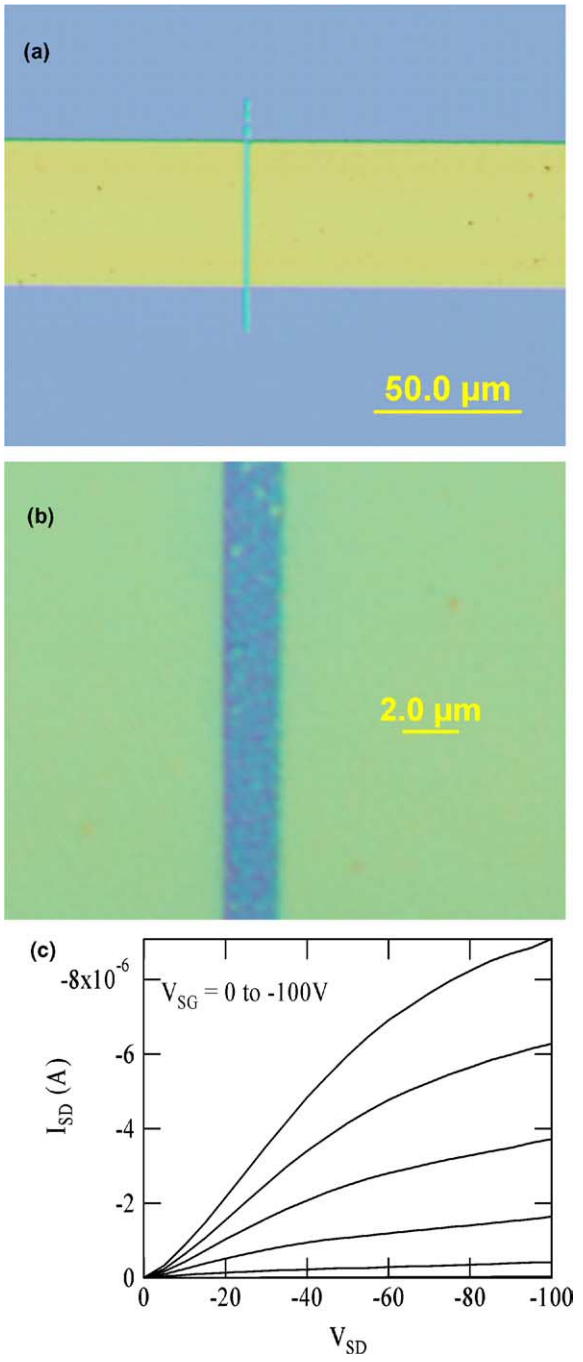

Fig. 4. Optical micrograph of a pentacene transistor with a 2 μm channel length and PEDOT:PSS electrodes fabricated by combining the subtractive and the additive approach (a). The channel region is shown in more detail in (b). Transistor characteristics are shown in (c).

is needed. Lefenfeld et al. [23] discussed contact issues for bottom electrode polymer transistors and demonstrate polymer transistors that perform well, showing the possibility for improvement with this process. The contact issues may be residual from the etch step creating a thin damaged region on the sidewalls of PEDOT:PSS. Since the parylene layer is more than a micron thick, and with ~1 μm or residual resist, shadowing of the pentacene may be a factor. Additionally, physical sputtering from the oxygen plasma step may cause roughening of the oxide layer, decreasing the mobility somewhat, but this has not yet been determined. It should be noted that devices with channel lengths of 25 μm exhibited less pronounced contact limited behavior and mobilities in the 10^{-2} cm^2/V s range.

The OTFT of Fig. 4 shows the applicability of this patterning approach to the fabrication of organic circuits. In addition to OTFTs, other devices can also be fabricated. For example, in systems where the parylene film can be peeled from the organic, the additive approach can be repeated to pattern different materials side-by-side. This way, red, green and blue pixels for full-color OLED displays can be sequentially patterned by repeating the additive approach three times. Similarly, sequential patterning of p-type and n-type organic semiconductor islands can be used for the fabrication of complementary OTFT circuits. The fabrication of such devices is currently underway.

6. Conclusions

In conclusion, we have demonstrated the photolithographic patterning of chemically sensitive organic electronic materials using parylene as an intermediary. With two complimentary patterning approaches available, a wide variety of structures with small dimensions may be fabricated out of low molecular weight as well as polymeric electronic materials. As a result, photolithography may yet play a role in future organic electronics manufacturing efforts.

Acknowledgements

This work was supported primarily by the Nanoscale Science and Engineering Initiative of the National Science Foundation (NSF) under Award Number EEC-0117770. A portion of this work was conducted at the Cornell Nanofabrication Facility (CNF) and the Nanobiotechnology Center (NBTC) which are supported by the NSF under Award Numbers ECS-9731293 and ECS-9876771, respectively. Thanks are due to Rob Ilic, Yuri Sylvester, Dan Bernards, Matt Lloyd, Ricardo

Ruiz, Yuanjia Zhang, and the staff at both the CNF and NBTC for help and useful discussions.

References

[1] U. Mitschke, P. Bauerle, J. Mater. Chem. 10 (2000) 1471.
[2] G. Horowitz, J. Mater. Res. 19 (2004) 1946.
[3] C.J. Brabec, N.S. Sariciftci, J.C. Hummelen, Adv. Funct. Mater. 11 (2001) 15.
[4] G.G. Malliaras, R.H. Friend, Phys. Today 58 (2005) 53.
[5] M. Chabinyc, A. Salleo, Chem. Mater. 16 (2004) 4509.
[6] M.J. Madou, Fundamentals of Microfabrication: The Science of Miniaturization, second ed., CRC Press, 2002.
[7] H. Sirringhaus, T. Kawase, R.H. Friend, T. Shimoda, M. Inbasekaran, W. Wu, E.P. Woo, Science 290 (2000) 2123.
[8] S.Y. Chou, P.R. Krauss, P.J. Renstrom, J. Vac. Sci. Technol. B 14 (1996) 4129.
[9] C.C. Cedeno, J. Seekamp, A.P. Kam, T. Hoffmann, S. Zankovych, C.M.S. Torres, C. Menozzi, M. Cavallini, M. Murgia, G. Ruani, F. Biscarini, M. Behl, R. Zentel, J. Ahopelto, Microelectron. Eng. 61-2 (2002) 25.
[10] J.A. Rogers, Z. Bao, M. Meier, A. Dodabalapur, O.J.A. Schueller, G.M. Whitesides, Synth. Met. 115 (2000) 5.
[11] M. Shtein, P. Peumans, J.B. Benziger, S.R. Forrest, Adv. Mater. 16 (2004) 1615.
[12] M. Halik, H. Klauk, U. Zschieschang, T. Kriem, G. Schmid, Appl. Phys. Lett. 81 (2002) 289.
[13] C.D. Müller, A. Falcou, N. Reckefuss, M. Rojahn, V. Wiederhirn, P. Rudati, H. Frohne, O. Nuyken, H. Becker, K. Meerholz, Nature 421 (2003) 829.
[14] W.F. Gorham, Mach. Des. 40 (1968) 65.
[15] I. Kymissis, C.D. Dimitrakopoulos, S. Purushothaman, J. Vac. Sci. Technol. B 20 (2002) 956.
[16] B. Ilic, H.G. Craighead, Biomed. Microdev. 2 (2000) 317.
[17] S. Takeuchi, D. Ziegler, Y. Yoshida, M. Mabuchi, T. Suzuki, Lab Chip 5 (2005) 519.
[18] J. Slinker, D. Bernards, P.L. Houston, H.D. Abruña, S. Bernhard, G.G. Malliaras, Chem. Commun. 19 (2003) 2392.
[19] K. Fujita, T. Yasuda, T. Tsutsui, Appl. Phys. Lett. 82 (2003) 4373.
[20] S.J. Limb, C.B. Labelle, K.K. Gleason, D.J. Edell, E.F. Gleason, Appl. Phys. Lett. 68 (1996) 2810.
[21] Y. Mao, N.M. Felix, P.T. Nguyen, C.K. Ober, K.K. Gleason, J. Vac. Sci. Technol. B 22 (2004) 2473.
[22] M. Lefenfeld, G. Blanchet, J.A. Rogers, Adv. Mater. 15 (2003) 1188.
[23] K.S. Lee, G.B. Blanchet, F. Gao, Y.L. Loo, Appl. Phys. Lett. 86 (2005) 074102.

Available online at www.sciencedirect.com
SCIENCE DIRECT
Organic Electronics 7 (2006) 29–37
Organic Electronics
www.elsevier.com/locate/orgel

Exciton quenching in highly efficient europium-complex based organic light-emitting diodes

T.W. Canzler *, J. Kido

Graduate School of Science and Engineering, Yamagata University, 4-3-16 Jonan, Yonezawa, Yamagata 992-8510, Japan

Received 5 August 2005; received in revised form 28 October 2005; accepted 31 October 2005
Available online 27 December 2005

Abstract

Red-light emitting organic electroluminescent devices using a trivalent europium complex (Eu^{3+}) as emitter were fabricated. A simple three-layer device, consisting of triphenyldiamine derivative (TPD) as hole transport layer, a 1,2,4-triazole derivative (TAZ) as electron injection layer, and europium(dibenzoylmethane)$_3$bathophenylphenathroline ($Eu(DBM)_3BPhen$) as electron transport and emission layer, exhibits efficient emission at very low currents. We attain peak external quantum efficiency of $7.5 \pm 0.5\%$ and a corresponding power efficiency of 10 ± 1 lm/W. For higher driving currents, we observe drastic decrease of efficiencies, accompanied by changes in the emission spectrum, i.e., an increase of emission from the $^5D_1$ state relative to the dominant $^5D_0$ emission. We show that both effects are caused by exciton–exciton annihilation. By co-evaporation of the Eu complex with TPD in the emitting layer, we can reduce quenching effects and color changes and achieve efficient electroluminescence also at higher currents.

Keywords: Europium; Exciton quenching; Electroluminescence

1. Introduction

The development of efficient organic light-emitting diodes (OLEDs) has lead to new possibilities for a low-cost, compact display technology. However, the spectrally broad emission of most organic molecules, due to vibrational broadening, makes it difficult to achieve the spectral purity required for full-color displays. On the other hand, it is widely known that lanthanide ions can exhibit spectrally narrow emission, due to intra-atomic transitions within the 4f shell, when suitably excited. It is the shielding of the 4f shell by the 5s5p electrons resulting in the narrow emission, which is only slightly perturbed by the host electric field. Europium complexes, which exhibit a dominant photoluminescence peak at 612 nm corresponding to the $^5D_0 - {}^7F_2$ transition of the Eu^{3+} ion, are hence promising materials for red EL devices [1]. The use of organolanthanide molecules in OLEDs also has the advantage of increasing the maximum theoretical internal quantum efficiency of the devices. In most OLEDs, emission is obtained from the recombination of singlet excitons only, limiting the internal quantum efficiency to 25%. Organolanthanides

* Corresponding author. Address: Novaled, Tatzberg 49, 01307 Dresden, Germany. Tel.: +49 3517965823; fax: +49 3517965829.
E-mail addresses: mail@tobias-canzler.de (T.W. Canzler), kid@yz.yamagata-u.ac.jp (J. Kido).

1566-1199/$ - see front matter © 2005 Elsevier B.V. All rights reserved.
doi:10.1016/j.orgel.2005.10.004

show highly efficient energy transfer from the ligand singlet and triplet to the rare earth ion. Thus, electroluminescence (EL) may arise from both singlet and triplet excitons increasing the theoretical internal quantum efficiency to 100%.

To estimate a realistic upper limit of the EL quantum efficiency, photoluminescence (PL) quantum efficiencies can be used. Values for europium complexes found in literature are up to ~80% in solution [2] and ~30% in diluted films [3]. As external quantum efficiencies of OLEDs on glass substrate (index of refraction $n = 1.5$) are about a factor $2n^2$ smaller than internal quantum efficiencies, we can roughly expect an external efficiency of ~6% for europium complex based OLEDs. In previous reports, the maximum external EL quantum efficiencies have exhibited values from ~1% up to 4.6% [4–7]. However, these best values are achieved only at very low current densities, i.e., for low luminance. One reason can be found in the nature of the characteristic Eu^{3+} transition $^5D_0 - {}^7F_2$ at 612 nm; such a transition is strictly forbidden for the free Eu^{3+} ion and only gets weakly electric dipole allowed in surroundings which break inversion symmetry. This results in a long lifetime of the excited sate in Eu^{3+} systems of several hundred μs [2,8].

In this work, the europium complex europium(dibenzoylmethane)$_3$bathophenylphenathroline (Eu(DBM)$_3$BPhen [21]) is used to fabricate red-light emitting devices. OLEDs based on undiluted Eu(DBM)$_3$BPhen as emission layer show pure Eu^{3+} emission with an external quantum efficiency of $7.5 \pm 0.5\%$ at low current densities. At higher current densities, a drastic decrease of efficiency accompanied by changes of the emission spectrum is observed. The emission from the $^5D_1$ state increases relative to the dominant $^5D_0$ emission. By analyzing the current dependencies, we can assign both effects to exciton–exciton (X–X) annihilation. This quenching process reduces the over-all quantum efficiency and feeds the $^5D_1$ state.

By co-evaporation of the Eu complex with TPD in the emitting layer, we can drastically reduce quenching effects and achieve efficient electroluminescence also at higher currents. Beside this, spectral changes of Eu^{3+} emission are much less pronounced in these devices, assuring good color purity.

2. Quenching theory

A significant issue in europium based devices is the decrease of quantum efficiency with increasing current. This is an intrinsic problem of Eu^{3+} phosphorescence because of the long lifetime of the quintet excited state. Depending on the specific surrounding of the Eu^{3+} ion, this lifetime is found to be in the range of 0.3–0.8 ms [2,8]. These values are orders of magnitude higher than those for other phosphorescent materials successfully applied in OLEDs, as for instance Ir(ppy)$_3$ with a phosphorescence lifetime in the order of 1 μs [9]. It has been proposed that the strong roll-off of quantum efficiency with current originates from quenching of the excited Eu^{3+} ion state with injected charge carriers, so called polaron–exciton (P–X) annihilation [10]. Alternatively, it has been suggested that X–X annihilation is responsible for this behavior [4,8,11]. The two quenching processes are described by

$$\text{X–X:} \quad M^* + M^* \rightarrow M^* + M, \tag{1}$$

$$\text{P–X:} \quad M^{\pm} + M^* \rightarrow M^{\pm} + M, \tag{2}$$

where M^* represents the excited molecular state, i.e., the quintet electronic state of Eu^{3+}. M represents its septet electronic ground state and $M^{\pm}$ a positive or negative charge carrier. In the case of X–X annihilation, the exciton concentration $[M^*]$ follows:

$$\frac{\mathrm{d}[M^*]}{\mathrm{d}t} = -\frac{[M^*]}{\tau} - \frac{k_{XX}}{2}[M^*]^2 + k_f \frac{J}{qd}, \tag{3}$$

where τ is the exciton lifetime, k_{XX} is the X–X annihilation parameter, J is the current density, q is the electron charge, d is the thickness of the exciton formation zone, and k_f is the probability for a charge carrier to form an excited Eu^{3+} ion. The current dependency of quantum efficiency η can be derived from the steady-state solution of Eq. (3):

$$\eta = \eta_0 \frac{J_0}{4J}\left[\sqrt{1 + 8\frac{J}{J_0}} - 1\right], \tag{4}$$

where η_0 is the quantum efficiency in the absence of X–X quenching, and

$$J_0 = \frac{4qd}{k_f k_{XX} \tau^2} \tag{5}$$

is the characteristic current density at which $\eta = \eta_0/2$.

Equivalent to Eq. (3), for the case of P–X annihilation the concentration of triplets follows:

$$\frac{\mathrm{d}[M^*]}{\mathrm{d}t} = -\frac{[M^*]}{\tau} - k_{PX}[M^*][M^{\pm}] + k_f \frac{J}{qd}, \tag{6}$$

where $[M^{\pm}]$ is the concentration of charge carriers and k_{PX} is the P–X quenching rate. Unfortunately, there is no straightforward solution to this equation. Adachi et al. solved the problem by assuming that $[M^{\pm}]$ is determined by trapped charge carriers in the case of trap-limited space charge current [4]. However, there remain doubts about this theory, as it does not cover the complexity of hetero structures, i.e., it assumes that space charge and exciton generation occur at the same position within the device.

Moreover, one should be aware that both Eqs. (3) and (6) already involve some serious simplifications, namely that (i) exciton generation is homogeneous within the generation zone and (ii) that the thickness of this generation zone is independent of the applied voltage and the resulting current density. Assumption (i) is certainly not justified, but this may only affect the derived rate constants. However, deviations from assumption (ii) will arise especially if the charge balance depends on applied voltage, which changes also the qualitative behavior.

3. Experiment

The inset of Fig. 1 shows the chemical structure of the emitter complex $Eu(DBM)_3BPhen$. The Eu^{3+} complex was prepared according to methods similar to those reported in literature [12]. It was previously shown that $Eu(DBM)_3BPhen$ possesses, besides efficient phosphorescence, good electron transporting properties [5,13]. The other organic materials used in this study are a hole transporting triphenyldiamine derivative (TPD) and a electron injecting and transporting 1,2,4-triazole derivative (TAZ). These materials were purified by vacuum gradient sublimation.

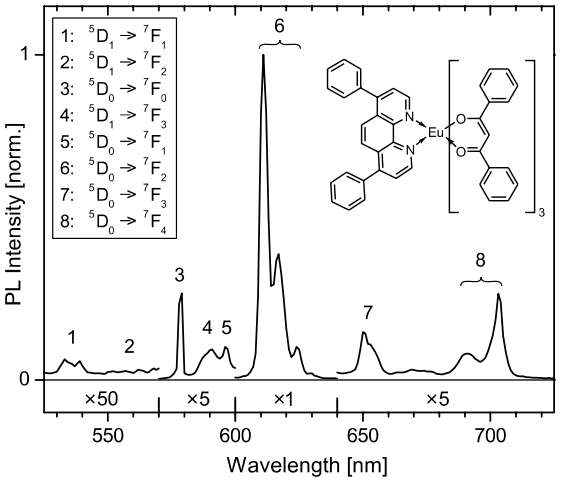

Fig. 1. PL spectrum and molecular structure of $Eu(DBM)_3BPhen$. The various transitions are labelled in the inset [17]. Transition 2 is too weak to show up in PL but appears in EL spectra at high currents (see Fig. 6). Different parts of the spectra are drawn to a larger scale as given beneath.

The organic layers were thermally deposited onto a solvent cleaned and ozone treated indium–tin–oxide (ITO) coated glass substrate at 5×10^{-6} Torr. Layer thickness calibration was performed using Dektak 3 surface profilometer. Mixed layers were produced by co-evaporation from two crucibles. The mixing ratio was established by independent quartz monitors and source control. The ITO serves as a transparent cathode with a sheet resistance of 15 Ω/sq. The Al top electrode was finally deposited at 2×10^{-5} Torr to define an emitting area of 5×5 mm^2. The electron injection from the Al cathode to the organic electron-injection layer is improved by a thin (0.5 nm) LiF layer [14].

It is worth mentioning that $Eu(DBM)_3BPhen$ is thermally not stable at temperatures required for evaporation and unavoidably decomposes during the deposition process. Thereby, the melted yellow material undergoes a slow darkening. Thus, continuous processing is required and the re-use of material, e.g., for a second sample, results in slightly decreased OLED performance.

Luminance measurements were carried out at room temperature under ambient atmosphere using a Topcon BM-8 luminance meter. Quantum efficiencies are calculated assuming Lambertian emission pattern and considering all spectral features in the visible.

Photoluminescence (PL) lifetimes were measured using a streak camera (C4334 from Hamamatsu Photonics). Photoexcitation of the samples was done by 500-ps pulses from a 10 Hz N_2 laser at a wavelength of $\lambda = 337$ nm. The streak camera is synchronized to the exciting laser and was used to run in single-photon counting mode. All measurements were performed at room temperature.

4. Efficient electroluminescence

Two device structures were chosen for investigating the EL properties of $Eu(DBM)_3BPhen$. They differ in their emission layer which consists either of pure $Eu(DBM)_3BPhen$ or of a mixed layer of $Eu(DBM)_3BPhen$ and TPD:

Device (I): [+] TPD (40 nm) | $Eu(DBM)_3BPhen$ (60 nm) | TAZ (10 nm) [−].
Device (II): [+] TPD (40 nm) | $Eu(DBM)_3BPhen$: TPD (1:2, 20 nm) | $Eu(DBM)_3BPhen$ (40 nm) | TAZ (10 nm) [−].

The given mixing ratio is the molecular ratio. Here, we present only data for one specific mixed-layer device. For the given mixing ratio of about 1:2, assuring both good electron and hole transport, the geometrical structure is optimized in terms of maximum quantum efficiency. Modification in the molecular ratio of the mixed layer will both affect exciton quenching as well as the carrier balance. Therefore, a systematic investigation of mixed layer devices requires additional optimization of device geometry and is beyond the scope of this report.

There are already reports on investigations of similar structures [5,15]. However, the results presented here differ significantly from previous reports. Especially the introduction of the thin TAZ layer improves the devices significantly. Lower onset voltages and higher efficiencies, compared to devices without the TAZ layer, suggest improved electron injection. Both devices (I) and (II) are designed to exhibit emission solely from Eu^{3+}.

TPD is energetically well-suited to dilute $Eu(DBM)_3BPhen$ and increase the effective interface area of hole transport and emission materials. This can be approved by time-resolved PL measurements. By photo-excitation of a $Eu(DBM)_3BPhen$:TPD (1:2) film using 337 nm light, we excite both TPD and DBM singlet excitons. However, the PL spectrum reveals solely $Eu(DBM)_3BPhen$ emission. The absence of any TPD contribution shows that TPD singlet excitons are efficiently transferred to $Eu(DBM)_3BPhen$. The transient PL decay is shown together with data of a pure $Eu(DBM)_3BPhen$ film in Fig. 2. The found phosphorescence lifetime for the mixed film at room temperature is of about 0.42 ms, the $Eu(DBM)_3BPhen$ film shows a comparable value of $\tau = 0.44$ ms. The difference of the found lifetimes is within the experimental error of the measurement.

In Fig. 3, the EL performance of the two devices is shown. Device (I) exhibits a maximum luminance of 380 cd/m^2 at around 60 mA/cm^2, whereas device (II) reaches its maximum luminance of about 1000 cd/m^2 at almost the double current density. Our interpretation is as follows: In device (I), excitons are formed at the sharp $Eu(DBM)_3BPhen$–TPD interface, whereas in device (II) exciton formation takes

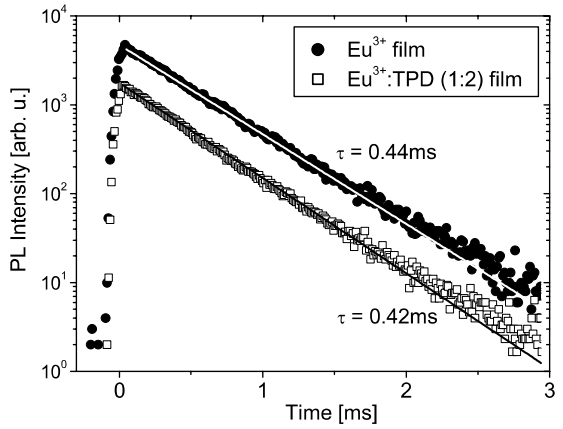

Fig. 2. Transient phosphorescence decay observed after pulsed photo-excitation of a $Eu(DBM)_3BPhen$ film and a $Eu(DBM)_3BPhen$:TPD (1:2) film. Initial exciton concentrations are about 10^{17} cm^{-3}. The fitted decay constants τ are given in the plot. The curves are separated vertically for clarity.

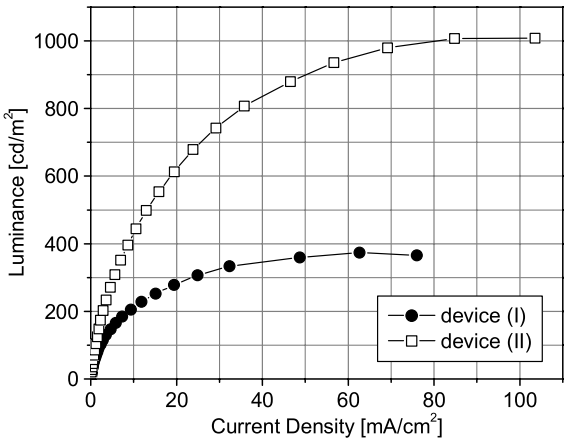

Fig. 3. Electroluminescence (EL) intensity versus driving current. Solid circles: undiluted $Eu(DBM)_3BPhen$ emission layer, device (I). Open squares: mixed emission layer of $Eu(DBM)_3BPhen$ and TPD, device (II).

place in the mixed $Eu(DBM)_3BPhen$:TPD layer, resulting in lower exciton densities. Thus, exciton quenching limits the performance of device (I) already at considerably lower currents. For higher currents than shown, luminance in both devices starts to decrease. This is partly due to irreversible degradation, strengthened by the fact of performing these measurements under ambient atmosphere.

Fig. 4 shows the external quantum efficiency η versus driving current. Device (I) exhibits a maximum external quantum efficiency of $\eta_{max} = 7.5 \pm 0.5\%$ ($\equiv$13.7 cd/A) at a current density of 0.02 mA/cm^2. To our knowledge, this is the highest

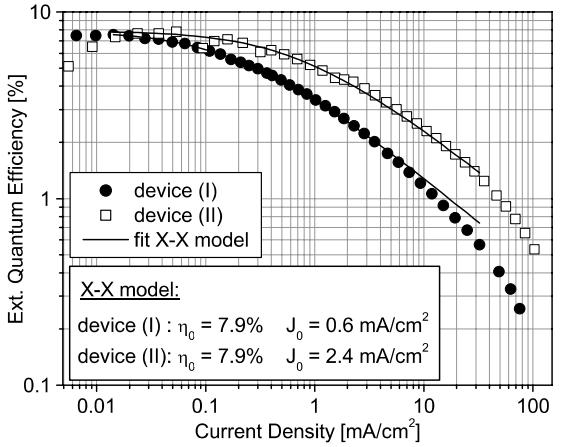

Fig. 4. The external quantum efficiency of the EL devices vs. current density. The calculated curves, based on the model of X–X annihilation, are also shown. The appendant fit parameters are given as an inset.

external quantum efficiency reported using a Eu^{3+} ion as a lumophore in an organic system. The power efficiency for this current was measured to be 10 ± 1 lm/W. Note, however, that efficiencies strongly decrease with increasing current, characteristic for luminescence originating from recombination of long-lived triplet excitons [4,16]. Device (II) with its broader exciton formation zone shows even slightly higher maximum efficiency $\eta_{max} = 7.8 \pm 0.5\%$ ($\equiv$14.0 cd/A). The broad exciton formation zone, i.e., the lower exciton density, results in a significantly weaker decrease of η with increasing current. For instance at a luminance of 100 cd/m^2, device (II) shows an external quantum efficiency of 4.9% whereas device (I) already dropped to 2.5%. From the comparison of the two devices it is obvious that the mixed TPD:$Eu(DBM)_3$BPhen layer in device (II) does not introduce additional quenching.

We have applied the X–X quenching model to the experiment. Adjusting Eq. (3) to the experimental data results in a good fit. However, for high currents we observe deviations of the fit. Especially for device (I), the decrease of efficiency is stronger than X–X annihilation predicts. This can be attributed to heat-up of the samples, reduced charge balance, and degradation, as well as other quenching mechanisms, e.g., P–X annihilation or higher order processes. The fit parameter for the initial quantum efficiency is for both devices the same, $\eta_0 = 7.9\%$. However, the parameter for the characteristic current density J_0, where η drops to half the initial value, is about four times larger for device (II) with $J_0 = 2.4$ mA/cm^2 compared to $J_0 = 0.6$ mA/cm^2 for device (I). This shows the strong impact of the mixed layer in reducing exciton density. In the next section, we will investigate spectral changes accompanying electroluminescence. This will give further evidence that X–X annihilation is the main quenching process.

5. Spectral changes

The europium complex exhibits an absorption spectrum which is determined by its DBM and BPhen ligands. The lowest energetic peak at around 360 nm can be assigned to the allowed π–π* transition of the β-diketone (DBM) ligand, the two next higher energetic peaks at 320 nm and 280 nm stem from BPhen. The PL spectrum exhibits a main sharp emission peak at 612 nm corresponding to the $^5D_0 - {}^7F_2$ transition of the trivalent europium ion accompanied by several weak peaks of various other $^5D_i - {}^7F_j$ ($i = 0, 1$; $j = 0$–4) transitions [17], as given in Fig. 1.

The emission from ^5D states is a result of highly efficient intra-molecular energy transfer from the DBM ligands to the Eu^{3+} ion, which is mediated by the ligand-to-metal charge-transfer (LMCT) state. LMCT state and emitting ^5D states exhibit resonance crossovers accompanied by thermal barriers. This can be depicted using a simple configurational coordinate diagram [18], as shown in Fig. 5. The feeding of LMCT state excitation into the ^5D states depends on the thermal barrier between the states. For $Eu(DBM)_3$BPhen, the $^5D_0$ and $^5D_1$ resonance crossovers to LMCT state are near the LMCT state minimum; energy transfer to these states can be activated thermally. Especially the LMCT $\rightarrow {}^5D_0$ feeding is very efficient already at room temperature, while the population of $^5D_1$ is almost negligible. The bent dotted arrows in Fig. 5 illustrate thermally activated excitation of $^5D_0$ and $^5D_1$ state.

The unusually large energy difference of optical transitions of the ligands and the Eu^{3+} core is worth some extra remarks concerning the possible quenching processes. Let us consider the possible processes that can occur when an excited Eu-complex meets a charge carrier (polaron). In general, the transitions of the charged ligand are smaller than the energy of the exciton on the complex core. In this case, transfer of the excitation energy from the core to the polaron via Förster process is possible, which favors P–X quenching. In our case, however, the transition energies of charged ligands might be larger than the energy of the exciton on the Eu^{3+} core.

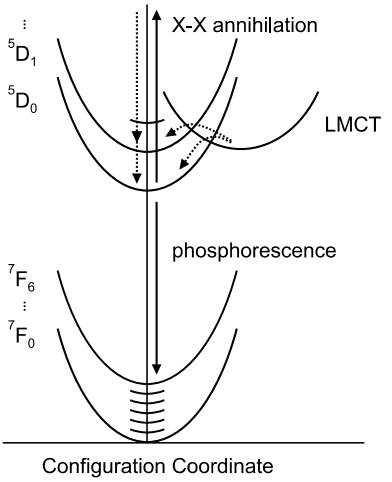

Fig. 5. Schematic configurational coordinate diagram for the ground ^7F, emitting ^5D, and the ligand-to-metal charge-transfer (LMCT) states for Eu^{3+} complexes. Unlabelled parabolas have been drawn in a reduced manner. The feeding of the emitting states from LMCT state is visualized by dotted arrows. The solid upward arrow represents the high excitation of one of the two excitons involved in an exciton–exciton annihilation process. The subsequent relaxation to the emitting states is given by dotted arrows.

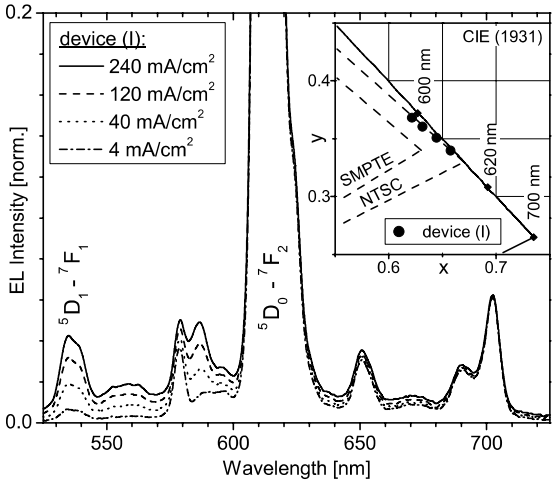

Fig. 6. EL spectra of device (I) for different driving currents. The spectra are normalized with regard to the main $^5D_0$ transition at 612 nm. With increasing current the $^5D_1$ transitions grow relatively stronger, shifting the emission from red to orange. The corresponding color changes are visualized in the CIE 1931 chromaticity diagram (inset). The solid and dashed black lines represent the red corner of the NTSC and SMPTE RGB triangle, respectively.

As the transition energies of $Eu(DBM)_3BPhen$ cations and anions are unknown, we can just speculate that the energetic situation might prohibit P–X quenching. In this case, a fusion of the exciton and the polaron becomes possible leading to an excited polaron. Such fusion process is favored by the fact that the self-polarizability is usually increased in the excited state. The excitation energy on the Eu^{3+} ion may be largely preserved due to the weak coupling between the ligands and the core. Consequently, the fusion cannot yet be regarded as a quenching process. However, the charged and excited complex can subsequently capture a complementary charge due to Coulomb attraction, leading to a higher excited state in a similar way to the X–X annihilation process. Even though the mechanism is different from conventional X–X quenching, the net effect is the same, namely that two pairs of carriers lead to one highly excited state instead of two excitons. Therefore, one can assume that the theory derived for X–X bimolecular quenching, as a first approximation, is also covering this special X–X quenching process.

Fig. 6 shows the evolution of EL spectra of device (I) with driving current. For comparison, the spectra are normalized with regard to the main emission at 612 nm. While peaks assigned to the $^5D_0$ transitions remain unchanged, we observe an increase of peaks originated from $^5D_1$ state. The two transitions, which are used for further analysis are labelled, for assigning other transitions see Fig. 1. A similar but less pronounced behavior was observed for device (II). Liang et al. already reported about the appearance of emission from $^5D_1$ state with increasing current [8]. They speculate that X–X annihilation may cause this effect, however, no further evidence is provided. In the following, we will show that the spectral changes are truly caused by X–X annihilation. For this reason, first, we have to exclude other possible mechanisms, as there are

- *Temperature effect* (heat up of sample),
- *Applied electric field*,
- *Charging of complex/local field effect*.

Actually, conventional P–X quenching will not lead to spectral changes as observed, because this process results in excited states of charged ligands with an excitation energy being lower than the exciton energy. Such states typically recombine radiationless and at least a blue shifted emission line is not to be expected.

Temperature effect: As the samples are heated up distinctly by the driving current, a temperature related effect might be considered to explain the

spectral changes. The temperature dependence of Eu^{3+} PL was observed already in 1970 [18]. These investigations resulted in semi-classical descriptions which can be visualized in a configuration coordinate diagram, as schematically drawn in Fig. 5. A recent publication even proposes the use of europium complexes for thermo-optical devices, as they provide accurate measurement of temperature [19]. However, the effects we observe in EL are too strong to be explained by heating up the samples in the approximate temperature range of 20–100 °C. Furthermore, we do not find any hysteresis of spectral changes by up and down switching of the driving current.

Applied electric field: To exclude any effect related to the applied electric field, we have prepared device (III), which suppresses carrier injection efficiently. For this purpose, we simply exchanged the hole and electron transport materials:

Device (III): [+] TAZ (40 nm) | $Eu(DBM)_3BPhen$ (50 nm) | TPD (30 nm) [−].

We have performed combined PL–EL measurements for device (I), (II) and (III) as a function of the applied electric field. The idea is that spectral changes due to an electric field would show up both in EL and PL. Therefore, in the following we do not distinct strictly between the two measures of EL and PL. We photoexcite the devices at 400 nm, where $Eu(DBM)_3BPhen$ still has considerable absorption while TPD and TAZ are transparent. At the same time, we apply an electric field and record the spectra of all luminescence leaving the devices. For low fields, below the onset of EL, the spectra represent solely PL. For higher fields, the EL signal quickly outshines the PL signal and the recorded spectra represent EL.

In Fig. 7, we show the peak-height ratio referred to as $^5D_1/^5D_0$ and equal to the emission intensities from $^5D_1 \rightarrow {}^7F_1$ divided by $^5D_0 \rightarrow {}^7F_2$. We have chosen these two transitions for analysis exemplarily; for other corresponding transitions we get comparable characteristics. For devices (I) and (II), the onset of EL is as low as 200 kV/cm^2, whereas device (III) does not show any EL up to 2000 kV/cm^2. We find that luminescence spectra do not change with field as long as there is no initiation of EL. As all three devices show strongly different behavior, it is straightforward to conclude that changes of Eu^{3+} emission are not caused by the applied electric field.

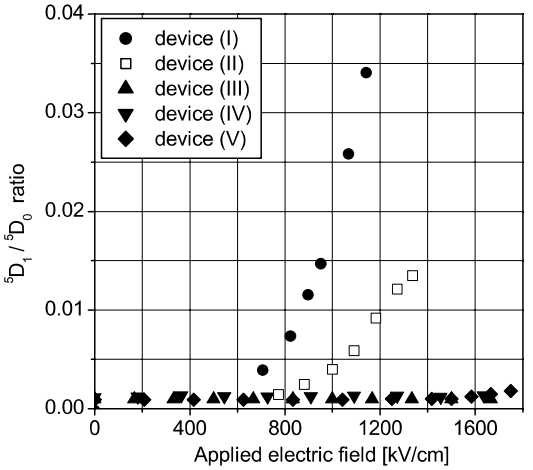

Fig. 7. The peak height ratio $^5D_1/^5D_0$ as a function of applied electric field. The given data stem both from PL and, if possible, from EL measurements.

Charging of complex/local field effect: The phosphorescent properties of Eu^{3+} are also used for cathodoluminescent display applications, as cathode ray tubes (CRTs) and field-emission displays (FEDs). Studies of Eu^{3+} cathodoluminescence report on changes of the $^5D_1/^5D_0$ ratio as a function of the electron-beam current [20]. This effect is partly described to originate from local redistribution of charge carriers. For our devices, strong charging effects seem not likely, however, we cannot exclude local field effects a priori. Therefore, we have prepared two devices, which suppress either electron or hole injection efficiently. For this purpose, we exchanged either the hole or electron transporting material:

Device (IV): [+] TPD (40 nm) | $Eu(DBM)_3BPhen$ (50 nm) | TPD (30 nm) [−].
Device (V): [+] TAZ (40 nm) | $Eu(DBM)_3BPhen$ (50 nm) | TAZ (30 nm) [−].

Device (IV) suppresses electron injection while hole injection remains efficient, which will lead to positive charging of $Eu(DBM)_3BPhen$. In contrast, device (V) suppresses hole injection while electron injection remains efficient, leading to negative charging of Eu^{3+} complexes. We are aware that charge carrier concentration in the Eu^{3+} layer of the devices does not necessarily follow the field in a linear way. Especially a comparison of the unipolar devices (IV) and (V) and the bipolar devices (I) and (II) seems questionable. The good carrier balance and efficient recombination in the bipolar

devices will reduce charging effects considerably. On the other hand, as charging effects should be stronger in unipolar devices (IV) and (V), they should clearly show up in combined PL–EL measurements. We have performed PL–EL measurements as a function of the applied electric field, as described above. The results are depicted in Fig. 7. Devices (IV) and (V) do not show any EL up to 1200 kV/cm^2, changes of the emission spectra are observed above 1600 kV/cm^2. As we observe only very small spectral changes in the unipolar devices compared to device (I) and (II), in which good carrier balance is assured, we can safely exclude local field effects to cause the observed spectral changes.

X–X annihilation: This process results in the high excitation of an already excited molecule for one of the two involved molecules. Fig. 5 visualizes this excitation as well as the subsequent relaxation. This relaxation may cause increased emission from higher levels such as $^5D_1$. The same holds for the speculated case of subsequent capture of two opposed charges by an already excited complex, as discussed above.

By definition, the internal quantum efficiency is given by the fraction of radiative-transition rate R_r relative to the sum of all rates. If we assume, besides nonradiative transitions, only X–X quenching to occur, the external quantum efficiency is given by

$$\eta(J) = \Phi_{\text{outcoupling}} \frac{R_r}{R_r + R_{nr} + R_{XX}}, \tag{7}$$

$$\eta_0 = \Phi_{\text{outcoupling}} \frac{R_r}{R_r + R_{nr}}, \tag{8}$$

where $\Phi_{\text{outcoupling}}$ is a factor to take into consideration outcoupling losses, R_{nr} is the nonradiative transition rate, and R_{XX} is the X–X quenching rate. Now, we assume that the change of peak-height ratio $^5D_1/^5D_0$ is direct proportional to the ratio of X–X quenching rate and radiative-transition rate:

$$^5D_1/^5D_0 \propto \frac{R_{XX}}{R_r}. \tag{9}$$

Connecting Eq. (9) with Eqs. (8) and (7) will finally result in

$$^5D_1/^5D_0 \propto \frac{1}{\eta(J)} - \frac{1}{\eta_0} \propto \frac{\eta_0}{\eta(J)} - 1. \tag{10}$$

This simple relation is a powerful tool to prove the nature of quenching by comparing two independently measured quantities. Fig. 8 shows the $^5D_1/^5D_0$ ratio for devices (I) and (II) as a function of current density. Additionally, we show the

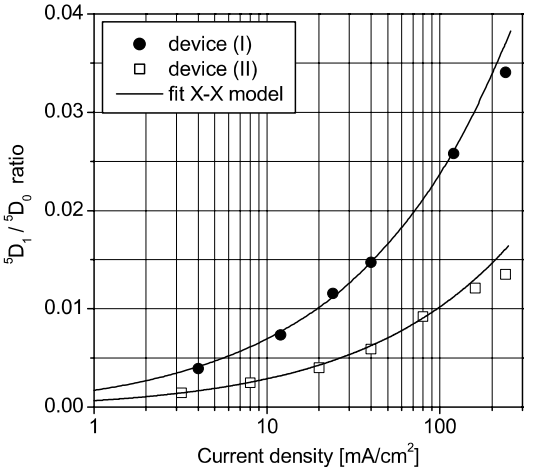

Fig. 8. The peak height ratio $^5D_1/^5D_0$ as a function of driving current. The curves are calculated using Eq. (10) based on the fit parameters of the X–X annihilation model.

behavior of this quantity, as it is predicted by the X–X annihilation model. For this simulation, we use the parameters from fitting the X–X model to the experimental efficiencies as given in Fig. 4. We find a nice correspondence of experiment and simulation giving strong proof that quenching and spectral changes in our devices truly stem from X–X annihilation.

6. Conclusion and outlook

We have demonstrated efficient electroluminescence of the lanthanide complex Eu(DBM)$_3$BPhen. Maximum external quantum efficiency of $\eta = 7.5 \pm 0.5\%$ at low current density <0.1 mA/cm^2 was achieved. The strong decrease of η with current was found to be due to X–X annihilation. We could show that this quenching mechanism is also responsible for changes in the emission spectra leading to significant color changes.

Further investigation of the spectral changes, e.g., analysis of density dependent PL, would allow to estimate the contribution of X–X annihilation not only qualitatively but also quantitatively. The quenching, and thus the color changes, can be successfully reduced by diluting the electron-transporting europium complex with the hole-transporting material TPD. We achieve comparable maximum efficiencies, however the roll-off for higher currents is drastically reduced, e.g., we keep η at 4.9% at a luminance of 100 cd/m^2.

However, europium-complex EL is still far from application. The used complex is not sufficiently

stable, neither thermally as needed for evaporation, nor electrically [5]. Future directions of work in this area will include the synthesis of new molecules with the aim of increasing stability and minimizing the lifetime of excited quintet states. Furthermore, high efficiencies at high current densities are possible when appropriate guest-host combinations are identified.

Acknowledgements

This work was supported by the Japan Society for the Promotion of Science (JSPS). The authors would like to thank Dr. M. Pfeiffer for useful discussions and S. Watanabe for experimental support.

References

[1] J. Kido, K. Nagai, Y. Okamoto, T. Skotheim, Chem. Lett. (1991) 1267.
[2] F. Halverson, J.S.R. Brinen, J. Leto, J. Chem. Phys. 41 (1964) 157.
[3] M.D. McGehee, T. Bergstedt, C. Zhang, A.P. Saab, M.B. O'Regan, G.C. Bazan, V.I. Srdanov, A.J. Heeger, Adv. Mater. 11 (1999) 1349.
[4] C. Adachi, M.A. Baldo, S.R. Forrest, J. Appl. Phys. 87 (2000) 8049.
[5] Z. Hong, C. Liang, R. Li, W. Li, D. Zhao, D. Fan, D. Wang, B. Chu, F. Zang, L.-S. Hung, et al., Adv. Mater. 13 (2001) 1241.
[6] M. Noto, K. Irie, M. Era, Chem. Lett. 4 (2001) 320.
[7] P.P. Sun, J.P. Duan, H.T. Shih, C.H. Cheng, Appl. Phys. Lett. 81 (2002) 792.
[8] C.J. Liang, T.C. Wong, L.S. Hung, S.T. Lee, Z.R. Hong, W.L. Li, J. Phys. D: Appl. Phys. 34 (2001) L61.
[9] M.A. Baldo, S. Lamansky, P.E. Burrows, M.E. Thompson, S.R. Forrest, Appl. Phys. Lett. 75 (1999) 4.
[10] J. Kido, H. Hayase, K. Hongawa, K. Nagai, K. Okuyama, Appl. Phys. Lett. 65 (1994) 2124.
[11] M.A. Baldo, C. Adachi, S.R. Forrest, Phys. Rev. B 62 (2000) 10967.
[12] L.R. Melby, N.J. Rose, E. Abramson, J.C. Caris, J. Am. Chem. Soc. 86 (1964) 5117.
[13] C.J. Liang, Z.R. Hong, X.Y. Liu, D.X. Zhao, D. Zhao, W.L. Li, J.B. Peng, J.Q. Yu, C.S. Lee, S.T. Lee, Thin Solid Films 359 (2000) 14.
[14] H. Heil, J. Steiger, S. Karg, M. Gastel, H. Ortner, H. von Seggern, M. Stöszel, J. Appl. Phys. 89 (2001) 420.
[15] C.J. Liang, D. Zhao, Z.R. Hong, D.X. Zhao, X.Y. Liu, W.L. Li, J.B. Peng, J.Q. Yu, C.S. Lee, S.T. Lee, Appl. Phys. Lett. 76 (2000) 67.
[16] M.A. Baldo, D.F. O'Brien, Y. You, A. Shoustikov, S. Sibley, M.E. Thompson, S.R. Forrest, Nature 395 (1998) 151.
[17] C. Kodaira, H. Brito, O. Malta, O. Serra, J. Lumin. 101 (2003) 11.
[18] W.H. Fonger, C.W. Struck, J. Chem. Phys. 52 (1970) 6364.
[19] G.E. Khalil, K. Lau, G.D. Phelan, B. Carlson, M. Gouterman, J.B. Callis, L.R. Dalton, Rev. Sci. Instrum. 75 (2004) 192.
[20] J. Bang, B. Abrams, P.H. Holloway, J. Appl. Phys. 94 (2003) 7091.
[21] An alternative abbreviation is $Eu(DBM)_3bath$.

Available online at www.sciencedirect.com
SCIENCE DIRECT®
Organic Electronics 7 (2006) 38–44
Organic Electronics
www.elsevier.com/locate/orgel

Layered organic film growth by substrate temperature tuning for efficiency-enhanced OLEDs

G. Wantz [a,*], O.J. Dautel [b], R. Almairac [c], L. Hirsch [a], F. Serein-Spirau [b], L. Vignau [a], J.P. Lère-Porte [b], J.P. Parneix [a], J.J.E. Moreau [b]

[a] *Fédération de Recherche SyMe CNRS FR2648, Laboratoires PIOM and IXL, Ecole Nationale Supérieure de Chimie et de Physique de Bordeaux, 16 Av. Pey Berland 33607 Pessac Cedex, France*
[b] *Hétérochimie Moléculaire et Macromoléculaire, UMR 5076, Ecole Nationale Supérieure de Chimie de Montpellier, 8 rue de l'Ecole Normale 34296 Montpellier Cedex 05, France*
[c] *LCVN, UMR 5587, cc26 Université Montpellier II, 34095 Montpellier Cedex 05, France*

Received 9 September 2005; received in revised form 6 November 2005; accepted 16 November 2005
Available online 9 December 2005

Abstract

Effects on resultant organic light-emitting device of substrate temperature during the evaporation process of a light-emitting material are reported. Light-emitting diodes are based on a novel bis-imido-phenylene vinylene (ImPV) derivative as green-emitting molecule. It is reported that the substrate temperature has a great influence on the thin film morphology. Heating the substrate results in a more ordered film. Using this technique, molecules of ImPV self-organise in an even layered film with 1.7 nm-thick molecular layers. Devices based on heated substrates exhibit higher operating voltages but enhanced quantum and luminous efficiencies.

PACS: 68.55.−a; 78.55.Kz; 78.60.Fi; 73.61.Ph; 71.20.Rv

Keywords: OLED; Substrate temperature; Organic vacuum deposition; Imido-phenylene vinylene

1. Introduction

Since Tang and VanSlyke demonstration of the electroluminescence of organic molecules [1], research around the world has expanded in order to develop a new display technology. Organic light-emitting diodes (OLEDs) present many attractive properties such as: low driving voltage, large color range, low cost and ease of processing. Small OLED-based displays are available for mobile solutions but quantum efficiencies and lifetimes are not yet sufficient to reach the market of large area displays and lighting [2].

In organic devices such as organic field-effect transistors (OFETs) [3], the morphology and the molecular/crystal orientation of the active organic layer are key factors for their electronic performances. For instance, charge transport will strongly depend not only on the molecular orientation due to the highly anisotropic charge carrier mobility in

* Corresponding author. Tel.: +33 5 4000 6630; fax: +33 5 4000 6631.
E-mail address: wantz@enscpb.fr (G. Wantz).

1566-1199/$ - see front matter
doi:10.1016/j.orgel.2005.11.001

organic crystals [4], but also on the film morphology because of grain boundaries [5].

This paper deals with OLEDs optoelectronic performances as a function of film morphology and molecular organization. The most basic structure of an OLED includes a single electroluminescent layer (ca. 100 nm-thick) sandwiched between two electrodes. It is well-known that multilayer devices are the most efficient due to a better charge balance using electron and hole transport layers, respectively on top and below the emitting layer, as well as blocking layers to confine excitons in the luminescent layer. Molecular layers are thermally evaporated under secondary vacuum (ca. 10^{-6} mbar). Typically, during deposition, substrates are kept at room temperature (RT), although substrate temperature is a key parameter to control the crystallinity of epitaxially grown layers [6]. This study deals with the effects of substrate temperature during the deposition of the active layer. Temperatures ranging between RT and the melting point of the organic material are considered. In order to avoid any desorption process and/or melting of successive organic layers, only single-layer devices have been studied.

The effect of the substrate temperature on devices with Tris-(8-hydroxyquinoline) aluminium (Alq_3) as emitting layer has already been reported [7–10]. Efficiency enhancements and retarded dark-spots growth have been observed with increasing substrate temperature. Morphological changes have also been reported but Alq_3 layers have always been found amorphous whatever the substrate temperature [11]. In this work, an electroluminescent material which enables non-amorphous growth is reported. Post-deposition annealing has not been investigated here because it has recently been shown that poor OLED performances are obtained [9].

2. Experimental

A novel bis-imido-phenylene vinylene (ImPV) derivative (Fig. 1) has been chosen as light-emitting material because this material exhibits good performances even in a single layer OLED. ImPV was synthesized in two steps from the 4-bromophthalic anhydride **1**. In a first step, cyclohehylamine and the 4-bromophthalic anhydride were condensed in refluxing toluene under a Dean–Stark trap to afford the corresponding halogenated cyclohexylphthalimide **2**. Finally, **2** readily underwent coupling reaction with the conjugated 1,4-divinyl-2,5-bis(octyloxy)benzene **3** in the presence of palladium catalyst. The Heck reaction was carried out in dry *N*,*N*-dimethylformamide at 110 °C in the presence of $Pd(OAc)_2$ and $P(o\text{-}C_6H_4Me)_3$. Yellow needles of ImPV were simply isolated through a filtration since it crystallised during the reaction mixture cooling. This new chromophore is highly soluble in common organic solvents, highly fluorescent and emits greenish blue light with a fluorescence quantum yield of 66% when irradiated at 425 nm in tetrahydrofuran [THF, $\lambda_{abs\_max} = 425$ nm; $\lambda_{em\_max} = 515$ nm ($\lambda_{ex} = 425$ nm), $\Phi_{f\mathrm{ImPV}} = 0.66$].

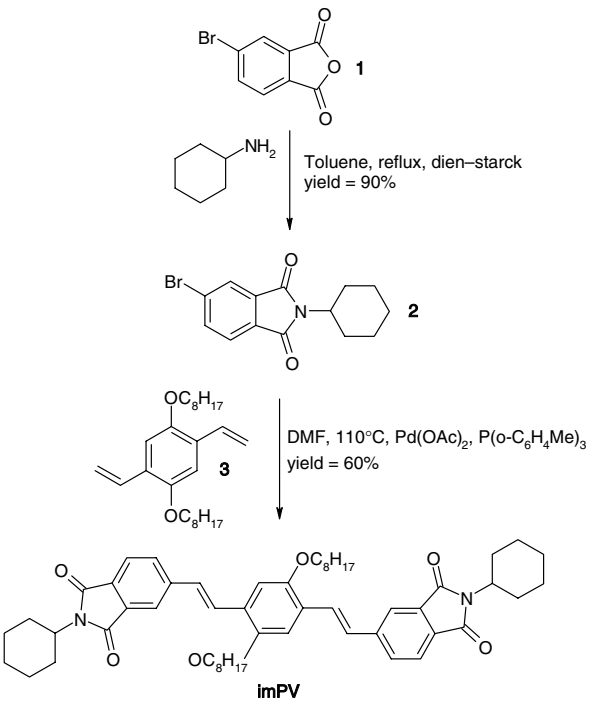

Fig. 1. Synthetic path to ImPV.

Diodes were fabricated using the following procedure. Indium-tin oxide (ITO) substrates on glass underwent a previously described preparation procedure [12]. A layer of poly(styrene sulfonate) doped poly(3,4-ethylene dioxythiophene) (PEDOT-PSS) was spun, from a 3 wt% water dispersion at 5000 rpm to form a 50 nm-thick layer. This conducting polymer layer was baked at 80 °C under rotary pump vacuum for 1 h. This layer improves hole injection from the ITO to the HOMO level of the organic material and increases the performances [13]. Then, the active layer was thermally evaporated under vacuum (ca. 10^{-6} mbar) at a low deposition rate of 0.1 nm s^{-1} and at different substrate temperatures in the same batch: Room temperature (RT), 45, 110 and 155 °C. Substrates were heated for 1 h

before evaporation in order to reach a stable temperature. Heating was kept during the evaporation process (at least 10 min) and after the deposition during 30 min. Then, the heating system was shut down and cooling operated naturally under high-vacuum. It took approximately 2.5 h to cool the substrates down to RT. We checked that PEDOT-PSS coatings on ITO were not affected by the temperature under high-vacuum since the substrate temperature does not exceed 200 °C. Nguyen et al. had already shown that PEDOT-PSS is not affected by such a thermal treatment [14]. The ImPV deposited thickness (50 nm) was monitored using a piezoelectric balance set-up inside the vacuum chamber close to the substrate holder. Thicknesses were subsequently checked using a *Tencor AS-IQ* profilometer.

Bi-layer cathodes of lithium fluoride LiF (~1 nm-thick) and aluminium Al (~55 nm-thick) were then sublimed under vacuum through a shadow mask. All investigated devices have an active area of 10 mm^2. Samples were then stored and characterized under inert atmosphere in a nitrogen glove box (O_2 and H_2O <1 ppm).

Contacts were taken using a prober (*Karl Suss PM5*). Current–voltage–luminance (*I–V–L*) curves were recorded using a *Keithley 2400 Sourcemeter* coupled to a photodiode calibrated with a *Minolta CS-100* luminancemeter. Electroluminescence spectra (EL) were investigated using an *Ocean Optics HR2000* Spectrometer. Atomic force microscopy measurements have been realized on a commercial optical deflection microscope (stand-alone configuration for a large sample, *Dimension 3100 Veeco Instruments* with a *Nanoscope IIIa, Digital Instrument*) operated in ambient conditions. Topographic images were taken in the tapping mode, and commercial silicon cantilever with a nominal radius of 5–10 nm and a spring constant in the range of 20–70 N/m were used. Data were acquired on 1 μm × 1 μm frames having 512 × 512 data points with a scan rate of 1.5 Hz. X-ray data were collected using a curve position sensitive detector *INEL CPS-120* equipped with a Cu K_α ($\lambda = 1.542$ Å) source and a Ge monochromator.

3. Results

3.1. Thin film analysis

AFM has been carried out on ImPV films deposited on silicon wafers (100) at different substrate temperatures. Fig. 2 shows the surface morphology

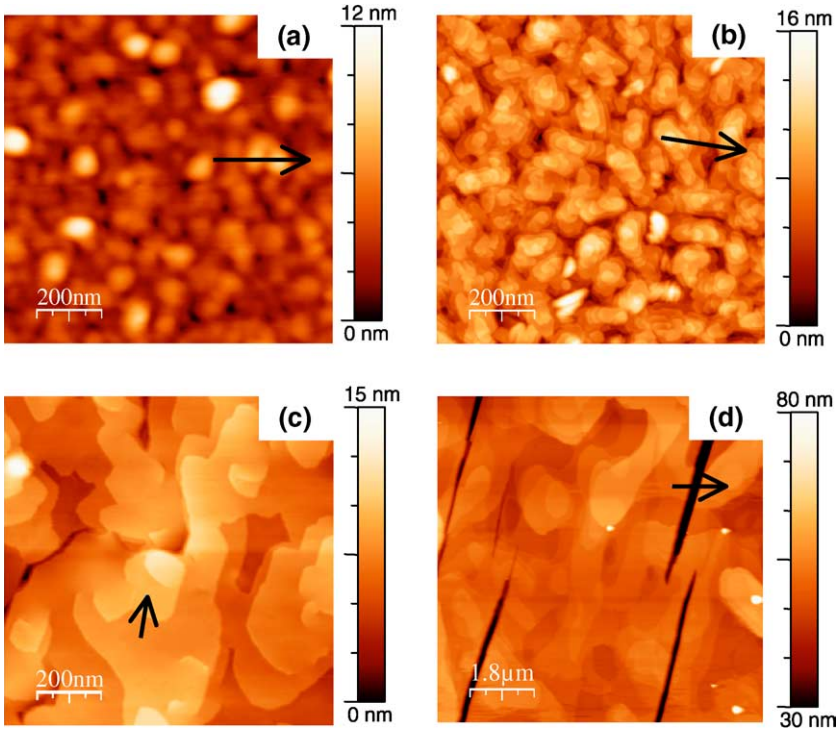

Fig. 2. AFM images of ImPV films deposited on silicon wafers at (a) room temperature, (b) 45 °C, (c) 110 °C and (d) 155 °C. Each arrow refer to profiles in Fig. 3.

of ImPV obtained with substrates at RT, 45, 110 and 155 °C. At RT, an irregular and granular structure is shown. With increasing temperature, the morphology gradually shifts toward a layered structure. Sub-layers are 1.7 nm-thick (Fig. 3c). This value corresponds to a tilted molecule since a single molecule is approximately 2.7 nm-long. At 45 °C, one can note that grain shapes exhibit small steps of 1.7 nm indicating a modified morphology. At 110 °C, the 1.7 nm-thick layers have expanded to form grains of around 1 μm of diameter and at higher temperature (155 °C), non-homogenous films have been obtained. In Fig. 2d, monocrystals of more than 1 μm-large are shown. But, many huge cracks are also observed, even in the middle of crystallites. These cracks are approximately 50 nm-deep, i.e. the layer thickness (Fig. 3d). We suppose that these defaults appeared after the deposition during the cooling step due to the mismatch in thermal expansion coefficients between the Si substrate and the organic semiconductor. Cracks are parallel to each others and parallel to the crystalline planes of silicon substrates. It has been verified that devices based on such crackled layers exhibit poor performances (see Table 1).

This type of morphological transition from grains below 110 °C to lamellae above 110 °C is different from the growth mechanism observed on

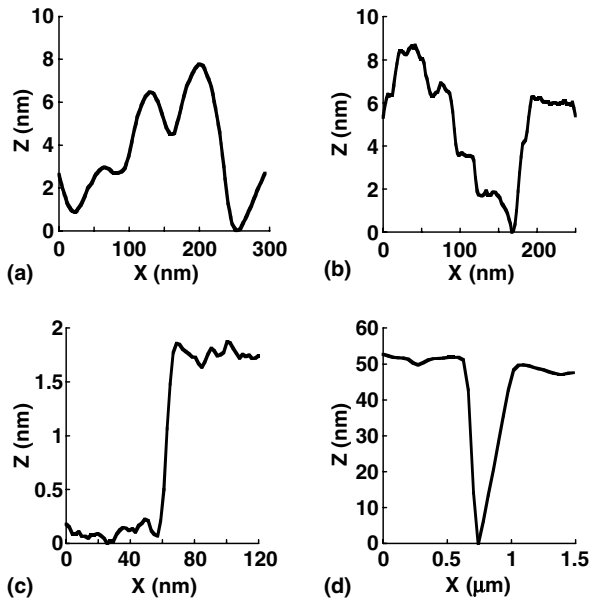

Fig. 3. Typical surface profile taken from the AFM images following the arrows plotted in Fig. 2. Samples: (a) room temperature, (b) 45 °C, (c) 110 °C and (d) 155 °C.

Table 1
Maximum quantum and luminous efficiencies

	Cd/A max	Lm/W max
RT	1.78	0.46
45 °C	1.94	0.48
110 °C	3.09	0.70
155 °C	0.1	0.03

Alq_3 film consisting of amorphous droplets with spherical cap shape growing according to a Capture Zone model (CZ) [11]. But the analogy with the investigation of Biscarini et al. [15,16], dealing with sexithienyl thin films, suggests that ImPV films evolve towards a self-affine topology as the morphology changes from grains to lamellae. This growth mechanism is based on the mobility of the molecules on the surface of the substrate which increases with temperature and on strong intermolecular interaction between ImPV molecules which can reach the terrace edge and be steadily absorbed. This is consistent with the film anisotropy revealed by X-ray diffraction measurements realized on ImPV thin films even at RT. X-ray diffraction patterns of ImPV films on silicon wafers, presented in Fig. 4, suggest a highly uniform out-of-plane lamellar structure with intermolecular period of 17.3 Å ($q = 0.36$ Å^{-1}) whatever the substrate temperature. This value is consistent with the AFM images. A tilt angle of 38.5° can be calculated from the idealized length of 27.8 Å (based on energy minimization using an MM2 force field). Contrary to Alq_3-based reported studies [11], ImPV films are non-amorphous, even at RT. The position of the XRD peaks are the same whatever the temperature which suggests similar molecular arrangements. The only difference lies in a slight narrowing of peaks when heating the substrate at 110 °C resulting in an increase of the crystallite size up to around 1 μm and resulting in a better out-of-plane orientation of crystalline planes. The mosaic angle varies from ~5° at RT to less than 1.5° at 110 °C, showing that in the latter case, the layer is better crystallized with planes parallel to the substrate.

3.2. OLED characterizations

OLEDs present substrate temperature dependent current–voltage–luminance curves (Fig. 5). Operating voltages increase with the substrate temperature while current densities are slightly reduced. As a consequence, quantum efficiencies are improved: a maximum of 3.1 Cd/A is obtained at 110 °C

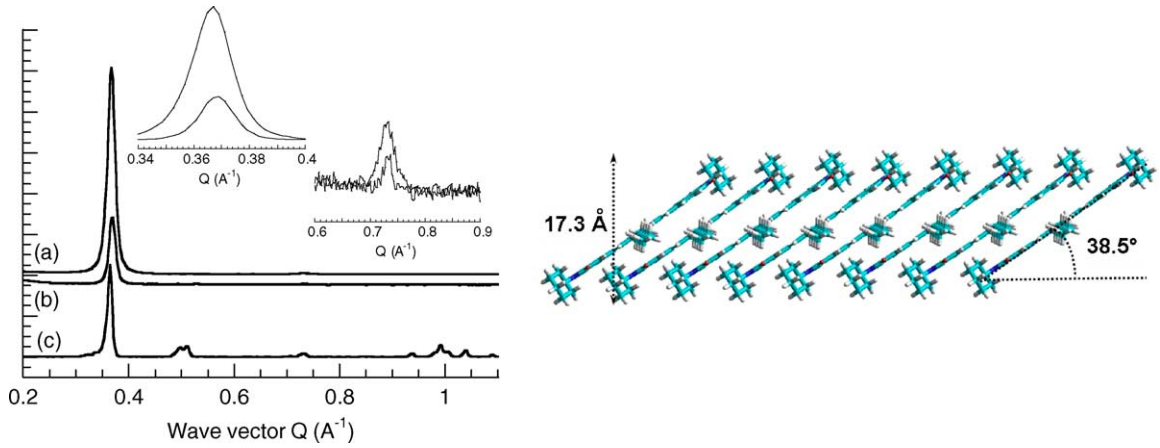

Fig. 4. X-ray diffraction patterns of ImPV films deposited on silicon wafers at (a) room temperature or 45 °C, and at (b) 110 °C. The pattern obtained on ImPV powder is shown on (c). Inset: detailed of the first and second order diffraction peaks corresponding to the lamellar organization. The tilted orientation of ImPV is schematically represented on the right for a single molecular layer.

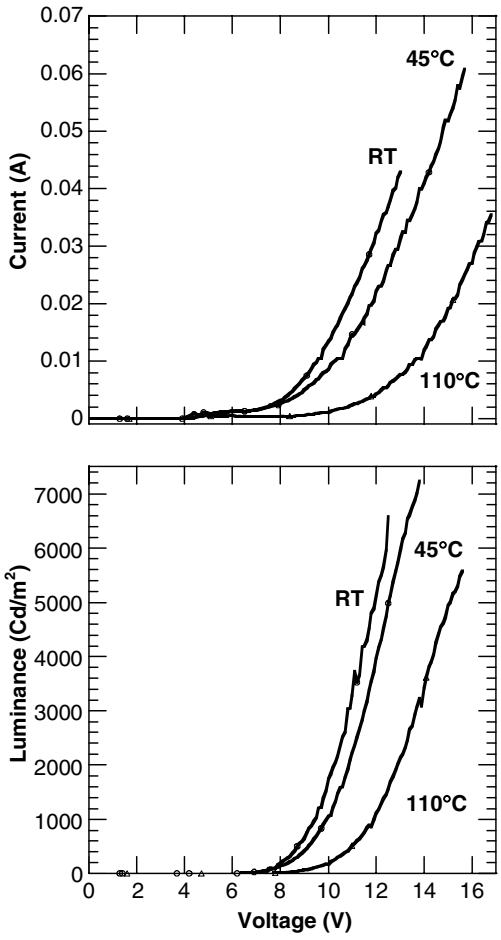

Fig. 5. Effects of substrate temperature on current–voltage–luminance curves of ITO/PEDOT-PSS/ImPV(50 nm)/LiF/Al devices.

whereas RT sample exhibits a maximum of 1.8 Cd/A. In spite of the operating voltage raise, the luminous efficiencies (Table 1), also increase with respect to the substrate temperature upon all the luminance range. The best efficiency is obtained for the 110 °C sample with a maximum of 0.7 lm/W. It corresponds to the most organised film without cracks. In an OLED structure, current direction between electrodes is orthogonal to the substrate. Due to the molecular crystallization (see Fig. 4), the charge carrier flow is perpendicular to the pi-stacking. The mobility is then reduced since electrons and holes have to cross a potential barrier to move layer by layer. Thus, such a film morphology is consistent with a voltage increase due to a charge carrier mobility shrink. The most organised morphology, the less grain boundaries amount, since in layered structure, grain boundaries act as percolation paths. *I–V* curves presented in Fig. 5 clearly show a current drop, at constant voltage, as a function of the substrate temperature which is consistent with a reduction of percolation path density. Moreover, enhanced efficiencies suggest a better exciton confinement in the layered organic film, as in multiple quantum wells inorganic LEDs and/or a reduction of non-radiative recombination centres.

Note that charge carrier mobility in plane directions, i.e. along molecular layers, must be higher due to the pi-stacking. Similar behaviours have already been reported on organic field-effect transistors (OFETs) based on anthracene derivatives [17] or based on different cyclohexyl-substituted molecules [18].

EL spectra of OLEDs made with substrate temperature set at RT, 45 and 110 °C have been recorded under inert atmosphere and at room temperature on devices operated at a constant current density of 100 mA/cm^2 (Fig. 6a). Spectra were found slightly different. The higher the substrate temperature, the higher the amount of light output. This is consistent with the efficiency improvement discussed in the previous paragraph.

The shape of each spectrum is accurately described by the sum of three Gaussian curves. Calculation was performed using a least square minimization fit (Fig. 6b). It corresponds to a vibronic structure as reported in crystallised 3,4,9,10-perylenetetracarboxylic diAnhydride (PTCDA) films [19]. The three main vibronic peaks are labelled 0–0 at 2.42 eV, 0–1 at 2.29 eV and 0–2 at 2.16 eV. These contributions correspond to emissive transitions between the zeroth vibronic level in the excited state and the consecutive levels in the ground state. The energy difference between the successive vibronic peaks is 0.13 eV. The energetic position of each Gaussian curve is independent on the temperature of the substrate whereas the full width at half maximum (FWHM) of each contribution is affected by the substrate temperature. The higher the substrate temperature, the lower the FWHM. Such phenomenon has already been observed on Raman spectra performed on PTCDA films grown at various substrate temperatures [20]. Salvan et al. proposed that the correlation between the FWHM of phonon bands and the structural order is similar to those observed in the case of inorganic semiconductor systems such as gallium arsenide [21]. The decrease in FWHM of the Gaussian peaks is then related to the development of larger and more perfect single crystalline domains. Furthermore, Sauvagol et al. [22] have studied polythiophene derivatives and demonstrated that the crystallinity as well as the presence of defects affect their photoluminescence spectra. They found that the higher the crystallinity the lower the FWHM of PL peaks. It is consistent with the exciton distribution energy narrowing related to a better molecular arrangement [23].

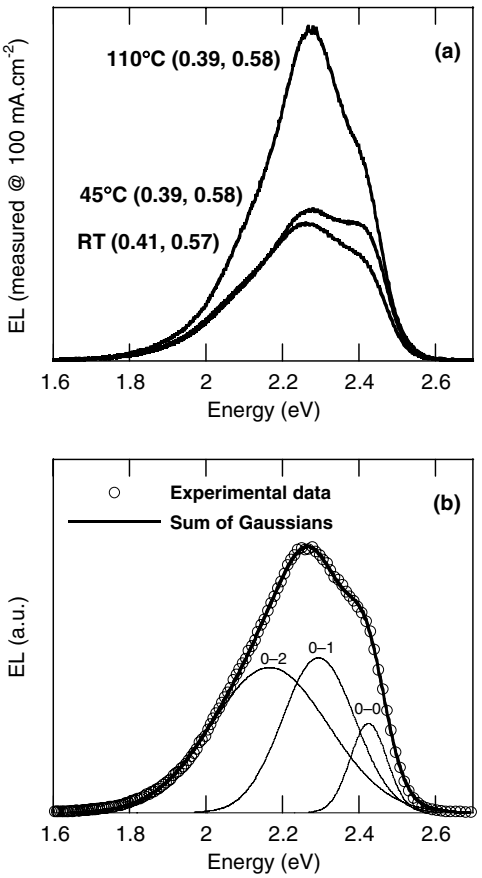

Fig. 6. (a) Electroluminescence spectra of devices made at room temperature, 45 and 110 °C; under brackets are given the related 1964 CIE chromatic coordinates. Spectra are plotted on a scale of light output measured when devices are operated at a constant current density of 100 mA cm^{-2}. (b) Spectrum at RT described as a sum of three Gaussian curves.

Moreover, the amplitude of the 2.29 eV peak clearly increases with the substrate temperature while the two other amplitudes are not significantly affected by the temperature of the substrate. Photoluminescence (PL) spectra have also been measured. A similar substrate temperature-dependence is observed. Further experiments are under investigation to find out the origin of this phenomenon.

4. Conclusion

In summary, single layer OLEDs fabricated by evaporating the organic layer at various substrate temperatures have been demonstrated. The films morphology is found highly dependent on the substrate temperature. Increasing temperature induces a lamellar organization. Each molecular plate is 17.3 Å-thick. A tilted angle of 38.5° has been deduced whatever the temperature of the substrate. The best layered and un-crackled film is obtained at 110 °C and exhibits the best performance, i.e. a luminance efficiency twice higher than the RT sample. The lamellar structure induces a lower charge carrier mobility perpendicular to the wafer. Further

experiments are under investigation to evaluate this mobility as well as the one in the wafer plane which is suspected higher.

This study shows an original approach to enhance performances of OLEDs. We believe that such an approach, applied on multilayer and highly efficient OLEDs, should enable to develop new display solutions. To reach this aim, the use of electron transport layers as well as hole transport layers should be a solution to prevent turn-on voltage increase due to mobility reduction.

Acknowledgements

This research has been made possible by the financial support of French CNRS and Région Aquitaine. We gratefully acknowledge Gilles Ruffié and Serge Destor for their technical contributions in this study. The authors also thank Professor A.S. Barrière for helpful comments.

References

[1] C.W. Tang, S.A. Vanslyke, Appl. Phys. Lett. 51 (1987) 913.
[2] S.R. Forrest, Org. Elec. 4 (2003) 45.
[3] G. Horowitz, Adv. Mater. 10 (1998) 365.
[4] V. Podzorov, E. Menard, A. Borissov, V. Kiryukhin, J.A. Rogers, M.E. Gershenson, Phys. Rev. Lett. 93 (2004) 086602.
[5] F. Cicoira, C. Santato, F. Dinelli, M. Murgia, M.A. Loi, F. Biscarini, R. Zamboni, P. Heremans, M. Muccini, Adv. Funct. Mater. 15 (2005) 375.
[6] S.R. Forrest, Chem. Rev. 97 (1997) 1793.
[7] D.S. Qin, D.C. Li, Y. Wang, J.D. Zhang, Z.Y. Xie, G. Wang, L.X. Wang, D.H. Yan, Appl. Phys. Lett. 78 (2001) 437.
[8] M.Y. Chan, S.L. Lai, F.L. Wong, O. Lengyel, C.S. Lee, S.T. Lee, Chem. Phys. Lett. 371 (2003) 700.
[9] C.Y. Kwong, A.B. Djurisic, V.A.L. Roy, P.T. Lai, W.K. Chan, Thin Solid Films 458 (2004) 281.
[10] A. Hepp, N.v. Malm, R. Schmechel, H.V. Seggern, Synth. Met. 138 (2003) 201.
[11] M. Brinkmann, F. Biscarini, C. Taliani, I. Aielo, M. Ghedini, Phys. Rev. B 61 (2000) R16339.
[12] G. Wantz, L. Hirsch, N. Huby, L. Vignau, J.F. Silvain, A.-S. Barrière, J.-P. Parneix, Thin Solid Films 485 (2005) 247.
[13] A.V. Dijken, A. Perro, E.A. Meulenkamp, K. Brunner, Org. Elec. 4 (2003) 131.
[14] T.P. Nguyen, P. Le Rendu, P.D. Long, S.A. De Vos, Surf. Coat. Technol. 180–181 (2004) 646.
[15] F. Biscarini, R. Zamboni, P. Samori, P. Ostoja, C. Taliani, Phys. Rev. B 52 (1995) 14868.
[16] F. Biscarini, P. Samori, O. Greco, R. Zamboni, Phys. Rev. Lett. 78 (1997) 2389.
[17] H. Meng, F. Sun, M.B. Goldfinger, G.D. Jaycox, Z. Li, W.J. Marschall, G.S. Blackman, J. Am. Chem. Soc. 127 (2005) 2406.
[18] J. Locklin, D. Li, S.C.B. Mannsfeld, E.-J. Borkent, H. Meng, R. Advincula, Z. Bao, J. Am. Chem. Soc. 17 (2005) 3366.
[19] W. Bala, M. Rebarz, P. Dalasinski, A. Bratkowski, Opt. Mater. 28 (2006) 94.
[20] G. Salvan, S. Silaghi, B. Paez, T.U. Kampen, D.R.T. Zahn, Synth. Met. 154 (2005) 165.
[21] P.S. Pizani, F. Lanciotti Jr., R.G. Jasinevicius, J.G. Duduch, A.J.V. Porto, J. Appl. Phys. 87 (2000) 1280.
[22] J.L. Sauvagol, J.P. Lère-Porte, J.J.E. Moreau, in: H.S. Nalwa (Ed.), Conjugated Polymers: Synthesis and Electrical Properties, vol. 2, Wiley, 1997.
[23] S. Tavazzi, M. Campione, M. Laicini, A. Papagni, A. Sassella, P. Spearman, S. Trabattoni, J. Lumin. 112 (2005) 312.

Available online at www.sciencedirect.com
SCIENCE DIRECT®
Organic Electronics 7 (2006) 45–54
Organic Electronics
www.elsevier.com/locate/orgel

A comprehensive study of short channel effects in organic field-effect transistors

Joshua N. Haddock [a], Xiaohong Zhang [a], Shijun Zheng [b], Qing Zhang [b], Seth R. Marder [b], Bernard Kippelen [a,*]

[a] Center for Organic Photonics and Electronics, School of Electrical and Computer Engineering, Georgia Institute of Technology, Atlanta, GA 30332, United States
[b] Center for Organic Photonics and Electronics, School of Chemistry and Biochemistry, Georgia Institute of Technology, Atlanta, GA 30332, United States

Received 22 July 2005; received in revised form 11 November 2005; accepted 17 November 2005
Available online 13 December 2005

Abstract

We present a comprehensive study of short channel effects in organic field-effect transistors by measuring the electrical characteristics of devices with fixed channel width and varying channel length. Our studies are conducted on a hole transport organic semiconductor, *E*,*E*-2,5-bis-{4′-bis-(4″-methoxy-phenyl)amino-styryl}-3,4-ethylenedioxy-thiophene, that is spin-coated from solution to form bottom contact organic field-effect transistors. Drain–source currents from transistors with a channel length of 50 μm show excellent agreement with the square law equations derived for crystalline Si MOSFETs in both the linear and saturation regimes. As the channel length is incrementally reduced to 1 μm, device characteristics such as saturation regime channel conductance, sub-threshold current and threshold voltage, behave in a manner similar to Si MOSFETs of decreasing channel length. Results of these studies indicate the presence of non-destructive current punch-through and in addition, behavior similar to channel-length modulation and threshold-voltage roll-off, neither of which have previously been reported in OFETs.

PACS: 85.30.Tv; 73.61.−r

Keywords: Integrated organic electronics; Thin-film transistors; Short channel effects; Channel-length modulation; Threshold-voltage roll-off; Current punch-through

1. Introduction

As the field of organic electronics matures it will be important to introduce organic based components and circuits to the electrical engineering community in as seamless a manner as possible. This will include reporting performance parameters and figures of merit [1] such that computer models (e.g.

* Corresponding author. Tel.: +1 404 385 5163; fax: +1 404 385 5170.
E-mail addresses: joshua.haddock@gmail.com (J.N. Haddock), Kippelen@ece.gatech.edu (B. Kippelen).

1566-1199/$ - see front matter © 2005 Elsevier B.V. All rights reserved.
doi:10.1016/j.orgel.2005.11.002

SPICE) may be developed to adequately simulate circuits that may be partly or completely comprised of organic electronic components. For organic field-effect transistors (OFETs) to be used in an increasing number of applications, the ability to accurately predict their electrical behavior will be critical.

One aspect of OFET design that needs to be addressed is that of device miniaturization for the purpose of creating organic integrated circuits with increased functionality. Within the field of integrated Si electronics the issues associated with decreasing MOSFET device dimensions can be effectively managed and the devices adequately modeled [2]. However, the behavior of OFETs with small device dimensions has yet to be fully explored and to date, only one analytical model (based on a model developed for α-Si thin-film transistors) has been presented for short channel organic devices [3]. In this work, we present a comprehensive characterization of the effects of reduced channel lengths in OFETs and show that these devices exhibit behaviors similar to those observed in crystalline Si MOSFETs.

2. Short channel inorganic field-effect transistors

Here, we first discuss short channel effects in traditional electronics. Inorganic Si MOSFETs with short channel lengths (L) are desirable for integrated digital logic circuits as they increase both functionality and clock speed by virtue of the fact that both packing density (#/area) and linear regime cut-off frequency (f) scale approximately as $1/L^2$ [4]

$$\text{Area} \propto L^2 \Rightarrow \text{Packing Density} \propto \frac{1}{L^2} \tag{1}$$

$$f = \frac{\mu V_{DS}}{2\pi L^2} \tag{2}$$

where μ is the field-effect mobility and V_{DS} is the drain–source voltage, which in the following will be referred to as the drain voltage. As the degree of integration is increased (L is decreased), it is essential to properly scale other device parameters such as gate oxide thickness (t_{ox}) and substrate doping concentration to maintain predictable long channel behavior [2]. Long channel behavior in the linear (Eq. (3)) and saturation regimes (Eq. (4)) can be described using the square-law equations

$$I_{DS} = \mu C_{ox} \frac{W}{L}\left((V_{GS} - V_T) - \frac{V_{DS}}{2}\right) V_{DS} \tag{3}$$

$$I_{DS} = \mu C_{ox} \frac{W}{2L}(V_{GS} - V_T)^2 \tag{4}$$

where I_{DS} is the drain–source current (or drain current), W is the channel width, C_{ox} is the gate oxide capacitance density (F/cm^2), and V_{GS}, and V_T are the gate–source (or gate), and threshold voltages, respectively. These equations are only valid under the constraints of the gradual-channel approximation which says that the electric field due to the gate voltage at the semiconductor/gate oxide interface is a one-dimensional function of channel position. Physically, the gradual channel approximation requires the gate (transverse) electric field E_{ox} to be much larger than the longitudinal electric field E_{DS}, formed between the source and drain electrodes [2]:

$$E_{ox} >> E_{DS}, \quad E_{ox} = \frac{V_{GS}}{t_{ox}}, \quad E_{DS} = \frac{V_{DS}}{L} \tag{5}$$

If channel lengths are reduced without regard to other device parameters, deviations from ideal long channel behavior are observed; such deviations are commonly referred to as short-channel effects [2,4,5]. As the channel length is decreased, the first short-channel effect to be observed is channel-length modulation. Channel-length modulation is characterized by the inability of the drain current to saturate above pinch-off and is defined by a non-zero channel conductance, g_d, where

$$g_d = \frac{\partial I_{DS}}{\partial V_{DS}} \neq 0 \tag{6}$$

In a device operating above pinch-off, the width of the depletion region surrounding the drain junction becomes comparable to the length of the conducting channel for increasing drain voltage which, in turn, causes a significant reduction in the physical channel length. As the drain current varies inversely with L in saturation (Eq. (4)), a dependence of the drain current on the drain voltage is observed. This dependence can be modeled to a first approximation by adding a term linear in V_{DS} to Eq. (4):

$$I_{DS} = I_{DS(\text{Saturation})}(1 + \lambda V_{DS}) \tag{7}$$

where λ (V^{-1}) is the channel-length modulation parameter. In analogy to bipolar junction transistors an early voltage V_A [4] can be determined from the linear dependence of the drain current in saturation by extrapolating back to a common intercept with the horizontal axis for various values of the gate voltage where,

$$V_A = -\frac{1}{\lambda} \tag{8}$$

For MOSFETs of various channel lengths that exhibit channel-length modulation, values of the early voltage are expected to scale linearly with channel length such that devices with channel lengths L_1, L_2 and associated early voltages $V_{A,1}$, $V_{A,2}$ are generally expected to follow the relation [6]:

$$\frac{L_1}{L_2} = \frac{V_{A,1}}{V_{A,2}} \tag{9}$$

If the channel length is decreased even further the magnitudes of the two electric fields in Eq. (5) become comparable and the resulting field in the channel becomes a two-dimensional function of position; thus the gradual-channel approximation is no longer valid. As a consequence, the depletion regions associated with the source and drain junctions can now occupy a large fraction of the channel and act to deplete it of charge carriers. This reduces the required applied gate voltage to reach inversion and hence lowers the device threshold voltage (V_T) [7]. For such devices the deviation of the threshold voltage from the long channel value (threshold-voltage shift ΔV_T) is inversely proportional to the channel length [8] where:

$$\Delta V_T = V_T(L) - V_{T,\text{Long Channel}} \propto \frac{1}{L} \tag{10}$$

Increased threshold-voltage shift (or threshold-voltage roll-off) ultimately transforms a normally-off (enhancement mode) device into a normally-on (depletion mode) device.

As a consequence of the larger depletion region the surface potential near the source will increase [2]. Below threshold, channel conduction is exponentially dependent upon the magnitude of the surface potential and at short channel lengths the increased sub-threshold current will degrade switching performance [9]. Furthermore, as the size of the depletion regions near source and drain are drain voltage dependent, threshold-voltage roll-off and sub-threshold current will also be functions of the drain voltage [8,10].

Finally, in the limit where the source and drain depletions regions come into contact, a space–charge limited current (SCLC) flows between source and drain. This is referred to as non-destructive punch-through and is similar to the effect observed in bipolar-junction transistors [4].

Elimination of these short-channel effects is most easily accomplished by scaling critical device parameters by a factor κ, such that the magnitudes of the electric fields remain unchanged from the original long-channel device (constant-field scaling) [11]. In constant-field scaling the channel dimensions (W and L), the gate oxide thickness, and the source and drain junction depths are scaled by $1/\kappa$ while the substrate doping concentration scales directly with κ. To maintain the constant field condition, the applied voltages must also be scaled by $1/\kappa$. The resulting device has a threshold voltage that scales as $1/\kappa$ and a cut-off frequency and packing density that scale as κ^2.

The previous analysis of short channel effects in MOSFETs is based on the fact that these devices are fabricated from selectively doped, bulk single crystal Si where p–n junctions (source and drain) and metal-oxide-semiconductor (MOS) capacitor structures (gate) are utilized to modulate the current flowing between source and drain. However, in OFET devices the semiconducting material is typically an intrinsic material deposited as either an amorphous or polycrystalline thin film and while a MOS capacitor structures is present there are no p–n junctions to define the source and drain. Furthermore, as Si is a crystalline material, charge carriers will undergo band type transport whereas in an amorphous/polycrystalline organic materials charge carriers can be subject to an electric field and/or carrier concentration dependent hopping type transport that can add complexity to the modeling of OFETs [12,13]. Despite these differences however, it will be shown that regardless of the semiconductor used and the principle of operation and/or charge transport, short channel effects are common to field-effect devices.

3. Short channel organic field-effect transistors

For organic electronics applications such as low-cost RFID, the issue of circuit integration is just as valid as for inorganic devices as both size and speed will be important. Of more importance, however, is that as the field-effect mobility values in organic materials are orders of magnitude lower than in Si ($\mu \sim 10^3\ \text{cm}^2/\text{Vs}$), organic transistors may be required to go to shorter channel lengths (on the order of 1 μm or less) to provide adequate drive currents while still maintaining relatively small channel widths (Eqs. (3, 4)) [14].

From a material standpoint short channels can also be preferable as many organic thin films tend to be polycrystalline and poor charge transport between adjacent crystalline domains decreases the overall carrier mobility [15,16]. To circumvent the

effects of domain boundaries short channel lengths may be used to bridge single crystal domains [17]. Efforts to fabricate short channel length OFETs have resulted in devices with non-zero channel conductance above pinch-off and increased, drain voltage dependent, sub-threshold current. Klauk et al. reported a channel length dependent threshold voltage [18] but large device-to-device variations made it unclear as to if a strict $1/L$ dependence was followed.

Short channel effects have been reported in polymers [19–22] and small molecules [23] processed from solution as well as in vacuum deposited small molecules [3,24]. In two separate cases OFETs fabricated using the same material, dihexylquarterthiophene (DH4T), were shown to exhibit short channel effects when the organic was processed either from solution [23] or by vacuum sublimation [24].

In this work, we present the characterization of solution processed hole transport OFETs with a fixed channel width of 500 μm but of varying channel lengths between 50 μm and 1 μm. OFETs with long channel lengths show typical transistor behavior whose output characteristics are well described using the square-law equations (Eq. (3)). As the channel length is reduced the various short-channel effects outlined above are observed and are found to behave in a manner similar to that of crystalline Si MOSFETs. To the best of our knowledge, these results represent the most comprehensive characterization of short-channel effects in OFETs to date.

4. Experimental

Transistors were fabricated on heavily n-doped silicon substrates (resistivity 0.005 Ω cm), which acted as the gate electrode with 200 nm of thermally grown oxide (SiO_x, $\varepsilon_r = 3.9$) as the gate dielectric. Interdigitated, bottom contact source and drain electrodes (e-beam evaporated Ti/Au, 10 nm/100 nm) with a channel width of 500 μm and channel lengths of 1, 2, 3, 4, 5, 10, 20 and 50 μm were fabricated on the oxide surface using lift-off photolithography (Fig. 1). The devices were fabricated with a common source, but individual drains. An external, common gate contact of e-beam evaporated Ti/Au (10 nm/100 nm) was deposited on the backside of the substrate. The organic semiconductor *E*,*E*-2,5-bis-{4′-bis-(4″-methoxy-phenyl)amino-styryl}-3,4-ethylenedioxy-thiophene (Fig. 2) was synthesized and cyclic-voltammetry measurements

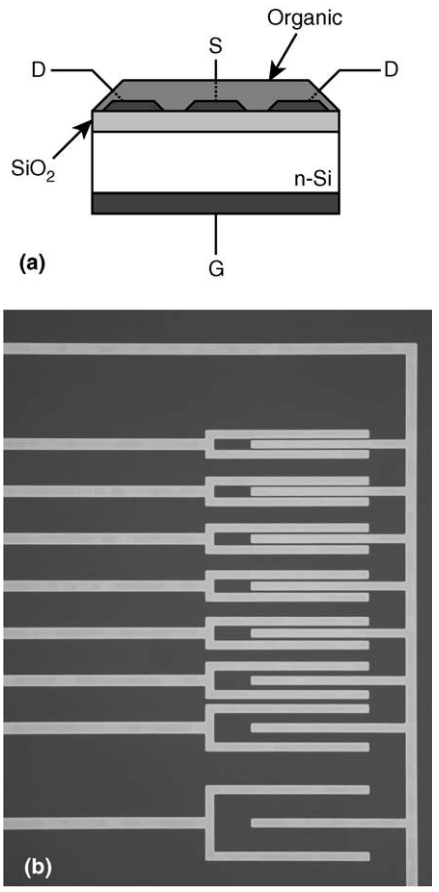

Fig. 1. Cross section (a) and micro photograph (b) of the OFET device geometry indicating the common source (S), individual drain (D), and common gate (G) electrodes.

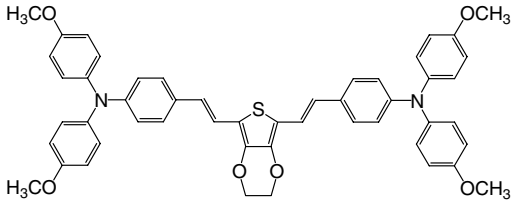

Fig. 2. Chemical structure of *E*,*E*-2,5-bis-{4′-bis-(4″-methoxy-phenyl)amino-styryl}-3,4-ethylenedioxy-thiophene.

using Cp_2Co^+/Cp_2Co as an internal reference in CH_2Cl_2 show the compound is easily oxidized with an oxidation potential of 0.02 V vs. Fc^+/Fc. From this, an ionization potential (HOMO) of approximately 5.2 eV can be estimated, indicating a low barrier for charge injection into the Au source and drain electrodes (work function approximately 5.1 eV [3]). Films of the compound were processed from solution in a nitrogen glove box (O_2, $H_2O < 1$ ppm) by dissolving the compound in

toluene at 20 mg/mL and spin coating over the source and drain electrodes to a thickness of 60 nm.

Fully fabricated devices were transferred in an air-tight vessel to a second nitrogen glove box (O_2, $H_2O < 0.1$ ppm) for electrical characterization. During testing electrical connections were made with a micro-probe station contained within the glove box and an Agilent E5272A medium power source/monitor unit, connected to the probe station, was used to perform the electrical measurements. At no point during and after spin coating of the organic layer were the devices exposed to air. For each device, output characteristics (I_{DS} vs. V_{DS} at multiple, discrete V_{GS} values) were measured for $0\ V > V_{DS}$, $V_{GS} > -60$ V. Transfer characteristics (I_{DS} vs. V_{GS} at discrete V_{DS} values) were also measured for $20\ V > V_{GS} > -60$ V at $V_{DS} = -20$, -40 and -60 V. From the transfer characteristics, linear fits to plots of $\sqrt{I_{DS}}$ vs. V_{GS} allowed extraction of threshold voltages and field-effect mobilities according to Eq. (4). Field-effect mobilities were also calculated from linear fits to the output characteristics at low V_{DS} by use of Eq. (3) for different values of the gate voltage.

5. Results and discussion

Transfer characteristics for the 50 μm channel length device are shown in Fig. 3. This hole transport device operated in enhancement mode with a threshold voltage of -3.8 V. The extracted field-effect mobility in the saturation regime was approximately 10^{-4} cm^2/Vs. In part, due to this low value, the on/off current ratio was kept to between 10^3 and

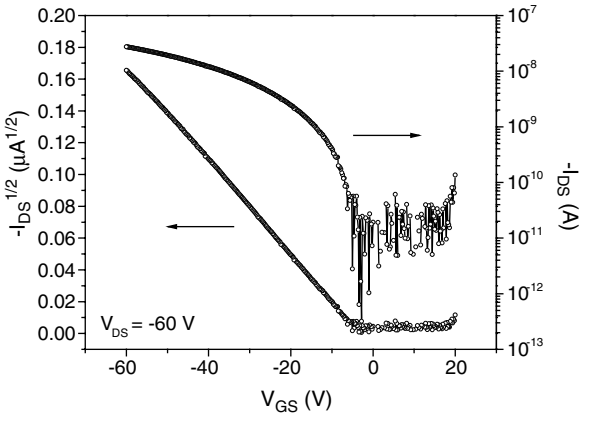

Fig. 3. Transfer characteristics for the 50 μm channel length device.

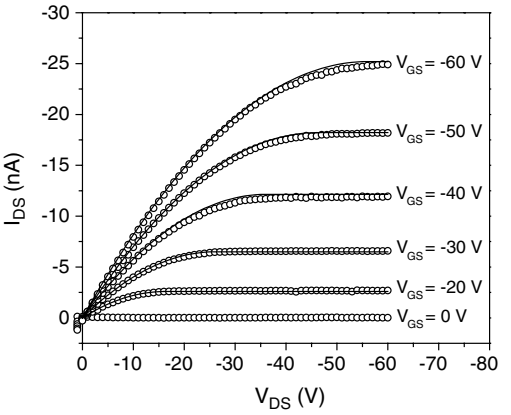

Fig. 4. Experimental output characteristics (circles) for the 50 μm channel length device fitted to the square-law equations using values of the field-effect mobility extracted in the linear regime at each value of the gate voltage.

10^4. Output characteristics for several gate voltage values are shown in Fig. 4 and show ohmic behavior at low drain voltages and drain current saturation above the pinch-off point. The data has been fitted to the square-law equations in both the linear (Eq. (3)) and saturation (Eq. (4)) regimes using the appropriate device dimensions and gate dielectric parameters, as well as the threshold voltage extracted from the transfer characteristic. To accurately fit the data to the square-law equations a gate voltage dependent mobility value had to be implemented as the single saturation regime value from the transfer characteristics tended to overestimate currents for gate voltages less than -30 V. Mobility as a function of the gate voltage was continuously determined from the slope of a fourth-order polynomial that was fitted to the transfer characteristic above threshold; but these values tended to underestimate currents for gate voltages less than -30 V. However, field-effect mobility values extracted from the linear region of the output characteristics at the various gate voltages using Eq. (3) yielded the fits shown in Fig. 4. No additional fitting parameters were used and the value of the field-effect mobility that was extracted in the linear regime was used in both the linear and saturation regime equations. Output characteristics for the device with the 20 μm channel length show similar ohmic behavior at low drain voltages and drain current saturation above pinch-off.

For the 10 μm channel length device we begin to see a lack of saturation above pinch-off and for the 5 μm channel length device the effect becomes quite

pronounced (Fig. 5). Using techniques similar to those used for the 50 μm channel length device, the square-law equations are plotted and while the agreement with the experimental data is good at low drain voltages it begins to break down as the pinch-off point is approached. Above pinch-off there is no agreement between experiment and theory and the current becomes linearly dependent on the drain voltage. This effect is observed to an increasing degree for shorter channel lengths down to 3 μm and is suggestive of channel-length modulation. For devices with channel lengths between 10 μm and 3 μm, early voltages were extracted for output characteristics with gate voltages between −10 V and −30 V and their values averaged. As shown in Fig. 6 the early voltages do scale linearly with channel length. It should be noted, however, that while the plots in Fig. 6 exhibit a linear dependence, the correlation between channel length and early voltage as predicted by Eq. (9) was not observed.

For channel lengths less than 3 μm the drain current above pinch-off begins to exhibit diode-like behavior suggestive of non-destructive current punch-through as shown in Fig. 7 for the 1 μm channel length device. In Si MOSFETs punch-through current is space–charge limited and expected to be quadratic with drain voltage. In a thin film with coplanar electrodes (similar to our OFET geometry, Fig. 1) this behavior is also expected and the space–charge limited current density J_{SC} is given by

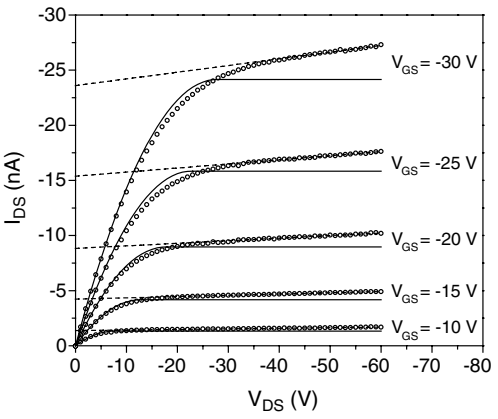

Fig. 5. Experimental output characteristics (circles) for the 5 μm channel length device at various gate voltages. The square-law equations (solid lines plotted using values of the field-effect mobility extracted in the linear regime) and linear fits to the data above pinch off (dashed lines) are also shown.

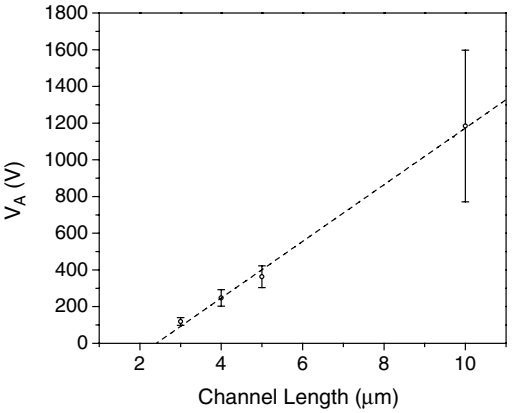

Fig. 6. Average values of the early voltage (and a linear fit) as a function of channel length for 3 μm ⩽ L ⩽ 10 μm. The error bars indicate the standard deviation due to a dependence on the gate voltage.

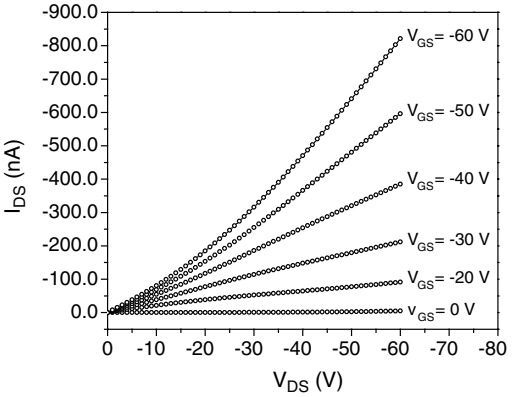

Fig. 7. Experimental output characteristics for the 1 μm channel length device at various gate voltages.

$$J_{SC} = \frac{I_{DS}}{W} = -0.57\varepsilon\mu\left(\frac{V_{DS}}{L}\right)^2 \tag{11}$$

where ε is the dielectric constant of the conductive/semiconductive material [25]. Space–charge limited punch-through currents in short channel OFETs have been observed previously by Austin and Chou [19], and by Chabinyc et al., whose results were found to agree well with Eq. (11) [20]. In their analysis, Austin and Chou plot drain current density as a function of longitudinal electric field (V_{DS}/L) for poly(3-hexylthiophene) OFETs on a log–log scale for channel lengths down to 70 nm. For the 70 nm channel length device at applied fields < 10 V/μm the response is ohmic but for applied fields between

10 V/μm and 100 V/μm, the drain current is found to follow the general SCLC relation

$$I_{DS} \propto V_{DS}^{n} \tag{12}$$

where $n \geqslant 2$ indicates operation in the SCLC regime. In the case of Austin and Chou $n = 2.4$, a good indicator of SCLC operation. A similar analysis for our 1 μm channel length device (Fig. 8) also results in ohmic behavior for applied fields < 10 V/μm ($n = 1.00$). However, for applied fields between 10 V/μm and 100 V/μm we find $n = 1.38$, suggesting that for our materials in this range of applied fields, the drain current is not space–charge limited as described by Eqs. (11) and (12). For comparison, Fig. 8 also shows plots of the drain current densities for the devices with 50 μm and 5 μm channel lengths which show saturation and channel length modulation behavior, respectively.

Over the entire range of channel lengths studied the sub-threshold current has also been found to behave in a manner similar to that of Si MOSFETs. For the long (50 μm) channel length device we observe sub-threshold currents that are independent of the drain voltage bias (Fig. 9a). At the shortest channel length of 1 μm the sub-threshold currents are higher than in the long channel device and are now drain voltage dependent (Fig. 9b). From Fig. 9c the increase of current and drain voltage dependence from the device with the longest to the device with the shortest channel length is readily apparent.

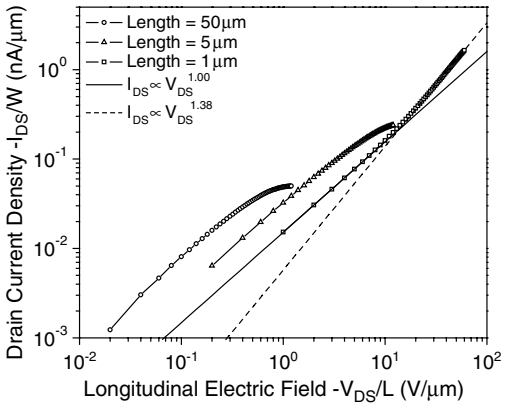

Fig. 8. Drain current density as a function of longitudinal electric field for the 50, 5 and 1 μm channel length devices. In all cases $V_{GS} = -60$ V.

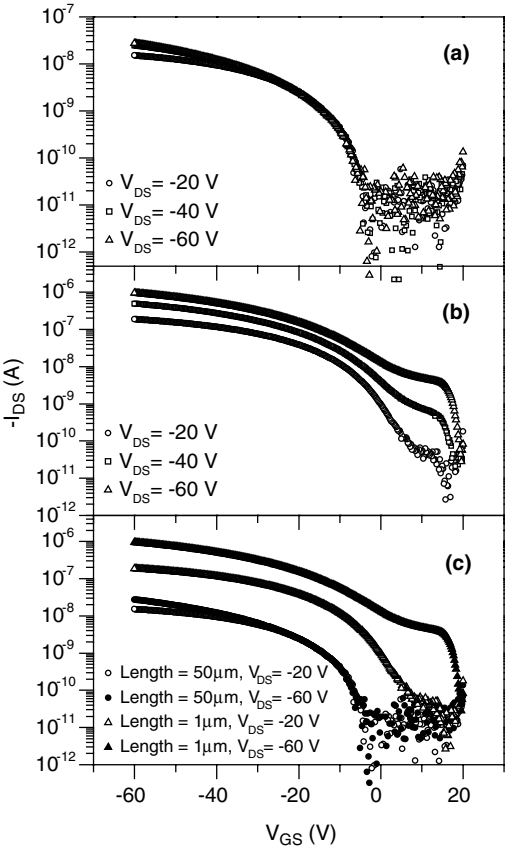

Fig. 9. Transfer characteristics for the 50 μm channel length device (a), 1 μm channel length device (b), and the 50 μm and 1 μm device plotted together (c), all at different drain voltages.

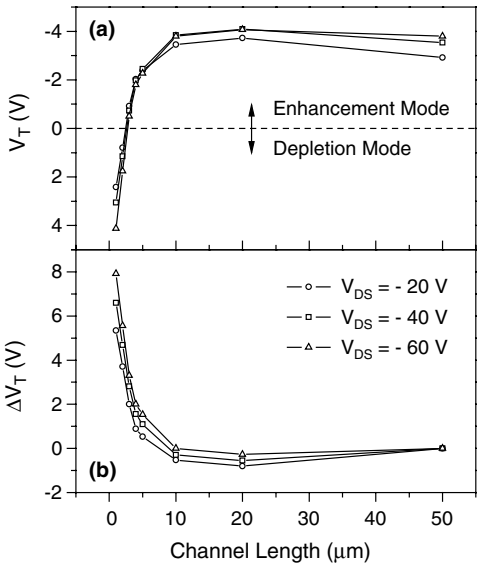

Fig. 10. Threshold voltage (a), and threshold voltage shift (b), as a function of channel length for three values of the drain voltage.

The data in Fig. 9 also shows a shift from enhancement mode to depletion mode operation ($|I_{DS}| > 0$ for positive V_{GS} in hole transport materials). Threshold voltages as a function of channel length (Fig. 10a) confirm the switch from enhancement mode to depletion mode operation for channel lengths < 3 μm. A plot of the threshold voltage shift as a function of both channel length and drain voltage (Fig. 10b) show the expected $1/L$ roll-off behavior and drain voltage dependence observed in Si devices.

As stated previously, elimination of short-channel effects is realized by making the transverse electric field much larger than the longitudinal electric field. For OFETs incorporating a given gate insulator material this can be accomplished by reducing the thickness of the insulator. Studies on vacuum deposited DH4T devices with severe short-channel effects have shown that long-channel operation can be regained by reducing the thickness of the gate insulator [24]. Work with ultra-thin (< 5 nm) gate insulators fabricated from organic self-assembled mono-layers (SAMs) has shown to reduce operating voltages for long-channel behavior to below 5 V [26,27] and holds promise for enabling the shortest possible channel lengths.

The degree to which the channel length of OFETs can be miniaturized depends on several factors such as the resolution of the electrode fabrication process, the thinnest employable gate insulator and more importantly, the semiconducting material and the degree to which the transverse electric field must exceed the longitudinal field. For Si MOSFETs an empirical relation exists that will determine the minimum channel length for long channel behavior based on oxide thickness and the junction depth and depletion region width of the source and drain [28]. Such a relation does not exist yet for OFETs, neither in general nor for any particular material/device geometry configuration. In surveying the literature it appears that there is some degree of variation in the conditions required for long channel and short channel behavior. Table 1 lists the material/deposition technique, gate insulator material and thickness (t), channel length (L), ratio of channel length to gate insulator thickness (L/t), and maximum longitudinal electric field ($E_{DS} = V_{DS}/L$) for semiconductor/gate insulator combinations that have shown previously both long channel and short channel behavior, as well as devices with physically short channel lengths ($L \leqslant 1$ μm) that exhibit long channel behavior. The examples are grouped in terms of channel length ($L > 1$ μm or $L \leqslant 1$ μm) for observed long channel behavior. Short channel behavior is observed for channel lengths ranging over two orders of magnitude and is generally characterized by $L/t < 20$ and longitudinal electric fields > 10 V/μm. Long channel behavior is somewhat less straight forward. For channel lengths > 1 μm long channel behavior is generally observed for devices

Table 1
Literature survey of OFETs that exhibit both long channel and short channel behavior as well as OFETs with channel lengths $\leqslant 1$ μm that exhibit long channel behavior

Ref.	Material/deposition	Long channel behavior				Short channel behavior			
		Insulator/t (nm)	L (μm)	L/t	Max E_{DS} (V/μm)	Insulator/t (nm)	L (μm)	L/t	Max E_{DS} (V/μm)
$L > 1$ μm									
[32]	Pentacene/vacuum	SiO_x/300	250.0	833.3	0.4	SiN_x/26	0.150	5.8	13.3
	This work	SiO_x/200	500.0	250.0	1.2	SiO_x/200	1.0	5.0	60.0
[22]	MEH-PPV/spin coat	SiO_x/100	12.0	120.0	1.3	SiO_x/100	0.5	5.0	10.0
[3]	α-6 T/vacuum	SiO_x/300	25.0	83.3	4.0	SiO_x/300	1.5	5.0	66.7
[24]	DH4T/vacuum	SiO_x/30	2.0	66.7	5.0	SiO_x/100	0.05	0.5	200.0
[21]	PT/spin coat	SiO_x/250	7.0	28.0	5.7	SiO_x/250	1.0	4.0	40.0
[33]	α-6 T/vacuum	SiO_x/300	12.0	40.0	8.3	SiO_x/300	1.5	5.0	66.7
$L \leqslant 1$ μm									
[19]	P3HT/spin coat	SiO_x/5	1.0	200.0	3.0	SiO_x/5	0.07	14.0	42.9
[26]	α-6 T/vacuum	SAM/3	0.5	166.7	4.0	SAM/3	0.03	10.0	50.0
[34]	P3HT/spin coat	SiO_x/30	0.88	29.3	5.7				
[29]	Pentacene/vacuum	SiO_x/150	1.0	6.7	20.0				
[31]	F_{16}CuPc & α-6 T/vacuum	SiO_x/20	0.1	5.0	50.0				
[30]	Pentacene/vacuum	SiO_x/30	0.03	1.0	66.7				

where $L/t > 20$ and for longitudinal electric fields $<$ 10 V/μm. When channel lengths drop below 1 μm these conditions apply in some cases but for others, long channel behavior is exhibited in devices where L/t and E_{DS} are more indicative of short channel behavior [29–31]. Zhang et al. [30] demonstrate a device for which $L/t = 1$ (transverse and longitudinal electric fields equal when $V_{DS} = V_{GS}$) where their output characteristics saturate fairly well (slight channel-length modulation appears possible), with no indication of non-destructive punch-through. While the results in Table 1 suggest general guidelines for designing OFETs with short physical channel lengths there is significant variation to warrant that for a given organic semiconductor in a given device geometry, the presence of short channel effects has to be confirmed experimentally.

6. Conclusion

In an effort to better characterize short channel effects in OFETs a novel, solution processed, hole transport semiconductor was used to fabricate devices with fixed channel width but varying channel length between 50 μm and 1 μm. Behavior of the long channel length devices was as expected and in excellent agreement with the square law relations. As the channel length was reduced, the devices exhibited behaviors similar to those observed in short channel Si MOSFETs; despite the fact that the physics of charge transport and device operation are different in the organic case. A comparison of other reports of short channel effects in OFETs indicates that in many instances, certain quantities such as the ratio of the channel length to the gate insulator thickness and the maximum longitudinal electric field may be used to predict the conditions necessary to induce short channel effects. However, in some instances these quantities are not accurate indicators and suggest that further studies will be required to gain a better understanding of the physical origin of short-channel effects in OFETs.

Acknowledgements

This material is based upon work supported in part by the STC Program of the National Science Foundation under Contract No. DMR-0120967, by the Office of Naval Research, by an NSF ECS program, an NSF NIRT program, and by an NSF CAREER program (B.K.).

References

[1] IEEE Standard Test Methods for the Characterization of Organic Transistors and Materials, IEEE Std. 1620-2004.
[2] Y. Tsividis, Operation and Modeling of The MOS Transistor, second ed., Oxford University Press, New York, 1999.
[3] L. Torsi, A. Dodabalapur, H.E. Katz, J. Appl. Phys. 78 (1995) 1088.
[4] S.M. Sze, Physics of Semiconductor Devices, second ed., John Wiley & Sons, New York, 1981.
[5] R.F. Pierret, Semiconductor Device Fundamentals, Addison-Wesley, Reading, 1996.
[6] A.S. Sedra, K.C. Smith, Microelectronic Circuits, Oxford University Press, New York, 1998.
[7] L.D. Yau, Solid State Electron. 17 (1974) 1059.
[8] W. Fitchner, H.W. Pötzl, Int. J. Elec. 46 (1979) 33.
[9] M.B. Barron, Solid State Electron. 15 (1972) 293.
[10] R.R. Troutman, A.G. Fortino, IEEE Trans. Electron. Dev. ED-24 (1977) 1266.
[11] R.H. Dennard, F.H. Gaensslen, H.N. Yu, V.L. Rideout, E. Bassouts, A.R. LeBlanc, IEEE J. Solid State Circ. SC-9 (1974) 256.
[12] G. Horowitz, Physics of organic field-effect transistors, in: G. Hadziioannou, P.F. van Hutten (Eds.), Semiconducting Polymers, Wiley-VCH, Weinheim, 2000, pp. 463–514.
[13] O. Katz, Y. Roichman, G. Bahir, N. Tessler, J. Salzman, Semicond. Sci. Technol. 20 (2005) 90.
[14] C.D. Dimitrakopoulos, P.R.L. Malenfant, Adv. Mater. 14 (2002) 99.
[15] A.B. Chwang, C.D. Frisbie, J. Appl. Phys. 90 (2001) 1342.
[16] G. Horowitz, J. Mater. Res. 19 (2004) 1946.
[17] E.L. Granstrom, C.D. Frisbie, J. Phys. Chem. B 103 (1999) 8842.
[18] H. Klauk, G. Schmid, W. Radlik, W. Weber, L. Zhou, C.D. Sheraw, J.A. Nichols, T.N. Jackson, Solid State Electron. 47 (2003) 297.
[19] M.D. Austin, S.Y. Chou, Appl. Phys. Lett. 81 (2002) 4431.
[20] M.L. Chabinyc, J.P. Lu, R.A. Street, Y. Wu, P. Liu, B.S. Ong, J. Appl. Phys. 96 (2004) 2063.
[21] Y. Xu, P.R. Berger, J. Appl. Phys. 95 (2004) 1497.
[22] Y. Chen, W.W. Zhu, S. Xiao, I. Shih, J. Vac. Sci. Technol. 22 (2004) 768.
[23] A.P. Kam, J. Seekamp, V. Solovyev, C.C. Cedeño, A. Goldschmidt, C.M.S. Torres, Microelectron. Eng. 73–74 (2004) 809.
[24] M. Leufgen, U. Bass, T. Muck, T. Borzenko, G. Schmidt, J. Geurts, V. Wagner, L.W. Molenkamp, Synth. Met. 146 (2004) 341.
[25] A.A. Grinberg, S. Luryi, M.R. Pinto, N.L. Schryer, IEEE Trans. Electron. Dev. 36 (1989) 1162.
[26] J. Collet, O. Tharaud, A. Chapoton, D. Vuillaume, Appl. Phys. Lett. 76 (2000) 1941.
[27] M. Halik, H. Klauk, U. Zschieschang, G. Schmid, C. Dehm, M. Schütz, S. Maisch, F. Effenberger, M. Brunnbauer, F. Stellacci, Nature 431 (2004) 963.
[28] J.R. Brews, W. Fitchner, E.H. Nicollian, S.M. Sze, IEEE Electron Dev. Lett. ED-1 (1980) 2.
[29] C. Pannemann, T. Diekmann, U. Hilleringmann, Microelectron. Eng. 67–68 (2003) 845.
[30] Y. Zhang, J.R. Petta, S. Ambily, Y. Shen, D.C. Ralph, G.G. Malliaras, Adv. Mater. 15 (2003) 1632.

[31] J.A. Rogers, A. Dodabalapur, Z. Bao, H.E. Katz, Appl. Phys. Lett. 75 (1999) 1010.
[32] J. Zaumseil, T. Someya, Z. Bao, Y.L. Loo, R. Cirelli, J.A. Rogers, Appl. Phys. Lett. 82 (2003) 793.
[33] L. Torsi, A. Dodabalapur, L.J. Rothberg, A.W.P. Fung, H.E. Katz, Phys. Rev. B 57 (1998) 2271.
[34] S. Scheinert, T. Doll, A. Scherer, G. Paasch, I. Hörselmann, Appl. Phys. Lett. 84 (2004) 4427.

Available online at www.sciencedirect.com
SCIENCE DIRECT®
Organic Electronics 7 (2006) 55–59
Organic Electronics
www.elsevier.com/locate/orgel

Letter

3,4-Diphenylmaleimide-thiophene-fluorene copolymers for polymeric orange–red light-emitting diodes

Li-Hsin Chan [a,b], Yu-Der Lee [a,*], Chin-Ti Chen [b,*]

[a] *Department of Chemical Engineering, National Tsing Hua University, Hsinchu 30013, Taiwan*
[b] *Institute of Chemistry, Academia Sinica, Taipei 11529, Taiwan*

Received 25 August 2005; received in revised form 2 December 2005; accepted 5 December 2005
Available online 27 December 2005

Abstract

Fluorescent copolymers based on 3,4-diphenylmaleimide-thiophene-fluorene triad were newly synthesized and characterized. The copolymers exhibited orange–red fluorescence (λ_{max}^{em} in the range of 598–620 nm) with fluorescence quantum yields of 32–37% in solution and of 13–22% in solid film. Polymer light-emitting diodes with simple device structure of ITO/PDOT:PSS/copolymers/LiF/Al, where PEDOT:PSS is (poly-ethylenedioxythiophene):poly(styrene sulfonate), were preliminarily fabricated and tested. Similar color to solution photoluminescence, the devices showed orange–red electroluminescence with a maximum electroluminance of 2020 cd/m^2 and peak efficiency of 1.25 cd/A.

Keywords: Polymer light-emitting diodes (PLEDs); Orange–red; Maleimide; Thiophene; Fluorene

We have recently reported *N*-methyl-3,4-bis(4-(*N*-(1-naphthyl)phenylamino)phenyl) maleimide as a novel red emitter in the fabrication of rare non-doped red organic light-emitting diodes (OLEDs) [1]. The precursor used in the preparation of the maleimide is a dibromo-substituted species, *N*-methyl derivative of 3,4-bis(4-bromophenyl)-maleimide, BrML (Scheme 1), which is readily synthesized in two-step from commercially available 4-bromophenylacetonitrile [1,2]. This is an ideal monomer in synthesizing high molecular weight polyarylenes through various type of polycondensation. About half a dozen of reports taking a good utilization of different alkyl derivatives of BrML in the preparation of 3,4-diphenylmaleimide-based polyaryl macromolecules have illustrated this point [3]. However, only yellow to orange fluorescent polymers derived from maleimides have been known thus far. Due to the low fluorescence quantum yields ($\phi^f s$) in the solid state arising from the formation of aggregation of red light-emitting polymeric materials, red polymer light-emitting diodes (PLEDs) show high efficiency and brightness are scarce [4]. Therefore, efficient and bright red polymeric light-emitting materials remain rather challenging and highly desired. In the design of long wavelength emissive copolymers, there are about a handful number of fluorene copolymers using "low-band-gap" approach [4]. Here we report a new type of orange–red light-emitting polymeric

* Corresponding authors. Tel.: +886 2 27898542; fax: +886 2 27831237 (C.-T. Chen).
E-mail address: cchen@chem.sinica.edu.tw (C.-T. Chen).

1566-1199/$ - see front matter © 2005 Elsevier B.V. All rights reserved.
doi:10.1016/j.orgel.2005.12.003

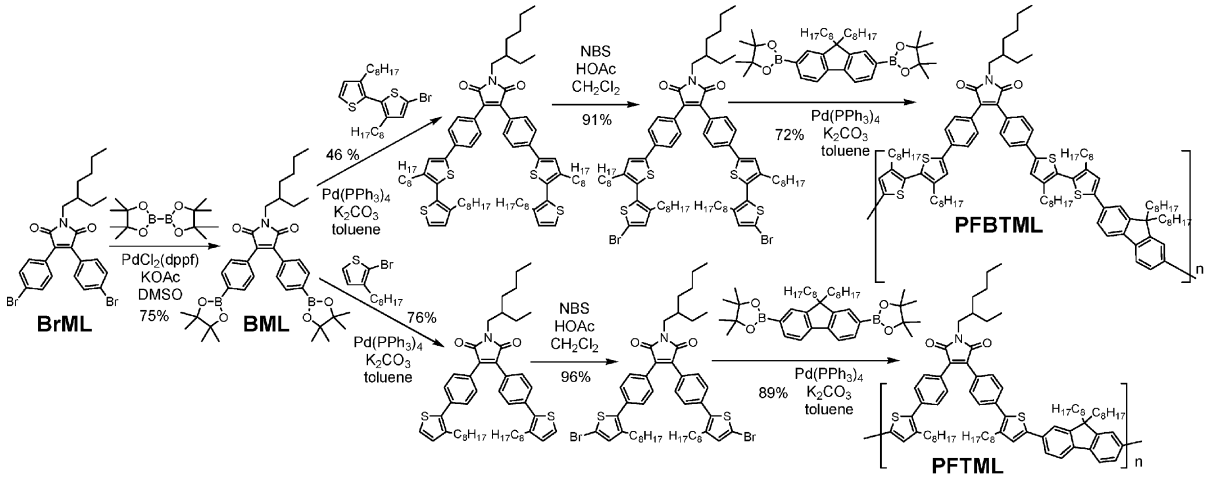

Scheme 1. Chemical synthesis of the copolymers of PFBTML and PFTML.

materials, copolymers of fluorene-thiophene-maleimide triads, PFTML and PFBTML (Scheme 1). The structural difference between two copolymers is just the number of thiophene ring of the triad. For PFTML and PFBTML, thiophene-maleimide-thiophene (donor–acceptor–donor) is the key "low-band-gap" moiety that emits orange to red fluorescence. Both copolymers behave reasonably well in terms of fluorescence color and intensity in solid state as well as PLED performance.

PFTML and PFBTML were readily prepared in a similar fashion via facile Suzuki cross-coupling between 2,7-bis(4,4,5,5-tetramethyl-1,3,2-dioxaborolan-2-yl)-9,9-dioctylfluorene and bromothiophene or bromobithiophene-substituted 3,4-diphenylmaleimide (Scheme 1). Both maleimide-thiophene brominated derivatives were obtained by the NBS (*N*-bromosuccinimide) bromination in high yields. Bisboron ester-substituted maleimide, BML, served as the common starting material that was easily converted from BrML by reacting with bis(pinacolato) diboron catalyzed by home made $PdCl_2$(dppf) (dppf = 1,1′-bis(diphenylphosphino)ferrocene). Both 2-bromo-3-octylthiophene and 5-bromo-3,3′-dioctylbithiophene were another two key starting materials, They were synthesized by controlled monobromination of known 3-octylthiophene and 3,3′-dioctylbithiophene, respectively, with NBS. Both copolymers and their monomeric intermediate compounds were characterized with elemental analysis and $^1H/^{13}C$ NMR (see supporting information). Their molecular weights were determined by gel permeation chromatography using polystyrene in THF as standard. These copolymers have weight-average molecular weights (M_w) of 20,500 or 34,000 and M_w/M_n (PDI) of 1.78 or 1.98, respectively (Table 1). Although copolymers have extended-conjugation along the rigid polymer backbone, many aliphatic long alkyl substituents (2-ethylhexyl and *n*-octyl) render both copolymers highly soluble in most common organic solvents, such as toluene, dichloromethane, and THF. However, the same reason also takes toll on the rigidity of the copolymer resulting relatively low glass transition temperatures (T_gs) of 75 and 112 °C.

The redox behaviors of the copolymers were investigated by cyclic voltammetry. The results are summarized in Table 1. From the oxidation potential relative to ferrocene/ferrocenenium one, which can correspond to 4.8 eV for ferrocene below the vacuum level), [5] and the onset energy estimated from UV–visible absorption spectra (Fig. 1), we can approximately calculate the HOMO and LUMO energy levels of two copolymers. As anticipated, whereas LUMO levels are about the same, PFBTML has 0.05 eV higher HOMO level than PFTML. This is logical because the electron-deficient maleimide moiety is the common site most susceptible to be reduced. The redox potential is also consistent with the most susceptible to be oxidized is the electron-rich thiophene rings and two thiophene rings of PFBTML pushing HOMO level higher than the single thiophene ring of PFTML. Therefore, both copolymers emit orange to red fluorescence in solution and solid state, but PFBTML has a redder fluorescence than PFTML in both solution and solid film. Interestingly, only limited solvatochromically red-shifting (less than 20 nm

Table 1
Physical data of PFTML and PFBTM and their PLED[a] characteristics

	M_w	M_n	PDI	T_g, T_d[b] (°C, °C)	E_{ox}, E_{red}[c] (mV, mV)	HOMO, LUMO (eV, eV)	Peak L (cd/m^2)	L and V[d] (cd/m^2, V)	Peak efficiency[e] (%, lm/W, cd/A)	λ_{max}^{EL} (nm)	FWHM (nm)	CIE 1931[f] (x, y)
PFTML	34,000	19,000	1.78	75, 435	+0.92, −1.16	5.43, 3.11	2020	215, 7.8	0.74, 0.78, 1.25 (5.0, 5.0, 5.0)	614	96	0.61, 0.39
PFBTML	20,500	10,400	1.97	112, 341	+0.87, −1.06	5.38, 3.11	1231	170, 8.1	0.70, 0.65,1.03 (5.0, 5.0, 5.0)	624	112	0.60, 0.40

[a] ITO/PEDOT:PSS(90 nm)/PFTML or PFBTM(60 nm)/LiF(0.5 nm)/Al(150 nm).
[b] By DSC and TGA measurements, respectively.
[c] E_{ox} and E_{red} were both measured in dry and deoxygenated CH_2Cl_2 with 0.1 M tetrabutylammonium perchlorate as the electrolyte in conjunction with a platinum working electrode and a saturated nonaqueous $Ag/AgNO_3$ referenced electrode. Ferrocene was used for potential calibration (all reported potentials are referenced against Ag/Ag^+) and for reversibility criteria.
[d] At 20 mA/cm^2.
[e] Numbers shown in parenthesis are the required driving voltage at peak efficiency.
[f] Commission Internationale de L'Eclairage chromaticity coordinates.

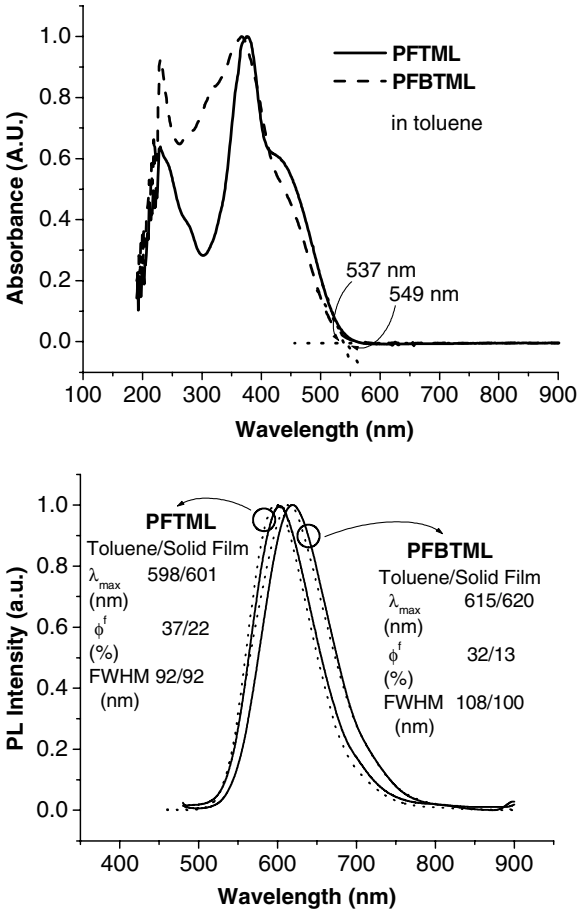

Fig. 1. Absorption (top) and PL (bottom) spectra of PFTML and PFBTML in toluene solution (dotted lines) and as solid film (solid lines). On-set absorption wavelength, emission wavelength (λ_{max}), fluorescence quantum yield (ϕ^f), and full-width-at-half-maximum (FWHW) are noted.

difference) observed on the copolymer PLs from the low polarity toluene solution to solid film.

Solid state fluorescence quantum yields were determined by integrating sphere method [6b] and it is 22% and 13% for PFTML and PFBTML, respectively. In toluene solution, PFTML and PFBTML show even higher ϕ^f of 37% and 32%, respectively. Clearly, thiophene ring is effective in red-shifting the fluorescence of the triad copolymer but is detrimental to the fluorescence intensity in both solution and solid state. Nevertheless, their solid state ϕ^f values, which is essential in electroluminescence (EL) concerns, are comparable with or better than 10–22% of orange MEH-PPV (2-methoxy-5-(2-ethylhexyl)-polyphenylenevinylene), [6] a bench mark polymer with long fluorescence wavelength in PLEDs application.

Two PLED devices with a same configuration containing thin film layer of PFTML or PFBTML (Table 1) were fabricated from toluene solution on PEDOT:PSS pre-coated ITO glass substrate by spin-casting method. The EL spectra (Fig. 2 top) of both copolymers are rather similar to their solid film PL spectra (Fig. 1), in terms of emission wavelength and FWHM (Table 1, Fig. 1, and Fig. 2 top), Considering the similarity between photoluminescence (PL) spectra of copolymer solution and solid film, this is a good lead to the origin of the EL and PL, i.e., they are all from the same singlet excited state of the pristine copolymers. However, the aggregation of polymer chains is probably substantial and considerable fluorescence is quenched in solid state, which is a common feature observed for most orange–red light-emitting polymeric

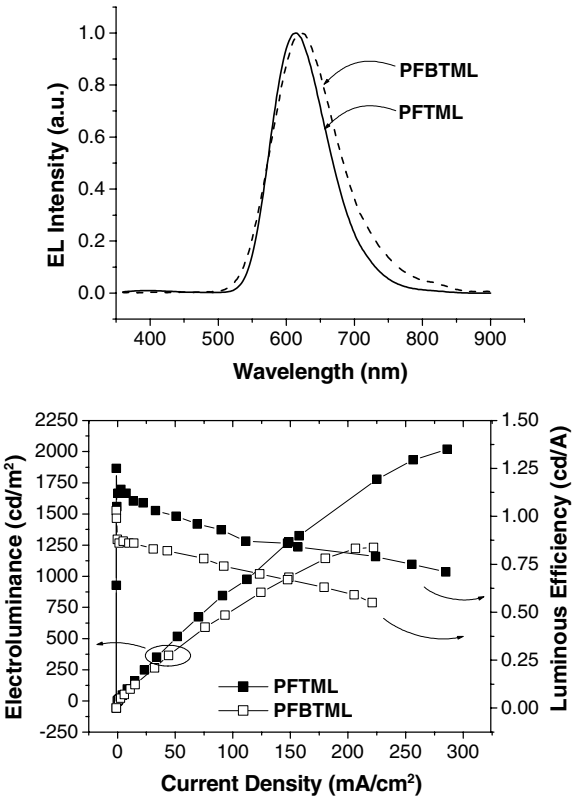

Fig. 2. (Top) Electroluminescence spectra of PLEDs containing PFTML or PFBTML. (Bottom) Current density (mA/cm^2) dependency of luminous efficiency (cd/A) and electroluminance (L, cd/m^2) of PFTML (solid squares) and PFBTML (hollow squares) PLEDs.

materials. Both devices show discernable orange–red EL at low voltage of 5 V. The brightness of PLEDs increases with higher voltage (or current density) and peaks at 2020 cd/m^2 (Fig. 2 bottom). This is a respectful intense electroluminance compared with other known orange to red PLEDs, [4] and can be attributed to the relatively high fluorescence quantum yields of two copolymers in solid state. Although λ_{max}^{EL} of PFBTML is 10 nm longer than that of PFTML, the estimated 1931 CIE chromaticity indicated that both PLEDs exhibited EL with rather similar red chromaticity. Nearly 1% external quantum efficiencies (or greater than 1 cd/A of luminous efficiencies) can be achieved at electroluminance of 1 cd/m^2 (Fig. 2 bottom) and driving voltage of 5 V. The efficiency performance of two PLEDs is not optimal but reasonably good considering the simple (single light-emitting layer without other electron-transporting material) and unprotected (from water and oxygen) device structure in EL characterization. This can be qualitatively attributed to the built-in electron-transporting structural moiety (maleimide) of two copolymers, which helps the balance of hole and electron in PLEDs. Maleimide moiety belongs to an electron-deficient imide family of phthalimide and naphthalimide, which are known for *n*-type organic filed-effect transistors and facilitates the transportation of electrons. Respectful performances of brightness and efficiency have proven that PFTML and PFBTML are potentially useful for orange–red PLEDs.

In summary, we have successfully designed and synthesized a new type of orange–red light-emitting copolymers, PFTML and PFBTM,with multiple structural components including 3,4-diphenylmaleimide, one or two thiophene rings, and fluorene. Our preliminary test of PLEDs has verified that these copolymers are valid for long wavelength (orange to red) polymeric electroluminescence application.

Acknowledgements

This work is support by National Science Council of Taiwan (NSC 93-2113-M-001-036). We also acknowledge the support from National Tsing Hua University and Academia Sinica.

Appendix A. Supplementary data

Supplementary data associated with this article can be found, in the online version, at doi:10.1016/j.orgel.2005.12.003.

References

[1] W.C. Wu, H.C. Yeh, L.H. Chan, C.T. Chen, Adv. Mater. 14 (2002) 1072.
[2] (a) H.C. Yeh, W.C. Wu, C.T. Chen, Chem. Commun. (2003) 404;
(b) H.C. Yeh, L.H. Chan, W.C. Wu, C.T. Chen, J. Mater. Chem. 14 (2004) 1293;
(c) H.C. Yeh, W.C. Wu, Y.S. Wen, D.C. Dai, J.K. Wang, C.T. Chen, J. Org. Chem. 69 (2004) 6455.
[3] (a) N.C. Yang, D.H. Suh, Polym. Bull. 46 (2001) 29;
(b) N.C. Yang, D.H. Suh, Macromol. Rapid Commun. 22 (2001) 335;
(c) N.C. Yang, Y.H. Park, D.H. Suh, React. Funct. Polym. 51 (2002) 121;
(d) J.K. Lee, N.C. Yang, H.W. Choi, D.H. Suh, Macromol. Res. 11 (2003) 92;
(e) N.C. Yang, D.H. Suh, Polymer 42 (2001) 7987;
(f) Q. Peng, Z. Lu, Y. Huang, M. Xie, D. Xiao, D. Zou, J. Mater. Chem. 13 (2003) 1570.

[4] (a) Q. Hou, Y. Xu, W. Yang, M. Yuan, J. Peng, Y. Cao, J. Mater. Chem. 12 (2002) 2887;
(b) N.S. Cho, D.H. Hwang, J.I. Lee, B.J. Jung, H.K. Shim, Macromolecules 35 (2002) 1224;
(c) S. Beaupré, M. Leclerc, Adv. Funct. Mater. 12 (2002) 192;
(d) R. Yang, R. Tain, Q. Hou, W. Yang, Y. Cao, Macromolecules 36 (2003) 7453;
(e) Q. Peng, Z.Y. Lu, Y. Huang, M.G. Xie, S.H. Han, J.B. Peng, Y. Cao, Macromolecules 37 (2004) 260;
(f) J. Yang, C. Jiang, Y. Zhang, R. Yang, W. Yang, Q. Hou, Y. Cao, Macromolecules 37 (2004) 1211;
(g) R.Q. Yang, R.Y. Tian, J.G. Yan, Y. Zhang, J. Yang, Q. Hou, W. Yang, C. Zhang, Y. Cao, Macromolecules 38 (2005) 244.

[5] (a) M. Thelakkat, H.W. Schmidt, Adv. Mater. 10 (1998) 219;
(b) S. Janietz, D.D.C. Bradley, M. Grell, C. Giebeler, M. Inbasekaran, E.P. Woo, App. Phys. Lett. 73 (1998) 2453.

[6] (a) N.C. Greenham, I.D.W. Samuel, G.R. Hayes, R.T. Philips, Y.A.R.R. Kessener, S.C. Moratti, A.B. Holmes, R.H. Friend, Chem. Phys. Lett. 242 (1995) 89;
(b) J.C. de Mello, H.F. Wittmann, R.H. Friend, Adv. Mater. 9 (1997) 230;
(c) Y.H. Niu, J. Hung, Y. Cao, Adv. Mater. 15 (2003) 807;
(d) C.L. Chiang, M.F. Wu, D.C. Dai, Y.S. Wen, J.K. Wang, C.T. Chen, Adv. Funct. Mater. 15 (2005) 231.

Available online at www.sciencedirect.com
SCIENCE DIRECT®
Organic Electronics 7 (2006) 61
Organic Electronics
www.elsevier.com/locate/orgel

Publisher's Announcement

Welcoming 4th Editor: Professor R.A.J. Janssen

We are delighted to announce to the readers of Organic Electronics that Prof. René Janssen has been appointed Editor of the journal as of March 1st 2006.

The contact details of Prof. Janssen are:

Prof. R.A.J. Janssen
Molecular Materials and Nanosystems
Eindhoven University of Technology
P.O. Box 513
5600 MB Eindhoven
The Netherlands
E-mail: r.a.j.janssen@tue.nl

The appointment of a fourth Editor is driven by the steady increase of manuscripts submitted to the journal and by the desire to maintain a high quality and personal care of the reviewing process. With this new appointment the Editorial Board of Organic Electronics consists of the following four Editors:

Prof. S.R. Forrest
Prof. R.A.J. Janssen
Prof. J. Salbeck
Prof. K. Seki

Authors are encouraged to submit their papers to one of the Editors using the Elsevier Editorial System, the journal's online submission tool at http://ees.elsevier.com/orgele.

Please join us welcoming Prof. René Janssen to the Organic Electronics editorial team.

The Publisher
March 2006

doi:10.1016/S1566-1199(06)00034-6

Available online at www.sciencedirect.com
SCIENCE DIRECT®
Organic Electronics 7 (2006) 62–76
Organic Electronics
www.elsevier.com/locate/orgel

Review

The discovery of organic semiconductors. Its light and shadow

Hiroo Inokuchi *

Japan Aerospace Exploration Agency, Tsukuba Space Center, 2-1-1 Sengen, Tsukuba-shi, Ibaraki 305-8505, Japan
Institute for Molecular Science, 38 Nishi-Gonaka, Myodaiji, Okazaki 444-8585, Japan

Received 9 March 2005; received in revised form 18 August 2005; accepted 16 December 2005
Available online 14 February 2006

Abstract

In this article I report why and how I became engaged in the study of organic semiconductors. My first step in the investigation of organic semiconductors was the measurement of electrical resistance of powdered carbon materials, which is a sort of solid colloid. Through the observation of electrical resistance of carbons, I accepted the property that carbon particles certainly conduct electric current. There, however, still remained a question as to how an electron could leap from one particle to another.

I noticed that functional groups bound to the edges of polycyclics in graphite do not cause swelling. Then, I hit upon an idea that polycyclic aromatic compounds with molecular structures similar to fragments of graphite might be electrically conductive. So I started by measuring the electrical resistance of violanthrone, a molecule containing nine benzene rings, with laborious experiments and hence found semiconductive behaviour in organic solids (1954).

In this article, I also report my encounter with charge transfer type organic semiconductors.

Keyword: Organic semiconductors

Contents

* Corresponding address: Japan Aerospace Exploration Agency, Tsukuba Space Center, 2-1-1 Sengen, Tsukuba-shi, Ibaraki 305-8505, Japan. Tel.: +81 (0)29 868 3760; fax: +81 (0)29 868 3956.
E-mail address: inokuchi.hiroo@jaxa.jp

1566-1199/$ - see front matter
doi:10.1016/j.orgel.2005.12.007

1. Introduction

A single molecule or a group of molecules could change the world.

I would like to look back to the history of my research since my student days, and relate how I came across organic semiconductors. I was fortunate enough to have elder professors, proficient seniors and colleagues to help and work with me, and these people should be remembered if the work is to find some place in the history of science. I would like to express my gratitude to all of them.

Since 1965, an organization called Chemical Abstracts Service (CAS) has been registering the number of chemical substances by accurately picking up newly obtained compounds from over 8000 scientific journals and patents over the world. The number, which was 211,934 in the first report of 1965, increased to 37 million in March, 2002. The number seems to be astronomical for chemists who are studying substances as their subject of research. However, it has increased extraordinarily in the last few years. The web site of the CAS (http://www.cas.org/cgi-bin/regreport.pl) now reveals the change in numbers per hour instead of per day! The total number reached 80 million on February 11, 2005. What does this rapid increase in number designate?

We have to admit that the chemistry of materials has been making remarkable progress, providing us with new knowledge, but I cannot be very confident about the future of this development. Since the registered number currently 80 million includes every molecule with different sequence of constituent atoms, the current massive increase in biological substances will accelerate the growth of the number. Expansion at the rate of about 7–8 million per year predicts that the figure of 100 million will be reached in the near future (Fig. 1).

One of the most fascinating aspects of chemistry is that a discovery of a single molecule or a new group of molecules might hold the possibility of changing the world. Chemical substances may be used in a harmful way, but that is a matter beyond the scope of this article. Chemists find real pleasure in a prospect of one substance or a single molecule transforming the world, and they are willing to make scientific exploration their lifework. Chemistry has three fields of research, that is, syntheses, properties and structures of substances. In each field, chemists are striving to advance research and technical developments, seeking substances, among the numerous materials on earth that benefit human life.

Prof. Mizuka Sano, my collleague for 40 years, translated this article from Japanese to English. I express my deep acknowledgement for his laborious work.

2. The encounter with organic semiconductors

Now let me explain how I came to be engaged in the study of organic semiconductors. All research works have tradition and succession, and they are further developed by the successors. My graduate research was carried out in Jitsusaburo Samejima's laboratory, in the Chemistry Department of the University of Tokyo. The photograph shown in

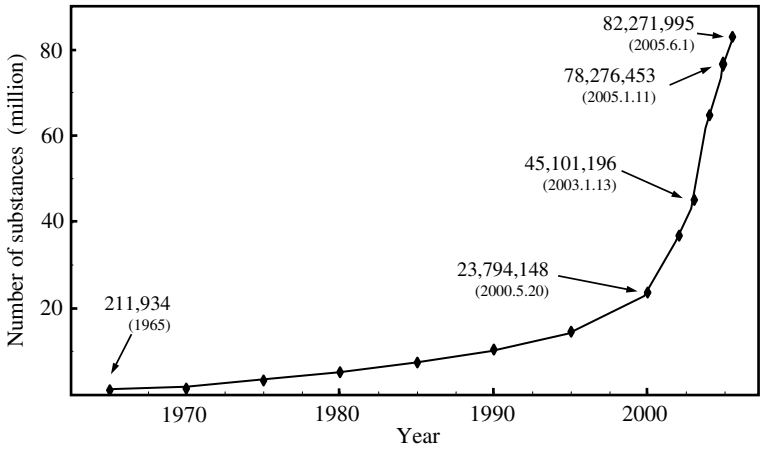

Fig. 1. The number of substances registered by the Chemical Abstracts Service.

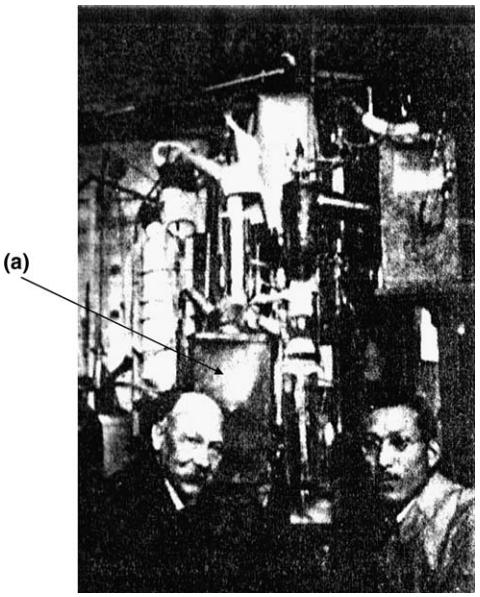

Fig. 2. H. Kamerlingh Onnes (left) and J. Samejima (right). (a) A large column of active charcoal.

Fig. 3. H. Akamatu at the Award Ceremony of the Prize of Japan Academy (1965).

Fig. 2 was taken in 1920, and displays at the back a helium-liquefier installed at Leiden University in the Netherlands. Samejima used to tell that Heike Kamerlingh Onnes affirmed he was the first Japanese to see liquid helium during his stay in Kamerlingh Onnes laboratory. A large amount of active charcoal was packed in a column, i.e., an adsorbing tower, located at the central part of the liquefier in order to remove moisture from gaseous helium for liquefaction.

Samejima returned to Japan, planning to embark on research in low-temperature chemistry, but the purchase of a helium-liquefier became extremely difficult due to the disastrous aftermath of the earthquake that struck the Kanto area of Japan in 1923. Therefore he shifted the object of his study to the field of colloid chemistry, starting research on active charcoal.

The measurement of electrical resistance of carbon materials, which was a sort of solid colloid, was the theme of the graduate project given to me by Samejima and Hideo Akamatu (Fig. 3) in 1947. I believe this was my first step towards investigating organic semiconductors and therefore the column of active charcoal shown in the photograph (Fig. 2) could be referred to as the origin of my lifelong study.

The damage from air raids was slight in the Hongo district, only a few university buildings having suffered from fires. Nevertheless, circumstances of experimental researches were quite inadequate; the power supply was insufficient, city gas was provided only for certain hours and chemicals were scarce. However, I had good friends who encouraged me, and we were keen on studying issues in other scientific fields. For example, someone proposed to read a book on solid state physics, and in fact we read and studied Seitz's *The Modern Theory of Solids.* The atmosphere of the laboratory was free and energetic, and besides, we had the benefit of time, when things were moving on rather slowly.

Subsequently my study of carbon materials shifted to organic compounds. It was known that carbons and graphite were composed of hexagonal networks made of condensed polycyclics. Each carbon atom located at the corners of the hexagons in the networks possessed a π-electron that brought about electrical conductivity in the entire network. It was, however, sometime later that I noticed a big error in a diagram of graphite shown in a textbook. The error occurred at the edge of a gigantic molecular plane, which terminated at the edge with dangling bonds, i.e., so-called free bonds of high reactivity, so that such a molecular plane of graphite did not exist as depicted in Fig. 4. In reality, the edge of graphite is terminated by various kinds of functional groups as shown in Fig. 5. The bonding of functional groups was realized through the following two experiments.

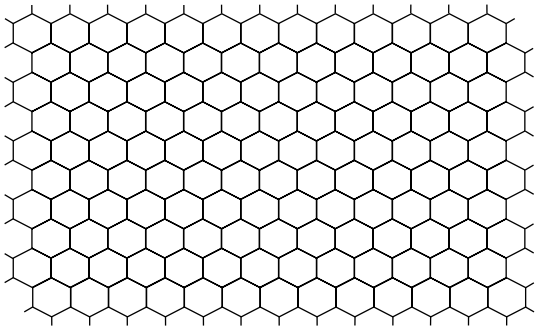

Fig. 4. A single gigantic molecular sheet of graphite.

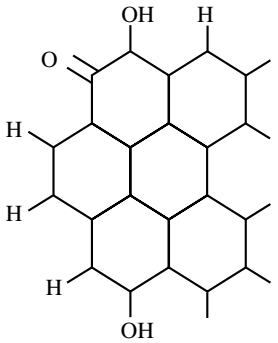

Fig. 5. Structure of graphite (molecular edge).

Carbon materials are classified into carbon blacks, acetylene blacks, active charcoal, bituminous coal and graphite, and the subject of my experiment was concerned with measuring their electrical resistance. The most valuable knowledge I learnt from my seniors is the philosophy that the essence of colloid science lies in simplifying complicated phenomena. Therefore, the first step in studying carbon materials was to plan how to simplify them so as to obtain reproducible values of their electrical resistance. Reproducible values were hardly obtained from the initial trials of packing carbon powder into an ebonite cylinder and measuring the electrical resistance. However, when the experiments were repeated many times, the values began to converge at a definite one. Finally, I could accept the conclusion that carbon particles certainly conducted electric current. There, however, still remained a question as to how electrons could leap from particle to particle.

One result obtained from a simple experiment greatly influenced my speculations about electrical conduction in carbon powders. The experiment was carried out with copper powders familiar in chemistry laboratories. They were the bright shining red copper powders used as a reducing agent. Since graphite powders were highly conductive, it could be assumed that the clean copper powders would show a high value, but the value of electrical conduction was feeble. I noticed that such a phenomenon as a jump of an electron from a copper particle to another did not occur, because an oxide film covering the particle obstructed the jump.

Concerning the edge of polycyclics, I noticed that functional groups bound to edges of these units in graphite did not swell. The bonds between functional groups and carbon networks began to break at the temperature around 400 °C, and therefore, thick films of oxide, hydrogen or hydroxide were not formed on a surface of graphite. Here I hit upon an idea that polycyclic aromatic compounds with molecular structures similar to pieces of graphite might likewise be electrically conductive.

Fig. 6 shows an apparatus for a measurement of electrical conductivity of carbon powders, manufactured by Takeo Ikeda in the machine shop at the Institute for Physical and Chemical Research (1947). It can compress a powder sample packed in a tube from the top up to a pressure of 150 kg cm^{-2}. I have a lot of memories related to this device, and it is still working for a class of physical chemistry laboratory in a university. It is mentioned here because it was the starting point for the study culminating in an experiment on the electrical conductivity of organic materials under high pressures, which will be related below. I believe this apparatus contributed much to establishing the concept of organic semiconductors.

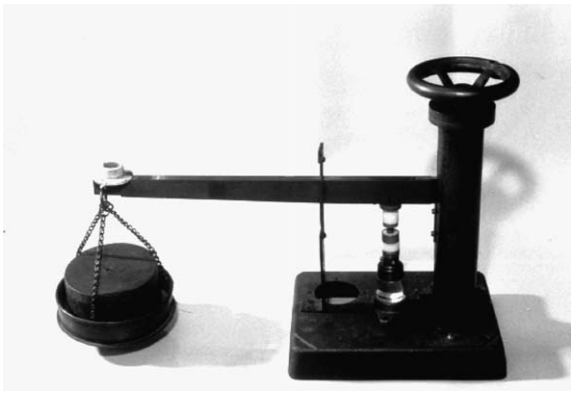

Fig. 6. An apparatus for compressing powders (for an electrical conductivity measurement).

The electrical resistance of carbon powders was measured by changing the applied pressure. It was supposed that a jump of an electron from one graphite molecule to an adjacent one occurred through a functional group similar to one found on an organic compound, because the edges of graphite were not covered with thick substitute films. It was already known that graphite was also conductive along the *c*-axis, so that the experiment was repeated in consideration of that fact, too.

At that time violanthrone was being studied by Akamatu and Kazuo Nagamatsu in the laboratory as a structural model of carbon blacks. Their paper concerning violanthrone had already been submitted to a foreign journal (1947), although at that time it was still quite difficult to submit papers to overseas journals. Thereupon I decided to measure the electrical resistance of violanthrone, which was a sort of condensed polycyclic aromatic compound. It was speculated that π-electrons might be able to transfer between polycyclic aromatic molecules possessing a molecular structure similar to graphite, though organic compounds containing fully saturated bonds had been regarded as electrical insulators. This is an image of organic semiconductors that has long been entertained in my mind, though it may seem very simple.

Violanthrone is a molecule with nine benzene rings, condensed as shown in Fig. 7. Since it had been used as dyestuff since 1904–1905, it was rather easily obtained. Organic compounds were naturally expected to be electrically conductive. However, the value of the electric current that would pass through such materials was hard to estimate, and it caused a serious problem. There was no clue how to choose and settle the method of measurement. It was extremely difficult to observe a weak current in those days. In a strenuous search for a breakthrough, I happened to think of an electrometer called a "quadrant electrometer" which had long been kept in our laboratory, and with that apparatus started to measure the electrical resistance of organic compounds.

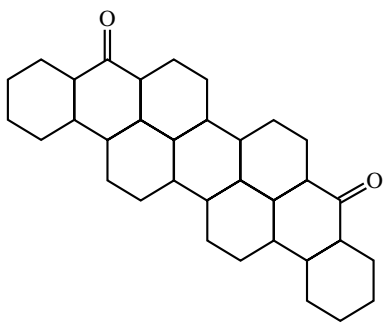

Fig. 7. Violanthrone.

The purity of samples was another crucial problem. The commercially available dyestuff, violanthrone, contained various kinds of impurities, which had to be removed. Thus a very hard task of purification started. For half a year, the measurements were repeated day by day on samples purified by dissolution into concentrated sulfuric acid followed by sublimation in vacuo. Through repetition, a real signal came to be distinguished from the noise, and with an increase in purity, the true signal could be finally detected by means of the "lamp and scale" of the electrometer. From these results, it was confirmed that even organic materials were undoubtedly electrically conductive, the value of electric current being 10^{-12}–10^{-13} A for an applied voltage of 1 V.

At that point it seemed to me clear that organic materials would also be able to pass electric current. The first paper on electrically conductive organic materials was prepared together with Akamatu, and submitted to an American journal. Even after the paper was accepted [1], I could not but feel uneasy about our conclusion that organic materials intrinsically conduct electric current. Colleagues in the laboratory positively supported us, but others were not always favorable and criticized with such comments that the current might have passed along a surface of the cylindrical container, or it might be something else, not inherent to the materials. Various kinds of experiments were performed to meet these criticisms, which brought conviction for the most part, but some concern still remained in our final result.

3. A conversion from anxiety to conviction

Several good results were obtained in the years 1949–1954. One of them was the determination of the electrical resistivity for violanthrone to be ca. $10^{12}\,\Omega\,\mathrm{cm}$, and therefore, an electric current of 10^{-12} A would pass through it for an applied voltage of 1 V. It was known that such a feeble current could be measured by an electrometer capable of amplification. Fortunately I was able to learn measuring techniques for high resistance under the guidance of Hideya Gamou and Goro Kuwabara of the Physics Department, Faculty of Science. Saburo

Izawa of Toshiba, who was an acquaintance of my father's, presented me with a vacuum tube UX-54 for high-resistance measurements. I remember how delighted I was when I visited the Matsuda Research Laboratory of Toshiba in Kawasaki, which was partially destroyed by aerial bombing, and brought back the tube, wrapping it with fluffy silk threads for protection.

Another course of research a chemist should pursue, it seemed to me, was to measure electrical resistance for a number of polycyclic aromatic compounds, in parallel with the determination of its value. Various sorts of aromatic compounds were synthesized or separated from coal tar. This type of work might be a routine for a chemist, but it was certainly what should be done. Japanese scientists had maintained a tradition of producing remarkable results in the field of research on polycyclic aromatic compounds. Lots of polycyclic aromatic compounds were prepared in cooperation with Takashi Handa and Junji Aoki in Toshio Maki's and Yoshio Nagai's laboratories of the Applied Chemistry Department, Faculty of Engineering, the University of Tokyo. Purifying them, which was exceedingly difficult, was my job and most of my time for experiment was spent on this work. The fact that the aim was clear might have encouraged my concentration and I worked many hours, exerting my youthful energy on the task.

The elucidation of the electronic band structure of graphite based on band theory by Coulson [2] and Wallace [3] further strengthened our confidence in the results on the electrical conductivity. While Coulson's paper was a short report, Wallace displayed the electronic band structure of graphite calculated in detail. I once heard a physicist say that the calculation is a good exercise for understanding band theory. Takeo Nagamiya has explained the process of the calculation in detail in his book, *Solid State Physics*, published by Kyoritsu. By that time it had become not too difficult to obtain that kind of foreign journal. Wallace's paper concluded that the energy band calculated for a single carbon network plane of graphite has exactly the same structure as that of an intrinsic semiconductor. The theoretical concept that organic compounds could be semiconductors, even though their band gaps would be wider with decreasing size of their network plane, sustained me in my effort to carry out experiments.

The greatest outcome was the success in measuring photoconductivity in organic materials. It is a special feature of organic materials that they are composed of independent molecules that easily form thin films upon sublimation in vacuo, and indeed the present article is based on this fact. Nowadays it is possible to make uncontaminated metallic thin films, but in the 1950s, it was inconceivable that the surface of metallic atoms was not influenced by residual oxygen in a vacuum chamber. The measurement of photoconduction in violanthrone (Fig. 8) was successful when a thin film was used [4,5], and the result confirmed the concept that this kind of organic material was electrically conductive. I named them "Organic Semiconductors" in 1954 in the paper that appeared in *Bull. Chem. Soc. Jpn.* [5].

Seven years passed since I first noticed the possibility of electrical conduction in organic materials. The long time needed for the confirmation of the concept, however, had not mattered much, since, I suppose, other things also progressed slowly.

I thought in those days that organic materials were stable, their bonds being completely filled, so that oxygen exerted no influence on the experimental results. I was therefore quite astonished one day to hear from Kozo Hirota of Osaka University that oxygen was dissolved in benzene, just as carbon oxide was dissolved in water. Although this was a phenomenon well known to spectroscopists, I had not realized the relationship between oxygen and benzene that was the starting point of polycyclics.

In order to determine the absolute values of electrical resistance, I should have used a so-called high-vacuum technique, but it might be said that I found organic semiconductors because I did not have

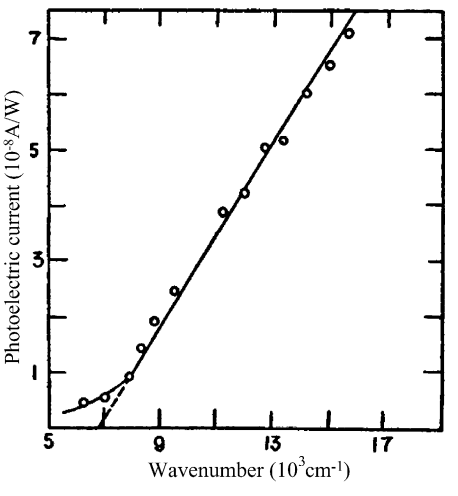

Fig. 8. "Organic semiconductors" (1954) [5], and the spectral response of photoconductivity for a violanthrone film [4].

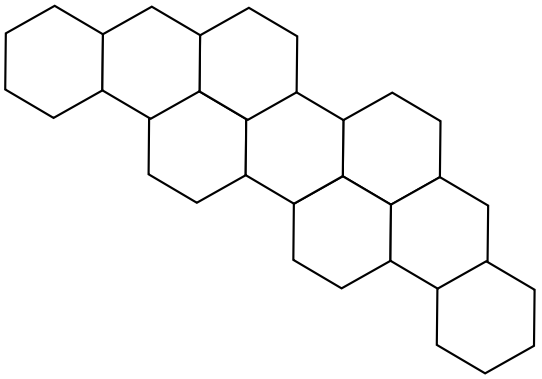

Fig. 9. Violanthrene.

enough knowledge. I also feel that if I had known about the effect of oxygen on the electrical resistance then, I might not have reached my conclusions, for I would have been engaged all the time in removing oxygen from organic thin films, and strayed into a dead end. Fortunately, violanthrone, possessing two oxygen atoms in itself, was found to be far less influenced by oxygen compared with violanthrene (Fig. 9), a polycyclic aromatic hydrocarbon corresponding to violanthrone without two oxygen atoms.

When carrying out a scientific research, it is sometimes necessary to distinguish between essential tasks and matters which can be disregarded for a while, in order to focus on the subject of the moment. I did not concern myself much about the oxygen effect, probably because I happened to lack the knowledge about it. Later, when I moved to the Institute for Solid State Physics at the University of Tokyo, the electrical resistance could be measured for completely oxygen-free organic solids under the ultra-high vacuum conditions, which were obtained by the skillful technique of my colleagues [6].

Another experimental success was the measurement of the effect of pressure on isoviolanthrone (Fig. 10). As described already, powders of carbons or organic material packed in a cylinder under the pressure of 80 kg cm^{-2} by means of the apparatus mentioned above gave a nearly constant value of electrical resistance, which seemed to imply the situation that powders were always packed uniformly. Then, without studying the essential part of a high-pressure experiment, I tried to perform an experiment under much higher pressures. Under such conditions, the electrical resistance was found to reduce to the easily measurable value of

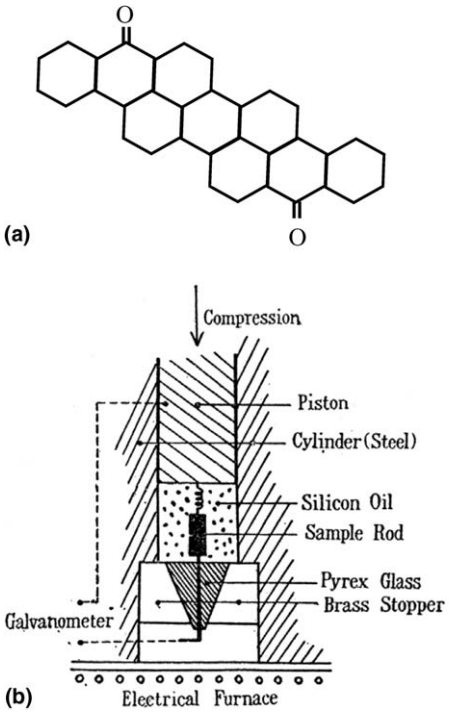

Fig. 10. (a) Isoviolanthrone and (b) a diagram of a compression apparatus [7].

10^7 Ω cm (Table 1), and moreover, the resistance reversibly returned to the original one when the applied pressure was removed [7]. These results brought a conception that intermolecular distances in organic crystals might shrink under high pressures. I was extremely pleased with this discovery. The equipment used for applying pressure was made from a piston for a scooter given by Tatsuhisa Fukushima of Fuji Heavy Industries (Fig. 10).

My eagerness, however, was soon to be disrupted. I told a distinguished scientist in the Physics Department that the experiments under high-pressure conditions would be interesting, since intermolecular distances in molecular crystals shrank under applied pressures. To my disappointment he just answered, "I'm afraid you might be mistaken."

Table 1
Semiconductivity of isoviolanthrone with compression (P) [7]

P (kg cm^{-2})	$\rho_{15°C}$ (Ω cm)	ΔE (eV)[a]
3×10^2	5×10^9	0.75
4.2×10^3	8.4×10^7	0.74
6.3×10^3	2.6×10^7	0.69
8.4×10^3	1.2×10^7	0.68

[a] $\rho = \rho_0 \exp(\Delta E/2kT)$.

I was not prepared to argue against him and even thought I might be wrong. The high-pressure experiment was therefore suspended for 10 years until I resumed the experiment of that type in 1965. The high-pressure experiment on organic solids was carried out together with Shigeru Minomura and Shunichi Akimoto in the Institute for Solid State Physics.

I am not complaining about the comment by the physicist, but regret the deficiency in my knowledge of basic science, which might partly be the result of the confusion during the last war. Since this instance it has become my custom to advise young people to learn fundamental sciences extensively. If the high-pressure experiment should have been performed without the interruption of 10 years, the study of organic semiconductors might have developed into another direction.

In the 1980s, I began to be concerned with another group of single-component organic semiconductors. In order to provide organic solids composed of the same sort of molecules with electrical conductivity, electrons must easily jump from molecule to molecule. One of the representative ways to shrink intermolecular distances is by applying high pressures, as has been mentioned. Another way of applying pressure was found for a group of substances, in which the pressure was induced from the additivity of intermolecular forces. Molecules attracted mutually so as to shorten intermolecular distances, and I named this phenomenon "Molecular Fastener Effect". The effect was discovered with such compounds wherein a highly electron-donating tetrathiafulvalene molecule (TTF) was bonded with four aliphatic hydrocarbon (paraffin) chains, i.e., alkylchalcogen-substituted TTF (molecular fastener). Peiji Wu of the Institute of Chemistry, Academia Sinica, who was staying to study at the Institute for Molecular Science, said one day that the compound was soft enough to be easily bent, but strangely, it still conducted electricity. In a crystal consisting of this compound, molecules are arranged favorably to attract each other, i.e., it has such a structure that the planes of the central TTF moiety of the molecules overlap perfectly in parallel and their four paraffin chains fasten the planes together (Fig. 11). The strong intermolecular force acting between the paraffin chains compresses the TTF moiety planes, which brings about high conductivity, in the range 10^5–10^7 Ω cm in resistivity (Table 2), values well beyond expectation for single-component organic semiconductors [8]. This kind of work was further developed by Kenichi Imaeda, and reached the study of single-component organic conductors with a characteristic metallic conductivity by Hisashi Tanaka, Hayao Kobayashi and Akiko Kobayashi. I know well that charge transfer type organic semiconductors which will be mentioned below are formed with components of great variety, and some of them show superconductivity, so that they seem to be a favorite among organic

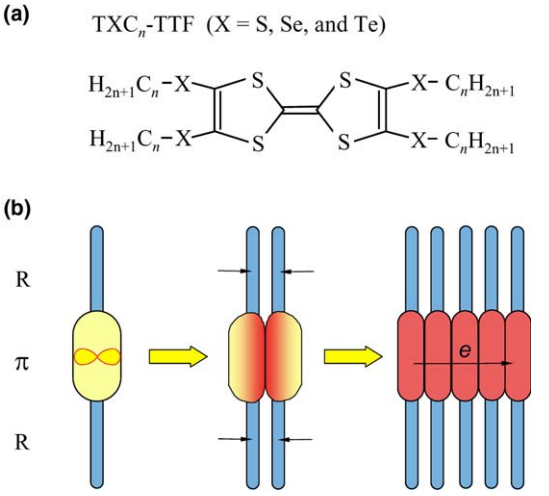

Fig. 11. (a) Molecular fasteners and (b) the molecular fastening principle.

Table 2
Electrical resistivities of molecular fastener (TXC$_n$-TTF) single-crystals [8]

n	X = S		X = Se		X = Te	
	ρ (Ω cm)	mp (°C)	ρ (Ω cm)	mp (°C)	ρ (Ω cm)	mp (°C)
1	2.9×10^{10}	96.5	1.0×10^{6}	92.5	8.1×10^{4}	175.2
3	9.6×10^{9}	30.4	6.6×10^{8}	38.9	7.5×10^{7}	62.2
5	6.4×10^{7}	32.2	3.5×10^{9}	30.8	2.4×10^{8}	56.9
9	5.0×10^{7}	56.8	(8.3×10^{5})	56.5	2.0×10^{6}	65.2
18	(6.8×10^{9})	85.0	(3.0×10^{7})	93.2	(3.5×10^{8})	97.5

ρ values in parentheses are for compaction pellet specimens.

semiconductors at the present situation. However, a search for materials in the field of simpler single-component organic semiconductors and conductors still seems promising to me.

Fifty years have passed since I kept watching day after day at a fan-shaped light spot of a quadrant electrometer shifting within 1 mm or so long on a scale bar. It is a great pleasure for a scientist like me, who has concentrated on experiment, to have witnessed the situation that the electrical conductivity of organic materials has been accepted without question.

4. Charge transfer type organic semiconductors

There is another significant branch of organic semiconductors, i.e., a group of charge transfer type. A semiconductor of this type consists of two components and has developed from quite a different origin. Nowadays binary organic semiconductors are being studied by a great number of scientists, since a variety of advances and applications are expected. The history of an encounter with charge transfer semiconductors seems to me an example of how to search for new materials. Although Yoshio Matsunaga (Fig. 12b), a colleague of mine, would be the best reporter of the details, here I will try to describe the circumstances. In our first paper on a charge transfer type semiconductor, we called it an addition compound, but then we learned about the concept of charge transfer established by Saburo Nagakura and Robert Sanderson Mulliken, and decided to call it a charge transfer organic semiconductor.

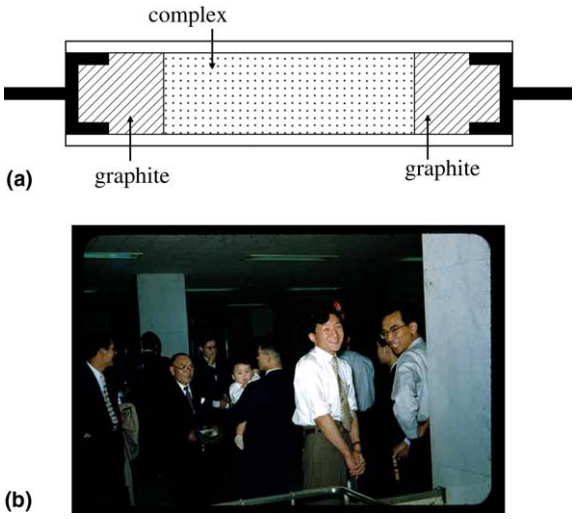

Fig. 12. (a) A specimen cell for a conductivity measurement of perylene-Br_2 [9] and (b) Y. Matsunaga (photo taken in 1960).

The binary organic semiconductors started from a historical background completely different from that of single-component ones. In the 1930s, Eric Clar in Germany and Alois Zinke in Austria were engaging in synthesizing polycyclic aromatic compounds, and there was a dispute between these two well-known chemists about the composition of a very dark blackish brown addition compound formed by reaction between perylene ($C_{20}H_{12}$) and bromine. Clar prepared it by dropping liquid bromine into perylene dissolved in benzene, while Zinke formed it by allowing bromine vapor to be absorbed by perylene crystalline powders. Matsunaga was interested in the compound, and we decided to synthesize it by Zinke's method. It was the time when Matsunaga was studying magnetic properties of organic materials under Akamatu's guidance, and it began to be known that radicals showed paramagnetism, whereas others generally showed diamagnetism. The addition compound showed an extraordinarily large paramagnetism and quite dark color, so that it was presumed that the solid of the compound might possess electrons moving freely in it. The measurement of its electrical conduction resulted in the recognition of charge transfer complexes as a further type of organic semiconductor. The research was performed in the years 1952–1953, and was favored by unexpected good fortune.

When a voltage was applied to a sample in an attempt to measure its resistance, an electric current passed for a moment and then diminished at once, due to an influence of bromine included in the sample. The electrodes on the sample were destroyed by reaction with bromine. At that time, graphite intercalation compounds were being studied in Akamatu's laboratory by mixing bromine with graphite to insert bromine molecules into the interlayer spaces of graphite. Then it dawned on me that an excess amount of bromine in the sample could be absorbed by graphite, and accordingly graphite powders were inserted between the electrode and the sample on both sides (Fig. 12a). The electric current was stabilized by this means, and measured successfully. In fact, an electric current much larger than our expectation passed through this system. After repeating the experiments, we came to the conclusion that the compound was quite highly conductive.

The next question was concerned with the type of charge carrier, whether it was an ion or electron.

Since the method of deciding the type of charge carrier had already been established in the field of physics, we repeated the confirmation work by the method, and proved it to be electronic. All the results were published as a rapid communication [9].

The electrical resistances of the addition compounds formed by reaction between polycyclics and halogen ranged in the order of $10^0\ \Omega$ cm, and this means they were extraordinarily conductive for organic semiconductors (Table 3) [10]. We prepared a number of complexes one after another and measured their electrical resistances. This was, I suppose, useful in obtaining plenty of results concerning charge transfer organic semiconductors. This is what is now called halogen-doping and enormous numbers of research results were achieved by means of halogen-doping.

I regret, however, the fact that we stuck too much to polycyclics. Later, when I stayed in England in 1955–1957, I prepared semiconductors by reaction between organic compounds under the guidance of Daniel D. Eley (Table 4). I think this was the time when organic semiconductors composed of only organic components were established [11]. The succeeding rapid developments in this field have been reported in numerous papers, so that I do not feel I need to explain them by myself, but I will mention two of them briefly. They are the syntheses of two kinds of substances. One is a synthesis of tetracyano-*p*-quinodimethane (TCNQ, Fig. 13) by the chemists of Du Pont in 1961, and the other is that of tetrathiafulvalene (TTF, Fig. 14) by Wudl et al. [12]. A complex prepared by mixing these two compounds contributed to the discovery of metallic conductivity in organic materials.

Table 3
Charge transfer organic semiconductors (halogen-doping) [10]

Complex (composition)	ρ (Ω cm)	ΔE (eV)
Perylene–bromine (1:4.4)	7.8	0.13
Pyranthrene–bromine (1:3.3)	220	0.20
Violanthrene–bromine (1:4.5)	66	0.20
Violanthrene–iodine (1:4.0)	45	0.15

Table 4
Charge transfer organic semiconductors formed by reaction between organic compounds [11]

Acceptor	Donor (*N*,*N*-dimethylaniline)			
		Chloranil	Bromanil	Iodanil
ρ (Ω cm)	a.c.	5.0×10^7	9.0×10^7	3.0×10^7
	d.c.	8.0×10^8	1.5×10^9	1.7×10^8

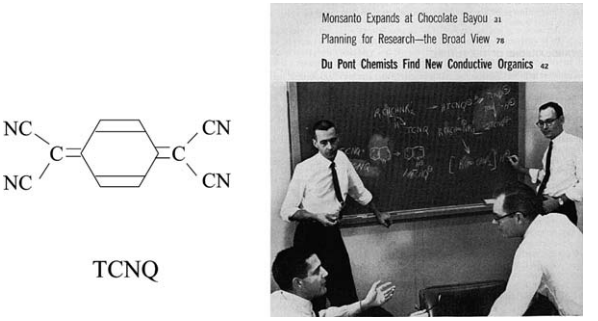

Fig. 13. Appearance of TCNQ (Chem. & Eng. News, January 9, 1961).

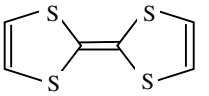

Fig. 14. Appearance of TTF [12].

The discovery of an organic superconductor made by Jerome et al. in France in 1980 (Fig. 15) resulted from a great evolution of a TTF–TCNQ binary system through an effective use of high pressure [13]. In our group, Saito et al. reported that the metallic conduction of bis(ethylenedithio)tetrathiafulvalene (BEDT-TTF, Fig. 16), synthesized by Mizuno et al. [14], with perchlorate in 1982 [15], and now we have about 150 organic superconductors over

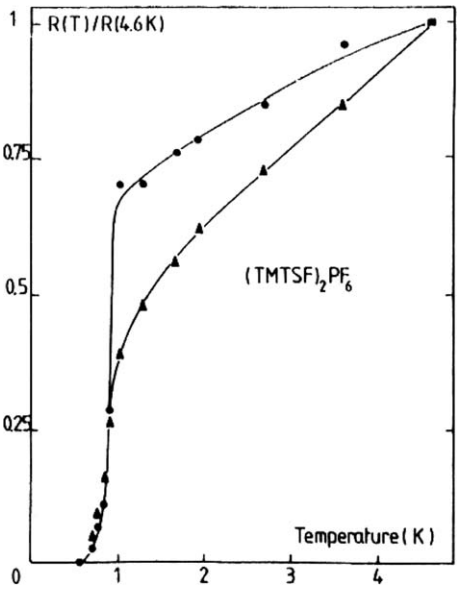

Fig. 15. The first report on an organic superconductor, $(TMTSF)_2PF_6$ [13].

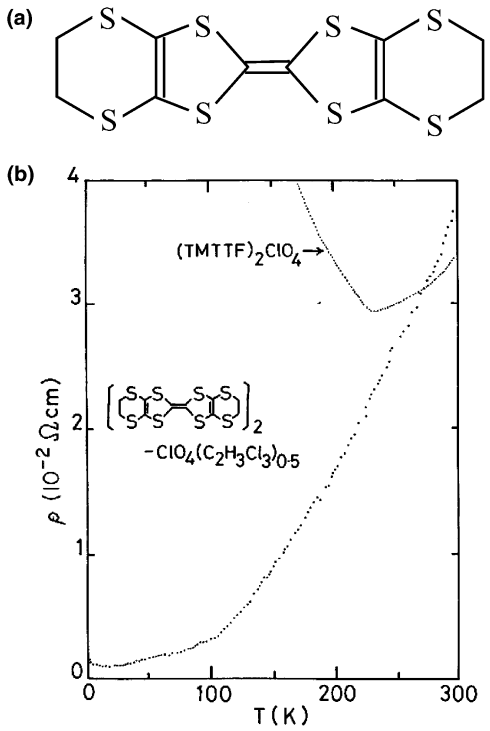

Fig. 16. BEDT-TTF and diagram of metallic conduction of BEDT-TTF–perchlorate complex [14].

the world, the majority of which were prepared on the base of BEDT-TTF. Organic superconductivity has been studied successfully and developed extensively even into the elucidation of its mechanism in the field of physics.

Ternary organic semiconductors have also been studied, in order to develop new materials. The origin of this endeavour is found in the graphite intercalation compounds mentioned above. Kenichi Imaeda and I happened to find a very interesting phenomenon in a ternary system. When hydrogen was used as one of three components, the hydrogen was not only simply accommodated in the system, but it also contributed to the electrical conductivity. This phenomenon is very fascinating to one who studies materials. Hydrogen, being a gaseous material, can be easily pumped out from the system, which changes its properties, and when hydrogen is absorbed into the system, it returns to the original one. This system was named a ''Breathing superconductor'', because this ternary system was an organic superconductor [16].

Compared with the early days when I first selected organic compounds as research objects, organic materials have been studied in greater

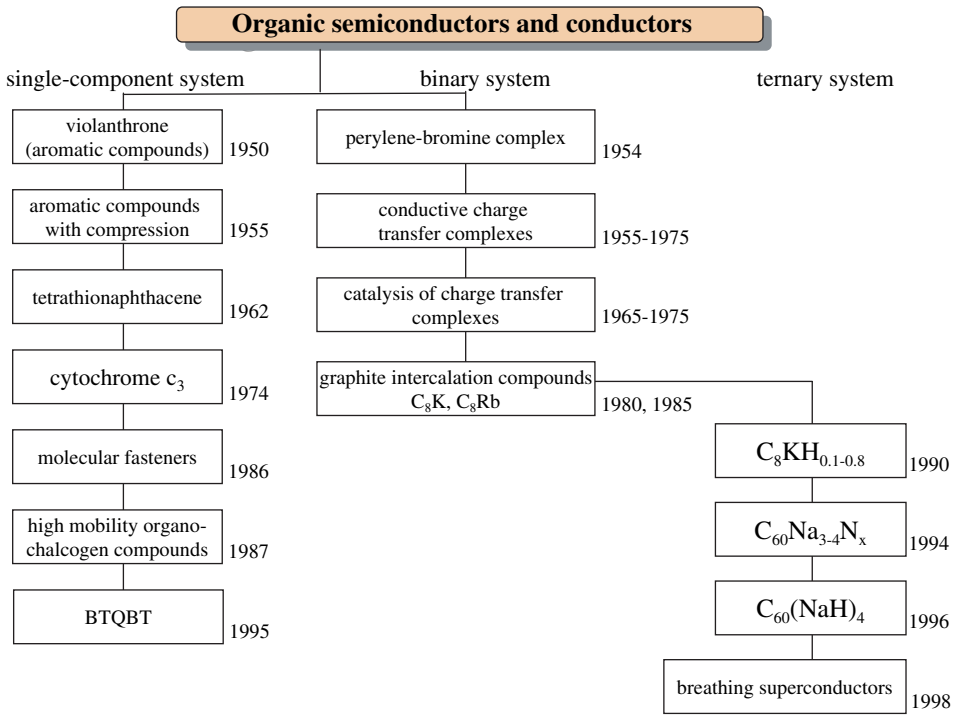

Fig. 17. The flow chart of research process of organic semiconductors and conductors of our group.

variety (Fig. 17). The most important feature of organic materials is that their constituent molecules are independent of each other, and that fact brings about various matters of interest. However, when they are in a form of an assembly, and the interaction between molecules is strong, further interesting properties appear. I have also dealt with this aspect of organic materials. My research has been concentrated on transferring electrons from one organic molecule to adjacent ones and the results have given rise to organic semiconductors.

5. Fundamental characteristics of molecules and molecular assemblies

It is sometimes necessary to push ahead with the subject of the moment in order to establish a certain concept in a field of science. An example is the study of oxygen effects on organic materials as mentioned above. This kind of practice provides us with a sense of satisfaction of having cleverly reached the destination, but on the other hand it leaves some uneasiness about its results. In my case, I was nervous about the essential mechanism of electrical conduction in organic solids.

One of the major works done after I moved to the Institute for Solid State Physics in 1965 was concerned with photoconduction, one of the photoelectric effects, i.e., the enhancement of electric current in organic solids under light illumination, and electron emission from organic solids (photoelectron emission). I read a German paper of the 1930s about enhancing photoelectron emission from alkali metals by mixing a small amount of anthracene with the metal, which was printed in the second volume of *The Progress of Quantum Physics* edited by Ryogo Kubo. Stimulated by the paper I started the study of photoelectron emission from organic solids. I am grateful to Hisao Miyazawa of the Matsuda Research Laboratory of Toshiba for his valuable instructions concerning the experiment. Fig. 18 shows a photoelectric cell made for a complex formed by reaction between a violanthrene film and caesium vapor [17]. The film was formed by sublimation of violanthrene from a sublimation gun in the cell. The observation that the violanthrene–Cs complex showed a quite high quantum yield in photoelectron emission pushed us to study electron emission from organic materials. This experiment triggered research on electronic properties of organic solids by means of photoelectron spectroscopy.

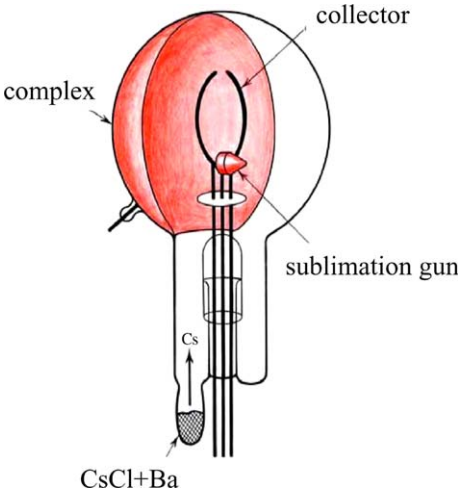

Fig. 18. Photoelectric cell of violanthrene–Cs complex [17].

The experiments on photoelectron spectroscopy exhibited an interesting feature derived from the fact that organic materials were assemblies of independent molecules. Fig. 19 shows photoelectron spectroscopic patterns of naphthacene ($C_{18}H_{12}$) [18]. It demonstrated very clear patterns for organic materials, though it was still the early days of photoelectron spectroscopy when the sample chamber could not be highly evacuated. I have mentioned that oxygen is dissolved in benzene, but the dissolution is quite different from the normal oxidation, for the bonding force acting between oxygen and

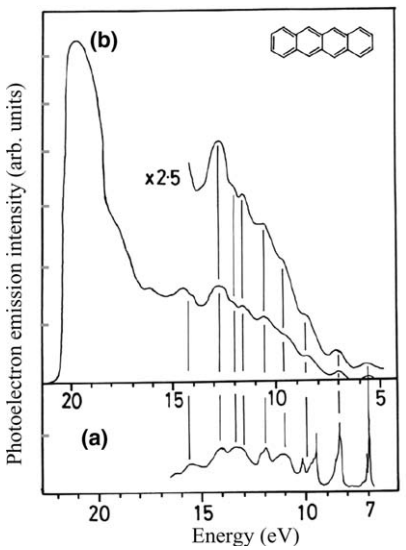

Fig. 19. Photoelectron spectroscopic patterns of naphthacene in the (a) gas and (b) solid phases (for the incident light of 21.2 eV) [18].

benzene is extremely weak. Due to the weak interaction, the photoelectron spectroscopy of a thin film of an organic solid displayed the energy level from which an electron emitted without being influenced by oxygen. This experiment was performed 30 years ago in the early 1970s, and the chamber was evacuated just high enough to evaporate some of naphthacene from the surface, thus forming a clean naphthacene film, which exhibited a spectroscopic pattern sharp enough at that time.

If we try to perform this kind of experiment for inorganic materials, we need to evacuate the chamber to a quite high degree of vacuum to make the surface of a sample clean. With respect to organic materials, however, the spectrum obtained for a sample in the solid state demonstrates a one-to-one correspondence with that obtained for a sample in the molecular state, as shown in Fig. 19. Plainly speaking, this is a basis for molecular electronics, and the fact that molecules form a molecular assembly, preserving their individual character is a very attractive feature found in organic materials. In the case of a strong intermolecular interaction, the assembly is a substance of high electrical conductivity, while in the case of a weak interaction, it keeps properties as a single molecule. The pattern of naphthacene shown in Fig. 19 demonstrates that the molecules condensed into an assembly still preserve the character of an individual molecule.

The way electrons are emitted from polycyclic aromatic compounds was confirmed by this experiment, and it became possible to determine accurately the forces necessary for emission, namely, their ionization potentials, from the threshold values of photoelectron spectra. The photoelectron spectra were observed for almost 100 organic materials, and the polarization energies were determined from the accurate values of the ionization potentials for materials in the solid state and those in the molecular state (Table 5) [19]. Consequently their electron-accepting abilities as well as electron-donating abilities were diagrammed. Electrically conductive charge transfer complexes have come to be designed on the basis of the diagram, and the electric action that induces electrical conduction has come to be discussed from a quantitative viewpoint. The scientists belonging to the group that studied organic materials by photoelectron spectroscopy are making great progress in carrying out the detailed research on organic solid surfaces and in solving problems concerning the interface between an organic material and a metal.

Table 5
Photo-ionization energies for molecules (I_g) and solids (I_s) determined by photoelectron spectroscopy, and polarization energies (P_+)

	I_g (eV)	I_s (eV)	P_+ (eV)
Naphthalene	8.12	6.4	1.7
Anthracene	7.42	5.75	1.67
Naphthacene	6.89	5.10	1.8
Pentacene	6.58	4.85	1.7
Perylene	6.90	5.2	1.7
Coronene	7.25	5.52	1.7
Violanthrone	6.42	4.9	1.6
Tetrabenzopentacene	6.13	4.98	1.15
Tetrathionaphthacene	6.07	4.4	1.7
TTF	6.4	5.0	1.4
TCNQ	9.5	7.4	2.1
I_2	9.26	6.34	2.92

I am grateful to the senior scientists and colleagues in the Institute for Solid State Physics for having helped me advance the study of electrical conduction onto the stage where it could be discussed quantitatively.

Fig. 20 shows electronic energy diagrams of an atom, a molecule, a molecular solid and an inorganic solid, drawn by Kazuhiko Seki. A molecular solid is an assembly of molecules, each of which is made of constituent atoms. On the other hand, an inorganic solid is constructed directly with atoms. The difference between an inorganic solid and an organic solid is the difference in assembling of components. A single atom of sodium is, as a matter of course, should be very reactive and hardly exist. In the case of organic materials, even a single molecule possesses its own property. Therefore, making the best use of the inherent property of a single molecule embues the development of molecular electronics.

Here let me refer to an example of molecular electronics connected with a polycyclic aromatic hydrocarbon. Compounds made of polycyclics are interesting substances. Tetrabenzopentacene (Fig. 21), one of the seven compounds containing nine benzene rings synthesized by a condensation reaction of benzanthrone followed by reduction, is especially interesting. It has a skeletal structure of the linear pentacyclic hydrocarbon pentacene at the center of the molecule. The color derived from the pentacene is clear blue, but it turns colorless when irradiated in air, and moreover, it returns to blue when heated, which means it has the property of photochromism. Photochromism is the characteristic that a substance changes color upon light

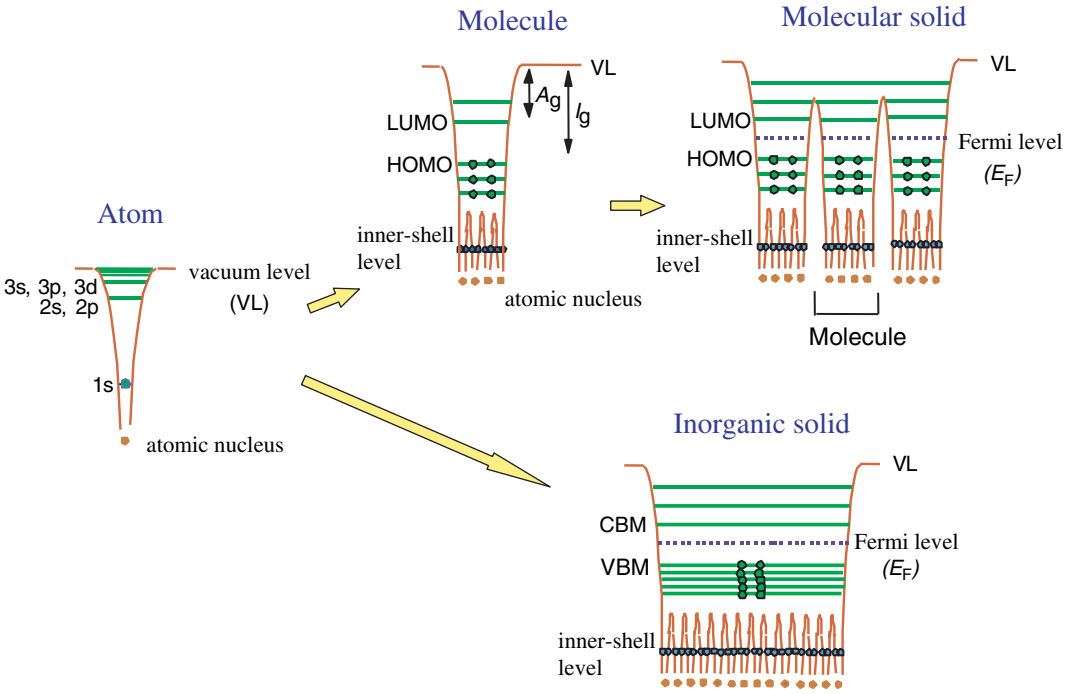

Fig. 20. Electronic energy diagrams of an atom, a molecule, a molecular solid and an inorganic solid.

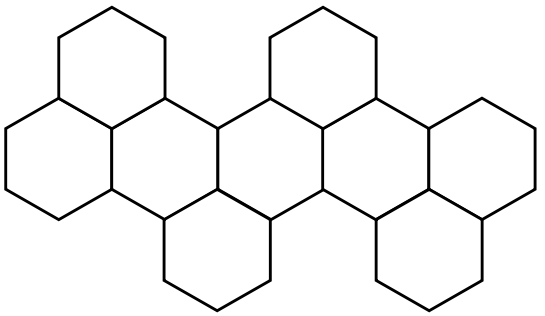

Fig. 21. Tetrabenzopentacene.

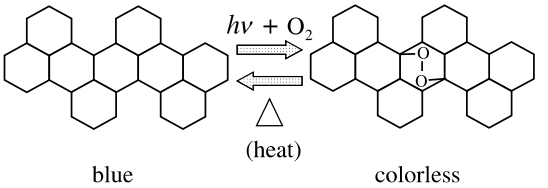

Fig. 22. Application of chemical reaction of polycyclic aromatics for a step to molecular devices [20,21].

illumination, and in this case, the color disappears. The color changes are caused by bond formation of oxygen in the air with the compound under illumination, and removal of the oxygen upon heating (Fig. 22) [20,21].

I think this is a first step towards molecular devices. The characteristic of a single molecule governs that of a molecular assembly as a whole. That is, the characteristic of a molecular assembly comes from a single molecule, so that an exhaustive study of molecular properties would lead to an understanding of the properties of an assembly. We have now come to the time when we can handle a single molecule. But some procedures such as wiring a single molecule are related to a fundamental principle in science. If we are too easy-going, we would be unsuccessful. After all, it is necessary for us to repeat steady experiments for further development. Smallness is not always useful for molecular devices. I think it is important to utilize effectively the property inherent in a molecule, and we have to proceed cautiously. I feel a little worried whenever I read some recent articles assuming that molecular devices would be realized soon.

The conditions necessary for molecular devices are the functions of transport, storage and control. In other words, molecular devices need to supply molecules or molecular assemblies with these three capabilities.

The function of transport corresponds to a transfer of an electron between molecules, and it has been extensively studied. The function of storage might be resolved with intercalation compounds. The most difficult part would be the problem of control. Discussions about its probability have recently appeared in newspapers and other media. But I suppose truly reliable results could be obtained only by furthering elaborate and thoughtful study of molecular properties. Although various sorts of difficulties are to be anticipated on the way, I believe we will be able to reach our goal of producing molecular devices.

References

[1] H. Akamatu, H. Inokuchi, J. Chem. Phys. 18 (1950) 810.
[2] C.A. Coulson, Nature 159 (1947) 265.
[3] P.A. Wallace, Phys. Rev. 71 (1947) 622.
[4] H. Akamatu, H. Inokuchi, J. Chem. Phys. 20 (1952) 1481.
[5] H. Inokuchi, Bull. Chem. Soc. Jpn. 27 (1954) 22.
[6] Y. Hori, S. Iwashima, H. Inokuchi, Bull. Chem. Soc. Jpn. 43 (1970) 3294.
[7] H. Inokuchi, Bull. Chem. Soc. Jpn. 28 (1955) 570.
[8] H. Inokuchi, G. Saito, P. Wu, K. Seki, T.B. Tang, T. Mori, K. Imaeda, T. Enoki, Y. Higuchi, K. Inaka, N. Yasuoka, Chem. Lett. (1986) 1263.
[9] H. Akamatu, H. Inokuchi, Y. Matsunaga, Nature 173 (1954) 168.
[10] H. Akamatu, H. Inokuchi, Y. Matsunaga, Bull. Chem. Soc. Jpn. 29 (1956) 213.
[11] D.D. Eley, H. Inokuchi, M.R. Willis, Faraday Soc. Discuss. 28 (1959) 54.
[12] F. Wudl, G.M. Smith, E.J. Hufnagel, J. Chem. Soc., Chem. Commun. (1970) 1453.
[13] D. Jerome, A. Mazaud, M. Ribau, K. Beckgaard, J. Phys. Lett. 41 (1980) L95.
[14] M. Mizuno, A. Garito, M.P. Cava, J. Chem. Soc., Chem. Commun. (1978) 18.
[15] G. Saito, T. Enoki, K. Toriumi, H. Inokuchi, Solid State Commun. 42 (1982) 557.
[16] K. Imaeda, J. Kröber, H. Inokuchi, Y. Yonehara, K. Ichimura, Solid State Commun. 99 (1996) 479.
[17] H. Inokuchi, Y. Harada, Nature 198 (1963) 477.
[18] K. Seki, Mol. Cryst. Liq. Cryst. 171 (1989) 255.
[19] H. Inokuchi, K. Seki, N. Sato, Phys. Scr. T 17 (1987) 93.
[20] H. Inokuchi, Mol. Cryst. Liq. Cryst. 125 (1985) 51.
[21] A. Izuoka, T. Murase, M. Tsukada, Y. Ito, T. Sugawara, A. Uchida, N. Sato, H. Inokuchi, Tetrahedron Lett. 38 (1997) 245.

Available online at www.sciencedirect.com
SCIENCE DIRECT
Organic Electronics 7 (2006) 77–84
Organic Electronics
www.elsevier.com/locate/orgel

N-type organic field-effect transistor using polymeric blend gate insulator with controlled surface properties

Youngnam Oh [a,1], Seungmoon Pyo [a,*,1], Mi Hye Yi [a,*], Soon-Ki Kwon [b]

[a] *Polymeric Nanomaterials Laboratory, Korea Research Institute of Chemical Technology, 100 Jang-dong, Yuseong-gu, Daejeon 305-610, Republic of Korea*

[b] *School of Nano & Advanced Materials and ERI, Gyeongsang National University, Jinju, 660-701, Republic of Korea*

Received 26 July 2005; received in revised form 6 October 2005; accepted 18 November 2005
Available online 19 December 2005

Abstract

Fabrication of n-type organic thin-film transistors (OTFTs) based on organic semiconductor and organic gate insulator is essential for the achievement of organic complementary logic circuit. This article deals with n-type OTFTs with copper hexadecafluorophthalocyanine (F16CuPc) and polymeric blend as an active semiconductor and a gate insulator, respectively. The gate insulator was prepared by blending poly(amic acid) and soluble polyimide with long alkyl side chains (C_{18} group), which make the surface of the gate insulator more hydrophobic. In order to reduce properties mismatch at interface between F16CuPc and the gate insulator, surface tension of the gate insulator was controlled to 39.1 dyn/cm, which is similar to that of F16CuPc (36.9 dyn/cm). AFM and X-ray diffraction measurements indicated that F16CuPc deposited on the gate insulator showed worm-like flat lying crystal and was highly ordered with a peak of 6.12°. The F16CuPc OTFTs with the gate insulator function as n-channel accumulation mode and their performance was better than that of F16CuPc OTFTs with SiO_2, demonstrating its potential applications for flexible organic display. Charge carrier field-effect mobility, I_{ON}/I_{OFF}, and subthreshold slope of the OTFT were 6×10^{-3} cm^2/V s, 5.4×10^3, and 7.3 V/dec, respectively.

PACS: 72.80.Le

Keywords: Organic semiconductor; Organic gate insulator; Polyimide; Organic field-effect transistor

1. Introduction

Organic semiconductors for electronic devices, such as thin-film transistors (OTFTs), light-emitting diodes, and photovoltaic cells have been widely investigated due to their low fabrication cost and flexibility. For organic complementary logic circuits, combination of n-type and p-type OTFTs is required, indicating the simultaneous development

* Corresponding authors. Tel.: +82 428607305; fax: +82 428614151 (S. Pyo), tel.: +82 42 8607291; fax: +82 42 8614151 (M.H. Yi).
E-mail addresses: pyosm@krict.re.kr (S. Pyo), mhyi@krict.re.kr (M.H. Yi).
[1] These authors equally contributed to this work.

1566-1199/$ - see front matter © 2005 Elsevier B.V. All rights reserved.
doi:10.1016/j.orgel.2005.11.004

of n-type and p-type organic semiconductors. Most organic semiconductors show mainly p-type behavior with field-effect mobilities (μ) ranging from 0.01 to 3 $cm^2 V^{-1} s^{-1}$ [1–3]. On the other hand, only several organic semiconductors show n-type behavior. Among them, C_{60} [4,5], C_{70} [6] and their derivatives [7], 3,4,9,10-perylene tetracarboxylic dianhydride [8], 3,4,9,10-perylene tetracarboxylic diimide [9] and intentionally-doped tetracyanoquinodimethane (TCNQ) [10] have been reported previously as n-type semiconductors. However, it is found that they are very air-sensitive which makes them unsuitable for practical applications. Recently, Chua et al. reported interesting results that n-type OTFTs with conjugated polymers can be obtained by the use of an appropriate hydroxyl-free gate insulator [11].

Metallophthalocyanines have been considered as potential candidates for organic electronics due to their excellent opto-electrical properties and film-growth properties, and good chemical stability [12–14]. However, most of them show p-type behavior. Modified metallophthalocyanines prepared by adding strong electron-withdrawing groups such as –CN, –F, and –Cl to their outer rings are also extensively studied due to their remarkable electronic properties and high chemical stability [15–17]. More recently, OTFTs using metallophthalocyanine composite have been reported to improve μ [18] and to obtain ambipolar characteristics [19]. Among them, copper hexadecafluorophthalocyanine (F16CuPc) is found to function as an n-channel semiconductor [15,20–24]. However, most of the OTFTs with F16CuPc are mainly fabricated with inorganic gate insulators such as SiO_2 and Ta_2O_5 [15,21,23–26]. For flexible display applications OTFTs should be fabricated on flexible substrates, and the material components of OTFTs should be flexible. It indicates that inorganic gate insulators should be replaced with organic ones.

Regarding organic and polymeric semiconductors, tremendous studies have been conducted to replace inorganic-based semiconductors [1,27]. However, there has been a lack of research on other material components, in particular, organic gate insulators. In this article, we report n-type F16CuPc OTFTs with chemically and mechanically stable polyimide blend gate insulator with non-polar long alkyl side chain (C_{18}, octadecyl group). In addition, we compare the performance of F16CuPc OTFT with the blended gate insulator with that of the device with SiO_2.

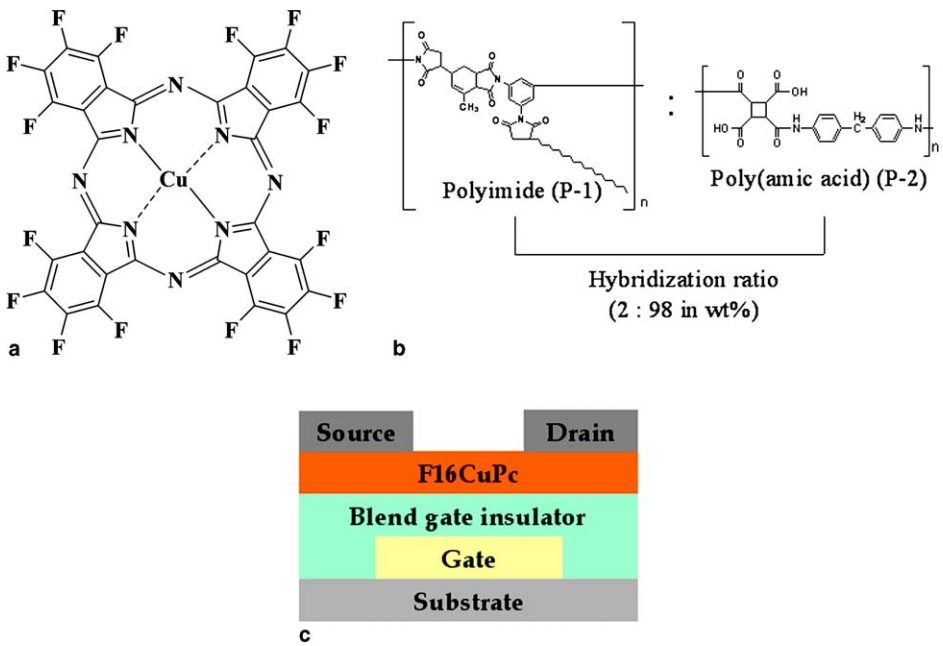

Fig. 1. Chemical structure of (a) copper hexadecafluorophthalocyanine (F16CuPc) and (b) the polymeric blend gate insulator, which is prepared by blending two polymers, polyimide (P-1) and poly(amic acid) (P-2). The blending ratio of polyimide to poly(amic acid) was 2:98 (described as 2/98 in the text). (c) Schematic device structure of F16CuPC OTFT used for this study.

2. Experimental

F16CuPc and hexamethyldisilazane (HMDS) were purchased from Aldrich Chemical Co. and used as received. Polyimide blend gate insulator was prepared by blending a soluble polyimide (P-1) and a poly(amic acid) (P-2) in our laboratory for this study. The blending ratio of P-1 to P-2 was 2:98 in wt.% (described as 2/98). The chemical structures of F16CuPc and the gate insulator are shown in Fig. 1a and b, respectively. P-1 was prepared from 5-(2,5-dioxotetrahydrofuryl)-3-methyl-3-cyclohexene-1,2-dicarboxylic anhydride (DOCDA) and 1-(3,5-diaminophenyl)-3-(1-octadecyl)-succinic-imide (DA18IM). P-2 was prepared from 1,2,3,4-cyclobutane-tetracarboxylic dianhydride (CBDA) and 4,4-diaminodiphenylmethane (MDA).

The geometry of OTFTs for all electrical characterizations was a top-contact as shown in Fig. 1c. Indium tin oxide (ITO) coated glass was used for a substrate and the ITO was patterned (2 mm wide stripes) for the formation of gate electrode by a conventional photolithographic method: photoresist coating, ultraviolet light exposure, developing and etching. The patterned ITO substrate was cleaned using the general cleaning process for electronic applications; sonication in detergent, deionized water, acetone and isopropanol in that order for 20 min at room temperature. The blend gate insulator solution in *N*-methylpyrrolidone was spin-coated on top of the gate electrodes, and soft-baked at 90 °C for 10 min on a hot plate in air. Subsequently, the soft-baked film was converted to the corresponding polyimide blend film by baking at 230 °C for 30 min on a hot plate in air. We understand that the baking temperature (230 °C) is relatively high for the fabrication of OTFTs on flexible substrates. So, we are currently working on the preparation of low-temperature processable hybrid gate insulator for n-type OTFTs by blending two soluble polyimide instead of using poly(amic acid). The final thickness of the fully-baked gate insulator was determined using alpha-step (KLA-Tencor α-step DC 50) surface profiler and was about 300 nm. A 60 nm-thick layer of F16CuPc was deposited on top of the gate insulator through a shadow mask by a thermal evaporation at a pressure of 3×10^{-6} Torr. The evaporation rate of the F16CuPc was 1 Å/s and substrate temperature was 90 °C. The fabrication of OTFTs was completed by thermally evaporating 100 nm-thick source and drain electrodes on top of F16CuPc through a shadow mask with a channel lengths (L) of 50 μm and width (W) of 500 μm. We also have fabricated F16CuPc OTFTs with an bare and HMDS-treated SiO_2 (60 nm) according to the fabrication conditions described above in order to compare the performance with that of F16CuPc OTFTs with the blend gate insulator. The HMDS-treated SiO_2 was obtained by spin-coating HMDS solution with a spin speed of 4k rpm, followed by baking at 120 °C for 5 min. Atomic force microscope (AFM) images were taken with a Digital Instrument Nanoscope IV operating in tapping mode in air based on a low-force imaging technique to get a high-resolution image. Scanning emission microscope (SEM) was obtained with a Jeol Model JSM-6700F. Wide angle X-ray diffraction (XRD) measurements were performed at room temperature using a Rigaku diffractometer (Model D/MAX-2200V). The CuK_α radiation source was operated at 40 kV and 60 mA. Output (I_{ds} vs V_{ds}) and transfer (I_{ds} vs V_{gs}) characteristic curves of OTFTs were obtained with an Agilent E5272 semiconductor parameter analyzer. Capacitance of the gate insulator was measured with an HP 4294A LCR meter. All electrical measurements were carried out in air without any encapsulation.

3. Results and discussion

3.1. Polyimide blend gate insulator and F16CuPc

It is well known that the hydrophobic surface of a gate insulator treated by primer, such as octadecyltrichlorosilane (OTS) and 1,1,1,3,3,3-hexamethyldisilazane (HMDS) gives positive effect on the performance of pentacene OTFTs. The treatment reduces interfacial properties mismatch between SiO_2 and organic semiconductor and leads to the improvement of the performance of OTFTs [28]. In order to confirm this we first have fabricated F16CuPc OTFTs with bare SiO_2 and HMDS-treated SiO_2 (more hydrophobic). The F16CuPc OTFTs with bare SiO_2 showed poorer performance than that of OTFTs with HMDS-treated SiO_2. Details about the device performance are summarized in Table 1. We found that more hydrophobic surface of HMDS-treated SiO_2 is more favorable in fabricating high performance F16CuPc OTFTs. Then, we tried to apply directly the result to the fabrication of OTFTs with polymeric gate insulators. However, in case of the polymeric gate insulators, unlike SiO_2, it was not possible to treat the surface with the

Table 1
The performance parameters of F16CuPc OTFTs with bare SiO_2 and HMDS-treated SiO_2

Device		Mobility (μ, $cm^2/V\,s$)	Threshold voltage (V_T, V)	Subthreshold slope (ss, V/dec)	I_{ON} (A)	I_{ON}/I_{OFF}
Bare SiO_2	Right after fabrication[a]	0.0010	9.1	2.97	7.9×10^{-11}	4.2×10^{2}
HMDS-treated SiO_2	Right after fabrication	0.0018	7.7	2.76	9.6×10^{-11}	8.1×10^{2}
	3 days later[b]	0.0015	7.1	2.56	1.0×10^{-10}	7.5×10^{2}
	5 days later[c]	0.0014	7.6	2.77	8.5×10^{-11}	7.3×10^{2}

[a] Measured right after fabrication in air.
[b] Devices are stored in air for 3 days and measured in air.
[c] Devices are stored in air for 5 days and measured in air.

primer because the polymeric gate insulators usually do not contain reaction sites, which is necessary for the surface treatment. So, new methods to control surface properties need to be developed.

In order to obtain polymeric gate insulator with more hydrophobic surface without any surface treatments such as primer treatment and buffer layer insertion, we have blended two polymers, polyimide (P-1) and poly(amic acid) (P-2). The P-1 has a long alkyl side chain (C_{18} group, see Fig. 1b), which is expected to contribute to make surface of the blend gate insulator hydrophobic. The effect of the C_{18} group on surface properties was investigated by surface tension measurements for both pure P-2 and the blended gate insulator (2/98). We found that the surface of 2/98 (39.1 dyn/cm) was much more hydrophobic than that of P-2 (51.1 dyn/cm). We believe that the non-polar C_{18} group of DA18IM protrudes to the surface and makes the surface more hydrophobic. This was confirmed by a pre-tilt angle measurement of liquid crystal molecules on the blend gate insulator [29]. The surface tension of the blended gate insulator (39.1 dyn/cm) was controlled to match with that (36.9 dyn/cm) of F16CuPc by controlling blending ratio.

One of the important concerns regarding any gate insulators, particularly for polymeric gate insulators, is gate leakage. To determine the electrical properties, such as gate leakage and capacitance, of the blend gate insulator, we have prepared metal–insulator–metal (MIM) capacitor structures on pre-cleaned glass. Leakage current as a function of applied electric field for the gate insulator is shown in Fig. 2. The leakage current was around 3.5×10^{-8} A/cm^2 at an electric field of 2.5 MV/cm. The electrical breakdown of the insulator was not detected up to 3.3 MV/cm. Inset of Fig. 2 shows capacitance–frequency (C–f) characteristic. Capacitance of the blended gate insulator was 97.5 pF/mm^2 at 10 kHz. It is well known that the surface

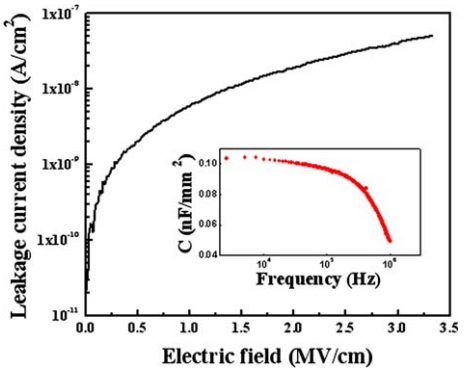

Fig. 2. Leakage current density as a function of the applied electric field for the MIM structure (gold/blended gate insulator (2/98)/gold). Inset: capacitance (C) as a function of frequency (f).

roughness of a gate insulator is one of the most important factors affecting the performance of OTFTs, and a smooth gate dielectric surface improves the molecular ordering of organic semiconductor, leading to improved μ [30]. The surface morphology of the gate insulator was investigated with AFM and the image is shown in Fig. 3. Its surface was smooth enough

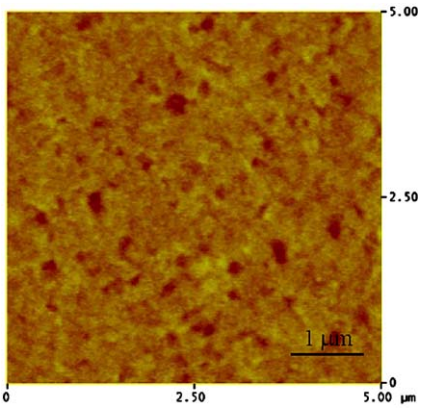

Fig. 3. AFM image of the blended gate insulator. The surface rms roughness is around 3 Å.

(rms roughness 3 Å) for the application of gate insulator.

F16CuPc on top of the gate insulator was characterized with AFM, SEM and XRD measurements. Fig. 4a shows AFM and SEM (inset) images of 60 nm-thick F16CuPc on the blended gate insulator. F16CuPc was composed of worm-like flat lying crystals ranging from a few tens of nm to a few hundred of nm in size. Orientation of F16CuPc molecules on the gate insulator and HMDS-treated SiO_2 was investigated with XRD measurements. The diffractograms are shown in Fig. 4c and indicates that the film is highly ordered with a peak of 6.12° corresponding to a *d*-spacing of 14.4 Å, which is very similar to that of the refraction peak at 6.9° (*d*-spacing = 12.6Å) of copper phthalocyanine (CuPc) [26–28]. The slight difference in the position of diffraction peak is due to the larger Van der Waals radius of *F* over *H*. AFM and XRD results for F16CuPc deposited on HMDS-treated SiO_2 are shown in Fig. 4b and c, and shows a highly ordered crystalline morphology, but it is slightly different in size and shape from the case on the blend gate insulator. Although more detail studies need to be done, we believe that the F16CuPc molecules on the blend gate insulator are standing and oriented perpendicular to the surface of the blended gate insulator based on simple calculation of tilt angel of F16CuPc molecules using the *d*-spacing and the length of one F16CuPc molecule and other reports [15,31–34].

3.2. Device characteristics

Before further discussion on the performance of F16CuPc OTFTs with the blended gate insulator, it is necessary to check the stability of F16CuPC in air since all electrical measurements of OTFTs were carried out in air. To do so, we have fabricated F16CuPc OTFTs with HMDS-treated SiO_2 and

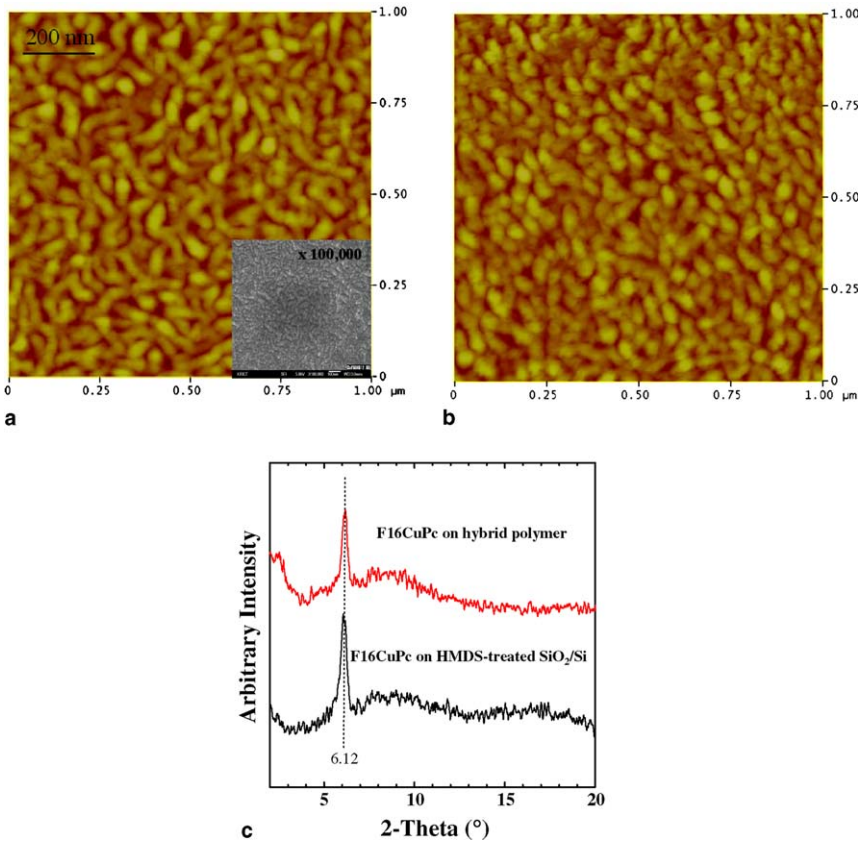

Fig. 4. AFM image of an F16CuPc deposited on (a) the blend gate insulator (inset: SEM image) and (b) HMDS-treated SiO_2. (c) X-ray diffractogram of an F16CuPc deposited on the blend gate insulator and HMDS-treated SiO_2.

checked their performance stability by measuring the OTFTs in air right after fabrication, 3 days and 5 days, respectively. The output characteristic curves (for drain current vs drain voltage, I_{ds} vs V_{ds}) at various positive gate voltages are shown in Fig. 5. Performance parameters of F16CuPC OTFTs with HMDS-treated SiO_2 were extracted from transfer characteristic curves (for drain current vs gate voltage, I_{ds} vs V_{gs}) and summarized in Table 1. The extraction of parameters will be discussed later. We found that the device showed a typical n-type behavior without any significant degradation even after 5 days in air indicating that the F16CuPc OTFTs are very stable in air.

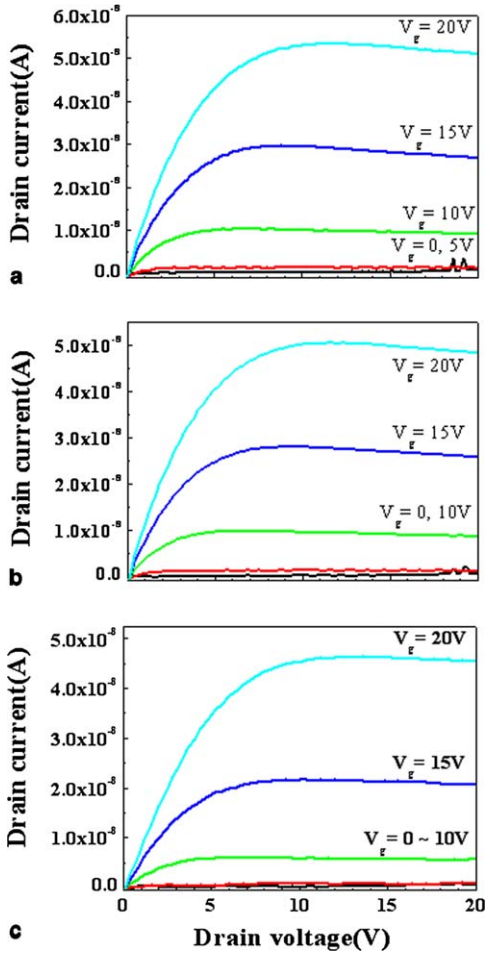

Fig. 5. The output characteristic curves (for drain current vs drain voltage, I_{ds} vs V_{ds}) of F16CuPc OTFTs with HMDS-treated SiO_2 at various positive gate voltages. Measured in air (a) right after fabrication, (b) 3 days later, (c) 5 days later. The devices showed a typical n-type behavior without any significant degradation even after 5 days after fabrication.

When F16CuPC was deposited on top of the blended gate insulator, the substrate temperature, which affects device performance significantly, was 90 °C. The substrate temperature was chosen based on studies about the effect of the substrate temperature on the performance of OTFTs. We have fabricated several F16CuPc OTFTs with HMDS-treated SiO_2 at different substrate temperatures, 30 °C, 60 °C, 90 °C and 120 °C, while fixing all the fabrication parameters. The best performance was extracted from OTFTs fabricated at 90 °C. Device fabricated at 30 °C showed the worst performance and the field-effect mobility was six times lower than that of OTFTs fabricated at 90 °C. So, we adopted 90 °C in fabricating F16CuPc OTFTs with the blended gate insulator in order to compare the performance directly with that of F16CuPc OTFTs with HMDS-treated SiO_2.

The output characteristic curves of the F16CuPc OTFTs with the blended gate insulator at various positive gate voltages are shown in Fig. 6. They shows typical n-type characteristics with a clear transition from linear to saturation behavior (due to a pinch off of the accumulation layer). Fig. 7 shows the transfer characteristic curves for the F16CuPc OTFTs with the blended gate insulator, therein the performance parameters were extracted in a saturation regime. The saturated I_{ds} is given by the following equation:

$$I_{ds} = \frac{WC_i}{2L}\mu(V_{gs} - V_T)^2$$

where I_{ds} is the drain current, W and L are, respectively, the channel width and length, C_i is the capacitance per unit area of the gate insulator layer, and V_{gs} and V_T are the gate voltage and the threshold voltage, respectively. V_T of the device in the saturation regime was determined from the plot of

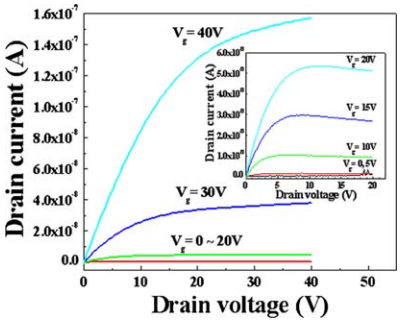

Fig. 6. Output characteristic curves of the F16CuPc OTFT with the blend gate insulator. Inset: out characteristic curves of the F16CuPc OTFT with HMDS-treated SiO_2.

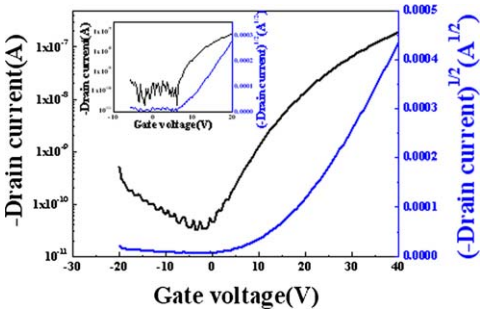

Fig. 7. Transfer characteristic curves of the F16CuPc OTFT with the polyimide hybrid gate insulator. The Y-axis is in $\log(-I_d)$. Inset: transfer characteristic curves of the F16CuPc OTFT with HMDS-treated SiO_2.

the square root of the drain current ($\sqrt{I_{ds}}$) and the gate voltage (V_{gs}) by extrapolating the measured data to $I_{ds} = 0$. μ was calculated from the plot of $\sqrt{I_{ds}}$ vs V_{gs}. The inverse subthreshold swing (ss), which is a measure of how sharply the device transits from the off to the on state, is given by $ss = \left[\frac{d\log(I_{ds})}{dV_{gs}}\right]^{-1}$. V_g was swept from -20 to $+40$ V while the drain voltage V_{ds} was set at $+40$ V. μ and threshold voltage were found to be 6×10^{-3} cm^2/V s and $+14.8$ V, respectively, for F16CuPc OTFTs with the blended gate insulator with a channel length (L) of 50 μm and width (W) of 500 μm. The current modulation ratio (I_{ON}/I_{OFF}) and OFF current (I_{OFF}) were around 5.4×10^3 and 3.5×10^{-11}, respectively, when V_{gs} was scanned from -20 to $+40$ V. The subthreshold swing (ss) was 7.3 V/dec. The threshold voltage was relatively large because of the use of a thick gate insulator. The voltage can be reduced by using a thinner gate insulator or a higher K insulator [21].

F16CuPc OTFTs with inorganic gate insulator have been previously reported by other groups [15,21,23–26]. Bao et al. has reported an F16CuPc OTFT with the mobility of 0.03 cm^2/V s, which is the highest so far [15]. Hoshino et al. has reported an OTFT with the mobility of 1.4×10^{-3} cm^2/V s using double layer (LiF/Al) source and drain electrode in order to improve the charge injection [26]. In addition, we have fabricated F16CuPc OTFTs with HMDS-treated SiO_2 gate insulator on n-type Si wafer. The output and transfer characteristic curves were shown in the inset of Figs. 6 and 7, respectively, and its performance parameters are summarized in Table 1. For transfer characteristic curve, V_g was swept from -20 to $+20$ V while the drain voltage V_{ds} was set at $+20$ V. μ and threshold voltage were found to be 1.8×10^{-3} cm^2/V s and $+7.7$ V, respectively. The current modulation ratio (I_{ON}/I_{OFF}) and I_{OFF} current were around 8×10^2 and 9.6×10^{-11}, respectively. Performance of the reported F16CuPc OTFTs cannot be compared directly with ours due to the difference of fabrication conditions, device geometry and material components. However, it should be mentioned that our F16CuPc OTFTs with the blended gate insulator showed comparable or even better device performance, although we used the polymeric blend gate insulator without any surface treatments and modification of source and drain electrodes for improving charge injection. This result indicates that the blended gate insulator could be an alternative gate insulator for the fabrication of n-type OTFTs for the achievement of organic complementary logic circuit.

4. Concluding remarks

We have prepared a polyimide blend gate insulator by blending two polymers (P-1 and P-2). Surface properties of the blended gate insulator were controlled without any primer treatments through a blending method. We have demonstrated n-type OTFTs with F16CuPc and the blended as an active semiconductor and gate insulator, respectively. The electrical properties of the F16CuPc OTFTs were investigated along with the structural characteristics of F16CuPc deposited on the blended gate insulator, whose surface r.m.s. roughness was around 3 Å. The F16CuPc on the blended gate insulator formed very uniform film, and showed a highly ordered crystalline morphology with a d-spacing of 14.4 Å. The field-effect mobility (μ) of F16CuPc OTFTs with the blended gate insulator was found to be 6×10^{-3} cm^2/V s. The performance was comparable to or even better than that of F16CuPc OTFTs with an inorganic gate insulator. By using the blended gate insulator, which is chemically, thermally, and mechanically stable, and F16CuPc, which is highly ordered, thermally and chemically stable semiconductor, our n-type F16CuPc OTFTs attracts more attention for the fabrication of complementary logic circuit for flexible organic display.

Acknowledgments

This research was supported by a grant from Information Display R&D Center, one of the 21st Century Frontier R&D Program funded by the

Ministry of Commerce, Industry and Energy of Korean Government and National Research Laboratory (NRL) program.

References

[1] C.D. Dimitrakopoulos, P.R.L. Malenfant, Adv. Mater. 14 (2002) 99.
[2] Y.-Y. Lin, D.J. Gundlach, S. Nelson, T.N. Jackson, IEEE Electron Dev. Lett. 18 (1997) 606.
[3] S.F. Nelson, Y.-Y. Lin, D.J. Gundlach, T.N. Jackson, Appl. Phys. Lett. 72 (1998) 1854.
[4] K. Horiuchi, K. Nakada, S. Uchino, S. Hashii, A. Hashimoto, N. Aoki, Y. Ochiai, M. Shimizu, Appl. Phys. Lett. 81 (2002) 1911.
[5] A. Kobayashi, T. Takenobu, S. Mori, A. Fujiwara, Y. Iwasa, Appl. Phys. Lett. 82 (2003) 4581.
[6] R.C. Haddon, J. Am. Chem. Soc. 118 (1996) 3041.
[7] R. Kumashiro, K. Tanigaki, H. Ohashi, N. Tagmatarchis, Hkato, H. Shinohara, T. Akasaka, K. Kato, S. Aoyagi, S. Kimura, M. Takata, Appl. Phys. Lett. 84 (2004) 2154.
[8] J.R. Ostrick, A. Dodabalapur, L. Torsi, A.J. Lovinger, E.W. Kwock, T.M. Miller, M. Galvin, M. Berggren, H.E. Katz, J. Appl. Phys. 81 (1997) 6804.
[9] K.N. Narayanan Unni, A.K. Pandey, J.-M. Nunzi, Chem. Phys. Lett. 407 (2005) 95.
[10] A.R. Brown, D.M. de Leeuw, E.J. Lous, E.E. Havinga, Synth. Met. 66 (1994) 257.
[11] L.L. Chua, J. Zaumseil, J.F. Chang, E.C.W. Ou, P.K.H. Ho, H. Sirringhaus, R.H. Friend, Nature 434 (2005) 194.
[12] Z. Bao, A.J. Lovinger, A. Dodabalapur, Appl. Phys. Lett. 69 (1996) 3066.
[13] H. Abdeldayem, D.O. Frazier, B.G. Penn, D.D. Smith, C.E. Banks, Thin Solid Films 350 (1999) 245.
[14] M.L. Rodriguez-Mendez, J. Souto, J.A. DeSaja, R. Aroca, J. Mater. Chem. 5 (1995) 639.
[15] Z. Bao, A.J. Lovinger, J. Brown, J. Am. Chem. Soc. 120 (1998) 207.
[16] K.Y. Law, Chem. Rev. 93 (1993) 449.
[17] H. Peisert, M. Knupfer, J. Fink, Surf. Sci. 515 (2002) 491.
[18] Z. Bao, Adv. Mater. 12 (2000) 227.
[19] J. Zhang, H. Wang, X. Yan, J. Wang, J. Shi, D. Yan, Adv. Mater. 17 (2005) 1191.
[20] J.H. Shon, C. Kloc, Z. Bao, B. Batlogg, Adv. Mater. 12 (2000) 1539.
[21] B.K. Crone, A. Dodabalapur, R. Sarpeshkar, R.W. Filas, Y.-Y. Lin, Z. Bao, J.H. O'Neill, W. Li, H.E. Katz, J. Appl. Phys. 89 (2001) 5125.
[22] H. Klauk, M. Halik, U. Zschieschang, F. Eder, D. Rohde, G. Schmid, C. Dehm, IEEE Trans. Electron Dev. 52 (2005) 618.
[23] Y.-Y. Lin, A. Dodabalapur, R. Sarpeshkar, Z. Bao, W. Li, K. Baldwin, V.R. Raju, H.E. Katz, Appl. Phys. Lett. 74 (1999) 2714.
[24] S.H. Kim, J.H. Lee, Y.S. Yang, T. Zyung, Mol. Cryst. Liq. Cryst. 405 (2003) 137.
[25] J. Wang, H. Wang, X. Yan, H. Huang, D. Yan, Chem. Phys. Lett. 407 (2005) 87.
[26] S. Hoshino, S. Nagamatsu, M. Chikamatsu, M. Misaki, Y. Yoshida, N. Tanigaki, K. Yase, Jpn. J. Appl. Phys. 41 (2002) L808.
[27] J. Yuan, J. Zhang, J. Wang, D. Yan, W. Xu, Thin Solid Films 450 (2004) 316.
[28] A. Salleo, M.L. Chabinyc, M.S. Yang, R.A. Street, Appl. Phys. Lett. 81 (2002) 4383.
[29] M.H. Yi, K.Y. Choi, J.H. Lee, J.K. Choi, Y.J. Lee, Korean Patent Application Serial No. 2004-0043770, 2004.
[30] D.J. Gundlach, Y.Y. Lin, T.N. Jackson, S.F. Nelson, D.G. Schlom, IEEE Electron Dev. Lett. 18 (1997) 87.
[31] M. Halik, H. Klauk, U. Zschieschang, T. Kriem, G. Schmid, W. Radlik, Appl. Phys. Lett. 81 (2002) 289.
[32] K. Xiao, Y. Liu, G. Yu, D. Zhu, Appl. Phys. A 77 (2003) 367.
[33] R. Ye, M. Baba, Y. Oishi, K. Suzuki, Appl. Phys. Lett. 86 (2005) 253505.
[34] M. Komiyama, Y. Sakakibara, H. Hiorai, Thin Solid Films 197 (1991) 335.

Available online at www.sciencedirect.com
SCIENCE DIRECT
Organic Electronics 7 (2006) 85–98
Organic Electronics
www.elsevier.com/locate/orgel

The synthesis and properties of iridium cored dendrimers with carbazole dendrons

Shih-Chun Lo [a], Ebinazar B. Namdas [b], Christopher P. Shipley [a], Jonathan P.J. Markham [b], Thomas D. Anthopolous [b], Paul L. Burn [a,*], Ifor D.W. Samuel [b,*]

[a] *Department of Chemistry, University of Oxford, Chemistry Research Laboratory, Mansfield Rd, Oxford OX1 3TA, United Kingdom*
[b] *Organic Semiconductor Centre, School of Physics and Astronomy, University of St Andrews, North Haugh, St Andrews, Fife KY16 9SS, United Kingdom*

Received 19 July 2005; received in revised form 8 November 2005; accepted 21 November 2005
Available online 15 December 2005

Abstract

A convergent procedure has been developed for the preparation of *fac*-tris(2-phenylpyridyl)iridium(III) cored dendrimers with first- and second-generation dendrons that each contain one and two carbazole units, respectively. The carbazole moieties are both an electroactive moiety and a branching unit in the dendron. The photoluminescence quantum yields of neat films of the first- and second-generation dendrimers were 48 ± 5% and 39 ± 4%, respectively. These values are substantially higher than for equivalent first- and second-generation dendrimers with phenyl moieties at the branching points of the dendrons instead of the carbazole units. The improved solid state luminescent properties can be attributed to the increased steric demand of the carbazole unit relative to the phenyl ring, which reduces more effectively the intermolecular interactions that cause the cores to be less emissive. Electrochemical experiments showed that both the core of the dendrimers and the dendrons were electroactive. Thin film hole mobilities of the first-generation dendrimer with the carbazolyl branching units in the dendrons were found to be higher than the equivalent dendrimer with biphenyl branching units across a range of fields.

PACS: 70; 80

Keywords: Dendrimer; Phosphorescence; Organic light-emitting diodes

1. Introduction

Highly efficient phosphorescent materials are likely to play an important role in the commercialisation of organic light-emitting diodes (OLEDs). The most developed family of phosphorescent materials are small molecules based on iridium complexes [1–7]. For these molecular complexes to

* Corresponding authors. Tel.: +44 (0) 1865 275643; fax: +44 (0) 1865 285002 (P.L. Burn), tel.: +44 (0) 1334 463114; fax: +44 (0) 1334 463104 (I.D.W. Samuel).
E-mail addresses: paul.burn@chem.ox.ac.uk (P.L. Burn), idws@st-andrews.ac.uk (I.D.W. Samuel).

1566-1199/$ - see front matter © 2005 Elsevier B.V. All rights reserved.
doi:10.1016/j.orgel.2005.11.003

work well in OLEDs it is normally necessary to deposit them as a guest in a host matrix. The performance of devices based on iridium(III) complexes blended into carbazole containing hosts is sensitive to the guest concentration or number of carbazole units. By having a low concentration of phosphorescent guest in the matrix the intermolecular interactions that lead to quenching of the luminescence can be avoided. However, this requires the guest to be evenly distributed throughout the film without phase separation and this is difficult to achieve reliably by techniques used to form blended films. We have been approaching controlling intermolecular interactions in light-emitting materials from a different direction by the development of solution processible light-emitting dendrimers for use in dendrimer light-emitting diodes (DLEDs) [8]. The light-emitting dendrimers have been comprised of surface groups to aid solubility and processing, and conjugated dendrons to control the intermolecular interactions of the emissive cores. For both fluorescent and phosphorescent dendrimers we have found that the efficiency of a device can be improved by simply changing the generation [8,9]. Generally, with emissive layers comprised of neat dendrimer films the efficiency increases in going from the first to the second generation. For example, with dendrimers comprised of 2-ethylhexyloxy surface groups, three biphenyl based dendrons, and phosphorescent *fac*-tris(2-phenylpyridyl)iridium(III) ($Irppy_3$) cores we have found that the efficiency of single layer devices increases by around a factor of 10 in moving from the first to the second generation [9]. However, in these simple phosphorescent dendrimers the single dendron per ligand was not sufficient to control the intermolecular interactions of the emissive cores, and the efficiencies of the single layer devices containing the neat dendrimer films were still below those reported for the highly tuned evaporated devices. For DLEDs a step change in efficiency was observed when the light-emitting layer was comprised of a blend of the phosphorescent dendrimer with a carbazole containing host and in moving from single layer to bilayer devices containing an electron transport layer [10–12]. The efficiencies of the bilayer devices were remarkably high at useable brightnesses and were similar to those reported for the more complex evaporated device architectures. One reason for the excellent blended DLED efficiencies is that the blended films have high photoluminescence quantum yields (PLQYs) [13]. A high PLQY suggests that the dendrimer guest is evenly

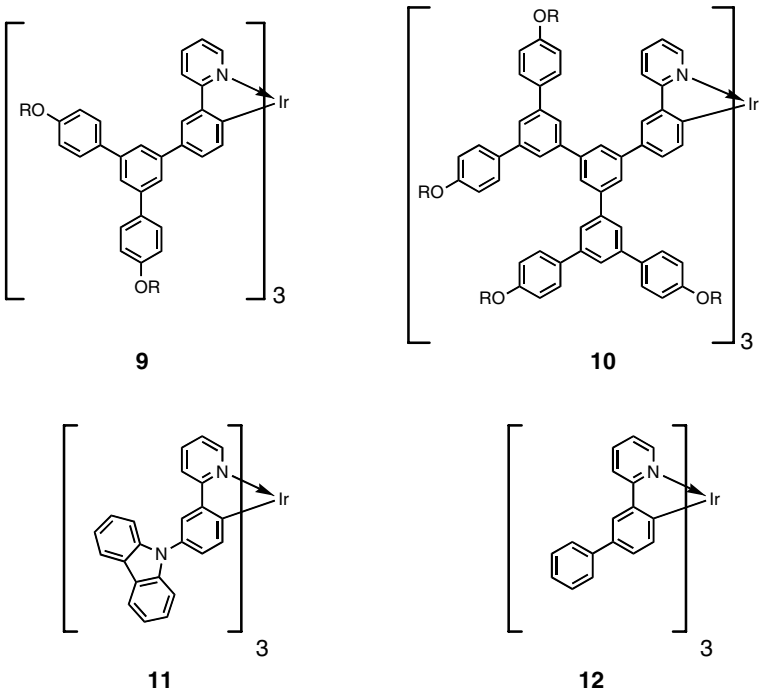

Fig. 1. Structures of first (**9**) and second-generation (**10**) dendrimers with R = 2-ethylhexyl and biphenyl dendrons, and model compounds **11** and **12** with pendant carbazole and phenyl groups, respectively.

distributed throughout the emissive film. Nevertheless, guest/host films are not ideal for manufacturing and hence the introduction of the host moiety into the structure may lead to enhanced properties. Copolymers containing carbazole units and iridium(III) complexes have been reported, although devices containing these materials have shown only modest performance [14,15]. The reason for this is difficult to ascertain due to the (often) complex polymer morphology. Dendrimers are ideal structures to investigate the relationship between the number of carbazole units and properties of the emissive core, as simply changing the generation can control the number of carbazole units. There have been only a few reports on carbazole containing dendrons [16–21] and the concept of using carbazole dendrons in conjunction with organometallic complexes was disclosed by us a few years ago [22]. More recently the synthesis and properties of several ruthenium complexes to which carbazole dendrons were attached has been described [23]. However, the ruthenium complex cored dendrimers are not useful in the context of DLEDs as they are charged macromolecules and have low photoluminescence quantum yields at room temperature.

In this paper we explore the effect of incorporating carbazole moieties into the structure of phosphorescent dendrimers. We report the synthesis of solution processable phosphorescent green-emissive dendrimers comprised of $Irppy_3$ cores and covalently attached dendrons. The dendrons contain carbazole units and 2-ethylhexyloxy groups are at the distal ends of the dendrons to give solubility. We report the physical, photophysical, and electrochemical properties of the first- and second-generation dendrimers that have three and six carbazole units, respectively. By comparing the photoluminescence quantum yield of solutions and neat films, we infer the extent to which intermolecular interactions are controlled by the dendrons. We also compare the properties of the dendrimers with the first- and second-generation dendrimers (Fig. 1: **9** and **10**, respectively) [24] containing the same emissive core and surface groups but biphenyl based dendrons.

2. Results and discussion

2.1. Synthesis

A convergent synthetic strategy (Scheme 1) was used for the preparation of the green emitting dendrimers with 2-ethylhexyloxy surface groups, three carbazole containing dendrons, and $Irppy_3$ cores. The first step in the synthesis was the palladium catalysed coupling of the pinacolylboronate ester **1** [24] with commercially available 3,6-dibromocarbazole. The correct choice of catalyst enabled the desired coupling to proceed without the need to protect the carbazole nitrogen. Tetrakis(triphenylphosphine)palladium(0) was a suitable catalyst and the first-generation dendron **3** was formed in a 43% yield from the reaction of the ''zeroeth''-generation boronate ester [G0-B($OCMe_2$)$_2$] **1** with 3,6-dibromocarbazole. Compound **3** was then simply coupled with 2-(3-bromophenyl)pyridine using tris(dibenzylideneactone)di-palladium(0) as catalyst to form the first-generation dendronised ligand **4** with one carbazole unit in a 96% yield. The second-generation dendronised ligand containing two carbazole units was formed by coupling **3** to 2-[3-(3,5-dibromophenyl)phenyl]pyridine **5** [24] under similar conditions used for the formation of **4**, giving **6** in a 91% yield. To form the first-generation dendrimer **7** from **4** a two-step procedure was used [25–27]. The dendronised ligand **4** was heated with iridium(III) chloride trihydrate in 2-ethoxyethanol to form the corresponding bis-iridium bis-chloro-bridged dimer in a 75% yield. The dimer was collected and in the second step reacted with an excess of ligand **4** in the melt using silver trifluoromethylsulfonate to drive the reaction forward. Under these conditions the first-generation dendrimer **7** was formed in a 49% yield. Although the second-generation dendrimer **8** could be formed under similar conditions it was found that a better yield of the desired material could be achieved by reacting **6** in a single step with iridium(III) acetylacetate in ethylene glycol heated at reflux. Under these conditions **8** was formed and isolated in a 32% yield. The characterisation data were all consistent with the structures of the dendrimers although the analysis of the ^{1}H NMR spectra was not always straightforward. The ^{1}H NMR of **7** was easily interpretable and from the relative simplicity of the ^{1}H NMR we concluded that the dendrimer was the *facial* isomer [26,27]. However, the ^{1}H NMR spectrum of **8** was found to be concentration dependent (Fig. 2). At concentrations normally used for ^{1}H NMR the proton signals of the dendrimer were broad and in addition more than one environment was observed for some protons (Fig. 2a). It is important to note that in spite of the multiplicity of some signals for a particular proton the integration ratios were consistent with the structure of **8**. When the concentration was reduced significantly

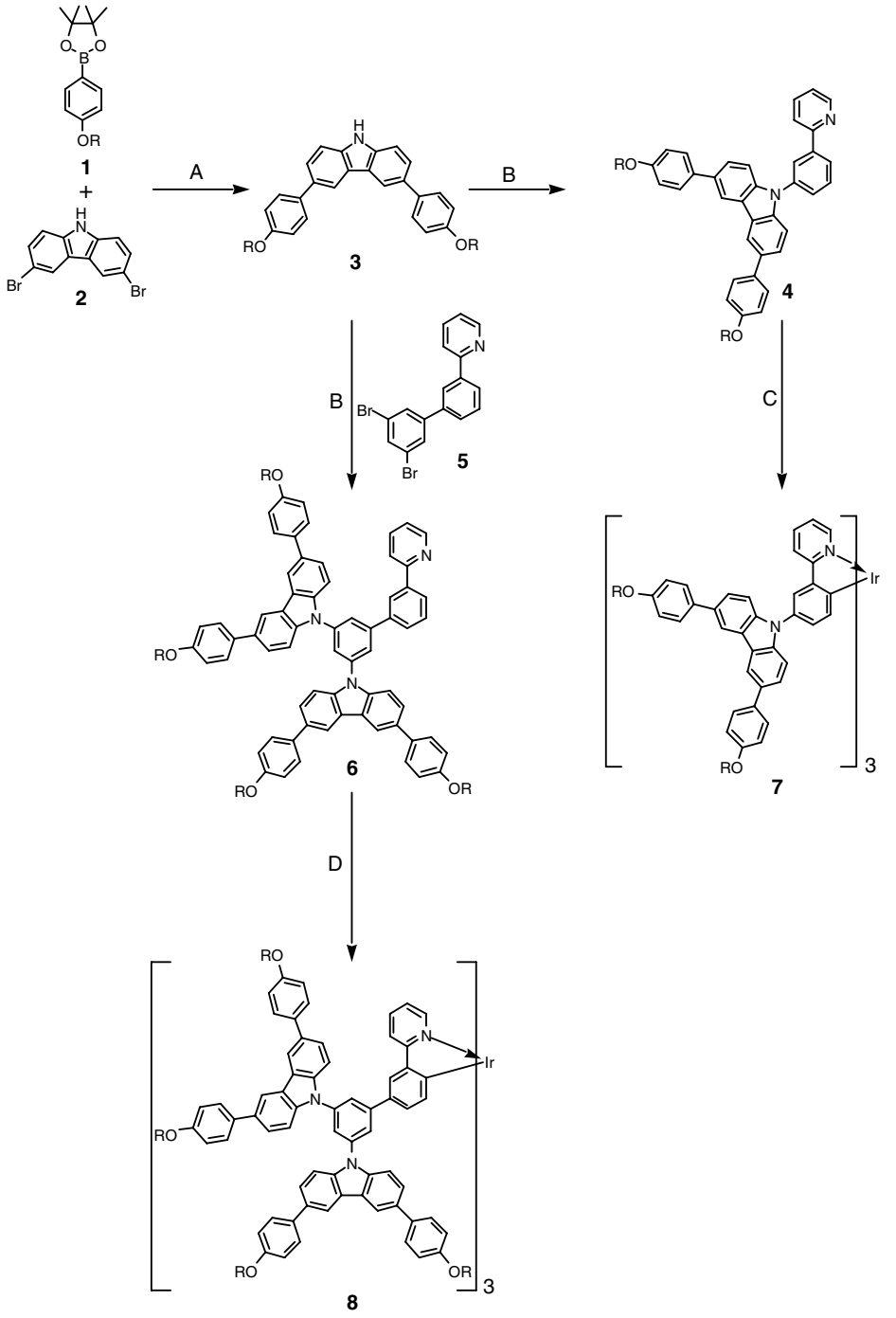

Scheme 1. Key: (A) Tetrakis(triphenylphosphine)palladium(0), aqueous sodium carbonate, ethanol, toluene, reflux, Ar. (B) Tris(dibenzylideneacetone)di-palladium(0), tri-*t*-butylphosphine, 2-(3-bromophenyl)pyridine, sodium *t*-butoxide, toluene, reflux, Ar. (C) Iridium(III) chloride tri-hydrate, water, 2-ethoxyethanol, reflux, Ar and then **4**, silver trifluoromethanesulfonate, heat, Ar. (D) Iridium(III) acetylacetonate, anhydrous ethylene glycol, reflux, Ar.

(≈0.4 mg/mL) the number of signals decreased and the peaks became more defined (Fig. 2b). This concentration dependence strongly suggests that **8** aggregates at higher concentrations in solution, which has important ramifications for films that are formed by solution processing.

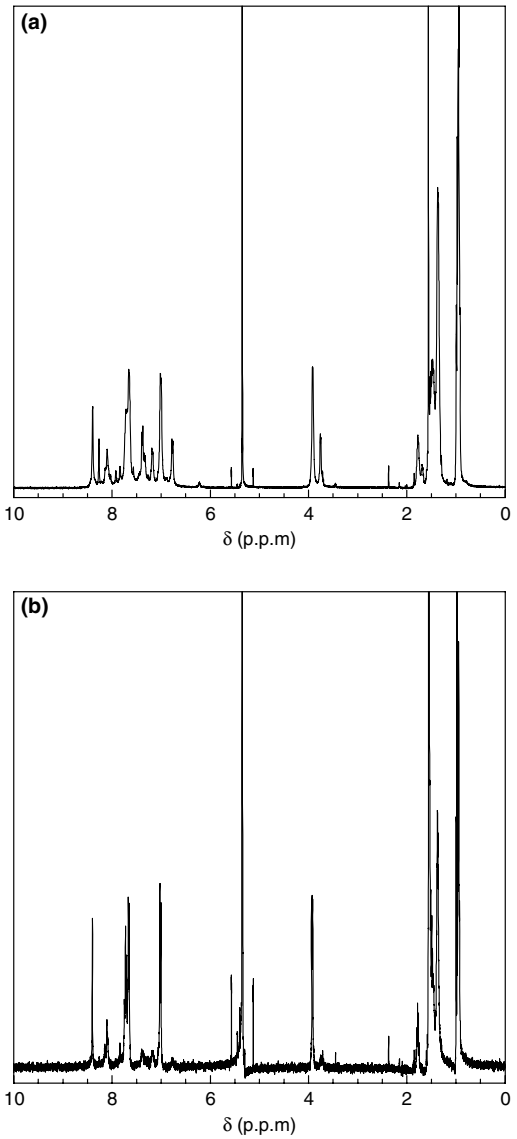

Fig. 2. ^{1}H NMR of **8** at (a) normal and (b) dilute concentrations in CD_2Cl_2. The concentrated spectrum is more complicated suggesting aggregation in solution.

2.2. Physical properties

The first and second-generation carbazole containing dendrimers differ in two distinct ways; first, the first-generation dendrimer **7** has the carbazole branching unit with the nitrogen of the carbazole unit directly attached to the phenyl ring that is complexed to the iridium(III). In contrast, the second-generation dendrimer **8** has two different branching points, the first branching point being a phenyl ring and the second being the carbazole unit. That is, in **8** the carbazole unit is not directly attached to the phenyl that is directly attached to the iridium(III). In fact because of the *meta* arrangement of the carbazole branching units around the first branching phenyl in **8** the nitrogen lone pair of the carbazole units cannot be delocalised into the ligand phenyl ring. Both dendrimers were soluble in solvents such as tetrahydrofuran, toluene, chloroform and dichloromethane. They could be spin-coated from solution to give thin films although it proved somewhat difficult to get good films reproducibly. This is in contrast to **9** and **10** (Fig. 1), which gave good quality thin films as neat layers and as blends with hosts such as 4,4′-bis(*N*-carbazolyl)biphenyl (CBP) [13]. In analysing the structure–property relationships of dendrimers it is useful to determine the hydrodynamic radii of the dendrimers. The hydrodynamic radii were determined by gel permeation chromatography (GPC) from the $\overline{M}_v$ in combination with the Hester-Mitchell equation and the Mark-Houwink relationship [28]. GPC analysis showed that the dendrimers were mono-disperse with the first (**7**) and second (**8**) generation dendrimers having $\overline{M}_v$s of 2508 and 4059, which correspond to hydrodynamic radii of 10.8 and 14.3 Å, respectively. The hydrodynamic radii of **9** and **10** (Fig. 1) that only contain phenyl units, were 10.2 and 13.3 Å, which are around 5% smaller than **7** and **8** with the larger carbazole units in the dendrons accounting for the increased radii.

Thermal gravimetric analysis was carried out at a heating rate of 10 °C/min under nitrogen. Both **7** and **8** were thermally stable with 5% weight loss being observed at 412 °C and 309 °C, respectively. Differential scanning calorimetry at a scan rate of 150 °C/min showed that **7** had a glass transition temperature (T_g) at 193 °C. The T_g of **7** is significantly higher than that observed for the first-generation dendrimer **9** (132 °C) [24] reflecting its higher molecular mass and the rigidity imparted by the carbazole units. No T_g was observed for **8** within the limits of the experiment. This is not surprising given the increased molecular weight and number of carbazole units in the dendrimer when compared to **7**.

2.3. Calculation of molecular orbitals

Density functional theory calculations for carbazole and phenyl substituted $Irppy_3$ analogues (**11** and **12**, respectively in Fig. 1) were carried out to determine the distribution and relative energies of the highest occupied (HOMO) and lowest

Table 1
Molecular orbital distribution (%) and energies for **11** and **12**

	Iridium d	Pyridine	Ligand Ph		Residual[a]	Energy (eV)
11				Carbazole		
HOMO	24.8	4.2	30.1	40.4	0.5	−5.06
LUMO	1.5	89.8	8.0	0.3	0.3	−1.99
12				Phenyl		
HOMO	52.1	7.5	33.4	6.2	0.8	−5.03
LUMO	1.6	91.4	6.3	0.3	0.3	−1.69

[a] Residual: The remaining orbital density not attributed to the main components.

unoccupied molecular orbitals (LUMO), and the results are summarised in Table 1. For **11** and **12** the LUMO distribution was similar with around 90% of the orbital density on the pyridyl ring and small but similar amounts on the iridium(III), ligand phenyls, and pendant aromatic moieties. In contrast there were significant differences in the HOMO distribution between **11** and **12**. For **12** with the pendant phenyl group the HOMO density was highest on the iridium(III) (52%) with the ligand phenyl ring also having substantial orbital density (33%). There was very little orbital density on the pyridyl or pendant phenyl rings. For **11** the calculations showed that the HOMO density was highest on the carbazole ring (40%) (with the largest proportion of this on the carbazole nitrogen) and the density on the iridium(III) was much lower than in **12**.

2.4. Photophysical properties

The UV–vis spectrum of $Irppy_3$, which is at the core of the dendrimers, can be divided into two main regions. The first region at around 280 nm corresponds to absorptions due to the π to π* transitions of the ligands with the longer wavelength overlapping absorptions between 325 and 475 nm arising from the metal complex [29]. For **9**, where the biphenyl dendrons are attached to the ligand phenyl *meta* to the pyridyl ring of $Irppy_3$, there is little change in either the strength or position of the absorptions of the core metal complex at longer wavelength [24]. However, at shorter wavelengths, around 280 nm, the molar absorptivity of **9** is much larger than $Irppy_3$ due to the biphenyl units in the dendron (Fig. 3). In addition, it is important to note that the absorption of the dendrons also partially overlaps the short wavelength absorptions of the core iridium(III) complex [24]. In moving from the biphenyl dendrons of **9** to the carbazole dendrons of **7** and **8** little difference is seen in the long wavelength absorptions (above 390 nm) implying that the carbazole dendrons are not substantially changing the energies of the 'metal-to-ligand charge transfer' (MLCT) states associated with the iridium(III) complex (Fig. 3). At shorter wavelengths both **7** and **8** have two absorption maxima at approximately 263 nm and 296 nm. Compound **8** is more strongly absorbing in this wavelength region due to the greater number of carbazole units in each of the dendrons. As in the case of **9** the longer wavelength absorptions of the dendrons in **7** and **8** overlap with the higher energy MLCT transitions of the $Irppy_3$ core.

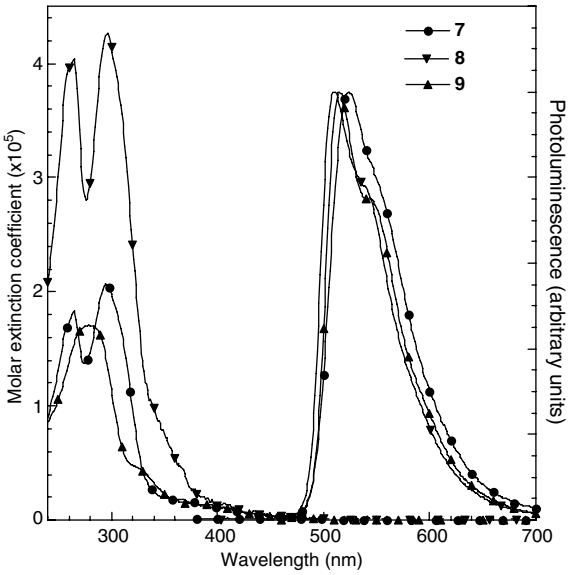

Fig. 3. Solution absorption (dichloromethane) and photoluminescence spectra of **7** and **8** (tetrahydrofuran), and **9** (toluene) (excitation wavelength = 360 nm).

The next step in the analysis of photophysical properties was to determine the emissive properties of **7** and **8**. Solutions of the dendrimers were excited at 360 nm, a wavelength where both the core and

the dendrons absorb light, and the photoluminescence (PL) spectra of dendrimers **7**, **8**, and **9** are shown in Fig. 3. It should be noted that the solution PL spectrum of **10** was identical to **9**. The first point to note is that the emission maxima and the general shape of the spectra of **7**, **8**, and **9** are similar implying that the emission arises from iridium(III) complexes with similar excited states and energies. As with other light-emitting dendrimers no emission was seen from the dendrons [24,31] indicating efficient energy transfer from the dendrons to the core. The emission maxima of **7**, **8**, and **9** were 523 nm, 510 nm and 515 nm, respectively. A reason for the PL spectra being so similar is that the connectivity around the aromatic rings means although the dendrons are fully conjugated the π-system is not fully delocalised. For example, the carbazole moiety of **7** and the first branching phenyl groups in **8**, **9**, and **10** are not in conjugation with the pyridyl ring of the ligand. It is interesting that although the distribution of the HOMO density of **7** is significantly different to **9** (based on model compounds **11** and **12**), the PL spectrum does not change dramatically.

We probed the effect of the carbazole dendrons on the photophysical properties of the dendrimers further by measuring the PL quantum yields (PLQYs). The PLQY of **7** in degassed tetrahydrofuran was $65 \pm 6\%$, which within the error of the experiment, is the same as the solution PLQYs of $70 \pm 7\%$ and $69 \pm 7\%$, respectively for first-generation **9** and second-generation **10** biphenyl dendroned dendrimers in degassed toluene [24]. This indicates that even though there is a substantial component of the HOMO on the carbazole rings of **7** it does not lead to new non-radiative pathways that can quench the luminescence. The PLQY of **8** at $48 \pm 5\%$ was a little lower than those of **7**, **9**, and **10**. A possible reason for the lower PLQY of **8** is that even at the low concentrations ($\approx 10^{-6}$ M) used for the measurement there may be some intermolecular interactions that lead to quenching of the luminescence. Although the concentration used for the PLQY measurement is significantly less than that used for the NMR experiment, both indicate that **8** has a propensity to interact in solution.

In moving from solution to the solid state significant differences in the PLQYs were observed. For **9** and **10** the solid state PLQY yields were $22 \pm 2\%$ and $31 \pm 3\%$, respectively. The higher solid state PLQY for **10** is at least in part due to the larger dendrons keeping the emissive cores further apart and thus reducing the core–core interactions that give rise to luminescence quenching. For the second-generation carbazole dendrimer **8** the solid state PLQY measured under similar conditions was found to be $39 \pm 4\%$. The decrease in PLQY in going from solution to the solid state for **8** (from 48% to 39%) is smaller than that of **10**, which decreases from 69% in solution to 31% in a neat film. The solid state PLQY of the first-generation carbazole dendrimer **7** was $48 \pm 5\%$, which is high for a neat film of an iridium(III) complex. It is also closer to the value in solution than is the case for its counterpart **9** with biphenyl dendrons (solution 70%, neat film 22%). These results show that the carbazole dendrons are more effective than biphenyl dendrons in protecting the emissive cores from quenching interactions, that is, they are more sterically demanding. The higher solid state PLQY observed for **7** when compared to **8** may be due to the larger carbazole branching group being closer to the emissive core, thus providing better protection of the core. Time-resolved luminescence measurements on films of **7** and **8** were performed. The decays are biexponential, with an average lifetime of 0.99 μs for **7** and 0.78 μs for **8**. The faster decay of **8** is consistent with its lower PLQY.

2.5. Electrochemical and charge transporting properties

In addition to controlling intermolecular interactions, the carbazole dendrons can also participate in the electrochemistry and charge transport of the dendrimers. $Irppy_3$ undergoes three chemically reversible one-electron reductions at −2.77, −2.95, and −3.19 V and one chemically reversible oxidation at 0.26 V [30]. The attachment of the first-generation biphenyl based dendrons to the $Irppy_3$ core did not significantly change the redox processes. Compound **9** also has three chemically reversible reductions with $E_{1/2}$s of −2.91, −3.10, and −3.28 V and a chemically reversible oxidation at 0.24 V [24]. The first-generation carbazole dendrimer **7** has significantly different electrochemical properties when compared to **9**. Compound **7** undergoes four chemically reversible oxidations (Fig. 4a) with $E_{1/2}$s of 0.31, 0.56, 0.72, and 0.87 V. The first oxidation of **7** is of the iridium(III) containing chromophore, and the fact that its potential is similar to **9** is consistent with the similarity of the calculated HOMO energies of **11** and **12** (Table 1). To determine the origin of the oxidations at more positive potentials in **7** the oxidative processes of

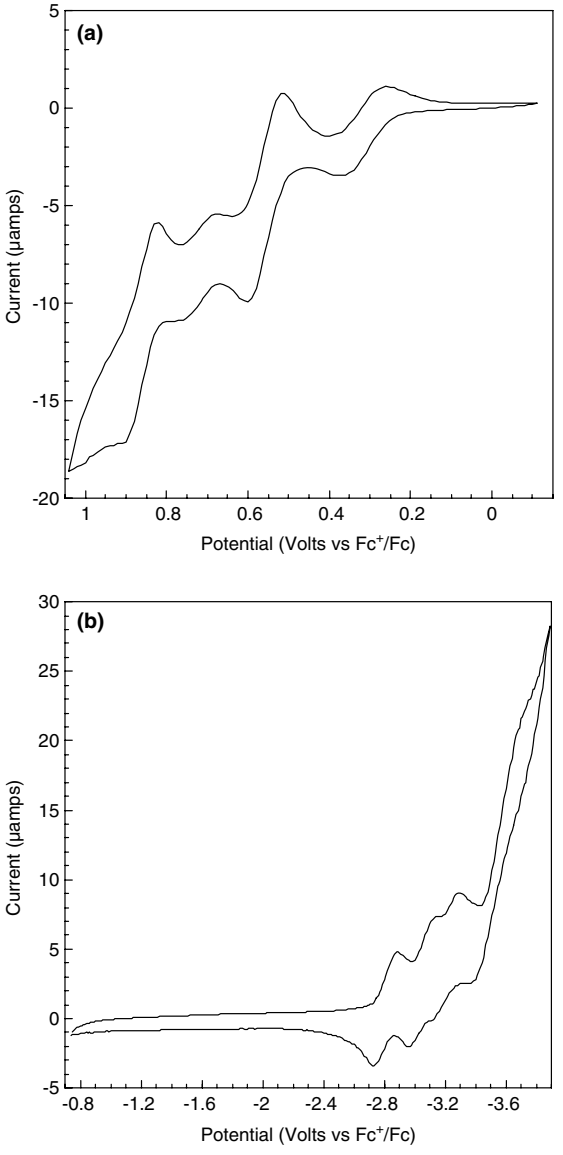

Fig. 4. (a) Oxidation cyclic voltammogram of **7**. Scan rate = 40 mV/s, solvent = dichloromethane, concentration = 1 mM, platinum working electrode, platinum counter electrode, Ag/0.1 M $AgNO_3$ in acetonitrile reference electrode. (b) Reduction cyclic voltammogram of **7**. Scan rate = 120 mV/s, solvent = tetrahydrofuran, concentration = 1 mM, glassy carbon working electrode, platinum counter electrode in 0.1 M tetra-*n*-butylammonium tetrafluoroborate in tetrahydrofuran, Ag/3 M NaCl/AgCl(sat) reference electrode. The potentials are referenced to the ferricenium/ferrocene couple.

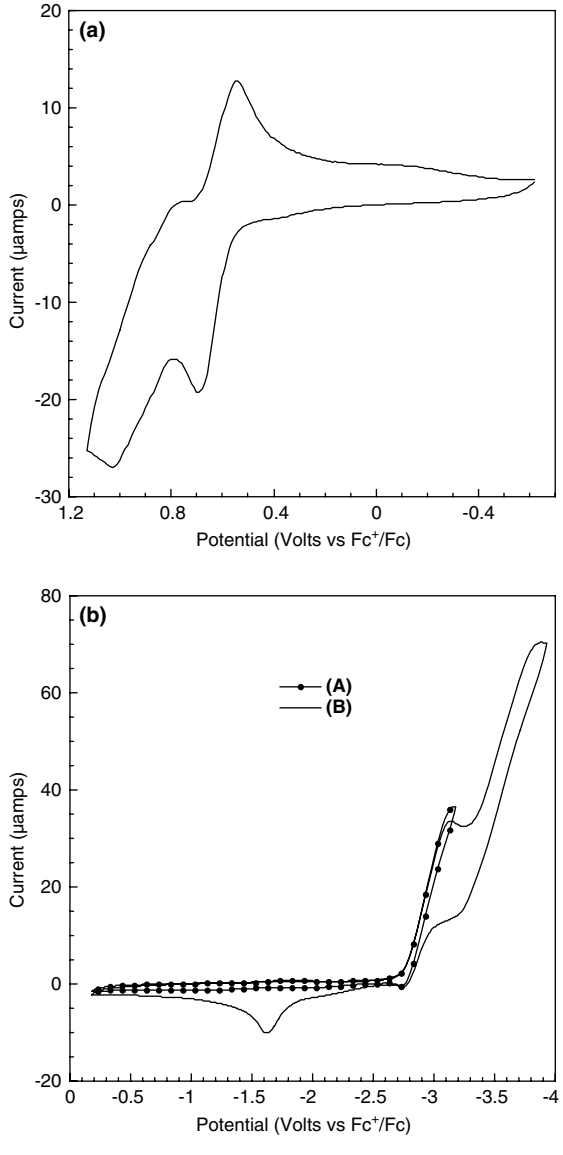

Fig. 5. (a) Oxidation cyclic voltammogram of **4**. Scan rate = 120 mV/s, solvent = dichloromethane, concentration = 1 mM, platinum working electrode, platinum counter electrode, Ag/0.1 M $AgNO_3$ in acetonitrile reference electrode. (b) Reduction cyclic voltammogram of **4**. Scan rate = 120 mV/s, solvent = tetrahydrofuran, concentration = 1 mM, platinum working electrode, platinum counter electrode in 0.1 M tetra-*n*-butylammonium tetrafluoroborate in tetrahydrofuran, Ag/0.1 M $AgNO_3$ in acetonitrile reference electrode. (A) Switching potential = −3.17 V and (B) switching potential = −3.92 V. The potentials are referenced to the ferricenium/ferrocene couple.

the first-generation dendronised ligand **4** were measured. The dendronised ligand **4** was found to undergo two chemically reversible oxidations with $E_{1/2}$s of 0.60 and 0.89 V (Fig. 5a). The oxidation of **4** at 0.60 V is close to the $E_{1/2}$ of the second oxidation of **7** indicating that the latter oxidations are due to the bis(phenyl)carbazole units in the dendrons. Four electrochemical reductions were also observed for **7** with half potentials of −2.81, −3.05, −3.23, and −3.55 V (Fig. 4b). The first three reductions are at similar potentials to those

observed for **9** and are normally assigned to the core iridium(III) complex. To understand the reductions of **7** more fully we studied the reduction processes of **4**. The reductions of **4** were difficult to measure due to the sensitivity of the reduced states to moisture and oxygen, and the observed cyclic voltammogram was strongly dependent on the switching potential used. When the switching potential was −3.17 V a single redox process, which was essentially chemically reversible, was observed (Fig. 5b). The $E_{1/2}$ of the reduction was −2.94 V, which is at a similar potential to the first reduction of the $Irppy_3$ complex and hence showing that the first reduction of **4** is of the ''ligand'' and not the dendron. If the switching potential was moved to −3.92 V then a second reduction process with E_{pc} of −3.88 V was observed (Fig. 5b). This second reduction is due to the bis(phenyl)carbazole unit of the dendron. However, the corresponding oxidation process was not seen although an oxidative wave at more positive potential (−1.63 V) was observed. Similar effects of high negative switching potentials have been reported for conjugated dendrimers and attributed to aggregation of the reduced species rather than chemical degradation [31,32]. Indeed for **4** the cyclic voltammogram does not change substantially over a number of cycles indicating that chemical degradation is not occurring. The second-generation carbazole dendrimer **8** was also more redox active than the second-generation biphenyl based dendrimer **10**. Compound **8** had two well-defined oxidation processes with $E_{1/2}$s of 0.36 and 0.63 V (Fig. 6). The potential of the first of these is similar to the $E_{1/2}$ of the first oxidation of **7** and can be assigned to the oxidation of the iridium(III) complex at the dendrimer core whilst the second corresponds to dendron-based oxidations. The latter was confirmed by determining the oxidation processes for the second-generation ligand **6**, which had chemically reversible oxidations with $E_{1/2}$s of 0.62 and 0.91 V (Fig. 7a). Two more oxidation processes could be observed for **8** on the anodic sweep but we could not differentiate the corresponding reduction waves due to the resolution of the experiment. Nevertheless, all the oxidative processes were chemically reversible. The reduction processes of the second-generation ligand **6** are shown in Fig. 6b and are similar to that observed for the first-generation ligand **4**. The reduction processes of the second-generation dendrimer **8** were difficult to elucidate and interpret. We believe the difficulty may arise from the fact that the concentrations used for the electrochemical experiment are above those at which the ^1H NMR indicates that the dendrimers are interacting or aggregating in solution.

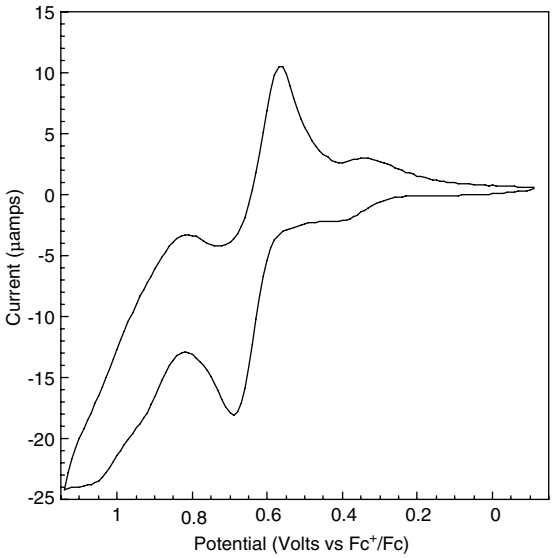

Fig. 6. Oxidation cyclic voltammogram of **8**. Scan rate = 40 mV/s, solvent = dichloromethane, concentration = 1 mM, platinum working electrode, platinum counter electrode, Ag/0.1 M $AgNO_3$ in acetonitrile reference electrode. The potentials are referenced to the ferricenium/ferrocene couple.

We have measured the hole mobilities of **7** and **9** using the time of flight technique with a charge generation layer (see Ref. [33] for further details). The results are shown in Fig. 8, and we find that over the entire range of fields measured, the hole mobility of **7** is much higher than that of **9**. We also find that the photocurrent transients of **7** are non-dispersive at room temperature, in contrast to **9** (data not shown). The difference in hole mobility can be understood from the molecular orbital calculations. For dendrimer **9**, which has the biphenyl dendrons, the HOMO is localised in the *fac*-tris(2-phenylpyridyl)iridium(III) core as in model compound **12**. Hence the mobility of the holes is dependent on the core-to-core distance in the film. However, for **7** the molecular orbital calculations on model compound **11** show that the HOMO has substantial character on the carbazole rings. Therefore, the hole mobility is not just reliant on the distance between the *fac*-tris(2-phenylpyridyl)iridium(III) cores in the solid state but also includes the interactions of the carbazole moieties on adjacent dendrimers. Given there are more hole transporting moieties in **7** than **9**, that is, in **7** the hole transporting moiety is not localised to the iridium(III) complex, and that

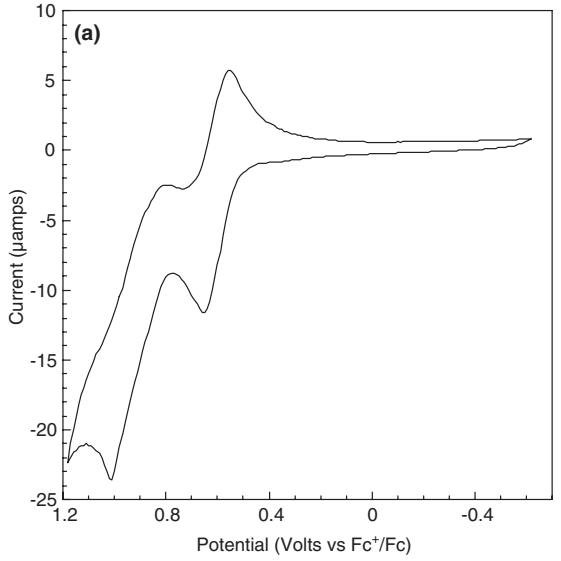

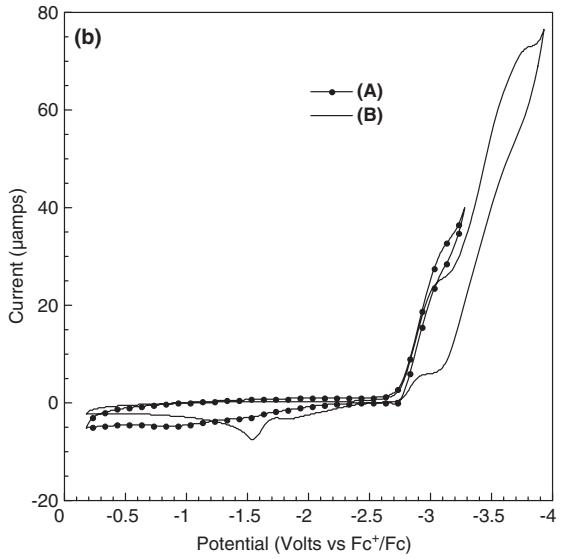

Fig. 7. (a) Oxidation cyclic voltammogram of **6**. Scan rate = 120 mV/s, solvent = dichloromethane, concentration = 1 mM, platinum working electrode, platinum counter electrode, Ag/0.1 M $AgNO_3$ in acetonitrile reference electrode. (b) Reduction cyclic voltammogram of **6**. Solvent = tetrahydrofuran, concentration = 1 mM, platinum working electrode, platinum counter electrode in 0.1 M tetra-*n*-butylammonium tetrafluoroborate in tetrahydrofuran, Ag/0.1 M $AgNO_3$ in acetonitrile reference electrode. (A) Switching potential = −3.27 V, scan rate = 600 mV/s, and (B) switching potential = −3.92 V, scan rate = 120 mV/s. The potentials are referenced to the ferricenium/ferrocene couple.

they can pack more closely it is not surprising the hole mobility of **7** is greater than **9**. In addition, the non-dispersive photocurrent transients at room

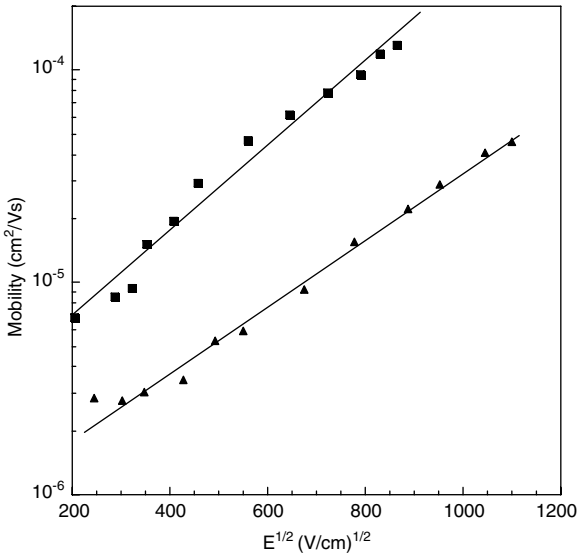

Fig. 8. Mobility versus electric field for the first-generation carbazolyl **7** (squares) and biphenyl **9** (triangles) dendrimers.

temperature indicate that films of **7** may be more ordered, and this would also give rise to improved hole mobility.

3. Conclusion

It has been shown that carbazole units, which are commonly used in host materials for phosphorescent LEDs, can be incorporated into phosphorescent dendrimers by a simple convergent synthetic route. The dendrimers, which have carbazole containing dendrons and iridium(III) complex cores, were found to be more electrochemically active, and had improved film PLQYs and charge transport.

4. Experimental

4.1. Measurements

NMR spectra were recorded on a Bruker DPX400, DQX400 or AMX500 spectrometers: sp H = surface phenyl H; bp H = branch phenyl H; CarbH = carbazole H, L-H = ligand phenyl H and pyridyl H. All *J* values are in Hertz and are rounded to the nearest 0.5 Hz. UV–vis spectra were recorded on a Perkin–Elmer UV–vis Lambda 14P spectrometer and were recorded as solutions in spectroscopic grade dichloromethane. Infrared spectra were recorded on a Perkin–Elmer Spectrum 1000 FT-IR

spectrometer. Mass spectra were recorded on a Fisons Platform for ESI, or a Micromass TofSpec 2E for matrix-assisted laser desorption/ionisation time-of-flight (MALDI-TOF) from dithranol (DITH) in reflectron mode, or a VG Platform for APCI. Melting points were recorded on a Gallenkamp melting point apparatus and are uncorrected. Microanalyses were carried out in the Inorganic Chemistry Laboratory, Oxford, UK. Gel permeation chromatography was carried out using PLgel Mixed-A columns (600 mm + 300 mm lengths, 7.5 mm diameter) from Polymer Laboratories calibrated with polystyrene narrow standards ($\overline{M}_p = 580–3.2 \times 10^6$) in tetrahydrofuran with toluene as flow marker. The tetrahydrofuran was degassed with helium and pumped with a rate of 1 mL/min at 30.0 °C. Thermal Gravimetric Analysis was performed on a Perkin–Elmer Thermogravimetric Analyzer TGA 7. Glass transition temperatures were measured on a Perkin–Elmer Differential Scanning Calorimeter Pyris 1. Light petroleum refers to the fraction of boiling point 40–60 °C. When solvent mixtures are used for chromatography over silica the proportions are given by volume.

Electrochemistry was performed using an EG&G Princeton Applied Research potentiostat/galvanostat model 263A. All measurements were made at room temperature on samples dissolved in dichloromethane or tetrahydrofuran, with 0.1 M tetra-*n*-butylammonium tetrafluoroborate as the electrolyte. The tetrahydrofuran was passed through a column of alumina, or distilled from sodium or potassium, and then distilled from lithium aluminium hydride under argon. HPLC grade dichloromethane was used for the oxidation studies. The electrolyte was purified by recrystallisation from ethylacetate. The solutions were deoxygenated with argon. The fericenium/ferrocene couple was used as standard [34], and the ferrocene was purified by sublimation. In all cases several scans were carried out to confirm the chemical reversibility of the redox processes.

Solution PLQYs were measured by a relative method using quinine sulfate in 0.5 M sulfuric acid which has a PLQY of 0.546, as the standard [35]. The dendrimers were dissolved in tetrahydrofuran and freeze–thaw degassed. Photoluminescence spectra were recorded in a JY Horiba Fluoromax 2 fluorimeter, with the dendrimer solutions excited at 360 nm. The optical densities of the standard and sample were similar and small (less than/equal to 0.1). The accuracy of these measurements is estimated to be ±10% of the stated value.

Neat films were spin-coated from chloroform solutions with a dendrimer concentration of 10 mg/mL at 800–1200 rpm for 1 min to give a thickness of about 100 nm. The PLQY of the films was measured using an integrating sphere with a Helium Cadmium laser (Kimmon) as the excitation source [36]. The excitation power was 0.2 mW at 325 nm and the sphere was purged with nitrogen during the measurement. The time-resolved luminescence measurements were performed using the time-correlated single photon counting technique, with excitation at 390 nm from a pulsed gallium nitride laser.

Density Functional Theory Calculations were performed for partially optimised structures with the pendant phenyl and carbazole units held at 30° to the ligand phenyl using the Gaussian 03 suite of programs [37] with a LanL2DZ basis set [38–41] and B3LYP level of theory [42] as employed therein. Compositions of molecular orbitals were calculated using the AOMix Program [43,44].

4.2. 3,6-Di[4′-(2″-ethylhexyloxy)phenyl]carbazole **3**

A mixture of 3,6-dibromocarbazole **2** (97 mg, 0.298 mmol), [G0-B($OCMe_2$)$_2$] **1** [24] (238 mg, 0.716 mmol), tetrakis(triphenylphosphine)palladium(0) (24 mg, 0.021 mmol), aqueous sodium carbonate solution (2 M, 0.2 mL), ethanol (0.2 mL) and toluene (0.6 mL) was degassed using a vacuum, placed under argon and then heated at reflux for 62 h. The mixture was allowed to cool to room temperature and water (8 mL) and ether (12 mL) were added. The organic layer was separated and the aqueous layer was extracted with ether (3 × 5 mL). The organic layer and the ether extracts were combined, washed with brine (15 mL), dried over anhydrous sodium sulfate and filtered. The filtrate was collected and the solvent completely removed. The residue was purified by column chromatography over silica using a dichloromethane–light petroleum mixture (1:40 to 1:3) as eluent to give **3** (73.8 mg, 43%) as a white solid; mp 121–122 °C; (Found: C 83.35, N 2.4, H 8.5. $C_{40}H_{49}NO_2$ requires C 83.4, N 2.4, H 8.6%); ν_{max} (KBr) 3399 (NH); λ_{max} (CH_2Cl_2)/nm 256 [log(ε/dm^3 mol^{-1} cm^{-1}) 4.72], 263 (4.72), 294 (4.72), and 339 (3.61); δ_H (400 MHz; $CDCl_3$) 0.97–1.08 (12H, m, Me), 1.36–1.68 (16H, m, CH_2), 1.77–1.89 (2H, m, CH), 3.96 (4H, m, $ArOCH_2$), 7.08 (4H, 1/2AA′BB′, sp H),

7.41 (2H, br d, $J = 7.5$ CarbH), 7.64–7.73 (6H, m, CarbH and sp H), 7.94 (1H, br s, NH), and 8.33 (2H, s, CarbH); δ_C (101 MHz; $CDCl_3$) 11.2, 14.2, 23.1, 23.9, 30.6, 39.45, 70.6, 110.9, 118.35, 124.0, 125.3, 128.2, 132.9, 134.4, 139.0, and 158.5; *m/z* [APCI$^+$] 576.4 (MH^+).

4.3. 2-(3′-{3″,6″-Di[4‴-(2⁗-ethylhexyloxy) phenyl]carbazolyl}phenyl)pyridine **4**

Tris(dibenzylideneacetone)di-palladium(0) (175 mg, 0.191 mmol) and tri-*t*-butylphosphine (10% in hexane, 1.6 mL) were added to a mixture of **3** (3.50 g, 6.08 mmol), 2-(3′-bromophenyl)pyridine [45] (2.85 g, 12.2 mmol), sodium *t*-butoxide (1.75 g, 18.2 mmol), and freshly distilled toluene (from sodium) (6.0 mL) which had been degassed with a vacuum and placed under argon using a Schlenk Line. The mixture was degassed and placed under argon a second time. The reaction mixture was then heated at reflux (with a bath temperature of 130–135 °C) under argon for 68 h. The mixture was allowed to cool to room temperature and then washed with water (15 mL), dried over anhydrous magnesium sulfate, and filtered. The solvent was completely removed and the residue was purified by column chromatography over silica using a dichloromethane–light petroleum mixture (1:4) as eluent to give **4** (4.27 g, 96%); (Found: C 83.8, N 4.2, H 7.5. $C_{51}H_{56}N_2O_2$ requires C 84.0, N 3.8, H 7.7%); λ_{max} (CH_2Cl_2)/nm 260sh [log (ε/dm^3 mol^{-1} cm^{-1}) 4.67], 265 (4.68), and 297 (4.66); δ_H (400 MHz; $CDCl_3$) 0.90–1.03 (12H, m, Me), 1.30–1.63 (16H, m, CH_2), 1.75–1.86 (2H, m, CH), 3.94 (4H, m, $ArOCH_2$), 7.05 (4H, 1/2AA′BB′, sp H), 7.30 (1H, m, L-H), 7.52 (2H, d, $J = 8$, CarbH), 7.62–7.70 (7H, m, CarbH, sp H, and L-H), 7.74 (1H, dd, $J = 8$, $J = 8$, L-H), 7.80 (2H, m, L-H), 8.16 (1H, m, L-H), 8.28 (1H, m, L-H), 8.38 (2H, d, $J = 1.5$, CarbH), and 8.75 (1H, m, L-H); δ_C (101 MHz; $CDCl_3$) 11.2, 14.2, 23.1, 23.9, 29.1, 30.6, 39.4, 70.6, 110.1, 114.9, 118.35, 120.7, 122.7, 124.1, 125.4, 125.5, 125.9, 127.4, 128.2, 130.4, 133.4, 134.3, 137.05, 138.3, 140.4, 141.3, 149.8, 156.3, and 158.5; *m/z* [ES] 729.3 (MH^+).

4.4. fac-Tris[2-(3′-{3″,6″-di[4‴-(2⁗-ethylhexyloxy) phenyl]carbazolyl}phenyl)pyridinyl] iridium(III) 7

A mixture of **4** (3.25 g, 4.46 mmol), iridium(III) chloride trihydrate (314 mg, 0.892 mmol), water (7.0 mL) and 2-ethoxyethanol (23 mL) was heated in an oil bath at 127 °C under argon for 40 h. The reaction mixture was allowed to cool to room temperature and the solvent was removed from the precipitate. The precipitate was dried under high vacuum and then purified in two steps by column chromatography over silica gel using; first, a dichloromethane–light petroleum mixture (1:30 to 1:0) as eluent to give **4** (244 mg). Second, the remaining bis-iridium chloro-bridged dimer and **4** were separated using a dichloromethane–light petroleum mixture (0:1 to 1:0) as eluent to give dimer (1.13 g, 75%); (Found: C 72.5, N 3.3, H 6.4. $C_{204}H_{220}Cl_2Ir_2N_8O_8$ requires C 72.8, N 3.3, H 6.6%); δ_H (400 MHz; $CDCl_3$) 0.92–1.04 (48H, m, Me), 1.30–1.63 (64H, m, CH_2), 1.72–1.87 (8H, m, CH), 3.92 (16H, m, $ArOCH_2$), 6.37 (4H, d, $J = 8$, L-H), 6.90–7.07 (24H, m, sp H and L-H), 7.37 (8H, br d, $J = 7.5$, CarbH), 7.54 (8H, br d, $J = 7.5$, CarbH), 7.63 (16H, 1/2AA′BB′, sp H), 7.78–7.87 (8H, m, L-H), 7.91 (4H, d, $J = 8$, L-H), 8.35 (8H, m, CarbH), and 9.48 (4H, d, $J = 5.5$, L-H); *m/z* [MALDI] [M+H] $C_{102}H_{111}ClIrN_4O_4$ requires 1681.8 (34%), 1682.8 (43%), 1683.8 (100%), 1684.8 (96%), 1685.8 (73%), 1686.8 (44%), 1687.8 (20%), and 1688.8 (8%), found 1681.9 (32%), 1682.8 (41%), 1683.8 (89%), 1684.8 (91%), 1685.9 (64%), 1686.8 (50%), 1687.8 (19%), and 1688.8 (12%); and **4** (1.42 g). A sample of the recovered **4** co-chromatographed with and had an identical ^{1}H NMR to and authentic sample. A mixture of the dimer (910 mg, 0.27 mmol), **4** (1.66 g, 2.28 mmol) and silver trifluoromethanesulfonate (277 mg, 1.08 mmol) was heated in an oil bath at 145 °C for 6.5 days under argon. The reaction was then allowed to cool to room temperature and the residue was purified by column chromatography over silica using a dichloromethane–light petroleum mixture (0:1 to 1:4) as eluent to give **7** (631 mg, 49%); mp 204–205 °C; $T_{g(150\,°C/min)}$ 193 °C, $TGA_{(5\%)}$ 412 °C; (Found: C 77.1, N 3.65, H 7.1. $C_{153}H_{165}IrN_6O_6$ requires C 77.3, N 3.5, H 7.0%); λ_{max} (CH_2Cl_2)/nm 258sh [log(ε/dm^3 mol^{-1} cm^{-1}) 5.22], 265 (5.26), 295 (5.32), 369sh (4.24), 410sh (3.99), 459sh (3.51), and 495sh (2.99); δ_H (400 MHz; CD_2Cl_2) 0.92–1.03 (36H, m, Me), 1.34–1.63 (48H, m, CH_2), 1.75–1.84 (6H, m, CH), 3.94 (12H, m, $ArOCH_2$), 7.03 and 7.66 (24H, AA′BB′, sp H), 7.13 (3H, m, L-H), 7.26 (3H, dd, $J = 2$, $J = 8$, L-H) 7.40 (3H, br m, L-H), 7.55 (6H, br m, CarbH) 7.60 (6H, br m, CarbH), 7.73 (3H, m, L-H), 7.82 (3H, d, $J = 5.5$, L-H), 7.96 (3H, d, $J = 8$, L-H), 7.98 (3H, d, $J = 2$, L-H), and 8.40 (6H, d,

$J = 1$, CarbH); *m/z* [MALDI] $C_{153}H_{165}IrN_6O_6$ requires 2373.2 (27%), 2374.2 (46%), 2375.2 (84%), 2376.3 (100%), 2377.3 (78%), 2378.3 (43%), 2379.3 (19%), and 2380.3 (6%), found 2373.6 (37%), 2374.6 (62%), 2375.6 (100%), 2376.7 (100%), 2377.7 (88%), 2378.8 (45%), and 2379.8 (20%). Excess **4** (1.45 g), a sample of which co-chromatographed with and had an identical ^{1}H NMR to and authentic sample was also recovered.

4.5. 2-[3′-(3″-5″-Di{3‴,6‴-di[4⁗-(2⁗′-ethylhexyloxy)phenyl]carbazolyl}phenyl)-phenyl] pyridine **6**

Tris(dibenzylideneacetone)di-palladium(0) (60 mg, 0.07 mmol) and tri-*t*-butylphosphine (10% in hexane, 1.0 mL) were added to a mixture of **3** (3.55 g, 6.17 mmol), 2-[3′-(3″,5″-dibromophenyl)phenyl]pyridine **5** [24] (1.00 g, 2.57 mmol), sodium *t*-butoxide (988 mg, 10.3 mmol), and fleshly distilled toluene (from sodium) (15 mL) that had been degassed with a vacuum and placed under argon using a Schlenk Line. The reaction mixture was degassed and placed under argon again before being heated for 17 h with an oil bath temperature of 70 °C and then at reflux with a bath temperature of 130–135 °C under argon for 5 days. The reaction was allowed to cool to room temperature and water (5 mL) was added. The organic portion was collected and purified by column chromatography over silica using a dichloromethane–light petroleum mixture (0:1 to 1:40) as eluent to give **6** (3.22 g, 91%); mp 208–209 °C; (Found: C 84.4, H 7.8, N 3.05. $C_{97}H_{107}N_3O_4$ requires C 84.5, H 7.8, N 3.05%); λ_{max} (CH_2Cl_2)/nm 258sh [log(ε/dm^3 mol^{-1} cm^{-1}) 5.16], 264 (5.16), 295 (5.07), and 360sh (3.83); δ_H (400 MHz; $CDCl_3$) 0.94–1.07 (24H, m, Me), 1.34–1.68 (32H, m, CH_2), 1.77–1.89 (4H, m, CH), 3.96 (8H, m, $ArOCH_2$), 7.07 (8H, 1/2AA′BB′, sp H), 7.27 (1H, m, L-H), 7.61–7.74 (17H, m, spH, L-H, and CarbH), 7.76–7.86 (3H, m, L-H), 7.91 (1H, s, G1-bp H), 8.07–8.13 (3H, m, G1-bp H and L-H), 8.40 (4H, s, CarbH), 8.46 (1H, s, L-H), and 8.74 (1H, m, L-H); δ_C (101 MHz; $CDCl_3$) 11.2, 14.2, 23.1, 23.9, 29.1, 30.6, 39.4, 70.6, 110.1, 114.9, 118.5, 120.65, 122.5, 123.5, 124.2, 124.4, 125.6, 126.0, 127.0, 127.7, 128.2, 129.65, 133.8, 134.1, 136.9, 139.8, 139.9, 140.1, 140.4, 144.7, 149.8, 156.8, and 158.6; *m/z* [MALDI] $C_{97}H_{107}N_3O_4$ requires 1377.8 (91%), 1378.8 (100%), 1379.8 (56%), 1380.8 (21%), and 1381.8 (6%), found 1377.7 (48%), 1378.8 (100%), 1379.7 (87%), 1380.7 (44%), and 1381.7 (20%).

4.6. fac-Tris{2-[3′-(3″,5″-di{3‴,6‴-di[4⁗-(2⁗′-ethylhexyloxy)phenyl]carbazolyl}phenyl)phenyl] pyridine} iridium(III) **8**

A mixture of **6** (1.00 g, 0.725 mmol), iridium(III) acetylacetonate (35 mg, 0.715 mmol) and anhydrous ethylene glycol (distilled from sodium) (0.7 mL) was deoxygenated before being heated at reflux under argon for 4.8 days. The reaction mixture was cooled to room temperature. The mixture was purified by column chromatography over silica in two stages. First, a dichloromethane–light petroleum mixture (0:1 to 2:1) as eluent was used and excess **6** (890 mg, 89%) was isolated, a sample of which co-chromatographed with and had an identical ^{1}H NMR to an authentic sample. The impure **8** was further purified using a dichloromethane–light petroleum mixture (0:1 to 1:10) as eluent to give **8** (100 mg, 32%); mp > 280 °C; (Found: C 80.65, H 7.5, N 2.8. $C_{291}H_{318}IrN_9O_{12}$ requires C 80.8, H 7.4, N 2.9%); λ_{max} (CH_2Cl_2)/nm 260sh [log(ε/dm^3 mol^{-1} cm^{-1}) 5.60], 265 (5.61), 297 (5.63), 369sh (4.65), 404sh (4.13), 458sh (3.55), and 491sh (3.07); δ_H (500 MHz; $CDCl_3$) 0.89–1.00 (72H, m, Me), 1.29–1.59 (96H, m, CH_2), 1.73–1.81 (12H, m, CH), 3.89 (24H, m, $ArOCH_2$), 6.99 (24H, 1/2AA′BB′, sp H), 7.18 (3H, br d, L-H), 7.37 (3H, br d, L-H), 7.58 (51H, m, CarbH, sp H, L-H), 7.76 (3H, s, G1-bp H or L-H), 8.00–8.08 (12H, m, G1-bp H, L-H), and 8.44 (12H, s, CarbH); *m/z* [MALDI] $C_{291}H_{318}IrN_9O_{12}$ requires 4322.4 (7%), 4323.4 (23%), 4324.4 (50%), 4325.4 (82%), 4326.4 (100%), 4327.4 (95%), 4328.4 (73%), 4329.4 (47%), 4330.4 (25%), and 4331.4 (12%), found 4326.7 (broad).

Acknowledgements

We are very grateful to H. Bässler for providing facilities for the time of flight mobility measurements. We thank CDT Oxford, the EPSRC and SHEFC for financial support. We also thank the EPSRC National Service for Computational Chemistry Software (URL: http://www.nsccs.ac.uk).

References

[1] M.A. Baldo, S. Lamansky, P.E. Burrows, M.E. Thompson, S.R. Forrest, Appl. Phys. Lett. 75 (1999) 4.
[2] M. Ikai, S. Tokito, Y. Sakamato, T. Suzuki, Y. Taga, Appl. Phys. Lett. 79 (2001) 156.
[3] T. Watanabe, E. Nakamura, S. Kawami, Y. Fukuda, T. Tsuji, T. Wakimoto, S. Miyaguchi, M. Yahiro, M.J. Yang, T. Tsutsui, Synth. Met. 122 (2001) 203.

[4] X. Zhou, D.S. Qin, M. Pfeiffer, J. Blochwitz-Nimoth, A. Werner, J. Dreschel, B. Maennig, K. Leo, M. Bold, P. Erk, H. Hartmann, Appl. Phys. Lett. 81 (2002) 4070.
[5] X.H. Yang, D. Neher, Appl. Phys. Lett. 84 (2004) 2476.
[6] X. Gong, W.L. Ma, J.C. Ostrowski, G.C. Bazan, D. Moses, A.J. Heeger, Adv. Mater. 16 (2004) 615.
[7] K.M. Vaeth, C.W. Tang, J. Appl. Phys. 92 (2002) 3447.
[8] M. Halim, J.N.G. Pillow, I.D.W. Samuel, P.L. Burn, Adv. Mater. 11 (1999) 371.
[9] J.P.J. Markham, S.-C. Lo, S.W. Magennis, P.L. Burn, I.D.W. Samuel, Appl. Phys. Lett. 80 (2002) 2645.
[10] S.-C. Lo, N.A.H. Male, J.P.J. Markham, S.W. Magennis, P.L. Burn, O.V. Salata, I.D.W. Samuel, Adv. Mater. 14 (2002) 975.
[11] T.D. Anthopoulos, M.J. Frampton, E.B. Namdas, P.L. Burn, I.D.W. Samuel, Adv. Mater. 16 (2004) 557.
[12] T.D. Anthopolous, J.P.J. Markham, E.B. Namdas, J.R. Lawrence, I.D.W. Samuel, S.-C. Lo, P.L. Burn, Org. Electron. 4 (2003) 71.
[13] E.B. Namdas, A. Ruseckas, I.D.W. Samuel, S.-C. Lo, P.L. Burn, J. Phys. Chem. B 108 (2004) 1570.
[14] C.-L. Lee, N.-G. Kang, Y.-S. Cho, J.-L. Lee, J.-J. Kim, Opt. Mater. 21 (2002) 119.
[15] X. Chen, Y. Liao, M.O. Ahmed, H.-E. Tseng, S.-A. Chen, J. Am. Chem. Soc. 125 (2003) 636.
[16] C.-W. Ko, Y.-T. Tao, J.T. Lin, K.R.J. Thomas, Chem. Mater. 14 (2002) 357.
[17] K.R.J. Thomas, J.T. Lin, Y.-T. Tao, C.-W. Ko, J. Am. Chem. Soc. 123 (2001) 9404.
[18] Z. Zhu, J.S. Moore, Macromolecules 33 (2000) 801.
[19] Z. Zhu, J.S. Moore, J. Org. Chem. 65 (2000) 116.
[20] K. Brunner, A. van Dijken, H. Börner, J.J.A.M. Bastiaansen, N.M.M. Kiggen, B.M.W. Langeveld, J. Am. Chem. Soc. 126 (2004) 6035.
[21] A. Kimoto, J.-S. Cho, M. Higuchi, K. Yamamoto, Macromol. Symp. 209 (2004) 51.
[22] S.-C. Lo, P.L. Burn, I.D.W. Samuel, T.D. Anthopolous, PCT Int. Appl. WO2003079736, 2003, 60 pp.
[23] N.D. McClenaghan, R. Passalacqua, F. Loiseau, S. Campagna, B. Verheyde, A. Hameurlaine, W. Dehaen, J. Am. Chem. Soc. 125 (2003) 5356.
[24] S.-C. Lo, E.B. Namdas, P.L. Burn, I.D.W. Samuel, Macromolecules 36 (2003) 9721.
[25] S. Sprouse, K.A. King, P.J. Spellane, R.J. Watts, J. Am. Chem. Soc. 106 (1984) 6647.
[26] H.G. Colombo, T.C. Brunold, T. Riedener, H.W. Güdel, Inorg. Chem. 33 (1994) 545.
[27] A.B. Tamayo, B.D. Alleyne, P.I. Djurovich, S. Lamansky, I. Tsyba, N.N. Ho, R. Bau, M.E. Thompson, J. Am. Chem. Soc. 125 (2003) 7377.
[28] P.L. Burn, R. Beavington, M.J. Frampton, J.N.G. Pillow, M. Halim, J.M. Lupton, I.D.W. Samuel, Mater. Sci. Eng. B 85 (2001) 190.
[29] C. Adachi, M.A. Baldo, S.R. Forrest, M.E. Thompson, Appl. Phys. Lett. 77 (2000) 904.
[30] V.V. Grushin, N. Herron, D.D. LeCloux, W.J. Marshall, V.A. Petrov, Chem. Commun. (2001) 1494.
[31] L.-O. Pålsson, R. Beavington, M.J. Frampton, J.M. Lupton, S.W. Magennis, J.P.J. Markham, J.N.G. Pillow, P.L. Burn, I.D.W. Samuel, Macromolecules 35 (2002) 7891.
[32] R. Beavington, M.J. Frampton, J.M. Lupton, P.L. Burn, I.D.W. Samuel, Adv. Funct. Mater. 13 (2003) 211.
[33] J.P.J. Markham, I.D.W. Samuel, S.-C. Lo, P.L. Burn, M. Weiter, H. Bässler, J. Appl. Phys. 95 (2004) 438.
[34] G. Gritzner, J. Kuta, Electrochim. Acta 29 (1984) 869.
[35] J.N. Demas, G.A.J. Crosby, J. Phys. Chem. 75 (1971) 991.
[36] N.C. Greenham, I.D.W. Samuel, G.R. Hayes, R.T. Phillips, Y.A.R.R. Kessener, S.C. Moratti, A.B. Holmes, R.H. Friend, Chem. Phys. Lett. 241 (1995) 89.
[37] M.J. Frisch, G.W. Trucks, H.B. Schlegel, G.E. Scuseria, M.A. Robb, J.R. Cheeseman, J.A. Montgomery Jr., T. Vreven, K.N. Kudin, J.C. Burant, J.M. Millam, S.S. Lyengar, J. Tomasi, V. Barone, B. Mennucci, M. Cossi, G. Scalmani, N. Rega, G.A. Petersson, H. Nakatsuji, M. Hada, M. Ehara, K. Toyota, R. Fukuda, J. Hasegawa, M. Ishida, T. Nakajima, Y. Honda, O. Kitao, H. Nakai, M. Klene, X. Li, J.E. Knox, H.P. Hratchian, J.B. Cross, C. Adamo, J. Jaramillo, R. Gomperts, R.E. Stratmann, O. Yazyev, A.J. Austin, R. Cammi, C. Pomelli, J.W. Ochterski, P.Y. Ayala, K. Morokuma, G.A. Voth, P. Salvador, J.J. Dannenberg, V.G. Akrzewski, S. Dapprich, A.D. Daniels, M.C. Strain, O. Farkas, D.K. Malick, A.D. Rabuck, K. Raghavachari, J.B. Foresman, J.V. Ortiz, Q. Cui, A.G. Baboul, S. Clifford, J. Cioslowski, B.B. Stefanov, G. Liu, A. Liashenko, P. Piskorz, I. Komaromi, R.L. Martin, D.J. Fox, T. Keith, M.A. Al-Laham, C.Y. Peng, A. Nanayakkara, M. Challacombe, P.M.W. Gill, B. Johnson, W. Chen, M.W. Wong, C. Gonzalez, J.A. Pople, Gaussian 03, revision C.01; Gaussian, Inc., Wallingford, CT, 2004.
[38] T.H. Dunning Jr., P.J. Hay, in: H.F. Schaefer III (Ed.), Modern Theoretical Chemistry, vol. 3, Plenum, New York, 1976, p. 1.
[39] P.J. Hay, W.R. Wadt, J. Chem. Phys. 82 (1985) 270.
[40] P.J. Hay, W.R. Wadt, J. Chem. Phys. 82 (1985) 284.
[41] P.J. Hay, W.R. Wadt, J. Chem. Phys. 82 (1985) 299.
[42] A.D. Becke, J. Chem. Phys. 98 (1993) 5648.
[43] S.I. Gorlesky, AOMix: Program for Molecular Orbital Analysis, York University, Toronto, Canada, 1997. Available from: <http://www.sg-chem.net>.
[44] S.I. Gorlesky, A.B.P. Lever, J. Organomet. Chem. 635 (2001) 187.
[45] M. Van der Sluis, V. Beverwijk, A. Termaten, F. Bickelhaupt, H. Kooijman, A.L. Spek, Organometallics 18 (1999) 1402.

Available online at www.sciencedirect.com
SCIENCE DIRECT®
Organic Electronics 7 (2006) 99–106
Organic Electronics
www.elsevier.com/locate/orgel

Polythiophene in strong electrostatic fields

L.R.C. Wang [a,b], H.J. Kreuzer [a,*], O. Nishikawa [b]

[a] Department of Physics and Atmospheric Science, Dalhousie University, Halifax, NS, Canada B3H 3J5
[b] Department of Materials Sciences and Engineering, Kanazawa Institute of Technology, 7-1 Ohgigaoka, Nonoichi, Ishikawa 921-8501, Japan

Received 16 May 2005; received in revised form 28 November 2005; accepted 29 November 2005
Available online 27 December 2005

Abstract

Field evaporation of polythiophene as studied in the scanning atom probe, yields as the dominant fragment $SC_4H_n^{2+}$, $n = 0, 1, 2, 3$, with a host of other singly and doubly charged fragments. Using density functional theory we show how this fragmentation is achieved in high electrostatic fields (larger than 1 V/Å) which are strong enough to close the HOMO–LUMO gap. The resulting charge transfer to the metal substrate weakens intramolecular bonds. The effect of boron substitution originating from the BF_4-dopant in the electrolyte used for the polymerization of polythiophene is also addressed.

PACS: 61.46.+w; 68.37.Vj; 68.47.Mn; 72.80.Le

Keywords: Field evaporation; Field fragmentation; Polymer conduction

1. Introduction

Oligomers of thiophene and polythiophene have attracted considerable interest in recent years for direct-writing of polymer nanostructures such as nanowires on semiconducting and insulating surfaces. They have appeared as active components in heterojunctions, photovoltaic cells, light-emitting diodes and field-effect transistors, mainly because of the ease with which the optical and electronic properties of oligothiophenes can be tuned by chemical modification [1]. More recently, the scanning atom probe has been used to mass analyze chemically modified polythiophene by field evaporation [2]. The dominant fragments observed were $SC_4H_n^{2+}$, $n = 0, 1, 2, 3$, with a host of other singly and doubly charged fragments, summarized in the mass spectrum, Fig. 1. A number of these also contained boron atoms which originated from the BF_4-dopant in the electrolyte used for the polymerization of polythiophene. Related field emission studies confirm that polythiophene is semiconductive.

Field evaporation or field desorption is the removal of atoms, molecules or molecular fragments as singly or doubly charged positive ions from a metal or semiconductor surface in strong electrostatic fields, typically several V/Å, as they occur at field emission tips in the field ion microscope [3,4]. Field evaporation can be viewed as a chemical reaction in which the field induces the

* Corresponding author. Tel.: +1 902 4946594; fax: +1 902 4945191.
E-mail address: h.j.kreuzer@dal.ca (H.J. Kreuzer).

1566-1199/$ - see front matter © 2005 Elsevier B.V. All rights reserved.
doi:10.1016/j.orgel.2005.11.006

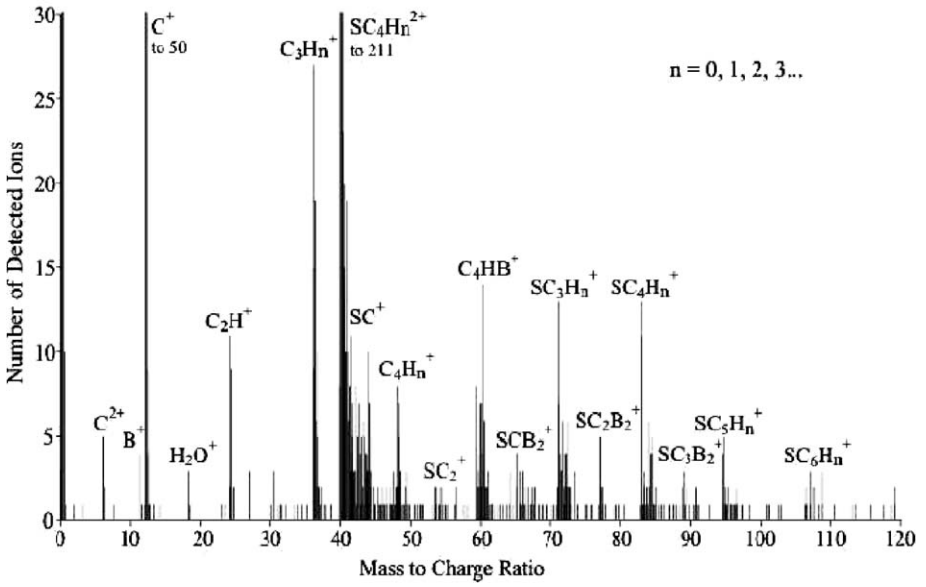

Fig. 1. Mass spectrum of poly(thiophene) obtained with the scanning atom probe [2].

transfer of electrons to the substrate leading to the rupture of a surface bond, after which a charged atom or molecular fragment is pulled away from the surface. The field-induced fragmentation of a polymer molecule adsorbed on a surface is a thermally activated process with a rate constant that can be parametrized according to Frenkel–Arrhenius as

$$r_d(T,F) = v(T,F)\exp[-Q(F)/k_B T] \quad (1)$$

in terms of a field-dependent prefactor, v, and a field-dependent activation barrier, Q [5–7]. Thus the fragmentation can be aided by heating the surface, for instance with laser pulses as it was done in this experiment.

In this paper we will present first principles calculations based on density functional theory to shed some light on the field-induced fragmentation and the evaporation of polythiophene. This approach has proven successful in recent studies on the intermolecular interactions in bithiophene [8] and for calculating excitation energies of terthiophene and its dioxide derivatives [9,10].

2. Theory

Our density functional calculations are done for short chains of polythiophene with up to eight units in electrostatic fields of the order of V/Å. We have used the GAUSSIAN'03 package with the B3LYP exchange/correlation potential and the 6-31G(d,p) basis set [11].

For fields below 1.6 V/Å the structure of neutral polythiophene does not change appreciably except that there is an intramolecular transfer of electrons down the electric field. In addition there is a substantial reduction in the HOMO–LUMO gap. The reason is that the field forces a concentration of the HOMO towards the end of the molecule in the field direction whereas the LUMO gets shifted towards the other end of the molecule. As a result the HOMO and LUMO energies are raised and lowered, respectively, by $\pm 1/2eFL$ with respect to the center of the molecule (of length L) This shift in the orbitals is clearly seen in the electron density plots of Fig. 2. For a neutral five-ring polythiophene the gap is 2.78 eV in zero field and only 0.07 eV for a field strength of 1.6 V/Å, see Table 1.

Whereas for zero field the electron density for the HOMO and the lowest two LUMOs are uniformly and symmetrically distributed along the molecule, the redistribution is already evident at 1.4 V/Å, particularly in the LUMO, and is completed at 1.6 V/Å. We note that as the HOMO–LUMO gap closes in the highest field there is still substantial overlap of the HOMO and LUMO π orbital wavefunctions suggesting that the molecule has become conductive. Although the overlap is larger at a field of 1.4 V/Å the gap is still too high, at 1.39 eV, for electron transfer along the molecule to occur at room

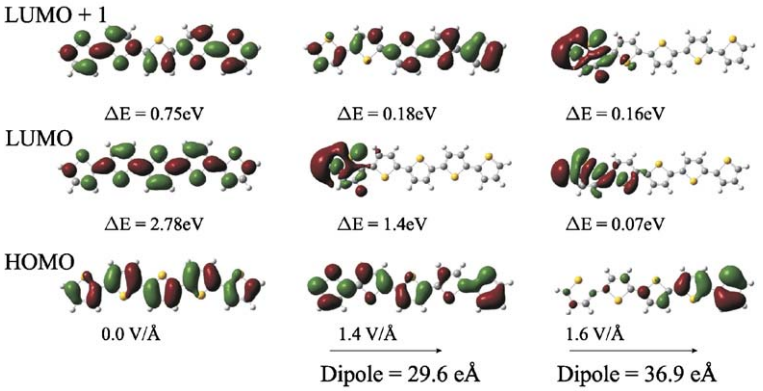

Fig. 2. π orbital charge density for the HOMO and two lowest LUMOs in various fields. Also noted are the energy differences between them and the induced dipole moments.

Table 1
HOMO–LUMO gap Δ as a function of field strength for a neutral five-ring of polythiophene

F (V/Å)	0.0	0.2	0.4	0.6	0.8	1.0	1.2	1.4	1.6
Δ (eV)	2.78	2.23	1.40	1.36	1.15	1.28	1.39	1.39	0.07

temperature. Table 1 also shows that the closure of the HOMO–LUMO gap is not monotonic as a function of field strength. The reason is that these orbitals are affected differently by the field as Fig. 2 clearly demonstrates.

Because for longer polymers the HOMO–LUMO gap is reduced, e.g. for an eight-ring polythiophene the gap is only 2.46 eV in zero field as compared to 2.76 eV for a five-ring, one expects that the HOMO–LUMO gap vanishes in longer molecules at smaller fields. As long as the molecule is isolated, an external field will lead to charge separation: for very low fields the induced dipole is linear in the field but becomes progressively nonlinear as the field increases. In Fig. 3 we show the accumulated charges on the various rings, obtained from a Mulliken analysis.

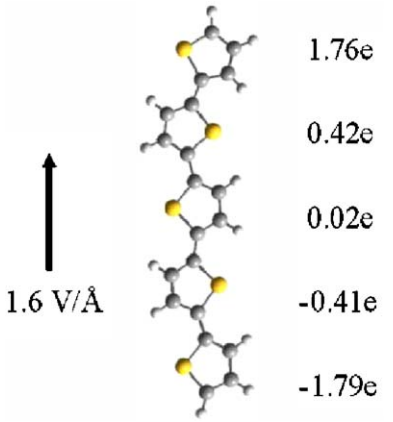

Fig. 3. Field-induced charge transfer in isolated poly(thiophene). Charges per ring, obtained by a Mullikan analysis.

We briefly comment on the advantage of density functional theory over Hartree–Fock calculations in situations where an external field leads to a vanishing HOMO–LUMO gap. In the HF calculations, the self-consistent-field convergence is determined by the total energy minimization, while the electron occupation on the calculated orbitals is obtained simply by filling with electrons from the lowest energy level up, regardless of whether this leads to the lowest energy configuration or not. In most cases, there is no conflict between these two rules. However, in cases when the HOMO–LUMO gap becomes very small, it is possible that the state of total energy minimum does not correspond to the state where all unoccupied orbitals are energetically above all occupied orbitals, rather it may have an unoccupied orbital with an energy lower than the HOMO energy. As a result one finds in some systems a critical field above which self-consistent-field convergence cannot be reached if one insists on the standard Hartree–Fock rule of filling orbitals. On the other hand, density functional theory provides an equation relating the total energy, E, the occupation, n_i, and the orbital energy, e_i, namely $\partial E/\partial n_i = e_i$. This guarantees that filling electrons

with all unoccupied orbitals staying above all occupied orbitals always leads to a configuration that has the total energy at a minimum [12].

It is of interest to see what happens when the molecule is adsorbed at a metal surface, i.e. to a metallic contact. As with other adsorbates high electric fields will effect the chemisorption bond significantly. In particular there is a charge transfer from the adsorbate to the metal which ultimately leads to field desorption as a positively charged ion. To see what happens with polythiophene we have attached a molecule to a small Al cluster. The amount of charge transfer from the oligomer to the metal, as measured rather arbitrarily by a Mulliken analysis, depends on the field strength and the number of monomers and is a continuous function of the field up to the point of field-induced dissociation or desorption of the oligomer. For longer oligomers significant charge transfer starts at smaller fields. It is worth recalling in this context that charges on atoms or subunits of a molecule are, strictly speaking, not quantum mechanically observable quantities. Thus any assignment of charges is qualitative and depends on the procedure chosen. For our example we have chosen a five-ring oligomer and adjusted the field so that the charge on the lowest unit of the oligomer, adsorbed on the metal, is more or less equals to zero which leads to a net transfer of about three electrons to the metal cluster. The resulting geometry in a field of 1 V/Å is shown in Fig. 4.

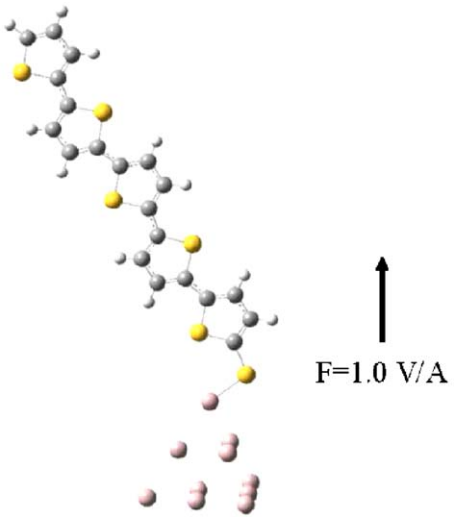

Fig. 4. Poly(thiophene) attached on a cluster of nine aluminum atoms in an external field of 1 V/Å.

This net transfer of about three electrons to the metal, obtained from a quantum mechanical calculation, has a simple analogue in classical electrostatics as shown previously for the adsorption of a single metal atom on a flat metal surface in an external electric field [13,14]. Approximating the adsorbed atom by a spherical (metallic) boss of radius R one finds that the total charge accumulation on the surface of the boss is $Q = 3\pi R^2\sigma_0$ where $\sigma_0 = F/4\pi$ is the surface charge density far from the boss given in terms of the applied electric field, σ [e/Å^2] $\approx 0.0055F$ [V/Å]. Thus for $R = 1$ Å and $F = 2$ V/Å we get $Q \approx 0.1e$ with an accompanying field enhancement above the atom of $3F$. To model polythiophene on a metal we take the boss to be half a prolate spheroid for which field and charge distributions have been calculated in Appendix A. Choosing $R \approx 2 - 3$ Å and a height of five rings we get $Q \approx 1 - 3e$ in qualitative agreement with the quantum mechanical calculations. Although rather qualitative, the agreement with a classical model in which the molecule is approximated by a metallic boss may be taken as confirmation that at this field strength polythiophene is conducting.

To account for the fact that the topmost units of a long polythiophene molecule will be highly charged we attach a molecule of five units to an Al cluster and remove three electrons, for reasons just discussed; on a metal surface these charges would spread laterally away. In a field of 1.4 V/Å the polymer is no longer stable as evidenced by the lack of convergence of the optimization algorithm towards selfconsistency. We used the Berny optimization in internal coordinates. In a field at which dissociation occurs, the total energy gets lower and lower with each iteration without reaching a minimum. As a result, the optimum geometry is mostly determined by the linear term, i.e. the forces acting on the bond lengths, bond angles and dihedral angles. For this reason the geometry optimization reflects the actual character of the dissociation dynamics. In Fig. 5 the various fragments are identified as single atoms and disconnected atomic groups. Criteria for a broken bond would be that the bond length is longer than the equilibrium value by a prescribed amount or that the field-reduced activation barrier for bond breakage is so low that thermal desorption is possible. For the latter, we should keep in mind that in the experiment field evaporation was assisted by intense YAG laser pulses that heated the sample considerably. Because neither criterion can be quantified

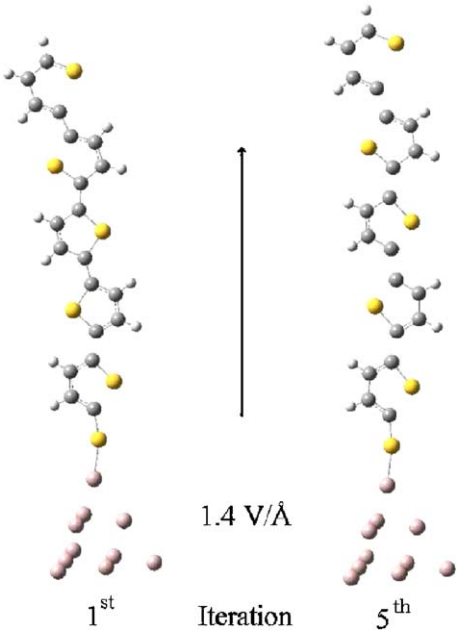

Fig. 5. Poly(thiophene) attached to an Al cluster total charge $Q=3e$. The field is so high that the molecule disintegrates as iterations progress.

sufficiently we use the criterion of GAUSSIAN'03 namely that a bond is about to break if it has stretched by more than 10% of its equilibrium value, e.g. for the S–C bond stretching from 1.73 Å to 1.9 Å with an accompanying reduction in bond energy of 0.4 eV. After five iterations these fragments are, from top to bottom in Fig. 5: H^+, SC_2^+, C_2H^+, $C_3H_2^+$, SC^+, and several $SC_4H_2^{2+}$. The interpretation that the laser pulses simply heat the sample thus enhancing desorption and fragmentation may well be only part of the effect: because these strong fields reduce the HOMO–LUMO gap considerably it might well be that optical absorption itself, i.e. promoting electrons to excited states, weakens the intramolecular bonds thus stimulating fragmentation and deterioration of the polythiophene film.

For longer polymer chains we expect more charging at their upper ends. The effect of removing electrons is shown in Fig. 6 for the top two units of an eight-ring molecule. Once three electrons have been removed the first S–C bond starts to break; removal of a further electron breaks the rings and stretches the units. Adding a field will then lead to the complete breakup of the chain. This is illustrated in Fig. 7 for a chain of eight units with a total of four electrons removed. The fragments that occur are H^+, SC_2^+, C_2H^+, $SC_4H_n^{2+}$ with $n=0,1,2$.

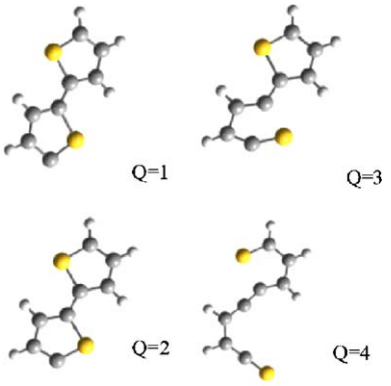

Fig. 6. The top two units of an eight-ring molecule in the absence of a field. Removing (Q) electrons leads to the break-up of the ring structure.

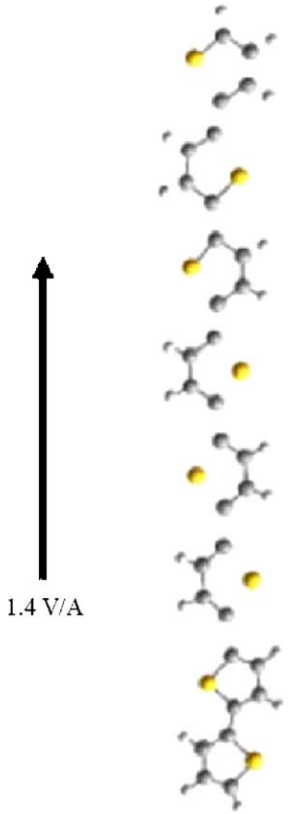

Fig. 7. Disintegration of an eight-ring poly(thiophene) molecule in a field.

As the charged fragments are accelerated away from the tip the external electric field they experience decreases rapidly. This will lead, in a qualitative way, to reconstruction of some of the rings for which the bonds have not been completely broken, and thus to a further abundance of $SC_4H_n^{2+}$.

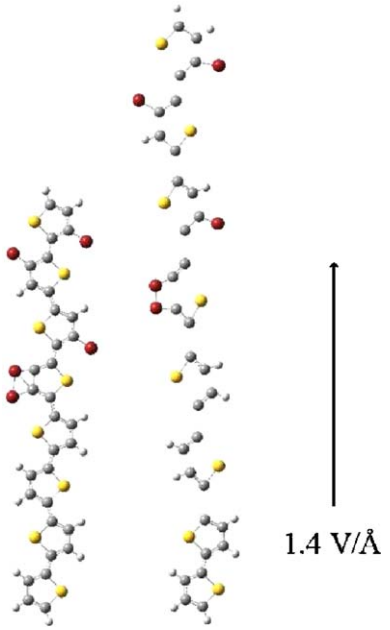

Fig. 8. Poly(thiophene) with some H atoms substituted by B without (left) and with (right) a field.

The quantification of this point needs not only a complete picture of the local field distribution but also a detailed kinetic picture of charge transfer and bond breaking. Although this has been done for simple molecules [15–17], the extension to polymer chains will not be attempted here.

Our last point addresses the issue of boron contamination of polythiophene. As mentioned in the introduction, the presence of BF_4^- dopant in the electrolyte used for the polymerization results in the replacement of some of the H atoms by B. An example is shown on the left of Fig. 8. Charging this molecule by removing four electrons and applying a field of 1.4 V/Å leads to the fragmentation of the molecule with charged fragments such as H^+, SC_2^+, BC_2^+, SC_2H^+, $SC_4H_2^+$, etc. as also seen in the mass spectrum of Fig. 1.

3. Discussion

Fragmentation or dissociative field desorption of polythiophene is caused foremost by the fact that in a strong electrostatic field this polymer becomes conducting so that charge transfer can occur easily along the molecule with the result that the end of the molecule in the field direction carries a substantial positive charge. This leads to the separation of the individual rings and also to their dissociation. However, as the fragments leave the high field region re-assembly of partially deformed rings may occur as this will minimize their energy substantially. This explains why mostly charged rings are observed in the mass spectrometer with much fewer small fragments.

The response of polythiophene to a strong electrostatic field is very different to that of poly(ethylene glycol) [18,19]. The latter retains its large HOMO–LUMO gap, severely limiting electron transfer down the molecule. All that happens is the creation of local dipole moments, more or less equal on each monomer. The result of this rather limited response is also very dramatic in that, for the helical conformer, a severe electrostriction of some 20% is observed in a field of 1.5 V/Å. Also, poly(ethylene glycol) field-desorbs gradually with fragments such as H^+, OCH^+, CH_2^+ leaving the end of the molecule in the field direction.

In discussions of the structure of organic layers sandwiched between metallic contacts the point has been raised that their performance in a device might be enhanced due to tunneling across the interface layer at "microtip" structures arising from rough interface morphology [20,21]. We recall that organic layers are typically 10^3 μm thick and voltages across them are of the order of 10 V. This gives rise to fields across the polymer film of the order of 10 mV/Å. At such strengths we do not expect significant field effects. However, if at weak spots the film thickness were reduced by an order of magnitude or more, field effects may become important. As mentioned in the previous paragraph different organic materials behave differently under high field conditions and detailed calculations have to be made for the particular material to see what constitutes a "high" field. All we can say in general is that high fields can be beneficial to reduce the band gap and may be detrimental, when they are strong enough, to lead to field-induced fragmentation.

Acknowledgments

The work at Dalhousie University was supported by grants from the NSERC and the Office of Naval Research. HJK would like to thank Ian Hill for illuminating discussions.

Appendix A. Prolate spheroidal boss in an electrostatic field

To understand charging effects on a conducting polymer in an electrostatic field we model the

polymer as half of a conducting prolate spheroid attached as a boss on a flat metal surface. We recall from electrostatics that for a spherical boss of radius R on a flat surface the field potential is given by

$$V(r,z) = -4\pi\sigma_0 z[1-(R/r)^3] \tag{A.1}$$

where σ_0 is the surface charge density far from the boss, and the charge distribution is

$$\sigma = \sigma_0[1-(R/r)^3] \tag{A.2}$$

on the flat surface and

$$\sigma = 3\sigma_0\frac{z}{R} \tag{A.3}$$

on the boss with a total charge accumulation $\Sigma = 3\pi\sigma_0 R^2$.

For a prolate spheroidal boss we use coordinates appropriate for a "two-center" problem

$$\begin{aligned}\xi_1 &= \cosh\xi\\ \xi_2 &= \cos\eta\\ \xi_3 &= \phi\end{aligned} \tag{A.4}$$

in terms of standard prolate spheroidal coordinates. Note that the z coordinate along the major axis of the spheroid is $z = a\xi_1\xi_2$. The large and small axes of a spheroid are given by $c = 2a\cosh h(\xi_0)$ and $b = 2a\sinh(\xi_0)$, respectively, with the ellipticity given by $e = [1-\tanh^2(\xi_0)]^{1/2}$. Its surface area is $S = 2\pi a^2\{\sinh^2\xi_0 + \sinh\xi_0\cosh\xi_0\sin^{-1}(1/\xi_0)\}$.

Solving Laplace's equation in these coordinates gives

$$V = -4\pi\sigma_0 z\left[1-(\xi_{10}/\xi_1)^3 f_{\rm ell}(\xi_1)/f_{\rm ell}(\xi_{10})\right] \tag{A.5}$$

where

$$f_{\rm ell}(\xi_1) = 1 + 3\xi_1^3\left[\coth^{-1}(\xi_1) - 1/(3\xi_1^3) - 1/\xi_1\right]. \tag{A.6}$$

Note that the first "correction" in $f_{\rm ell}$ is of order ξ_1^{-5}. Also observe that we can express $\xi_1 = (r_1+r_2)/2a$ in terms of the distances from the two foci of the spheroid. Thus, far from the surface of the spheroid we recover the results for a spherical boss. The charge distribution on the flat surface is given by

$$\begin{aligned}\sigma &= -\frac{1}{4\pi}\left.\frac{\partial V}{\partial z}\right|_{\xi_1}\\ &= \sigma_0\left[1-(\xi_{10}/\xi_1)^3 f_{\rm ell}(\xi_1)/f_{\rm ell}(\xi_{10})\right]\end{aligned} \tag{A.7}$$

and on the spheroid boss by

$$\sigma = -\frac{1}{4\pi}\left.\frac{\partial V}{\partial\xi_1}\right|_z = 3\sigma_0\cos\eta\,\frac{\xi_{10}^2}{(\xi_{10}^2-1)}\,\frac{1}{f_{\rm ell}(\xi_{10})}$$

so that the total charge accumulated on the boss is

$$Q = 3\pi\sigma_0 a^2\left(\xi_{10}^2 - \frac{1}{2}\right)\frac{\xi_{10}^2}{(\xi_{10}^2-1)}\,\frac{1}{f_{\rm ell}(\xi_{10})} \tag{A.8}$$

These formulae have been used in the text to estimate the accumulated charge on a polythiophene molecule in contact with a metal.

References

[1] D. Fichou (Ed.), Handbook of Oligo and Polythiophene, Wiley-VCN, Weinheim, Germany, 1999.
[2] O. Nishikawa, M. Taniguchi, Chin. J. Phys. 43 (2005) 111.
[3] E.W. Müller, T.T. Tsong, Field Ion Microscopy, Principles and Applications, American Elsevier Publishing Co., 1969.
[4] T.T. Tsong, Atom Probe Field Ion Microscopy, Cambridge University Press, 1990.
[5] H.J. Kreuzer, in: R. Vanselow (Ed.), Physics and Chemistry at Solid Surfaces VIII, Springer-Verlag, Berlin, Germany, 1990, pp. 133–158.
[6] H.J. Kreuzer, in: D.J. Dwyer, F.M. Hoffmann (Eds.), Surface Science of Catalysis: In situ Probes and Reaction Kinetics, ACS Symposium Series, 482, American Chemical Society, Washington, 1992.
[7] H.J. Kreuzer, Surf. Interface Anal. 36 (2004) 372.
[8] L. van Eijck, M.R. Johnson, G.J. Kearley, J. Phys. Chem. A 107 (2003) 8980.
[9] F. Della Sala, H.H. Heinze, A. Görling, Chem. Phys. Lett. 339 (2001) 343.
[10] R. Telesca, H. Bolink, S. Yunoki, G. Haziioannou, P.Th. van Duijen, J.G. Snijders, H.T. Jonkman, G.A. Sawatzky, Phys. Rev. B 63 (2001) 155112.
[11] Gaussian 98 (Revision A.1), M.J. Frisch, G.W. Trucks, H.B. Schlegel, G.E. Scuseria, M.A. Robb, J.R. Cheeseman, V.G. Zakrzewski, J.A. Montgomery, R.E. Stratmann, J.C. Burant, S. Dapprich, J.M. Millam, A.D. Daniels, K.N. Kudin, M.C. Strain, O. Faraks, J.Tomasi, V. Barone, M. Cossi, R. Cammi, B. Mennucci, C. Pomelli, C. Adamo, S. Clifford, J. Ochterski, G.A. Peterson, P.A. Ayala, Q. Cui, K. Morokuma, D.K. Malick, A.D. Rabuck, K. Raghavachari, J.B. Foresman, J. Cioslowski, J.V. Ortiz, B.B. Stefanov, G. Liu, A. Liashenko, P. Piskorz, I. Komaromi, R. Gomperts, R.L. Martin, D.J. Fox, T.Keith, M.A. Al-Laham, C.Y. Peng, A. Nanayakkara, C. Gonzalez, M. Challacombe, P.M.W. Gill, B.G. Johnson, W. Chen, M.W. Wong, J.K. Andres, M. Head-Gordon, E.S. Replogle, J.A. Pople, Gaussian, Inc., Pittsburgh PA, 1998.
[12] J.F. Janak, Phys. Rev. B 18 (1978) 7165.
[13] H.J. Kreuzer, L.C. Wang, N.D. Lang, Phys. Rev. B 45 (1992) 12050.
[14] Yu. Suchorski, N. Ernst, W.A. Schmidt, V.K. Medvedev, H.J. Kreuzer, R.L.C. Wang, Prog. Surf. Sci. 53 (1996) 135.

[15] H.J. Kreuzer, K. Watanabe, L.C. Wang, Surf. Sci. 232 (1990) 379.
[16] L.C. Wang, H.J. Kreuzer, Surf. Sci. 237 (1990) 337.
[17] H.J. Kreuzer, Chin. J. Phys. 43 (2005) 249.
[18] R.L.C. Wang, H.J. Kreuzer, M. Grunze, A.J. Pertsin, Phys. Chem. Chem. Phys. 2 (2000) 1721.
[19] A.J. Pertsin, M. Grunze, H.J. Kreuzer, R.L.C. Wang, Phys. Chem. Chem. Phys. 2 (2000) 1729.
[20] H. Kanai, S. Ichinosawa, Y. Sato, Synth. Met. 91 (1997) 195.
[21] I.G. Hill, A. Rajagopal, A. Kahn, J. Appl. Phys. 84 (1998) 3236.

Available online at www.sciencedirect.com
SCIENCE DIRECT®
Organic Electronics 7 (2006) 107–113
Organic Electronics
www.elsevier.com/locate/orgel

Photoemission study of the interface properties of aminothiophene derivatives in contact to Au as a function of conjugation length

X. Liu [a], M. Knupfer [a,*], L. Dunsch [a], A. Tabet [b], H. Hartmann [b]

[a] *Leibniz-Institut für Festkörper- und Werkstoffforschung Dresden, D-01069 Dresden, Germany*
[b] *University of Applied Sciences, Geusaer Strasse, D-06217 Merseburg, Germany*

Received 5 September 2005; received in revised form 23 November 2005; accepted 30 November 2005
Available online 27 December 2005

Abstract

The electronic properties of aminothiophene/gold interfaces have been investigated by photoemission spectroscopy in dependence of the amonithiophene conjugation length. The valence band onset as a measure for the charge injection barrier at these interfaces as well as the ionization potential depend on the length of the conjugated thiophene chain while the value of the interface dipole hardly varies. These results are discussed on the basis of recent theoretical approaches that aim to explain the interface dipoles.

PACS: 79.60.Dp; 79.60.Fr; 73.61.Ph

Keywords: Organic semiconductors; Photoemission spectroscopy; Aminothiophene; Interface

1. Introduction

Charge transport in organic opto-electronic devices, such as organic light emitting diodes, organic field effect transistors or organic solar cells, depends not only on the chemical nature of the materials used but also on the interfaces between them and the metal or metal oxide electrodes. Therefore, the morphological and electronic properties of interfaces between organic semiconductors and metals or metal oxides have been studied extensively during the last years [1–7]. Often, these interfaces are characterized by the presence of a rather large interface dipole. The previous investigations have provided us with substantial insight into the interface dipoles and have identified several contributions to these dipoles.

In order to differentiate between universal properties of metal–organic interfaces, which are determined by the bulk properties of the two materials in contact only, and effects that arise from the particular interface structure, morphology, and chemistry, studies of general, material independent and fundamental changes of the interface dipoles as a

* Corresponding author. Tel.: +49 351 4659 544; fax: +49 351 4659 440.
E-mail address: m.knupfer@ifw-dresden.de (M. Knupfer).

1566-1199/$ - see front matter
doi:10.1016/j.orgel.2005.11.005

function of the electronic properties of the materials have been very instructive and successful [1,2,8–14].

Previously, a large variety of organic monomeric, oligomeric as well as polymeric materials useful for manufacturing different types of opto-electronic devices have been developed [15–17]. Most of these materials are required for the transport of charged species generated, e.g., by anodic oxidation, cathodic reduction, or optical excitation. As a very promising class of such materials different types of *N*-peraryl-substituted aromatic or heteroaraomtic amines, such as of the *N*,*N*′-tetraphenylbenzidine (TPB) and the so-called starburst (SB) compounds, were proposed. Due to their electron-donating amino moieties these compounds can be easily transformed into mono- or higher cationic species (polarons or bipolarons) which act as essential hole-transport materials [18].

Very recently, *a*,*a*′-bis(diarylamino)-functionalised oligothiophenes of the general structure A-*n*T (Fig. 1) as heterocyclic analogues of the TPB series have received a strong interest. They have been prepared, e.g. by means of a heavy-metal catalysed *C*,*N*-coupling reaction of halo-substituted oligothiophenes with diphenylamine [17] and were intensively studied in respect to the formation of amorphous glasses and charged species. Thus, it was found that depending on the number of thiophene moieties mono-, bis-, tris- and tetra-charged cationic species can be oxidatively generated in this series [18].

In this paper, we will report on photoemission spectroscopy studies of the interface formation between the first four representatives of the A-*n*T series ($n = 1, 2, 3, 4$) and polycrystalline gold. The results indicate the formation of interface dipoles of about 1.2–1.3 eV which are hardly dependent on the thiophene chain length *n*. With increasing *n* the corresponding valence band onset and the ionization potential decrease. These trends are helpful for the design of materials able to influence the electronic properties of interfaces by modification of their molecular structure and for fundamental studies of metal–organic interfaces.

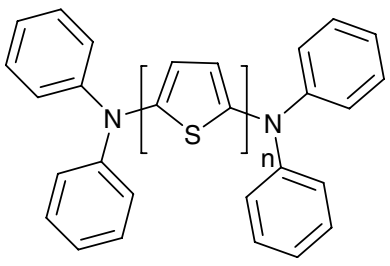

Fig. 1. The molecular structure of aminothiophenes, $n = 1$–4.

2. Experimental

The photoemission measurement were performed in a commercial PHI 5600 spectrometer which was equipped with a He-discharge lamp and a monochromatic Al-K_α X-ray source providing photons with 21.22 eV for UPS (ultraviolet photoemission spectroscopy) and 1486.6 eV for XPS (X-ray photoemission spectroscopy), respectively. The total energy resolution of the spectrometer, determined by analyzing the width of a Au Fermi edge, is about 0.1 eV (UPS) and 0.35 eV (XPS). The UPS spectra have been corrected for the contributions from He satellite radiation. Thin films of aminothiophenes with different thicknesses were prepared on a sputter-cleaned polycrystalline Au foil by in situ vacuum evaporation in a preparation chamber (base pressure 2×10^{-10} mbar). Subsequently, the films were transferred to the measurement chamber (base pressure 10^{-10} mbar). The films were characterized taking a full range XPS spectrum and the number of impurities in the deposited films is below the detection limit of XPS. There was no signature of decomposition of the amonithiophenes during evaporation or deposition onto the gold substrate. The thickness of the respective layer was estimated by monitoring the attenuation of the intensity of the Au $4f_{7/2}$ substrate peak by the organic overlayer [19,20]. This procedure to determine the film thickness is only correct for a layer by layer growth of the organic film. If the organic film is not uniform, this method underestimates the real film thickness. The work function Φ of the films was extracted from the high binding energy cut-off of the UPS spectra by applying a bias of 5 V to the sample, which enables the determination of the secondary cut-off at appropriate electron kinetic energies (see for instance Ref. [21]).

3. Results and discussion

3.1. The Au/A-3T interface

The photoemission valence band spectra of the Au substrate and A-3T films are presented in the left panel of Fig. 2 as a typical example of A-*n*T structures. With increasing A-3T coverage, new features

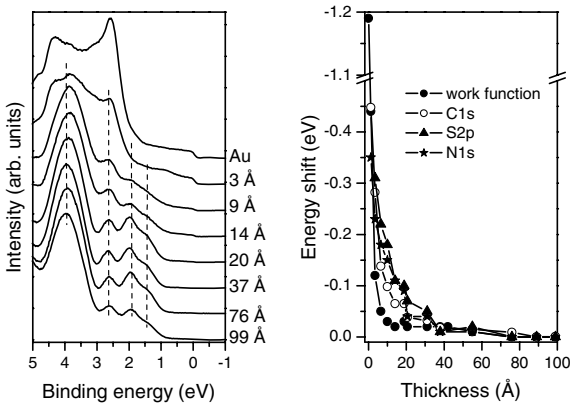

Fig. 2. Left: The evolution of A-3T UPS spectra with increasing thickness on Au. The labels indicate the corresponding film thickness. Right: Dependence of the work function, and the C 1s, S 2p, and N 1s core level peak position on the A-3T layer thickness.

due to photoemission from the molecular orbitals of A-3T appear. Simultaneously, the characteristic Au structures at binding energies between 2 and 5 eV are suppressed but do not completely disappear until the valence band photoemission features of A-3T are fully developed above a nominal thickness of about 20 Å. Four clear peaks are observed at about 1.4, 1.9, 2.6, and 4 eV as indicated by the dashed lines in Fig. 2. The energy position of these peaks is independent of film thickness for thicknesses larger than 20 Å, indicating that the formation of the interface is complete at this value.

The relative changes of the work function and the energy position of the A-3T photoemission core-level spectra as a function of the film thickness are shown in the right panel of Fig. 2. The work function changes abruptly by about 1.2 eV at initial A-3T deposition and remains essentially constant thereafter. This abrupt shift of the work function points to the formation of an interface dipole confined to a very narrow region around the interface. Moreover, the thickness range in which the work function saturates indicates that A-3T deposition onto gold results in the formation of a rather closed organic layer of the order of 1–2 ML. Similar observations have been reported for other organic semiconductors deposited on gold [22–26]. Furthermore, the binding energy of all core levels of A-3T layers behaves similar to the work function with only a slight broadening as a function of A-3T layer thickness as seen in Fig. 2. This demonstrates that the ionization potential of the core levels is rather independent of the A-3T film thickness which essentially rules out a chemical interaction at the interface. We therefore conclude that the A-3T molecules are physisorbed on gold. This is fully consistent with the absence of valence band photoemission features in the energy region of the gap of A-3T for low coverages, which are often observed in case of chemisorption of organic molecules on metal surfaces [27–29]. The fact that the core level binding energies do not change as rapidly as the work function is a consequence of final state screening in the core level photoemission process which near a metal surface is considerably enhanced due to image charge screening [30].

It is well accepted that there are several possible reasons for the interface dipole at organic–metal interfaces [1–7,14]. Since we can rule out a chemical interaction at the A-3T/Au interface we attribute the large interface dipole to a combination of (i) a reduction of the gold work function upon adsorption of the organic molecules, (ii) unconventional band bending as a consequence of a broadening of the valence and conduction levels in A-3T films and/or (iii) an induced density of interface states with a charge neutrality level that is able to pin the Fermi level (for further details see discussion below) [1,7,14].

3.2. A-nT, n = 1–4

The data shown in Fig. 2 are representative of the other A-*n*T materials under consideration in this study ($n = 1$–4). In particular, there is no binding energy shift of the valence band photoemission features with increasing film thickness after the interface has been completed abruptly. Fig. 3 depicts a comparison of the UPS valence band spectra of all A-*n*T films at a thickness of about 5.5 nm. The main features are quite similar in all A-*n*T UPS spectra, where an intense maximum appears at about 4 eV, and features at lower binding energy are located between 1 and 3 eV.

Firstly, we consider the valence band onset of the A-*n*Ts which measures the hole injection barrier for the corresponding junction to gold. The valence band onset position was determined from the low binding energy emission edge by linear extrapolation, and this valence band onset in the UPS spectra of the A-*n*T films shifts towards lower binding energies as the number of thiophene rings (n) increases from one to four. However, this increase is not smooth.

Instead, there is a low binding energy shoulder appearing for A-3T and A-4T which is absent for

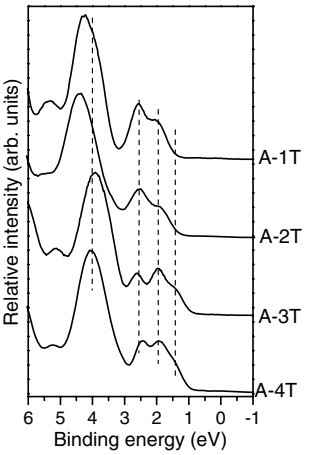

Fig. 3. UPS spectra of aminothiophenes (A-*n*T) at a film thickness of about 5.5 nm on gold as a function of the number of thiophene rings from top to bottom. The dashed lines indicate the energy position of the main valence band features.

the two shorter aminothiophenes, and the spectral onset consequently rather jumps to lower energy for the larger molecules. Recently, cyclic voltammetry studies have demonstrated that the first and second electron transfer of aminothiophenes coincide for $n \geqslant 3$ [18], i.e. when the low binding energy shoulder in our photoemission spectra appear. It is tempting to infer that both spectroscopic results have a common microscopic origin.

Interestingly, the spectrum for A-1T with its features at 1.9, 2.6 and 4.0 eV very much resembles that of A-2T (the only significant difference being the slight upshift of the 4 eV maximum) but also that of TPD (*N*,*N*′-diphenyl-*N*,*N*′-bis(3-methylphenyl)(1,1)biphenyl-4,4′diamine) with a similar chemical structure [20], while a similarity to corresponding spectra of bithiophene [31] is not observed. For TPD, calculations have shown that the highest occupied molecular orbital (HOMO) is delocalized over the entire π conjugated molecular system with a substantial wave function probability on the nitrogen sites [32]. From the close similarity of the valence band photoemission spectra of A-1T and A-2T to that of TPD, we assume that the same wave function distribution is true for the two shorter aminothiophenes where the HOMO is represented by the feature at about 1.9 eV. The peak at 2.6 eV then is due to emission from the HOMO-1 molecular orbital, and that at around 4 eV can be attributed to the emission from non-bonding π states [31,32], i.e. electronic molecular states that do not contribute to the formation energy of the molecule.

Extending the thiophene chain of the molecule will hardly affect the HOMO distribution over the entire molecule, but will result in a gain of kinetic energy due to delocalization. Simultaneously, the number of molecular orbitals is increasing as a consequence of the larger number of structural units. The energy shift of the spectral onset in Fig. 3 is related to the growing delocalization which decreases the ionization potential of the respective molecules. It can also be expected that the HOMO wave function has an increasing relative weight at thiophene units of the aminothiophenes with increasing molecule length. Possibly, this larger thiophene weight of the HOMO stabilizes the dications in larger aminothiophenes as indicated by cyclic voltammetry [18]. In addition, the growing number of molecular orbitals is also in correspondence to what is seen in Fig. 3 as a function of the length of the A-*n*T molecules. The fact that the changes of ionization potential and injection barrier as a function of chain length are not smooth but appear quite abruptly going from A-2T to A-3T is reminiscent to what is predicted and observed for unsubstituted oligithiophenes where the evolution of ionization potential and spectral onset in photoemission data is also not smooth as a function of the molecule length [31,33]. A detailed microscopic understanding will require calculations of the electronic properties of aminothiophene molecules which are beyond the scope of this work.

3.3. Energy levels at Au/A-nT interfaces

The energy level alignment at the metal–organic gold/aminothiophene interfaces is summarized in Fig. 4. The size of the interface dipole has been determined from the change of the work function upon A-*n*T deposition. The ionization potential of the A-*n*T films is given by the difference between the photon energy (UPS, $h\nu = 21.2$ eV) and the energy width of the UPS spectrum. The latter is the difference of the spectral thresholds at lowest and highest binding energies, i.e. the onset of the HOMO and the secondary cut-off, respectively.

Fig. 4 reveals that the interface dipole ($-eD$) of all studied Au/A-*n*T interfaces hardly changes, although the ionization potential significantly decreases with the A-*n*T chain length. Therefore, the ionization potential of the organic semiconductor cannot be a parameter that determines the size of the interface dipole. The work function of the A-*n*T films also does not show a significant varia-

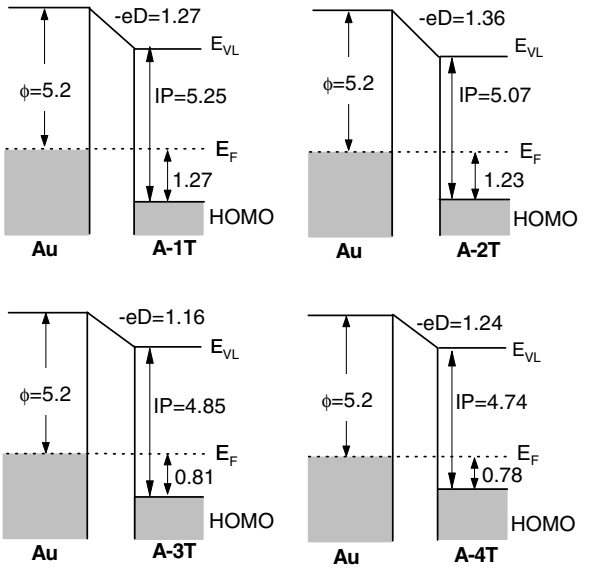

Fig. 4. Energy diagrams of the interfaces between aminothiophenes with different number of thiophene rings and Au. All energy values are expressed in eV.

tion within the aminothiophenes under consideration. This is supplementary and well consistent to previous studies that came to the conclusion that the short range interface dipole often found for metal/organic interfaces is a function of the work function difference of the two materials in contact [1,10–13]. Interestingly, while the work function and not the ionization potential or the electron affinity is decisive for the interface dipole, there is evidence that the electron affinity plays a major role concerning the type of interaction which is present at a particular metal/organic interface—physisorption or chemisorption [34].

Recently, a number of studies have shown that the interface dipoles can in part be explained by the alteration of the metal surface dipole as a consequence of adsorption of organic molecules [7,12,35–39]. Thereby, the electron wave function of the metal that spills out into vacuum is repelled by the physisorbed molecules. This effect can cause work function changes at metal/organic interfaces up to 0.5 eV. We note that the actual size of this contribution to the interface dipole might depend on the orientation of the deposited organic molecules with respect to the metal surface, an issue which can be influenced by growth parameters and the molecular structure [40,41]. However, this mechanism cannot be fully responsible for the interface dipoles of more than 1 eV as reported here, and thus other contributions have to be considered.

A successful microscopic description of the interface dipoles at many organic/metal interfaces in addition must reproduce its dependence on the work function of the organic semiconductor. Recently, there have been two proposals for mechanisms that could lead to relatively large contributions to the interface dipoles at metal/organic interfaces and which also could reflect the work function dependence. One of them argued that as a consequence of an energetic broadening of the valence and conduction levels due to disorder in the films, as concluded from transport studies [42–45], there is unconventional band bending at these interfaces caused by the tails of the valence and conduction level distributions into the energy gap [13]. As indicated by the decreasing ionization energy with increasing aminothiophene chain length and a red shift of the optical absorption of aminothiophenes in toluene solution [18], the energy gap also decreases. This is well known in π conjugated systems and has also been calculated for unsubstituted thiophene molecules [33]. In order to obtain an essentially constant interface dipole via the unconventional band bending due to an energy broadening of the transport levels, this broadening also has to decrease with increasing number of thiophene rings. As there are no data available yet on the energy broadening of the transport levels in aminothiophenes, the clarification of this point requires further experiments.

Another theoretical consideration gave rise to the argument that there is an induced density of interface states at metal/organic interfaces which defines the charge neutrality level of the organic semiconductor and is large enough to essentially pin the Fermi level close to the charge neutrality level [46,47]. Indeed, recent calculations of some particular metal/organic interfaces within the density-functional theory provided evidence for a interface induced density of states around the Fermi level [48,49]. Our experimental results now require for this scenario to be applicable to rationalize the interface dipoles summarized in Fig. 4, that the charge neutrality level of all A-*n*T materials is located near the mid point of the energy gap independent of the size of the gap. Again, this needs to be verified experimentally. Interestingly, the induced density of interface states model would predict a negligible interface dipole for organic heterointerfaces made out of two different A-*n*T materials.

The injection barrier for holes at the Au/A-*n*T interfaces is decreasing with increasing A-*n*T length

which demonstrates that it is in principle possible to a adjust the injection barrier by extending the thiophene chain. This confirms similar trends which have been observed for other organic semiconductors recently [8,9].

4. Summary

Our photoemission study of four different aminothiophenes, A-1T, A-2T, A-3T and A-4T and their interfaces to gold exhibits well defined molecular orbitals for all of these materials and allowed the determination of the corresponding energy level alignment at the interfaces. We have shown that the interface dipole hardly changes with increasing chain length of the aminothiophene. This behavior has been discussed in consideration of previous models which microscopically describe the presence of interface dipoles at metal/organic interfaces. We have demonstrated that studies as reported here can help to finally identify the mechanism of interface dipole formation at these interfaces. Moreover, the hole injection barrier and the ionization potentials change in a non-monotonous manner with increasing aminothiophene length which might be related to a relative transfer of the HOMO wave function probability to thiophene structural units.

Acknowledgements

The project was supported by BMBF under grant no. 01 BI 163. Technical support by R. Hübel, R. Schönfelder and S. Leger is appreciated.

References

[1] H. Ishii, K. Sugiyama, E. Ito, K. Seki, Adv. Mater. 11 (1999) 605.
[2] W.R. Salaneck, K. Seki, A. Kahn, J.-J. Pireaux, Conjugated Polymer and Molecular Interfaces, Marcel Dekker Inc., New York, 2002.
[3] A. Kahn, N. Koch, W. Gao, J. Polym. Sci. B 41 (2003) 2529.
[4] W.R. Salaneck, M. Fahlman, J. Mater. Res. 19 (2004) 1917.
[5] H. Ishii, N. Hayashi, E. Ito, Y. Washizu, K. Sugi, Y. Kimura, M. Niwano, Y. Ouchi, K. Seki, Phys. Status Solidi A 201 (2004) 1075.
[6] M. Knupfer, H. Peisert, Phys. Status Solidi A 201 (2004) 1055.
[7] M. Knupfer, G. Paasch, J. Vac. Sci. Technol. A 23 (2005) 1072.
[8] A.J. Mäkinen, I.G. Hill, M. Kinoshita, T. Noda, Y. Shirota, Z.H. Kafafi, J. Appl. Phys. 91 (2002) 5456.
[9] A.J. Mäkinen, I.G. Hill, T. Noda, Y. Shirota, Z.H. Kafafi, Appl. Phys. Lett. 78 (2001) 670.
[10] G. Greczynski, Th. Kugler, W.R. Salaneck, J. Appl. Phys. 88 (2000) 7187.
[11] S. Park, T.U. Kampen, D.R.T. Zahn, W. Braun, Appl. Phys. Lett. 79 (2001) 4124.
[12] H. Peisert, M. Knupfer, J. Fink, Appl. Phys. Lett. 81 (2002) 2400.
[13] G. Paasch, H. Peisert, M. Knupfer, J. Fink, S. Scheinert, J. Appl. Phys. 93 (2003) 6084.
[14] H. Vazquez, W. Gao, F. Flores, A. Kahn, Phys. Rev. B 71 (2005) 041306(R).
[15] R. Hajlaoui, D. Fichou, G. Horowitz, B. Nessakh, M. Constant, F. Garnier, Adv. Mater. 9 (1997) 557.
[16] G. Horowitz, J. Mater. Res. 19 (2004) 1946.
[17] H. Hartmann, P. Gerstner, D. Rohde, Org. Lett. 3 (2001) 1673.
[18] A. Tabet, A. Schröder, H. Hartmann, D. Rohde, L. Dunsch, Org. Lett. 5 (2003) 1817;
D. Rohde, L. Dunsch, A. Tabet, H. Hartmann, J. Fabian, J. Phys. Chem. B, submitted for publication.
[19] M.P. Seah, W.A. Dench, Surf. Interface Anal. 1 (1976) 2.
[20] H. Peisert, T. Schwieger, M. Knupfer, M.S. Golden, J. Fink, J. Appl. Phys. 88 (2000) 1535.
[21] K. Horn, Appl. Surf. Sci. 166 (2000) 1.
[22] F. Baier, F.V. Ludowig, A. Soukopp, C. Väterlein, J. Laubender, P. Bäuerle, M. Sokolowski, E. Umbach, Opt. Mater. 12 (1999) 285.
[23] T.S. Ellis, K.T. Park, S.L. Hulbert, M.D. Ullrich, J.E. Rowe, J. Appl. Phys. 95 (2004) 982.
[24] O. Tal, W. Gao, C.K. Chan, A. Kahn, Y. Rosenwaks, Appl. Phys. Lett. 85 (2004) 4148.
[25] T. Schwieger, X. Liu, H. Peisert, B. Adolphi, N. Kiriy, M. Knupfer, J. Appl. Phys. 97 (2005) 123712.
[26] X. Liu, M. Knupfer, B.-H. Huisman, Surf. Sci. 595 (2005) 165.
[27] L.H. Tjeng, R. Hesper, A.C.L. Heessels, A. Heeres, H.T. Jonkman, G.A. Sawatzky, Solid State Commun. 103 (1997) 31.
[28] F.S. Tautz, M. Eremtchenko, J.A. Schaefer, M. Sokolowski, V. Shklover, E. Umbach, Phys. Rev. B 65 (2002) 125405.
[29] T. Schwieger, H. Peisert, M. Knupfer, Chem. Phys. Lett. 384 (2004) 197.
[30] H. Peisert, M. Knupfer, T. Schwieger, J.M. Auerhammer, M.S. Golden, J. Fink, J. Appl. Phys. 91 (2002) 4872.
[31] H. Fujimoto, U. Nagashima, H. Inokuchi, K. Seki, Y. Cao, H. Nakahara, J. Nakayama, M. Hoshino, K. Fukuda, J. Chem. Phys. 92 (1990) 4077;
H. Fujimoto, U. Nagashima, H. Inokuchi, K. Seki, Y. Cao, H. Nakahara, J. Nakayama, M. Hoshino, K. Fukuda, J. Chem. Phys. 89 (1988) 1198.
[32] K. Sugiyama, D. Yoshimura, T. Miyamae, T. Miyazaki, H. Ishii, Y. Ouchi, K. Seki, J. Appl. Phys. 83 (1998) 4928.
[33] R. Telesca, H. Bolink, S. Yunoki, G. Hadziioannou, P.Th. Van Dijnen, J.G. Snijders, H.T. Jonkman, G.A. Sawatzky, Phys. Rev. B 63 (2001) 155112.
[34] M. Knupfer, T. Schwieger, Appl. Surf. Sci. 252 (2005) 77.
[35] X. Crispin, Sol. Energy Mater. Sol. Cells 83 (2004) 147.
[36] X. Crispin, V. Geskin, A. Crispin, J. Cornil, R. Lazzaroni, W.R. Salaneck, J.-L. Bredas, J. Am. Chem. Soc. 124 (2002) 8131.
[37] P.S. Bagus, V. Staemmler, Ch. Wöll, Phys. Rev. Lett. 89 (2002) 096104.
[38] L. Yan, N.J. Watkins, S. Zorba, Y. Gao, C.W. Tang, Appl. Phys. Lett. 81 (2002) 2752.

[39] N. Koch, A. Kahn, J. Ghijsen, J.-J. Pireaux, J. Schwartz, R.L. Johnson, A. Elschner, Appl. Phys. Lett. 82 (2003) 70.
[40] H. Peisert, I. Biswas, L. Zhang, M. Knupfer, M. Hanak, D. Dini, M.J. Cook, I. Chambrier, T. Schmidt, D. Batchelor, T. Chasse, Chem. Phys. Lett. 403 (2005) 1.
[41] I. Biswas, H. Peisert, T. Schwieger, D. Dini, M. Hanak, M. Knupfer, T. Schmidt, T. Chasse, J. Chem. Phys. 122 (2005) 064710.
[42] H. Bässler, Phys. Status Solidi B 175 (1993) 15.
[43] M.C.J.M. Vissenberg, M. Matters, Phys. Rev. B 57 (1998) 12964.
[44] R. Schmechel, H. von Seggern, Phys. Status Solidi A 201 (2004) 1215.
[45] I.N. Hulea, H.B. Brom, A.J. Houtepen, D. Vanmaekelbergh, J.J. Kelly, E.A. Meulenkamp, Phys. Rev. Lett. 93 (2004) 166601.
[46] H. Vazquez, R. Oszwaldowski, P. Pou, J. Ortega, R. Perez, F. Flores, A. Kahn, Europhys. Lett. 65 (2004) 802.
[47] H. Vazquez, F. Flores, R. Oszwaldowski, J. Ortega, R. Perez, A. Kahn, Appl. Surf. Sci. 234 (2004) 107.
[48] S. Picozzi, A. Pecchia, M. Gheorghe, A. Di Carlo, P. Lugli, B. Delley, M. Elstner, Phys. Rev. B 68 (2003) 195309.
[49] M. Simeoni, S. Picozzi, D. Delley, Surf. Sci. 562 (2004) 43.

Available online at www.sciencedirect.com
SCIENCE DIRECT®
Organic Electronics 7 (2006) 114–120
Organic Electronics
www.elsevier.com/locate/orgel

Optical proximity and touch sensors based on monolithically integrated polymer photodiodes and polymer LEDs

Lukas Bürgi *, Reto Pfeiffer, Mario Mücklich, Peter Metzler, Michael Kiy, Carsten Winnewisser

CSEM SA, Badenerstrasse 569, 8048 Zürich, Switzerland

Received 10 October 2005; received in revised form 28 November 2005; accepted 1 December 2005
Available online 28 December 2005

Abstract

An optical touch and proximity sensor based on polymer light-emitting diodes and polymer photodiodes is presented. The sensor's thin-film light sources and detectors are monolithically integrated in the same plane of a common substrate and are processed from the liquid phase at room-temperature. These key features make the sensor potentially attractive for applications where low cost, small device thickness, tight space requirements or mechanical flexibility matter, such as simple information displays with touch switch functionality, for example. A static light-emitting sign with integrated touch switch is demonstrated here.

PACS: 42.40.My; 42.68.Wt; 42.79.Kr; 42.82.Gw

Keywords: Optical sensor; Proximity detector; Polymer LED; Polymer photodiode; Monolithic integration

1. Introduction

The monolithic integration of all components of an optoelectronic device on a single substrate—as opposed to the assembly or packaging from a number of discrete components—offers benefits in terms of cost, reliability, size, short signal paths and/or reduced complexity of the fabrication process, which are useful or even necessary attributes for many applications ranging from routing in telecommunications to disposable optical bio-sensors.

Organic semiconductor technology offers completely new and attractive routes for monolithic integration, due to comparatively simple thin-film device architectures and fabrication processes that differ radically from the ones of silicon industry. With this respect, a major strength of organic optoelectronics, particularly polymer optoelectronics based on solution processing, is the possibility to deposit the materials by additive processes in only those areas, where their specific functionality is required, as exemplified by ink-jet printed red,

* Corresponding author. Tel.: +41 44 497 14 16; fax: +41 44 497 14 00.
E-mail address: lukas.burgi@csem.ch (L. Bürgi).

1566-1199/$ - see front matter
doi:10.1016/j.orgel.2005.12.002

green, and blue emitting pixels in polymer LED displays [1].

Although organic optoelectronic devices are generally perceived to have a large potential for monolithic integration, only a limited number of classes of functional devices comprising monolithically integrated organic components have been reported so far. Most prominently, organic light-emitting diode (OLED) displays with more than 1 million OLED pixels have been demonstrated [2], with smaller sized OLED displays being already on the market. Integrated circuits consisting of more than 1000 organic field-effect transistors have been shown, e.g., in the form of shift registers [3]. Relatively early on, the possibility to use organic field-effect transistors to drive single OLEDs monolithically integrated on the same substrate was demonstrated by the Cambridge and Bell Lab groups simultaneously [4,5]. Meanwhile, thousands of organic transistors have been integrated in display backplanes, however, not to drive OLEDs—the drive currents of organic transistors do currently not meet the needs of OLED displays—but capacitive media such as electrophoretic displays [3,6]. Organic photodiodes have also been integrated in arrays and matrices for image sensing and position detector applications [7–9]. Only since recently, however, monolithically integrated organic LEDs and photodiodes are being explored in promising new application areas such as chemical sensing [10,11], bio-sensing [12], or optical integrated systems [13].

Here, we present an optical touch and proximity sensor based on the monolithic integration of polymer light-emitting diodes (PLEDs) and polymer photodiodes (PPDs) [14]. Although similar devices have been proposed in patents [15], none has been demonstrated so far. Furthermore, small molecule organic photodiodes have been integrated on top of OLEDs to form an optical bistable switch in Forrest's group before [16]. However, to the best of our knowledge, our work demonstrates the first functional device combining solution-processed *polymer* LEDs and photodiodes.

For the optical thin-film sensor discussed in this paper, PLED and PPD pixels have been integrated on the same side of a common substrate. Fig. 1 sketches the device architecture and illustrates the principle of operation. The sensor can be operated either in proximity mode or as touch sensor. For the former, light emitted by the PLED is reflected from nearby objects and falls back onto the photodiode pixels, leading to a signal enhancement (left PPD in Fig. 1). On the other hand, the functioning of the touch sensor relies on the fact that the slightest touch of the device leads to a change of the effective refractive index, which in turn influences the angle of total reflection and therefore the guided modes in the substrate. This results in a change (generally a decrease) of the photodiode signals (right PPD in Fig. 1). Apart from serving as thin-film illuminators, which act as the light source for touch and proximity detection, the PLEDs can also function as information display at the same time, e.g., in the form of a passive matrix display or a static light emitting logo. An example for the latter is presented in this paper.

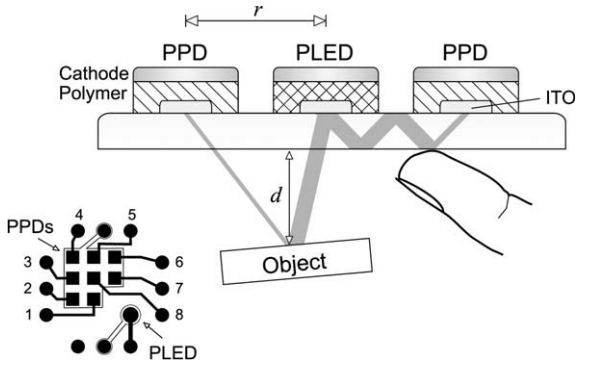

Fig. 1. Schematic diagram of device architecture and device operation. Also shown is the ITO pattern—consisting of one circular PLED and eight square PPD pixels, contact strips and pads—for one example layout in the lower left of the figure. The thin lines drawn in this layout indicate the outline of the cathodes.

2. Experimental details

The devices were fabricated on 1 inch square Corning 1737F glass substrates of 1.1 mm thickness with an indium tin oxide (ITO) layer of 150 nm (12 Ω/□) on its top surface. LED pixel and photodiode pixels were defined by patterning the ITO layer using conventional photolithography in combination with wet etching. Anode contact strips as well as contact pads were directly patterned into the ITO layer, too as illustrated in Fig. 1. Prior to the deposition of the organic layers, the substrates were carefully cleaned by sonication in water, acetone, and isopropanol, followed by an oxygen plasma treatment.

A 50 nm thick layer of PEDOT:PSS [17] was then applied by spin coating and subsequently baked at 180 °C for 10 min. Next, the active polymer layers

were deposited. First, a continuous polyfluorene-based film was applied, serving as light-emitting layer in the LED pixel. This 70 nm thick film was spin coated from a 1.1 wt.% solution of a 1:2:2 blend (by weight) of F8BT:F8:TFB [18] in toluene. Second, the light-emitting layer was removed again from those areas of the substrate, which do not require its functionality, i.e. the photodiode pixels. To achieve this, droplets of pure toluene were pipetted to the areas outside the periphery of the LED pixel and immediately after this the substrate was rotated around the centre of the LED pixel at 1300 rpm. This procedure first dissolves and then carries away the surplus polyfluorene material without affecting the polyfluorene layer of the LED pixel. Third, the 70–150 nm thick photoactive layers were deposited on the photodiode pixels by spin coating a 2:1 blend (by weight) of PCBM:P3HT [19] from 0.6–1.4 wt.% solutions in chloroform. To avoid cross-contamination as well as partial dissolution of the active material on the LED pixel, the PCBM:P3HT blend was pipetted to the areas outside the periphery of the LED pixel only. This method of sequential spin coating was chosen here due to the fact that in our laboratories we do not currently have access to more appropriate tools for additive thin-film deposition from solution of different functional materials onto different areas of one substrate, such as e.g., ink-jet printing [20,21]. Clearly, by using an adequate additive printing method one could overcome the main shortcomings of the sequential spin coating method, which are the very limited resolution of about 1 mm as well as the restrictions in pixel layout [22]. However, the deposition technique used here is fully adequate for the demonstration of functionality and feasibility of the monolithic sensors.

To finish the device, the cathode—consisting of a 20 nm thick layer of calcium capped by 70 nm of aluminium—was deposited through a shadow mask by vacuum evaporation. The mask design was such that all photodiodes on one substrate were contacted by a common cathode, whereas a separate cathode contacted the LED (Fig. 1). Prior to taking the finished devices into ambient atmosphere they were encapsulated with a <10 μm thick epoxy layer and a microscope cover glass.

The PLEDs show green electroluminescence with peak emission at 530 nm, as seen in Fig. 2. A low turn-on voltage of 2.5 V [23] allows one to operate the PLEDs at voltages lower than 8 V. The initial efficacy of the PLEDs is 0.6 cd/A.

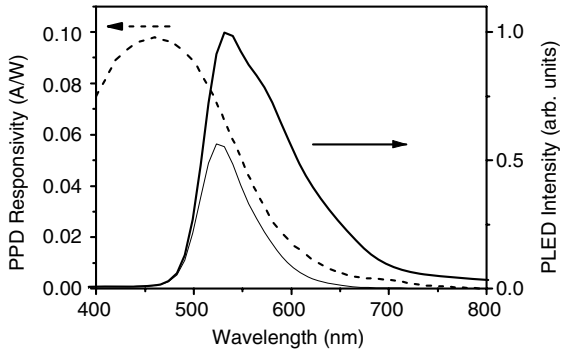

Fig. 2. Electroluminescence spectrum of a polyfluorene LED (full line) and responsivity of a PCBM:P3HT photodiode (dashed line, 70 nm thick active layer). The product of the two (thin full line, arbitrary scale) highlights the wavelength range, which is relevant for the sensor.

At 0 V applied bias, the bulk heterojunction polymer photodiodes show responsivities larger than 0.02 A/W at wavelengths ranging from the blue to 600 nm (Fig. 2) [24]. The overlap between the PLED emission spectrum and the PPD responsivity is reasonably good and fully sufficient for the purpose of this work. In fact, the spectral match of PLED and PPD allows the photodiodes in our devices to collect 35–50% of the maximal photocurrent they could collect if the PLED would emit its total radiant power at the wavelength of maximal PPD sensitivity [25].

Our PLED and PPD efficiencies are a factor of about 50 and 3 inferior to literature values for comparable spectral response, respectively [24,26]. In the case of the PLED, this is partly due to the different material class used in this study—polyfluorene emitter as compared to iridium complex [26]—and partly to the quality of the commercial materials. Although our efficiencies are fully sufficient for the purpose of this work, it is clear that the overall efficiency of the sensor as well as the signal to noise ratio would benefit from improvements in PLED and PPD efficiency.

3. Results and discussion

PLED and PPD performance of a sensor placed at a safe distance from any light scattering or reflecting surfaces is shown in Fig. 3. The curves were measured in the dark on a device with an eight photodiode pixel layout as depicted in Fig. 1. The guided modes of the substrate, which are schematically illustrated in Fig. 1, couple part of the light emitted by the PLED into the photodiode pixels

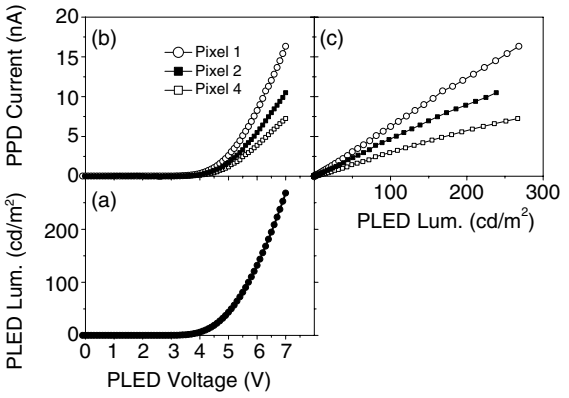

Fig. 3. PLED and PPD characteristics of a device with pixel layout shown in Fig. 1. (a) PLED luminance in forward direction versus driving voltage. The simultaneously measured response of three PPD pixels is shown in (b) and (c) as a function of PLED voltage and luminance in forward direction, respectively. The photocurrent was measured at 0 V.

and give rise to the photocurrent of Fig. 3(b). Evidently, coupling through the substrate decreases with increasing distance between PLED and PPD. Pixel 4, being at double the distance from the PLED than pixel 1, shows less than half of the latter's photocurrent. In fact, the decay of the substrate coupling I_{sub} is well described by

$$I_{\mathrm{sub}}(r) \propto \frac{1}{r}\exp(-r/L), \tag{1}$$

where r is the distance between PLED and PPD pixel (Fig. 4, upper right inset). The term inversely

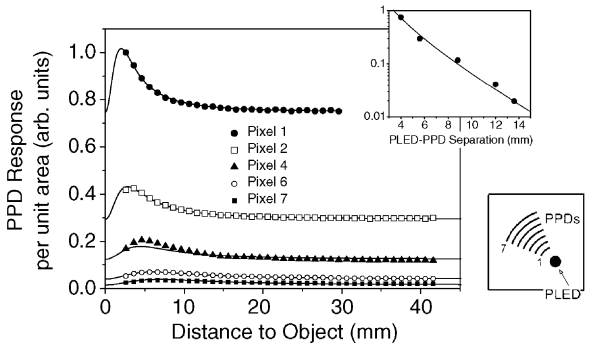

Fig. 4. Response of a sensor operated in proximity mode. The layout of the seven pixel sensor is shown in the lower right. The signal of the photodiode pixels as a function of distance between sensor and object—a coplanar flat surface covered with white paper—is shown in the main graph. The full lines depict the model of Eq. (2) (α identical for all curves, I_{sub} fitted individually). Inset: Signal of the individual PPD pixels as a function of their distance from the PLED for large sensor-object distances ($d = 40$ mm). The full line depicts a fit with Eq. (1) with $L = 4.0$ mm.

proportional to r is typical for a wave spreading in two dimensions, and the exponential attenuation results from absorption of the guided modes at the substrate/polymer interface giving rise to decay constants L of a few mm in our devices [27].

The photodiode response is close to linear over the range of intensities of interest in this study, as seen in Fig. 3 (c). The quantum efficiency of the substrate coupling was measured to be of the order of 10^{-6} in our devices, i.e. a few charge carriers are photogenerated in a PPD pixel per 10^6 carriers passing through the PLED. For example, pixel 1 in Fig. 3 shows an efficiency of 4×10^{-6}, as determined from the ratio of PPD photocurrent and PLED driving current.

Operation of a sensor in proximity modus is demonstrated in Fig. 4. It shows the response of the PPD pixels upon positioning an object, which in case of Fig. 4 is a coplanar white surface, at a distance d in front of the sensor. The signal on the PPDs increases as the distance between object and sensor decreases. It becomes distinguishable from the substrate-coupled background at distances below about 15 mm.

The basic features of the proximity sensor's response can be well understood in a simple model, for which the PLED is assumed to be a Lambertian emitter and the object a coplanar mirror [28]. The angle ϑ under which the PLED "sees" the PPD in the object mirror is given by $tg\vartheta = r/2d$, where d is the distance between object and sensor and r is the separation between PLED and PPD (Fig. 1). For a Lambertian emitter, the intensity that is reflected back onto the PPD is proportional to $\cos\vartheta \times \Omega$, where $\Omega = A_{\mathrm{PPD}}\cos\vartheta/(r^2 + 4d^2)$ is the solid angle spanned by the PPD and A_{PPD} is the area of the photodiode pixel. Putting all together, one obtains the following expression for the photodiode current in proximity mode:

$$I_{\mathrm{prox}}(r,d) = \alpha\frac{d^2}{(4d^2 + r^2)^2} + I_{\mathrm{sub}}(r). \tag{2}$$

Here, α is a proportionality factor and $I_{\mathrm{sub}}(r)$ is the contribution due to substrate coupling (Eq. (1)).

As seen in the main panel of Fig. 4, there is a satisfactory agreement between the simple model (full lines) and the measured data. In particular, the model reproduces the maxima observed in the sensor response at distances around 5 mm. These maxima result from the competition between the angle of incidence, which becomes more grazing with decreasing object–sensor distance and thus results

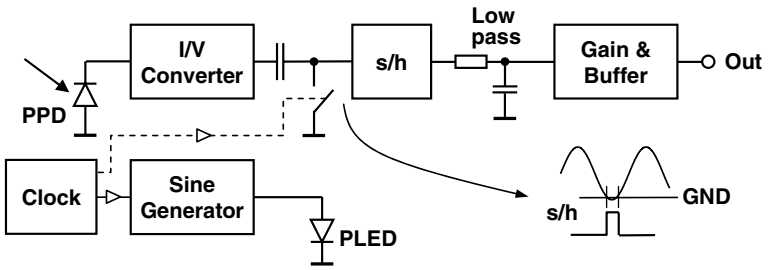

Fig. 5. Schematic diagram of the PLED driving circuit and one of the eight channels of the PPD readout electronics.

in a signal decrease, and the decrease in optical path length with decreasing object–sensor distance, which results in a signal increase. In the simple model of Eq. 2 the maxima in the PPD response occur at $d = r/2$, i.e. at an object–sensor distance that corresponds to half the PLED–PPD separation. The maximum in the response shifts to very low distances if the PLED–PPD separation is minimized ($r \to 0$). In practice, one can achieve a monotonically increasing response by placing small PLED and PPD pixels very close to each other, resulting in an inverse square law dependence on the object–sensor distance, and thus a high sensitivity in the short range.

For any practical application of the sensor presented here one needs to deal with unwanted light from the surrounding. We developed the sample and hold (s/h) circuit shown in Fig. 5 to operate our demonstrators under normal indoors lighting conditions. Signal detection and background subtraction is achieved by modulation of the PLED driving current and a corresponding pixel-wise demodulation of the photodiode signals by virtue of a sample and hold stage followed by a low pass filter.

An example of such a demonstrator is presented in Fig. 6. The demonstrator combines a simple static information display with a touch sensor. In this case, the PLED serves both as a light emitting sign and as the light source for the touch sensor. The patterning of the light-emitting sign was achieved by inserting a thin (300 nm) insulating polyimide layer between the ITO, which itself was coarsely patterned into a sign-enclosing rectangle, and the PEDOT:PSS in those areas where the PLED should not light up. The polyimide was patterned using conventional photolithography combined with dry etching.

Fig. 6(c) illustrates the functioning of the touch sensor. The sensor signal shows a clear drop of about 0.7 V when a finger is brought into contact with the sensor surface (left arrow in Fig. 6). Upon

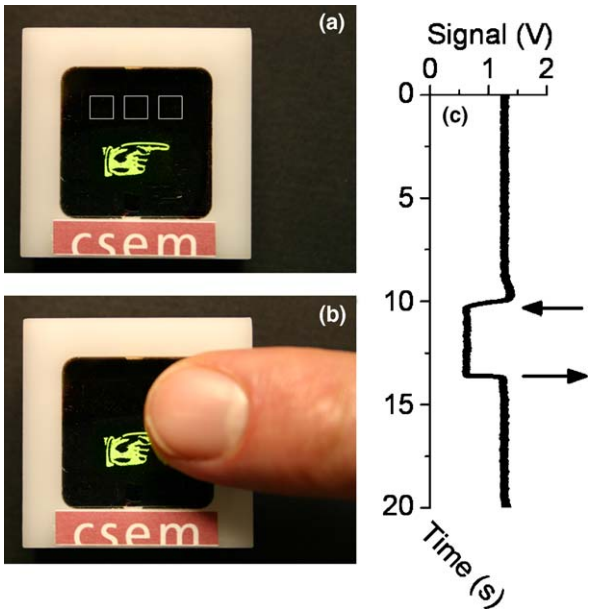

Fig. 6. Polymer light-emitting sign with touch-switch functionality. The three monolithically integrated PPD sensor pixels are indicated by the white squares in (a). Touching the sensor with a finger (b) leads to a clear drop in the PPD signals, as seen for the middle pixel in (c).

removing the finger again (right arrow), the signal recovers to its initial value of about 1.3 V. Note that this value is non-zero due to the through-substrate coupling discussed above. The presence of human skin (or other soft material) on the sensor surface leads to a damping of the substrate modes and thus results in a decrease of the PPD photocurrent. In touch modus, the drop of the sensor signal to below a given threshold value could be used to trigger any desired event, such as e.g., switching a light on or calling an elevator.

Furthermore, the demonstrator of Fig. 6 can also be run in proximity mode. Fig. 7 shows the response of the sensor to the presence of either a coplanar white paper surface (a) or the palm of a hand (b) in close proximity. Light reflected from the nearby

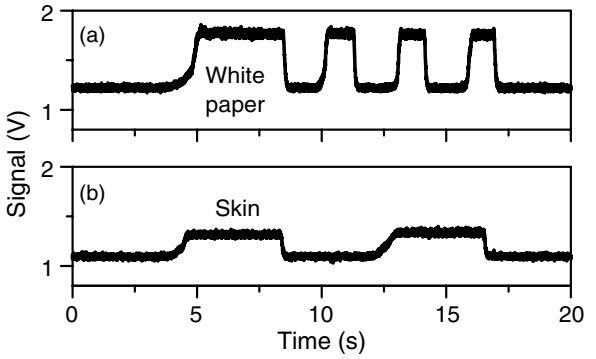

Fig. 7. Sensor of Fig. 6 operated in proximity mode. The response of the sensor to white paper and human skin brought repeatedly into close proximity (~1.5 mm distance) is shown in (a) and (b), respectively.

surfaces results in a clear increase of the current generated in the PPDs. White paper having a higher reflectivity than human skin explains the stronger response of the sensor to the former.

4. Summary and outlook

Polymer LEDs and polymer photodetectors have been monolithically integrated in the same plane of a common substrate in order to demonstrate a sensor with touch-switch and proximity detection functionality. The proximity sensing range of these devices extends to a few centimetres and large sensitivities are achieved for small object–sensor distances ($1/d^2$ dependence).

The all-polymer thin-film sensor is compatible with ultra-thin, light-weight, flexible and/or large-area substrates. On the other hand, due to fact that light source and detector are fully integrated, it could also be miniaturized to a great degree in order to be fitted into applications with tightest space requirements. Furthermore, processing from solution together with the simplicity of the sensor design should make its production accessible for low cost, high-volume fabrication methods such as e.g., roll-to-roll print processes. For all these attractive features, this new type of sensor might be useful for many applications. For example, simple static light-emitting signs with touch-switch functionality are a possible low-end application, which would benefit from the potentially low cost. More advanced possible applications include matrix displays with integrated touch-screen, (large area) position sensitive proximity detectors or even flexible sheets with artificial haptics [29].

Acknowledgements

We gratefully acknowledge the Merck Chemicals Ltd. for supplying the P3HT. This work was partly funded by the Swiss Federal Office for Professional Education and Technology (OPET).

References

[1] B.-J. de Gans, P.C. Duineveld, U.S. Schubert, Inkjet printing of polymers: state of the art and future developments, Advanced Materials 16 (2004) 203, and references therein.
[2] L.S. Hung, C.H. Chen, Recent progress of molecular organic electroluminescent materials and devices, Materials Science and Engineering R 39 (2002) 143.
[3] G.H. Gelinck, H.E.A. Huitema, E. van Veenendaal, E. Cantatore, L. Schrijnemakers, J.B.P.H. van der Putten, T.C.T. Geuns, M. Beenhakkers, J.B. Giesbers, B.-H. Huisman, E.J. Meijer, E. Mena Benito, F.J. Touwslager, A.W. Marsman, B.J.E. van Rens, D.M. de Leeuw, Flexible active-matrix displays and shift registers based on solution-processed organic transistors, Nature Materials 3 (2004) 106.
[4] H. Sirringhaus, N. Tessler, R.H. Friend, Integrated optoelectronics devices based on conjugated polymers, Science 280 (1998) 1741.
[5] A. Dodabalapur, Z. Bao, A. Makhija, J.G. Laquindanum, V.R. Raju, Y. Feng, H.E. Katz, J. Rogers, Organic smart pixels, Applied Physics Letters 73 (1998) 142.
[6] A.C. Arias, S.E. Ready, R. Lujan, W.S. Wong, K.E. Paul, A. Salleo, M.L. Chabinyc, R. Apte, Robert A. Street, All jet-printed polymer thin-film transistor active-matrix backplanes, Applied Physics Letters 85 (2004) 3304.
[7] G. Yu, G. Srdanov, J. Wang, H. Wang, Y. Cao, A.J. Heeger, Large area full-color digital sensors made with semiconducting polymers, Synthetic Metals 111–112 (2000) 133.
[8] R.A. Street, M. Mulato, R. Lau, J. Ho, J. Graham, Z. Popovic, J. Hor, Image capture array with an organic light sensor, Applied Physics Letters 78 (2001) 4193.
[9] D. Kabra, Th.B. Singh, K.S. Narayan, Semiconducting-polymer-based position-sensitive detectors, Applied Physics Letters 85 (2004) 5073.
[10] V. Savvate'ev, Z. Chen-Esterlit, J.W. Aylott, B. Choudhury, C.-H. Kim, L. Zou, J.H. Friedl, R. Shinar, J. Shinar, R. Kopelman, Integrated organic light-emitting device/fluorescence-based chemical sensors, Applied Physics Letters 81 (2002) 4652.
[11] O. Hofmann, P. Miller, P. Sullivan, T.S. Jones, J.C. deMello, D.D.C. Bradley, A.J. deMello, Thin-film organic photodiodes as integrated detectors for microscale chemiluminescence assays, Sensors and Acutators B 106 (2005) 878.
[12] B. Choudhury, R. Shinar, J. Shinar, Glucose biosensors based on organic light-emitting devices structurally integrated with a luminescent sensing element, Journal of Applied Physics 96 (2004) 2949.
[13] Y. Ohmori, H. Kajii, M. Kaneko, K. Yoshino, M. Ozaki, A. Fujii, M. Hikita, H. Takenaka, T. Taneda, Realization of polymeric optical integrated devices utilizing organic light-emitting diodes and photodetectors fabricated on a polymeric waveguide, IEEE Journal of Selected Topics in Quantum Electronics 10 (2004) 70.

[14] We have termed this new type of sensor SENSoLED™.
[15] P. May, K. Pichler, UK Patent 2315594.;
P. Seitz, U. Claessen, S. Rechsteiner, European Patent Application 1467224.;
J. Halls and M. Shade, WO Patent Application 2004/006350.
[16] J. Xue, S.R. Forrest, Organic optical bistable switch, Applied Physics Letters 82 (2003) 136.
[17] Baytron P VP AI 4083 from H.C. Starck.
[18] F8BT = poly[(9,9-dioctylfluorenyl-2,7-diyl)-co-(1,4-benzo-{2,1′-3}-thiadiazole)]. TFB = poly[(9,9-dioctylfluorenyl-2,7-diyl)-co-(4,4′-(*N*-(4-sec-butylphenyl))dipheylamine)].
F8 = poly[9,9-dioctylfluorenyl-2,7-diyl]. All polyfluorenes were purchased from the American Dye Source Inc.
[19] PCBM = [6,6]-phenyl C_{61} butyric acid methyl ester, purchased from Nano-C Inc.
P3HT = regioregular poly[3-hexylthiophene], supplied by Merck Chemicals Ltd.
[20] E. Tekin, E. Holder, V. Marin, B.-J. de Gans, U.S. Schubert, Ink-jet printing of luminescent ruthenium- and iridium-containing polymers for applications in light-emitting devices, Macromolecular Rapid Communications 26 (2005) 293.
[21] V. Marin, E. Holder, M.M. Wienk, E. Tekin, D. Kozodaev, U.S. Schubert, Ink-jet printing of electron donor/acceptor blends: towards bulk heterojunction solar cells, Macromolecular Rapid Communications 26 (2005) 319.
[22] The smallest circle containing all the LED pixels may not contain any photodiode pixel.
[23] A luminance of 1 cd/m^2 is achieved at 2.5 V.
[24] P. Schilinsky, C. Waldauf, J. Hauch, C.J. Brabec, Polymer photovoltaic detectors: progress and recent developments, Thin Solid Films 451–452 (2004) 105.
[25] Spectral match $\eta_s = \frac{1}{r_{\max} S} \int \mathrm{d}\lambda r(\lambda) s(\lambda)$, where $r(\lambda)$ [$r_{\max}$] and $s(\lambda)$ [S] are the responsivity [maximal responsivity] and spectrum [total spectral weight] of PPD and PLED, respectively.
[26] X.H. Yang, D. Neher, Polymer electrophosphorescence devices with high power conversion efficiencies, Applied Physics Letters 84 (2004) 2476.
[27] In the absence of absorption, the total energy flux must be conserved, thus in two dimensions $2\pi(r+\Delta r)\cdot I_{\mathrm{sub}}(r+\Delta r) = 2\pi r \cdot I_{\mathrm{sub}}(r)$. In the presence of absorption, the energy losses have to be taken into account, i.e. $2\pi(r+\Delta r)\cdot I_{\mathrm{sub}}(r+\Delta r) = 2\pi r \cdot I_{\mathrm{sub}}(r) - \frac{\Delta r}{L} 2\pi r I_{\mathrm{sub}}(r)$, where L^{-1} is the absorption coefficient. From this, one derives the following differential equation $\frac{\partial I_{\mathrm{sub}}}{\partial r} = -(\frac{1}{r} + \frac{1}{L}) I_{\mathrm{sub}}(r)$, which has as a solution the expression given in Eq. 1.
[28] A mirror object rather than a Lambertian surface is chosen for the model since the former results in an analytic expression whereas the latter does not. We note that the model predictions for both surfaces are very similar.
[29] T. Someya, T. Sekitani, S. Iba, Y. Kato, H. Kawaguchi, T. Sakurai, A large-area flexible pressure sensor matrix with organic field-effect transistors for artificial skin applications, Proceedings of the National Sciences of the United States of America 101 (2004) 9966.

Available online at www.sciencedirect.com
SCIENCE DIRECT®
Organic Electronics 7 (2006) 121–131
Organic Electronics
www.elsevier.com/locate/orgel

Nanoscale thin-film morphologies and field-effect transistor behavior of oligothiophene derivatives

Eunhee Lim [a], Byung-Jun Jung [a,1], Hong-Ku Shim [a,*], Tomohiro Taguchi [b], Bunpei Noda [b], Takuya Kambayashi [b], Takehiko Mori [b], Ken Ishikawa [b], Hideo Takezoe [b], Lee-Mi Do [c]

[a] *Department of Chemistry, Korea Advanced Institute of Science and Technology (KAIST), 373-1 Guseong-dong, Yuseong-ku, Daejeon 305-701, Republic of Korea*
[b] *Department of Organic and Polymeric Materials, Tokyo Institute of Technology (TIT), Tokyo 152-8552, Japan*
[c] *Electronics and Telecommunications Research Institute, Daejeon 305-350, Republic of Korea*

Received 8 August 2005; received in revised form 1 December 2005; accepted 1 December 2005
Available online 27 December 2005

Abstract

The field-effect transistor (FET) performances of two thiophene-based semiconducting materials (T2TT and T2FL) were examined. Through studies of the thin-film morphology using X-ray diffraction (XRD) and atomic force microscopy (AFM), we could access the behavior and structure of the thin-film devices at the nanoscale level in single molecular layers and determine the correlation between molecular alignment and device performance. Due to the extended π-conjugation, efficient hole injection, and good molecular alignment, the T2TT and T2FL FET devices exhibited hole mobilities of up to 0.03 $cm^2 V^{-1} s^{-1}$, when the films were deposited at T_{sub} = RT and 80 °C, respectively. In spite of the large number of small grains in the film deposited at room temperature, the T2TT molecules were aligned perpendicular to the substrate when deposited at this low substrate temperature, which favored π–π overlap between adjacent molecules, resulting in high OFET performance.

Keywords: Field-effect transistor; Charge carrier mobility; Morphology; Oligomer; Fluorene; Thiophene

1. Introduction

In recent years, interest in organic semiconductors has increased due to their applications in optoelectronic devices such as light-emitting diodes (OLEDs) [1–3], field-effect transistors (FETs) [4–7], and photovoltaic devices [8,9]. These organic electronics have several advantages over conventional inorganic electronics, including facile processability, chemical tunability, compatibility with plastic substrates, and low cost. Applications of OFETs include low-cost memories, smart cards, and driving circuits for large-area display devices [10–12]. Many studies have demonstrated the potential of

* Corresponding author. Tel.: +82 42 869 2827; fax: +82 42 869 2810.
E-mail address: hkshim@kaist.ac.kr (H.-K. Shim).
[1] Present address: Samsung SDI, Yongin, Kyunggi-do 449-577, Republic of Korea.

1566-1199/$ - see front matter © 2005 Elsevier B.V. All rights reserved.
doi:10.1016/j.orgel.2005.12.001

pentacene, pentacene derivatives, oligothiophenes, and poly(3-alkyl-thiophene) (P3HT) as candidate materials for use in OFETs. In particular OFETs based on these materials have been found to be characterized by excellent performance and environmental stability. Improvements in fabrication techniques have enhanced OFETs to the point where their performance is now approaching that of FETs based on inorganic amorphous silicon [13].

To obtain high carrier mobility, it is crucial that the organic molecules be arranged in particular molecular architectures. Specifically, a high degree of molecular alignment and a molecular orientation that is favorable for intermolecular charge migration are needed for efficient charge transport and thus for good device performance. In the development of semiconducting materials, molecules with fused rings in their backbone [14–16] and/or with alkyl chains at their ends [17] have been used to obtain highly crystalline films via enhanced intermolecular ordering and π–π stacking. With the development of OFET semiconducting materials, the charge transport mechanism and structural organization in conjugated oligomers have also been studied in terms of the link between these characteristics and the experimental conditions (e.g. film deposition and treatment conditions) [17–20]. Previous studies have established that the thin-film morphology of the oligomers depends on the processing conditions, and interestingly, that the FET device performance strongly depends on the thin-film morphology. Many attempts have been made to elucidate the correlation between morphology and device performance in the fields of solar cells and light-emitting diodes as well as FETs [21,22]. In organic semiconductor materials, charge carrier transport between adjacent molecules is affected not only by the electronic properties of the material, but also by its morphology. Here we report on the OFET characteristics of two oligothiophene derivatives, with a focus on their charge carrier transport behavior. In particular, we demonstrate that variation of the deposition temperature causes changes in the molecular orientation and film morphology, which in turn result in large changes in the carrier transport behavior and OFET performance.

2. Experimental

The syntheses of the 2,5-bis-(5′-hexyl-[2,2′]bithiophenyl-5-yl)-thieno[3,2-*b*]thiophene (T2TT) and 2,5-bis-(5′-hexyl-[2,2′]bithiophenyl-5-yl)-fluorene (T2FL) were carried out using the well-known palladium-catalyzed Suzuki coupling between dibromoaryl and diborolanylaryl compounds [23–25]. A well-known thiophene-based semiconducting material, dihexylquarterthiophene (DH4T) and two semiconducting materials containing thieno[3,2-*b*]thiophene (2,5-bis-(5-hexyl-thiophen-2-yl)-thieno[3,2-*b*]thiophene, T1TT) or fluorene (2,5-bis-(5-hexyl-thiophen-2-yl)-fluorene, T1FL) were also prepared for comparison. These molecules were synthesized with alkyl chains at both ends and a fused ring system at the core in order to increase the π–π stacking of the oligomer molecules. The chemical structures of the oligomers, which were verified by ^{1}H and ^{13}C NMR spectroscopy as well as elemental analysis, are shown in Fig. 1.

UV–Vis spectra were obtained using a Jasco V-530 UV/Vis. spectrometer, and PL spectra were obtained using a Spex Fluorolog-3 spectrofluorometer. The films used in the UV–Vis and PL measurements were prepared by solution-casting of the oligomers (1.0 wt% in dichlorobenzene). Cyclic voltammograms were recorded at a scan rate of 100 mV/s at room temperature in a solution of tetrabutylammonium hexafluorophosphate (Bu_4NPF_6) dissolved in benzonitrile. A Pt wire was used as the counter electrode and an Ag/AgCl electrode was used as the reference electrode. The oxidation potentials were calibrated using the ferrocene (Fc) value of −4.8 eV as the standard [26]. HOMO values are calculated using the empirical equation: $I_p(\mathrm{HOMO}) = -(E_{\mathrm{onset}} + 4.39)$, where E_{onset} is the onset potential of oxidation [27,28]. Film thicknesses were measured using a Dektak 3ST surface profiler.

FETs were fabricated using the bottom contact geometry (channel length $L = 50\ \mu m$, width $W = 250\ \mu m$). This geometry was chosen over the top contact geometry with the practical consideration that OFETs will ultimately be manufactured in the bottom contact configuration [29]. In our devices, source and drain contacts were made of gold and the dielectric was silicon oxide (SiO_2; thickness 300 nm). Onto a cleaned SiO_2 surface, the organic semiconductors were vacuum-deposited under a pressure of $\sim 2.0 \times 10^{-6}$ Torr to a final thickness of 200 nm. The substrate temperature during deposition was controlled by heating the platform on which the substrate was mounted. The electrical characteristics of the OFET devices were measured in air using a Keithley 4200 Semiconductor Characterization System. For morphological characterizations, the semiconducting materials

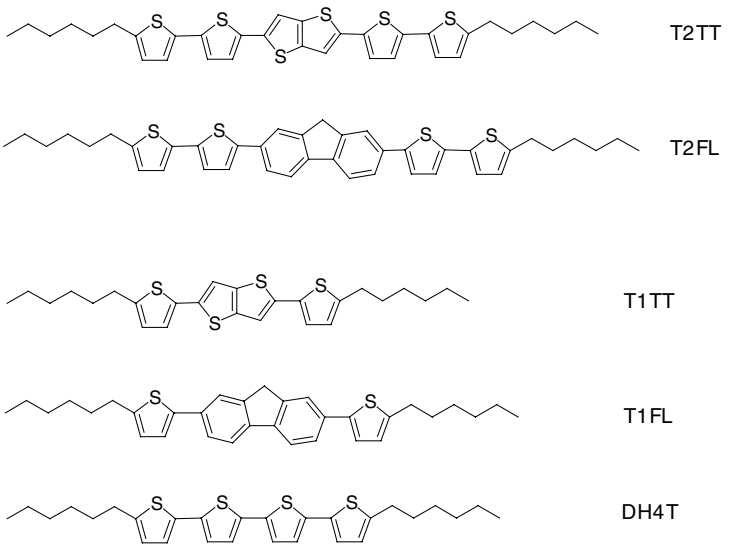

Fig. 1. Chemical structures of the thiophene-based semiconducting materials containing thieno[3,2-*b*]thiophene or fluorene groups.

were deposited onto SiO_2/Si substrates simultaneously with the FET devices. XRD patterns were recorded using an X'Pert-MPD System (Philips) in reflection mode at 40 kV and 30 mA with a scanning rate of 0.08° per second and Cu Kα radiation (with wavelength $\lambda = 1.5406$ Å) with a θ–2θ scans configuration. Contact-mode AFM images were recorded using a Seiko Instruments SPA-300/SPI3800 probe system, equipped with a SiN cantilever (Olympus, OMCL-TR400PSA-1, force constant 0.09 N/m, tip curvature radius −15 nm).

3. Results and discussion

3.1. Optical properties

The intermolecular interactions between adjacent molecules of the oligomers in the solid state were confirmed by UV–Vis absorption and photoluminescence (PL) emission spectroscopy (Fig. 2). The PL emission peaks of the T2FL and T2TT films are clearly red-shifted with respect to those in solution, indicating increased interactions between neighboring molecules in the film state. In addition, compared to the corresponding solution spectra, the PL emission of the T2TT film is considerably weaker and the spectrum of the T2TT film exhibits a blue-shifted absorption maximum at 349 nm. Similar behavior has been reported for oligothiophenes, which were found to have low PL yields and blue-shifted absorption maxima when prepared as thin films [30]. It has been reported that in oligothiophene films, the closed-packed arrangement of the molecules leads to a splitting of the excited state into

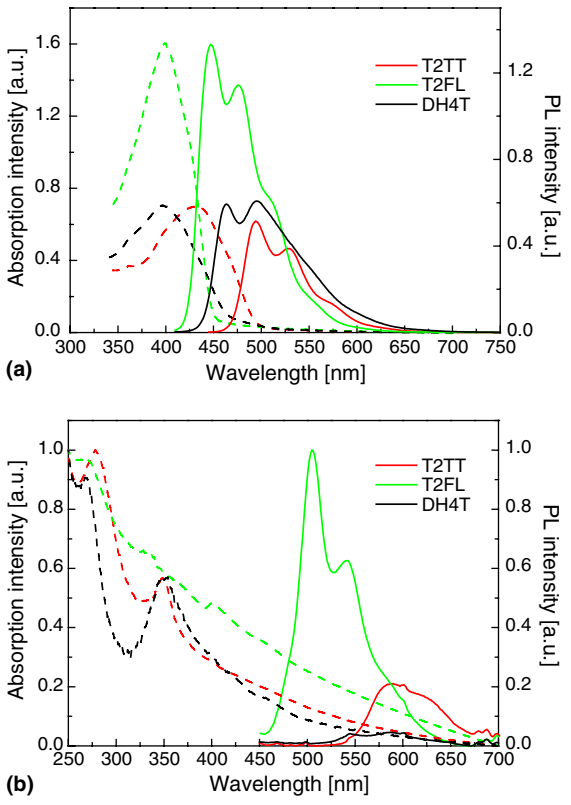

Fig. 2. UV–Vis absorption (dotted line) and PL emission (solid line) spectra of the oligomers (a) in chloroform solution and (b) as films.

two exciton states (Davydov splitting) [31,32]. The optical properties of the two oligomers considered in the present work confirm the existence of strong interactions among their π-conjugated systems in the solid state.

3.2. FET characteristics

FETs were fabricated using the bottom contact geometry (channel length $L = 50$ μm, width $W = 250$ μm). A schematic cross-section of the bottom contact device is shown in Fig. 3. The device performance was measured in air and the results are shown in Table 1. The thin-film transistors of T2TT and T2FL showed characteristics typical of a *p*-channel field-effect transistor, i.e. when a negative bias was applied, the drain–source current scaled with the negative gate voltage due to the increased number of charge carriers (holes). The output curves [i.e., $I_D = f(V_D)$] at different gate biases and the transfer curves [i.e., $I_D = f(V_G)$] at constant V_D for the T2TT and T2FL films are shown in Figs. 4 and 5, respectively. The output curves show very good saturation behavior. The field-effect mobilities (μ_{FET}) were calculated in the saturation regime at a drain voltage of $V_D = -80$ V using the equation $I_D = (WC_i/2L)\,\mu_{FET}(V_G - V_T)^2$, where C_i is the capacitance of the SiO_2 insulator

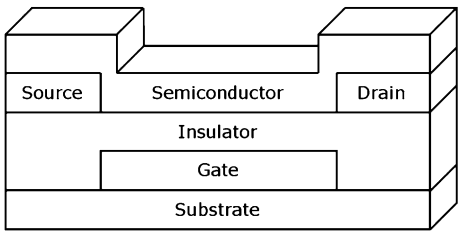

Fig. 3. A schematic cross-section of the bottom contact FET device.

Table 1
Field-effect mobility (μ_{FET}) and threshold voltage (V_{th}) for oligomer transistors prepared at different substrate temperatures (T_{sub})

Material	T_{sub} [°C]	μ_{FET} [$cm^2\,V^{-1}\,s^{-1}$]	V_{th} [V]
T2TT	25 (RT)	0.030–0.023	−2 to −5
	80	0.012–0.011	−5 to −12
	100	0.002–0.001	−8 to −28
T2FL	25 (RT)	0.008–0.006	−38 to −44
	80	0.031–0.020	−2 to −14
	100	0.022–0.016	−16 to −25
	120	0.0007	−28 to −40

($C_i = 12.3 \times 10^{-9}$ F cm^{-2}) and V_G and V_T are the gate and threshold voltages, respectively.

The T2TT and T2FL devices showed hole mobilities of ca. 0.03 $cm^2\,V^{-1}\,s^{-1}$ and threshold voltages of −4 V and −14 V when deposited at T_{sub} = RT and 80 °C respectively; this mobility was comparable to that of DH4T (0.02 $cm^2\,V^{-1}\,s^{-1}$) under the same conditions. Considering that FETs were fabricated using the bottom contact geometry with the SiO_2 gate dielectric, this FET performance is one of the best among thin-film organic semiconductors. In addition, the OFET devices made from these two oligomers showed good stability in air. Only slight changes of the device performances have been observed after the transistors have been exposed to ambient air for 10 days. (e.g., $I_{off,\,fresh} = 2$ nA, $I_{off,\,10\,days} = 6.8$ nA, $I_{on,\,fresh} = 3.3$ μA, and $I_{on,\,10\,days} = 5.2$ μA for T2FL at T_{sub}=80 °C).

For comparison, we have also prepared two semiconducting materials containing thieno[3,2-*b*] thiophene (T1TT) or fluorene (T1FL). Although the chemical structures of T1TT and T1FL are analogous to T2TT and T2FL respectively, other than that the number of thiophene rings is reduced to half, the films of T1TT and T1FL showed relatively low FET hole mobility of an order of 10^{-3}–10^{-4} $cm^2\,V^{-1}\,s^{-1}$ at all substrate temperatures (RT and 80 °C). The extension of π-conjugation from thiophene to bithiophenyl substitution effectively improves the FET performance, indicating that the extended π-conjugation length results in increased π–π stacking between the oligomer molecules for efficient carrier transport.

The good performances of the T2TT and T2FL devices can be attributed to the good match between the ionization potential of each oligomer and the work function of the gold electrodes. The HOMO levels of the materials were determined using the onset potential of the oxidation process of each oligomer [33]. The onset of oxidation of T2TT and T2FL occurs at 0.66 V and 0.76 V (vs SCE), which correspond to E_{HOMO} values of −5.10 eV and −5.20 eV, respectively. Thus the HOMO levels of T2TT and T2FL match well with the work function of gold metal, resulting in efficient hole injection in OFETs.

The FET characteristics of OFETs depend primarily on the molecular alignment in the film and on the injection of holes from the electrodes. Generally, oligomeric semiconducting materials such as pentacene show a vertical alignment in which the molecular long axes are oriented perpendicular to

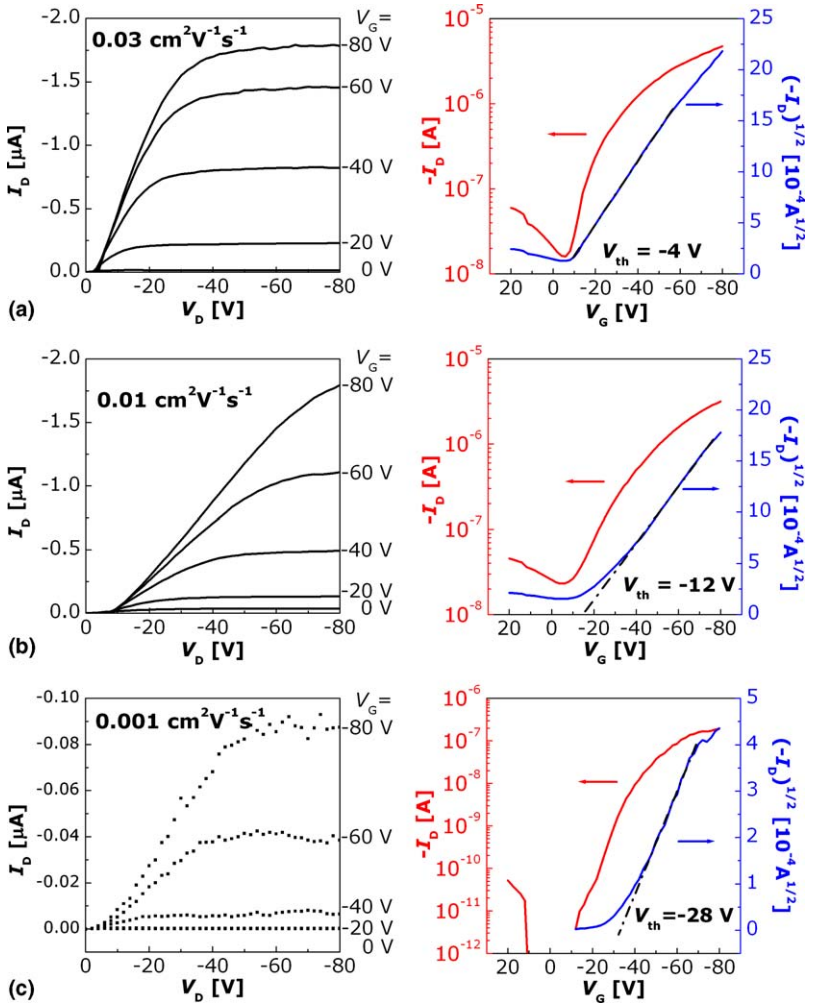

Fig. 4. Output characteristics of the T2TT FET devices at different gate biases (left) and plots of the transfer at constant $V_D = -80$ V (right) (semilogarithmic plot of $-I_D$ versus V_G (left axis) and plot of $(-I_D)^{1/2}$ versus V_G (right axis)), when deposited at T_{sub} = (a) RT, (b) 80 °C, and (c) 100 °C, respectively.

the substrate surface [34,35]. The degree of alignment is an important determinant of the degree of carrier transport between adjacent molecules. In the present work, we additionally performed AFM and X-ray diffraction (XRD) studies to further investigate the relationship between molecular alignment and device performance. The AFM micrographs of the oligomer films showed 3- or 2-dimensional morphologies that varied with substrate temperature. For all of the oligomer films, the XRD θ–2θ scans were highly textured and showed well-resolved multiple (h00) reflections with a strong (100) reflection corresponding to the calculated molecular length. This indicates that, similar to other organic semiconducting materials, the oligomers are oriented perpendicular to the substrate. The characteristics of T2TT and T2FL—most notably their extended π-conjugation length, appropriate ionization potentials, and good molecular alignment—thus result in reasonable performance characteristics for FETs based on these oligomers.

3.3. Relationship between thin-film morphology and FET performance

As shown in Table 1, the FET performances of the oligomers depended on the substrate temperature (T_{sub}), with optimum performances being achieved when T2TT and T2FL were deposited at

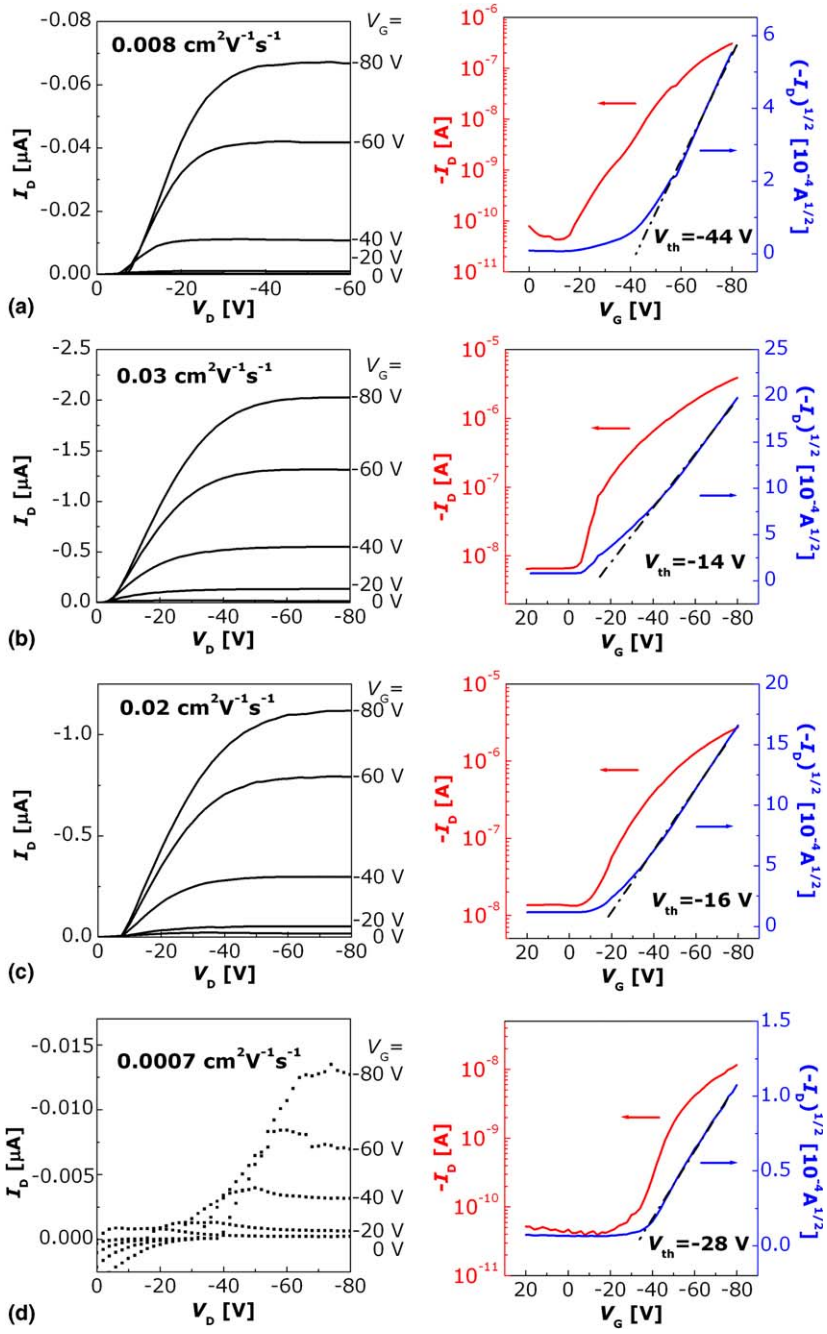

Fig. 5. Output characteristics of the T2FL FET devices at different gate biases (left) and plots of the transfer at constant $V_D = -80$ V (right) (semilogarithmic plot of $-I_D$ versus V_G (left axis) and plot of $(-I_D)^{1/2}$ versus V_G (right axis)), when deposited at T_{sub} = (a) RT, (b) 80 °C, (c) 100 °C, and (d) 120 °C, respectively.

substrate temperatures of RT and 80 °C respectively ($0.03\ cm^2\ V^{-1}\ s^{-1}$). The FET characteristics of T2TT and T2FL at different substrate temperatures are summarized in Table 1. To determine the source of this dependence of FET performance on T_{sub}, we studied the thin-film morphologies and FET performances of devices fabricated at various substrate temperatures. AFM images and XRD patterns of T2TT are shown in Fig. 6. In terms of OFET performance, T2TT had the highest hole mobility (0.03

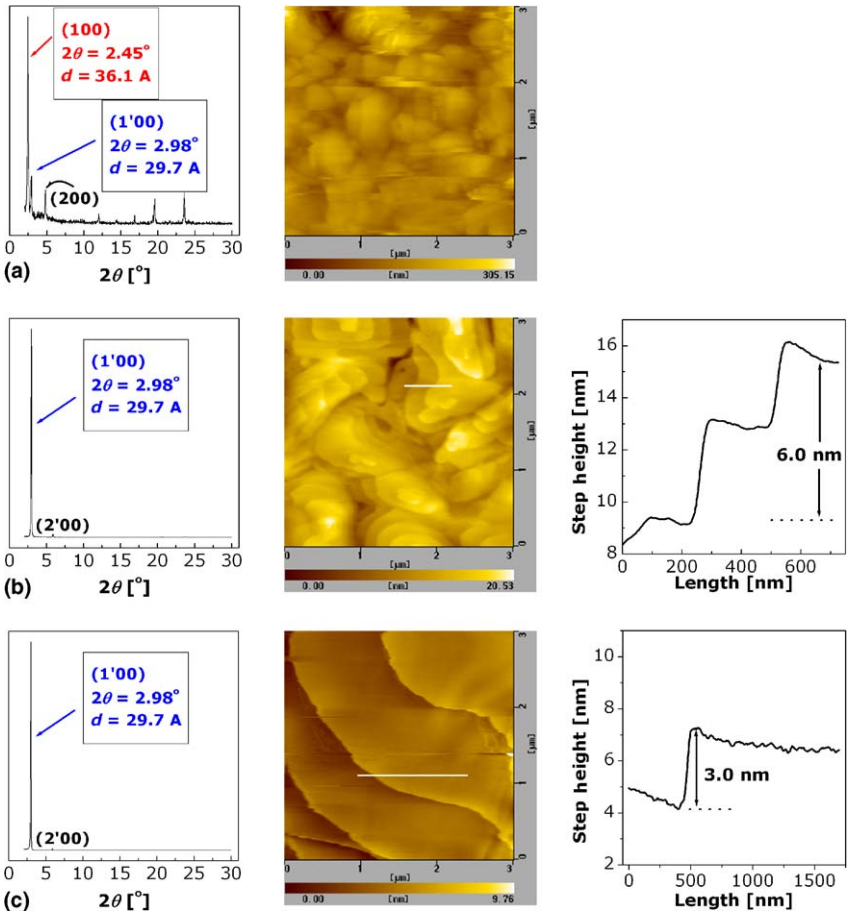

Fig. 6. XRD patterns and AFM images (with profiles) of T2TT films deposited at T_{sub} = (a) RT, (b) 80 °C, and (c) 100 °C, respectively.

$cm^2\ V^{-1}\ s^{-1}$) when deposited at RT, and maintained a hole mobility of 0.01 $cm^2\ V^{-1}\ s^{-1}$up to 80 °C; above 100 °C, however, the hole mobility of the T2TT device decreased to values on the order of 10^{-3} $cm^2\ V^{-1}\ s^{-1}$'. Generally, oligomeric semiconducting materials have higher mobilities at higher substrate temperatures because the grain size tends to increase and the number of grain boundaries tends to decrease with increasing temperature [20,36]. Consistent with this, the grain size of T2TT increases with increasing substrate temperature, as shown in Fig. 6. In T2TT, the domain size is 0.5–1 μm at T_{sub} = RT and more than 3 μm at T_{sub} = 100 °C. The grain size of the T2TT film at T_{sub} = RT is greater than the grain sizes in thin films of other semiconductors [20,33,37–39], supporting the good FET performance of T2TT films at T_{sub} = RT. In spite of the increase in grain size, however, the FET hole mobility of the T2TT device decreases with increasing T_{sub}. This finding indicates that the molecular alignment and FET characteristics are affected by factors other than the grain size and grain boundaries. Information on the molecular arrangement in the crystal grains can be obtained by XRD analyses of thin films of the oligomers. As mentioned above, a series of multiple (h00) reflections with a strong (100) reflection is observed in the XRD patterns of T2TT at all substrate temperatures, T_{sub} = RT, 80 °C, and 100 °C. The calculated interlayer spacings (d) and the estimated molecular lengths (l) are summarized in Table 2. Interestingly, the interlayer spacing, which was determined from the (100) reflection, was 36.1 Å at T_{sub} = RT but 29.7 Å at both T_{sub} = 80 °C and 100 °C. While the T2TT films at T_{sub} = 80 °C and 100 °C showed their first reflection peak at $2\theta = 2.98°$, indicative of a d spacing of 29.7 Å, the T2TT film deposited at T_{sub} = RT showed the first strong reflection peak at $2\theta = 2.45°$, indicative of a d spacing 36.1 Å, and only a very small

Table 2
Estimated molecular lengths (l),[a] calculated interlayer spacing (d)[b] and calculated tilt angles (θ_{tilt})[c] of the oligomer films prepared at different substrate temperatures (T_{sub})

	l [Å]	T_{sub} = RT (25 °C)		T_{sub} = 80 °C		T_{sub} = 100 °C		T_{sub} = 120 °C	
		d [Å]	θ_{tilt} [deg]	d [Å]	θ_{tilt} [deg]	d [Å]	θ_{tilt} [deg]	d [Å]	θ_{tilt} [deg]
T2TT	36.6	36.1	9.5	29.7	35.8	29.7	35.8		
T2FL	39.1	32.5	33.8	33.3	31.6	32.9	32.7	31.8	35.6

[a] Estimated by MOPAC-PM3 calculation.
[b] Determined on the basis of the first-layer line in the θ–2θ scan of the thin films.
[c] Calculated by $\theta_{tilt} = \cos^{-1}(d/l)$.

reflection peak corresponding to a d spacing of 29.7 Å. Surprisingly, the calculated d spacings from the first reflection peaks of the XRD patterns match exactly with the step heights of the films in the AFM images (~3 nm). The d spacing for the film at T_{sub} = RT (36.1 Å) is very close to the molecular length calculated using MOPAC-PM3 (36.6 Å), indicating that the molecules have an edge-on orientation relative to the substrate. When the molecules are aligned perpendicular to the substrate, the π–π overlap between adjacent molecules is maximized and carrier transport can occur effectively. The planarity and rigidity of thieno[3,2-*b*]thiophene result in high crystallinity of the oligomer and vertical alignment into the favorable molecular orientation. On the other hand, when the T2TT films were deposited at the higher substrate temperatures of T_{sub} = 80 °C and 100 °C, the observed d spacings were smaller than the corresponding extended chain lengths, indicating that the molecules may be inclined away from the direction normal to the substrate, resulting in a lower mobility. Taken together, the above results thus suggest that when deposited at higher substrate temperatures, the T2TT film is comprised of large domains and small grain boundaries, but the molecules in each domain are inclined with a tilt angle of about 36°, which diminishes the π–π overlap between adjacent molecules and hence degrades the OFET performance. In addition, it has been reported that the dependence of OFET performance on deposition temperature can be understood in terms of the existence of crystal grains with different phases, such as the "thin-film phase" and "single-crystal phase" [20]. In that work, an oligomer film in the "single-crystal phase" showed a lower hole mobility than a film of the same material in the "thin-film phase", due to the smaller degree of intermolecular overlap in the former film. In the present work, the decrease of the layer spacing and the increase of the tilt angle of molecules in films fabricated at higher T_{sub} can also be understood as originating from a morphological change into a different phase. Further research into the crystal structures of our derivatives is currently underway.

The T2FL films showed features similar to those described above for the T2TT films. As shown in Fig. 7, the grain size of the T2FL films increased with increasing deposition temperature, which is not consistent with the temperature dependence of the device performance. It is worth noting that the T2FL film deposited at 120 °C exhibits a well-defined 2-dimensional morphology with a domain size of more than 10 μm. The multistep structures of T2TT and T2FL (shown in Fig. 6c and 7d respectively) indicate that these films consist of regularly stacked molecular layers similar to a self-assembled monolayer (SAM). Thus, our XRD and AFM studies allow us to access the behavior and structure of the thin-film devices at the nanoscale level in single molecular layers. The T2FL films exhibited more complicated XRD patterns than those observed for the T2TT films. Films grown at all four substrate temperatures showed strong (1 0 0) reflections with multiple (h 0 0) reflections; however, the d spacings obtained from the (1 0 0) reflections varied with the substrate temperature, as summarized in Table 2. The interlayer d spacings of the T2FL films were 32.5, 33.3, 32.9, and 31.8 Å when deposited at RT, 80 °C, 100 °C, and 120 °C, respectively. Inspection of the data reveals that the hole mobilities of the T2FL films increase as the difference between the d spacing of the film and the estimated molecular length (39.1 Å) decreases. The d spacings indicate that the molecules in the T2FL films deposited at T_{sub} = RT and 120 °C are more inclined with respect to the substrate than those in the films deposited at T_{sub} = 80 °C and 100 °C, suggesting that the T2FL films deposited at these temperatures show higher hole mobilities because their molecular orientation is more favorable for carrier transport. In addition, the large decrease in hole mobility at T_{sub} = 120 °C

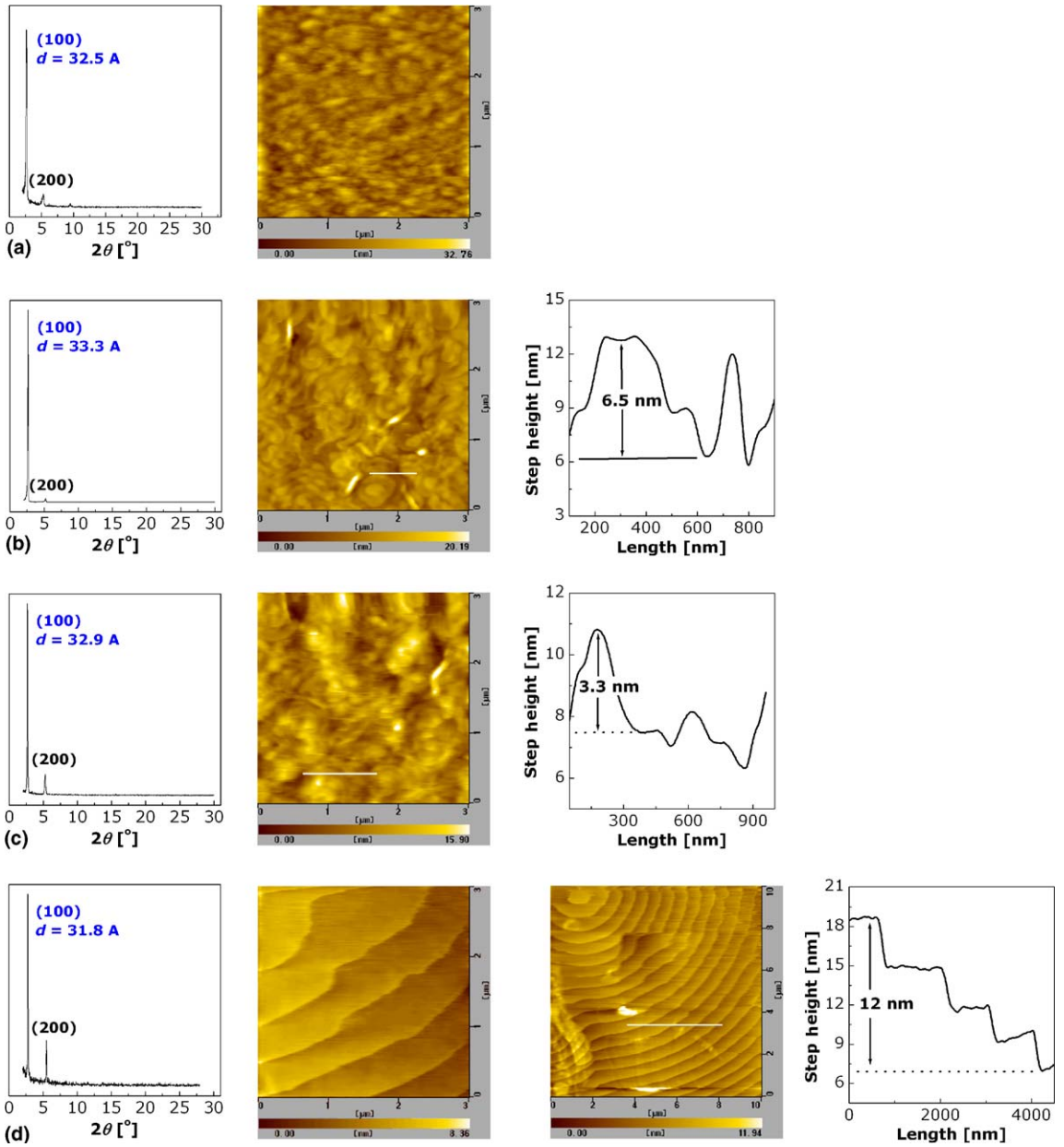

Fig. 7. XRD patterns and AFM images (with profiles) of T2FL films deposited at T_{sub} = (a) RT, (b) 80 °C, (c) 100 °C, and (d) 120 °C, respectively.

may also be caused by the poor wetting of an organic semiconductor to the electrode [29] and cracking of the film which was observed by AFM [37]. A crack-induced reduction in mobility has been observed for films of other oligothiophene derivatives deposited at $T_{sub} > 130$ °C [37]. The cracking of oligomer films has been attributed to mechanical stresses originating from the different thermal expansion coefficients of the film and the Si wafer.

Fig. 8 shows the hole mobilities and *d*-spacings for T2FL and T2TT films deposited at various substrate temperatures, from which we can determine the effect of molecular orientation on FET performance. Collectively, our analyses of the FET characteristics and thin-film morphologies indicate that the best mobility of the semiconducting materials is obtained when the material is deposited at a substrate temperature that gives films that have not

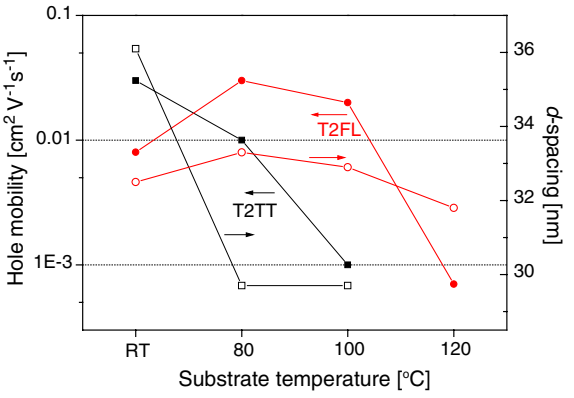

Fig. 8. Hole mobilities and *d*-spacings at various substrate temperatures.

only a large grain size but also a molecular orientation favoring intermolecular charge migration.

4. Conclusions

In summary, we have synthesized two new thiophene-based semiconducting materials containing thieno[3,2-*b*]thiophene or fluorene groups, T2TT and T2FL, and fabricated OFETs using these oligomers as the active layer. Due to the (1) extended π-conjugation, (2) efficient hole injection, and (3) good alignment of the molecules, the T2TT and T2FL FET devices exhibited hole mobilities of up to 0.03 $cm^2 V^{-1} s^{-1}$, when the films were deposited at T_{sub} = RT and 80 °C respectively. In oligomer films, the carriers (holes) move effectively, and thus the FET characteristics are better, when the molecular orientation favors π–π overlap and the grains are large in size and separated by small grain boundaries. For T2TT, the molecules tended to align almost perpendicular to the substrate at a low substrate temperature (RT), which favors π–π overlap between adjacent molecules. In spite of the large number of small grains in the film deposited at this low substrate temperature, the T2TT device showed high hole mobility due to the efficient transport of the carriers. Further improvements in FET performance should be possible by optimizing the fabrication conditions and the surface treatment.

Acknowledgements

This work was supported by the Center for Advanced Functional Polymers (CAFPoly) through KOSEF and the Information Display R&D Center (No. AOD 02-A) through the 21st Century Frontier R&D Program of Ministry of Science and Technology (MOST). We gratefully acknowledge Dr. T. Hayakawa (TIT) and Mr. M. Seo (KAIST) for the helpful discussion for XRD studies.

References

[1] J.H. Burroughes, D.D.C. Bradley, A.R. Brown, R.N. Marks, K. Mackey, R.H. Friend, P.L. Burns, A.B. Holmes, Nature 347 (1990) 539.
[2] R.H. Friend, R.W. Gymer, A.B. Holmes, J.H. Burroughes, R.N. Marks, C. Taliani, D.D.C. Bradley, D.A. Dos Santos, J.L. Brédas, M. Lögdlund, W.R. Salaneck, Nature 397 (1999) 121.
[3] H.-K. Shim, J. Jin, Adv. Polym. Sci. 158 (2002) 193.
[4] H.E. Katz, Z. Bao, S.L. Gilat, Acc. Chem. Res. 34 (2001) 359.
[5] G. Horowitz, Adv. Mater. 10 (1998) 365.
[6] A. Babel, S.A. Jenekhe, Macromolecules 36 (2003) 7759.
[7] T.P.I. Saragi, T. Fuhrmann-Lieker, J. Salbeck, Synth. Met. 148 (2005) 267.
[8] L. Schmidt-Mende, A. Fechtenkötter, K. Müllen, E. Moons, R.H. Friend, J.D. MacKenzie, Science 293 (2001) 1119.
[9] C.J. Brabec, N.S. Sariciftci, J.C. Hummelen, Adv. Funct. Mater. 11 (2001) 15.
[10] B. Crone, A. Dodabalapur, Y.-Y Lin, R.W. Filas, Z. Bao, A. LaDuca, R. Sarpeshkar, H.E. Katz, W. Li, Nature 403 (2000) 521.
[11] G.H. Gelinck, T.C.T. Geuns, D.M. de Leeuw, Appl. Phys. Lett. 77 (2000) 1487.
[12] H. Klauk, H.N. Jackson, Solid State Technol. 43 (2000) 63.
[13] H. Sirringhaus, N. Tessler, R.H. Friend, Science 280 (1998) 1741.
[14] J.G. Laquindanum, H.E. Katz, A.J. Lovinger, J. Am. Chem. Soc. 120 (1998) 664.
[15] J.G. Laquindanum, H.E. Katz, A.J. Lovinger, A. Dodabalapur, Adv. Mater. 9 (1997) 36.
[16] E. Lim, B.-J. Jung, J. Lee, J.H.-K. Shim, J.-I. Lee, Y.S. Yang, L.-M. Do, Macromolecules 38 (2005) 4531.
[17] H. Meng, Z. Bao, A.J. Lovinger, B.-C. Wang, A.M. Mujsce, J. Am. Chem. Soc. 123 (2001) 9214.
[18] D.J. Gundlach, Y.Y. Lin, T.N. Jackson, S.F. Nelson, D.G. Schlom, IEEE Electron. Dev. Lett. 18 (1997) 87.
[19] F. Garnier, Philos. Trans.: Math. Phys. Eng. Sci. 355 (1997) 815.
[20] K. Takimiya, Y. Kunugi, Y. Toyoshima, T. Otsubo, J. Am. Chem. Soc. 127 (2005) 3605.
[21] M. Chiesa, L. Burgi, J.-S. Kim, R. Shidler, R.F. Friend, H. Sirringhaus, Nano Lett. 5 (2005) 559.
[22] X. Yang, J. Loos, S.C. Veenstra, W.J.H. Verhees, M.-M. Wienk, J.M. Kroon, M.A.J. Michels, R.A.J. Janssen, Nano Lett. 5 (2005) 579.
[23] E. Lim, B.-J. Jung, H.-K. Shim, Macromolecules 36 (2003) 4288.
[24] P. Bauerle, F. Wurthner, G. Gotz, F. Effenberger, Synthesis (1993) 1099.
[25] M.D. Iosip, S. Destric, M. Pasini, W. Porzio, K.P. Pernstich, B. Batlogg, Synth. Met. 146 (2004) 251.
[26] J. Pommerehe, H. Vestweber, W. Guss, R.F. Mahrt, H. Bassler, M. Porsch, J. Daub, Adv. Mater. 7 (1995) 55.

[27] D.M. de Leeuw, M.M.J. Simenon, A.R. Brown, R.E.F. Einerhand, Synth. Met. 87 (1997) 53.
[28] A. Charas, J. Morgado, J.M.G. Martinho, L. Alcacer, F. Cacialli, Synth. Met. 127 (2002) 251.
[29] C.D. Dimitrakopoulos, R.L. Malenfant, Adv. Mater. 14 (2002) 99.
[30] C. Videlot, J. Ackermann, P. Blanchard, J.-M. Raimundo, P. Frere, M. Allain, R. Bettignies, E. Levillain, J. Roncali, Adv. Mater. 15 (2003) 306.
[31] A. Yassar, G. Horowitz, P. Valat, V. Wintgens, M. Hmyene, F. Deloffre, P. Srivastava, P. Lang, F. Garnier, J. Phys. Chem. 99 (1995) 9155.
[32] F. Garnier, Acc. Chem. Res. 32 (1999) 209.
[33] H. Meng, J. Zheng, A.J. Lovinger, B.-C. Wang, P.G.V. Patten, Z. Bao, Chem. Mater. 15 (2003) 1778.
[34] C.D. Dimitrakopoulos, S. Purushothaman, J. Kymissis, A. Callegari, J.M. Shaw, Science 283 (1999) 822.
[35] F. Garnier, A. Yassar, R. Hajlaoui, G. Horowitz, F. Deloffre, B. Servet, S. Ries, P. Alnot, J. Am. Chem. Soc. 115 (1993) 8716.
[36] S. Ando, J.-i. Nishida, H. Tada, Y. Inoue, S. Tokito, Y. Yamashita, J. Am. Chem. Soc. 127 (2005) 5336.
[37] J. Locklin, D. Li, S.C.B. Mannsfeld, E.-J. Borkent, H. Meng, R. Advincula, Z. Bao, Chem. Mater. 17 (2005) 3366.
[38] A. Facchetti, M. Mushrush, M.-H. Yoon, G.R. Hutchison, M.A. Ratner, T.J. Marks, J. Am. Chem. Soc. 126 (2004) 13859.
[39] Y. Wu, Y. Li, S. Gardner, B.S. Ong, J. Am. Chem. Soc. 127 (2005) 614.

Available online at www.sciencedirect.com
SCIENCE DIRECT®
Organic Electronics 7 (2006) 132–136
Organic Electronics
www.elsevier.com/locate/orgel

High charge density and mobility in poly(3-hexylthiophene) using a polarizable gate dielectric

R.C.G. Naber [a], M. Mulder [a], B. de Boer [a], P.W.M. Blom [a,*], D.M. de Leeuw [b]

[a] *Molecular Electronics, Materials Science Centre[Plus], University of Groningen, Nijenborgh 4, 9747 AG, Groningen, The Netherlands*
[b] *Philips Research Laboratories, Professor Holstlaan 4, 5656 AA, Eindhoven, The Netherlands*

Received 3 November 2005; accepted 30 November 2005
Available online 10 February 2006

Abstract

Organic field-effect transistors (OFETs) typically exhibit either a high charge transport mobility or a high charge density. Here we demonstrate an OFET in which both the mobility and the charge density have high values of 0.1 $cm^2/V\,s$ and 28 mC/m^2, respectively. The high charge density is induced by the ferroelectric polarization of the gate dielectric poly(vinylidene fluoride/trifluoroethylene). The high mobility is achieved in a regioregular poly(3-hexylthiophene) semiconductor using a transistor with a top-gate layout that inherently exhibits a smooth semiconductor–dielectric interface. The combination of high mobility and charge density yields a record conductance value for polymer-based FETs of 0.3 μS.

PACS: 72.80.Le; 77.84.Jd; 85.30.Tv

Keywords: Poly(3-hexylthiophene); Ferroelectric polymer; Field-effect transistor

1. Introduction

Organic field-effect transistors (OFETs) have reached a technological level where they might be applied in a number of products, ranging from RFID tags to active-matrix (AM) driven displays. Active-matrix electronic-paper displays driven by OFETs have recently been demonstrated [1], and application of OFETs for AM liquid crystal displays is also considered. An inherent disadvantage of organic FETs is that the current driving capability is limited by the relatively low mobility, as compared to their inorganic counterparts. A high current response/conductance is advantageous for driving organic light-emitting diodes (OLEDs) and it reduces the charging time of gate capacitors in integrated circuits. The conductance is determined by the product of charge carrier density in the channel, governed by the capacitance of the gate dielectric, and the charge carrier mobility. In a recent demonstration of an AM driven OLED display pentacene-based drive transistors were used, exhibiting a conductance of typically 0.2 μS [2]. These pentacene FETs make use of the high carrier mobility of 0.6 $cm^2/V\,s$ that can be achieved in

* Corresponding author. Tel.: +31 50 363 4376/8336; fax: +31 50 363 8751.
E-mail addresses: r.c.g.naber@rug.nl (R.C.G. Naber), p.w.m.blom@rug.nl (P.W.M. Blom).

1566-1199/$ - see front matter
doi:10.1016/j.orgel.2005.11.007

vacuum-deposited small molecules. An important question is whether such a large conductance can also be achieved in solution-processed polymer transistors, of which the mobility is at least an order of magnitude lower as compared to their small-molecule based counterparts. For this a large carrier density and carrier mobility needs to be combined in one single polymer transistor.

One way to increase the maximum charge carrier density is by increasing the capacitance of the gate dielectric. It has been shown that the high capacitance of a polymer electrolyte can induce a charge density of 3 C/m^2 [3], but only in combination with a strongly limited carrier mobility of 4×10^{-4} cm^2/V s in pentacene, which results in a low conductance value of 0.07 μS. Another approach is to use a thin polymer film with a high dielectric constant k [4]. One promising candidate material is polyvinylidene fluoride (PVDF) and its co- and terpolymers because it has a high dielectric constant and dielectric strength [5]. A pentacene-based transistor using a PVDF terpolymer gate dielectric with a mobility of 1 cm^2/V s has been demonstrated [6]. However, the transistor was made with a low-k buffer layer on top of the dielectric which lowered the effective k-value by 50%. The buffer layer was necessary because of the high surface roughness of the dielectric layer, which would have lowered the mobility due to charge trapping effects inside roughness valleys at the dielectric–semiconductor interface [7]. Field-effect transistors based on pentacene and regioregular poly(3-hexylthiophene) (rr-P3HT) with a PVDF gate dielectric without a buffer layer have also been demonstrated [8,9]. The highest mobility was 8×10^{-3} cm^2/V s in rr-P3HT, which was obtained using a PVDF gate dielectric with a surface roughness of 5 nm [9]. In recent literature the reported mobility of rr-P3HT is most often higher than 1×10^{-2} cm^2/V s [10]. The fact that the mobility of rr-P3HT is generally higher confirms that the mobility on PVDF without a buffer layer is limited by the surface roughness of PVDF. In this manuscript we demonstrate that a top-gate transistor layout enables a smooth interface between rr-P3HT and PVDF copolymer poly(vinylidene fluoride/trifluoroethylene) (P(VDF-TrFE)). The change from a bottom-gate to a top-gate layout is a more expedient solution to the roughness problem than using a buffer layer, because it does not lower the effective k-value of the gate dielectric. With the top-gate transistor layout a semiconductor mobility of 0.1 cm^2/V s is obtained in rr-P3HT, which is an increase of about one order of magnitude. Furthermore, we demonstrate that a charge density of 28 mC/m^2 is induced by the ferroelectric and dielectric polarization of P(VDF-TrFE). The combination of high mobility and charge density induces a large conductance of 0.3 μS. It is this large conductance value that makes the transistors applicable as drive transistors in active-matrix OLED displays [2,11].

2. Experimental

The top-gate field-effect transistor layout is shown in Fig. 1(a), with silver source, drain and gate electrodes and a P(VDF-TrFE) gate dielectric film on top of the rr-P3HT semiconductor film. The transistors were prepared upon clean glass substrates onto which silver source–drain electrodes were deposited with shadow mask evaporation, using a wire to create the channel. The substrates were subsequently annealed at 140 °C in air to increase the adhesion. The workfunction of the annealed silver measured with a Kelvin probe was 4.4 eV. Regioregular poly(3-hexylthiophene) (electronic grade; 98.5% regioregular; Rieke Metals, Inc.) was purified as described in a previous report [9]. Chloroform solutions were spin coated in a N_2 filled glovebox. A rotation speed of 4000 rpm was used to minimize the surface roughness. The layer

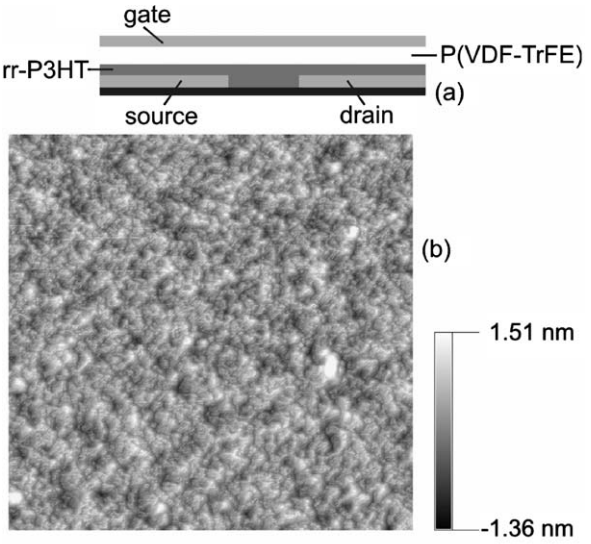

Fig. 1. (a) The top-gate transistor layout. (b) The topography of an annealed rr-P3HT layer, as measured with an AFM. The area is 3×3 μm^2.

thickness was typically 60 nm. The samples were subsequently annealed in a vacuum oven at 140 °C to enhance the crystallinity of the rr-P3HT. The topography of an annealed rr-P3HT layer as measured with an AFM is presented in Fig. 1(b). The root-mean-square roughness derived is about 0.7 nm. On top of this layer, the gate dielectric was applied by spin coating filtered 2-butanone solutions of either polytrifluoroethylene (PTrFE) or poly(vinylidene fluoride-trifluoroethylene) 65–35 mol% random copolymer (Solvay, Belgium). It is crucial in this step that the semiconductor layer does not dissolve in the solvent 2-butanone. A solubility test showed no coloration of this colorless solvent after prolonged stirring, indicating that 2-butanone is a non-solvent to rr-P3HT. The samples were annealed again in a vacuum oven at 138 °C to enhance the crystallinity of the gate dielectric. The transistors were finalized by evaporation of silver gate electrodes. Current transport measurements were performed in dark and vacuum using a Keithley 4200 semiconductor analyzer. Polymer layer thicknesses were determined using a Dektak profilometer.

3. Results and discussion

Fig. 2 shows a typical transfer curve measurement of a top-gate ferroelectric FET (FeFET) as depicted in Fig. 1(a). The drain current has a bistability at zero gate bias due to the ferroelectric polarization of the gate dielectric, similar to the results obtained for FeFETs with a bottom-gate layout and a poly(*p*-phenylene vinylene) derivative as the semiconductor [12]. The charge transport mobility value derived from the drain current slope in the on-state at zero gate bias is 0.12 $cm^2/V\,s$. We can compare this mobility value to the results obtained by us with rr-P3HT bottom-gate FeFETs because all the active materials used were identical [9]. The mobility for the bottom-gate FeFETs was $8 \times 10^{-3}\ cm^2/V\,s$ which shows that changing the transistor layout from a bottom-gate to a top-gate geometry increases the mobility by more than one order of magnitude. The mobility increase can be explained by the semiconductor interface roughness of the transistors. For the bottom-gate transistors, this roughness is determined by the surface roughness of 5 nm of P(VDF-TrFE), but for the top-gate transistors it is determined by the roughness of 0.7 nm of rr-P3HT. The surface roughness of the bottom layers determine the semiconductor interface roughness, because the bottom layers are insoluble in the solvents used for depositing the second layer (see Section 2).

In Fig. 3, the induced charge density in the FeFET is estimated by comparing the current response of non-ferroelectric with ferroelectric FETs. The non-ferroelectric FETs were prepared

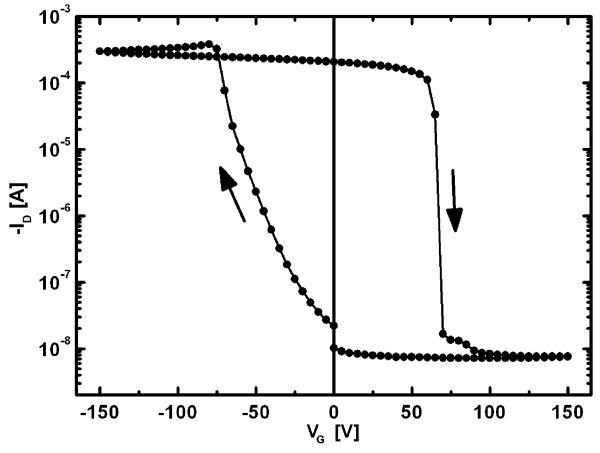

Fig. 2. Hysteretic transfer curve measurement on a top-gate FeFET with P(VDF-TrFE) as the gate dielectric and rr-P3HT as the semiconductor. The gate insulator layer thickness and dielectric capacitance are 1.8 μm and 5.5 nF/cm^2, respectively. The drain voltage V_D, channel length L and width W are −5 V, 30 μm and 6 mm, respectively.

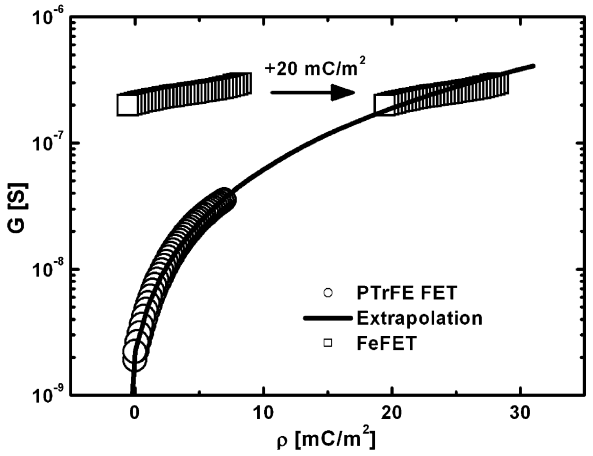

Fig. 3. Estimation of the remanent charge density ρ in a FeFET, using data from Fig. 2 (squares) and transfer curve measurements on a similar transistor but with a non-ferroelectric PTrFE gate dielectric (circles). By extrapolating the current response of the non-ferroelectric FET, we obtain a model curve. A surface charge of 20 mC/m^2 is added to the FeFET data to match the model curve. Semiconductor channel conductance G is defined by $(LI_D)/(WV_D)$. The charge density ρ is equal to the product of gate voltage V_G and dielectric capacitance per unit area C_i.

in an identical way to the FeFETs, but with polytrifluoroethylene (PTrFE) as the gate dielectric. PTrFE is a highly polar fluoropolymer with the same dielectric constant as P(VDF-TrFE), but it has a negligible ferroelectric polarization [12]. In this way, an estimate of 20 mC/m^2 is obtained for the induced charge in the FeFET at zero gate bias. This value is consistent with a previous value of 18 mC/m^2 found for FeFETs with a poly(*p*-phenylene vinylene) derivative as the semiconductor [12]. At a gate voltage of −150 V the induced charge increases to 28 mC/m^2. This induced surface charge density is a high value compared to what can be obtained with conventional Si^{++}/SiO_2 transistors, because these transistors are limited by the dielectric breakdown of SiO_2 at high applied fields [12]. The maximum conductance in Fig. 3 is 0.3 μS which to our knowledge is the largest value ever reported for a semiconducting polymer. The large conductance is a consequence of the high semiconductor mobility and induced charge density because it is the product of these two.

Having determined the charge density in the FeFET, we can confirm the linear mobility value using the current–voltage characteristics of the FeFET and

$$I_D = \frac{W}{L}\mu C_i(V_G - V_T)V_D, \quad (1)$$

which is the standard equation for a FET operating in the linear regime [13]. We can neglect the threshold voltage in Eq. (1) because the effective gate voltage, that consists of an applied gate voltage and the ferroelectric polarization, is high. If we also replace the product of V_G and C_i by the induced charge density ρ we obtain

$$I_D = \frac{W}{L}\mu\rho V_D. \quad (2)$$

Fig. 4 presents the current–voltage characteristic of the FeFETs at a gate voltage of −100 V, operating in the linear regime. Using a ρ value of 25 mC/m^2, extracted from Fig. 3 for a gate voltage of −100 V, we obtain a good fit with Eq. (2) for a mobility value of 0.15 cm^2/V s. This value confirms the mobility value derived from Fig. 2. Fig. 4 also demonstrates the high current response of the transistor in the milliamp regime that enables it to drive organic light-emitting diodes. For practical applications the gate voltage of −100 V would need to be reduced by using a thinner gate dielectric. FeFETs with a gate dielectric thickness of 200 nm have been

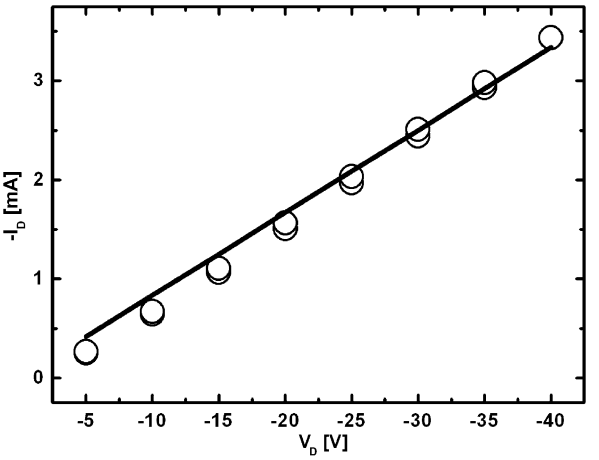

Fig. 4. Current–voltage characteristic of a FeFET (circles) identical to the FeFET in Fig. 2 at a gate voltage of −100 V and the fit obtained with Eq. (2), a charge density value of 25 mC/m^2 and a mobility value of 0.15 cm^2/V s.

demonstrated [9], which would reduce the gate voltage from −100 V to −11 V.

An increase of the *k*-value of the gate dielectric generally leads to a sharp decrease of the mobility of organic semiconductors [14]. This decrease is due to the dipolar disorder inside polar dielectrics which broadens the density of states and ultimately increases the energy barrier for hopping transport. The highest mobility reported for rr-P3HT is 0.3 cm^2/V s [15]. Considering the *k*-value of P(VDF-TrFE) of 11 and the dependence of the mobility on the *k*-value of the gate dielectric, a maximum semiconductor mobility of 0.03 cm^2/V s is expected for a FeFET. This is about one order of magnitude lower than the observed mobility of 0.1 cm^2/V s in the FeFET. However, the charge density in the FeFET has a high value and the mobility of most organic semiconductors increases with the charge density [16]. The high charge density can therefore explain the high mobility in the FeFET.

We note that a recent report demonstrated a transistor that is similar to the one presented here [17]. However, the measurement results are dissimilar to the present results: the rr-P3HT charge transport mobility and the maximum conductance had low values of 3.4×10^{-3} cm^2/V s and 9 nS, respectively; the gate bias attenuates the drain current by a factor of 2.5, while the on/off ratio in Fig. 2 is 10^4; the gate insulator leakage current was 200 mA/m^2 (=2×10^{-5} A/cm^2) at an applied field of 25 MV/m (=250 kV/cm), which is 100 times

higher than our result of 2 mA/m^2 at an applied field of 90 MV/m [9]. The lower performance suggests an adverse effect caused by a suboptimal device processing.

4. Conclusions

We have shown that the mobility of a transistor with rr-P3HT as the semiconductor and P(VDF-TrFE) as the gate dielectric was increased by an order of magnitude to 0.1 $cm^2/V\,s$ by using a top-gate transistor layout, because this reduces the semiconductor–dielectric interface roughness from 5 to 0.7 nm. A high charge density of 28 mC/m^2 was induced by the polarizable gate dielectric which led to a record conductance value for polymer FETs of 0.3 μS.

Acknowledgements

We thank E. Cantatore for fruitful disussions, M. Morariu and J. de Wit for technical assistance and we gratefully acknowledge financial support by the Dutch Science Foundation NWO/FOM and the EC (project PolyApply IST-IP-507143).

References

[1] G.H. Gelinck, E.H. Huitema, E. van Veenendaal, E. Cantatore, L. Schrijnemakers, J.B.P.H. van der Putten, T.C.T. Geuns, M. Beenhakkers, J.B. Giesbers, B.H. Huisman, E.J. Meijer, E.M. Benito, F.J. Touwslager, A.W. Marsman, B.J.E. van Rens, D.M. de Leeuw, Nat. Mater. 3 (2004) 106.
[2] L. Zhou, S. Park, B. Bai, J. Sun, S.-C. Wu, T.N. Jackson, S. Nelson, D. Freeman, Y. Hong, IEEE Electr. Dev. Lett. 26 (2005) 640.
[3] M.J. Panzer, C.D. Frisbie, J. Am. Chem. Soc. 127 (2005) 6960.
[4] A. Facchetti, M.-H. Yoon, T.J. Marks, Adv. Mater. 17 (2005) 1705.
[5] H.S. Nalwa (Ed.), Ferroelectric Polymers, Marcel Dekker, Inc., New York, 1995.
[6] B. Stadlober, M. Zirkl, M. Beutl, G. Leising, S. Bauer-Gogonea, S. Bauer, Appl. Phys. Lett. 86 (2005) 242902.
[7] S. Steudel, S. de Vusser, S. de Jonge, D. Janssen, S. Verlaak, J. Genoe, P. Heremans, Appl. Phys. Lett. 85 (2004) 4400.
[8] K.N.N. Unni, R. de Bettignies, S. Dabos-Seignon, J.-M. Nunzi, Appl. Phys. Lett. 85 (2004) 1823.
[9] R.C.G. Naber, B. de Boer, P.W.M. Blom, D.M. de Leeuw, Appl. Phys. Lett. 87 (2005) 203509.
[10] J. Veres, S. Ogier, G. Lloyd, D.M. de Leeuw, Chem. Mater. 16 (2004) 4543.
[11] H. Sirringhaus, N. Tessler, R.H. Friend, Science 280 (1998) 1741.
[12] R.C.G. Naber, C. Tanase, P.W.M. Blom, G.H. Gelinck, A.W. Marsman, F.J. Touwslager, S. Setayesh, D.M. de Leeuw, Nat. Mater. 4 (2005) 243.
[13] S.M. Sze, Physics of Semiconductor Devices, Wiley, New York, 1981.
[14] J. Veres, S.D. Ogier, S.W. Leeming, D.C. Cupertino, S.M. Khaffaf, Adv. Funct. Mater. 13 (2003) 199.
[15] D.H. Kim, Y.D. Park, Y. Jang, H. Yang, Y.H. Kim, J.I. Han, D.G. Moon, S. Park, T. Chang, C. Chang, M. Joo, C.Y. Ryu, K. Cho, Adv. Funct. Mater. 15 (2005) 77.
[16] C. Tanase, E.J. Meijer, P.W.M. Blom, D.M. de Leeuw, Phys. Rev. Lett. 91 (2003) 216601.
[17] K. Müller, I. Paloumpa, K. Henkel, D. Schmeisser, J. Appl. Phys. 98 (2005) 056104.

Available online at www.sciencedirect.com
SCIENCE DIRECT
Organic Electronics 7 (2006) 137–143
Organic Electronics
www.elsevier.com/locate/orgel

All non-dopant red–green–blue composing white organic light-emitting diodes

Shi-Jay Yeh [a], Hung-Yang Chen [a], Min-Fei Wu [a], Li-Hsin Chan [a], Chih-Long Chiang [a], Hsiu-Chih Yeh [a], Chin-Ti Chen [a,*], Jiun-Haw Lee [b,*]

[a] *Institute of Chemistry, Academia Sinica, Taipei 11529, Taiwan, ROC*
[b] *Graduate Institute of Electro-Optical Engineering and Department of Electrical Engineering, National Taiwan University, Taipei 10617, Taiwan, ROC*

Received 2 August 2005; received in revised form 10 December 2005; accepted 13 December 2005
Available online 11 January 2006

Abstract

All non-dopant white organic light-emitting diodes (WOLEDs) have been realized by using solid state highly fluorescent red bis(4-(*N*-(1-naphthyl)phenylamino)phenyl)fumaronitrile (**NPAFN**) and amorphous bipolar blue light-emitting 2-(4-diphenylamino)phenyl-5-(4-triphenylsilyl)phenyl-1,3,4-oxadiazole (**TPAOXD**), together with well known green fluorophore tris(8-hydroxyquinolinato)aluminum (**Alq$_3$**). The fabrication of multilayer WOLEDs did not involve the hard-to-control doping process. Two WOLEDs, Device B and C, different in layer thickness of **Alq$_3$**, 30 and 15 nm, respectively, emitted strong electroluminescence (EL) as intense as 25,000 cd/m^2. For practical solid state lighting application, EL intensity exceeding 1000 cd/m^2 was achieved at current density of 18–19 mA/cm^2 or driving voltage of 6.5–8 V and the devices exhibited external quantum efficiency (η_{ext}) of 2.6–2.9% corresponding to power efficiency (η_P) of 2.1–2.3 lm/W at the required brightness. The thickness of **Alq$_3$** layer is decisive in color quality of non-dopant WOLEDs. The Commission Internationale de l'Eclairage (CIE) coordinates of fairly white EL of Device B varied only little from (0.34, 0.39) to (0.34, 0.38) at driving voltage between 6 and 14 V. Device B exhibited relatively high color rendering indexes (CRIs) in the range of 74–81, which were essentially voltage-independent. The other WOLED, Device C, showed even better color purity of white EL (CIE$_{x,y}$ = 0.34, 0.31) along with higher CRI of 83 at 8 V, although higher voltage deteriorated the color quality of WOLED.

PACS: 71.20.Rv; 72.80.Le; 73.61.Ph

Keywords: White; Organic light-emitting diode; Non-dopant; Red; Blue

1. Introduction

Organic light-emitting diodes (OLEDs) have rapidly developed over the last decade and have become the highly competitive alternative of full color flat panel display [1–5], which is currently

* Corresponding authors. Tel.: +886 227898542; fax: +886 227831237.
E-mail addresses: cchen@chem.sinica.edu.tw (C.-T. Chen), jhlee@cc.ee.ntu.edu.tw (J.-H. Lee).

1566-1199/$ - see front matter © 2005 Elsevier B.V. All rights reserved.
doi:10.1016/j.orgel.2005.12.004

dominated by the liquid-crystal display (LCD) [6]. Besides glamorous displays, an intriguing and potentially energy-saving application for OLEDs are decorative or domestic solid-state lighting (SSL) and the flat panel display backlight [6–10], OLEDs for SSL or back light for flat panel display have not been considered to be realistic until recent discovery of highly efficient organometallic phosphorophores [11,12]. The introduction of electrophosphorescence moves the upper limit of the power efficiency (η_P) from ~20 lm/W for electrofluorescent materials to ~80 lm/W, which surpasses 15 lm/W for incandescent light bulb and is comparable with that of a fluorescent lamp. With exceptions of low efficient singlet exciplexes or triplet excimers emitting broad-band (white) emission, satisfactory white organic light-emitting diodes (WOLEDs) are always constructed on a multilayer device structure with two (green blue/orange red or blue/yellow) to three (red, green, and blue) light-emitting components that can be fluorophores and/or phosphorophores [12–31]. Among these color components of WOLEDs, many blue, most of yellow, and nearly all orange to red fluorophores suffer from a common problem, namely the concentration quenching of fluorescence in solid state. Consequently, the dopant light-emitter of guest–host system becomes a universal method for solving the quenching problem of these long-wavelength, orange to red fluorophores [32]. Emission quenching due to the long lifetime of the triplet state (phosphorescence) causes severe triplet–triplet annihilation of electroluminescence (EL) which is significant even at medium current density greater than 50 mA/cm^2 for most cases. Doping is also an inevitable solution to all colors of phosphorophores. Therefore, the doping process seems to be a must in the fabrication of WOLEDs based on small molecular materials, either fluorophores or phosphorophores. However, in practical OLED manufacture, the doping process is not a trivial task to handle, considering the reproducibility of the optimum doping level, which is normally low and less than 1–2% and let along that it should be carefully controlled in a narrow effective range of ±0.5% for a consistent performance of the devices.

Recently, we have successfully developed a few bright (electroluminance (L) of 8000–12,400 cd/m^2) and efficient (external quantum efficiency, η_{ext}, of 2.4–3.6% or η_P of 0.9–1.8 lm/W) non-doped red OLEDs based on extraordinary red light-emitting materials [33–36]. **NPAFN** (Scheme 1) is one of those rare materials that have an unusual property

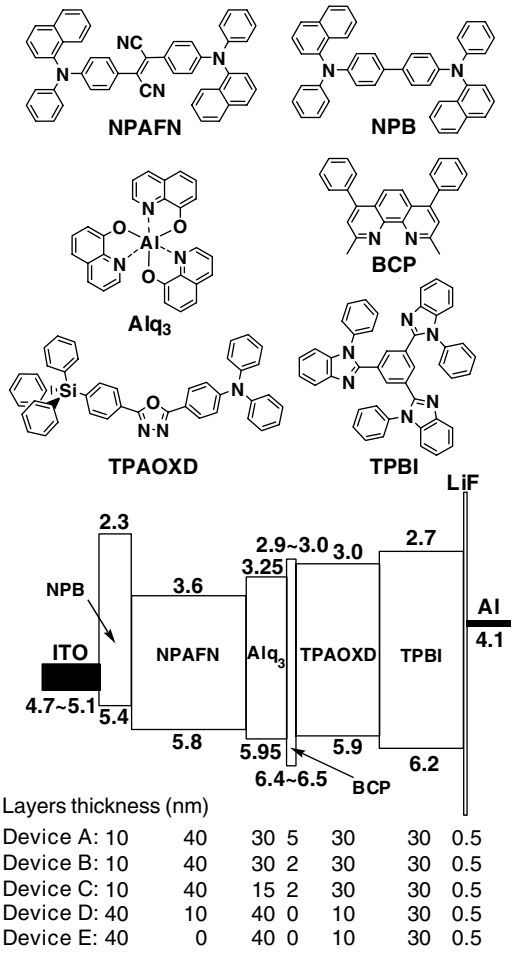

Scheme 1. Chemical structures and their relative energy level (HOMO and LUMO) diagram of **NPAFN**, **Alq$_3$**, **TPAOXD**, **NPB**, **BCP**, and **TPBI**. Layer structures of Device A–E are also schematically shown here with the layer thickness indicated therein.

of aggregation-induced emission (AIE) and it was adopt here as non-dopant red light-emitting material for WOLEDs [37]. In addition to **NPAFN**, we have also explored a new type of blue fluorophore, **TPAOXD** (Scheme 1), which is bipolar in nature but is an authentic amorphous molecular material [38]. High-performance (maximum brightness ~20,000 cd/m^2 and maximum external quantum efficiency ~2.4%) blue (1931 Commission Internationale de L'Eclairage, CIE$_{x,y}$ of $x = 0.16$ and $y = 0.18$) OLEDs containing **TPAOXD** as the non-dopant blue emitter was found to be relatively stable with little decay of external quantum efficiency at ~2.3% from low to high current density (10–500 mA/cm^2) [39]. In this work, three devices A, B, and C, were fabricated to test the idea of

bright and efficient all non-dopant WOLEDs using **NPAFN**, **Alq_3**, and **TPAOXD** for red, green, and blue emitters, respectively (see photoluminescence, PL, spectra in Fig. 1).

There was one preceding report about ''nondoped-type'' WOLED by Tsuji et al. [40].

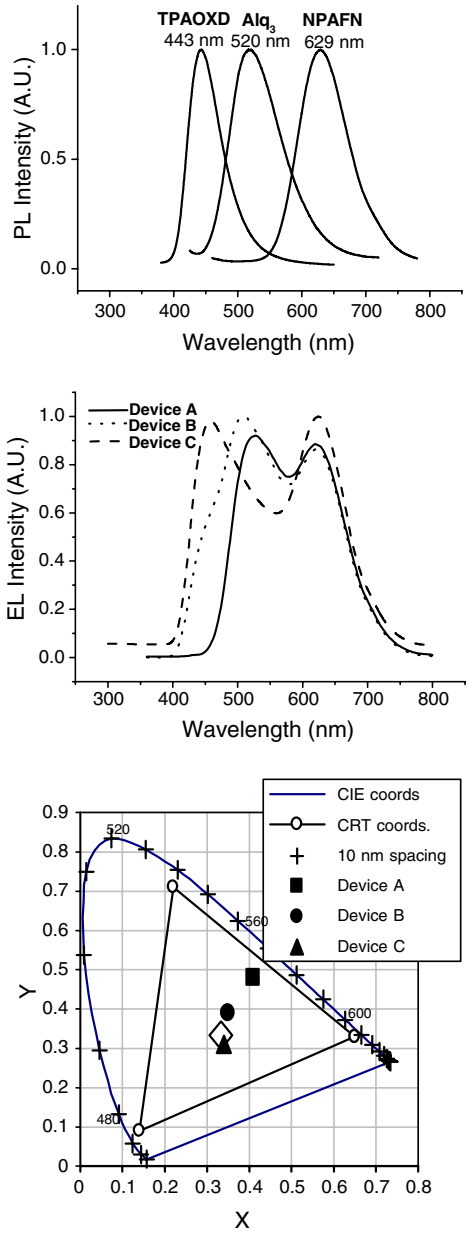

Fig. 1. Normalized photoluminescence spectra of vacuum thermal deposited thin films of **TPAOXD**, **Alq_3**, and **NPAFN**; EL spectra (center) and 1931 CIE coordinates (bottom) of Device A–C at driving voltage of 8 V. CRT (cathode ray tube) coordinates mean the standard red–green–blue color coordinates of CRT screen (traditional color television screen).

However, they were utilizing complementary two-color system, blue emission (445 and 480 nm) from **NPB** and orange emission (558 nm) from DCM (4-(dicyanomethylene)-2-methyl-6-(*p*-dimethylaminostyryl)-4*H*-pyran), in composing white emission. Furthermore, their WOLEDs adopt an ultrathin layer (only 1 nm thickness) of DCM as one of the complementary colors. Such a thin layer is unlikely to make DCM to be a ''nondoped type'' emitter (more likely to be a blending of DCM and **NPB**) and hence unlikely the ''nondoped type'' WOLED. This is because the authentic ''nondoped type'' DCM (neat DCM) emitter should have a deep red emission at wavelength greater than 620 nm instead of orange 558 nm [32,41]. Furthermore, their WOLED is weakly electroluminescent (maximum luminance ~1000 cd/m^2) due to the dim blue **NPB** and concentration quenching orange DCM. The EL efficiency of such WOLED is expected to be low, which in fact is not available from the report.

2. Experimental

Device A–E were fabricated by sequential thermal vacuum deposition of thin layer of organic materials and LiF–Al as the final cathode electrode on ITO (indium-thin-oxide)-coated glass substrate. The configuration of these devices is depicted in Scheme 1. The current, voltage, and light intensity measurements have been described before [39]. All measurements, including the recording of EL spectra, were carried out at room temperature under ambient condition without the encapsulation of the devices. Whereas literature known figures were adopt for **Alq_3**, **BCP**, and **TPBI**, HOMO energy levels of **NPB**, **NPAFN**, and **TPAOXD** were measured with a low-energy photo-electron spectrometer (Riken-Keiki AC-2). The addition of the absorption on-set energy to the HOMO energy levels led to LUMO energy levels of these materials. The absorption on-set energy was estimated from the solution UV–visible absorption spectra. In CRI calculation, eight test-color samples were chosen followed the definition of DIN 6169 standards. CIE 1976 ($L^*u^*v^*$) color-difference formula was used to determine the resultant color shift [42]. In order to demonstrate the easy control of the white color EL from these all non-dopant devices, we fixed the thickness of **NPB**, **NPAFN**, **TPAOXD**, and **TPBI** layers at 10, 40, 30 and 30 nm, respectively, in Device A, B, and C, although these can be the adjustable parameters in optimizing performance of the devices. By just

varying the thickness of **Alq$_3$** and **BCP** layers we were able to tune the color of the devices showing CIE coordinates as close as to (0.33, 0.33), a standard figure for color-balanced WOLED.

3. Results and discussion

Device A is our testing model and is not a color-balanced WOLED since the 5 nm layer of hole-blocking **BCP** (2,6-dimethyl-4,7-diphenyl-1,10-phenanthroline) is simply too much for WOLED. In current case, 5 nm layer of **BCP** effectively blocks the hole from entering **TPAOXD** and hence limits the charge recombination and/or exciton diffusion on it. This greatly prevents the blue emission ($\lambda_{max} \sim 460$ nm) from **TPAOXD** in EL spectra (Device A in Fig. 1). Reducing the thickness of **BCP** layer to half as in Device B turned out to be just fine for white EL of Device B. CIE coordinates of it is (0.35, 0.39), which is a respectful improvement of white EL from (0.41, 0.48) of CIE coordinates of yellow–orange Device A (Fig. 1). Even higher color purity of white EL has been achieved by adjusting the thickness of **Alq$_3$** layer. In Device C, the thickness of **Alq$_3$** layer was further reduced to half (15 nm) from 30 nm of Device B. Having both thin layers of green light-emitting **Alq$_3$** and hole-blocking **BCP**, Device C showed significant increase of the blue emission from **TPAOXD** as well as the decrease of green emission from **Alq$_3$** (Fig. 1). Such changes of relative contribution of emission color rendered virtually white EL of Device C as indicated by the CIE coordinates (0.34, 0.31) (Fig. 1). In principle, all non-dopant WOLED with any CIE coordinates as close as to (0.33, 0.33) can be achieved with the variation of the thickness of **Alq$_3$** and **BCP** layers.

WOLEDs reached 1000 cd/m^2 of EL intensity, the general requirement for SSL application, at a reasonable current density range of 18–19 mA/cm^2 (Fig. 2), which corresponded to 6.5–8 V for Devices B and C. The maximum EL intensity of 25,000 cd/m^2 was observed for Device B at 790 mA/cm^2 and 15 V. At low current density near 0.1 mA/cm^2, high η_Ps over 5 lm/W were observed for Device C and slightly lower 4.0–4.5 lm/W were found for Device B, although both devices display a roll-off of η_P at elevated current density (Fig. 2). However, high η_{ext}s of 2.9–3.3% remained relatively stable with only slight decay to 2.6–2.9% (corresponding to 2.1–2.3 lm/W) when the current density up to 20 mA/cm^2 (or 1000 cd/m^2 lighting intensity). Even

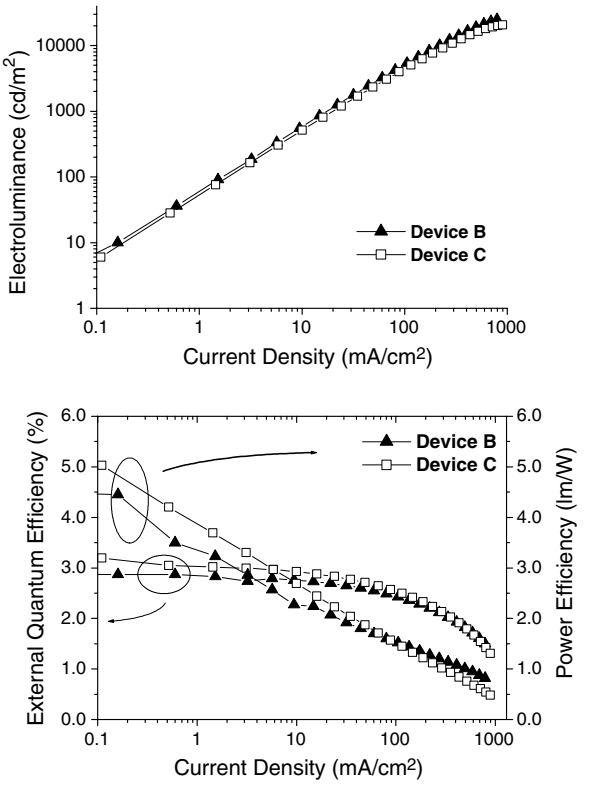

Fig. 2. Electroluminance (L)–current density (I)–efficiency (η_{ext} and η_P) characteristics of Device B and C.

at relatively high current density of 100 mA/cm^2 (where WOLED showed EL intensity of ~5000 cd/m^2, Fig. 2), η_{ext}s stayed reasonably high around 2.4–2.6%. The rather current-stable external quantum efficiency can be partially attributed to the relatively stable blue emitter **TPAOXD**. Similar stability of η_{ext} was previously known for blue OLEDs based on amorphous **TPAOXD** [39]. Containing both electron-poor oxadiazole and electron-rich triphenylamine moieties, bipolar **TPAOXD** possesses electro-transporting characteristic, which is crucial for a good performance WOLEDs here. We have fabricated the same WOLED by using **XTPS** (*trans*-4-(bis(2,4-dimethylphenyl)amino)-2′,3′,4′,5′-tetraphenylstilbene), another highly efficient (maximum external quantum efficiency up to 4.1%) non-dopant blue light ($\lambda_{max}^{EL} \sim 462$ nm) emitter [43]. However, the **XTPS**-containing WOLEDs performed poorly. Unlike bipolar **TPAOXD**, **XTPS** is stilbene-type triarylamine and preferentially transports hole instead of electron. This is not appropriate for using **XTPS** as blue light-emitting material that is insufficient for electron-transporting in current devices.

Device B was unusually stable regarding CIE coordinates and CRIs. The CIE coordinates of Device B were virtually unchanged with CIE coordinates $x = 0.34$–0.35 and $y = 0.38$–0.39 at the driving voltage range of 6–14 V (Fig. 3). CRIs of Device B were rather high in the range of 74–81 and they also remained reasonably steady in the driving voltage between 6 and 14 V (Fig. 3). However, we noted that Device C was less stable considering either CIE coordinates or CRIs. With increasing driving voltage, CIE coordinates of Device C shifted to smaller figures and CRIs dropped to smaller numbers from 83 to less than 50 (Fig. 3). This is in sharp contrast to Device B. Furthermore, Device C exhibited complicate up and down of CIE coordinates and CRIs when driving voltage varied from 6 to 14 V. Usually, such nonlinear changes imply that there are at least two different processes that are responsible for the color changes of devices. For Device C, blue EL first increased in intensity relative to the red EL (CIE coordinates changed to smaller figures) when the driving voltage was raised from 6 to 12 V (Fig. 3). Significant decrease of blue EL was then observed when driving voltage was further up to 14 V (Device C in Fig. 3). It is not so clear at the moment that why Device B is more stable in general than Device C. We can surmise that it is probably due to the instability of blue **TPAOXD** because the device having thinner **Alq_3** tends to have more portion of blue EL from **TPAOXD** (see below).

Among several possible causes for color changes, we can assume that the shifting of the charge recombination zone and/or exciton diffusion toward cathode side of the device under higher driving voltage as one of the possibilities. Such zone shifting and/or exciton diffusing takes place in both Device B and C but the thick **Alq_3** layer (30 nm) in between **NPAFN** and **TPAODX** layers taking up large portion of it that alleviate most of the color changes in Device B. The second possible process that changes the color of the device is the potential degradation of blue emitter **TPAODX**, particularly, under high voltage of 14 V (corresponding to very high current density $\sim$1000 mA/cm^2), which has been identified before [39]. The lowering CRIs of Device C with rising voltage is mainly due to the diminished relative contribution of green EL from **Alq_3** as the charge recombination zone shifting or exciton diffusing toward blue emitter **TPAODX**. At high voltage of 14 V, the relative intensity of the blue emission from **TPAODX** became weaken-

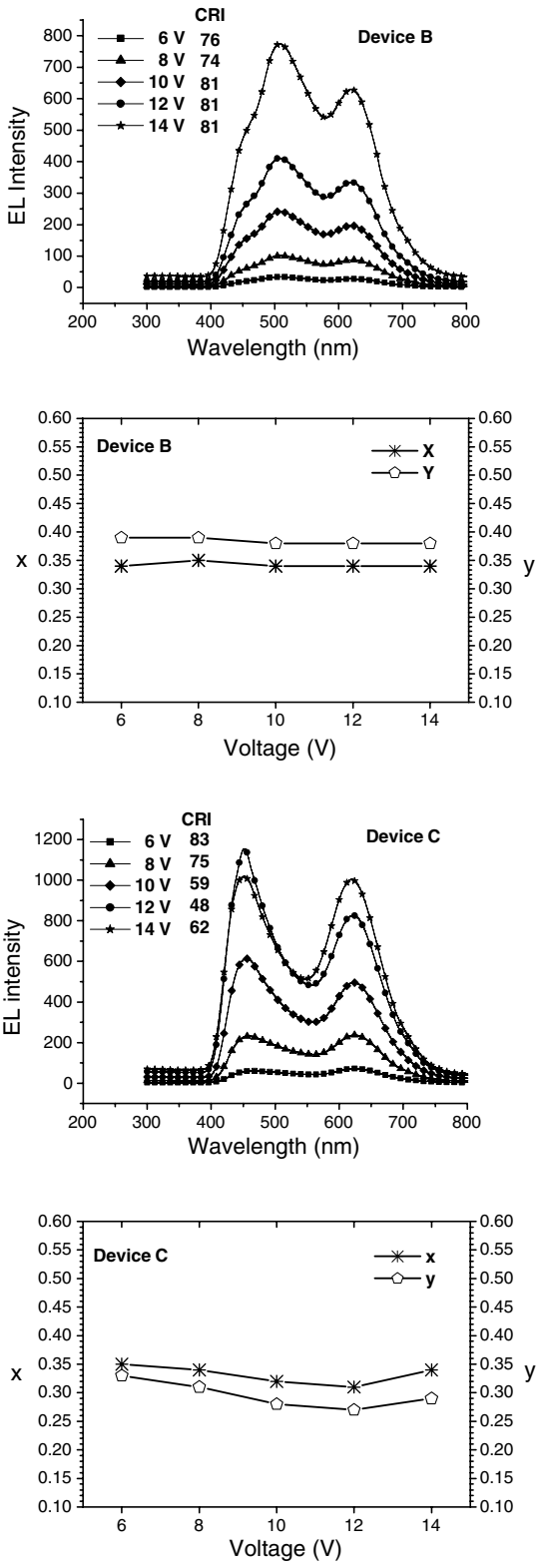

Fig. 3. The voltage dependency of EL spectra and CIE coordinates (x, y), and CRIs of Device B and C under different voltage of 6, 8, 10, 12, and 14 V.

ing and the profile of white EL spectrum became less dented, which turned the CRI to a larger figure.

Among several vital issues mentioned above, the success of such WOLED depends on the appropriate adjustment of the relative EL intensity of red–green–blue three components via the thickness control of individual light-emitting layer. Through the organ–red dye-doped spacial sensing layer in **Alq_3**, it has been demonstrated before by Tang et al. that charge-recombination is confined about 5 nm near the hole-transport interface in the bilayer OLED [40]. At a glance, observing the blue EL from **TPAOXD** from our devices, particularly Device B and C, was rather unbelievable because of the thickness of **Alq_3** layer is way beyond 5 nm and it is 30 and 15 nm, respectively. However, we have recognized that Tang et al. also had reported that EL emission zone in the undoped **Alq_3** system was considerably larger than the charge-recombination zone due to the exciton diffusion. The migration of the exciton was carefully estimated by Tang et al. to be more than 20 nm in undoped **Alq_3** [42]. In order to get a clear picture of the thickness-dependent EL of all non-dopant devices here, we have fabricated two more devices, Device D and E. These devices are similar to Device A–C but **Alq_3** layer is thicker (40 nm) and we remove **BCP** hole-blocking layer to simplify the issue (Scheme 1). Particularly, Device E contains no red **NPAFN** and we see only strong EL from **Alq_3** accompanying with weak emission side band around 440 nm, which strongly resembles the blue EL from **TPAOXD** (Fig. 4). The result of Device E indicates that the charge-recombination zone and/or exciton diffusion is beyond the whole 40 nm thick **Alq_3** layer and entering blue **TPAOXD** layer. The result is somewhat reconfirmed what Tang et al. found earlier, although 40 nm was a bit beyond the estimated exciton diffusion length ($\geqslant$20 nm) for **Alq_3**. Here, according to the current results, we have a new proposal that the zone of charge-recombination and/or the range of exciton diffusion of non-doped **Alq_3** depend on the HOMO energy level of hole-transport layer adjacent to the **Alq_3**. This is based on the result of Device D, which has a similar structure to Device E except a thin layer (10 nm) of red **NPAFN** inserted in between **NPB** and **Alq_3**. In addition to the strong EL from red **NPAFN** around 615 nm, when compared with Device D, a significant increase of blue EL from **TPAOXD** relative to the green EL from **Alq_3** was observed (Fig. 4). **NPAFN** has HOMO energy level of 5.8 eV, which is 0.4 eV lower than **NPB** HOMO energy level (Scheme 1). **NPAFN** has been proven to be an efficient non-dopant red-light emitter and hole-transport material as well in the non-dopant red OLEDs [34]. We assume that the closer of the HOMO energy level of hole-transport material to that of **Alq_3** is, the deeper of the charge recombination zone is inside **Alq_3**. Assuming the same range of exciton diffusion (a function of diffusion coefficient and the lifetime) [40], the closer charge recombination zone to the interface of **Alq_3** and **TPAOXD** layers will presumably facilitates the exciton taking place in the blue light-emitting **TPAOXD** layer.

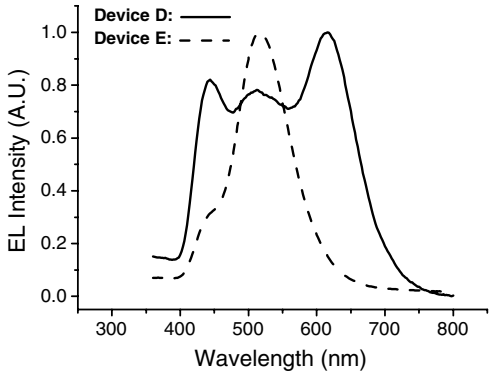

Fig. 4. EL spectra of Device D and E under voltage of 8 V.

4. Conclusion

In summary, we have studied the EL properties of a series of multilayer OLEDs containing all non-dopant emitters. Devices with the structure configuration of ITO/**NPB**/**NPAFN**/**Alq_3**/**BCP**/**TPAOXD**/**TPBI**/LiF/Al emit color-balanced white EL. The success of the all non-dopant WOLEDs here hinges on the unusual AIE red emitter of **NPAFN** as well as the amorphous bipolar blue emitter **TPAOXD**. Green light-emitting **Alq_3** also plays a crucial role of white color purity and stability of non-dopant WOLEDs. Under the condition of sufficient amount of blue EL contributed to the color-balanced WOLED, such as Device B and C, we propose that a thick **Alq_3**-containing device can cover most of the charge-recombination zone and reduce the number of exciton migrating into blue **TPAOXD**. The relatively unstable blue EL from **TPAOXD** is limited and CIE- or CRI-stability can thus be enhanced. WOLEDs, particularly the thick (30 nm) **Alq_3**-containing Device B, has been demonstrated to show satisfactory performances, including EL intensity, efficiency, CRIs, and voltage-stable

white EL, which are comparable with or better than conventional electrofluorescence-based WOLEDs that are exclusively based on hard-to-control doping process.

Acknowledgements

This work was supported by Academia Sinica and National Science Council. We thank Prof. Yu-Tai Tao for his instruction in the fabrication and measurement of OLEDs.

References

[1] S.M. Kelly, Flat Panel Display: Advanced Organic Materials, Royal Society of Chemistry, Cambridge, 2000.
[2] B. Johnstone, Technol. Rev. 104 (September) (2001) 80.
[3] O. Gelson, Opt. Laser Eur. 107 (June) (2003) 33.
[4] W.E. Howard, Sci. Am. 290 (February) (2004) 76.
[5] J.R. Sheats, J. Mater. Res. 19 (2004) 1974.
[6] B. Yang, Inf. Disp. 21 (February) (2005) 22.
[7] A. Bergh, D. Craford, A. Duggal, R. Haitz, Phys. Today 54 (2001) 42.
[8] T. Whitaker, Opt. Laser Eur. 126 (March) (2004) 5.
[9] B.W. D'Andrate, R.J. Holmes, S.R. Forrest, Adv. Mater. 16 (2004) 624.
[10] T. Whitaker, Comp. Semicond. 10 (October) (2004) 20.
[11] S.R. Forrest, Org. Electron. 4 (2003) 45.
[12] B.W. D'Andrade, S.R. Forrest, Adv. Mater. 16 (2004) 1585.
[13] J. Kido, M. Kimura, K. Nagai, Science 267 (1995) 1332.
[14] R.S. Deshpande, V. Bulovic, S.R. Forrest, Appl. Phys. Lett. 75 (1999) 888.
[15] Z.Y. Xie, J.S. Huang, C.N. Li, S.Y. Liu, Y. Wang, Y.Q. Li, J.C. Shen, Appl. Phys. Lett. 74 (1999) 641.
[16] M. Strukelj, R.H. Jordan, A. Dodabalapur, J. Am. Chem. Soc. 118 (1996) 1213.
[17] R.H. Jordan, A. Dodabalapur, M. Strukelj, T.M. Miller, Appl. Phys. Lett. 68 (1996) 1192.
[18] F. Steuber, J. Staudigel, M. Stossel, J. Simmerer, A. Winnacker, H. Spreitzer, F. Weissörtel, J. Salbeck, Adv. Mater. 12 (2000) 130.
[19] S. Liu, J. Huang, Z. Xie, Y. Wang, B. Chen, Thin Solid Films 363 (2000) 294.
[20] C.W. Ko, Y.T. Tao, Appl. Phys. Lett. 79 (2001) 4234.
[21] K.O. Cheon, J. Shinar, Appl. Phys. Lett. 81 (2002) 1738.
[22] Y.S. Hunag, J.H. Jou, W.K. Weng, J.M. Liu, Appl. Phys. Lett. 80 (2002) 2782.
[23] B.W. D'Andrade, M.E. Thompson, S.R. Forrest, Adv. Mater. 14 (2002) 147.
[24] C.H. Chuen, Y.T. Tao, Appl. Phys. Lett. 81 (2002) 4499.
[25] G. Li, J. Shinar, Appl. Phys. Lett. 83 (2003) 5359.
[26] X.H. Zhang, M.W. Liu, O.Y. Wong, C.S. Lee, H.L. Kwong, S.T. Lee, S.K. Wu, Chem. Phys. Lett. 369 (2003) 478.
[27] S. Tokito, T. Iijima, T. Tsuzuki, F. Sato, Appl. Phys. Lett. 83 (2003) 2459.
[28] T.-H. Liu, Y.-S. Wu, M.-T. Lee, H.-H. Chen, C.-H. Liao, C.H. Chen, Appl. Phys. Lett. 85 (2004) 4304.
[29] G. Cheng, Y. Zhao, Y. Zhang, S. Liu, F. He, H. Zhang, Y. Ma, Appl. Phys. Lett. 84 (2004) 4457.
[30] D. Qin, Y. Tao, Appl. Phys. Lett. 86 (2005) 113507.
[31] Y. Xu, J. Peng, Y. Mo, Q. Hou, Y. Cao, Appl. Phys. Lett. 86 (2005) 163502.
[32] C.-T. Chen, Chem. Mater. 16 (2004) 4389.
[33] W.-C. Wu, H.-C. Yeh, L.-H. Chan, C.-T. Chen, Adv. Mater. 14 (2002) 1072.
[34] H.-C. Yeh, S.-J. Yeh, C.-T. Chen, Chem. Commun. (2003) 2632.
[35] H.-C. Yeh, L.-H. Chan, W.-C. Wu, C.-T. Chen, J. Mater. Chem. 14 (2004) 1293.
[36] C.-L. Chiang, M.-F. Wu, D.-C. Dai, Y.-S. Wen, J.-K. Wang, C.-T. Chen, Adv. Funct. Mater. 15 (2005) 231.
[37] J. Chen, B. Xu, X. Ouyang, B. Tang, Y. Cao, J. Phys. Chem. A 108 (2004) 7522.
[38] L.-H. Chan, H.-C. Yeh, C.-T. Chen, Adv. Mater. 13 (2001) 1637.
[39] L.-H. Chan, R.-H. Lee, C.-F. Hsieh, H.-C. Yeh, C.-T. Chen, J. Am. Chem. Soc. 124 (2002) 6469.
[40] T. Tsuji, S. Naka, H. Okada, H. Onnagawa, J. Appl. Phys. 81 (2002) 3329.
[41] C.W. Tang, S.A. VanSlyke, C.H. Chen, J. Appl. Phys. 65 (1989) 3610.
[42] G. Wyszecki, W.S. Stiles, Color Science, second ed., Wiley, New York, 1982, CIE 1931 is commonly used to describe the color of an light-emitting device. However, a uniform color space, such as CIE 1976 Luv or Lab ($L^*u^*v^*$) space, is needed for calculating CRI and color difference.
[43] C.-T. Chen, C.-L. Chiang, Y.-C. Lin, L.-H. Chan, C.-H. Huang, Z.-W. Tsai, C.-T. Chen, Org. Lett. 5 (2003) 1261.

Available online at www.sciencedirect.com
SCIENCE DIRECT®
Organic Electronics 7 (2006) 144–154
Organic Electronics
www.elsevier.com/locate/orgel

Hydrogen bonding and π-stacking in highly organized arenes-based molecular wire

É. Bayard, S. Hamel [1], A. Rochefort *

École Polytechnique de Montréal, Department of Engineering Physics and Regroupement, québécois sur les matériaux de pointe (RQMP), Montréal, Que., Canada

Received 18 November 2005; received in revised form 14 December 2005; accepted 16 December 2005
Available online 19 January 2006

Abstract

We have theoretically investigated the stacking of promising arenes-based molecules into a highly organized columnar structure in which hydrogen bonding plays a major role. The nature of the functional groups attached to benzene creates a strong net dipole moment which initiates and favors a symmetric π-stacking of the molecules. The formation of multiple hydrogen bonds between molecular units enforces the stacking of arenes, dramatically improves the overall stability of the assemblies, and leads to relatively large intermolecular distances. In contrast, the variation of electronic properties, such as a decreasing band gap, during the formation of the molecular wire indicates the presence of a significant delocalization of π-electron over the entire assembly. The asymptotic variation of cohesion energy and other calculated properties over a relatively small molecular assembly indicates a rapid convergence of the electronic structure of the system toward its extended 1D limit.

PACS: 31.15.Ar; 31.15.Ew; 31.70.−f; 73.61.Ph; 73.20.At

Keywords: π-stacking; Low dimensional systems; Ab initio calculations; Hydrogen bonding; Organic materials; Electronic properties

1. Introduction

The integration of organic materials into high performance electronic devices such as transistors [1] and other molecular components [2] constitutes a major scientific challenge of the last few decades [3]. Molecules and polymers with conjugated π-orbitals are of primary interest, especially when they stack into supramolecular low dimensional structures. Although organic materials are generally characterized by relatively low mobilities [4] (10^{-5}–10^{-4} cm^2/V s), recent theoretical and experimental works on such organized systems suggest much larger values [5]. For example, it has been demonstrated on several occasions that electrical transport strongly depends on the molecular configuration, which defines the magnitude of π-overlapping along the propagation direction [6,7]. The control of the

* Corresponding author.
E-mail address: alain.rochefort@polymtl.ca (A. Rochefort).
[1] Present address: University of California, Lawrence Livermore National Laboratory, P.O. Box 808, Livermore, CA 94551-0808, USA.

1566-1199/$ - see front matter
doi:10.1016/j.orgel.2005.12.005

molecular packing should allow one to improve the magnitude of π-overlap between molecular units, and to displace the transport regime from the slow polaronic to the fast band-transport limit [6].

An efficient route to improve the conduction of carriers into organic materials is to increase the packing densities within specific molecular conformations. For example, high pressure on a biphenyl crystal decreases the distance between molecules, and hence improves its intrinsic mobility through improved π-interaction [8]. Similarly, impressive electrical properties such as large conductance modulation are predicted for perfectly aligned and tightly stacked 4,4′-biphenyldithiol molecules when intermolecular distances are below 4 Å [9]. An interesting possibility to create π-stacking is the self-directed growth of aromatic molecules such as styrene on a hydrogen-terminated Si(0 0 1)[2 × 1] surface [10]. This chain reaction growth leads to the formation of a tightly packed molecular line in which molecules are separated by 3.8 Å, and where significant π-coupling is expected along the dimer row direction. Another well-ordered grafting process on Si(1 0 0) surface was also proposed by theoretical DFT/LSD calculations in which strong covalent Si–C bonds and stabilizing intermolecular interactions are predicted [11]. Finally, a recent experimental achievement regarding the self-alignment of substituted benzene ring into a columnar structure has been demonstrated [12]. The formation and cohesion of these molecular wires is based on the alignment of strong dipole moments and the formation of multiple hydrogen bonds [13]. X-ray diffraction experiments and force field (AMBER) molecular mechanics simulations have predicted a tightly packed structure where molecules are separated by around 3.8 Å [12,13]. Except for these structural predictions, our understanding of the electronic and structural properties for isolated and assembled molecules are practically nonexistent. The aim of the present study is to give a more quantitative description of the structural and electronic properties of such strongly packed organic wires.

In this study, we present results obtained from first principles calculations of the electronic and structural properties of a columnar structure made of substituted benzene rings. Our main focus is on the variation of properties upon the wire formation where the molecules form a rigid stacking through hydrogen bonding. The presence of low energy π-electrons facilitates the orbital coupling between molecules for the creation of a well-delocalized π-wavefunction at an energy around the Fermi level. Although hydrogen bonding favors the relatively strong cohesion of molecules into the columnar structure, the molecule studied here does not appear the most appropriate building unit for creating tightly packed supramolecular structures.

2. Computational details

The electronic structure calculations on the different molecular systems were performed at the ab initio Hartree–Fock (HF) level with the GAMESS [14] software package, and at the density functional theory (DFT) level with the help of the NWChem [15,16] package. Most of the calculations were carried out at HF level with double-ζ quality basis sets for carbon, nitrogen, oxygen and hydrogen atoms. In addition, more extended basis set (6-311G) was also used in conjunction with HF and more accurate DFT/B3LYP [17] computational methods. The use of the B3LYP functional was originally motivated by its relatively good performance in describing weak hydrogen bonding that occurs in organic systems [18,19], and for the possibility to reasonably evaluate band gap [20]. It was also observed that the B3LYP functional allows a reasonable description of both intra- and intermolecular hydrogen bonds [24]. The molecular structures were fully optimized with the quasi-Newton method until a gradient convergence factor better than 10^{-5} Hartree/Bohr was reached. Since we are focusing on the relative stability of the oligomers, we have not calculated the basis set superposition error (BSSE) for correcting the cohesion energies. Most of the graphics presented here were produced with the help of the molekel software [21].

3. Results and discussion

3.1. The monomer

The original molecule used in the synthesis of 1D molecular wires is shown in Fig. 1 where most of the long hydrocarbon side chains are represented by a R group. With first-principles methods, a single molecule (a monomer) that may contain up to about 254 atoms cannot easily be treated explicitly in a large assembly. When the use of highly accurate computational technique is crucial, e.g. when the structure is driven by weak interaction such as hydrogen bonding, a small molecular model has to be

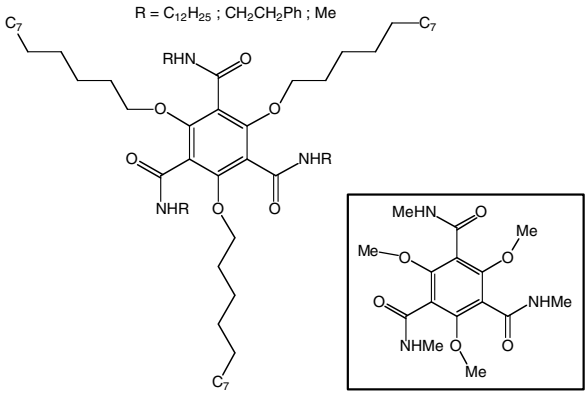

Fig. 1. Representation of the molecule used during the synthesis of crowded arene stacks. The inset shows the model considered in our calculations where Me corresponds to a methyl group and Ph to a phenyl group.

considered. The first obvious approximation we may consider in our model is to replace the long hydrocarbon chains that are bonded to oxygen atoms by a methyl (Me) group. Since this OR fragment is not dominating the intermolecular hydrogen bonding, this does not appear to be a drastic approximation.

For the other R chain bonded to the nitrogen atom in CONHR, we have considered the following three groups H, CH_3 and CH_2CH_3. Since this CONHR group directly participates in the formation of hydrogen bonds between molecules, we need a more accurate description of the polar nature of this fragment. We will use the value of the dipole moment as well as the net Mulliken charge on the nitrogen atom as criteria for the accuracy of the approximation to the R chain (Table 1). We find that the results obtained for R=H are drastically different than with CH_3 or CH_2CH_3 groups; the dipole moment is much lower and is also related to a higher charge transfer on the nitrogen atom. Hence, this approximation has been discarded. As the smaller CH_3 group leads to similar results than CH_2CH_3, it was used to investigate larger assembly models (see inset of Fig. 1).

Table 1
Variation of physical properties of functional groups following different approximations

Model	Net charge on N[a] (e)	Net dipole moment[b] μ_D (Debye)
H	0.75	1.89 (2.86)
CH_3	0.63	2.60 (3.77)
CH_2CH_3	0.63	2.56 (3.71)

[a] *N* refers to the atom directly bonded to H, CH_3 or CH_2CH_3, and the net charge is obtained from a Mulliken population analysis.

[b] Modulus of net dipole moment calculated with DFT(HF) methods. The different CONHR groups are pointing in opposite direction, then the component of the dipole moment that are parallel to the benzene ring cancel. The direction of the net dipole is clearly is along the C_3 symmetry axis for the monomer.

The more difficult task in the structural optimization of the monomer is to clearly identify the global minimum of the potential energy surface. For example, the presence of polar groups attached to the benzene ring increases the number of possible internal interactions that contribute to stabilize the molecule into a local or global minimum. Hence, the stability of the monomer has been carefully investigated by considering several configurations of the functional groups around the benzene ring prior to the optimization process. Most of the conformations considered have lead to a similar energy minimum in which the monomer shows a C_3 symmetry. In addition, the structure obtained with the DFT/B3LYP method shows the presence of multiple intramolecular hydrogen bonds involving $CONHCH_3$ and OCH_3 groups (see Fig. 2) which suggests that the B3LYP hybrid functional tends to favor the formation of internal hydrogen bonds. The presence of intramolecular hydrogen bonds reduces the helical twist angle between the CO group and the benzene ring, making the molecule flatter, and hence reducing the dipole moment of the molecule (see Table 1).

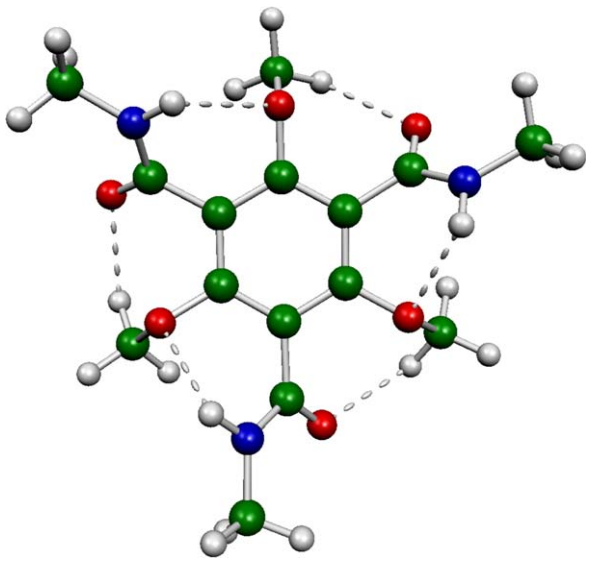

Fig. 2. DFT optimized structure that clearly indicates the presence of multiple intramolecular hydrogen bonds identified by the dashed lines.

The strong net dipole moment reported in Table 1 is well aligned along the main molecular C_3 axis. The difference in dipole moments from DFT to HF can be easily explained by a variation in the geometry of the polar CONHR groups. As mentioned, DFT/B3LYP gives a final molecular geometry in which the CO group in the CONHR fragment is around 10° closer to the benzene plane (normal to the C_3 axis) compared to HF results. Since the DFT geometry is flatter due to internal hydrogen bonds, it gives smaller contributions from the polar groups to the net dipole moment. This difference could induce two important but related consequences; the formation of weaker intermolecular hydrogen bonds but an improvement of π-stacking upon the creation of such hydrogen bonds. Finally, Fig. 3 shows frontier orbitals (HOMO and LUMO) for the monomer, and reveals well-localized wavefunctions, mostly over the benzene ring region. The overall shape of frontier orbitals are similar to those of a single benzene molecule where the HOMO is a bonding π-orbital and the LUMO is an anti-bonding π^*-orbital. The calculated HOMO–LUMO gap (HLG) is 5.34 eV and 12.2 eV with DFT/B3LYP and HF respectively. The larger HLG with HF relative to DFT is a well-known characteristic between the two theoretical approaches and is related to the weakness of HF in evaluating exchange-correlation energy [22].

3.2. The molecular assembly

In this section, we focus the discussion on the progressive formation of an assembly of up to five

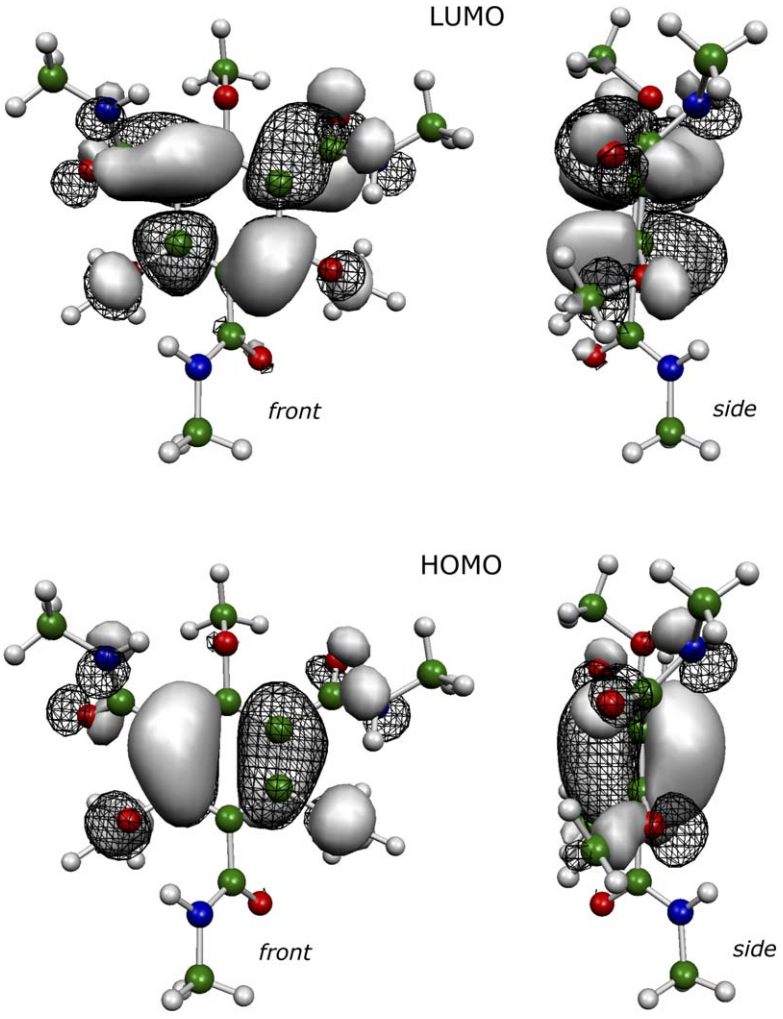

Fig. 3. Composition of frontier orbitals (HOMO, LUMO) in the monomer.

molecular units. We describe the different conformations obtained on small assemblies along with their electronic and energetic properties. One of the most interesting characteristics for the existence of a molecular assembly remains the cohesion energy which translates into the stability of the assembly. The cohesion energy per molecular units is evaluated using

$$\Delta E = \frac{(E_{\text{wire}} - nE_{\text{mol}})}{(n-1)}$$

where E_{wire} is the total energy of the wire considered, E_{mol} is the total energy for a monomer, and n is the number of molecular units in the assembly. The variation of this cohesion energy as a function of the assembly length is shown in Fig. 4. We note that the substantial cohesion energy found for a two units assembly (0.66 eV) essentially involves hydrogen bonds. A slightly larger energy value is found (0.75 eV) when a more extended 6-311G basis set is used for both the DFT and the HF methods, but the obtained conformations are very similar. In addition, the cohesion energy increases with the number of units but rapidly saturates for wires containing more than four units. Although the cohesion energy is mostly related to the presence of hydrogen bonds between molecules, the slight increase during the formation of the assembly suggests an additional stabilization energy that may be related to the existence of other energy contribution such a cooperative hydrogen bond effect [23] or simply a model size effect. The calculated energy related to the formation of hydrogen bonds between the units, i.e. 5–6 kcal mol^{-1} per hydrogen bond formed, is in very good agreement with the usual energy (2–10 kcal mol^{-1}) ascribed to this type of weak bonding. More importantly, the cohesion energy for extended systems can be estimated from Fig. 4 to around 1.0 eV (~23 kcal mol^{-1}) per molecule, which represents a substantial stabilization energy for a H-bonded system.

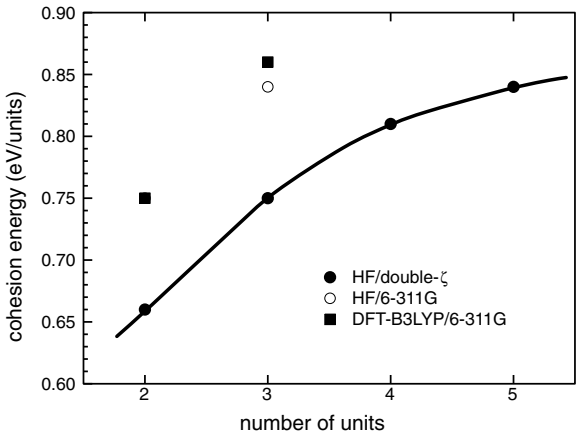

Fig. 4. Variation of the cohesion energy with the number of molecular units within the assembly obtained at HF/6-31G level. Values obtained with higher level of theory (HF/6-311G and DFT/B3LYP/6-311G) are also reported.

In this type of π-stacked system, it is also important to consider the existence of π–π interaction which could contribute to the stability of the assembly. In fact, it was found that such weak dispersive interactions are absent within HF, and are found to be slightly repulsive with B3LYP for several van der Waals complexes [24,25]. In contrast, hydrogen bonding is generally underestimated with HF while it is slightly overestimated with B3LYP. For the benzene dimer where the stability is mainly related to the dispersive π–π interaction, a binding energy of approximately 2.4 kcal mol^{-1} was measured [26]. This weak energy value is supported by Hartree–Fock dispersion (HFD) and MP2 calculations [27] in which T-shaped and parallel displaced complexes were proposed. Hence, we can expect a lower stabilizing energy related to dispersion for our systems where benzene rings are perfectly organized into a columnar shape. From this, we can assume that dispersion will play a minor role (<10%) in the interaction energy between molecular units in the wire, and that the cohesion of the molecules is essentially due to H-bonding. Consequently, we anticipate to observe few variations in terms of energy between HF and DFT/B3LYP methods due to a weak contribution of dispersion, and also by its potential compensation through the specific treatment of H-bonding discussed above.

3.2.1. Molecular conformation

Since we observed that the monomer is characterized by a relatively smooth potential energy surface with several local minima, we can expect a similar and even flatter energy surface for the assemblies due to the presence of several weak hydrogen bonds. First, we need to emphasize that the formation and the cohesion of the molecular units are clearly driven by the strong molecular dipole moment. This driving force favors the molecules to assemble into a specific face-to-face π-stacking configuration, where the formation of hydrogen bonds reinsures the strength and cohesion of the molecular assembly. The helical twist angle and

the distance between molecular units will be shown to be intimately related. The assemblies we have considered are characterized by an overall helical shape in which the molecular planes are separated by a relatively long distance of around 4.8–5.0 Å. Fig. 5 gives a schematic representation of the five molecules assembly, including the general helical structure of the backbone. Considering our approximation for the monomer, the calculated geometries differ but are consistent with previous experimental data [12,13].

For the formation of the assembly, Fig. 6 reveals structural features for which we can establish a clear relation between the interplanar distance and the helical twist angle between functional groups. Briefly, an increasing intermolecular distance can be simultaneously translated into a smaller helical twist angle between functional groups of the molecular units. To understand the different variations observed, we have to realize that the formation of the assembly is a compromise between various but weak energy contributions. Hence, a typical assembling process successively involves (1) the breaking of intramolecular hydrogen bonds, followed by (2) the rotation of functional groups to establish intermolecular hydrogen bonds, and (3) the displacement of molecules toward each other which, in order to occur, (4) have to overcome possible π–π repulsion. Our calculations indicate that intermolecular hydrogen bond lengths are practically constant for the different interplanar distances and helical twist angles considered. This means that the formation of hydrogen bond is at the source of the relation between the interplanar distances and helical twist angles: as the helical twist angle decreases, in other words as the CONHR groups become well-aligned in the assembly, molecules need to be slightly repelled in order to maintain a constant hydrogen bond length.

The balance between intra and intermolecular hydrogen bonds remains the major factor that directs the helical geometry of the assembly. Intramolecular hydrogen bonds make the molecule flatter, and favors larger helical twist angle between functional groups and shorter interplanar distances between benzene rings in the assembly. For example, calculations with a 6-311G basis set give an interplanar distance of 4.53 Å and 4.86 Å when calculated with DFT and HF respectively. The shortest value obtained with DFT is mainly due to the use of the B3LYP functional because it allows a better description of hydrogen bonding over HF. As expected, the molecular units do not perfectly align within a low dimensional wire structure but show a significant torsion between molecular units; the 6-311G calculated helical twist angle is 40° and 30°, with DFT/B3LYP and HF respectively.

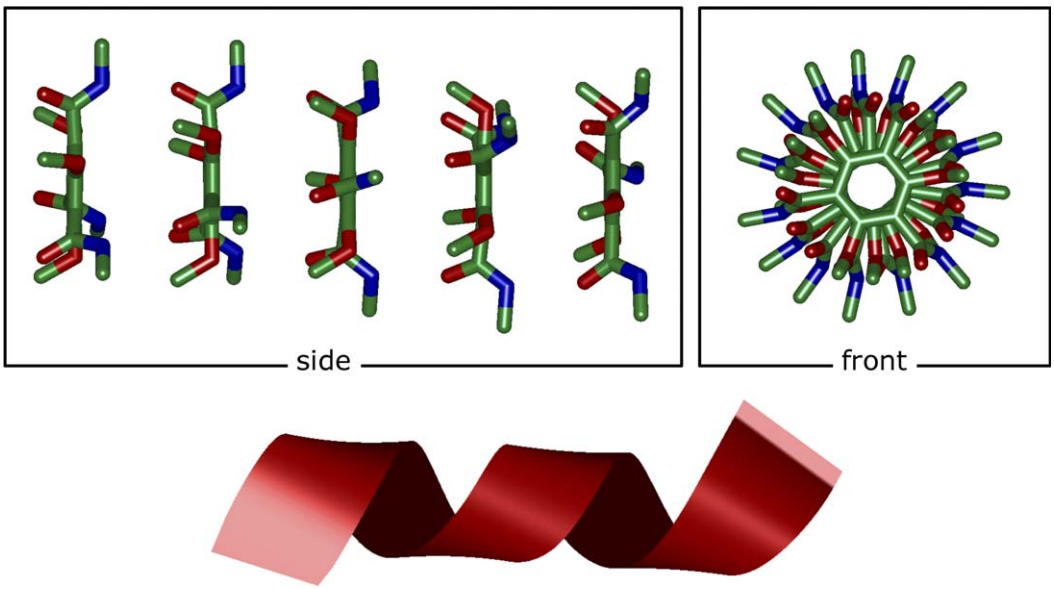

Fig. 5. Molecular structure obtained for an assembly made of five monomers that should in principle constitute a complete unit cell. The helical representation of the general backbone structure is also represented.

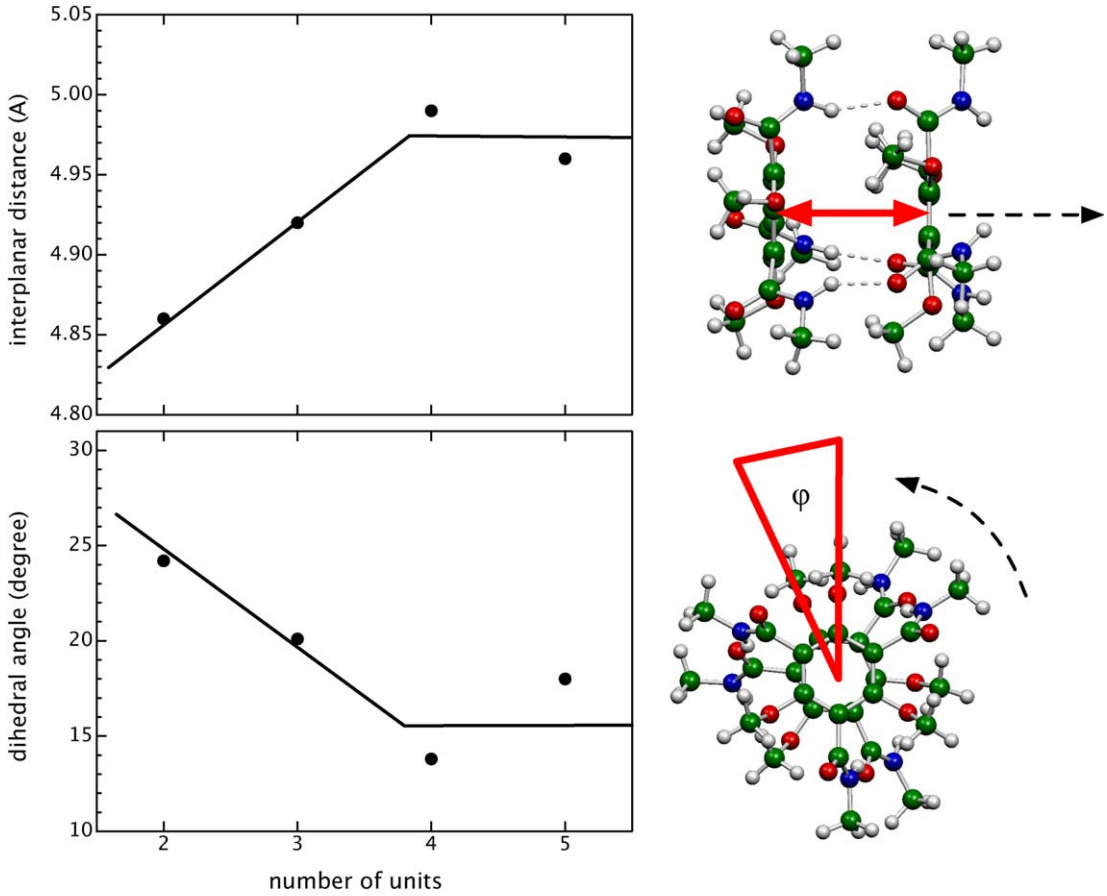

Fig. 6. Influence of the number of molecules in the assembly and the relation existing between the intermolecular distance (upper panels) and the helical twist angle (lower panels).

We now focus on the variation of structural properties observed in Fig. 6 for small assemblies. The distances and helical twist angles represented in this figure are average values. Thus, more scattered data near the asymptote is mainly related to the presence of molecules near the ends of the assembly that have different structural properties compared to those in the middle of the wire. The dispersion of these structural parameters should rapidly converge for larger assemblies. We have estimated the asymptotic behavior from the values obtained on the more central molecules of the assembly. X-ray diffraction on similar systems shows sharp (1 0 0) reflection at 18.4 Å that suggests an unit cell containing four molecules separated by 4.6 Å or five molecules separated by 3.7 Å [12]. Our theoretical results support an intermolecular separation of around 4.6 Å with four molecules in the unit cell. In fact, we obtained very consistent interplanar distances with different approaches (DFT vs HF, 6-31G vs 6-311G), and this distance does not drastically change with respect to the variation of the helical twist angle. Therefore, we can confidently exclude the 3.7 Å interplanar distance value that was previously proposed [12]. More recent STM works [28] on similar systems also support our evaluation of 4.6 Å for intermolecular separation. Nevertheless, the calculated average helical twist angle between two adjacent molecules in the five units assembly shown in Fig. 5 is much lower (18°) than the expected value (30°) from XRD data [12,29].

This important difference between experimental and theoretical helical twist angle could probably be ascribed to the model used in which the absence of the long side carbon chains could underestimate the steric interactions between side chains. Nevertheless, preliminary results on systems that include long side chains do no support this possibility. The presence of solvant in the vicinity of these long

hydrocarbon chains could also influence the electrostatic interaction between molecular units. As we observed for a small assembly of two units using both HF and DFT, our limited 6-31G/HF computational approach also contributes to give lower helical twist angle by underestimating the hydrogen bonding. Nevertheless, our theoretical results are in agreement with previous experimental works [12,29] including recent STM results [28] predicting a general α-helix structure for this type of molecular assembly. Finally, as we will see in the next section, the nature of the bands near E_F originating from the π-stacking is strongly influenced by the overall molecular conformation.

3.2.2. Electronic properties

In this last section, we want to emphasize the effect of intermolecular interactions on the resulting electronic properties, and more specifically on the variation of the net dipole moment, the band gap (HLG), the charge distribution and the wavefunction during the formation of the assembly. The variation of the net dipole moment with the addition of a molecular unit in the assembly strongly depends on the fluctuation of charge among the CONHR groups where the hydrogen bonds are formed. As revealed in Fig. 7, the linear variation of the net dipole moment with the progressive formation of a five units assembly confirms a very weak charge transfer between the molecular units. Although the numerical determination of an accurate dipole moment value generally remains a difficult task, we calculate very small variations with the computational techniques used. This points to a weak perturbation of the electronic properties of individual molecules within the wire, and consequently, a relatively weak electron perturbation of weakly bonded π-electrons.

Fig. 8 shows the change in the HOMO–LUMO gap evaluated with different computational approaches as a function of the number of molecules in the assembly. In contrast to the results obtained for the dipole moment, we observe an important HLG decrease by more than 2.0 eV when growing the assembly from a single molecule to five units. This significant HLG variation suggests the existence of electronic coupling between molecules within the wire, and is consistent with fluorescence results obtained on similar systems [30]. An extrapolation of the HLG values following a predicted asymptotic decrease for conjugated polymers [31] gives stable values from approximately 8–10 molecular units. For the geometrically optimized structure, we estimate the HLG values at around 3.0 eV for DFT and 10.0 eV for HF. Given the relatively large distance (4.8–5.0 Å) separating the molecules in the assembly, this important modulation of the HLG strongly contrasts with previous prediction on thiolarene where weak variations were observed for such large separations [9]. This difference can be explained by the large net dipole moment of the present molecule which influences the ability of the π-electron cloud to be polarized in order to create significant overlaps between low energy π-orbital of the individual molecular units. The helical geometry of the assemblies should also

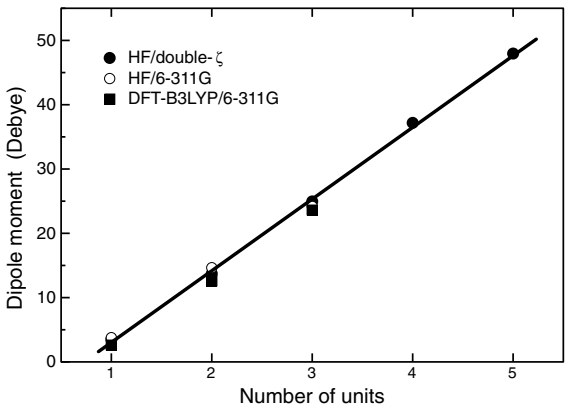

Fig. 7. The linear variation of the net dipole moment during the formation of an assembly containing up to five molecular units, and comparison to higher level of theory. The vector direction of the net dipole moment is along the stack axis for every oligomer, and along the C_3 symmetry axis for the monomer.

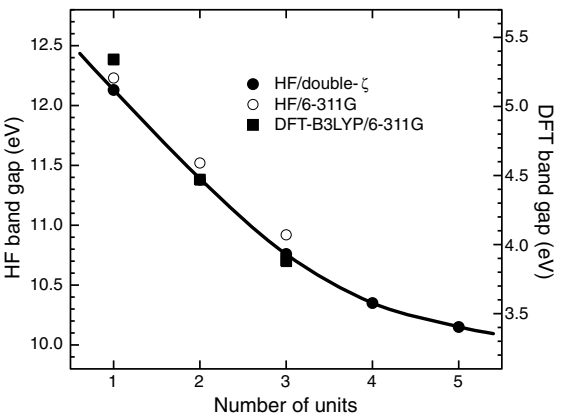

Fig. 8. Variation of the HOMO–LUMO gap (HLG) along the formation of the assembly obtained from HF and DFT/B3LYP level of theory.

contribute to reduce the band gap because of the symmetry breaking of both π and π*-bands near E_F.

From the results obtained on these relatively small assemblies, we can conclude than the two more important parameters for the characterization of electron transport in this type of assembly which are the band gap value, and the magnitude of π-electron overlap (i.e. the intermolecular distance)

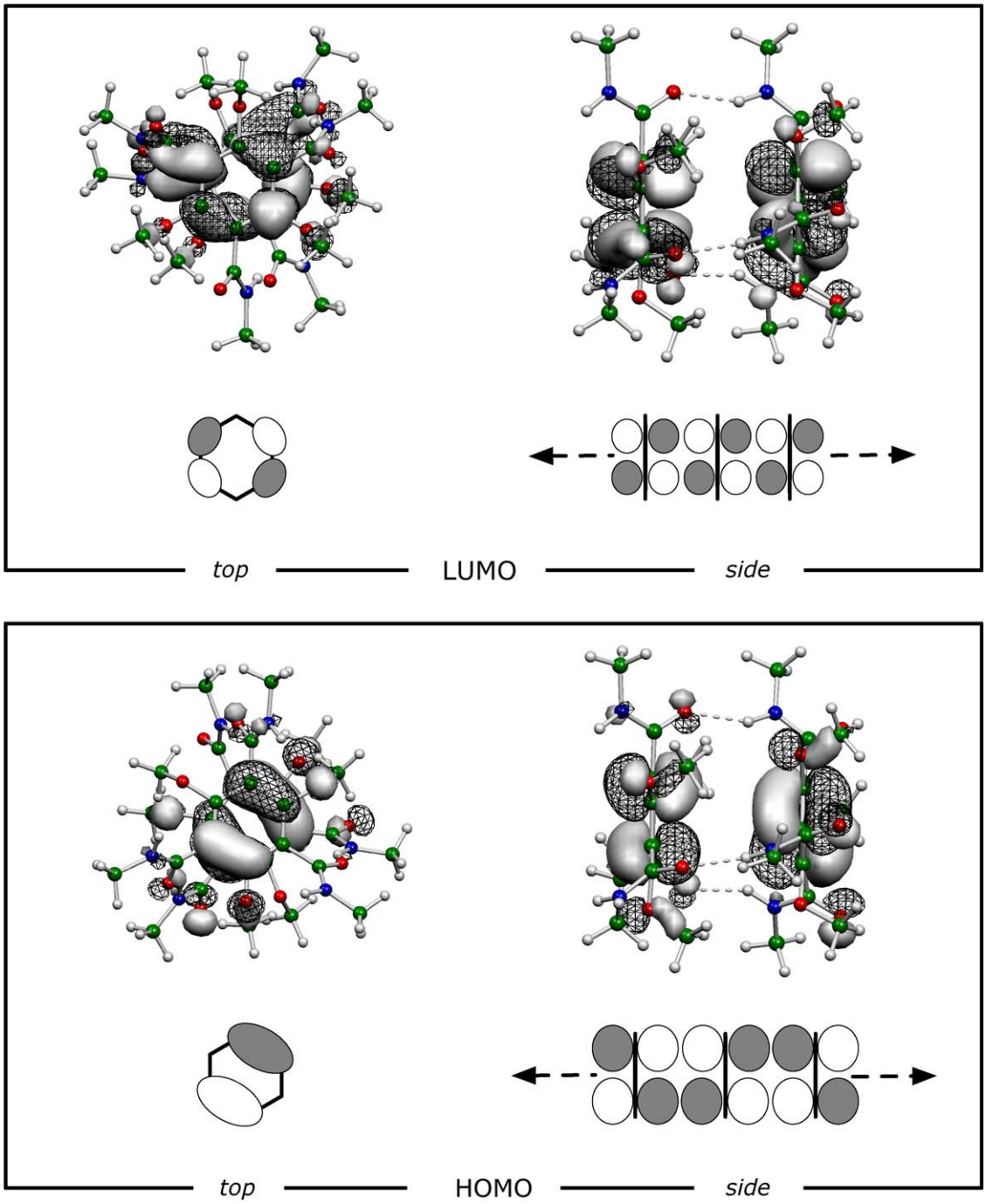

Fig. 9. Composition of the frontier orbital shown here for a short two units assembly for clarity. We can clearly observe the nature of the packing where the HOMO is formed from $\pi + \pi = \pi$ combination while the LUMO is originating from $\pi^* - \pi^* = \pi^*$ mixing.

between molecules rapidly converge to stable values of extended systems. Based on our previous works [9] where both finite and periodic approaches were used, even five to six members oligomer would qualitatively reproduce the main electronic properties of periodic systems. In addition, although an apparent π-electron coupling occurs in small and more extended systems, preliminary transport calculations within Landauer–Buttiker formalism [9] on a 10 nm long assembly suggest a polaronic rather than a band transport regime. This result is supported with the relatively large intermolecular distances calculated in these assemblies.

In order to characterize the variation of the HLG along the formation of large assemblies, and more importantly to estimate the fluctuations of the band-gap upon the creation of similar but more tightly packed systems, we have carefully analyzed the nature of the frontier orbitals. For example, Fig. 9 shows the wavefunction composition of the top-HOMO and bottom-LUMO bands [32] for a short assembly of two units. As we showed for a single molecule, HOMO and LUMO on the small assembly are π-bonding and π^*-antibonding, respectively. Once the molecules are packed into an unidimensional structure, the nature of the HOMO (top-band) which is made of π-stacked states remains π-bonding ($\pi + \pi = \pi$) while the LUMO (bottom-band) is π^*-antibonding ($\pi^* - \pi^* = \pi^*$). This description drastically contrasts with our previous results on well organized systems where the top of the HOMO-band was found anti-bonding ($\pi - \pi = \pi^*$) and the bottom of the LUMO-band was found to be bonding ($\pi^* + \pi^* = \pi$) [9]. This is an interesting result which suggests that a compression of the wire, i.e. a decreasing interplanar distance, should contribute to open the HLG of the wire, as the HOMO would stabilize and the LUMO destabilize.

Finally, the shape of individual frontier orbitals and their combination within the assembly are consistent with the helical wire structure found. Fig. 9 suggests that a perfect alignment (twisting angle = 0) of the molecules could stabilize the HOMO ($\pi + \pi = \pi$) but destabilize the LUMO ($\pi^* - \pi^* = \pi^*$). In contrast, introducing a π/2 rotation between molecules within this 1D wire would destabilize the HOMO ($\pi - \pi = \pi^*$) and stabilize the LUMO ($\pi^* + \pi^* = \pi$). Thus, the helical conformation obtained for our assemblies appears a compromise between these two cases. This change in electronic structure properties when introducing a helical symmetry has already been described for hypothetical one-dimensional band structured materials [33]. Our results on finite assemblies support this theoretical band structure description of helical materials. This wavefunction feature in addition to the balance between intra and intermolecular hydrogen bondings, characterize the overall helical conformation of the molecular assembly.

4. Conclusions

We studied the structural and electronic properties of an organic assembly in which the cohesion between the molecular units is directed by hydrogen bonding. The cohesion energy of the assembly increases linearly for small wires then saturates for molecular wires containing more than four molecules. Although the variation of the dipole moment as a function of assembly size does not show an apparent electronic interaction between molecules, the variation of the HOMO–LUMO gap clearly shows a significant but moderate π-coupling between molecular units. This moderate π-electron coupling, in conjunction to the relatively long distances separating the molecules in the assembly do not suggest very promising transport properties for such molecular assembly.

Acknowledgements

This work was supported by the Natural Sciences and Engineering Research Council of Canada (NSERC), Ministère du Développement économique et régional (MDER) and Canadian Funds for Innovation (CFI). We thank Richard Martel for stimulating discussions and the Réseau québécois de calcul haute performance (RQCHP) for providing computational facilities.

References

[1] C.D. Dimitrakopoulos, D.J. Mascaro, IBM J. Res. Dev. 45 (2001) 11.
[2] (a) A. Aviram, M.A. Ratner (Eds.), Molecular Electronics: Science and Technology, New York Academy of Science, New York, 1998;
(b) M.A. Reed, Proc. IEEE 87 (1999) 652.
[3] D.R. Gamota, P. Brazis, K. Kalyanasundaram, J. Zhang, Printed Organic and Molecular Electronics, Kluwer Academic, Boston, 2004.
[4] C. Reese, M. Roberts, M.M. Ling, Z. Bao, Mater. Today (2004) 20.
[5] J.G. Laquindanum, H.E. Katz, A.J. Lovinger, J. Am. Chem. Soc. 120 (1998) 664.

[6] H. Sirringhaus, P.J. Brown, R.H. Friend, M.M. Nielsen, K. Bechgaard, B.M.W. Langeveld-Voss, A.J.H. Spiering, R.A.J. Janssen, E.W. Meijer, P. Herwig, D.M. de Leeuw, Nature 401 (1999) 685.
[7] H. Sirringhaus, R.J. Wilson, R.H. Friend, M. Inbasekaran, W. Wu, E.P. Woo, M. Grell, D.D.C. Bradley, App. Phys. Lett. 77 (2000) 406.
[8] (a) P. Puschnig, C. Ambrosch-Draxl, G. Heimel, E. Zojer, R. Resel, G. Leising, M. Kriechbaum, W. Graupner, Synth. Met. 116 (2001) 327;
(b) P. Puschnig, C. Ambrosch-Draxl, K. Hummer, G. Heimel, M. Oehzelt, R. Resel, Phys. Rev. B 67 (2003) 235321;
(c) M. Chandrasekhar, S. Guha, W. Graupner, Adv. Mater. 13 (2001) 613.
[9] A. Rochefort, R. Martel, Ph. Avouris, Nano Letters 2 (2002) 877.
[10] G.P. Lopinski, D.D.M. Wayner, R.A. Wolkow, Nature 406 (2000) 48.
[11] A. Rochefort, A. Beausoleil, Chem. Phys. Lett. 400 (2004) 347.
[12] M.L. Bushey, A. Hwang, P.W. Stephens, C. Nuckolls, J. Am. Chem. Soc. 123 (2001) 8157.
[13] M.L. Bushey, A. Hwang, P.W. Stephens, C. Nuckolls, Angew. Chem. Int. Ed. 41 (2002) 2828.
[14] M.W. Schmidt, K.K. Baldridge, J.A. Boatz, S.T. Elbert, M.S. Gordon, J.H. Jensen, S. Koseki, N. Matsunaga, K.A. Nguyen, S. Su, T.L. Windus, M. Dupuis, J.A. Montgomery Jr., J. Comput. Chem. 14 (1993) 1347.
[15] R.A. Kendall, E. Aprà, D.E. Bernholdt, E.J. Bylaska, M. Dupuis, G.I. Fann, R.J. Harrison, J. Ju, J.A. Nichols, J. Nieplocha, T.P. Straatsma, T.L. Windus, Comput. Phys. Commun. 128 (2000) 260.
[16] T.P. Straatsma, E. Aprà, T.L. Windus, M. Dupuis, E.J. Bylaska, W. de Jong, S. Hirata, D.M.A. Smith, M. Hackler, L. Pollack, R. Harrison, J. Nieplocha, V. Tipparaju, M. Krishnan, E. Brown, G. Cisneros, G. Fann, H. Fruchtl, J. Garza, K. Hirao, R. Kendall, J. Nichols, K. Tsemekhman, M. Valiev, K. Wolinski, J. Anchell, D. Bernholdt, P. Borowski, T. Clark, D. Clerc, H. Dachsel, M. Deegan, K. Dyall, D. Elwood, E. Glendening, M. Gutowski, A. Hess, J. Jaffe, B. Johnson, J. Ju, R. Kobayashi, R. Kutteh, Z. Lin, R. Littlefield, X. Long, B. Meng, T. Nakajima, S. Niu, M. Rosing, G. Sandrone, M. Stave, H. Taylor, G. Thomas, J. van Lenthe, A. Wong, Z. Zhang, "NWChem, A Computational Chemistry Package for Parallel Computers, Version 4.5" (2003), Pacific Northwest National Laboratory, Richland, Washington 99352-0999, USA.
[17] A.D. Becke, J. Chem. Phys. 98 (1993) 5648.
[18] F. Sim, A. St-Amant, I. Papai, D.R. Salahub, J. Am. Chem. Soc. 114 (1992) 4391.
[19] A.T. Pudzianowski, J. Phys. Chem. 100 (1996) 4781.
[20] (a) S. Yang, P. Olishevski, M. Kertesz, Synth. Met. 141 (2004) 171;
(b) C.-G. Zhang, J.A. Nichols, D.A. Dixon, J. Phys. Chem. A 107 (2003) 4184.
[21] S. Portmann, H.P. Lüthi, Chimia 54 (2000) 766.
[22] R. Stowasser, R. Hoffmann, J. Am. Chem. Soc. 121 (1999) 3414.
[23] H. Guo, D.R. Salahub, Angew. Chem. Int. Ed. 37 (1998) 2985.
[24] Y. Zhao, D.G. Truhlar, J. Chem. Theory Comput. 1 (2005) 415.
[25] E.R. Johnson, R.A. Wolkow, G.A. DiLabio, Chem. Phys. Lett. 394 (2004) 334.
[26] J.R. Grover, E.A. Walters, E.T. Hiu, J. Phys. Chem. 91 (1989) 3233.
[27] C. Gonzalez, E.C. Lim, J. Phys. Chem. A 107 (2003) 10105.
[28] T.-Q. Nguyen, R. Martel, C. Nuckolls, in preparation.
[29] M.L. Bushey, T.-Q. Nguyen, C. Nuckolls, J. Am. Chem. Soc. 125 (2003) 8264.
[30] T.-Q. Nguyen, R. Martel, Ph. Avouris, M.L. Bushey, L. Brus, C. Nuckolls, J. Am. Chem. Soc. 126 (2004) 5234.
[31] A.J. Heeger, S. Kivelson, J.R. Schrieffer, W.-P. Su, Rev. Mod. Phys. 60 (1988) 781.
[32] We used the term band because the represented HOMO (LUMO) contains the first four highest occupied orbitals, two on each molecule.
[33] W.V. Glassey, R. Hoffmann, Theor. Chem. Acc. 107 (2002) 272.

Available online at www.sciencedirect.com
SCIENCE DIRECT
Organic Electronics 7 (2006) 155–162
Organic Electronics
www.elsevier.com/locate/orgel

Fluorene-substituted pyrenes—Novel pyrene derivatives as emitters in nondoped blue OLEDs

Chao Tang, Feng Liu, Yi-Jie Xia, Jian Lin, Ling-Hai Xie, Gao-Yu Zhong, Qu-Li Fan, Wei Huang *

Institute of Advanced Materials (IAM), Fudan University, 220 Handan Road, Shanghai 200433, China

Received 2 October 2005; received in revised form 5 January 2006; accepted 5 January 2006
Available online 25 January 2006

Abstract

Two highly efficient blue light-emitting materials, 9-phenyl-9-pyrenylfluorene substituted pyrenes (**P1**, **P2**), were designed and synthesized. The two compounds demonstrated highly thermal stability and bright blue emission both in solution and in the solid state. Even after being annealed at 150 °C under nitrogen for 24 h, the solid emission spectra showed no obvious changes. The high energy levels of the HOMO (about −5.2 eV) exhibit that they have improved hole-injection/transporting ability. A three layer blue OLED of ITO/TCTA (8 nm)/**P2** (30 nm)/BCP (40 nm)/Mg:Ag was obtained with high efficiency (3.08 cd/A, 1.17 lm/W), low turn-on voltage (3.5 V) and high brightness (19885 cd/m^2) in ambient air, which is competitive with the best of the doped and nondoped blue OLEDs. These results revealed that these materials are promising as blue emitters for high efficiency OLEDs with a much simpler architecture. We thus exemplified that introducing 9-phenyl-9-pyrenylfluorene onto large aromatic rings is a new method to employ fluorescent dyes with large planar aromatic rings as the blue emitters in nondoped OLEDs without a hole-injection layer.

Keywords: 9-Phenyl-9-pyrenylfluorene substituted pyrenes; Hole-injection; Organic electroluminescence

1. Introduction

Since the breakthrough discovery by Tang and van Slyke in organic light emitting diodes (OLEDs), [1] research into OLEDs has been pursued intensively because of their potential use in information displays such as TVs, computer monitors and cellular phones [2–6]. Developing blue light emitters is essential for the development of full color displays [7,8]. It is much more difficult to produce blue emission due to the intrinsic characteristic of having a wide bandgap irrespective of the type of materials. Because of their high solution and solid-state photoluminescence (PL) quantum yields, recently much research into blue-emitting materials has centered on fluorene conjugated derivatives [9]. In order to block the interchain interaction and improve the thermal stability, two bulky aryl groups are introduced at C9 position of fluorene moiety [10]. However, the difference between ionization potential (IP) of conjugated fluorene derivatives (5.6–5.8 eV) and

* Corresponding author. Tel.: +86 21 5566 4188; fax: +86 21 6565 5123.
E-mail addresses: wei-huang@fudan.edu.cn, iamdirector@fudan.edu.cn (W. Huang).

1566-1199/$ - see front matter © 2006 Elsevier B.V. All rights reserved.
doi:10.1016/j.orgel.2006.01.001

work-function of the indium tin oxide (ITO) ($\phi \sim 4.7$ eV) requires the use of hole-injection layers to obtain efficient hole-injection, [11] and the poly(3,4-ethylenedioxythiophene):poly(styrenesulfonate) (PEDOT:PSS) is commonly used as the hole-injection materials. But it is not ideal because of its absorption in the visible region and the unstable interface between ITO and PEDOT:PSS [12]. In order to avoid above disadvantages and simplify the OLEDs device, triarylamines was incorporated into the fluorene moiety to improve the hole-injection ability [13].

Due to the large planar conjugated aromatic characteristic, pyrene has strong π electron delocalization energy and efficient fluorescence property, which makes its derivatives widely used as probes in recognized DNA labels [14]. More recently, some pyrene derivatives have been used in OLEDs in order to improve hole transporting ability because of its electron-rich property [15], yet the performance of those OLEDs is not satisfactory in brightness and efficiency. On the other hand, due to the high carrier mobility of large planar conjugated aromatic rings, blue doped OLEDs using these compounds as dopants, such as perylene, always have high brightness and high efficiency [16]. Although such doping procedure is easy to be done and enables one to take advantage of the commercially available dyes, recent work has shown that the blends of the host materials and the dopant dyes have a tendency to show phase separation over time, which leads to instability in the performance of devices [17]. In addition to the high PL efficiency and high carrier mobility, large planar aromatic rings such as pyrene and perylene also have better hole-injection ability than conjugated fluorene derivatives because of its electron-rich characteristic.

In the present work, we report the synthesis and characterization of two novel 9-phenyl-9-pyrenylfluorene subsitituted pyrenes (**P1**, **P2**) (Scheme 1), which is noncoplanar in structure because of the steric tortional hindrance of 9-phenyl-9-pyrenylfluorenes. Our motivation for the design of the materials is to combine the thermal stability of the 9-phenyl-9-pyrenylfluorene Section [10] with the high efficiency, high carrier mobility and hole-injection advantage of large planar aromatic rings. This report provides clear evidence that we have not only significantly improved the thermal stability of large planar pyrene rings, but also improved the hole-injection ability compared with the conjugated fluorene derivatives. The device ITO/TCTA (8 nm)/**P2** (30 nm)/BCP (40 nm)/Mg:Ag, without the need for hole-injection layer, shows very bright blue electroluminescence (EL) (19 885 cd/m^2), with the low turn-on voltage of 3.5 V, the current efficiency of 3.08 cd/A and power efficiency of 1.17 lm/W. The high performance and simple device structure are competitive with the best of the doped [16,18] and nondoped [19] blue OLEDs. We thus have exemplified that introducing 9-phenyl-9-pyrenylfluorene onto large aromatic rings is a new method to employ the fluorescene dyes with large planar aromatic rings as the blue emitters in nondoped OLEDs without the needs for hole-injection layers, which is essential for simplifying device fabrication

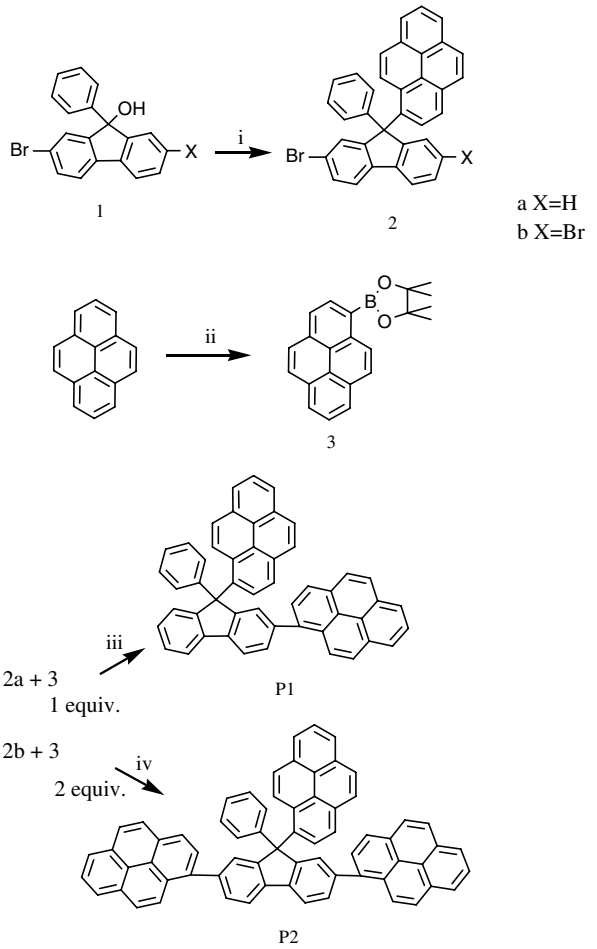

Scheme 1. Reagents and conditions: (i) pyrene (5 equiv), $CHCl_3$, CH_3SO_3H (1 equiv), 60 °C, 20 min; (ii) (1) NBS/DMF, (2) *n*-BuLi, THF, −78 °C, 2 h, (3) $B(OMe)_3$, THF, −78 °C to room temp., 36 h, (4) 2 M HCl, (5) pinacol/CH_2Cl_2; 48 h; (iii) **2a**/**3** (1:1), $Pd(PPh_3)_4$, toluene, K_2CO_3 (2.0 M, aq.), 90 °C, 48 h; (iv) **2b**/**3** (1:2), $Pd(PPh_3)_4$, toluene, K_2CO_3 (2.0 M, aq.), 90 °C, 48 h.

processes so as to cut the cost of full color displays. It is noted that a similar work was reported [20] after this paper was submitted for publication.

2. Results and discussion

2.1. Preparation and characterization

The detailed synthesis of the two pyrenes, **P1** and **P2**, is sketched in Scheme 1. Compounds **1a** and **1b**, prepared according to our previous procedure, [9a] underwent Friedel–Crafts reaction with an excess amount of pyrene in chloroform promoted by methanesulfonic acid to achieve the compound **2a** and **2b** (>78% yield), respectively. Pyrene was brominated with *N*-bromosuccinimide (NBS) in *N*,*N*-dimethylformamide (DMF), then the crude bromopyrene was subjected to halogen-lithium exchange with *n*-BuLi at −78 °C in THF and subsequent reaction of the anion with $B(OMe)_3$ gave the corresponding pyrene boronic acid, whose esterification with pinacol obtained the desired boronic ester **3** (55% yield). Suzuki coupling reaction was employed between the monobromide **2a**, dibromide **2b** and pyrene boronic ester **3** to obtain the target compounds **P1** and **P2** (>70% yield) [21]. Both the two fluorene substituted pyrenes in this report were purified by flash column chromatography. They were fully characterized by ^1H and ^{13}C NMR, laser desorption/ionization time-of-flight mass spectrometer (LDI-TOF-MASS) and elemental analysis. The results were consistent with the proposed structures.

2.2. Thermal properties

Thermal properties of the two materials were evaluated using thermogravimetric analysis (TGA) and differential scanning calorimetry (DSC). TGA (10 °C /min) showed that the two materials were highly stable in nitrogen, with the thermal decomposition temperature (T_d) at 459 and 478 °C, for **P1** and **P2**, respectively, which means the materials are stable enough to endure the temperature of the vacuum vapor deposition. In the first DSC trace of heating (10 °C /min), the two materials have the melting transition at 274 °C and 359 °C for **P1** and **P2**, respectively. **P2** is more thermally stable than **P1** because **P2** has a more symmetric structure and a higher molecular weight resulting from an additional pyrene group at the C7 of the fluorene moiety (Scheme 1). After the samples were cooled to room temperature, during the second DSC trace of heating (10 °C /min), **P2** has a high glass transition temperature of 217 °C, and **P1** has no obvious glass transition. No crystallization procedure was observed during the DSC trace. These results show that **P1** and **P2** have good thermal stability even though they are low molecular weight organic compounds. In contrast, pyrene has a melting point of 150 °C, so the thermal stability was enhanced significantly by incorporating the more rigid 9-phenyl-9-pyrenylfluorene group, which may in turn improve the stability and operating lifetime of the EL device.

2.3. Optical and electrochemical properties

The spectroscopic properties of the two materials were measured in dichloromethane (CH_2Cl_2) solution and the corresponding data were summarized in Table 1. They showed absorption with the λ_{max} at 351 and 352 nm, respectively, due to π–π* transition derived from the conjugated substituted pyrene backbone (Fig. 1(a)). Additional absorption bands around 336 nm might be originated from the absorption of pyrene at the C9 of the fluorene core, which is not conjugated to the fluorene–pyrene conjugation chain, because the pyrene, in CH_2Cl_2, has an absorption with λ_{max} at 336 nm. From the **P1** to **P2**, the absorption shows red-shift due to the increasing of conjugation length, resulting from the pyrene group at the C7 of fluorene moiety. Upon excitation of the pyrene–fluorene conjugation

Table 1
Physical properties of **P1** and **P2**

Pyrenes	Φ (%)	Abs. λ_{max} (nm)	PL λ_{max} (nm)		HOMO (eV)	LUMO[c] (eV)	ΔE
			Solution[a]	Film[b]			
P1	71	351	408	462	−5.24	−2.23	3.05
P2	75	352	424	450	−5.22	−2.51	2.88

[a] In CH_2Cl_2 solution, the excitation light wavelength is the absorption maxima (λ_{max}).
[b] Prepared by vacuum vapor deposition (100 nm), the excitation light wavelength is the absorption maxima (λ_{max}).
[c] LUMO = HOMO − ΔE (band gap).

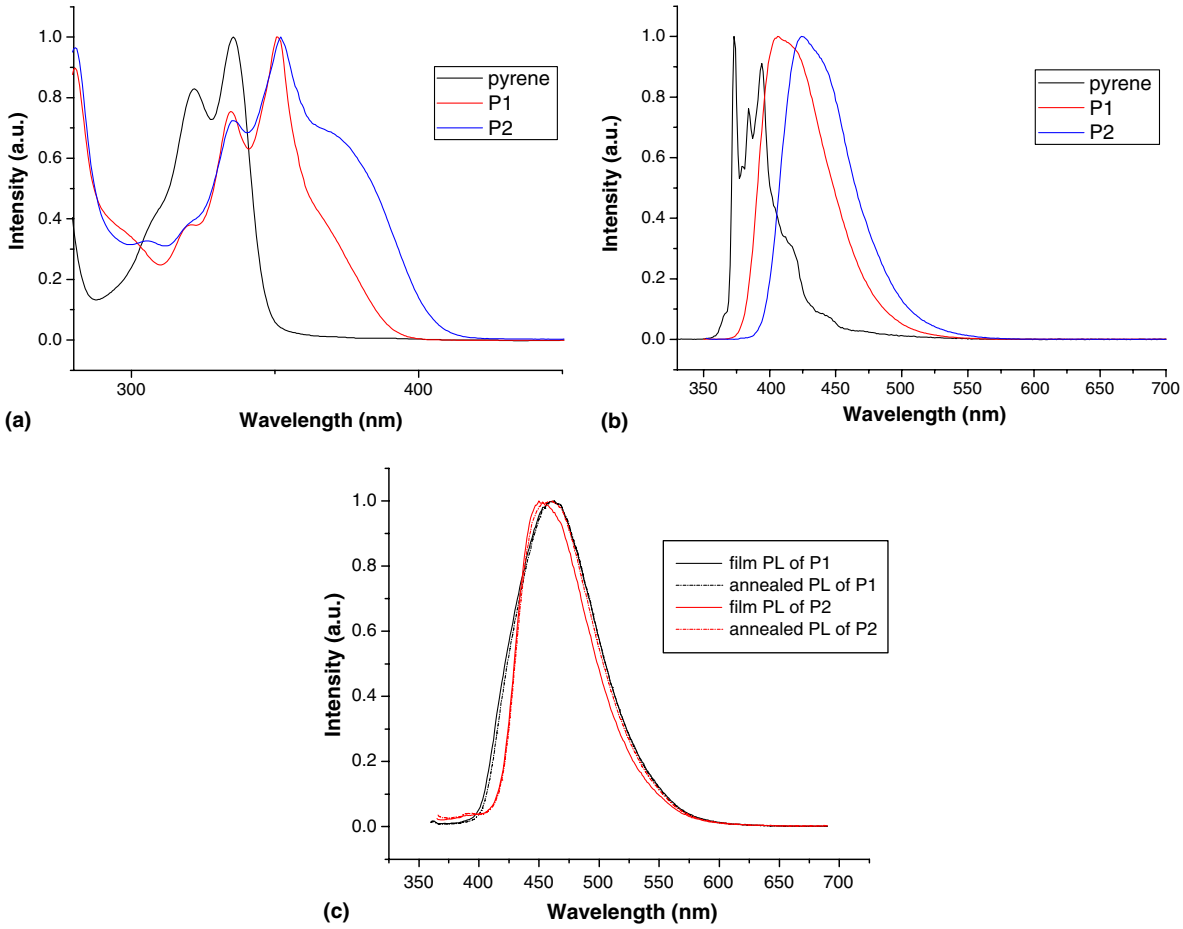

Fig. 1. (a) UV–visible absorption. (b) Emission spectra of pyrene, **P1** and **P2**. (c) Solid PL of **P1** and **P2**, also included are the PL spectra of **P1** and **P2** film after annealed at 150 °C for 24 h.

at 351 nm and 352 nm, the emission spectra display maxima at 408 and 424 nm, for **P1** and **P2**, respectively. From the unsubstituted pyrene to substituted **P1** to **P2**, the PL spectra also show a gradual red-shift, concomitant with the increasing conjugation length (Fig. 1(b)). The PL quantum yield of the materials in dichloromethane solution was estimated to be 0.71 and 0.75 by using 9,10-diphenylanthrancene as the reference standard (cyclohexane solution, $\Phi = 0.9$) [22].

Both the film PL of **P1** and **P2**, prepared by vacuum vapor deposition (100 nm), show obvious red-shift than the PL in CH_2Cl_2 (Fig. 1(c)). The solid state PL quantum yields were measured to be 0.50 and 0.61 for **P1** and **P2**, respectively. No obvious change in the emission film was observed even after annealing at 150 °C for 24 h under nitrogen, which indicates that we have successfully improved the thermal and luminescent stability of pyrene by incorporating the bulky 9-phenyl-9-pyrenylfluorene group onto the pyrene ring.

The electrochemical behavior of **P1** and **P2** was investigated by cyclic voltammetry (CV) with a standard three electrodes electrochemical cell in a 0.1 M tetrabutylammonium tetrafluoroborate (Bu_4NBF_4) in dichloromethane at room temperature under nitrogen with a scanning rate of 200 mV/s. A platinum working electrode, a platinum counter electrode and an $Ag/AgNO_3$ (0.1 M) reference electrode were used. The oxidation onset potentials were measured to be 0.54 and 0.52 V, respectively. The corresponding HOMO energy levels were thus estimated to be −5.24 and −5.22 eV, [23] indicating that the electron-rich pyrene derivatives do have an increase in hole affinity and an improvement in hole-injection ability than conjugated fluorene derivatives [9]. From the UV–visible absorption spectra, the onset absorption of **P1** and **P2** were measured to be

407 nm and 431 nm, and the band gap (ΔE) were thus calculated to be 3.05 and 2.88 eV for **P1** and **P2**, respectively. Then the LUMO can be estimated to be −2.23 and −2.88 eV, respectively. The corresponding data were also summarized in Table 1.

2.4. Electroluminescence properties

Because the HOMO of two fluorene substituted pyrenes (Table 1) were close to that of PEDOT:PSS (∼−5.2 eV), the hole-injection layers were not necessary in the light-emitting devices. So we fabricated devices of ITO/TCTA (8 nm)/**P1** or **P2** (30 nm)/BCP (40 nm)/Mg:Ag (**Device 1** or **2**), where the TCTA (4,4′,4″-tri(*N*-carbazolyl)triphenylamine) was used as both the buffer layer and hole-transporting layer, and BCP (2,9-dimethyl-4,7-diphenyl-1,10-phenanthroline) as both the buffer layer and electron-transporting layer. The three-layer devices exhibit blue EL (Fig. 2) from **P1** and **P2**. High brightness of 16664 cd/m^2 (15 V) and 19885 cd/m^2 (13 V) were obtained for **Devices 1** and **2**, respectively (Fig. 3(a)). The devices have low turn-on voltages of 4 and 3.5 V, with high current efficiency of 2.56 (9.5 V) and 3.08 cd/A (9 V), high power efficiency of 0.85 lm/W (7.5 V) and 1.17 lm/W (7.5 V) for **Devices 1** and **2**, respectively (Fig. 3(b)). The peaks of the blue EL spectra were all at 454 nm, with 1931 CIE coordinate of $(x = 0.17, y = 0.17)$ and $(x = 0.17, y = 0.19)$ for **Devices 1** and **2**, respectively. Long wavelength emission was not observed in our devices, which could be attributed to the non-planar molecular structure of the materials. It is noteworthy that the EL efficiency of the devices do not drop obviously when current density increased (Fig. 3(b)), and when the current density reaches its maximum, the devices have still maintain a efficiency of 2.53 cd/m^2 and 2.84 cd/m^2 for **Devices 1** and **2**, respectively, which indicates that the devices are still stable under extreme operating conditions. The low turn-on voltage, high brightness, high efficiency and simple architecture make the devices competitive with the best of the doped [16,18] and nondoped [19] blue OLEDs. The performance of **Device 2** is obviously better than that of **Device 1** in turn-on voltage, brightness and efficiency, which might be attributed to the higher PL efficiency of **P2** than that of **P1**. In contrast, the device of ITO/TCTA (8 nm)/pyrene (30 nm)/BCP (40 nm), where the un-substituted pyrene was used as emitting materials, no EL emission was observed. So, the high performance of **Devices 1** and **2** can be attributed to intrinsic feature of the pyrene derivatives with high thermal stability, much improved hole-injection ability, which results from the elaborate combination of the stable 9-phenyl-9-pyrenylfluorene moiety with the large planar aromatic ring of pyrene.

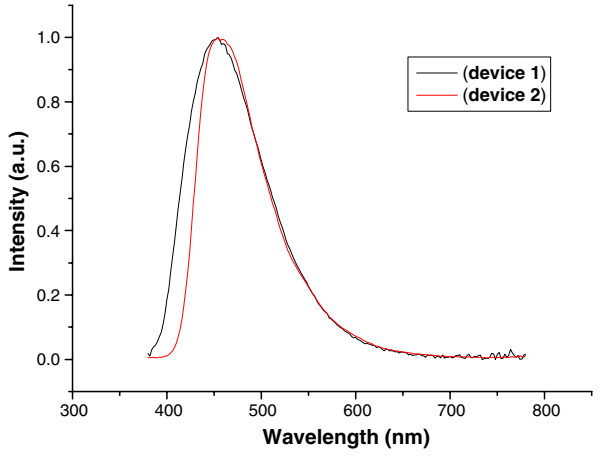

Fig. 2. EL spectra from **Devices 1** and **2**.

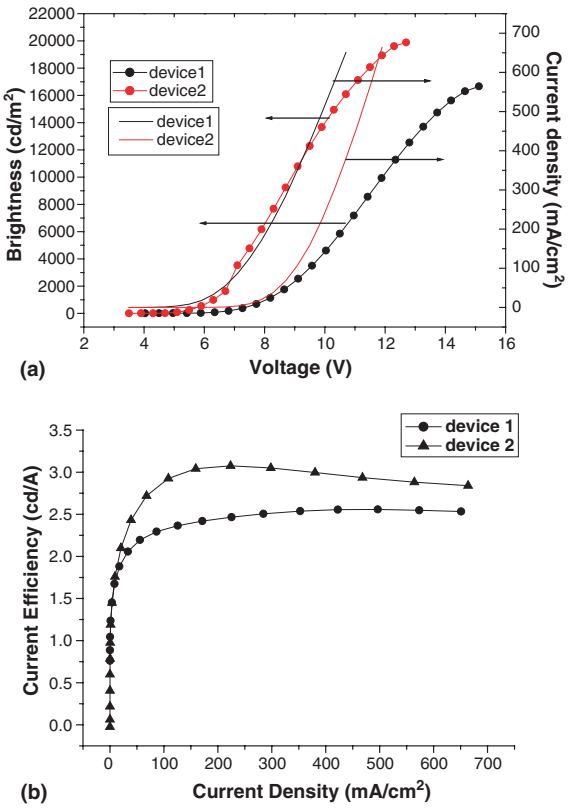

Fig. 3. (a) Brightness–current density–voltage, and (b) Current efficiency–current density of **Devices 1** and **2**.

3. Conclusions

Two new 9-phenyl-9-pyrenylfluorene substituted pyrenes, **P1** and **P2** were designed and synthesized. The materials have not only shown high thermal stability, but also shown improved hole-injection and hole-transporting ability over conjugated fluorene derivatives. A blue OLED using **P2** as emitting materials, ITO/TCTA (8 nm)/**P2** (30 nm)/BCP (40 nm)/Mg:Ag, was obtained with high efficiency (3.08 cd/A, 1.17 lm/W), low turn-on voltage (3.5 V), high brightness (19 885 cd/m^2), which is competitive with the best of the doped and nondoped blue OLEDs. High efficiency and high stabi- lity in junction with easily synthesizing route render the materials a very promising class of optoelectronic materials. This method of material design, introducing 9-phenyl-9-pyrenylfluorene onto large aromatic rings, can also be applied in the design and synthesis of other efficient blue emitters containing other large planar aromatic rings such as perylene, and this is current in progress in our group. Therefore we, in fact, have provided a new simple method to make full use of the efficient fluorescence dyes with large planar aromatic rings for acting as efficient blue emitters in nondoped OLEDs, without need for the hole-injection layers.

4. Experimental

4.1. General information and materials

Commercial grade reagents were used without further purification unless otherwise stated. All the solvents for characterization were used after redistillation. THF was refluxed with sodium filament in the presence of benzophenone until a persistent violet–blue color appears and then distilled. All reactions were monitored by TLC using pre-coated glass sheets purchased by Yantai Huiyou Silica Gel Developing Co., Ltd. (0.20 mm with fluorescent indicator UV_{254}). Compounds were visualized with UV light at 254 nm. Column chromatography was carried out using flash silica gel from Qingdao Haiyang Chemical Co., Ltd. (200–300 mesh). ^1H and ^{13}C NMR were recorded using a Varian spectrometer at 400 MHz. Molecular masses were determined by a SHIMADZU laser desorption/ionization time-of-flight mass spectrometer (LDI-TOF-MASS). Elemental analyses were performed on a Vario III elemental analyzer. Thermogravimetric analysis (TGA) and differential scanning calorimetry (DSC) were performed under nitrogen atmosphere at a heating rate of 10 °C/min. Absorption and photoluminescence (PL) emission spectra of the target compounds were measured in dichloromethane using a SHIMADZU UV-3150 spectrophotometer and a SHIMADZU RF-5301PC spectrophotometer, respectively. Quantum yield was determined in CH_2Cl_2 solution and was calculated by comparing emission with that of the standard solution of 9,10-diphenylanthracene in cyclohexanane ($\Phi = 0.9$) at room temperature. The film quantum yield was measured on a Labsphere's URS-600 uniform source systems with an optical power meter of Model 1830-C. Cyclic voltammetry (CV) was performed on an Eco Chemie's Autolab.

4.2. Synthesis

2,7-Dibromo-9-phenyl-9-pyrenylfluorene (**2b**). To a solution of pyrene (5 g, 24.7 mmol) and CH_3SO_3H (0.72 g, 4.8 mmol) in chloroform (100 mL) was added dropwise 2,7-dibromo-9-phenyl-fluoren-9-ol (**1b**) (2.0 g, 4.8 mmol) in chloroform (50 mL). The mixture was heated to 60 °C, and stirred for another 20 min. Then saturated sodium bicarbonate solution was added into the mixture to quench the reaction. The organic phase was separated and washed by saturated sodium bicarbonate (100 mL), and the water phase was extracted three times with dichloromethane. The combined organic solution was dried with anhydrous $MgSO_4$. The solvent was removed by rotary evaporation, and the residue was purified by column chromatography using petroleum ether/dichloromethane (5:1) as eluent to get a white solid (2.3 g, 79%). ^1H NMR (400 MHz, $CDCl_3$) δ (ppm): 7.58–8.24 (m, 11H); 7.67 (d, $J = 8.0$ Hz, 2H); 7.52 (dd, $J = 8.0$ Hz, 2.0 Hz); 7.23–7.32 (br., 3H), 7.12–7.23 (br., 2H). LDI-TOF-MS (m/z); calcd. for $C_{35}H_{20}{}^{79}Br^{79}Br$ 598.0, found 598.1; calcd. for $C_{35}H_{20}{}^{79}Br^{81}Br$ 600.0, found 600.0; calcd. for $C_{35}H_{20}{}^{81}Br^{81}Br$ 602.0, found 602.3. Anal. calcd. C, 70.02; H, 3.36. Found C, 70.08; H, 3.40.

2-Bromo-9-phenyl-9-pyrenylfluorene (**2a**). **2a** was synthesized according to the procedure described for **2b** using 2-bromo-9-phenyl-fluoren-9-ol (**1a**) (2.0 g, 6 mmol) in chloroform (50 mL) and pyrene (6 g, 30 mmol) in chloroform (120 mL) to get a white solid (2.5 g) in 80% yield. ^1H NMR (400 MHz, $CDCl_3$) δ (ppm): 7.90–8.20 (m, 8H); 7.78–7.86 (br., 2H); 7.64–7.76 (m, 3H); 7.56–7.64 (br., 1H); 7.52 (d, $J = 8.0$ Hz, 1H); 7.39 (t, 8.0 Hz,

1H); 7.16–7.26 (br., 5H). LDI-TOF-MS (*m*/*z*); calcd. for $C_{35}H_{21}{}^{79}Br$ 520.1, found 520.8; calcd. for $C_{35}H_{21}{}^{81}Br$ 522.1, found 522.2. Anal. calcd. C, 80.62; H. 4.06. Found C, 80.70; H, 4.16.

1-(4,4,5,5-Tetramethyl-1,3,2-dioxaborolan-2-yl)pyrene (**3**). To a solution of pyrene (8.1 g, 40 mmol) in DMF (250 mL), NBS (3.6 g, 20 mmol) in DMF (150 mL) was added dropwise and stirred for another 2 h. The mixture was treated with hydrochloric acid (2 M, 500 mL) and dicloromethane, and the water phase was then extracted several times with dichloromethane. The solvents were removed under reduced pressure to yield the crude 1-bromopyrene. Then the crude 1-brompyrene was reacted successively with *n*-butyllithium (1.6 M in hexane) (25 mL, 40 mmol), $B(OMe)_3$ (20 g, 190 mmol), HCl (2 M, 300 mL) and pinacol (23 g, 200 mmol) according to the literature procedure. At last, the solvent was removed by rotary evaporation, and the residue was purified by column chromatography using petroleum ether/ethyl acetate (10:1) as eluent to provide **3** (3.6 g, 55%). ^{1}H NMR (400 MHz, $CDCl_3$) δ (ppm): 9.10 (d, $J = 9.2$ Hz, 1H); 8.56 (d, $J = 7.6$ Hz, 1H); 8.25–7.98 (m, 7H); 1.51 (s, 12H). LDI-TOF-MS (*m*/*z*); calcd. for $C_{22}H_{21}{}^{10}BO_2$ 328.2, found 328.1; calcd. for $C_{22}H_{21}{}^{11}BO_2$ 329.2, found 329.1. Anal. calcd. C, 80.51; H, 6.45. Found C, 80.65; H, 6.72.

2-Pyrenyl-9-phenyl-9-pyrenylfluorene (**P1**): 1-(4,4,5,5-Tetramethyl-1,3,2-dioxaborolan-2-yl)pyrene (**3**) (0.5 g, 1.5 mmol), 2-bromo-9-phenyl-9-pyrenylfluorene (**2a**) (0.78 g, 1.5 mmol), and $Pd(PPh_3)_4$ (0.05 mmol) and aqueous 2.0 M K_2CO_3 (2 mL) were mixed in a flask containing with nitrogen saturated toluene (50 mL). The reaction mixture was stirred at 90 °C for 48 h. After it was cooled to room temperature, the reaction mixture was quenched with saturated sodium bicarbonate solution and extracted twice with dichloromethane. The combined organic extracts were dried with anhydrous $MgSO_4$. The crude product was purified by column chromatography using petroleum ether/dichloromethane (4:1) as eluent to provide a pale white powder (0.75 g, 78%). ^{1}H NMR (400 MHz, $CDCl_3$) δ (ppm): 8.15 (t, $J = 9.2$ Hz, 4H); 8.08–7.90 (m, 15H); 7.90–7.80 (d, $J = 8.0$ Hz, 2H); 7.76–7.66 (t, $J = 9.2$ Hz, 3H); 7.46 (t, $J = 7.6$ Hz); 7.40–7.30 (m, 3H); 7.30–7.18 (m, 2H). ^{13}C NMR (400 MHz, $CDCl_3$) δ (ppm): 152.35, 147.18, 140.81, 140.05, 139.22, 137.77, 131.63, 131.23, 131.05, 130.73, 130.58, 130.39, 129.82, 129.13, 128.55, 128.26, 128.11, 127.79, 127.68, 127.58, 126.90, 126.82, 126.40, 126.17, 125.37, 125.24, 125.18, 124.94, 124.83, 120.82, 120.71, 67.18. LDI-TOF-MS (*m*/*z*); calcd. for $C_{51}H_{30}$ 642.2, found 642.4. Anal. calcd. C, 95.30; H, 4.70. Found C, 95.25; H, 4.62.

2,7-Dipyrenyl-9-phenyl-9-pyrenylfluorene (**P2**). **P2** was synthesized according to the procedure described for **P1** using **3** (0.5 g, 1.5 mmol), **2b** (0.40 g, 0.7 mmol), $Pd(PPh_3)_4$ (0.02 mmol), 2.0 M K_2CO_3 (1 mL) and toluene (30 mL). The crude product was purified by column chromatography using petroleum ether/dichloromethane (3:1) as eluent to provide a pale green powder (0.47 g, 70%). ^{1}H NMR (400 MHz, $CDCl_3$) δ (ppm): 8.24–8.12 (m, 8H); 8.10–7.92 (m, 19H); 7.77 (dd, $J = 8.4$ Hz, 1.6 Hz, 2H); 7.64 (d, 8.4 Hz, 2H); 7.46 (s, 2H); 7.34–7.28 (s, 3H); 7.27–7.22 (m, 2H). ^{13}C NMR (400 MHz, $CDCl_3$) δ (ppm): 152.80, 140.92, 139.04, 137.75, 131.63, 131.06, 130.76, 130.62, 129.27, 128.56, 128.48, 127.85, 127.60, 126.98, 126.57, 126.18, 125.37, 125.28, 125.04, 124.98, 124.88. LDI-TOF-MS (*m*/*z*); calcd. for $C_{67}H_{38}$ 842.3, found 842.2. Anal. calcd. C, 95.46; H, 4.54. Found C, 95.36; H, 4.58.

4.3. OLED device fabrication

Organic EL device were fabricated by using successive vacuum-deposition of the materials on top of the ITO glass substrate under a pressure of about 1×10^{-4} Pa with the deposition rate of about 0.1 nm/s. ITO glass was etched for the anode electrode pattern and cleaned in ultrasonic baths of chloroform, acetone and alcohol. The overlap area of Mg:Ag alloy cathode and ITO electrodes is 6 mm^2. A UV zone cleaner was used for further cleaning before vacuum deposition of the organic materials. The evaporation rate and the thickness of the film were measured with a quartz oscillator. Current–voltage–luminescence (*I*–*V*–*L*) characteristics and CIE color coordinates were measured with a Keithley SMU238 and a ST-86LA luminance-meter. EL spectra were measured with a Photo Research's PR 705.

Acknowledgements

This work was financially supported by the National Natural Science Foundation of China under Grants 60325412 and 90406021 and the Shanghai Commission of Science and Technology under Grants 03DZ11016 and 04XD14002 as well as the Shanghai Commission of Education under Grant 2003SG03. Helpful discussions with Prof.

Wei Wei, Prof. Lian-Hui Wang, Prof. Bo Peng, Dr. Jia-Chun Feng, and Ms. Xiao-Mei Lu are highly appreciated. CT would also like to extend his gratitude to Fudan University and IAM for the scholarships offered.

References

[1] C.W. Tang, S.A. van Slyke, Appl. Phys. Lett. 51 (1987) 913.
[2] S. Miyata, H.S. Nalwa, Organic Electroluminescent Materials and Devices, Gordon and Breach Publishers, New York, 1997.
[3] C.H. Chen, J. Shi, C.W. Tang, Macromol. Symp. 125 (1997) 1.
[4] C.H. Chen, J. Shi, C.W. Tang, Coord. Chem. Rev. 171 (1998) 161.
[5] U. Mitschke, P. Bauerle, J. Mater. Chem. 10 (2000) 1471.
[6] L.S. Hung, C.H. Chen, Mater. Sci. Eng. R 39 (2002) 143.
[7] C.H. Chen, J.M. Shi, Coord. Chem. Rev. 171 (1998) 161.
[8] J. Kido, K. Hongawa, K. Okuyama, K. Nagai, Appl. Phys. Lett. 64 (1994) 815;
J. Kido, H. Shionoya, K. Nagai, Appl. Phys. Lett. 67 (1995) 2281;
F.C. Chen, Y. Yang, M.E. Thompson, J. Kido, Appl. Phys. Lett. 80 (2002) 2308;
G. Gu, S.R. Forrest, IEEE J. Sel. Top. Quantum Electron. 4 (1998) 83.
[9] W.-L. Yu, J. Pei, W. Huang, A.J. Heeger, Adv. Mater. 12 (2000) 828;
K.T. Wong, Y.Y. Chien, R.T. Chen, C.F. Wang, Y.T. Lin, H.H. Chiang, P.Y. Hsieh, C.C. Wu, C.H. Chou, Y.O. Su, G.P. Lee, S.M. Peng, J. Am. Chem. Soc. 124 (2002) 11576;
Y.H. Kim, D.C. Shin, S.H. Kim, C.H. Ko, H.S. Yu, Y.S. Chae, S.K. Kwon, Adv. Mater. 13 (2001) 1690.
[10] G. Zeng, W.L. Yu, S.J. Chua, W. Huang, Macromolecules 35 (2002) 6907;
X. Gong, P.K. Iyer, D. Moses, G.C. Bazan, A.J. Heeger, S.S. Xiao, Adv. Funct. Mater. 13 (2003) 325;
M. Gaal, E.J.W. List, U. Scherf, Macromolecules 36 (2003) 4236;
Q. Pei, Y. Yang, J. Am. Chem. Soc. 79 (1996) 934;
M. Kreyenschmidt, G. Klaerner, T. Fuhrer, S. Ashenhurst, J. Karg, W.D. Chen, V.Y. Lee, J.C. Scott, R.D. Miller, Macromolecules 31 (1998) 1099;
U. Scherf, E.J.W. List, Adv. Mater. 14 (2002) 477.
[11] A. Grice, D.D.C. Bradley, M. Grell, M.D. Bradley, M.T. Bernius, M. Inbasekaran, W.W. Wu, E.P. Woo, Appl. Phys. Lett. 73 (1998) 629.
[12] M.P. de Jong, L.J. Ijzendoorn, M.J.A. de Voigt, Appl. Phys. Lett. 77 (2000) 2255;
K.W. Wong, H.L. Yip, Y. Luo, K.Y. Wong, W.M. Lau, K.H. Low, H.F. Chow, Z.Q. Gao, W.L. Yeung, C.C. Chang, Appl. Phys. Lett. 80 (2002) 2788.
[13] B.C. Ego, F.U. Grimsdale, G. Yu, G. Srdanov, K. Müllen, Adv. Mater. 14 (2002) 809.
[14] K. Yamana, M. Takei, H. Nakano, Tetrahedron Lett. 38 (1997) 6051.
[15] T. Otsubo, Y. Aso, K.J. Takimiya, J. Mater. Chem. 12 (2002) 2565;
W.L. Jia, T.M. Cormick, Q.D. Liu, H. Fukutani, M. Motala, R.Y. Wang, Y. Tao, S.J. Wang, J. Mater. Chem. 14 (2004) 3344.
[16] C.C. Wu, Y.T. Lin, H.H. Chiang, T.Y. Cho, C.W. Chen, K.T. Wong, Y.L. Liao, G.H. Lee, S.M. Peng, Appl. Phys. Lett. 81 (2002) 577;
W.J. Shen, R. Dodda, C.C. Wu, F.I. Wu, T.H. Liu, H.H. Chen, C.H. Chen, C.F. Shu, Chem. Mater. 16 (2004) 930.
[17] G.Y. Zhong, Z. Xu, J. He, S.T. Zhang, Y.Q. Zhan, X.J. Wang, Z.H. Xiong, H.Z. Shi, X.M. Ding, W. Huang, X.Y. Hou, Appl. Phys. Lett. 81 (2002) 1122;
C. Ego, D. Marsitzky, S. Becker, J. Zhang, G.C. Grimsdale, K. Müllen, J.D. MacKenzie, C. Silva, R.H. Friend, J. Am. Chem. Soc. 125 (2003) 437;
J.-R. Gong, L.-J. Wan, S.-B. Lei, C.-L. Bai, X.-H. Zhang, S.-T. Lee, J. Phys. Chem. B. 109 (2005) 1675.
[18] J. Shi, C.W. Tang, Appl. Phys. Lett. 80 (2002) 3201;
C. Hosokawa, H. Higashi, H. Nakamura, T. Kusumoto, Appl. Phys. Lett. 67 (1995) 3853;
Y. Li, M.K. Fung, Z. Xie, S.-T. Lee, L.-S. Hung, J. Shi, Adv. Mater. 14 (2002) 1317.
[19] L.-H. Chan, H.-C. Yeh, C.-T. Chen, Adv. Mater. 13 (2001) 1637;
Y.H. Kim, D.C. Shin, S.H. Kim, C.H. Ko, H.S. Yu, Y.S. Chae, S.K. Kwon, Adv. Mater. 13 (2001) 1690;
C.C. Wu, Y.-T. Lin, K.-T. Wong, R.-T. Chen, Y.-Y. Chien, Adv. Mater. 16 (2004) 61;
A.P. Kulkarni, A.P. Gifford, C.J. Tonzola, S.A. Jenekhea, Appl. Phys. Lett. 86 (2005) 061106.
[20] S. Tao, Z. Peng, X. Zhang, P. Wang, C.-S. Lee, S.-T. Lee, Adv. Funct. Mater. 15 (2005) 1716.
[21] N. Miyaura, A. Suzuki, Chem. Rev. 95 (1995) 2457.
[22] S. Hamal, F. Hirayama, J. Phys. Chem. 87 (1983) 83.
[23] D.M. de Leeuw, M.M.J. Simenon, A.R. Brown, R.E.F. Einerhand, Synth. Met. 87 (1997) 53;
R. Cervini, X.C. Li, G.W.C. Spencer, A.B. Holmes, S.C. Moratti, R.H. Friend, Synth. Met. 84 (1997) 359.

Available online at www.sciencedirect.com
SCIENCE DIRECT
Organic Electronics 7 (2006) 163–172
Organic Electronics
www.elsevier.com/locate/orgel

Reduced geminate recombination in iridium-based electrophosphorescent materials

R.J. Holmes [a], S.R. Forrest [a,*], T. Sajoto [b], A. Tamayo [b], P.I. Djurovich [b], M.E. Thompson [b]

[a] *Department of Electrical Engineering, Princeton Institute for the Science and Technology of Materials (PRISM), Princeton University, Princeton, NJ 08544, United States*
[b] *Department of Chemistry, University of Southern California, Los Angeles, CA 90089, United States*

Received 25 November 2005; received in revised form 20 February 2006; accepted 2 March 2006
Available online 4 April 2006

Abstract

We demonstrate reduced geminate recombination of excitons in electrophosphorescent organic light emitting devices using the green phosphor *fac*-tris(1-(9′,9′-dimethyl-2′-fluorenyl)pyrazolato,N,C^2)iridium(III). At low phosphor doping concentrations (<20 wt.%) in a N,N'-dicarbazolyl-3,5-benzene host, transient electroluminescence spectra show no bimolecular quenching at the highest excitation densities used. At higher doping concentrations (>60 wt.%), the transient decay reflects the presence of phosphor molecular aggregates. The roll-off in external quantum efficiency at high current densities is attributed to the field-assisted dissociation of charge pairs prior to exciton formation.

PACS: 73.61.Ph; 78.30.Jw; 78.60.Fi

Keywords: Phosphorescence; Organic light emitting devices; Exciton quenching

1. Introduction

Phosphorescent materials consisting of cyclometalated iridium complexes have been used to demonstrate efficient electrophosphorescence with near unity internal quantum efficiencies [1]. Organic light emitting devices (OLEDs) employing phosphor light emitting materials typically experience a pronounced decrease in the external quantum efficiency (η_{EXT}) under intense electrical excitation [2–4]. These bimolecular quenching processes have limited the use of phosphorescent emitters in high brightness applications accessed at large current densities. Further, lasing from phosphorescent emitters has seldom been considered as a result of strong exciton–exciton and exciton–polaron quenching [5]. Hence, the reduction of non-radiative pathways has the potential to enable the application of these highly efficient emitters in a greater variety of optoelectronic devices.

In materials systems that employ host-dopant energy transfer, including most Pt-based phosphor

* Corresponding author.
E-mail address: stevefor@umich.edu (S.R. Forrest).

1566-1199/$ - see front matter © 2006 Elsevier B.V. All rights reserved.
doi:10.1016/j.orgel.2006.03.009

OLEDs, the roll-off in η_{EXT} is attributed to triplet–triplet (T–T) annihilation [2,6]. However, the current understanding of bimolecular quenching remains incomplete in Ir-based phosphor OLEDs. For example, in the archetypical *fac*-tris(2-phenylpyridine)iridium(III) [Ir(ppy)$_3$], the T–T model does not fully describe the steady-state and transient luminescent behavior under both optical and electrical excitation [2–4]. To our knowledge, no discussion of the biexponential transient decay characteristic of Ir(ppy)$_3$ OLEDs under pulsed electrical excitation has been offered beyond that of a modified T–T annihilation model [2].

In this work, we examine phosphorescence from the green emitter *fac*-tris(1-(9′,9′-dimethyl-2′-fluorenyl)pyrazolato,N,C^2)iridium(III) [Ir(flz)$_3$] [7] under both optical and electrical excitation. Transient photoluminescence (PL) measurements show no evidence for bimolecular quenching, even at the highest excitation densities employed. Transient electroluminescence (EL) from the phosphor exhibits biexponential decay at low excitation densities, with the short lifetime component of the decay originating from the quenching of triplet excitons by Ir(flz)$_3$ cations. Under high excitation, this additional source of non-radiative loss is reduced, and the resulting decay is characterized by the natural radiative lifetime of the phosphor. Under steady-state electrical excitation, the roll-off in η_{EXT} with brightness results from the electric-field induced quenching of charge pairs (CPs) prior to exciton formation [4,8]. At high concentrations of Ir(flz)$_3$ (>60 wt.%) in a N,N'-dicarbazolyl-3,5-benzene (mCP) host [9,10], both the steady-state and transient behaviors are dominated by emission from phosphor molecular aggregate states.

2. Theory

2.1. Exciton quenching by trapped charge

Exciton formation in phosphorescent guest–conductive host systems generally relies on a combination of host–guest energy transfer [10–12], and charge trapping directly on the phosphor dopant [13,14]. Charge trapping is particularly important for deep-blue phosphorescent OLEDs where exciton formation on the wide energy gap host becomes energetically difficult to achieve [13,14]. Depending on the host and phosphor transport energy levels, such systems may exhibit poor charge balance at low current densities due to the preferential injection and/or transport of one type of carrier in the device emissive layer (EML). In such unbalanced systems, preferential build-up of one type of charge can serve as a quenching site for excitons [15]. In this discussion, the triplet quenching centers are holes trapped on the phosphorescent guest. Assuming that the number of trapped holes is much larger than that of electrons or excitons in the EML, the injected hole density is approximately voltage independent. For excitons located far from a trapped hole, the transient luminescence decay time is the natural lifetime of the phosphor, namely $1/k_T$, where k_T is the sum of the radiative (k_R) and non-radiative (k_{NR}) decay rates. However, in the presence of a trapped hole, the rate equation governing the triplet exciton density ($[T^*(t)]$) is [15]

$$\frac{d[T^*(t)]}{dt} = -k_T[T^*(t)] - k_{hT}[h][T^*(t)] \quad (1)$$

where k_{hT} is the rate constant for interactions between trapped holes of density $[h]$, and triplet excitons. Accounting for both cases leads to the following biexponential solution:

$$[T^*(t)] = [T^*(0)]\left[\left(1 - \frac{[h]}{N}\right)\exp(-k_T t) + \frac{[h]}{N}\exp(-(k_T + k_{hT}[h])t)\right], \quad (2)$$

where N is the total number of Ir(flz)$_3$ molecules in the film. The coefficients containing $[h]/N$ are branching probabilities for exciton formation on a neutral Ir(flz)$_3$ molecule versus a quenching site. In this simplified model we assume that a triplet is quenched when it occupies the same molecular site as a trapped hole. This is expected to be valid for systems where exciton formation occurs directly on phosphorescent molecules by charge trapping, a process that ultimately reduces exciton diffusivity.

Exciton quenching by trapped charges is expected to be strongly dependent on both $[T^*]$ and $[h]$. The number of trapped holes remains constant over time since hole injection into the EML is highly efficient. In contrast, the number of electrons increases steeply with applied voltage due to injection barrier lowering. The increased electron density in the EML leads to a reduction in the number of trapped holes since they pair with injected electrons to form triplets. As a result, quenching is expected to decrease with increasing excitation density, reducing the contribution of the second term in Eq. (1).

2.2. Electric field induced dissociation of charge pairs

The electric field in an OLED is often sufficient to separate CPs prior to exciton formation, giving rise to the roll-off in luminance often observed at high steady state voltages (and hence correspondingly high current densities) [4]. In this case, the CP can be treated as an electron in a positively ionized trap (molecular cation) whose depth is determined by the external electric field, F. Using the Poole–Frenkel model, the rate of dissociation is expressed as [8]

$$k_{\mathrm{PF}}(F) = k_0 \exp(\beta\sqrt{F}/k_{\mathrm{B}}T) \tag{3}$$

where k_0 is the zero-field rate of dissociation, k_{B} is Boltzmann's constant, T is the temperature. In one dimension, $\beta = (e^3/\pi\varepsilon\varepsilon_0)^{1/2}$ where e is the elementary charge, ε is the material dielectric constant, and ε_0 is the permittivity of free space. If a CP ultimately forms an exciton, its recombination rate is governed by the natural lifetime of the exciton. If, instead, it dissociates, the carrier pair may reform a CP, non-radiatively recombine, or contribute to current. In all cases, field dissociation ultimately reduces the radiative efficiency. The probability for CP dissociation is [4]

$$\eta_{\mathrm{PF}}(F) = \frac{1}{1 + \frac{k_{\mathrm{Ex}}}{k_0}\exp(-\beta\sqrt{F}/k_{\mathrm{B}}T)} \tag{4}$$

where k_{Ex} is the rate at which a CP relaxes to form an exciton. The quenching efficiency, δ, can be expressed as

$$\delta = \frac{\eta_{\mathrm{EXT}}(F_0) - \eta_{\mathrm{EXT}}(F)}{\eta_{\mathrm{EXT}}(F_0)} = \frac{\eta_{\mathrm{PF}}(F) - \eta_{\mathrm{PF}}(F_0)}{1 - \eta_{\mathrm{PF}}(F_0)} \tag{5}$$

Hence, when field assisted dissociation is dominant, then

$$\eta_{\mathrm{EXT}}(F) = \eta_{\mathrm{EXT}}(F_0)(1 - \delta) \tag{6}$$

leading to a roll-off in luminance with F.

3. Experimental methods

The electrophosphorescent properties of Ir(flz)$_3$ were investigated using thin film structures grown by vacuum thermal sublimation at a base pressure of $\sim 1 \times 10^{-7}$ Torr, on a pre-cleaned [13], glass substrate coated with a ~150-nm-thick layer of indium-tin-oxide (ITO) having a sheet resistance of ~20 Ω/□. The devices consisted of a 30-nm-thick 4-4′-bis[*N*-(1-naphthyl)-*N*-phenyl-amino]biphenyl (NPD) hole transport layer (HTL), followed by a 10-nm-thick layer of the electron–exciton blocker (EBL) *fac*-tris(1-phenylpyrazolato,*N*,$C^{2'}$)iridium(III) [Ir(ppz)$_3$] [9]. The 30-nm-thick EML consisted of Ir(flz)$_3$ co-deposited with mCP at various doping concentrations. Finally, a 40-nm-thick electron transport layer (ETL) of 2,9-dimethyl-4,7-diphenyl-1,10-phenanthroline (bathocuproine, BCP) was deposited to confine holes and excitons within the EML. Cathodes consisted of a 0.5-nm-thick layer of LiF followed by a 50-nm-thick layer of Al deposited through 1 mm diameter openings in a shadow mask. Literature procedures were used to prepare NPD [16], Ir(ppz)$_3$ [9], mCP [9], and Ir(flz)$_3$ [7], while BCP was commercially obtained [17]. All materials were purified prior to use by thermal gradient vacuum sublimation [18].

Devices were tested under steady-state[19] and pulsed excitation. Transient EL and PL (excited at a wavelength of $\lambda = 337$ nm, with 1 ns pulses and a 60 Hz repetition rate) were collected using a streak camera.

4. Results

Fig. 1 shows the molecular structure, and the EL and PL spectra of Ir(flz)$_3$ doped at 10 wt.% into mCP [9,10]. The EL originates solely from Ir(flz)$_3$ and has Commission Internationale de l'Eclairage (CIE) chromaticity co-ordinates of ($x = 0.26$, $y = 0.56$). The inset of Fig. 1 shows the highest occupied (HOMO) and lowest unoccupied molecular orbital (LUMO) energies for the materials used. The HOMO energies were measured using photoelectron spectroscopy, while the LUMO levels were estimated from the optical absorption edge energy for each material [20,21]. This method tends to underestimate the HOMO–LUMO transport gap since it includes the binding energy of the exciton. The low HOMO energy of Ir(flz)$_3$ relative to mCP allows this dopant to trap and transport holes to the EML/BCP interface. This is apparent from the data in the inset in Fig. 2 where the device operating voltage decreases with increasing doping concentration [13]. Hence, we infer that the LUMO of Ir(flz)$_3$ is not directly populated by injected electrons. Peak quantum and power efficiencies (η_{P}), of $\eta_{\mathrm{EXT}} = (6.1 \pm 0.6)\%$ and $\eta_{\mathrm{P}} = (11.3 \pm 1.1)$ lm/W (measured through the anode normal to the substrate plane) are obtained for mCP:10 wt.% Ir(flz)$_3$ OLEDs, respectively. The hole mobility of the NPD HTL is significantly larger

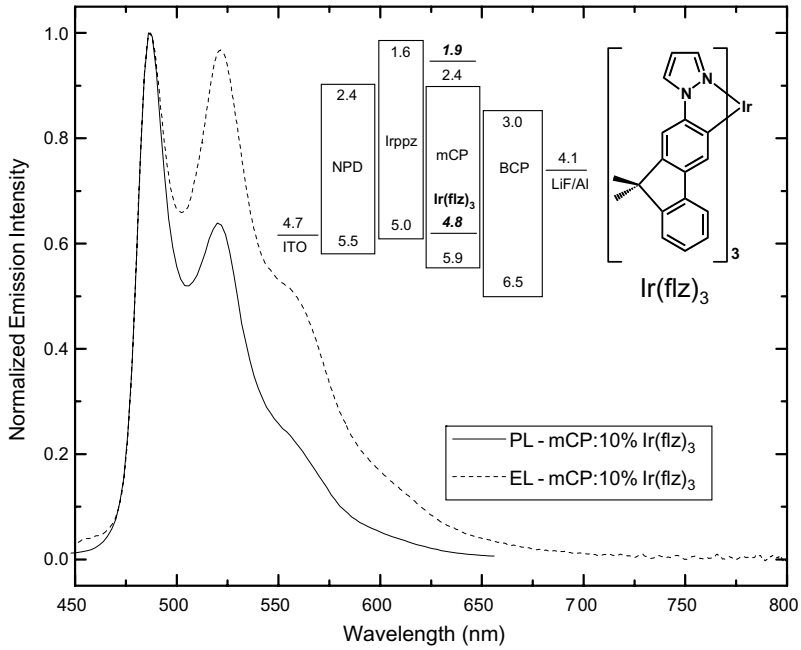

Fig. 1. The molecular structural formula, photoluminescence and electroluminescence spectra of 10 wt.% $Ir(flz)_3$ in mCP. Inset: Proposed equilibrium energy level scheme for the device used to observe electrophosphorescence.

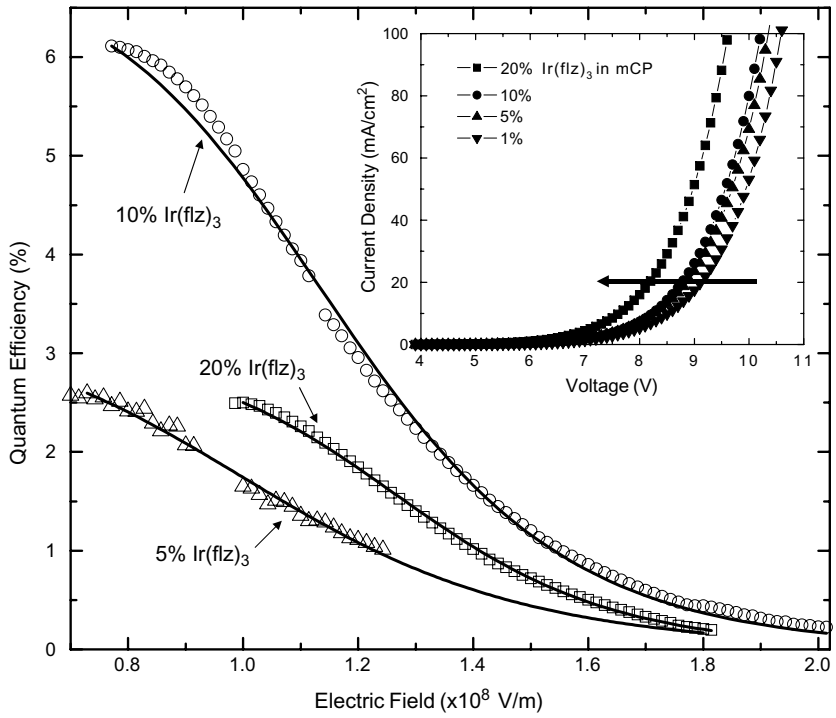

Fig. 2. Device quantum efficiency plotted versus external electric field as a function of doping concentration for a ITO/NPD (30 nm)/$Ir(ppz)_3$ (10 nm)/mCP:*x* wt.% $Ir(flz)_3$ (30 nm)/BCP (40 nm)/LiF (0.5 nm)/Al (50 nm) test OLED. The quantum efficiency is fit (—) using the Poole–Frenkel model of field assisted charge pair dissociation described in text. Inset: Current density–voltage characteristics for devices in the figure as a function of the $Ir(flz)_3$ concentration in mCP. The arrow indicates the direction of increasing $Ir(flz)_3$ concentration.

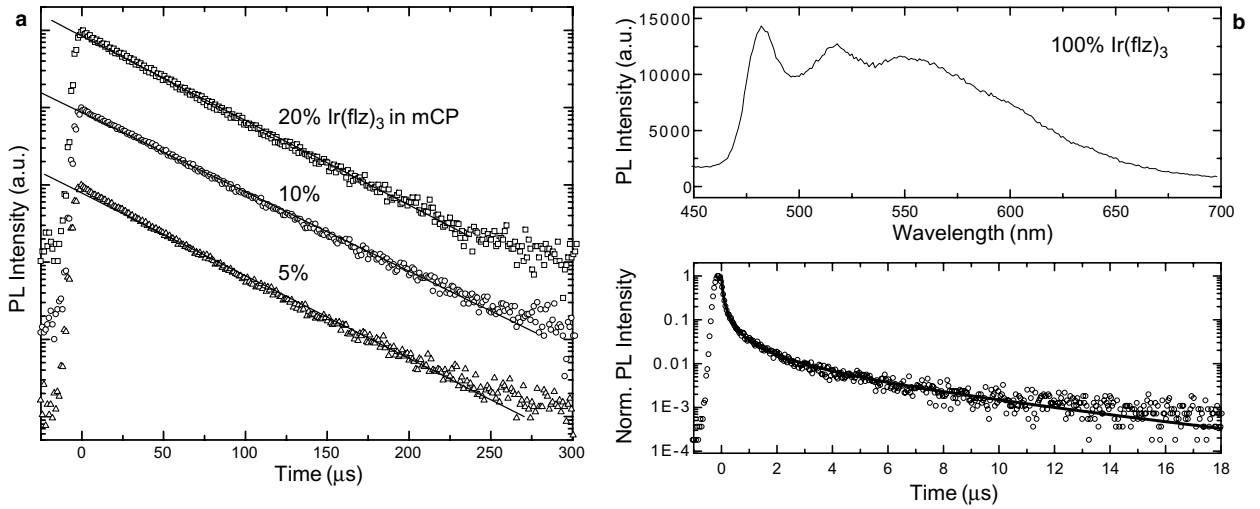

Fig. 3. (a) Transient photoluminescence decay for $Ir(flz)_3$ in mCP as a function of doping concentration, for an excitation density of 10^{13} photons/cm^2 (per 1 ns pulse) at a wavelength of $\lambda = 337$ nm. (b) Top: The photoluminescence spectrum of a neat film of $Ir(flz)_3$ under excitation at $\lambda = 337$ nm. Bottom: The corresponding transient decay for a neat film of $Ir(flz)_3$, fit to a model of triplet–triplet annihilation (—); see Ref. [2].

than the electron mobility of the BCP ETL, hence the external electric field is calculated by dividing the applied voltage by the combined thicknesses of the EML and ETL.

Bimolecular quenching was probed under both transient optical and electrical excitation. Fig. 3a shows the transient PL decay under an excitation density of 10^{13} photons/cm^2 for films of 5–20 wt.% $Ir(flz)_3$ doped into mCP. For reference, Fig. 3b depicts the PL spectrum and transient decay of a neat $Ir(flz)_3$ film. The broad spectral feature spanning wavelengths from $\lambda = 550$ to 650 nm is

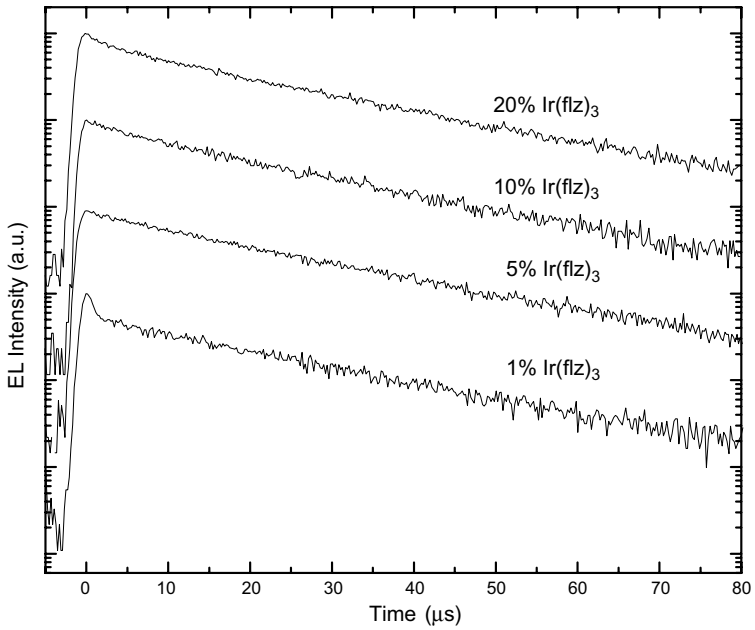

Fig. 4. Transient electroluminescent decay for devices in Fig. 2 as a function of $Ir(flz)_3$ concentration in mCP. The exciting pulse width is 500 ns, with an amplitude of 0–11.5 V.

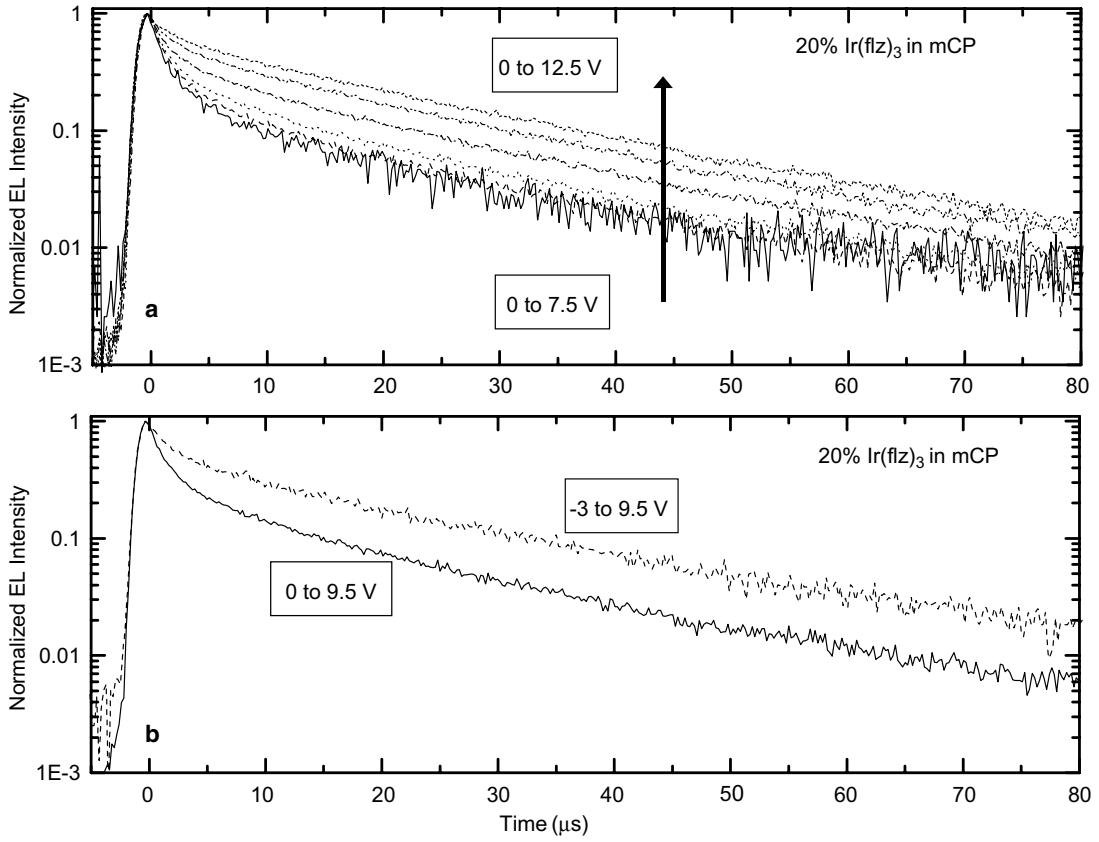

Fig. 5. (a) Transient electroluminescent decay for the device in Fig. 2 as a function of voltage pulse amplitude. The arrow indicates the direction of increasing peak pulse voltage, from 7.5 V to 12.5 V in 1 V steps. (b) Transient electroluminescent decay of the same device for 9.5 V voltage pulses with a baseline of either 0 V or −3 V.

emission from aggregates formed between neighboring molecules.

Fig. 4 shows the dependence of the transient EL decay on $Ir(flz)_3$ concentration; the drive current density in all cases is >100 mA/cm^2. Under these high injection levels, the transient decays are linear, showing little evidence for bimolecular quenching. Fig. 5a shows the transient EL decay as a function of drive voltage (with the return-to-zero pulse amplitude varied from 7.5 V to 12.5 V) for an EML consisting of 20 wt.% $Ir(flz)_3$ in mCP. Biexponential decays are observed at small input pulse amplitudes, with the initial rapid decay reduced at large pulse amplitudes. Similar trends are observed as a function of pulse amplitude for lower doping concentrations, with the initial rapid decay becoming less pronounced at reduced doping levels. When the pulse baseline is moved from 0 V to −3 V, as in Fig. 5b, the initial rapid decay is also suppressed.

Fig. 6a shows representative transient EL decays collected for devices doped at 10 wt.% and 20 wt.% $Ir(flz)_3$ in mCP.

5. Discussion

5.1. Steady state quantum efficiency roll-off

The exponential decays observed in transient PL and EL (Figs. 3 and 4) provide evidence that bimolecular exciton quenching processes are not responsible for the roll-off in η_{EXT} observed at high electric fields in Fig. 2, but rather they may be due to field induced dissociation of CP states, as previously suggested for similar iridium-based phosphors [4].

In Fig. 2, the roll-off in η_{EXT} at room temperature as a function of applied electric field and doping concentration is fit using Eq. (6) and the parameters in Table 1. Here, $\eta_{EXT}(F_0)$ and F_0 are

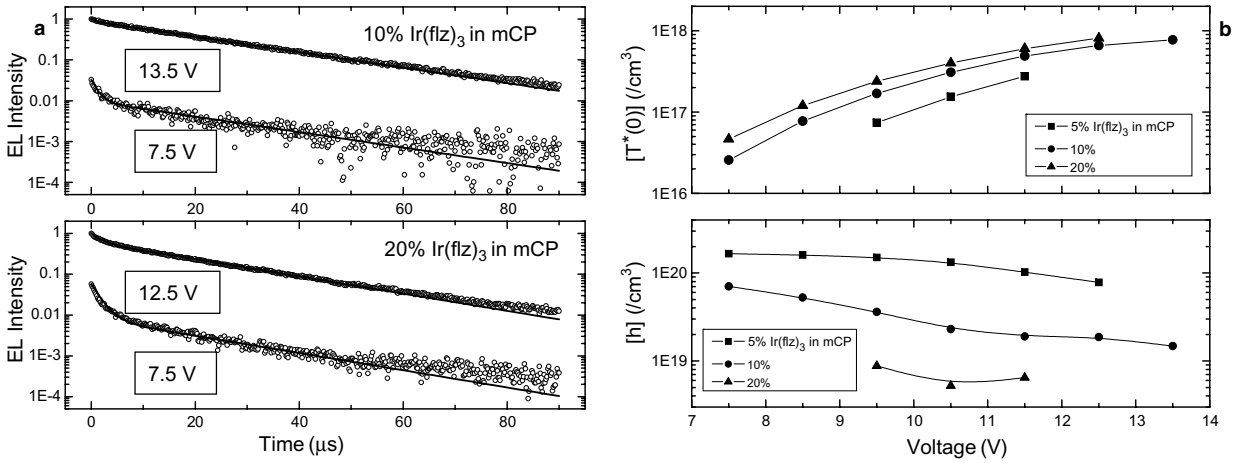

Fig. 6. (a) Transient electroluminescent decays at low and high applied bias for devices containing 10 wt.% (top) and 20 wt.% (bottom) $Ir(flz)_3$ in mCP. Solid line indicates best fit to Eq. (2) in text. (b) Variation of parameters obtained from fitting transient electroluminescence decays with Eq. (2) as a function of both voltage and doping concentration.

Table 1
Parameters for the field induced quenching fits of Fig. 2

% $Ir(flz)_3$	$\beta(C^2mV)^{1/2}$	$F_0(V/m)$	$k_{Ex}/k(F=0)$	$\eta_{EXT}(F_0)$
5	3.99×10^{-24}	7.3×10^{7}	1.9×10^{3}	2.6%
10	4.75×10^{-24}	7.7×10^{7}	2.0×10^{4}	6.1%
20	5.44×10^{-24}	1.0×10^{8}	2.2×10^{5}	2.5%

taken from the experimental data in Fig. 2 at the electric field where η_{EXT} is at a maximum. Since the exciton non-radiative decay rate is nearly constant as a function of doping concentration, the variation of $\eta_{EXT}(F_0)$ reflects changes in charge trapping efficiency and charge balance in the EML.

The ratio, k_{Ex}/k_0, increases with doping concentration, suggesting that at $F=0$, exciton formation becomes increasingly favorable relative to dissociation as the doping concentration is increased. Since the CPs span multiple molecular sites, k_{Ex} will reflect the ability of the two carriers to migrate to a common molecular site and undergo exciton formation. This migration should be strongly influenced by the conductivity of the EML, which is observed to increase with doping concentration (Fig. 2, inset). The values obtained for β are consistent with a material dielectric constant of $\varepsilon \sim 5$, 7 and 9 for doping concentrations of 20 wt.%, 10 wt.% and 5 wt.% $Ir(flz)_3$, respectively. These values are somewhat larger than those typically encountered in organic materials and reflect the limitations of the 1D analysis employed. Improvements to the current analysis can be made by implementing a 3D model of Poole–Frenkel barrier lowering to account for dissociation out of the plane [22]. Further adjustments to the model are needed to account for the significant number of positive charges trapped in the EML, and potentially large built-in fields at low applied voltages.

5.2. Transient photoluminescence

In Fig. 3a, the transient photoluminescence for films of 5 wt.%, 10 wt.% and 20 wt.% $Ir(flz)_3$ doped into mCP are fit with single exponential decays to yield an average phosphorescent lifetime of (37.1 ± 1.4) μs. These intensity independent fits confirm the absence of bimolecular quenching under optical excitation at low doping concentrations ($\leqslant$20%). Fig. 3b shows the PL spectrum and transient decay for a neat film of $Ir(flz)_3$. In contrast to the data in Fig. 3a, the transient decay of the spectrally broad feature with a peak at $\lambda = 550$ nm that is attributed to phosphorescence from aggregates shows significant curvature. The decay is fit to a model of T–T annihilation to give $k_{TT} = 1.7\times10^{-11}$ cm^3/s and $\tau = 5.9$ μs for the T–T annihilation rate and natural radiative lifetime of the phosphor, respectively [2]. Thus, under optical excitation T–T

annihilation becomes significant only at the highest doping concentrations (>60 wt.%) explored.

5.3. Exciton quenching by trapped charge

From the energy level diagram in Fig. 1, we infer that holes are readily injected from the ITO anode into the Ir(flz)$_3$ HOMO. In contrast, electron injection from the LiF/Al cathode is less efficient due to the several large energy barriers interposed between the contact and the Ir(flz)$_3$ LUMO. Therefore, we conclude that the short lifetime component of the biexponential decay observed at low voltage in Fig. 5a arises from triplet excitons that are quenched by Ir(flz)$_3$ cations (see Section 2). At low pulse amplitudes, trapped holes on Ir(flz)$_3$ cations act as exciton quenching centers. As the voltage is increased, the barrier to electron injection is lowered, resulting in improved charge balance. This in turn leads to a decrease in the number of Ir(flz)$_3$ cations, and hence a reduction in the number of excitons quenched by trapped charges. In Fig. 5b, the transient decay for a device containing 20 wt.% Ir(flz)$_3$ in mCP is shown for 9.5 V pulses, with either a 0 V or −3 V reverse bias applied between pulses. When a −3 V bias is applied, trapped positive charge is swept out of the EML reducing the number of Ir(flz)$_3$ cations and, hence, quenching is also reduced. This results in the initial rapid decay becoming less pronounced, as observed.

The rapid component of the biexponential decay at low voltage is more prominent at higher doping concentrations ($\geqslant$20 wt.%). As the concentration of Ir(flz)$_3$ is increased, there are more hole trapping sites, and hence more quenching. At reduced doping concentrations, the initial rapid decay vanishes at low voltage since fewer electrons are required to neutralize the trapped holes.

The fits in Fig. 6a (solid lines) to the transient data for OLEDs doped with 10 wt.% and 20 wt.% Ir(flz)$_3$ in mCP are obtained using Eq. (2). The parameters used for the fits are listed in Table 2, and are plotted in Fig. 6b. The bimolecular quenching parameter k_{hT} is expected to vary only weakly with doping concentration. In Fig. 6b (top) the triplet exciton density at $t = 0$ is estimated from steady state optical power density ($P_{optical}$) measurements using $[T^*(0)] = P_{optical}\tau_R/(\eta_{OC}d_{rec})$, where η_{OC} is the outcoupling efficiency (~0.2) [23,24], d_{rec} is the width of the exciton recombination zone, approximately equal to the EML thickness (~30 nm), and τ_R is the exciton radiative lifetime. In Ref. [7], the thin film PL efficiency of Ir(flz)$_3$ is estimated to be ~1 from the temperature dependence of the PL decay rate, such that τ_R should equal the PL decay lifetime of (37.1 ± 1.5) μs.

Table 2
Parameters for the biexponential fits of Fig. 6

% Ir(flz)$_3$	k_T (μs^{-1})	k_{hT} (cm^3/μs)
5	0.043	4.8×10^{-20}
10	0.043	1.2×10^{-20}
20	0.052	3.8×10^{-21}

The density of trapped positive charge is extracted directly from the fits of Fig. 6a, and is plotted versus voltage in Fig. 6b. The total number of Ir(flz)$_3$ molecules, N is taken as 2×10^{20} cm^{-3}, 1×10^{20} cm^{-3} and 5×10^{19} cm^{-3} for doping levels of 20 wt.%, 10 wt.% and 5 wt.% Ir(flz)$_3$ in mCP, respectively. The density of quenching sites remains constant as a function of voltage for the 5 wt.% Ir(flz)$_3$ in mCP device. For 10 wt.% Ir(flz)$_3$ in mCP, the trap density decreases monotonically until it saturates near the same density obtained for the 5 wt.% device. The 20 wt.% Ir(flz)$_3$ in mCP film is expected to saturate as well, but at a larger voltage since more electrons are required to neutralize the quenching sites than in the more lightly doped films.

The voltage dependence of $[h]$ depends on the mechanism for electron injection into the EML. If electron injection increases exponentially with applied voltage due to Poole–Frenkel field induced barrier lowering [8], $[h]$ is expected to remain constant until the exponential term becomes significant, after which point the hole density decreases exponentially as trapped holes are paired with electrons to form excitons. This dependence is inferred from Fig. 6b in the dependence of $[h]$ on voltage for both 10 wt.% and 20 wt.% Ir(flz)$_3$ in mCP. The natural phosphorescent decay rate (k_T) in Table 2, is roughly independent of doping concentration. Experimentally, the quenching constant k_{hT} is observed to decrease with increasing doping concentration (Table 2). For low doping concentrations (5 wt.%), hole transport may actually occur on both host and guest molecules. Thus, in treating only phosphor sites as hole traps, the maximum number of trapping sites N (Eq. (2)) is underestimated. This underestimate leads to an overestimation of the quenching constant and to the dependence of k_{hT} on doping concentration already noted. At 20 wt.% doping, hole transport is expected to occur exclusively on the phosphor guest, allowing for a more accurate estimate of k_{hT}.

The triplet energy of BCP is smaller than that of $Ir(flz)_3$ [11], thus it is important to rule out possible energy transfer from $Ir(flz)_3$ to BCP as the origin of the biexponential decays observed under electrical excitation. This process is expected to occur by Dexter transfer between the triplet levels of $Ir(flz)_3$ and BCP since Förster transfer from the $Ir(flz)_3$ triplet to the BCP singlet is not energetically favorable.

To test whether this process is occurring, we compare the transient EL decays of mCP:$Ir(flz)_3$ (Figs. 5 and 6a) to those reported for a stacked, 2-cell, white organic light emitting device (WOLED) that also uses $Ir(flz)_3$ doped into mCP as an active layer [25,26]. In the device of Ref. [25], the mCP:$Ir(flz)_3$ layer is spatially separated from the ETL (consisting of 4,7-diphenyl-1,10-phenanthroline or BPhen), and hence, the quenching interface by a 5 nm thick layer of *N*,*N*′-dicarbazolyl-4-4′-biphenyl (CBP) doped with the phosphors *fac*-tris(2-phenylpyridinato-$N,C^{2'}$)iridium(III) [$Ir(ppy)_3$] and bis(2-phenyl quinolyl-$N,C^{2'}$)acetylacetonate iridium(III) (PQIr). This interlayer prevents direct Dexter transfer between $Ir(flz)_3$ and BPhen. Exciton diffusion to the quenching interface should also be limited since triplet excitons that diffuse into CBP should rapidly transfer to lower energy $Ir(ppy)_3$ and PQIr molecules before reaching the interface. Thus, if interface quenching was responsible for the biexponential decays observed in Figs. 5 and 6a, no such behavior should be observed in the WOLED structure under similar conditions. However, the transient EL from the WOLED structure is characterized by biexponential decays that are analogous to those observed for $Ir(flz)_3$-only devices [26]. This suggests that the interface is not the source of the quenching observed for the WOLED, nor for the $Ir(flz)_3$ structure shown in the inset of Fig. 1. In fact, the dependence of the WOLED transients on voltage is very similar to that of the $Ir(flz)_3$ devices discussed here [26]. Further, the fact that the quenching in the stacked WOLED persists at even larger voltages than those of Fig. 6 is consistent with the mCP:$Ir(flz)_3$ layer of the WOLED remaining hole-rich/electron-starved to larger drive voltages as a result of electron trapping on $Ir(ppy)_3$ and PQIr.

6. Conclusion

Reduced bimolecular exciton quenching is observed under high excitation of the green phosphor $Ir(flz)_3$. Under low excitation, quenching results from trapped positive charge on the phosphorescent guest. The roll-off in η_{EXT} is attributed to field-assisted dissociation of CPs prior to exciton formation. Since the remaining, dominant non-radiative loss mechanism depends exclusively on the device electric field, additional refinements in device design should ultimately allow this quenching mechanism to be minimized.

Reduced geminate recombination in $Ir(flz)_3$ is of general importance as it provides insight into the behavior of phosphors under intense electrical excitation. Specifically, applications that seek to use phosphorescent OLEDs for solid state lighting [27,28] can benefit from reduced non-radiative loss under high device luminance conditions. These materials may also aid in the design of potential active media for organic lasers; a phenomenon that to our knowledge has yet to be reported under either optical or electrical excitation of phosphors due to their strong luminance-dependent excited state quenching properties.

Acknowledgement

This work was partially supported by the Air Force Office of Scientific Research, the Department of Energy Solid State Lighting Program, and Universal Display Corporation.

References

[1] C. Adachi, M.A. Baldo, M.E. Thompson, S.R. Forrest, J. Appl. Phys. 90 (2001) 5048.
[2] M.A. Baldo, C. Adachi, S.R. Forrest, Phys. Rev. B 62 (2000) 10967.
[3] J. Kalinowski, J. Mezyk, F. Meinardi, R. Tubino, M. Cocchi, D. Virgili, J. Appl. Phys. 98 (2005) 063532.
[4] J. Kalinowski, W. Stampor, J. Mezyk, M. Cocchi, D. Virgili, V. Fattori, P. Di Marco, Phys. Rev. B 66 (2002) 235321.
[5] M.A. Baldo, R.J. Holmes, S.R. Forrest, Phys. Rev. B 66 (2002) 035321.
[6] M.A. Baldo, D.F. O'Brien, Y. You, A. Shoustikov, S. Sibley, M.E. Thompson, S.R. Forrest, Nature (London) 395 (1998) 151.
[7] T. Sajoto, P.I. Djurovich, A. Tamayo, M. Yousufuddin, R. Bau, M.E. Thompson, R.J. Holmes, S.R. Forrest, Inorg. Chem. 44 (2005) 7992.
[8] J. Frenkel, Phys. Rev. 54 (1938) 647.
[9] V. Adamovich, J. Brooks, A. Tamayo, A.M. Alexander, P. Djurovich, B.W. D'Andrade, C. Adachi, S.R. Forrest, M.E. Thompson, New J. Chem. 26 (2002) 1171.
[10] R.J. Holmes, S.R. Forrest, Y.-J. Tung, R.C. Kwong, J.J. Brown, S. Garon, M.E. Thompson, Appl. Phys. Lett. 82 (2003) 2422.
[11] M.A. Baldo, S.R. Forrest, Phys. Rev. B 62 (2000) 10958.

[12] M.A. Baldo, S. Lamansky, P.E. Burrows, M.E. Thompson, S.R. Forrest, Appl. Phys. Lett. 75 (1999) 4.
[13] R.J. Holmes, B.W. D'Andrade, S.R. Forrest, X. Ren, J. Li, M.E. Thompson, Appl. Phys. Lett. 83 (2003) 3818.
[14] R.J. Holmes, S.R. Forrest, T. Sajoto, A. Tamayo, P.I. Djurovich, M.E. Thompson, J. Brooks, Y.-J. Tung, B.W. D'Andrade, M.S. Weaver, R.C. Kowng, J.J. Brown, Appl. Phys. Lett. 87 (2005) 243507.
[15] M. Pope, C.E. Swenberg, Electronic Processes in Organic Crystals and Polymers, second ed., Oxford University Press, New York, 1999.
[16] D.E. Loy, B.E. Koene, M.E. Thompson, P.E. Burrows, S.R. Forrest, Chem. Mater. 10 (1998) 2235.
[17] Bathocuproine, Cat. 14,091-0, Sigma–Aldrich Corp., St. Louis, MO.
[18] R.A. Laudise, C. Kloc, P.G. Simpkins, T. Siegrist, J. Cryst. Growth 187 (1998) 449.
[19] S.R. Forrest, D.D.C. Bradley, M.E. Thompson, Adv. Mater. 15 (2003) 1043.
[20] I.G. Hill, A. Kahn, J. Appl. Phys. 86 (1999) 4515.
[21] B.W. D'Andrade, S. Datta, S.R. Forrest, P. Djurovich E. Polikarpov, M.E. Thompson, Org. Electron. 6 (2005) 11.
[22] K.C. Kao, W. Hwang, Electrical Transport in Solids, Pergamon Press, New York, 1981.
[23] V. Bulovic, V.B. Khalfin, G. Gu, P.E. Burrows, D.Z. Garbuzov, S.R. Forrest, Phys. Rev. B 58 (1998) 3730.
[24] G. Gu, P.E. Burrows, S. Venkatesh, S.R. Forrest, M.E. Thompson, Opt. Lett. 22 (1997) 396.
[25] H. Kanno, R.J. Holmes, Y. Sun, S. Kena-Cohen, S.R. Forrest, Adv. Mater. 18 (2006) 339.
[26] H. Kanno, R.J. Holmes, Y. Sun, S. Kena-Cohen, S.R. Forrest, Presented at the Materials Research Society Fall Meeting, Boston, MA, 2005 (unpublished).
[27] B.W. D'Andrade, R.J. Holmes, S.R. Forrest, Adv. Mater. 16 (2004) 624.
[28] B.W. D'Andrade, S.R. Forrest, Adv. Mater. 16 (2004) 1585.

Available online at www.sciencedirect.com
SCIENCE DIRECT
Organic Electronics 7 (2006) 173–180
Organic Electronics
www.elsevier.com/locate/orgel

Letter

Non-volatile WORM memory device based on an acrylate polymer with electron donating carbazole pendant groups

E.Y.H. Teo [a], Q.D. Ling [b], Y. Song [a], Y.P. Tan [a], W. Wang [b], E.T. Kang [b], D.S.H. Chan [a], Chunxiang Zhu [a,*]

[a] Department of Electrical and Computer Engineering, National University of Singapore, 10 Kent Ridge, 119260, Singapore
[b] Department of Chemical and Biomolecular Engineering, National University of Singapore, 10 Kent Ridge, 119260, Singapore

Received 28 November 2005; received in revised form 6 March 2006; accepted 7 March 2006
Available online 18 April 2006

Abstract

A write-once read-many-times (WORM) memory device based on an acrylate polymer containing electron donating carbazole pendant groups, or poly(2-(9H-carbazol-9-yl)ethyl methacrylate) (PCz), was demonstrated. The as-fabricated device was found to be at its OFF state and could be programmed irreversibly to the ON state. The WORM device exhibited a high ON/OFF current ratio of up to 10^6, a long retention time in both ON and OFF states, a switching time of 1 ms, and number of read cycles up to $\sim 10^7$. Compared to that of poly(*N*-vinylcarbazole) (PVK), the well-defined memory property of PCz can be attributed to the presence of the spacer between the pendant carbazole group and the polymer backbone. The molecular spacer has allowed the transition of the pendant carbazole groups from the disoriented state to the ordered face-to-face conformation at the threshold voltage.

PACS: 73.61.Ph

Keywords: Polymer; Carbazole; Donor; Memory; WORM

1. Introduction

In recent years, several types of electronic devices based on conjugated polymers and molecules have been demonstrated, including light-emitting diodes [1], transistors [2], photo-detectors [3], thyristor [4] and switches [5]. The advantages of using organic materials lie in the ease of fabrication and low cost. Unlike the low molecular weight materials that are processed normally via evaporation under high vacuum, many polymers can be easily deposited by spin-coating. Recently, several excellent studies on functional memory devices based on organic materials have been reported [6,9–13]. For an organic material to function viably as a memory device, two basic features must be present: (1) it must possess a high ON/OFF current ratio between the conducting and non-conducting states in order to

* Corresponding author. Tel.: +65 65168930.
E-mail address: elezhucx@nus.edu.sg (C. Zhu).

1566-1199/$ - see front matter © 2006 Elsevier B.V. All rights reserved.
doi:10.1016/j.orgel.2006.03.003

minimize any error during the read cycle, and (2) the retention time in both ON and OFF states must be sufficiently long. Several studies have devoted to the understanding of memory effects in organic materials. These studies have included the understanding of conformation change [7], modification of conjugation [8,9] and oxidation–reduction process [11–13]. It has been shown that in the supramolecular structure of the Rose Bengal system, the presence of acceptor groups for the oxidation–reduction process is essential for the memory effect to achieve a reasonable ON/OFF current ratio [13]. Recently, a write-once read-many times (WORM) memory, utilizing the mechanism of current-controlled and thermally activated un-doping of a two-component electrochromic conducting polymer, viz., polyethylenedioxythiophene: poly(styrene sulfonic acid) (PEDOT) [14], has also been demonstrated. Among the reported non-volatile memory devices fabricated from polymers, the WORM type memory devices show the best retention time, which is critical to real applications. In this study, we show that an acrylate polymer containing the carbazole donor moiety in the pendant groups (PCz, structure shown in Fig. 1) also exhibits bi-stable states for WORM memory applications. By comparing the electrical characteristics of this polymer to those of poly(*N*-vinylcarbazole) (PVK), whose conductivity has been found to be related to the presence of carbazole groups [15–17], the memory effect or bi-stable states of PCz can be attributed to the susceptibility of carbazole groups to form a ''face-to-face conformation''. The flexible molecular spacer between the carbazole groups and the polymer backbone in PCz play an important role in the conduction mechanism of the polymer material.

2. Experimental

2.1. Preparation of the PCz

Poly(2-(9H-carbazol-9-yl)ethyl methacrylate), or PCz, was prepared in three steps: (1) synthesis of 2-(9H-carbazol-9-yl)ethanol (A1) from the reaction of 9H-cabarzole with 2-chloroethanol in the presence of potassium hydroxide and *N*,*N*′-dimethylformamide (DMF), (2) synthesis of the monomer, 2-(9H-carbazol-9-yl)ethyl methacrylate (M1), from the reaction of A1 with methacryloyl chloride in the presence of triethylamine and dry tetrahydrofuran, (3) polymerization of M1 to PCz in the presence of the 2,2′-azobisisobutyronitrile (AIBN) initiator [18]. The polymerization was carried out at 60 °C in DMF and under an argon atmosphere for 48 h. The resulting polymer, PCz, has a weight-average molecular weight of about 15,800 and a polydispersity index of about 2.36, as revealed by gel permeation chromatography (GPC) measurement. The

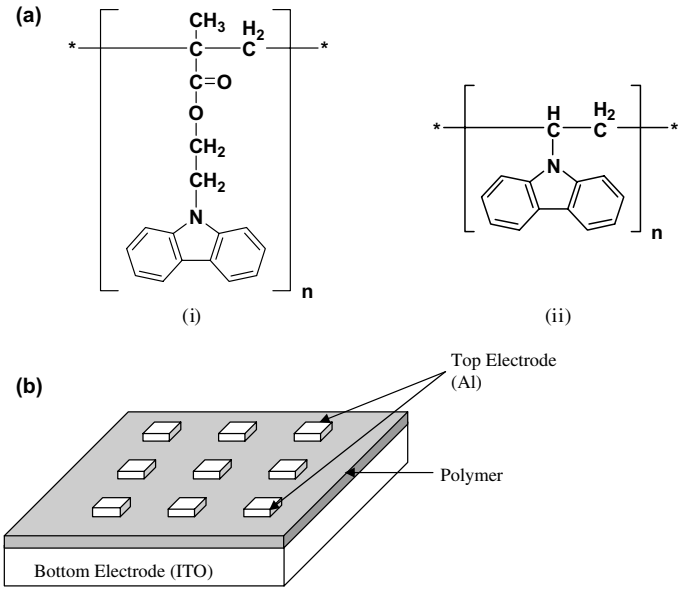

Fig. 1. (a) Molecular structure of (i) PCz and (ii) PVK, and (b) schematic diagram of the memory device consisting of a thin film (~50 nm) of PCz sandwiched between an indium–tin-oxide (ITO) substrate and an aluminum top electrode (0.2×0.2 mm^2, ~150 nm in thickness).

FT-IR spectrum of PCz shows the characteristic absorption bands at 3050 and 2938 cm^{-1} (C–H stretching of aliphatic segments), at 1729 cm^{-1} (C=O stretching vibration), and at 750 and 723 cm^{-1} (carbazole ring vibration). PCz exhibited good thermal stability, with an onset decomposition temperature of about 300 °C, and a glass transition temperature (T_g) of about 196 °C, as determined by thermogravimetric analysis and differential scanning calorimetry, respectively.

2.2. Fabrication and measurement of the memory device

Film of PCz of ~50 nm in thickness was spin-coated on indium–tin-oxide (ITO) glass substrate. The latter was cleaned, a prior, with deionized water, acetone and isopropanol, in an ultrasonic bath for 20 min. A portion of the polymer was removed to expose the bottom ITO electrode. A layer of Al of ~150 nm in thickness was deposited through a shadow mask to form the top electrode and to define a device structure of 0.2×0.2 mm^2. The current–voltage (I–V) measurements were carried out using a HP4155C semiconductor parameter analyzer. All electrical measurements were conducted under ambient conditions without any encapsulation of the devices.

3. Results and discussion

The structure of the synthesized poly(2-(9H-carbazol-9-yl)ethyl methacrylate) (PCz) is shown in Fig. 1(a). For comparison purpose, the structure of poly(*N*-vinylcarbazole) (PVK) is also shown in Fig. 1(a). Both polymers contain the electron donating or hole-transporting carbazole groups. They differ in the length and structure of the side chain joining the carbazole pendant group to the polymer backbone. In PCz, the carbazole group is separated from the main chain by the O=C–O–C–C spacer, while in PVK, the carbazole group is linked directly to the main chain. The flexible molecular spacer between the carbazole group and the backbone in PCz reduces initially the interactions among the carbazole groups. Fig. 1(b) shows schematically, an ITO/PCz/Al memory test structure.

The electrical properties of the devices are measured at room temperature under ambient conditions. Fig. 2(a) shows the current density-voltage (J–V) characteristics of the ITO/PCz/Al device. The top Al electrode and bottom ITO electrode were connected to a varying voltage source. The bottom ITO was grounded and the current passing through the electrodes was monitored. For the as-fabricated device, the conductance was very low. The as-fabricated device showed the current density of the low-conductivity state (~10^{-6} A cm^{-2}, OFF-state) at a read voltage of −1 V. By sweeping the voltage from 0 V to −3 V, a switch in the conductivity state was observed. Upon reaching the threshold voltage of around −1.8 V, the devices switched from the low conductivity (OFF) state to a high conductivity (ON) state with a current density of ~1 A cm^{-2}. The device remained in the ON state as the voltage was swept from −1.8 V to −3 V. With subsequent sweeping of the voltage under negative bias, the current density was characteristic of that of the ON state current in Fig. 2(a). By using a read voltage of −1 V, an ON/OFF current ratio larger than 10^6 was obtained. This high ON–OFF ratio is essential for the device to function with minimal misreading error. Fig. 2(b) shows the J–V characteristic of an equivalent ITO/PVK/Al device. Using a similar sweep from 0 V to −3 V, the device exhibits only a single ON state, without any discernible transitions.

The transition from the OFF state to the ON state for the PCz device serves as a 'write' operation in the memory device. It was found that the transition to the ON state was irreversible. The switching time of the device was found to be around 1 ms, as measured by applying a voltage pulse duration to observe an OFF-to-ON transition at the threshold voltage. After the device is switched to its ON state, it remains in the ON state even after the power has been turned off. It cannot return to its OFF state by subsequent application of a positive or negative bias. Furthermore, once the ON state is reached, the device exhibits the high conductivity state in both the negative and positive voltage sweep. Thus, the device based on PCz behaves as a write-once read-many-times (WORM) electronic memory. Biasing the device with a higher voltage stress was attempted. At a negative bias exceeding −6 V, the device showed a sudden drop in current density, due to device failure at the high electric field stress of ~1.2×10^6 V cm^{-1} (not shown).

The thermal stability of the device in the ON-state was measured in the same J–V set-up, except that the device was placed on a hot chuck that was connected to a heating source. The actual temperature was measured using a thermocouple. The current density of the devices was measured with a

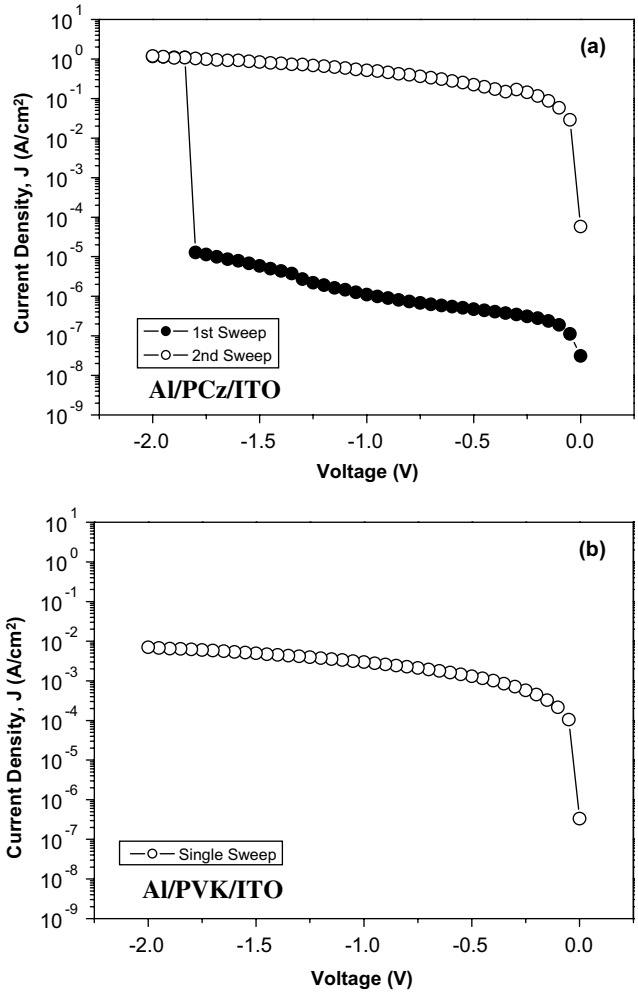

Fig. 2. (a) Typical J–V characteristics of an Al/PCz/ITO device in the ON and OFF state, showing an OFF–ON transition when voltage reaches −1.8 V. (b) Typical J–V characteristics of an Al/PVK/ITO device, showing PVK always exhibiting an ON state.

read voltage sweep of 1 V, first at room temperature, and then at several increasing temperature step. The device was found to be stable in its ON state from room temperature to around 120 °C (Fig. 3(a)). The result is expected as PCz has a relatively high glass transition (T_g) of 196 °C. For a substrate temperature of about 300 K, an ON-state current density of 1 A cm^{-2} at an applied voltage of 2 V, and thermal conduction of the PCz film according to the following equation [14]:

$$P = -\kappa \frac{\partial T}{\partial x} - c_v \rho d \frac{\partial T}{\partial t} \quad (1)$$

where $P = J \cdot V$ is the power density dissipated in the film, T is the film temperature, and κ, ρ and c_v are the thermal conductivity, density and heat capacity for a fixed volume of the PCz film, respectively, the maximum temperature in the film is substantially below 120 °C. Therefore, the PCz device will remain in its regioregular conducting ON-state, rather than undergoes a transition back to the regiorandom non-conducting OFF-state. Furthermore, the regioregular conducting ON-state, produced by the initial electrostatic ordering, is retained as long as the polymer remains below its glass transition temperature.

The retention time of the ON and OFF states of PCz was tested under ambient conditions. Initially, the device in the OFF-state was subjected to a constant voltage stress of −1 V, and the OFF-state current was recorded every minute, up to a time of 24 h. Then the device was programmed by a voltage

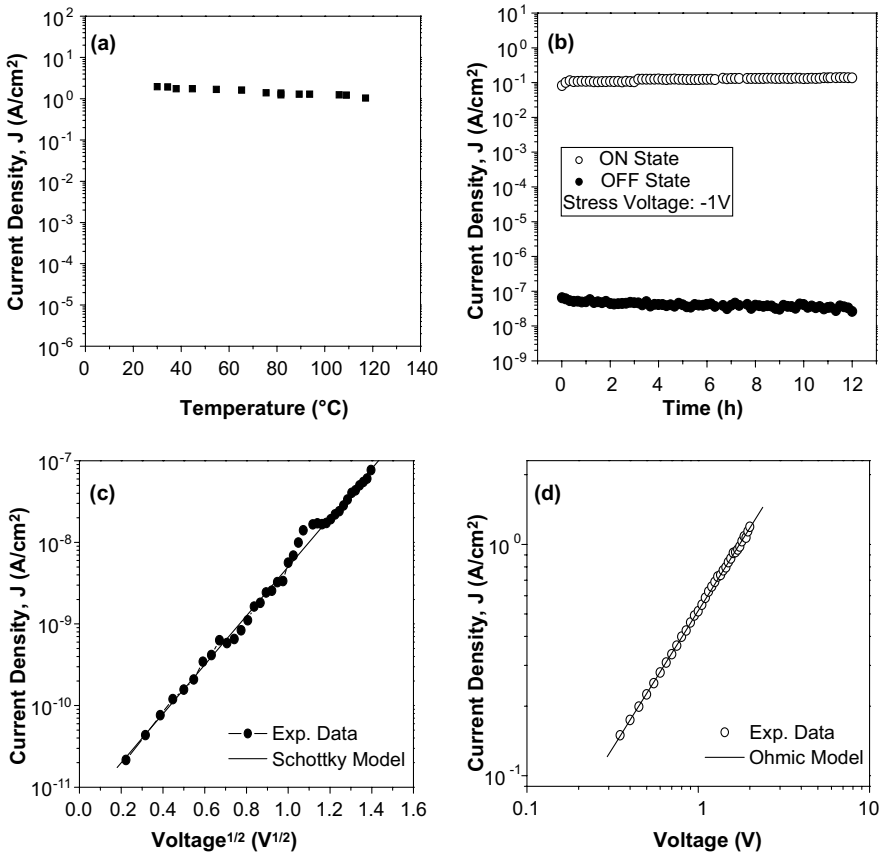

Fig. 3. (a) The current density-temperature plot of a turned-ON Al/PCz/ITO device, obtained at a read voltage of 1 V. The device shows stability at its ON-state from room temperature to around 120 °C. (b) Stability of the Al/PCz/ITO device in either the OFF or ON state under a constant stress of −1 V. The device shows stability up to 12 h, with an ON/OFF ratio of $\sim 10^6$. Fitted J–V curves of the Al/PCz/ITO device: (c) OFF-state with the charge injection model, and (d) ON-state with the ohmic conduction.

sweep and the ON-state was measured under the same stress conditions. Fig. 3(b) shows that the device has both stable ON and OFF state current within the 12 h time frame, which can be extrapolated to sustain for 10 years. Also, the ON/OFF current ratio of 10^6 is sustained. The J–V curves of the PCz device in the ON and OFF state were fitted to the conduction models. As shown in Fig. 3(c), the J–V curve in the OFF-state can be fitted by the Schottky emission model, whereas Fig. 3(d) shows that the ON-state current can be fitted by the ohmic model. The ohmic nature of the PCz device in the ON state is similar to the ohmic characteristic of conduction in PVK [16].

From the cyclic voltammograms of PCz in the applied potential range between −2.3 V and 2.3 V (vs. Ag/AgCl electrode), PCz containing the carbazole groups shows only one irreversible oxidation peak. This suggests that the carbazole group is an efficient hole transport site with a high tendency to donate electrons. The HOMO energy level of PCz can be calculated from the onset oxidation potential $E_{\text{onset}}(\text{ox})$, based on the reference energy level of ferrocene (4.8 eV below the vacuum level) [19,20]:

$$\text{HOMO} = E_{\text{onset}}(\text{ox}) + 4.8 - E_{\text{FOC}}$$
$$\text{LUMO} = \text{HOMO} + E_{\text{g}}(\text{bandgap})$$

wherein E_{FOC} is the potential of Foc(ferrocene)/Foc^+ vs. Ag/AgCl. The value of E_{Foc} is 0.46 V [21]. The bandgap of PCz calculated from UV absorption edge is 3.52 eV. According to the above equation, the HOMO and LUMO energy level of PCz relative to the vacuum level is estimated to be about 5.30 eV and 1.78 eV respectively. Fig. 4(a) shows the schematic energy diagram of the ITO/PCz/Al sandwich structure. PCz, with the presence of the hole-transporting carbazole groups, acts as

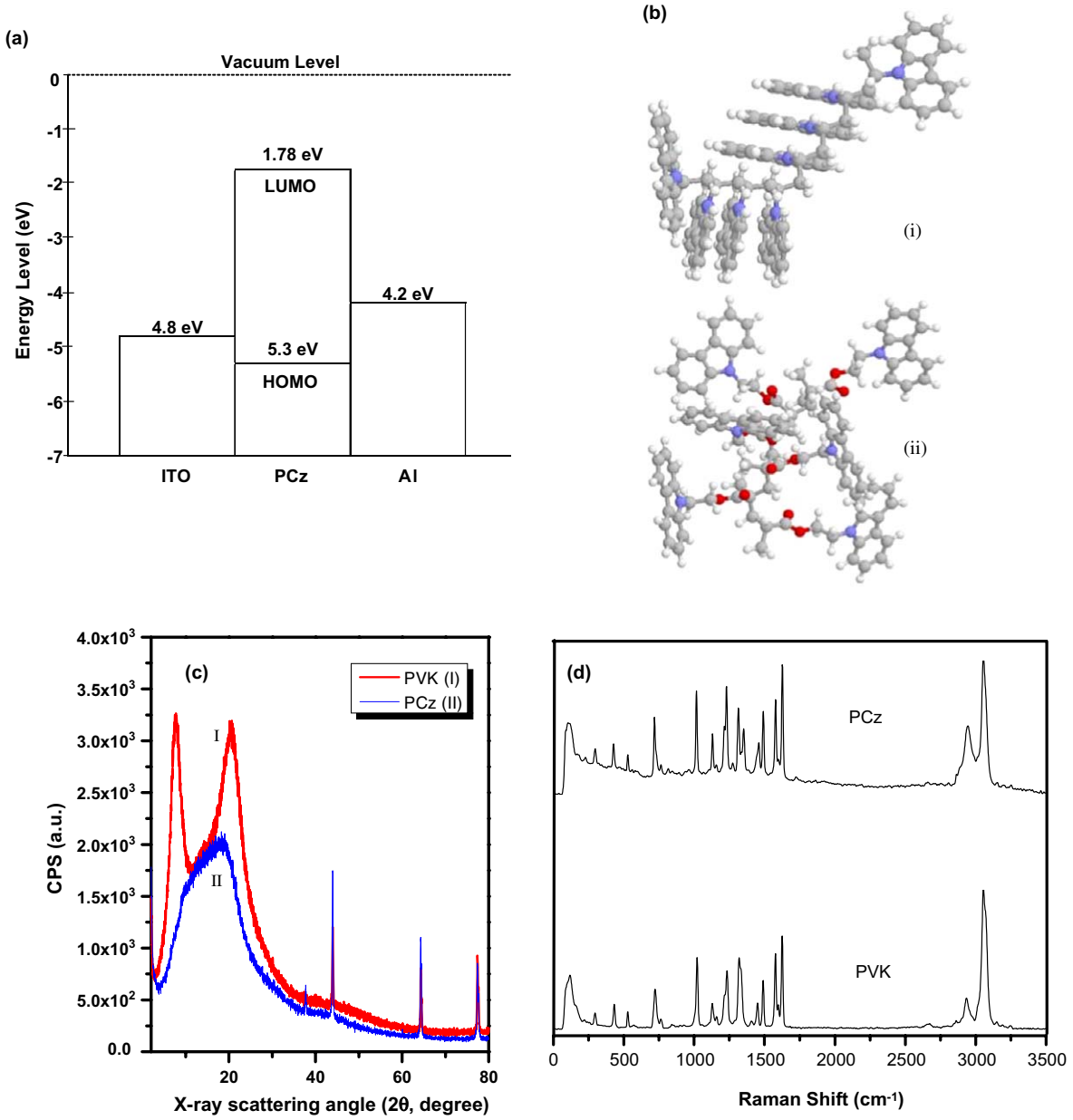

Fig. 4. (a) Schematic energy diagram of an Al/PCz/ITO structure. (b) Simulation results by molecular mechanics showing the optimized geometry corresponding to the minimized energy states in (i) PVK and (ii) PCz. (c) X-ray diffraction patterns of PVK and PCz at ground state. (d) Raman spectra of PVK and PCz.

a donor. It favors the injection of holes rather than electrons. As seen in the energy diagram, the barrier to hole injection from the ITO electrode (0.5 eV) is smaller, compared to the barrier to hole injection from the Al electrode (1.1 eV). Thus, the bi-stable states performance of the device was observed in the reverse bias, with holes transport as the conducting mechanism.

It is well known that the high conductivity of poly(*N*-vinylcarbazole) (PVK) is due to the charge carriers (holes) hopping through the neighboring carbazole groups rather than migrating through the polymer backbone since it is not a conjugated polymer [16]. The neighboring carbazole groups in PVK have a high tendency to form the face-to-face conformations in the ground state, as seen by the

simulation results in part (i) of Fig. 4(b) [22]. As a result, the region of electron delocalization is extended to several carbazole groups. The charge carriers (holes) can be shared as such and hop through the regioregular carbazole groups in the direction of electric field (E-field). Since PCz has the similar molecular structure to PVK, its conductivity mechanism should be similar to that of PVK. However, at low E-field, the current density of the device based on PCz is low and the device is in its OFF state. The J–V characteristic of the OFF state follows the Schottky emission model (Fig. 3(c)). In comparison with the molecular structure of PVK, PCz has a relatively extended side chain. The flexible molecular spacer between the carbazole group and the backbone does not favor interaction of the carbazole groups, but promoting them to form regiorandom structure at the ground state (part (ii) of Fig. 4(b)). The charge carriers (holes) will have difficulty to hop through the neighboring carbazole groups due to the absence of face-to-face conformations and the long distance between the neighboring carbazole groups.

The X-ray diffraction (XRD) patterns of both PVK and PCz samples at ground state are shown in Fig. 4(c). The diffraction peaks at around 38.31°, 44.18°, 64.55° and 77.60° arise from contamination by the aluminum sample holder. Two diffraction peaks centered at $2\theta = 20.56°$ (4.32 Å) and 7.76° (11.38 Å) were observed (the magnitude in the brackets represents the corresponding d-value for 2θ peak) for PVK [23,24]. The former peak is an amorphous halo which is broad, diffuse and strong, while the latter peak has been shown to be a function of the chain parallelism [25], with the nearest chain-to-chain distance of about 11.38 Å. The result indicates that PVK is regioregular. The XRD pattern of PCz consists of only one broad peak at around $2\theta = 18.73°$ (4.73 Å), similar to the one at $2\theta = 20.56°$ for PVK. The results indicate that PCz is amorphous in the ground state. The holes are still the majority carrier in the amorphous polymer. However, carrier generation and mobility are substantially reduced compared to those in the unsubstituted PVK with paracrystalline structure [24]. XRD results indicate that the spacer between the carbazole group and the backbone interferes with chain interaction and ordering in the amorphous polymer, hence eliminating the unusual degree of chain parallelism and destroying the ability to crystallize. As a result, PCz is in its regiorandom non-conductive state at a low field.

As the E-field increases in the reverse bias, hole injection from the ITO causes the carbazole groups near the ITO region to be oxidized, forming positive species. Driven by the applied field, the charged carbazole group has the tendency to attract the nearby neutral carbazole groups to form partial or full face-to-face conformation. The positive charge will then be delocalized to neighboring carbazole groups through the more ordered conformation. As the delocalization process increases with the increase in electric field up to the required threshold value, the carbazole groups in the bulk material re-organized from a regiorandom to a regioregular structure, in the general direction of the electric field towards the Al cathode. As a result, a high conductivity path among the hole-transporting carbazole groups is established and the device is switched to its ON state. The oxidized carbazole groups are further stabilized by the neighboring electron-withdrawing –O–C=O groups. The high conductivity (ON) state of PCz follows the ohmic conduction model (Fig. 3(c)).

To characterize the influence of electric field on the conformation changes during measurement, the Raman scattering technique, in which laser excitation produced the similar effect as an electric field, was employed. The Raman spectra of PVK and PCz are shown in Fig. 4(d). Most of the scattering frequencies of PVK are also observed in the Raman spectrum of PCz. In addition, the frequencies associated with the $-OCH_2-$ group in PCz are also observed at around 1350 and 2860 cm^{-1}. The conductivity of PVK has been attributed to the presence of the 1,2,4-substituted aromatic rings and the quinonoidal C=C structure, which have Raman peaks in the range of 750–850 and around 1600 cm^{-1}, respectively [26,27]. The Raman spectrum of PCz also shows the presence of 1,2,4-substituted benzene rings (at 835 cm^{-1}) and the quinonoidal C=C structure (at 1596 cm^{-1}) under laser excitation. The results indicate that PCz has transformed into a conductive conformation, similar to that of PVK, under laser excitation.

4. Summary

A WORM memory device based on a newly synthesized acylate polymer containing a carbazole pendant group was demonstrated. The WORM device exhibited a high ON/OFF current ratio of 10^6, a long retention time in both ON and OFF states, and a short switching time of ~1 ms. The

device could be read up to $\sim 10^7$ times. All these characteristics make the device potentially viable. When the 90 nm technology is used, a high density of 1×10^4 Mb/cm^2 WORM can be expected, and when it is stacked to a 3D structure, the capacity of data storage can be significantly enlarged. Finally, the use of the relatively simple homopolymer of PCz makes the production of memory economical, simple, and easily compatible with other organic or inorganic electronic processes.

Acknowledgements

This work was supported by research grants R-263-000-327-112 and R-279-000-167-112 (NUS, Singapore), and IME/04-410004 (IME, Singapore).

References

[1] C.W. Tang, S.A. VanSlyke, Appl. Phys. Lett. 51 (1987) 913.
[2] F. Garnier, R. Hajlaoui, A. Yassar, P. Srivastava, Science 265 (1994) 1684.
[3] G. Yu, K. Parbaz, A.J. Heeger, Appl. Phys. Lett. 64 (1994) 3422.
[4] A.C. Arias, I.A. Hümmelgen, A. Meneguzzi, C.A. Ferreira, Adv. Mater. 9 (1997) 972.
[5] J.R. de Lima, L.O. Péres, J.R. Garcia, J.R. Garcia, J. Gruber, I.A. Hümmelgen, Solid-State Electron. 44 (2000) 565.
[6] J.Y. Ouyang, C.W. Chu, D. Sieves, Y. Yang, Appl. Phys. Lett. 86 (2005) 123507.
[7] Z.J. Donhauser, B.A. Mantooth, T.P. Pearl, K.F. Keey, S.U. Nanayakkara, P.S. Weiss, Jpn. J. Appl. Phys. Part 1 41 (2002) 4871.
[8] J. Chen, M.A. Reed, A.M. Rawlett, J.M. Tour, Science 286 (1999) 1550.
[9] A. Bandyopadhyay, A.J. Pal, Appl. Phys. Lett. 82 (2003) 1215.
[10] J. Chen, J. Su, W. Wang, M.A. Reed, Physica E 16 (2003) 17.
[11] W.C. Chih, J.Y. Ouyang, J.H. Tseng, Y. Yang, Adv. Mater. 17 (2005) 1440.
[12] Q. Ling, Y. Song, S.J. Ding, C.X. Zhu, D.S.H. Chan, D.L. Kwong, E.T. Kang, K.G. Neoh, Adv. Mater. 17 (2005) 455.
[13] A. Bandhopadhyay, A.J. Pal, J. Phys. Chem. B 107 (2003) 2531.
[14] S. Moller, C. Perlov, W. Jackson, C. Taussing, S.R. Forrest, Nature 426 (2003).
[15] D.M. Pai, J. Phys. Rev. B. 52 (1970) 2285.
[16] G. Safoula, K. Napo, J.C. Bernede, S. Touihri, K. Alimi, Euro. Polym. J. 37 (2001) 843.
[17] J.V. Grazulevicius, P. Strohriegl, J. Pielichowski, K. Piechowski, Prog. Polym. Sci. 28 (2003) 197.
[18] J. Sanetra, D. Bogdal, M. Warzala, A. Boron, Chem. Mater. 14 (1) (2002) 89.
[19] J.L. Bredas, R. Silbey, D.S. Boudreaux, R.R. Chance, J. Am. Chem. Soc. 105 (1983) 6555.
[20] Y.Z. Lee, X.W. Chen, S.A. Chen, P.K. Wei, W.S. Fann, J. Am. Chem. Soc. 123 (2001) 2296.
[21] T.Y. Wu, R.B. Sheu, Y. Chen, Macromolecules 37 (2004) 725.
[22] J. Vandendriessche, P. Palmans, S. Toppet, N. Boens, F.C. De Schryver, H. Masuhara, J. Am. Chem. Soc. 106 (1984) 8057.
[23] G.C. Richards, Macromolecules 4 (1971) 379.
[24] C.H. Griffiths, K. Okumura, A. Van Laeken, J. Polym. Sci: Polym. Phys. Ed. 15 (1977) 1627.
[25] C.H. Griffiths, J. Polym. Sci.: Polym. Phys. Ed. 13 (1975) 1167.
[26] R. Anandhi, S. Umapathy, J. Raman Spectrosc. 29 (1998) 901.
[27] M. Sacak, U. Akbulut, C. Cheng, D.N. Batchelder, Polymer 35 (1994) 2495.

Available online at www.sciencedirect.com
SCIENCE DIRECT
Organic Electronics 7 (2006) 181–187
Organic Electronics
www.elsevier.com/locate/orgel

Non-lithographic fabrication of PEDOT nano-wires between fixed Au electrodes

A. Das [a,*], C.H. Lei [a], M. Elliott [a], J.E. Macdonald [a], M.L. Turner [b]

[a] School of Physics and Astronomy, Cardiff University, 5 The Parade, Cardiff, CF24 3YB, United Kingdom
[b] School of Chemistry, University of Manchester, Oxford Road, Manchester M13 9PL, United Kingdom

Received 22 November 2005; received in revised form 22 December 2005; accepted 22 December 2005
Available online 23 January 2006

Abstract

Poly(3,4-ethylenedioxythiophene) (PEDOT) nano-wires have been electrochemically grown between fixed Au electrodes on an insulating SiO_2 substrate. The local DC electric field between the electrodes was used to control the diffusion of the 3,4-ethylenedioxythiophene (EDOT) monomer which was then polymerised in situ by the same applied field to create a stable, insoluble wire of width 500–700 nm. Relatively smooth and conducting nano-wires ($\sim$10 S cm^{-1}) resulted from the application of step-wise decreasing DC voltages. The PEDOT wire was characterised using Raman spectroscopy and atomic force microscopy (AFM). Current-voltage measurements indicate Ohmic and space-charge limited conduction, depending on applied bias, for Au electrodes.

PACS: 82.35.Cd; 82.45.Bb; 73.61.Ph

Keywords: Poly(3,4-ethylenedioxythiophene); Nano-wires; Atomic force microscopy; Raman spectroscopy and conductivity

1. Introduction

There is growing interest in the fabrication of micro- and nano-scale conducting and semiconducting wires, because of the potential for application in nano-electronics devices such as solar cells [1], biochemical sensors [2], and other molecular devices [3]. While there is considerable excitement regarding potential single molecule devices to complement silicon technology, progress on easily processible and compatible interconnect technology has been slow. Considerable progress has been made in the growth of metallic and semiconducting one-dimensional structures [4,5]. Electrochemical formation of metallic and semiconducting wires between electrodes selected by simple application of a bias is an attractive route, which could reduce dependence on lithographic fabrication. Such an approach has been utilised to produce addressable nano-metal (Pd) [6] and polymer wires e.g. polyaniline and polypyrrole [7].

Poly(3,4,-ethylenedioxythiophene) (PEDOT) is viewed as a promising conducting polymer for

* Corresponding author. Tel.: +44 2920870166; fax: +44 2920874056.
E-mail addresses: spxad@cf.ac.uk, adas_69@yahoo.com (A. Das).

1566-1199/$ - see front matter © 2006 Elsevier B.V. All rights reserved.
doi:10.1016/j.orgel.2005.12.006

making organic based electronic devices due to its excellent transparency in the visible range, good electrical conductivity, and environmental stability [8,9]. However, lack of processability due to its insolubility and infusibility has been a major impediment to the widespread application of this polymer. A water dispersion of PEDOT doped with poly(styrenesulfonate)(PSS) is widely used as hole injecting material in OLED devices [10,11]. However, the dispersion, being very acidic, causes problems during application and often needs binders for wetting organic substrates. Addition of these binders generally decreases the conductivity of the resulting film.

There have been several attempts at synthesising PEDOT films [12], nano-rods [13], wires [14,15] and hollow particles by chemical or electrochemical routes [16]. These routes sometimes require multi-step processes or templates and invariably involve other chemical reagents used during synthesis, which can act as dopants in the material. The opto-electronic properties of PEDOT are also strongly influenced by the preparation conditions [17]. Nano-epitaxial growth of thiophene based polymer has been reported on Al(1 1 1) surfaces by stepwise electropolymerisation from an STM tip using an I_2-containing electrolyte [18].

Metallic nano-wires (Pd) [19] and polymer wires e.g. polyaniline and polypyrrole [7] have also been realised by an electrochemical route. Predefined metal micro-electrodes written by e-beam lithography were employed for the nano-wire deposition, and the thickness of the nano-wire was dependent on the dimensions of the prefabricated electrodes. However, in these reports the polymer wire is not free from dopant effects due to the use of a chloride based reagent in a three-electrode set-up.

Herein we demonstrate a simple but robust method for fabrication of PEDOT wires between fixed Au electrodes. The local electric field between the electrodes is used to direct the flow of the active monomer species which is then polymerised in situ by the applied field, creating a stable, insoluble electrode or wire. The formed wire is conducting and the *I–V* characteristics demonstrate good Ohmic contact with the electrodes.

2. Experimental

Liquid EDOT monomer was obtained from Sigma-Aldrich and used without any further purification. EDOT was dissolved in acetonitrile (Fisher chemicals, HPLC grade) to form a solution of concentration of 0.1 M. Au electrodes 15 nm thick were evaporated onto a SiO_2/Si surface by a wire shadow mask method [20]. The wire shadow mask left a gap of about 5 μm between the Au films, which act as micro-electrodes. For growth of triangular tip-like electrodes, a pair of wires were mounted in a crossed-configuration to create a gap of 8 μm.

An electrometer (Keithley 617) and a voltage source (Keithley 230) were used to perform *I–V* measurements. Micro-Raman spectra of the PEDOT wires were taken using a RENISHAW system (2000 micro-Raman spectrometer) with the 785 nm line of a laser. The AFM measurements were performed in ambient conditions with an n-type Si cantilever using a NanoScope IIIa Multimode (Digital Instruments).

3. Results and discussion

3.1. Multi-wire growth

The choice of solvent is crucial to the stability of a solution. Acetonitrile (CH_3CN) has been used in the present case as an electrolyte for EDOT to produce high quality PEDOT, because of its high dielectric constant (36.6) and poor nucleophilicity, ensuring good electrochemical resistance against decomposition at the potential required to oxidize the EDOT ring (~1.0 V vs. SCE) [21,22].

Fig. 1 shows an optical micrograph of sub-micron wires fabricated between two electrodes made of gold with a gap of 4 μm, created by a

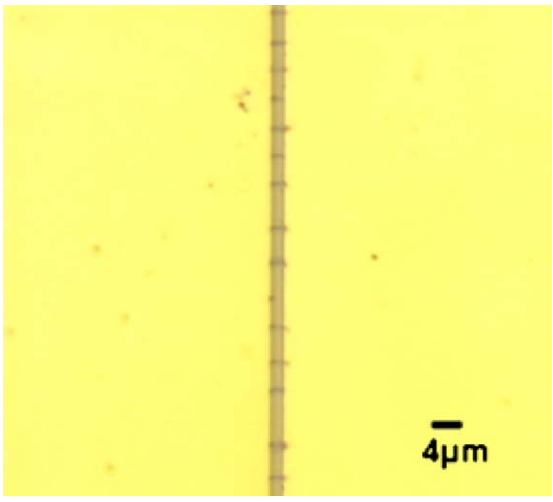

Fig. 1. Optical image of PEDOT arrays between parallel Au electrodes with an application of +5 V for 3 s to the left electrode.

simple wire shadow mask method. To prepare these wires a drop of 0.1 M EDOT solution (~20 μl) was placed on the substrate to fill the electrode gap. Application of a constant electrical potential for 5 s (+5 V, potentiostatic method) resulted in wires growing from the anode to the cathode across the gap. These bridges are conductive with a total parallel resistance of 47 kΩ for about 50 wires connected along the length of the electrode (3 mm). Once PEDOT formation is complete, surplus solution is blown off the substrate surface with nitrogen gas. The resulting PEDOT wires are stable and are not washed away by CH_3CN or deionised water, indicating strong adherence of the wires to the SiO_2 substrate surface. No wire growth is observed for a potential less than 2 V between the electrodes. This potential is slightly higher than the ionisation potential reported for EDOT [21]. It is believed that, like the electropolymerisation process of thiophene [22], the EDOT monomer is oxidised to its radical cation at the anode. This assertion is supported by the observation of partially-formed wires only at the anode when the bias is switched off prematurely. As the electron-transfer reaction is much faster than the diffusion of the monomer from the bulk solution, a high concentration of radicals is continuously maintained near the electrode surface. The ionised EDOT moieties then migrate in solution driven by the spatially varying electric field in the region of the electrodes. There is no need to use a supporting electrolyte, usually required for mobility of ions in the electrochemical cell, since these charged species are dispersed by the non-uniform electric field. Competition between the formation of a high concentration of ions at the anode and the migration of the ions away from the electrode can influence strongly the wire thickness near the electrode. This has been realised during step wise growth for a single smooth PEDOT wire, and is discussed later.

The formation of PEDOT is further confirmed by the micro-Raman spectroscopy which has been applied to characterise the wire. Raman shifts are measured at $\lambda = 785$ nm with a spot size ~1 μm. Fig. 2 shows Raman shifts for an EDOT layer (under no bias) and for the conducting wires formed between two electrodes. The Raman spectrum of the wire can be well correlated with various vibrational modes for PEDOT [14,23]. The features at 1498 and 1434 cm^{-1} match with asymmetric and symmetric stretching modes of —C=C— bonds, respectively whereas the weak peaks at 1365 and 1235 cm^{-1} originate from —C—C— bonds. The weaker bands at 1127 and 1100 cm^{-1}, related to distorted C—C inter-ring bonds and the strong presence of —C=C— modes indicate formation of a highly planar structure with extended conjugation [24].

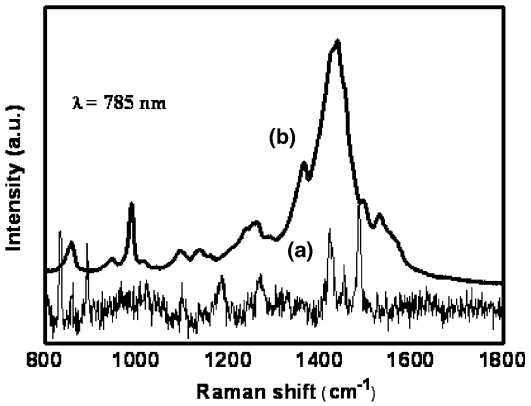

Fig. 2. Raman spectra of (a) EDOT layer (b) PEDOT nano-wire formed between parallel Au electrodes.

The polymer chain tends to grow along the local electric field direction, so a tiny protrusion on the electrode can initiate fast polymer growth, forming a growing electrode front, until it reaches the opposite electrode. This idea is supported by the fact that growth of PEDOT is always seen at the edges of an electrode. The most striking feature of growth between two extended electrodes (Fig. 1) is the periodic array of wires formed. The most probable explanation of this periodic separation is distortion of the local electric field deviation in the proximity of a growing conducting wire. The electric field between ideal parallel Au electrodes is uniform. Once a conducting wire starts growing from the anode, it causes a decrease in the local field close to the sides of the growing wire. This can, in turn create a local reduction in the concentration of the active species and therefore inhibit the initiation of new wires close to the existing growing wire. Qualitatively, this can be understood to suppress growth of a new wire close to the existing wire, giving rise to quasi-periodic wires. Periodic array has also been reported in the case of the Pd nano-wire growth, induced by an AC applied bias from a palladium acetate solution [19].

Fig. 3 displays an AFM image of the formed PEDOT wire between extended Au electrodes. Analysis of the AFM image shows that the PEDOT wire is ~50 nm high with a root mean square roughness value of 20 nm. It is reported [13] that thin film

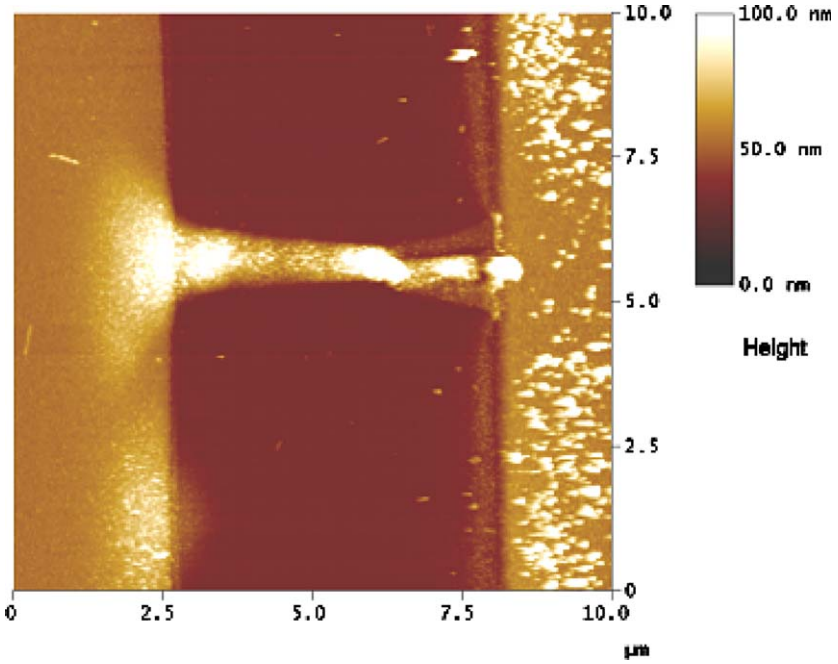

Fig. 3. AFM images of a fully grown PEDOT bridge between parallel Au electrodes with +5 V to the left electrode.

of PEDOT formed from CH_3CN solvent via a chemical oxidation route also produces high roughness ~60 nm. The poor surface morphology of PEDOT wire in the present case might have resulted from multiple deposits of polymer molecules under applied bias and the width of the PEDOT wires is in the range 600–700 nm.

3.2. Growth of single wire

Growth of a single PEDOT wire between triangular electrodes, 15 nm thick, is shown in Fig. 4. The electrodes were produced using a simple crossed-wire shadow mask on SiO_2/Si substrate, giving four electrodes with gaps of about 8 μm between opposing electrodes. By applying a bias to one pair of opposing electrodes with the other pair floating, growth is induced in the region of high electric field between the tip-like electrodes. To deposit the PEDOT wire, 0.1M EDOT solution was dropped onto the substrate to cover the electrode gap, and a series of continuous step voltages of 10 V, 8 V, and 6 V applied to the left electrode each with duration of 100 ms. The bias was then switched off, and the remaining solution was blown away with compressed nitrogen. A single PEDOT wire can be seen between the electrodes in the AFM image in Fig. 4a. This wire has a smooth surface with a roughness ~5 nm, average thickness 50 nm and width ~500 nm. In contrast to the single potential used previously for the flat electrodes, a series of potentials is preferred with triangular electrodes to form a single wire. The triangular electrodes give a divergent electric field in the electrode gap with the largest field along the straight line connecting the two electrodes tips. When a single constant bias (10 V for 400 ms) between the electrodes was applied, thick, rough multi-wire growth with branches was formed (Fig. 4b). However, by controlling reaction conditions such as the rate of migration of the reactive species along the electric field, a smooth and single wire can be produced. By reducing the bias as the wire grows, multi-wire growth of PEDOT can also be prevented (Fig. 4a). Although a series of steps in the potential source was used in this study, a continuously decreasing potential source may be preferred, as the profile of the potential may be finely tuned to the electrode arrangement, EDOT states and concentration, in order to grow a uniform wire.

3.3. Electrical measurements

The *I–V* characteristics of the single nano-wire in the range of ±4 V are displayed in Fig. 5. In the low potential regime (0–1.0 V), a linear Ohmic depen-

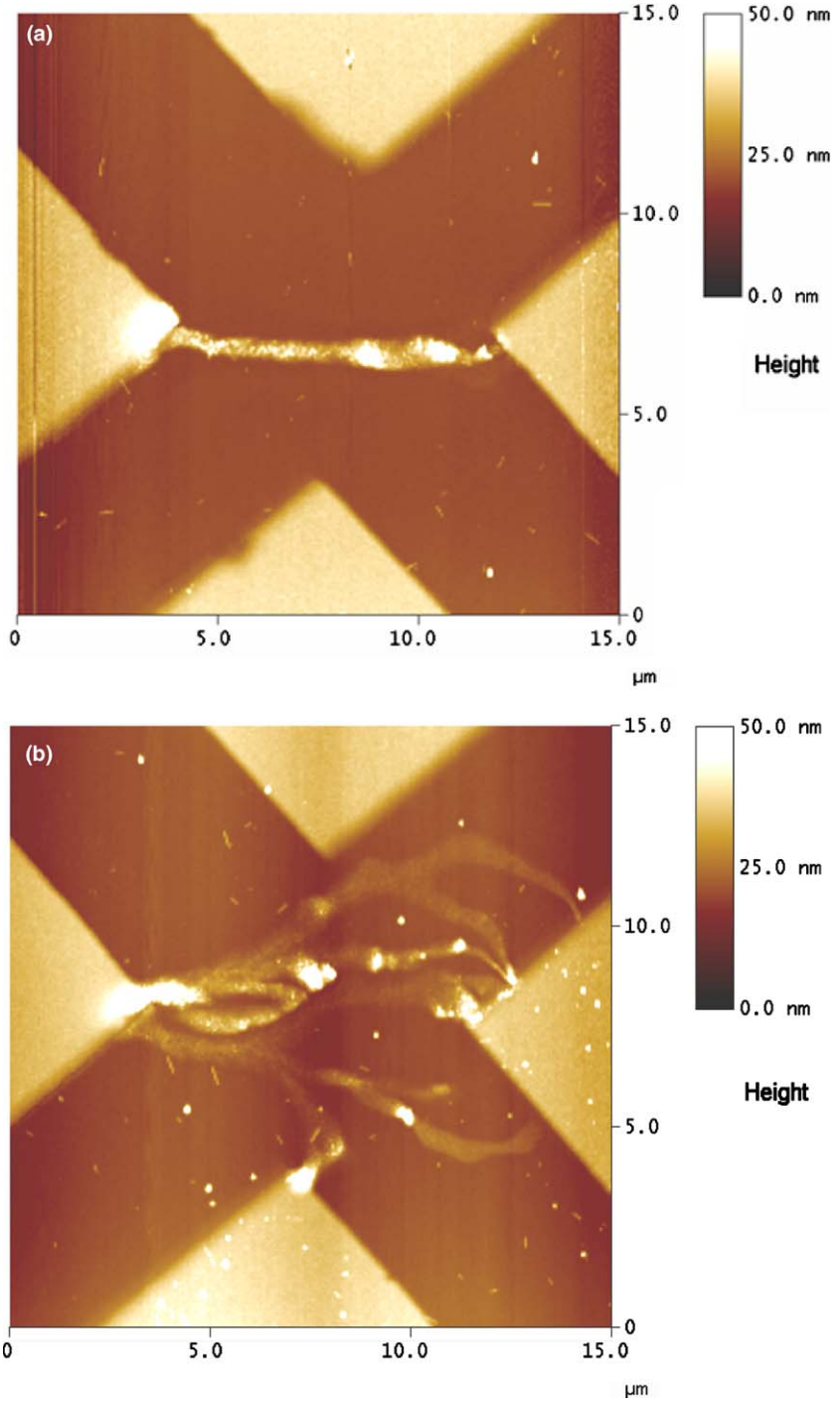

Fig. 4. AFM image of (a) single PEDOT bridge fabricated with decreasing bias voltages between triangle electrodes (b) branched PEDOT wires with constant 10 V bias.

dence of the current on the voltage is observed. This is followed by a steep rise in current for a bias in the range of 1.0–3.8 V and then a sudden drop in current at above 4 V. The steep rise in current at greater than 1 V is an indication of a space-charge limited current (SCLC), where the current density changes depends on V^2 [25,26], rather than a thermionic emission mechanism occurring at low voltages.

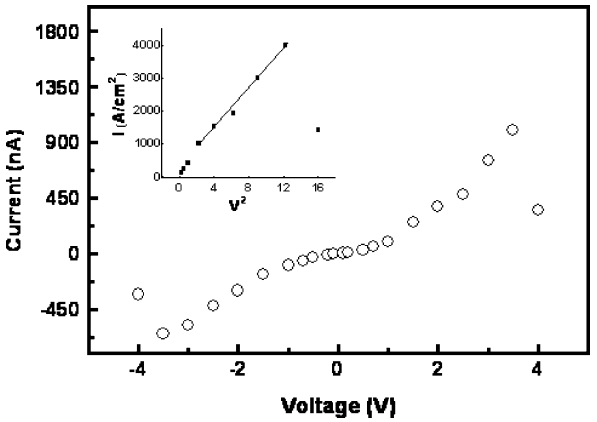

Fig. 5. *I–V* measurement of the single PEDOT wire as shown in Fig. 4. Inset shows a plot of current density vs. V^2 for indicating a SCL mechanism.

Current density is calculated using AFM data of the contact area (average thickness 50 nm and width 500 nm) and current density vs. V^2 is displayed in Fig. 5 as an inset. A straight line fit in the region of 1.5–3.5 V as shown in Fig. 5 supports the SCL mechanism proposed. It appears that for small voltages (<1 V), SCLC is not observed due to fewer injected space charges where the conduction is approximately Ohmic. The conductivity estimated at 0.2 V for the 8 μm long PEDOT wire is $\sim$10 S cm^{-1}. Ohmic behaviour at low potential (at 0.1 V) has also been reported for very thin nanowires of PEDOT/PSS [27]; although in this case the role of ionic PSS is not fully understood. In the present case, as the voltage increases the additional space charge is also injected and therefore, a transition from Ohmic to SCL behaviour is observed for the single PEDOT nano-wire. At a voltage greater than 3.8 V, a sudden drop in current is observed which can be ascribed to the thermal damage caused by a strong current flow, this damage is permanent if the bias is increased to more than 5 V. Therefore, *I–V* measurements were recorded for a maximum voltage of 4 V. Intriguingly, it has been shown [28] that conducting PEDOT/PSS can be transformed to a open state at a potential above 10 V and this process has potential to be exploited in a WORM (write once read many) memory chip. The nanowires described in this report are clearly of interest for application in these types of devices. The *I–V* measurements were performed under ambient condition and the conductivity of the wires was found to be stable for a few (2–3) days, in contrast to the few hours reported for polyaniline wires [6].

4. Conclusion

In summary, a simple electrochemical technique is described that enables the fabrication of PEDOT nano-wires between electrodes. The composition and conducting nature of the PEDOT wires were confirmed by Raman spectroscopy and *I–V* measurements. Smooth single PEDOT wires were produced from EDOT/CH_3CN solution with a stepwise potential source with no additional reagents or electrolytes, in contrast to electropolymerisation or chemical synthesis previously reported [12–16]. The growth conditions need to be optimised for the electrode geometry, the EDOT states and the EDOT concentration, in order to produce a well-confined PEDOT wire. *I–V* measurement shows a transition from Ohmic behaviour with Au electrodes to SCL conduction. This non-lithographic approach might be extended to other polymeric materials in a fast, single step process, including a way to use this conducting polymer as components in electronic nano-devices or even molecular electronics, such as transistors, diodes, or sensors. Further investigation is needed to understand the effect of EDOT concentration, electrode geometry and other factors, such as growth rate, for practical applications.

Acknowledgments

The authors would like to thank Dr. Yimin Lu for help in recording Raman spectra. This research has been partially supported by the EPSRC, Grant GR/S02280.

References

[1] B. Das, S.P. McGinnis, P. Sines, NCPV Program Review Meeting Proceedings, 2001, p. 326.
[2] M. Yun, N.V. Myung, R.P. Vasquez, C. Lee, E. Menke, R.M. Penner, Nano Lett. 4 (2004) 419.
[3] J.A. Misewich, R. Martel, Ph. Avouris, J.C. Tsang, S. Heinze, J. Tersoff, Science 300 (2003) 783.
[4] Z.L. Wang. Nanowires and Nanobelts Materials, Properties and Devices Metal and Semiconductor Nanowires, Vol. I, Kluwer Academic Publishers, 2003.
[5] S. Ciraci, A. Buldum, I.P. Batra, J. Phys.: Condens. Matter 13 (2001) R537.
[6] M.A. Bangar, K. Ramanathan, M. Yun, C. Lee, C. Hangarter, N.V. Myung, Chem. Mater. 16 (2004) 4955.
[7] K. Ramanathan, M.A. Bangar, M. Yun, W. Chen, A. Mulchandani, N.V. Myung, Nano Lett. 4 (2004) 1237.
[8] F. Jonas, L. Schrader, Synth. Met. 41/42 (1991) 831.
[9] G. Heywang, F. Jonas, Adv. Mater. 4 (1992) 116.
[10] B. Xiao, B. Yao, C. Ma, S. Liu, Z. Xie, S. Wang, Semicond. Sci. Technol. 20 (2005) 952.

[11] W.H. Kim, G.P. Kushto, H. Kim, Z.H. Kafafi, Org. Light-Emitting Dev. (2003) 2522.
[12] D. Hohnholz, A.G. MacDiarmid, D.M. Sarno, W.E. Jones Jr., Chem. Commun. (2001) 2444.
[13] T. Hatano, M. Takeuchi, A. Ikeda, A.S. Shinkai, Org. Lett. 5 (2003) 1395.
[14] J.L. Duvail, P. Retho, S. Garreau, G. Louarn, C. Godon, S.D. Champagne, Synth. Met. 131 (2002) 123.
[15] B.H. Kim, M.S. Kim, K.T. Park, J.K. Lee, D.H. Park, J. Joo, S.G. Yu, S. Lee, Appl. Phys. Lett. 83 (2003) 539.
[16] M.G. Han, S.H. Foulger, Chem. Commun. (2004) 2154.
[17] T. Tran-Van, S. Garreau, G. Louarn, G. Froyerb, C. Chevrot, J. Mater. Chem. 11 (2001) 1378.
[18] H. Sakagichi, H. Matsumura, H. Gong, Nature Mater. 3 (2004) 551.
[19] C. Cheng, R.K. Gonela, Q. Gu, D.T. Haynie, Nano Lett. 5 (2005) 175.
[20] C.H. Lei, A. Das, M. Elliott, J.E. Macdonald, Appl. Phys. Lett. 83 (2003) 482.
[21] J. Roncali, Chem. Rev. 92 (1992) 711.
[22] Z. Mekhalif, F. Plumier, J. Delhalle, Appl. Surf. Sci. 212–213 (2003) 472.
[23] S. Garreau, G. Louarn, J.P. Buisson, G. Froyer, S. Lefrant, Macromolecules 32 (1999) 6807.
[24] N. Sakmeche, S. Aeiyach, J.J. Aaron, M. Jouini, J.C. Lacroix, P.C. Lacaze, Langmuir 15 (1999) 2566.
[25] K.C. Kao, W. Hwang, Electrical Transport in Solids, vol. 14, Pergamon Press, New York, 1981.
[26] R.W. Silveira, J.A. Marohn, Phys. Rev. Lett. 93 (2004) 116104.
[27] S. Samitsu, T. Shimomura, K. Ito, M. Fujimori, S. Heike, T. Hashizume, Appl. Phys. Lett. 86 (2005) 233103.
[28] S. Moller, C. Perlov, W. Jackson, C. Taussig, S.R. Forrest, Nature 426 (2003) 166.

Available online at www.sciencedirect.com
SCIENCE DIRECT®
Organic Electronics 7 (2006) 188–194
Organic Electronics
www.elsevier.com/locate/orgel

Photoresponse of organic field-effect transistors based on conjugated polymer/fullerene blends

N. Marjanović [a,*], Th.B. Singh [a], G. Dennler [a], S. Günes [a], H. Neugebauer [a], N.S. Sariciftci [a], R. Schwödiauer [b], S. Bauer [b]

[a] *Linz Institute for Organic Solar Cells (LIOS), Physical Chemistry, Johannes Kepler University Linz, Altenbergerstrasse 69, Linz, A-4040, Austria*

[b] *Soft Matter Physics, Johannes Kepler University Linz, Altenbergerstrasse 69, Linz, A-4040, Austria*

Received 22 November 2005; accepted 9 January 2006
Available online 7 February 2006

Abstract

Results on photoresponsive organic field-effect transistors (photOFETs) based on conjugated polymer/fullerene solid-state mixtures as active semiconductor layer and poly-vinyl-alcohol (PVA) or divinyltetramethyldisiloxane-bis(benzocyclobutene) (BCB) as gate dielectrics are presented. With LiF/Al top source–drain contacts all devices show dominantly n-type transistor behaviour. Devices fabricated with PVA as gate insulator reveal gate voltage induced saturation upon illumination but low photostability. Contrary, devices fabricated with BCB as gate insulator show transistor amplification in a wide range of illumination intensities. The increase of the drain–source current by more than two orders of magnitudes upon illumination is explained by the generation of a large carrier concentration due to photoinduced charge transfer at the conjugated polymer/fullerene bulk heterojunction upon illumination (photodoping). After illumination, a change of the dark transfer characteristics with respect to the initial transfer characteristics was observed. The initial dark state is achieved either by applying a large negative gate bias or by annealing.

PACS: 85.60.Dw; 85.30.Tv

Keywords: Phototransistors; Organic field-effect transistors (OFETs); Organic dielectrics; Conjugated polymer/fullerene bulk heterojunction

1. Introduction

Organic field-effect transistors (OFETs) play a prominent role in organic semiconductor based electronic devices due to the possibility of switching and driving thin film transistors (TFT) in flexible displays, smart cards, radio frequency identification (RFID) tags and large area sensor arrays [1–3]. An advantage of organic devices is the capability of being processed from solution allowing low cost/large scale fabrication techniques, such as ink-dot printing [4]. Light emitting diodes and

* Corresponding author. Tel.: +43 732 2468 8767; fax: +43 732 2468 8770.
E-mail address: nenad.marjanovic@jku.at (N. Marjanović).

1566-1199/$ - see front matter © 2006 Elsevier B.V. All rights reserved.
doi:10.1016/j.orgel.2006.01.002

displays based on organic semiconductors are already entering the market. Organic solar cells have reached efficiencies exceeding 4% [5a,b]. OFETs with mobilities up to 1 cm^2/V s are investigated in academic as well as in industrial laboratories catching up fast with the performance of amorphous silicon TFT devices [6a,b].

Photoresponsivity of organic field-effect transistors (photOFETs) is interesting since it is the basis for light sensitive transistors. PhotOFETs can be used e.g. for light induced switches, light triggered amplification, detection circuits and, in photOFET arrays, for highly sensitive image sensors. The realisation of photoactive organic field-effect transistors has been demonstrated using various organic and polymeric semiconductors. Responsivity as high as 0.5–1 A/W has been achieved using pristine poly(3-octylthiophene) [7], polyfluorene [8], bifunctional spiro compounds [9] and polyphenyleneethynylene derivative [10]. Among the various concepts for achieving a highly efficient photoinduced charge generation, one of the well-known routes is ''the bulk heterojunction concept'', which uses acceptor materials with high electron affinity (such as C_{60} or soluble derivatives of C_{60}) mixed with conjugated polymers as electron donors [11a,b,c]. The behaviour of OFETs based on conjugated polymer/fullerene blends as active layers in FET configuration in the dark (including ambipolar transport) has been reported [12a,b,13]. However, photOFETs based on conjugated polymer/fullerene blends, which are expected to show higher photoresponsivity in comparison to devices with single components [7–10], have not been reported until now.

In this paper, we report on photOFETs based on conjugated polymer/fullerene blends as the photoactive semiconductor layer and poly-vinyl-alchocol (PVA) or divinyltetramethyldisiloxane-bis(benzocyclobutene) (BCB) as a highly transparent polymeric gate dielectrics. PhotOFETs fabricated on PVA show high responsivity but weak photostability, whereas photOFETs fabricated on BCB show transistor behaviour in a broad range of illumination intensities and good photostability even at high illumination. For devices with both dielectrics, the increase in drain–source current under illumination suggests the generation of carriers in the bulk of the highly photoactive conjugated polymer/fullerene blend. Interface charging effects, i.e. charge trapping at the interface between the dielectric and the bulk, resulting in hysteresis in transfer curves, is observed.

2. Experimental

A scheme of the device structure is presented in Fig. 1 together with the chemical structures of the materials used. PhotOFETs were fabricated on cleaned and patterned indium tin oxide (ITO) glass substrates. For PVA based devices, PVA with an average molecular weight of 127,000 (Sigma–Aldrich Mowiol® 40–88) was used as received. A pinhole free film of PVA gate dielectric was cast from a 10 wt.% aqueous solution by spin coating with 1500 rpm. From the thickness of the dielectric layer $d = 3.8$ μm and the dielectric constant $\varepsilon_{PVA} = 8$, a capacitance of $C_{PVA} = 1.8$ nF/cm^2 is estimated. BCB precursor solution (used as received from Dow Chemicals) was spin coated at 1500 rpm resulting in a 2-μm thick pinhole free film. The cross-linking to BCB was done as described previously [6b,14,15]. BCB forms an inert dielectric layer with excellent mechanical properties and chemical stability, however with a rather low dielectric constant $\varepsilon_{BCB} = 2.6$ ($C_{BCB} = 1.2$ nF/cm^2). As photoactive material, a blend of MDMO-PPV (poly[2-methoxy-5-(3,7-dimethyloctyloxy)]-1,4-phenylenevinylene) and (PCBM) methanofullerene [6,6]-phenyl C_{61}-butyric acid methyl ester (1: 4 wt. ratio) was spin coated at 1500 rpm from 0.5 wt.% chlorobenzene solution, yielding films around 170 nm, inside a glove box under argon atmosphere. The surface morphology and the thickness of the dielectric and the blend film were determined with a Digital Instrument 3100 atomic force microscope (AFM) and a Dektak surface profilometer. As top source and drain contacts, LiF/Al (0.6/60 nm) was evaporated under vacuum (5×10^{-6} mbar) through a shadow mask. The channel length, L, of all devices was 35 μm and the channel width, W, was 2 mm. All electrical characterisations were carried out under inert argon environment inside a glove box system or under vacuum. For the steady state current–voltage measurements, Keithley 2400 and Keithley 236 instruments were used. For the characterisation of the devices under illumination, a solar simulator (K.H. Steuernagel Lichttechnik GmbH) with intensities varying from 0.1 to 100 mW/cm^2 by using neutral density filters was used. The devices were illuminated through the ITO glass and the transparent dielectric layer as shown in Fig. 1(c).

3. Results and discussion

Output characteristics of a photOFET based on MDMO-PPV:PCBM (1:4) blends fabricated on

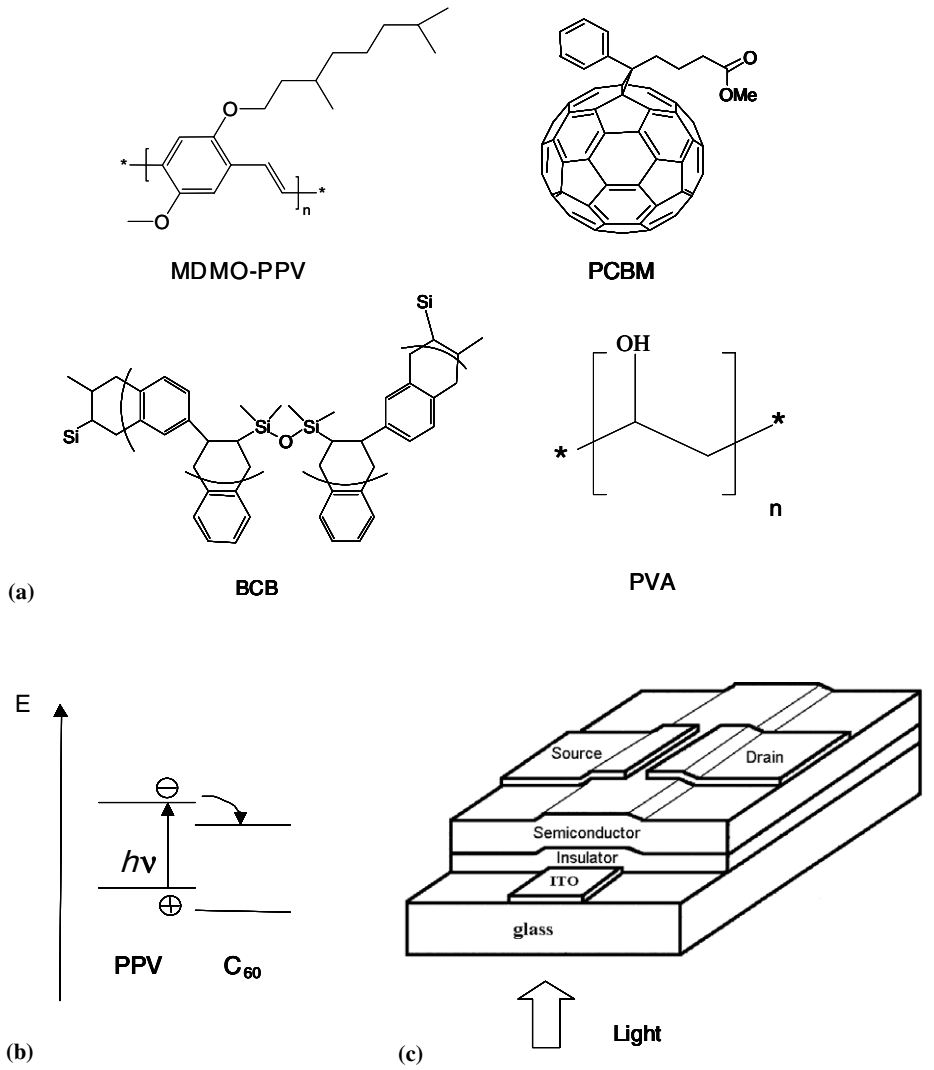

Fig. 1. (a) Molecular structure of MDMO-PPV, PCBM, BCB and PVA; (b) scheme of the photoinduced charge transfer between the PPV donor and the C_{60} acceptor; (c) photOFET device structure.

top of the PVA gate-insulator with LiF/Al top source–drain contacts in dark are shown in Fig. 2(a). Electron accumulation mode is achieved with a positively biased gate voltage, V_{gs}, demonstrating n-type transistor behaviour, similar to the behaviour reported in pristine PCBM based devices [17]. It is assumed that LiF/Al forms ohmic contacts with the blend layer, especially with respect to charge injection and collection from the fullerene phase [16a,b,c]. Fig. 2(b) shows device transfer characteristics in dark (bottom curve). The calculated electron field-effect mobility, μ, was obtained from the saturation regime by using the following equation [18]:

$$I_{ds} = \frac{\mu W C_{PVA}}{2L}(V_{gs} - V_{th})^2, \quad (1)$$

where V_{th} is the threshold voltage, and found to be 10^{-2} cm^2/V s. In pristine PCBM based OFETs, calculated electron mobilities as high as 0.2 cm^2/V s have been observed [17], at least one order of magnitude higher than in the present blend devices. We presume that, in the blend, polymer chains significantly disturb the inter-molecular hopping transport in the fullerenes. A significant hysteresis in the dark transfer characteristics curve (Fig. 2(b)), when changing the sweep direction of the gate voltage, is observed. In other systems, the occurrence of a hysteresis has been attributed to charge trapping

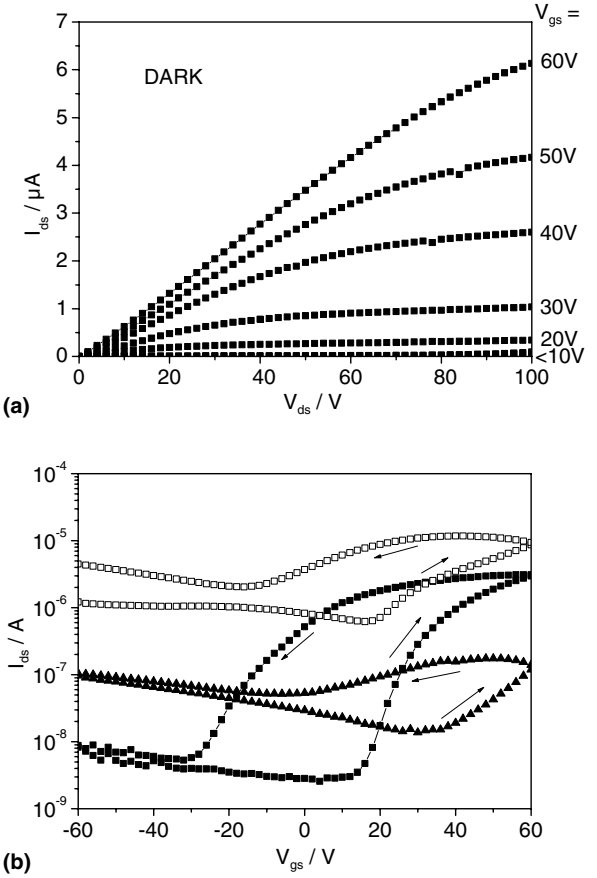

Fig. 2. (a) Output characteristics of the MDMO-PPV:PCBM (1:4) based photOFET fabricated on top of a PVA gate-insulator with LiF/Al as top source and drain electrodes in dark; (b) Transfer characteristics of the device in dark (filled square symbol curves), under AM1.5 (1 mW/cm^2) illumination (open square symbol curves) and in dark after illumination (filled triangular symbol curves) measured at $V_{ds} = +80$ V. The arrows show the sweep directions.

effects at the semiconductor/dielectric interface or in the bulk of the dielectric [17,19,20]. Similar effects are expected to be the reason for the hysteresis in our devices as well.

The curves with open squares symbols (upper curve) in Fig. 2(b) show the photoresponse of the devices. At low white light (AM1.5) intensity of 1 mW/cm^2, the transfer characteristics show gate voltage induced electron enhanced regime. In the depletion regime, I_{ds} increases more than two orders of magnitude in comparison to the currents in dark. The responsivity of the devices calculated (using Eq. (2)) from the depletion and the accumulation region, are 1.4 A/W and 5 A/W, respectively. At higher light intensities the drain–source current, I_{ds} increases even more, becoming gate voltage independent and the device performance changes to a two terminal photoresistor.

The increase in I_{ds} can be explained by the generation of a large number of charge carriers due to the photoinduced charge transfer at the conjugated polymer/fullerene bulk heterojunction (photodoping). In contrast to expectations, still a high field is required for reaching the threshold voltage in the PVA based photOFET devices upon illumination, presumably due to complex interactions of different effects like charge trapping at the PVA/blend interface or in bulk of the dielectric or additional electric field induced charges. After switching off the light, a significant irreversible shift of the transfer curve in respect to the initial dark transfer characteristic was found (filled triangular symbol curves in Fig. 2(b)). We attribute that behaviour to photoinstability of the device. The origin and nature of the processes, which lead to photoinstability, are still under investigation.

In contrast to PVA, BCB as gate-insulator forms a much more photostable system. As mentioned above, cross-linked BCB forms an inert dielectric layer with excellent mechanical properties and chemical stability. On top of BCB, bulk heterojunction MDMO-PPV:PCBM (1:4) based photOFETs were fabricated. Electron enhanced mode in dark and under AM1.5 (100 mW/cm^2) illumination is achieved by biasing the devices with positive gate-source voltages, V_{gs} (Fig. 3(a)). The light response of the device is clearly observed by comparing the values of the drain–source current in dark and under illumination. Again, the increase of I_{ds} is caused by the creation of a large number of charge carriers due to photoinduced charge transfer between the conjugated polymer and the fullerene in the blend. A negligible hysteresis in the initial dark transfer characteristics is observed (filled squares symbol curves in Fig. 3(b)). A calculated electron mobility, μ_e of 10^{-2} cm^2/V s is derived from the initial dark transfer characteristics at $V_{ds} = +80$ V. The transfer characteristics of the device upon illumination with white light (AM1.5) and different illumination intensities (from 0.1 to 100 mW/cm^2) are shown in Fig. 3(b) with open symbol curves. The drain–source current of the device is significantly increased upon illumination, especially in the depletion regime. In the accumulation regime, the increase of the drain–source current is less pronounced.

The *responsivity*, R (expressed in A/W) of the device, can be defined as [8]:

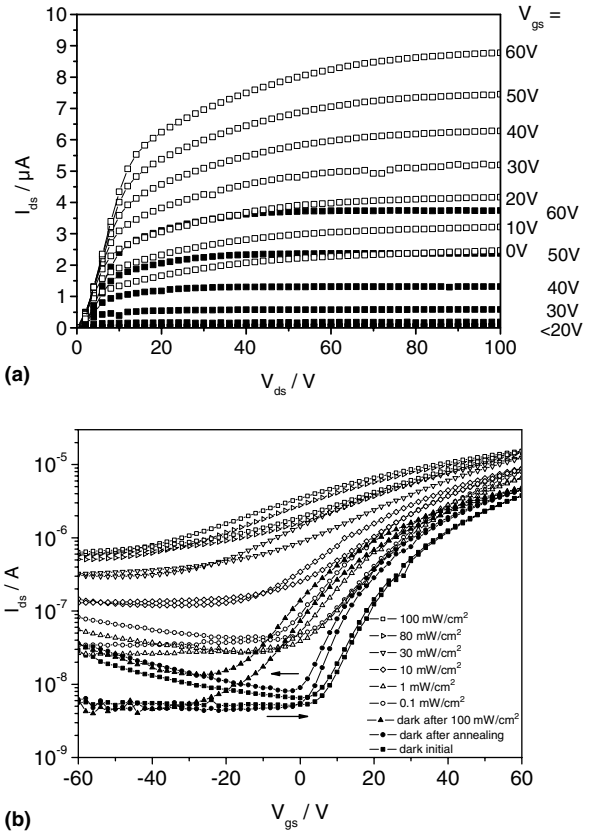

Fig. 3. (a) Output characteristics of the MDMO-PPV:PCBM (1:4) based photOFET fabricated on top of a BCB gate insulator with LiF/Al as top source and drain electrodes in dark (filled square symbol curves) and under AM1.5 (100 mW/cm^2) (open square symbol curves); (b) transfer characteristics of the device in dark (filled square symbol curves), under AM1.5 illumination for different illumination intensities from 0.1 to 100 mW/cm^2 (open symbol curves), in dark after illumination (filled triangular symbol curves) and in dark after annealing at 130 °C for 3 min (filled circle symbol curves), measured at $V_{ds} = +80$ V. The arrows show the sweep directions.

$$R = \frac{I_{ph}}{P_{opt}} = \frac{(I_{ds,illum} - I_{ds,dark})S^{-1}}{P_{inc}}, \qquad (2)$$

where I_{ph} is the drain–source photocurrent, P_{opt} is the incident optical power, P_{inc} the power of the incident light per unit area, $I_{ds,illum}$ the drain–source current under illumination, $I_{ds,dark}$ the drain–source current in the dark and S is the effective device area. The photOFET responsivity calculated from Eq. (2) in the depletion region was found to be 10 mA/W and in the accumulation regime 0.15 A/W, respectively. The threshold voltage for reaching the accumulation mode and opening of the transistor shifts to lower values upon illumination, suggesting that the trap carrier density in the channel is enhanced by photodoping. The higher responsivity in the accumulation regime than in the depletion regime is attributed to the number of photogenerated charge carriers in the blend, which depends mostly on the light intensity and not on the applied gate voltage.

Upon illumination two different effects occur in the active layer of the transistor, i.e. *photoconductivity* and *photovoltaic effect*. When the transistor is in the ON-state the photocurrent is dominated by the photovoltaic effect and is given by Eq. (3) [21]:

$$I_{ph,pv} = G_M \Delta V_{th} = \frac{AkT}{q} \ln\left(1 + \frac{\eta q \lambda P_{opt}}{I_{pd} hc}\right), \qquad (3)$$

where η is the quantum efficiency (i.e. number of carriers generated per photon), q is elementary charge, P_{opt} the incident optical power, I_{pd} the dark current for electrons, hc/λ the photon energy, G_M the transconductance, ΔV_{th} the threshold voltage shift, and A a fit parameter. The photovoltaic effect together with a shift of the threshold voltage is caused by the large number of trapped charge carriers under the source [7–10].

When the transistor is in the OFF-state, the photocurrent, dominated by photoconductivity is given by Eq. (4) [18]:

$$I_{ph,pc} = (q\mu nE)WD = BP_{opt}, \qquad (4)$$

where μ is the charge carrier mobility, n is the carrier density, E the electrical field in the channel, W the gate width, and D the thickness of the active layer. $I_{ph,pc}$ is therefore directly proportional to P_{opt} with a proportionality factor B. The experimental result of photOFETs based on MDMO-PPV:PCBM

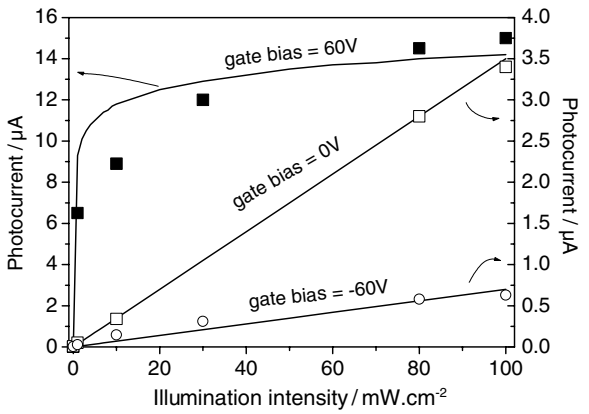

Fig. 4. Photocurrent as a function of illumination intensity in the ON-state ($V_{gs} = 60$ V, filled square symbols), under low gate bias ($V_{gs} = 0$ V, open square symbols) and in the OFF-state ($V_{gs} = -60$ V, open circle symbols). Solid lines are fits using Eqs. (3) and (4).

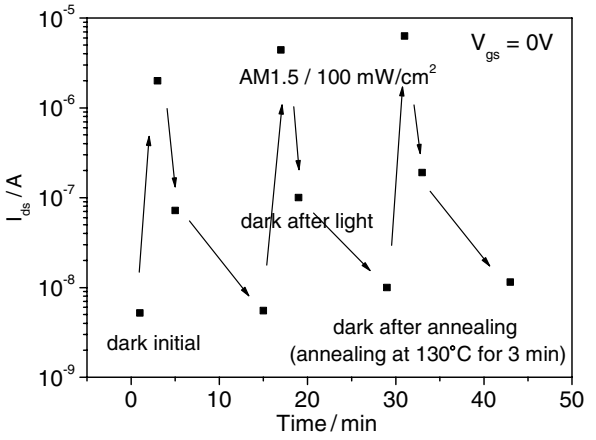

Fig. 5. Drain–source current for the MDMO-PPV:PCBM (1:4) photOFET recorded at $V_{gs} = 0$ V in the dark, under AM1.5 (100 mW/cm^2) illumination, again in the dark, and after annealing, for the first three cycles.

(1:4) blend as active layer and BCB as gate-insulator (Fig. 4) are in good agreement with the calculations.

After illumination, a shift in the dark transfer curve with respect to the initial dark transfer characteristics was observed (filled triangular symbol curves Fig. 3(b)) presumably due to the persistent interface effects, i.e. charge trapping, bias stressing, etc. [17,19,20,22]. In contrast to PVA, the initial dark can be recovered by annealing the device at 130 °C for 3 min (filled circle symbol curves, Fig. 3(b)). Fig. 5 shows the drain–source current recorded sequentially at $V_{gs} = 0$ V in the dark, under AM1.5 (100 mW/cm^2) illumination, again in the dark and after annealing, for the first three cycles. The similar values for the respective dark/illumination situations show the good reversibility of the device. The existence of a state in the device with a larger current after illumination and prior to annealing may be considered as a memory state, which can be set by light and erased either by annealing or by applying a large negative gate voltage. It is proposed to exploit the effect of an increased dark state current after illumination in applications such as a light activated memory (''light memory device'').

4. Summary

In summary, we demonstrate photoresponsive OFETs (photOFET) based on MDMO-PPV:PCBM (1:4) blends with transparent insulating PVA or BCB layers as gate-dielectrics. The devices shown-type transistor characteristics with LiF/Al as top source and drain electrodes. Devices fabricated with PVA as gate insulator show phototransistor behaviour at low light intensities with a high response. However, irreversibilities in the device properties after illumination occurred. PhotOFETs fabricated on top of cross-linked BCB as dielectric show phototransistor behaviour in a wide range of illumination intensities with sufficiently good photo- stability. The observation of an intermediate state (dark after illumination) has been proposed for use in ''light memory devices''.

Acknowledgements

Special thanks are to G.J. Matt, A.J. Mozer, and A. Tanda for fruitful discussions. Financial support from the Austrian Foundation for the Advancement of Scientific Research (FWF P15629-N08) is gratefully acknowledged. S. Günes acknowledges the national award scholarship from Yildiz Technical University allocated from the Council of Higher Education of Turkey (YÖK).

References

[1] H.E.A. Huitema, G.H. Gelinck, J.B.P.H. van der Putten, K.E. Kuijk, C.M. Hart, E. Cantatore, P.T. Herwig, A.J.J.M. van Breemen, D.M. de Leeuw, Nature 414 (2001) 599.
[2] W. Clemens, W. Fix, J. Ficker, A. Knobloch, A. Ullmann, J. Mater. Res. 19 (2004) 1963.
[3] B. Crone, A. Dodabalapur, A. Gelperin, L. Torsi, H.E. Katz, A.J. Lovinger, Z. Bao, Appl. Phys. Lett. 78 (2001) 2229.
[4] A. Knobloch, A. Manuelli, A. Bernds, W. Clemens, J. Appl. Phys. 96 (2004) 2286.
[5] (a) S.E. Shaheen, C.J. Brabec, N.N. Sariciftci, F. Padinger, T. Fromherz, J.C. Hummelen, Appl. Phys. Lett. 78 (2001) 841; (b) M.M. Wienk, J.M. Kroon, W.J.H. Varhees, J. Knol, J.C. Hummelen, P.A. Van Hal, R.A.J. Jansen, Angew. Chem. Int. Ed. 42 (2003) 3371.
[6] (a) C.D. Dimitrakopoulos, P.R.L. Malenfant, Adv. Mater. 14 (2002) 99;
(b) Th.B. Singh, N. Marjanović, G.J. Matt, S. Günes, N.S. Sariciftci, A.M. Ramil, A. Andreev, H. Sitter, R. Schwödiauer, S. Bauer, Org. Electron. 6 (2005) 105.
[7] K.S. Narayan, N. Kumar, Appl. Phys. Lett. 79 (2001) 1891.
[8] M.C. Hamilton, S. Martin, J. Kanicki, IEEE Trans. Electron Dev. 51 (2004) 877.
[9] T.P.I. Saragi, R. Pudzich, T. Fuhrmann, J. Salbeck, Appl. Phys. Lett. 84 (2004) 2334.
[10] Y. Xu, P.R. Berger, J.N. Wilson, U.H.F. Bunz, Appl. Phys. Lett. 85 (2004) 4219.
[11] (a) N.S. Sariciftci, L. Smilowitz, A.J. Heeger, F. Wudl, Science 258 (1992) 1474;
(b) C.H. Lee, G. Yu, D. Moses, K. Pakbaz, C. Zhang, N.S. Sariciftci, A.J. Heeger, F. Wudl, Phys. Rev. B 48 (1993) 15425;
(c) C.J. Brabec, N.S. Sariciftci, J.C. Hummelen, Adv. Func. Mater. 11 (2001) 15.

[12] (a) E.J. Meier, D.M. de Leeuw, S. Setayesh, E. van Veenendaal, B.-H. Huisman, P.W.M. Blom, J.C. Hummelen, U. Scherf, T.M. Klapwijk, Nature Mater. 2 (2003) 678;
(b) W. Geens, T. Martens, J. Poortmans, T. Aernouts, J. Manca, L. Lutsen, P. Heremans, S. Borghs, R. Mertens, D. Vanderzande, Thin Solid Films 451–452 (2004) 498.
[13] Th.B. Singh, S. Günes, N. Marjanović, N.S. Sariciftci, R. Menon, J. Appl. Phys. 97 (2005) 114508.
[14] L.-L. Chua, P.K.H. Ho, H. Sirringhaus, R.H. Friend, Appl. Phys. Lett. 84 (2004) 3400.
[15] R. Schwödiauer, G.S. Neugschwandtner, S. Bauer-Gogonea, S. Bauer, W. Wirges, Appl. Phys. Lett. 75 (1999) 3998.
[16] (a) V.D. Mihailetchi, J.K.J. van Duren, P.W.M. Blom, J.C. Hummelen, R.A.J. Janssen, J.M. Kroon, M.T. Rispens, W.J.H. Verhees, M.M. Wienk, Adv. Func. Mater. 13 (2003) 43;
(b) G.J. Matt, N.S. Sariciftci, T. Fromherz, Appl. Phys. Lett. 84 (2004) 1570;
(c) C.J. Brabec, A. Cravino, D. Meissner, N.S. Sariciftci, T. Fromherz, M.T. Rispens, L. Sanchez, J.C. Hummelen, Adv. Funct. Mater. 11 (2001) 374.
[17] Th.B. Singh, N. Marjanović, P. Stadler, M. Auinger, G.J. Matt, S. Günes, N.S. Sariciftci, R. Schwödiauer, S. Bauer, J. Appl. Phys. 97 (2005) 083714.
[18] S.M. Sze, Physics of Semiconductor Devices, Wiley, New York, 1981.
[19] Th.B. Singh, N. Marjanović, G.J. Matt, N.S. Sariciftci, R. Schwödiauer, S. Bauer, Appl. Phys. Lett. 85 (2004) 5409.
[20] L.-L. Chua, J. Zaumsell, J.-F. Chang, E.C.-W. Ou, P.K.-H. Ho, H. Sirringhaus, R.H. Friend, Nature 434 (2005) 194.
[21] H.-S. Kang, C.S. Choi, W.-Y. Choi, D.-H. Kim, K.-W. Seo, Appl. Phys. Lett. 84 (2004) 3780.
[22] A. Sallelo, M.L. Chabinyc, M.S. Yang, R.A. Street, Appl. Phys. Lett. 81 (2002) 4383.

Available online at www.sciencedirect.com
SCIENCE DIRECT®
Organic Electronics 7 (2006) 195–204
Organic Electronics
www.elsevier.com/locate/orgel

Stoichiometry dependence of charge transport in polymer/methanofullerene and polymer/C_{70} derivative based solar cells

Abay Gadisa [a,*], Xiangjun Wang [a], Shimelis Admassie [b,a], Erik Perzon [c], Frédéric Oswald [d], Fernando Langa [d], Mats R. Andersson [b,c], Olle Inganäs [b,a]

[a] *Biomolecular and Organic Electronics (IFM), Linköping University, S-581 83 Linköping, Sweden*
[b] *Center of Organic Electronics, Linköping University, S-581 83 Linköping, Sweden*
[c] *Department of Organic Chemistry and Polymer Technology, Chalmers University of Technology, S-41296 Göteborg, Sweden*
[d] *Facultad de Ciencias del Medio Ambiente, Universidad de Castilla-La Mancha, 45071 Toledo, Spain*

Received 3 November 2005; received in revised form 22 December 2005; accepted 26 January 2006
Available online 28 February 2006

Abstract

Charge transport in a near infrared absorbing polyfluorene copolymer (APFO-Green1) and its blends with methanofullerene [6,6]-phenyl C_{61}-butyric acid methyl ester (PCBM), and 3′-(3,5-bis-trifluoromethylphenyl)-1′-(4-nitrophenyl)pyrazolino[70]fullerene (BTPF70) is reported. PCBM and BTPF70 are electron acceptor and transporting molecules in polymer based solar cells. The BTPF70 has emerged as a new electron acceptor molecule that provides adequate exciton dissociation when blended with the low band gap polyfluorene copolymer APFO-Green1. Electron transport in both net PCBM and BTPF70 films are subjected to positional and energetic disorder, with the degree of disorder being more pronounced in BTPF70. On the other hand, mixing PCBM with conjugated polymers usually leads to increased hole mobility. We have investigated and compared the acceptor concentration dependence of charge transport in APFO-Green1/PCBM and APFO-Green1/BTPF70 blend films. For better understanding of the charge transport in the heterojunction films, the field and temperature dependence of hole transport in pure APFO-Green1 films has also been studied. It is observed that the behavior of hole mobility in the blend layer is sensitive to the acceptor type. For APFO-Green1/PCBM hole only devices, the hole mobility attains a local maximum at 67 wt.% of PCBM, while on the contrary mixing any amount of BTPF70 with APFO-Green1 results into degradation of hole transport. Electron transport in both blends, however, increases monotonically as a function of acceptor loading.

PACS: 73.61.Ph; 73.61.Wp

Keywords: Solar cells; Acceptor concentration; Charge transport; Space charge limited current

* Corresponding author. Tel.: +46 13 288917; fax: +46 13 288969.
E-mail address: abay@ifm.liu.se (A. Gadisa).

1566-1199/$ - see front matter © 2006 Elsevier B.V. All rights reserved.
doi:10.1016/j.orgel.2006.01.003

1. Introduction

Conjugated polymers have a potential to be used in solar cells. However, unlike in inorganic semiconductors, photocurrent generation in polymer solar cells is a several step process. Shining light on a polymer solar cell generates electron–hole pairs (exciton) that have a binding energy of several tenths of electron volts. Dissociation of the excitons into free carriers gives rise to output current. Hence the current of polymer solar cells is influenced by the exciton dissociation rate and mobility of the free carriers. Efficient exciton dissociation can be achieved by mixing electron accepting and transporting (EAT) materials with the exciton generating polymers, while the free charge collection efficiency is greatly improved by enhancing both hole and electron mobility within the polymer/electron acceptor matrix. Methanofullerene [6,6]-phenyl C_{61}-butyric acid methyl ester (PCBM) is a well-known EAT molecule. In pure PCBM layer, the mobility of an electron was reported to be as high as 2×10^{-7} $m^2/V\,s$ [1]. PCBM is an efficient EAT material when mixed with various types of polymers including polythiophene derivatives [2,3], poly(*p*-phenylene vinylene) (PPV) derivatives [4,5], and polyfluorene derivatives [6,7]. Moreover, charge transport studies in solar cells with poly(2-methoxy-5(3′,7′-dimethyloctyloxy)-*p*-phenylene) vinylene/PCBM active layer showed that the presence of PCBM enhances both hole and electron mobility [8,9].

To harvest more energy from the solar spectrum, it is necessary to have low band gap polymers that absorb the red and infrared part of the solar light. Recently, we have demonstrated solar cells that comprise a low band gap polyfluorene copolymer (APFO-Green1) blended with electron acceptor materials [10,11]. APFO-Green1 has a number average molecular weight (M_n) of 3600 and weight average molecular weight (M_W) of 6200. It has an onset of absorption at 1 μm, while photoluminescence and electroluminescence of devices with APFO-Green1 extends into infrared [12]. It was observed that in solar cells with APFO-Green1/PCBM heterojunction active film, solar energy conversion to electricity was not efficient, in particular near the infrared region [10]. This is due to low driving forces for exciton dissociation at APFO-Green1/PCBM interfaces

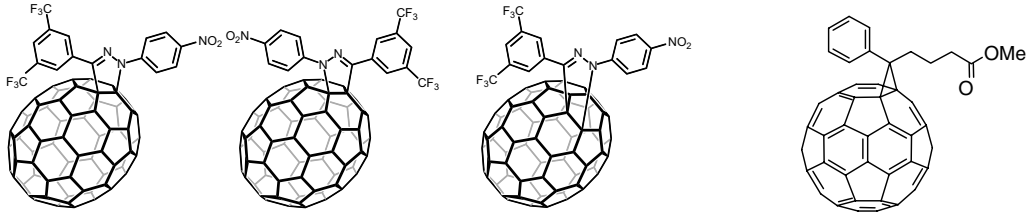

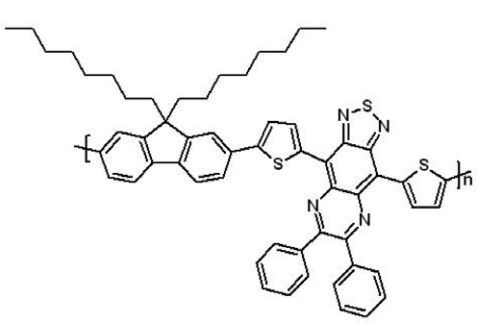

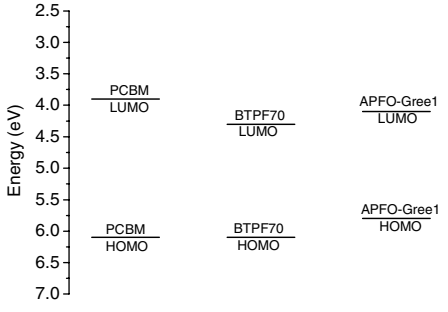

Fig. 1. Chemical structures of the electron acceptor materials and APFO-Green1. The energy band diagram of the materials is also sketched. The energy levels of APFO-Green1 and the LUMO of BTPF70 are taken from Refs. [13,26]. The HOMO level of BTPF70 was estimated from its LUMO energy and the onset of its optical absorption spectrum. The energy levels of BCPM are adopted from Ref. [1].

(see Fig. 1); this is demonstrated by moderate luminescence quenching in these blends. In addition, such solar cells give smaller open circuit voltage mainly due to the reduced energy difference between the highest occupied molecular level (HOMO) of APFO-Green1 and lowest unoccupied molecular level (LUMO) of PCBM [10]. This indicates that PCBM is not an efficient acceptor for solar cells that rely on near infrared absorbing polymers. Consequently, alternative acceptor materials that deliver efficient driving force should be synthesized. We have demonstrated two types of new acceptor molecules, namely, 3′-(3,5-bis-trifluoromethylphenyl)-1′-(4-nitrophenyl)pyrazolino[60]fullerene (BTPF) [10], and 3′-(3,5-bis-trifluoromethylphenyl)-1′-(4-nitrophenyl)pyrazolino[70]fullerene (BTPF70) [13]. Compared to solar cells with APFO-Green1/PCBM, devices with both APFO-Green1/BTPF and APFO-Green1/BTPF70 gave better conversion of light to electricity, with devices based on APFO-Green1/BTPF70 active layer being the best.

In order to develop solar cells with APFO-Green1/BTPF70 active films, the knowledge of charge transport in each material is indispensable. BTPF70 is a mixture of three isomers [13] that have similar electrochemical behaviors in solution. It has a LUMO energy level of 4.3 ± 0.1 eV as determined from electrochemical measurements. Electron transport in BTPF70 was found to be field and temperature dependent, and at room temperature 6×10^{-9} m^2/V s electron mobility was calculated from current–voltage (I–V) measurements of diodes with pure BTPF70 active film [14]. Here, we report the influence of acceptor type on hole and electron transport in diodes that comprise APFO-Green1/BTPF70 and APFO-Green1/PCBM active films. Moreover, detailed studies of field and temperature dependent hole transport in pure APFO-Green1 films will also be presented and discussed.

2. Trap free space charge limited transport

Charge transport in conjugated polymer films is dominated by hopping of charge carriers among localized states as a consequence of the intrinsically amorphous nature of the polymers. Particularly, hopping transport of holes in pure polymer films is field and temperature dependent owing to a positional and energetic disorder limited charge carrier mobility [15,16]. As a consequence, the I–V characteristics of polymer diodes are space charge limited (SCL). In the absence of traps, the SCL I–V characteristics of polymer [15] or molecule [1] based devices are well-described by field and temperature dependent empirical relation

$$\mu = \mu_0 \exp(\gamma\sqrt{E}) \tag{1}$$

where μ_0 is the zero-field mobility, and γ the field activation factor. It has also been demonstrated that for carrier concentration exceeding 10^{22} m^{-3}, charge mobility scales with carrier concentration as a power law [17]. Such power law increase is described by a variable range-hopping model [18].

Charge transport in polymer-based diodes is often simplified as a one-dimensional process. In this context, the basic transport equations describing charge transport behavior are the Poisson's and continuity equations for electrons and holes. In particular, if the effects of traps are negligibly small, the drift-diffusion current equations and the Poisson's equation, respectively, are given by [19]

$$J_n = e\left(-\mu_n(x)n(x)\frac{d\psi}{dx} + D_n\frac{dn}{dx}\right) \tag{2}$$

$$J_p = e\left(-\mu_p(x)p(x)\frac{d\psi}{dx} - D_p\frac{dp}{dx}\right) \tag{3}$$

$$\frac{dE(x)}{dx} = \frac{e}{\varepsilon}(p(x) - n(x)) \tag{4}$$

where J_n (J_p) is the electron (hole) current density, $n(x)$($p(x)$) is the electron (hole) density, e is the electronic charge, D_n (D_p) is electron (hole) diffusion constant, μ_e (μ_p) is the electron (hole) mobility, and ε is the static dielectric constant. The electric field strength $E(x)$ is related to the electrostatic potential $\psi(x)$ as $E(x) = -\frac{d\psi}{dx}$. Under the condition of SCL transport, the drift current dominates the net current flow and the diffusion part is often neglected. Thus, experimental I–V characteristics can, in principle, be analyzed by solving the relevant current equations, and Poisson's equation together with the Poole–Frenkel mobility equations. Due to field dependence of mobility, exact analytic solutions are, however, not possible. This leaves us with either approximate analytic solutions or numerical calculations. Under ohmic boundary conditions, experimental SCL I–V characteristics of holes in polymer [15], and electrons in PCBM [1] thin films, in diode configuration, were successfully described by numerically calculating Eqs. (1)–(4).

The charge transport studies reported in this paper are based on the measurement and analysis of SCL current of sandwich structure devices. Transport parameters were extracted from the fits

of experimental *I–V* data, which were generated by numerically solving Eqs. (1)–(4).

3. Experimental details

3.1. Construction methods of hole only devices

The hole only APFO-Green1 based devices were constructed by sandwiching the polymer film between glass/ITO/PEDOT:PSS, and gold (Au) electrodes. The thickness of the PEDOT:PSS layer was 45 nm while that of Au was 80 nm. The detailed device preparation procedures can be found in Ref. [3]. APFO-Green1 films were formed by spin coating from chloroform solution. Gold is well-known for forming dipoles at Au/PCBM interface giving rise to lowering of injection barrier for electrons [20]. Thus, to discriminate electron injection, the second electrode of polymer/acceptor based hole only devices was constructed from palladium (Pd). However, direct evaporation of Pd onto the active layer was found to give short-circuited devices. To circumvent the later problem, hole only devices that are based on blends of APFO-Green1 and PCBM or BTPF70 were constructed by soft contact lamination technique. Quite recently, non-invasive techniques, termed soft contact lamination, have emerged as an alternative method for formation of electrodes [21]. Soft contact lamination technique exploits the good adhesion property of soft elastomeric materials when brought in conformal contact with smooth surfaces. The adhesion of such elastomeric materials are attributed to only van der Waals forces, but facilitates good electrical contact when conducting materials are applied on the elastomer. This technique has been effectively used in organic light emitting diodes (OLED) [22,23] that generate uniform and stable light. The hole only APFO-Green1/acceptor based devices has two parts. The bottom part comprises the active layer, which was spin coated on a glass/ITO/PEDOT:PSS substrate. The construction of the glass/ITO/PEDOT:PSS was done through the steps described in Ref. [3]. The active layers of APFO-Green1/PCBM were formed by spin coating from chloroform solution. However, due to poor solubility of BTPF70 in chloroform, APFO-Green1/BTPF70 films were formed by spin coating from blends of chloroform and dichlorobenzene solution. The top component of the later devices composes an elastometric polymer Sylgard 184 polydimethylsiloxane (PDMS) as a supporting substrate. The PDMS was initially prepared and cured on a silicon wafer to achieve a smooth surface. The cured PDMS was cut into appropriate pieces onto which thin layer (2–4 nm) of titanium (Ti), and 30 nm of palladium (Pd) metals were consequently evaporated under shadow mask. The presence of Ti between PDMS and Pd facilitates the adhesion of Pd to PDMS, thereby avoiding the cracking of Pd layer. Putting the two parts in intimate contact completes the devices. No additional pressure or heating is applied to construct the complete devices.

3.2. Construction methods of electron only devices

The electron only devices were also constructed in a sandwich structure. One of the electrodes was formed by a highly conductive vapor phase polymerised polymer poly(3,4-ethylenedioxy)thiophene (VPP PEDOT) (~60 nm), which is supported by glass substrates. The synthesis sequences of VPP PEDOT is described elsewhere [24,25]. The conductivity of the VPP PEDOT can reach as high as 1000 S/cm [24] while its work function, as measured by UV photoemission spectroscopy, is about 4.4 eV. The active layer of electron only devices were formed by spin coating respective solutions on the VPP PEDOT layer. The devices were completed by evaporating thin layers of LiF (~1 nm) and aluminium (80 nm) on to the active layer.

3.3. I–V measurements

The *I–V* characteristics of all the devices were measured by a semiconductor parameter analyzer (HP 4156 A). The *I–V* characteristic at various temperatures was recorded by mounting the sample inside a liquid nitrogen cryostat.

4. Results and discussion

4.1. Hole transport in APFO-Green1

According to electrochemical measurements, APFO-Green1 has a HOMO level of 5.2 eV and a LUMO level of 4.0 eV [13]; however, when evaluated from the peak of electrochemical cyclic voltammograms the location should be 5.8 eV and 4.1 eV, respectively [26]. The work function of PEDOT:PSS is about 5.2 eV, and that of Au is close to 5.1 eV. As can be inferred from the *I–V* characteristics, which is depicted in Fig. 2(a), its non-rectifying, and almost symmetric behavior is an indication of a

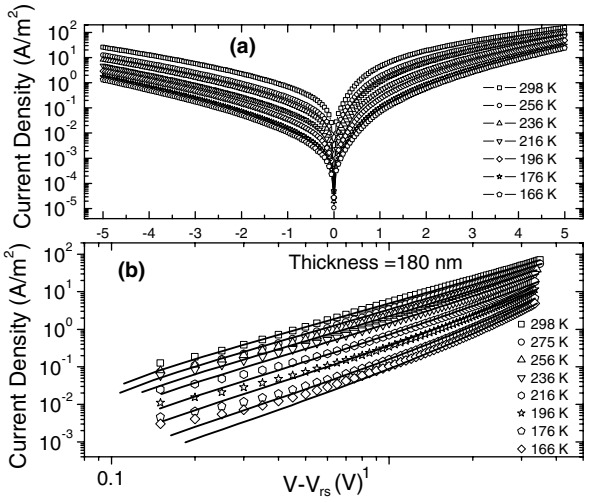

Fig. 2. (a) Semilog plot of SCL I–V characteristics of ITO/PEDOT:PSS/APFO-Gree1n/Au hole only devices both in the reverse and forward bias regions. (b) Log–log plot of the SCL I–V characteristics of ITO/PEDOT:PSS/APFO-Gree1/Au hole only devices in the forward bias. The symbols are experimental data points and the lines are fits generated by a single carrier SCL current model with field and temperature dependent mobility. The device potential is corrected for a contact resistance V_{rs} at the ITO/PEDOT electrode.

negligible built-in potential, which results from the very small difference of the work function of the two electrodes. Consequently, it can be concluded that in the ITO/PEDOT:PSS/APFO-Green1/Au devices studied here, the work functions of the two electrodes are approximately equal and both are hole injecting, making the devices hole dominated.

The average carrier density in the devices can be approximated by $p_{av} = (3/2)(\varepsilon_0\varepsilon_r V/qL^2)$ [19] where ε_0 is the permittivity of free space, ε_r is the dielectric constant of the polymer, V is the net potential, L is the thickness of the active film and q is an elementary charge. Accordingly, at room temperature, the estimated carrier density in ITO/PEDOT:PSS/APFO-Green1/Au devices of thickness 180 nm, $\varepsilon_r = 3$, is about $10^{22}\,m^{-3}$ for a bias voltage of 1.3 V and above. Assuming carrier dependent hole mobility, Tanase et al. [27], described the current of hole dominated devices as $J = 0.8ep_{av}\mu_h(p_{av})E_{av}$, where $E_{av} = V/L$. As discussed earlier, in the field range of interest, the calculated carrier concentration in our hole only devices is almost constant, with a value less than $4 \times 10^{22}\,m^{-3}$. Thus, we describe the temperature and field dependence of the SCL I–V curves of ITO/PEDOT:PSS/APFO-Green1/Au devices by considering field and temperature dependent mobility relation of Eq. (1).

As can be seen from Fig. 2, the very low onset potential for hole injection and the immediate occurrence of SCL current can be taken as the signature of ohmic contacts. We have, therefore, fitted the I–V curves by solving Eqs. (1), (3) and (4) by considering ohmic boundary conditions and taking $N_V = 2.5 \times 10^{25}\,m^{-3}$ [15]. The numerical fits to the experimental I–V curves are depicted in Fig. 2(b). The good agreements between the experimental and calculated curves enabled us to calculate the zero-field mobility (μ_0) and the field activation factor (γ) at various temperatures. Figs. 3 and 4 show the zero-field mobility (μ_0) and the field activation factor (γ), respectively, as a function of temperature. In particular, at room temperature, the hole mobility was found to be $\mu_0 = (8.0 \pm 0.4) \times 10^{-10}\,m^2/V\,s$ while the field activation factor amounts to $\gamma = (8.76 \pm 0.2) \times 10^{-5}\,(m/V)^{1/2}$. The strong temperature dependence of μ_0 and γ is a typical feature of hopping transport among localized transport sites.

Based on the data of temperature dependent mobility (μ_0) (Fig. 3) and the field activation factor (γ) (Fig. 4), more quantitative description of hole transport can be done by elaborating other transport models. The empirical mobility Eq. (1) is typical for hopping transport in a Gaussian density of states (GDS). Under hopping transport conditions, which are subjected to long-range energy correlations, the

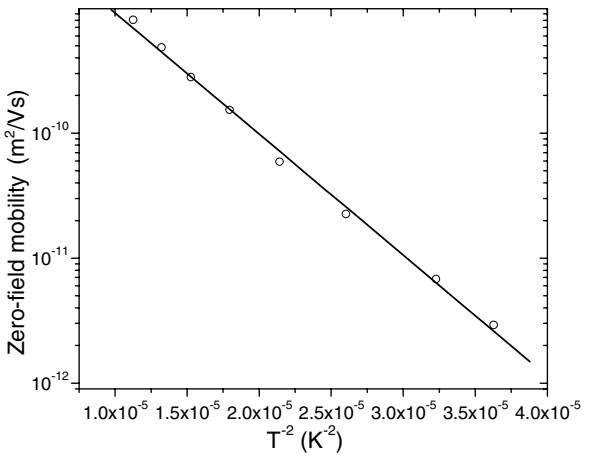

Fig. 3. The variation of zero-field mobility (μ_0) with temperature. The symbols represent the values extracted from numerical calculations of Eqs. (1)–(3), by using the experimentally measured current density as an input. The line is a fit, which was generated by using Eq. (5).

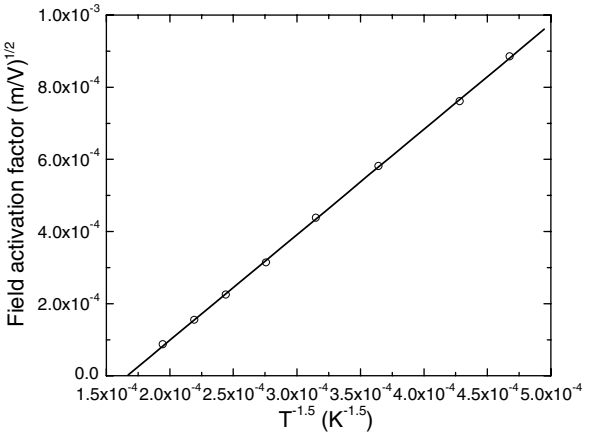

Fig. 4. The variation of field activation factor (γ) with temperature. The symbols represent the values extracted from numerical calculations of Eqs. (1)–(3), by using the experimentally measured current density as an input. The line is a fit, which was generated by using Eq. (5).

empirical mobility Eq. (1) was formulated through Monte Carlo simulation as [28]

$$\mu = \mu_\infty \exp\left[-\left(\frac{3\sigma}{5k_BT}\right)^2 + 0.78\left(\left(\frac{\sigma}{k_BT}\right)^{3/2} - 2\right)\sqrt{\frac{eaE}{\sigma}}\right] \quad (5)$$

Here, μ_∞ is the mobility at $T \to \infty$, σ is the width of the GDS, a is the average intersite distance between hopping sites, and k_B is the Boltzmann's constant. This model was found to agree very well with experimental data of hole only devices based on conjugated polymers [15], and a SCL electron current in PCBM [1] thin films. Therefore, we have chosen to use the correlated Gaussian disorder model (Eq. (5)) to further relate mobility with intrinsic parameters of the polymer. Using Eq. (5), σ can be calculated from the slope of the plot of μ_0 versus T^{-2} (Fig. 3). Once σ is known, the value of a can be obtained from the plot of γ versus $T^{-3/2}$ (Fig. 4). The best fitting parameters are $\sigma = 70 \pm 1$ meV and $a = 1.95 \pm 0.02$ nm.

4.2. Hole and electron transport in APFO-Green1/PCBM blend films

Mixing polymers with PCBM usually ends up with phase-separated domains rich either in PCBM or polymer. From transport point of view, the most peculiar feature of polymer/PCBM blend is the monotonically increasing electron and hole mobility as the PCBM concentration in the blend is gradually increased. This has clearly been demonstrated in time-of-flight (TOF) [29,30] and solar cell measurements [8,9].

For APFO-Green1/PCBM based diodes, both hole and electron transport parameters were extracted from the respective I–V curves that were measured under dark condition at room temperature. Typical I–V curves are depicted in Fig. 5. The hole only and electron only devices resulted into SCL transport as can be seen from Fig. 5. The I–V curves were fitted using a model of single carrier SCL current where the carrier mobility is described by Eq. (1).

Extracted hole and electron mobility are depicted in Fig. 6 as a function of PCBM concentration. As

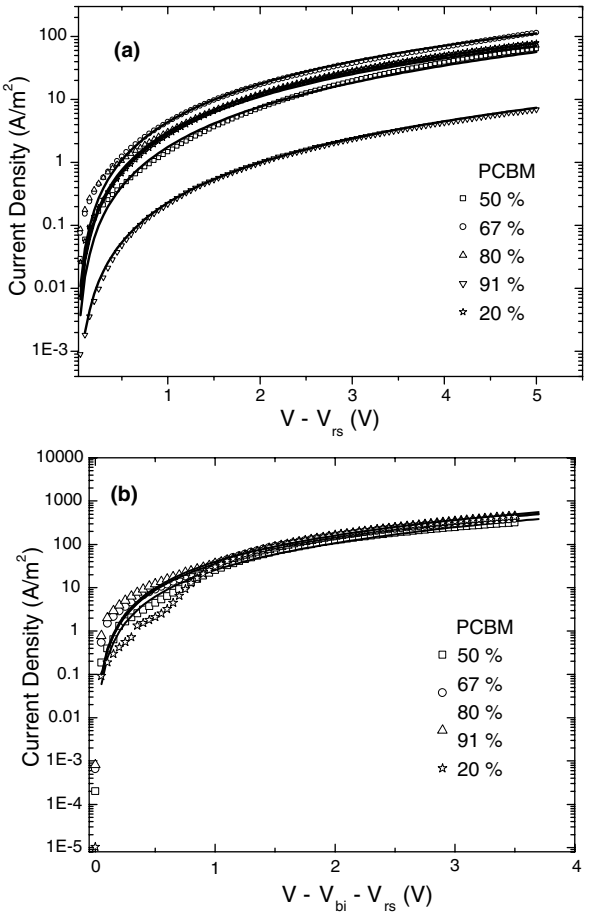

Fig. 5. The dark current–voltage characteristics of the (a) hole only, and (b) electron only devices with APFO-Green1:PCBM charge transporting layer. The lines represent the predictions of single carrier SCL current model that incorporates the Poole–Frenkel mobility $\mu = \mu_0 \exp(\gamma\sqrt{E})$, the built-in potential, V_{bi}, and the potential drop across the ITO/PEDOT:PSS contact, V_{rs}.

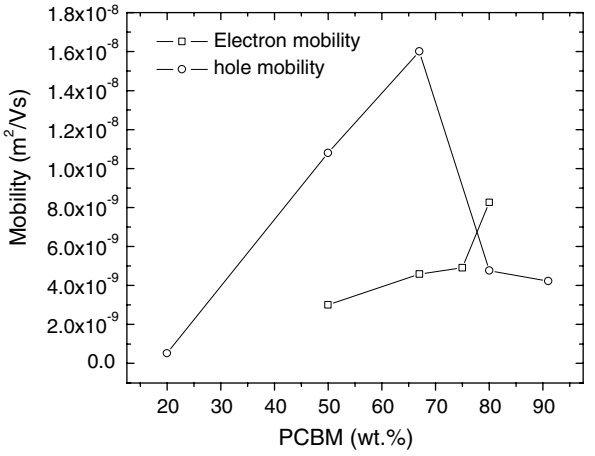

Fig. 6. Hole and electron mobility as a function of PCBM concentration. Lines between data points are only guides to the eye.

can be observed from Fig. 6, hole mobility varies as a function of PCBM concentration, where the monotonic variation includes a local maximum at around 67 wt.% of PCBM. On the contrary, loading more and more PCBM seems to enhance electron mobility.

Spin coated films of polymer/polymer [31,32] or polymer/molecule [33,34] thin films are usually accompanied by phase separation processes as a result of low entropy of mixing. Among others, the morphology of solar cells based on blends of MDMO-PPV poly(2-methoxy-5(3′,7′-dimethyloctyloxy)-1,4-phenylene vinylene) and PCBM has been well-studied [33,34]. According to the report of Hoppe et al. [34], the morphology of MDMO-PPV:PCBM films is nanoclusters which are exclusively rich with either of the materials. Such big nanoclusters of PCBM were observed to initiate at MDMO-PPV:PCBM ratio of 1:2 and grow as a function of PCBM loading. The transition of morphology from smooth to uneven behavior in MDMO-PPV:PCBM solid films was further confirmed through a detailed study of morphology [33]. In general, it has been shown that increasing the concentration of PCBM enhances electron mobility while inducing more phase separation. On the other hand, it has been demonstrated that for solar cells based on MDMO-PPV/PCBM, increasing PCBM concentration was found to enhance both electron and hole mobility [8,9,29]. However, the reason for enhancement of hole mobility as a function of more PCBM loading is not clear yet.

Contrary to what is observed for other polymers, hole mobility in APFO-Green1/PCBM films has a local maximum at a PCBM concentration of 67 wt.% (APFO-Green1/PCBM mixed at 1:2 by wt.). The local peak is followed by a sharp decrease in hole mobility. The reason for breaking of hole percolation path beyond PCBM concentration of 67 wt.% is not clear yet. However, it appears that more interconnected domains that are rich of either of the materials coexist at PCBM concentration of about 67%. While increasing PCBM concentration obviously enhances connection of the PCBM rich domains (increasing electron percolation path), the polymer rich domains might further be separated from each other thereby suppressing hole percolation paths.

4.3. Hole and electron transport in APFO-Green1/BTPF70 blend films

As stated earlier, solar cells based on APFO-Green1 as electron donors are efficient when BTPF70 is used as an electron acceptor [13]. Hence, it is quite important to investigate the behavior of electron and hole transport in APFO-Green1/BTPF70 heterojunction films. Here, electron and hole transport in APFO-Green1/BTPF70 thin films were investigated separately following similar procedures of the previous sections. The *I–V* characteristics of electron and hole only currents were measured and depicted in Fig. 7. The *I–V* curves were fitted by a single carrier SCL model, which is governed by the mobility given in Eq. (1).

Fig. 8 shows the calculated electron and hole mobility as a function of BTPF70 concentration. As can be observed from the figure, blending BTPF70 with APFO-Green1 does not favor hole transport at all. In addition, though electron mobility seems to increase with increasing concentration of BTPF70, better electron mobility was measured in pure BTPF70 film. Similarly, comparing the results of this section with that of Section 4.1 shows that hole mobility in pure APFO-Green1 is about an order of magnitude greater than hole mobility measured in blend films. In a separate study of electron transport in pure BTPF70 film [14] we observed that the electron transport is severely limited by positional and energetic disorder. Hopping transport in a disordered media takes place at an expense of an energy that is supplied to the electron to increase jumping rates over barriers. Assuming a Gaussian site energy distribution (GED), we

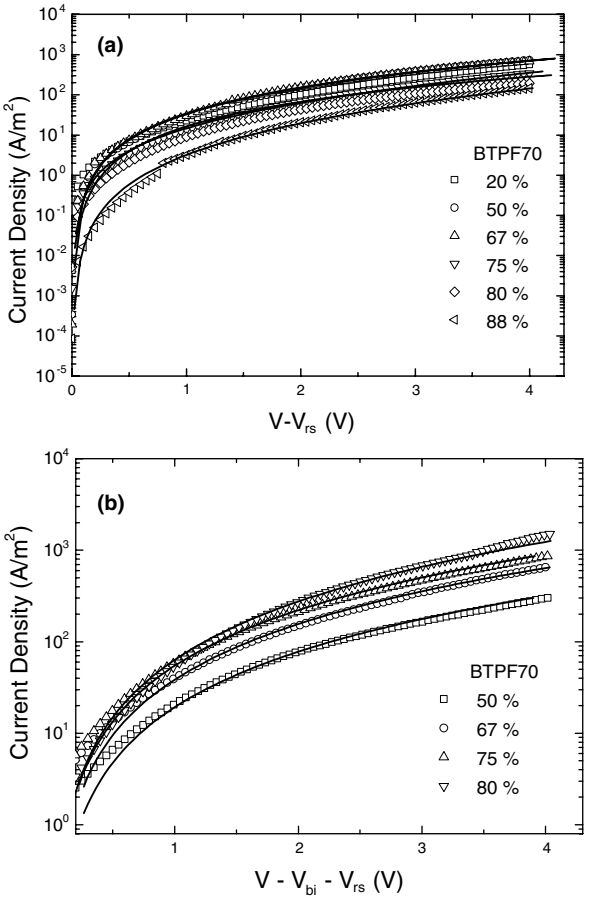

Fig. 7. The dark current–voltage characteristics of the (a) hole only, and (b) electron only devices with APFO-Green1:BTPF70 charge transporting layer. The lines represent the predictions of single carrier SCL current model that incorporates the Poole–Frenkel mobility $\mu = \mu_0 \exp(\gamma\sqrt{E})$, the built-in potential, V_{bi}, and the potential drop across ITO/PEDOT:PSS contact, V_{rs}.

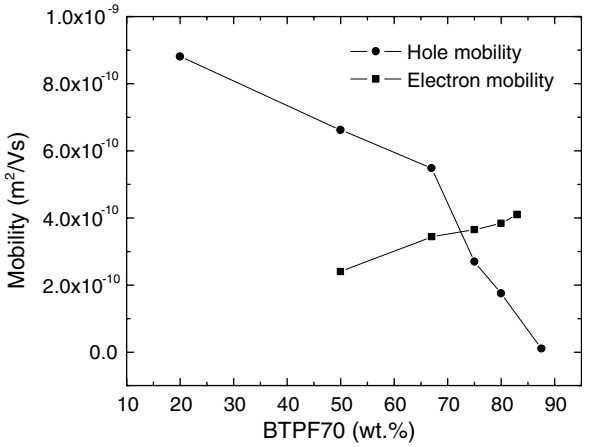

Fig. 8. Hole and electron mobility as a function of BTPF70 concentration. Lines between data points are only guides to the eye.

estimated the width of the GED for electron hopping in BTPF70 film to be about 150 meV [14]. The reported GED width for electron transport in PCBM is 73 meV [1]. The later result indicates that electron hopping transport in BTPF70 is highly subjected to energetic disorder. We attributed the origin of the disorder to structural inhomogeneity that must be generated by the three different isomers of BTPF70. Hence, the suppression of both electron and hole transport in blends of APFO-Green1 and BTPF70 is due to severe disorder. However, the interplay between morphology and charge transport, as a function of varying acceptor concentration, is not totally reflected in the current investigation and it is an issue to be explored further through other methods including microscopy.

In general, the studies reported here shows that charge transport in polymer/acceptor based solar cells is highly influenced by the nature of the polymer as well as the EAT molecule. The hole transport in pure APFO-Green1 film, in general, is enhanced in the presence of PCBM while addition of BTPF70 reduces hole transport. Structurally, PCBM and BTPF70 are quite different from each other. At room temperature, PCBM forms nanocrystals in solar cells [34], a condition that might favor exciton dissociation and creates better transport paths. Quite recently, Yang et al. [35] have shown that thermal annealing of blends of poly(3-hexylthiophene) (P3HT) and PCBM produces nanoscale interpenetrating networks with crystalline order in both materials. They demonstrated that solar cells with annealed P3HT/PCBM films are quite stable and efficient. On the other hand, annealed MDMO-PPV/PCBM films were found to form large PCBM single crystals [36]. So far, no ordering has been observed in BTPF70 films even under elevated temperature conditions. Thus, the different transport behavior of the blend layers should mainly originate from the structural difference of the two EAT materials. Structural tuning can easily induce morphological changes.

4.4. Ambipolar transport in BTPF70 and PCBM films

It was demonstrated that PCBM exhibits ambipolar transport characteristics in field effect transistors [37,38]. Tuladhar et al., using TOF measurements, argued that enhancement of hole mobility of polymer/PCBM blend films might originate from ambipolar transport behavior of PCBM

[29]. Electro-luminescence (EL) studies can be considered as a very direct method of probing ambipolar transport in a given material. However, so far, no evidence of light emission has been demonstrated either from PCBM or from BTPF70 films. In addition to transport studies, we have also investigated the EL behavior of both acceptor materials in a sandwich configuration. These studies were made on diodes with either ITO or ITO/PEDOT:PSS anode, and LiF/Al cathode. While devices with ITO anode have shown no evidence of light even at high applied potential (10 V), devices with ITO/PEDOT:PSS anode emits light. To our surprise, the onset of light emission was quite low (close to 1 V) both for PCBM and BTPF70 based diodes. From electroluminescence spectra we can identify the source of light to be the acceptor, as they agree with the photoluminescence spectra of the films. Typical EL characteristics are shown in Fig. 9. Optimized EL studies will be reported elsewhere.

This demonstrates that under appropriate electrode configurations, PCBM and BTPF70 can conduct both electrons and holes. Comparing the EL measurement with the studies of hole transport in polymer/acceptor phase leads to the conclusion that the enhancement of hole mobility in blends may be partly due to the ambipolar transport behavior of the acceptor materials. This is, in particular, plausible for polymer/PCBM blends as hole and electron mobilities in pure PCBM are high and comparable [37]. The complex interplay of electron and hole transport in similar blends is further demonstrated by a recent report, where EL emission from polymer/PCBM blends is substantial at high-bias potential [39].

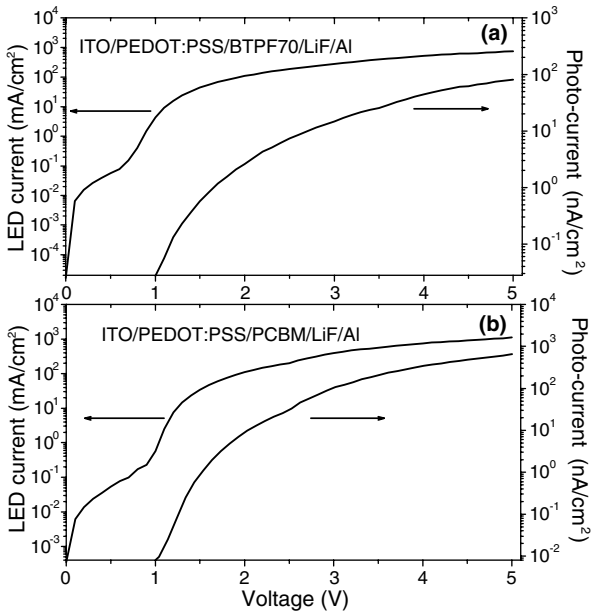

Fig. 9. The current density and emitted light intensity as a function of bias voltage for LED with (a) BTPF70, and (b) PCBM emitting layer.

5. Conclusions

In summary, charge transport in diodes with APFO-Green1, APFO-Green1:PCBM and APFO-Green1:BTPF70 thin films was investigated by analyzing the SCL I–V characteristics of the respective devices. The hole transport in APFO-Green1 is space charge limited, and the hole mobility is governed by field and temperature. At room temperature, a hole mobility of $\mu_0 = (8.0 \pm 0.4) \times 10^{-10}$ m^2/V s was calculated. On the other hand, comparative study of hole transport in the various blends show that the hole mobility has a local maximum at 67 wt.% of PCBM concentration while it falls down as a function of BTPF70 loading. The electron mobility seems to increase with increasing level of both acceptors. As compared to PCBM, BTPF70 provides better driving force for exciton dissociation when mixed with APFO-Green1. However, its structural inhomogeneity leads to poor charge transport in the blend films.

Acknowledgements

One of the authors (Abay Gadisa) gratefully acknowledges the financial support from the International Program in the Physical Sciences (IPPS) of Uppsala University, Sweden. X. Wang and E. Perzon are grateful to Swedish Ministry of Education and Swedish Research Council for the financial support. These investigations were financially supported by the Center of Organic Electronics (COE) at Linköping University, Sweden, financed by the Strategic Research Foundation SSF. This work has also been supported by the DGESIC of Spain (Project CTQ2004-00364/BQU) and FEDER funds.

References

[1] V.D. Mihailetchi, J.K.J. van Duren, P.W.M. Blom, J.C. Hummelen, R.A.J. Janssen, J.M. Kroon, M.T. Rispens, W.J.H. Verhees, M.M. Wienk, Adv. Funct. Mater. 13 (2003) 43.

[2] M. Reyes-Reyes, K. Kim, D.L. Carroll, Appl. Phys. Lett. 87 (2005) 083506.
[3] A. Gadisa, M. Svensson, M.R. Andersson, O. Inganäs, Appl. Phys. Lett. 84 (2004) 1609.
[4] S.E. Shaheen, C.J. Brabec, N.S. Sariciftci, F. Padinger, T. Fromherz, J.C. Hummelen, Appl. Phys. Lett. 78 (2001) 841.
[5] F.L. Zhang, M. Johansson, M.R. Andersson, J.C. Hummelen, O. Inganäs, Synth. Met. 137 (2003) 1401.
[6] M. Svensson, F. Zhang, S.C. Veenstra, W.J.H. Verhees, J.C. Hummelene, J.M. Kroon, O. Inganäs, M.R. Andersson, Adv. Mater. 15 (2003) 988.
[7] O. Inganäs, M. Svensson, F. Zhang, A. Gadisa, N.K. Persson, X. Wang, M.R. Andersson, Appl. Phys. A: Mater. Sci. Process. 79 (2004) 31.
[8] C. Melzer, E.J. Koop, V.D. Mihailetchi, P.W.M. Blom, Adv. Funct. Mater. 14 (2004) 865.
[9] V.D. Mihailetchi, L.J.A. Koster, P.W.M. Blom, C. Melzer, B. de Boer, J.K.J. van Duren, R.A.J. Janssen, Adv. Funct. Mater. 15 (2005) 795.
[10] X. Wang, E. Perzon, J.L. Delgado, P. de la Cruz, F. Zhang, F. Langa, M.R. Andersson, O. Inganäs, Appl. Phys. Lett. 85 (2004) 5081.
[11] E. Perzon, X. Wang, F. Zhang, W. Mammo, J.L. Delgado, P. de la Cruz, O. Inganäs, F. Langa, M.R. Andersson, Synth. Met. 154 (2005) 53.
[12] M. Chen, E. Perzon, M.R. Andersson, S. Marcinkevicius, S.K.M. Jönsson, M. Fahlman, M. Berggren, Appl. Phys. Lett. 84 (2004) 3570.
[13] X. Wang, E. Perzon, F. Oswald, F. Langa, S. Admassie, M.R. Andersson, O. Inganäs, Adv. Funct. Mater. 15 (2005) 1665.
[14] A. Gadisa, X. Wang, E. Perzon, F. Oswald, F. Langa, M.R. Andersson, O. Inganäs, unpublished.
[15] H.C.F. Martens, P.W. Blom, H.F.M. Schoo, Phys. Rev. B 61 (2000) 7489.
[16] A.R. Inigo, H.-C. Chiu, W. Fann, Y.-S. Huang, U-S. Jeng, T.-L. Lin, C.-H. Hsu, K.-Y. Peng, S.-A. Chen, Phys. Rev. B 69 (2004) 075201.
[17] C. Tanase, E.J. Meijer, P.W. Blom, D.M. de Leeuw, Phys. Rev. Lett. 91 (2003) 216601.
[18] W.F. Pasveer, J. Cottaar, C. Tanase, R. Coehoorn, P.A. Bobbert, P.W.M. Blom, D.M. de Leeuw, M.A.J. Michels, Phys. Rev. Lett. 94 (2005) 206601.
[19] M.A. Lampert, P. Mark, Current Injection in Solids, Academic, New York, 1970.
[20] E.J. Meijer, D.M. De Leeuw, S. Setayesh, E. Van Veenendaal, B.-H. Huisman, P.W.M. Blom, J.C. Hummelen, U. Scherf, T.M. Klapwijk, Nat. Mater. 2 (2003) 678.
[21] J. Zaumseil, T. Someya, Z. Bao, Y.-L. Loo, R. Cirelli, J.A. Rogers, Appl. Phys. Lett. 82 (2003) 793.
[22] D.A. Bernards, T. Biegala, Z.A. Samuels, J.D. Slinker, G.G. Malliaras, Appl. Phys. Lett. 84 (2004) 3675.
[23] T.-W. Lee, J. Zaumseil, S.H. Kim, J.W.P. Hsu, Adv. Mater. 16 (2004) 2040.
[24] S. Admassie, F. Zhang, A.G. Manoj, M. Svensson, M.R. Andersson, O. Inganäs, Sol. Energy Mater. Sol. Cells 90 (2006) 133.
[25] B.W. Jensen, K. West, Macromolecules 37 (2004) 4538.
[26] S. Admassie, O. Inganäs, W. Mammo, E. Perzon, M.R. Andersson, Synth. Met., submitted for publication.
[27] C. Tanase, P.W.M. Blom, D.M. de Leeuw, Phys. Rev. B 70 (2004) 193202.
[28] S.V. Novikov, D.H. Dunlap, V.M. Kenkre, P.E. Parris, A.V. Vannikov, Phys. Rev. Lett. 81 (1998) 4472.
[29] S.M. Tuladhar, D. Poplavskyy, S.A. Choulis, J.R. Durrant, D.D.C. Bradley, J. Nelson, Adv. Funct. Mater. 15 (2005) 1171.
[30] S.A. Choulis, J. Nelson, Y. Kim, D. Poplavskyy, T. Kreouzis, J.R. Durrant, D.D.C. Bradley, Appl. Phys. Lett. 83 (2003) 3812.
[31] A.M. Higgins, S.J. Martin, R.L. Thompson, J. Chappell, M. Voigt, D.G. Lidzey, Richard A.L. Jones, M. Geoghegan, J. Phys.: Condens. Matter 17 (2005) 1319.
[32] J.J.M. Halls, A.C. Arias, J.D. MacKenzie, W. Wu, M. Inbasekaran, E.P. Woo, R.H. Friend, Adv. Mater. 12 (2000) 498.
[33] J.K.J. van Duren, X. Yang, J. Loose, C.W.T. Bulle-Lieuwma, A.B. Sieval, J.C. Hummelen, R.A.J. Janssen, Adv. Funct. Mater. 14 (2004) 425.
[34] H. Hoppe, M. Niggemann, C. Winder, J. Kraut, R. Hiesgen, A. Hinsch, D. Meissner, N.S. Sariciftci, Adv. Funct. Mater. 14 (2004) 1005.
[35] X. Yang, J. Loos, S.C. Venenstra, Wiljan J.H. Verhees, M.M. Wienk, J.M. Kroon, Matthias A.J. Michels, René A.J. Janssen, Nano Letters 5 (2005) 579.
[36] X. Yang, J.K.J. van Duren, R.A.J. Janssen, M.A.J. Michels, J. Loos, Macromolecules 37 (2004) 2151.
[37] T.D. Anthopoulos, C. Tanase, S. Setayesh, E.J. Meijer, J.C. Hummelen, P.W.M. Blom, D.M. De Leeuw, Adv. Mater. 16 (2004) 2174.
[38] T. Nishikawa, S. Kobayashi, T. Nakanowatari, T. Mitani, T. Shimoda, Y. Kubozono, G. Yamamato, H. Ishii, M. Miwano, Y. Iwasa, J. Appl. Phys. 97 (2005) 104509.
[39] H. Kim, J.Y. Kim, S.H. Park, K. Lee, Y. Jin, J. Kim, H. Suh, Appl. Phys. Lett. 86 (2005) 183502.

Available online at www.sciencedirect.com
SCIENCE DIRECT®
Organic Electronics 7 (2006) 205–212
Organic Electronics
www.elsevier.com/locate/orgel

Electronic characterization of Al/PMMA[poly(methyl methacrylate)]/p-Si and Al/CEP(cyanoethyl pullulan)/p-Si structures

Moonkyong Na, Shi-Woo Rhee *

Laboratory for Advanced Molecular Processing (LAMP), Department of Chemical Engineering, Pohang University of Science and Technology (POSTECH), Pohang, Gyeongbuk 790-784, Republic of Korea

Received 7 November 2005; received in revised form 1 February 2006; accepted 2 February 2006
Available online 4 April 2006

Abstract

Thin films of poly(methyl methacrylate) (PMMA) and cyanoethyl pullulan (CEP) were prepared by spin coating on p-Si substrate. Capacitance–voltage (*C–V*) and current–voltage (*I–V*) behavior of the aluminum/PMMA/p-Si and Al/CEP(cyanoethyl pullulan)/p-Si MIS (metal–insulator–semiconductor) structures was studied at various frequencies ranging from 20 kHz to 1 MHz and for a bias voltage range of −50 V to +20 V. No hysteresis was observed in the *C–V* curve for both films as deposited and annealed (70–200 °C). Flat band voltage (V_{FB}) of aluminum/PMMA/p-Si structure with as deposited films was about −15 V and increased up to −30 V with annealing. This suggested that a large amount of positive charge was generated in the film. Electronic properties of the annealed PMMA film at above glass transition temperature were degraded substantially with larger shift in flat band voltage, low dielectric constant and low breakdown voltage. Al/CEP(cyanoethyl pullulan)/p-Si showed V_{FB} about −1 V for both as deposited or annealed film and CEP is more stable than PMMA. Frequency dependence of the electronic properties was also studied.

Keywords: Poly(methyl methacrylate); Cyanoethyl pullulan; Polymer gate dielectric; Organic thin film transistor

1. Introduction

Poly(methyl methacrylate) (PMMA) is one of the promising polymeric materials and there are numerous papers for its application as a gate dielectric in organic thin film transistors (OTFTs) [1–3]. Also cyanoethyl pullulan (CEP) draws much attention as a high dielectric constant polymeric insulator [4,5]. As a dielectric layer in OTFT structure, it should have a small number of charge traps, good processability, reproducibility and stability against degradation, small leakage current and high breakdown potential. PMMA's thermal and mechanical stability, together with its high resistivity ($>2\times10^{15}\ \Omega$ cm), suitable dielectric constant and thin film processability on large areas by spin coating make it an ideal candidate as a dielectric layer in organic electronics. Also cyanoethyl pullulan is expected to improve the OTFT characteristics such as a

* Corresponding author. Tel.: +82 54 279 2265; fax: +82 54 279 8619.
E-mail address: srhee@postech.ac.kr (S.-W. Rhee).

1566-1199/$ - see front matter © 2006 Elsevier B.V. All rights reserved.
doi:10.1016/j.orgel.2006.02.003

reduction of threshold voltage with its high dielectric constant.

Puigdollers et al. [1,2] fabricated pentacene thin film transistor using PMMA and SiO_2 as gate dielectrics. They reported that transistors using PMMA as a gate dielectric showed better electrical characteristics than SiO_2. They also observed that PMMA surface favors the formation of bigger crystalline grains than SiO_2 surface, which consequently leads to improved field effect mobility. Uemura et al. [3] investigated the effect of surface modification of PMMA with clay mineral and showed that leakage current was smaller than unmodified PMMA diode structure. El-Shahawy [6] studied the dielectric constant (ε) of solution cast PMMA film (thickness = ! 1 mm) and PMMA mixed with some organic laser dyes at different temperatures ranging from 30 °C to 130 °C and for various frequencies ranging from 0.6 to 10 kHz. They observed that the ε value increased from 3.6 to 5.1 with the increase of temperature for 10 kHz. Davis and Pathrick [7] reported the variation of dielectric constant and dielectric loss of PMMA ($M_w = 136000$) with frequency (1×10^2 to 1×10^5 Hz) for different annealing temperatures (30, 50 and 120 °C) and for various annealing times (0–64 h).

To our knowledge, there is no report on the electronic characteristics such as capacitance–voltage (C–V) and current–voltage (I–V) behavior of the aluminum/PMMA/p-Si or the aluminum/CEP/p-Si MIS (metal–insulator–semiconductor) structure (also called MPS: metal–polymer–semiconductor). The study of C–V and I–V characteristics of MIS structure gives useful information about the properties of the insulator and insulator–semiconductor interface [8]. In this study, electrical properties of PMMA and CEP were studied by making MIS structure and measuring C–V and I–V characteristics. The effect of annealing on the PMMA films and CEP films prepared by spin coating technique on silicon was studied. These measurements give information about charges in the insulating films [9,10]. Our present work also deals with the effect of the frequency ranging from 20 kHz to 1 MHz.

2. Experimental

PMMA having a molecular weight of 96700 was obtained from Sigma–Aldrich and CEP having a molecular weight of 489000 was obtained from Shin Etsu Chemical Co. Molecular structure of these two polymers are shown in Fig. 1 and both were used

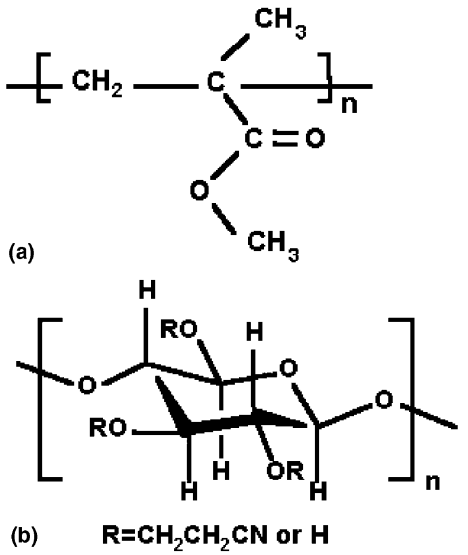

Fig. 1. Molecular structure of (a) poly(methyl methacrylate) (PMMA) and (b) cyanoethyl pullulan (CEP).

without further purification to form the insulator layer. Anisole was used as a solvent to dissolve PMMA and *N*,*N*-dimethyl formamide was used for CEP. The solution was spun on boron doped Si (1 0 0) substrate (p-type Si) at room temperature to prepare thin films. Before deposition, the surface preparations of silicon wafers were done by degreasing it with organic solvents such as trichloroethylene (TCE), ethanol and then followed by a rinse in deionized (DI) water. The solution concentration was between 5.6 and 11.2 wt.% (0.06–0.12 g polymer/cc solvent). 0.25 ml of the solution was introduced at the center of the substrate and spinning was about a minute. For the electronic characterization, 300 nm thick polymer film was made at the spin speed of 4000 rpm with 9.0% solution. After spin coating process, the samples were dried in the vacuum chamber for 3–4 h to evaporate the solvent remained in the film and then the films were annealed at 70–200 °C for 60 min in argon (Ar) ambient. The bottom metal contact was formed by evaporating aluminum (Al) on the back side of the Si substrate and the top metal contact was formed by evaporating Al over the polymer film surface by using a suitable metal mask (dot size, 5×10^{-3} cm^2). The polymer films coated were identified by using a FT-IR spectrometer and small angle X-ray diffractometer was used to examine the structure of the as grown and annealed films. Thermo gravimetric analyzer (TGA) was used to identify the thermal stability of the film. The glass

transition temperature (T_g) range of the film was measured by using differential scanning calorimetry (DSC). Spectroscopic ellipsometry (SE, J.A. Woolam Co., Model WVASE32) was used to measure the thickness of the films coated on Si substrate. The surface morphology of the as grown and annealed films was investigated with SEM and AFM. The capacitance–voltage (C–V) measurements were performed using HP 4284A. The C–V measurements were carried out at a voltage range of −50 V to 20 V for various frequencies from 20 kHz to 1 MHz. The current–voltage (I–V) characteristics were studied by using HP 5270A. Surface energy of the film was obtained by measuring the contact angle with water with static contact angle goniometry.

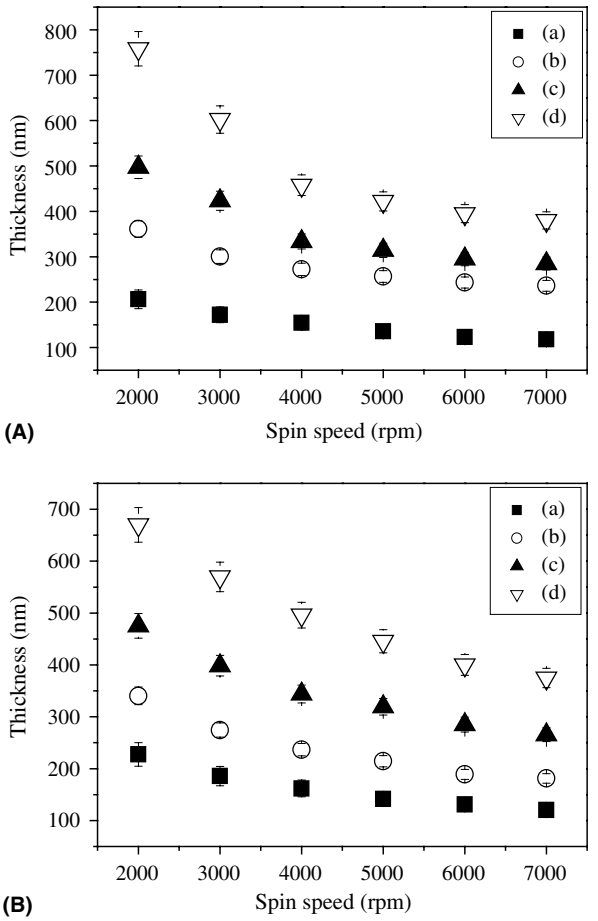

Fig. 2. Thickness variation of (A) PMMA films at different spin speeds and solution concentrations in anisole (a) 5.65 wt.% (b) 7.45 wt.% (c) 9.08 wt.% (d) 10.72 wt.% and (B) cyanoethyl pullulan films dissolved in *N*,*N*-dimethyl formamide solvent (a) 5.98 wt.% (b) 7.77 wt.% (c) 9.50 wt.% (d) 11.18 wt.%.

3. Results and discussion

Fig. 2 shows the thickness of the film as a function of the spin speed and the concentration. With thicker solution, the film thickness was larger. With higher spin speed, film became thinner and the film thickness was saturated when the spin was greater than 4000 rpm. For the electronic characterization, 300 nm thick film was made at the spin speed of 4000 rpm with 9% solution.

The glass transition temperature (T_g) range of the film was measured to be 96–120 °C by using differential scanning calorimetry (DSC) for both polymers and TG (thermogravimetric) analysis showed that PMMA was stable up to 270 °C [11] and CEP up to 250 °C [12]. Annealing is a process related with stress relief and local structural rearrangement of polymer chains and it is expected that annealing effect can be different below or above the glass transition temperature. To know the annealing effect on the dielectric and capacitance–voltage behavior of the film, investigations were carried out for various annealing temperatures ranging from 70 °C to 200 °C. X-ray diffraction spectrum of as grown PMMA films and films subjected to various annealing temperatures ranging from 70 °C to 200 °C are shown in Fig. 3. Almost similar XRD spectrum was observed for films subjected to repeated annealing cycles at 100 °C (figures not included). The X-ray diffraction pattern indicates the amorphous nature with large diffraction maxima that decreases at large diffraction angles. The shape of

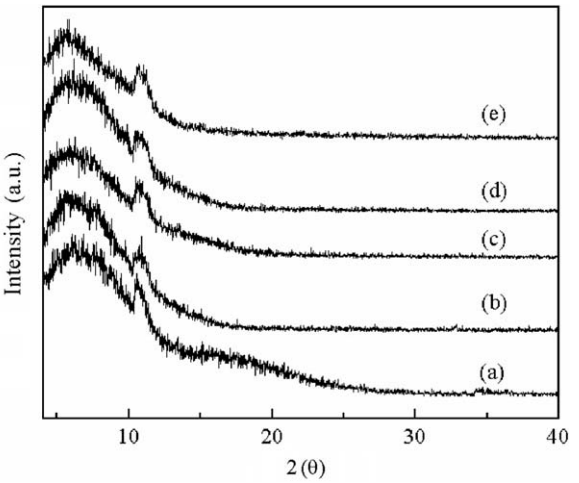

Fig. 3. XRD spectrum of PMMA films, (a) as grown, (b) 70 °C annealed, (c) 100 °C annealed, (d) 150 °C annealed and (e) 200 °C annealed samples.

the first main maximum indicates the ordered packing of the polymer chains. The intensity and shape of the second maxima are related to the effect of ordering inside the main chains. The observed broad humps in the XRD spectrum indicate the presence of crystallites of very low dimensions. The absence of any prominent peaks in the as grown and annealed PMMA thin films indicates the predominantly amorphous nature of the films.

Surface morphology of dielectric layer is very important because it affects the property of the semiconductor layer deposited over it. Fig. 4 shows the SEM image of the as grown and annealed PMMA films. The film surface of as grown and films annealed at 70 °C, 100 °C, 150 °C and 200 °C is compact. No pits and pinholes were found on the surface. Macroscopic granular chains appear at the surface in the stretching direction of PMMA film. The granular structures (grooves) vary in size from few nanometers to hundreds of nanometers. Improved surface smoothness and greater grooves were found for films annealed at 100 °C. PMMA films subjected to repeated annealing cycles at 100 °C (figures not included) showed very smooth surface. The observed change in the morphology with increase of annealing temperature above 70 °C may be assigned to the reasons such as intensified thermal oscillations of molecules at higher temperatures leading to the diminished order of their orientation, the improved stoichiometry, reduction of defects and faster structural relaxation. The surface morphology of both as grown and annealed films is quite homogeneous and amorphous nature. The atomic force micrographs of as

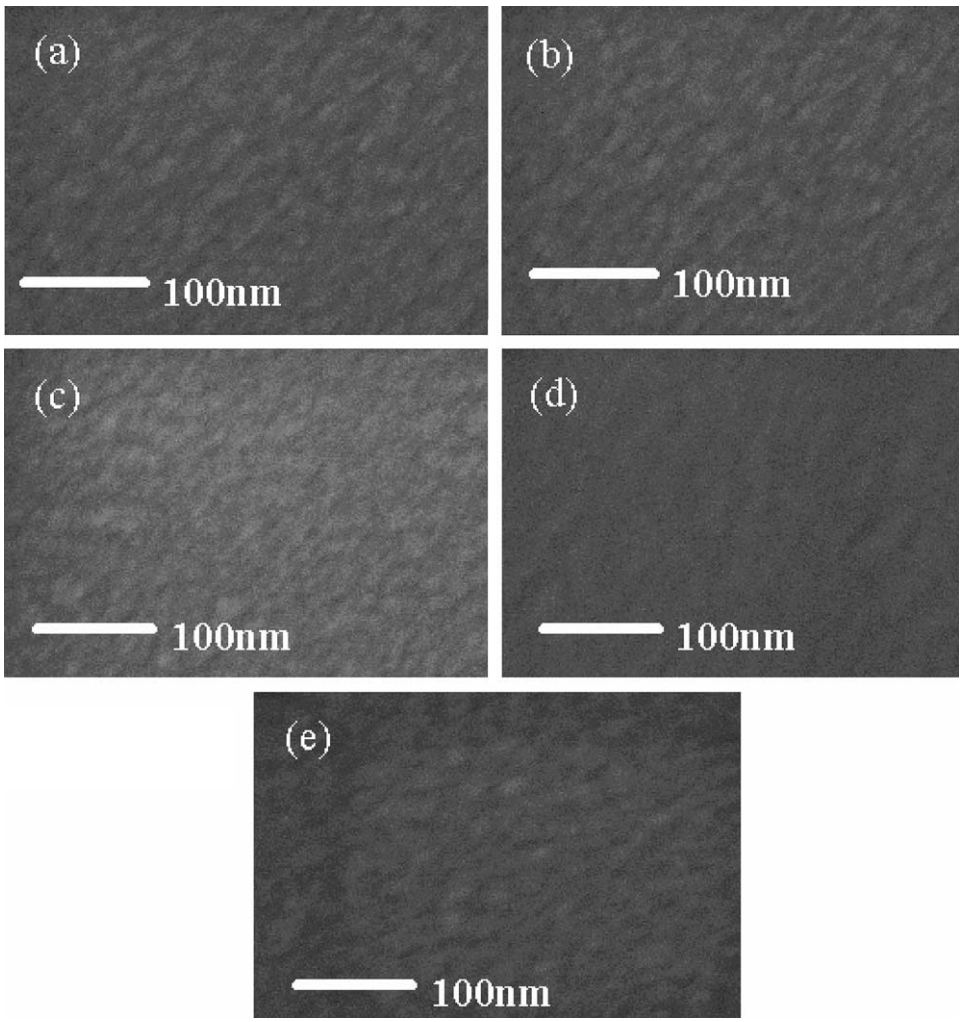

Fig. 4. SEM image of PMMA films, (a) as grown, annealed at (b) 70 °C, (c) 100 °C, (d) 150 °C and (e) 200 °C.

grown and annealed PMMA films are shown in Fig. 5. The film surface of as grown and films subjected to repeated annealing cycles at 100 °C is compact. Both as grown and annealed films exhibited random morphologies with smooth surface having microdomains of less than 100 nm. The RMS roughness was found to be very low for as grown and annealed films. The roughness increased a bit with annealing cycle. No pits and pin holes are observed in the AFM topographical image of the samples studied. The only topographic features observed is the hillock of about 10–100 nm large and a peak to valley distance of about 0.5–1 nm.

Fig. 6 shows the capacitance–voltage characteristics of the aluminum/PMMA/p-Si and the aluminum/CEP/p-Si MIS (metal–insulator–semiconductor) structure. Accumulation, depletion and inversion regions [8] are observed for both as grown and annealed films. *C–V* measurements were performed with a small superimposed AC signal at a frequency of 1 MHz on top of a preselected DC voltage. The voltage was swept forward from negative to positive. At negative voltage, it showed maximum capacitance with accumulation of holes in the p type silicon at the polymer–silicon interface. The dielectric constant of the polymer film was obtained from this capacitance. As the voltage increases, depletion and inversion region were clearly observed with the decrease of the capacitance because now the total capacitance comes from the serial coupling of the capacitance from the polymer dielectric and the silicon layer. The flat band voltage was shifted in the negative direction, which indicates that positive fixed charges exist in the polymer film [9]. For PMMA films (Fig. 6(A)), the shift was large with more than −15 V for films as-deposited and annealed at 70–100 °C and more than −30 V for films annealed at 100–200 °C. The ideal MOS capacitor has zero flat band voltage if we neglect the work function difference between aluminum and silicon and assume that there is no mobile or fixed charge in the dielectric film and interface. In the present work with the Al/PMMA/p-Si capacitor structure, the V_{FB} shift observed for both as grown and annealed films is significant and it is mainly due to the charges in the PMMA film. It seems that as we increased the annealing temperature, more chemical bonds were broken in the film and positive charges were formed. For CEP films (Fig. 6(B)), the flat band voltage shift was small at about −1 V for films as-deposited or annealed at 70–200 °C. CEP is thermally more stable than PMMA probably due to the ring structure and accumulation and inversion occurs at lower voltage. It is expected that threshold

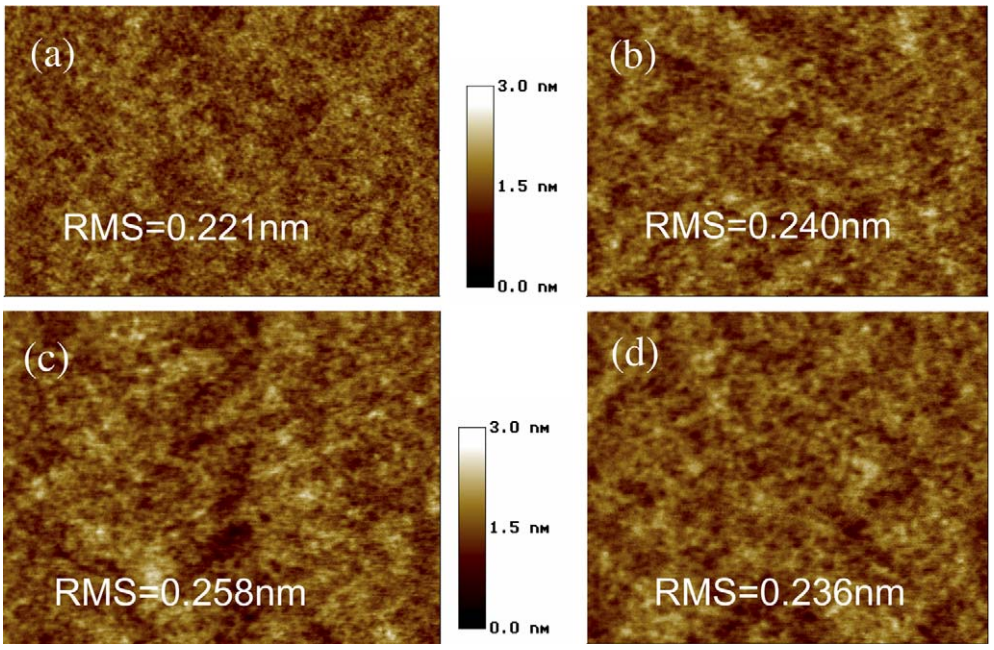

Fig. 5. AFM image of (a) as grown, (b) 1st cycle of annealing at 100 °C, (c) 2nd cycle of annealing at 100 °C and (d) 3rd cycle of annealing at 100 °C.

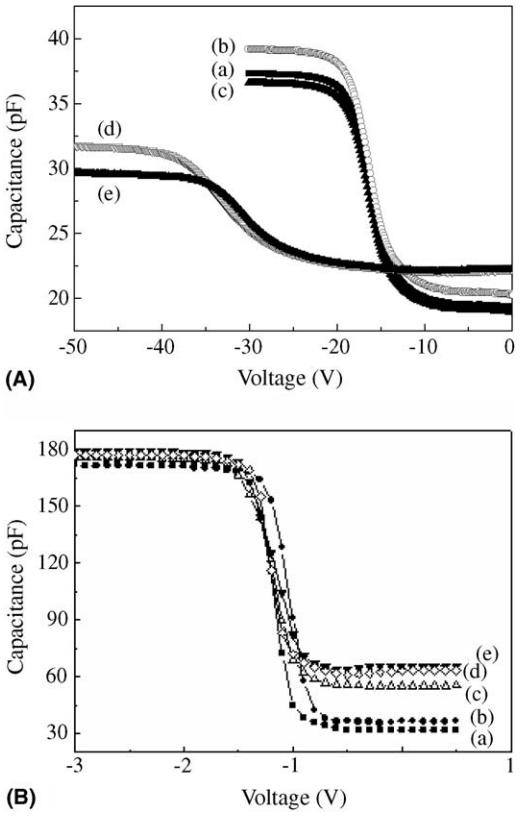

Fig. 6. Capacitance–voltage (C–V) characteristics (A) of the Al/PMMA/p-type Si structure at 1 MHz (a) as-dep. and annealed at (b) 70 °C (c) 100 °C (d) 150 °C and (e) 200 °C and (B) of the Al/CEP/p-type Si structure at 1 MHz (a) as-dep. and annealed at (b) 70 °C (c) 100 °C (d) 150 °C and (e) 200 °C.

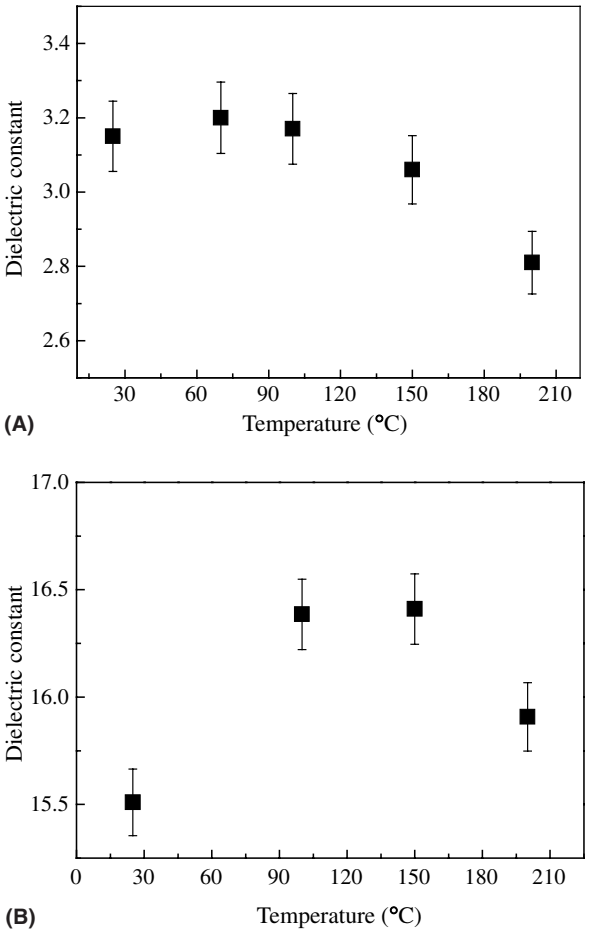

Fig. 7. Dielectric constant of (A) PMMA films and (B) cyanoethyl pullulan films at 1 MHz as a function of the annealing temperature.

voltage of the device made with CEP will be much lower. This result shows that electrical characterization of MIS structure is quite effective to identify the characteristics of the polymer film. Similar C–V behavior (with a V_{FB} shift value of −8 V to −12 V) was reported by LEE and Muraka [9] for Cu/fluorinated polyimide/SiO_2/Si capacitor structure and by Musa and Eccleston [10] for Al/poly(3-octylthiophene) (P3OT)/p-Si structure.

Fig. 7 shows the dielectric constant of PMMA and CEP film as deposited and annealed at various temperatures obtained from C–V measurement at a frequency of 1 MHz. As grown PMMA films showed a relative dielectric constant value of 3.15. Films annealed at 70 °C showed a little increase in the dielectric constant whereas films subjected to annealing above 70 °C showed a decrease in dielectric constant with the increase of annealing temperature. As the annealing temperature increases, the rate of decrease of the dielectric constant increases. The observed dielectric behavior indicates the weak polar nature of the PMMA film studied [13,14]. The increase in the value of the dielectric constant obtained for temperature up to 70 °C is due to an increase of total polarization arising from dipoles and trapped charge carriers. As grown CEP films showed a relative dielectric constant value of 15.5. Films annealed at 70–150 °C showed an increase in the dielectric constant whereas films subjected to annealing above 150 °C showed a decrease in dielectric constant with the increase of the annealing temperature. The dielectric constant is much higher than PMMA due to the polar nature of CEP arising from –C≡N and C–O–C.

Fig. 8 shows the variation of dielectric constant (ε) with frequency (20 kHz–1 MHz) for as grown and annealed PMMA and CEP films. The observed decrease of dielectric constant with increasing

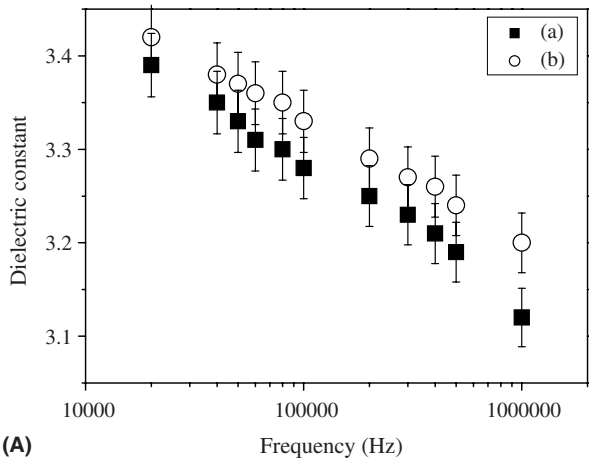

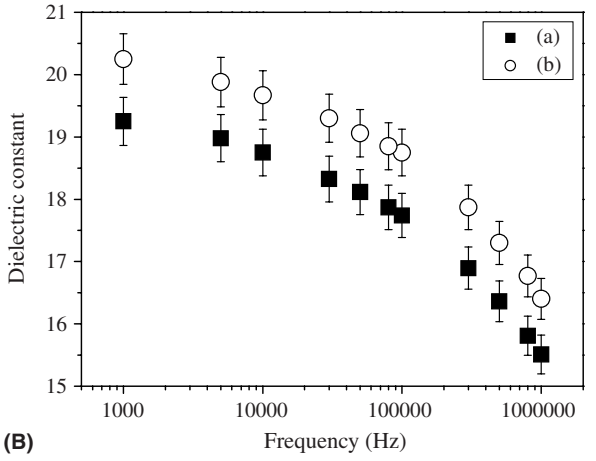

Fig. 8. Dielectric constant of (A) PMMA films and (B) CEP films at various frequencies (a) as-deposited and (b) annealed at 100 °C.

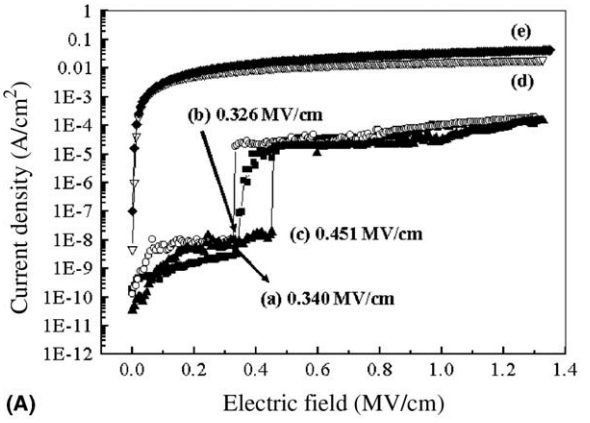

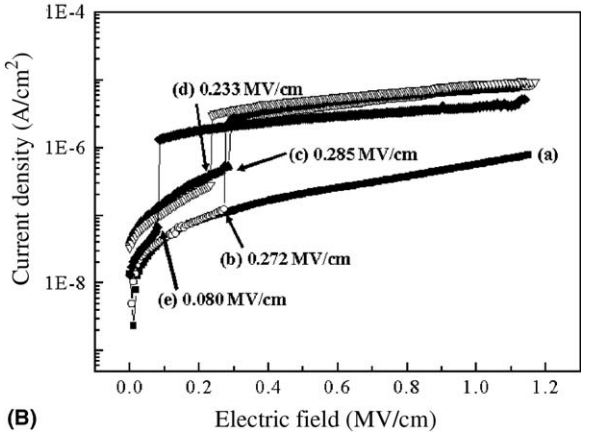

Fig. 9. Current–voltage (I–V) characteristics of (A) PMMA film and (B) CEP film (a) as deposited and annealed at (b) 70 °C (c) 100 °C (d) 150 °C and (e) 200 °C.

frequency may be due to the tendency of induced dipoles in the film to orient themselves in the direction of the applied field. In organic molecules, dipoles cannot orient themselves in a rapidly varying electric field and charge carriers are released slowly from relatively deep traps in the amorphous state.

Fig. 9 shows the current–voltage characteristics of 300 nm thick PMMA and CEP films. For as deposited PMMA films, the leakage current level is low at 10^{-9}–10^{-8} A/cm^2 up to 0.3 MV/cm. The leakage current increased up to the order of 10^{-5} when the field strength was higher than 0.3 MV/cm. PMMA films annealed at 150 and 200 °C showed very poor insulating property and the annealing above the glass transition temperature degraded film properties as was already shown in C–V measurement (Fig. 6). For both polymers, thermal annealing above the glass transition temperature degraded the electrical properties of the film and it was more severe for PMMA.

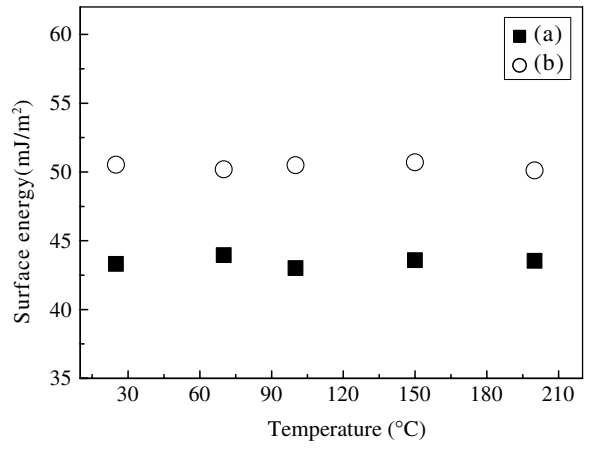

Fig. 10. Surface energy of (a) PMMA and (b) CEP film formed at different annealing temperatures measured by static contact angle goniometry.

Fig. 10 shows the surface energy of the two polymer films obtained by measuring the contact angle with water using static contact angle goniometry [15]. For PMMA films, surface energy was 43 mJ/m^2 while it was 50 mJ/m^2 for CEP films. CEP films contain polar groups like –C≡N and C–O–C– and the surface energy was higher and the surface was more hydrophilic than PMMA. PMMA surface is more hydrophobic with higher contact angle. For both films annealing did not affect surface energy very much, which indicates that annealing did change the bulk property due to the rotation and twisting of the polymer chain but did not affect the surface state much.

4. Conclusions

Smooth and compact thin films of poly(methyl methacrylate) (PMMA) and cyanoethyl pullulan (CEP) were obtained by spin coating. SEM and AFM studies revealed that there were no pits and pin holes on the surface. Both as grown and annealed films showed smooth surface. The XRD spectrum of as grown and films subjected to various annealing temperatures indicated the amorphous nature. *C–V* characteristics of the Al/PMMA/p-Si and Al/CEP(cyanoethyl pullulan)/p-Si MIS(metal–insulator–semiconductor) structures showed good depletion behavior. Flat band voltage (V_{FB}) of aluminum/PMMA/p-Si structure with as deposited films was about −15 V and increased up to −30 V with annealing. This suggested that a large amount of positive charge was generated in the film. Electronic properties of the annealed PMMA film at above glass transition temperature were degraded substantially with larger shift in flat band voltage, low dielectric constant and low breakdown voltage. Al/CEP(cyanoethyl pullulan)/p-Si showed V_{FB} about −1 V for both as deposited or annealed film and CEP is more stable than PMMA. The study of *C–V* and *I–V* characteristics of MIS structure gives useful information about the properties of the insulator and insulator–semiconductor interface.

Acknowledgement

This research was supported by the Korea Science and Engineering Foundation (KOSEF) through the National Research Laboratory Project and Polymer Gel Cluster group of the Korea government.

References

[1] J. Puigdollers, C. Voss, I. Martin, A. Rosella, M. Vetter, R. Alcubilla, J. Non-Cryst. Solids 338–340 (2004) 617.
[2] J. Puigdollers, C. Voz, A. Orpella, R. Quidant, I. Martín, M. Vetter, R. Alcubilla, Org. Electron. 5 (2004) 67.
[3] S. Uemura, M. Yoshida, S. Hoshino, T. Kodzasa, T. Kamata, Thin Solid Films 438–439 (2003) 378.
[4] W. Sakai, C.K. Chiang, Mater. Res. Soc. Symp. Proc. 710 (2002) DD6.17.
[5] W. Sakai, T. Yoshiji, N. Tsutsumi, C.K. Chiang, Mater. Res. Soc. Symp. Proc. 769 (2003) H10.8.
[6] M.A. El-Shahawy, Polym. Test. 18 (1999) 389.
[7] W.J. Davis, R.A. Pethrick, Polymer 39 (1998) 255.
[8] S.M. Sze, Physics of Semiconductor Devices, second ed., Wiley, New York, 1981, Chapter 7.
[9] Y.K. Lee, S.P. Muraka, Mater. Res. Bull. 34 (6) (1999) 869.
[10] I. Musa, W. Eccleston, Thin Solid Films 343–344 (1999) 469.
[11] J.A. Chandrasiri, D.E. Roberts, C.A. Wilkie, Polym. Degrad. Stab. 45 (1994) 97.
[12] S.P.S. Yen, C.R. Lewis. In: Proc. 35th Int. Power Source Symp., 1992, p. 381.
[13] B. Tareev, Physics of Dielectric Materials, MIR, Moscow, 1979.
[14] R. Vijayalakshmi, P.V. Ashokan, M.H. Shridhar, Mater. Sci. Eng. 281A (2000) 213.
[15] D.G. Rance, Industrial Adhesion Problems, Orbital Press, Oxford, 1985, p. 48.

Available online at www.sciencedirect.com
SCIENCE DIRECT®
Organic Electronics 7 (2006) 213–221
Organic Electronics
www.elsevier.com/locate/orgel

Electro-optical studies on MDMO-PPV:PCBM bulk-heterojunction solar cells on the millisecond time scale: Trapped carriers

Ton Offermans, Stefan C.J. Meskers, René A.J. Janssen *

Molecular Materials and Nanosystems, Department of Chemical Engineering and Chemistry, Eindhoven University of Technology, P.O. Box 513, 5600 MB, Eindhoven, The Netherlands
Dutch Polymer Institute (DPI), P.O. Box 902, 5600 AX Eindhoven, The Netherlands

Received 9 January 2006; received in revised form 12 February 2006; accepted 14 February 2006
Available online 10 March 2006

Abstract

The influence of a periodically modulated electric field on the concentration of photogenerated charges in bulk-heterojunction solar cells of poly[2-methoxy-5-(3′,7′-dimethyloctyloxy)-1,4-phenylene vinylene] (MDMO-PPV) and 1-(3-methoxycarbonyl)-propyl-1-phenyl-[6,6]C_{61} (PCBM) is studied at 80 K by near-steady-state photoinduced absorption (PIA) spectroscopy. Measurements are complemented with recording the photocurrent. The results show that the lifetime of extractable charge carriers under conditions where the built-in electrical field is largely compensated, is in the sub-millisecond time domain. PIA is dominated by the contribution from trapped carriers and application of a −4 V bias increases the number of trap sites available to the carriers in comparison with a +1 V bias voltage. The reverse bias voltage also leads to an enhancement in the generation rate of carriers that can be trapped and/or the lifetime of the trapped carriers. The experiment indicates that the lifetime of the trapped carriers at −4 V bias voltage remains in the sub-millisecond time domain.

PACS: 85.65.+h; 73.50.Pz; 72.20.Jv; 72.40+w

Keywords: Photovoltaic devices; Charge generation; Conjugated polymers; Fullerenes; Photoinduced absorption

1. Introduction

Bulk-heterojunction solar cells use a nanoscopic phase-separated blend of an electron donating and an electron accepting material as the active layer [1,2]. When light is absorbed in the active layer by either of the two components, a photoinduced charge transfer across the interface can produce a geminate electron–hole pair. Provided that percolation pathways exist to the two electrodes, the photogenerated electrons and holes may be collected in an external circuit before they recombine.

Near-steady state photoinduced absorption (PIA) has often been used to probe the formation and recombination of photoinduced charge carriers in π-conjugated molecular materials for photovoltaic

* Corresponding author. Tel.: +31 40 247 3596; fax: +31 40 245 1035.
E-mail address: r.a.j.janssen@tue.nl (R.A.J. Janssen).

1566-1199/$ - see front matter
doi:10.1016/j.orgel.2006.02.001

applications [3,4]. To approach conditions that are present in photovoltaic devices under operation, the influence of an externally applied electric field on the dynamics of the charge carriers has recently come under investigation with PIA [5–8].

It is well established that an electric field can stabilize metastable photogenerated charge pairs, facilitate their dissociation, and enhance the generation efficiency of long lived carriers [9–17]. Hence, an electric field can influence the near-steady state PIA signal associated with charge carriers changes by changing their generation efficiency or lifetime. The latter is important in near-steady state PIA measurements because the time averaged density of charge carriers is probed and, hence, the signal intensity depends on the lifetime of the carriers.

PIA studies on polythiophene:PCBM cells have revealed an enhanced signal under a reverse bias voltage [8]. Under the conditions, the lifetime of the charge carriers did not change and the increase was attributed to an enhanced probability for escape of the charge carriers from their mutual Coulombic potential well in the electric field [8]. An increased PIA signal of charge carriers by application of a moderate electric field has also been observed in MDMO-PPV:PCBM bulk heterojunction cells [5]. Here the increase was attributed to liberation of persistent charge carriers with lifetimes much larger than the inverse modulation frequency, due to a lowering of the trap energy by the high internal electric field [5]. By detrapping, the lifetime of persistent carriers is lowered below the inverse modulation frequency and they become detectable in the photomodulation experiment. In contrast, electromodulated photoinduced absorption (EPA) measurements on MEH-PPV:C_{60} films showed that a moderate electric field (10^4–10^5 V/cm) can also reduce the magnitude of the PIA, which was interpreted in terms of a reduction of the lifetime of the charge transfer complex at the donor–acceptor interface [18].

To discriminate between the various effects of an electrical field, we use a periodically modulated external bias having an identical frequency but variable phase relative to the photomodulation. For our study we use bulk-heterojunction MDMO-PPV:PCBM solar cells. In this experiment, photoinduced charges are simultaneously probed optically and electrically by recording the PIA signal and the photocurrent collected at the electrodes. By monitoring the PIA as a function of the phase difference between the photomodulation and field modulation, we experimentally test the notion that an applied electric field stabilizes photogenerated charge carriers. If this is indeed the case, the PIA signal is expected to be higher when the field modulation lags behind in phase because photogenerated carriers are longer lived in comparison to the situation where the voltage modulation precedes.

In short, we find that the lifetime of the field-stabilized photogenerated charge carriers is still in the sub-millisecond time domain. An increase of both PIA and photocurrent is observed upon applying an external electric field. As we will discuss, the increase of both PIA and the photocurrent is due to an enhancement in the generation rate of long-lived carriers.

2. Experiment

Photovoltaic devices were prepared using glass substrates with patterned indium tin oxide (ITO). After careful scrubbing, cleaning, and UV-ozone treatment, a 100 nm thin layer of poly(3,4-ethylenedioxythipophene):poly(styrene sulfonate) (PEDOT:PSS) (Baytron P, H.C. Starck) was applied by spin coating, followed by a 100 nm composite layer of poly[2-methoxy-5-(3′,7′-dimethyloctyloxy)-1,4-phenylene vinylene] and 1-(3-methoxycarbonyl)-propyl-1-phenyl-[6,6]C_{61} (MDMO-PPV:PCBM) in a 1:4 wt ratio from a chlorobenzene solution. The back electrode consisting of LiF (1 nm) and Al (150 nm) was evaporated at 5×10^{-6} mbar through a shadow mask. Photocurrent densities are calculated with respect to the illuminated area (0.071 cm^2).

PIA experiments were performed in reflection geometry (Fig. 1a). The laser excitation (458 nm) was modulated at 70 Hz (14.3 ms) by a mechanical chopper unless stated otherwise. The resulting change in transmission ΔR of a tungsten–halogen white–light probe beam was monitored at 1.47 eV after reflection at the back electrode of the device, dispersion by a grating monochromator, and detection by a Si detector with a phase-sensitive lock-in amplifier and normalized for the reflection R of the probe light in absence of photoexcitation. The pump power incident on the sample was typically 25 mW with a spot diameter of 3 mm. The devices were held in vacuum using an Oxford Optistat cryostat at 80 K.

A voltage pulse was applied to the device during the modulation period of the photoexcitation to extract the photogenerated charges (Fig. 1b). The extracted current was measured by recording the

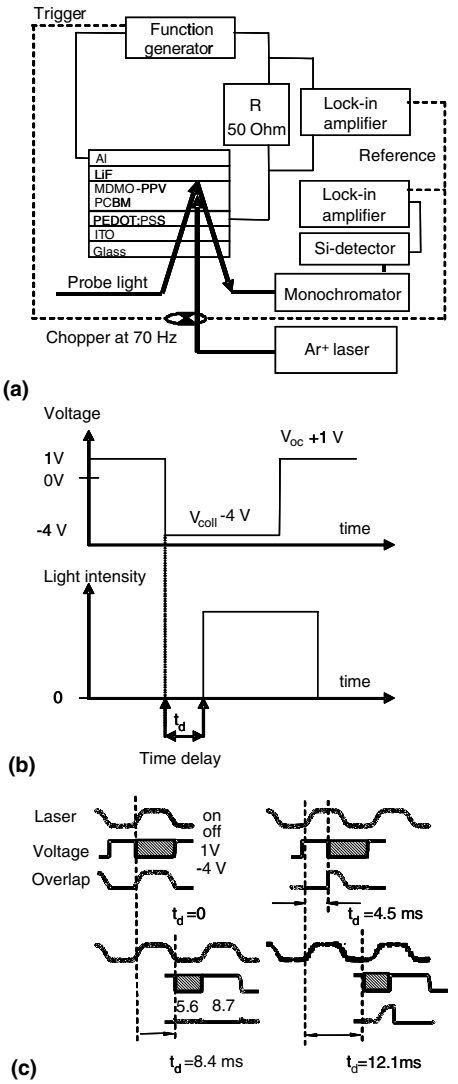

Fig. 1. (a) Experimental setup, (b) detailed view of the voltage pulse used and (c) overview of the timing of the pulses used for four different delay times and the overlap. The dashed area represents the duty cycle of the pulse, note that on and off times are different.

amplitude of the oscillating voltage over a probe resistance R (50 Ω) connected in series with the device using a lock-in amplifier (Fig. 1a). Positive bias voltage corresponds to the ITO/PEDOT:PSS electrode being charged positive. Constant bias voltages were applied using a Keithley 2400 sourcemeter. The voltage pulse over the device was generated using an Agilent 33120A function generator triggered by the chopper, creating a pulse with a width smaller than the period of the trigger signal (14.3 ms) to ensure synchronization. The phase difference between the applied voltage pulse and photoexcitation was changed in steps of 10°, causing the voltage pulse to be shifted with respect to the excitation in time and allowing the concentration of photogenerated charges to be followed as a function of time t_d. Going from a positive to a negative phase difference, however, caused the duty cycle of the applied voltage pulse to be reversed and a change in the pulse width (5.6 ms–8.7 ms) (Fig. 1c).

The photocurrent was measured under the same conditions as the PIA, thus under both laser and white light illumination. We corrected for the contribution to the photocurrent measurement of the white–light probe by subtracting the photocurrent induced by the probe light only.

3. Results

3.1. PIA and photocurrent in electric field

MDMO-PPV radical cations formed in the photoinduced charge transfer reaction with PCBM exhibit two characteristic, broad sub gap absorptions at 0.40 and 1.35 eV [19]. In our experiment we monitor photogenerated MDMO-PPV radical cations in photovoltaic devices by measuring the PIA in reflection (Fig. 1a). In this experiment, the modulated laser light results in a periodic variation of the intensity of the reflected probe light (ΔR). By using a probe energy of 1.47 eV within the broad absorption band at 1.35 eV, we ensure that the contribution of the thermoreflection signal from the aluminum back electrode to the photoinduced reflection is negligible [20,21]. The thermoreflection signal is a change in reflectivity near the spectral position of the interband transition of the Al due to a variation of the temperature of the Al layer between laser-on and laser-off periods.

In the PIA experiments a bias voltage (V_{bias}) can be applied over the ITO/PEDOT:PSS front and LiF/Al back electrodes of the devices and the photocurrent can be measured simultaneously. At 80 K, the open-circuit voltage (V_{oc}) of the MDMO-PPV:PCBM cells is +1 V. Fig. 2a shows that at 80 K a static reverse bias voltage ($V_{bias} < V_{oc}$) gives rise to a significant increase of the PIA signal ($-\Delta R/R$) at 1.47 eV when compared to open circuit conditions ($V_{bias} = V_{oc}$). At 80 K, the photocurrent increases approximately linearly with the applied reverse bias voltage (Fig. 2b). The external quantum efficiency of the device for 2.71 eV photons at short circuit equals 0.2 at room temperature and decreases

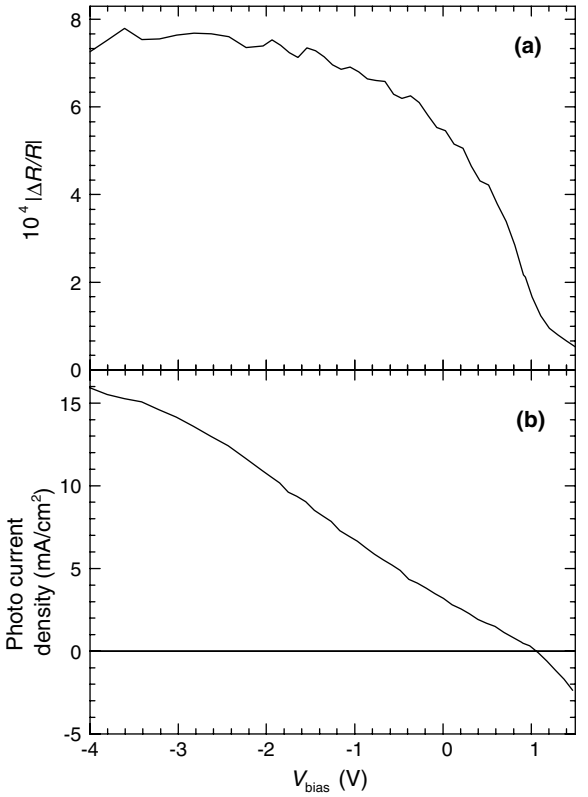

Fig. 2. (a) Near-steady-state PIA of a MDMO-PPV:PCBM photovoltaic device measured in reflection mode with a probe energy of 1.47 eV as function of applied voltage. There is no significant phase lag between the PIA signal and excitation modulation and the in-phase component is shown and (b) photocurrent as a function of applied bias. Again there is no significant phase lag between photocurrent and excitation modulation and the in-phase component is shown. In both experiments $T = 80$ K and modulation frequency 77 Hz.

to 0.05 upon lowering the temperature to 80 K. When V_{bias} is close to V_{oc}, extraction of charge carriers is strongly suppressed because the internal electric field arising from the use of two electrodes with different work function is largely compensated. Under these conditions the lifetime of the carriers may be expected to be determined by recombination processes. At $V_{bias} = -4$ V the charges are extracted. At each bias, the differential reflection ($-\Delta R/R$) signal was found to be almost 180° out of phase with respect to the photomodulation, signifying that the photoinduced charge carriers detected by PIA have an average lifetime that is short in comparison with the modulation period.

To investigate the field-enhanced PIA signal in more detail, a modulated bias voltage was applied to the cell with the same frequency as the photomodulation. The modulation waveform used is illustrated in Fig. 1b. In the first half of the cycle, a bias voltage of $V_{bias} = +1$ V close to V_{oc} suppresses the extraction of charge carriers, while in the second half period a reverse bias collection voltage $V_{coll} = -4$ V extracts the majority of charge carriers present in the device. The modulated voltage is applied together with the modulated laser light and the time delay t_d between the half period where the excitation light is on and the half period where the collection voltage is applied can be varied (Fig. 1c).

Fig. 3a shows the PIA signal versus t_d for one full period of the modulation (14.3 ms). Data between $t_d = 4$ and $t_d = 8$ ms are missing, because of a reversal of the duty cycle of the applied voltage pulse. Increasing the phase difference between laser light and voltage pulse results in a jump after $t_d = 4$ to $t_d = 8$ ms when the duty cycle reverses (Fig. 1c). The constant PIA signal for $t_d < 1$ ms has the same

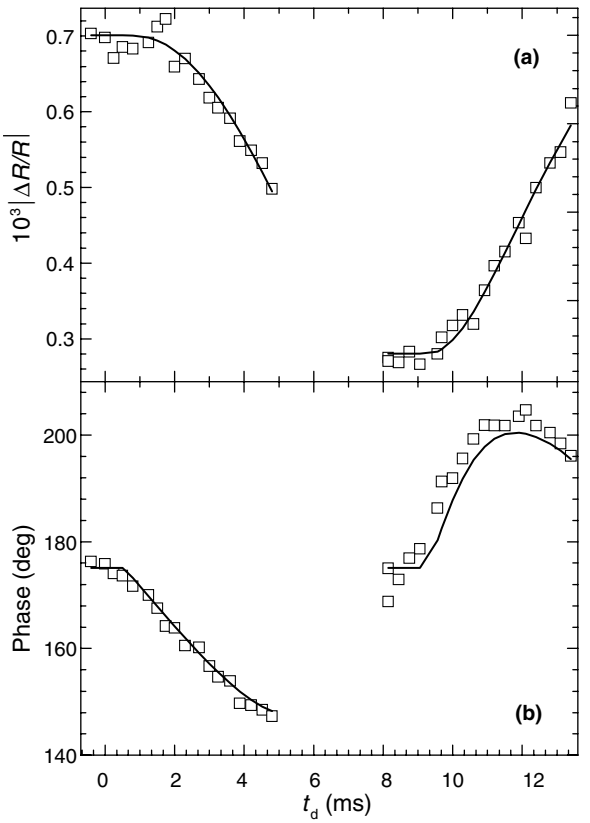

Fig. 3. PIA intensity (a) and phase (b) at 1.47 eV of charge carriers in a MDMO-PPV:PCBM solar cell measured at 80 K in reflection geometry with simultaneous photoexcitation and voltage modulation versus the delay time t_d between the two modulation cycles. The phase is referenced with respect to the photoexcitation. Symbols correspond to experimental values and the solid lines give the results of the model calculations.

origin; here the width of the voltage pulse is larger than half the period of the laser light during several milliseconds (Fig. 1c).

At $t_d = 0$, the applied field and the illumination overlap in time and a maximum in the PIA signal is observed. At $t_d = 8.4$ ms, where illumination and the electric field are 180° out of phase, a minimum in the PIA intensity is observed ($-\Delta R/R = 0.27 \times 10^{-3}$). This minimum is in good agreement with the value of $-\Delta R/R = 0.26 \times 10^{-3}$ obtained when the electrical circuit was opened. Clearly, the applied voltage of −4 V enhances the PIA signal and the concentration of charge carriers probed by PIA is maximal when the laser light and the electric field overlap in time.

Similar to the static experiments discussed above, a phase angle close to 180° is also observed in the field modulated experiments for $t_d = 0$ and 8.4 ms (Fig. 3b). This indicates that for these two time delays, the lifetime of the photogenerated charge carriers detected by PIA is short in comparison to the modulation period. For the other delay times we find that the phase angle of the PIA signal varies slowly between 150° and 210° (Fig. 3b). The maximum field induced change in the phase lag amounts to ±30°.

Fig. 4 shows the amplitude and phase angle of the photocurrent versus t_d, recorded simultaneously with the PIA measurements. When $t_d = 0$, the applied field and the illumination overlap in time and a maximum in the photocurrent is observed (Fig. 4a). At $t_d = 8.4$ ms, i.e. at the smallest temporal overlap of illumination and field, the photocurrent is practically zero. This indicates that there are virtually no carriers with a lifetime comparable to the modulation period, when $V_{bias} = +1$ V. The photocurrent is in phase with respect to the photoexcitation at $t_d = 0$ (Fig. 4b) and its phase angle increases to 120° when t_d approaches half the modulation period. For larger delay times, the phase switches sign and decreases again to zero. The sign difference arises because in the first half period the excitation precedes the collection pulse and in the second half the collection pulse precedes the excitation.

As stated in Section 2, the photocurrent signal shown in Fig. 4 was corrected for a contribution of the continuous probe light. We checked the validity of this correction by blocking the continuous probe light and measuring the photocurrent due to the laser illumination only. The values for the photocurrent thus obtained, which differ little from the values with probe light, can be subtracted from photocurrent measurement where the cell is illuminated with both laser light and continuous probe light. The result is a practically constant and small contribution to the photocurrent (solid symbols, Fig. 4c). This contribution is equal in magnitude to the photocurrent measured with white light only and corrected for the dark current (open symbols, Fig. 4c). From the comparison it can be concluded that the background illumination does not interfere with the photocurrent resulting from laser illumination in this experiment and that the contributions from the laser and probe light are additive. Thus, the correction for the white probe light applied to the photocurrent measurements appears justified.

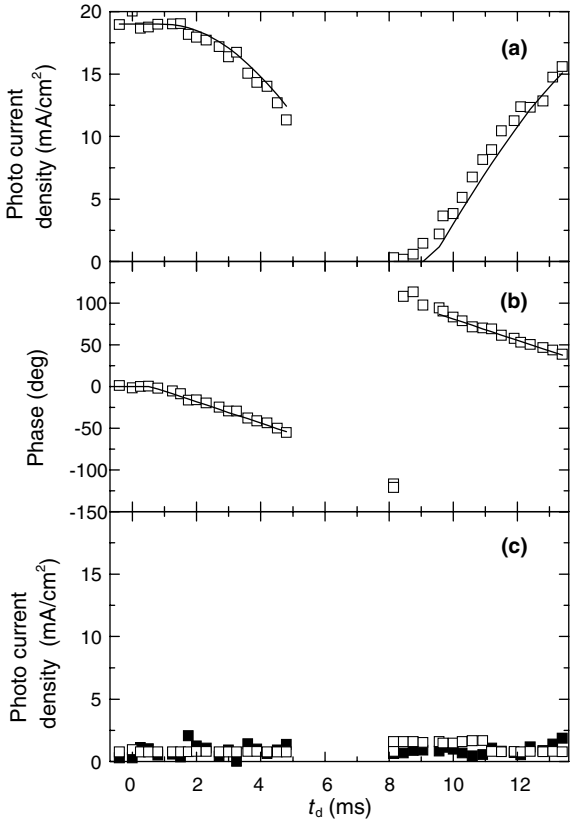

Fig. 4. Amplitude of the photocurrent density (a) and phase (b) for a MDMO-PPV:PCBM solar cell measured at 80 K with simultaneous photoexcitation and voltage modulation versus the delay time t_d between the two modulation cycles. Symbols represent experimental data and lines the model calculations. The measured values are corrected for the background illumination. Panel (c) gives the photocurrent density due to the background illumination after subtraction of the laser induced contribution (solid symbols) and the photocurrent density due to the background illumination measured with laser beam blocked and corrected for the dark current (open symbols).

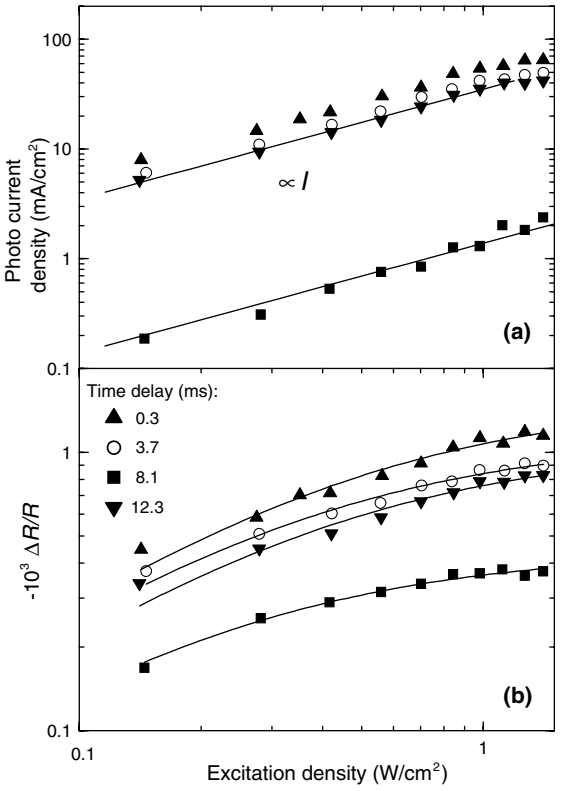

Fig. 5. Excitation density dependence at different collection delay times (symbol, see inset) of (a) the photocurrent density and (b) the photoinduced absorption signal. The fits (solid lines) to the PIA signals are according to a monomolecular trap filling model. The fit (solid line) to the photocurrent (I) is linear (solid) for excitation density below 1 W/cm^2.

Apart from the delay time t_d, also the intensity of the illumination is an easily controllable experimental parameter. The dependence of the amplitude of the photocurrent and the PIA on the excitation density is shown for different delay times. For excitation densities below 1 W/cm^2, the photocurrent is almost linear with excitation density I (Fig. 5a). Above 1 W/cm^2 the photocurrent seems to approach saturation and can be fitted according to $I^{0.5}$. The dependence of the PIA signal on the illumination intensity is less strong (Fig. 5b) showing a sublinear dependence ($I^{0.4}$) also below 1 W/cm^2. In the experiments the phase angle did not changes significantly with changing excitation density.

3.2. Model

The dependence of the PIA and photocurrent signal on the delay time t_d contains information on the lifetime and dynamics of the charge carriers. In order to retrieve this information we present a model to describe the experimental photocurrent and PIA signals.

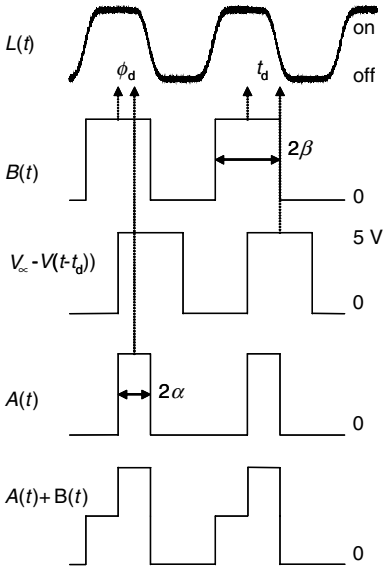

Fig. 6. Schematic illustration of the functions involved in modeling the photocurrent and the photoinduced absorption signal.

In the model, the laser light illumination ($L(t)$) is approximated by a square wave $B(t)$ with a frequency of $\omega_0/2\pi = 70$ Hz (Fig. 6). $B(t)$ is set to zero when the chopper blocks the laser beam. We assume that the experimental photocurrent at t_d is proportional to the overlap S between the half period of laser illumination $B(t)$ and the effective collection voltage pulse $V_{oc} - V(t - t_d)$ integrated over a full period (Fig. 6).

$$S(t_d) = \int_{t_0}^{t_0+2\pi/\omega_0} B(t)(V_{oc} - V(t - t_d))\,dt. \quad (1)$$

This relation assumes that the extraction of photogenerated charge carriers upon application of the collection voltage $V_{coll} = -4$ V is quasi-instantaneous on the time scale of the experiment (ms). This assumption is supported by measurements of the photocurrent under application of a continuous -4 V bias voltage, showing no significant phase difference of the photocurrent with respect to the modulated illumination. No extraction of carriers is assumed to occur when applying V_{oc} because V_{oc} compensates the built-in voltage of the device. Thus the internal electrical field E will be proportional to $V_{oc} - V(t - t_d)$. Here, the band bending at the interface of the device is neglected and it is assumed that

the photocurrent is proportional to the electric field. Furthermore, $V_{oc} - V(t - t_d)$ is approximated by a square wave function.

Another, important, assumption in this model is that the lifetime of photogenerated carriers under application at $V_{oc} = +1$ V is very short in comparison to the modulation period. This assumption is open to question, and its validity will be investigated here.

The product of the laser illumination profile $B(t)$ and the effective collection voltage $V_{oc} - V(t - t_d)$ used in Eq. (1) can be expressed as a Fourier series $A(t)$:

$$B(t)(V_{oc} - V(t - t_d)) = A(t) = A_0(t) + A_1(t) + \cdots \quad (2)$$

The term in this series at the fundamental frequency, $A_1(t)$, is of particular interest because it corresponds to the output of the lock-in amplifier used to record the photocurrent. For a square wave, the Fourier component at the fundamental frequency is given by

$$A_1(t) = a\frac{2\sin\alpha}{\pi}\cos(\omega_0 t + \phi_d) = A_{1X}\cos(\omega_0 t) + A_{1Y}(t)\sin(\omega_0 t),$$
$$A_{1X} = a\frac{2\sin\alpha}{\pi}\cos(\phi_d), \quad A_{1Y} = -a\frac{2\sin\alpha}{\pi}\sin(\phi_d), \quad (3)$$

where 2α is the width of the square wave $A(t)$. This width depends on the delay time t_d. ϕ_d is the phase difference between $B(t)$ and $A(t)$ which depends in a straightforward manner on the delay time t_d used in the experiment (Fig. 6). A_{1X} and A_{1Y} are the amplitudes of the in-phase (X or cosine) and 90° out-of-phase (Y or sine) component of $A_1(t)$ respectively. At this stage we normalize the amplitude of the overlap function $A(t)$ (i.e. we set $a = 1$) and describe the experimental photocurrent (J) by a proportionality constant c_J

$$J_X = c_J A_{1X}; \quad J_Y = c_J A_{1Y}. \quad (4)$$

The total calculated amplitude $J = c_J\sqrt{A_{1X}^2 + A_{1Y}^2}$ is plotted in Fig. 4a. Eqs. (2)–(4) can also be used to predict the phase angle of the experimentally recorded photocurrent (Fig. 4b) via $\phi_J = \tan^{-1}(A_{1Y}/A_{1X})$. The model calculations agree quite well with the experimental data (Fig. 4). For points between $t_d = 8$ and 9 ms we notice some discrepancies. For these delay times, the model predicts zero amplitude whereas in the experiment a very small current is measured. The deviation is most likely due to the approximation of the laser light by a square wave. Furthermore, upon close inspection it can be seen that for $t_d = 2$–4 ms the measured photocurrent is lower than predicted, while for $t_d = 9$–11 ms the experimental current is actually higher than expected. For $t_d = 2$–4 ms the extraction pulse is delayed with respect to the illumination while for $t_d = 9$–11 ms the extraction pulse precedes the illumination. Thus, the differences between prediction and experiment are not compatible with the notion of long-lived carriers whose extraction is delayed with respect to their generation because this would result in a higher photocurrent when the collection pulse lags behind the illumination. The good agreement between measured and predicted phase angle also speaks against long-lived ($\tau > 14.3$ ms) carriers. The discrepancy between experiment and model may therefore indicate that charge carrier extraction or generation are more efficient at the beginning of the illumination pulse than at the end. This may be related to e.g. trap filling effects or built-up of space charge during illumination; in the absence of an electric field at the beginning of the illumination, space charge may be built up and counteract charge carrier extraction upon applying the voltage pulse at the end of the illumination.

It is possible to describe the t_d dependence of the PIA signal in a similar way as for the photocurrent. Here, we assume that when the device is illuminated by the laser during the half period of the modulation cycle, charge carriers are generated with a lifetime short in comparison to the modulation cycle, giving rise to a PIA signal proportional to and in phase with the laser intensity profile $B(t)$ [21]. Application of the collection voltage $V_{coll} = -4$ V is assumed to result in an additional contribution to the PIA signal only at those instants where V_{coll} coincides with the laser light. If the laser is off when V_{coll} is on, the PIA signal is zero. This implies that the lifetime of the charge carriers giving rise to the PIA signal when applying V_{coll} is short in comparison with the modulation period. The enhancement of the PIA signal when applying V_{coll} may be due to an enhanced generation of carriers giving rise to PIA or in a change of the lifetime of this type of carrier provided that its modified lifetime is still short in comparison with $2\pi/\omega_0$. Under these premises, the additional electric field induced contribution to the PIA is proportional to the overlap $A(t)$ between the effective collection voltage and the illumination (Fig. 6). The total experimental PIA signal

can be expressed as the sum of the field dependent (A) and field-independent (B) Fourier component at the fundamental frequencies with appropriate proportionality factors c_P and c'_P for the field dependent and field-independent contributions of the PIA signal respectively

$$\begin{aligned}(-\Delta R/R)_X &= c_P A_{1X} + c'_P B_{1X} \\ (-\Delta R/R)_Y &= c_P A_{1Y}.\end{aligned} \tag{5}$$

The amplitude and phase angle of total PIA signal can now be expressed as

$$\begin{aligned}(-\Delta R/R) &= \sqrt{(c_P A_{1X} + c'_P B_{1X})^2 + (c_P A_{1Y})^2} \\ \phi_P &= \tan^{-1}\left(\frac{c_P A_{1Y}}{c_P A_{1X} + c'_P B_{1X}}\right),\end{aligned} \tag{6}$$

where the quadrant in which $-\Delta R/R$ lies has to be taken into account.

A good fit between modeled and measured PIA signal is obtained for a 3:2 ratio between the amplitudes of the field dependent and field-independent contributions c_P:c'_P (Fig. 3a). This gives a factor $(c_P + c'_P)/c'_P = 2.5$ for the increase of the PIA signal when a constant -4 V voltage is applied compared to the PIA signal at (constant) $+1$ V. Thus far, PIA experiments under application of a constant bias voltage on a similar device have yielded an increase of the PIA signal with a factor of 3.5 when changing the bias from $+1$ to -4 V (Fig. 2a). In Fig. 3b the predicted phase of the PIA signal, as calculated using Eq. (6), is compared to the measured phase. The model satisfactorily predicts the phase behavior of the signal.

4. Discussion

From the close agreement between calculated and measured photocurrent and PIA signals we can now draw a number of conclusions. First, from the proportionality of the photocurrent and the overlap S of the illumination and effective collection voltage we can conclude that the lifetime of extractable carriers when applying a bias voltage of $+1$ V is short compared to the modulation period used. Recent photo-CELIV measurements on similar photovoltaic cells have shown that, at room temperature, a major fraction of the photogenerated charge carriers recombine within 10 μs at a $+1$ V bias voltage [22].

The proportionality of the excess PIA signal induced by the electric field with the overlap S of the illumination and effective collection voltage indicates that the charge separated state giving rise to the PIA cannot be stabilized to such an extent that its lifetime becomes comparable to the modulation period used. The observation of an enhanced PIA signal upon application of a reverse bias voltage shows however that the carriers are affected by the applied electric field. The PIA is proportional to the time averaged concentration of charge carriers in the device, provided that all carriers have a lifetime short compared to the modulation period. Under these conditions, long lived or trapped carriers make up an important contribution to the signal, while short lived carriers hardly contribute. Therefore, the enhancement of the PIA may result from a more efficient generation of (trapped) carriers or an extension of their lifetime. The extended lifetime should be in the sub-ms time range in order to be compatible with the experimental data. In principle, application of a voltage may also reduce the lifetime of carriers because of faster extraction of the charges. Apparently this latter possibility does not apply to the carriers responsible for the PIA signal since this would result in a reduction of the PIA signal upon application of a -4 V bias.

Additional information on the origin of the enhancement of the PIA signal by the applied electric field comes from the study of the excitation density dependence. In Fig. 6, a monomolecular trap filling model has been fitted to the experimental data [23,24]

$$-\frac{\Delta R}{R}(I) = \frac{pI}{I + q^{-1}}, \tag{7}$$

where $q = \frac{g\tau}{n_0}$ and $p = An_0$. Here g represents the generation efficiency of photogenerated charges that can be trapped, τ the lifetime of the trapped carriers, n_0 the trap site density, and A is the proportionality factor between the PIA signal $-\Delta R/R$ and the concentration of photogenerated charges. In this model a limited number of trap sites is available to photogenerated carriers and it is assumed that the PIA signal results from trapped carriers only. The short lived 'free' carriers make a negligible contribution. In the fitting procedure used here, both p and q are taken to be dependent on the delay time between laser and voltage pulses. Keeping either p or q constant, i.e. independent of the field, did not produce a good fit for all delay times. From the fits we find for the ratio of p at time $t_d = 0.3$ ms (where the overlap between illumination and the applied voltage is maximum) and p at $t_d = 8.1$ ms (where the overlap is minimum) a value of 3.5. For the ratio of the values of q at time $t_d = 0.3$ ms and at $t_d = 8.1$ ms, a factor of

0.5 is obtained. Following Eq. (7) we find the ratio of the values of $g\tau$ at the delay times $t_d = 0.3$ ms and at $t_d = 8.1$ ms equals 1.7. Thus, upon application of an external electric field the number of available trap sites n_0 increases by a factor 3.5, which results in a more efficient generation of trapped, long-lived charge carriers. This increase in the number of trap sites could be interpreted in a tentative way in terms of a stabilization of pairs of oppositely charged carriers by the electric field. Application of a moderately strong electric field would in this view lead to trapping of a larger number of carriers inside the device.

The increase of it $g\tau$ implies that either τ increases and/or g increases. An increase of τ may be interpreted in terms of a stabilization of trapped carriers as mentioned above and a rise in g may result from suppression of the initial rate of charge carrier recombination giving the charge carriers more time to reach a trap site.

5. Conclusions

By applying a periodically modulated voltage and controlling the phase difference between the applied voltage modulation and the photoexcitation modulation an additional time dimension can be introduced in near-steady state PIA measurements on MDMO-PPV:PCBM solar cells. This method provides information of the dynamical behavior of charge carriers and offers some insight in the origin of the enhancement of the PIA by application of a moderate reverse bias potential. Although no direct evidence for a change in the lifetime of trapped carriers by application of an electric field could be obtained, it was established that the modified lifetime must still be in the sub-ms time domain. With this method also the intensity of the excitation light can be varied and this reveals that the enhancement of the PIA is at least in part due to a more efficient generation of trapped charge carriers under influence of the reverse bias voltage. Thus, we have demonstrated that an electric field is not only necessary for efficient charge extraction, but also facilitates the generation of long-lived charge carriers as evidenced from the PIA measurements.

Acknowledgements

The work of TO forms part of the research programme of the Dutch Polymer Institute (DPI), project DPI#324. The research of SCJM has been made possible by a fellowship of the Royal Dutch Academy of Arts and Sciences.

References

[1] J.J.M. Halls, C.A. Walsh, N.C. Greenham, E.A. Marseglia, R.H. Friend, S.C. Moratti, A.B. Holmes, Nature 376 (1995) 498.
[2] G. Yu, J. Gao, J.C. Hummelen, F. Wudl, A.J. Heeger, Science 270 (1995) 1789.
[3] L. Smilowitz, N.S. Sariciftci, R. Wu, C. Gettinger, A.J. Heeger, F. Wudl, Phys. Rev. B 47 (1993) 13835.
[4] R.A.J. Janssen, J.C. Hummelen, K. Pakbaz, N.S. Sariciftci, A.J. Heeger, F. Wudl, J. Chem. Phys. 103 (1995) 788.
[5] C. Arndt, U. Zhokhavets, G. Gobsch, C. Winder, C. Lungenschmied, N.S. Sariciftci, Thin Solid Films 451 (2004) 60.
[6] C. Arndt, U. Zhokavets, M. Mohr, G. Gobsch, M. Al-Ibrahim, S. Sensfuss, Synth. Met. 147 (2004) 257.
[7] C. Winder, C. Lungenschmied, G. Matt, N.S. Sariciftci, A.F. Nogueira, I. Montanari, J.R. Durrant, C. Arndt, U. Zhokhavets, G. Gobsch, Synth. Met. 139 (2003) 577.
[8] C.J. Brabec, C. Winder, M.C. Scharber, N.S. Sariciftci, J.C. Hummelen, M. Svensson, M.R. Andersson, J. Chem. Phys. 115 (2001) 7235.
[9] H.J. Snaith, I.B. Malone, C.M. Ramsdale, R.H. Friend, N.C. Greenham, in: Z.H. Kafafi, P.A. Lane (Eds.), Proceedings of SPIE, Denver, 2004, 5520, University of Denver, Denver, CO, 2004, pp. 26–35.
[10] B. Schweitzer, V.I. Arkhipov, H. Bässler, Chem. Phys. Lett. 304 (1999) 365.
[11] M. Reufer, M.J. Walter, P.G. Lagoudakis, B. Hummel, J.S. Kolb, H.G. Roskos, U. Scherf, J.M. Lupton, Nature Mater. 4 (2005) 340.
[12] P. Peumans, S.R. Forrest, Chem. Phys. Lett. 398 (2004) 27.
[13] M. Esteghamatian, Z.D. Popovic, G. Xu, J. Phys. Chem. 100 (1996) 13716.
[14] V. Arkhipov, H. Bässler, E. Emelyanova, D. Hertel, V. Gulbinas, L. Rothberg, Macromol. Symp. 212 (2004) 13.
[15] S. Barth, D. Hertel, Y.H. Tak, H. Bässler, H.H. Hörhold, Chem. Phys. Lett. 274 (1997) 165.
[16] V.D. Mihailetchi, L.J.A. Koster, J.C. Hummelen, P.W.M. Blom, Phys. Rev. Lett. 93 (2004) 216601.
[17] T. Offermans, S.C.J. Meskers, R.A.J. Janssen, Chem. Phys. 308 (2005) 125.
[18] M. Liess, Z.V. Vardeny, P.A. Lane, Phys. Rev. B 59 (1999) 11053.
[19] M.M. Wienk, J.M. Kroon, W.J.H. Verhees, J. Knol, J.C. Hummelen, P.A. van Hal, R.A.J. Janssen, Angew. Chem. 115 (2003) 3493.
[20] R. Rosei, D.W. Lynch, Phys. Rev. B 5 (1972) 3883.
[21] T. Offermans, S.C.J. Meskers, R.A.J. Janssen, submitted for publication.
[22] A.J. Mozer, N.S. Sariciftci, L. Lutsen, D. Vanderzande, R. Österbacka, M. Westerling, G. Juska, Appl. Phys. Lett. 86 (2005) 112104.
[23] P.A. Lane, X. Wei, Z.V. Vardeny, J. Poplawski, E. Ehrenfreund, M. Ibrahim, A.J. Frank, Synth. Met. 76 (1996) 57.
[24] D. Comoretto, M. Ottonelli, G.F. Musso, G. Dellepiane, C. Soci, F. Marabelli, Phys. Rev. B 69 (2004) 115215.

Available online at www.sciencedirect.com
SCIENCE DIRECT®
Organic Electronics 7 (2006) 222–228
Organic Electronics
www.elsevier.com/locate/orgel

Improving the light extraction efficiency of polymeric light emitting diodes using two-dimensional photonic crystals

A.M. Adawi [a], R. Kullock [a], J.L. Turner [a], C. Vasilev [a], D.G. Lidzey [a,*], A. Tahraoui [b], P.W. Fry [b], D. Gibson [c], E. Smith [d], C. Foden [d], M. Roberts [d], F. Qureshi [d], N. Athanassopoulou [d]

[a] *Department of Physics and Astronomy, The University of Sheffield, Hicks Building, Hounsfield Road, Sheffield S3 7RH, United Kingdom*
[b] *Department of Electronic and Electrical Engineering, The University of Sheffield, Mappin Street, Sheffield S1 3JD, United Kingdom*
[c] *Applied Multilayers Ltd., West Stone House, West Stone, Berry Hill Industrial Estate, Droitwich Worcestershire WR9 9AS, United Kingdom*
[d] *Cambridge Display Technology, Greenwich House, Madingley Road, Madingley Rise, Cambridge CB3 0TX, United Kingdom*

Received 23 December 2005; received in revised form 17 February 2006; accepted 21 February 2006
Available online 22 March 2006

Abstract

We have fabricated light emitting diodes based on a conjugated polymer, in which a planarized two-dimensional photonic crystal (PC) was inserted between the glass substrate and the ITO anode. Planarized PCs were fabricated into a high-index layer via interference lithography, followed by dry-etching and the spin-casting of a low-index glass. We characterize the electroluminescence (EL) emission from devices containing a PC, and compare this with photoluminescence (PL) generated from within the same structure. We show that LEDs incorporating the PC have an increased EL external quantum efficiency of (2.3 ± 1.0) times compared to a standard non-patterned control. This efficiency increase is in excellent agreement with PL measurements on similar structures, which also demonstrate relative increases in external emission intensity of 2.3 times.

Keywords: Polymeric light emitting diodes; Photonic crystal

Over the last decade polymeric light emitting diodes (PLEDs) have received significant attention from both academic and industrial research groups as systems for use in flat panel display technologies due to their low fabrication cost, low power consumption, wide viewing angle and fast switching times [1–5]. Improving the external efficiency of organic LEDs is a critical issue in addressing their commercial uptake, as this plays a significant role in determining their useful operational lifetime. Standard organic LEDs are composed of a glass

* Corresponding author.
E-mail addresses: a.adawi@sheffield.ac.uk (A.M. Adawi), d.g.lidzey@sheffield.ac.uk (D.G. Lidzey).

1566-1199/$ - see front matter © 2006 Elsevier B.V. All rights reserved.
doi:10.1016/j.orgel.2006.02.002

substrate coated with a transparent anode layer such as indium tin oxide (ITO), one or more of organic layers and a low work-function metallic cathode. In such a configuration only ~20% [6] of the light generated within the device can usefully escape to an external observer, with the remainder of the light being trapped in optical modes in the substrate, or in the ITO/organic layers [6].

Several methods have been explored to extract more light from organic LEDs, including the introduction of scattering centres within the device to overcome the critical angle condition [7,8] the incorporation of microcavities [9], the use of microlenses [10], the insertion of Bragg diffraction gratings [11–13], or the use photonic crystals (PCs) within the device [14–22]. There are several positions in which such a grating or a photonic crystal can be inserted into an LED; these include placing it between the metallic cathode and the active organic [22], between the active region and the ITO layer [14–17] or between the ITO layer and the glass substrate [18–21]. The latter approach is probably the most promising for practical applications, as it does not result in a modification in the electronic properties of the device. In this letter, we demonstrate the effect of inserting a deep photonic crystal (PC) between the glass substrate and the ITO layer. To create a flat surface on which the device is deposited, we use a simple spin-casting technique to planarize the surface of the grating on which an ITO anode is deposited. This approach permits us to improve the external luminous EL efficiency of red-emitting PLEDs by a factor of (2.3 ± 1.0) times (defined within an external emission cone angle of 35°). We show that the electrical properties of the patterned PLEDs are identical to un-patterned control devices, and use photoluminescence (PL) measurements to confirm that the improvement in external EL efficiency results from purely optical effects. Furthermore, we demonstrate that there are no unwanted colour shifts associated with utilizing such a PC structure. We argue that this approach to improving PLED efficiency could also be applied over large areas by using low-cost embossing techniques to create suitably patterned substrates.

A PC is a structure in which a periodic variation in refractive index occurs at the scale of the wavelength of light in one or more direction [23]. If the refractive index contrast of the PC is sufficiently large, it can result in the formation of a photonic bandgap (a range of frequencies in which the propagation of light is forbidden) [23]. In principle, there are two methods to use PCs to improve the external efficiency of organic LEDs. One approach is to match the trapped waveguide modes within the LED to the bandgap of the photonic crystal. The waveguided light thus lies within the bandgap of the PC, blocking its propagation in lateral directions within the structure, leaving only the external emission channel for light to exit the device [24]. Such an approach is however difficult to realize in practice, as there are significant material processing problems associated in creating a planarized structure having a sufficiently large refractive index contrast to open a full optical-bandgap. A second approach (which we use here) is to utilize the refractive index periodicity of a PC to diffract waveguide modes above a certain cut-off frequency into externally propagating modes (as schematically illustrated in Fig. 1(c)), which thus improves the

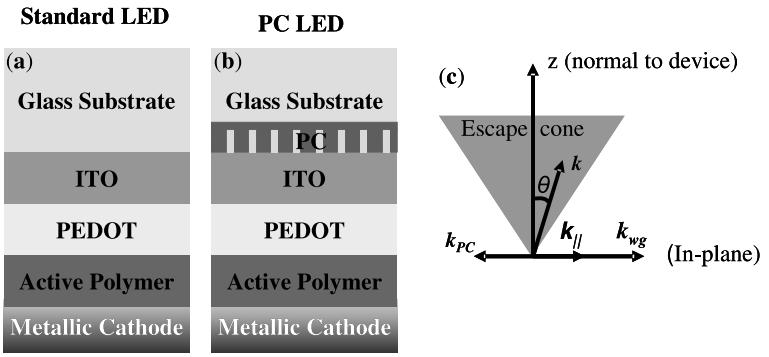

Fig. 1. A schematic of the conjugated polymer LEDs explored in this work. The structure shown in part (a) is a standard device, whilst that shown in part (b) is deposited upon a photonic grating. Part (c) shows how a periodic grating can be used to couple waveguide modes in an LED into propagating modes and therefore improve optical extraction efficiency. Here, $\vec{k}_{wg}$ is the wave-vector of a trapped waveguide mode, $\vec{k}_{pc}$ is the reciprocal lattice vector of the photonic crystal and $\vec{k}_{\parallel}$ is the wave-vector of the diffracted light. The diffracted light propagates with a wave-vector $\vec{k}$, where $|\vec{k}_{\parallel}| = |\vec{k}| \sin\theta$.

extraction efficiency of the device [24]. In Fig. 1(c), $\vec{k}_{wg}$ is the component of the waveguided light parallel to the device plane and $\vec{k}_{pc}$ is the reciprocal wave-vector of the photonic crystal, given by $\vec{k}_{pc} = \left(\frac{2\pi}{a_x}\right)\hat{i} + \left(\frac{2\pi}{a_y}\right)\hat{j}$, where a_x and a_y are the periodicity of the lattice in the x and y directions, respectively. The effect of the photonic crystal on the waveguided modes is to change their in-plane wave-vector to $\vec{k}_{\parallel}$, where $\vec{k}_{\parallel} = \vec{k}_{wg} \pm n\vec{k}_{pc}$, where n is an integer number. Such diffracted modes will escape from the device provided that $\vec{k}_{\parallel}$, is less than the wave-vector above which light is totally internally reflected.

Recently Lee et al. [18] have made an experimental and theoretical study of the effect of inserting a PC between the glass substrate and the ITO layer in an organic LED based on vapor deposited low molecular-mass materials. Their results indicated that the extraction efficiency increases with *increasing depth* of the photonic crystal, and also showed that the external efficiency of the device *is maximized* when the periodicity of the photonic crystal is larger than the (vacuum) wavelength of the emitted light. This allowed them to demonstrate an improvement in external efficiency by a factor of 1.5 times using a 200 nm deep grating. Whilst this is clearly a promising result, we note that it is less than the enhancement factors that have been demonstrated when PC structures have been incorporated into inorganic LEDs. In particular, a PC etched into the surface of an AlGaN LED [25] improved the power output of the device by a factor of 2.5 times. Here, the depth of the PC was 190 nm, with a periodicity approximately 3 times that of the AlGaN emission wavelength. In this paper, we have explored the use of a deep optical grating to enhance the extraction efficiency of a polymer LED. The grating used had a depth of 450 nm with a periodicity approximately twice that of the polymer emission wavelength. Using this approach we demonstrate improvements in external efficiency of a red-emitting polymer LED by a factor of 2.3 times. This enhancement is close to the largest enhancement observed in inorganic devices, and suggests a promising method to gain significant improvements in the external efficiency of organic LED.

The devices that were fabricated and evaluated are shown schematically in Fig. 1(a) and (b). Fig. 1(a) shows a standard PLED device, composed of a glass substrate coated with a 150 nm thick layer of ITO (deposited using closed field magnetron sputtering), a 150 nm thick layer of the conducting polymer PEDOT:PSS (poly(3,4-ethylendioxythiophene)/polystyrene-sulfonic acid) (Baytron P PE FL supplied by H.C. Starck Ltd.) included to facilitate hole injection, and a 70 nm thick layer of an active red polymer (supplied by Covion Organic Semiconductors GmbH). Here, each polymer layer was deposited by spin coating, with the PEDOT:PSS being annealed at 150 °C in air for 15 min. The device was then finished by the thermal evaporation of a cathode, composed of a 20 nm thick film of calcium used to aid electron injection, capped by an optically thick (50 nm) film of silver. The cathode was evaporated through a shadow-mask onto the surface of the conjugated polymer, with each individual LED having an active area of $\sim 5\,mm^2$. All metal depositions were made at a base-pressure of 10^{-8} mbar in a Kurt J. Leskar Spectros deposition system.

Fig. 1(b) shows a schematic of an LED whose structure is identical to that shown in Fig. 1(a), however, it is fabricated on a planarized PC. The PC was created by first depositing a 500 nm thick layer of Si_xN_y ($n = 1.95$) on a $12 \times 12\,mm^2$ glass substrate using plasma-enhanced chemical vapor deposition. Interference lithography [26–28] was then used to write a photonic structure into a 1 μm thick layer of a high sensitivity positive photoresist (SPR350 supplied by Chestech Ltd.) spin-cast onto the Si_xN_y layer. Interference lithography was achieved using a HeCd laser ($\lambda = 442$ nm), which was split into two beams using a beam splitter. Each beam was expanded using a 10× microscope objective lens, and then recombined onto the substrate surface (with the beams having a mutual angular separation of 20°). The diameter of the expanded beams was ~6 cm, permitting us to micro-pattern the entire PLED substrate. To do this, the photoresist was first exposed to the laser having a power of $5\,mW\,cm^{-2}$ for 20 s. The sample was then rotated by 90° and the exposure repeated. This resulted in the creation of a square lattice PC having a pitch of 1.2 μm. The photoresist was then developed for 10 s in a developer (MF26 supplied by Chestech Ltd.). This pattern was then transferred into the Si_xN_y layer using a CHF_3 coupled plasma-etching technique.

Fig. 2(a) shows an AFM image of a patterned Si_xN_y layer following dry-etching. The pattern is comprised of holes having a diameter of 930 nm, with a periodicity of 1245 nm and depth of 430 nm.

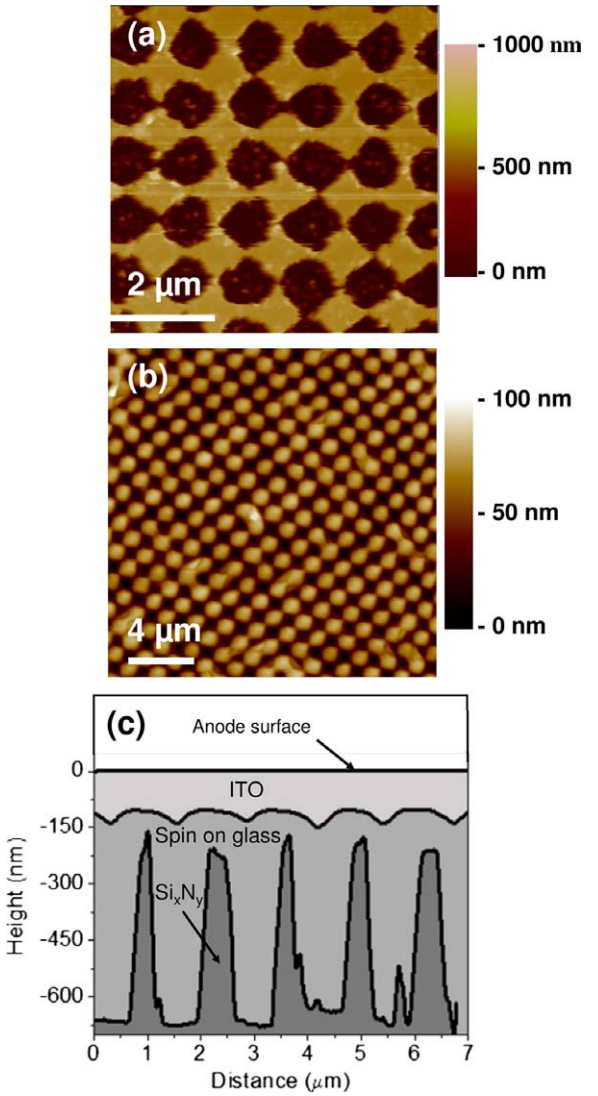

Fig. 2. Part (a) shows an AFM image of the photonic crystal (PC) structure after dry-etching. Part (b) shows the same grating after filling with a spin-on glass material. Part (c) shows a series of topographic cross-sections of the PC anode surface recorded (using an AFM) at various steps in its fabrication.

To planarize the grating, a low refractive index ($n = 1.45$) spin-on glass (supplied by Allied Signal Inc.) was coated onto the surface and then thermally annealed in air at 280 °C for 1 h. As the thickness of the spin-on glass layer was (after annealing) 150 nm, the coating process was repeated three times to totally infill the holes in the Si_xN_y and thus planarize the grating (see the AFM image presented in Fig. 2(b)). This structure was then coated by a 150 nm thick layer of ITO. The internal structure of the ITO-covered PC can be visualized by plotting a series of AFM cross-sections taken at various stages during its fabrication as shown in Fig. 2(c). It can be seen that the spin-on glass largely planarized the Si_xN_y grating and created a surface having a height modulation of ±25 nm. This planarization process was completed by the ITO deposition, which reduced the amplitude of the surface corrugations to ±2 nm.

Current–voltage–luminance measurements of the PC LED and control devices were made in an overpressure nitrogen glove-box, having water and O_2 background levels less than 0.1 ppm. To measure luminance, a calibrated photodiode was placed above the sample, subtending a cone angle of 35° to the device. The current generated by the photodiode was converted to an equivalent brightness (in units of cd m^{-2}) using a pre-determined correction factor obtained using a calibrated Topcon luminance meter. As we show below, there is very little difference in the EL emission spectra between the control devices and the PC LEDs (both at normal incidence and as a function of external viewing angle). Thus the efficiency of the device in terms of cd A^{-1} can be thought of as being a relative measurement of external quantum efficiency. Emission spectra were also measured from both control and patterned devices using a fibre-coupled CCD-spectrograph. We emphasise that both PC LEDs and control devices emitted uniform EL across their active area and were free from so-called 'black spots'.

We have complemented the electrical measurements on the devices using optical excitation to generate photoluminescence (PL) within the structure. Importantly, this permits us to obtain a second measurement of the effect of the periodic patterning on the device emission, and – as we show below – it demonstrates that the external efficiency enhancements observed are purely optical in nature and do not rely on effects relating to charge injection and transport. For PL measurements, we studied structures identical to those shown in Fig. 1(a) and (b), however, the thin calcium layer was omitted to avoid any problems due to photo-oxidation (as all excitation and emission measurements were performed in air). To generate PL, the sample surface was excited at normal incident using a 4 mW 405 nm diode laser, with emission being measured as a function of viewing angle.

In Fig. 3(a) we plot the *I–V* characteristics of both patterned and control devices. It can be seen that both types of device have (as expected) similar *I–V* characteristics. Fig. 3(b) plots the *L–V* characteristics of control and patterned devices. It can be

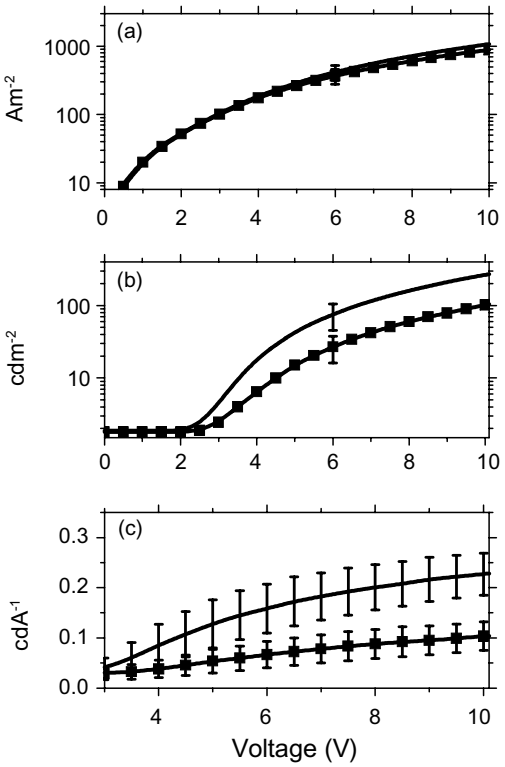

Fig. 3. Part (a) shows current–voltage curves recorded for control and laterally patterned devices. The luminance versus voltage for the same devices is shown in part (b), which is then used to calculate external emission efficiency as shown in part (c). Note, that all data shown are an average deduced from a large number of measurements made on individual devices as discussed in the text.

seen that both patterned and control devices emit light at voltages greater than 2.5 V. The luminance of the patterned device is higher than that of the control device by a factor of ~2.7 times at all voltages. Fig. 3(c) compares the luminous efficiency (in terms of cd A^{-1}) as a function of driving voltage for both patterned device and the control. Here, the data presented in Fig. 3(a)–(c) is an average of measurements made from seven identical patterned devices and 10 control devices. It can be seen that there is a clear enhancement by a factor of (2.3 ± 1.0) times in the external efficiency of the patterned LED, which – as indicated by the I–V data shown in Fig. 3(a) – is not related to changes in the electronic properties of the device. Note that the absolute efficiency of the patterned or control devices presented in Fig. 3 is significantly lower than that of state-of-the-art devices. This was due to the fact that the ITO used here was not optimized for OLED operation. Despite this, our results indicate

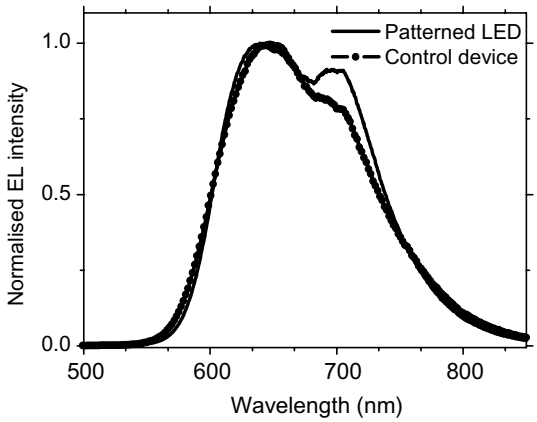

Fig. 4. Normalised EL spectra recorded at normal incidence from a control device (closed circles), and a laterally patterned LED (solid line).

that the observed improvements in the external efficiency in Fig. 3(c) originate from inserting PC beneath the ITO.

In Fig. 4, we plot the normal incidence EL emission spectrum recorded from the patterned device and the control PLED. It can be seen that the EL emission spectrum of both devices are quite similar, indicating that the adoption of a PC structure does not cause an apparent shift in the emission colour of the LED. We have also characterized the CIE (x, y) emission colour-coordinates from both control and patterned devices as a function of external viewing angle and find them to be largely identical, being $(0.66, 0.33)$ and $(0.67, 0.33)$ at normal incident from the control devices and patterned devices, respectively, and $(0.67, 0.33)$, $(0.67, 0.32)$ from the control devices and the patterned devices at a viewing angle of 40°. Such differences in the CIE coordinates are clearly very small, permitting us to conclude that the observed enhancement in the efficiency (in terms of cd A^{-1}) from the patterned devices come as a result of increasing the relative external efficiency rather than tuning the EL emission to a part of the spectrum where the eye has an improved sensitivity. This also demonstrates that unlike microcavity-based LEDs, the enhancements in external efficiency observed here do not come at the cost of a severe angular-dependent colour-shift.

We can gain further confidence in the effect of the PC on the improved output coupling by comparing the PL emission from a patterned LED with a control device. This is shown in Fig. 5(a), where we plot the PL spectra from a control LED with a patterned device as a function of viewing angle. It can be seen

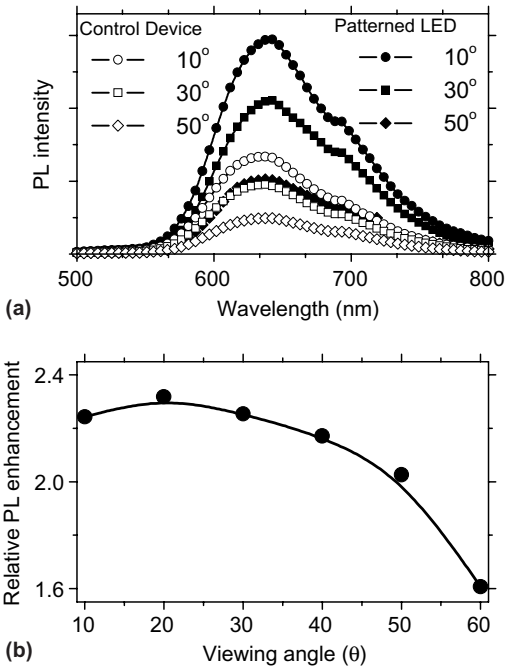

Fig. 5. Part (a) shows the PL spectra from standard device and a laterally patterned structure as a function of external viewing angle. Part (b) shows the enhancement in PL emission intensity (averaged over wavelength), also presented as a function of viewing angle.

that the emission spectra are very similar to those generated via electrical excitation, with the PL intensity from both devices decreasing with increasing viewing angle as expected. As was observed under electrical excitation, the device emission colour is angle-independent. Importantly, the PL emission intensity from the laterally patterned structure is higher than from the control at all external viewing-angles. This is illustrated in Fig. 5(b), where we plot the PL enhancement factor as a function of viewing angle. This enhancement factor was calculated as the ratio of the PL intensity (integrated over 500–800 nm) from the patterned structure to that of the control. It can be seen that close to normal incidence, the PL from the patterned structure was enhanced by approximately 2.3 times – a value in good agreement with the results of the EL enhancement as presented above. This enhancement in relative PL emission efficiency also survives to large off-axis angles, being a factor of 1.6 times at a viewing angle of 60°. This observation further confirms that inserting a photonic crystal between the glass substrate and the ITO anode improves the fraction of light that can escape from of the structure.

We have therefore investigated the effect of inserting a two-dimensional PC having a pitch of 1.2 μm between the glass substrate and the ITO anode layer of red-emitting polymer LED. Such periodic patterning can be used to generate a significant improvement in device external emission efficiency (in this case by a factor of >2 times). Usefully, the enhancements that we observe are not accompanied by an angular-dependent colour shift. The grating used here was not sufficient to open up a photonic bandgap, however, we argued that the PC effectively diffracted waveguided modes trapped in the ITO layer into useful external emission. It is also possible however, that the close proximity of the PC to the active emissive region of the LED can modify the optical density of states within the device, which may also have an effect on the spontaneous emission process itself. The approach that we used to pattern the LED substrate was based on interference lithography. Such a process would probably not be scalable to a manufacturing environment, however, we note that many other techniques can be used to pattern large areas at this resolution. For example, polymer embossing techniques can be used in a manufacturing environment to pattern relatively large areas with a resolution of around 100 nm [29]. Thus the simple approach prototyped here could be used to significantly improve the efficiency of a number of organic light-emitting devices, ranging from light emitting displays to organic flat panel lighting systems.

Acknowledgements

We wish to thank the UK EPSRC and DTI for support of this research via grant GR/S05687/01 'Light Emission for Active Polymers' (LEAP).

References

[1] G. Gu, S.R. Forrest, IEEE J. Sel. Top. Quant. Electron. 4 (1998) 83.
[2] K. Ziemelis, Nature 399 (1999) 408.
[3] I.D.W. Samuel, A. Beeby, Nature 403 (2002) 710.
[4] M. Pfeiffer, S.R. Forrest, K. Leo, M.E. Thompson, Adv. Mater. 14 (2002) 1633.
[5] A.B. Chwang, M.A. Rothman, S.Y. Mao, R.H. Hewitt, M.S. Weaver, J.A. Silvernail, K. Rajan, M. Hack, J.J. Brown, X. Chu, L. Moro, T. Krajewski, N. Rutherford, Appl. Phys. Lett. 83 (2003) 413.
[6] C.F. Madigan, M.H. Lu, J.C. Sturm, Appl. Phys. Lett. 76 (2000) 1650.
[7] T. Yamasaki, K. Sumioka, T. Tsustui, Appl. Phys. Lett. 76 (2000) 1243.

[8] H.J. Peng, Y.L. Ho, X.J. Yu, H.S. Kwok, J. Appl. Phys. 96 (2004) 1649.
[9] R.H. Jordan, L.J. Rothberg, A. Dodabablapur, R.E. Slusher, Appl. Phys. Lett. 69 (1996) 1997.
[10] S. Moller, S.R. Forrest, J. Appl. Phys. 91 (2002) 3324.
[11] J.M. Lupton, B.J. Matterson, I.D.W. Samuel, M.J. Jory, W.L. Barnes, Appl. Phys. Lett. 77 (2000) 3340.
[12] B.J. Matterson, J.M. Lupton, A.F. Safonov, M.G. Salt, W.L. Barnes, I.D.W. Samuel, Adv. Mater. 13 (2001) 123.
[13] P.A. Hobson, S. Wedge, J.A.E. Wasey, I. Sage, W.L. Barnes, Adv. Mater. 14 (2002) 1393.
[14] J.M. Ziebarth, A.K. Saafir, S. Fan, M.D. McGehee, Adv. Funct. Mater. 14 (2004) 451.
[15] M. Fujita, T. Ueno, T. Asano, S. Noda, H. Ohhata, T. Tsuji, H. Nakada, N. Shimoji, Electron. Lett. 39 (2003) 1750.
[16] M. Fujita, K. Ishihara, T. Ueno, T. Asano, S. Noda, H. Ohata, T. Tsuji, H. Nakada, N. Shimoji, Jpn. J. Appl. Phys. 44 (2005) 3669.
[17] G. Fichet, N. Corcoran, P.K.H. Ho, A.C. Arias, J.D. MacKenzie, W.T.S. Huck, R.H. Friend, Adv. Mater. 16 (2004) 1908.
[18] Y.-J. Lee, S.-H. Kim, J. Huh, G.-H. Kim, Y.-H. Lee, S.-H. Cho, Y.-C. Kim, Y.R. Do, Appl. Phys. Lett. 82 (2003) 3779.
[19] Y.R. Do, Y.-C. Kim, Y.-W. Song, C.-O. Cho, H. Jeon, Y.-J. Lee, S.-H. Kim, Adv. Mater. 15 (2003) 1214.
[20] M. Kitamura, S. Iwamoto, Y. Arakawa, Jpn. J. Appl. Phys. 44 (2005) 2844.
[21] Y.R. Do, Y.-C. Kim, Y.-W. Song, Y.-H. Lee, J. Appl. Phys. 96 (2004) 7629.
[22] C. Liu, V. Kamaev, Z.V. Vardeny, Appl. Phys. Lett. 86 (2005) 143501-1.
[23] J.D. Joannopoulos, R.D. Meade, J.N. Win, Photonic Crystals, Princeton University Press, 1995.
[24] S. Fan, P. Villeneuve, J.D. Joannopoulos, Phys. Rev. Lett. 78 (1997) 3294.
[25] J. Shaky, K.H. Kim, J.Y. Lin, H.X. Jiang, Appl. Phys. Lett. 85 (2004) 142.
[26] J.P. Spallas, A.M. Hawryluk, D.R. Kania, J. Vac. Sci. Technol. B 13 (1995) 1973.
[27] S.C. Kitson, W.L. Barnes, J.R. Sambles, IEE Photonics Technol. Lett. 8 (1996) 1041.
[28] I. Mikulskas, J. Mickevicius, J. Vaitkus, R. Tomasiunas, V. Grigaliunas, V. Kopusyainskas, S. Meskinins, Appl. Surf. Sci. 186 (2002) 599.
[29] L.S. Roman, O. Inganäs, T. Granlund, T. Nyberg, M. Svensson, M.R. Andersson, J.C. Hummelen, Adv. Mater. 12 (2000) 189.

Available online at www.sciencedirect.com
SCIENCE DIRECT®
Organic Electronics 7 (2006) 229–234
Organic Electronics
www.elsevier.com/locate/orgel

Charge carrier mobility and lifetime versus composition of conjugated polymer/fullerene bulk-heterojunction solar cells

G. Dennler [a,*], A.J. Mozer [b], G. Juška [c], A. Pivrikas [d], R. Österbacka [d], A. Fuchsbauer [a], N.S. Sariciftci [a]

[a] *Linz Institute for Organic Solar Cells (LIOS), Johannes Kepler University Linz, Altenbergerstrasse 69, A-4040 Linz, Austria*
[b] *Molecular Process Engineering, Graduate School of Engineering, Osaka University, Japan*
[c] *Department of Solid State Electronics, Vilnius University, Lithuania*
[d] *Department of Physics, Åbo Akademi University, Turku, Finland*

Received 22 December 2005; received in revised form 27 February 2006; accepted 28 February 2006
Available online 18 April 2006

Abstract

Charge carrier mobility (μ), recombination kinetics, and lifetime (τ) have been investigated with the photo-induced charge carrier extraction by linearly increasing voltage technique (photo-CELIV) in blends of poly[2-methoxy-5-(3,7-dimethyloctyloxy)-phenylene vinylene] (MDMO-PPV) and 1-(3-methoxycarbonyl)propyl-1-phenyl-(6,6)-C_{61}(PCBM). Different MDMO-PPV/PCBM ratios have been studied showing that increasing the PCBM content induces an increase of the photo-CELIV mobility up to two orders of magnitude. Simultaneously, the lifetime of the charge carriers decreases in such a way that the product $\mu \times \tau$ appears almost constant independently of the blend composition. Recombination kinetics close to the Langevin one is observed for all PCBM concentrations studied.

PACS: 72.20.Jv; 72.80.Le; 73.50.Pz

Keywords: Mobility; Recombination kinetics; Lifetime; Bulk-heterojunction; Conjugated polymer; Fullerene; Organic solar cells

1. Introduction

During the last five years, important research efforts have been devoted to acquire a better understanding of the working principle of conjugated polymer:fullerene based bulk-heterojunction solar cells [1]. This knowledge sounds mandatory to allow further optimization and potential increase of the efficiency of these devices [2]. It appeared quickly that the ratio donor/acceptor does dictate not only the number of charge carriers created per incoming photons [3], but as well the ability of the device to collect the photo-induced charge carriers, that is, the transport properties of the active blend [4].

Several previous works focused on the investigation of solar cells characteristics versus conjugated

* Corresponding author. Tel.: +43 732 2468 1213; fax: +43 732 2468 8770.
E-mail address: gilles.dennler@jku.at (G. Dennler).

1566-1199/$ - see front matter © 2006 Elsevier B.V. All rights reserved.
doi:10.1016/j.orgel.2006.02.004

polymer/fullerene ratio [4–9]. In the case of poly [2-methoxy-5-(3,7-dimethyloctyloxy)-phenylenevinylene] (MDMO-PPV):1-(3-methoxycarbonyl)propyl-1-phenyl-(6,6)-C_{61}(PCBM) blends, short circuit current (I_{sc}), fill factor (FF) and overall efficiency (η) were reported to show optimum values for PCBM concentration about 80% [7,9]. These results have been interpreted in terms of competing effects between charge generation, taking essentially place in the MDMO-PPV molecules, and hole and electron respective mobilities. These latter have both been reported to increase up to two orders of magnitude upon increasing the PCBM concentration [9,10]. Among others, ordering effects have been invoked to explain this unexpected phenomenon. This hypothesis has been substantiated by the numerous morphology studies performed on MDMO-PPV:PCBM, which show that PCBM tends to form nano-clusters due to its quite high diffusion coefficient in amorphous MDMO-PPV [7,8]. This nano-clusters have been proposed to enhance the organization of the long MDMO-PPV chains, and hence the hole mobility [11].

In several models proposed to describe the working principle of conjugated polymer:fullerene solar cells, the charge collection is considered to be mostly ensured by field driven drift, yet diffusion might play a non-negligible role, especially close to the electrodes [9,12,13]. In this perspective, the distance performed by the charge carriers is given by

$$l = \mu \cdot \tau \cdot E, \tag{1}$$

where μ is the mobility of the charge carriers, τ their lifetime, and E the electric field in the device. Thus, the mobility indeed plays a major role in the collection of charge carriers. But so does as well the charge carrier lifetime. To the best of our knowledge, no one did yet report the evolution of τ versus the concentration of the MDMO-PPV:PCBM blend. Mihailetchi et al. expressed the necessity of their model to suppose increasing τ with decreasing PCBM to fit properly the experiment data, especially in the range below 50% of PCBM [9]. But no direct evaluation of τ was performed. Nevertheless, it has to be mentioned that Montanari et al. studied the recombination kinetic of charge carriers by transient absorption spectroscopy (TAS) [14]. However, the authors reported a PCBM concentration independent recombination kinetics as detected with this optical method.

Thus, we have used photo-induced charge carrier extraction by linearly increasing voltage technique (photo-CELIV) to investigate the charge carrier mobility, recombination kinetic and lifetime.

2. Experimental

As described in details elsewhere [15–17], photo-CELIV is a powerful method that allows the determination of charge carrier transport properties in the μs to ms range: a short laser pulse (3 ns, 532 nm, 0.5 mJ/pulse, Nd-YAG laser in our case) is absorbed by the device to be characterized; the charge carriers created are forced to recombine in the device thanks to an offset bias applied to compensate the Voc of the solar cell, what ensures flat-band condition; after a certain delay time τ_{del}, the remaining charges are extracted by a linearly increasing voltage $A = dU/dt$ applied in the reverse, non-injecting polarization of the photodiode. The devices studied in this work are MDMO-PPV:PCBM bulk-heterojunctions solar cells with PCBM concentrations varying from 0% to 80% (in weight, in the entire text). The chlorobenzene based solutions have been spin-cast on indium tin oxide (ITO), and coated with evaporated aluminum (Al, 70 nm) after drying in vacuum. The thickness of the device is comprised between 150 and 250 nm and the active surface area between 4 and 6 mm^2. All the photo-CELIV measurements have been carried out under high vacuum (10^{-6} mbar) at room temperature.

3. Results and discussion

Fig. 1a shows the photo-CELIV curves collected in the case of a 30% MDMO-PPV:70% PCBM active layer for various τ_{del}. One can observe a capacitance induced displacement current to which is superimposed an extraction current [15–17]. This latter disappears after 8 μs, indicating a complete extraction of the charge carrier photogenerated. The mobility of the carriers can be calculated according to Eq. (2):

$$\mu = \frac{2.d^2}{3 \cdot A \cdot t_{max}^2 \left[1 + 0.36 \frac{\Delta j}{j(0)}\right]} \quad \text{if } \Delta j \leqslant j(0) \tag{2}$$

where d is the thickness of the device, A is the voltage rise speed, t_{max} is the time at the maximum Δj of the extraction peak, and $j(0)$ is the displacement current of the capacitance. Using Eq. (2), we find a mobility $\mu = 1.9 \times 10^{-4}\ cm^2\ V^{-1}\ s^{-1}$. Moreover, it can be noted that the number of extracted charge

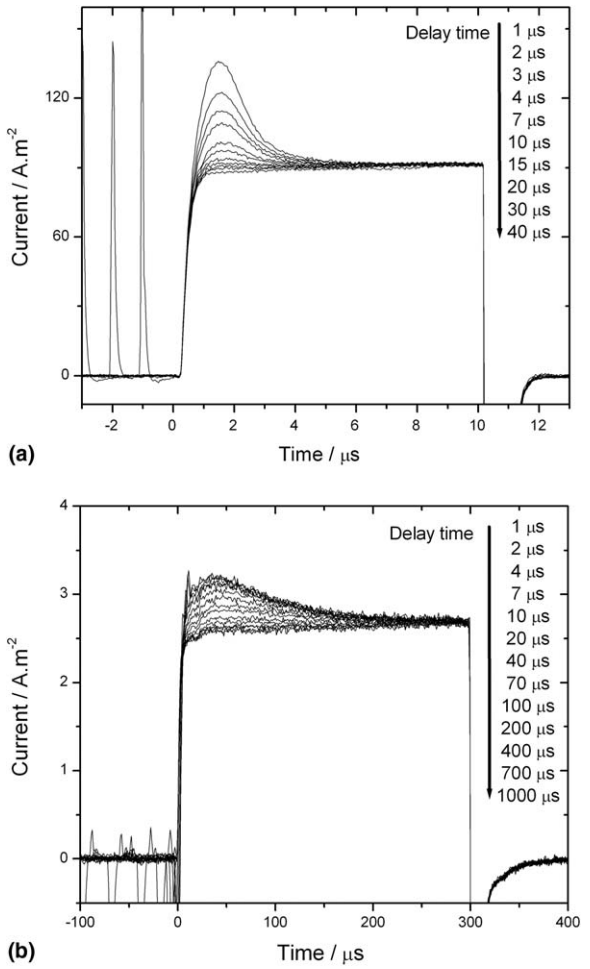

Fig. 1. Photo-CELIV curves for various delay times between the light pulse and the extraction voltage ramp in the case of (a) a 30% MDMO-PPV:70% PCBM blend ($A = 5$ V/10 µs, $d = 155$ nm) and (b) a 70% MDMO-PPV:30% PCBM blend ($A = 5$ V/300 µs, $d = 200$ nm).

carriers, that is the area under the extraction peak, decreases with increasing delay time between the light pulse and the beginning of the extraction. This indicates that a recombination process takes place during τ_{del}, while flat-band condition is ensured in the device thanks to the applied offset voltage.

Fig. 1b exhibits the photo-CELIV transients collected in the case of a 70% MDMO-PPV:30% PCBM active layer for various τ_{del}. Although the curves show qualitatively the same behavior than in Fig. 1a, a quantitative analysis suggests major differences. The application of Eq. (2) reveals that the mobility of the charge carriers drastically decreases with decreasing PCBM concentration: μ is found to be about $1 \times 10^{-5}\,cm^2\,V^{-1}\,s^{-1}$. Moreover, long lived charges can still be extracted after several hundreds of µs after the light pulse, what suggests that the lifetime of the charges is considerably enhanced compared to the situation displayed in Fig. 1a, where all the carriers recombine within less than 100 µs. Finally, a close observation reveals that the shape of the photo-CELIV peak changes from Fig. 1a and b. This shape can be numerically analyzed by calculating the ratio $t_{1/2}/t_{max}$, where t_{max} is the time at the maximum of the peak, and $t_{1/2}$ is the width at half maximum of the extraction peak [18]. In the case of ideal non-dispersive transients $t_{1/2}/t_{max} = 1.2$, and this ratio increases with increasing dispersivity. The value extracted for Fig. 1a and b are 1.2 and 2.4, respectively. This shows that the dispersive character of the transient decreases with increasing PCBM concentration, as observed by Pacios et al. in the case polyfluorene:PCBM blends [19].

A more detailed investigation of the charge carrier mobility and decay versus blend composition has been performed. Fig. 2 exhibits the time dependence of the charge carrier mobility and the number of charge carriers extracted. As a first observation, one can note that, as mentioned above and reported previously by several groups [9,10], the charge carrier mobility increases with increasing PCBM concentration, from $3 \times 10^{-6}\,cm^2\,V^{-1}\,s^{-1}$ for the pure MDMO-PPV to about $3 \times 10^{-4}\,cm^2\,V^{-1}\,s^{-1}$ for the 1:4 ratio (at $\tau_{del} = 1$ µs). Though the sign of the charge carriers investigated with photo-CELIV remains under debate, these values are believed to be related to the slowest carriers [20], namely the holes. These values are in close accordance to the hole mobilities reported by Mihailetchi et al. [9]. Moreover, Fig. 2a indicates a slightly time dependent mobility for almost all PCBM concentrations studied. This phenomenon, already reported elsewhere for 20% MDMO-PPV: 80% PCBM solar cell, has been attributed to energy relaxation of the charge carriers towards the tail states of the density of states (DOS) distribution [20].

Fig. 2b shows the number of charge carriers extracted versus the delay time between light pulse and extraction. As illustrated in Fig. 1, $n(t)$ drastically decreases with increasing time since the charge carriers are forced to recombine in the device. The saturation of the number of carriers extracted versus light intensity (not shown here), observed for all PCBM concentration suggests that the recombination kinetic is of bimolecular nature in the regime studied. This bimolecular regime has been proposed

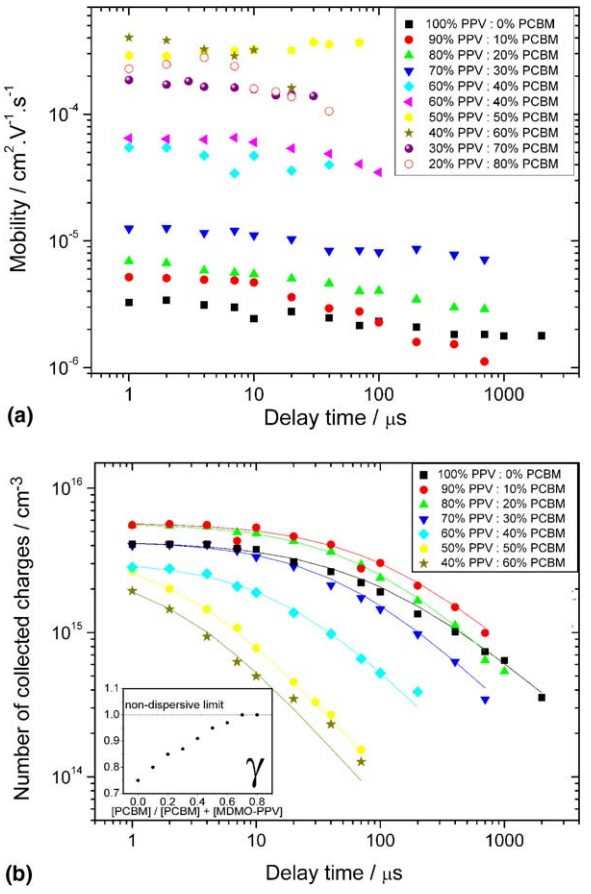

Fig. 2. (a) Photo-CELIV mobility and (b) number of extracted charge carriers versus delay time measured for different MDMO-PPV:PCBM ratios. In (b), the solid lines are fits realized using Eq. (5). The inset in (b) shows the evolution of γ versus the composition of the blend.

to be of primary importance in the recombination kinetics in solar cells in operation [21], especially in situations close to the open circuit condition.

Moreover, Fig. 2b shows that for low PCBM concentrations, the lifetime of the charge carriers is much longer than for high PCBM concentrations. In order to extract the value of the charge carriers bimolecular lifetime, the $n(t)$ data have been fitted with a dispersive bimolecular recombination dynamics model [20]: The observation of a time dependent mobility during thermalization suggests a time dependent bimolecular recombination rate

$$\frac{dn}{dt} = \frac{dp}{dt} = -\beta(t) \cdot n \cdot p, \tag{3}$$

where n and p are the concentration of electrons and hole, respectively, and $\beta(t)$ the time dependent bimolecular recombination coefficient.

Assuming charge neutrality, and using the following functional form of $\beta(t)$

$$\beta(t) = \beta_0 \cdot t^{-(1-\gamma)}, \tag{4}$$

where β_0 and γ are time independent parameters, Eq. (5) can be yielded:

$$n(t) = p(t) = \frac{n(0)}{1 + (t/\tau_B)^{\gamma}}. \tag{5}$$

τ_B, called the "effective" bimolecular lifetime, can be expressed as follow:

$$\tau_B = \left(\frac{\gamma}{n(0) \cdot \beta_0}\right)^{\frac{1}{\gamma}} \tag{6}$$

The fits to the decay data, displayed as solid lines in Fig. 2b, show good agreement with the experimental data. The values of γ, extracted for each PCBM concentrations are found to evolves from 0.75 to 1 with increasing PCBM concentration, indicating a transition form a dispersive to a non-dispersive regime, as already noticed above. Finally μ and τ_B extracted for each concentration are shown in Fig. 3. While the mobility clearly increases by two orders of magnitude upon adding PCBM, the "effective" bimolecular lifetime decreases by the same factor, evolving from about 100 µs to 2 µs. Interestingly, these opposite evolutions induce a constant product $\mu \times \tau_B$ independent of the PCBM concentration, as revealed in the inset of Fig. 3.

It has been previously reported that the bimolecular recombination kinetics in PPV [22] and 20% MDMO-PPV:80% PCBM [20] is of Langevin type [23]. In this case, the Langevin bimolecular recombination coefficient β_L in given by

$$\beta_L(t) = B \cdot \mu(t) \quad \text{where } B = e/\varepsilon \cdot \varepsilon_0, \tag{7}$$

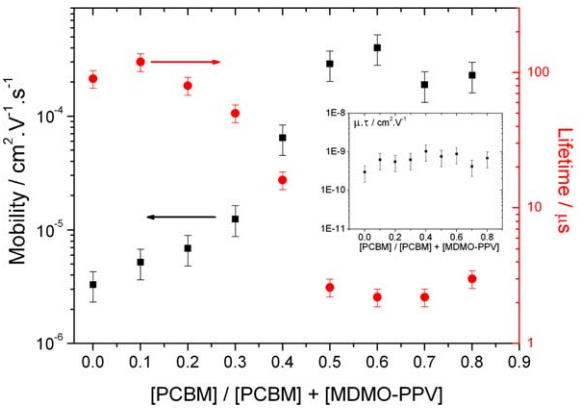

Fig. 3. Photo-CELIV mobility (μ) of charge carriers, "effective" bimolecular lifetime (τ_B) of charge carriers, and (inset) product $\mu \times \tau_B$ versus MDMO-PPV:PCBM ratio.

e being the elementary charge, ε the relative dielectric constant of the semiconductor (3 in our case), and ε_0 the permittivity of vacuum. In order to verify the nature of the bimolecular recombination kinetic observed in this study, we have fitted the $n(t)$ data of each PCBM concentration with Eq. (8). It should be noted here that while Eq. (6) (used to fit the data in Fig. 2b) supposes a bimolecular recombination kinetic (Eq. (3)) with a power law decay of the bimolecular recombination coefficient (Eq. (4)), Eq. (8) results from the supposition of a purely Langevin (Eq. (7)) bimolecular recombination kinetic (Eq. (3)):

$$n(t) = \frac{n(0)}{1 + n(0) \cdot B \cdot \int_0^t \mu(t) \cdot \mathrm{d}t}. \tag{8}$$

The results are exhibited in Fig. 4. It is visible that accurate fits are achieved for all PCBM concentrations with value of B comprised between 3 and 9×10^{-7} V cm that is very close to the theoretical value of $B = 6 \times 10^{-7}$ V cm. This allows us to conclude that in all cases investigated here, the nature of the bimolecular recombination kinetic is very close to being Langevin. This conclusion is consistent with the fact that the product $\mu \times \tau_B$ is constant for all PCBM concentrations. Indeed, surprisingly the $n(0)$ obtained by fitting the data in Fig. 2b are found to be all very close, comprised between 3 and 8×10^{15} cm^{-3}. Thus the variation of τ_B versus PCBM concentration appears to be directly related to the variation of the mobility (Eq. (7)), since $n(0)$ can be considered as almost constant.

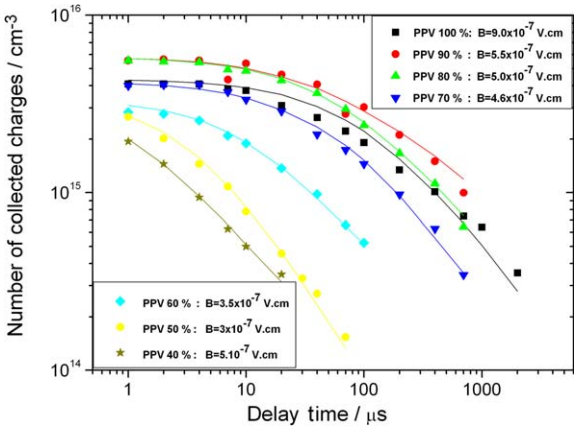

Fig. 4. Number of extracted charge carriers versus delay time measured for different MDMO-PPV:PCBM ratios and fitted with Eq. (8). The values of B used in the fits are indicated for each PCBM concentration. The values of the mobility used in Eq. (8) have been numerically integrated from Fig. 2a.

Finally, the intriguing point of the constancy of $n(0)$ versus PCBM concentration has to be addressed. As mentioned above, it is of common knowledge that the short circuit current of a MDMO-PPV:PCBM based solar cell is drastically dependent on the PCBM content in the blend. Contrarily to one's expectation, Fig. 2b shows that the number of charge carriers collected during photo-CELIV experiments does not obviously increase with PCBM concentration, but rather fluctuates within a factor 3. A rough estimation of the quantum efficiency yields values by orders of magnitude lower than that of a device in operation. This low efficiency might arise from the fact that the device is investigated in a bimolecular mode and that the light intensity used is important: according to Eq. (5), the number of extractable charges does saturate. Lower light intensities would yield higher quantum efficiencies. Moreover, Montanari et al. [14] have shown that charge carrier decay studied by TAS can be separated into two distinguished phases. The fist one, $\leqslant$20 ns, is light intensity dependent while the second one, extending to the ms range was found to be light intensity independent above a certain threshold. This second decay regime exhibited a power law type behavior OD $\sim t^{\alpha}$, where OD is the optical density of the device at a certain wavelength, and α equals 0.4 in the case of MDMO-PPV:PCBM blends, independently of the PCBM concentration. This phenomenon was explained by diffusion controlled recombination kinetic combined with the presence of a mobility edge in the PPV derivative [24]: when the number of charge carriers photo-created exceeds the number of available localized states evaluated about 10^{17} cm^{-3} in MDMO-PPV phase, charge carrier located above the MDMO-PPV mobility edge can diffuse faster, and therefore recombine faster ($\leqslant$20 ns). Contrarily to TAS data, the transient decays measured by photo-CELIV do not follow a power law, and do depend on the PCBM concentration. Moreover, $n(0)$ was found to fluctuate around 5×10^{15} cm^{-3}, that is abound 20 times less than the number of localized states available in MDMO-PPV, as proposed by Nelson. These differences might come from the different nature of the charge carriers probed by the two techniques: TAS is sensitive to optically active carriers, while photo-CELIV detects mobile charges able to contribute to an electrical current. However, the time scale investigated by photo-CELIV does correspond to the second decay phase described by Nelson [24] what might explain

why $n(0)$ does not vary with PCBM concentration. This leads us to the conclusion that, though photo-CELIV transients allow us to investigate the transport and recombination kinetics of long lived charges, it does not give access to the very fast (ns range) phenomena, which might be relevant for the understanding of the device operation.

4. Conclusion

In conclusion, we have studied the transient mobility, charge carrier recombination kinetic (in the μs range) and charge carrier lifetime in MDMO-PPV:PCBM blends by photo-CELIV. We have observed that the charge carrier mobility increases by two orders of magnitude with increasing PCBM concentration, while the "effective" bimolecular lifetime of charge carriers decreases drastically, as theoretically proposed by Mihailetchi et al. Hence, the product mobility × lifetime of long lived charge carriers is found to be independent of the PCBM concentration. This effect is believed to be induced by Langevin type bimolecular recombination, found to control the recombination kinetics for all PCBM concentrations studied. Moreover, the dispersive character of the photo-CELIV transient and of the recombination kinetics is found to decrease with increasing PCBM concentration.

Acknowledgements

The authors gratefully acknowledge the financial support of the Austrian Foundation for the Advancement of Science (FWF NANORAC Contract No: FWF-N00103000). They thank H. Neugebauer and C. Lungenschmied for fruitful discussions.

References

[1] C.J. Brabec, V. Dyakonov, J. Parisi, N.S. Sariciftci (Eds.), Organic Photovoltaics: Concepts and Realization, Springer, 2003.
[2] C.J. Brabec, Sol. Energy Mater. Sol. Cells 83 (2004) 273.
[3] H. Lee, G. Yu, D. Moses, K. Pakbaz, C. Zhang, N.S. Sariciftci, A.J. Heeger, F. Wudl, Phys. Rev. B 48 (1993) 15425.
[4] G. Yu, J. Gao, J.C. Hummelen, F. Wudl, A.J. Heeger, Science 270 (1995) 1789.
[5] J. Gao, F. Hide, H. Wang, Synth. Met. 84 (1997) 979.
[6] D. Chirvase, J. Parisi, J.C. Hummelen, V. Dyakonov, Nanotechnology 15 (2004) 1317.
[7] J.K.J. Van Duren, X. Yang, J. Loos, C.W.T. Bulle-Lieuwma, A.B. Sieval, J.C. Hummelen, R.A.J. Janssen, Adv. Funct. Mater. 14 (2004) 425.
[8] H. Hoppe, M. Niggemann, C. Winder, J. Kraut, R. Hiesgen, A. Hinsch, D. Meissner, N.S. Sariciftci, Adv. Funct. Mater. 14 (2004) 1005.
[9] V.D. Mihailetchi, L.J.A. Koster, P.W.M. Blom, C. Melzer, B. De Boer, J.K.J. Van Duren, R.A.J. Janssen, Adv. Funct. Mater. 15 (2005) 795.
[10] W. Geens, T. Martens, J. Poortmans, T. Aernouts, J. Manca, L. Lutsen, P. Heremans, S. Borghs, R. Mertens, D. Vanderzande, Thin Solid Films 451–452 (2004) 498.
[11] R. Pacios, D.D.C. Bradley, J. Nelson, C.J. Brabec, Synth. Met. 137 (2003) 1469.
[12] P. Schilinsky, C. Waldauf, J. Hauch, C.J. Brabec, J. Appl. Phys. 95 (2004) 2816.
[13] L.J.A. Koster, E.C.P. Smits, V.D. Mihailetchi, P.W.M. Blom, Phys. Rev. B 72 (2005) 085205.
[14] I. Montanari, A.F. Nogueira, J. Nelson, J. Durrant, C. Winder, M.A. Loi, N.S. Sariciftci, C.J. Brabec, Appl. Phys. Lett. 81 (2002) 3001.
[15] G. Juška, K. Arlauskas, M. Viliūnas, J. Kočka, Phys. Rev. Lett. 84 (2000) 4946.
[16] R. Österbacka, A. Pivrikas, G. Juška, K. Genevičius, K. Arlauskas, H. Stubb, Curr. Appl. Phys. 4 (2004) 534.
[17] A.J. Mozer, N.S. Sariciftci, L. Lutsen, D. Vanderzande, R. Österbacka, M. Westerling, G. Juška, Appl. Phys. Lett. 86 (2005) 112104.
[18] G. Juska, N. Nekrasas, K. Genevicius, J. Stuchlik, J. Kocka, Thin Solid Films 451–452 (2004) 290.
[19] R. Pacios, J. Nelson, D.D.C. Bradley, C.J. Brabec, Appl. Phys. Lett. 83 (2003) 4764.
[20] A.J. Mozer, G. Dennler, N.S. Sariciftci, M. Westerling, A. Pivrikas, R. Österbacka, G. Juska, Phys. Rev. B 72 (2005) 035217.
[21] H.H.P. Gommans, K. Kemerink, J.M. Kramer, R.A.J. Janssen, Appl. Phys. Lett. 87 (2005) 122104.
[22] P.W.M. Blom, M.J.M. De Jong, S. Breedijk, App. Phys. Lett. 71 (1997) 930.
[23] P. Langevin, Ann. Chem. Phys. 28 (1903) 289.
[24] J. Nelson, Phys. Rev. B 67 (2003) 155209.

Available online at www.sciencedirect.com
SCIENCE DIRECT
Organic Electronics 7 (2006) 235–242
Organic Electronics
www.elsevier.com/locate/orgel

Charge formation and transport in bulk-heterojunction solar cells based on alternating polyfluorene copolymers blended with fullerenes

Kim G. Jespersen [a], Fengling Zhang [b,*], Abay Gadisa [b], Villy Sundström [a], Arkady Yartsev [a], Olle Inganäs [b]

[a] *Chemical Physics, Kemicentrum, Getingevägen 60, SE-22100 Lund, Sweden*
[b] *Biomolecular and Organic Electronics, Center of Organic Electronics, Linköping University, SE-58183 Linköping, Sweden*

Received 27 December 2005; received in revised form 1 March 2006; accepted 3 March 2006
Available online 4 April 2006

Abstract

We investigate charge formation in bulk-heterojunction solar cells based on conjugated polymers in the form of alternating polyfluorene copolymers and the methanofullerene PCBM. Using transient absorption spectroscopy we show that optimal charge formation is obtained with 20–50 wt% PCBM. This is in contrast to the maximum short circuit current density obtained at ~80 wt% PCBM as determined by steady state current density–voltage characterization. Hence, we show explicitly that the solar cell performance of these interpenetrating polymer networks containing PCBM is limited by charge transport rather than by formation of charges.

PACS: 73.50.Pz; 73.61.ph; 78.47.+p

Keywords: Transient absorption spectroscopy; Charge transport; Bulk-heterojunction solar cells

1. Introduction

The conversion of solar energy into electrical energy using thin films of photovoltaic plastic has showed great potential as a renewable energy source [1]. Typical polymeric solar cells are based on interpenetrating polymer networks in which a photosensitive hole-conducting polymer is combined with an electron-conducting acceptor moiety [2,3]. The two co-continuous phases create a bulk-heterojunction in which photoinduced charge separation is highly efficient and where charge transport can take place. A common electron-conducting acceptor is the soluble methanofullerene derivative [6,6]-phenyl-C_{61}-butyric acid methyl ester (PCBM) [4]. The forward electron transfer from polymer to PCBM is very fast [5] (~45 fs as measured by Brabec et al. [6]), and generates a metastable charge separated state with μs lifetime. The electron mobility of neat PCBM is reported to be 2×10^{-3} cm^2/V s [7], while that of

* Corresponding author. Tel.: +46 13 281257; fax: +46 13 288969.
E-mail address: fenzh@ifm.liu.se (F. Zhang).

1566-1199/$ - see front matter © 2006 Elsevier B.V. All rights reserved.
doi:10.1016/j.orgel.2006.03.001

the conjugated polymer is typically an order of magnitude lower. In bulk-heterojunctions these values have a complex dependency on the relative PCBM concentration and the morphology of the polymer–fullerene blend, i.e. the degree of phase separation and percolation (see e.g. Ref [8]). Several groups have reported power conversion efficiencies (PCE) exceeding 2.5% under AM 1.5 solar illumination [9–11]. An interesting common denominator in these bulk-heterojunction solar cells is a rather high concentration of PCBM. Typically, the ratio of polymer to PCBM is 1:4 by weight for optimal PCE. This is observed in PPV derivatives [9,12] as well as in polyfluorene [13,14] and polythiophene [10] derivatives. In general, the highest PCE is a compromise between charge formation and the electron and hole transport in the two compounds. Both charge formation and charge transport are assumed to be strongly influenced by the morphology of the blend. In previous photocurrent experiments [8] and device modelling [15] it has been suggested that the efficiency is mostly limited by charge transport.

Recent publications on bulk-heterojunction solar cells based on P3HT:PCBM have shown that the PCE can be increased up to 5% by annealing. Somewhat surprisingly the highest PCE was achieved with relatively low PCBM concentrations of 0.8:1 [16,17] and 1:1 [18]. These results indicate that an improvement of the transport properties by annealing in P3HT:PCBM leads to an optimal PCBM concentration that is significantly reduced as compared to those reported in the past.

Here, we address the relative importance of charge formation and charge transport for the overall performance of a polymer–fullerene bulk-heterojunction. Using femtosecond time-resolved spectroscopy and steady state photocurrent measurements, we show explicitly that a high concentration of PCBM is not favorable in terms of the number of charges generated, and we give an estimate for the optimal PCBM concentration in bulk-heterojunctions based on alternating polyfluorene copolymers.

2. Experimental

The experiments are based on the alternating polyfluorene copolymer poly(2,7-(9-di-octyl-fluorene)-*alt*-5,5-(4′,7′-di-2-thienyl-2′,1′,3′-benzothiadiazole)) (APFO3) [19] in combination with PCBM (see repeat unit of APFO3 and molecular structure of PCBM in the inset of Fig. 1). The APFO3 copolymer belongs to a new generation of low-bandgap conjugated polymers with improved overlap between the absorption spectrum and the solar radiation spectrum [14,20]. For a detailed study of APFO3, see Ref. [21]. Samples for optical characterization, with APFO3:PCBM weight ratios 1:0, 4:1, 1:1 and 1:4 were fabricated by spin coating on glass substrates from chloroform solutions. The samples were subsequently sealed to prevent photo degradation. After the experiments, the samples were opened and the film thickness was determined using a standard profilometer. For electrical characterization, the samples were spin-coated onto ITO substrates and an Al electrode was evaporated (for details see Ref. [20]). For transport measurements, hole-only diodes were constructed by sandwiching the active layer between ITO/PEDOT:PSS and palladium (Pd) electrodes. Transport parameters are extracted from space charge limited current–voltage characteristics of the hole only diodes, which is measured under dark condition. Measurement and transport description details can be found in Ref. [22]. In Fig. 1 the absorption spectra of neat APFO3, PCBM and the APFO3:PCBM weight ratio 4:1, 1:1 and 1:4 are plotted. The absorbance is linearly scaled to a film thickness of 100 nm for comparison. This simple scaling approach is observed to be valid for the different blend ratios and thickness used in this work. The strong absorption below 400 nm in the 1:4 sample is dominated by PCBM absorption, while the region

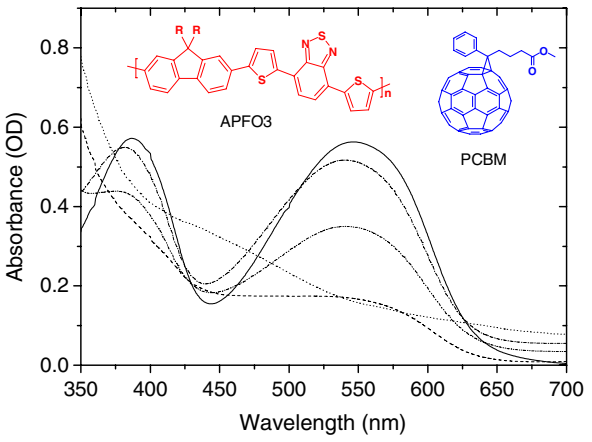

Fig. 1. Absorption spectrum of neat APFO3 (solid), PCBM (dot), APFO3:PCBM in the weight ratio 4:1 (dash dot), 1:1 (dash dot dot) and 1:4 (dash). Inset shows the APFO3 repeat unit ($R = C_8H_{17}$ indicating 'octyl' side-groups) and the PCBM molecular structure.

above 500 nm is predominant absorption by APFO3.

Time-resolved absorption experiments were performed using a transient absorption spectrometer with 120 fs pulses. The experimental setup was based on a commercial 1 kHz Clark MXR CPA-2001 femtosecond laser pumping two non-colinear optical parametric amplifiers (NOPA) for generation of single color pump pulses and a broad probe continuum. The excitation wavelength was 570 nm corresponding to the red tail of the lowest absorption band of APFO3. The probe continuum covered the spectral region from 550 nm to 750 nm. The pump pulse was polarized at magic angle to the probe polarization. To have approximately linear optical excitation and thereby minimize the influence of bimolecular annihilation we limited the pump intensity to $\sim 10^{14}$ ph/cm^2/pulse.

Steady state photocurrent measurements were performed under low intensity monochromatic light illumination from a halogen lamp passing through a monochromator with the intensity of 0.2 mW/cm^2. The wavelength chosen to illuminate the diodes was the same as for the excitation pulse in the time-resolved absorption experiments. The current density–voltage measurements were carried out by applying negative potential on the Al electrode and positive potential on the ITO electrode. Photocurrent was measured using a Keithley 485 picoammeter. All fabrications and characterizations were performed in an ambient environment without protective atmosphere.

3. Results and discussion

3.1. Charge generation

In Fig. 2 the transient absorption spectra of APFO3:PCBM are shown for different concentration ratios. Here the raw data have been scaled to a 100 nm thick film for direct comparison of the spectra. The explicit scaling factor is given by the ratio between the number of absorbed photons in the measured film and in a corresponding film of 100 nm thickness, and is given by $(1–10^{-A^{\text{scaled}}})/(1–10^{-A})$, where A is the transient absorption of the film at the excitation wavelength, and $A^{\text{scaled}} = A \times 100\ \text{nm}/d$ is the transient absorption at the excitation wavelength for a corresponding 100 nm thick film (d is the thickness of the measured film in nm). We show the spectra at 0.5 ps and 466 ps pump–probe delay. The upper panel shows the spectra of

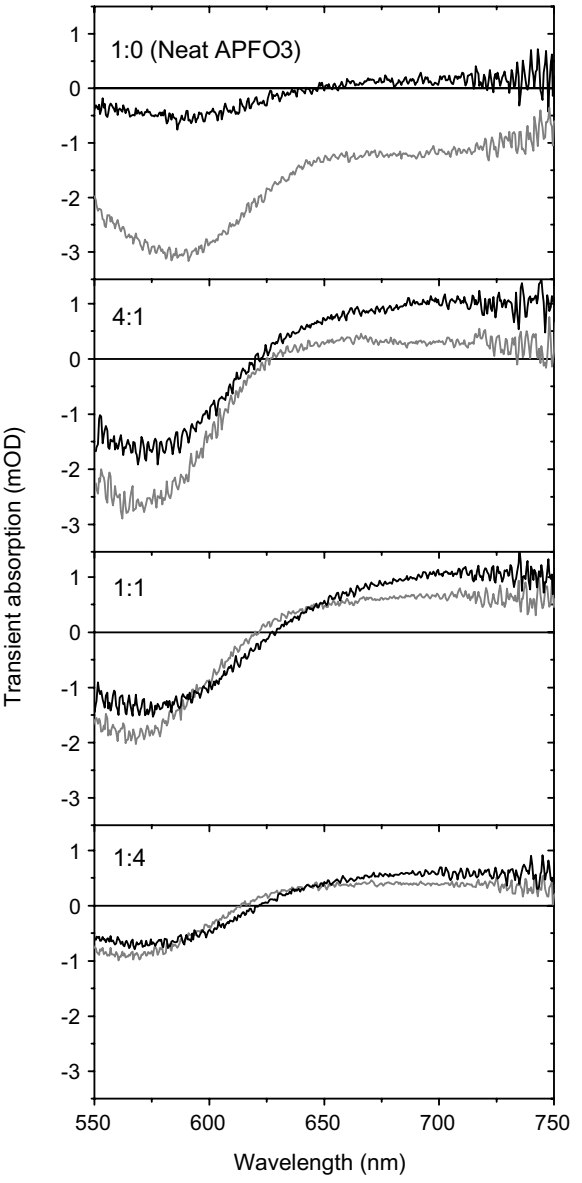

Fig. 2. Transient absorption spectra of APFO3:PCBM 1:0, 4:1, 1:1, and 1:4. The spectra are scaled to 100 nm film thicknesses. Gray is at 0.5 ps; black is 466 ps.

neat APFO3 (1:0). Initially, the spectral features are due to stimulated emission (SE) (centered at 700 nm) and photobleaching (PB) (centered at 580 nm). The excited state dynamics is found to be non-exponential by fluorescence lifetime measurements (data not shown), and can be approximated by three decay components, where the major contribution decays within 100 ps. Hence, at 466 ps the excited state population is heavily reduced, such that there is only a negligible SE contribution to

the transient spectrum, and what is left is a long-lived residual signal in the form of photoinduced absorption (PA) together with a partly recovered PB. When increasing the PCBM concentration (the three lower panels), the amplitude of the long-lived feature increases and a faster quenching of the excited state is observed, which is correlated with a faster formation of the long-lived PA feature. This is seen in the early time spectra, in the 4:1 sample (second panel), the 0.5 ps spectrum indicates a contribution from SE decay and PA formation at 700 nm, while for the 1:1 and 1:4 samples (third and fourth panels), the 0.5 ps spectra are very similar to the long time spectra indicating that the major part of the excited state is quenched within 0.5 ps. The amplitude of the initial bleach for all PCBM concentrations is approximately proportional to the number of absorbed photons in the APFO3 compound. At the excitation wavelength used in the experiments, the total absorbance is primarily a result of absorption in APFO3 molecules. The long-lived PA signal is considered to be due to absorption from the polymer cation in the case of the bulk-heterojunction, since PCBM is known to be an effective electron scavenger. In neat copolymer we believe that the long-lived PA signal is due to charge-separated species. This is corroborated by the fact that the PA signal is located at the same spectral position as in the APFO3:PCBM blends. Moreover, long-lived PA signals in the visible spectrum have been assigned to charge separated species in other conjugated polymers (see e.g. Ref. [23]). In the following we shall assume a linear correlation between the long-lived PA amplitude and the number of generated charges in the case of APFO3:PCBM and the number of charge-separated species in the case of neat APFO3. This is valid since we do not observe any significant spectral shifts that could result in signal amplitude 'moving' out of the detection window of the spectrometer.

In order to compare charge formation in samples with different PCBM concentrations, we have extracted (1) the efficiency of charge formation and (2) the relative number of generated charges from the amplitude of the long-lived PA. The charge formation efficiency (1) is defined by the number of generated charges per absorbed photon in APFO3 and is calculated from the raw data by dividing the long-lived PA amplitude at 700 nm by the number of absorbed photons at the excitation wavelength. We note that the reflectivity is approximately the same for samples of blend ratios 1:0, 1:4, and 0:1

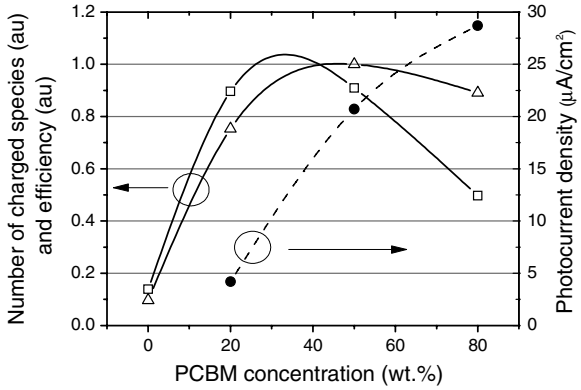

Fig. 3. Number of charged species generated (□), charge formation efficiency (△), and the short circuit current density J_{SC} (●; dash). The data points are connected via an arbitrary function.

at 570 nm, such that we may ignore deviations in reflection loss for samples with different blend ratios. The charge formation efficiency is plotted in Fig. 3 (–△–). It indicates that maximum efficiency is obtained at a PCBM concentration close to 50 wt%. The relative number of generated charges (2) in films of equal thickness is obtained from the raw data by scaling the thickness to 100 nm as described above (see spectra in Fig. 2). Thus, the relative number of charges formed in films of equal thickness is given directly by the long-lived PA amplitude at 700 nm. We note that the relative number of charges can be considered as an overall efficiency that treats the sample as a whole including glass substrate and active polymer. From Fig. 2 it is seen that the low PCBM concentration (4:1) leads to a final PA amplitude close to that of the 1:1 sample and clearly larger than the amplitude found in the 1:4 sample. Hence, the total number of charges generated is higher for samples 4:1 and 1:1 as compared to the sample with the APFO3:PCBM weight ratio 1:4. This interesting observation is also shown in Fig. 3, where the amplitude (at 700 nm) of the long-lived PA due to charges in samples of 100 nm thickness is mapped against PCBM concentration (–□–). The solid line connecting the data points is chosen arbitrarily, however, the maximum number of generated charges is expected to lie in the range 20–50 wt%. The reason for this is that a significant 'loss' in the form of photoluminescence is observed at 20 wt% PCBM, while photoluminescence is effectively quenched at 50 wt% PCBM (data not shown). Furthermore, the charge formation efficiency curve in Fig. 3 (–△–) indicates that photoinduced charge

separation is more efficient at 50 wt% than at 20 wt%. Hence, we expect the maximum number of charges to occur above 20 wt% PCBM.

3.2. Photocurrent collected in the devices

In general, the optimal PCBM concentration for best solar cell performance should be seen as a compromise between the number of charge carriers generated in the polymer blend and the number of PCBM molecules required to facilitate efficient charge transport. Steady state photocurrent measurements show that the best performance of APFO3:PCBM solar cell devices was achieved in the ratio of 1:4, which is in sharp contrast to the results on photogeneration presented above. Photocurrent collected in the devices is mainly determined by three processes: photon absorption, exciton dissociation or charge generation, and charge carrier collection.

We measured the photocurrent collected in devices with different blend ratios as a function of film thickness. The diodes were characterized under monochromatic light at 570 nm, which is the same wavelength as the excitation pulse in the time-resolved absorption experiments. In Fig. 4 the short circuit current density (J_{sc}) of APFO3:PCBM samples with composition ratios 4:1, 1:1, and 1:4 are displayed. The diodes with the ratios 4:1, 1:1, and 1:4 present very different behaviors. It shows that the J_{sc} of the diodes with the ratio 4:1 and 1:1 decreases with increasing thickness, which indicates that the transport property of the active-layer limits the J_{sc}. Oppositely, it seems that the J_{sc} of the diodes with the ratio 1:4 increases with increasing thickness up to 255 nm, and thereafter decreases with the thickness. The fact that J_{sc} has a maximum implies that absorption limits J_{sc} at thinner active layers, and transport becomes a limitation for J_{sc} at thicker layers.

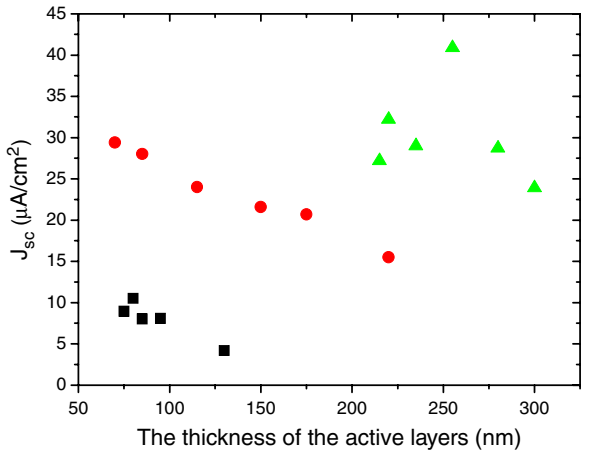

Fig. 4. The J_{sc} of APFO3:PCBM solar cells vs the thickness of the active layers under monochromatic illumination(570 nm, 0.2 mW/cm^2), where the square symbols are for the diodes with ratio of 4:1, circles for 1:1 and up-triangles for 1:4.

In order to make a comparison between the charge generation results of the previous section and the photocurrent density measurements presented above it must be taken into account that the samples used in the electrical characterization vary in thickness. That is, we consider the samples with ratio 4:1, 1:1, and 1:4 having thickness 130–160 nm, 150–170 nm, and 250–300 nm, respectively. This could make a comparison with the charge generation results difficult. However, the absorption spectra of the films with these varied thicknesses all present comparable absorption at 570 nm (the wavelength used in the time-resolved absorption experiments) as seen in Fig. 5. Thus, a similar number of photons are absorbed by these specific films of different PCBM concentrations.

If we compare the J_{sc} of those diodes (Fig. 4) with similar absorption in Fig. 5, it is clear that the diode of blend ratio 4:1 (130 nm) presents much lower J_{sc} (~4 μA/cm^2) than the diode 1:1 (175 nm) (~21 μA/cm^2), and 1:4 (280 nm) (~29 μA/cm^2). The current density is displayed in Fig. 3 for visual comparison. It is seen that J_{sc} increases monotonically up to 80 wt% PCBM. Moreover, optimization of the solar cell performance indicates that the highest current density is indeed found at a ratio close to 1:4, in good agreement with previous results on solar cells based on other conjugated polymers

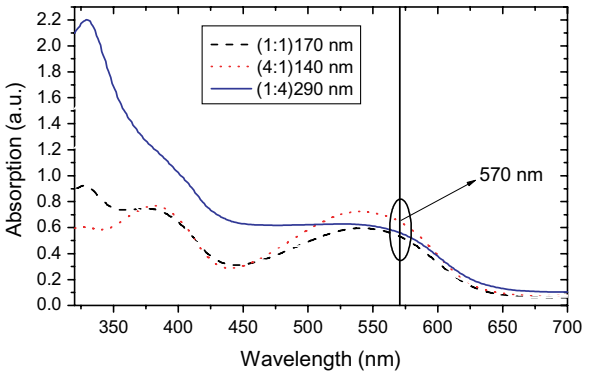

Fig. 5. Absorption spectra of APFO3:PCBM in the 'solar cell' with the ratio of 4:1 (dot line), 1:1 (dash line), and 1:4 (solid line).

and PCBM. This is significantly different to the results on charge generation. A notable point is that the small deviations in optical density for the specific films as seen in Fig. 5 are insufficient to account for this difference.

The photocurrent peaks at higher PCBM concentrations as compared to charge generation. Therefore, the fact that we observe a maximum charge formation efficiency at ~50 wt% and a maximum number of charged species at 20–50 wt% PCBM, while the short circuit current density peaks at ~80 wt% argues that the solar cell performance of APFO3:PCBM is limited by charge transport rather than by charge formation.

3.3. Transport properties of the devices

To understand the different results between charge generation and photocurrent of the devices, we need to take into account charge transport in the active layer because the photocurrent collected in the devices not only depends on the charge generation, but also the charge transport, that is, the mobility. Charge transport properties in bulk-heterojunction solar cells are very sensitive to the morphology of the active layer [17,18]. Björström et al investigated the morphologies of the films with same composition, but different stoichiometries (1:0, 1:1, 1:2, 1:3, and 1:4) using atomic force microscopy [24,25]. AFM images presented little evidence for phase separation in all blends. There were no pronounced differences among those films with different PCBM loadings. Fig. 6 presents the fill factors (FFs) of the same devices with the section above. It is obvious that the FFs of the diodes show monotonic increase with increasing PCBM concentration, irrespective of thickness. The FF of diodes 4:1 is between 0.23 and 0.27, for diode 1:1 it is 0.34 to 0.44, and for diode 1:4 it is 0.63 and 0.72. This strongly suggests that the transport properties are improved when adding more PCBM. Therefore, the transport property in the devices may be responsible for the deviation of photocurrent and charge generation.

It is tempting to assign this limiting process to electron transport in the PCBM phase since one could imagine that a high concentration of PCBM is required to facilitate efficient electron hopping. However, it has been reported that not only does electron mobility depend on PCBM concentration but also hole mobility seems to be increasing with PCBM concentration [26]. Tuladhar et al. found that PCBM can support ambipolar transport, which can

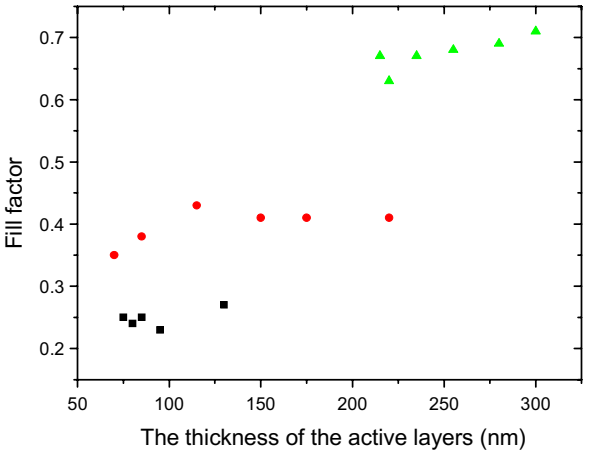

Fig. 6. The FFs of APFO3:PCBM solar cells vs the thickness of the active layers under monochromatic illumination(570 nm, 0.2 mW/cm^2), where the squares symbols are for the diodes with ratio of 4:1, circles for 1:1 and up-triangles for 1:4.

explain the relative high PCBM to polymer ratio needed in previous studies [27]. This is in very good, keeping with the results on annealed P3HT:PCBM mentioned in the introduction. Annealing of the P3HT:PCBM blend results in self-organization [18,28] creating domains of crystalline polymer phase with high hole mobility. This reduces the role of PCBM in hole transport in the annealed blend and makes it possible to approach a lower and more favorable PCBM concentration for the solar cell performance. In this study we have measured the optimal PCBM contents to be 20–50 wt% for the APFO3:PCBM bulk-heterojunction using femtosecond transient absorption spectroscopy, which is in very good agreement with the optimal ratio of 1:0.8 (44 wt% PCBM) and 1:1 (50 wt% PCBM) found in the annealed P3HT:PCBM solar cells.

In order to understand the influence of PCBM on transport, we have investigated hole transport in blend APFO3:PCBM films with weight ratio of 1:1, 1:3, 1:4, and 1:5, using the space charge limited current–voltage characteristics of hole only diodes. The variation of hole mobility with acceptor concentration is depicted in Fig. 7. The hole mobility is enhanced as a consequence of varying PCBM concentration from 50 to 83 wt.%. This confirms that the large amount of PCBM content in polymer-based solar cells results into facilitating charge transport while charge generation is already complete at a small PCBM concentration. The influence of PCBM loading on hole mobility was also observed in field effect transistors (FET) based on the same blends [29].

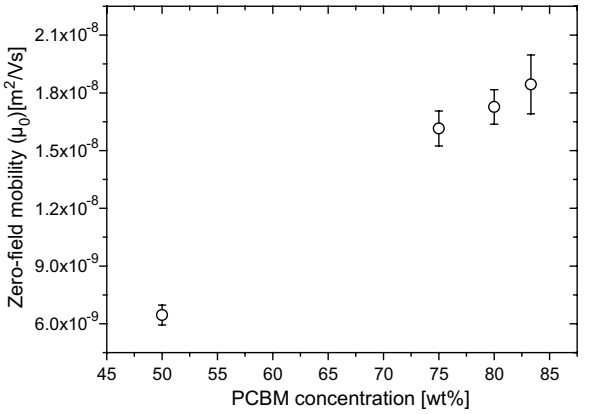

Fig. 7. Hole mobility as a function of PCBM concentration.

The above discussion suggests more precisely that hole transport in the polymer phase is the performance limiting process. It is well known that the electron mobility of PCBM is 1–2 orders of magnitude larger than the hole mobility in most polymers, which means that the bottleneck for charge transport is hole mobility in polymer. The hole mobility increase when adding more PCBM, which also means the better balance between hole and electron transport. This is consistent with our observation from solar cells and also supported by Rappaport et al. [30] who calculated that in order to obtain an ideal fill factor the hole mobility in the polymer phase should increase by two orders of magnitude compared to previous non-annealed solar cells. In our work we find that the fill factor is very sensitive to the PCBM concentration; the more PCBM, the larger FF.

The transport limited performance in APFO3:PCBM blends suggests that the power conversion efficiency in APFO3:PCBM solar cells could be increased if proper material processing leads to a high hole mobility. Polyfluorenes are known to have liquid crystalline phases with an enhanced hole mobility [31]. If this phase can be obtained, either by thermal treatment or by other means of processing, it would result in an increase in the solar cell performance of APFO3:PCBM. A high PCE solar cell based on polyfluorene copolymers is attractive since polyfluorenes are relatively stable against photochemical degradation, compared to other conjugated polymers.

4. Conclusion

In conclusion we have used time-resolved spectroscopy to show that charge formation in APFO3:PCBM bulk-heterojunctions is optimal at 20–50 wt% PCBM concentration. On the other hand, we found that J_{sc} is monotonically increasing up to 80 wt% PCBM. This proves that charge formation is not the performance limiting process. On the contrary, the results show that a high PCBM concentration is a requirement for maximum short circuit current density and that charge transport is limiting the performance of the investigated bulk-heterojunction solar cell. The results indicate that the high PCBM concentration needed in the best performing APFO3:PCBM solar cells enhances the effective hole transport in the blend. The solar cell performance of the APFO3:PCBM blend is likely to be increased by improving the hole transport in the polymer phase.

Acknowledgements

We thank Prof. Mats Andersson for providing the APFO3 copolymer, Dr. Nils-Krister Persson for valuable discussions. Financial support is acknowledged from the Center of Organic Electronics financed by the Swedish Strategic Research Foundation and the Swedish Research Council.

References

[1] P. Fairley, Technol. Rev. 107 (2004) 34.
[2] J.M. Halls, C.A. Walsh, N.C. Greenham, E.A. Marseglia, R.H. Friend, S.C. Moratti, A.B. Holmes, Nature 376 (1995) 498.
[3] G. Yu, J. Gao, J.C. Hummelen, F. Wudl, A.J. Heeger, Science 270 (1995) 1789.
[4] J.C. Hummelen, B.W. Knight, F. Lepeq, F. Wudl, J. Yao, C.L. Wilkins, J. Org. Chem. 60 (1995) 532.
[5] Q.H. Xu, D. Moses, A.J. Heeger, Phys. Rev. B 67 (2003) 245417.
[6] C.J. Brabec, G. Zerza, G. Cerullo, S. De Silvestri, S. Luzzati, J.C. Hummelen, N.S. Sariciftci, Chem. Phys. Lett. 340 (2001) 232.
[7] V.D. Mihailetchi, J.K.J. van Duren, P.W.M. Blom, J.C. Hummelen, R.A.J. Janssen, J.M. Kroon, M.T. Rispens, W.J.H. Verhees, M.M. Wienk, Adv. Funct. Mater. 13 (2003) 43.
[8] S.A. Choulis, J. Nelson, Y. Kim, D. Poplavskyy, T. Kreouzis, J.R. Durrant, D.D.C. Bradley, Appl. Phys. Lett. 83 (2003) 3812.
[9] S.E. Shaheen, C.J. Brabec, N.S. Sariciftci, F. Padinger, T. Fromherz, J.C. Hummelen, Appl. Phys. Lett. 78 (2001) 841.
[10] F. Padinger, R.S. Rittberger, N.S. Sariciftci, Adv. Funct. Mater. 13 (2003) 85.
[11] C.J. Brabec, A. Cravino, G. Zerza, N.S. Sariciftci, R. Kiebooms, D. Vanderzande, J.C. Hummelen, J. Phys. Chem. B 105 (2001) 1528.

[12] F.L. Zhang, M. Johansson, M.R. Andersson, J.C. Hummelen, O. Inganäs, Synth. Met. 137 (2003) 1401.
[13] R. Pacios, D.C. Bradley, J. Nelson, C.J. Brabec, Synth. Met. 137 (2003) 1469.
[14] O. Inganäs, M. Svensson, F. Zhang, A. Gadisa, N.K. Persson, X. Wang, M.R. Andersson, Appl. Phys. A–Mater. 79 (2004) 31.
[15] S. Lacic, O. Inganäs, J. Appl. Phys. 97 (2005) 124901.
[16] M. Reyes-Reyes, K. Kim, D.L. Carroll, Appl. Phys. Lett. 87 (2005) 083506.
[17] W.L. Ma, C.Y. Yang, X. Gong, K. Lee, A.J. Heeger, Adv. Funct. Mater. 15 (2005) 1617.
[18] G. Li, V. Shrotriya, J.S. Huang, Y. Yao, T. Moriarty, K. Emery, Y. Yang, Nature Mater. 4 (2005) 864.
[19] M. Svensson, F.L. Zhang, S.C. Veenstra, W.J.H. Verhees, J.C. Hummelen, J.M. Kroon, O. Inganäs, M.R. Andersson, Adv. Mater. 15 (2003) 988.
[20] T. Yohannes, F. Zhang, M. Svensson, J.C. Hummelen, M.R. Andersson, O. Inganäs, Thin Solid Films 449 (2004) 152.
[21] K.G. Jespersen, W.J.D. Beenken, Y. Zaushitsyn, A. Yartsev, M. Andersson, T. Pullerits, V. Sundstrom, J. Chem. Phys. 121 (2004) 12613.
[22] A. Gadisa, X. Wang, S. Admassie, E. Perzon, F. Oswald, F. Langa, M.R. Andersson, O. Inganäs, Organic Electronics, in press.
[23] A. Ruseckas, M. Theander, M.R. Andersson, M. Svensson, M. Prato, O. Inganäs, V. Sundstrom, Chem. Phys. Lett. 322 (2000) 136.
[24] C.M. Björström, K.O. Magnusson, E. Moons, Synth. Met. 152 (2005) 109.
[25] O. Inganäs, F. Zhang, X. Wang, A. Gadisa, N-K. Persson, M. Svensson, E. Perzon, W. Mammo, M.R. Andersson, in: S. Sun, S. Sariciftci (Eds.), "Organic Photovoltaics: Mechanisms, Materials and Devices", CRC, 2005 (Chapter 17).
[26] C. Melzer, E.J. Koop, V.D. Mihailetchi, P.W.M. Blom, Adv. Funct. Mater. 14 (2004) 865.
[27] S.M. Tuladhar, D. Poplavskyy, S.A. Choulis, J.R. Durrant, D.D.C. Bradley, J. Nelson, Adv. Funct. Mater. 15 (2005) 1171.
[28] T. Erb, U. Zhokhavets, G. Gobsch, S. Raleva, B. Stühn, P. Schilinsky, C. Waldauf, C.J. Brabec, Adv. Funct. Mater. 15 (2005) 1193.
[29] L.M. Andersson, O. Inganäs, Acceptor influence on hole mobility in fullerene blends with alternating copolymers of fluorene, Appl. Phys. Lett. 88 (2006) 082103.
[30] N. Rappaport, O. Solomesch, N. Tessler, J. Appl. Phys. 98 (2005) 033714.
[31] M. Chen, C. Xavier, E. Perzon, M.R. Andersson, T. Pullerits, M. Andersson, O. Inganäs, M. Berggren, Appl. Phys. Lett. 87 (2005) 252105.

Available online at www.sciencedirect.com
ScienceDirect
Organic Electronics 7 (2006) 243–248
Organic Electronics
www.elsevier.com/locate/orgel

Photovoltaic cells from a soluble pentacene derivative

M.T. Lloyd [a], A.C. Mayer [a], A.S. Tayi [a], A.M. Bowen [a], T.G. Kasen [a], D.J. Herman [a], D.A. Mourey [a], J.E. Anthony [b], G.G. Malliaras [a,*]

[a] Department of Materials Science and Engineering, Cornell University, 327 Bard Hall, Ithaca, NY 14853-1501, United States
[b] Department of Chemistry, University of Kentucky, Lexington, KY 40506-0055, United States

Received 13 January 2006; accepted 3 March 2006
Available online 4 April 2006

Abstract

Multilayer heterojunction photovoltaic cells were fabricated using a solution processable pentacene derivative as the donor layer. Upon annealing of these devices, the open circuit voltage was found to gradually increase with temperature up to 265 °C. Further improvement in the photovoltaic performance was achieved with the incorporation of mobile ions into the donor material for concentrations of lithium triflate up to 1.4 mg/ml. Finally, after introducing an exciton blocking layer, an optimized white-light (100 mW/cm^2) power conversion efficiency of 0.52% was achieved.

PACS: 85.60.−q; 72.40.+w

Keywords: Organic photovoltaics; Functionalized pentacene; Pentacene derivatives; Mobile ions; Annealing

1. Introduction

Pentacene is a thoroughly characterized prototypical organic semiconductor [1] and is well suited for use as the donor material in organic photovoltaic cells [2,3]. Work has been done to further improve the already high charge carrier mobility in pentacene by making changes at the molecular level. One example is the work of Anthony et al., who functionalize pentacene with silyl groups attached to the 6, 13 positions [4]. In doing so, the side groups disrupt face-to-edge interactions of condensed phase pentacene and decrease intermolecular carbon–carbon spacing. In theory, an increase in π–π interaction will improve mobility and give rise to band-like transport [5]. Functionalization also significantly improves the solubility in common organic solvents and opens new routes to processing from solution. Already, promising results for solution processed thin film transistors have been obtained utilizing this class of materials. Bottom-contact transistors of pentacene derivatives yield mobilities of 0.17 cm^2/Vs, while anthradithiophene derivatives show mobilities as high as 1.0 cm^2/Vs [6].

The first reported use of pentacene in a solar cell was by Yoo et al., with a calculated AM1.5 efficiency of 1.5% in a double heterojunction configuration [2]. Vacuum sublimed bi-layers consisting of an

* Corresponding author. Tel.: +1 607 255 1956; fax: +1 607 255 2365.
E-mail address: ggm1@cornell.edu (G.G. Malliaras).

1566-1199/$ - see front matter © 2006 Elsevier B.V. All rights reserved.
doi:10.1016/j.orgel.2006.03.002

unsubstituted pentacene/fullerene heterojunction achieve white-light power conversion efficiencies as high as 1.07% [3]. Pentacene derivatives, in particular bis(triisopropylsilylethynyl)pentacenes (TIPS–pentacene), should be able to replace pentacene in such solar cells to yield comparable if not higher efficiencies. Via fine tuning of the molecular structure, one can tailor the oxidation and reduction potentials as well as the optical gap of acene derivatives to provide optimal overlap with the solar spectrum [7,8]. With an absorption onset of 750 nm, TIPS–pentacene absorbs approximately 50 nm further into the red than pentacene [5]. Another advantage of TIPS–pentacene stems from a highest occupied molecular orbital (HOMO) which is 280 meV lower than that of pentacene, leading to a potentially larger open circuit voltage (V_{OC}). Additionally, TIPS–pentacene is a crystal forming small molecule that retains a high charge mobility when deposited from solution.

As a first step towards all-solution processable organic solar cells from small molecules, we investigate the viability of TIPS–pentacene as the donor layer in bi- and tri-layer device configurations. We show that thermal annealing of a bi-layer device tends to enhance performance by steadily increasing the V_{OC}. X-ray diffraction scans as a function of annealing temperature point to significant structural changes taking place in TIPS–pentacene films; however, it appears that the behavior of the V_{OC} does not strongly depend upon the observed microstructural changes. We also report that mobile ions, introduced in the solution deposited layer in the form of lithium triflate (LiTF), significantly affect the shunt resistance, fill factor, and short circuit current (I_{SC}). Lastly, TIPS–pentacene/C_{60} cells are subject to thermally induced damage to the acceptor during the deposition of the cathode. As a consequence, the performance of all cells fabricated here increased with the addition of a thin bathrocuprine (BCP) buffer layer.

2. Experimental

The pentacene derivatives were prepared as reported in an earlier publication [4]. All other chemicals were purchased from commercial suppliers and used without further purification unless otherwise noted. For X-ray measurements, thin films of TIPS–pentacene were spin coated and annealed for 1 min on a hot-plate in a nitrogen environment. X-ray data were collected with both a Bruker-AXS general area detector diffraction system (GADDS) as well as a Scintag, Inc. theta–theta diffractometer with a Cu-Kα_2 source. Atomic force microscopy images were taken in tapping mode using a DI 3100 Dimension microscope.

Photovoltaic cells were fabricated on pre-patterned indium tin oxide (ITO) coated glass plates (Thin Film Devices, Anaheim, CA). The substrates were cleaned in a deionized water bath followed by a UV/O_3 treatment. Poly(3,4-ethylenedioxythiophene):poly(styrene sulfonate) (PEDOT:PSS) was filtered and spin coated onto the ITO to give a smooth, 80 nm thick film. To dry the PEDOT layer, the samples were heated to 125 °C for 1 h and allowed to cool under low vacuum overnight. Distilled toluene was added to crystals of TIPS–pentacene to form solutions of 20 mg/ml. Solutions were stirred for a minimum of 1 h and filtered (0.2 μm) immediately before forming films. When mobile ions were used, LiTF and 4-tertbutylpyridine (4TBP) were added to toluene, maintaining a fixed weight ratio of LiTF to 4TBP at 1:1.83. After spin coating a ~70 nm thick layer of TIPS–pentacene, 30 nm of C_{60} were thermally deposited at a rate of ~0.2 Å/s in a high vacuum chamber ($<10^{-6}$ Torr). Next, 11 nm of BCP were deposited at a rate (>4.0 Å/s) necessary to inhibit crystallization. A 100 nm silver cathode was deposited onto devices containing BCP, otherwise the cathode included ~1 nm CsF capped with 40 nm of aluminum. The testing apparatus consisted of a halogen lamp calibrated to 100 mW/cm^2 with a Si photodiode coupled to an integrating sphere. Current–voltage sweeps were taken with a Keithley 237 controlled with LabVIEW software. All fabrication and testing was carried out in a nitrogen environment.

3. Results and discussion

In order to better understand microstructural changes that occur during heating, we subjected crystals of TIPS–pentacene to thermal gravimetric analysis and amorphous films of TIPS–pentacene to a thermal annealing sequence. To obtain amorphous films of TIPS–pentacene, standard spin coated techniques can be used with a solvent of sufficiently low boiling point, such as toluene. During the spin coating procedure, solvent rapidly escapes from the thin film to trap molecules in a meta-stable phase. X-ray diffraction analysis in Fig. 1 confirms the absence of crystallinity in the film after spin coating. Room temperature X-ray traces of films

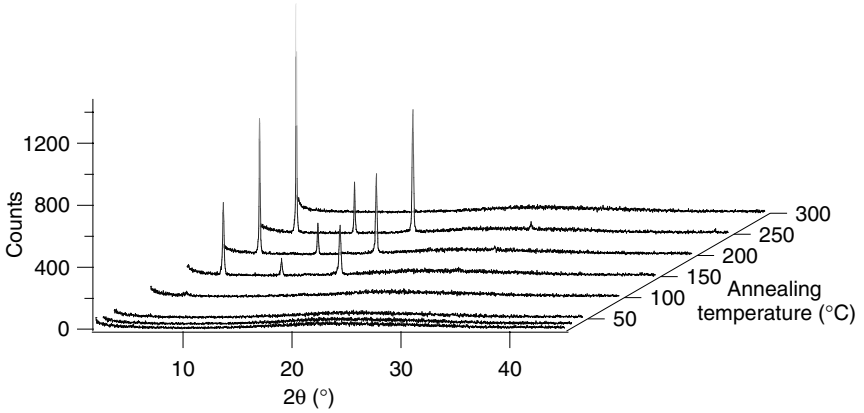

Fig. 1. X-ray diffraction from thin films of TIPS–pentacene as a function of annealing temperature.

annealed at higher temperatures show an onset of crystallization between the temperatures of 100 and 150 °C. The angular position of the X-ray peaks of the annealed crystalline films indicate a layer separation of 16.61 Å, in close agreement with 16.83 Å measured by Anthony et al. [4]. A general area detection X-ray scan (not shown) of crystallized films shows no preferential orientation of the crystallites. The intensity of diffracted X-rays increases with increasing temperature, indicating an enhancement of the crystal structure with each consecutive annealing temperature. The scan at 300 °C indicates that melting takes place between 250 and 300 °C.

Thermal annealing has been shown to significantly enhance the photovoltaic performance of organic solar cells [9,10]. Peumans et al., found that when thin organic layers are physically confined beneath a metal electrode, annealing-induced morphological changes are particularly beneficial to device performance [10]. Specifically, a 30% increase in quantum efficiency was achieved by maintaining a smooth surface topography, while permitting the formation of an interpenetrating bulk heterojunction. Mayer et al., addressed the increase in performance with annealing in pentacene photovoltaics [3]. An increase in shunt resistance and rectification ratio was attributed to the elimination of microscopic shorts, and an increase in J_{SC} was explained by an enhancement of the crystallinity of the organic films.

In an annealing sequence similar to that carried out for X-ray diffraction experiments, we measured the effect of annealing on the performance of TIPS–pentacene based photovoltaic cells. Fig. 2 shows a plot of V_{OC} and J_{SC} after annealing for a typical cell. Under white-light illumination, the V_{OC} gradually increased with annealing temperature. An increase was also observed for the J_{SC}, but to a negligible extent in comparison to the unusually large change in V_{OC}. TIPS–pentacene has an amorphous-to-crystalline and a solid-to-liquid phase transformation taking place over the temperature

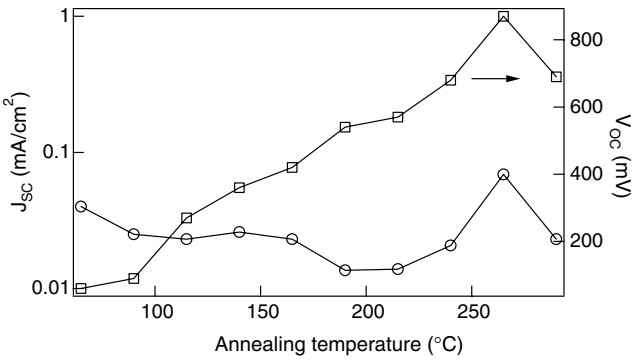

Fig. 2. Short circuit current (○) and open circuit voltage (□) vs. annealing temperature for a ITO/PEDOT:PSS/TIPS–pentacene/C_{60}/CsF/Al device.

range for which the V_{OC} was monitored. Transmission electron microscopy studies of TIPS–pentacene films reveal mesoscale cracks that appear in unconstrained films at approximately 130 °C [11]. Atomic force microscopy images of annealed films of TIPS–pentacene show a tendency for micro-crystalline domains to separate at the grain boundaries and grow normal to the substrate to reduce their surface area. Despite these abrupt changes in the microstructure of the film, we see a very smooth increase in the V_{OC} between 65 and 265 °C. One possible explanation for the smooth increase in V_{OC} is a result of two-dimensional crystalline growth due to confinement by the C_{60} layer and the aluminum cathode during annealing. This will hinder the surface roughening observed on unconfined TIPS–pentacene films, and result in crystalline, yet continuous films. Rough or discontinuous films cause the thermally evaporated electrode to form microscopic shorts. By smoothing the layers of the device, and eliminating these shorts, a large open circuit voltage can be obtained. Indeed, the open circuit voltage is shown to approach 900 mV, which is very high value for small molecule-based solar cells [12].

Mobile ions have been shown to facilitate charge injection at the electrode/organic interface [13,14]. Following previous work on hole transport materials for dye-sensitized solar cells [15,16], LiTF was dissolved in 4TBP and incorporated into the solution cast donor layer. By increasing the Li^+ concentration, Haque and colleagues found the J_{SC} increased by a factor of 10, and V_{OC} decreased by about 25% [17]. For concentrations of LiTF up to an optimum, we also found the V_{OC} to be relatively unaffected by the presence of mobile ions. As shown in Fig. 3c, we saw a slight enhancement (34%) in the

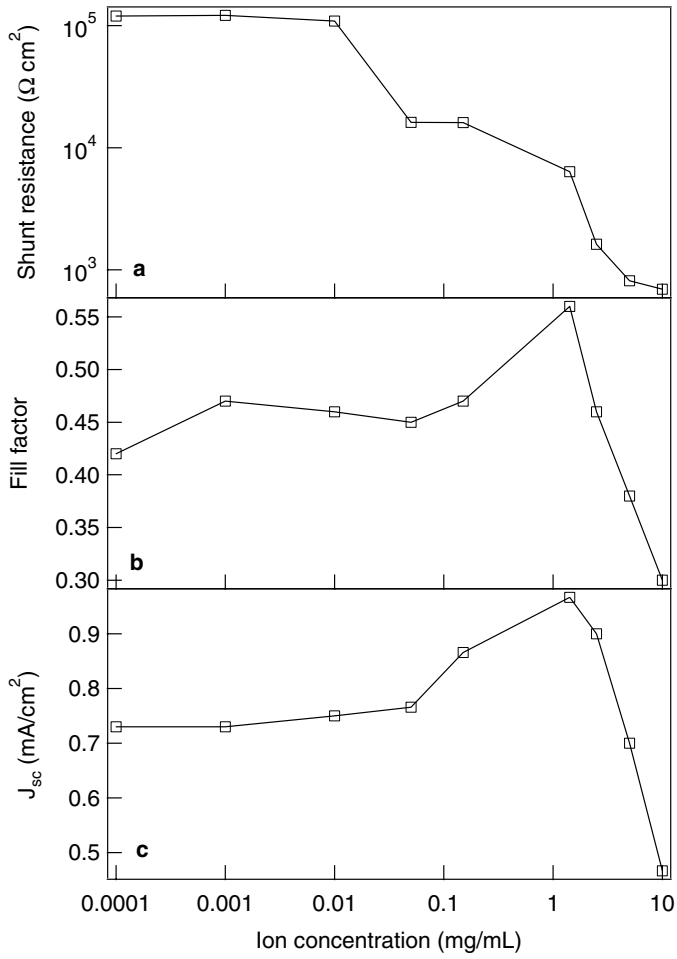

Fig. 3. Effect of LiTF concentration of the (a) shunt resistance (in the dark), (b) fill factor, and (c) short circuit current for ITO/PEDOT:PSS/TIPS–pentacene/C_{60}/BCP/Ag devices.

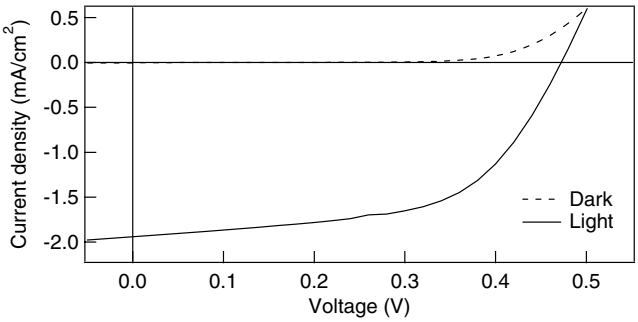

Fig. 4. Current–voltage characteristics for an optimized ITO/TIPS–pentacene/C_{60}/BCP/Ag device in the dark and under illumination by 100 mW/cm^2 halogen lamp.

short circuit current (J_{SC}), peaking at a concentration of 1.42 mg/ml. Likewise, Fig. 3b shows that the fill factor is increased by 33%. This increase in performance is consistent with enhanced exciton dissociation. In analogy to the electrodynamic model [13], the ionic charge will redistribute to minimize an applied electric field within the TIPS–pentacene layer. At short circuit conditions, the Fermi levels of the metal electrodes align to establish a built-in field that drives Li^+ ions towards the anode and the triflate ions towards the organic/organic interface. This will result in a steep electric field at the interface, which will sweep holes away from the heterojunction and will increase J_{SC} as well as the fill factor by reducing recombination [18]. At higher ion concentrations, ion conduction becomes increasing dominant as evidenced by the drop in shunt resistance (Fig. 3a).

Many vacuum sublimed solar cells see a significant increase in power conversion efficiency with in inclusion of a large bandgap exciton blocking layer (EBL). Puemans et al., used BCP to optimize the internal optical field. It is also thought that BCP prevents quenching of long lived excitons at metal interfaces, leading to a decrease in charge recombination [12]. An additional benefit of BCP is that it might fill imperfections in the underlying films and protect the active organic layers from damage induced by thermally deposited top contacts [19]. Consistent with previous work, an increase in device performance was measured with the inclusion of a 110 Å BCP layer between the C_{60} and Ag cathode. The application of BCP in TIPS–pentacene devices increased dark current rectification ratio at ±1 V from 16 to 86, and the fill factor from 0.30 to 0.42. The J_{SC} increased from 0.02 mA/cm^2 to 0.73 mA/cm^2, and the V_{OC} increased from 220 mV to 335 mV.

With an optimized LiTF concentration of 1.4 mg/ml of and a 110 Å thick BCP layer, the best cell produced a white-light power conversion efficiency of 0.52%. Unfortunately, any attempts to anneal such cells resulted in rapid degradation in efficiency due to BCP crystallization and concomitant delamination of the metal cathode. The *I–V* characteristics in Fig. 4 show a J_{SC} of 1.9 mA/cm^2, a V_{OC} of 470 mV, a fill factor of 0.52, a rectification ratio $>10^3$, and a series resistance under illumination of 16 Ω cm^2.

To continue to increase the efficiency of this system we envision an exploration of changes to the molecular structure of pentacene derivatives. It is possible to synthesize pentacene derivatives with ionization potentials greater than TIPS–pentacene [7] which should further increase V_{OC}. Similarly, the bandgap of functionalized acenes can be altered to absorb a larger portion of the solar spectrum [8]. Efforts are also underway to enhance the film-forming characteristics of crystalline films by introducing inert high molecular weight polymer binders. Additionally, blending with soluble acceptor molecules might help optimize exciton dissociation. Despite multiple attempts to form a bulk heterojunction by blending TIPS–pentacene with soluble derivates of C_{60}, such devices did not show an appreciable photovoltaic response. One possible explanation is the formation of C_{60}:TIPS–pentacene adducts with energy levels that prevent exciton separation. By sterically blocking reaction sites on the pentacene backbone, adduct formation could be eliminated.

4. Conclusions

In conclusion, we have shown that TIPS–pentacene is a promising solution processable donor material in organic heterojunction solar cells.

Thermal annealing tends to monotonically increases V_{OC} in these cells without a corresponding loss in J_{SC} up to 265 °C. With the addition of mobile ions the performance of the cells increased for LiTF concentrations up to 1.4 mg/ml. With the introduction of an exciton blocking layer, the white-light power conversion efficiency surpassed 0.5%. Through molecular level engineering of pentacene derivatives, higher efficiencies are likely in solar cells based on solution processed small molecules.

Acknowledgements

This work was made possible by funding from the Office of Naval Research. Additional thanks are due to the Cornell Center of Materials Research, as well as Christopher Umbach, Anthony Condon, and Maura Weathers for assistance with AFM, TGA, and XRD measurements.

References

[1] R. Ruiz, D. Choudhary, B. Nickel, T. Toccoli, K.C. Chang, A.C. Mayer, P. Clancy, J.M. Blakely, R.L. Headrick, S. Iannotta, G.G. Malliaras, Chemistry of Materials 16 (2004) 4497–4508.
[2] S. Yoo, B. Domercq, B. Kippelen, Applied Physics Letters 85 (2004) 5427–5429.
[3] A.C. Mayer, M.T. Lloyd, D.J. Herman, T.G. Kasen, G.G. Malliaras, Applied Physics Letters 85 (2004) 6272–6274.
[4] J.E. Anthony, J.S. Brooks, D.L. Eaton, S.R. Parkin, Journal of the American Chemical Society 123 (2001) 9482–9483.
[5] O. Ostroverkhova, D.G. Cooke, S. Shcherbyna, R.F. Egerton, F.A. Hegmann, R.R. Tykwinski, J.E. Anthony, Physical Review B 71 (2005) 035204/1-6.
[6] M.M. Payne, S.R. Parkin, J.E. Anthony, C.C. Kuo, T.N. Jackson, Journal of the American Chemical Society 127 (2005) 4986–4987.
[7] C.R. Swartz, S.R. Parkin, J.E. Bullock, J.E. Anthony, A.C. Mayer, G.G. Malliaras, Organic Letters 7 (2005) 3163–3166.
[8] M.M. Payne, S.R. Parkin, J.E. Anthony, Journal of the American Chemical Society 127 (2005) 8028–8029.
[9] G. Li, V. Shrotriya, Y. Yao, Y. Yang, Journal of Applied Physics 98 (2005) 043704/1-5.
[10] P. Peumans, S. Uchida, S.R. Forrest, Nature 425 (2003) 158–162.
[11] D.C. Martin, J.H. Chen, J.Y. Yang, L.F. Drummy, C. Kubel, Journal of Polymer Science Part B—Polymer Physics 43 (2005) 1749–1778.
[12] P. Peumans, A. Yakimov, S.R. Forrest, Journal of Applied Physics 93 (2003) 3693–3723.
[13] J.C. deMello, N. Tessler, S.C. Graham, R.H. Friend, Physical Review B 57 (1998) 12951–12963.
[14] Y.L. Shen, A.R. Hosseini, M.H. Wong, G.G. Malliaras, Chemphyschem 5 (2004) 16–25.
[15] J. Kruger, R. Plass, L. Cevey, M. Piccirelli, M. Gratzel, U. Bach, Applied Physics Letters 79 (2001) 2085–2087.
[16] T. Park, S.A. Haque, R.J. Potter, A.B. Holmes, J.R. Durrant, Chemical Communications (2003) 2878–2879.
[17] S.A. Haque, T. Park, C. Xu, S. Koops, N. Schulte, R.J. Potter, A.B. Holmes, J.R. Durrant, Advanced Functional Materials 14 (2004) 435–440.
[18] J.A. Barker, C.M. Ramsdale, N.C. Greenham, Physical Review B 67 (2003) 075205/1-9.
[19] K. Suemori, T. Miyata, M. Yokoyama, M. Hiramoto, Applied Physics Letters 85 (2004) 6269–6271.

Available online at www.sciencedirect.com
ScienceDirect
Organic Electronics 7 (2006) 249–255
Organic Electronics
www.elsevier.com/locate/orgel

Tuning of electrical bistability in organic devices through electrochemical potential of metal contacts

Biswanath Mukherjee, Amlan J. Pal *

Indian Association for the Cultivation of Science, Department of Solid State Physics, Jadavpur, Kolkata 700 032, India

Received 18 October 2005; received in revised form 28 January 2006; accepted 15 March 2006
Available online 18 April 2006

Abstract

The effect of different electrode combinations on conductance switching devices has been studied. A number of base electrodes were chosen while the top electrode was kept the same. With a suitable electrode combination, we could observe a large conductance switching (On/Off ratio = 10^7). Such a high ratio as compared to other electrode combinations has been discussed in terms of reversible electrochemical changes of charge transfer complexes and change in conduction mechanism. The switching devices showed an associated memory effect for data-storage applications. We could ''write'' or ''erase'' a state and ''read'' it for many cycles. The high On/Off ratio was maintained at the ''read'' pulse of ''write–read–erase–read'' sequence and also during long-time retention test. The results showed a novel route to select right electrode combination for efficient conductance-switching devices.

PACS: 85.65.+h; 85.37.+q; 73.61.Ph; 72.80.Le

Keywords: Electrical bistability; Memory-switching devices; On/Off ratio; Data-storage applications; Molecular electronics

1. Introduction

The drive toward miniaturization of silicon-based electronics has led scientists to work with organic molecule based electronic and optoelectronic devices. Apart from light-emitting diodes, field-effect transistors, sensors, photovoltaic devices, and complex lasers [1–4], there are recent in-depth reports on voltage-induced switching phenomenon in conjugated organics [5–10], which was first observed more than 30 years ago [11,12]. Such switching phenomenon can also lead to molecular scale memory elements and logic gates.

In switching devices, two conducting states exist at the same applied voltage. One can switch a state to the other by applying a suitable voltage. The electrical bistability has been explained in terms of a number of possible mechanisms. The conducting states observed in anthracene thin films [12] and in structures based on Cr-doped inorganic thin oxide films [13] were explained to be due to presence of traps, which were filled under high fields leading to high carrier mobility and filamentary condition. In a complicated tri-layer structure, an additional layer

* Corresponding author. Tel.: +91 33 24734971; fax: +91 33 24732805.
E-mail address: sspajp@iacs.res.in (A.J. Pal).

1566-1199/$ - see front matter © 2006 Elsevier B.V. All rights reserved.
doi:10.1016/j.orgel.2006.03.004

of metal nanoclusters was introduced between two active organic layers to store charges and to provide large On/Off ratio [10]. In copper– and cyanine–tetracyanoquinodimethanide (Cu–TCNQ) complex based devices, the proposed mechanism involved formation of charge transfer complex with metal ions, so that a field induced solid-state reversible electrochemical reaction could take place. Recently, Yang's group [14] has shown bistability with Cu electrode and proposed that switching occurred due to migration of Cu ions into the active organic material. By controlling the concentration of Cu ions, it was possible to switch the device to either of the states. In these high-performing devices, where switching mechanism is a bulk property, their miniaturization to molecular scale is however restricted.

Though the contact of the metallic electrodes with the organic films can often play a crucial role in determining the current–voltage (I–V) characteristics of the devices, a true molecular device can be fabricated only in single layer switching devices. In such devices, thickness can be aimed to reduce down to molecular limit. By ensuring ohmic contact with the molecule, molecular switching or molecular memory will be possible and lead to true molecular electronic devices.

The electrical bistability, which is due to conformational changes and/or electroreduction of the molecules, should be sensitive to the type of contacts between the molecule and the metals. It is hence important to know how the electrodes can control the current levels of the two conducting states. In this article, we aimed to study the effect of the metal electrodes on switching mechanism of a quinone derivative. We report the effect of different electrode combinations on the electric field induced switching and memory phenomenon for data storage applications.

2. Experimental

The device fabrication procedure involved deposition of base electrode, e.g., silver (Ag), chromium (Cr), and aluminum (Al), on thoroughly cleaned glass substrate by thermal evaporation under vacuum (below 10^{-5} Torr). Width of the electrode strips was 2 mm. In addition, indium tin oxide (ITO) coated glass substrates, purchased from Optical Filters Limited, were used as another base electrode. Active material chosen for the present work was 2,3-dichloro-5,6-dicyano-1,4-benzoquinone (DDQ), whose molecular structure is shown in the inset of Fig. 1. To avoid any formation of oxide layer over the metallic electrodes, they are exposed to the organic solution soon after the deposition process was over. Chloroform solution of DDQ (2 mg/ml) was spun on the electrode-coated glass substrates at 2000 rpm for 30 s. The thin films were annealed in a vacuum oven (10^{-3} Torr) at 90 °C for 12 h. Thickness of the active layer was around 80–100 nm. On top of the annealed films, Al was vacuum-evaporated from a tungsten filament basket. A mechanical shutter protected the films from excess heat before and after metal evaporation. A shadow mask used during top electrode evaporation defined the active area of the devices, which were 4 mm^2.

The devices were kept in a shielded vacuum chamber (10^{-3} Torr) at room temperature for 10 h before a set of I–V characteristics was taken. For each pair of electrodes, we have characterized at least three devices. The I–Vs showed high degree of reproducibility. The variation in current values for a combination of electrodes was at least 10 times lower than the difference due to change in electrode. The I–V characteristics were recorded with a Yokogawa 7651 dc source and a Keithley 486 picoammeter. In all the cases, bias was applied with respect to the top Al electrode. Voltage was changed in steps of 0.01 V and device current was measured after 2 s, resulting in a scan speed of 5 mV/s. The dc source coupled with fast switching transistors were used to generate voltage pulse of different widths and amplitudes, which were used to "write" or "erase" a state and consequently "read" the states of different devices. Solartron 1260 Impedance Analyzer recorded the impedance characteristics of the

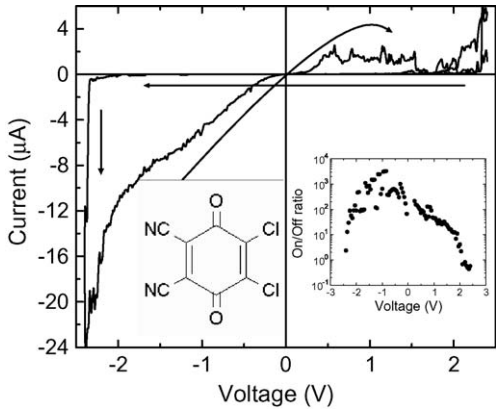

Fig. 1. Typical I–V characteristics of an ITO/DDQ/Al device for two voltage sweeps. Arrows show the direction of voltage sweep. Inset shows the molecular structure of DDQ and voltage dependence of On/Off ratio.

devices in a parallel mode. The test voltage of the analyzer was 100 mV rms. Open- and short-circuit compensations were performed with standard normalization procedure in order to minimize the effect of any stray and wire capacitances. The measurements were carried out with SMaRT software. Real and imaginary parts of impedance, Z' and Z'', respectively, of the devices were measured with and without dc bias. The instruments were controlled with a personal computer via a general-purpose interface bus (GPIB).

3. Results and discussion

3.1. ITO/DDQ/Al switching devices

I–V characteristics of different devices based on DDQ films were recorded by scanning applied voltage to different voltage amplitudes (V_{Max}). In general, voltage sweeps were carried out from 0 to $+V_{Max}$ followed by $+V_{Max}$ to $-V_{Max}$ and finally from $-V_{Max}$ to $+V_{Max}$. A typical *I–V* for an ITO/DDQ/Al device for the two sweep directions is shown in Fig. 1. The plot distinctly displays presence of two conducting states at any voltage during the two sweeps. When the voltage was swept from $+V_{Max}$ to $-V_{Max}$, the device exhibited its low-conducting neutral state (Off-state). When bias exceeded a critical amplitude above reduction potential, the DDQ molecules were reduced and the device underwent a transition from the low- to a high-conducting state (On-state). The high-conducting On-state persisted during the sweep from $-V_{Max}$ to $+V_{Max}$, showing a bistable nature of the devices at any voltage. The device finally switched off to its low-conducting state as the voltage approached $+V_{Max}$ oxidizing the molecules to their neutral state. When bias was looped for many times, the electrochemical reaction processes also cycled resulting in reproducible *I–V* characteristics.

The ratio between the On-state current and the Off-state current at a particular voltage, the On/Off ratio depended on the measured voltage (inset of Fig. 1). The ratio ranged up to more than 3000 in devices with ITO and Al. The On/Off ratio also depended on V_{Max} and increased with increasing V_{Max}. The ratio increased from 200 to 3000 as V_{Max} ranged from 2 to 2.8 V. The dependence of On/Off ratio on V_{Max} suggests that the density of the reduced species changes with V_{Max} and can have a role on the overall conductivity of a device. When Off- and On-state currents for different V_{Max}s are compared (Fig. 2) for an ITO/DDQ/Al device, we find that the *I–V* characteristics for the Off-state remained mostly identical. The characteristics for the On-state show that the device current at a voltage was higher with increase in V_{Max}. As V_{Max} increased, the density of high-conducting reduced molecules in the device became more. This opened up a number of percolating conducting channels through the device and resulted in a higher level of conductivity [15]. Finally at a sufficiently higher voltage, the density reached saturation as evidenced by invariant *I–V* characteristics with V_{Max} ranging from 2.5 to 2.8 V.

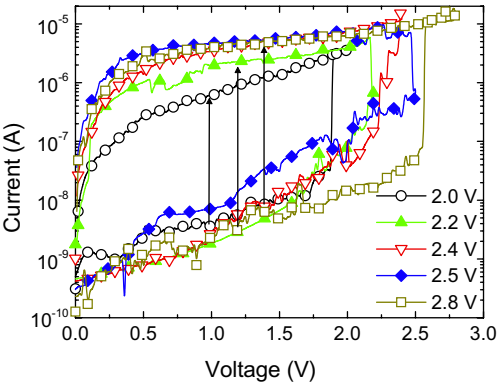

Fig. 2. *I–V* characteristics for two voltage sweep directions of an ITO/DDQ/Al device for different amplitude of maximum voltage (V_{Max}). The plot shows only the negative bias section of the characteristics. Amplitudes of voltage and current are plotted for clarity. The vertical arrows indicate transitions from Off-state to different On-states in each of the cases. Different V_{Max}s are represented in the figure.

3.2. Electrode variation

The On/Off ratio can also be modulated by selecting different electrode combinations. We have varied the base electrode and kept Al as the top electrode. *I–V* characteristics of devices with four different electrode combinations are shown in Fig. 3. The V_{Max} chosen for each of the cases was in the voltage range, where *I–V* characteristics did not vary with V_{Max}. The characteristics were for both voltage sweep directions. All the devices exhibited reproducible switching behavior. The On/Off ratio varied between 300 in Al/Al case to 10^7 in Ag/Al combination. The results in Fig. 3 show that the On-state current in the device with Al as base electrode was lower by several orders in magnitude as compared to other electrode cases. This could be due to formation of aluminum oxide layer over Al electrode during DDQ

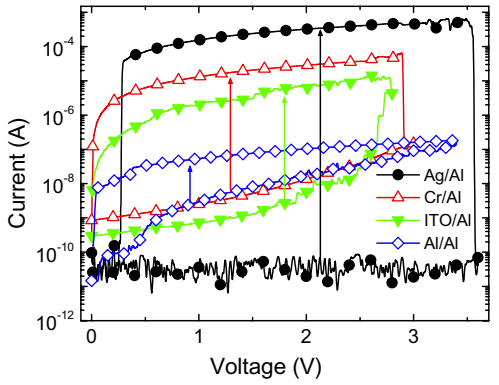

Fig. 3. *I–V* characteristics for On- and Off-states of DDQ devices with different electrode combinations. The plot shows only the negative bias section of the characteristics (except for the Ag/Al case). Amplitudes of voltage and current are plotted for clarity. The vertical arrows indicate transitions from Off- to On-state for each of the cases.

deposition. Apart from the system with Ag electrode, which is known to form a complex with DDQ [16], the On-state current of a device depended on the base metal's work-function. This is due to the fact that injected electrons electroreduce the molecules to their high-conducting state [15]. The On-state current (in the reverse bias) hence depended on the work-function of the base electrode. The maximum On/Off ratio for ITO/DDQ/Al and Cr/DDQ/Al devices were 3000 and 10^4, respectively. The variation of On/Off ratio with base electrode can be explained in terms of energy band diagram. Since the devices switch to a high-state in the reverse bias, electrons that are injected from the base-electrode electroreduce the DDQ molecules. The energy difference between metal Fermi level and lowest unoccupied molecular orbital (LUMO) of DDQ (1.9 eV) or the barrier height for electrons, which is less for Cr (work function $\varphi = 4.5$ eV) electrode than the ITO ($\varphi = 4.7$ eV) one, hence determined the On-state current. This explains higher current with Cr as compared to that with ITO as base electrode.

In devices based on Ag electrode, where switching to the high state occurred at a positive bias, the high ratio at room temperature and in single layer sandwich structures is itself of interest. The key features for such a high On/Off ratio in Ag/DDQ/Al devices are their low Off-state current and high On-state current as compared to the other devices. For Ag/DDQ/Al devices, the high On/Off ratio can be attributed to the formation of charge transfer salts between Ag and DDQ, which may modify the highest occupied molecular orbital (HOMO) and LUMO levels of DDQ. The changes in HOMO and LUMO leading to lowering of band gap would offer a low barrier height for charge injection in the On-state and high barrier height in the Off-state. Additionally, it could also lead to switching in the forward bias direction.

Apart from barrier height, transport mechanisms may also dictate On- and Off-state currents. We have aimed to fit the *I–V* plots with different existing models. Transport mechanism in devices based on ITO, Cr, and Al was found to follow thermionic emission model. Fig. 4 shows ln(*I*) versus $V^{0.5}$ plots for an ITO/DDQ/Al device in its On- and Off-states. The plots seem to fit to two straight lines at low- and high-voltage regimes. Such linearity suggests that the conduction mechanism was dominated by injection process in these devices. At higher voltages, the plots for the Off- and On-states fit with same slope, showing no change in dielectric constant during conductance switching. The intercept is however lower in the Off-state. This shows that barrier height was higher for the Off-state than that in the On-state.

For the Ag/DDQ/Al case, where On/Off ratio was the highest, both of the *I–V* plots cannot be fitted through thermionic emission model. The Off-state current, shown in Fig. 5(a), exhibits an excellent fit to the model. In the On-state, transport through the device seems to obey Poole–Frankel model. In Fig. 5(b), a plot of ln(*I*/*V*) versus $V^{0.5}$ fits to a straight line in the high voltage regime. Hence the conduction process in the high-state is dominated by charge transport through the bulk of the device. Thus the conduction mechanism is different for the two types

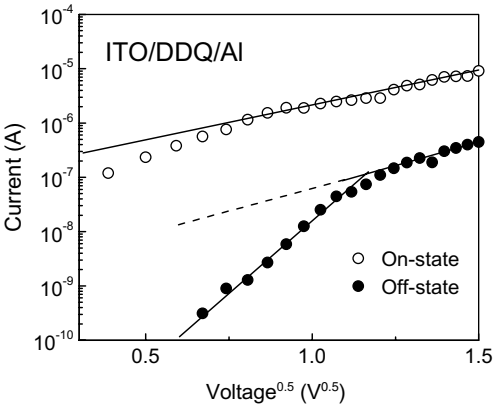

Fig. 4. Thermionic emission fitting of an ITO/DDQ/Al device in its high-conducting On-state and low-conducting Off-state. The lines are best fits to the experimental points.

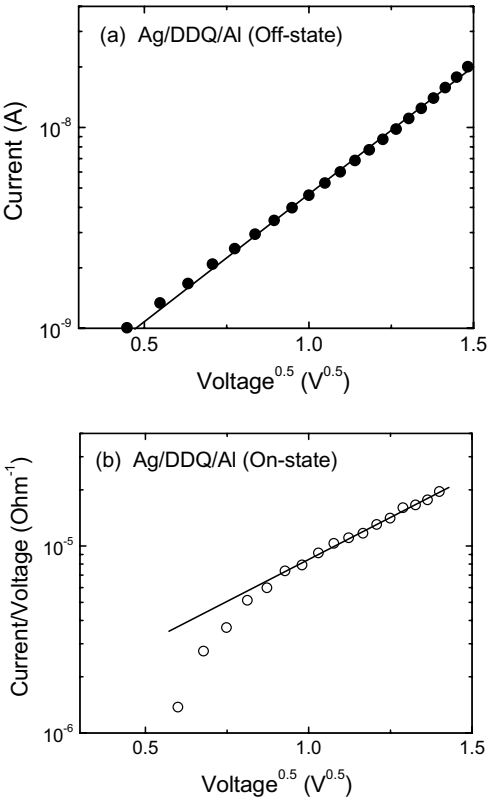

Fig. 5. Thermionic emission and Poole–Frenkel fittings of an Ag/DDQ/Al device in its (a) low-conducting Off-state and (b) high-conducting On-state. The lines are best fits to the experimental points following the respective models.

of devices. For devices with ITO, Cr, or Al as base electrodes, current conduction is injection-limited in both Off- and On-states. In Ag/DDQ/Al devices, conduction is limited by carrier injection only in the Off-state. After switching, it changed to a transport dominated mechanism in the On-state for Ag/Al based devices.

3.3. Impedance characteristics

The complex impedance of the devices at the On- and Off-states were characterized using dielectric spectroscopy. The advantages of dielectric measurements are that it is sensitive to any electrical polarization. The devices can also be modeled to an equivalent circuit. The devices were first switched to an Off- or On-state by suitable voltage pulse. Frequency scans were made from 12 MHz to 1 Hz at 0 V dc bias. Real and imaginary parts of complex impedance of the devices in their high- and low-conducting states are plotted in Fig. 6 with frequency of test voltage as the independent parameter. Such

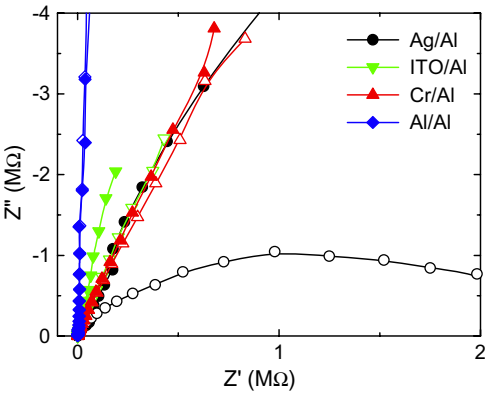

Fig. 6. Imaginary versus real part of complex impedance (Cole–Cole plot) of DDQ-based devices with different electrode combinations. Plots for high-and low-conducting states are represented by open and filled symbols, respectively. High-conducting state was induced by applying a suitable voltage pulse. Frequency scans were carried out without any dc bias.

plots, known as Cole–Cole plots show semicircular arcs. The devices can hence be modeled to a parallel combination of a resistor and a capacitor network. The diameter of the semicircle, which represents the bulk resistance of a device, shows a large change in Ag/DDQ/Al device due to switching. For other devices, however, the change is comparatively small. The results hence show that the observed high On/Off ratio in Ag/DDQ/Al devices is also due to large change in bulk resistance. The dielectric properties of the Ag/DDQ/Al device also showed a large increase during the conductance transition. The dielectric constant of the materials increased during the switching. The capacitance of the device at low frequencies increased from a few pF to about 10 nF during the transition. For other devices, the change in capacitance was however small.

3.4. Memory phenomenon

We also have observed an associated memory phenomenon in these switching devices. The active material retained its high-conducting state till a reverse bias erased it. Such a phenomenon can lead to data-storage applications in these device structures. In the two panels of Fig. 7, we represent random-access memory (RAM) and read-only memory (ROM) applications of an Ag/DDQ/Al device. In the upper panel, the two states were induced repeatedly by applying a suitable voltage pulse, and probed by measuring device current under a small voltage pulse. In a pristine structure, a 10 s 4 V pulse was applied to "write" the high-conducting state.

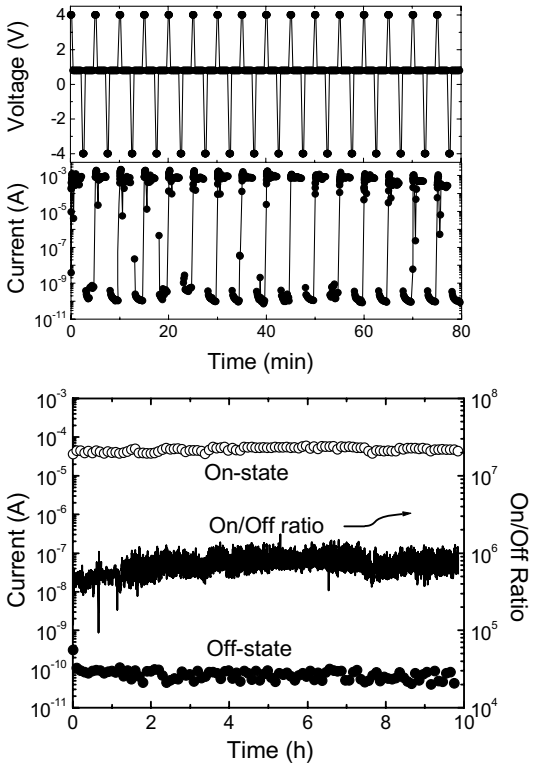

Fig. 7. Switching performance of a pristine Ag/DDQ/Al device during a "write–read–erase–read" sequence for data storage applications. The sequence of voltage pulse and the current response are shown in upper plot. "Write", "read" and "erase" voltages were 4, 0.8, and −4 V, respectively. The lower plot shows the retention ability of the two states of the device. The plot shows time response of current under 0.8 V probe voltage pulse (width = 2 s). The low-conducting Off-state and high-conducting On-state were induced by −4 and 4 V pulse (width = 10 s), respectively. The corresponding On/Off ratio as a function of time is also shown in the lower figure.

The state was probed after 10 s by measuring the current under 0.8 V pulse (width = 2 s). The state was "read" once in 4 s for 30 times. A −4 V pulse was then applied to "erase" the high-state and switched to a low-one, which was again probed or "read" by the same 0.8 V pulse. The "write–read–erase–read" sequence was repeated for many cycles. The current under the probe voltage pulse for high- and the low-conducting states had a ratio greater than 10^6. Such a high On/Off ratio under continuous flip-flop condition (RAM applications) is indeed very novel. The figure clearly shows that the electrical bistability of the device between two distinctly different states could be repeatedly observed without any significant device degradation.

Moreover, once the device was switched to either of the states, it remained in the state for a prolonged period of time. The retention ability of the device was tested by switching it to either of the states by a suitable voltage pulse and probed the state by a series of small voltage pulses. Lower panel of Fig. 7 demonstrates the long run plot for an Ag/DDQ/Al device for ROM applications. The device was switched to high and low states by applying a voltage pulse of 4 and −4 V, respectively. The state of the device was "read" by measuring current under 0.8 V pulse for several hours. The probe current for the high-conducting state was at least five orders in magnitude higher as compared to the case when low-state was probed. Also, there was no significant change in probe current in each of the states even after 10 h. The figure also shows the On/Off ratio (ratio between the probe currents) with time. The two states were clearly distinguishable after 10 h of continuous probing. The On/Off ratio also maintained a very high and stable value of around 10^6 with no detectable degradation. These "write–read–erase–read" cycles and the durability test demonstrate that the devices have the basic requirement necessary for binary information storage and present the potential for operation as non-volatile memory elements.

We have also observed multilevel memory in these devices. Width of +4 V "write" voltage pulse was varied from 1 to 20 s. After applying the "write" pulse to switch to different high-conducting states, current was measured by scanning probe voltage in the 0 to 1.5 V range (Fig. 8). The current

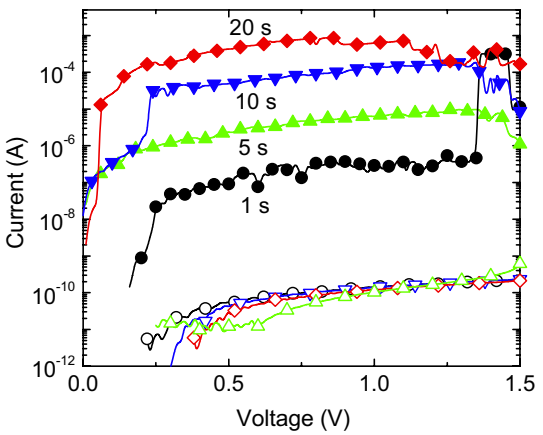

Fig. 8. Multilevel memory application of an Ag/DDQ/Al device. Different high-conducting states were induced by +4 V pulse of different widths (as shown in the figure). Probe voltage was swept from 0 to +1.5 V after each "write" pulse width and current was measured (plotted as filled symbols). Open symbols represent Off-state current under the same probe voltage scans after −4 V pulse of different widths was applied.

under probe voltage depended on the width of "write" voltage pulse. Here, with increase in width of "write"-pulse, the density of high-conducting molecules increased and resulted in different levels of conductivity in the devices. When −4 V pulse was used to "erase" the state, the probe current remained independent of "erase" voltage pulse width. The results show that different high conductivity levels can be introduced by applying "write" pulse of different widths and the states can be "read" for multilevel memory applications.

4. Conclusions

In conclusion, we have fabricated organic bistable devices based on DDQ with a number of electrode combinations. We have showed that appropriate electrode combination could lead to a stable bistability in conductance with a very high On/Off ratio. We have shown that such a high On/Off ratio was due to (1) lowering of injecting barrier height, (2) change in conduction mechanism, and (3) decrease in bulk resistance during conductance-switching. While the low-state current was restricted by carrier injection, conduction through the bulk of the device determined the current in the high-state. The devices exhibited RAM and ROM applications for several hours. The currents under probe voltage of "write–read–erase–read" and retention sequences also showed a high ratio between high- and low-conducting states. The results presented here shows that DDQ molecules can be considered as a potential candidate for molecular memory and logic elements and switching ratio can be tuned if sandwiched between appropriate electrode combination.

Acknowledgements

B.M. acknowledges CSIR Junior Research Fellowship No. F.NO.2-56/2002(I) EU.II (Roll No. 506120). The authors also acknowledge financial supports from the Department of Science and Technology, Government of India through Project SP/S2/M-44/99.

References

[1] W. Brütting, S. Berleb, A.G. Mückl, Org. Electron. 2 (2001) 1.
[2] R.H. Friend, R.W. Gymer, A.B. Holmes, J.H. Burroughes, R.N. Marks, C. Taliani, D.D.C. Bradley, D.A. Dos Santos, J.L. Brédas, M. Lögdlund, W.R. Salaneck, Nature 397 (1999) 121.
[3] B. Crone, A. Dodabalapur, Y.Y. Lin, R.W. Filas, Z. Bao, A. Laduca, R. Sarpeskar, H.E. Katz, W. Li, Nature 403 (2001) 521.
[4] F.M. Raymo, Adv. Mater. 14 (2002) 401.
[5] J. Chen, M.A. Reed, A.M. Rawlett, J.M. Tour, Science 286 (1999) 1550.
[6] C.P. Collier, G. Mattersteig, E.W. Wong, Y. Luo, K. Beverly, J. Sampaio, F.M. Raymo, J.F. Stoddart, J.R. Heath, Science 285 (1999) 391.
[7] Z.J. Donhauser, B.A. Mantooth, K.F. Kelly, L.A. Bumm, J.D. Monnell, J.J. Stapleton, D.W. Price Jr., A.M. Rawlett, D.L. Allara, J.M. Tour, P.S. Weiss, Science 292 (2001) 2303.
[8] J.M. Seminario, A.G. Zacarias, A.P. Derosa, J. Chem. Phys. 116 (2002) 1671.
[9] D.M. Taylor, C.A. Mills, J. Appl. Phys. 90 (2001) 306.
[10] L. Ma, J. Liu, S. Pyo, Y. Yang, Appl. Phys. Lett. 80 (2002) 362.
[11] S.R. Ovshinsky, Phys. Rev. Lett. 21 (1968) 1450.
[12] A.R. Elsharkawi, K.C. Kao, J. Phys. Chem. Solids 38 (1977) 95.
[13] A. Beck, J.G. Bednorz, Ch. Gerber, C. Rossel, D. Widmer, Appl. Phys. Lett. 77 (2000) 139.
[14] L. Ma, Q. Xu, Y. Yang, Appl. Phys. Lett. 84 (2004) 4908.
[15] B. Mukherjee, A.J. Pal, Appl. Phys. Lett. 85 (2004) 2116.
[16] R.S. Potember, T.O. Poehler Jr., D.O. Cowan, U.S. Patent 4371883, February 1, 1983.

Available online at www.sciencedirect.com
ScienceDirect
Organic Electronics 7 (2006) 256–260
Organic Electronics
www.elsevier.com/locate/orgel

High-mobility polymer thin-film transistors fabricated by solvent-assisted drop-casting

Joonhyung Park, Sangwoon Lee, Hong H. Lee *

School of Chemical and Biological Engineering, Seoul National University, Seoul, 151-744, Republic of Korea

Received 10 January 2006; received in revised form 24 January 2006; accepted 16 March 2006
Available online 18 April 2006

Abstract

A solvent-assisted drop-casting technique is introduced for the active layer formation in fabricating polymer thin-film transistors (TFTs). This method allows one to lower the rate of film formation (or deposition) of polymer semiconductor and to use a higher temperature, both factors contributing to better ordering of the semiconducting polymer. A notable increase in mobility results when the technique is applied to fabricating the polymer TFT. More important is the stability of the device that the method provides.

PACS: 85.30.Tv; 73.61.Ph

Keywords: Polymer thin-film transistor; Solvent; Conjugated polymer; Poly(3-hexylthiophene)

There has been a great deal of interest in organic thin-film transistors (TFTs) recently because they can be utilized for driving circuits of active matrix display and flexible displays at low cost [1–4]. Both small molecule organic semiconductors and conjugated polymers can be used for the active layer of organic TFTs. The best performance has been achieved with vacuum evaporated pentacene as active layer and silicon dioxide as gate dielectric. The carrier mobility is higher than 1 $cm^2 V^{-1} s^{-1}$, which is comparable to that obtainable with hydrogenated amorphous silicon [5,6].

Polymers have also been used as a semiconductor or a gate dielectric [7–10]. Organic TFTs using polymers show relatively poor device performance compared to that of the devices using small molecule organic semiconductors or inorganic dielectrics. However, polymers allow solution processability in the fabrication which is cost effective [11–13]. Various processes have been studied, including ink-jet printing, screen printing, and others [14–16].

In organic TFTs, the device performance is mainly determined by the structural order of the molecules in the organic semiconductor film. The molecular structure can be controlled by synthesizing molecules that show optimal characteristics or by controlling the process conditions. Annealing process, for instance, has widely been used to control the molecular structure of the semiconductor

* Corresponding author. Tel.: +82 2 880 7403; fax: +82 2 878 5043.
E-mail address: honghlee@snu.ac.kr (H.H. Lee).

1566-1199/$ - see front matter
doi:10.1016/j.orgel.2006.03.008

film either by heating the substrate prior to the deposition or by post-annealing of the deposited film [17–28]. For a given material, it is known that increasing the substrate temperature and/or lowering the deposition rate usually improves the device performance [29–31]. At higher substrate temperature, semiconductor molecules have higher mobility on the surface and more easily move to the equilibrium position in the crystalline structure. When the deposition rate is lower, the molecules have more time to form an ordered crystalline structure. Therefore, a higher temperature and a lower deposition rate lead to a better ordering of the organic semiconductor and thus a better performance. Our motivation is that higher temperature and low deposition rate, which was very effective for pentacene-based TFT, could be applied to polymer-based TFT.

For small molecule organic semiconductors such as pentacene, the films are deposited by thermal evaporation in high vacuum. Therefore, the substrate temperature and the deposition rate can easily be controlled by changing process parameters. When polymer semiconductors are used for the active layer, it is known that the deposition rate can be slightly changed by using solvents with high boiling points [25]. However, it is difficult to control both the deposition rate and the temperature because of solution-based processing. As the substrate temperature increases, so does the evaporation rate of the solvent. Consequently, the deposition or film formation rate increases with increasing temperature, when in fact a decrease in the deposition rate and an increase in the temperature are desired.

In this article, we present a solvent-assisted drop-casting method for forming a polymer semiconductor layer at elevated temperature, which also leads to reduced deposition rate. Because of the additional solvent available during the drop-casting process, the solvent evaporation rate could be lowered even at the higher temperature, resulting in better device performance. More importantly, failures in device operation are significantly reduced and more stable devices could be obtained.

The polymer TFTs fabricated in this work are of bottom gate and top contact type, the device structure of which is shown in Fig. 1(a). Fig. 1(b) illustrates the equipment set-up for the solvent-assisted drop-casting method, which is discussed in detail shortly. To fabricate the device, glass substrates were first cleaned and then aluminum was deposited through a shadow mask by thermal evaporation to

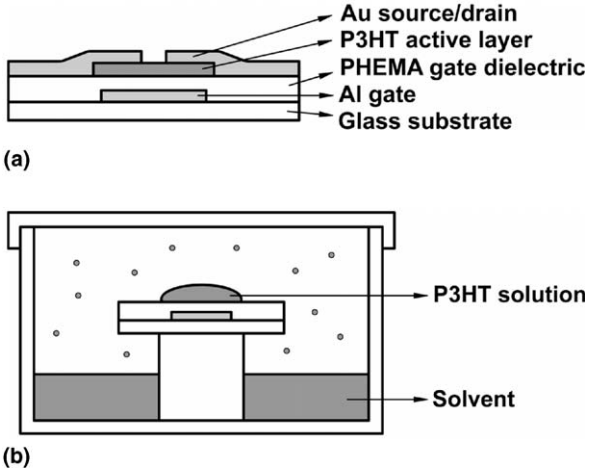

Fig. 1. (a) Schematic cross section of P3HT TFT. (b) Schematic illustration of solvent-assisted drop-casting process.

define the gate electrode. Onto the gate electrode, poly(2-hydroxyethyl methacrylate) (PHEMA) in methanol was spin-coated for the gate dielectric [10,32]. Onto this polymer gate dielectric, the active layer of poly(3-hexylthiophene) (P3HT) in toluene was coated by drop-casting. Toluene was selected to minimize the deleterious effect of the solvent on the polymer gate dielectric [10]. Finally, the source and drain contacts were formed by thermal evaporation of gold through a shadow mask. The channel length and width were 120 μm and 3 mm, respectively.

For the polymer TFTs fabricated, the carrier mobility was determined from the following relationship in the saturation regime:

$$I_D = \frac{WC_i}{2L}\mu_{eff}(V_G - V_T)^2, \quad (1)$$

where I_D is the drain current, W and L are the channel width and length, respectively, μ_{eff} is the effective mobility, C_i is the capacitance per unit area, V_G is the gate voltage, and V_T is the threshold voltage. The saturation regime mobility was determined at a drain–source voltage, V_{DS}, of −60 V.

We fabricated devices by drop-casting of P3HT solution at room temperature (25 °C) and 70 °C to compare the drying time and its effects on device performance. When the P3HT drop was dispensed on the insulator layer at room temperature, it took about 3 min for complete drying. When the substrate was heated to 70 °C before the drop-casting process, on the other hand, the drying was completed within 30 s. To compare the performance

between the devices fabricated at the two temperatures, the electrical characteristics were measured for each device. The drain current–gate voltage characteristics of the devices fabricated under different conditions are shown in Fig. 2(a). It can clearly be seen that the device fabricated at room temperature is superior in performance to that of the device fabricated at 70 °C. The carrier mobility decreased from 7.1×10^{-2} cm^2 V^{-1} s^{-1} to 3.8×10^{-3} cm^2 V^{-1} s^{-1} when the temperature was increased to 70 °C. It is known that the device with P3HT film formed by drop-casting gives a better device performance than that by spin-coating due to slower growth of the semiconductor film and consequently better ordering of the polymer [7,9,10]. At 70 °C, the formation rate of the film was so high that the positive effect of the elevated temperature was not sufficient enough to surmount the deleterious effect of the fast growth of the film.

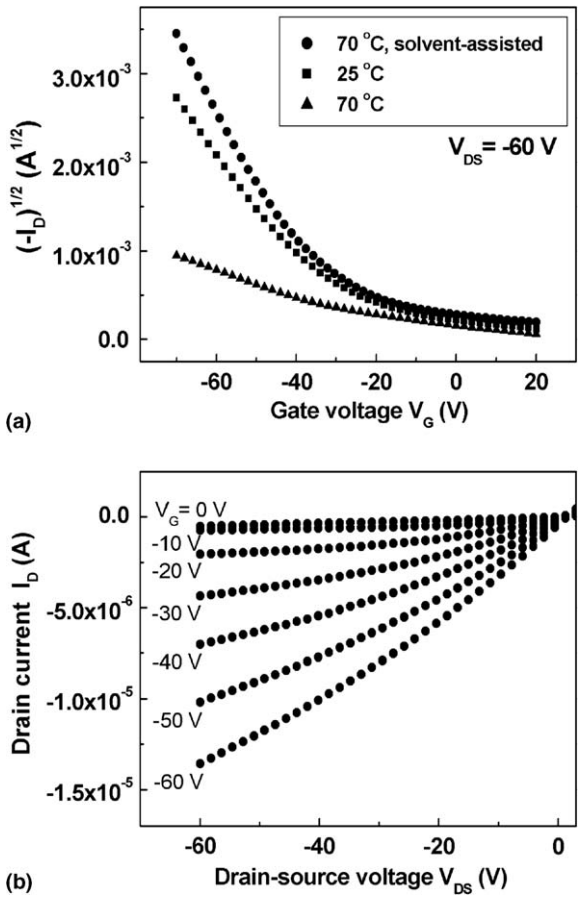

Fig. 2. Electrical characteristics of P3HT TFTs. (a) Electrical transfer characteristics of the device with PHEMA gate dielectric and P3HT active layer formed by drop-casting methods under different conditions. (b) Electrical output characteristics of the device with PHEMA gate dielectric and P3HT active layer formed by solvent-assisted drop-casting at 70 °C. The gate voltage varies between 0 and −60 V in steps of 10 V.

To overcome this problem, we introduced a solvent-assisted drop-casting method. The fabrication procedure is illustrated in Fig. 1(b). We devised a small chamber that has a solvent reservoir inside. The chamber was filled with the toluene vapor that is used for the P3HT solution and as a result the solvent drying was suppressed in the chamber due to the high vapor pressure. To fabricate the devices, we carried out drop-casting in the chamber and the temperature was maintained at 70 °C. The solvent drying was completed in 15 min, which is five times longer than that of the drying at 25 °C even at the higher temperature. We expect the process time can be reduced by optimizing the process with respect to the way the solvent vapor pressure is controlled. The electrical characteristic of the device fabricated in this way is also shown in Fig. 2(a). The carrier mobility increased up to 1.2×10^{-1} cm^2 V^{-1} s^{-1} when the solvent-assisted drop-casting method was used at the elevated temperature. The electrical output characteristics of the device are shown in Fig. 2(b).

To understand the role of the increased drying time and the higher temperature in improving the device performance, we fabricated devices by the solvent-assisted drop-casting method at room temperature. In this case, the drying time was also 15 min, which is identical with that of the solvent-assisted drop-casting process at 70 °C. We could obtain a carrier mobility of 7.8×10^{-2} cm^2 V^{-1} s^{-1}, which is slightly higher than that of the device fabricated by normal drop-casting at the same temperature (7.1×10^{-2} cm^2 V^{-1} s^{-1}). The result shows that the device performance was not significantly improved when only the deposition rate is decreased. Therefore, the improvement in the device performance by solvent-assisted drop-casting method at the higher temperature is mainly due to the increased mobility of the semiconductor molecules at the elevated temperature. The device characteristics of the TFTs for the four cases are summarized in Table 1.

The solvent-assisted drop-casting method leads not only to improved performance but more importantly to more stable device operation. When the device is fabricated by the normal drop-casting method, abnormal behavior in the electrical characteristics is frequently observed. Examples of the

Table 1
Field-effect mobilities in saturation regime, threshold voltages, and on/off ratios for various film formation methods

	Mobility ($cm^2 V^{-1} s^{-1}$)	Threshold voltage (V)	On/off ratio
25 °C, Drop-casting	7.1×10^{-2}	−22	2×10^3
25 °C, Solvent-assisted drop-casting	7.8×10^{-2}	−20	2×10^3
70 °C, Drop-casting	3.8×10^{-3}	−14	3×10^2
70 °C, Solvent-assisted drop-casting	1.2×10^{-1}	−24	4×10^3

abnormal device characteristics are shown in Fig. 3(a) and (b). When the drain–source voltage or the gate voltage is varied, abrupt changes in the drain current were observed. This abnormality was not observed for all the devices fabricated, but for some devices, it was.

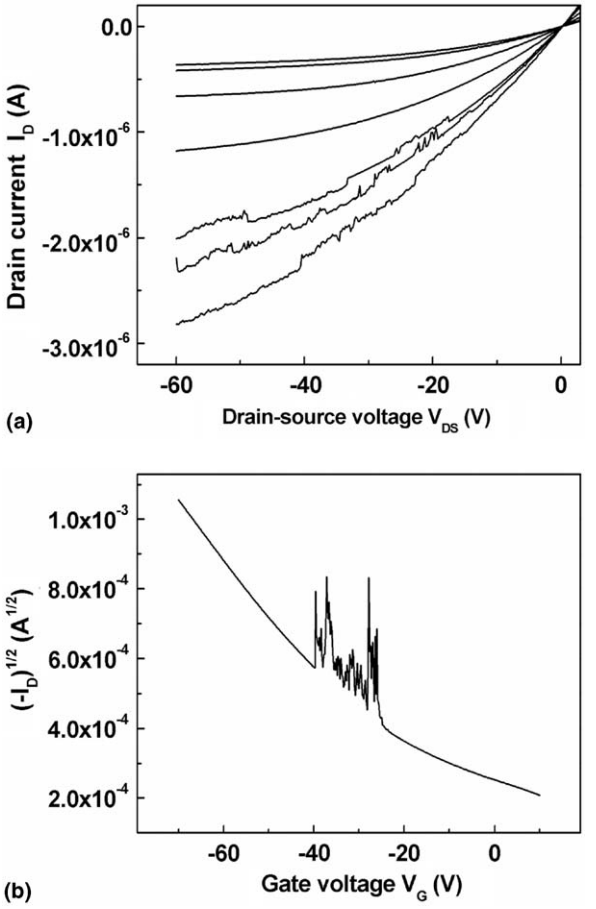

Fig. 3. Examples of failure in electrical characteristics of P3HT TFTs. Abnormal behavior in (a) electrical output characteristics and (b) electrical transfer characteristics.

The pattern of the abnormal behavior is not regular but rather changes with each measurement even with the same device. The mechanism of the failure in electrical characteristics is not fully understood yet, but it might be due to an intermittent contact or the defects in the crystalline structure of the polymer semiconductor film. To compare the stability between the device fabricated by the normal drop-casting and the solvent-assisted drop-casting, we fabricated 50 devices for each case. With the normal drop-casting method, the abnormal behavior in the electrical performance was observed for 30% of all the device fabricated. However, the failure ratio was significantly reduced from 30% to 10% with the solvent-assisted drop-casting method. The improvement was observed regardless of the temperature at which the solvent-assisted drop-casting was performed. In contrast, the normal drop-casting at higher temperature led to higher failure ratio. The improved stability can be attributed mainly to more stable film formation during the active layer deposition because all the process variables other than the rate of film formation were kept identical. Possible defect formation within the semiconductor film or at the interface between layers could be reduced by allowing sufficient time for the layer to form a well-oriented ordered structure.

In summary, a solvent-assisted drop-casting technique has been introduced for forming the polymer semiconductor layer in polymer TFTs. The method is effective in increasing both the substrate temperature and the solvent drying time, both of which lead to a better device performance. It has been found that the substrate temperature plays a more important role in improving the performance. The device stability in operation, which is critical in any application, could also be significantly improved with the solvent-assisted drop-casting method. These results suggest that less defects form in the polymer semiconductor film due to higher temperature and lower deposition rate, which has been made possible by the solvent-assisted drop-casting method.

References

[1] A. Dodabalapur, L. Torsi, H.E. Katz, Science 268 (1995) 270.
[2] C.D. Dimitrakopoulos, A.R. Brown, A. Pomp, J. Appl. Phys. 80 (1996) 2501.
[3] H. Sirringhaus, N. Tessler, R.H. Friend, Science 280 (1998) 1741.
[4] B.K. Crone, A. Dodabalapur, R. Sarpeshkar, R.W. Filas, Y.-Y. Lin, Z. Bao, J.H. O'Neill, W. Li, H.E. Katz, J. Appl. Phys. 89 (2001) 5125.

[5] Y.-Y. Lin, D.J. Gundlach, S.F. Nelson, T.N. Jackson, IEEE Electron. Dev. Lett. 18 (1997) 606.
[6] C.D. Sheraw, L. Zhou, J.R. Huang, D.J. Gundlach, T.N. Jackson, M.G. Kane, I.G. Hill, M.S. Hammond, J. Campi, B.K. Greening, J. Francl, J. West, Appl. Phys. Lett. 80 (2002) 1088.
[7] Z. Bao, A. Dodabalapur, A.J. Lovinger, Appl. Phys. Lett. 69 (1996) 4108.
[8] H. Klauk, M. Halik, U. Zschieschang, G. Schmid, W. Radlik, W. Weber, J. Appl. Phys. 92 (2002) 5259.
[9] G. Wang, J. Swensen, D. Moses, A.J. Heeger, J. Appl. Phys. 93 (2003) 6137.
[10] J. Park, S.Y. Park, S.-O. Shim, H. Kang, H.H. Lee, Appl. Phys. Lett. 85 (2004) 3283.
[11] F. Garnier, R. Hajlaoui, A. Yassar, P. Srivastava, Science 265 (1994) 1684.
[12] G.H. Gelinck, T.C.T. Geuns, D.M. de Leeuw, Appl. Phys. Lett. 77 (2000) 1487.
[13] M. Halik, H. Klauk, U. Zschieschang, T. Kriem, G. Schmid, W. Radlik, K. Wussow, Appl. Phys. Lett. 81 (2002) 289.
[14] J.A. Rogers, Z. Bao, V.R. Raju, Appl. Phys. Lett. 72 (1998) 2716.
[15] H. Sirringhaus, T. Kawase, R.H. Friend, T. Shimoda, M. Inbasekaran, W. Wu, E.P. Woo, Science 290 (2000) 2123.
[16] J. Zaumseil, T. Someya, Z. Bao, Y.-L. Loo, R. Cirelli, J.A. Rogers, Appl. Phys. Lett. 82 (2003) 793.
[17] A. Afzali, T.L. Breen, C.R. Kagan, Chem. Mater. 14 (2002) 1742.
[18] M.J. Banach, R.H. Friend, H. Sirringhaus, Macromolecules 36 (2003) 2838.
[19] M. Mushrush, A. Facchetti, M. Lefenfeld, H.E. Katz, T.J. Marks, J. Am. Chem. Soc. 125 (2003) 9414.
[20] L. Burgi, T.J. Richards, R.H. Friend, H. Sirringhaus, J. Appl. Phys. 94 (2003) 6129.
[21] A. Afzali, C.D. Dimitrakopoulos, T.O. Graham, Adv. Mater. 15 (2003) 2066.
[22] H.E. Katz, T. Siegrist, M. Lefenfeld, P. Gopalan, M. Mushrush, B. Ocko, O. Gang, N. Jisrawl, J. Phys. Chem. B 108 (2004) 8567.
[23] D.B. Mitzi, L.L. Kosbar, C.E. Murray, M. Copel, A. Afzali, Nature 428 (2004) 299.
[24] B.S. Ong, Y. Wu, P. Liu, S. Gardner, J. Am. Chem. Soc. 126 (2004) 3378.
[25] J.-F. Chang, B. Sun, D.W. Breiby, M.M. Nielsen, T.I. Solling, M. Giles, I. McCulloch, H. Sirringhaus, Chem. Mater. 16 (2004) 4772.
[26] A. Facchetti, J. Letizia, M.-H. Yoon, M. Mushrush, H.E. Katz, T.J. Marks, Chem. Mater. 16 (2004) 4715.
[27] B.S. Ong, Y. Wu, P. Liu, S. Gardner, Adv. Mater. 17 (2005) 1141.
[28] Y. Wu, P. Liu, B.S. Ong, T. Srikumar, N. Zhao, G. Botton, S. Zhu, Appl. Phys. Lett. 86 (2005) 142102.
[29] J.G. Laquindanum, H.E. Katz, A.J. Lovinger, A. Dodabalapur, Chem. Mater. 8 (1996) 2542.
[30] M. Shtein, J. Mapel, J.B. Benziger, S.R. Forrest, Appl. Phys. Lett. 81 (2002) 268.
[31] D. Knipp, R.A. Street, A. Volkel, J. Ho, J. Appl. Phys. 93 (2003) 347.
[32] J. Park, S.-O. Shim, H.H. Lee, Appl. Phys. Lett. 86 (2005) 073505.

Available online at www.sciencedirect.com
ScienceDirect
Organic Electronics 7 (2006) 261–270
Organic Electronics
www.elsevier.com/locate/orgel

Influence of temperature and frequency on the electrical conductivity and the dielectric properties of nickel phthalocyanine

M.M. EL-Nahass *, A.F. EL-Deeb, F. Abd-El-Salam

Physics Department, Faculty of Education, Ain Shams University, Heliopolies, Cairo 11757, Egypt

Received 29 December 2005; received in revised form 2 March 2006; accepted 16 March 2006
Available online 18 April 2006

Abstract

The temperature and frequency dependence of the AC conductivity $\sigma_{ac}(\omega)$, the dielectric constant $\varepsilon'(\omega)$ and the dielectric loss $\varepsilon''(\omega)$ were studied on pellet samples of nickel phthalocyanine (NiPc) with evaporated ohmic Au electrodes in the frequency range from 20 kHz to 10 MHz and within the temperature range from 303 to 600 K. The DC conductivity σ_{dc} has also been measured in the considered range of temperature. Two temperatures – induced changes in the thermal activation energy ΔE have been observed. For $T \leqslant 435$ K, $\Delta E_1 = 0.322$ eV; for 435 K $\leqslant T \leqslant 525$ K, $\Delta E_2 = 0.497$ eV; for $T \geqslant 525$ K, $\Delta E_3 = 0.703$ eV. These variations in the activation energy were attributed to a partial phase transformation from α- to β-NiPc phase and as a change from extrinsic to intrinsic conduction mechanism. The AC conductivity $\sigma_{ac}(\omega)$ showed temperature independence and it has been found to vary with angular frequency as ω^s with the index $s \leqslant 1$ suggesting a hopping conduction mechanism at low temperatures and high frequency. At higher temperatures and lower frequencies a free-band conduction mechanism was observed. Both the dielectric constant $\varepsilon'(\omega)$ and the dielectric loss $\varepsilon''(\omega)$ increased with temperature and decreased with frequency in the investigated ranges. Such characteristics, reveal that the tested organic NiPc exists in the form of molecular dipoles which remain frozen at low temperature, whereas at higher temperatures, when the dipoles attaining rotational freedom, the dielectric constant was found to decrease with increasing frequency and increase with increasing temperature. The increase in the dielectric loss $\varepsilon''(\omega)$ with increasing temperature at low frequencies can be understood in terms of an increase in DC conductivity.

PACS: 72.20.−i; 77.22.−d

Keywords: Organic semiconductor; Nickel phthalocyanine; Electrical conductivity; Dielectric properties

1. Introduction

Phthalocyanines are aromatic compounds having semiconducting properties. Besides they are chemically stable and have dense colors; arising from an intense absorption in the UV–VIS region of spectra,

* Corresponding author. Tel.: +20 012 4168621.
E-mail address: prof_nahhas@yahoo.com (M.M. EL-Nahass).

1566-1199/$ - see front matter © 2006 Elsevier B.V. All rights reserved.
doi:10.1016/j.orgel.2006.03.007

that make them suitable to be employed as dyes and pigments in textile and paint industries. There are more than 70 different phthalocyanine complexes that can be obtained by replacing the two hydrogen atoms at the center of the molecular structure of metal-free phthalocyanine, H_2Pc, molecule [1]. Phthalocyanine compounds may have the potential to be used as gas sensors [2–6], optical data storage systems [7], solar cells [8,9], light emitting diodes [10,11] and to generate various types of switching devices [12]. In addition, zinc phthalocyanine, ZnPc, was employed in some medical application due to its selective binding to tumor-selective antibodies, and it has been used in the synthesis of a novel compound appropriate in photodynamic therapy of cancer [13,14]. The DC electrical properties of phthalocyanines have received the greatest attention in both single crystal [15–17] and thin film forms [18–20]. The AC electrical properties of metal phthalocyanine have attracted several researchers in the last decades, such as cobalt phthalocyanine, CoPc [21–24], copper phthalocyanine, CuPc [25–27], zinc phthalocyanine, ZnPc [28,29], molybdenum phthalocyanine, MoPc [30] and nickel phthalocyanine, NiPc [26,28]. AC measurements in various phthalocyanines have generally shown an $\sigma \propto \omega^s$ dependence for low temperatures and high frequencies, corresponding to hopping conduction. At higher temperatures and lower frequencies free – band conductivity with activation energy of a few tenths of an electron volt is fairly common [31].

In the present work, we report on AC electrical conductivity and the dielectric measurements of NiPc in pellets form with evaporated Au electrodes. Studies covered the frequency range from 20 kHz to 10 MHz and in the temperature range from 303 to 600 K. The DC conductivity has been measured in the same temperature range to determine the predominant electrical conduction mechanism in nickel phthalocyanine.

2. Experimental techniques

The nickel phthalocyanine (NiPc) powder used in this study was obtained from Kodak, UK. The pellets of NiPc were prepared (diameter 1 cm; thickness ~0.13 cm) by compressing the powder in a die under a pressure $\sim 1.96 \times 10^8$ N m^{-2}. The pellets were sandwiched between two evaporated gold electrodes which provide ohmic contacts to the phthalocyanines. The AC and DC conductivity measurements were made in air in the temperature range from 303 to 600 K, using a temperature controller (model TC-15 A) which can maintain constant temperature within ±0.5 K. The AC measurements were measured in the frequency range from 20 kHz to 10 MHz using a Hewlett–Packard (model 4275A) LCR bridge equipped with a three-terminal test fixture to avoid any stray capacitance and minimize the experimental error. The AC conductivity $\sigma_{ac}(\omega)$ was calculated by using the relation; $\sigma_{tot}(\omega) = \sigma_{ac}(\omega) + \sigma_{dc}$, where σ_{dc} (DC conductivity) was measured using a Keithley electrometer (model 6512 programmable electrometer) in series with a standard regulated power supply. The dielectric constant ε' (real part of the dielectric constant) was calculated using the relation: $\varepsilon' = Ct/\varepsilon_0 a$, where t is the disk thickness, C is the capacitance of the sample, a is the cross-sectional area and ε_0 is the permittivity of free space. The dielectric loss ε'' (imaginary part of the dielectric constant) was calculated from the relation: $\varepsilon'' = \varepsilon' \tan\delta$, where $(\delta = 90 - \varphi)$, φ is the phase angle. The experimental error during the measurements is ±2%.

3. Results and discussion

3.1. The frequency and temperature dependence of conductivity

Fig. 1 demonstrates the measured total conductivity $\sigma_{tot}(\omega)$ as a function of reciprocal temperature at various frequencies, along with the DC conductivity σ_{dc} of NiPc sample. This figure reveals that, frequency has a pronounced effect on $\sigma_{tot}(\omega)$, while there is no effect of temperature on it except at high temperatures region. At low frequencies and high temperatures the values of $\sigma_{tot}(\omega)$ and σ_{dc} approach each other. The DC curve shows an increase in the conductivity starting from 303 K up to 345 K, followed by a decrease in it with increasing temperature from 345 K to 370 K. Above 370 K the DC conductivity increases again with increasing the temperatures. This variation in the conductivity may be caused by the oxygen exhaustion from the sample. Similar behaviour has been observed in both thin films and pressed pellets of H_2Pc [32,33], in α-CuPc thin films [34], in NiPc thin films [35] and in ZnPc thin films [36]. These workers have ascribed this behaviour to oxygen exhaustion too. Above 370 K, the change of the DC conductivity with temperature shows three regions associated with three activation energies separated by two transition temperatures,

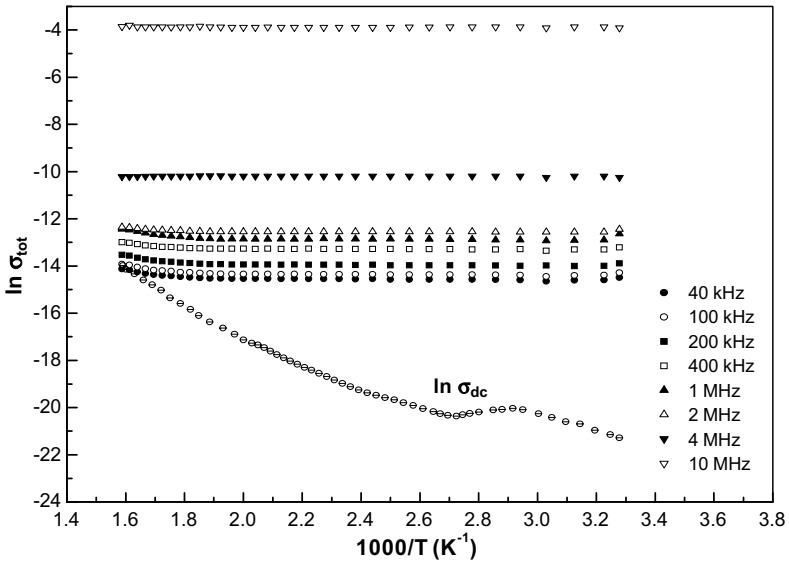

Fig. 1. Temperature dependence of the measured total electrical conductivity $\sigma_{tot}(\omega)$ at different frequencies and DC electrical conductivity for NiPc sample.

$T_1 = 435$ K and $T_2 = 525$ K. The activation energies obtained from the slopes of the three straight line segments using the well-known relationship [37]:

$$\sigma_{dc} = \sigma_0 \exp(-\Delta E/kT), \quad (1)$$

where σ_{dc} is the DC conductivity at temperature T, σ_0 is the pre-exponential factor, k is Boltzmann's constant and ΔE is the thermal activation energy. For $T \leqslant 435$ K, $\Delta E_1 = 0.322$ eV; for $435\ \text{K} \leqslant T \leqslant 525$ K, $\Delta E_2 = 0.497$ eV; for $T \geqslant 525$ K, $\Delta E_3 = 0.703$ eV. Phthalocyanines exist in several crystalline polymorphs, including the α-, β- and γ-structures [38]. Sharp [39] showed that in phthalocyanine compounds, the α-form is converted to the β-form by annealing in the temperature range of 473–573 K. Hence in Fig. 1, region 1 for $T \leqslant 435$ K may represents the α-form having thermal activation energy $\Delta E_1 = 0.322$ eV; region 2 extending over the range $435\ \text{K} \leqslant T \leqslant 525$ K may be related to the existing of preferential orientation in the α-form prior to the phase change associated with activation energy $\Delta E_2 = 0.497$ eV. On passing through the second transition temperature $T \geqslant 525$ K, we get region 3 which represents a smooth progression from the α-phase to the β-phase having thermal activation energy $\Delta E_3 = 0.703$ eV, while the transformation to β-NiPc phase is completed at 623 K [40]. The change in the activation energy could be interpreted as a change from extrinsic to intrinsic conduction too. The presence of extrinsic behaviour in phthalocyanine is attributed to the presence of energy states above the valence band, and act as donors' levels. The presence of the energy states is confirmed by the SCLC measurements [16,40]. The intrinsic conduction probably results from the removal of states. Similar behaviour has also been observed in DC conductivity measurements of both NiPc single crystals [16] and thin films [35], which were considered to be due to oxygen exhaustion and phase transformation from α- to β-phase. Abdel-Malik et al. [16] attributed the variation of the activation energy in β-NiPc single crystals to a transition from an extrinsic to a non-extrinsic conduction mechanism in a partially compensated specimen.

To further check the decrease in the DC conductivity in the temperature range from 345 to 370 K, we measured the conductivity of another NiPc sample and recycled the temperature of the sample between room temperature and 385 K. Fig. 2 shows the DC conductivity for temperature increasing up to 385 K (curve A), followed by the characteristics obtained with temperature decreasing down to room temperature (curve B). The disappearance of the conductivity peak during the decreasing temperature measurements can be attributed to the oxygen exhaustion from the sample during the heating cycle. To ensure that the peak is not due to a hysteretic effect or a phase transition, the sample was heated again to 385 K. No peak was observed in the second heating cycle, confirming the oxygen drain from the

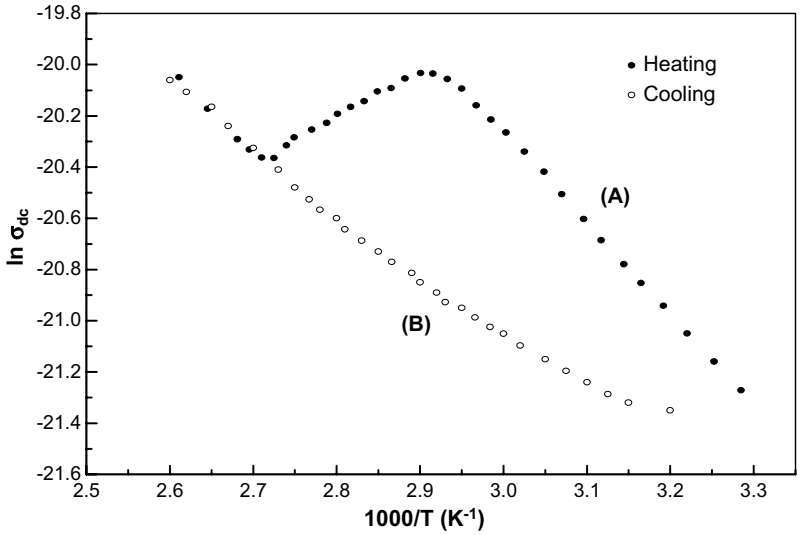

Fig. 2. The DC conductivity dependence on inverse temperature for increasing temperature (curve A), and decreasing temperature (curve B) for NiPc sample.

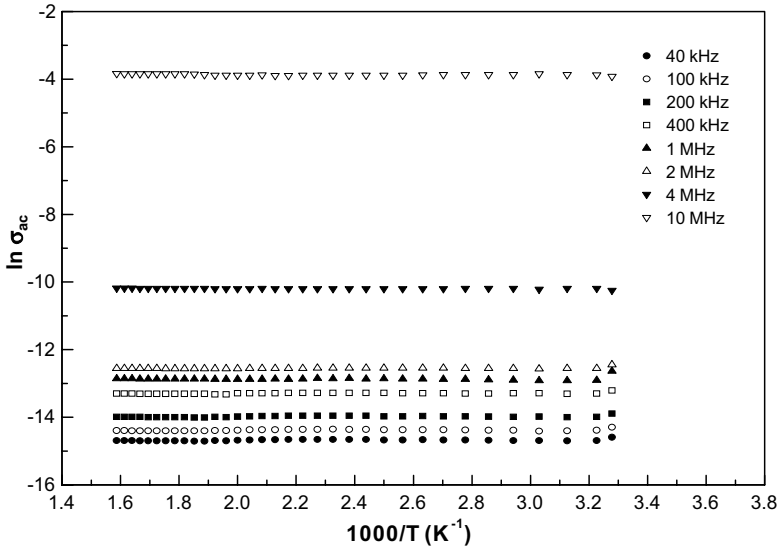

Fig. 3. Temperature dependence of AC conductivity $\sigma_{ac}(\omega)$ for NiPc at different frequencies.

sample. Therefore it is apparent that annealing or heating the sample to high temperature will stabilize the electrical properties due to oxygen exhaustion and structural changes [1,16,29,33–36,40].

Fig. 3 shows the AC conductivity $\sigma_{ac}(\omega)$, obtained by subtracting the DC conductivity from the measured total conductivity, as a function of reciprocal temperature at various frequencies. This figure depicts the temperature independence and the frequency dependence of $\sigma_{ac}(\omega)$ in the investigated temperature and frequency ranges; this means that $\sigma_{ac}(\omega)$ is not thermally activated in this range of temperature.

The frequency dependence of the AC conductivity for different temperatures is shown in Fig. 4. The conductivity obeyed the power law [37]:

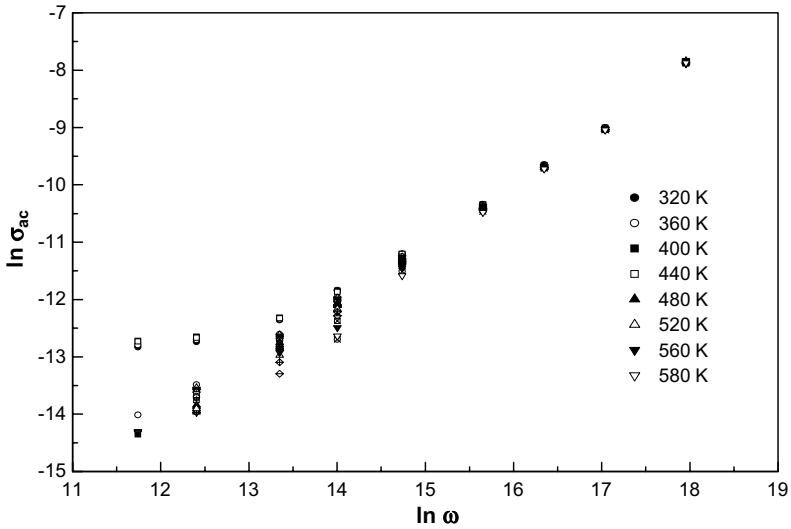

Fig. 4. Frequency dependence of AC conductivity $\sigma_{ac}(\omega)$ for NiPc at various temperatures.

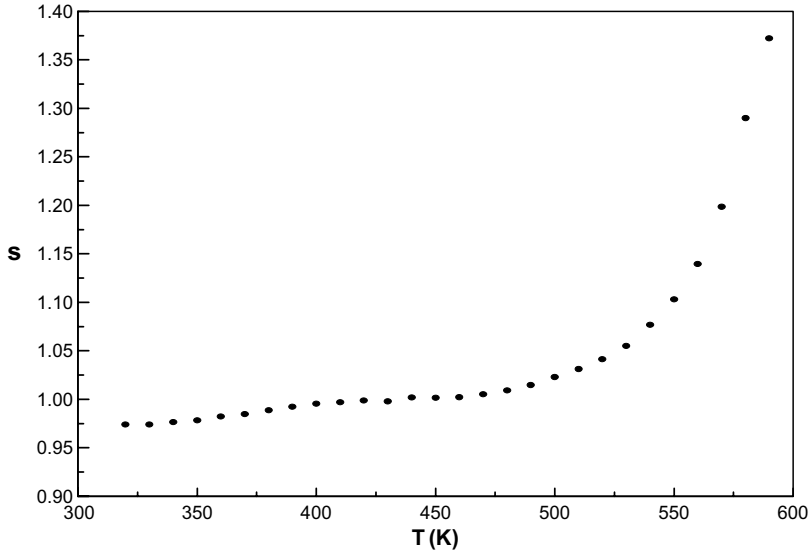

Fig. 5. Temperature dependence of the frequency exponent s for NiPc sample.

$$\sigma_{ac}(\omega) = A\omega^{s}, \tag{2}$$

where A is a constant dependent on temperature, ω is the angular frequency and the exponent s denotes the frequency dependence of $\sigma_{ac}(\omega)$.

As can be seen from Fig. 4, the conductivity shows strong frequency dependence at low temperatures, while at higher temperatures and low frequencies the conductivity becomes less frequency dependent. The index s in the present work was found to vary with temperature, as can be seen from Fig. 5, where it has values very close to unity at low temperatures, while at high temperatures ($T > 460$ K) the index s increases with increasing temperature reaching a maximum value of 1.37 at $T = 580$ K.

It is apparent from the derived values of the index s that the hopping conduction process as proposed by Elliott [41] is applicable for the present low temperatures case. In this model, hopping of carriers is most likely to occur between adjacent localized sites. Additionally, the AC conductivity is given by the following equation [42]:

$$\sigma_{ac}(\omega) = (n\pi^3/24)N^2\omega\varepsilon\varepsilon_0 R_\omega^6, \tag{3}$$

where ε is the dielectric constant of the material, ε_0 that of free space, N the concentration of localized sites, $n = 1$ for single-electron hopping, $n = 2$ for hopping of two electrons and R_ω is the hopping distance at a given frequency; given by

$$R_\omega = \frac{ne^2}{\pi\varepsilon\varepsilon_0[W_M + kT\ln(\omega\tau_0)]}, \tag{4}$$

where τ_0 is the effective relaxation time of approximately 10^{-13} s [42], e the electronic charge, k the Boltzmann, s constant and W_M is the energy required to move the electron from one site to the infinite. The frequency exponent s for this model is evaluated as:

$$s = 1 - \frac{6kT}{W_M + [kT\ln(\omega\tau_0)]}, \tag{5}$$

which, to a first approximation reduces to the simple expression:

$$s = 1 - \beta = 1 - \frac{6kT}{W_M}, \tag{6}$$

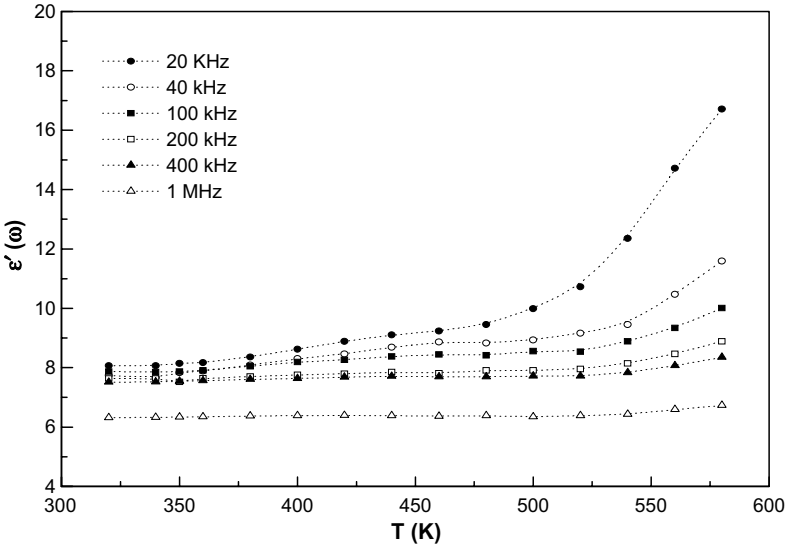

Fig. 6. Variation of the dielectric constant $\varepsilon'(\omega)$ with temperature at different frequencies for NiPc.

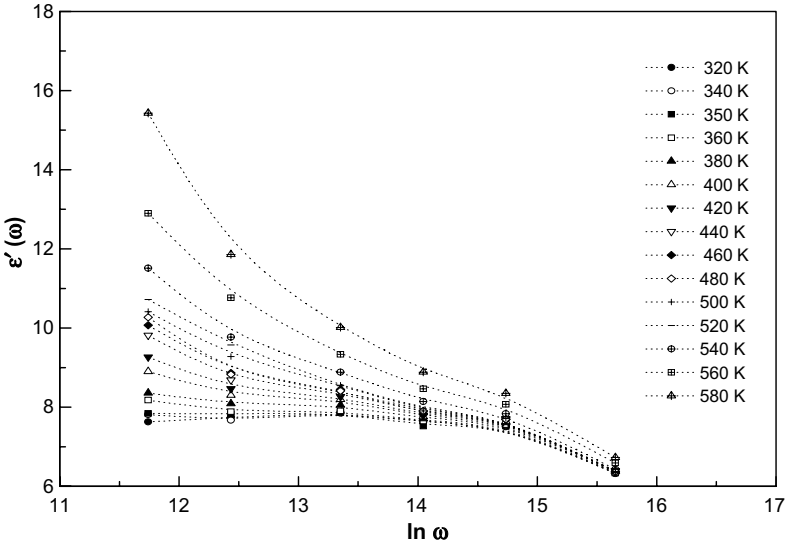

Fig. 7. Frequency dependence of the dielectric constant $\varepsilon'(\omega)$ at various temperatures for NiPc.

where the parameter β is small in comparison to unity. It is worth mentioning here that the derived values of the index s, particularly at low temperatures approaches one, and is in good qualitative agreement with the predicted value as proposed by Elliott model.

At temperatures exceeding 460 K, the index s behaviour reveals a free band conduction mechanism as suggested by Vidadi et al. [43]. Such frequency dependence is in reasonable agreement with those observed for other phthalocyanines compounds like CoPc [22,25], CuPc [25–27,43,44], H_2Pc [26,33], ZnPc [29,36], PbPc [25], NiPc [26,35] and MgPc [43]. These researchers pointed out that for low temperatures and high frequencies hopping was believed to occur, and was mainly by free-band conductivity with an activation energy of a few tenths of an electron volt at higher temperatures and lower frequencies.

3.2. Frequency and temperature dependence of the dielectric properties

Figs. 6 and 7 show the temperature and the frequency dependences of the dielectric constant $\varepsilon'(\omega)$. These figures indicate that the increase in the dielectric constant $\varepsilon'(\omega)$ with temperature is more clear at lower frequencies, and a strong dielectric dispersion occurs at temperatures greater than 525 K. The increase in the dielectric of the sample is due to the electric field which is accompanied by the applied frequencies. Such field will cause some ordering inside the sample as well as the formation of an electric moment in the entire volume of the dielectric and in each separate polarizing molecule. The molecular dipoles in polar material cannot orient themselves at low temperature. When the temperature rises the dipoles orientation is facilitated, and this increases the dielectric constant $\varepsilon'(\omega)$. In slowly varying fields at low frequency, the dipoles align themselves along the field direction and fully contribute to the total polarization. As the frequency is increased, the variation in the field become too rapid for the molecular dipoles to follow, so that their contribution to the polarization becomes less with a measurable lag because of internal frictional forces. The phase transformation from α- to β-phase in phthalocyanine compounds is accompanied by a gradual change of the electronic configuration inside the sample [15]. So, the space charge polarization is expected to give a drastic increase in $\varepsilon'(\omega)$ around 525 K and is responsible for the behaviour of the dielectric constant at different frequencies.

The variation in the dielectric loss $\varepsilon''(\omega)$ as a function of temperature and frequency is similar to that for the dielectric constant $\varepsilon'(\omega)$, this is clear from Figs. 8 and 9. These figures illustrate that $\varepsilon''(\omega)$ exhibit strong temperature dependence at higher temperatures and lower frequencies. There are two types of polarization [45], deformational polarization

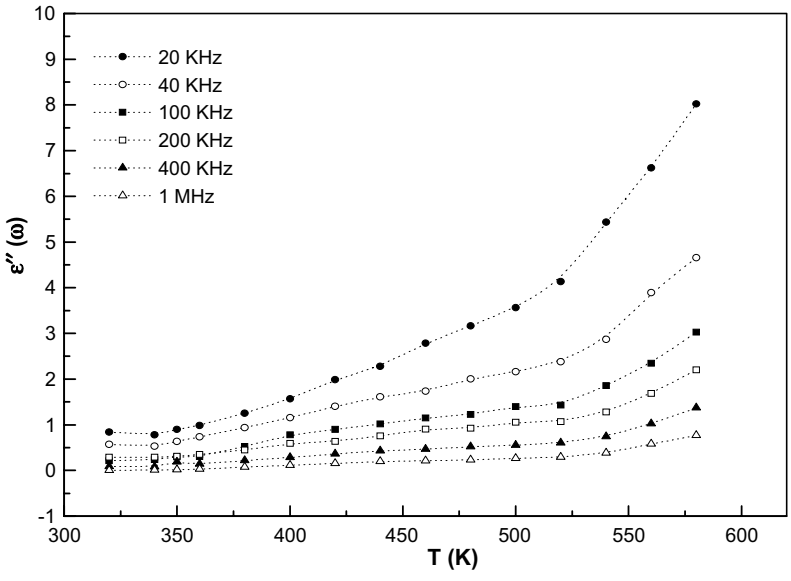

Fig. 8. Variation of the dielectric loss $\varepsilon''(\omega)$ with temperature at different frequencies for NiPc.

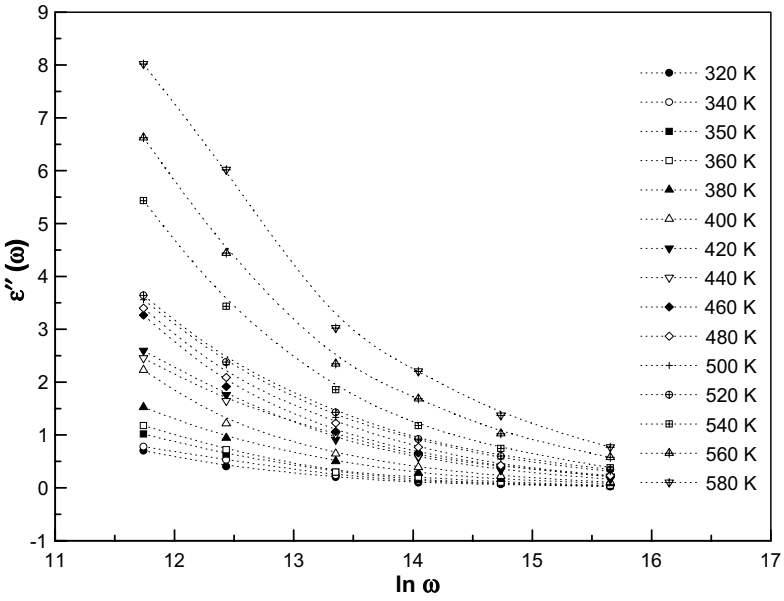

Fig. 9. Frequency dependence of the dielectric loss $\varepsilon''(\omega)$ at various temperatures for NiPc.

(electronic and ionic polarization) and relaxation polarization (orientation and interfacial polarization). Electronic polarization is the displacement of electrons with respect to the atomic nucleus, it can be observed in all dielectrics and occur during a very brief interval of time ($\sim 10^{-15}$ s). Ionic polarization is the mutual displacement of ions forming a heteropolar (ionic) molecule. It occurs during a short time (10^{-13}–10^{-12} s), which is longer than that of electronic polarization. The process of deformational polarization is practically unaffected by the temperature of the dielectric and is not connected with an irreversible dissipation of energy. So, the samples polarization here is not of the deformational type. Orientational polarization is not only a direct rotation of polar molecules under the action of an electric field, but it is connected with the thermal motion of molecules. So temperature must exert an appreciable effect on the phenomenon of dipole polarization. In fact, the rise in temperature and the resulting drop in viscosity exert a double effect on the amount of losses due to the friction of the rotating dipoles: on one hand, the degree of dipole orientation increases, and on the other hand, there is a reduction in the energy require to overcome the resistance of the viscous medium (internal friction of matter) when the dipole rotates through a unit angle. Interfacial or space charge polarization arises from the migration of electrons or ions over distances of macroscopic magnitude. Some of these charge carries may be trapped and accumulated at the interfaces of different dielectrics; lattice defects, impurity centers, voids, strains, or at electrode surfaces. So it distort the field and produce an apparent increase in the dielectric loss $\varepsilon''(\omega)$ [46]. As distinct from deformational polarization, relaxation polarization requires a relatively long time and dissipates electric energy which transforms into heat in a dielectric, i.e., this energy causes dielectric losses.

Owing to Stevels [47], the origins of the dielectric loss are conduction losses, dipole losses and vibrational losses. As the temperature increases, the electrical conduction losses increase which increases the dielectric loss $\varepsilon''(\omega)$. A comparative study to the following equation [48]:

$$\tilde{\varepsilon}(\omega) = \varepsilon'(\omega) - \mathrm{i}[\varepsilon''(\omega) + \sigma_{\mathrm{dc}}/\omega] = \varepsilon_0\{1 + \chi'(\omega) - \mathrm{i}[\chi''(\omega) + \sigma_{\mathrm{dc}}/\varepsilon_0\omega]\}, \quad (7)$$

where $\tilde{\varepsilon}(\omega)$ denotes the effective permittivity as measured by the instrument, $\chi'(\omega)$ and $\chi''(\omega)$ are the real and imaginary parts of the susceptibility of the material medium itself, and σ_{dc} is the DC conductivity. The significance of the last term in the above equation is that the DC conductivity makes a contribution to the apparent dielectric loss measured by a bridge or other instrument. This is not a true dielectric response, since it is not accompanied by any contribution to the real part of the permittivity

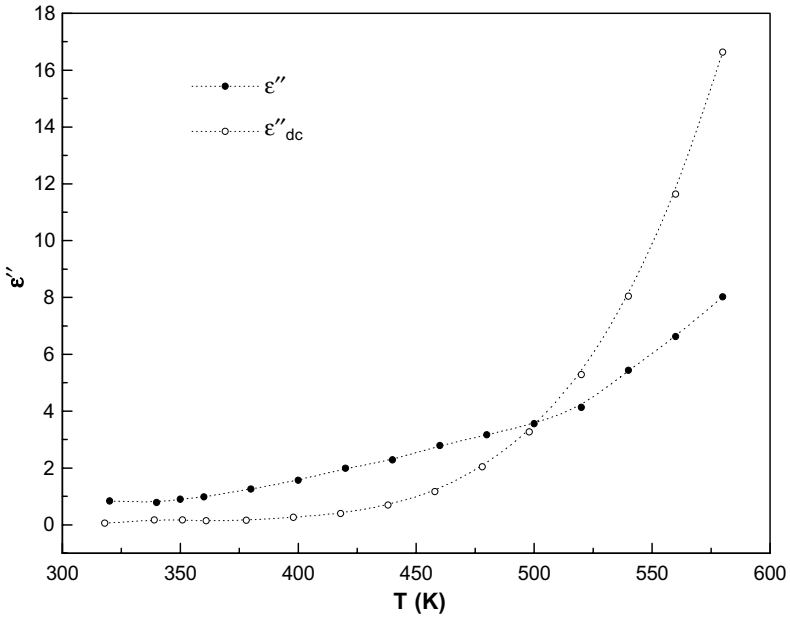

Fig. 10. Temperature dependence of the observed dielectric loss $\varepsilon''(\omega)$ and the DC conduction loss ε''_{dc} at frequency 20 kHz for NiPc sample.

and it arises because no instrument can distinguish between true dielectric response which does not contain σ_{dc} and the effective which does. To ascertain the contribution of the DC conduction loss ε''_{dc} to the dielectric dispersion; ε''_{dc} was calculated from the above relation [48]:

$$\varepsilon''_{dc} = \sigma_{dc}/\varepsilon_0\omega. \quad (8)$$

From Fig. 10 it has been observed that the DC conduction loss is comparable to the observed loss at a certain frequency (20 kHz). The DC conduction loss ε''_{dc} is smaller than the observed loss $\varepsilon''(\omega)$ up to a certain temperature 500 K, and after that ε''_{dc} dominates over the observed dielectric loss $\varepsilon''(\omega)$.

It can be assumed that the increase in the dielectric loss ε'' (ω) may be due to an increase in the DC conductivity. Similar trend has been reported by other workers [49,50].

4. Summary and conclusion

AC conductivity measurements have been carried out on pellet samples of NiPc sandwiched between two evaporated Au electrodes. The measurements covered the temperature range of 303–600 K and frequency range of 20 kHz to 10 MHz. The AC conductivity shows a strong frequency dependence and temperature independence in the investigated temperature and frequency ranges. It has been observed that the AC conductivity vary with the angular frequency as ω^s with index $s \leqslant 1$ at low temperatures, while at high temperatures the index s increased with increasing temperature having a maximum value of 1.37 at 580 K. Such behaviour indicating a hopping conduction mechanism at lower temperatures and a band conduction mechanism dominates at higher temperatures. The DC conductivity has also been measured in the considered range of temperature. There is a decrease in the DC conductivity in the temperature range from 345 K to 370 K, then after that started to increase once again. This behaviour was attributed to drain of oxygen molecules out of the sample during heating. This phenomenon was not a hysteretic effect since the peak disappeared in a second heating cycle. A partial phase transformation from α- to β-phase in NiPc was identified with the change in the thermal activation energy ΔE from 0.497 eV to 0.703 eV around 525 K. The dielectric constant $\varepsilon'(\omega)$ and the dielectric loss $\varepsilon''(\omega)$ were found to decrease with increasing frequency and increase with increasing temperature. Such behaviour reveals that the tested organic NiPc exists in the form of molecular dipoles. The phase transformation from α- to β-phase in NiPc is accompanied by a gradual change of the electronic configuration which gives a drastic increase in $\varepsilon'(\omega)$ around

525 K. The increase in the dielectric loss $\varepsilon''(\omega)$ with increasing the temperature at low frequencies can be understood in terms of an increase in DC conductivity.

In conclusion, the results of the present study are qualitatively in good agreement with the results of other phthalocyanine compounds. Despite of this agreement, more research effort is seriously required to fully understand the electrical behaviour of these compounds due to their importance in science, technology and industry. The proposed study should include more refine investigation of the compounds that include a wider temperature and frequency ranges.

References

[1] E. Orti, J.L. Brades, J. Chem. Phys. 89 (1988) 1009.
[2] J.W. Gardner, M.Z. Iskandari, B. Bott, Sens. Actuators B 9 (1992) 133.
[3] A. Mrwa, M. Friedrich, A. Hofman, Sens. Actuators B 24 (1995) 596.
[4] L. Hou, L. Cao, X. Li, H. Cui, D. Jiang, G. Zeng, S. Xi, Thin Solid Films 365 (2000) 129.
[5] K. Chuan Ho, Y. Ham Tsou, Sens. Actuators B 77 (2001) 253.
[6] R. Rellaa, A. Rzzob, A. Licciullic, P. Sicilianoa, L. Troisid, L. Vallic, Mater. Sci. Eng. C 22 (2002) 439.
[7] L. Kilmmert, D. Haarer, Adv. Mater. 7 (1995) 495.
[8] H.R. Kerb, E.E. Van Faassen, Chem. Phys. Lett. 5 (2000) 332.
[9] M. Pfeiffer, A. Beyer, B. Plonnigs, A. Nollau, T. Fritz, K. Leo, D. Schlettwein, S. Hiller, D. Wohrle, Sol. Energy Mater. Sol. Cells 63 (2000) 83.
[10] S.T. Lee, Y.M. Wang, X.Y. Hou, C.W. Tang, Appl. Phys. Lett. 74 (1999) 670.
[11] Z. Zhilin, J. Xueyin, Z. Wenquing, Z. Buxin, X. Shaohong, J. Phys. D Appl. Phys. 34 (2001) 188.
[12] F.Z. Henari, J. Opt. A Pure Appl. Opt. 3 (2001) 188.
[13] U. Drechsles, M. Ptaff, M. Hanack, Eur. J. Org. Chem. 1999 (1999) 3411.
[14] L. Gao, X. Qian, L. Zhang, Y. Zhang, J. Photochem. Photobiol. 65 (2001) 35.
[15] G.H. Helimeier, S.E. Harrison, Phys. Rev. 132 (1963) 2010.
[16] T.G. Abdel-Malik, G.A. Cox, J. Phys. C: Solid State Phys. 10 (1977) 63.
[17] A.S. Riad, A.E. El-Samahy, S.M. Khalil, Physica B 215 (1995) 217.
[18] R.D. Gould, Thin Solid Films 125 (1985) 63.
[19] R. Signerski, J. Kallnowski, I. Davoliand, S. Stizza, Phys. Status Solidi A 125 (1991) 597.
[20] K.P. Krishnakumar, C.S. Menon, J. Solid State Chem. 128 (1997) 27.
[21] H.S. Nalwa, P. Vazudevan, J. Mater. Sci. Lett. 2 (1983) 22.
[22] S.I. Shihub, R.D. Gould, Thin Solid Films 254 (1995) 187.
[23] A.S. Riad, M.T. Korayem, T.G. Abdel-Malik, Physica B 270 (1999) 140.
[24] S.I. Shihub, R.D. Gould, S. Gravano, Physica B 222 (1996) 136.
[25] W. Waclawek, M. Kulesza, M. Zabkowska, Mater. Sci. 7 (1981) 385.
[26] T.G. Abdel-Malik, R.M. Abdel-Latif, M. El-Shabasy, M. Abdel-Hamid, Indian J. Phys. 62A (1988) 17.
[27] R.D. Gould, A.K. Hassan, Thin Solid Films 223 (1993) 334.
[28] B. Boudjema, G. Guillard, M. Gamoudi, M. Maitrot, J.J. Andre, M. Martin, J. Simon, J. Appl. Phys. 56 (1984) 2323.
[29] A.M. Saleh, R.D. Gould, A.K. Hassan, Phys. Status Solidi A 139 (1993) 379.
[30] S.A. James, A.K. Ray, S. Silver, Phys. Status Solidi A 129 (1992) 453.
[31] R.D. Gould, Coord. Chem. Rev. 156 (1996) 237.
[32] K. Wihksne, A.E. Newkirk, J. Chem. Phys. 34 (1961) 2184.
[33] N.M. Amar, A.M. Saleh, R.D. Gould, Appl. Phys. A 76 (2003) 77.
[34] S.E. Harrison, K.H. Ludewig, J. Chem. Phys. 45 (1966) 343.
[35] A.K. Hassan, R.D. Gould, Int. J. Electron. 74 (1993) 59.
[36] A.O. Abu-Hilal, A.M. Saleh, R.D. Gould, Mater. Chem. Phys. 94 (2005) 165.
[37] N.F. Mott, E.A. Davis, Electronic Processes in Non-Crystalline Materials, second ed., Clarendon Press, Oxford, 1979.
[38] J.M Assour, W.K. Kahan, J. Amer. Chem. Soc. 87 (1965) 207.
[39] J.H. Sharp, M. Lardon, J. Phys. Chem. 72 (1968) 3230.
[40] M.M. El-Nahass, K.F. Abd-El-Rahman, A.A.M. Farag, A.A.A. Darwish, Phys. Scr. 37 (2006) 40.
[41] S.R. Elliott, Philos. Mag. 36 (1977) 1291.
[42] S.R. Elliott, Adv. Phys. 36 (1987) 135.
[43] Yu.A. Vidadi, L.D. Rozenshtein, E.A. Chistyakov, Sov. Phys. Solid State 11 (1969) 173.
[44] J.J. Fendley, A.K. Jonscher, J. Chem. Soc. Faraday Trans. I 69 (1973) 1213.
[45] B. Tareev, Physics of Dielectric Materials, Izd. Mir, Moscow, 1988, p. 105.
[46] A. Simon, R. Ravez, M.P. Crosnier, Y. Piffard, Tournoux, J. Phys. Chem. Solids 52 (1991) 11.
[47] J.M. Stevels, in: S. Flugge (Ed.), Handbuch der Physik, Springer, Berlin, 1957, p. 350.
[48] A.K. Jonsher, Dielectric Relaxation in Solids, Chelsea Dielectrics Press, London, 1983, p. 45.
[49] R. Arora, A. Kumar, Phys. Status Solidi A 115 (1989) 307.
[50] M. Ilyas, M. Zulferquar, H.K. Zishan, M. Hussain, Physica B 254 (1998) 57.

Available online at www.sciencedirect.com
ScienceDirect
Organic Electronics 7 (2006) 271–275
Organic Electronics
www.elsevier.com/locate/orgel

Root cause of hysteresis in organic thin film transistor with polymer dielectric

Young H. Noh, S. Young Park, Soon-Min Seo, Hong H. Lee *

School of Chemical and Biological Engineering, Seoul National University, 49-1 Shinlimdongsan, Seoul 151-742, Republic of Korea

Received 12 January 2006; received in revised form 11 March 2006; accepted 16 March 2006
Available online 17 April 2006

Abstract

Moisture is identified as the root cause of the hysteresis problem that can occur in the organic thin film transistor with a polymer gate dielectric. The hysteresis problem can be eliminated by simply drying the dielectric layer sufficiently prior to the deposition of semiconductor. The moisture effects are reversible such that the device output characteristics can be made to change from moisture-affected to moisture-free state and then back to the original moisture-affected state. The extent of hysteresis can be related to solubility parameter, a physical property unique to a polymer.

PACS: 85.30.Tv; 85.50.−n; 81.05.Lg

Keywords: Organic thin film transistor; Hysteresis problem; Polymer dielectric; Moisture

Organic thin film transistors (OTFTs) have now been utilized for various applications as in integrated circuits [1,2], flat panel display [3], and chemical vapor sensors [4,5]. While inorganic dielectrics such as silicon oxides can be used for the thin film transistor, polymer dielectrics have been explored because of the advantages that the solution processing with polymer can offer and the need for flexible device applications. Of the polymer dielectrics explored, the best dielectrics in terms of mobility are poly(vinylphenol) (PVPh) [6] with pentacene semiconductor and poly(2-hydroxyethyl methacrylate) (PHEMA) [7] with poly(3-hexylthiophene) (P3HT) semiconductor. The mobility obtainable with these polymer dielectrics is fairly close to that with silicon dioxide, i.e., about 0.1 $cm^2/V\,s$ for the polymer dielectrics and about 0.4 $cm^2/V\,s$ for SiO_2.

One major hurdle in utilizing polymer dielectrics for OTFTs is the hysteresis problem such an use of a polymer dielectric presents. Peng et al. [8] found that the exposure of the device in laboratory environment led to huge leakage currents due to moisture uptake when polyvinyl alcohol was used as the dielectric. It is known [9] in silicon devices that moisture, oxygen, or mobile charges cause hysteresis. In a recent study [10], a bilayer of dielectric was used to remedy the hysteresis problem. One of the findings in the study was that the hysteresis is bulk-related rather than interface-related.

* Corresponding author. Tel.: +82 2 880 7403; fax: +82 2 878 5043.
E-mail address: honghlee@snu.ac.kr (H.H. Lee).

1566-1199/$ - see front matter
doi:10.1016/j.orgel.2006.03.006

In this article, we look into the major cause of the hysteresis that can occur in OTFT when a polymer gate dielectric is used and investigate annealing effects on the hysteresis. We also relate a measure of the extent of hysteresis to a physical parameter unique to a given polymer dielectric. Metal–insulator–semiconductor (MIS) structure and pentacene OTFT are used for the investigation.

A literature survey of polymer gate dielectrics reveals that in general, the device with hydrophilic polymer dielectric tends to exhibit hysteresis in current–voltage (I–V) and capacitance–voltage (C–V) outputs whereas the device with hydrophobic polymer dielectric does not in many cases. It should be noted in this regard that the device even with hydrophobic dielectric does show hysteresis as in a self-assembled monolayer [11]. This revelation has led us to investigate the moisture effects on the device behavior.

The hysteresis is well revealed by capacitance–voltage (C–V) output. Therefore, MIS structure was fabricated to obtain C–V outputs for various polymer dielectrics. For the fabrication, aluminum layer was deposited on a cleaned glass substrate by thermal evaporation in a vacuum of 5.0×10^{-6} Torr, onto which a polymer dielectric was spin coated. Pentacene was then deposited by thermal evaporation to a thickness of 100 nm. Gold electrode 70 nm thick was defined by thermal deposition through a shadow mask. Dynamic C–V measurements were made with the MIS capacitor from −40 V to +40 V at a frequency of 100 kHz.

A stark contrast is shown in Fig. 1 between the capacitor with poly(methyl methacrylate) (PMMA) dielectric and that with poly(vinylphenol) (PVPh): no hysteresis with PMMA but a large hysteresis with PVPh. To investigate the hysteresis behavior, C–V measurements were also made with several other polymer dielectrics and the results are summarized in Table 1. The half width at the mid-capacitance (HWMC) (refer to Fig. 1b) was taken as a measure of the extent of hysteresis and this value is given in the last column of Table 1 for each of six polymer dielectrics tested. The higher the value of HWMC is, therefore, the lager the extent of hysteresis is. Also given in the next to the last column of the table is the solubility parameter for each of the polymers. With water as the reference, for which the solubility parameter is 47.8 $(MPa)^{1/2}$, the closer the solubility parameter of a polymer is to that of water, the more easily the polymer dissolves in water. Also given in the table are the molecular

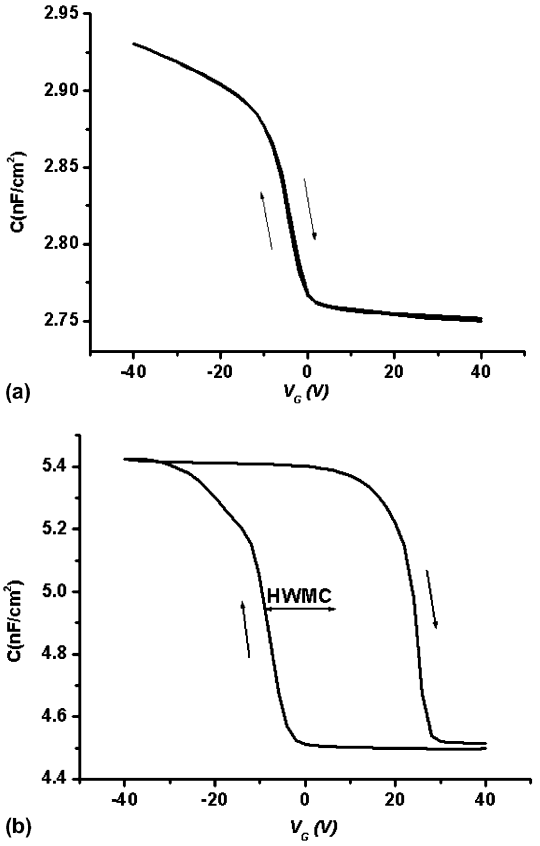

Fig. 1. Typical hysteresis behavior of polymer gate dielectric in MIS structure: (a) PMMA and (b) PVPh dielectric.

weight (M_w), the polymer solution concentration (C), the solvent used for spin coating, and the polymer film thickness (T).

There are two conclusions that can be made from Table 1. One is that the extent of hysteresis is small when a non-polar, organic solvent is used when compared with polar solvent. The other is that the solubility parameter is a trend indicator of the extent of hysteresis: a larger solubility parameter of polymer leads to a larger HWMC or a larger extent of hysteresis. The fact that the affinity of polymer dielectric to water can be related to the extent of hysteresis motivated us to look into the effects that the annealing of the gate polymer dielectric has on the device characteristics.

For the investigation, top-contact pentacene TFTs were fabricated with polymer gate dielectrics of PVPh and PMMA. Pentacene TFTs were first fabricated according to the usual procedure for them to be used as reference devices. To investigate the annealing effects, the PVPh dielectric layer was

Table 1
Extent of hysteresis for each of six polymer dielectrics tested: poly(methyl methacrylate) (PMMA), polystyrene (PS), poly(vinylacetate) (PVAc), poly(hydroxyethyl methacrylate) (PHEMA), poly(vinylphenol) (PVPh), poly(vinylalcohol) (PVA)

Polymer	M_w	C (wt%)/solvent	T(nm)	δ (MPa)$^{1/2}$	HWMC (V)
PMMA	300,000	10/toluene	940	18.2	0.5
PS	500,000	6/toluene	600	17.5	0
PVAc	500,000	5/toluene	450	19.2	2
PVPh	20,000	10/isopropanol	650	23.9	16.5
PHEMA	300,000	11/methanol	700	26.9	12
PVA	90,000	6/water	300	25.8	16.5

Solubility parameters of PVPh and PHEMA are from Refs. [13,14], respectively, and the rest from Ref. [12]. The solubility parameter of water is 47.8 (MPa)$^{1/2}$.

annealed at 120 °C (glass transition temperature of PVPh: 150–180 °C) in a high vacuum for an hour prior to pentacene deposition, which will be simply termed ''annealing'' henceforth. The electrical characteristics obtained with the devices are shown in Fig. 2(a)–(c) for the PVPh dielectric. Shown in the lower part of Fig. 2(a) for the reference device is the square root of the drain current ($I_D^{1/2}$) plotted against the gate voltage (V_G) scanned from +10 V to −80 V (forward scan) and then from −80 to +10 (backward scan) with a fixed source–drain voltage (V_{SD}) at −80 V. The hysteresis in the I–V curve is quite apparent. Given in the upper part of Fig. 2(a) is the drain current plotted against V_{SD} at a fixed V_G of −80 V. The upper curve was obtained by charging at a gate bias of −80 V for an hour and then scanning backward. The discrepancy in the saturation current shown in Fig. 2(a) between the V_G scan and the V_{SD} scan is another indicator of the hysteresis. The characteristics of the device made with annealed dielectric, shown in Fig. 2(b), reveal that the hysteresis is completely removed as a result of the annealing. Annealing at 120 °C in a high vacuum for 1 h should be sufficient enough for removing the moisture in the dielectric layer. This result is a clear evidence that moisture in the dielectric layer is responsible for the hysteresis. To investigate further the moisture effects, the annealed PVPh dielectric layer was exposed to the moisture at a relative humidity of 80% in Ar gas for 12 h prior to pentacene deposition, which will be simply termed ''moisture-exposed'' henceforth. The electrical characteristics of the device thus fabricated are shown in Fig. 2(c). It can be seen that the hysteresis appears again as a result of the exposure to moisture. In fact, the hysteresis problem is worse than with the reference device, which is a confirmation that moisture is at the root of the hysteresis problem. Note in this regard that annealing did not cause any noticeable change in the morphology. Although not shown, the reference device made with PMMA dielectric did not exhibit any hysteresis and there was no discrepancy in the saturation current. When the dielectric was exposed to moisture in the same way as for the PVPh dielectric, there was no hysteresis in I–V characteristics but some discrepancy in the saturation current.

To further confirm that moisture is at the root of the hysteresis, we set out to check whether the moisture effects are reversible. The results are shown in Fig. 3 in the form of $I_D^{1/2}$ vs V_G. The curve given by open rectangles represents the $I_D^{1/2}$ vs V_G curve for the reference device with PVPh dielectric that was obtained by sweeping from +10 V to −80 V. When the dielectric layer was annealed, the $I_D^{1/2}$ vs V_G curve shifted upward as indicated by the pointer 1. When this annealed dielectric layer was then exposed to moisture, the curve shifted downward as shown by the pointer 2. To show reversibility, this exposed dielectric layer was annealed again and as the pointer 3 indicates, the $I_D^{1/2}$ vs V_G curve shifted upward to the original moisture-exposed curve. The effective mobility, μ_{eff}, can be determined from:

$$|I_D| = \frac{1}{2}\mu_{eff} C_i \frac{W}{L}(V_G - V_T)^2 \quad (1)$$

where W and L are the channel width (3 mm) and length (130 μm), respectively, C_i is the insulator capacitance, and V_T is the threshold voltage. The mobilities thus determined show that the moisture effects are not significant. The mobilities for the device with annealed dielectric, the reference device and that with the moisture-exposed dielectric are 1.2×10^{-1}, 0.96×10^{-1} and 0.85×10^{-1} cm^2/V s, respectively.

As indicated earlier, there was a finding [10] that the hysteresis is bulk-related rather than interface-related. To further confirm the finding, we

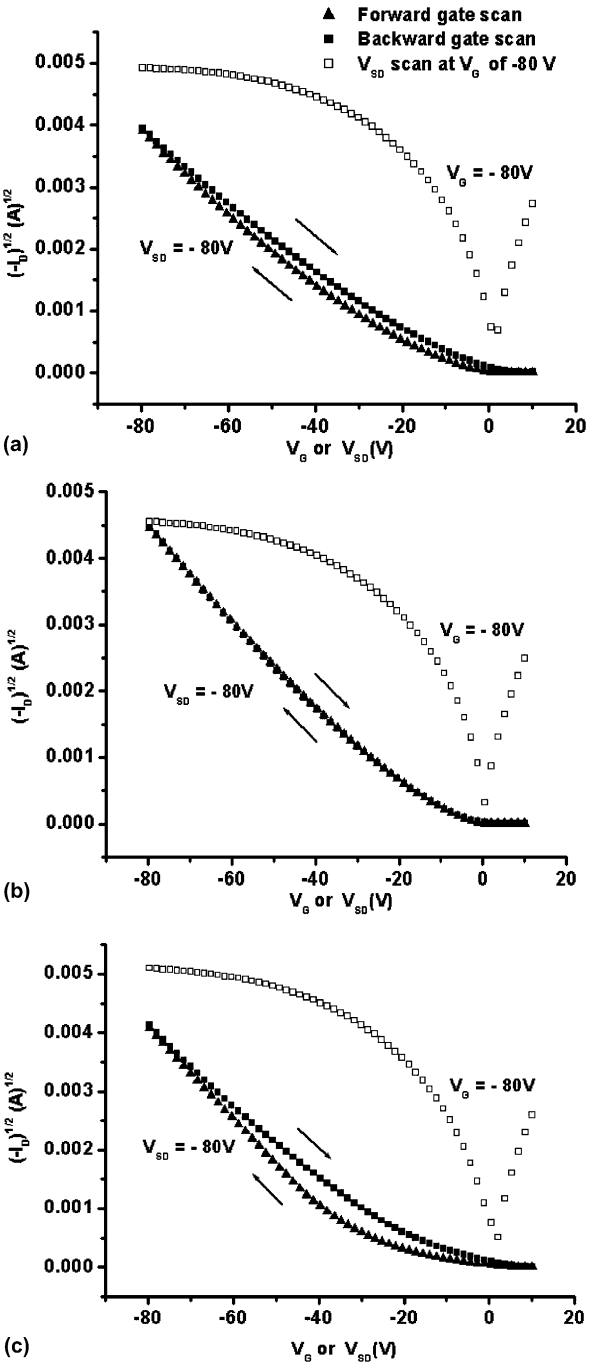

Fig. 2. *I–V* characteristics of Pentacene OTFT with PVPh gate dielectric: (a) a reference OTFT, (b) OTFT annealed 120 °C for an hour, (c) OTFT exposed to moisture for 12 h.

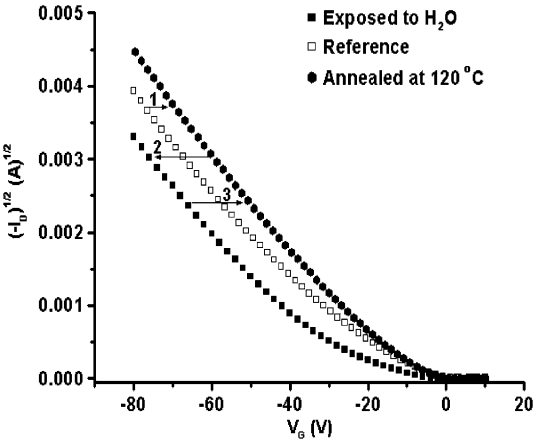

Fig. 3. $I_D^{1/2}$ vs V_G characteristics, showing the reversibility of moisture effects. Pointer 1 shows the change when the reference device was annealed, pointer 2 the change when the annealed device was exposed to moisture and pointer 3 the change when the exposed device was annealed again.

fabricated a double layer dielectric device, in which a relatively thick PVPh layer (10 wt%) was first formed on the gate followed by the formation of relatively thin PMMA layer (4 wt%) on the thick PVPh layer such that PMMA is in contact with pentacene. When compared with a single PVPh dielectric device, the extent of hysteresis was found to be larger. If the moisture charge traps at the semiconductor–dielectric interface were responsible for the hysteresis, the device with the double dielectric layer should not have any hysteresis since the device with a single PMMA dielectric does not show any hysteresis. Because of the presence of the top PMMA layer in the double layer dielectric, less moisture will evaporate in the course of pentacene deposition under high vacuum from the PVPh layer capped with the PMMA layer than from the bare PVPh layer. Therefore, the moisture concentration in the underlying PVPh layer is larger than that in a single PVPh layer, which led to a larger hysteresis.

Several evidences have been obtained that support the argument that moisture is at the root of the hysteresis. The most evident is that the hysteresis disappears upon annealing or sufficient drying. Another is the reversibility of moisture effects. When an annealed device, which does not show the hysteresis, is exposed to moisture and then it is annealed again, the hysteresis disappears again and the *I–V* characteristics are the same as those of the device initially annealed. Yet another is that the hysteresis is bulk-related rather than interface-related. Lastly, there are evidences that a hydrophobic polymer dielectric does not lead to the hysteresis, which can be explained by the fact that such a polymer repels moisture. There is a question, however, as to the

extent of the hydrophobicity. In term of solubility parameter, a polymer is more hydrophobic when its solubility parameter is further away from the solubility parameter of water. If the results in Table 1 are any indication, a polymer gate dielectric would not lead to any significant hysteresis when its solubility parameter is less than, say, 18 $(MPa)^{1/2}$.

In summary, we have shown that moisture is at the root of the hysteresis problem that can arise when a polymer gate dielectric is used for OTFT. The hysteresis can be completely removed by sufficiently drying the dielectric layer or annealing. The moisture effects are reversible in terms of presence/absence of hysteresis and $I_D^{1/2}$–V_G characteristics such that one can go from moisture-affected state to moisture-free state and backward without affecting the characteristics. For an OTFT with a polymer gate dielectric, the smaller the solubility parameter of the polymer is, the more the device is free from the hysteresis problem. For such an OTFT, the device may be considered free of the hysteresis problem if the solubility parameter of the polymer is less than 18 $(MPa)^{1/2}$.

Acknowledgements

This work was supported by the Nano-systems Institute National Core Research Center program of Korea Science and Engineering Foundation (NSI-NCRC program of KOSEF).

References

[1] H. Sirringhaus, N. Tessler, R.H. Friend, Science 280 (1998) 1741.
[2] B. Crone, A. Dodabalapur, Y.Y. Lin, R.W. Filas, Z. Bao, A. LaDuca, R. Sarpeshkar, H.E. Katz, W. Li, Nature (London) 403 (2000) 521.
[3] P. Mach, S.J. Rodirguez, R. Nortrup, P. Wiltzius, J.A. Rogers, Appl. Phys. Lett. 78 (2001) 3592.
[4] B. Crone, A. Dodabalapur, A. Gelperin, L. Torsi, H.E. Katz, A.J. Lovinger, Z. Bao, Appl. Phys. Lett. 78 (2001) 2229.
[5] Z. Zhu, J.T. Mason, R. Dieckmann, G.G. Malliaras, Appl. Phys. Lett. 81 (2002) 4643.
[6] H. Klauk, M. Halik, U. Zsxhieschang, G. Schmid, W. Radlik, W. Weber, J. Appl. Phys. 92 (2002) 5259.
[7] J. Park, S.Y. Park, S. Shim, H. Kang, H.H. Lee, Appl. Phys. Lett. 85 (2004) 3283.
[8] X. Peng, G. Horowitz, D. Fichou, F. Garnier, Appl. Phys. Lett. 57 (1990) 2013.
[9] D.K. Schroder, Semiconductor Material and Device Characterization, second ed., Wiley, New York, 1998, Chapter 6, pp. 337–419.
[10] S.Y. Park, M. Park, H.H. Lee, Appl. Phys. Lett. 85 (2004) 2283.
[11] H. Klauk, M. Halik, F. Eder, G. Schmid, C. Dehm, D. Rohde, S. Maisch, F. Effenberger, U. Zschieschang, IEDM Tech. Digest. IEEE 369 (2004);
M. Halik, H. Klauk, U. Zschieschang, G. Schmid, C. Dehm, M. Schütz, S. Maisch, F. Effenberger, M. Brunnbauer, F. Stellacci, Nature 431 (2004) 963.
[12] J. Brandrup, E.H. Immergut, Polymer Handbook, Wiley, New York, 1989.
[13] T. Çaykara, C. Özyürek, Ö. Kantolu, O. Güven, Journal of Polymer Science Part B 40 (2002) 1995.
[14] S. Arichi, S. Himuro, Polymer 30 (1989) 686.

Available online at www.sciencedirect.com
ScienceDirect
Organic Electronics 7 (2006) 276–286
Organic Electronics
www.elsevier.com/locate/orgel

Differences of interface and bulk transport properties in polymer field-effect devices

S. Grecu, M. Roggenbuck, A. Opitz, W. Brütting *

Experimentalphysik IV, Universität Augsburg, 86135 Augsburg, Germany

Received 8 July 2005; received in revised form 23 February 2006; accepted 15 March 2006
Available online 18 April 2006

Abstract

The influence of substrate treatment with self-assembled monolayers and thermal annealing was analysed by electrical and structural measurements on field-effect transistors (FETs) and metal–insulator–semiconductor (MIS) diodes using poly(3-hexylthiophene) (P3HT) as a semiconducting polymer and Si/SiO_2 wafers as a substrate.

It is found that surface treatment using silanising agents like hexamethyldisilazane (HMDS) and octadecyltrichlorosilane (OTS) can increase the field-effect mobility by up to a factor of 50, reaching values in saturation of more than 4×10^{-2} cm^2/V s at room temperature. While there is a clear correlation between the obtained field-effect mobility and the contact angle of water on the treated substrates, X-ray diffraction and capacitance measurements on MIS diodes show that structural and electrical properties in the bulk of the P3HT films are not influenced by the surface treatment. On the other hand, thermal annealing is found to cause an increase of grain size, bulk relaxation frequency and thereby of the mobility perpendicular to the SiO_2/P3HT interface, but has very little influence on the field-effect mobility. Temperature dependent investigations on MIS diodes and FETs show that the transport perpendicular to the substrate plane is thermally activated and can be described by hopping in a Gaussian density of states, whereas the field-effect mobility in the substrate plane is almost temperature independent over a wide range. Thus, our investigations reveal significant differences between interface and bulk transport properties in polymer field-effect devices.

PACS: 61.41.+e; 61.10.Eq; 72.80.Le; 73.61.Ph; 82.35.Gh

Keywords: Organic transistor; MIS diode; Self-assembled monolayer; Polythiophene; P3HT

1. Introduction

In recent years conjugated polymers have gained increasing interest as active materials in organic electronics. Their wide range of chemical variability in combination with low-cost solution processing make them attractive candidates for the fabrication of electronic devices such as light-emitting diodes (LEDs), photovoltaic cells (PVCs) and field-effect transistors (FETs) [1,2]. For the latter, high field-effect mobility is required and this is usually associated with high degree of structural order of the films. Poly(alkylthiophenes) have proven to be very promising candidates to achieve this goal. Charge

* Corresponding author.
E-mail address: Wolfgang.Bruetting@physik.uni-augsburg.de (W. Brütting).

1566-1199/$ - see front matter
doi:10.1016/j.orgel.2006.03.005

carrier mobility as high as 0.1 $cm^2/V\,s$ has been reported in regioregular poly(3-hexylthiophene) (rr-P3HT) [3], its structure being shown in Fig. 1.

In field-effect transistors the charge transport in the active channel is restricted to a few monolayers close to the interface [4], so it is to be expected that the surface treatment of the underlying substrate has a strong influence on the charge carrier mobility of P3HT FETs [5]. Another issue that comes into play is the anisotropy of charge carrier transport in polymeric field-effect devices. The regular arrangement of the alkane side groups promotes the formation of a lamellar stacking of the polymer chains with good π-orbital overlap between neighbouring chains. This orientation is expected to result in anisotropy of the mobility in the parallel and perpendicular direction with respect to the substrate. From the comparison of MIS diodes and FET data Scheinert et al. [6,7] and our group [8] have suggested that the charge carrier mobility in the substrate plane and perpendicular to it may differ by up to four orders of magnitude. Contrarily, Tanase et al. [9] have shown that differences between the values of the field-effect mobility and the values obtained from space-charge limited currents in diode structures is due to a charge carrier density dependence of the mobility in disordered hopping systems. In amorphous films of OC_1C_{10}-PPV and P3HT having field-effect mobility in the range 10^{-5} to 10^{-4} $cm^2/V\,s$, at room temperature, no evidence for a pronounced anisotropy of charge carrier transport was found.

In this paper we will demonstrate that by suitable substrate treatment the field-effect mobility of P3HT can be varied over a wide range whereby the surface energy of the Si/SiO_2 substrate will turn out to be the decisive control parameter. We will further show that by silanisation highly ordered films with field-effect mobility approaching 0.1 $cm^2/V\,s$ can be achieved in which the mobility in the substrate plane and perpendicular to it is strongly anisotropic.

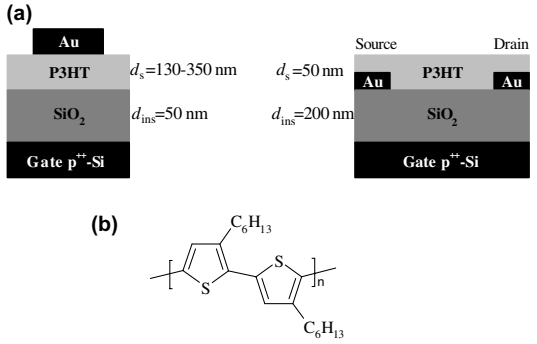

Fig. 1. (a) Device structure of MIS diode and field-effect transistor. (b) Chemical structure of regioregular poly-(3-hexylthiophene).

2. Experimental

2.1. Sample preparation

The substrates used in this work were highly p-doped Si wafers (1–5 mΩ cm) with high quality, thermally grown oxide as the gate insulator. Four different types of surface treatments were employed prior to the deposition of P3HT. The first substrate type was only wet-cleaned in an ultrasonic bath with solvents (acetone, isopropyl), in the following termed untreated. The other three were additionally exposed to oxygen plasma in order to create a hydrophilic surface which is required for the growth of self assembled monolayers through a silanisation reaction. One of these substrates, to which we will refer to as the O_2 plasma treated one, was used to prepare field-effect devices without any further treatment. The other two were used for silanisation immediately after the O_2 plasma treatment. Two types of silane molecules, hexamethyldisilazane (HMDS) and octadecyltrichlorosilane (OTS), respectively, were used. The HMDS treatment was done in the liquid phase at 60 °C for 24 h. The OTS treatment was carried out at room temperature, in a solution of OTS in *n*-heptane (0.86 mM), in an exsiccator. Samples were subsequently cleaned from residual OTS in chloroform in an ultrasonic bath. The values of the contact angles of water droplets on these substrates are summarized in Table 1.

The MIS diodes have been prepared on Si substrates with a 50 nm thin oxide layer (Fig. 1(a)). Solutions of regioregular P3HT in toluene (5 wt.%) were spin-coated at 2000 rpm resulting in films with a thickness of about 240–265 nm, except for the O_2 sample where it was about 130 nm. The P3HT was obtained from Merck and used without any additional purification. The molecular weight of P3HT was about 14 000. After a drying step (12 h, 10^{-3} mbar, 330 K), for all samples, top gold

Table 1
Contact angles of water for the different types of substrates

Sample type	O_2 plasma	Untreated	HMDS	OTS
Contact angle (°)	<5	60 ± 2	95 ± 1	110 ± 1

contacts were evaporated through a shadow mask, defining an area of about 28–33 mm^2. The FETs were prepared by spin-coating a 50 nm thick P3HT film onto Si/SiO_2 substrates with photolithographically patterned source and drain electrodes from Au, having a circular geometry to reduce leakage currents. The insulator thickness in this case was 200 nm, the channel length 5 μm and channel width 1000 μm. Thus, the resulting FETs were in the bottom-gate, bottom-contact configuration (Fig. 1). To avoid unintentional doping by oxygen the whole film preparation was performed in a glove-box system under inert atmosphere (<0.1 ppm oxygen and <1 ppm water content). The substrates for the X-ray diffraction analysis were normal glass. In this case the P3HT films were spin-coated from a 5 wt.% solution in toluene at 1000 rpm resulting in a thickness of about 400–450 nm. Additionally, heating at 350–420 K in high vacuum was applied to the samples in order to study the influence of further thermal annealing.

2.2. Measurement details

The X-ray diffraction (XRD) measurements were performed on a Siemens D-5000 diffractometer in grazing incidence geometry (0.03° between the incident beam and the sample, wavelength 1.54 Å), on pristine and annealed films for all types of samples.

The MIS diodes were characterized by measuring the capacitance–voltage (*C–V*) and capacitance–frequency (*C–f*) dependence, using a Solartron 1260 impedance/gain-phase analyzer coupled with a Solartron 1296 dielectric interface, in the frequency range from 1 to 10^6 Hz. An a.c. amplitude of 0.5 V and bias between −10 and +10 V was used to operate the diodes either in accumulation or depletion. Measurements of the output and transfer characteristics of FETs were performed using two independent source-measure units (Keithley 236). Both types of devices were measured and annealed in a cryostat in high vacuum ($<10^{-6}$ mbar) and darkness. The transfer between the glove-box and the cryostat was performed in a load–lock system so that the samples were not exposed to air at any time.

3. Results and discussion

3.1. Structural investigations

The structural ordering of the P3HT films was analysed by XRD measurements. P3HT films were prepared on untreated as well as O_2 plasma, HMDS and OTS treated substrates, as previously mentioned. Additionally the changes upon thermal annealing of the films (up to 24 h, 350 K) were analysed. A typical XRD spectrum of a P3HT film deposited on an OTS treated substrate is shown in Fig. 2(a). Clearly visible is the (100) peak at about 5.5° and additionally, much weaker, the (200) peak at 11°. The effect of thermal annealing resulting in an increase of peak height is shown as an example for the untreated substrate in Fig. 2(b).

The observed first order diffraction peaks were fitted in order to calculate the lattice constant *a* from the Bragg condition

$$2a\sin(\theta) = n\lambda. \quad (1)$$

In polycrystalline materials, the crystallite size *l* can be obtained from the Scherrer equation using the relation between full width at half maximum FWHM (2θ) of the diffraction peak and the diffraction angle 2θ

$$\mathrm{FWHM}(2\theta) = 0.94 \cdot \lambda / l \cdot \cos(\theta). \quad (2)$$

In polymers, however, the FWHM is usually dominated by variations in interplanar spacings. Thus the width of the XRD peaks can only give a qualitative hint to the degree of crystallinity. The calculated crystallite size from the Scherrer equation is about 10–11 nm for the as-prepared samples and increases up to 13 nm upon annealing. The increase of peak intensity after annealing indicates an increase of crystallinity which can be due to a higher number of crystallites and also an increase of

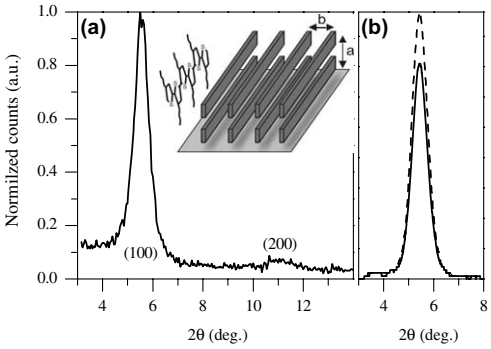

Fig. 2. Gracing incidence X-ray diffraction patterns of P3HT films on glass substrate: (a) P3HT on OTS treated substrate with first and second order diffraction peak. The inset shows a cartoon of the lamellar structure and layer spacing. (b) XRD peak of P3HT on an untreated substrate before and after annealing for 12 h at 350 K.

crystallite size. As other groups have shown, the structure model of rr-P3HT films consists of crystallites embedded into an amorphous polymer matrix [10,11]. All spectra show a diffraction peak at about 5.4° which is known for the organized lamellar structure of rr-P3HT with π–π-interchain stacking within the crystallites as shown in the inset of Fig. 2(a). This corresponds to a layer spacing for the (1 0 0) direction of about $a = 16$ Å which is comparable to literature data [12]. No evidence for the other two possible orientations of P3HT with respect to the substrate (corresponding to diffraction peaks around 23°) was found.

3.2. Capacitance measurements on MIS diodes

Capacitance-voltage (C–V) and capacitance–frequency (C–f) measurements were performed on MIS diodes prepared with different substrate treatment (Figs. 3 and 4). In general, the C–V characteristics of p-conducting organic MIS diodes show two regimes: accumulation at negative bias and depletion at positive bias with the measured value of C corresponding either to the insulator capacitance (C_{ins}) or to the series sum of the insulator capacitance and the capacitance of the organic semiconductor ($((C_{ins}^{-1} + C_S^{-1})^{-1}$), respectively. The absence of inversion is explained by the extraordinarily long generation times for minority carriers in wide-gap organic semiconductors [7].

Using the standard Schottky–Mott analysis, the doping concentration N_A can be extracted from the slope of the C–V curves in the transition region between accumulation and depletion via [13]

$$\frac{\partial}{\partial V}(C^{-2}) = \frac{2}{\varepsilon_0 \varepsilon_S q N_A A^2}, \tag{3}$$

where ε_0 is the permittivity of vacuum, ε_S the dielectric constant of the semiconductor and A the active diode area. Thus N_A can be extracted from a plot of $1/C^2$ versus the voltage applied to the Si bottom gate electrode as shown in Fig. 3(b) for the untreated sample. Also included in this figure is a simulation using an analytical expression for the C–V characteristics given by Scheinert and Paasch [7]. Within the error limits, both methods give the same values for the doping concentration N_A. We note that the simulated curves show inversion at voltages above 2 V, which is not seen experimentally for reasons discussed above. The simulation also yields information on the flat-band voltage. In an MIS structure the flat-band voltage

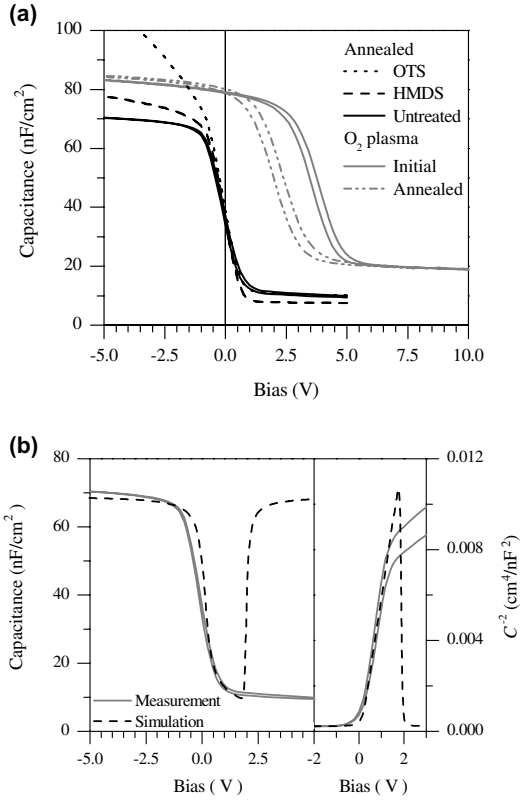

Fig. 3. (a) Capacitance–voltage characteristics of Au/P3HT/SiO_2/Si MIS diodes. The curves for the untreated, HMDS and OTS treated SiO_2 surface are shown only after annealing because there are no significant changes during annealing (measurement frequency = 1 Hz, apart from the untreated one, measured at 10 Hz). The characteristics for the O_2 plasma treatment are shown before and after annealing (measurement frequency = 1 Hz). (b) Comparison of measured and simulated C–V curves for the untreated substrate with $N_A = 7.2 \times 10^{15}$ cm^{-3} and $V_{FB} = +0.1$ V.

$$V_{FB} = \phi_{MS} - \frac{Q_{SS}}{C_{ins}} \tag{4}$$

incorporates the metal–semiconductor work function difference ϕ_{MS} and the equivalent fixed oxide charges Q_{SS} [14].

Applying the Schottky–Mott analysis to the C–V curves shown in Fig. 3(a) yields very similar doping concentrations in the range 2.5–7 × 10^{15} cm^{-3} for all samples, with the exception of the O_2 plasma treated one, where N_A is up to one order of magnitude higher (see Table 2). A closer look at the C–V curves reveals some interesting details: Whereas the untreated, HMDS and OTS-treated MIS diodes show a sharp transition between accumulation and depletion at zero or slightly positive flat-band voltage with only marginal hysteresis between

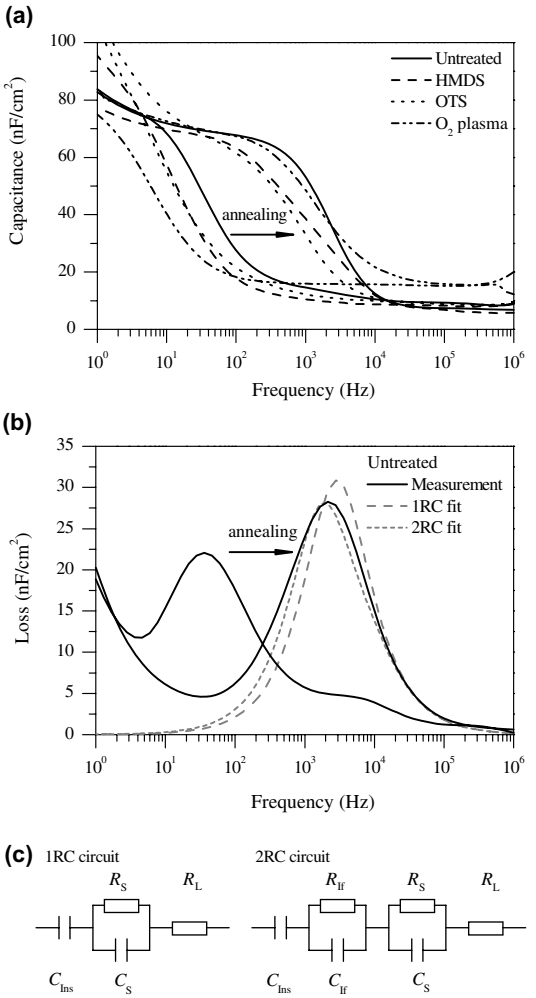

Fig. 4. (a) Capacitance–frequency characteristics of MIS diodes for the different substrate treatments before and after annealing. The changes due to annealing are indicated by the arrow. The curves are measured at $V_{BIAS} = -10$ V. (b) Example of loss-frequency characteristics of MIS diodes for the untreated substrate before and after annealing (at $V_{BIAS} = -10$ V). Comparison between the measured and fitted curves for annealed sample, using the 1RC and the 2RC circuit ($R_{S,1RC} = 2413\ \Omega$, $C_{S,1RC} = 2.4$ nF; $R_{S,2RC} = 1980\ \Omega$, $C_{S,2RC} = 2.6$ nF, $R_{If,2RC} = 1498\ \Omega$, $C_{If,2RC} = 20.7$ nF; the lead resistance is always negligible). The loss is defined as conductance over frequency (G/ω). (c) Schematic of the equivalent circuits used for the simulations.

increasing and decreasing bias sweeps, the O_2 plasma treated diode has a larger hysteretic behaviour and the transition between accumulation and depletion takes place at higher V_{FB} (between 2.1 and 3.6 V). This can be seen as an indication of interface states at the P3HT/SiO_2 interface created by the O_2 plasma treatment. We note that the measured capacitance does not saturate at the value of the oxide capacitance in the accumulation regime, but increases significantly above $C_{ins} \approx 70$ nF/cm^2. This can be explained by charge spreading beyond the active area defined by the top contact [15]. This effect is particularly pronounced for the OTS treated substrate which can be seen as an indication for the high in-plane charge carrier mobility for this treatment (see below).

The C–f curves measured at negative gate bias show a relaxation step from the accumulation capacitance to the lower value in depletion (Fig. 4(a)). The reason is the finite semiconductor bulk conductivity which sets an upper limit for the frequency up to which the injected majority carriers can follow the applied a.c. frequency and reach the accumulation layer at the interface to the oxide. Thus, this relaxation process yields information on the transport properties perpendicular to the substrate. The relaxation frequency f_R can be obtained from the maximum in the dielectric loss function (the conductance G divided by the angular frequency ω) as shown in Fig. 4(b). Using a simple equivalent circuit (with a capacitance C_{ins} for the insulator, one RC element for semiconductor and a lead resistance R_L, see Fig. 4(c)) the corresponding relaxation time $\tau_R = (2\pi f_R)^{-1}$ then directly yields the semiconductor bulk resistance according to [8,16]

$$\tau_R = R_S(C_{ins} + C_S). \tag{5}$$

We note that the simple circuit used here is not sufficient for a full description of the dielectric response of these MIS structures. For example, it has been demonstrated by Scheinert and Paasch [7] that another RC element for the accumulation layer should be included in the circuit. A comparison of fits using both the simple and the extended circuit model is included in Fig. 4(b). Even more sophisticated models have been suggested recently by Torres et al. [16]. However, by comparing fits with different circuit models we have carefully checked that the error in the semiconductor bulk resistance using the simplified analysis used here is always less than 20%.

With the knowledge of the doping concentration N_A from the C–V analysis one can then calculate the charge carrier mobility $\mu_\perp$ perpendicular to the insulator via:

$$R_S = \frac{d_S}{qN_A\mu_\perp A}. \tag{6}$$

Table 2
MIS diode parameters (relaxation frequency f_R, doping concentration N_A, flatband voltage V_{FB}, mobility perpendicular to the interface $\mu_\perp$) for different substrate treatments and thermal annealing

Treatment		f_R (Hz)	N_A (cm^{-3})	V_{FB} [V]	$\mu_\perp$ (cm^2/V s)
Untreated	As prepared	35	3.0×10^{15}	−0.1	9.3×10^{-7}
	Annealed	2190	7.2×10^{15}	+0.1	2.5×10^{-5}
HMDS	As prepared	10	3.1×10^{15}	+0.25	2.4×10^{-7}
	Annealed	1135	2.5×10^{15}	+0.2	3.3×10^{-5}
OTS	As prepared	7	7.1×10^{15}	+0.2	7.8×10^{-8}
	Annealed	667	5.8×10^{15}	+0.1	8.9×10^{-6}
O_2 plasma	As prepared	6	2.4×10^{16}	+3.6	1.1×10^{-8}
	Annealed	1488	3.0×10^{16}	+2.1	2.3×10^{-6}

From the comparison of different samples as shown in Fig. 4 one can notice two important features: On the one hand, substrate treatment has only a weak influence on the relaxation frequency, but on the other hand there is a strong effect of annealing on it. Whereas the pristine MIS diodes show relaxation frequencies in the range of 10–100 Hz the annealed devices have significantly higher values of f_R in the kHz range (see Fig. 4(b) and Table 2). This clearly indicates that the semiconductor bulk resistance in MIS diodes can be drastically reduced by up to three orders of magnitude by thermal annealing, whereas substrate treatment has little influence on it. Since the changes in doping upon annealing as determined from the C–V data are comparatively small, one has to conclude that the charge carrier mobility perpendicular to the insulator interface is strongly enhanced by annealing and can be correlated with the increase of crystallinity, as seen in the XRD measurements.

3.3. Current–voltage characteristics of OFETs

The output and transfer characteristics of bottom-gate bottom-contact FETs for the different treatments of SiO_2 substrates are shown in Fig. 5. The output characteristics (Fig. 5(a)) show a linear onset with little evidence for contact resistances and a well-defined saturation region for $|V_D| > |V_G|$. As seen from the output characteristics, at a given gate voltage (10 V), the current increases, from the untreated substrate towards the OTS-treated one, by more than one order of magnitude. This can either be caused by an increase of the charge carrier mobility or/and by a positive shift of the threshold voltage. Therefore one has to look at the transfer characteristics in more detail.

In the saturation regime the drain current is given by

$$I_{D,Sat} = \frac{W}{2L}\mu \cdot C_{ins}(V_G - V_T)^2. \quad (7)$$

Therein W and L are the channel width and channel length, respectively, C_{ins} is the specific capacitance of the oxide, V_G is the gate voltage and V_T the threshold voltage. The threshold voltage V_T in the Shockley model is related to the flat-band voltage, the bulk doping N_A and the bulk potential ϕ_B and is classically defined as the voltage where inversion starts

$$V_T = V_{FB} + \frac{eN_A d_S}{C_{ins}} - 2\varphi_B. \quad (8)$$

Here the transistors operate only in accumulation and the threshold voltage is determined as an experimental parameter from the fit of $\sqrt{I_{D,\,Sat}}$ versus V_G (Fig. 5(c)). Additionally, for analysing the subthreshold behaviour the switch-on voltage V_{SO} and the subthreshold slope were determined. The former is defined as the gate voltage where the current starts to increase [17] in the semi-logarithmic plot (Fig. 5(b)). The resulting parameters for the four different substrate treatments before and after annealing are summarized in Table 3.

Comparing the different treatments the most striking observation is the increase of the field-effect mobility by a factor of about 40 from the O_2 plasma treated substrate to the OTS-treated one before annealing (after annealing the increase is approximately 50). At the same time, the FET on the untreated substrate has the highest ON–OFF ratio, the most negative threshold voltage, and the lowest value of the inverse subthreshold slope. The ON–OFF ratio for the OTS-treatment is significantly

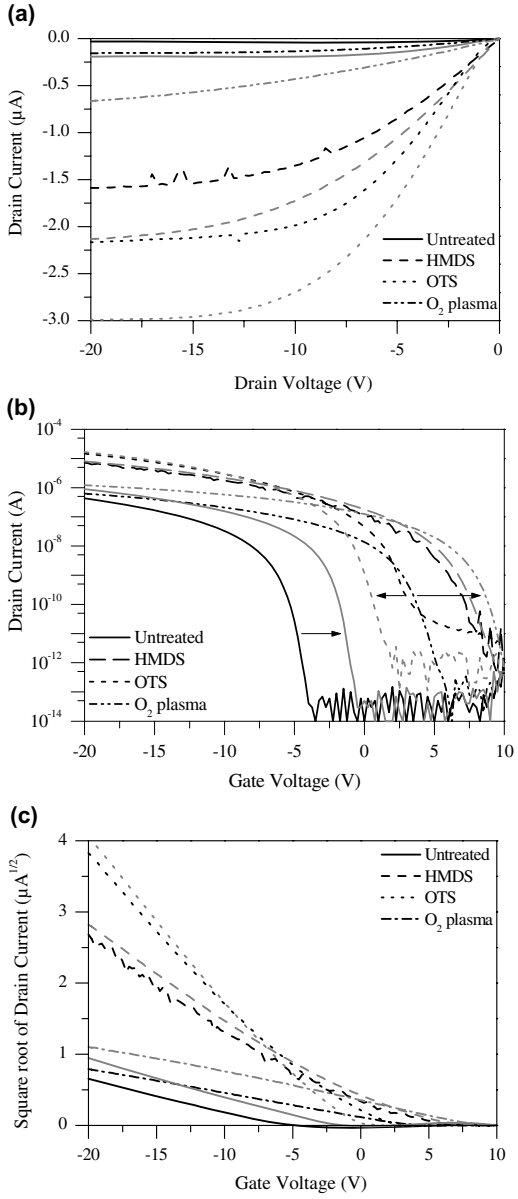

Fig. 5. (a) Output characteristics ($V_G = -10$ V) and (b, c) transfer characteristics ($V_D = -20$ V) of P3HT field-effect transistors with different substrate treatments before and after thermal annealing. The black curves are the initial ones and the grey curves after annealing. The changes are marked in Fig (b) by an arrow, except for the HMDS treatment. The transfer characteristics are shown on semi-logarithmic scale (b) and as the square root of the drain current (c).

lower but still acceptable. The HMDS-treated substrate has a high threshold voltage and also a high value of the inverse subthreshold slope. The highest value of V_T, however, is found for the O_2 plasma treated sample.

After thermal annealing the transfer characteristics show a shift of the switch-on and threshold voltage, but the magnitude and direction of the shift are not the same for all the samples. The FET on the untreated substrate shows a positive shift, whereas the shift for the OTS treated sample is smaller and negative. The HMDS treated FET is almost unchanged, while the V_T of the O_2 plasma treated sample increases dramatically. Further, the ON–OFF ratio and the inverse subthreshold slope are slightly improved by thermal annealing. Most remarkable, however, is the fact that there is no significant change in the field-effect mobility, reflected by the slopes of the curves in Fig. 5(c).

A comparison to MIS diode parameters (Table 2) does not show a direct correlation between flat-band voltage and threshold voltage as would be expected from Eq. (8). Nevertheless, there is a clear indication that oxygen plasma treatment leads in both devices to high positive values of V_{FB} and V_T.

3.4. Temperature dependence of MIS diode and FET characteristics

In order to get further insight into the transport mechanism in the substrate plane and perpendicular to it, we measured the temperature dependence of the *C–f* characteristics in MIS diodes and the transfer characteristics in FETs. The obtained curves in the temperature range between 200 and 420 K are shown in Fig. 6 for the OTS treated substrates. As shown in Fig. 6(a), the bulk relaxation frequency in the MIS diode shifts over almost four orders of magnitude in the investigated temperature range. We have also measured the temperature dependence of the *C–V* characteristics (not shown here). As reported in the literature [7], the flat band voltage is shifting towards higher positive values with increasing temperature; however, no significant changes in the doping concentration with temperature were observed up to 350 K. Thus, the strong shift of f_R directly reflects a strong temperature dependence of the perpendicular mobility in MIS diodes. Contrarily, in FETs (see Fig. 6(b)) the current at large gate voltage changes by only a factor of two over the whole temperature range indicating a very weak temperature dependence of the field-effect mobility parallel to the substrate. Even if the temperature is lowered to 40 K (not shown here) the mobility stays at about 1×10^{-2} cm^2/V s.

In Fig. 7(a) the temperature dependence of the mobility for MIS diodes and field-effect transistors

Table 3
OFET parameters (mobility μ_{sat}, switch-on voltage V_{SO}, threshold voltage V_T, ON/OFF ratio and inverse subthreshold slope S) for different surface treatments before and after thermal annealing

Treatment		μ_{sat} (cm^2/V s)	V_T (V)	V_{SO} (V)	ON/OFF	S (V/dec)
Untreated	As prepared	1.7×10^{-3}	−6.34	−4.06	1.2×10^{7}	0.44
	After annealing	2.2×10^{-3}	−2.90	−0.65	2.6×10^{7}	0.36
HMDS	As prepared	1.3×10^{-2}	−0.20	7.50	7.8×10^{7}	1.56
	After annealing	1.3×10^{-2}	0.90	9.50	1.9×10^{7}	0.85
OTS	As prepared	3.4×10^{-2}	−2.30	3.65	1.4×10^{6}	0.92
	After annealing	4.1×10^{-2}	−2.75	1.52	1.7×10^{7}	0.62
O_2 plasma	As prepared	8.4×10^{-4}	3.81	6.25	3×10^{6}	0.60
	After annealing	8.7×10^{-4}	12.64	10	4×10^{7}	0.49

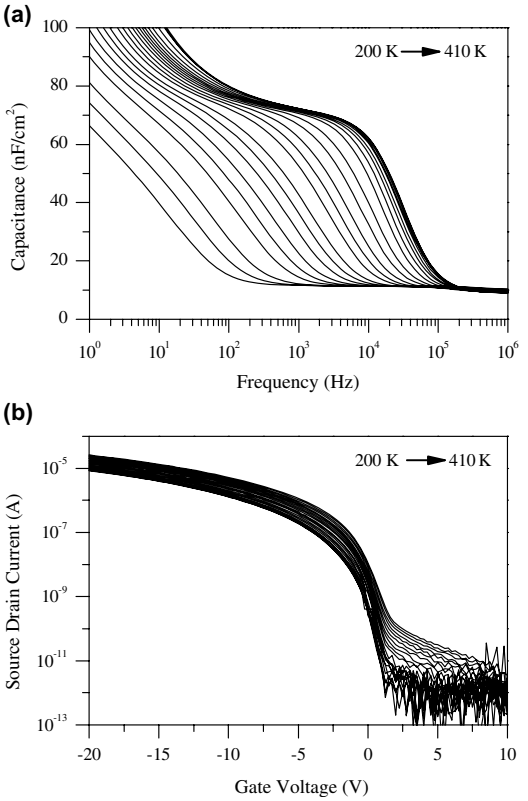

Fig. 6. Temperature dependence of MIS diode and FET characteristics of samples with OTS treated substrates and thermal annealing at 420 K, measured from 200 to 410 K in steps of 10 K: (a) C–f characteristics in accumulation ($V_{BIAS} = -10$ V), (b) transfer characteristics in saturation ($V_D = -20$ V).

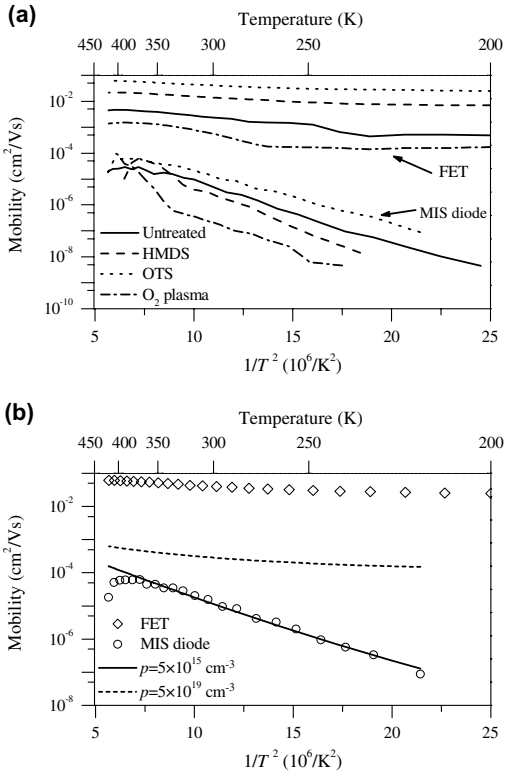

Fig. 7. (a) Temperature dependence of the field-effect mobility and the mobility from the bulk relaxation time in MIS diodes for different substrate treatments. The plot versus $1/T^2$ is in accordance with the correlated disorder model. (b) Comparison of FET and MIS diode mobility for the OTS treated substrates with the predictions of an analytical model for carrier density dependent hopping transport. The used parameters are: width of the DOS $\sigma = 98$ meV, intersite spacing $a = 1.4$ nm, carrier densities $p_{MIS} = 5\times10^{15}$ cm^{-3}, $p_{FET} = 5\times10^{19}$ cm^{-3}.

on the different substrates is shown. The change of the mobility in MIS diodes amounts to several orders of magnitude for all the samples and shows the typical behaviour of hopping transport.

It has been shown that charge transport in semiconducting polymers is well described by hopping models based on a Gaussian density of states [18–21]. Considering the correlated disorder model, where the expression for the mobility at low electric fields is given by

$$\mu(E \to 0) = \mu_0 \exp\left[-\left(\frac{3\sigma}{5kT}\right)^2\right], \quad (9)$$

with σ, the width of the Gaussian DOS, k is the Boltzmann's constant, T, the absolute temperature and μ_0, the microscopic mobility. Values for σ of 98 meV for the OTS treated MIS diode, 118 meV for the HMDS treated one, 110 meV for the O_2 treated one and 105 meV for the untreated substrate are obtained, while the prefactor μ_0 lies in the range $0.2–4 \times 10^{-3}$ cm^2/V s for all samples. As σ is a measure of disorder, this indicates that the degree of disorder in the bulk of the polymer films increases from the OTS treated substrate to the HMDS treated ones. The observed decrease of mobility above 380 K for the untreated, HMDS and OTS treated substrates is probably due to morphological changes rather than thermal degradation of the polymer. The O_2 treated sample, however, shows a steep increase of the perpendicular mobility at temperatures above 335 K, which could be related to changes at the oxygen plasma treated SiO_2-P3HT interface upon annealing at higher temperatures. This indicates that this substrate treatment is less stable as compared to the other three methods.

In contrast to the MIS diodes, the temperature variation of the field-effect mobility is very small. Among the different substrates, the OTS treated one shows the weakest dependence which also results in the highest mobility values at all temperatures. For the other samples, with smaller values of the field-effect mobility, the temperature dependence is somewhat stronger, but still less than one order of magnitude.

A central issue with respect to the observed big differences in the mobilities between FETs and MIS diodes is the question whether this is caused by a density dependent charge carrier mobility. Therefore we have compared our data with the predictions of an isotropic hopping model developed recently by Pasveer et al. [20,21] As an example, Fig. 7(b) shows a comparison of the temperature dependent mobility data for OTS treated structures with simulations based on this model. The required parameters are a hopping distance of 1.4 nm and a disorder parameter $\sigma = 100$ meV which are in going with the numbers given in Ref. [9]. The prefactor for the hopping mobility is adjusted to give the best agreement with our data for the MIS diode. Since there are no other free parameters in this model, the only difference between MIS diodes and FETs lies in the charge carrier densities. For the simulation we have taken the value of the doping $N_A = 5 \times 10^{15}$ cm^{-3} for the MIS diode and the estimated density of field-effect induced carriers at $V_G = -20$ V of about 5×10^{19} cm^{-3} (in agreement with Ref. [9]). The comparison shows that the different temperature dependencies of the mobility in MIS diodes and FETs are qualitatively reproduced by the isotropic hopping model; however, there is a quantitative difference of about two orders of magnitude by which the experimentally observed FET mobility is higher than predicted by this model.

3.5. Discussion

In this work, we have addressed interface and bulk transport in polymeric field-effect devices. We have seen significant differences between the field-effect mobility parallel to the polymer–SiO_2 interface and the mobility perpendicular to it. The room temperature mobility values in MIS diodes and FETs for different treatments are listed in Tables 2 and 3. The values are distinguished by surface treatment, which is characterized by a distinct contact angle, as well as by heat treatment. Clearly, the field-effect mobility increases by almost two orders of magnitude with the surface treatment, but does not change very much due to thermal annealing over the measured temperature range. Contrarily, the perpendicular mobility in MIS diodes increases upon annealing by up to four orders of magnitude and becomes almost independent of the substrate treatment. Thus, the effect of substrate treatment and thermal annealing is complementary in FETs and MIS diodes. Interestingly, the field-effect mobility shows a close correlation with the water contact angle on the substrate, increasing with the hydrophobicity of the SiO_2 surface. Such behaviour has recently also been observed by Veres et al. [5]. Fig. 8 shows their data together with the values obtained in this work. The excellent agreement is remarkable; the only exception being the O_2 plasma treated FET. However, this may be related to the fact that the O_2 plasma treatment additionally causes acceptor-like doping of the P3HT layer, which can enhance the observed mobility [22]. Thus one has to conclude that the modification of the surface energy of silicon oxide by appropriate treatments is of outmost importance for achieving high field-effect mobilities in OFETs with P3HT as a semiconducting polymer. As an explanation one can take the suggested lamellar structure of the

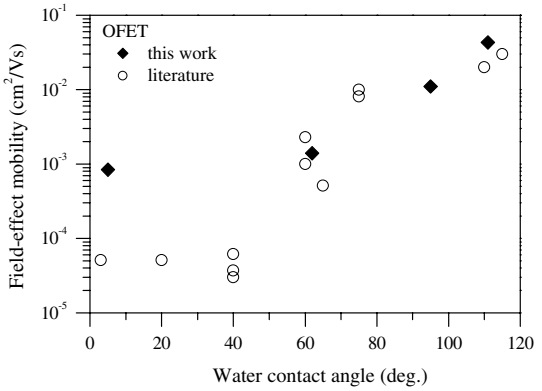

Fig. 8. Field-effect mobility versus water contact angle for different surface treatments of the SiO_2 insulator. The data shown as open circles are taken from Ref. [5].

P3HT chains (see. Fig. 2) in which the aliphatic side chains are standing upright on the substrate. Obviously, this structural motive within the first few monolayers is crucial for achieving good π–π-interchain stacking and thus high charge carrier mobility parallel to the surface of the SiO_2 gate dielectric.

These results are in going with recent publications on the charge carrier distribution within the active channel of organic FETs. Tanase et al. have shown that in disordered organic FETs the charge carrier density decreases already by one order of magnitude within the first nanometers away from the gate dielectric [4]. Taking into account the carrier density dependence of the mobility in disordered systems they could show that the macroscopically measured field-effect mobility corresponds to the local mobility of charge carriers directly at the interface. By performing in situ electrical measurements during layer growth Dinelli et al. came to a similar result for FETs with ordered layers of sexithienyl molecules [23]. They could show that the first two monolayers next to the dielectric interface dominate the charge transport. Therefore, it is understandable that the substrate treatment in bottom-gate FETs, based on rr-P3HT, has such a strong influence on the field-effect mobility. If this crucial parameter is not properly controlled in the experiment, large scattering of the field-effect mobility can be obtained in nominally identical devices (see e.g. the compilation of data from different groups in Ref. [5]). Further consequences of different surface treatments are seen in variations of related transistor parameters such as switch-on or threshold voltage, ON–OFF ratio and subthreshold slope. Pernstich et al. have recently published a comprehensive survey of these effects in pentacene FETs [24]. Although we have not studied these effects in detail, our data show that substrate treatment also has a strong influence on these parameters. Their control will be crucial for fabricating electronic circuits based on organic FETs.

Another outcome of our work is the huge difference of charge carrier mobility for OFETs and MIS-diodes. The perpendicular mobility is orders of magnitude smaller than the field-effect mobility parallel to the interface even after thermal annealing. Such differences between in-plane and sandwich geometry have been observed before on polymeric devices [6–9]. However, there was a debate whether this difference is due to a structural and electrical anisotropy of the polymer film or a consequence of the mobility depending on the carrier density. As Tanase et al. [9] have demonstrated by a comparison of FET mobility data with mobility data obtained from space-charge limited currents on diodes an apparent anisotropy of about a factor of 10 could be explained in amorphous polymers by the latter effect. Nevertheless, they also found that in ordered polymers (e.g. $OC_{10}C_{10}$-PPV) there exists a true electrical anisotropy which is not explained by different carrier densities in OFETs and diodes [25]. For the case of P3HT, they have observed FET mobilities up to 6×10^{-4} cm^2/V s at $V_G = -19$ V which is almost two orders of magnitude lower than the mobilities obtained here on silanised substrates. Thus it is questionable whether P3HT as prepared here can be treated as an amorphous polymer. The XRD data rather indicate that our P3HT films are nanocrystalline. Such a picture has recently been put forward also by Street et al. for regioregular poly(3,3‴-didodecylquarterthiophene) (PQT-12) [26]. We therefore suggest that the observed huge differences between the mobilities for transport parallel and perpendicular to the gate insulator interface are caused by a structural anisotropy. Preliminary ellipsometric measurements on our P3HT films have also indicated considerable optical anisotropy in P3HT comparable to poly(3-octylthiophene) [27].

Moreover, the most convincing argument for a true electrical anisotropy of P3HT films comes from our temperature dependent investigations on MIS diodes and FETs. The temperature dependent mobility data for both types of devices clearly show that charge carrier transport parallel and perpendicular to the dielectric interface can not be described by an isotropic hopping model. Thus, highly ordered films of rr-P3HT display a true electrical

anisotropy which emphasises the importance of the first few monolayers of the film for charge transport even more.

4. Conclusion

In conclusion, we have found that the mobility in P3HT field-effect transistors depends very sensitively on the nature of the interface to the gate dielectric. Using silanisation of SiO_2 with different agents the mobility can be increased by almost two orders of magnitude and reaches values of about 4×10^{-2} cm^2/V s. Interestingly, the structural ordering in the bulk of the films as controlled by thermal annealing has almost no influence on the field-effect mobility.

By comparing OFETs with MIS diodes we have found a large difference of charge carrier mobility parallel and perpendicular to the gate dielectric which can not be explained alone on the basis of a carrier density dependent hopping mobility. Owing to their lamellar structure, highly ordered P3HT films thus display anisotropic transport which needs to be considered in extended hopping models.

Acknowledgements

This work was supported by the Deutsche Forschungsgemeinschaft (Focus Programme 1121, "Organic Field-Effect Transistors") and the German Bundesministerium für Bildung und Forschung (Focus Programme "Polymer Electronics", POLITAG project). We thank Dago de Leeuw and Maxim Shkunov for helpful discussions and the companies Merck and Philips for providing materials and financial support.

References

[1] R.H. Friend, R.W. Gymer, A.B. Holmes, J.H. Burroughes, R.N. Marks, C. Taliani, D.D.C. Bradlay, D.A. Dos Santos, J.L. Brédas, M. Löglund, W.R. Salaneck, Nature 397 (1999) 121.

[2] C.J. Brabec, C. Winder, N.S. Sariciftci, J.C. Hummelen, A. Dhanabalan, P.A. Van Hal, R.A.J. Janssen, Adv. Func. Mat. 12 (2002) 709.

[3] H. Sirringhaus, P.J. Brown, R.H. Friend, M.M. Nielsen, K. Bechgaard, B.M.W. Langeveld-Voss, A.J.H. Spiering, R.A.J. Janssen, E.W. Meijer, P. Herwig, D.M. de Leeuw, Nature 401 (1999) 1038.

[4] C. Tanase, E.J. Meijer, P.W.M. Blom, D.M. de Leeuw, Org. Electron. 4 (2003) 33.

[5] J. Veres, S. Ogier, G. Lloyd, D. de Leeuw, Chem. Mater. 16 (2004) 4543.

[6] S. Scheinert, W. Schliefke, Synth. Met. 139 (2003) 501.

[7] S. Scheinert, G. Paasch, Phys. Stat. Sol. A 201 (2004) 1263.

[8] S. Grecu, M. Bronner, A. Opitz, W. Brütting, Synth. Met. 146 (2004) 359.

[9] C. Tanase, E.J. Meijer, P.W.M. Blom, D.M. de Leeuw, Phys. Rev. Lett. 91 (2003) 216601.

[10] A. Zen, J. Pflaum, S. Hirschmann, W. Zhuang, F. Jaiser, U. Asawapirom, J.P. Rabe, U. Scherf, D. Neher, Adv. Func. Mat. 14 (2004) 757.

[11] R.J. Kline, M.D. McGehee, E.N. Kadnikova, J.S. Liu, J.M.J. Frechet, M.F. Toney, Macromolecules 38 (2005) 3312.

[12] T.J. Prosa, M.J. Winokur, J. Moulton, P. Smith, A.J. Heeger, Macromolecules 25 (1992) 4363.

[13] S.M. Sze, Physics of Semiconductor Devices, Wiley, New York, 1982.

[14] D.A. Neaman, Semiconductor Physics and Devices: Basic Principles, third ed., McGraw-Hill, 2003.

[15] S. Ogawa, Y. Kimura, H. Ishii, M. Niwano, Jpn. J. Appl. Phys. 42 (2003) L1275.

[16] I. Torres, D.M. Taylor, E. Itoh, Appl. Phys. Lett. 85 (2004) 314.

[17] According to E.J. Meijer, C. Tanase, P.W.M. Blom, E. Van Veenendaal, B.-H. Huisman, D.M. de Leeuw, T.M. Klapwijk, Appl. Phys. Lett. 80 (2002) 3838, the switch-on voltage V_{SO} is related to the flat-band condition in the transistor and is an alternative measure of the turn-on voltage in polymeric field-effect transistors.

[18] H.C.F. Martens, P.W.M. Blom, H.F.M. Schoo, Phys. Rev. B 61 (2000) 7489.

[19] W.F. Pasveer, J. Cottaar, C. Tanase, R. Coehoorn, P.A. Bobbert, P.W.M. Blom, D.M. de Leeuw, M.A.J. Michels, Phys. Rev. Lett. 94 (2005) 206601.

[20] R. Coehoorn, W.F. Pasveer, P.A. Bobbert, M.A.J. Michels, Phys. Rev. B 72 (2005) 155206.

[21] P.W.M. Blom, M.C.J.M. Vissenberg, Mater. Sci. Eng. 27 (2000) 53.

[22] A.R. Brown, D.M. de Leeuw, E.E. Havinga, A. Pomp, Synth. Met. 68 (1994) 65.

[23] F. Dinelli, M. Murgia, P. Levy, M. Cavallini, F. Biscarini, D.M. de Leeuw, Phys. Rev. Lett. 92 (2004) 116802.

[24] K.P. Pernstich, S. Haas, D. Oberhoff, C. Goldmann, D.J. Gundlach, B. Batlogg, A.N. Rashid, G. Schitter, J. Appl. Phys. 96 (2004) 6431.

[25] C. Tanase, P.W.M. Blom, D.M. de Leeuw, E.J. Meijer, Phys. Stat. Sol. A 201 (2004) 1236.

[26] R.A. Street, J.E. Northrup, A. Salleo, Phys. Rev. B 71 (2005) 165202.

[27] U. Zhokhavets, G. Gobsch, H. Hoppe, N.S. Sariciftci, Synth. Met. 143 (2004) 113.

Available online at www.sciencedirect.com
ScienceDirect
Organic Electronics 7 (2006) 287–294
Organic Electronics
www.elsevier.com/locate/orgel

Scanning tunneling and photoemission spectroscopies at the PTCDA/Au(1 1 1) interface

Nicoleta Nicoara [a,b], Elisa Román [a], José M. Gómez-Rodríguez [b], José A. Martín-Gago [a], Javier Méndez [a,*]

[a] *Instituto de Ciencia de Materiales de Madrid CSIC, Fisica e Ingenieria de Superficies, Campus de Cantoblanco, E-28049 Madrid, Spain*
[b] *Departamento de Física de la Materia Condensada, Universidad Autónoma de Madrid, E-28049 Madrid, Spain*

Received 11 January 2006; received in revised form 17 March 2006; accepted 21 March 2006
Available online 19 April 2006

Abstract

We have studied the electronic properties at the interface of a PTCDA molecular film on Au(1 1 1) by means of scanning tunneling microscopy (STM), scanning tunneling spectroscopy (STS) and angle resolved ultraviolet photoelectron spectroscopy (ARUPS). Measurements were performed for the clean Au(1 1 1) surface as well as for 1 ML and multilayer coverage of PTCDA. STS curves recorded for 1 ML PTCDA film show a feature at the density of states inside the PTCDA gap and a metallic behavior, in contrast to higher coverage, where a semiconductor behavior is observed. By relating this information to the band dispersion of the electronic states close to the Fermi edge, we can assign this electronic feature to the Au(1 1 1) Shockley surface state. By comparison of intramolecularly resolved STM images with first-principles calculations of the free molecule we show that the electronic molecular states at the interface are not altered by the gold surface. All these facts indicate a weak interaction of the PTCDA molecules with the Au surface and we conclude that the observed metallicity of the interface is provided by the gold substrate rather than by the organic layer.

PACS: 68.37.Ef; 79.60.Fr; 73.20.−r

Keywords: Scanning tunneling microscopy; Scanning tunneling spectroscopy; Photoemission spectroscopy; PTCDA; Organic molecules; Surface states

1. Introduction

In the last years, an intensive research has been focused on organic materials with promising applications in optoelectronic devices [1,2]. These materials incorporate interesting properties such as self-organization, flexibility, new electronic (semiconducting or metallic) and optoelectronic properties. The interface between the organic film and the inorganic material is of special interest, because it influences the structure and morphology of the molecular layers, and hence, also their properties. Therefore, a detailed understanding of the processes taking place at the interface and how they affect the

* Corresponding author. Tel.: +34 913348983; fax: +34 913720623.
E-mail address: jmendez@icmm.csic.es (J. Méndez).

1566-1199/$ - see front matter © 2006 Elsevier B.V. All rights reserved.
doi:10.1016/j.orgel.2006.03.010

electronic properties of the organic/inorganic system [3] is not only of fundamental importance, but also of technological relevance.

PTCDA (3,4,9,10, perylene tetracarboxylic dianhydride, $C_{24}O_6H_8$) are small conjugated molecules belonging to perylene derivatives, which have been extensively studied along the past years. These molecules are considered as a model system, due to their ability of forming well-ordered layers on a variety of substrates. PTCDA films present semiconducting behavior, strong anisotropy in electronic transport and relevant optical properties [2].

Several studies have focused on the growth mode and structural properties of PTCDA on different metallic substrates: silver [4–8], copper [9,10] and gold [11–16]. Particularly, for PTCDA on Au(1 1 1) the structure and morphology of this system have been studied as a function of growth parameters [14]. A layer-by-layer growth has been reported for the first several layers [11], followed by island formation for multilayer coverage [15]. Even in the sub-monolayer regime PTCDA forms large domains with well-ordered molecules. PTCDA molecules typically assemble on most substrates in a herringbone structure, with a rectangular unit cell consisting of two almost coplanar molecules [13,14,16]. For the Au(1 1 1) substrate, also a less dense square assembling can be obtained [15], which is not treated in this paper.

Scanning tunneling microscope (STM) has demonstrated its ability for the investigation of ordered organic films grown on different substrates, providing structural and morphological properties. Besides the topographical imaging, information about the surface density of states from the voltage dependence of the current can be obtained from scanning tunneling spectroscopy (STS). The advantage of STS, compared to other spectroscopic techniques, is to locally probe the electronic properties. On the other hand its interpretation is not straightforward due to the convolution with the tip states. In this sense the combination of STS and ultraviolet photoemission spectroscopy (UPS) is a powerful tool to determine electronic properties at the interface.

One aspect treated in this paper is the interaction of the PTCDA molecules with the metallic substrate. In previous works, the interaction of PTCDA molecules with silver surfaces has been described as strong [17], involving an interaction between the π molecular orbitals and the metallic surface. For the Ag(1 1 1) substrate, a metallic behavior for the first PTCDA monolayer has been reported [18]. In the case of Au substrates a weaker interaction has been observed [19]. STS measurements for PTCDA grown on gold have been performed [20,21], however, the metallicity of the first monolayer has not been addressed up to now.

Another aspect here mentioned is the influence of the organic molecules on the gold surface state. Tunneling spectroscopic studies have reported on the behavior of the surface states of noble metals [22], and how these surface states are modified by adsorbates [23–27].

In this work we focus on the electronic states close to the Fermi energy of the PTCDA/Au interface by combining STM, STS and angle resolved UPS (ARUPS). Through several experimental observations we assert that there is a weak interaction between the gold substrate and the first organic monolayer, which does not disrupt the Au(1 1 1) surface state even though the PTCDA overlayer completely covers the Au surface. We conclude that the metallic behavior of the interface is provided by the gold substrate beneath.

2. Experimental

STM and STS experiments were carried out with a home-built UHV STM [28]. Ultraviolet photoelectron spectroscopy measurements were performed in a separate UHV chamber equipped with a HeI (21.2 eV) radiation source and a hemispheric electron analyzer. The angular aperture of the analyzer is 2°.

Au(1 1 1) single crystal sample was cleaned by several sputtering and annealing cycles (sputtering at $\sim 1 \times 10^{-6}$ Ar pressure, annealing at $\sim$700 K).

The organic films were deposited under ultra-high vacuum from home-made sublimation cells. Previous degassing of the PTCDA cell was performed. The deposition rate was about 0.5 ML per minute and was calibrated via scanning tunneling microscopy and previously by a quartz microbalance. Prior to the photoemission experiments, a careful estimation of the PTCDA coverage was performed from XPS measurements (data not shown here).

All the measurements were taken at room temperature. For the STM/STS experiments, tungsten (electrochemically etched) and Pt–Ir (mechanically cut) tips were used. W tips were prepared in situ by thermal annealing and field emission, until stable field emission currents were obtained. For the system investigated here, the most reproducible spec-

troscopic data were obtained with mechanically cut Pt–Ir tips. They were recorded at stabilization bias voltages between −1 and −2.5 V, with voltages referred to the sample. Higher voltages damaged or lifted up the molecules from the surface. Tunneling spectroscopy was performed with set-point currents as low as possible, in order to avoid strong interaction between the tip and the organic layer [29], but high enough to have signal at zero voltage [30]. STS curves were measured by averaging several successive plots obtained on the same position and conditions. All the STM/STS data acquisition and processing were done using the WSxM software [31].

3. Results and discussion

3.1. Scanning tunneling microscopy

Detailed characterizations of the structural properties and the growth mode of PTCDA/Au have been previously reported [11–16]. However, for sub-monolayer coverage several aspects can be discussed from topographic STM images. In Fig. 1 we show a representative STM image of PTCDA molecules deposited at room temperature on a Au(1 1 1) substrate for a sub-monolayer coverage. On the left side of the STM image, the clean Au(1 1 1) substrate is observed with the characteristic $(22 \times \sqrt{3})$ reconstruction. On the right side, adsorbed PTCDA molecules form an ordered domain assembled in the so-called herringbone structure [13,14]. This structure is characteristic of the (1 0 2) plane of PTCDA bulk [13]. The noisy appearance in the STM images at the boundary of the PTCDA area is due to a high mobility of PTCDA at room temperature, with molecules diffusing on the surface. Isolated molecules are only observed when they are stacked along the steps or pinned at surface defects.

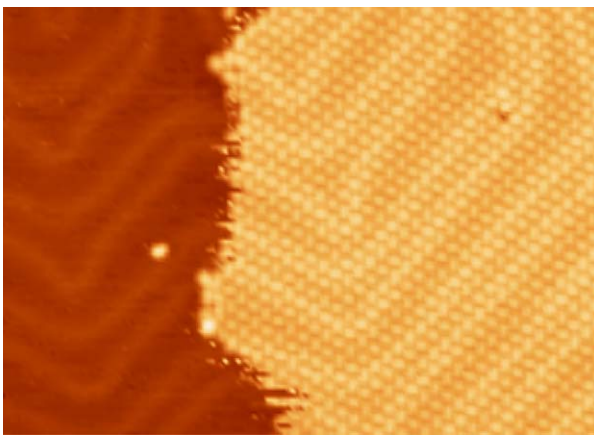

Fig. 1. Constant current STM image of sub-monolayer PTCDA coverage on Au(1 1 1). The right side of the image corresponds to a gold terrace covered with 1 ML of PTCDA. The left side corresponds to the clean substrate. The substrate reconstruction is still visible through the organic layer (57 nm × 40 nm, $V = -2.0$ V, $I = 0.16$ nA).

Another interesting fact is that already in the first monolayer PTCDA molecules adopt a structure similar to the bulk molecular crystal [32]. Furthermore, it can be noticed in Fig. 1 that the Au(1 1 1) reconstruction is not lifted up upon PTCDA monolayer adsorption [13,15,16]. The gold reconstruction is still visible underneath the PTCDA molecular layer. All these statements point out towards a weak interaction of the molecules with the gold substrate and that the molecule–molecule interaction dominates over the molecule–substrate interaction [15].

Additional proofs for the weak interaction come from the bias-dependent imaging of PTCDA on gold. In Fig. 2(a) and (c) we show STM images acquired at both polarities on a region covered by 1 ML. In these constant current images we resolve intramolecular features of the PTCDA molecules. The images reveal distinct internal structures for unoccupied molecular states ($V = +1.0$ V) and for occupied molecular states ($V = -1.8$ V).

For the positive biased sample, where the electrons tunnel into the unoccupied states of the sample, we observe 10 maxima in the STM topographic images (Fig. 2(a)). In the case of a negative bias applied to the sample, which means electrons tunneling from the occupied states, the image reveals eight maxima for each molecule (Fig. 2(c)), and all the molecules present a deeper area parallel to the long axis, which splits the molecules in two parts. Profiles along the molecules have been added for better recognition of the maxima.

In order to gain insight into the meaning of these intramolecular features, we have performed first-principles calculations for the PTCDA free molecule. These calculations were done within density functional theory (DFT) in the local density approximation (LDA) [33], using the SIESTA method [34,35]. Core electrons were replaced by norm-conserving pseudopotentials [36], whereas valence electrons were described using a double-ζ plus polarization (DZP) basis set. A real-space grid with a cutoff of 50 Ry was used. Only the Γ point was used in reciprocal space. The geometries were

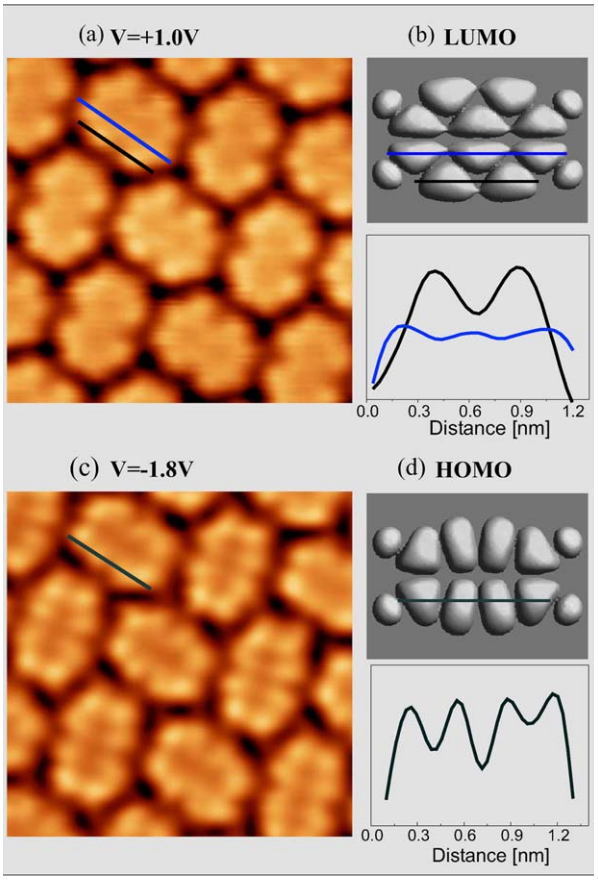

Fig. 2. (a,c) STM images of 1 ML PTCDA on Au(1 1 1) at RT obtained at $V = +1.0$ V (unoccupied) and $V = -1.8$ V (occupied), respectively (4.2 nm × 4.2 nm, $I = 0.6$ nA). Notice the similarity between the unoccupied (occupied) states resolved in single molecules and the corresponding calculated LUMO (HOMO) of the free molecule, displayed in (b) and (d), respectively. Profiles along a molecule are shown for better comparison.

relaxed until the maximum residual force was below 0.04 eV/Å.

Fig. 2(b) and (d) present charge density isosurfaces obtained from the DFT calculation and corresponding to the lowest-unoccupied molecular orbital (LUMO) and the highest-occupied molecular orbital (HOMO) of the free molecule [37]. These images are in good agreement with previous calculations by Scholz et al. [38]. The experimental STM image shown in Fig. 2(a), measured at +1.0 V clearly resembles the calculated LUMO of the isolated molecule, while the STM image measured at −1.8 V can be directly related to the calculated HOMO. Although broadening of the orbitals cannot be excluded, the strong similarity between the calculated orbitals and the STM images (see Fig. 2) suggests that the HOMO and LUMO molecular orbitals, are not significantly modified upon adsorption of PTCDA on gold.

When there is a strong coupling between adsorbate and substrate states, a modification of the electronic structure is expected, and this is generally reflected in the STM image. Thus, for systems with a strong bonding between the organic molecules and the substrate, as PTCDA on Si(1 0 0) [39] and on Si(1 1 1) [40], high-resolution STM images show that the intramolecular features differ from the HOMO and LUMO of the isolated molecule. Similarly, for PTCDA on silver [41,42] and for PTCDA on graphite [43], where a charge transfer is proposed, shifting of the LUMO towards the Fermi level partially filling this band has been reported [41,43]. In this case, images at both polarities around the Fermi level look like the LUMO. In contrast, for systems where the molecule has a rather weak interaction with the substrate, as reported for pentacene on isolating layers [44] or for the results described in this paper, the intramolecular features resemble the molecular orbitals of the isolated molecule, and this occurs at the corresponding voltages. Again, these findings point out to a rather weak interaction of PTCDA molecules with the gold substrate.

3.2. Scanning tunneling spectroscopy

The main STS measurements were performed for samples with sub-monolayer PTCDA coverage, so that clean gold and PTCDA covered areas could be simultaneously imaged (Fig. 1). Before and after recording spectroscopic data on the adsorbate layer, reference I–V curves were recorded on the clean fcc-gold area. Only when the Au(1 1 1) spectrum with the characteristic Shockley-type surface state is achieved, we follow recording current–voltage curves on the PTCDA molecules. With this approach, we ensure a "*good state of the tip*" and therefore, that the additional features which appear in the case of STS on molecules, are indeed related to PTCDA molecular states.

Fig. 3(a) shows tunneling spectroscopy results acquired on the clean Au(1 1 1) surface (dashed line) and on the 1 ML PTCDA region (solid line). STS results for 2 ML PTCDA/Au(1 1 1) are also included (gray line) for comparison. The spectra are displayed as the differential conductance (dI/dV) vs. V plot. The curve for the clean gold exhibits a characteristic feature, with the onset at ∼− 0.4 eV,

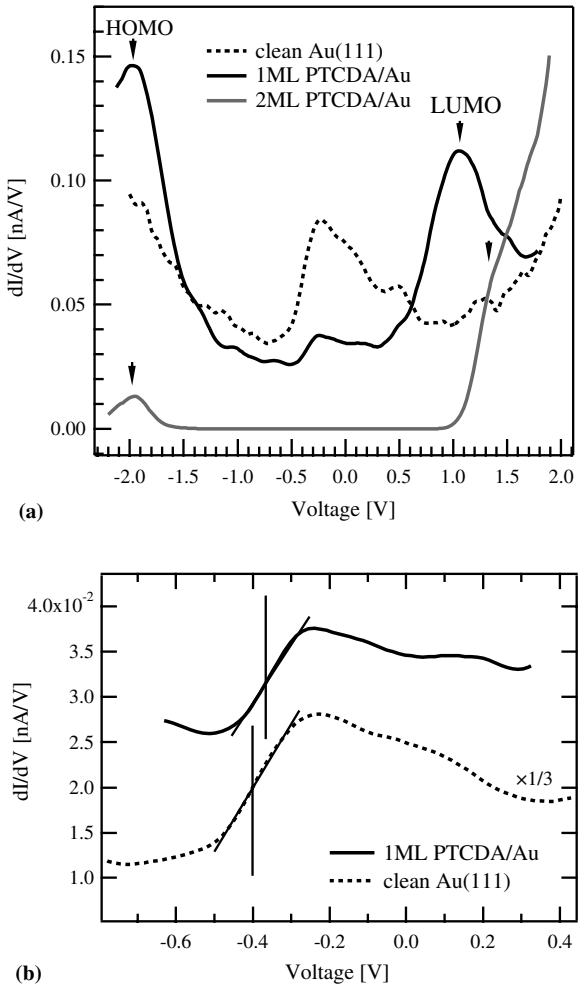

Fig. 3. (a) Tunneling spectroscopy performed at RT on clean Au(1 1 1) and on 1 ML PTCDA covered gold. For clean gold (dashed line) the onset of Shockley surface states is identified around −0.4 V. A similar peak and the molecular related features HOMO and LUMO appear in the differential conductance spectra recorded on PTCDA monolayer (solid line). STS for 2 ML PTCDA on gold (gray line) shows semiconducting behaviour characteristic for PTCDA. The plots correspond to the differential conductance that was derived from averaging several *IV* curves and subsequent mathematical differentiation. (b) Detail of the gold surface state region where a shift of ∼40 meV can be observed.

corresponding to the Shockley-type surface state of the Au(1 1 1) surface [45,46]. Subsequent spectroscopic curves acquired for 1 ML PTCDA on Au(1 1 1) show a metallic behavior characterized by a non-zero density of states at zero voltage. The differential conductance plot for this case (solid line in Fig. 3(a)) shows a peak close to the Fermi level similar to the one observed for the clean substrate though slightly shifted in energy. In the limit of the room temperature STS experimental resolution,[1] a shift of ∼40 meV toward the Fermi level for the PTCDA monolayer has been reproducibly obtained (Fig. 3(b)). The value of this shift and its direction toward the Fermi level are comparable with STS results reported for rare gases on Au(1 1 1) [27], where shifts of 150 meV for Xe and 80 meV for Kr have been obtained. For other adsorbates, the reported energy shift of the bottom of the band is much higher: 300 meV for Pd on Au(1 1 1) [25] and 230 meV for NaCl on Cu(1 1 1) [26]. These energy shifts can be qualitatively understood as induced by a modification of the image potential and work function of the surface upon coverage [26].

Two additional peaks are observed in the STS results for 1 ML PTCDA (solid line in Fig. 3(a)): one centered around +1.0 V above the Fermi level, and another one around −1.9 V below the Fermi level. These features can be attributed to the lowest-unoccupied (LUMO) and the highest-occupied (HOMO) molecular states of the PTCDA respectively. Tsiper et al. [21] reported these peaks located at +1.3 V and −2.2 V. A possible explanation for this discrepancy could be related to different tip–surface interaction or tunneling distance [29,30].

The STS measurements for 2 ML PTCDA coverage (gray line in Fig. 3(a)) do not show any structure close to the Fermi level, corresponding to the expected semiconductor behavior of the organic layer. In the curve we observe the onset of the LUMO at around +1.0 V, and in the filled states, a peak centered at about −2.0 V attributed to HOMO. The position in energies of both features may slightly shift in the STS spectra depending on the tunneling conditions; the value of the band gap varies between 2.7 and 3.0 eV, when measured from peak-to-peak in the differential conductance (2.4–2.5 eV when measured in the logarithmic representation). For higher PTCDA coverage (3–8 ML), the results are similar to the 2 ML case but the gap increases slightly, approaching a value of 3.3 eV (2.6 eV in the logarithm), in comparison with 2.44–2.55 eV reported for the transport gap of PTCDA [47]. Other authors have reported even lar-

[1] The thermal broadening of the STS data measured at room temperature can be estimated as ∼4 kT ≈ 100 meV. This value is compatible with the width of the Au(1 1 1) surface-state band onset measured in Fig. 3.

ger gap values [21,48] with a similar dependence with coverage, interpreted as a change in the polarization with the organic layer thickness [21].

The presence of the peak in the STS curves of 1 ML of PTCDA at ~ -0.4 eV (see Fig. 3) is somehow unexpected, since it is known that the organic semiconductor PTCDA has no molecular states in this region, and LUMO and HOMO molecular orbitals are far from the Fermi level. Moreover, this feature being localized close to the Fermi level may confer metallicity to the PTCDA adsorbed layer. Metallicity of the surface overlayer has been reported for PTCDA on the Ag(1 1 1) surface [18], where a chemisorption process takes place at the interface. These authors [18] have suggested that the surface state of the Ag(1 1 1) could play a significant role in this effect. The question that arises in our case is whether the feature observed in the STS plots belongs to the Au(1 1 1) surface states or is rather due to new electronic states formed at the PTCDA/Au interface. The first case suggests a tunneling process of the surface states through the PTCDA layer. On the other hand, the second one points out toward a PTCDA–Au bonding different than a simple Van der Waals interaction that could lead to the formation of states in the overlayer gap. In order to solve this question we have performed ARUPS measurements.

3.3. Angle resolved photoemission

Fig. 4 shows the valence band photoemission spectra recorded at normal emission in the region close to the Fermi level as a function of PTCDA coverage. The peak with a binding energy of 0.4 eV in the upper curve corresponds to the Au(1 1 1) Shockley-type surface state [45,46]. In the subsequent spectra we observe that the gold surface state is progressively attenuated as the coverage is increased, being still visible at approximately 1 ML and disappearing at $\sim$2 ML coverage (the surface state is still visible at 1.5 ML, as can be observed in Fig. 4). There is no shift, within the experimental resolution, of this electronic state as coverage increases, indicating the absence of important interaction between the layer and the Au surface.

PTCDA related electronic states are not visible in the UPS spectra up to few layers coverage due to the huge contribution and the large mean free path of the valence band gold electrons. No extra states close to the Fermi level can be resolved, neither for the PTCDA/Au interface, nor for coverages larger than 1 ML.

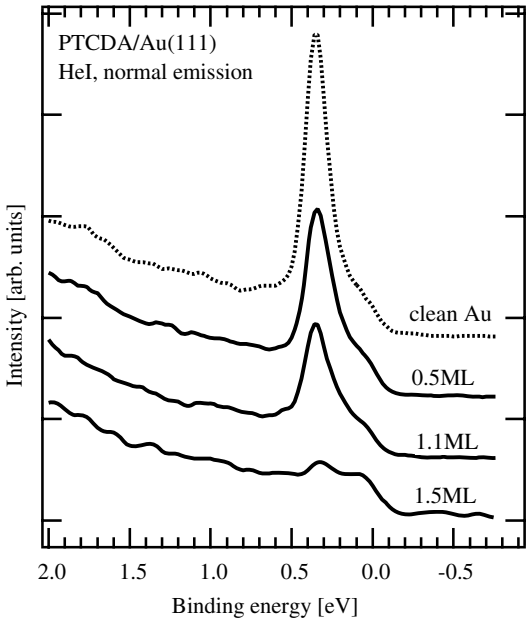

Fig. 4. Normal emission photoemission spectra obtained at room temperature for different coverages of PTCDA on Au(1 1 1). The clean Au(1 1 1) spectrum shows the Shockley-type surface state at a binding energy of 0.4 eV. For 1.1 ML PTCDA the peak corresponding to the Au(1 1 1) surface state is attenuated, but still visible. Binding energies are referred to the Fermi level.

Further proofs concerning the behavior and nature of the surface states are provided by angle resolve photoemission (ARUPS) measurements. In Fig. 5 we present the comparison between the photoemission spectra for the clean gold substrate and for a 1 ML PTCDA covered surface as the emission angle is varied close to the surface normal. Both UPS spectra show an identical dispersion, corresponding to the well-known nearly free-electron-like parabolic dispersion of the Shockley-type surface state [46]. It is important to remark that any electronic state related to the single well-ordered PTCDA overlayer should present a band dispersion induced by the lateral periodicity of the layer, which is different from that of Au. Hence, the electronic features should repeat with the surface reciprocal-space lattice i.e., about 0.15 Å^{-1}. This small k-parallel periodicity will be measured in our photoemission experiment as a non-dispersive band. This is not the case of the band shown in Fig. 5, which disperse following the Au(1 1 1) periodicity. We can conclude that there are no new electronic features related to the PTCDA–substrate interaction. Hence

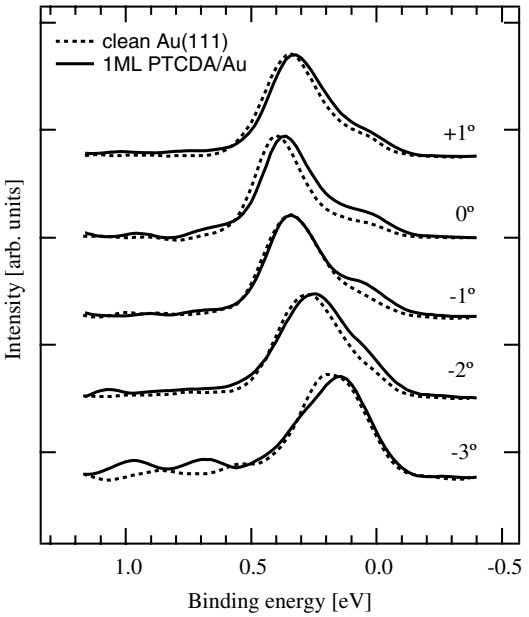

Fig. 5. Angular resolved photoemission spectra for the surface state of clean (dashed line) and 1 ML PTCDA covered Au(1 1 1) surface (solid line). Both surfaces display an identical angular dispersion.

the peak observed in the STS curves for the first PTCDA monolayer can be attributed to the Au(1 1 1) Shockley surface state. Consequently, the apparent metallicity of the PTCDA monolayer solely arises from the gold substrate beneath; the gold states are detected in the STS experiment via a tunneling process through the PTCDA monolayer.

As mentioned above, adsorption processes typically modify the surface electronic states of the (1 1 1) face of noble metals. By means of photoemission spectroscopy a wide range of effects has been reported depending on the adsorbates and their interaction with the substrate. Chemisorbed atoms often completely quench the surface state [49]. For adsorption (physisorption) of rare gases [27,50], where a weak interaction can be expected, the reported ARUPS energy shift of the bottom of the band is rather small, varying from 150 to 170 meV for Xe, 80 to 100 meV for Kr, and 60 to 87 meV for Ar (Refs. [50,27], respectively). In the case of PTCDA here reported, limited by the experimental resolution of our room temperature photoemission spectroscopy, the ARUPS spectra is compatible with a small energy shift (lower than 100 meV), in agreement with the STS data shown in Fig. 3(b). This places the organic monolayer of PTCDA as a very weak interacting layer, only comparable to noble gases physisorption.

4. Conclusions

To summarize, we present experimental results obtained from a combination of different spectroscopic methods for the PTCDA/Au(1 1 1) interface. The qualitative agreement between experimental data obtained by both techniques, STS and photoemission, gives a clear evidence that the interaction between PTCDA molecules and the Au(1 1 1) surface is very weak. The Au(1 1 1) Shockley surface state is not disrupted by one single and complete adsorbed layer of PTCDA, but only an small energy shift towards the Fermi level (<100 meV) is observed by both spectroscopies. Therefore, the metallicity observed by STS for the first PTCDA monolayer is provided by the electronic states of the gold substrate tunneling through the organic layer.

Acknowledgments

Fruitful discussion are acknowledged to F. Flores, H. Vázquez, J.J. Palacios, O. Paz and J.M. Soler. Critical reading and comments are also acknowledged to J. Cerdá and A.M. Baró. The authors acknowledge EU-RT-Network DIODE HPRN-CT-1999-00164 and the Spanish Ministerio de Educación y Ciencia, project numbers MAT2005-3866 and MAT2004-03129 for financial support.

References

[1] Hardis Morkoç, Advanced Semiconductor and Organic Techniques, Academic Press, London, 2003.
[2] S.R. Forrest, Chem. Rev. 97 (1997) 1793.
[3] M. Pope, Ch.E. Swenberg, Electronic Processes in Organic Crystals and Polymers, University Press, Oxford, 1999.
[4] C. Siedel, C. Awater, X.D. Liu, L. Ellerbrake, H. Fuchs, Surf. Sci. 371 (1997) 123.
[5] B. Krause, A.C. Dürr, K. Ritley, F. Schreiber, H. Dosch, D. Smilgies, Phys. Rev. B 66 (2002) 235404.
[6] L. Chkoda, M. Schneider, V. Shklover, L. Kilian, M. Sokolowski, C. Heske, E. Umbach, Chem. Phys. Lett. 371 (2003) 548.
[7] L. Kilian, E. Umbach, M. Sokolowski, Surf. Sci. 573 (2004) 359.
[8] D. Braun, A. Schirmeisen, H. Fuchs, Surf. Sci. 75 (2005) 3.
[9] M. Stöhr, M. Gabriel, R. Möller, Surf. Sci. 507–510 (2002) 330.
[10] Th. Wagner, A. Bannani, C. Bobisch, H. Karacuban, M. Stöhr, M. Gabriel, R. Möller, Org. Electron. 5 (2004) 35.

[11] P. Fenter, P.E. Burrows, P. Eisenberger, S.R. Forrest, J. Cryst. Growth 152 (1995) 65.
[12] P. Fenter, P. Eisenberger, P. Burrows, S.R. Forrest, K.S. Liang, Physica B 221 (1996) 145.
[13] T. Schmitz-Hübsch, T. Fritz, R. Sellam, R. Staub, K. Leo, Phys. Rev. B 55 (1997) 7972.
[14] P. Fenter, F. Schreiber, L. Zhou, P. Eisenberger, S.R. Forrest, Phys. Rev. B 56 (1997) 3046.
[15] I. Chizhov, A. Kahn, G. Scoles, J. Cryst. Growth 208 (2000) 449.
[16] S. Mannsfeld, M. Toerker, T. Schmitz-Hübsch, F. Sellam, T. Fritz, K. Leo, Org. Electron. 2 (2001) 121.
[17] V. Shklover, F.S. Tautz, R. Scholz, S. Sloboshanin, M. Sokolowski, J.A. Schaefer, E. Umbach, Surf. Sci. 454–456 (2000) 60.
[18] F.S. Tautz, M. Eremtchenko, J.A. Schaefer, M. Sokolowski, V. Shklover, K. Glockler, E. Umbach, Surf. Sci. 502 (2002) 176.
[19] M. Eremtchenko, D. Bauer, J.A. Schaefer, F.S. Tautz, New J. Phys. 6 (2004) 4.
[20] M. Toerker, T. Fritz, H. Proehl, F. Sellam, K. Leo, Surf. Sci. 491 (2001) 255.
[21] E.V. Tsiper, Z.G. Soos, W. Gao, A. Kahn, Chem. Phys. Lett. 360 (2002) 47.
[22] J. Kliewer, R. Berndt, E.V. Chulkov, V.M. Silkin, P.M. Echenique, S. Crampin, Science 288 (2000) 1399.
[23] J.Y. Park, U.D. Ham, S.-J. Kahng, Y. Kuk, K. Miyake, K. Hata, H. Shigekawa, Phys. Rev. B 62 (2000) R16341.
[24] H. Hövel, B. Grimm, B. Riel, Surf. Sci. 477 (2001) 43.
[25] T. Suzuki, Y. Hasegawa, Z.-Q. Li, K. Ohno, Y. Kawazoe, T. Sakurai, Phys. Rev. B 64 (2001) R081403.
[26] J. Repp, G. Meyer, K.-H. Rieder, Phys. Rev. Lett. 92 (2004) 036803.
[27] T. Andreev, I. Barke, H. Hövel, Phys. Rev. B 70 (2004) 205426.
[28] J.I. Pascual, Ph.D. thesis, Universidad Autónoma de Madrid, 1998; O. Custance, Ph.D. thesis, Universidad Autónoma de Madrid, 2002.
[29] N. Nicoara, O. Custance, D. Granados, J.M. García, J.M. Gómez- Rodríguez, A.M. Baró, J. Méndez, J. Phys.: Condens. Matter 15 (2003) S2619.
[30] R.M. Feenstra, J.A. Stroscio, A.P. Fein, Surf. Sci. 181 (1987) 295.
[31] WSxM-software from http://www.nanotec.es.
[32] S.R. Forrest, Y. Zhang, Phys. Rev. B 49 (1994) 11297.
[33] J.P. Perdew, A. Zunger, Phys. Rev. B 23 (1981) 5048.
[34] P. Ordejón, E. Artacho, J.M. Soler, Phys. Rev. B 53 (1996) R10441.
[35] J.M. Soler, E. Artacho, J. Gale, A. García, J. Junquera, P. Ordejón, D. Sánchez-Portal, J. Phys.: Condens. Matter 14 (2002) 2745.
[36] N. Troullier, J.L. Martins, Phys. Rev. B 43 (1991) 1993.
[37] According to our DFT calculations, the energy difference between the HOMO and the LUMO is 1.6 eV. This value, much lower than the experimental one (it is well known that DFT methods underestimate gap values), is consistent with previous DFT calculations see, e.g., R. Oszwaldowski, H. Vázquez, P. Pou, J. Ortega, R. Pérez, F. Flores, J. Phys.: Condens. Matter 15 (2003) S2665.
[38] R. Scholz, A.Yu. Kobitski, T.U. Kampen, M. Schreiber, D.R.T. Zahn, G. Jungnickel, M. Elstner, M. Sternberg, Th. Frauenheim, Phys. Rev. B 61 (2000) 13659.
[39] T. Soubiron, F. Vaurette, J.P. Nys, B. Grandidier, X. Wallart, D. Stiévenard, Surf. Sci. 581 (2005) 178.
[40] N. Nicoara, O. Paz, J.M. Soler, A.M. Baró, J. Méndez, J.M. Gómez- Rodríguez, in press.
[41] K. Glöckler, C. Seidel, A. Soukopp, M. Sokolowski, E. Umbach, M. Böhringer, R. Berndt, W.-D. Schneider, Surf. Sci. 405 (1998) 1.
[42] A. Hauschild, K. Karki, B.C.C. Cowie, M. Rohlfing, F.S. Tautz, M. Sokolowski, Phys. Rev. Lett. 94 (2005) 036106.
[43] A. Hoshino, S. Isoda, H. Kurata, T. Kobayashi, J. Appl. Phys. 76 (1994) 4113.
[44] J. Repp, G. Meyer, S.M. Stojkovic, A. Gourdon, C. Joachim, Phys. Rev. Lett. 94 (2005) 026803.
[45] S.D. Kevan, R.H. Gaylord, Phys. Rev. B 36 (1987) 5809.
[46] F. Reinert, G. Nicolay, S. Schmidt, D. Ehm, S. Hüfner, Phys. Rev. B 63 (2001) 115415.
[47] T.U. Kampen, G. Gavrila, H. Méndez, D.R.T. Zahn, A.R. Vearey-Roberts, D.A. Evans, J. Wells, I. Mc Govern, W. Braun, J. Phys.: Condens. Matter 15 (2003) S2679.
[48] I.G. Hill, A. Kahn, Z.G. Soos, R.A. Pascal Jr., Chem. Phys. Lett. 327 (2000) 181.
[49] S.A. Lindgren, L. Wallden, Solid State Commun. 28 (1978) 283.
[50] F. Forster, G. Nicolay, F. Reinert, D. Ehm, S. Schmidt, S. Hüfner, Surf. Sci. 532–535 (2003) 160;
F. Forster, S. Hüfner, F. Reinert, J. Phys. Chem. B 108 (2004) 14692.

Available online at www.sciencedirect.com
ScienceDirect
Organic Electronics 7 (2006) 295–299
Organic Electronics
www.elsevier.com/locate/orgel

Electrically tunable binary liquid crystal grating device consisting of homeotropic monodomain and non-aligned multidomain geometry

Suk-Won Choi [a], Shin Matsumoto [a], Yoichi Takanishi [a], Ken Ishikawa [a], Isa Nishiyama [b], Joji Kawamura [b], Hirokazu Takada [b], Hideo Takezoe [a,*]

[a] *Department of Organic and Polymeric Materials, Tokyo Institute of Technology, O-okayama, Meguro-ku, Tokyo 152-8552, Japan*
[b] *Dainippon Ink and Chemicals, Incorporated, Central Research Laboratories, Pioneering Technology Center, 631 Sakato, Sakura-shi, Chiba-ken 285-8668, Japan*

Received 4 July 2005; accepted 8 February 2006
Available online 2 May 2006

Abstract

Electrically tunable binary liquid crystal (LC) diffraction grating has been designed and fabricated in a simple technique using an LC composite containing photo-curable LC pre-polymer. The binary grating consists of alternating stripes of homeotropic monodomain and non-aligned multidomain. The diffraction efficiency can be modulated by an applied electric field, and is independent of the polarization of incident light.

PACS: 78.20.Jq

Keywords: Electro-optical device; Low molecular nematic liquid crystal; Photo-curable LC pre-polymer; Diffraction grating; Simple fabrication

1. Introduction

Electro-optical devices are keys in current information and communication technologies. In recent years, electrically tunable diffraction gratings are of interest for a number of optical and photonic applications. Liquid crystals (LCs) are the materials of choice for fabricating such grating devices, and are actually applied to light modulators [1,2], display devices [3,4], beam steering [5,6], optical computing [7] and etc. The control of the diffraction efficiency is easily possible due to altering the LC alignment state or texture by applying external stimuli (ex. electric field and magnetic field, etc.). The LC gratings have been developed in various ways such as patterned electrodes [5,8], patterned alignment layers [3,4,9], LC-filled periodic grooves [10] and LC-monomer mixtures [11–13]. An easy fabrication [14,15] and reliability are indispensable to practical application for efficient devices. Moreover,

* Corresponding author. Tel.: +81 3 57342436; fax: +81 3 57342876.
E-mail address: htakezoe@o.cc.titech.ac.jp (H. Takezoe).

1566-1199/$ - see front matter
doi:10.1016/j.orgel.2006.02.005

the diffraction performance independent of incident polarization is desirable to increase the optical efficiency. In this work, we report an electrically tunable binary LC diffraction grating device that is fabricated easily and has stable performance as an electro-optical device.

2. Experimental

2.1. Material and measurement set-up

The anisotropic composite prepared for this work was a mixture of 90 wt% of low molecular nematic LC (ZLI-2293, $\Delta\varepsilon > 0$, $n_e = 1.6312$, $n_o = 1.4990$, $\Delta n = 0.1322$, Merck) and 10 wt% of a photo-curable LC pre-polymer (UCL-002-K1, Dainippon Ink and Chemicals, Incorporated) with a small amount of photoinitiator. The prepared mixture was injected into an empty cell whose inner surfaces were coated with indium-tin-oxide (ITO) as an electrode. The cell gap was measured to be about 3 μm. In our case, the processes for alignment of LC director (coating and rubbing processes of the alignment layer) are not always necessary to make non-aligned multidomain.

The diffraction properties of the fabricated LC grating were investigated using a normally incident circularly polarized He–Ne (633 nm) laser. Polarization of the incident light was set with a rotating polarizer. The intensity of the diffraction was measured by a photodetector with an aperture whose diameter was smaller than the size of the diffraction spot.

2.2. Fabrication procedure for binary LC grating

The processes of fabricating binary LC grating devices are illustrated in Fig. 1. In the first step, an external ac electric field (30 V_{pp}, 10 kHz) was applied across the cell to align the low molecular nematic LC molecules homeotropically. Incorporated photo-curable LC pre-polymer also could be aligned in the template of the low molecular nematic LC. Next, the cell was irradiated at room temperature with a collimated UV light ($\lambda = 365$ nm) from a high pressure Hg-lamp for 60 s through a striped patterned photo-mask of 50 μm grating period (second step). The UV light power was about 1.5 mW/cm^2. Photo-induced phase migration of LC/pre-polymer occurred between the UV-irradiated domains and the non-irradiated domains. Generally, the area with a stronger UV light would accelerate the photo-polymerization process, resulting

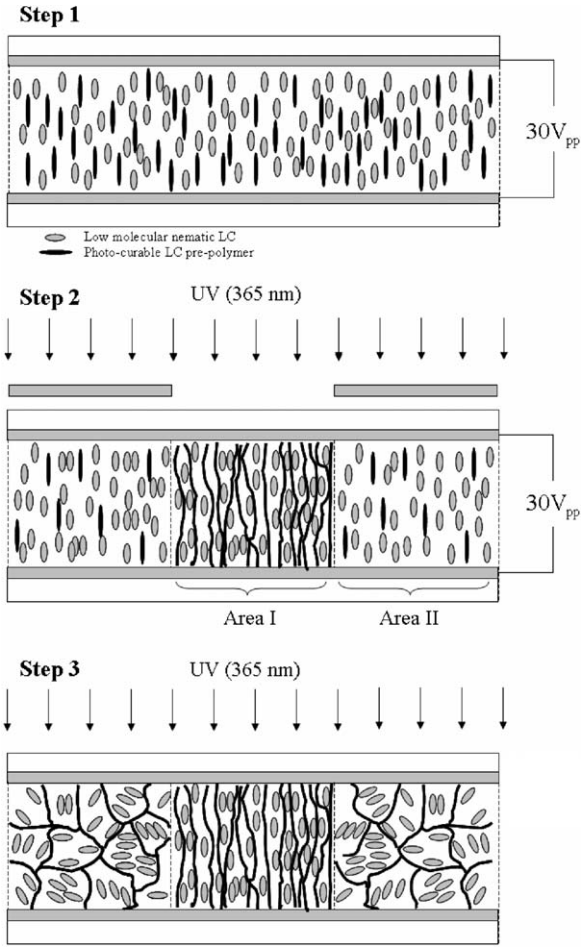

Fig. 1. Fabrication process of our LC grating.

in a higher polymer concentration. Thus, in the UV-irradiated domains, high photo-curable pre-polymers come together and aggregate to form supporting networks for homeotropically aligned low molecular nematic LC molecules (Area I). On the contrary, non-irradiated areas are remained non-fixed for the low molecular nematic LC. Finally, without applying electric fields, the overall cell was then exposed to UV light at room temperature for 60 s (third step). This exposure polymerizes the residual pre-polymer in non-fixed low molecular nematic LC and induces polymer-networks-stabilized non-aligned multidomain geometry (Area II). In this step, our binary LC grating device consisting of alternating homeotropic monodomain (Area I) and non-aligned multidomain (Area II) is completed. This second exposure can also play a role in improving the device reliability; namely, residual pre-polymer is fully exhausted and non-intentioned degradation of device may be prevented.

3. Results and discussion

Fig. 2(a), (b) and (c) shows the microphotographs and diffraction patterns of the fabricated binary LC grating at different electric stimuli, 0 V_{pp}, 10 V_{pp} and 30 V_{pp}, respectively. In Fig. 2(a), under crossed polarizers, dark and bright areas show the homeotropic monodomain (Area I) and non-aligned multidomain geometry (Area II), respectively. At $V = 0$ V_{pp}, distinct higher order-diffraction patterns are observed. Then, as the applied electric field increases, the bright area gradually darkened under crossed polarizers. Associated with this process, the higher-order diffraction patterns were extinguished, as shown in Fig. 2(b) and (c). The diffraction can be easily and reversibly modulated by an applied electric field.

Fig. 3 plots the measured voltage-dependent diffraction efficiencies of the single first-order diffracted light. The efficiency is defined by $\eta_1 = I_1/I_0$, where I_1 and I_0 are the intensities of the first order diffracted and incident beams, respectively [16]. In our case, the intensity of incident beams was used as that of the zeroth-order light passed through the fabricated cell, without higher-order diffraction and light scattering, under applying 30 V_{pp}. We also observed light scattering property of the fabricated grating as a function of the applied voltage V. As shown in Fig. 3, the diffraction efficiency slightly increased with increasing applied voltage in the range of $V < 3$ V_{pp}. The

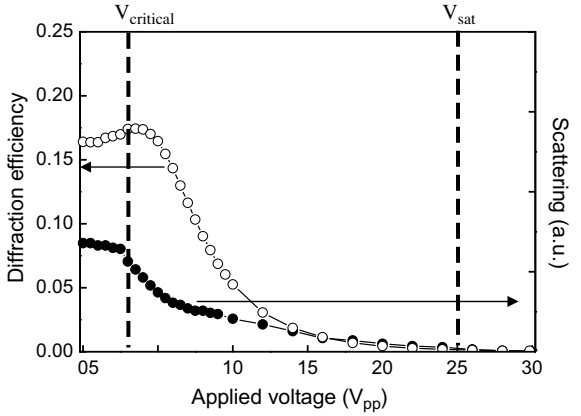

Fig. 3. The diffraction efficiencies of the first-order diffracted light and light scattering as a function of applied voltage V.

observed light scattering was prominent and slightly decreased at the same range ($V < 3$ V_{pp}). We define this voltage (3 V_{pp}) as a critical voltage ($V_{critical}$). Then the diffraction efficiency gradually decreased with increasing applied voltage (3 $V_{pp} \leqslant V < 25$ V_{pp}) after showing a maximum. The observed light scattering also gradually decreased with increasing applied voltage. When the applied voltages exceeded 25 V_{pp}, our binary grating could not be operated as a diffraction device. We also define this voltage (25 V_{pp}) as a saturation voltage (V_{sat}).

In order to explain the above experimental result, Fig. 4 illustrates cross-sectional schematic views parallel to the surfaces of the substrates of our

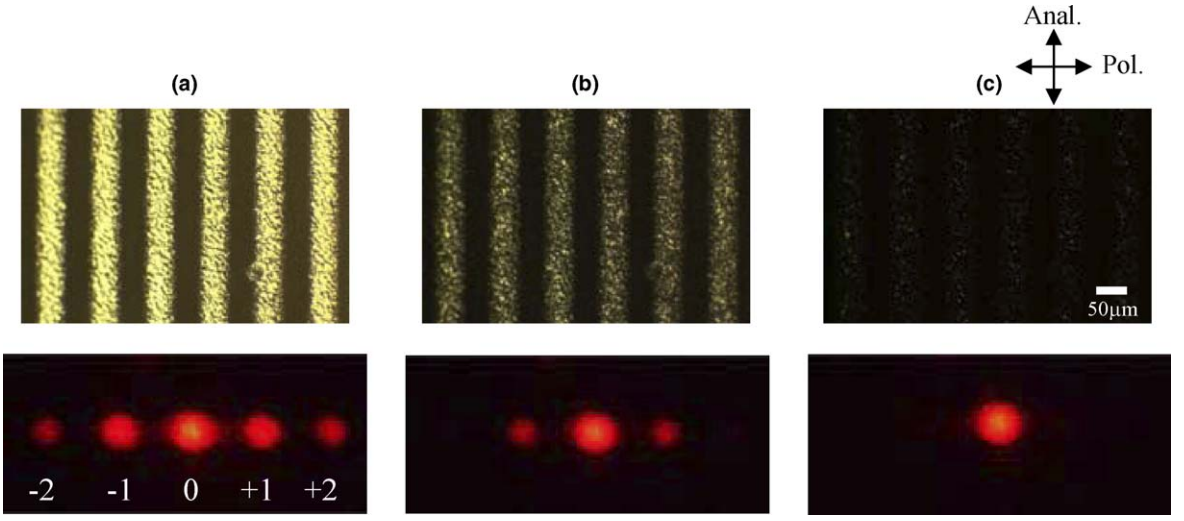

Fig. 2. The microphotographs and diffraction patterns of the fabricated binary LC grating at different electric stimuli: (a) 0 V_{pp}, (b) 10 V_{pp}, and (c) 30 V_{pp}.

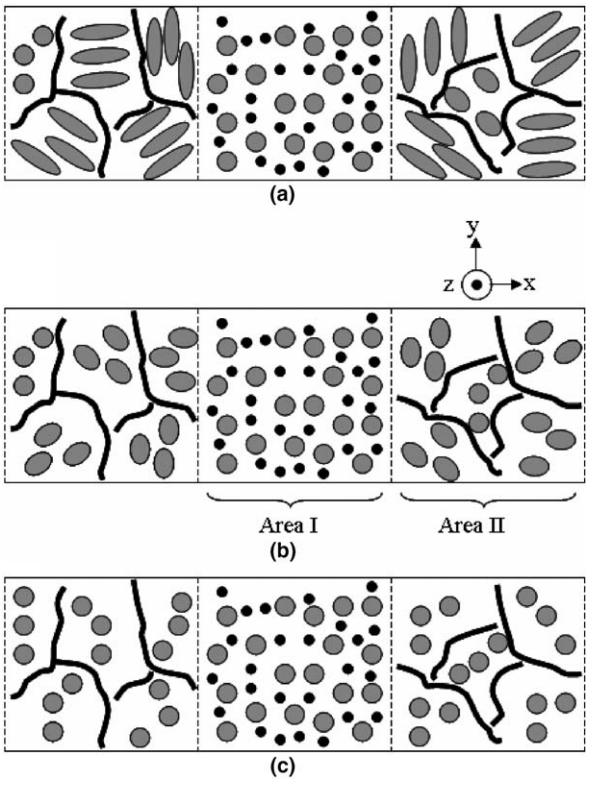

Fig. 4. A simple model of LC molecular orientation state of non-aligned multidomain and homeotropic monodomain at (a) $V < V_{\text{critical}}$, (b) $V_{\text{critical}} \leqslant V < V_{\text{sat}}$, and (c) $V \geqslant V_{\text{sat}}$ (top view of a cell).

binary LC grating device cell. The low molecular nematic LC directors are randomly aligned in Area II. At $V < V_{\text{critical}}$, because of the large refractive index mismatch between the adjacent domains, light scattering is prominent (see Fig. 4(a)). However, as the applied voltage increases ($V_{\text{critical}} \leqslant V < V_{\text{sat}}$), the LC directors are reoriented along the electric field direction, where V_{critical} and V_{sat} are the critical voltage (the minimum voltage of the critical LC-reorientation in Area II) and the saturation voltage (the voltage of no more LC-reorientation in Area II), respectively. As the refractive index gradually changes and matches between the domains at $V_{\text{critical}} \leqslant V < V_{\text{sat}}$, the Area II becomes transparent because of decreasing light scattering (see Fig. 4(b)). When the voltage increases further ($V \geqslant V_{\text{sat}}$), LCs in Area II are completely reoriented along the electric field direction, as shown in Fig. 4(c). While the alignment of low molecular namatic LCs was easily changed and modulated by an electric field in the Area II, the alignment of the Area I is fixed at any electric fields because low molecular nematic LC molecules are fixed homeotropically by a homeotropically oriented polymer network. The observed diffraction property is due to phase grating effect, i.e., the relative phase difference for passing through two adjacent domains (Area I and Area II) of the fabricated grating device. The slight increase of diffraction efficiencies with increasing applied voltage in the range of $V < V_{\text{critical}}$ is attributed to slight decrease of light scattering effect which causes diffraction loss.

We have to take into account two causes for the diffraction for $V_{\text{critical}} \leqslant V < V_{\text{sat}}$; amplitude grating effect due to light scattering and phase grating effect due to optical anisotropy. The area I is essentially transparent, whereas the area II scatters light at least at low electric field strength (see closed circles in Fig. 3), resulting in the amplitude grating. The diffraction efficiency due to this effect decreases with decreasing scattered intensity with electric stimuli. As for the phase grating effect, the diffraction efficiency decreases with electric stimuli, since the refractive indices in two areas approach to each other. In any events, it is reasonable to observe the decrease in the diffraction efficiency with increasing the applied voltage ($V_{\text{critical}} \leqslant V < V_{\text{sat}}$).

Fig. 5 shows the diffraction characteristics depending on the polarization of incident light. Polarization-independent diffraction characteristics were observed in our LC grating device under an applied voltage in the range of $V_{\text{critical}} \leqslant V < V_{\text{sat}}$, i.e., 5 V and 10 V. To understand the polarization-independency of the diffraction efficiency, a simple model of the LC molecular orientation state of fabricated grating for $V_{\text{critical}} \leqslant V < V_{\text{sat}}$ is shown in Fig. 4(b). While the refractive index of the Area I

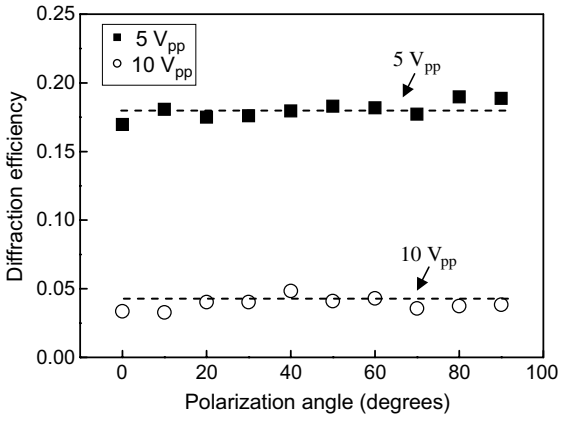

Fig. 5. Diffraction characteristics depending on the polarization of incident light at 5 V_{pp} and 10 V_{pp}.

is n_o irrespective of incident polarization, the refractive index of the Area II is described as n_{eff}^x and n_{eff}^y for x- and y-directions, respectively. Since there is no preferential LC director orientation, the refractive indices for x- and y-directions are almost the same, i.e., $n_{eff}^x \approx n_{eff}^y$. Thus, the values of absolute difference of refractive indices for the x- and y-directions are the same, i.e., $|n_o - n_{eff}^x| \approx |n_o - n_{eff}^y|$. Since diffraction efficiency depends only on the absolute value of the refractive index difference, those with respect to the x- and y-directions are almost the same. Even if we take into account the amplitude grating effect, the diffraction efficiency is independent of the polarization anyway. Therefore, polarization independent diffraction occurs. For $V \geqslant V_{sat}$, molecules in the Area II perfectly realign parallel to the cell surface normal, thus, the refractive indices for x- and y-directions are n_o. Therefore phase diffraction characteristics are extinguished.

4. Conclusion

In summary, a simple technique for fabricating electrically controllable polarization independent binary LC diffraction gratings has been reported. The reliability-improved binary grating consists of alternating stripes of homeotropic monodomain and non-aligned multidomain. Dependence of the diffraction efficiency on the applied electric field was shown to occur because of the refractive index (phase) change due to the reorientation of the LC molecules depending on the applied field in the Area II. The efficiency is almost independent of the polarization angle of the incident beam. The diffraction characteristics were discussed using a simple model.

References

[1] M. Schadt, W. Helfrich, Appl. Phys. Lett. 18 (1971) 127.
[2] K.A. Crandall, M.R. Fisch, R.G. Petschek, C. Rosenblatt, Appl. Phys. Lett. 64 (1994) 1741.
[3] J. Chen, P.J. Bos, H. Vithana, D.L. Johnson, Appl. Phys. Lett. 67 (1995) 2588.
[4] C.M. Titus, P.J. Bos, Appl. Phys. Lett. 71 (1997) 2239.
[5] D.P. Rester, D.S. Hobbs, R.C. Sharp, L.J. Friedman, T.A. Dorschner, Opt. Lett. 21 (1996) 689.
[6] D. Subacius, S.V. Shiyanovskii, P. Bos, O.D. Lavrentovich, Appl. Phys. Lett. 71 (1997) 3323.
[7] B.H. Soffer, J.D. Margerum, A.M. lackner, D. Boswell, A.R. Tanguay Jr., T.C. Strand, A.A. Sawchuk, P. Chavel, Mol. Cryst. Liq. Cryst. 70 (1981) 145.
[8] I. Fujieda, Appl. Opt. 40 (2001) 6252.
[9] M. Honma, T. Nose, Jpn. J. Appl. Phys. 42 (2003) 6992.
[10] H. Sakata, M. Nishimura, Jpn. J. Appl. Phys. 39 (2000) 1516.
[11] R.L. Sutherland, V.P. Tondiglia, L.V. Natarajan, T.J. Bunning, W.W. Adams, Appl. Phys. Lett. 64 (1994) 1074.
[12] J. Qi, M.E. Sousa, A.K. Fontecchio, G.P. Crawford, Appl. Phys. Lett. 82 (2003) 1652.
[13] H. Ren, Y.H. Fan, S.T. Wu, Appl. Phys. Lett. 82 (2003) 3168.
[14] A.K. Ghosh, Y. Takanishi, K. Ishikawa, Y. Ono, J. Kawamura, H. Takezoe, J. Appl. Phys. 95 (2004) 5241.
[15] A.K. Ghosh, S.-W. Choi, Y. Takanishi, B. Park, K. Ishikawa, Y. Ono, J. Kawamura, H. Takezoe, J. Appl. Phys. 96 (2004) 5909.
[16] I.C. Khoo, S.T. Wu, Optics and Nonlinear Optics of Liquid Crystals, World Scientific, Singapore, 1993.

Available online at www.sciencedirect.com
ScienceDirect
Organic Electronics 7 (2006) 300–304
Organic Electronics
www.elsevier.com/locate/orgel

Fabrication and photoresponse of novel carboxymethylcellulose (CMC) based bacteriorhodopsin (bR) sensor

P. Vengadesh [a,*], Wan Haliza Abdul Majid [a], S. Anandan Shanmugam [b], K.S. Low [a]

[a] *Department of Physics, University of Malaya, Lembah Pantai, 50603 Kuala Lumpur, Malaysia*
[b] *Department of Biomedical Engineering, University of Malaya, Lembah Pantai, 50603 Kuala Lumpur, Malaysia*

Received 19 November 2005; received in revised form 26 March 2006; accepted 29 March 2006
Available online 2 May 2006

Abstract

A single-pixel dry-type reconstituted bacteriorhodopsin (bR) sensor (Au/CMC + bR/ITO) incorporating carboxymethylcellulose (CMC) as the artificial membrane is fabricated according to a protocol developed to investigate signal acquisition from the proposed biosensor. Droplets of reconstituted purple membrane (PM) containing bR applied onto a gel-like solution of CMC placed on gold electrodes (anode) are allowed to dry under an electric field, utilising the PM fragment's net negative charge and electric dipole moment. The resulting bR matrix thin film with high molecular orientation is finally sandwiched together with a semi-transparent indium titanium oxide (ITO) counter electrode and proper electrical connections made to form a single pixel bR-CMC photosensor. Efficient and reproducible photoresponse observed upon illumination clearly exhibits the potential of the proposed biosensor for future photosensing works.

PACS: 85.65.+h; 85.60.Bt; 87.14.Ee; 07.07.Df

Keywords: Bacteriorhodopsin; bR-photosensor; Organic optoelectronic material; Light-driven proton pump

1. Introduction

Bacterial-rhodopsin or bacteriorhodopsin (bR) is a family of the retinal-containing proteins found in extremely halophilic bacteria known as *Halobacterium halobium* thriving in salt marshes [1]. The only protein component in the purple membrane (PM) of the bacteria and contains a binary mixture of two proteins [2], one containing 13-*cis* retinal (dark-adapted bR) and the other all-*trans* retinal (light-adapted bR) at ambient temperature and low-light conditions. It is the simplest known light-driven ion pump performing photosynthesis that provides light-dependent ion (proton, H^+)

* Corresponding author. Address: No. 37, Jalan Kemboja 7, Taman Aman, 42700 Banting, Selangor Darul Ehsan, Malaysia. Tel.: +60 3 79674435; fax: +60 3 79674146.
E-mail address: vengadeshp@hotmail.com (P. Vengadesh).

1566-1199/$ - see front matter
doi:10.1016/j.orgel.2006.03.012

transport and sensory functions for these organisms. This is achieved by converting light energy into an electrochemical gradient by means of pumping out protons from the cytoplasmic region into the extracellular region of the biological membrane.

bR of the halobacterial cell membrane consist of a 2-dimensional crystalline cell membrane embedded into a lipid bilayer (3:1 to protein:lipid) and grown by the bacterium when the concentration of oxygen becomes too low to sustain the generation of adenosine triphosphate (ATP) via oxidative phosphorylation, which is also how ATP is formed in cellular respiration. ATP production in the absence of oxygen is achieved by using bR as a proton pump by participating in a photocycle process [1,3] and [4], which produces H^+ for every photon of light absorbed. The process in turn changes the bR's shape (kinked shapes) and creates many intermediate forms while moving the protons produced across the membrane. This trans-membrane movement from the cytoplasmic side to the extracellular side creates an H^+ gradient. The resulting energy of the H^+ gradient is then harnessed by using ATP-ase to form ATP from inorganic phosphate and ADP in the same manner it occurs in cellular respiration.

Many bR-based photosensors as proposed by various research groups [5–15] and [16] worldwide were configured in a multilayered thin film sandwiched between two conducting electrodes. Crucial steps usually involve the incorporation of reconstituted bR into suitable mediums [5–15] acting as "artificial membranes. The medium to be chosen should be transparent enough to allow light penetration to reach the embedded bR in the "artificial membrane". It should also possess cation-selective capabilities that enable proton transport through the medium. Most research groups concentrate into separate formation of bR thin film layers and "artificial membrane" medium [8,11,12,15] before sandwiching the bR-matrix together to enable forced incorporation of highly orientated bR into the active medium. In the work proposed however, an unconventional approach is used by allowing the bR to directly fuse into the medium in the form of a thick and viscous electrolyte gel that restricts free movements and rotations of the bR. By allowing the rotation limited bR-matrix to dry naturally under an electric field, bR with high molecular orientation embedded in an almost uniform multilayered matrix is formed.

2. Experiment

2.1. Materials

PM (molecular weight without retinal of 26784 kDa) of variant type V1 containing lyophilized powder of bR molecules from *Halobacterium salinarium* were obtained from MIB, Munich Innovative Biomaterials, Germany. Product information stated absorption maximum of bR in deionized water after light adaptation at 566 nm, while absorbance ratio (referring to the ratio of maximum optical densities, ODs at 280 nm and 570 nm), OD_{280} / OD_{570} at 2,3. For the purpose of the study, bR was suspended in pure deionized water to form a bR solution with a concentration of 0.2 mg/ml. The gel-like "artificial membrane" CMC-salt viscous gel electrolyte, bought in the form of powder from Sigma chemicals (product number 419273-100G), was prepared by slowly dissolving 6% CMC in 1 M of KCl (pH 7.4) prepared earlier in purified deionized water. Homogeneity of the gel electrolyte and the bR solution was achieved by means of using an agitator (Model 34524), supplied by Snijders Scientific, Holland. Gold coating (resistivity of 11.5 Ω/cm) formed on standard glass slides (2.5 cm × 7.5 cm) used in the work was achieved by using a BIO-RAD SEM sputtering system. The counter electrode used, the semi-transparent ITO conducting electrode (2.5 cm × 7.7 cm) had a surface resistivity of about 75.0 Ω/cm. Single pixel light-receptive area of 1.3 cm × 0.9 cm on the gold sputtered electrode was prepared by simply using a sharp metal point to define the dimensions of the light receiving area and thoroughly wiping of the rest of the sputtered gold on the slide with a filter paper. Electrical connections for the pixel from the edge to the underside of the pixel bearing glass slide were made using silver conductive paint (resistivity of 1.20 Ω/cm) obtained from RS Components, UK, while copper wires were attached to the individual electrical connections using the silver conductive paint. Sensor sealing was accomplished using a silicon based adhesive sealant (Selley Silicone Sealant).

2.2. Device optimizations and fabrication

bR-sensors fabricated by many researchers in their previous publications [8–10,12,15] seems to centre on the semi-dry type version, which basically involves the junction type bR-matrix sensor (metal /

bR / medium (electrolyte gel) / metal). Incorporating bR layers deposited as single or multilayered thin films employed through various deposition techniques and additions of charge enhancing ionophores [17] and [18] increases the production of efficient photoresponse from the fabricated photosensor. Much more basic configurations were employed in this work, yet still allowing a high level of photosensitivity to be achieved.

A glass slide prepared and washed with methanol and deionized water is sputtered with gold using a Scanning Electron Microscope (SEM) coating unit. Using the sharp metal point as mentioned earlier, a single pixel configuration is prepared on the gold coated glass slide (working electrode), which acts as the gold electrode. Electrical connection is made by using silver conductive paint on the edge of the gold pixel (the side of the glass slide) to the underside of the gold electrode. A copper wire is then attached by using the silver conductive paint to the electrical connection made on the underside of the pixel bearing glass slide. Using a 1 ml syringe, a drop of the gel-like CMC solution (about 0.1 ml) is applied onto the gold pixel. The use of CMC as the active medium was mainly due to ready availability and the intrinsic cation exchange capability possessed by the negatively charged carboxymethyl groups in CMC, enabling proton transport through the matrix. A drop of bR solution, about 0.1 ml applied from a 1 ml syringe is later deposited directly onto the CMC droplet. The OD measurement of the resulting light adapted bR-CMC mixture placed in a cuvette showed a value of 0.345 at 566 nm.

To induce high molecular orientation of bR as it rotates and fuses into the CMC material, the gold pixel bearing the bR-matrix is placed on an aluminium base and kept under a high electric field of 50 V/cm to utilise the bR's net negative charge and electric dipole moment. Silver paint connecting the edge of the gold pixel to the underside of the glass slide bearing the pixel enables electrical connection to the aluminium base, which is connected to the positive polarity of the dc supply. Puu et al. [19], in his paper has shown that this method of bR matrix film formation will retain their molecular orientation even after the removal of the electric field and the drying of the electrode while retaining the natural intrinsic properties of bR. Such thin films incorporated into the dry-type photosensor design enables a high efficiency in generating photoelectric current as shown by Nicolini et al. [20], since almost all proton pathways are orientated in the same direction.

The whole setup is kept in dark for about 48 h to allow the pixel bearing electrode to dry naturally under the electric field and normal room temperature. An ITO slide washed with methanol and deionized water is dried and used as a counter electrode by sandwiching it with the prepared bR-matrix on the gold pixel. To allow good adhesion, the working electrode is wetted using a drop of deionized water from a 1 ml syringe before sandwiching. If the weight of the ITO slide is placed immediately on top of the "gel-like" bR matrix

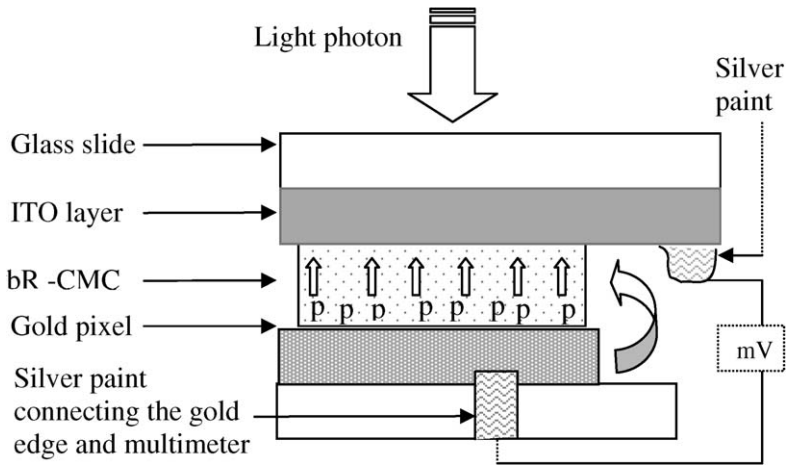

Fig. 1. Proton transfer mechanism as been suggested for the study carried out using the proposed CMC-based bR sensor. Light photon activates the photocycle process within the PM. The process produces a proton gradient across the membrane, activating the proton pumping mechanism from the cytoplasmic to the extracellular region.

before allowing complete drying, the viscous matrix will spread all over and flow out of the gold pixel. By keeping the fabricated bR-sensor overnight in dark conditions to dry naturally under the same electric field and room temperature, the electric dipole moment of bR will be oriented in the same direction. After complete drying, the edge of the sensor is sealed using the silicon based adhesive sealant to reduce the effects of humidity fluctuations. Finally the entire sensor is placed permanently by using adhesive tapes onto a solid polystyrene base to give physical support and kept in dry and dark conditions overnight [21] before any signal acquisition works are carried out (see Fig. 1).

2.3. Signal acquisition

Signal acquisition from the biosensor was carried out using a 500 W halogen projector lamp as the light source. To reduce excessive heat build-up, a distance of 0.5 m was maintained between the protein-based biosensor and the light source, allowing about 1.3 mW/cm^2 of light intensity to fall onto the pixel of the sensor.

3. Results and discussions

When the light source was switched on, an increase or "rise" in open voltage generation was observed. As a result of using a continuous source of illumination, a steady photovoltage generation or open voltage is observed. The peak values registered characterized by the bR concentration and light intensity used in the experiment shows a steady state photovoltage, which represents the proportional open voltage measurement of the net charge (proton) transport. When the light source was removed, a sudden decrease or "fall" in photovoltage generation was observed indicating sudden loss of proton gradient.

The sensors' switching profiles on days 1, 2, 3 and 4 registered different initial (at $t = 0$ s) or starting open voltage values suggesting incomplete proton discharging of the sensor or exposure to background light before signal acquisition was obtained. It was evident that the initial values registered do not alter the switching profiles of the sensor but inversely influences the time it takes to reach the peak photovoltage (see Fig. 2).

The basic underlying mechanism that occurs, involves creation of the build-up of positive charges or protons through direct response towards absorption of light photons through the ITO semi-transparent electrode. This being as a consequence of the photocycle process triggered in the bR incorporated into the CMC matrix, creating a proton gradient across the "artificial membrane". As in nature, the single pixel gold electrode represents the cytoplasmic side from where the proton or charge transfer takes place towards the extracellular side of the "artificial membrane", which is represented by the ITO slide. The ITO slide collecting the charges or the electrical current produced will then be registered as photoresponse or an open voltage value.

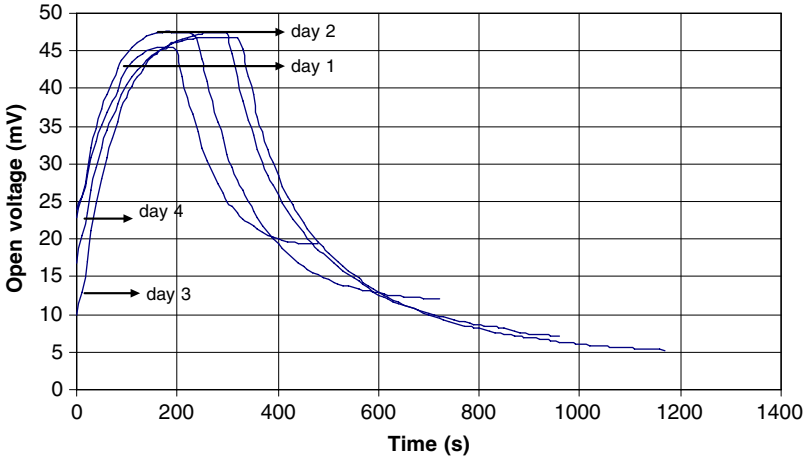

Fig. 2. Switching profiles of the bR sensor as obtained on days 1, 2, 3 and 4, exhibiting similar stable profiles. Peak values for days 1, 2, 3 and 4, self-stabilising at about 45.5 mV, 47.6 mV, 47.5 mV and 46.7 mV respectively were achieved after 170–270 s. On day 1, an initial open voltage value of 24 mV takes 170 s to reach peak value, day 2 with 22.9 mV takes 180 s, day 3 with 10 mV takes 270 s and day 4 registers 16.9 mV and 260 s.

As discussed earlier, there are many methods for immobilizing bR into the ''artificial membrane''. Most of these works involve either the semi-dry sandwich-type voltaic cells with metal-bR matrix-metal [11,12,14] or liquid junction cells comprising a bR-loaded membrane separating two aqueous solutions [8,22]. But the work presented in this paper involves a truly robust and easy to fabricate completely dry sandwich-type photosensor with repeatable and stable switching profiles.

4. Conclusions and future works

The work presented serves as a crucial preliminary investigation into the possibility of fabricating a multi-pixel CMC-based bR sensor to be integrated into an optical data processing system. Observation of photoresponse results clearly exhibits the switching profile of the proposed biosensor and by further perfecting the bR-matrix deposition method a faster rise-time could be achieved allowing fabrication of a more sensitive and practical photosensing device. Future works will also include important characterization works on the proposed bR sensor so as to better understand the light sensing mechanisms involved.

The basic bR-based photosensor design architecture presented and fabricated in this work demonstrates good photoresponse as shown by the switching profiles obtained while keeping many aspects of the fabrication process as simple as possible.

Acknowledgements

This work was partially supported by VOTE-F grant IPP/UPDiT/Geran (PJP)/F0161/2003D. We would like to extend our gratitude to Prof. Vicky of Plant Mycology and Pathology and to the staffs at the Institute of Postgraduate Studies, University of Malaya for their assistance and all others for contributing positively towards the success of this project.

References

[1] S.B. Hwang, J.I. Korenbrot, W. Stoeckenius, J. Memb. Biol. 36 (1977) 115.
[2] S. Walter, N.F. Charles, D.K. Klaus, A.D. Norbert, Febbs Lett. 97 (1978) 129.
[3] B. Robertson, E.P. Lukashev, Biophy. J. 68 (1995) 1507.
[4] M. Tsutomu, K. Koichi, Chem. Lett. (1991) 1645.
[5] J.W. Kevin, B.G. Nathan, A.S. Jeffrey, P.K. Mark, R.B. Robert, Trends Biotech. 20 (2002) 387.
[6] K.L. Janos, Biochim. Ac. 1460 (2000) 1.
[7] T.H. Felix, BioSystematics 35 (1995) 117.
[8] M. Tsutomu, K. Koichi, Appl. Opt. 32 (1993) 1645.
[9] F. Michael, S. Pertti, P. Sinikka, P. Jussi, J. Timo, BioSyst. 54 (2000) 131.
[10] B. Aurelie, D. Michel, S. Pattrick, A. Claude, B. Francois, Biosen. Bioelect. 10 (1995) 415.
[11] C. Zhongping, R.B. Robert, Tibtechniques 11 (1993) 292.
[12] G.C. Hyun, C.J. Woo, M. Junhong, H.L. Won, W.C. Jeong, Biosen. Bioelect. 16 (2001) 925.
[13] C. Jinfang, L. Xingchang, Z. Jianping, T. Jian, Biochem. Biophy. Res. Comm. 305 (2003) 116.
[14] M. Tsutomu, K. Koichi, I. Isamu, Science 255 (1992) 342.
[15] G.C. Hyun, C.J. Woo, M. Junhong, H.L. Won, W.C. Jeong, Biosen. Bioelect. 16 (2001) 917.
[16] M. Eisenbach, C. Weissmann, G. Tanny, S.R. Caplan, Febbs Lett. 81 (1977) 77.
[17] F.L. Bao, R.L. Jin, C.S. Yu, L.J. Song, Mat. Sci. Eng. C3 (1995) 219.
[18] M.B. Lindner, Y.A. Dor, Febbs Lett. 101 (1979) 113.
[19] G. Puu, I. Gustafson, E. Artursson, P.A. Ohlsson, Biosen. Bioelect. 10 (1995) 463.
[20] C. Nicolini, V. Erokhin, S. Paddeu, C. Paternolli, M.K. Ram, Biosen. Bioelect. 14 (1999) 427.
[21] B. Yaoli, Y. Zheng, Y. Wang, M. Lei, G. Chen, N. Hampp, Opt. Commun. 218 (2003) 25.
[22] V.P. Skulachev, Febbs Lett. 64 (1976) 23.

Available online at www.sciencedirect.com
ScienceDirect
Organic Electronics 7 (2006) 305–312
Organic Electronics
www.elsevier.com/locate/orgel

Switching and filamentary conduction in non-volatile organic memories

Michael Cölle *, Michael Büchel, Dago M. de Leeuw

Philips Research Laboratories, High Tech Campus 4 (WAG 11), 5656 AE Eindhoven, The Netherlands

Received 11 November 2005; received in revised form 7 March 2006; accepted 26 March 2006
Available online 27 April 2006

Abstract

Switching in metal/organic/metal structures for non-volatile memory applications was investigated. The electrodes turned out to be crucial for obtaining reversible switching, whereas the organic material had only minor influence. Electron-only devices with aluminum electrodes showed reversible resistive switching due to external bias. Transport and switching mechanism were studied by measuring *I–V* characteristics, retention, impedance spectroscopy and temperature dependence. The results suggest that switching is due to the oxide layer at the electrode and transport through filaments. Spatially resolved infrared photographs prove the filamentary nature.
Published by Elsevier B.V.

PACS: 73.40.Sx; 84.37.+q; 73.61.Ph; 85.65.+h

Keywords: Organic memory; Switching; Polymers; Filaments; Oxide

1. Introduction

Non-volatile organic memories are presently being investigated as a low-end replacement for standard NAND flash circuitry. The devices consist of a thin semiconducting organic film sandwiched between two electrodes. Resistance switching has been reported for a wide variety of semiconductors such as pentacene [1], anthracene [2], copper-tetracyano-quinodimethane (Cu TCNQ) [3], blends of organic materials [4,5] and doping with nanoparticles [6–8]. It is noteworthy that one of the electrodes is typically aluminum. In some of the devices on which reports have been written, reproducible switching is only observed when the aluminum electrode is deliberately oxidized or unintentionally passivated with native oxide. The devices switch reversibly between a high resistance off-state and one or more low resistance on-states at fields much lower than the breakdown fields. The current modulation at low bias is typically several orders of magnitude. Nanosecond switching times have been reported [6]. In the on-state, the transport is symmetric for forward and reverse bias and transport has a negligibly small thermal activation energy. Data retention times and programming cycle endurance are both excellent. Shelf-life data is not yet available but data for similar devices, e.g. organic

* Corresponding author. Tel.: +31 (0)40 27 42117; fax: +31 (0)40 27 46505.
E-mail address: michael.coelle@philips.com (M. Cölle).

1566-1199/$ - see front matter Published by Elsevier B.V.
doi:10.1016/j.orgel.2006.03.014

light-emitting diodes, suggests it will be environmentally stable.

The nature of the switching mechanism is still unknown. For heterogeneous systems, it has been suggested that field-induced charge transfer that leads to a building up of space charges and inhibits injection could explain switching combined with negative differential resistances [8,9]. As an alternative, charge tunneling and polarization of the trapped charge has been proposed [6]. In homogenous organic systems switching has been ascribed to several different mechanism, including bulk charge transfer [3], charge trapping [7], electroreduction and conformational changes [10]. Finally, formation of conducting filaments [1,11] and influence of aluminum oxide [12] has also been suggested.

For practical application in electronic devices, the properties of the organic memory must be adjustable. Memory circuit design imposes specific windows for both on and off resistance. For instance, selection transistors cannot deliver the current to switch large arrays of metallic conductors. Moreover, the resistances of the cell should scale with the lateral dimensions. Hence, it is of paramount importance to know whether the switching is a bulk property or due to the formation of filaments. To address this question we investigated resistance switching in electron-only, hole-only and bipolar polymeric light-emitting diodes. Our findings suggest that switching is related to the nature of the electrode. By using a heat-sensitive camera, we show that the conduction in the on-state is due to the presence of conducting paths through the bulk of the semiconductor. A phenomenological interpretation of the switching is presented and the consequences for scaling are discussed.

2. Experimental

Devices were glass/bottom electrode/organic layer/top electrode sandwich structures. Glass substrates were cleaned carefully and checked by SEM and AFM measurements. Furthermore, the whole process was carried out in a cleanroom environment to exclude any influence from dust particles as reported by Tang et al. [13] and references therein. The bottom electrode was indium tin oxide (ITO)/polyethylenedioxythiophene:polystyrene sulfonic acid (PEDOT) (100 nm) or Al (30 nm). For the organic layer we used polymers with different chemical structure and bandgaps (e.g. Polystyrene, poly[2-methoxy-5-(3′,7′-dimethyloctyloxy)-1,4-phenylene vinylene] (OC_1OC_{10}), SuperYellow (Merck) and polyspirofluorene of red, green and blue color) and the small molecule material tris-(8-hydroxyquinoline)aluminum (Alq_3). Polymer films were spincoated while Alq_3 films were evaporated. The semiconductor layer thickness was varied between 60 nm and 170 nm. Top electrodes were deposited at a pressure of 10^{-6} mbar. Thereafter devices were encapsulated. The active device area was 3×3 mm^2. Depending on the electrodes, unipolar or bipolar devices are obtained. For electron-only devices we used glass/Al (30 nm)/organic/Ba/Al, Al or LiF/Al as the top electrode. The hole-only device structure was glass/ITO/PEDOT/organic/Au and for bipolar devices glass/ITO/PEDOT/organic/Ba/Al structures were used. By variation of the electrodes and the polymers about fifty different device structures were studied and at least 27 identical devices were fabricated for each structure. The data shown in the figures was measured on devices with blue polyspirofluorenes as the organic layer with a thickness of 80 nm.

An HP4155B was used to measure the *I–V* characteristics and to monitor the current during the temperature-dependent measurements. Forward or positive bias was defined with a positive bias at the bottom electrode. Temperature-dependent measurements were carried out under continuous readout conditions at 1 V and temperature was swept at a speed of 0.5 K/min. For retention measurements and read/write cycles a Keithley 2400 was used, which was controlled by a self-made computer program and compliance was set to 10 mA. A Schlumberger SI 1260 impedance analyzer was used for the *C–V* measurements. A Semicaps SOM 3000 was used for spatially resolved IR measurements. The InGaAs camera has a spectral response from 950 to 1700 nm and a spatial resolution of 10 μm.

3. Results and discussion

By variation of the electrode materials and the organic materials a large number of different device structures with an electrode/organic layer/electrode configuration were studied. Hole-only and bipolar diodes exhibited hardly any switching behavior. However, over 30% of the electron-only devices did exhibit resistive switching. Treatment of the aluminum bottom electrode with UV/O_3 or with oxygen plasma increased the yield. We conclude that

formation of a thin aluminum oxide layer is crucial for the fabrication of reliable switching devices. The bottom electrode can be much better controlled than the interface to the top contact. In some cases, if aluminum was directly evaporated on the organic layer we obtained bipolar diodes that can exhibit switching, but with significantly reduced reproducibility. Parameters like vacuum pressure during evaporation and evaporation speed seem to be important and are difficult to control. By using Ba/Al as top electrode the bipolar devices hardly switched. This indicates that Ba has a major impact on the interface formation and further that the interface between organic semiconductor and aluminum is related to the switching properties of these devices.

We deliberately varied the type of semiconductor. However, the chemical structure has no influence on the yield, and only changes in the read/write voltages were found. A polymer thickness of about 80 nm turned out to be best for reproducible and controllable switching.

Typical current–voltage characteristics of a switching diode are presented on a semi-logarithmic scale in Fig. 1. The inset shows the same data on a double logarithmic scale. Three states, labeled A, B and C, are shown. State A corresponds to the pristine device. The I–V characteristics are typical for an electron-only diode. The transport is non-symmetric with a superlinear increase in the current above a built-in voltage of approximately 1 V. We calculated the space charge limited current using a hopping transport model that takes into account a charge-carrier-dependent mobility [14]. The solid line was calculated by assuming ohmic contacts and trap-free transport, and represents an upper limit for bulk limited transport.

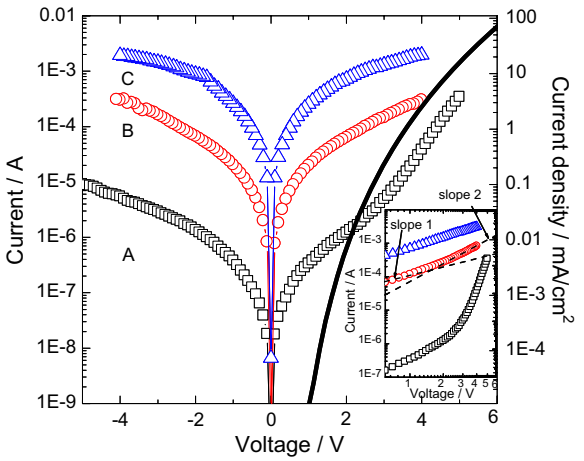

Fig. 1. Current–voltage (I–V) characteristics of an electron-only device (Al/blue polyspirofluorene/BaAl) with three different states labeled A, B and C, respectively, measured at room temperature. By using external bias stress it is possible to switch between these levels at will (see text). The black solid line indicates the upper limit for bulk transport obtained from simulations based on SCLC. The inset shows the double logarithmic representation of the data, indicating a slope between 1 and 2 of the two upper states. This indicates a different transport mechanism from the pristine state A.

States B and C are formed upon application of an external pulsed bias. In the example of Fig. 1 we used 5 s at +11 V for the transition from state A to B and 1 s at +7 V for the transition from B to C. The process is totally electrically reversible. Upon application of −10 V for 1 s, state C transforms back into state B, and when −15 V is applied for 5 s state C transforms into state A. States B and C are two examples of upper states. Several discrete upper levels can be formed in these devices, depending on the biasing conditions. Hence, the devices behave like multi-level memories.

The I–V characteristics are smooth at biases below the switching voltage. Instabilities are observed but they are typically close to the switching voltage. In the upper states and at low biases the current increases linearly with applied voltage. As shown in the inset of Fig. 1, with increasing bias the slope changes from 1 to 2, indicating a transition from ohmic to space charge limited current transport. In some devices and at higher bias the current decreases with increasing bias, but the occurrence of this negative differential resistance is not a prerequisite for switching. We note that Fig. 1 shows that in the upper states the current density exceeds the calculated limits by more than an order of magnitude. The transport in the upper states therefore cannot be limited by the bulk of the semiconductor.

Programming cycle endurance was investigated for the upper two states by applying repetitive write, read and erase cycles. As shown in the upper part and the zoomed-in inset in Fig. 2, we used a +7 V writing, +1 V read and −10 V erase bias. The switching times are smaller than the experimental resolution of our set-up of about 10 ms. However, reliability increases with increasing pulse duration. For this reason, the pulse durations were kept constant at about 1 s. Fig. 2 shows that switching is reversible and that the currents for the two states differ by about a factor of 20. There is a small variation in current levels but the switching between the two states is reliable and reproducible. The inset of

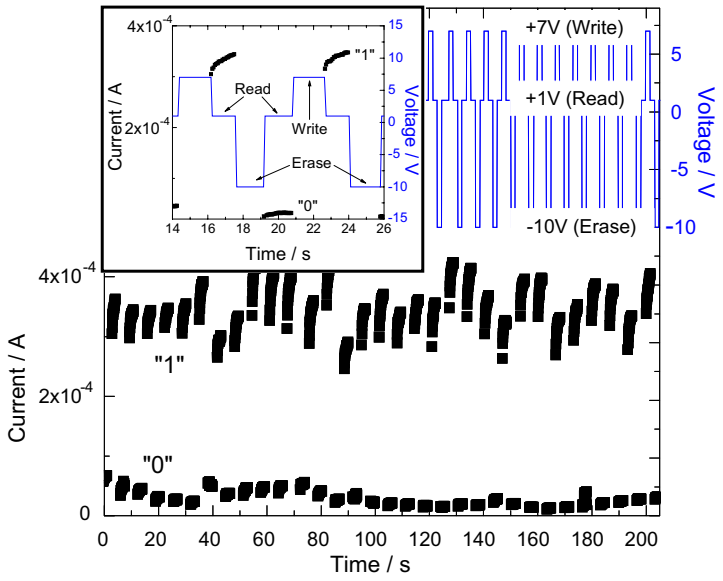

Fig. 2. Repeated read/write cycles. The upper line shows the bias sequence using 7 V to write, 1 V to read, −10 V to erase and 1 V to read again. The lower part shows the corresponding current during readout. "1" and "0" indicate the device in the C- and B-state of Fig. 1, respectively. The inset shows a zoomed-out image of two read/write cycles.

Fig. 2 shows that within a given reading pulse the current slowly increases with time. The origin for this current increase is still unknown. Fig. 2 shows the reading currents for about 30 cycles. However, over a thousand fault-free cycles could be obtained. The memory diodes investigated showed similar programming cycle endurance, but write and erase voltages had to be adjusted for each diode separately.

By adapting the pulse sequence, switching between the upper states and the pristine state is possible. However, when large numbers of cycles were measured read/write errors were obtained. Parameters such as pulse–time and voltage levels then had to be readjusted.

Data retention was measured under constant readout, the so-called stress condition, as well as with disconnected contacts in between the measurements. A readout voltage of 1 V was used. The readout currents for states A, B and C as a function of time are presented in Fig. 3a and b. The data of Fig. 3a is similar to that of Fig. 3b, showing that there is no difference between the two types of measurements. Readout is therefore non-destructive. Fig. 3 shows that over a period of months the current does not change with time. Programmed devices are remarkably stable. We note that the long data retention times eliminate bulk charge trapping as a switching mechanism. The maximum trap depth in organic semiconductors is in the order of 1 eV. For example values of 0.6 eV and less for polyfluorene were reported [15]. Studies with techniques such as thermally stimulated current show that these traps are released at temperatures below room temperature with applied voltages below 1 V and even at zero bias [16]. Therefore bulk charge trapping cannot explain the long retention times.

Trapping and release of charges and/or dipole reorganizations at one of the interfaces might lead to variations in the injection barriers and hence to switching [17]. Formation of such an interface layer should be accompanied by a change in the diode capacitance. Hence, we measured impedance spectra of the two upper states of the sample in Fig. 1. Cole–Cole plots of the measurements are presented in Fig. 4, showing semicircles that can be described by a single parallel RC circuit shown in the inset. For both states in Fig. 4 an identical value for the capacitance of 3.4×10^{-9} F was found. This value is in the same order as the geometric capacitance of the sample. The different semicircles are a result of the differences in the resistances, about a factor of 20, which are similar to the differences measured in the I–V characteristics. This shows that the memory effect is due to resistive switching. In Fig. 1 the impedance was measured at 1 V that we used as readout voltage. Voltage dependent impedance spectroscopy revealed a more complex

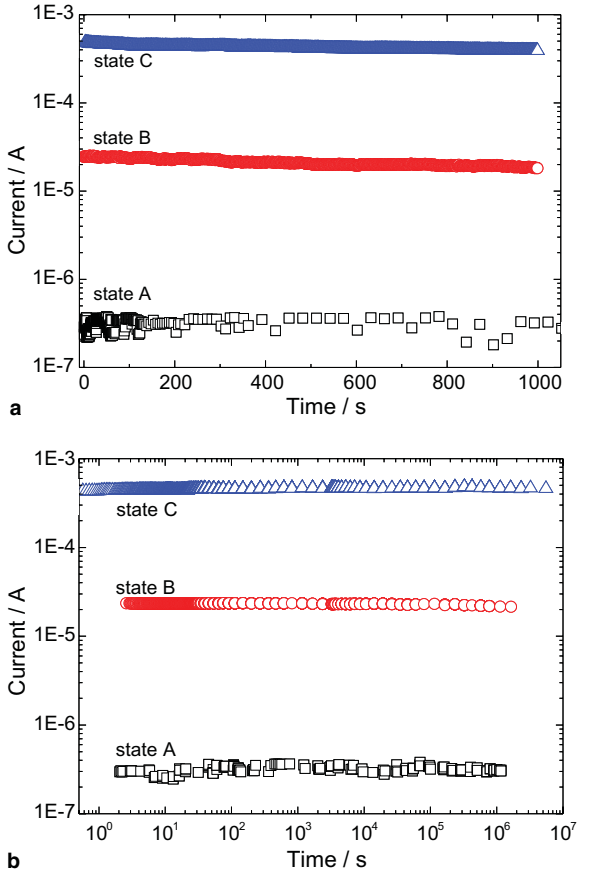

Fig. 3. Retention of the three states A, B and C from Fig. 1. (a) Measured under continuous readout (stress condition). (b) With no bias applied between measurement points. Measurements were started several seconds after writing, which is why the slight increase in current during the initial seconds is not visible. The readout voltage was 1 V. In both cases the devices are stable and exhibit remarkable retention, even after months. Furthermore, we note that readout is non-destructive.

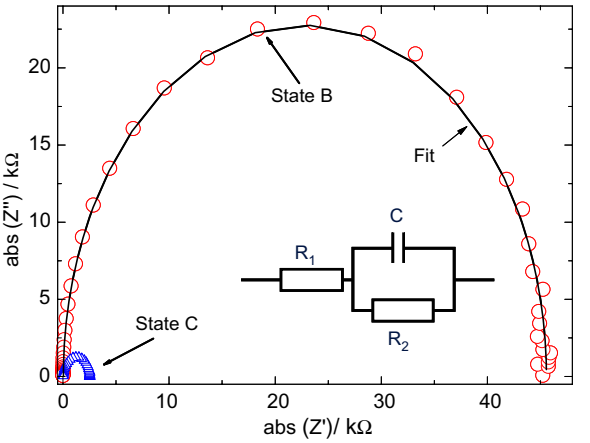

Fig. 4. Impedance spectroscopy of states B and C in Fig. 1, measured at room temperature with a bias of 1 V. Points are the measured data and lines are the fits with the equivalent circuit given in the inset. R_1 corresponds to the resistance of cables and connections, R_2 and C to the resistance and capacity of the device, respectively. In both cases R_1 and C resulted in identical values ($40\,\Omega$, 3.4×10^{-9} F), with C equal to the geometric capacity. Only R_2 changed between 2.5 kΩ and 45 kΩ.

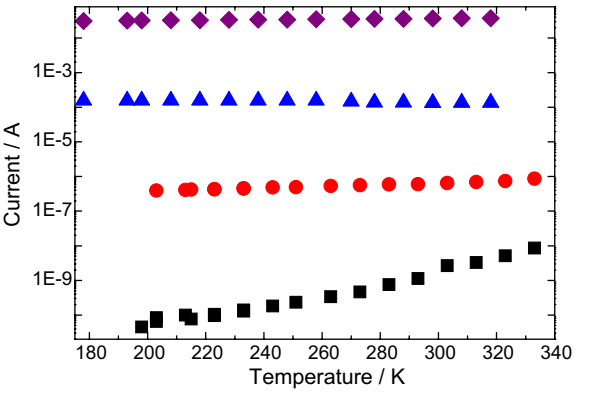

Fig. 5. Temperature dependence of the current in four different states. The lowest state that corresponds to the standard I–V characteristic (similar to state A in Fig. 1) shows a decrease in the current with decreasing temperature and is therefore thermally activated, whereas the other levels are only weakly influenced by or almost independent of temperature.

behavior that goes beyond the scope of this report and will be presented elsewhere.

Further information about the transport mechanism is obtained from temperature-dependent measurements. A diode was programmed in one of four possible states, in this case the pristine state and, in this diode, there were three accessible upper levels. The current was subsequently measured at 1 V whilst the temperature was swept at a speed of 0.5 K/min. Data integrity was checked by sweeping the temperature down and up again. The currents as a function of temperature are presented in Fig. 5. The pristine state, the original electron-only diode, shows thermally activated transport, where the current increases with increasing temperature. An exact value of the activation energy cannot be presented as the readout is close to the built-in voltage where transport is due to both drift and diffusion. Hence, the Arrhenius representation is not linear. Fig. 5 shows that the currents in the upper levels do not change with temperature. The negligible activation energies point to either metallic-like filaments or tunneling transport.

Switching of an electron-only device with 50 nm of polystyrene further supports the filamentary nature of the transport. As polystyrene is not

semiconducting, a diode characteristic corresponding to state A in Fig. 1 was not measured. However, symmetric and highly conductive states can be selected, which indicates a similar switching mechanism to that in the devices using semiconducting polymers.

Filamentary conduction in the upper states suggests that current will be transported via a limited number of filaments. If such a hypothesis is true, the filaments should show up in thermal images of the diode area. For this purpose, we investigated the homogeneity of switching diodes with an IR-enhanced CCD camera. The spatial resolution was about 10 μm. We used a constant bias of 1 V. A representative series of thermal images is presented in Fig. 6. The diode (glass/Al (30 nm)/blue polyspirofluorene/BaAl) is switched between two upper states

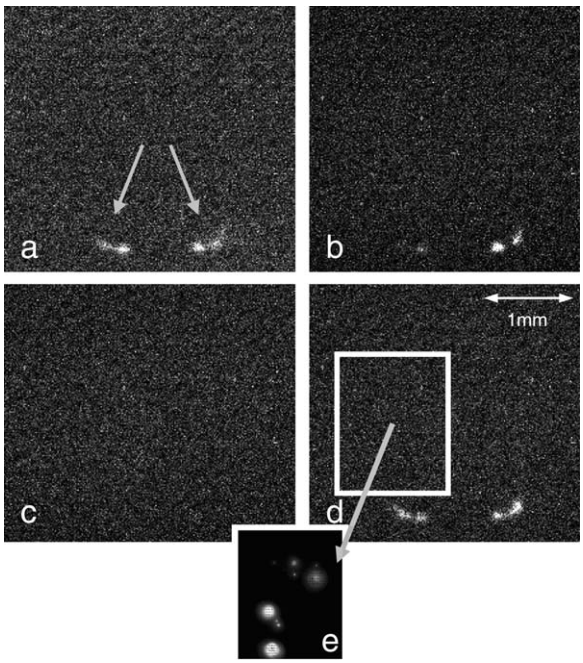

Fig. 6. Series of spatially resolved photographs made with an IR detection system showing the entire device area of 3×3 mm^2. The device is switched from the highest state (a) to a lower state (b), then to the pristine state (c) and subsequently back to the highest state (d) again. Two spots, which are located in the lower part of the device, are monitored at a bias of 1 V. In (b) the spots are still visible, but their intensity is reduced. Thus, a lower state was formed. Further negative bias stress results in the pristine state and the spots disappear (c). The identical filaments are reactivated after applying positive bias (d). This series demonstrates that transport is through filaments and that current through the filaments can be modified by bias treatment. In (e) we zoomed in on the rectangular device area marked in (d) and the readout voltage was increased to 3 V. The picture shows that a large number of filaments is present.

in Fig. 6a and b. Fig. 6c shows the thermal image when the diode is switched to the pristine state. Subsequently, in Fig. 6d, the diode is switched back to the upper state with which this series started.

In the upper high-conductance state (Fig. 6a), the image shows clearly two groups of hot spots marked by arrows. The diameters of these spots in the device are probably smaller than recorded with the CCD as the Al layer (30 nm) and the glass substrate lead to a lateral dissipation of heat. When the diode is switched into the lower upper state (Fig. 6b) one group of hot spots has nearly disappeared. Upon switching to the pristine diode (Fig. 6c), filaments can no longer be detected. The hot spots are due to highly conductive paths. However, they are not created and destroyed upon switching. Fig. 6d shows that when the original state is restored, the same original hot spots as in Fig. 6a are detected in the thermal image. We therefore conclude that upon switching the filaments are not generated nor destroyed, but that individual filaments are turned on and off, like switches.

Fig. 6a–d shows the most intense spots. However, there are many more filaments. In Fig. 6d we zoomed in on the area indicated by the dark rectangle while at the same time increasing the bias to 3 V. The resulting image is shown in Fig. 6e. It is evident that many more filaments are present. The series of pictures in Fig. 6 provides further experimental evidence of the existence of multi-state levels. The stable upper states in the switching diodes correspond to groups of filaments. Depending on the programming sequence of writing biases and pulse widths, different groups of filaments are gradually tuned or switched on and off.

The microscopic switches are most probably formed in the aluminum oxide. Aluminum is known to form natural oxide of about 2–4 nm at the surface, even if processed in a nitrogen glovebox with a concentration of water and oxygen of less than 1 ppm. Our devices therefore have an Al/oxide/organic semiconductor interface. The structure of naturally formed aluminum oxide is disordered or even amorphous [18]. Naturally formed aluminum oxide films are known to have large spatial differences in conductivity [19,20]. The differences have been attributed to variations in the local atomic structure, which lead to a broad distribution of electronic states and injection barrier heights. It has been shown that bias treatment can lead to changes in the local conductivity by orders of magnitude [18,19]. The local breakdown of tunnel junctions

has also been attributed to the formation of high-conductance aluminum oxide spots [21,22]. Theoretical models suggest that field-induced displacement of atoms in aluminum oxide is reversible [23]. This was confirmed by Kurnosikov et al. They demonstrated reversible switching of the local conductivity of natural aluminum oxide films by using an AFM tip [24]. Furthermore, by comparing *I–V* characteristics, switching behavior, switching and retention times with results obtained on metal/oxide/metal devices [25], we can conclude that switching is due to the oxide layer at the contact.

The switching mechanism can phenomenologically be understood by assuming the formation of highly conductive paths within the organic semiconducting film. We note, however, that the microscopic formation process of the filaments is still unknown. It appears that the filaments are turned on and off by reversible microscopic switches in the aluminum oxide films. The ensembles of switches are defined by the write and erase biases and pulse widths. Different pulse sequences will open and close different sets of filaments or gradually tune the current through individual filaments. This explains the multi-level stages. The highly conductive paths dominate the conduction. Hence, the current density is high and the temperature dependence in the upper states is negligible. The equivalent circuit of the diode is a single RC circuit with a geometric capacitance and variable resistance. In the off-state all switches are closed and the transport is similar to standard bulk limited semiconducting diodes. The reliability of the memory diodes is dominated by the persistence of the aluminum oxide switches. As long as the switching parameters do not change, the same set of switches is addressed. This explains the data endurance, the programming cycle endurance and its sensitivity for changes in the programming conditions.

Scaling of the device resistance with surface area is crucial for memory applications. The filamentary switching mechanism in organic memory cells fundamentally limits the scaling at small lateral dimensions. Furthermore, selection transistors cannot deliver the current to switch the metallic filaments.

Several organic memories have been published, proposing a large variety of different mechanisms that refer mainly to the bulk or change of molecular properties. Interestingly, most of these devices use aluminum as the electrode material. Although we have not investigated all different types of published organic memory devices, there are significant similarities in the reported properties with our data and a similar operation mechanism can be expected in these devices. Therefore the various mechanism for organic memories proposed in literature should be tested by using other electrode materials.

In conclusion, metal/organic/metal structures were investigated and electron-only devices with aluminum electrodes showed reversible resistive switching due to external bias. Transport and switching mechanism were studied by measuring *I–V* characteristics, retention, impedance spectroscopy and temperature dependence. Our results suggest that switching is due to the oxide layer at the electrode and transport through filaments. Photographs with a spatially resolved infrared camera proved the filamentary nature. Several published organic memory devices show comparable characteristics and a similar operation mechanism may play a role in these devices, especially when using electrodes that form oxides like aluminum. The scientific challenge now is to understand the formation of the filaments. The practical challenge is to manipulate the switching properties of the aluminum oxide films to give rise to scalable, non-volatile organic memories of which the resistances can be tuned at will.

Acknowledgements

We would like to thank Simone Vulto and Reinder Coehoorn for their helpful discussions, Edsger Smits for experimental support and Jan Jansen for sample preparation. We also gratefully acknowledge the financial support received from the EC (project PolyApply IST-IP-507143).

References

[1] D. Tondelier, K. Lmimouni, D. Vuillaume, C. Fery, G. Haas, Appl. Phys. Lett. 85 (2004) 5763.
[2] A.R. Elsharkawi, K.C. Kao, J. Phys. Chem. Solids 38 (1977) 95.
[3] R.S. Potember, T.O. Poehler, D.O. Cowan, Appl. Phys. Lett. 34 (1979) 405.
[4] C.W. Chu, J. Ouyang, J.H. Tseng, Y. Yang, Adv. Mat. 17 (2005) 1440.
[5] H.S. Majumdar, J. Baral, R. Oesterbacka, O. Ikkala, H. Stubb, Org. Electr. 6 (2005) 188.
[6] Y. Yang, L. Ma, J. Wu, MRS Bull. (November) (2004) 833.
[7] J. Ouyang, C.W. Chu, C.R. Szmanda, L. Ma, Y. Yang, Nat. Mat. 3 (2004) 918.
[8] J.G. Simmons, R.R. Verderber, Proc. R Soc. Lond. Ser. A 301 (1967) 77.
[9] L.D. Bozano, B.W. Kean, V.R. Deline, J.R. Salem, J.C. Scott, Appl. Phys. Lett. 84 (2004) 607.

[10] A. Bandyopadhyay, A.J. Pal, Appl. Phys. Lett. 82 (2003) 1215.
[11] Y.S. Lai, C.H. Tu, D.L. Kwong, J.S. Chen, Appl. Phys. Lett. 87 (2005) 122101.
[12] T. Oyamada, H. Tanaka, K. Matsushige, H. Sasabe, C. Adachi, Appl. Phys. Lett. 83 (2003) 1252.
[13] W. Tang, H. Shi, G. Xu, B.S. Ong, Z.D. Popovic, J. Deng, J. Zhao, G. Rao, Adv. Mat. 17 (2005) 2307.
[14] W.F. Pasveer, J. Cottaar, C. Tanase, R. Coehoorn, P.A. Bobbert, P.W.M. Blom, D.M. de Leeuw, M.A.J. Michels, Phys. Rev. Lett. 94 (2005) 206601.
[15] A. Kadashchuk, R. Schmechel, H. von Seggern, U. Scherf, A. Vakhnin, J. Appl. Phys. 98 (2005) 024101.
[16] R. Schmechel, H. von Seggern, Phys. Stat. Sol. A 201 (2004) 1215.
[17] T. van Woudenbergh, J. Wildeman, P.W.M. Blom, J.J.A.M. Bastiaansen, B.M.W. Langeveld-Voss, Adv. Funct. Mat. 14 (2004) 677.
[18] M.J. Plisch, J.L. Chang, J. Silcox, R.A. Buhrmann, Appl. Phys. Lett. 79 (2001) 391.
[19] E.Y. Luo, S.K. Wong, A.B. Pakhomov, J.B. Xu, I.H. Wilson, C.Y. Wong, J. Appl. Phys. 90 (2001) 5202.
[20] W.H. Rippard, A.C. Perrella, F.J. Albert, R.A. Buhrman, Phys. Rev. Lett. 88 (2002) 046805.
[21] H. Watanabe, K. Fujita, M. Ichikawa, Appl. Phys. Lett. 72 (1998) 1987.
[22] V. Da Costa, C. Tiusan, T. Dimopoulos, K. Ounadjela, Phys. Rev. Lett. 85 (2000) 876.
[23] W. Oepts, H.J. Verhagen, R. Coehoorn, W.J.M. de Jonge, J. Appl. Phys. 86 (1999) 3863.
[24] O. Kurnosikov, F.C. de Nooij, P. LeClair, J.T. Kohlhepp, H.J.M. Swagten, W.J.M. de Jonge, Phys. Rev. B 64 (2001) 153407.
[25] A. Beck, J.G. Bednorz, Ch. Germber, C. Rossel, D. Widmer, Appl. Phys. Lett. 77 (2000) 139.

Available online at www.sciencedirect.com
ScienceDirect
Organic Electronics 7 (2006) 313–318
Organic Electronics
www.elsevier.com/locate/orgel

Influence of charge balance and microcavity effects on resultant efficiency of organic-light emitting devices

Benjamin Krummacher [a,c,*], Mathew K. Mathai [b], Vi-En Choong [b], Stelios A. Choulis [b], Franky So [b], Albrecht Winnacker [c]

[a] OSRAM Opto Semiconductors GmbH, Leibniz Strasse 4, D-93055 Regensburg, Bavaria, Germany
[b] OSRAM Opto Semiconductors Inc., 3870 N 1st Street, San Jose, CA 95134, United States
[c] Department of Material Science VI, University of Erlangen-Nuremberg, Martensstrasse 7, 91058 Erlangen, Germany

Received 3 January 2006; received in revised form 30 March 2006; accepted 30 March 2006
Available online 2 May 2006

Abstract

The contribution of charge balance and optical microcavity effects in solution processed OLEDs cannot be easily quantified due to the absence of a well defined location for the emission zone. In this paper, we study the device efficiency of a solution processed blue electrophosphorescent OLED where the relative electron–hole balance is varied by means of molecular doping with an electron transport material. Changes in the electroluminescent spectra for the device series indicate the presence of optical microcavity effects, which we quantify by means of optical simulation. Furthermore, this enables us to factor out the contribution of microcavity effects on device efficiency enabling the quantification of the charge balance effect on device performance.

PACS: 85.60.Jb; 78.66.Qn; 78.60.Fi

Keywords: Organic light emitting diode (OLED); Microcavity effect; Optical simulation

1. Introduction

The efficiency of organic light-emitting diodes (OLEDs) has improved to an extent where they are being considered for lighting applications [1]. At present, the various designs for lighting fixtures are based on flat panels emitting light in the forward direction to yield diffuse light sources. This design is fully compatible with the basic architecture of OLEDs which involve organic thin films sandwiched between conducting electrodes.

However, this OLED architecture results in the formation of a microcavity, due to the double mirror structure given by the two electrodes and the organic layers embedded in between. From the perspective of charge balance within the device, electrons and holes injected from the respective contacts recombine in the emission zone (EMZ) to

* Corresponding author. Address: OSRAM Opto Semiconductors GmbH, Leibniz Strasse 4, D-93055 Regensburg, Bavaria, Germany. Tel.: +49 941 850 1983; fax: +49 941 850 444 3508.
E-mail address: Benjamin.Krummacher@osram-os.com (B. Krummacher).

1566-1199/$ - see front matter
doi:10.1016/j.orgel.2006.03.011

form excitons which undergo radiative emission to generate light. The rate and direction of emission of excitons that are physically close to the highly reflective cathode, are strongly affected by optical interference effects [2], which in turn affects the efficiency of the device. The internal device efficiency is related to the rate of emission. The external device efficiency is determined by the fraction of light, which is generated in the device stack and extracted to air. The mismatch of the refractive index between air and the OLED reduces the light output due to poor extraction of generated light. Total internal reflection into wave guiding modes and self-absorption are two mechanisms responsible for this reduction. Thus, the light emitted by the device can be classified into three modes: the external mode, the substrate waveguided mode and the anode/organic waveguided mode, as shown in Fig. 1. The distribution of the light into the three modes is affected by the emission angle of the light and the location of the emission zone.

However, in an OLED device, the internal device efficiency is highly dependent on the charge balance of the device. At the same time a modification of charge balance could lead to a change in the location of the emission zone. This can result in variations in the extent to which light is outcoupled from the device due to the dependence of the microcavity effect on the location of the EMZ [3]. Thus the resultant change in device efficiency is a combined effect of improved charge balance and alterations in the microcavity effect. Improvements in device efficiency are often assigned entirely to charge balance effects without considering microcavity effects. This is because a general methodology has not been rigorously defined to isolate the relative contribution of both effects on enhancement in device performance. In this paper we show a method, which enables the separate quantification of both effects using optical simulation.

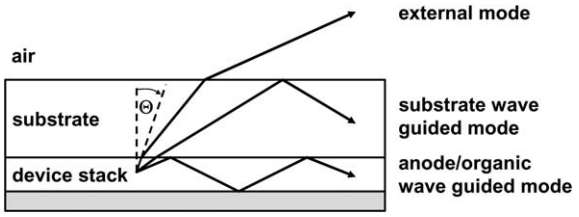

Fig. 1. The external mode, the substrate waveguided mode and the anode/organic waveguided mode in an organic EL device. Dependent on the emission angle Θ the generated photons are outcoupled or waveguided.

2. Method

2.1. OLED devices

Fig. 2 shows the structure of the devices used in this study. The light emitting polymer layer (LEP) in these OLEDs are comprised of polyvinylcarbazole (PVK) as the hole transporting matrix, 1,3,4-oxadiazole, 2,2′-(1,3-phenylene)bis(5-(4-(1,1-dimethylethyl)phenyl) or OXD-7 as an electron transporter and the blue phosphorescent dye Iridium (III)bis[(4,6-di-fluorophenyl)-pyridinato-N,C^2]picolinate (FIrpic) [4]. Keeping the amount of FIrpic in the LEP constant at 10% by weight, the relative concentrations of PVK and OXD-7 are changed in order to vary the hole and electron transport within the LEP. PEDOT and the LEP are deposited on indium tin oxide (ITO) coated glass substrates respectively, followed by thermal evaporation of the cathode layers comprising CsF and Al. The LEP (thickness of 75 nm) is spin coated from chlorobenzene and is baked at 80 °C for 30 min. Device characterization is carried out after encapsulating the OLEDs. All device fabrication steps are carried out in an inert atmosphere except for the PEDOT spin coating.

2.2. Optical modeling

Optical simulation of the experimental results was performed using the microcavity simulation tool UniMCO 4.0 by UniCAD [5]. The radiative emission from the recombining excitons is modeled by oscillating dipoles in front of a mirror. The recombining exciton is modeled as a two-level system whose transition rate is given by Fermi's golden

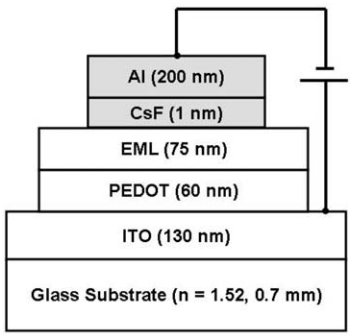

Device	% OXD-7
A	0
B	10
C	20
D	30
E	40

Fig. 2. Architecture of the devices used in this study. The table contains the device nomenclature based on the composition of the LEP.

rule [6]. The method used in UniMCO is based on the transfer matrix formalism including additional source terms for electric field (i.e. the diplole emission terms). The electric field emitted by electric dipoles can be expressed in terms of superposition of s-(TE) and p-(TM) polarized waves, while the dipole source can be decomposed into three orthogonal components (d_s, d_p, d_v), where d_s and d_p are in-plane dipole components, and d_v is the out-of plane component. It can be shown that the powers per solid angle θ and surface emitted by such dipoles in an unbounded medium of refractive index n_{emit} are of the form:

$$P_0^s = \frac{3}{8\pi} \tag{1a}$$

$$P_0^p = \frac{3}{8\pi}\cos^2\theta \tag{1b}$$

$$P_0^v = \frac{3}{8\pi}\sin^2\theta \tag{1c}$$

For a sheet of dipoles at distance z from the cathode-reflector, the power per unit solid angle and surface $P_{front}^{s,p,v}$ radiated outside the microcavity by the s-, p- and v-dipoles can be calculated from the following equations:

$$P_{front}^s = |1 + r_1^s e^{2i\varphi^I}|^2 \frac{1 - |r_2^s|}{|1 - r_1^s r_2^s e^{2i\varphi}|^2} P_0^s \tag{2a}$$

$$P_{front}^p = |1 + r_1^p e^{2i\varphi^I}|^2 \frac{1 - |r_2^p|}{|1 - r_1^p r_2^p e^{2i\varphi}|^2} P_0^p \tag{2b}$$

$$P_{front}^v = |1 + r_1^v e^{2i\varphi^I}|^2 \frac{1 - |r_2^v|}{|1 - r_1^v r_2^v e^{2i\varphi}|^2} P_0^v \tag{2c}$$

where r_1 is the reflectivity coefficient of the anode mirror and r_2 the reflectivity of the cathode mirror of the microcavity, φ and φ^I are given by

$$\varphi = \frac{2\pi z}{\lambda} n_{emit}\cos\theta_{emit} \tag{3}$$

$$\varphi^I = \frac{2\pi d}{\lambda} n_{emit}\cos\theta_{emit} \tag{4}$$

where λ is the wave length of the emitted light and d is the optical path length.

Only the radiation emitted in the source medium (refractive index n_{emit}) with angles θ_{emit} smaller than the critical angle: $\theta_{emit}^0 = \arcsin(n_a/n_{emit})$, where n_a is the refractive index of the outside medium, can be extracted out of the microcavity. The interval $[0, \theta_{emit}^0]$ corresponds to the escape window of the radiation. If $\theta_{emit} > \theta_{emit}^0$, the light will undergo total internal reflection. The amount of extracted light is a fraction of the light generated in a distance z from the cathode:

$$P_{extr}^{s,p,v} = P_{front}^{s,p,v} \quad \text{for } 0 \leqslant \theta_{emit} \leqslant \theta_{emit}^0 \tag{5}$$

Considering an emission zone profile $E(z)$ $(0 < z < Z)$, the total power radiated out of the device is given by

$$P_{total}^{s,p,v} = \int_0^z E(z)\,dz \int_0^{\theta_{emit}^0} \sin\theta\,d\theta \int_0^\infty d\lambda P_{front}^{s,p,v}(\theta,\lambda) \tag{6}$$

Further refinements are based on the optical constants as a function of wavelength for all layers of the device stack.

Considering Eqs. (1)–(6), it is obvious that the variation in the location and shape of the exciton profile ($E(z)$) formed within the LEP can result in significant differences in the extent to which light can be outcoupled from the device due to the presence of a microcavity in the OLED stack. It is also evident that such microcavity effects can lead to changes in the electro luminescence (EL) spectrum, as light corresponding to different wavelengths are outcoupled to a different extent for a given location of the emission zone.

Furthermore the model allows the determination of the emission spectrum of the emitter in a space filled with the emitting medium without any interfaces, EL0. EL0 is extracted from experimental data, using the EL-spectrum of the device measured in the direction normal to the device substrate, and performing numerical back calculation based on the model described above.

3. Results and discussion

The devices utilized in this study involve a given emitter (FIrpic) which is contained in an LEP where the electron and hole charge balance is systematically varied by varying the relative concentration of PVK and OXD-7 [4]. In Fig. 3, the luminous efficiency of these devices is plotted as a function of current density.[1] Given that the device in the absence of OXD-7 is hole dominated [4] the rise in

[1] The light output of the devices was measured using a large area (18 mm × 18 mm) Si photodiode. The distance between the Si photodiode and the OLED substrate's surface was kept at <0.5 mm. Considering the size of the OLED's active area of 4 mm^2 in comparison to the area of the Si photodiode, this setup offers a nearly entire solid angle collection of the light emitted by the devices.

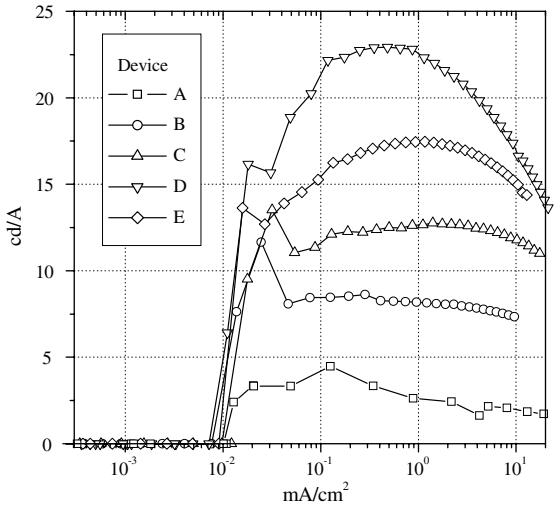

Fig. 3. Current efficiency (cd/A) versus current density for devices with varying OXD-7 concentration in the light emitting spin coated layer.

device efficiency with increasing OXD-7 concentration in the LEP is the result of better injection and transport of electrons within the LEP. This trend is seen to exist between devices A–D. The fall in efficiency of device E could be due to too much electron injection into the LEP.

However, this explanation does not consider the microcavity effects. Using the EL-spectra of devices A–E (Fig. 4), the presence of microcavity effects can be demonstrated. The spectra were measured at a fixed current density of 1 mA/cm^2. The inset shows the entire spectrum, while the main portion of the figure is a magnified portion of the same spectrum in the 500 nm region for all devices. As observed, the shoulder at 500 nm is seen to increase with increasing OXD-7 concentration in the LEP. Thus, at a fixed current density, the spectrum of the FIrpic devices changes as a function of the OXD-7 content in the LEP. This takes place in spite of the absence of any emission from species other than FIrpic in the LEP. Changes in the PL-spectra due to the different OXD-7 concentrations were not observed for the devices used in this study. We will show that these changes observed in the EL spectra can be attributed to the variation in the location of the exciton recombination zone within the LEP as its composition is changed.

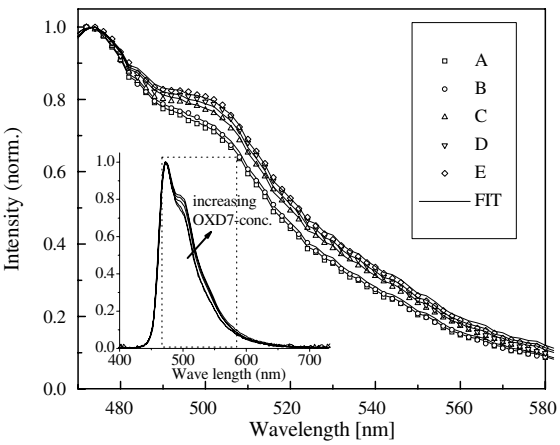

Fig. 4. Variation in EL-spectra at a fixed current density of 1 mA/cm^2 for devices with varying OXD-7 concentration. The inset shows the total EL spectrum for the devices over the entire wavelength range in the visible region.

Using the microcavity simulation tool described above, the EL-spectra in Fig. 4 were fitted. The parameters used for the fit were the location of the EMZ and the internal emission spectrum of the material (EL0). We assume that the photoluminescence spectrum of FIrpic corresponds to EL0. The complex index of refraction as a function of wavelength was determined by the means of standard ellipsometry for all organic layers and electrode materials used in this study in order to ensure accurate simulation. For the calculation, the location of the EMZ is needed. The location of the EMZ is defined as the distance between the cathode and the centre of a Gaussian distribution of excitons within the LEP. In a work published by Wu et al. a scope of the exciton distribution of approximately 25 nm was determined experimentally for FIrpic in DCB [7]. As both PVK and DCB contain carbazole as functional group a similar behavior for exciton diffusion is expected. Thus, a full width at half maximum of 20 nm was chosen for the distribution of excitons within the LEP in the simulation. Given the EL spectrum of each device, the distance between the EMZ and the cathode was varied till the calculated EL0 matched the PL spectrum of FIrpic, which is considered to be the actual EL0 as stated above. According to the simulation results the distance between cathode and EMZ increased from 20 nm for device A to 60 nm for device E. This can be explained as follows: As the amount of OXD-7 in the LEP increases, more electrons are able to penetrate into the LEP. This results in a higher extent of exciton formation in those regions of the LEP which are farther from the cathode.

In the following, we quantify the effect of the change in the location of the EMZ on device performance due to improved charge balance and

microcavity. First, the external light output as a function of the location of the EMZ was determined for the device geometry used in this study (Fig. 5). In the calculation, a constant electron–hole balance leading to a uniform recombination rate was assumed. Finally, by analyzing the external light output, the microcavity effect is determined. The circles in Fig. 5 mark the light output for the imaginary devices A′, B′, C′, D′, E′, which all have the same locations of the EMZ as the corresponding real devices A, B, C, D, E. To obtain the actual effect of charge balance, the microcavity effect is superimposed onto the actual measured experimental data. The portion of the light output not due to microcavity effects is attributed to the charge balance. We will illustrate this with devices A and D.

When considering microcavity effects alone, we see that the light output of Device D′ is almost twice as high as the output of device A′ (Fig. 5). However in the case of the real devices A and D, the light output of device D is 8.5 times more than that of device A for the same current density (Fig. 3). Based on the comparison of devices A′ and D′, the improvement in device efficiency due to the microcavity effect is given by the measured output of device D divided by two. The rest of the improvement is due to the effect of improved charge balance.

A more rigorous description of the above calculation can be stated as follows: the improvement due to better charge balance in comparison to device A is given by

$$\Delta_1(X) = \frac{O_m(X)}{O(X')} - O_m(A) \tag{7}$$

where $O_m(X)$ ($X \in [B, C, D, E]$) is the measured light output at constant current density and $O(X')$ ($X' \in [B', C', D', E']$) is the light output of the imaginary devices normalized on the output of A′. The improvement compared to device A due to the microcavity effect is given by

$$\begin{aligned}\Delta_2(X) &= O_m(X) - [\Delta_1(X) + O_m(A)] \\ &= O_m(X) - \frac{O_m(X)}{O(X')}\end{aligned} \tag{8}$$

The block graph in Fig. 6 shows the external light output of the devices used in this study normalized on the output of device A (current density of 1 mA/cm^2). The cross-hatched area represents the efficiency improvement compared to device A due to the microcavity effect. The improvement in device efficiency due to better charge balance is marked by the double ended arrows. The effect on the efficiency due to microcavity and charge balance increase from device A to device D. In comparison to device A the internal efficiency of device D is increased by a factor of 4.4 due to the effect of improved charge balance. The microcavity effect caused by the change in the location of the EMZ further improves the efficiency by a factor of 1.93 (an overall improvement of 8.5) from device A to D. The drop of device efficiency from device D to

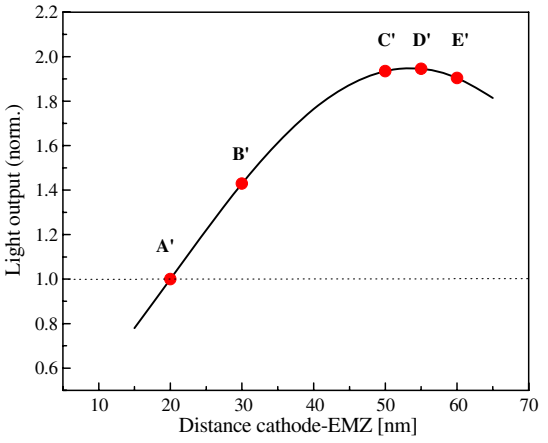

Fig. 5. Calculated external light output (for constant current density) as a function of the location of the EMZ. The exciton formation rate was assumed to be constant. The circles in the graph mark the light output for the imaginary devices A′, B′, C′, D′, E′, which all have the corresponding locations of the EMZ as the real devices A, B, C, D, E. The graph describes the efficiency improvement in comparison to device A due to the microcavity effect dependent on the location of the EMZ.

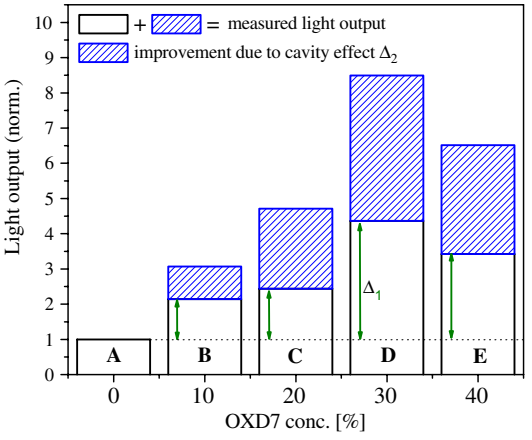

Fig. 6. Measured external light output of the devices used in this study. The cross-hatched area represents the efficiency improvement compared to device A due to the microcavity effect. The improvement in efficiency due to better charge balance is marked by the double ended arrows.

device E is mainly caused by a decrease in internal device efficiency. This is attributed to the achievement of optimum charge balance for device D. Additional increase in OXD-7 tilts charge balance and makes device E electron dominant. Quenching effects due to the proximity to the PEDOT layer also begin to have a larger contribution.

4. Conclusion

To summarize, the evolution of device efficiency for a class of OLEDs with different hole–electron balance in the LEP was studied. While charge balance is observed to play a major role, optical microcavity effects also contribute to the improved efficiency. These effects are the result of the movement of the exciton profile within the LEP, and are often not taken into consideration when analyzing the effect of charge balance on device performance. By analyzing the changes in EL-spectra from the series of devices we can pinpoint the location of the EMZ within the LEP, from which the microcavity effect can be quantified. Based on this, we illustrate a general methodology to determine the contribution of both charge balance and optical effects while analyzing the performance of devices.

Acknowledgements

We would like to thank Dr. Ji-Hai Xu from UniCAD, Inc. for useful discussions and support. This work is supported by the Department of Energy (Polymer OLED White Light Development Program; award number DE-FC26-04NT41947).

References

[1] M.A. Baldo, S. Lamansky, P.E. Burrows, M.E. Thompson, S.R. Forrest, Appl. Phys. Lett. 75 (1999) 4.
[2] J.-S. Kim, P.K.H. Ho, N.C. Greenham, R.H. Friend, J. Appl. Phys. 88 (2) (2000) 1073.
[3] C. Adachi, M.A. Baldo, M.E. Thompson, S.R. Forrest, J. Appl. Phys. 90 (2001) 5048.
[4] M.K. Mathai, V.-E. Choong, S.A. Choulis, B. Krummacher, F. So, Appl. Phys. Lett., in press.
[5] Available from: <www.unicadinc.com>.
[6] V. Bulovic, V.B. Khalfin, G. Gu, P.E. Burrows, D.Z. Garbuzov, S.R. Forrest, Phys. Rev. B 58 (1998) 3730.
[7] Z. Wu, L. Wang, G. Lei, Y. Qiu, J. Appl. Phys. 97 (2005) 103105-1.

Available online at www.sciencedirect.com
ScienceDirect
Organic Electronics 7 (2006) 319–329
Organic Electronics
www.elsevier.com/locate/orgel

Concentration dependence of amplified spontaneous emission in organic-based waveguides

Eva M. Calzado [a,b], José M. Villalvilla [a,b], Pedro G. Boj [a,c], José A. Quintana [a,c], María A. Díaz-García [a,b,d,*]

[a] Instituto Universitario de Materiales de Alicante (IUMA), Universidad de Alicante, 03080 Alicante, Spain
[b] Departamento de Física Aplicada, Universidad de Alicante, 03080 Alicante, Spain
[c] Departamento Interuniversitario de Óptica, Universidad de Alicante, 03080 Alicante, Spain
[d] Unidad Asociada CSIC-UA, Universidad de Alicante, 03080 Alicante, Spain

Received 23 December 2005; received in revised form 23 March 2006; accepted 3 April 2006
Available online 2 May 2006

Abstract

The concentration dependence of amplified spontaneous emission (ASE) in optically pumped polystyrene (PS) films containing a variable concentration (between 2.5 and 100 wt%) of the luminescent and hole-transporting organic molecule *N*,*N*′-Bis(3-methylphenyl)-*N*,*N*′-diphenylbenzidine (TPD) is reported. It is observed that both, the ASE threshold and linewidth above threshold, decrease with concentration up to 20 wt% doped films and then keeps a constant value up to concentrations of 100 wt% (neat films). Accordingly, photoluminescence (PL) efficiency increases with concentration up to 20 wt% and then saturates. Results also show that the position of ASE can be tuned between 413 and 421 nm by changing the concentration of TPD. These shifts are also observed in the PL emission and are presumably due to the increase of absorption, as well as polarity of the medium, with concentration. Measurements and modeling of the waveguiding characteristics of the films, show that the observed shifts are not due to cut-off thickness limitations. In addition, although the different confinement of the waveguide modes might be influencing the ASE performance, it seems to be determined mostly by the PL efficiency. Results show that the most efficient films are those doped with 20–30 wt% TPD. Finally, a study of the photostability of the samples is also included.

Keywords: Amplified spontaneous emission; Organic lasers; Photoluminescence; TPD; Light-emitting devices

1. Introduction

In the last years, organic solid-state lasers, based on both, polymers and small organic molecules have been the subject of numerous investigations [1–3]. The main advantage of organic materials is that they can be fabricated onto almost any type of substrate (including flexible ones) by inexpensive

* Corresponding author. Address: Departamento de Física Aplicada, Universidad de Alicante, Facultad de Ciencias Fase II Univ., 03080-Alicante, Alicante, Spain, Tel.: +34 96 5903400x 2905; fax: +34 96 5909726.
E-mail address: maria.diaz@ua.es (M.A. Díaz-García).

1566-1199/$ - see front matter © 2006 Elsevier B.V. All rights reserved.
doi:10.1016/j.orgel.2006.04.002

techniques, such as spin-coating, photolithography, ink-jet printing, etc., in contrast with the sophisticated technology used with inorganic materials. At present, optically pumped organic lasers have been demonstrated in a large variety of materials. However, the organic diode laser (electrically pumped) keeps being a goal to achieve.

A few years after the discovery of the laser in 1960, the first solid-state organic lasers, consisting of small organic molecules (dyes) inserted in different kind of matrices, were reported [2]. The main problem of these materials is the stability. In addition, generally they can not be electrically pumped and there is a limit in the amount of dye that can be introduced, since at high concentrations molecular interactions lead to photoluminescence (PL) quenching [4,5]. In 1996 the interest in the field grew considerably with the first reports of laser action in optically pumped semiconducting polymer films [6–8]. As contrary to most dyes, these materials are semiconductors, thus offering the possibility of being pumped electrically. Moreover, in most cases quenching of the PL and the stimulated emission (due to molecular interaction) is not observed in neat films. So, in the following years optically pumped polymeric lasers were demonstrated in many different configurations (microcavities, distributed feedback (DFB), microrings, etc.,) [1]. Today, a very good level of threshold optimisation has been achieved, and their application as optical amplifiers might become soon a reality [3]. Concerning solid-state lasers based on low molecular weight materials, the previously mentioned limitations of dye concentration, where circumvented in 1997 by using guest-host systems, so very low laser thresholds were achieved [1]. Besides guest-host systems, stimulated emission has been reported from oligothiophene single crystals [9–11] and oligophenylenes in the form of fibers grown by epitaxy [12,13]. Just a few materials, such as various thiophene-based oligomers [14–16], as well as several spiro-type materials [17,18], have shown laser action in the form of neat films. In the case of the oligothiophenes, their functionalization with thienyl-S,S-dioxide groups led to high solid-state PL efficiencies [19] while keeping good chemical stability. This increase in PL efficiency was due to the reduction of nonradiative processes in the functionalised molecules induced by the variation of both, the supramolecular organization in the solid-state and the single molecule properties [20]. On the other hand, for the spiro-type materials, the concept of spiro-linkage of a chromophore to other molecular group was used in order to enhance film quality, that has been proven to be a relevant factor in preventing the PL quenching due to intermolecular interaction. Very recently the usage of *tert*-butyl groups in sexiphenyl molecules [21] has served to prevent crystallization of the dyes, so stimulated emission was observed, as contrary to the simple p-sexiphenyl molecule. Another interesting material, that has received attention from our group and others, is the hole-transporting molecule *N*,*N*′-Bis(3-methylphenyl)-*N*,*N*′-diphenylbenzidine (TPD). Laser action has been reported in both, neat [22] and diluted [23] (in polystyrene (PS)) films.

The simplest method to study the laser properties of a certain material consists of identifying the presence of amplified spontaneous emission (ASE) by photopumping films of the material. If ASE takes place, a collapse of the width of its PL spectrum (at a certain pump intensity) is observed [1,6,7]. This spectral narrowing is normally accompanied by a large enhancement of the output intensity and accounts for the presence of gain due to stimulated emission. By studying the dependence of the emitted signal with the length of the pump stripe, gain coefficients can be determined [24]. These studies were carried out in 15 wt% TPD doped PS films, so a gain coefficient of 16 cm^{-1} at 12.4 kW/cm^2 was obtained [25].

Generally, ASE takes place when the active films constitute waveguides, i.e., the refractive index of the film is larger than that of the substrate and the thickness is larger than the cut-off thickness for the propagation of one mode. Several groups have investigated the influence of the waveguiding properties of the films in the ASE performance [26–28]. Recently we reported on the dependence of ASE with film thickness in PS films doped with 15 wt% TPD [29]. The position of ASE could be tuned between 404 and 417 nm by changing film thickness. Moreover, the position and the threshold of ASE were explained in terms of the different confinement of the propagation modes due to thickness variations. Another way to tune the ASE wavelength consists on changing the concentration of active material. These type of shifts have been observed in blends of two polyfluorenes [28]. In that case the process was rather complicated by the existence of energy transfer, so the origin of these shifts was not clear. In the present work we study the dependence of ASE (in terms of threshold, final linewidth and wavelength position) with the concentration of

TPD in PS films. In addition, the influence of the waveguiding properties in the ASE performance is investigated in detail.

One of the main problems of solid-state dye-doped polymer devices is the poor photostability of the chromophores [30]. Although many attempts have been made in order to improve the photostability of the materials [30,31], as far as we know, commercial systems based on these materials are not still available. Given the importance of this issue, the photostability of our samples is also discussed in this work.

2. Sample preparation and experimental procedures

The samples were prepared by the spin-coating technique. Toluene solutions containing PS as an inert polymer doped with a varying concentration of TPD (ranging from 5% to 90% by weight (wt%) of the total mass) were prepared and spin-coated over glass substrates (BK7). The concentration of the solid material with respect to the solvent was adjusted in order to get films with similar thickness (around 425 nm). Also, neat films of TPD (i.e., 100 wt% of TPD and no PS) were deposited by spin-coating a solution containing 40 mg of TPD in 1 ml of toluene. In this case films of 150 nm thick were obtained.

Film quality (transparency and homogeneity) was very good for concentrations of TPD up to 70 wt%. On the other hand, for high concentrations of TPD (>80 wt%), and specially for the neat films, problems of lack of homogeneity and stability appeared (films remained transparent just for a few hours after preparation). It should be noted that this stability refers to samples left in air and in the dark. Photodegradation, i.e., degradation under the excitation beam, is discussed in detail below.

The thickness of the samples was measured by means of an interferometer coupled to an optical microscope. The waveguiding properties of the films were characterized by the m-line technique at 633 nm. The linear absorption was measured in a Shimadzu spectrophotometer. Standard PL spectra were obtained in a Jasco FP-6500/6600 fluorimeter, exciting the samples at 355 nm and then collecting the transmitted beam at a 45° angle to avoid the pump beam.

The experimental setup used to investigate the presence of stimulated emission in these materials has been reported elsewhere [23,24,29]. Samples were photopumped at normal incidence with a pulsed Nd:YAG laser (10 ns, 10 Hz) operating at 355 nm, which lies in the absorption region of TPD. The energy of the pulses was controlled using neutral density filters. The laser beam was expanded, collimated and only the central part was selected in order to ensure uniform intensity. A cylindrical lens and an adjustable slit were then used to shape the beam into a stripe width of approximately 0.53 mm by 3.5 mm. When ASE occurs in a long, narrow stripe, most of the light is emitted from the ends of the stripe. Therefore, the pump stripe was placed right up to the edge of the film where the emitted light was collected with a fiber spectrometer.

3. Waveguide modeling

The films under study constitute asymmetric planar waveguides, since their refractive index is larger than those of the substrate (glass, s) and the cover (air, c). The equation for the guided modes is given by [32]

$$k n_f h \cos\theta_m + \phi_s + \phi_c = m\pi \tag{1}$$

where k is the free space wave vector, n_f and h are respectively the refractive index and the thickness of the organic film, m is an integer that accounts for the mode order, θ_{m} is the angle of propagation for mode of m-order and ϕ_s and ϕ_c are half of the phase changes at the interfaces film-substrate and film-air, respectively. The equations for ϕ_s and ϕ_c for TE and TM polarizations read:

$$\tan\phi_{c,s}^{\mathrm{TE}} = -\sqrt{N_{\mathrm{eff}}^2 - n_{c,s}^2}/(n_f\cos\vartheta) \quad \text{and}$$
$$\tan\phi_{c,s}^{\mathrm{TM}} = (n_f^2/n_{c,s}^2)\tan\phi_{c,s}^{\mathrm{TE}} \tag{2}$$

where $N_{\mathrm{eff}} = n_f \sin\theta$ is the so-called effective index.

The procedure we generally use consists in experimentally determining the effective indexes for the different modes of a certain waveguide by the m-line technique. Then, by solving Eq. (1) numerically, the refractive index and the thickness of the film can be determined. As described in next section, all the waveguides studied here had just one propagation mode (for each polarization), so Eq. (1) was used to determine the refractive index of the film by using the film thickness values measured by interferometry.

It can be shown that for h/λ values below a certain quantity there is no solution for Eq. (1). In other words, for a certain mode, there is a minimum thickness (at a given wavelength) below which the

mode can not propagate. Similarly, for a given thickness, the mode can not propagate for wavelengths above the so-called cut-off wavelength. The cut-off condition for the zero-order mode at TE polarization is given by [32]:

$$(h/\lambda) = \tan^{-1}\sqrt{(n_s^2 - n_c^2)/(n_f^2 - n_s^2)}/(2\pi\sqrt{n_f^2 - n_s^2}) \quad (3)$$

In order to evaluate the confinement of the different propagation modes one should take into account that the light penetrates in the substrate and the cover. These penetration depths ($x_{s,c}$) can be expressed as [32]:

$$x_{s,c} = z_{s,c}/\tan\vartheta \quad (4)$$

where $z_{s,c}$ values for TE and TM polarizations are given by:

$$z_{s,c}^{\mathrm{TE}} = \tan\vartheta \Big/ (k\sqrt{N_{\mathrm{eff}}^2 - n_{s,c}^2}) \quad \text{and}$$

$$z_{s,c}^{\mathrm{TM}} = z_{s,c}^{\mathrm{TE}} \Big/ \left(\frac{N_{\mathrm{eff}}^2}{n_{s,c}^2} + \frac{N_{\mathrm{eff}}^2}{n_f^2} - 1\right) \quad (5)$$

The larger the penetration depth, less confined the mode becomes. Therefore, the lack of confinement of the mode is directly related to the total penetration depth into the substrate and the cover (air in this case):

$$x_{\mathrm{total}} = x_s + x_c \quad (6)$$

4. Results and discussion

4.1. Absorption and emission spectra

Photoluminescence spectra for films containing a varying concentration of TPD (from 2.5 to 100 wt%) were obtained in the fluorimeter (PL), as well as in the setup for the ASE characterization, where light is collected from the edge of the sample. In the latter case, spectra below (denoted as PL-e, referring to PL-edge) and above (ASE) the threshold for ASE were obtained. The expected [23] collapse of the spectrum due to ASE at sufficiently high pump intensity (above the threshold) was observed for all films, even for non-diluted films (100 wt% TPD), as contrary to most laser dyes [4]. As an illustration, spectra for the 50 wt% TPD doped film are presented in Fig. 1. Absorption is also plotted in the figure. As observed, the PL spectrum consists of a main band (0-0 transition) with a maximum at 403 nm and the first vibronic

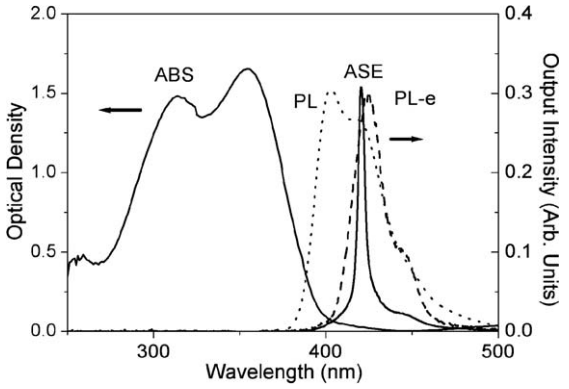

Fig. 1. Optical absorption and emission spectra of a 50 wt% TPD doped PS film: Optical density (ABS, full line, left axis), standard photoluminescence (PL, dotted line, right axis), photoluminescence spectra collected from the edge of the sample at low pump intensity (0.69 kw/cm^2; PL-e, dashed line, right axis) and at high pump intensity (16.5 kw/cm^2; ASE, full line, right axis). The intensity of the ASE curve has been divided by 80 for comparison purposes.

peak (0-1 transition) at around 420 nm. ASE takes place at the wavelength of the 0-1 transition and the spectrum reaches a linewidth of 4.8 nm. For the regime of concentrations studied here, gain-narrowing takes place at the first vibronic peak, as contrary to dilute liquid solutions, for which ASE occurs at the main 0-0 band [22]. This is due to the fact that in the films, absorption (and consequently losses), is larger at the blue end of the emission spectrum, where spectral overlap occurs between absorption and emission. So, net gain at the 0-1 transition is larger than at the main band. It is also interesting to note that the PL-e spectrum (obtained in the ASE setup below threshold) differs from the PL spectrum (obtained in the fluorimeter). For the 50 wt% TPD doped film (shown in Fig. 1), the PL-e spectrum is dominated by the 0-1 transition, while the 0-0 transition practically is not observed. In fact, the shape of the PL-e spectra obtained in the ASE setup depend on concentration as illustrated in Fig. 2. For low TPD concentrations the shape of the PL-e spectra are very similar to those of the PL. When the concentration is increased, the intensity of the 0-1 transition grows with respect to that of the 0-0 band. For high TPD concentrations, the 0-1 transition is dominant and new transitions appear at longer wavelengths. These variations in the shape of the PL-e spectra are due to the experimental configuration used. In the ASE setup, emitted light travels along the waveguide, being amplified in its way until is collected

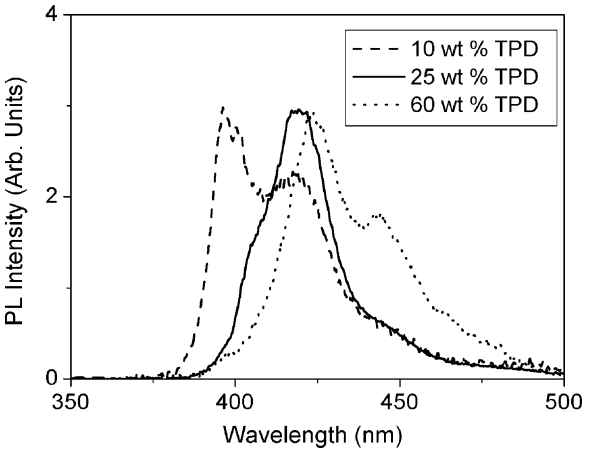

Fig. 2. Photoluminescence emission spectra collected from the edge of the sample at pumping intensities below the ASE threshold (PL-e) for PS films of various TPD concentrations (wt%).

from the edge. On the other hand, in the fluorimeter, the collected light has not been guided, so it travels a much shorter distance across the film. Since gain takes place at the wavelength of the 0-1 transition, in the ASE setup the 0-1 transition will be enhanced with respect to the main band, even below the threshold. Obviously, the larger the TPD concentration, the larger the gain, justifying the fact that these changes are more evident in highly doped films. On the contrary, the shape of the PL spectra (obtained in the fluorimeter) do not depend on TPD concentration, since in this case emitted light travels a much shorter distance across the film until it is collected. Concerning absorption spectra, their shape do not change with concentration.

Kruhlak et al. used side-illumination fluorescence spectroscopy (SIF) [33] to study dye-doped polymer fibers [34]. By looking at the changes in the PL spectrum due to absorption along the fiber, the linear absorption spectrum could be determined. The SIF experiment has some similarities with our ASE setup, since the sample (planar waveguide or fiber) is excited in a direction perpendicular to the waveguide plane or the fiber length, while the emitted luminescence is collected in the propagation direction. As a consequence, the PL emitted in the excited region travels some distance along the waveguide or fiber until it is collected. Therefore, the gain or absorption experienced by the light will result in changes in the PL spectrum. As previously discussed for TPD waveguides, the existence of gain at the 0-1 band at 420 nm explains the fact that the shape of the PL spectrum collected from the edge (PL-e) is different than the PL spectrum obtained in the fluorimeter. In the case of the fibers studied with SIF, different PL spectra are obtained when the distance traveled by the emitted light is changed, since the absorption increases with the distance. The main difference between both setups consists in the fact that in the SIF experiment the fiber is excited with a spot of light at a certain distance from the end of the fiber, so the emitted light travels that distance until it is collected. On the other hand, in the ASE setup the excited region is a stripe of light that reaches the edge of the sample, where light is collected. Thus, in this case, depending on the particular spot of the stripe from where light has been emitted, the distance traveled by the light is different. As a consequence, results obtained by these two experiments, can not be directly compared.

As previously mentioned, the quality of the neat films was not very good and they degraded quickly after preparation, so reproducibility was a main problem, specially when they wanted to be compared with the rest of the films. For that reason, data related to neat films are not shown in the various figures presented below. Nevertheless, they follow the same trend in the concentration dependence that the rest of the films.

The normalized PL intensity (integrated area/film thickness) is plotted in the left axis of Fig. 3 as a function of concentration. Absorption at the excitation wavelength (355 nm) divided by film thickness has been also represented in Fig. 3 (right

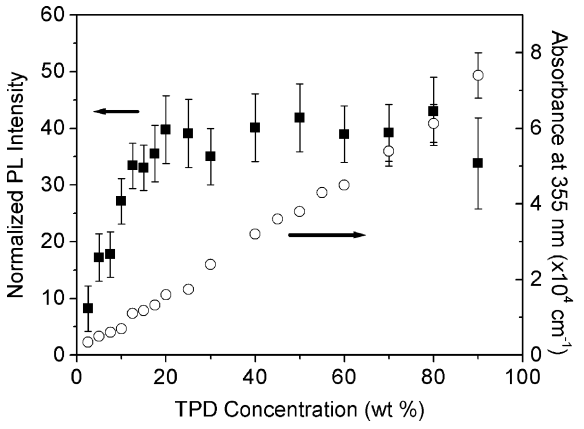

Fig. 3. Normalized PL intensity (total integrated area/thickness) (full squares, left axis) and absorbance at the excitation wavelength (optical density at 355 nm/thickness) (open circles, right axis) as a function of TPD concentration (wt%) in PS films.

axis). As contrary to absorption, that has a linear dependence with concentration, the PL curve increases up to around 20 wt% and then saturates and keeps constant with concentration. Presumably, the saturation of the PL is due to molecular interaction, that seems to be more important for TPD concentrations above 20 wt%. However, some aspects remains unclear, i.e. the type of interactions that take place, why they occur for concentrations above 20 wt% and why the PL is not completely quenched as it happens in most of molecular laser dyes. In thiophene-based oligomers, as previously mentioned, the functionalization with thienyl-S,S-dioxide groups led to high solid-state PL efficiencies and stimulated emission, that was explained in terms of the different supramolecular organization in the solid-state and the single molecule properties [20]. Since interchain interactions seem to play a major role in the luminescence and hence the laser properties of organic systems [5], the study of the interchain effects in TPD would be important to understand the observed behavior. There exist some density functional theoretical studies of the geometric structure and energetics of TPD [35,36], that have been compared with the crystal structure determined crystallographically [37,38]. However, the main objective of these reports was to relate the structure of TPD with its transport properties, since TPD has been extensively used as a hole-transporting material in LED devices. Concerning the optical properties of TPD, as far as we know, calculations in order to elucidate its PL and lasing properties, have not been reported so far. In our group some work in this direction is currently being performed. In particular, ab initio calculations for both, the isolated molecule and the dimmer, and comparison with the absorption and PL spectra experimentally obtained, are already available and will be published elsewhere [39]. For the neat films, the role of charge-transfer excitons in the PL and ASE efficiencies could be investigated by calculating the exciton resonance interaction, as well as the interchain transfer integrals [20], for each couple of molecules along all directions, using the available X-ray structure [37]. On the other hand, for the TPD doped PS films no structural information is available. We have estimated the molecular density in the diluted films by simply dividing their weight by their volume. Then, by assuming that the molecules are isolated, the distance between two of them would be around 16, 14 and 12 Å for the 10, 20 and 30 wt% doped films respectively. These distances are comparable to the size of TPD (around 13 Å), so point-dipole approximation is not valid and consequently, as in the case of neat films, we must deal with distribution of overlap charges. Our calculations [39] show that the distance between molecules in the dimmer is around 6 Å. Taking into account that the distance between molecules in the TPD doped films is rather small, molecules could be forming dimmers. A detail description of the influence of dimmer formation in the optical properties and its role in the PL saturation observed at 20 wt% is out of the scope of this paper. In any case, it should be noted that such studies are complicated by the fact that no structural information is available.

4.2. ASE performance: Concentration dependence

The concentration dependence of ASE has been studied through three parameters: pump intensity threshold, final linewidth (full width at half of the maximum, FWHM) and wavelength of emission.

Firstly, ASE thresholds were calculated for each film as the intensity at which the FWHM of the spectrum decreases at half of its maximum value. They have been represented in Fig. 4 as a function of TPD concentration. It is observed that for low concentrations the threshold is large, it decreases up to 20 wt% when the concentration increases and then keeps a similar value up to 90 wt%. These results are in agreement with the behavior described in Fig. 3 for the normalized PL intensity, that increases up to around 20 wt% and then keeps

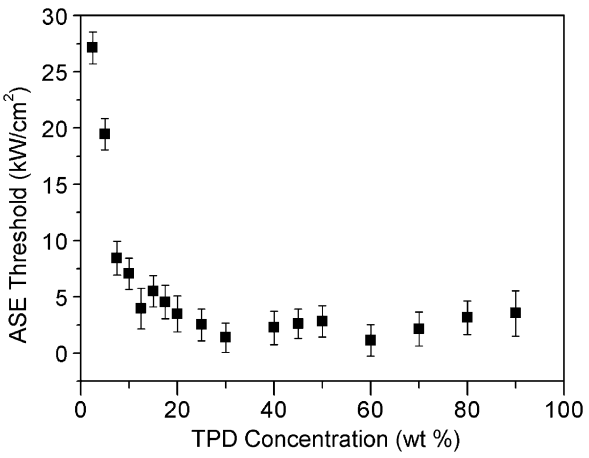

Fig. 4. ASE thresholds as a function of TPD concentration (wt%) in PS films.

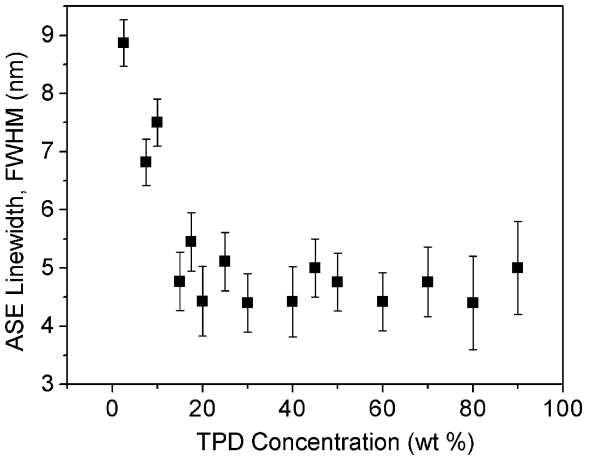

Fig. 5. ASE linewidth (FWHM) as a function of TPD concentration (wt%) in PS films.

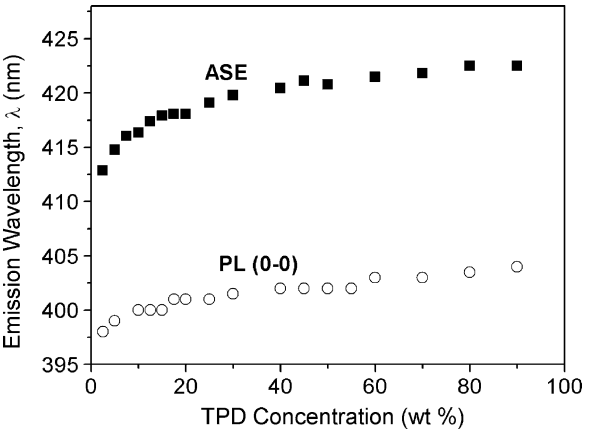

Fig. 6. Wavelength of ASE emission (full squares) and of 0-0 band of the standard PL emission (open circles) as a function of TPD concentration (wt%) in PS films. The error in the emission wavelength is around 0.2%.

constant with concentration. Moreover, the same trend is observed in the final ASE linewidth (above threshold). This is illustrated in Fig. 5 where the final FWHM (at high pump intensity), denoted as ASE linewidth, has been represented versus concentration. The ASE linewidth decreases up to 20 wt% and then keeps constant for larger concentrations. Therefore, the ASE performance (in terms of threshold and final linewidth) follows that of the efficiency of the PL process.

It is important to note that when the TPD concentration increases, absorption at the blue end of the emission spectrum (where spectral overlap occurs between absorption and emission) also increases. In addition, the polarity of the medium also grows when the concentration of TPD gets larger, due to the polarity of TPD. As a result, emission would tend to shift to longer wavelengths. In fact, these shifts are observed in both, the PL and the ASE. This is shown in Fig. 6, where the position of both, ASE and PL(0-0) peak are plotted as a function of TPD concentration. As observed, both, ASE and PL(0-0), shift to longer wavelengths when the TPD concentration is increased. Similar total energy shifts are obtained for both cases: $\Delta E = 0.07$ eV ($\Delta\lambda = 10$ nm) for ASE and $\Delta E = 0.05$ eV ($\Delta\lambda = 6$ nm) for PL(0-0). This indicates that the observed variations in the ASE position with concentration are due to shifts of the PL emission as a result of the increase in absorption and polarity of the medium. Kruhlak et al. also observed shifts of the fluorescence peak to the red when the dye concentration was increased in dye-doped polymer fibers, by using SIF spectroscopy [34]. These shifts were attributed to the increase of absorption with concentration.

4.3. Waveguide characterization and relation with the ASE properties

In recent studies of ASE in TPD films, shifts of the ASE wavelength due to film thickness variations were reported [29]. In that case, most of the observations were explained in terms of the confinement of the waveguide modes. Since the waveguiding properties seem to play a relevant role in the ASE performance, we decided to investigated them in our films, in an attempt to determine their possible influence in the ASE shifts and the observed concentration dependence of the threshold and linewidth. Therefore, the waveguiding properties of the films were both, measured and modeled. The experimental characterization was performed by the m-line technique at 633 nm. Two propagation modes were observed (one TE and one TM) and their effective indexes measured. These data were used to calculate from Eq. (1) the refractive index of the film at 633 nm. Approximately, the same values were obtained for both polarizations (TE and TM), indicating that the films are isotropic. The so-calculated refractive indexes (at 633 nm) for TE polarization are represented in Fig. 7 (solid squares) as a function of the concentration of TPD in the film. As observed, a linear increase of the index is observed up to around 70 wt% (a linear fit is represented as a solid line in Fig. 7). For larger concentrations the quality of the films was not very good, so less

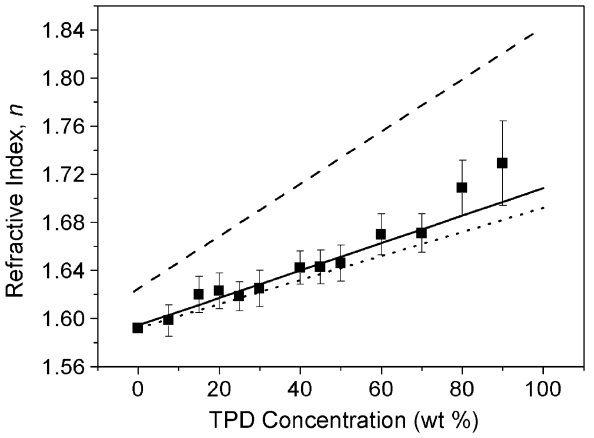

Fig. 7. Refractive index (n) as a function of TPD concentration (wt %) in PS films: n measured at 633 nm by the m-line technique (full squares) and linear fit (full line); n calculated from Refs. [22,40] at 633 nm (dotted line) and at the ASE wavelength (dashed line).

precision in the determination of the modes position (by the m-line technique) is achieved, resulting in slightly larger values. In fact, no waveguide modes could be measured in the neat films, due to their poor quality. For comparison purposes, the refractive indexes at 633 nm were calculated by using the refractive index spectra for a neat TPD film [22] and also for pure PS [40], and assuming that the refractive index is proportional to the concentration of each component. The results of this calculation are plotted as a dotted line in Fig. 7. The good agreement between both (full line and dotted line) is an indication of the validity of this assumption, so this can be used to calculate the refractive index at any wavelength. Therefore, refractive indexes at the ASE wavelength (reported in Fig. 6) were calculated following this method and represented in Fig. 7 (dashed line).

It could be expected that the observed variations of the ASE wavelength with the concentration of TPD might be influenced by cut-off thickness limitations. So, the cut-off thickness for the propagation of one mode were calculated from Eq. (3) for each film at the corresponding ASE wavelength. The dashed curve shown in Fig. 7, as well as the refractive index dispersion of the substrate (glass) were taken into account. The so-calculated cut-off thickness varied between 120 and 60 nm, well below the thickness for all the films. This is an indication that the observed variations of the ASE position with TPD concentration are not due to thickness limitations.

Recent reports about TPD showed that the different confinement of the waveguide modes due to thickness and/or refractive index variations influenced the ASE properties [29]. For very well confined modes, most of the emitted light would propagate in the gain medium so it would get amplified. On the other hand, for poorly confined modes, most of the emitted light would radiate to the substrate where no amplification could take place. In order to investigate the possible influence of the mode confinement in the ASE properties in our present case, we calculated the total penetration depth x_{total} (Eq. (6)) for films with varying TPD concentrations. Results are presented in Fig. 8. For the calculation of x_{total} from Eqs. (4)–(6), the value of N_{eff} (for a certain concentration with a given thickness) has been evaluated from Eq. (1) at the corresponding emission wavelength (shown in Fig. 6). Also, the variation of the refractive index with concentration has been taken into account for both, the film (Fig. 7-dashed line) and the substrate. As observed, x_{total} decreases (mode confinement increases) with concentration. The important parameters in x_{total} are the thickness, the ASE wavelength and the refractive index. When the concentration increases, both the ASE wavelength and the refractive index increase (see Figs. 6 and 7 respectively). The increase in the ASE position with concentration would lead to an increase in x_{total}. On the other hand, the increase in refractive index with concentration would result in a decrease in x_{total}. The influence of the wavelength shifts in the behavior of x_{total} were analyzed by calculating x_{total} at a constant wavelength (420 nm). Results were

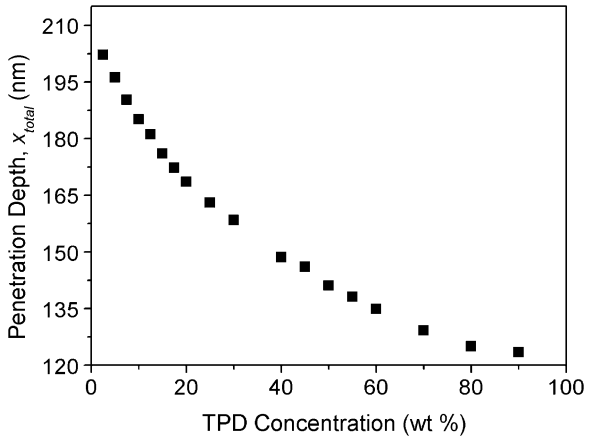

Fig. 8. Penetration depth (x_{total}), calculated from Eqs. (4)–(6), as a function of TPD concentration (wt%) in PS.

practically the same as for variable wavelength (given in Fig. 6), indicating that the type of dependence observed in Fig. 8 is a consequence of the variation of refractive index with concentration.

The ASE behavior could be influenced by the confinement of the waveguide modes. The larger the confinement, the better the ASE performance, so one should obtain lower thresholds and linewidths for films with better mode confinement. In order to check that possibility, the concentration dependence of x_{total} (Fig. 8) is compared to that of the ASE threshold and linewidth (Figs. 3 and 4 respectively). A rough correlation is observed in the sense that x_{total} gets the maximum value (poor confinement) for very diluted films and then decreases with increasing concentration (better confinement). However, it should be noted that x_{total} diminish continuously with concentration, in contrast with the ASE threshold and linewidth that reach a constant value at around 20 wt%. This indicates that although the confinement of the modes might be influencing the ASE performance, it seems to be driven mostly by PL efficiency.

4.4. Photodegradation

The photostability of TPD in PS was studied by recording the total ASE intensity emitted as a function of time, by keeping a constant pump intensity. The presence of photodegradation is evident in the observation of a decrease in the total ASE output. Results are illustrated in Fig. 9 for three representative concentrations (20, 50 and 80 wt%), where the ASE intensity has been represented versus time (lower axis). In order to compare with previous works, the total number of pulses irradiating the sample have also been indicated in the figure (top axis). The pump intensity was around 5 kW/cm^2 (i.e., 0.9 μJ/pulse) just above the ASE threshold. As observed in Fig. 9, the ASE output decreases with time, reaching half of its maximum value (halflife) at around 2.5–3 min (i.e., at 1500–1750 pulses). In terms of halflife, no differences are observed for the different concentrations shown in Fig. 9. However, at longer times, slight differences appear. The larger the TPD concentration in the films, the slower the decrease in the emitted intensity. This is probably due to the fact that the number of active molecules is bigger. In any case, it is important to note that after 10–12 min, the emission spectra get broad, indicating that ASE does no longer exist. As compared to some of the most photostable materials reported in the literature, the photodegradation of TPD doped PS films is faster. For example, PMMA films doped with disperse orange 11 showed ASE halflives of several hundreds of minutes [31]. For other materials, such as dipyrromethane-BF_2 dyes, the emission intensities decreased to half of their initial values after being irradiated with 10000–20000 pulses [30].

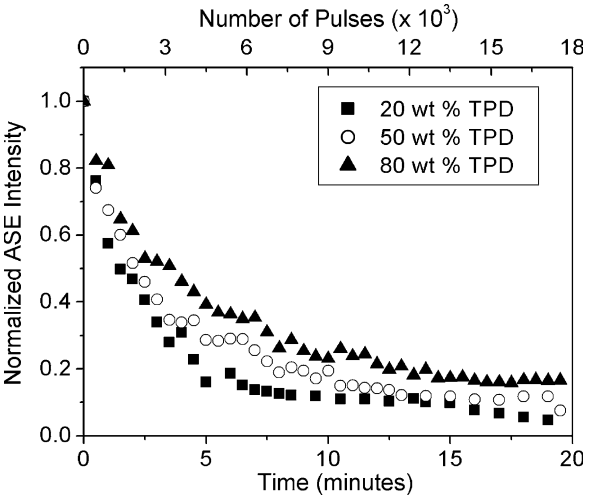

Fig. 9. Normalized ASE intensity versus irradiation time (bottom axis) and versus the number of pump pulses (10 ns, 10 Hz, 0.9 μJ/pulse; top axis) for PS films doped with various TPD concentrations. The error in the normalized intensity is around ±0.03.

It was observed that photodegradation depended on pump intensity, since at higher pump intensities the samples degraded faster. For example, at a pump intensity of around 2.8 MW/cm^2, the 20 wt% TPD doped film showed a haflife of around 1 min. In this case, the emission spectrum became broad (i.e., ASE disappeared) after 5 min of irradiation.

Since photodegradation depends on both, irradiation time and pump intensity, the definition of 'damage threshold' is not obvious. A possible definition of 'damage threshold' would be the pump intensity at which the ASE halflife gets lower than 1 min. Then, the damage threshold for ASE in TPD doped films would be around 2.8 MW/cm^2.

We also investigated the possibility of recoverability of a photodegraded sample, as reported for disperse red orange [31]. For such purpose, a TPD doped PS film that had been photodegraded to 50% of its original ASE output, was allowed to rest unpumped for approximately 24 h at room temperature. Subsequently the sample was pumped under identical conditions, and the ASE was measured.

Unfortunately, a recovery of the ASE efficiency was not observed.

5. Conclusions

Amplified spontaneous emission (ASE) has been reported in optically pumped polystyrene films containing a varying concentration (from 2.5 to 100 wt%) of the luminescent and hole-transporting organic molecule *N*,*N*′-Bis(3-methylphenyl)-*N*,*N*′-diphenylbenzidine (TPD). The photoluminescence (PL) efficiency increases with TPD concentration up to around 20 wt% and then saturates. Accordingly, the ASE threshold and linewidth decrease up to concentrations of 20 wt%, keeping a constant value for larger concentrations. It has been also observed that the position of both, the PL and the ASE, shift to longer wavelengths for increasing TPD concentrations due to the corresponding increases in absorption and polarity of the medium. Measurements and modeling the waveguide modes indicate that the observed shifts are not due to cut-off thickness limitations. Moreover, although the different confinement of the waveguide modes might be influencing the ASE performance, it seems to be driven mostly by PL efficiency. According to the results reported in this work, the best ASE performance is obtained for films with concentrations between 20 and 90 wt%. Since at high doping levels, degradation problems and mechanical instabilities appear, and more active material is used, the most efficient films would be those doped with 20–30 wt% of TPD. Finally, the photostability of these materials has also been studied. When samples are pumped just above the ASE threshold, the ASE intensity decreases rapidly with irradiation time, reaching half of its maximum value in 2.5–3 min and disappearing completely after 10 min.

Acknowledgments

This work was supported by the Spanish Ministry of Education and Science (grant numbers MAT2002-04429-C03-3 and MAT2005-07369-C03-1) and by FEDER funding. We also thank Vicente Esteve for technical assistance and Igor Vragovic for useful discussions.

References

[1] M.D. McGehee, A.J. Heeger, Adv. Mater. 12 (2000) 1655.
[2] N. Tessler, Adv. Mater. 11 (1999) 363.
[3] I.D.W. Samuel, C.A. Turnbull, Mat. Today (Sept.) (2004).
[4] F.J. Duarte, L.W. Hillman (Eds.), Dye Laser Principles with Applications, Academic Press, Boston, 1990.
[5] J. Cornil, D. Beljonne, J.P. Calbert, J.L. Brédas, Adv. Mater. 13 (2001) 1053.
[6] F. Hide, B. Schwartz, M.A. Díaz-García, A.J. Heeger, Chem. Phys. Lett. 257 (1996) 424.
[7] F. Hide, M.A. Díaz-García, B. Schwartz, M. Andersson, Q. Pei, A.J. Heeger, Science 273 (1996) 1833.
[8] N. Tessler, G.J. Denton, R.H. Friend, Nature 382 (1996) 695.
[9] D. Fichou, S. Delysse, J.-M. Nunzi, Adv. Mater. (Weinheim, Ger.) 9 (1997) 1178.
[10] G. Horowitz, P. Valat, F. Garnier, F. Kouki, V. Wintgens, Opt. Mater. 9 (1998) 46.
[11] M. Nagawa, R. Hibino, S. Hotta, H. Yanagi, M. Ichikawa, T. Koyama, Y. Taniguchi, Appl. Phys. Lett. 80 (2002) 544.
[12] Y. Yanagi, T. Ohara, T. Morikawa, Adv. Mater. (Weinheim. Ger.) 13 (2001) 1452.
[13] F. Quochi, F. Cordella, R. Orru, J.E. Communal, P. Verzeroli, A. Mura, G. Bongiovanni, Appl. Phys. Lett. 84 (2004) 4454.
[14] M. Anni, G. Gigli, R. Cingolani, M. Zavelani-Rossi, C. Gadermaier, G. Lanzani, G. Barbarella, L. Favaretto, Appl. Phys. Lett. 78 (2001) 2679.
[15] M. Zavelani-Rossi, G. Lanzani, S. De Silvestri, M. Anni, G. Gigli, R. Cingolani, G. Barbarella, L. Favaretto, Appl. Phys. Lett. 79 (2001) 4082.
[16] D. Pisignano, M. Anni, G. Gigli, R. Cingolani, M. Zavelani-Rossi, G. Lanzani, G. Barbarella, L. Favaretto, Appl. Phys. Lett. 81 (2002) 3543.
[17] N. Johansson, J. Salbeck, J. Bauer, F. Weissörtel, P. Bröms, A. Andersson, W.R. Salaneck, Adv. Mater. (Weinheim, Ger.) 10 (1998) 1136.
[18] D. Schneider, T. Rabe, T. Riedl, T. Dobbertin, O. Werner, M. Kröger, E. Becker, H.-H. Johannes, W. Kowalsky, T. Weimann, J. Wang, P. Hinze, A. Gerhard, P. Stössel, H. Vestweber, Appl. Phys. Lett. 84 (2004) 4693.
[19] G. Gigli, G. Barbarella, L. Favaretto, F. Cacialli, R. Cingolani, Appl. Phys. Lett. 75 (1999) 439.
[20] F. Della Sala, G. Gigli, M.F. Raganato, M. Anni, D. Pisignano, R. Cingolani, L. Favaretto, G. Sotgiu, G. Barbarella, L. Antolini, Organ. Electron. 3 (2004) 129.
[21] D. Schneider, T. Rabe, T. Riedl, T. Dobbertin, M. Kröger, E. Becker, H.-H. Johannes, W. Kowalsky, T. Weimann, J. Wang, P. Hinze, J. Appl. Phys. 98 (2005) 043104.
[22] W. Holzer, A. Penzkofer, H.-H. Hörhold, Synth. Met. 113 (2000) 281.
[23] M.A. Díaz-García, S.F. De Avila, M.D. Kuzyk, Appl. Phys. Lett. 80 (2002) 4486.
[24] M. McGehee, R. Gupta, S. Veenstra, E.K. Miller, M.A. Díaz-García, A.J. Heeger, Phys. Rev. B 58 (1998) 7035.
[25] M.A. Díaz-García, E.M. Calzado, J.M. Villalvilla, P.G. Boj, J.A. Quintana, M. Kuzyk, J. Nonl. Opt. Phys. and Mater. 13 (2004) 621.
[26] X. Peng, L. Liu, J. Wu, Y. Li, Z. Hou, L. Xu, W. Wang, F. Li, Opt. Lett. 25 (2000) 214.
[27] A.K. Sheridan, G.A. Turnbull, A.N. Safonov, I.D.W. Samuel, Phys. Rev. B 62 (2000) R11929.
[28] R. Xia, G. Heliots, Y. Hou, D.D.C. Bradley, Organ. Electron. 4 (2003) 165.

[29] E.M. Calzado, J.M. Villalvilla, P.G. Boj, J.A. Quintana, M.A. Díaz-García, J. Appl. Phys. 97 (2005) 093103.
[30] A. Costela, J. García-Moreno, R. Sastre, Phys. Chem. Chem. Phys. 5 (2003) 4745.
[31] B.F. Howell, M.G. Kuzyk, J. Opt. Soc. Am. B 19 (2002) 1790.
[32] H. Kogelnik, in: T. Tamir (Ed.), Theory of Optical Waveguides in Guided Wave Optoelectronics, second ed., Springer-Verlag, New York, 1990.
[33] R.J. Kruhlak, M.G. Kuzyk, J. Opt. Soc. Am. B 16 (1999) 1749.
[34] R.J. Kruhlak, M.G. Kuzyk, J. Opt. Soc. Am. B 16 (1999) 1756.
[35] M. Malagoli, J.L. Brédas, Chem. Phys. Lett. 327 (2000) 13.
[36] M. Malagoli, M. Manoharan, B. Kippelen, J.L. Brédas, Chem. Phys. Lett. 354 (2002) 283.
[37] A.R. Kennedy, W.E. Smith, D.R. Tackley, W.I.F. David, D. Shankland, B. Brown, S.J. Teat, J. Mat. Chem. 12 (2002) 168.
[38] P.J. Low, M.A.J. Paterson, H. Puschmann, A.E. Goeta, J.A.K. Howard, C. Lambert, J.C. Cherryman, D.R. Tackley, S. Leeming, B. Brown, Chem. Eur. J. 10 (2004) 83.
[39] I. Vragovic, M.A. Díaz-García. Unpublished results.
[40] R.H. Boundy, R.F. Raymond, Styrene. Its Polymers, Copolymers and Derivatives, Reinhold Publishing Corp., New York, 1952.

Available online at www.sciencedirect.com
ScienceDirect
Organic Electronics 7 (2006) 330–336
Organic Electronics
www.elsevier.com/locate/orgel

The host materials containing carbazole and oxadiazole fragment for red triplet emitter in organic light-emitting diodes

Min Guan [a], ZhuQi Chen [a], ZuQiang Bian [a,*], ZhiWei Liu [a], ZeLiang Gong [a], Woonphil Baik [b], HyunJoo Lee [b], ChunHui Huang [a]

[a] *Beijing National Laboratory for Molecular Sciences (BNLMS), State Key Laboratory of Rare Earth Materials Chemistry and Applications, College of Chemistry and Molecular Engineering, Peking University, Beijing 100871, China*
[b] *Department of Chemistry, Myong Ji University, Yong In City, Kyong Ki Do 449-728, Republic of Korea*

Received 9 February 2006; received in revised form 25 April 2006; accepted 25 April 2006
Available online 19 May 2006

Abstract

Three new oxadiazole substituted carbazole derivatives 9-{4-[5-(4-*tert*-butylphenyl)-[1,3,4] oxadiazol-2-yl]-benzyl}-9*H*-carbazole (t-CmOxa), 9-[4-5-phenyl-[1,3,4]oxadiazol-2-yl-benzyl]-9*H*-carbazole (p-CmOxa) and 9-[4-5-biphenyl-[1,3,4] oxadiazol-2-yl-benzyl]-9*H*-carbazole (d-CmOxa) were successfully synthesized and characterized by spectroscopy (NMR, UV–vis, mass spectrum and photoluminescence) and cyclic voltammetry measurements. Employing t-CmOxa as a host and $Ir(DBQ)_2(acac)$ (DBQ = dibenzo[*f*,*h*]quinoxaline, acac = acetylacetonate) as the dopant emitter, OLEDs with structures of ITO/NPB(30 nm)/$Ir(DBQ)_2(acac)$: t-CmOxa (30 nm, x%)/Alq_3(30 nm)/$Mg_{0.9}$:$Ag_{0.1}$ were fabricated without using BCP as the hole blocking layer. Red emission was obtained with CIE coordinates ($x = 0.66$, and $y = 0.34$) at 5 V and a very high external electroluminescent (EL) quantum efficiency of 9.5 ± 0.1%, and an energy conversion efficiency of 9.9 ± 0.1 lm/W were achieved for the device when the doping concentration x is equal to 4%.

PACS: 73.21.Ac; 73.61.Ph; 81.15.Ef

Keywords: Oxadiazole; Carbazole; OLED; Red; Host material

1. Introduction

Much effort has been devoted to increase the emission efficiency of organic light-emitting diodes (OLEDs). Energy transfer from a conductive host to a luminescent guest molecule can result in high external quantum efficiency (η_{ext}). In particular, the use of phosphorescent emitters as guests, which harvests both singlet and triplet excitons, leads to internal quantum efficiency (η_{int}) approaching 100% [1–5]. In general, host materials should be selected to follow after those that have a higher triplet energy level than that of the guest molecules benefits the energy transfer from the host to the guest

* Corresponding author. Tel.: +86 10 62757156; fax: +86 10 62751708.
E-mail address: chhuang@pku.edu.cn (C. Huang).

1566-1199/$ - see front matter
doi:10.1016/j.orgel.2006.04.006

while prohibits the energy transfer of triplet excitons from the guest to the host material. In addition, the charge transporting properties of host materials are also important. For example, although 4,4-*N*,*N*-dicarbazolebiphenyl (CBP), 2,9-dimethyl-4,7-diphenyl-9,10-phenanthroline (BCP), triazole (TAZ), and oxadiazole (OXD) derivatives have been revealed to be excellent hosts [6–8], they are often described as a unipolar hole or electron transporters. In order to confine the emission zone to be in the emitter layer and consequently to improve the electroluminescence performance of OLEDs, it is very important to balance between the hole, electron injection, and transportation. The multi-functional electroluminescent small molecules and polymers have already been discussed whereby light emission and electron- and hole-transporting properties are combined in one material to achieve high efficiency [9–11].

Currently, many carbazole compounds have been used as host materials for OLEDs [12–15]. Oxadiazole molecules and polymers are the most widely investigated electron transport materials (ETM) for OLEDs since the initial studies using 5-(4-biphenyl)-2-(4-*tert*-butyl-phenyl)-1,3,4-oxadiazole (PBD) as ETM in EL devices [16]. In our previous work [17], it has been demonstrated that one carbazole derivative containing 1,3,4-oxadiazole, CzOxa (see Fig. 3), has an excellent hole- and electron-transfer ability. However, the conjugated system of this molecule is large in some extent due to the carbazole group directly connecting with phenyl, and the emission peak shifts toward the red side. Furthermore, the singlet energy gap of CzOxa is narrow, and the triplet energy level may be low. On the other hand, the hole transporting ability of CzOxa is too strong such that a hole-blocking layer is needed if it is used as a host layer. In this report, the purpose is to decrease the π-conjugation of the carbazole ring with phenyl and to make a blue-shift in the PL peak, three similar carbazole derivatives containing 1,3,4-oxadiazole, t-CmOxa, p-CmOxa and d-CmOxa, respectively, were synthesized by introducing one methylene between the carbazole and the phenyl rings, and characterized by spectroscopy (NMR, UV–vis, mass spectrum and photoluminescence) and cyclic voltammetry measurements. In order to study their properties as a host, we chose one compound t-CmOxa as the host and a reported triplet emitter, $Ir(DBQ)_2(acac)$ [18], as the guest, and a series of electroluminescent devices were fabricated. The results showed that such molecules have a better bipolar balanced charge transporting character than CBP. Unlike in most cases, a blocking layer is no longer required if they were used as the host material in OLEDs.

2. Experiments

All reagents and solvents were used as received or purified using standard procedures. ^{1}H NMR spectra were recorded with a Bruker ARX400 MHz spectrometer. The mass spectra were recorded on a ZAB-HS mass spectrometer. The elemental analyses were performed with a Vario EL elemental analyzer. UV–vis absorption spectra were recorded in a chloroform solution with a Shimadzu 3100 UV–VIS-NIR spectrophotometer. The emission spectra were measured in thin film with an F-4500 fluorescence spectrophotometer. The morphological properties (T_g, glass transition temperature and T_m, melting point) were evaluated by DSC analysis with a Shimadzu DSC-60 instrument. A thermogravimetric analyzer (Dupont Model TGA1090B) was used to measure the onset decomposition temperature (T_d) and the weight loss of compounds during the temperature scan from 0 °C to 600 °C, with a heating rate of 10 °C/min in an atmosphere of nitrogen.

The synthetic routes of t-CmOxa, p-CmOxa and d-CmOxa are shown in Scheme 1.

9-[4-5-phenyl-[1,3,4]oxadiazol-2-yl-benzyl]-9*H*-carbazole (p-CmOxa): Yield: 75%. ^{1}H NMR (400 MHz, $CDCl_3$), δ: 8.17–8.15 (d, 2H), 8.12–8.09 (dd, 2H), 8.04–8.03 (d, 2H), 7.54–7.52 (m, 3H), 7.48–7.44 (t, 2H), 7.37–7.35 (d, 2H), 7.31–7.26 (m, 4H), 5.60 (s, 2H). MS (*m*/*z*): calcd for $C_{27}H_{19}N_3O$ 401, found 401. Anal. calcd. C: 80.78%, H: 4.77%, and N: 10.47%, and found C: 80.95%, H: 4.75%, and N: 10.34%.

9-{4-[5-(4-*tert*-butylphenyl)-[1,3,4]oxadiazol-2-yl]-benzyl}-9*H*-carbazole (t-CmOxa): Yield: 85%. ^{1}H NMR (400 MHz, $CDCl_3$), δ: 8.16–8.14 (d, 2H), 8.03–8.00 (m, 4H), 7.53–7.51 (d, 2H), 7.46–7.42 (m, 2H), 7.36–7.33 (d, 2H), 7.29–7.25 (m, 4H), 5.58 (s, 2H), 1.35 (s, 9H). MS (*m*/*z*): calcd for $C_{31}H_{27}N_3O$ 457, found 457. Anal. calcd. C: 81.37%, H: 5.95%, and N: 9.18%, and found C: 81.25%, H: 5.95%, and N: 9.88%.

9-[4-5-biphenyl-[1,3,4]oxadiazol-2-yl-benzyl]-9*H*-carbazole (d-CmOxa): Yield: 85%. ^{1}H NMR (400 MHz, $CDCl_3$), δ: 8.18–8.16 (d, 4H), 8.07–8.05 (d, 2H), 7.76–7.74 (d, 2H), 7.66–7.64 (t, 2H), 7.50–7.36 (m, 7H), 7.32–7.26 (m, 4H), 5.61 (s, 2H). MS (*m*/*z*): calcd for $C_{33}H_{23}N_3O$ 477, found 477. Anal.

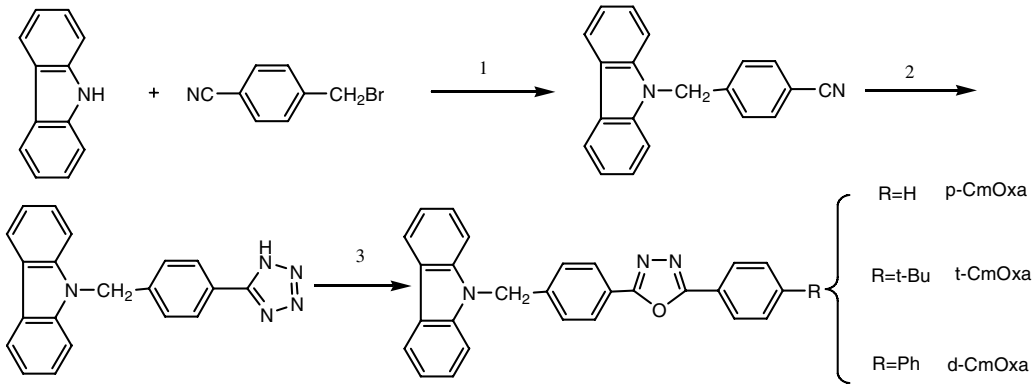

Scheme 1. Synthetic route. *Reagents and conditions*: 1, toluene/$(C_4H_9)_4NBr$/KOH, 5 h, 77%; 2, NaN_3/NH_4Cl/DMF, 100 °C, 24 h, 65%; 3, carbonyl chloride/pyridine, refluxing 2 h, ~80%.

calcd. C: 83.00%, H: 4.85%, and N: 8.80%, and found C: 83.05%, H: 4.88%, and N: 8.85%.

Devices with a configuration of indium tin oxide (ITO, 6 Ω/□)/NPB (30 nm)/Ir(DBQ)$_2$(acac): t-CmOxa (or CBP) (30 nm, *x*%)/Alq_3 (30 nm)/ $Mg_{0.9}$:$Ag_{0.1}$ were fabricated by vacuum deposition. The ITO substrates were cleaned with deionised water, acetone and ethanol, and finally treated with UV-ozone for about 5 min. The devices were fabricated by evaporating multiple organic layers onto the ITO substrate sequentially in one run under a pressure below 2×10^{-7} Torr. The doped layer of Ir(DBQ)$_2$(acac) in t-CmOxa or CBP was prepared by co-evaporation with the guess concentration controlled by carefully adjusting the evaporating rates of the guest and the host. A cathode layer of $Mg_{0.9}$:$Ag_{0.1}$ (mass ratio) was evaporated onto the Alq_3 layer. The EL spectra and current–voltage–luminescence characteristics were measured with a Spectra Scan PR 650 photometer and a computer-controlled dc power supply under ambient conditions. The emission area of the devices is 0.09 cm^2 as determined by the overlap area of the anode and the cathode. All compounds used for EL devices were sublimated in vacuum prior to use.

Cyclic voltammetry measurements were recorded in dichloromethane with 0.1 M tetrabutylammonium hexafluorophosphate as the supporting electrolyte. The working electrode was a platinum disk (0.1 cm^2), the counter electrode was a platinum plate and an Ag/AgCl electrode was used as a reference electrode, calibrated against an Fc/Fc^+ couple. Since the oxidation potential of Ag/AgCl relative to the vacuum level is known (4.72 V[19]), the measured oxidation potentials can be converted into ionization potentials if the effect of solvent is neglected. In this report, we use the ionization potential as a measure for the energy of the highest occupied molecular orbital (HOMO).

3. Results and discussion

Three carbazole derivatives were synthesized as shown in Scheme 1. All appears as white solids. Their optical and thermal characteristics are summarized in Tables 1 and 2, respectively. Their UV–vis absorption spectra in chloroform show that all of them have multiple absorptions ranging from 240 to 350 nm with a tail extending to about 360 nm (see Fig. 1). For example, p-CmOxa absorbs at 243, 264, 293 and 341 nm originated from the π–π* transitions of the conjugated π electron in the system. When a *tert*-butyl group was joined to the end of phenyl, the t-CmOxa was formed. The

Table 1
Absorption peaks (λ^{ab}), emission peak (λ_{em}), half-wave oxidation potentials ($E^{ox}_{1/2}$, irreversible), HOMO and LUMO energy level for carbazole derivatives

Comp.	λ^{ab} (nm)	λ_{em} (nm)	$E^{ox}_{1/2}$ (eV)	HOMO (eV)	LUMO (eV)
p-CmOxa	341, 293, 264, 243	390	1.40	6.13	2.61
t-CmOxa	341, 293, 264, 241	394	1.41	6.14	2.62
d-CmOxa	308, 294, 262, 241	410	1.41	6.14	2.67

Table 2
Thermal characteristics of three carbazole derivatives

Comp.	T_m (°C)	T_g (°C)	T_d (°C)
p-CmOxa	198	61	375
t-CmOxa	211	76	387
d-CmOxa	229	83	415

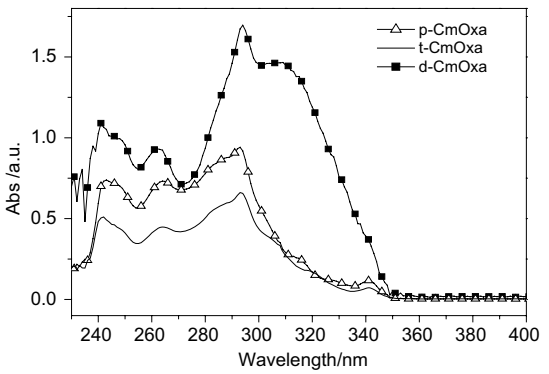

Fig. 1. UV–vis absorption spectra of p-CmOxa, t-CmOxa and d-CmOxa in chloroform solution (concentration = 10^{-5} M).

UV absorption of t-CmOxa and p-CmOxa are nearly identical. However, when the phenyl group was added into the p-CmOxa, a new absorption appears at 308 nm, indicating an enlargement of the conjugated system.

The emission spectra of the three congeners in solid state are shown in Fig. 2. The emission peaks (λ_{em}) locate 390, 394 and 410 nm for p-CmOxa, t-CmOxa and d-CmOxa, respectively, implying that the energy level of the singlet state is lowed along with the enlargement of the conjugated systems of these compounds. The values of stokes shift are 69, 73 and 102 nm for p-CmOxa, t-CmOxa and d-CmOxa, respectively. This observation reveals that the energy loss between the absorption and emission caused by the vibration and configuration change of the molecules has increased, especially along with the enlarged conjugated system when one more phenyl group was added onto the molecule in the case of d-CmOxa compared with the other two.

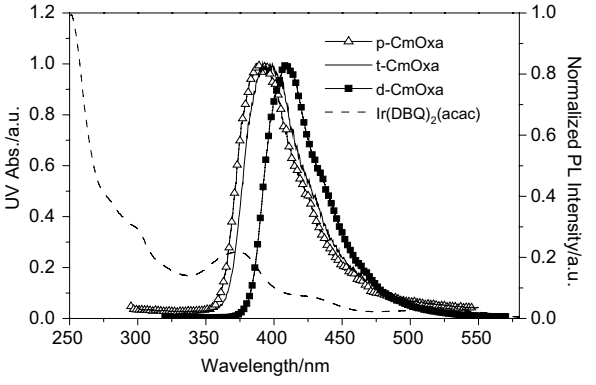

Fig. 2. Normalized PL spectra of p-CmOxa, t-CmOxa and d-CmOxa in the solid state and the UV–vis absorption spectrum of $Ir(DBQ)_2(acac)$.

A good host material is expected to have a lower occupied molecular orbital energy level (HOMO) and a higher unoccupied molecular orbital energy level (LUMO) for charge injection from neighboring layers. The HOMO and LUMO energy levels for the three carbazole compounds were determined and listed in Table. 1. The HOMO energy levels were deduced from their oxidation potentials measured by cyclic voltammetry (CV), while the LUMO energy levels were estimated based on the HOMO energy levels and the optical band gaps obtained from the absorption spectra. In the CV measurement, they showed irreversible oxidation waves, indicating all of these oxadiazole-containing species are in unstable reduced forms under the electrochemical condition. The HOMO energy levels are 6.13, 6.14 and 6.14 eV for p-CmOxa, t-CmOxa and d-CmOxa, respectively. Although the conjugated systems are structurally different, the HOMO energy levels of the three compounds are almost the same and lower than that of CBP (6.00 eV[20]), suggesting that their hole injection ability is weakened, which would benefit the recombination zone to be confined within the emission layer. Also, a wide singlet energy gap ($E_g \sim 3.5$ eV) for them is expected for a wide triplet energy gap. Moreover, comparing with CzOxa ($E_g = 3.1$ eV), the HOMO/LUMO gap is also enlarged, which would maintain the excitations within the guest.

Onset decomposition temperatures (T_d) of p-CmOxa, t-CmOxa, and d-CmOxa were determined to be 375, 387 and 415 °C, respectively, which are all higher than that of PBD (313 °C). It demonstrates that introducing carbazole group into oxadiazole compounds enhances the thermal stability. In addition, these compounds have excellent film forming qualities and can be evaporated without decomposition. Furthermore, the glass transition temperature (T_g) and T_d increase as the conjugated system enlarged.

Compared with d-CmOxa, the overlap of UV–vis absorptions of $Ir(DBQ)_2(acac)$ with the PL spectrum of t-CmOxa is wider (see Fig. 2). Furthermore,

compared with p-CmOxa, t-CmOxa has higher T_d and T_g. Therefore we believe that t-CmOxa is more suitable as a host layer than the other two compounds. And thus, OLEDs with t-CmOxa as the host and different mass ratio of $Ir(DBQ)_2(acac)$, which exhibited strong emission at $\sim$ 630 nm (ref [18]), as the guest were constructed. Fig. 3 shows the molecular structures of the compounds used in these devices and their energy level diagram. The device structures were ITO/NPB(30 nm)/$Ir(DBQ)_2(acac)$:t-CmOxa(30 nm, x%)/Alq_3(30 nm)/$Mg_{0.9}$:$Ag_{0.1}$ ($x = 22, 18, 13, 9, 6, 4$). It is worthy to point out that the hole blocking layer of BCP was not used as usually in these devices. Since t-CmOxa has a relatively lower HOMO level (6.14 eV) than that of CBP, using it as a host will weaken the ability of hole injection. In addition, the introduction of the oxadiazole group to the host will improve its electron transportation, so the hole blocking layer is no longer needed.

The electroluminescence spectra of all devices consist only of red emission from $Ir(DBQ)_2(acac)$ without any residual emission from the host and Alq_3 layer (see Fig. 4), moreover the EL spectra of

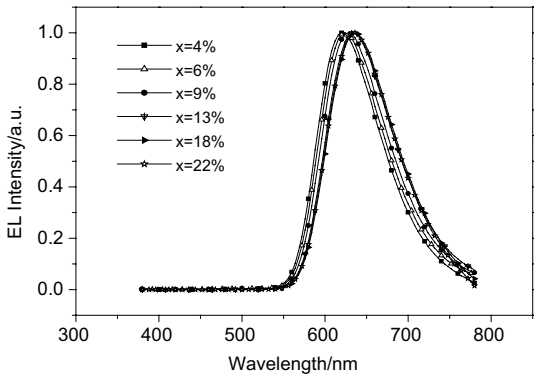

Fig. 4. The electroluminescence spectra of the devices at 10 V.

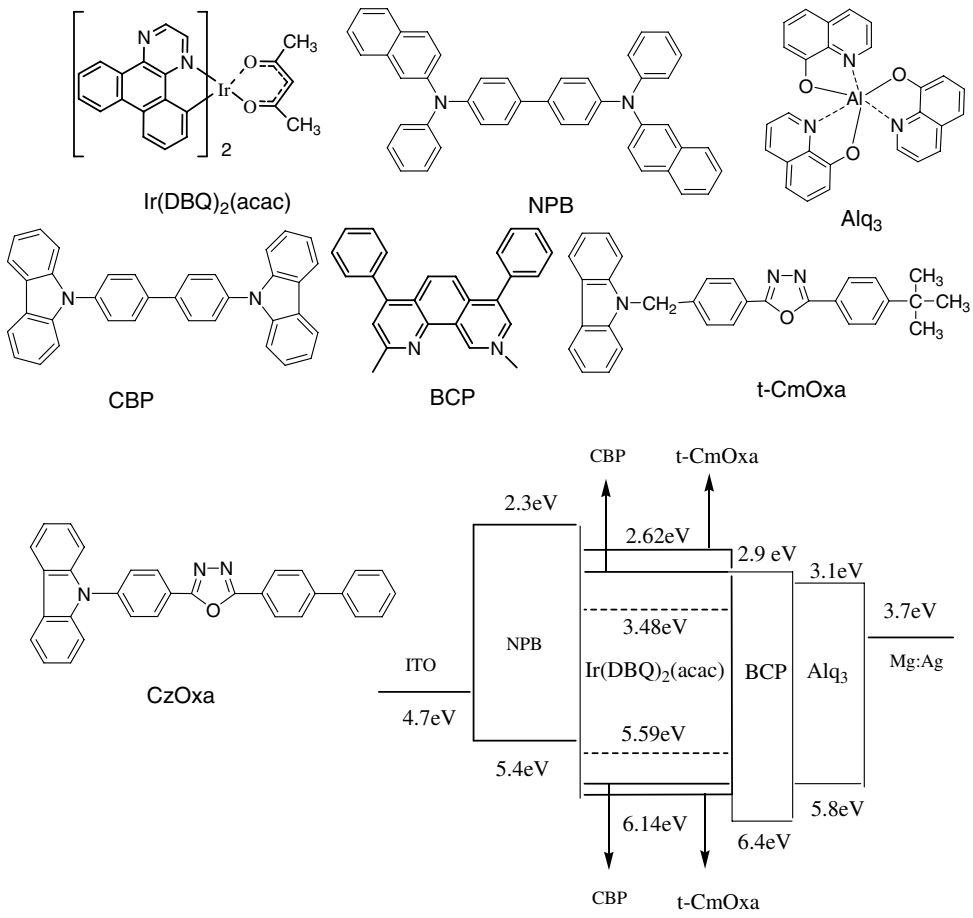

Fig. 3. The molecular structures of the compounds used in the devices and energy level diagram.

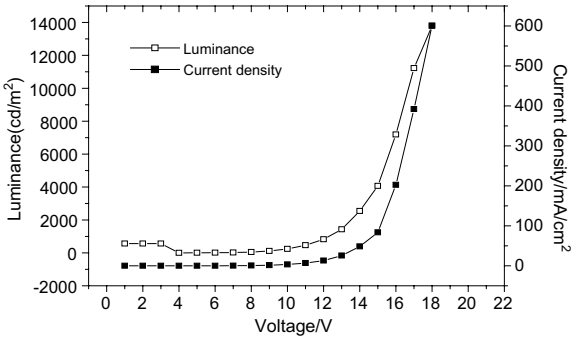

Fig. 5. The voltage–luminescence (□) and voltage–current density (■) characteristics of device 1.

these devices do not change significantly with variation of the applied voltage.

Comparison of the performance of these devices indicates that the **device 1** with 4% $Ir(DBQ)_2(acac)$ has the highest efficiency. The current–voltage and voltage–luminescence characteristics are presented in Fig. 5. A turn-on voltage of 4 V, maximum brightness of 13 790 cd/m^2 at 18 V, power efficiency of 9.89 lm/W and external efficiency of 9.52% at 5 V were achieved, which are so far the best results among the red emission devices. Commission Internationale de l'Eclairage coordinates, x and y, were calculated to be 0.66 and 0.34 at 5 V. At 100 cd/m^2, the power efficiency and external quantum efficiency are 2.60 lm/W and 4.52%, respectively.

To compare with a CBP host, the **device 2** with a configuration of ITO/NPB(30 nm)/$Ir(DBQ)_2(acac)$: CBP(30 nm, 4%)/BCP(10 nm)/Alq_3(30 nm)/$Mg_{0.9}$:$Ag_{0.1}$ was fabricated under the same condition and its electrical characteristics were measured. A turn-on voltage of 6.5 V, maximum brightness of 19350 cd/m^2 at 18 V, power efficiency of 2.36 lm/W and external efficiency of 3.18% at 7 V were achieved. At 100 cd/m^2, the power efficiency and external quantum efficiency are 2.07 lm/W and 3.98%. It is noted that although the maximum brightness decreased, the maximum efficiency increased from 2.36 to 9.89 lm/W, and the turn-on voltage reduced from 6.5 to 4 V upon replacing CBP by t-CmOxa as the host material. Compared with device 2, the device 1 using t-CmOxa as a host would be destroyed at low current density before it achieves the highest brightness due to crystallization of the materials during operation. However, since the joule heat is small at low applied voltage, the effective energy transfer from the host to the guest as mentioned above and the balanced hole and electron transport result in a high efficiency of the device 1. As shown in Fig. 3, the HOMO of $Ir(DBQ)_2(acac)$ is positioned only slightly above the HOMO of CBP, thus $Ir(DBQ)_2$(acac) acts as a shallow trap for positive charge carriers. The positive charge carriers will therefore not only reside in the guest emitter but also in the host. It prevents efficient charge recombination on the guest, thus it is necessary to use BCP as a hole blocking layer. BCP has been known to be insufficient and may further decrease durability of the devices [21,22]. However, when it was replaced by a multi-functional molecule and dispersed in t-CmOxa, $Ir(DBQ)_2(acac)$ acts as a deep trap for both types of charge carriers. The efficiency of recombination via sequential trapping is increased and the efficiency of device is also increased. On the other hand, a good host material is expected to have an appropriate hole or electron mobility so that the recombination zone of excitons could be confined to the emitting layer in the multilayer device at the applied bias. For example, though the HOMO energy level of CzOxa [17] is little lower than that of t-CmOxa, the trap for positive charge carriers is deeper. However, the hole hops faster in CzOxa than t-CmOxa layer thus the charge carriers jump over the emitting layer to the electron transporting layer in the presence of bias. A device with the structure of ITO/NPB(30 nm)/$Ir(DBQ)_2(acac)$: CzOxa (30 nm, 20%)/Alq_3(30 nm)/$Mg_{0.9}$:$Ag_{0.1}$ was fabricated, and its EL spectrum is presented in the following Fig. 6, which shows the 520 nm peak belonging to the associated Alq_3 layer.

OLEDs with t-CmOxa as the host and varied mass ratio of $Ir(DBQ)_2(acac)$ as the guest were also constructed. The general structure and key

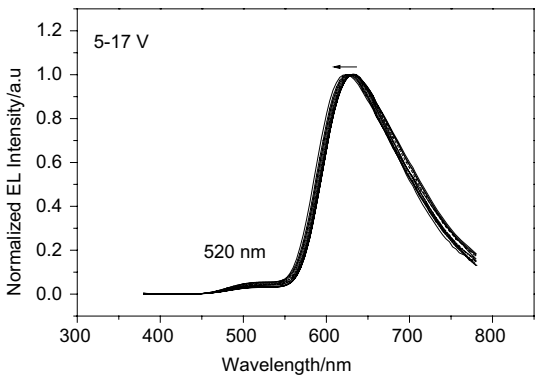

Fig. 6. The electroluminescence spectra of the device ITO/NPB(30 nm)/$Ir(DBQ)_2(acac)$:CzOxa (30 nm, 20%)/Alq_3(30 nm)/$Mg_{0.9}$:$Ag_{0.1}$ at different bias.

characteristics for the devices are listed in Table A (see the supporting information).

4. Conclusion

In summary, three new host materials containing carbazole and oxadiazole fragment connected through a methylene bridge were synthesized and characterized. The OLEDs performances were investigated using t-CmOxa as a host material. Our data demonstrate that this novel multi-functional material not only be able to transfer energy efficiently in a red emission OLED, but also make the balanced electrons and holes recombination within the emitting layer. Importantly, unlike in most OLED, the blocking layer is no longer required in our devices. The investigation on the long-term stability of this novel device is under processing (see the supporting information).

Acknowledgements

The authors thank the national basic research 973 program (2006CB601103), NNSFC (20221011, 20471004, 50372002 and 90401028), China education foundation for doctorial program (20030001065) and the RRC program of Korea ministry of commerce, industry and Energy for the financial supports.

Appendix A. Supplementary data

Supplementary data associated with this article can be found, in the online version, at doi:10.1016/j.orgel.2006.04.006.

References

[1] C. Adachi, M.A. Baldo, S.R. Forrest, M.E. Thompson, Appl. Phys. Lett. 77 (2000) 904.
[2] R.J. Holmes, S.R. Forrest, Y.J. Tung, R.C. Kwong, J.J. Browm, S. Garon, M.E. Thompson, Appl. Phys. Lett. 82 (2003) 2422.
[3] C. Adachi, M.A. Baldo, S.R. Forrest, M.E. Thompson, J. Appl. Phys. 90 (2001) 4058.
[4] M. Ikai, S. Tokito, Y. Sakamoto, T. Suzuki, Y. Taga, Appl. Phys. Lett. 79 (2001) 156.
[5] Md.K. Nazeeruddin, R. Humphry-Baker, D. Berner, S. Rivier, L. Zuppiroli, M. Graetzel, J. Am. Chem. Soc. 125 (2003) 8790.
[6] H. Inomata, K. Goushi, T. Masuko, T. Konno, T. Imai, H. Sasabe, J.J. Brown, C. Adachi, Chem. Mater. 16 (2004) 1285.
[7] C. Adachi, S. Tokito, S. Saito, J. Appl. Phys. Part 1 27 (1988) 713.
[8] A.R. Brown, J.H. Burroughes, N.C. Greenham, R.H. Friend, D.C. Bradley, P.L. Burn, A. Kraft, A.B. Holmes, Appl. Phys. Lett. 61 (1992) 2793.
[9] A.P. Kulkarni, C.J. Tonzola, A. Batel, S.A. Jenekhe, Chem. Mater. 16 (2004) 4556.
[10] G. Hughes, M.R. Bryce, J. Mater. Chem. 15 (2005) 94.
[11] N. Tamoto, C. Adachi, K. Nagai, Chem. Mater. 9 (1997) 1077.
[12] D.F. O'Brien, M.A. Baldo, M.E. Thompson, S.R. Forrest, Appl. Phys. Lett. 74 (1999) 442.
[13] P.E. Burrows, S.R. Forrest, T.X. Zhou, L. Michalski, Appl. Phys. Lett. 76 (2000) 2493.
[14] K. Brunner, A. van Dijken, H. Borner, J.J.A.M. Bastiaansen, N.M.M. Kiggen, B.M.W. Langeveld, J. Am. Chem. Soc. 126 (2004) 6035.
[15] X. Gong, M.R. Robinson, J.C. Ostrowski, D. Moses, G.C. Bazan, A.J. Heeger, Adv. Mater. 14 (2002) 581.
[16] C. Adachi, T. Tsutsui, S. Saito, Appl. Phys. Lett. 56 (1990) 799.
[17] M. Guan, Z.Q. Bian, Y.F. Zhou, F.Y. Li, Z.J. Li, C.H. Huang, Chem. Commun. (2003) 2708.
[18] J.P. Duan, P.P. Sun, C.H. Cheng, Adv. Mater. 15 (2003) 224.
[19] J.O.M. Bockris, S.U.M. Khan, Surface Electrochemistry. A Molecular Level Approach, Kluwer Academic/Plenum Publishers, New York, 1993.
[20] I.G. Hill, A. Kahn, J. Appl. Phys. 86 (1999) 4515.
[21] H. Nakada, S. Kawami, N. Nagayama, Y. Yonemoto, R. Muayama, J. Funaki, T. Wakimoto, K. Imai, Polymer 43 (1994) 2450, Preprints.
[22] Teruichi Watanabe, Kenji Nakamura, Shin Kawami, Yoshinori Fukuda, Taishi Tsuji, Takeo Wakimoto, Satoshi Miyaguchi, Proc. SPIE 4105 (2001) 175.

Available online at www.sciencedirect.com
ScienceDirect
Organic Electronics 7 (2006) 337–350
Organic Electronics
www.elsevier.com/locate/orgel

Binary mixtures of self-assembled monolayers of 1,8-octanedithiol and 1-octanethiol for a controlled growth of gold nanoparticles

Anne Kathrena A. Aliganga [a,c], Anne-Sophie Duwez [a,b], Silvia Mittler [a,c,*]

[a] *Max Planck Institute for Polymer Research, Ackermann Weg 10, D-55128 Mainz, Germany*
[b] *Unité de Chimie et de Physique des Hauts Polymères and Research Center in Micro and Nanoscopic Electronic Devices and Materials (CERMIN), Université catholique de Louvain, Place Croix du Sud 1, B-1348 Louvain-la-Neuve, Belgium*
[c] *Department of Physics and Astronomy, University of Western Ontario, London, Ont., Canada N6A 3K7*

Received 24 January 2006; received in revised form 31 March 2006; accepted 31 March 2006
Available online 2 May 2006

Abstract

The physical response of gold nanoparticles, e.g. electronic, magnetic, and photonic behaviours due to quantum confinement effects, does not only depend on their size, but also on the shape and the density of the nanoparticles and therefore on the probability for the formation of clusters of nanoparticles. Nanocluster-based devices are envisioned as the next generation in electronics miniaturization. Organometallic chemical vapor deposition (OMCVD) is a straight forward method to grow these kinds of Au nanoparticles and clusters covalently attached on self-assembled monolayers (SAMs) carrying nucleation sites for particle growth. The control of density and location of these nucleation sites is a crucial point for the development of new nanoparticle based devices. The OMCVD particles grown here are nucleated by –SH groups at the head group of a SAM. Therefore, it is important to control and understand structure, order, composition, and lateral distribution of the SH-terminated molecules in a templating SAM for OMCVD grown gold nanoparticles.

This paper presents a characterization of self-assembled monolayers of 1-octanethiol (C8-T) and 1,8-octanedithiol (C8-DT) and their binary mixtures immobilized on gold substrates using contact angle investigations, spontaneous desorption time-of-flight mass spectrometry (SD-ToF-MS) and X-ray photoelectron spectroscopy (XPS). We examined the relationship between the molar ratio of C8-T and C8-DT molecules in solution versus their corresponding molar ratio in the binary mixed SAMs and the ratio between standing up and lying down species of C8-DT.

The growth of gold nanoparticles was investigated with respect to the dilution of the nucleation sites in the templating SAM. Influences on the growth velocities were found depending on the amount of available nucleation sites.

Keywords: Self-assembled monolayer; Binary mixture; Thiol; Dithiol; Conformation; Standing up conformation; Lying flat conformation; Gold nanoparticle; OMCVD

* Corresponding author. Address: Department of Physics and Astronomy, University of Western Ontario, London, Ont., Canada N6A 3K7. Tel.: +1 519 661 2111x88592; fax: +1 519 661 2033.
E-mail address: smittler@uwo.ca (S. Mittler).

1566-1199/$ - see front matter
doi:10.1016/j.orgel.2006.03.013

1. Introduction

The extensive research interest in nanometer-dimension inorganic nanoparticles was mainly driven by their broad impact on the emerging disciplines of nanoengineering [1], nanoelectronics [2], and nanobioelectronics [3]. Gold nanoparticles, in particular, were the focus of numerous investigations in recent years because of promises offered by their optical, electronic, and chemical properties [4]. Of particular interest are their tunable electronic, magnetic, and photonic behaviours due to quantum confinement effects, with nanoparticle and nanoparticle cluster-based devices being envisioned as the next generation in electronics miniaturization [5]. Recent years have also seen a tremendous impact on silver and gold nanoparticles and nanobjects in biological assays, detection, labeling and sensing [6].

One of the technological challenges is to fabricate robust and organized assemblies of these nanoscale building blocks [7] where the collective structural properties and functions might be manipulated by the nature, size, cluster-size, position and overall composition of the nanoparticles e.g. on a substrate. Among the various techniques developed, self-assembly was quite effective in creating ordered superlattices of nanoparticles by exploiting the molecular interactions such as van der Waals forces, chemisorptive bonding, electrostatic interactions, etc. [4,5,8]. A key structural element is a bifunctional bridge which links the nanoparticles to the substrate surfaces and/or allows layering of nanoparticles, such as aliphatic dithiols. These processes can be achieved by simple beaker chemistry.

Self-assembled monolayers of organosulfur compounds like thiols, sulfides and disulfides on the surface of coinage metals like Cu, Ag and Au, have attracted much attention because of their ease of preparation and their applicability ranging from medicine [9–11] to microelectronic device fabrication [12,13]. Research on alkanethiol SAMs has increased enormously since the pioneering work of Nuzzo et al. [14–16]. Ulman [17,18] gives good reviews in these aspects. The principle of these systems is simple: A molecule, which is essentially an alkane chain, is given an anchor group with a strong preferential adsorption to the substrate used and a head group, which carries a functional group. Thiol (–SH) anchor groups and Au(1 1 1) substrates have shown to work excellently. The thiol molecules adsorb readily from solution onto the gold substrate, creating a dense monolayer with the head group pointing outwards from the surface. By using thiol molecules with different head groups, the resulting chemical surface functionality can be varied within a wide range. In addition, it is also possible to chemically functionalize the head groups by performing reactions after assembly of the SAMs. While the nature of the thiol–gold bond on the substrate is still subject to controversy and the structural properties of the resulting SAMs are still matters of intense current research efforts, the focus of several activities is the deposition of inorganic materials on the surfaces of SAMs [19–23]. The present study is part of a general objective to prepare SAMs carrying a specific density of reactive groups for a templated nucleation and growth of OMCVD gold nanoparticles. It focuses on using 1,8-octanedithiol (C8-DT) to yield monolayers presenting –SH reactive groups at the surface of the SAM. For dilution the length adequate 1-octanethiol (C8-T) is mixed to C8-DT.

It is not necessarily clear that α,ω-alkanedithiols form well-ordered SAMs. With some dependence on chain length, these layers have been reported to anchor to gold surfaces with one or both thiol groups and to orient in an upright, looped, or flat arrangement [24–32]. It seems that short chain dithiols, such as hexanedithiol, form well-ordered monolayers where both thiol groups bind to the surface and the chain is parallel to the substrate [24]. Intermediate chain length dithiols, such as octanedithiol or nonanedithiol, form monolayers where either thiol group bonding and chain orientation are similar to that of the short chain dithiols [25–28], or one thiol group binds to the surface and the second one projecting outward, the chain being oriented upright to the surface [29–31]. Long chain dithiols, such as dodecanedithiol, form monolayers where the bonding involves both thiol groups with the chain in a looped conformation [30,33] and/or a single thiol group with the chain extending outward [32]. Whether the chemisorption of both thiol groups, or the van der Waals interactions between the alkyl chains leading to well-ordered structures, is the dominating effect depends on the particular system and the conditions employed [34–38].

A previous XPS study has shown that C8-DT SAMs can form nicely ordered SAMs on gold and silver, yielding a surface which is terminated by thiol functions [29]. For the purpose of using thiol-terminated SAMs as nucleation sites for the deposition of

Au by OMCVD, the amount of C8-DT in the SAMs is an important parameter giving control over the amount, size and form of Au nanoparticles on the surface [39]. It is also a step towards the fabrication of well-defined arrays of gold nanoparticles on SAMs.

To control the density of functional –SH groups for gold nanoparticle nucleation on the SAM surface, we chose to fabricate binary mixtures of SAMs of C8-DT and C8-T (which has a methyl ($-CH_3$)-terminal function as a non-reactive site for the employed gold precursor). Such films were prepared by self-assembly out of binary mixtures of these thiols in solution. The relative proportion of the two functionalities in the final SAMs depends upon several parameters, like the mixing ratio in solution, the alkane chain lengths, the solubility of the thiols in the solvent used and the properties of the chain-terminating groups. In general, the composition in the SAM differs from that in the preparation solution. Measurements with surface sensitive probes are necessary to calibrate the mixing ratio in the final SAM.

TOF-SDMS and XPS were used to determine the relationship between the solution concentration ratio of C8-DT and its concentration ratio on the surface. Finally various mixed monolayers are used to grow gold nanoparticles. Both the overall deposited gold as well as the height of the particles and their distributions are investigated by spontaneous desorption ToF mass spectrometry (SD-ToF-MS), STM and AFM.

2. Experimental

2.1. Au(1 1 1) substrate preparation

Gold (Balzers, 99.99%) was deposited onto freshly cleaved mica substrates using a vacuum coating system (Edwards, FL 400) at $p \leqslant 5 \times 10^{-6}$ mbar. Before deposition, the mica was heated to 650 °C for 3–4 min under N_2 atmosphere. It was immediately placed inside the vacuum evaporation machine. The typical evaporation rate was 1 Å/s, and the thickness of the gold film was 60 nm. Prior to the self-assembly process, these freshly evaporated Au/mica samples were annealed to form large areas with (1 1 1) orientation on the surface. Annealing was carried out at 650 °C for 1 min under a N_2 atmosphere in a tubular oven (Heraeus) and chilled to room temperature under N_2 atmosphere. This method produced flat Au(1 1 1) terraces as large as $300\,\text{nm} \times 300\,\text{nm}$ basing from AFM measurements.

2.2. SAM preparation

1-Octanethiol (C8-T; Aldrich, 98.5+%), deuterated C8-T (purchased from Dr. R.K. Thomas, Physical Chemistry Laboratory, Oxford University, UK), 1,8-octanedithiol (C8-DT; Aldrich, 97+%) and ethanol (Chromasolv®, Riedel-de Haën, 99.9%) were used without further purification. SAMs were prepared by immersing freshly prepared Au(1 1 1) in a 1 mM ethanolic solution of the respective alkanethiol or –dithiol for approximately 15 h. The samples were then cleaned by rinsing extensively with ethanol, dried with N_2, and stored under inert conditions (sealed in a glass flask under Ar atmosphere). Binary mixed SAMs of C8-T and C8-DT were prepared from 1 mM stock solutions of each thiol.

2.3. Spontaneous desorption time-of-flight mass spectrometry (SD-ToF-MS)

The SD-ToF-MS measurements were performed using a linear time-of-flight mass spectrometer in high vacuum at a pressure of about 1×10^{-6} mbar. Atomic and molecular ions from the sample were released by spontaneous desorption, a secondary ion process in which the sample is not bombarded by particles from an external source [40].

Primary ions of adsorbates are field desorbed from the edges of an acceleration grid located in front of the sample. These ions are accelerated towards the sample gaining keV energies. They finally sputter secondary ions from the sample. Spectra of negative secondary ions are recorded using the simultaneously emitted secondary electrons from the sample surface as trigger particles. An acceleration voltage of 9.5 kV was applied to the sample. The recording time of a spectrum was 20–40 min. Within one spectrum mass peaks of interest were integrated and normalized with the number of start events with one or more corresponding stop events. This leads to a relative ion yield that allows the comparison of the intensities of equivalent peaks in different spectra. Fragments of masses m/z up to 2000 u can be analyzed by this setup. In order to analyze the concentration ratio of immobilized species by SD-ToF-MS one needs to calibrate the counts in specific peak with the help of spectra of the pure substances. A detailed data analysis is given in elsewhere [41].

2.4. X-ray photoelectron spectroscopy

The surface chemical composition was determined using a SSIX probe (SSX 100/206) spectrometer from Fisons, operating at a pressure in the 10^{-9} Torr range, equipped with an aluminum anode and a quartz monochromator. No flood-gun was used to minimize the appearance of beam-induced species. When the flood-gun is used, beam-induced sulfur species appear after only a few minutes of accumulation. When no flood-gun is used, such species appear after 2 h of accumulation. The acquisition parameters have been adjusted to avoid the appearance of beam-induced species while keeping an acceptable signal to noise ratio. We have checked that no charging effects occurred. Spectra were recorded at a take-off angle of 35° (angle between the plane of the sample surface and the entrance lens of the analyzer) and with a pass energy of 150 eV. Intensity ratios were converted into atomic ratios by using the sensitivity factors proposed by the manufacturer (Scoffield photoemission cross sections, variation of the electron mean free path according to the 0.7th power of the kinetic energy, constant transmission function). The S 2p spectra were fitted by a function describing a doublet with spin–orbit coupling of 1.18 eV and area ratio of 1:2 for $2p_{1/2}$ and $2p_{3/2}$ components using a Gaussian-Lorentzian (85–15%) linear combination and a linear background [42].

2.5. Contact angle measurements

Advancing and receding contact angles of water on the films were measured using a contact angle microscope (Krüss G-1) under ambient conditions, while the volume of the drop (2.5 μL) was increased or decreased at the minimum rate required for movement of the water/air/solid triple point.

2.6. Scanning tunnelling microscopy

STM was performed with a homebuilt scan head in combination with a commercial controller (RHK SPM 1000). PtIr tips were used for imaging. The imaging parameters were 500 mV bias, currents below 100 pA under ambient conditions.

2.7. Organometallic chemical vapor deposition (OMCVD) of gold onto SAMs

The vapor deposition of $[(CH_3)_3P]AuCH_3$ [43] onto SAMs was carried out in a home build vacuum sealed glass reactor chamber, which contained the SAM sample and a small glass vessel with 20 mg of the gold precursor. The reactor was evacuated ($p_{max} = 2.0 \times 10^{-2}$ mbar) and placed in an oven at 70 °C [22,23]. Thirty minutes of deposition time was employed in this work. Subsequently, the SAMs were quickly removed, rinsed with dry ethanol and stored under inert conditions.

2.8. Atomic force microscopy (AFM)

AFM topography images were acquired using a Nanoscope™ IIIa Atomic Force Microscope (Digital Instruments, Santa Barbara, CA). Imaging was done in tapping mode at ambient conditions. Silicon nitride cantilevers of 100 μm length (spring constant 0.1 N/m) with integrated sharpened tips (Olympus, Tokyo, Japan) were used.

All AFM tips used to determine the height of the particles were calibrated by imaging colloidal gold with known shape and size as a reference sample. In addition to that, in comparing gold nanoparticles on mixed SAMs with different ratios, very dilute samples were prepared in order to avoid the tip convolution effects due to particles that are too close to each other.

3. Results and discussion

3.1. Determination of the surface composition in the mixed SAMs

Binary mixed SAMs were prepared by the deposition of C8-DT and C8-T from solutions in ethanol onto gold substrates. Within each series, the molar fractions of the adsorbates in solution (χ_{sol}) were varied from 0 to 1 in order to produce monolayers with a range of surface compositions. The aim is to determine the relationship between χ_{sol} and χ_{SAM}, the molar fraction of adsorbates on the surface.

3.1.1. Characterization of SAMs by contact angle measurements

Contact angle measurements were performed to check the quality of the SAMs prepared. As shown in Fig. 1, the advancing contact angle of water on pure C8-T SAMs is $103° \pm 2°$. The criterion for a good monolayer in the case of long chain methyl-terminated molecules (for $n > 10$, where n is the number of CH_2 units) is a contact angle above 110° [18]. For shorter chains ($n < 10$), the contact angles become progressively lower (100–105°). This

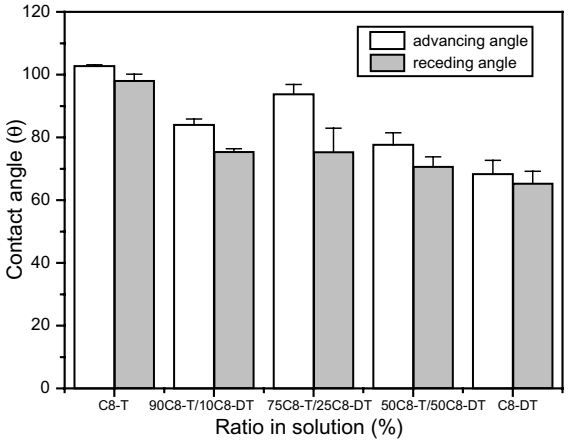

Fig. 1. Contact angle of water on pure and binary mixed SAMs of C8-T and C8-DT.

trend is due to the increasing disorder of short chains, exposing their methylene units. The value we found for the C8-T SAMs is in very good agreement with the values reported in the literature for short alkylthiol chains. The advancing contact angle of pure C8-DT is $68° \pm 4°$, which is in good agreement with the reported value for –SH head groups, 70° [44]. The contact angle hysteresis, which is the difference between the advancing and the receding angle, for C8-T and C8-DT films are 5° and 3°, respectively. This small hysteresis can be attributed to a very low surface roughness and a high surface homogeneity [44]. Contact angle measurements were also performed on mixed SAMs (Fig. 1). The contact angles of mixed SAMs lie between the values of 103° for C8-T and 68° for C8-DT. The contact angle values decrease with increasing C8-DT content, but showing enhanced individual hysteresis measures indicating surface roughness enhancements within the mixed regime [44,45].

3.1.2. Characterization of SAMs by SD-ToF-MS

Fig. 2 shows the SD-ToF-mass spectra for pure C8-T SAMs on Au. The molecular fragment of C8-T, octanethiolate ($^{-}S–(CH_2)_7–CH_3$), is observed at $m/z = 145$ u. From the spectra, the signals corresponding to gold peaks, $m/z = 197$ u (Au^{-}), 394 u (Au_2^{-}) and 591 u (Au_3^{-}) are not observed. This indicates a density of the C8-T in the SAM being high enough to mask the gold substrate. The assignment of the other peaks can be found in Table 1. There is no drawn-out-mechanism of the molecules from the surface [44]. In SD-ToF-MS the desorption process randomly cleaves off species on the surface when they are hit by the bombarding particles from the grid. Therefore the most accessible species, the topmost layer on the surface, have the highest probability to be desorbed first. In the case of C8-T SAMs, the Au substrate is masked completely by the alkanethiolate monolayer.

In the mass spectra of C8-DT (Fig. 3), the 1-octanethiol-8-thiolate ($^{-}S–(CH_2)_8–SH$) fragment is

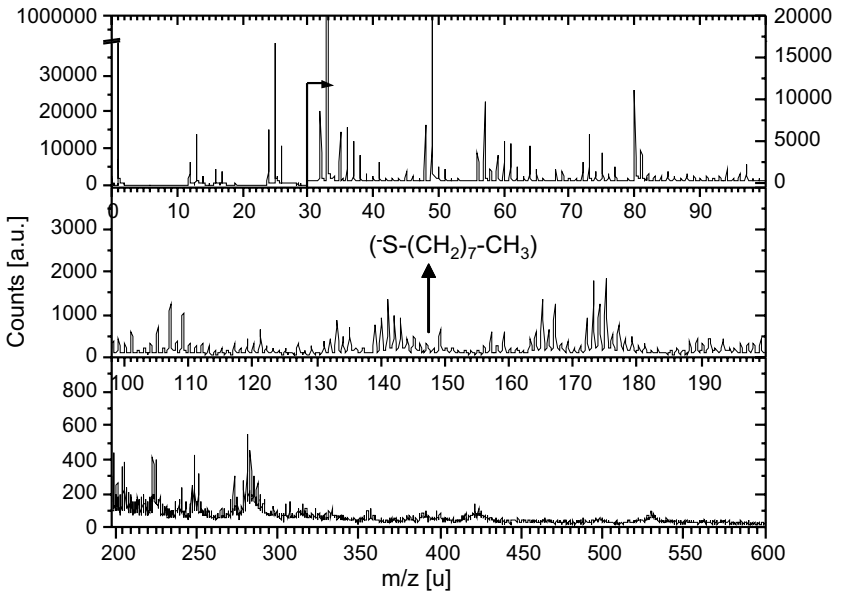

Fig. 2. SD-ToF-mass spectra of C8-T SAMs on Au.

Table 1
Assignment of mass peaks of Fig. 2, C8-T SAM

	m/z (u)	Molecular fragments
Peaks that are also observed in clean, bare gold substrates	12	C
	13	CH
	24	C–C
	25	CH–C
	26	CH–CH
	32	S
	33	SH
	48, 49	Probably C_4, C_4H
	229	AuS, AuO_2
Other peaks	80	SO_3
	109	$SO_3(CH_2)_2$
	146	$SH(CH_2)_8$
	167	$SO_3(CH_2)_6$
	174	$SO_3(CH_2)_7$
	275	$AuSO_3$

Table 2
Assignment of mass peaks of Fig. 3, C8-DT SAM

	m/z (u)	Molecular fragments
Peaks that are also observed in clean, bare gold substrates	12	C
	13	CH
	24	C–C
	25	CH–C
	26	CH–CH
	32	S
	33	SH
	48, 49	Probably C_4, C_4H
	229	AuS, AuO_2
Other peaks	60	$SH–(CH_2)_2$
	197	Au
	229	AuS, AuO_2
	245	AuSO, AuO_2
	591	Au_3

There are many peaks here that can be found also in bare gold substrate. This supports the interpretation that C8-DT SAM is not as ordered as C8-T SAM due to its dithiol moiety.

found at $m/z = 177$ u. This fragment is a finger print of the single bound, standing up chains. A signal from the gold substrate is also detected, indicating a non-shielding of the gold substrate by the C8-DT SAM. This can be due to the presence of double bound, lying flat C8-DT molecules, which do not mask the gold from the substrate efficiently, and at the same time have a much lesser probability to be found in a SD-TOF-mass spectrum due to the double bonding [40c]. The assignment of the other peaks can be found in Table 2.

Further examination of the mass spectra of C8-T and C8-DT SAMs, does not yield any more reliable mass fragment peaks for comparison and for the calibration of the mixing ratio in the mixed SAMs. The molecular fragments of C8-T and C8-DT are not distinctive from each other, which is not surprising taking the very similar molecular structure into account. The typical fragments of these two molecules are found in both spectra.

Since there are no distinctive peaks obtained for C8-T and C8-DT, a completely deuterated octanethiol, C8-T_d, is used instead, presuming that the self-assembly thermodynamics do not change by

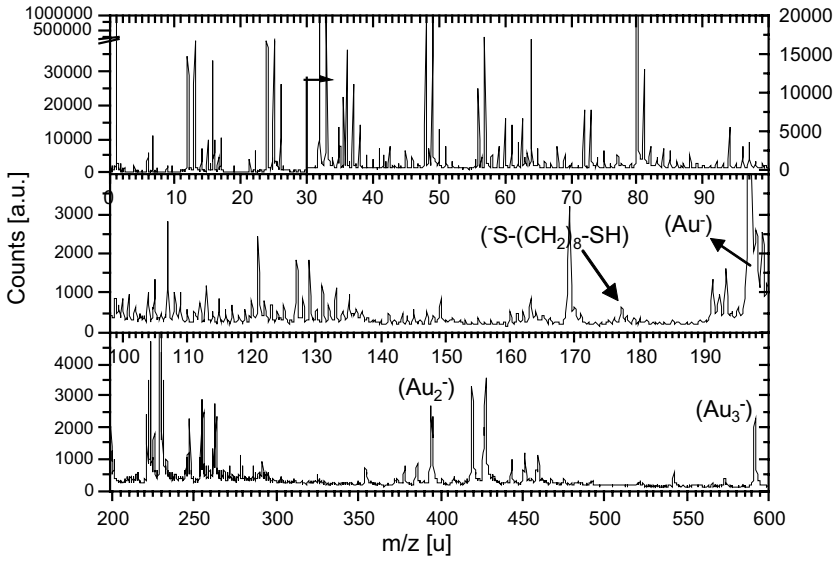

Fig. 3. SD-ToF-mass spectra of C8-DT SAMs on Au.

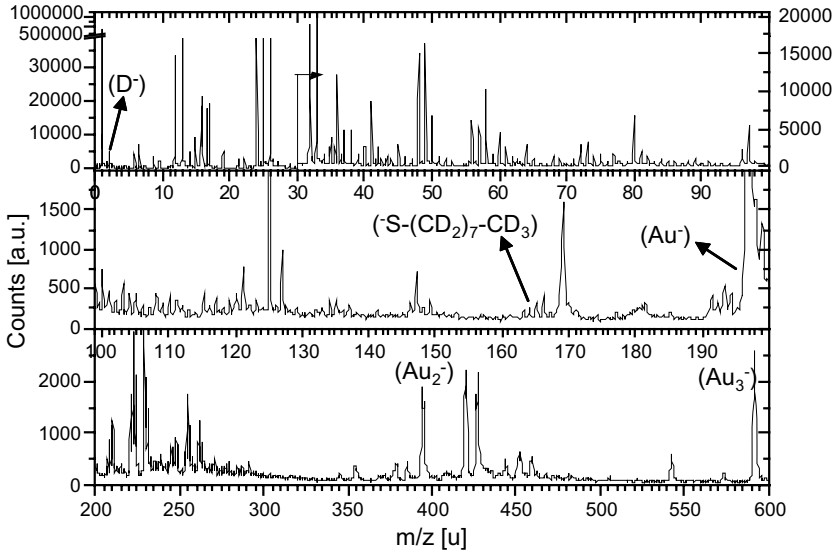

Fig. 4. SD-ToF-mass spectra of perdeuterated C8-T SAMs on Au.

the deuterium. Fig. 4 shows the SD-ToF-mass spectra of SAMs prepared from perdeuterated C8-T_d on Au. There is a strong signal of deuterium (D) at peak $m/z = 2$ u which was used to identify the presence of C8-T_d in the SAMs. The assignment of the other peaks can be found in Table 3.

Fig. 5 shows the mass spectra of pure and mixed SAMs of C8-DT and perdeuterated C8-T_d on Au in a directly comparable fashion, for the $\chi_{sol}^{C8\text{-}DT} = 0.1$. The relationship between the molar fraction of C8-DT in solution ($\chi_{sol}^{C8\text{-}DT}$) and on the surface ($\chi_{SAM}^{C8\text{-}DT}$) can be determined from these spectra, the pure SAMs and a series of mixed SAMs with systematically changing C8-DT mole fractions in the self-assembling solution. This is obtained by integrating and normalizing the mass peak of interest, which is deuterium (D) in this case, within one spectrum, with the number of start events with one or more corresponding stop events. This then leads to a relative ion yield that allows the comparison of the intensities of equivalent peaks in different spectra. This yields an individual data set of surface molar fractions (χ_{SAM}) for each species. The sum of the individual surface molar fractions ($\chi_{SAM}^{C8\text{-}DT}(\chi_{sol} = x) + \chi_{SAM}^{C8\text{-}Td}(\chi_{sol} = x)$) at a given solution mole fraction ($\chi_{sol} = x$) has to be 1 for reliable data, being the case in this study.

Table 3
Assignment of mass peaks of Fig. 4, C8-T_D SAM

m/z (u)	Molecular fragments
50	$SD–CD_2$
80	SO_3, $S–(CD_2)_3$
96	$S–(CD_2)_4$
164	$SD–(CD_2)_8$
210	$SO_3–(CD_2)_8$
197	Au
229	AuS, AuO_2
245	AuSO, AuO_3
426	Au_2S, Au_2O_2
591	Au_3

There are many peaks here that can be found also in bare gold substrate.

Fig. 6 shows the molar fractions (χ_{SAM}) of both species in the mixed C8-T_d/C8-DT SAMs on Au substrates versus the molar fractions (χ_{sol}) of C8-DT in solution. The amount of C8-DT within the SAMs dominates nearly the entire mixing regime. Only at very small C8-DT concentrations, in the $\chi_{sol} = 0.01$–0.03 regime, C8-T molecules are found in comparable amounts. This very asymmetric binary assembly map suggests that C8-DT with its two binding sites has a much stronger affinity to the gold substrate surface as compared to C8-T with one binding site only. For example, a very dilute solution of C8-DT, approximately a $\chi_{sol} = 0.005$, is needed to have a 1:1 mixture of both thiols on the surface.

At this point, we can conclude that in order to achieve the main goal—to have diluted –SH head groups on the surface for gold nanoparticle deposition—it is interesting to explore $\chi_{SAM}^{C8\text{-}DT}$ of 0.5 and lower only. The actual solution concentrations of

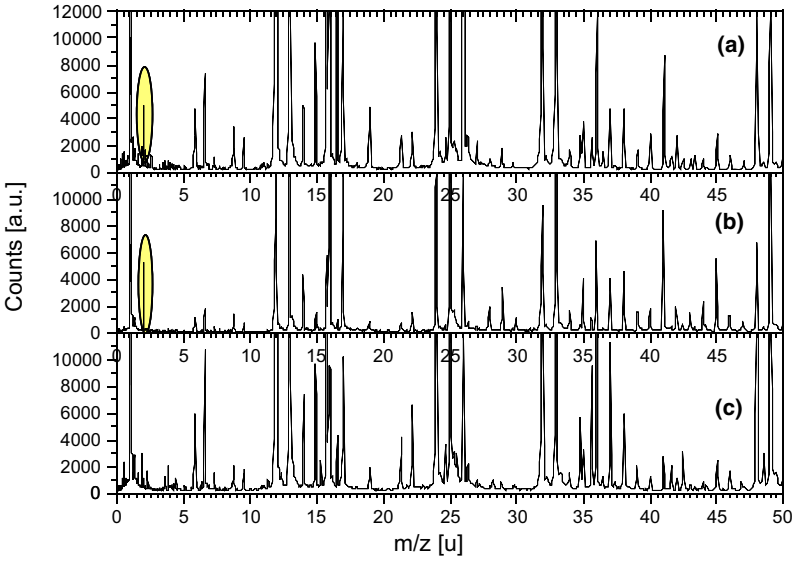

Fig. 5. SD-ToF-mass spectra of pure and mixed SAMs on Au. (a) perdeuterated C8-T SAM, (b) $\chi_{sol}^{C8\text{-}DT} = 0.1$ ($\chi_{sol}^{perdeuterated\ C8\text{-}T} = 0.9$), (c) C8-DT SAM.

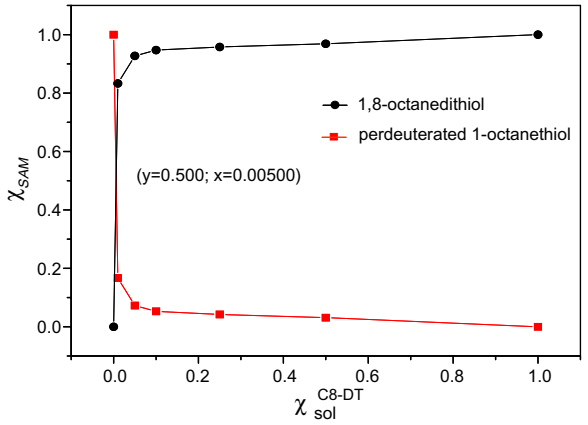

Fig. 6. Molar fraction (χ_{SAM}) of C8-T and C8-DT in SAMs on Au substrates versus molar fraction of C8-DT ($\chi_{sol}^{C8\text{-}DT}$) in solution.

C8-DT yielding dilute concentrations of C8-DT in the mixed SAM on the surface are listed in Table 4.

3.1.3. X-ray photoelectron spectroscopy (XPS) studies of SAMs

To estimate the amount of free thiol head groups on the surface, the SAMs were investigated by XPS. And since it is desired to achieve a dilute concentration of C8-DT SAMs with free-SH on the surface, molar fractions $\chi_{SAM}^{C8\text{-}DT}$ of 0.5 and below were explored, on the basis of the SD-ToF-MS results (Table 4).

Table 4
Solution concentrations relative ($\chi_{sol}^{C8\text{-}DT}$) and in moles (M) required for the formation of diluted C8-DT molecules in a matrix of C8-T in mixed SAMs up to $\chi_{SAM}^{C8\text{-}DT} = 0.5$

$\chi_{SAM}^{C8\text{-}DT}$	$\chi_{sol}^{C8\text{-}DT}$	C8-DT concentration in solution (M)
0.005	0.00005	5.0×10^{-8}
0.01	0.0001	1.0×10^{-7}
0.05	0.0005	5.3×10^{-7}
0.1	0.001	1.0×10^{-6}
0.15	0.0015	1.5×10^{-6}
0.2	0.002	2.0×10^{-6}
0.5	0.005	5.0×10^{-6}

XPS has been popularly used as a tool in characterizing alkanethiol SAMs [For a review see ref. [46]]. In Fig. 7a–e, the X-ray photoelectron spectra of the S 2p region are displayed as obtained from pure SAMs of C8-T and of C8-DT and a series of binary mixtures. Two main peaks, centered on 162 and 169 eV can be observed. The dominant peak centered at 162.0 eV was previously assigned to thiolate moiety and proves the existence of a chemical gold-sulfur bond [46–48]. The second peak around 169 eV can be attributed to oxidized sulfur species [46,49,50]. The presence of these oxidized species is a well-known phenomenon for monolayers made out of short chain thiols in which oxidation on the sulfur occurs fast [46,49].

The larger FWHM of the S 2p component situated at 162 eV in the C8-DT SAM (2.9 eV) and in

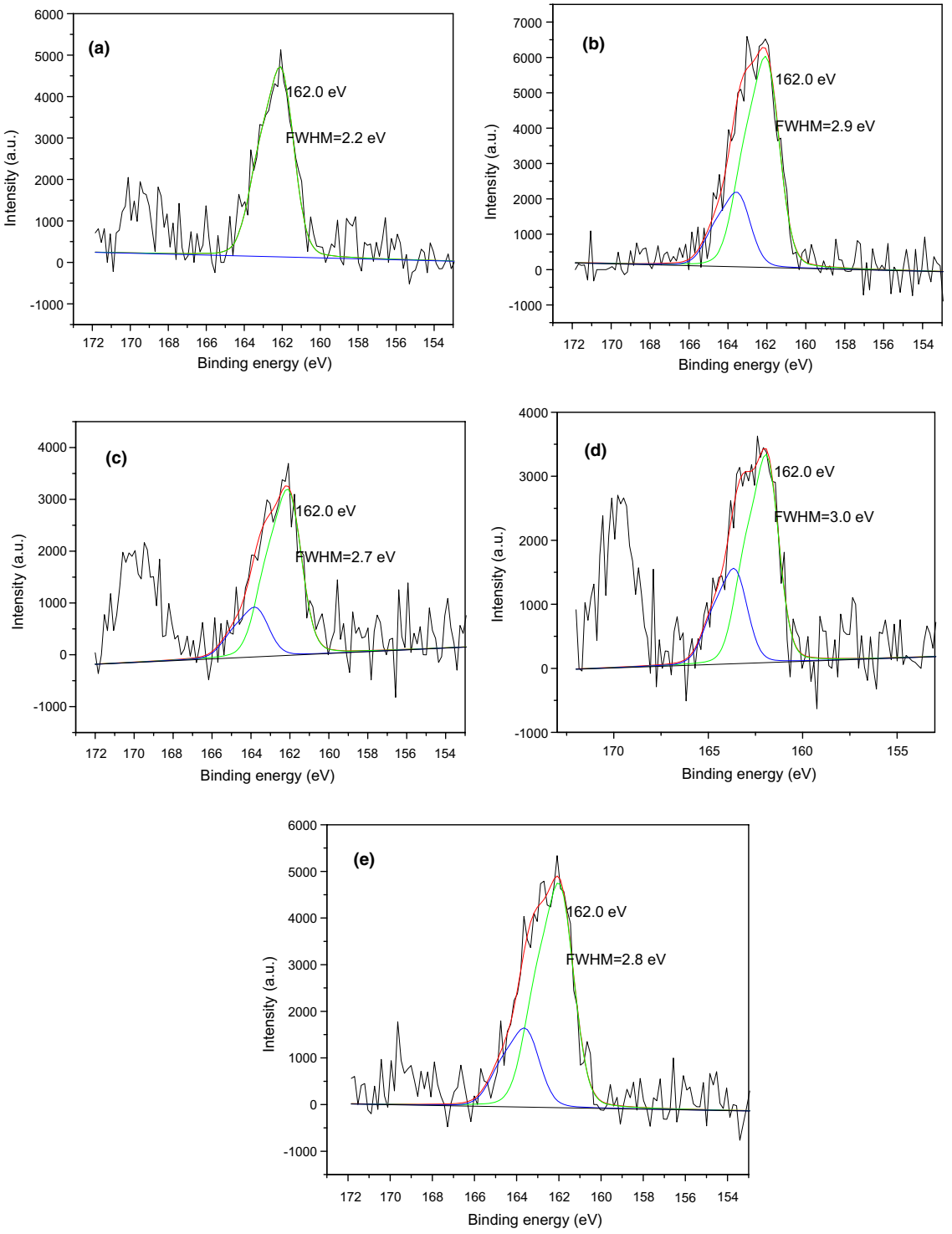

Fig. 7. X-ray photoelectron spectra of the S2p region of SAMs prepared from (a) C8-T, (b) C8-DT and binary mixed SAMs with C8-DT surface molar fractions ($\chi_{SAM}^{C8\text{-}DT}$) of (c) 0.1 (d) 0.2, and (e) 0.5. The peaks were fitted by functions describing doublets with spin–orbit coupling of 1.18 eV and area ratio of 1:2 for $2p_{1/2}$ and $2p_{3/2}$ components, using a Gaussian-Lorentzian (85–15%) linear combination and a linear background. The FWHM of the doublet corresponding to the S–Au species (green line) in figures b–e has been fixed to the value obtained when fitting the pure C8-T sample. (For interpretation of the references in color in this figure legend, the reader is referred to the web version of this article.)

the mixed SAMs (2.7–3.0 eV) as compared to the one from the C8-T SAM (2.2 eV) strongly suggests that the peak envelope contains an additional structure. The spectrum deconvolution (doublets with spin–orbit coupling of 1.18 eV and area ratio of 1:2 for S $2p_{1/2}$ and S $2p_{3/2}$ components) reveals the presence of one additional doublet positioned at 163.5 eV. This is typically the position of the S $2p_{3/2}$ component of a free S–H [27,29,46]. This is a fingerprint of the standing up dithiol molecules bound with one SH-group only to the gold substrate. To note, the peak positioned at 162.0 eV, which is referring to the S–Au binding, is much more dominant than the free S–H peak. This should be the contrary in a C8-DT monolayer in which the dithiols are in a standing up structure. The photoelectrons coming from the Au–S interface are attenuated by the SAM as an overlayer to travel through and we would thus observe a smaller intensity for the Au–S peak than for the SH peak. This means that a large amount of molecules are lying down on the substrate. Table 5 summarizes the relative area and position of the two doublets obtained from the deconvolution for all SAMs samples measured. This means that a large amount of molecules are lying down on the substrate, as confirmed by a lower attenuation of the Au signal for the C8-DT SAMs as compared to the monothiol SAMs.

Both the standing up and lying down dithiols contribute to the Au–S signal. The ratio between the Au–S and SH component can give a rough estimation of the amount of dithiols that are standing up. The intensity of the sulfur originating from the S–Au bond is attenuated by the carbon overlayer following the classical equation [46,51]:

$$I_{S\text{–}Au} = I_0 e^{-d/\lambda \sin\theta} \quad (1)$$

where I_0 is the intensity without overlayer, d is the layer thickness, θ is the takeoff angle and λ is the electron mean free path of the S 2p electrons. θ is equal to 35°, λ can be estimated to be equal to 39 Å [46] and d can be calculated (8.8 Å). Thus, $I_{S\text{–}Au}/I_0$ is equal to 0.67. As an example calculation for the pure C8-DT SAM, the area of the S–Au peak (74.6, Table 5) should be equal to 111, as calculated from Eq. (1). The electrons from S–H are not attenuated since S–H is situated on top of the film. Therefore there are 111 S–Au species and 25 S–H species (Table 5). Among the 111 species, 25 come from the molecules having S–H moieties outside the film. Thus 86 (111 − 25) S–Au come from molecules that are lying down on the substrate having two S–Au bonds each. Therefore 86 bound S–Au groups mean 46 flat lying molecules. So 25 molecules carrying a free SH-group and 43 flat lying molecules gives a standing up ratio of 37% (100% being 43 + 25 = 68). This is a rough estimation since only the standing up molecules contribute to the Au–S attenuation. This is thus a borderline case, corresponding to a system with a thickness of 8.8 Å, where the entire Au–S signal is attenuated. The true layer thickness is probably lower than 8.8 Å, because of the contribution of lying down molecules. Another borderline case is a system into which there is no attenuation of the Au–S signal. In this case, the estimation yields 50% of standing up molecules. We can thus conclude that in a pure C8-DT SAM, between 37% and 50% of the dithiols are standing up. It is much more difficult to estimate the amount of standing up structures in mixed monolayers since both the monothiol and dithiols contribute to the Au–S signal. Moreover, the presence of oxidized sulfur species in the mixed layers may lead to wrong estimations. It is extremely difficult, if not impossible, to determine exactly how much oxidized species originates from S–H and from S–Au. However, we can still derive a relationship between the free S–H peak area and the Au–S peak area (Fig. 8). Here the integrated area ratios between the SH and the S–Au peaks are plotted versus the amount of C8-DT present in the SAM. The area ratio SH/S–Au is proportional to the amount of free SH-groups, but not necessarily directly linear, because of the hidden, unknown attenuation factor for the S–Au species.

The ratio of free S–H/Au–S species reveals two relationships within the concentration regime of C8-DT in the mixed SAMs. From 0% to 20% C8-DT content or $\chi_{SAM}^{C8\text{-}DT} = 0\text{–}0.2$ (Fig. 8), the ratio of S–H/S–Au on the surface rapidly increases with increasing C8-DT concentration. From 20% to 100% (or $\chi_{SAM}^{C8\text{-}DT} < 0.2$) it decreases slightly.

Table 5
Peak position (eV) and relative area (%) of the sulfur components obtained from the deconvolution of the S 2p spectrum of mixed SAMs

χ_{SAM}	Peak position (eV)–relative area (%)	
	S–H	S–Au
C8-DT	163.5–25.4	162.0–74.6
0.5 C8-DT/0.5 C8-T	163.5–25.7	161.9–74.3
0.2 C8-DT/0.8 C8-T	163.5–31.0	161.9–69.0
0.1 C8-DT/0.9 C8-T	163.7–22.0	162.0–78.0
C8-T	–	162.0–100.0

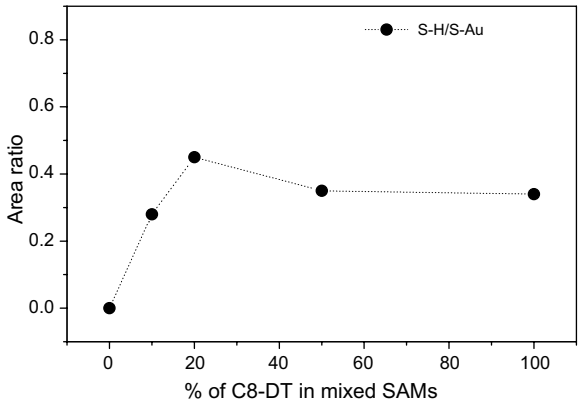

Fig. 8. Area ratio of the free S–H component to the Au–S component versus $\chi_{SAM}^{C8\text{-}DT}$ in binary mixed SAMs. The line is a guide to the eye only.

This behaviour gives us several hints on the mixed SAMs structure. First, from 0.2 to 1 $\chi_{SAM}^{C8\text{-}DT}$, there is an inverse relation between the amount of C8-DT present and the free SH groups. This means with respect to the diluter molecule C8-T, that there is a small increase in free S–H groups with increasing amount of C8-T on the surface. Second, an increase in the area ratio of SH/S–Au means there is an increased percentage of standing up molecules of C8-DT in the SAMs: the amount of lying-flat-molecules increases with increasing surface concentration of C8-DT. Third, from 0 to 0.2 $\chi_{SAM}^{C8\text{-}DT}$, the amount of C8-DT in the SAM is increasing due to an effective onset of the dilution with C8-T and at the same time an increase in C8-DT concentration leads to a nearly linear increase in the SH/S–Au area ratio. This can only be the case when most of the dithiol molecules in the SAMs with in this C8-DT low concentration range are in the standing up geometry. As a tentative explanation, the van der Waals interaction becomes the more dominant driving force in the overall self-assembly process with high C8-T concentrations in the binary mixtures of SAMs of C8-T and C8-DT.

3.2. OMCVD of gold nanoparticles

Chemical vapor deposition (CVD) is a method for depositing films of various materials, which involves the thermally induced reaction of a material-containing molecule on a heated surface [52]. First, a volatile precursor is transported into the reactor and to the substrate leading to an adsorption and a surface reaction, whereby the metal is deposited and the by-products are subsequently desorbed. The metal atoms then diffuse to form a stable nucleus at a nucleation site, where subsequent growth occurs. The volatile organometallic precursor used for the organo metallic CVD (OMCVD) of gold is trimethylphosphinegoldmethyl ($(((CH_3)_3P)AuCH_3)$), which is known to give pure gold films at low temperatures [52]. Here we use the exposed SH-groups at the SAM surface as nucleation sites.

Fig. 9 shows a (a) STM and an (b) AFM image of the OMCVD deposited gold nanoparticles grown onto C8-DT SAMs. Disc-like structures were observed with an average particles' height of approximately 5 Å as obtained from the AFM measurements (Fig. 9b) and lateral diameters of about 5 nm as determined from STM measurements (Fig. 9a), yielding an aspect ratio of 1:10.

C8-DT samples systematically diluted with C8-T were used as templates for the gold nanoparticle

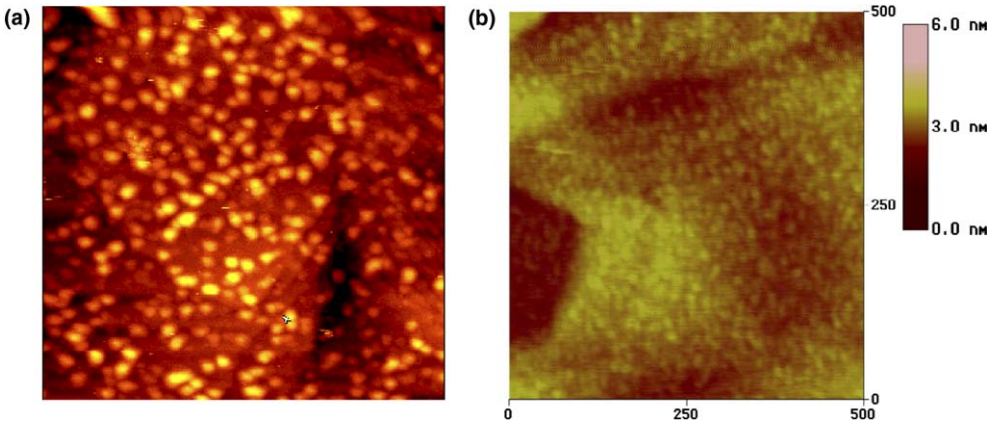

Fig. 9. (a) STM (195 nm × 195 nm) and (b) AFM (500 nm × 500 nm) images of OMCVD gold nanoparticles on C8-DT SAMs on Au(1 1 1) substrate.

growth. Fig. 10 shows the height histograms obtained from AFM images with decreasing amount of C8-DT in the SAM. Clearly with decreasing amount −10% in (a), 5% in (b) to 1% in (c)—the average height rises from 2.4 nm along 3.5 nm to 4.5 nm. Nevertheless the average deposited amount of gold increases with increasing amount of C8-DT content as seen in Fig. 11 showing relative gold amount data obtained by SD-ToF-MS.

Because available nucleation sites compete at a given precursor pressure for each available gold atom the average height per present particle increases when the amount of competing binding sites decreases. This is similar but not identical to Oswald ripening [53]. But still the overall amount of gold decreases. The non-linear curve form in Fig. 11 represents the non-linear immobilization probability of the C8-DT/C8-T binary mixture (Fig. 6) and the available free-SH-groups due to the two possible C8-DT binding geometries: standing up and lying down (Fig. 8). Especially at small

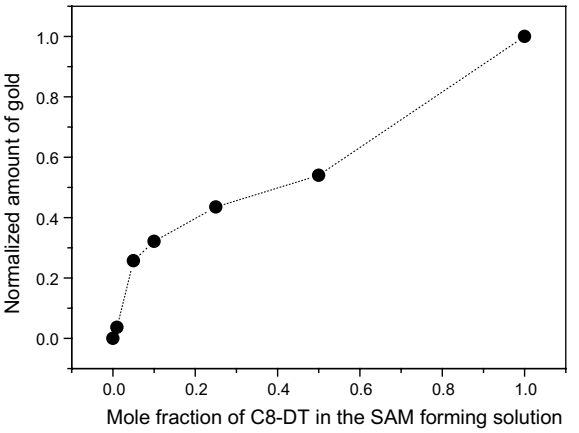

Fig. 11. Plot of the normalized amount of gold versus the percentage ratio of C8-DT in solution in a binary mixture of C8-T and C8-DT SAMs.

C8-DT concentrations the amount of surface bound C8-DT is over-proportionally high because of the double probability to find a binding position due to the two binding thiol groups. On the other hand,

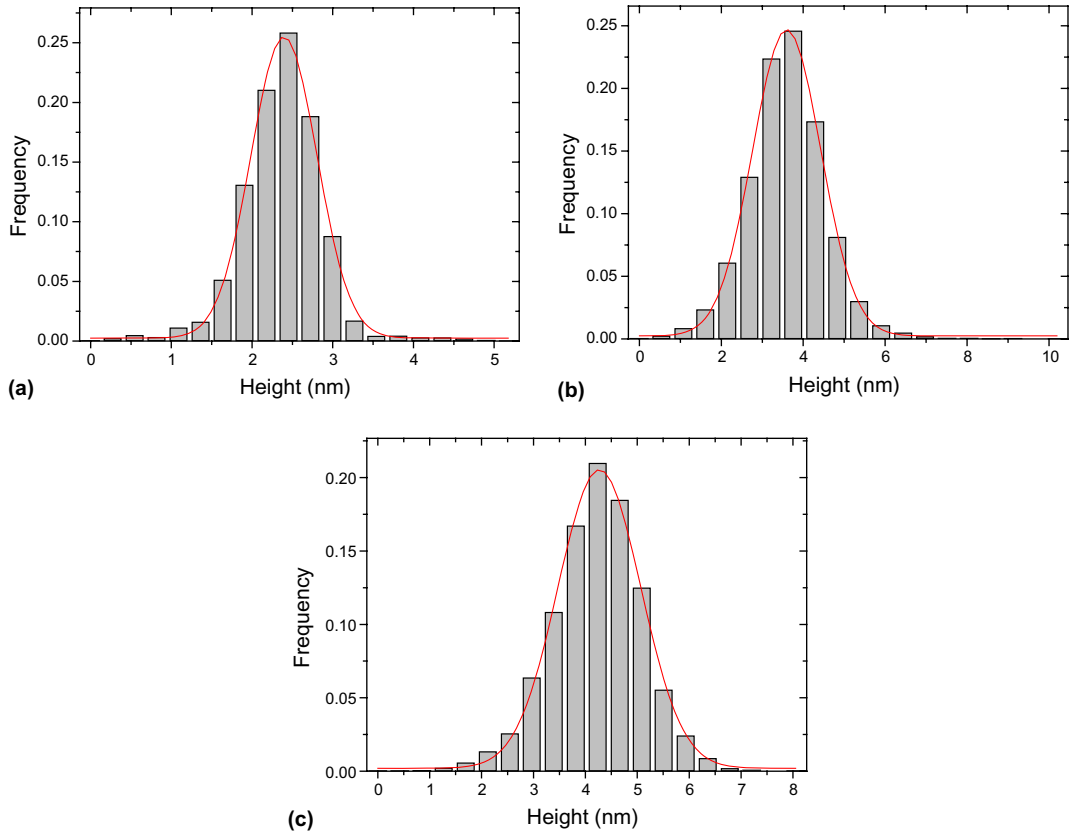

Fig. 10. Height histograms of gold nanoparticles grown on diluted C8-DT SAMs obtained from AFM images: (a) 10%, (b) 5% and (c) 1% C8-DT in the SAM.

as more C8-DT molecules are present the amount of flat lying, with both SH-groups bound to the gold, C8-DT molecules are enhanced and less SH-nucleation sites are present. Indeed it was found in the AFM images that the number of gold nanoparticles per unit area decreased with increasing C8-T content.

4. Conclusions

The combination of contact angle measurements, SD-ToF-MS and XPS yield a detailed picture of the formation and structure of C8-T/C8-DT mixed monolayers. Additional information deducted from by the growth behaviour of gold nanoparticles on pure and diluted C8-DT SAMs investigated by AFM, STM, and SD-ToF-MS gave valuable information to understand the templating action of mixed SAMs.

C8-DT shows a stronger affinity to the Au surface compared to C8-T. In order to have a $\chi_{SAM}^{C8\text{-}DT}$ of 0.5 in the mixed SAMs, a $\chi_{sol}^{C8\text{-}DT}$ of 0.005 (and thus a $\chi_{sol}^{C8\text{-}T}$ of 0.995) in solution is needed. For $\chi_{SAM}^{C8\text{-}DT}$ ranging from 0.2 to 1, a decrease in monothiol concentration results in a decrease in standing up structures of the dithiols. While for surface molar fractions of C8-DT ranging from 0 to 0.2, increasing dithiol concentration increases the amount of standing up structures of dithiol. The behaviour corresponding to $\chi_{SAM}^{C8\text{-}DT}$ of 0–0.2 displays the van der Waals interactions as the most dominant driving force in the overall self-assembly process driven by the high amount of C8-T in the mixture. In order to yield a diluted amount of –SH groups on the surface of the binary mixed SAMs and to avoid the lying down structures, it is best to explore C8-DT surface molar fraction between 0 and 0.2.

One hundred percent of C8-DT SAMs yield disc-like nanoparticles with an aspect ratio of 1:10. The flat lying domains here and in the high concentration C8-DT mixing regime seem not to play a role in the nanoparticle growth, because no SH-groups as nucleation sites are exposed. The gold nanoparticles show a higher average height and therefore a faster height growth with increasing C8-T dilution due to binding site competition. Also the number of gold nanoparticles per unit area decreases with increasing dilution.

The phase behaviour, or with other words, the lateral distribution of the two components of the binary mixture, was not studied here. A systematic study on a possible miscibility gap and the resulting domain structure needs to be done to gain more insight into the gold growth behaviour, especially the positioning of the nucleation sites.

Acknowledgements

The authors like to thank Wolfgang Knoll, Bo Liedberg and Roland Fischer for useful discussions in various aspects, and the Unité de Chimie des Interfaces (UCL) of the Université catholique de Louvain for access to the XPS facilities. A.-S.D. thanks the Belgian National Fund for Scientific Research for her Collaborateur Scientifique position and NATO for an Advanced Science Fellowship. S.M. and A.K.A.A. want to acknowledge the financial support from the BMBF (Germany) and its Center for Multifunctional Materials, the DFG (Germany), the Academic Development Fund of the University of Western Ontario. S.M. like to thank the Ontario Photonics Consortium, NSERC (Canada) and the CRC Program of the Canadian Government for financial support.

References

[1] (a) K.E. Drexler (Ed.), Nanosystems, Molecular Machinery, Manufacturing and Computation, Wiley, New York, 1992;
(b) F.L. Carter, A. Schultz, D. Duckworth, in: F.L. Carter (Ed.), Molecular Electronic Devices, Marcel Decker, New York, 1987, p. 183.
[2] (a) P. Ball, L. Garwin, Nature 355 (1992) 761;
(b) G.J. Ashwell (Ed.), Molecular Electronics, Wiley, New York, 1992.
[3] (a) I. Willner, E. Katz, B. Willner, in: H. Baltes, W. Göpel, J. Hesse (Eds.), Sensors Update, Vol. 5, Wiley, Weinheim, 1999, p. 45;
(b) W. Göpel, Biosens. Bioelectron. 13 (1998) 723.
[4] (a) X.Y. Zhang, L.D. Zhang, Y. Lei, L.X. Zhao, Y.Q. Mao, J. Mater. Chem. 11 (2001) 1732;
(b) S. Sun, C.B. Murray, D. Weller, L. Folks, A. Moser, Science 287 (2000) 1989;
(c) C.J. Kiely, J. Fink, M. Brust, D. Bethell, D.J. Schiffrin, Nature 396 (1998) 444;
(d) D.I. Gittins, D. Bethell, D.J. Schiffrin, R.J. Nichols, Nature 408 (2000) 67;
(e) R.G. Osifchin, R.P. Andres, J.I. Henderson, C.P. Kubiak, R.N. Dominey, Nanotechnology 7 (1996) 412;
(f) M.A. Hayat (Ed.), Colloidal Gold. Principles, Methods and Applications, Academic Press, 1989.
[5] (a) A.P. Alivisatos, Science 271 (1996) 933;
(b) A.P. Alivisatos, J. Phys. Chem. 100 (1996) 13226;
(c) D.L. Feldheim, C.D. Keating, Chem. Soc. Rev. 27 (1998) 1.
[6] (a) A.J. Haes, D.A. Stuart, S. Nie, R.P. Duyne, J. Fluorescence 14 (4) (2004) 355;
(b) K. Aslan, J. Zhang, J.R. Lakowicz, C.D. Geddes, J. Fluorescence 14 (4) (2004) 391;

(c) G.-J. Zhang, R. Möller, R. Kreyschmer, A. Csaki, W. Fritsche, J. Fluorescence 14 (4) (2004) 369;
(d) C. Mirkin, R.L. Letsinger, R.C. Mucic, J.J. Storhoff, Nature 382 (6592) (1996) 607;
(e) M.D. Malinsky, K.L. Kelly, G.C. Schatz, R.P. Van Duyne, J. Am. Chem. Soc. 123 (7) (2002) 1471.
[7] C. Sönnichsen, C.S. Geier, N.E. Hecker, G. Von Plessen, J. Feldmann, H. Ditlbacher, B. Lamprecht, J.R. Krenn, F.R. Aussenegg, V.Z.-H. Chan, J.P. Spartyz, M. Möller, Appl. Phys. Lett. 77 (19) (2000) 2949.
[8] (a) S. Chen, J. Phys. Chem. B 104 (2000) 663;
(b) S. Chen, J. Am. Chem. Soc. 122 (2000) 7420.
[9] R. Singhvi, A. Kumar, G.P. Lopez, G.N. Stephanopoulos, D.I.C. Wang, G.M. Whitesides, D.E. Ingber, Science 264 (1994) 696.
[10] M. Mrksich, L.E. Dike, J. Tien, D.E. Ingber, G.M. Whitesides, Exp. Cell. Res. 235 (1997) 305.
[11] E. Cooper, R. Wiggs, D.A. Hutt, L. Parker, G.J. Leggett, T.L. Parker, J. Mater. Chem. 7 (1997) 435.
[12] A. Kumar, H.A. Biebuyck, G.M. Whitesides, Langmuir 10 (1994) 1498.
[13] T.J. Gardner, C.D. Frisbie, M.S. Wrighton, J. Am. Chem. Soc. 117 (1995) 6927.
[14] R.G. Nuzzo, D.L. Allara, J. Am. Chem. Soc. 105 (1983) 4481.
[15] C.D. Bain, B.E. Troughton, Y.T. Tao, J. Evall, G.M. Whitesides, R.G. Nuzzo, J. Am. Chem. Soc. 111 (1989) 321.
[16] R.G. Nuzzo, F.A. Fusco, D.L. Allara, J. Am. Chem. Soc. 109 (1987) 2358.
[17] A. Ulman, Chem. Rev. 96 (1996) 1533.
[18] A. Ulman, Thin Films: Self-Assembled Monolayers of Thiols, Academic Press Inc., San Diego, CA, 1998.
[19] (a) R.P. Andres, T. Bein, M. Dorogi, S. Feng, J.I. Henderson, C.P. Kubiak, W. Mahoney, R.G. Osifchin, R. Reifenberger, Science 272 (1996) 1323;
(b) J.I. Henderson, S. Feng, G.M. Ferrence, T. Bein, C. Kubiak, Inorg. Chim. Acta 242 (1996) 115.
[20] M. Brust, D. Bethell, C.J. Kiely, D.J. Schiffrin, Langmuir 14 (1998) 5452.
[21] J. Käshammer, P. Wohlfart, J. Weiß, C. Winter, R. Fischer, S. Mittler-Neher, Opt. Mater. 9 (1998) 406.
[22] P. Wohlfart, J. Weiß, J. Käshammer, C. Winter, V. Scheumann, R. Fischer, S. Mittler-Neher, Thin Solid Films 340 (1999) 274.
[23] S. Busse, J. Käshammer, S. Krämer, S. Mittler, Sens. Actuators B 60 (1999) 148.
[24] T.Y.B. Leung, M.C. Gerstenberg, D.J. Lavrich, G. Scoles, Langmuir 16 (2000) 549.
[25] K. Kobayashi, J. Umemura, T. Horiuchi, H. Yamada, K. Matsushige, Jpn. J. Appl. Phys. 37 (1998) L297.
[26] P. Kohli, K.K. Taylor, J.J. Harris, G.J. Blanchard, J. Am. Chem. Soc. 120 (1998) 11962.
[27] K. Kobayashi, T. Horiuchi, H. Yamada, K. Matsushige, Thin Solid Films 331 (1998) 210.
[28] K. Kobayashi, H. Yamada, T. Horiuchi, K. Matsushige, Appl. Surf. Sci. 144–145 (1999) 435.
[29] H. Rieley, G.K. Kendall, F.W. Zemicael, T.L. Smith, S. Yang, Langmuir 14 (1998) 5147.
[30] C. Winter, U. Weckenmann, R.A. Fischer, J. Käshammer, V. Scheumann, S. Mittler, Chem. Vap. Deposition 6 (2000) 199.
[31] W. Deng, D. Fujita, L. Yang, H. Nejo, C. Bai, Jpn. J. Appl. Phys. 39 (2000) L751.
[32] T. Nakamura, H. Kondoh, M. Matsumoto, H. Nozoye, Langmuir 12 (1996) 5977.
[33] A.-S. Duwez, G. Pfister-Guillouzo, J. Delhalle, J. Riga, J. Phys. Chem. B 104 (2000) 9029.
[34] M.D. Porter, T.B. Bright, D.L. Allara, C.E.D. Chidsey, J. Am. Chem. Soc. 109 (1987) 3559.
[35] P. Fenter, P. Eisenberger, K.S. Liang, Phys. Rev. Lett. 70 (1993) 2447.
[36] J.N. Israelachvili, Intermolecular and Surface Forces, Academic Press, London, 1992.
[37] A.J. Pertsin, M. Grunze, Langmuir 10 (1994) 3668.
[38] G.M. Whitesides, P.E. Laibinis, Langmuir 6 (1990) 87.
[39] A.K.A. Aliganga, I. Lieberwirth, G. Glasser, A.-S. Duwez, Y. Sun, S. Mittler, Org. Electron, submitted.
[40] (a) H. Voit, C. Schoppmann, D. Brandl, Phys. Rev. B 48 (1993) 17517;
(b) S. Della Negra, C. Deprun, Y. Le Beyec, F. Röllgen, K. Standing, B. Monart, G. Bolbach, Int. J. Mass Spectrom. Ion Process. 75 (1987) 319;
(c) G. Nelles, M. Weisser, R. Back, P. Wohlfart, G. Wenz, S. Mittler-Neher, J. Am. Chem. Soc. 118 (21) (1996) 5039.
[41] M. Weisser, J. Käshammer, B. Menges, J. Matsumoto, F. Nakamura, K. Ijiro, M. Shimomura, S. Mittler, J. Am. Chem. Soc. 122 (2000) 87.
[42] A.-S. Duwez, C. Poleunis, P. Bertrand, B. Nysten, Langmuir 17 (2001) 6351.
[43] H. Schmidbaur, A. Shiotani, Chem. Ber. 104 (1971) 2821.
[44] S. Wu, Polymer Interface and Adhesion, Marcel Dekker Inc., New York, 1982.
[45] L.-H. Lee, Fundamentals of Adhesion, Plenum Press, New York, 1991.
[46] A.-S. Duwez, J. Electron Spectrosc. Relat. Phenom. 134 (2004) 97.
[47] C.D. Bain, H.A. Biebuyck, G.M. Whitesides, Langmuir 5 (1989) 723.
[48] R.G. Nuzzo, L.H. Dubois, D.L. Allara, J. Am. Chem. Soc. 112 (1990) 558.
[49] M.J. Tarlov, D.R.F. Burgess, G. Gillen, J. Am. Chem. Soc. 115 (1993) 5305.
[50] L. Sun, J.A. Gardella Jr., Langmuir 18 (2002) 9289.
[51] J.F. Watts, An Introduction to Surface Analysis by Electron Spectroscopy, Oxford University Press, New York, 1990.
[52] M.J. Hampden-Smith, T.T. Kodas, Chem. Vap. Deposition 1 (1995) 8.
[53] L. Ratke, P.W. Voorhees, Growth and Coarsening: Ostwald Ripening, Springer, Berlin, New York, 2002.

Available online at www.sciencedirect.com
ScienceDirect
Organic Electronics 7 (2006) 351–362
Organic Electronics
www.elsevier.com/locate/orgel

Synthesis and characterization of a new soluble conducting polymer and its electrochromic devices

Elif Sahin [a,b], Ertugrul Sahmetlioglu [a,c], Idris M. Akhmedov [a], Cihangir Tanyeli [a], Levent Toppare [a,*]

[a] Department of Chemistry, Middle East Technical University, 06531 Ankara, Turkey
[b] Department of Chemistry, Dicle University, 21280 Diyarbakir, Turkey
[c] Department of Chemistry, Nigde University, 51100 Nigde, Turkey

Received 21 January 2006; received in revised form 16 March 2006; accepted 3 April 2006
Available online 2 May 2006

Abstract

A new polythiophene derivative was synthesized by both chemical and electrochemical oxidative polymerization of 1-(perfluorophenyl)-2,5-di(2-thienyl)-1*H*-pyrrole (FPTPy). The structures of both the monomer and the soluble polymer were elucidated by nuclear magnetic resonance (^{1}H-NMR) and fourier transform infrared (FTIR). Polymer of FPTPy was also synthesized via potentiostatic electrochemical polymerization in acetonitrile (AN)/$NaClO_4$/$LiClO_4$ (0.1 M:0.1 M) solvent–electrolyte couple. Characterizations of the resulting insoluble polymer were performed by cyclic voltammetry (CV), FTIR, scanning electron microscopy (SEM) and UV–Vis Spectroscopy. Four-probe technique was used to measure the conductivities of the samples. Moreover, the spectroelectrochemical and electrochromic properties of the polymer film were investigated. In addition, dual type polymer electrochromic devices (ECDs) based on P(FPTPy) with poly(3,4-ethylenedioxythiophene) (PEDOT) were constructed. Spectroelectrochemistry, electrochromic switching and open circuit stability of the devices were studied. They were found to have good switching times, reasonable contrasts and optical memories.

PACS: 85.60.Pg

Keywords: Conducting polymers; UV–vis spectroscopy; Electrochemistry; Morphology

1. Introduction

Since the discovery of electrical conductivity in polyacetylene [1], the field of conducting polymers has aroused a great deal of interest among scientists both in industry and academia [2,3].

A great deal of attention was focused on conjugated polymers due to the broad range of applications for which they are potentially useful [2]. Photovoltaic devices [4], light emitting diodes [5], field effect transistors [6], electrochromic devices [7], and various types of sensors [8] based on conjugated polymers are under investigation by numerous researchers around the world. As such, the search for new functional and responsive conjugated polymers exhibiting electrochromism [9], photochromism [10], or non-linear

* Corresponding author. Tel.: +90 312 2103251; fax: +90 312 2101280.
E-mail address: toppare@metu.edu.tr (L. Toppare).

1566-1199/$ - see front matter © 2006 Elsevier B.V. All rights reserved.
doi:10.1016/j.orgel.2006.04.001

optics properties are especially sought after for such applications in display technology or data storage. A polymer that possesses a combination of several of these properties is especially an attractive target [11].

An electrochromic material is the one that changes color in a persistent but reversible manner by an electrochemical reaction and the phenomenon is called electrochromism. Electrochromism is reversible and visible change in transmittance and/or reflectance that is associated with an electrochemically induced oxidation–reduction reactions. It results from the generation of different visible region electronic absorption bands upon switching between redox states. The color change is commonly between a transparent (bleached) and a colored state or between two colored states. In case where more than two redox states are electrochemically available, the electrochromic material may exhibit several colors and may be termed as polyelectrochromic. This optical change is affected by a small electric current at low direct current potentials in the order of a fraction of a volt to a few volts [12].

An electrochromic device is a two-electrode electrochemical cell in a sandwich configuration of thin layers. The arrangement of these layers depends on the operation mode, which can be reflective or transmissive [13]. The reflective mode is used to display or to decrease the reflected light, for example, in a car rear-view mirror. In these devices, one of the electrical contacts should be covered with a reflective layer as a mirror. Transmissive mode operation is very similar, but all layers must become fully transparent when desired. For this reason, optically transparent electrodes must be used [14].

This study aims the synthesis of 1-(perfluorophenyl)-2,5-di(2-thienyl)-1*H*-pyrrole (FPTPy) via the reaction between 1,4-bis(2-thienyl)butane-1,4-dione and 2,3,4,5,6-pentafluoroaniline. The monomer was characterized via ^{1}H-NMR, FTIR. A new soluble conducting polymer was chemically synthesized and characterized. The spectroelectrochormic properties of electrochemically synthesized polymer were determined. Possibility of using the polymer as a p-type conducting material in an electrochromic device was investigated.

2. Experimental

2.1. Materials

$AlCl_3$ (Aldrich), succinyl chloride (Aldrich), dichloromethane (DCM) (Merck), *p*-toluene sulfonic acid (PTSA) (Sigma), 2,3,4,5,6-pentafluoroaniline (Aldrich), toluene (Sigma), nitromethane (Aldrich), methanol (Merck), ferric(III) chloride (Aldrich), acetonitrile (AN) (Merck), NaOH (Merck), $LiClO_4$ (Aldrich), $NaClO_4$ (Aldrich), propylene carbonate (PC) (Aldrich) and poly(methyl methacrylate) (PMMA) (Aldrich) were used without further purification. 3,4-ethylenedioxythiophene (EDOT) (Aldrich) were used as received.

2.2. Equipments

NMR spectrum of the monomer was recorded on a Bruker-Instrument-NMR Spectrometer (DPX-400) using $CDCl_3$ as the solvent. The FTIR spectrum was recorded on a Varian 1000 FTIR spectrometer. Mn for the soluble polymer was measured by gel permeation chromatography (GPC PL220). The surface morphologies of the polymer films were analyzed using JEOL JSM-6400 scanning electron microscope. Cyclic voltammograms were recorded in $NaClO_4$ (0.1 M) and $LiClO_4$ (0.1 M)/AN electrolyte-solvent couple with a system consisting of a potentiostat (Wenking POS 73), an X–Y recorder and a CV cell containing indium/tin oxide (ITO)-coated glass plate working and Pt counter electrodes, and a Ag/Ag^+ reference electrode. Measurements were carried out at room temperature under nitrogen atmosphere. VoltaLab-50 Potentiostat was used to supply constant potential during electrochemical synthesis. Varian Cary 5000 UV–Vis spectrophotometer was used in order to perform the spectroelectrochemical studies of the polymer and the characterization of the devices. Colorimetry measurements were done with Minolta CS-100 spectrophotometer.

2.3. Synthesis of 1-(perfluorophenyl)-2, 5-di (2-thienyl)-1H-pyrrole (FPTPy)

The starting material, 1,4-di (2-thienyl)-1,4-butanedione **1**, was synthesized according to literature procedure [15]. To a suspension of $AlCl_3$ (16 g, 0.12 mol) in CH_2Cl_2(15 mL), a solution of thiophene (9.6 mL, 0.12 mol) and succinyl chloride (5.5 mL, 0.05 mol) in CH_2Cl_2 were added dropwise. The mixture was stirred at 18–20 °C for 4 h. This was then poured into ice and concentrated HCl (5 mL) mixture. The dark green organic phase was washed with concentrated $NaHCO_3$ (3×25 mL), and dried over $MgSO_4$. After evaporation of the solvent, a blue green solid was remained which

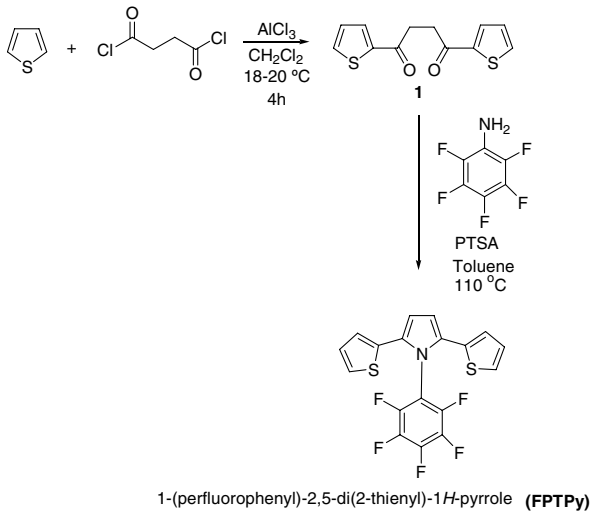

Scheme 1. The synthetic route of the monomer.

was suspended in ethanol. Filtration and washing with ethanol yielded 1, 4-bis(2-thienyl)butane-1,4-dione.

The monomer (FPTPy) was synthesized from 1,4-bis(2-thienyl)butane-1,4-dione and 2,3,4,5,6-pentafluoroaniline in the presence of catalytical amount of *p*-toluene sulphonic acid (PTSA) [16,17]. A round-bottomed flask equipped with an argon inlet and magnetic stirrer was charged with 1,4-bis(2-thienyl)butane-1,4-dione (5 mmol, 1.25 g), 1.28 g (7 mmol) 2,3,4,5,6-pentafluoroaniline, 0.1 g (0.58 mmol) PTSA and 20 mL of toluene were added. The resultant mixture was stirred and refluxed for 24 h under argon. Evaporation of the toluene, followed by flash column chromatography (SiO_2 column, elution with dichloromethane) afforded the desired compound as pale brown powder. The synthetic route of the monomer is shown in Scheme 1.

2.4. Chemical polymerization of (FPTPy) with iron (III) chloride

FPTPy (1×10^{-3} M) was dissolved in nitromethane (15 mL) and placed in a three-necked flask. Iron (III) chloride (2×10^{-3} M) is placed in 15 mL nitromethane. Monomer solution was added drop wise to the solution of iron (III) chloride at 0 °C. The reaction was carried out for 5 min. with constant stirring. The dark blue oxidized polymer was first washed with methanol, filtered, compensated with 30% NaOH, and dried under vacuum for ^{1}H-NMR analyses.

2.5. Cyclic voltammetry (CV)

The oxidation/reduction behavior of polymer was investigated by CV in $NaClO_4$ (0.1 M) and $LiClO_4$ (0.1 M)/AN solvent–electrolyte couple. Experiments were carried out in an electrolysis cell equipped with indium/tin oxide (ITO)-coated glass plates as the working, a Pt wire counter and Ag/Ag^+ reference electrodes. The measurements were carried out at room temperature under nitrogen atmosphere.

2.6. Electrochemical polymerization of FPTPy

Preparative electrochemical polymerization was performed by sweeping the potential between 0.0 V and +1.4 V with 500 mV/s scan rate. 50 mg FPTPy were dissolved in AN and $NaClO_4$ (0.1 M) and $LiClO_4$ (0.1 M) were used as the supporting electrolyte. Electrolyses were carried out using Pt working and counter electrodes and a Ag/Ag^+ reference electrode at room temperature for 1 h. The free standing films were washed with AN several times to remove unreacted monomer and the electrolyte. A similar method was used to synthesize the polymer on an ITO coated glass plate.

2.7. Preparation of the gel electrolyte

Gel electrolyte was prepared utilizing $NaClO_4$:$LiClO_4$:AN:PMMA:PC in the ratio of 1.5:1.5:70:7:20 by weight. After $NaClO_4/LiClO_4$ was dissolved in AN, PMMA was added into the solution. In order to dissolve PMMA, vigorous stirring and heating were required. Propylene carbonate (PC), as plasticizer, was introduced to the reaction medium when all the PMMA was completely dissolved. The mixture was stirred and heated until a highly conducting transparent gel was produced.

2.8. Construction of electrochromic devices

Poly (3,4-ethylenedioxythiophene) (PEDOT) was potentiostatically deposited on ITO working electrode by applying +1.5 V in $AN/NaClO_4/LiClO_4$ (0.1 M) solvent–electrolyte. P(FPTPy) was obtained by sweeping the potential between 0.0 V and +1.4 V versus Ag/Ag^+ in $AN/NaClO_4/LiClO_4$ (0.1 M:0.1 M). It is important to balance the charge capacities of the devices prior to assembling the devices. Otherwise, there would be incomplete electrochemical reaction and residual charges would remain during

the redox process [18]. Therefore, redox charges of the anodically and cathodically coloring polymers were matched by chronocoulometry. In order to obtain the complementary operating conditions, anodically coloring polymers were fully reduced and the cathodically coloring polymer was fully oxidized. By sandwiching the gel electrolyte between the anodically and the cathodically coloring polymers, the device was constructed.

3. Results and discussion

3.1. Synthesis

For the synthesis of 1,4-di(2-thienyl)-1,4-butanedione, the double Friedel–Crafts reactions propose by Merz and Ellinger [15] was chosen. However we found that the reaction time can be considerable reduced, the reaction mixture being refluxed at 18–20 °C for 4 h (instead of 24 h stirring at ambient temperature) without loss of yield (75%).

3.2. Cyclic voltammetry

Cyclic voltammogram of FPTPy in AN/$LiClO_4$–$NaClO_4$ solvent/electrolyte couple indicated an oxidation peak at 1.1 V and a reduction peak at 0.4 V. When the range between 0.0 V and +1.4 V (Fig. 1) was scanned, it was observed that the electroactivity increased with increasing scan number. This process promotes an electrochromic change on the polymer film to a yellow color, while a greenish cloud is formed around the electrode due to the partial dissolution of neutral oligomers of low molecular weight present in the reduced P(FPTPy). Under these conditions, the monomer yields a polymer which is subsequently oxidized at the same potential to produce polarons balanced with ClO_4^- counterions. Further reduction of this polymer at 0.4 V peak involves the neutralization of polarons with the loss of ClO_4^- and the resulting short linear species are dissolved [19].

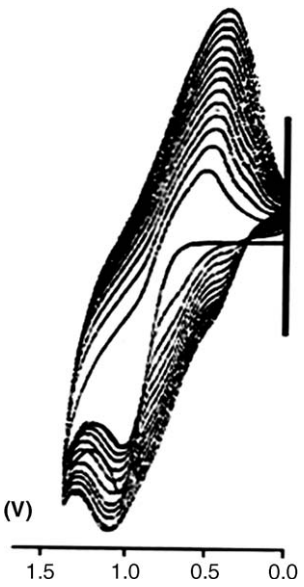

Fig. 1. Cyclic voltammogram of FPTPy.

3.3. NMR spectra of FPTPy and P(FPTPy)

^{1}H-NMR spectrum of monomer (Fig. 2(A)) reveals: (Pale yellow viscous product) $C_{18}H_8NF_5$, δ_H ($CDCl_3$): 6.63 (s, 2 H, pyrrolyl), 6.84 (d, 2H, $J = 3.34$ Hz, 3-thienyl), 6.96 (dd, 2H, $J = 4.61$ Hz, 3.34 Hz, 4-thienyl), 7.22 (d, 2H, $J = 4.61$ Hz, 5-thienyl).

^{1}H-NMR spectrum of polymer (Fig. 2(B)) ($CDCl_3$): 6.53–6.47 (2H, broad s, pyrrolyl), 6.86–6.75 (2H, d, 3-thienyl), 7.19–7.11 (2H, d, 4-thienyl).

GPC data revealed $Mn = 8.0 \times 10^3$ for P(FPTPy) prepared by chemical polymerization.

3.4. FTIR spectra

FTIR spectrum of the FPTPy shows the following absorption peaks: 3096 cm^{-1} (aromatic C–H stretching), 3020 cm^{-1} (C–H_α stretching of thiophene), 1515 cm^{-1} (C–F stretching of benzene), 1416–1261 cm^{-1} (aromatic C=C, C–N stretching due to pyrrole and benzene), 1073 cm^{-1} (aromatic C=C–F), 801 cm^{-1} (C–H_α out of plane bending of thiophene).

Most of the characteristic peaks of FPTPy remained unperturbed upon chemical polymerization. The intensity absorption bands of the monomer at 3020 cm^{-1} arising from C–H_α stretching of thiophene moiety, disappeared completely. This is an evidence of the polymerization from 2,5 positions of thiophene moiety of the monomer. Whereas, two new bands related to C–H_β out-of-plane bending of 2,5 disubstituted thiophene and C–S stretching appeared at 836 and 773 cm^{-1}, respectively. The broad band observed at around 1649 cm^{-1} proves the presence of polyconjugation

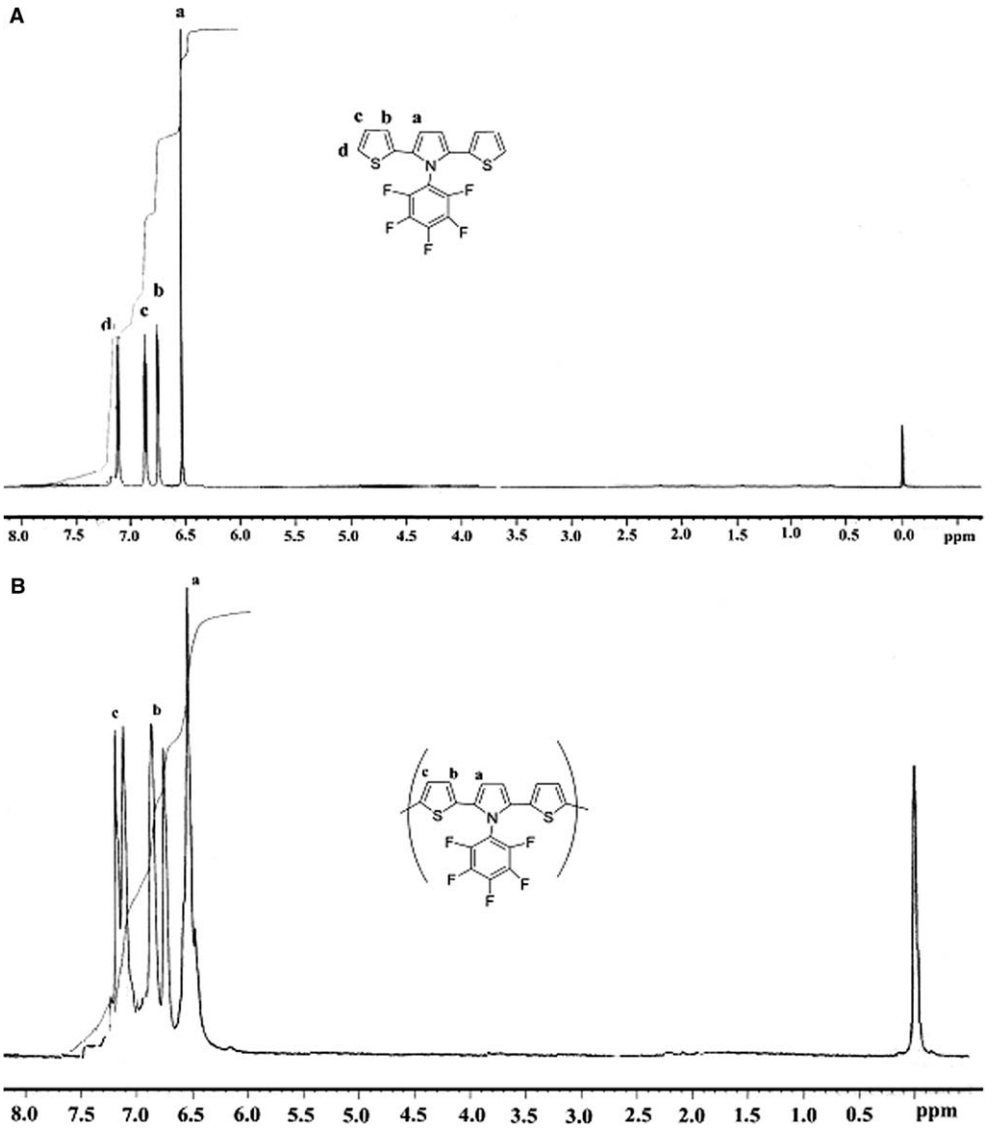

Fig. 2. ^{1}H-NMR spectra of monomer (A), polymer in $CDCl_3$(B).

and the new peak at 642 cm^{-1} indicates the presence of the dopant ion (Cl^-).

FTIR spectra of electrochemically synthesized P(FPTPy) showed the characteristic peaks of the monomer. The peaks related to C–H_α stretching of thiophene disappeared completely. The new broad band at around 1622 cm^{-1} was due to poly-conjugation. The strong absorption peak at 1129, 1052 cm^{-1} were attributed to the incorporation ClO_4^- ions into the polymer film during doping process. Results of the FTIR studies clearly indicated the polymerization of the monomer.

3.5. Conductivities of the films

The conductivities of electrochemically and chemically prepared P(FPTPy) were measured as 1.3×10^{-4} S/cm and 4.2×10^{-5} S/cm respectively via four probe technique.

3.6. Scanning electron microscopy (SEM)

Analysis of the surface morphologies of films was done using JEOL JSM-6400 scanning electron microscope. SEM micrograph of solution side of

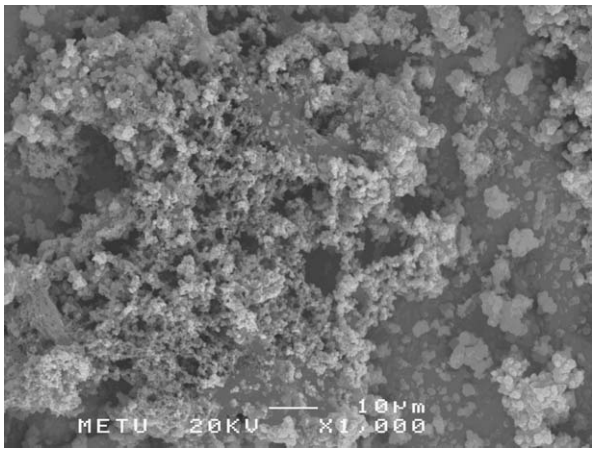

Fig. 3. SEM micrographs of P(FPTPy).

P(FPTPy) film showed droplet like structures (Fig. 3).

3.7. Electrochromic properties of the electrochemically synthesized conducting polymer

We investigated the in situ electrochemical polymerization of FPTPy by UV–Vis spectrophotometer via applying 1.4 V in AN/$LiClO_4$–$NaClO_4$ (0.1 M:0.1 M) at every 10 s time intervals (Fig. 4). There was a gradual increase in the peak intensity at around 760 and 850 nm for P(FPTPy) revealing the formation of the charge carriers.

The best way of examining the changes in optical properties of conducting polymers upon voltage change is spectroelectrochemistry. It also gives information about the electronic structure of the polymer such as its band gap (E_g) and the intergap states that appear upon doping. P(FPTPy) film was also potentiodynamically synthesized on ITO electrode in the presence of 50 mg FPTPy, while the potential was swept between 0.0 V and 1.4 V in AN/$NaClO_4$/$LiClO_4$. The spectroelectrochemical and electrochromic properties of the resultant polymer were studied by applying potentials ranging between 0.0 V and +1.1 V in monomer free AN/$NaClO_4$/$LiClO_4$ medium. At the neutral state λ_{max} value due to the π–π^* transition of the polymer was found to be 420 nm and E_g was calculated as 2.11 eV. Upon applied voltage, reduction in the intensity of the π–π^* transitions and formation of charge carrier bands were observed. Thus, appearance of peaks around 700 nm and 1000 nm are attributed to the evolution of polaron and bipolaron bands, respectively (Fig. 5).

The colors of the electrochromic materials were defined accurately by performing colorimetry measurements. CIE system was used as a quantitative

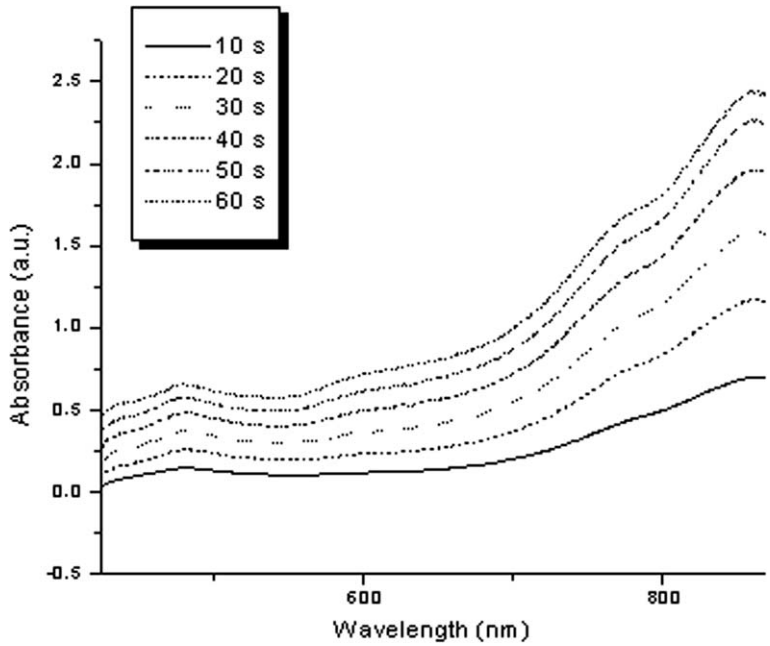

Fig. 4. In situ electrochemical polymerization of FPTPy.

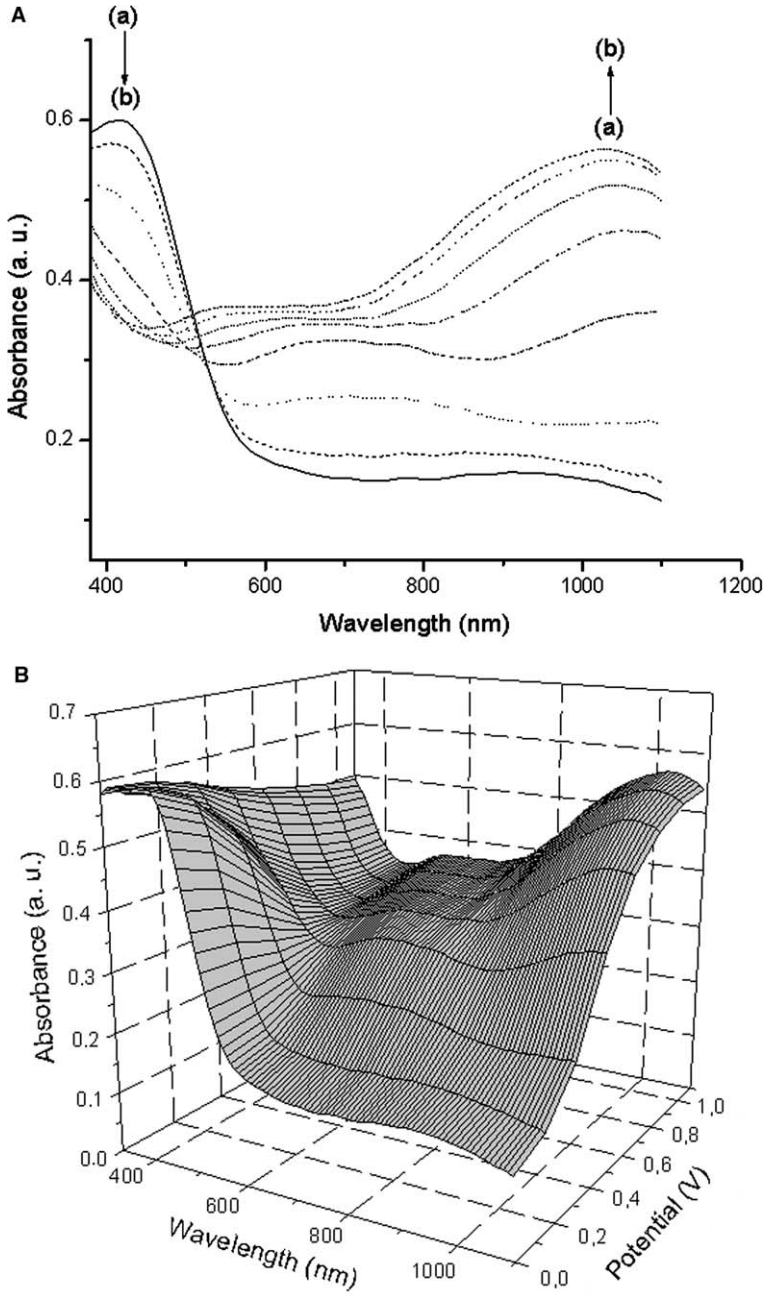

Fig. 5. Optoelectrochemical spectrum of (A) two dimensional representation of P(FPTPy) as applied potentials between 0.0 V and +1.1 V in AN/$NaClO_4$/$LiClO_4$ (0.1 M); (a) 0.0 V, (b) +0.5 V, (c) +0.6 V, (d) +0.7 V, (e) +0.8 V, (f) +0.9 V, (g) +1.0 V, (h) +1.1 V. (B) Three dimensional representation.

scale to define and compare colors. Three attributes of color; hue (a), saturation (b) and luminance (L) were measured and recorded. The P(FPTPy) film shows different colors in the fully reduced state (0.0 V), half oxidized state (0.9 V) and fully oxidized state (1.1 V) (Table 1).

3.8. Electrochromic switching

The polymers that can switch rapidly and exhibit striking color changes reveal superior results in electrochromic applications. The experiments carried out via spectroelectrochemistry proved the ability

Table 1
Colorimetric properties of polymer and device

Material	Color	*L*	*a*	*b*
P(FPTPy)	Yellow (0.0 V)	75	4	27
	Green (0.9 V)	75	−1	12
	Light purple (1.1 V)	67	−5	−5
P(FPTPy)/PEDOT	Brown (0.0 V)	70	1	28
	Blue (2.6 V)	49	−3	13

of P(FPTPy) to switch between its neutral and doped states with a change in transmittance at a fixed wavelength. Square wave potentials, as determined from the spectroelectrochemical experiments, were applied to the polymer. The polymer film was synthesized on ITO-coated glass slides. During the experiment, the % transmittance (%*T*) at 420 nm was measured using a UV–Vis spectrophotometer. Upon switching P(FPTPy) between 0.0 V and +1.1 V with a residence time of 5 s, optical contrast and the time needed to reach 95% of the total transmittance change for the homopolymer was measured. P(FPTPy) was found to have 18% optical contrast with a switching time of 1.3 s (Fig. 6).

3.9. Spectroelectrochemistry of Electrochromic Devices (ECDs)

A dual-type ECD consists of two electrochromic materials (one revealing anodic coloration, the other revealing cathodic coloration) deposited on transparent ITO, placed in a position to face each other and a gel electrolyte in between. In order to maintain a balanced number of redox sites for switching, the redox charges of the two complementary polymer films were matched by chronocoulometry. Before constructing the ECD, the anodically coloring polymer film, P(FPTPy), was fully reduced and the cathodically coloring polymer (PEDOT) was fully oxidized. Upon application of voltage, the doped polymer will be neutralized, whereas the other component will be oxidized, resulting in the color change. Colorimetry analyses of the ECDs were performed by using the same procedure as described. The luminance (L), hue (a) and saturation (b) values of the devices were measured and recorded in Table 1.

Spectroelectrochemistry experiments were performed to investigate the changes of the electronic transitions of the ECD by increasing the applied potential. Fig. 7 represents the absorption spectra of the ECD, recorded during application of different voltages between 0.0 V and +2.6 V. The polymer was in its neutral state at 0.0 V, where the absorption at 420 nm was due to π–π^* transition of the polymer. At this potential, PEDOT was in oxidized state showing no pronounced absorption at the UV–Vis region of the spectrum, thus the color of the device was yellow. As the applied potential

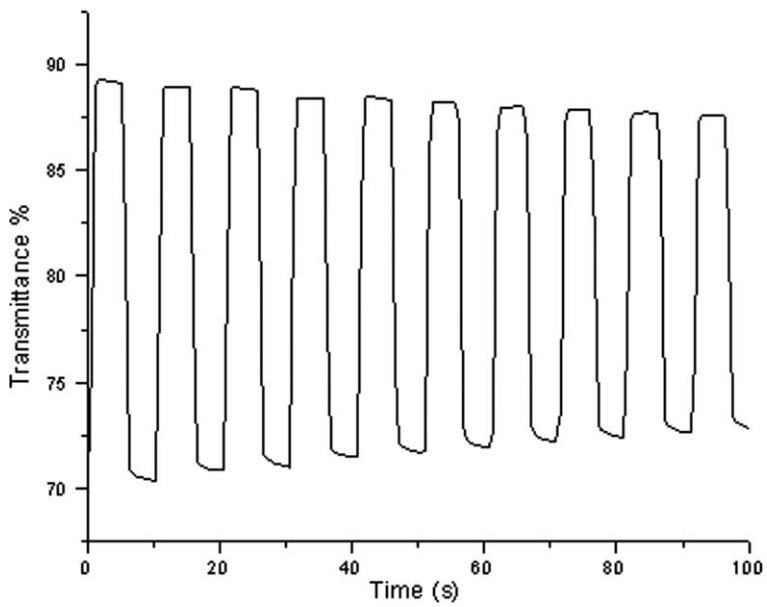

Fig. 6. Electrochromic switching, optical absorbance change monitored at 420 nm for P(FPTPy) between 0.0 V and 1.1 V in AN/$NaClO_4$/$LiClO_4$ (0.1 M:0.1 M).

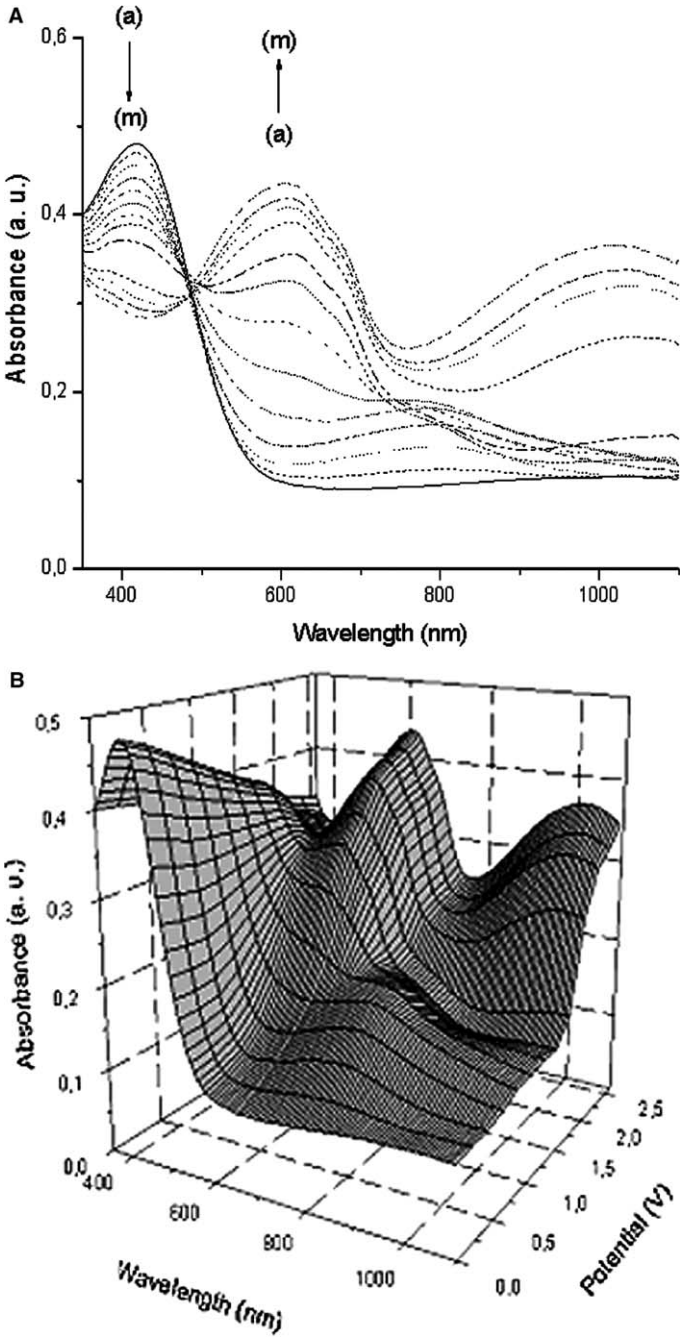

Fig. 7. Optoelectrochemical spectrum of (A) two dimensional representation of P(FPTPy)/PEDOT ECD at applied potentials between 0.0 V and +2.6 V; (a) 0.0 V, (b) +0.2 V, (c) +0.4 V, (d) +0.6 V, (e) +0.8 V, (f) +1.0 V, (g) +1.2 V, (h) +1.4 V, (i) +1.8 V, (j) +2.0 V, (k) +2.2 V, (l) +2.4 V, (m) +2.6 V. (B) Three dimensional representation.

increased the homopolymer layer started to get oxidized, and a decrease in the intensity of the absorption was observed. Meanwhile, PEDOT layer was in its reduced state, which was followed by the appearance of the new absorption at 607 nm, dominating the color of the device as blue.

3.10. Switching of ECDs

One of the most important characteristics of ECDs is the response time needed to perform switching between the two colored states. Another important parameter is the optical contrast, which

can be defined as the transmittance difference between the redox states [20]. Chronoabsorptometry, a square wave potential step method coupled with optical spectroscopy, was used to evaluate the response time of the device. The potential was set at an initial potential for a residence time of 5 s and than a second potential was applied for the same set period of time until being switched back to the initial potential again. Applied potentials were determined from the spectroelectrochemical studies, where the ultimate states of the devices were achieved. The experiment was carried out at 607 nm for P(FPTPy) /PEDOT device. The device was switched between 0.0 V and +2.6 V. The maximum transmittance difference between the oxidized and reduced states was measured as 29%. The time required to attain 95% of the total transmittance difference was found as 1.2 s for the device (Fig. 8).

3.11. Stability of ECDs

Redox stability is an important requirement for production of reliable electrochromic devices with long lifetimes. Main reasons for device failure are different applied voltages and environmental conditions. Cyclic voltammetry was employed by monitoring current alterations to visualize the long term stability of the ECD. The voltage was continuously swept between 0.0 V and +2.6 V with 500 mV/s scan rate. After 500 cycles, almost all initial electroactivity was maintained proving that ECD has reasonable environmental and redox stability (Fig. 9).

3.12. Open circuit memory of ECDs

The color persistence is an important feature since it is directly related to aspects involved in its utilization and energy consumption during use [21]. After setting the device in one of the colored state and removing the applied voltage, it should retain that color with no further current requirement. This is known as open circuit memory. To test this property a potential was applied for one second and the device was left under open circuit conditions for 100 s while monitoring the percent transmittance change at a fixed wavelength. The open circuit memory of P(FPTPy)/PEDOT device was tested at 0.0 V (yellow colored state) and +2.6 V (blue colored state) at 420 nm. As given in Fig. 10, P(FPTPy)/PEDOT device shows quite good optical memories both in oxidized (with only 5% transmittance change) and reduced states (with almost no transmittance change).

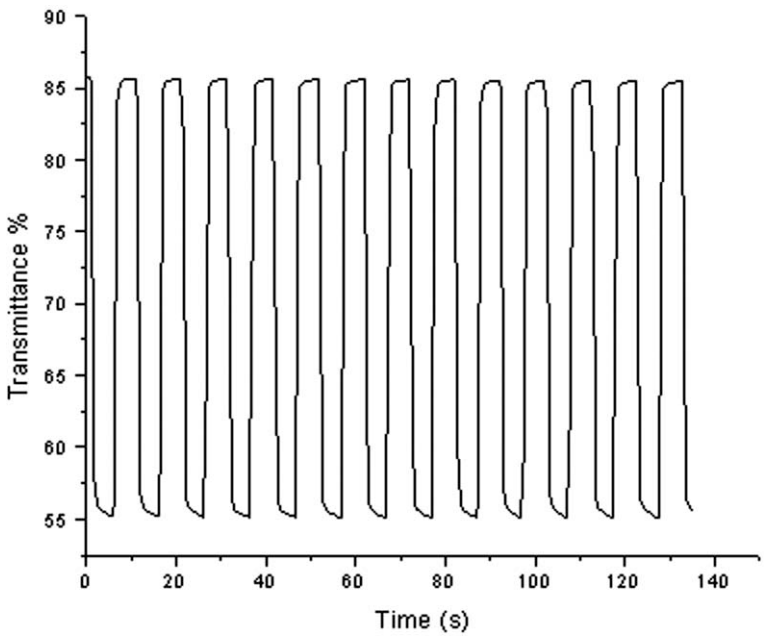

Fig. 8. Electrochromic switching, optical absorbance change monitored at 607 nm for device between 0.0 V and +2.6 V.

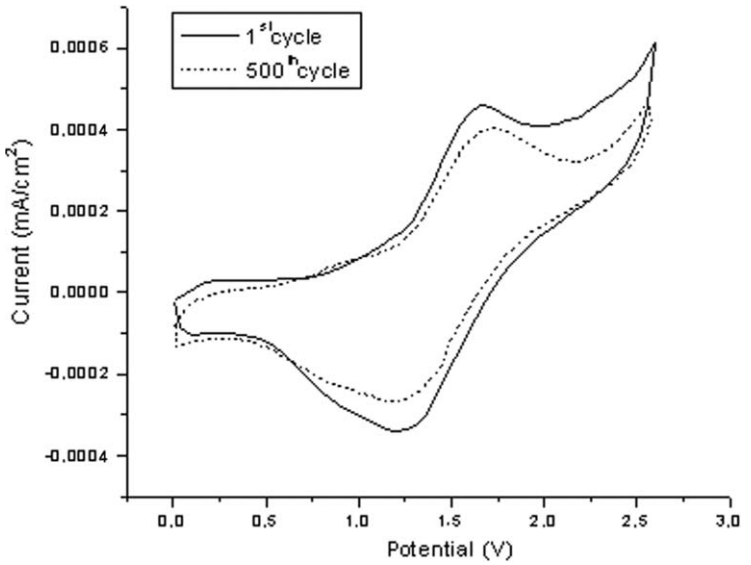

Fig. 9. Cyclic voltammogram of the device as a function of repeated scans 500 mV/s: after 1st cycle (plain), after 500th cycles (dash).

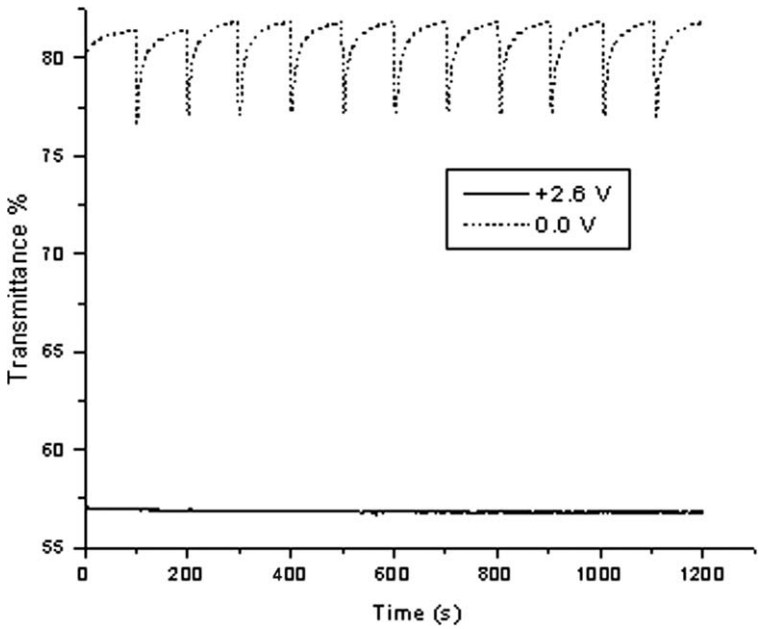

Fig. 10. Open circuit memory of P(FPTPy)/PEDOT ECD monitored at 420 nm, 0.0 V and +2.6 V potentials were applied for one second for each 100 s time interval.

4. Conclusions

The synthesis of a new monomer; 1-(perfluorophenyl)-2,5-di(2-thienyl)-1*H*-pyrrole FPTPy was successfully achieved. P(FPTPy) was synthesized by both chemical and electrochemical oxidative polymerizations. Chemically synthesized homopolymer of FPTPy is soluble in common organic solvents. This property provides several applications. The homopolymer of P(FPTPy) was also synthesized via potentiodynamically in AN/$NaClO_4$/$LiClO_4$ (0.1 M) solvent–electrolyte couple. Spectroelectrochemical analyses revealed that this polymer has an electronic band gap of 2.11 eV. The contrast

is measured as the difference between $\%T$ in the reduced and oxidized forms and is noted as $18\%T$ at 420 nm.

In the second part of the study, dual-type complementary colored polymer ECD made up of P(FPTPy)/PEDOT was constructed and its characteristics were examined. A potential range from 0.0 V to +2.6 V was found suitable for operating the device. The color changes were distinctive and aesthetically pleasing. Good switching time and optical contrast values were obtained. In addition, the device showed good environmental and redox stability. Considering these results, polymer of FPTPy is a feasible candidate for electrochromic layers in ECDs.

Acknowledgements

Authors gratefully thank to DPT-2005K120580, BAP2005-01-03-06 and TUBA grants.

References

[1] H. Shirakawa, E.J. Lewis, A.G. MacDiarmind, C.K. Chiang, A.J. Heeger, J. Chem. Soc., Chem.Commun. 16 (1977) 578.
[2] T.A. Skotheim, R.L. Elsenbaumer, J.R. Reynolds (Eds.), Handbook of Conducting Polymers, second ed., Marcel Dekker, New York, 1998.
[3] G. Sonmez, P. Schottland, J.R. Reynolds, Synt. Met. 155 (2005) 130.
[4] C.J. Brabec, N.S. Sariciftci, J.C. Hummelen, Adv. Funct. Mater. 11 (2001) 15.
[5] R.H. Friend, R.W. Gymer, A.B. Holmes, J.H. Burroughes, N. Marks, C. Taliani, D.D.C. Bradley, D.A. Dos Santos, J.L. Bredas, M. Logdlund, W.R. Salaneck, Nature 121 (1999) 397.
[6] N. Stutzmann, R.H. Friend, H. Sirringhaus, Science 299 (2003) 1881.
[7] A.A. Argun, A. Cirpan, J.R. Reynolds, Adv. Mater. 15 (2003) 1338.
[8] D.T. McQuade, A.E. Pullen, T.M. Swager, Chem. Rev. 100 (2000) 2537.
[9] A.A. Argun, P.-H. Aubert, B.C. Thompson, I. Schwendeman, C.L. Gaupp, J. Hwang, N.J. Pinto, D.B. Tanner, A.G. Mac-Diarmid, J.R. Reynolds, Chem. Mater. 23 (2004) 4401.
[10] M.J. Marsella, Z.-Q. Wang, R.H. Mitchell, Org. Lett. 2 (2000) 2979.
[11] B.C. Thompson, K.A. Abboun, J.R. Reynolds, K. Nakatani, P. Audedert, New J. Chem. 29 (2005) 1128.
[12] P.R. Somani, S. Radhakrishnan, Mater. Chem. Phy. 77 (2002) 117.
[13] W.A. Gazotti, A.F. Nogueira, E.M. Girotto, L. Micaroni, M. Martini, S. Neves, M.-A. De Paoli, In: H.S. Nalwa (Eds.), Handbook of Advanced Electronic and Photonic Materials and Devices, Academic Press, San Diego, 2001.
[14] M.D. Paoli, W.A. Gazotti, J. Braz, Chem. Soc. 13 (2002) 410.
[15] A. Merz, F. Ellinger, Synthesis 6 (1991) 462.
[16] G.G. McLeod, M.G.B. Mahboubian-Jones, R.A. Pethrick, S.D. Watson, N.D. Truong, J.C. Galin, J. Francois, Polymer 27 (1986) 455.
[17] P.E. Just, K.I. Chane-Ching, P.C. Lacaze, Tetrahedron 58 (2002) 3467.
[18] O. Turkarslan, A. Erden, E. Sahin, L. Toppare, J. Macr. Sci. Part:A Pure Appl. Chem. 43 (2005) 115.
[19] R.E. Niziurski-Mann, C. Scordilis-Kellev, T.L. Liu, M.P. Cava, R.T. Carlin, J. Am. Chem. Soc. 115 (1993) 887.
[20] E. Brillas, J. Carrasco, R. Oliver, F. Estrany, J. Vilar, J.M. Morlans, Electrochim. Acta 45 (2000) 4049.
[21] S.A. Sapp, G.A. Sotzing, J.R. Reynolds, Chem. Mater. 10 (1998) 2101.

Available online at www.sciencedirect.com
ScienceDirect
Organic Electronics 7 (2006) 363–368
Organic Electronics
www.elsevier.com/locate/orgel

Sensitization of thin-film-silicon by a phthalocyanine as strong organic absorber

C. Kelting [a], U. Weiler [b], T. Mayer [b], W. Jaegermann [b], S. Makarov [c], D. Wöhrle [c], O. Abdallah [d], M. Kunst [d], D. Schlettwein [a,*]

[a] *Institute of Applied Physics, Justus-Liebig-University Gießen, D-35390 Gießen, Germany*
[b] *Surface Science Department, Institute of Materials Science, Technical University Darmstadt, D-64287 Darmstadt, Germany*
[c] *Institute for Organic und Macromolecular Chemistry, University Bremen, D-28334 Bremen, Germany*
[d] *Department Solar Energy, Hahn-Meitner-Institute, D-14109 Berlin, Germany*

Received 9 January 2006; received in revised form 20 March 2006; accepted 3 April 2006
Available online 11 May 2006

Abstract

Interfaces of either microcrystalline Si (μc-Si) on the organic sensitizer phthalocyaninatozinc (PcZn) or of PcZn on amorphous Si (a-Si) were prepared to study the compatibility of the film growth of Si by chemical vapor deposition with the thermal and chemical stability of PcZn. The compatibility could be reached and, composite structures were prepared of a-Si with PcZn by simultaneous deposition. An electronic interaction of Si and PcZn was indicated by an observed fluorescence quenching in PcZn by subsequently deposited μc-Si. The photoconductivity of a-Si was increased by absorption of light either in subsequently or simultaneously deposited PcZn as seen in photoconductivity spectra. The sensitization of Si by PcZn was thereby proven. The conditions to utilize this effect for a further development of thin film photovoltaic devices are discussed.

PACS: 73.22.−f; 73.25.+i; 73.50.Pz; 73.61.−r

Keywords: Sensitization; Microcrystalline silicon; Amorphous silicon; Organic dye; Solar cell; Composite material

1. Introduction

To establish a sustainable energy cycle on national as well as international levels thin film photovoltaics will play a decisive role [1]. Aside from compound semiconductor thin film cells like those based on CdTe or on representatives of the Copper–Indium–Gallium–Sulphide–Selenide (chalkopyrite) family, cells based on Si thin films are one of the most promising candidates [2]. Si thin films are typically prepared by chemical vapor deposition (CVD) using a mixture of silane and hydrogen or by reactive sputtering [1–4]. Depending on the choice of preparation parameters, either amorphous silicon films (a-Si) or microcrystalline silicon films (μc-Si) are obtained. Because of a higher mobility of charge carriers, prolonged lifetime of minority charge carriers and hence a decreased recombination

* Corresponding author. Tel.: +49 641 99 33400; fax: +49 441 99 33409.
E-mail address: schlettwein@uni-giessen.de (D. Schlettwein).

1566-1199/$ - see front matter © 2006 Elsevier B.V. All rights reserved.
doi:10.1016/j.orgel.2006.04.003

probability, cells based on μc-Si generally have the higher potential to reach technically interesting conversion efficiencies [3,4]. The beneficial photophysical properties of crystalline Si directly dwell on the indirect character of the Si band-gap [5] which, however, leads to a rather weak optical absorbance of Si, in particular within the red part of the visible spectrum (Fig. 1). Therefore, a substantial film thickness of μc-Si in the cells is needed. This is in contradiction to the largest benefit of thin film photovoltaics, namely a decreased need of electrical film quality that directly leads to decreased process costs and, further, a minimized consumption of electrode material also lowering the costs of the technology.

Organic pigments or dye molecules, on the other hand, are designed to strongly absorb visible light (Fig. 1). Phthalocyanines are one of the technically most important group of such materials absorbing with molar extinction coefficients easily above 10^5 L mol^{-1} cm^{-1} [6] in the red part of the visible spectrum (Fig. 1). Considering the strength of this absorption, purely organic thin film photovoltaic junctions have also been studied extensively leading, however, to rather poor performance because of a limited mobility of charge carriers and rapid recombination [7]. Some of these problems can be overcome by the use of junctions with a maximized surface area and decreased average film thickness but reported efficiencies still lie well below 5% even for laboratory cells [8–11]. Another approach to utilize the strong absorption of organic dyes and, for example, (substituted) phthalocyanines consists in the sensitization of porous wide band-gap semiconductor electrodes like TiO_2 or ZnO [12,13]. In these photosensitization cells the organic absorber injects an electron from its excited state to the conduction band of the wide band-gap semiconductor and in turn has to be regenerated by a reaction with either a redox electrolyte or a hole–conductor penetrating to the pore system of the composite electrode. Cells with liquid electrolytes lead to acceptable efficiencies above 10% at, however, technical difficulties to ensure their stable operation. Cells with hole–conductors to avoid the stability problems still lead to considerably lower efficiency [14,15].

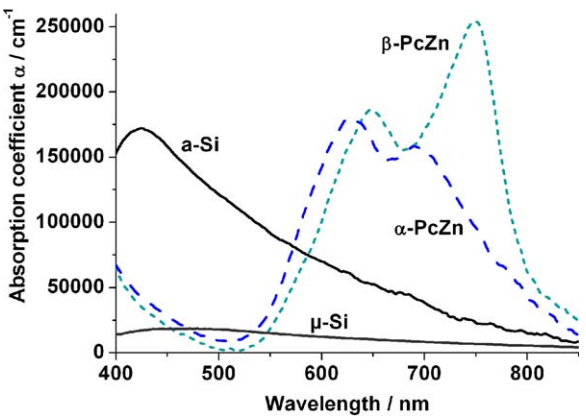

Fig. 1. Optical absorption coefficient α calculated from optical absorption spectra of 50 nm thick amorphous Si film (a-Si), 2 μm thick microcrystalline Si (μc-Si), 50 nm PcZn deposited at room temperature (α-PcZn) and 50 nm PcZn deposited at a substrate temperature of 250 °C (β-PcZn), all films deposited on glass.

In this paper, we report about a new approach to utilize a strongly absorbing organic dye as a sensitizer to enhance the optical absorbance of Si thin films. In this approach, we combine a material of optimized electrical properties (μc-Si) with a material of complementary optimized optical absorption (phthalocyanine). Phthalocyanines were deposited earlier on different crystalline orientations of either H-terminated [16,17] or native Si [18,19]. A rather strong interaction with the Si substrate was indicated by a high degree of order in the films [18] in some cases even leading to epitaxial relations of crystal growth [16,17]. Among the phthalocyanines, the zinc complex (PcZn) has shown to be one of the best sensitizer molecules because of a long lifetime of its molecular excited state [20]. For the interface of PcZn with Si a photovoltaic effect was already reported, speaking for electron transfer from the excited state of PcZn to Si [19]. Recently we have shown the feasibility of adjusting the deposition of μc-Si to the chemical and thermal stability limits of PcZn. Thereby we could show the preparation of the first such organic/Si composite materials [21]. In a previous paper, we have also shown that the energetic alignment of energy levels in a contact of PcZn with crystalline (wafer) Si should allow the injection of both types of charge carriers from the illuminated dye molecule to Si: excited electron from the Pc-LUMO to the Si conduction band, excited hole from the Pc-HOMO to the conduction band of Si [22]. As a composite, such a combination represents an optimized absorber material for thin film photovoltaics since it combines the best of the two specialists (Si and organic dye) without the need of a separate transport layer (electrolyte or hole–conductor in the injection cells with wide band-gap semiconductors). In this present paper, we will now present photoconduction measurements that clearly show sensitization of Si by PcZn and thereby proof the concept lined out above.

2. Experimental

PcZn was received from Aldrich and purified by zone sublimation at 10^{-6} mbar. PcZn was deposited by physical vapor deposition in a high vacuum chamber at a rate of around 1 nm min^{-1} from a resistively heated BN or Al_2O_3 crucible at 300 °C. The substrate was kept at room temperature for depositions on either glass or Si thin films (see below) and at 250 °C for the preparation of the composite materials. The amount of deposited PcZn as monitored by a quartz crystal microbalance is presented as an equivalent to an average film thickness, although closed films can barely be expected at the low coverage of this study. Silicon thin films were deposited either on top of PcZn or on glass slides by a hot wire CVD technique in a mixed atmosphere of silane and hydrogen in high vacuum chambers. For the preparation of the composite material, the hot wire to activate the Si precursors was placed in a remote position out of the PcZn beam to avoid thermal decomposition of PcZn. Details were reported elsewhere [21]. The thickness of the Si and composite films was determined by a surface profiler (Tencor Industries Alpha-Step). For the photoconductivity experiments, silver electrodes (100 nm thickness) with a gap of 50 μm × 10 mm were Ar^+-RF-sputtered (Leybold Z 400, 10^{-3} mbar, 1500 V) on top of Si to contact the samples. For the films of pure Si, the photoconduction of the pure film was used as a reference before 10 nm PcZn was deposited. The photoconductivity measurements were made in air with a Keithley 6517 electrometer at 10 V bias under illumination with a water-filtered beam of an Oriel 1000 W xenon arc lamp at 100 mW cm^{-2} and using interference filters (LOT Oriel; FWHM 10 nm). All reported photoconductivity values are steady state values. Optical absorption spectra were obtained with a Tec5 Evaluation line diode array spectrometer. The Raman experiments were performed in a Dilor confocal spectrometer using the 633 nm line of a Helium–Neon-laser.

3. Results and discussion

For the preparation of a composite material consisting of microcrystalline Si (μc-Si) with embedded molecular clusters of phthalocyaninatozinc (PcZn) the compatibility of the chemical vapor deposition (CVD) of μc-Si and the physical vapor deposition (PVD) of PcZn had to be ensured. Since the crystallinity of Si thin films generally can be increased easily at higher substrate temperatures, the upper limit of the thermal stability of solid PcZn thin films was investigated. Films of PcZn were deposited on Si wafers at room temperature and at elevated temperatures. Films could only be grown at a reasonable growth rate up to about 250 °C substrate temperature. The films were monitored by optical reflection spectra. At room temperature, PcZn crystallized in its α-crystalline structure (Fig. 1) [23]. At 250 °C, PcZn crystallized in the high-temperature β-phase (Fig. 1) [23]. These films were left in vacuum and changes in the reflection spectra were monitored in situ under increasing substrate temperatures. PcZn was stable up to 300 °C. Even at this temperature only slow evaporation at a rate of about 10 nm h^{-1} was observed. This temperature can therefore serve as an upper limit of substrate temperatures during preparation of Si on PcZn in bilayer test devices (see below). For the preparation of composites of PcZn with Si, however, 250 °C is the upper limit because of a lower sticking probability of individual molecules and rather slow crystallization kinetics.

To analyze the chemical integrity of PcZn under the conditions of the CVD process, about 1 μm Si was prepared at a substrate temperature of 200 °C on top of an equivalent of 100 nm PcZn that was PVD-deposited on glass in a prior step. Raman spectra were used to analyze both, the chemical structure of PcZn and the crystalline character of the Si film. The results are summarized in Fig. 2. The crystallinity of the deposited Si film was shown by the clear Raman line at 520 cm^{-1} [24] for the Si film deposited on glass as well as for Si deposited on top of PcZn. On the other hand, the Raman lines characteristic for PcZn [25] were detected for the film as deposited, for the one that was present during Si deposition but not covered with Si and also for the film with Si deposited on top of it. So it is concluded that the chemical structure of PcZn was not altered by the CVD process and that μc-Si could be deposited also on top of PcZn, both fundamental prerequisites for the preparation of a composite material of the two constituents. Further, the Raman experiments indicated electrical interaction of PcZn and μc-Si. The increase in the Raman spectra towards higher wavenumbers is caused by a strong fluorescence background of the PcZn [25]. This is observed for pure PcZn before and after the CVD conditions, but not for the one with μc-Si deposited on top of it (see arrow in Fig. 2), a quite

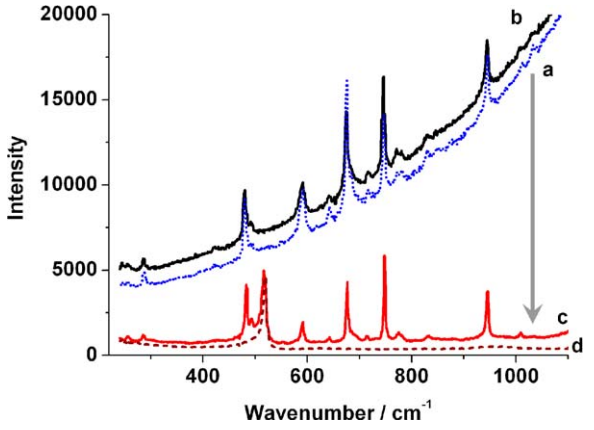

Fig. 2. Raman spectra of a 100 nm thick PcZn film on glass (a), the same film following the conditions of Si-CVD but without deposited Si (b), for Si on top of PcZn (c) and for pure Si deposited next to the PcZn film onto bare glass (d), layer thickness of Si about 1 μm. Fluorescence quenching of PcZn (see text) is indicated by the arrow.

positive hint towards the desired sensitization of μc-Si by PcZn. Light absorption in solid PcZn leads to the formation of a singlet exciton [26]. To allow charge transfer to an adjacent film, the exciton has to reach this interface by diffusion. In evaporated thin films of PcZn a diffusion length of (30 ± 10) nm was reported [26]. The quenching of luminescence of PcZn films with an average film thickness of 100 nm (Fig. 2) speaks for a similar diffusion length in these films, considering possible inhomogeneities in film growth.

The sensitization of silicon by PcZn was directly measured in photoconduction experiments starting with a pure a-Si thin film and observed following deposition of α-PcZn. To ensure sufficient exciton diffusion and to avoid the formation of a closed PcZn film [27] an equivalent of 10 nm average film thickness of PcZn was deposited. Fig. 3a shows the spectral dependence of the photoconduction in the visible range. The strong contribution of photons absorbed in Si was detected in the broad band centered around 500 nm, dominating the photoresponse. Photons absorbed in PcZn also contributed to the observed photoconductivity as detected as a shoulder on the long wavelength part of the band between 600 and 700 nm proving the sensitization of Si by PcZn. A direct comparison of the photocurrents measured at the PcZn-sensitized film with the same Si film prior to PcZn deposition is presented in Fig. 3b for selected wavelengths. 500 nm was chosen as a wavelength at which PcZn showed only minor absorption and Si still absorbed at reasonable intensity (Fig. 1). Here the deposition of PcZn only resulted in a subtle decrease of the observed photocurrent, probably caused by additional scattering of light or by defect states introduced by the interaction with PcZn. At the wavelengths of 600, 620 or 700 nm, however, at which the PcZn showed intense optical absorption (Fig. 1), the observed photocurrent was increased significantly. Since the dark current was observed at a constant level of 0.1 nA throughout the experiments, the observations clearly demonstrate sensitization of the Si film by

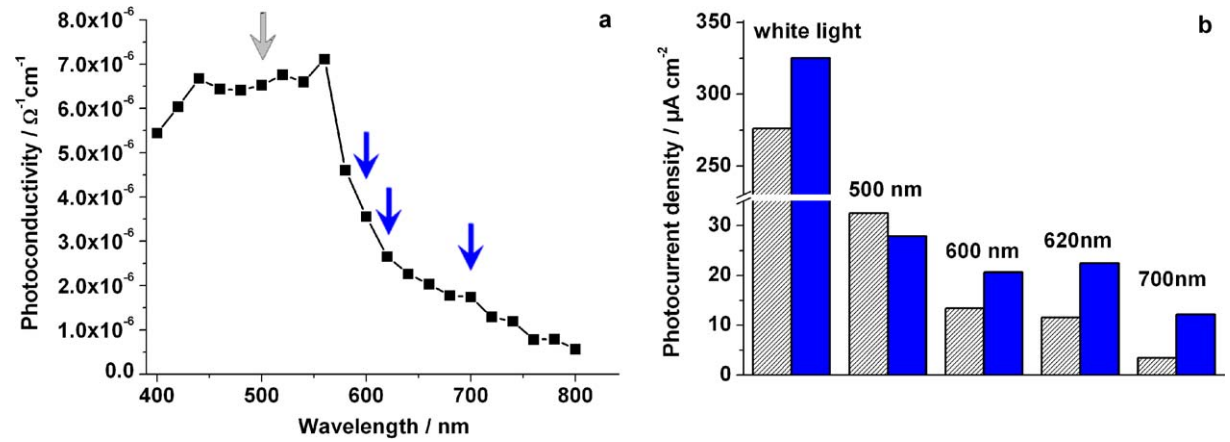

Fig. 3. (a) Spectral dependence of the photoconductivity normalized to a photon flux of 10^{15} photons cm^{-2} s^{-1} observed at a 120 nm thick film of a-Si following room-temperature deposition of α-PcZn (equivalent amount of 10 nm thickness) measured at 2000 V cm^{-1}; (b) Comparison of the photocurrent density at 2000 V cm^{-1} observed under white light and at selected wavelengths (indicated by arrows in part a) for a pure 120 nm a-Si film (hatched columns) and the same covered with an equivalent amount of 10 nm α-PcZn (solid columns).

the deposited PcZn. The effects were accumulated to an increase of the photoconduction of about 15% under white light illumination, a remarkable value considering the small interfacial contact area of PcZn with the smooth Si films.

Composite films of Si and PcZn were prepared by simultaneous PVD of PcZn during CVD of Si at around 250 °C substrate temperature with a remote position of the hot wire to prevent thermal decomposition of PcZn. Under these conditions, amorphous rather than microcrystalline Si was formed [21]. Fig. 4a shows an optical absorption spectrum of such a composite film. The contribution of both constituents was clearly detected when compared to Fig. 1. By the absorption band at 760 nm it was shown that PcZn clusters of the β-structure were formed under these preparation conditions, as also seen for PcZn deposition on heated substrates (Fig. 1) [23]. From the optical data, an approximate content of 90% Si and 10% PcZn can be estimated.

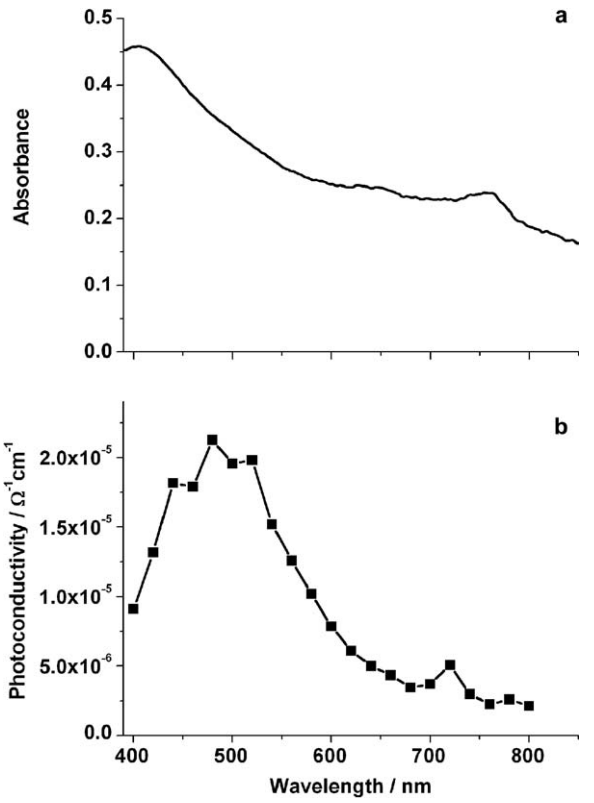

Fig. 4. (a) Optical absorption spectrum of a 170 nm thick composite Si–PcZn film prepared at 250 °C substrate temperature consisting of a-Si and β-PcZn (see text); (b) Photoconductivity spectrum measured for a film prepared under the same conditions as in (a) measured at 2000 V cm^{-1}.

Also in the photoconduction data at such composite films, the sensitization by PcZn was observed by a contribution in the PcZn absorption region around 700 nm (Fig. 4b), although again absorption in Si characterized by the broad band around 500 nm clearly dominated the spectrum. This contribution within the overall photocurrent spectrum approximately equals the contribution of the PcZn absorption to the absorption spectrum, indicating a similar quantum efficiency for both, photons absorbed in Si and photons absorbed in PcZn. This can be considered a great success since the photoconductivity quantum efficiency for pure Si thin films often approaches unity. We are presently working on a further quantification of this efficiency.

4. Conclusions and outlook

A composite material of a-Si and β-PcZn was prepared and sensitization of Si by PcZn was shown by photoconductivity measurements. The sensitization reaction was also detected in smooth interfaces of either a-Si or μc-Si with α-PcZn, either directly in PcZn-sensitized photoconductivity or, indirectly, by fluorescence quenching of PcZn by deposited Si. Since sensitization was observed in a steady state it is concluded that both types of charge carriers, electrons from the sensitizer LUMO and holes from the sensitizer HOMO have been successfully transferred to the conduction band and valence band of Si, respectively. These results are consistent with the reported relative positions of the energy levels of PcZn/Si [22] and the reported exciton diffusion length [26] in PcZn. The concept of a Si material sensitized by strongly absorbing organic dye molecules has thereby been proven and we are now heading towards the next step of a photovoltaic test device.

Acknowledgement

Financial support by the Volkswagen foundation (I/78203, I/78204, I/78205, I/78206 and I/80315) is gratefully acknowledged.

References

[1] J. Yang, A. Banerjee, S. Guha, Sol. Energ. Mat. Sol. C. 78 (2003) 597.
[2] H.W. Schock, Appl. Surf. Sci. 92 (1996) 606.
[3] B. Rech B, T. Roschek, T. Repmann, J. Muller, R. Schmitz, W. Appenzeller, Thin Solid Films 427 (2003) 157.
[4] R.E.I. Schropp, Thin Solid Films 451–452 (2004) 455.

[5] K.F. Brennan, The Physics of Semiconductors, Cambridge University Press, 1999.
[6] E.A. Lukyanets (Ed.), Electronic Spectra of Phthalocyanines and Related Compounds (in Russian), NIITEHIM, Cherkassy, 1989.
[7] D. Wöhrle, D. Meissner, Adv. Mater. 3 (1991) 129.
[8] B. Maennig, J. Drechsel, D. Gebeyehu, P. Simon, F. Kozlowski, A. Werner, F. Li, S. Grundmann, S. Sonntag, M. Koch, K. Leo, M. Pfeiffer, H. Hoppe, D. Meissner, N.S. Sariciftci, I. Riedel, V. Dyakonov, J. Parisi, Appl. Phys. A-Mater. 79 (2004) 1.
[9] C.J. Brabec, N.S. Sariciftci, J.C. Hummelen, Adv. Funct. Mater. 11 (2001) 15.
[10] L. Schmidt-Mende, A. Fechtenkotter, K. Müllen, R.H. Friend, J.D. MacKenzie, Physica E 14 (2002) 263.
[11] P. Peumans, S. Uchida, S.R. Forrest, Nature 425 (2003) 158.
[12] M.K. Nazeeruddin, R. Humphry-Baker, M. Grätzel, D. Wöhrle, G. Schnurpfeil, G. Schneider, A. Hirth, N. Trombach, J. Porphyr. Phthalocya. 3 (1999) 230.
[13] T. Yoshida, M. Iwaya, H. Ando, T. Oekermann, K. Nonomura, D. Schlettwein, D. Wöhrle, H. Minoura, Chem. Commun. (2004) 400.
[14] M. Grätzel, MRS Bull. 30 (2005) 23.
[15] L. Schmidt-Mende, U. Bach, R. Humphry-Baker, T. Horiuchi, H. Miura, S. Ito, S. Uchida, M. Grätzel, Adv. Mater. 17 (2005) 813.
[16] T. Kawaguchi, H. Tada, A. Koma, J. Appl. Phys. 75 (1994) 1486.
[17] M. Nakamura, T. Matsunobe, H. Tokumoto, J. Appl. Phys. 89 (2001) 7860.
[18] R. Hiesgen, M. Räbisch, H. Böttcher, D. Meissner, Sol. Energ. Mat. Sol. C. 61 (2000) 73.
[19] M.M. El-Nahass, H.M. Zeyada, M.S. Aziz, N.A. El-Ghamaz, Solid State Electron. 49 (2005) 1314.
[20] J.R. Darwent, P. Douglas, A. Harriman, G. Porter, M.-C. Richoux, Coordin. Chem. Rev. 44 (1982) 83.
[21] U. Weiler, K. Schwanitz, T. Mayer, W. Jaegermann, C Kelting, D. Schlettwein, D. Wöhrle, Thin Solid Films, in press.
[22] U. Weiler, T. Mayer, W. Jaegermann, C. Kelting, D. Schlettwein, S. Makarov, D. Wöhrle, J. Phys. Chem. B 108 (2004) 19398.
[23] J. Simon, J.-J. Andre, Molecular Semiconductors, Springer, Berlin, 1985.
[24] J.H. Parker Jr., D.W. Feldman, M. Ashkin, Phys. Rev. 155 (1967) 712.
[25] D.R. Tackley, G. Dent, W.E. Smith, Phys. Chem. Chem. Phys. 3 (2001) 1419.
[26] H.R. Kerp, H. Donker, R.B.M. Koehorst, T.J. Schaafsma, E.E. van Faassen, Chem. Phys. Lett. 298 (1998) 302.
[27] A.K. Hassan, R.D. Gould, Phys. Stat. Sol. (a) 132 (1992) 91.

Available online at www.sciencedirect.com
ScienceDirect
Organic Electronics 7 (2006) 369–374
Organic Electronics
www.elsevier.com/locate/orgel

Organic heterojunction with reverse rectifying characteristics and its application in field-effect transistors

Haibo Wang, Jun Wang, Haichao Huang, Xuanjun Yan, Donghang Yan *

State Key Laboratory of Polymer Physics and Chemistry, Changchun Institute of Applied Chemistry, Chinese Academy of Sciences, Graduate School of Chinese Academy of Sciences, Changchun 130022, PR China

Received 24 November 2005; received in revised form 12 March 2006; accepted 17 April 2006
Available online 11 May 2006

Abstract

A diode with a reverse rectifying characteristics was fabricated based on the organic heterojunction of copper phthalocyanine (CuPc) and copper-hexadecafluoro-phthalocyanine (F_{16}CuPc). At the heterojunction interface, HOMO of CuPc is bended upwards and LUMO of F_{16}CuPc is bended downwards, since the charge carriers were accumulated at both side of the interface, electrons in F_{16}CuPc and holes in CuPc. The thickness of holes accumulated at the CuPc layer is about 10 nm, which was determined by fabricating organic field-effect transistors with active layers in series of thickness. By utilizing the heterojunction-effect, the threshold voltage in organic transistors can be modified.

PACS: 73.40.Lq; 73.61.Ph; 85.30.Kk; 85.30.Tv

Keywords: Organic heterojunction; Phthalocyanine; Interfacial electronic structure; Field-effect transistors; Threshold voltage

1. Introduction

Organic electronics has been focused on developing low-cost, flexible, and large-area consumptive productions in recent decades [1,2]. The organic heterojunction has been an important component in organic electronic devices, such as organic photovoltaic (PV) cells [3–5], organic light-emitting diodes (OLEDs) [6], and organic field-effect transistors [7–14]. The utilizing of organic heterojunction has significantly improved the device performance or implemented some new function. However, the understanding of the property of organic heterojunction is still an emerging issue. In our previous work, it was realized that free charge carriers exist at both sides of the heterojunction interface between p-type copper phthalocyanine (CuPc) [15,16] and n-type copper-hexadecafluoro-phthalocyanine (F_{16}CuPc) [17], which induces an effective transport channel for ambipolar organic field-effect transistors (OFETs) and normally-on OFETs [18,19]. In this paper, we fabricated the diode with CuPc and F_{16}CuPc, which showed the reverse rectifying characteristics. The interfacial electric structure was revealed by the experiment results. The thickness of the charge accumulation at both sides of the hetero-

* Corresponding author. Tel.: +86 431 5262165; fax: +86 431 5262266.
E-mail address: yandh@ciac.jl.cn (D. Yan).

1566-1199/$ - see front matter © 2006 Elsevier B.V. All rights reserved.
doi:10.1016/j.orgel.2006.04.004

junction interface, an important feature of organic heterojunction, was also determined by way of varying the thickness of the active layer in OFETs.

2. Experiment

Diodes were fabricated on glass substrate, which were previously coated with indium tin oxide (ITO, as anode). The CuPc and F_{16}CuPc samples were purchased from Aldrich Company (USA), and purified two times by thermal gradient sublimation prior to processing. Then, the purified CuPc and F_{16}CuPc were deposited on the ITO anode in vacuum of 10^{-4}–10^{-5} Pa at a rate of about 1 nm/min. The substrate temperatures were kept at 200 °C during deposition. Au was thermally evaporated with a mask shadow on the F_{16}CuPc layer as cathode. Schematic structure of the diode with a heterojunction of CuPc and F_{16}CuPc is shown in Fig. 1(a). The current–voltage measurement was performed with a Keithley 236 source-measurement unit under ambient conditions at room temperature.

Schematic diagram of heterojunction OFETs with a sandwich configuration is shown in Fig. 1(b). A highly n-doped silicon wafer was used as the gate electrode and the substrate. A 150 nm thermally oxidation SiO_2 layer was adopted as the gate insulator. An F_{16}CuPc and a CuPc layers were, respectively, deposited on the insulator SiO_2 with the substrate held at 200 °C. Details on deposition process and current–voltage characteristics measurement can be found in Ref. [18]. For comparison, the transistors based on only single layer F_{16}CuPc as the active layer were also fabricated.

The X-ray diffraction patterns of organic thin films were recorded using a Rigaku D/max 2500 PC X-ray diffractometer with a Cu Kα source ($\lambda = 1.54056$ Å).

3. Results and discussion

3.1. X-ray diffraction spectra of organic thin films

X-ray diffraction (XRD) pattern of CuPc, F_{16}CuPc and CuPc/F_{16}CuPc thin films are shown in the Fig. 2. For CuPc and F_{16}CuPc thin films, a sharp diffraction peak at $2\theta = 6.78$ and 5.92, corresponding to d_{200} spacing of 13.02 and 14.92 Å, is observed, respectively. These results indicated that the CuPc and F_{16}CuPc thin film is highly ordered with the metastable α-phase, and the molecular arrangement is the herringbone pattern parallel to the substrate [15–17]. For the double layer of CuPc/F_{16}CuPc thin film, two sharp peaks at $2\theta = 6.66$ and 6.04 have a slight deviation from the CuPc and F_{16}CuPc single layers. It possibly originates from the interaction between CuPc and F_{16}CuPc interface [14]. The results also indicated the CuPc/F_{16}CuPc heterojunction thin film still was high crystalline.

3.2. CuPc/F_{16}CuPc heterojunction diode

The typical current–voltage curve of a diode with 180 nm CuPc and 140 nm F_{16}CuPc is shown in Fig. 3. It can be seen that a reverse rectifying characteristic was observed. Because the interfaces of ITO/CuPc and F_{16}CuPc/Au had a good ohmic contact, the current–voltage plot can indicate the

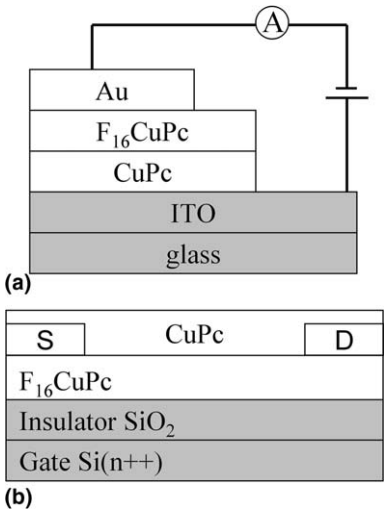

Fig. 1. The schematic cross-section of the diode (a) and organic field-effect transistors (b) used in this study.

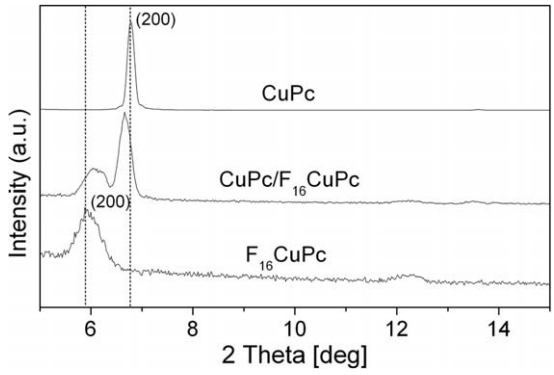

Fig. 2. X-ray diffraction spectra of CuPc, F_{16}CuPc and CuPc/F_{16}CuPc thin films.

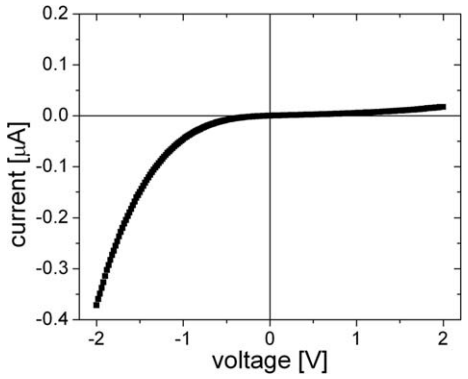

Fig. 3. Typical current–voltage curve of diode with F_{16}CuPc and CuPc heterojunction.

interfacial characteristics of CuPc and F_{16}CuPc. The energy levels of CuPc and F_{16}CuPc were obtained from Ref. [20], as shown in Fig. 4(a). When CuPc and F_{16}CuPc are brought together into contact, energy bands will have a bending, highest occupied molecular orbital (HOMO) of CuPc bent upwards and lowest unoccupied molecular orbital (LUMO) of F_{16}CuPc bent downwards (Fig. 4(b)). Carriers, electrons in F_{16}CuPc and holes in CuPc, are accumulated at both sides of the heterojunction interface (Fig. 4(c)). Heterojunction thus produces a build-in electrical field, self-bias, at the interface. This may be caused by the charge transfer between CuPc and F_{16}CuPc, which lead to an interface dipole and was hinted in the literatures [19,21]. Similar phenomena have been also observed in a metal/semiconductor contacts [20]. The electronic structure at the interface of CuPc and F_{16}CuPc under zero bias conditions is shown in Fig. 4(b). When a forward bias is applied on the diode, the potential barrier at the junction is enhanced since the direction of applied electrical field is the same as that of build-in field. So, current through the junction is restricted. It is noted that the forward bias strengthens the reverse band-bending. When a reverse bias is applied, the potential barrier is lowered since the applied electrical field opposes the built-in field. The reverse band-bending is weakened. Current can flow through the junction. Therefore, the diode has a small current for a forward bias and a large current for a reverse bias.

3.3. Interfacial electronic structure for diode and OTFT

At the heterojunction interface, the charge carriers induced by the heterojunction-effect will fill the localized states within the energy gap. But the induced holes exceed the localized states in CuPc layer, and the partial holes are free (Fig. 4(c)), since a high conduction is observed at zero gate voltage and a normally-on p-channel behavior can be obtained based on the same material pair [19]. Therefore, the aligned Fermi-level E_F crosses the bending HOMO of CuPc (Fig. 4(b)). For the induced electrons, they all may fill the localized states in F_{16}CuPc layer.

For transistors with double-layer structure, the performance of bottom-layer semiconductor is shown easier than that of top-layer semiconductor. In this case, the CuPc layer has a high conduction due to the heterojunction-effect, so the normally-on transistors can be easily realized when CuPc layer is used as the first semiconductor (bottom-layer) [19]. The schematic structure of normally-on device is shown in Fig. 5(a). While ambipolar transistors can be achieved when CuPc layer is used as the second semiconductor (top-layer, Fig. 5(b)) [14,18,19], since the hole transport can be easily realized under certain bias.

3.4. Accumulation length of crystalline CuPc

Because the charge carriers are accumulated at both sides of CuPc/F_{16}CuPc interface, a self-bias is produced, thus the threshold voltage in OFETs can be modified by utilizing the heterojunction-effect. Fig. 6 shows the output characteristics of a 10 nm F_{16}CuPc single layer device in comparison with a heterojunction device with a 3 nm F_{16}CuPc/10 nm CuPc. It can be seen that the drain current I_{DS} of heterojunction OFETs at 0 V gate voltage is clearly higher than that at 40 V for the single layer F_{16}CuPc device, i.e., a high conduction at 0 V gate voltage in the heterojunction device. This indicates that mobile charges accumulate at the heterojunction interface even without applying gate voltage in a heterojunction device.

The field-effect mobility and threshold voltage were estimated from the saturation region ($V_D =$ 50 V) according to the following equation:

$$I_{DS} = \frac{W}{2L} C_i \mu (V_{GS} - V_T)^2$$

where W and L are the width and length of the channel, C_i is the capacitance of the gate insulator; μ is the field-effect mobility, and V_T is the threshold voltage. Fig. 6 shows the transfer characteristics (Fig. 7(a)) and $I_{DS}^{1/2} \sim V_{GS}$ (Fig. 7(b)) of the single

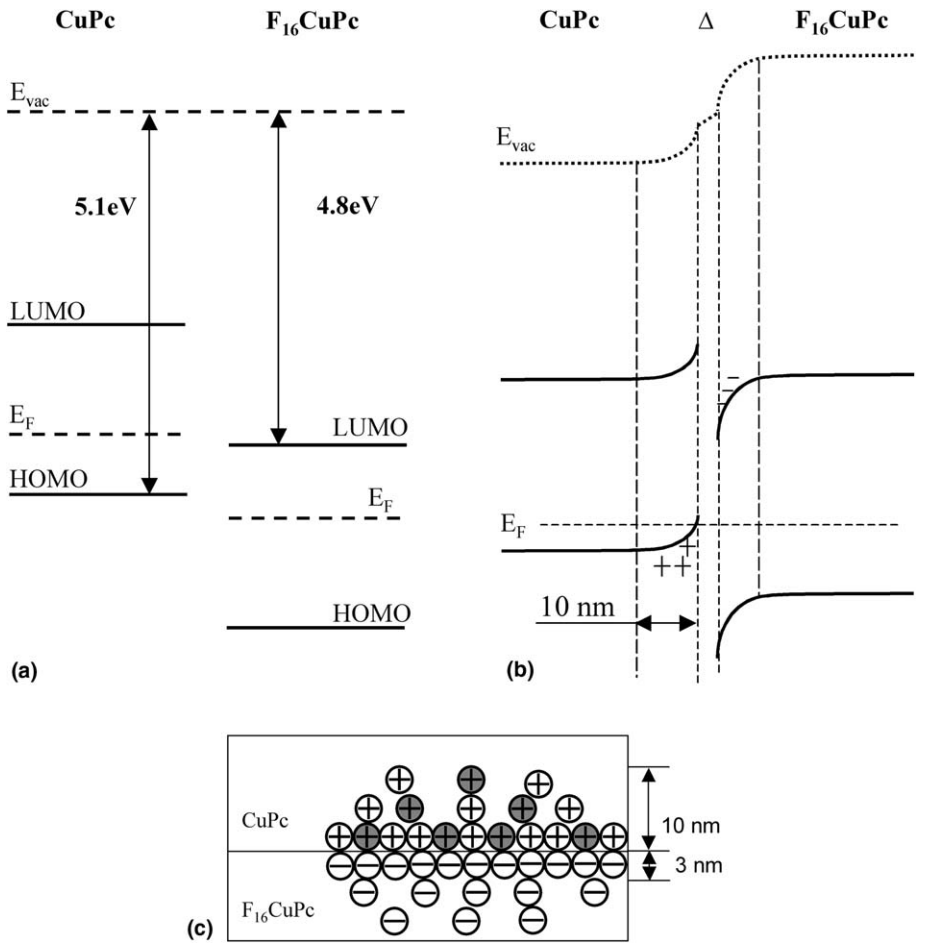

Fig. 4. (a) Energy diagram of CuPc and F_{16}CuPc before (a) and after (b) contact. E_{vac} and E_F denote the vacuum level and Fermi level, respectively. (c) The charge carrier distribution at the heterojunction interface of CuPc and F_{16}CuPc under zero bias conditions. The filled symbols indicate that the hole charges are free.

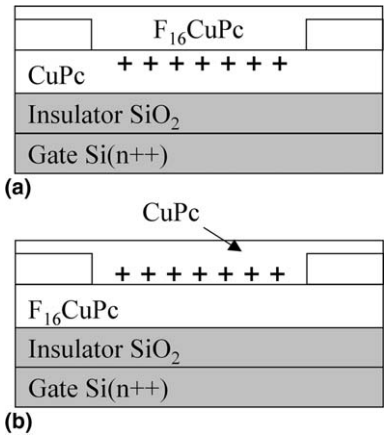

Fig. 5. The schematic structure of organic transistors with a heterojunction of F_{16}CuPc/CuPc and CuPc/F_{16}CuPc. The cross-shaped symbols indicate the hole charges are free in the CuPc layer.

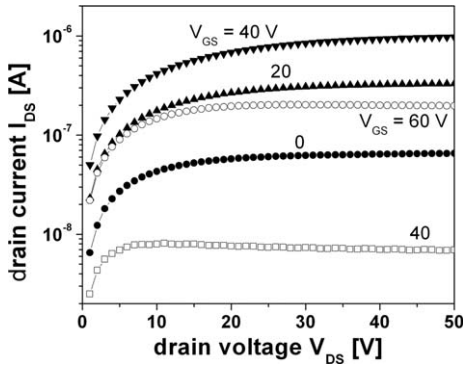

Fig. 6. The output characteristics of single layer F_{16}CuPc transistors with 10 nm thickness (open symbols) and heterojunction OFETs with 3 nm F_{16}CuPc and 10 nm CuPc (solid symbols).

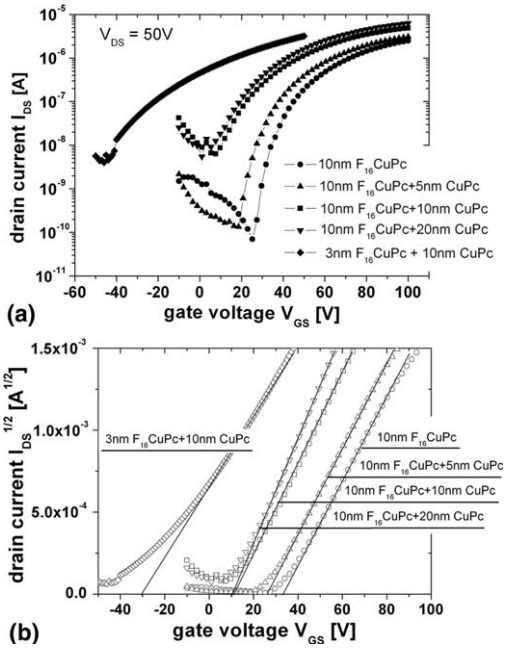

Fig. 7. (a) Transfer characteristics of CuPc/F_{16}CuPc heterojunction with different thicknesses at 50 V drain voltage. (b) $I_{DS}{}^{1/2} \sim V_{GS}$ characteristics of above heterojunction OFETs.

layer device together with heterojunction devices, including a 10 nm F_{16}CuPc/5 nm CuPc, a 10 nm F_{16}CuPc/10 nm CuPc, a 10 nm F_{16}CuPc/20 nm CuPc and the 3 nm F_{16}CuPc/10 nm CuPc devices. A mobility of 0.0062 cm^2/V s was extracted for the 3 nm F_{16}CuPc/10 nm CuPc device. For the 10 nm F_{16}CuPc/10 nm CuPc and the 10 nm F_{16}CuPc/20 nm CuPc devices, the mobilities increases to 0.0086 cm^2/V s and 0.0112 cm^2/V s, respectively. The approximately same order level of mobilities in all devices indicates that the drain current is predominated by the accumulation electrons in the F_{16}CuPc. Moreover, the threshold voltage have a significant shift from +33 V for F_{16}CuPc single layer device to +10 V for the 10 nm F_{16}CuPc/10 nm CuPc and the 10 nm F_{16}CuPc/20 nm CuPc heterojunction devices. For the device of 3 nm F_{16}CuPc/10 nm CuPc, V_T shifts to −30 V. The shift of threshold voltage was attributed to the heterojunction-effect. The threshold voltage can be continuously controlled from −30 to 33 V by varying the thickness of the active layer. Therefore, it supplied a new method to control the threshold voltage to meet different requirements.

The concept of threshold voltage had been explained by Shur in amorphous-Si thin-film transistors [22]. At below-threshold regime, the charges induced by field-effect fill the localized states within the energy gap, and transport occurs via activated hopping between these states. Therefore, the shift of V_T indicates the decrease of the localized states in F_{16}CuPc at equilibrium with increasing the thickness of CuPc. The decreased localized states are filled by increased electrons, which is attributed to organic heterojunction-effect. The heterojunction may induce the same number of electrons and holes at both sides of the interface for being neutral in the whole semiconductor thin-film. Therefore, the induced holes in CuPc also increase with increasing the thickness of CuPc. Finally, the induced holes and electrons reaches a saturation value when CuPc thickness is larger than 10 nm, and V_T also reaches the saturation value of 10 V for the 10 nm F_{16}CuPc/10 (or 20) nm CuPc device. This indicates that the accumulation thickness for holes is about 10 nm at CuPc side (Fig. 4(b) and (c)). For a thinner F_{16}CuPc, for example a 3 nm F_{16}CuPc/10 nm CuPc device, electrons induced by the heterojunction-effect exceed the localized states in the F_{16}CuPc layer, so the free electrons occur in the semiconductor layer. Therefore, a high conduction is observed at the zero gate voltage, and a negative V_T can be obtained. This indicates that the accumulation thickness of electrons is larger than 3 nm at the F_{16}CuPc side.

4. Conclusions

The diode with the organic heterojunction of CuPc and F_{16}CuPc showed a reverse rectifying characteristic. HOMO of CuPc is bended upwards and LUMO of F_{16}CuPc is bended downwards since the electrons and holes are accumulated at both sides of the organic heterojunction interface, which produce a built-in electric field. The thickness of the charges accumulated at CuPc layer is 10 nm. An application of heterojunction-effect of charge accumulation has been demonstrated to control the threshold voltage of organic field-effect transistors. Therefore, it supplies a physical method by the utilization of the heterojunction-effect to optimize the threshold voltage of organic transistors to meet different requirements, such as stabilizing threshold voltage for OTFT integration or minimizing threshold voltage for OTFT employing polymer dielectrics. We believe that a further understanding of the features of organic heterojunction will be helpful for developing novel organic electronic devices.

Acknowledgements

The work was financially supported by the Special Funds for Major State Basic Research Projects (2002CB613400) and the National Natural Science Foundation of China (90301008, 20025413). The authors thank Prof. Dongge Ma for discussions.

References

[1] G. Horowitz, Adv. Mater. 10 (1998) 365.
[2] C.D. Dimitrakopoulos, P.R.L. Malenfant, Adv. Mater. 14 (2002) 99.
[3] C.W. Tang, Appl. Phys. Lett. 48 (1986) 183.
[4] P. Peumans, S.R. Forrest, Appl. Phys. Lett. 79 (2001) 126.
[5] P. Peumans, S. Uchida, S.R. Forrest, Nature 425 (2003) 158.
[6] C.W. Tang, S.A. VanSlyke, Appl. Phys. Lett. 51 (1987) 913.
[7] A. Dodabalapor, H.E. Katz, L. Torsi, R.C. Haddon, Science 269 (1995) 1560.
[8] K. Tada, H. Harada, K. Yoshinio, Jpn. J. Appl. Phys. Part 2 35 (1996) L944.
[9] E.J. Meijer, D.M. de Leeuw, S. Setayesh, E. van Veenendaal, B.-H. Huisman, P.W.M. Blom, J.C. Hummelen, U. Scherf, T.M. Klapwijk, Nat. Mater. 2 (2003) 678.
[10] C. Rost, D.J. Gundlach, S. Karg, W. Rieß, J. Appl. Phys. 95 (2004) 5782.
[11] R. Hajlaoui, G. Horowitz, F. Garnier, A. Arce-Brouchet, L. Laigre, A. El Kassmi, F. Demanze, F. Kouki, Adv. Mater. 5 (1997) 389.
[12] M. Yoshida, S. Uemura, T. Kodzasa, H. Ushijima, T. Kamata, Synth. Met. 137 (2003) 893.
[13] Y. Abe, T. Hasegawa, Y. Takahashi, T. Yamada, Y. Tokura, Appl. Phys. Lett. 87 (2005) 153506.
[14] R. Ye, M. Baba, Y. Oishi, K. Mori, Appl. Phys. Lett. 86 (2005) 253505.
[15] Z. Bao, A.J. Lovinger, A. Dodabalapur, Adv. Mater. 9 (1997) 42.
[16] Z. Bao, A.J. Lovinger, A. Dodabalapur, Appl. Phys. Lett. 69 (1996) 3066.
[17] Z. Bao, A.J. Lovinger, J. Brown, J. Am. Chem. Soc. 120 (1998) 207.
[18] J. Wang, H. Wang, X. Yan, H. Huang, D. Yan, Chem. Phys. Lett. 407 (2005) 87.
[19] J. Wang, H. Wang, X. Yan, H. Huang, D. Yan, Appl. Phys. Lett. 87 (2005) 093507.
[20] H. Peisert, M. Knupfer, T. Schwieger, G.G. Fuentes, D. Olligs, J. Fink, J. Appl. Phys. 93 (2003) 9683.
[21] D. Schlettwein, K. Hesse, N.E. Gruhn, P.A. Lee, K.W. Nebesny, N.R. Armstrong, J. Phys. Chem. B 105 (2001) 4791.
[22] M. Shur, Physics of Semiconductor Devices, Prentice-Hall, Englewood Cliffs, New Jersey, 1990.

Available online at www.sciencedirect.com
ScienceDirect
Organic Electronics 7 (2006) 375–386
Organic Electronics
www.elsevier.com/locate/orgel

Transient analysis of triplet exciton dynamics in amorphous organic semiconductor thin films

N.C. Giebink [a], Y. Sun [a], S.R. Forrest [b,*]

[a] Princeton Institute for the Science and Technology of Materials (PRISM), Department of Electrical Engineering, Princeton University, Princeton, NJ 08544, USA
[b] Departments of Electrical Engineering and Computer Science, Physics, Materials Science and Engineering, University of Michigan, Ann Arbor, MI 48109, USA

Received 1 March 2006; received in revised form 12 April 2006; accepted 20 April 2006
Available online 6 June 2006

Abstract

We study triplet exciton diffusion in the archetype organic material 4,4′-bis(*N*-carbazolyl)biphenyl (CBP) commonly used as a conductive host in the emissive zone of organic light emitting devices. Using time-resolved spectral decay ensuing from the diffusion of an initially localized triplet population to a spatially separated phosphor doped region, we model the delayed fluorescence and phosphorescence decays based on non-dispersive triplet transport. Fits to the model yield a diffusion coefficient of $D = (1.4 \pm 0.3) \times 10^{-8}$ cm^2/s, and a triplet–triplet bimolecular quenching rate constant of $K_{TT} = (1.6 \pm 0.4) \times 10^{-14}$ cm^3/s. The results are extended by doping a wide energy-gap molecule into CBP that serves to frustrate triplet transport, lowering both the diffusion coefficient and annihilation rate. These results are used to model a recently demonstrated white organic light emitting device that depends on triplet diffusion in CBP to excite spatially separate fluorescent and phosphorescent doped regions of the emissive layer. We determine the extent to which diffusion contributes to light emission in this structure, and predict its performance based on ideal lumophores with unity quantum yield.

Keywords: Exciton; Electrophosphorescence; Organic light emitting device; Triplet; Diffusion

1. Introduction

Energy transport by exciton diffusion in organic thin films plays a significant role in many practical applications, including organic light emitting devices [1,2] (OLEDs), and organic photovoltaic cells [3]. For example, Sun et al. recently introduced a white light emitting device that depends on diffusive energy transport to achieve the desired color balance at high luminous efficiency [4]. Exciton diffusion also controls the performance of organic photovoltaics, linking exciton generation to the subsequent dissociation into a free electron and hole at a nearby donor/acceptor interface [3]. In both of these examples, efficient energy transport is required to achieve high device performance.

* Corresponding author. Tel.: +1 734 936 2680; fax: +1 734 763 0085.
E-mail address: stevefor@umich.edu (S.R. Forrest).

1566-1199/$ - see front matter
doi:10.1016/j.orgel.2006.04.007

The diffusive characteristics of spin singlet and triplet excitons are considerably different. The forbidden triplet exciton decay transition typically takes 10^6 times longer than the allowed singlet decay of 1–10 ns [5]. This leads to a triplet diffusion length >100 nm [6,7] in amorphous organic thin films that is often an order of magnitude larger than for singlets [8,9]. Triplet excitons thus provide a means for efficient energy transport within an organic solid. For example, intersystem crossing following photon absorption in C_{60}-based organic solar cells is a source of triplets that leads to an exciton diffusion length (~40 nm) that is comparable to the optical absorption length [3], resulting in a high device efficiency.

Control of exciton diffusion is the basis for the white-emitting fluorescent/phosphorescent (*F*/*P*) hybrid OLED architecture recently reported by Sun et al. [4]. That device uses the different diffusive characteristics of singlet and triplet excitons to spatially separate the decay channels for each species. In constraining singlet decay to a blue fluorescent zone and triplet decay to spatially remote red and green phosphorescent regions, high efficiency white emission was observed. In principle, this device concept offers a lower operating voltage and a more stable white emission spectrum with drive current than conventional all-phosphorescent white organic light emitting devices (WOLEDs), while maintaining the possibility for 100% internal quantum efficiency. Improved understanding of the diffusive process in such a device is one motivation for this current study.

Diffusion also plays an important role in both energy transport and triplet–triplet (T–T) annihilation [5,10], both of which are central to understanding the operation of practical devices. Several studies have examined triplet diffusion in organic molecular crystals [5]. Focus has also been given to thin films by employing both steady-state [7] and time-of-flight experiments under electrical excitation [11]. The simple experimental procedure and easily interpretable results presented here serve to complement these previous investigations.

We employ optically pumped pseudo-time-of-flight measurements to obtain both the triplet diffusion coefficient, D, and the T–T annihilation rate, K_{TT}, for the commonly used OLED host material, 4,4′-bis(*N*-carbazolyl)biphenyl (CBP). These measurements use the delayed fluorescence from CBP and the delayed phosphorescence from a phosphor-doped "sensing layer" to monitor the evolution of the triplet spatial profile. In addition, we demonstrate that the diffusion coefficient is decreased by doping into CBP a wide energy-gap molecule that scatters triplets and frustrates their transport. The results are employed to understand the mechanisms that control the performance of fluorescent/phosphorescent WOLEDs, and to determine the limitations of such an architecture using CBP as a host material.

In Section 2 we develop a theory describing triplet exciton migration and annihilation processes. Experimental details are given in Section 3, and in Section 4 we present the results from transient measurements. In Section 5 we fit and discuss these results in terms of the theory in Section 2, and in Section 6 these results are used to analyze the fluorescent/phosphorescent WOLED. Section 7 provides a summary.

2. Theory

Intermolecular triplet transfer is fundamentally different from that for singlets. Transfer of a singlet exciton is often dominated by long-range (~5 nm) Förster dipole–dipole coupling [9]; however, this mechanism contributes negligibly to triplet transfer since both donor and acceptor transitions are disallowed. Triplets, instead, transfer by the short range (<1 nm) Dexter process [12], an exchange coupling between nearest-neighbor molecules that is permitted by a simultaneous interchange of spin on both the donor and acceptor molecules. Triplet migration thus proceeds as a series of incoherent hops between adjacent molecules that have considerable intermolecular electronic orbital overlap. Both Förster and Dexter processes are modeled as diffusive in the continuum limit [9].

The morphological disorder present in an amorphous organic solid leads to a distribution of both molecular site energies and intersite exchange couplings [13,14]. This results in an inhomogeneously broadened density of states (DOS) within which triplet transport occurs. Relaxation of triplets into the low-energy tail of this DOS gives rise to dispersive transport [13,14], which is typically described by a time-dependent diffusion coefficient. At room temperature, however, thermal energy is generally sufficient to ensure that equilibrium is rapidly approached [14]. Thus, transport quickly moves from the dispersive to the classical regime, at which point it can be described by a time-independent diffusion coefficient.

The encounter of two triplet excitons (T_1) may result in an annihilation reaction that proceeds as

$$T_1 + T_1 \overset{K_{TT}}{\rightarrow} \{(T_n + S_0) \text{ or } (S_n + S_0)\},$$

where the reaction products are a ground state (S_0), and a triplet (T_n) or singlet (S_n) in the nth electronic manifold ($n \geqslant 1$) [5]. The creation of a singlet exciton in the latter reaction is responsible for delayed fluorescence [5,15]. The triplet–triplet annihilation rate, K_{TT}, is related to the diffusion coefficient since the triplet mobility controls their encounter probability. That is [15,16]:

$$K_{TT} = 4\pi D R_{eff}, \tag{1}$$

where D is the non-dispersive diffusion coefficient, and R_{eff} is the effective radius for quenching such that triplets approaching within this distance are assumed to annihilate with unity probability.

In this work, we combine the results of several experiments to study the one-dimensional evolution of the CBP triplet density, $T_H(x,t)$. Assuming non-dispersive transport, $T_H(x,t)$ obeys the following diffusion equation:

$$\frac{\partial T_H}{\partial t} = D\frac{\partial^2 T_H}{\partial x^2} - \frac{T_H}{\tau_T} - K_{TT}T_H^2. \tag{2}$$

Here, triplets are lost via natural decay in time, τ_T, as well as via T–T annihilation at a rate, K_{TT}. The annihilation reaction can yield singlets that give rise to delayed fluorescence. In this case, the singlet density, $S_H(x,t)$, is

$$\frac{\partial S_H}{\partial t} = -\frac{S_H}{\tau_S} + \frac{1}{2}K_{TT}T_H^2, \tag{3}$$

where the generation term (second on the right-hand side) has a prefactor of 1/2 since annihilation of two triplets produces one singlet. We assume for simplicity that all T–T annihilation reactions yield singlets that decay naturally in time, τ_S. There is no explicit spatial dependence in Eq. (3) since the effects of singlet diffusion are not relevant on the time scales of our experiments.

Similar equations are obtained for the case of a doped film. The dopant provides an additional decay route for host triplets – namely Dexter transfer to the guest dopant molecules at a rate, K_{TG}. Hence, in the presence of a guest:

$$\frac{\partial T_H}{\partial t} = D\frac{\partial^2 T_H}{\partial x^2} - K_{TT}T_H^2 - \left(K_{TG} + \frac{1}{\tau_T}\right)T_H. \tag{4}$$

For exothermic $T_H \rightarrow T_G$ transfer, back-transfer from guest to host is not energetically favorable, resulting in triplet localization on the dopant. In this case, the guest triplet density, $T_G(x,t)$, is

$$\frac{\partial T_G}{\partial t} = -\frac{T_G}{\tau_G} + K_{TG}T_H. \tag{5}$$

Eqs. (2)–(5) provide the required framework for the analysis of the experimental results that follow.

3. Experimental

A schematic of the sample structure, as well as the processes leading to luminescence, are shown in Fig. 1. For all samples, a 200 Å thick layer of CBP doped at 10 wt.% with a metallorganic phosphor is thermally evaporated onto the surface of a freshly cleaned and deoxidized Si substrate. The phosphors used are *fac*-tris(2-phenylpyridine) iridium ($Ir(ppy)_3$) [17] emitting in the green, and iridium(III) bis(2-phenyl quinolyl-$NC^{2'}$) acetylacetonate (PQIr) [18] that emits in the red. The doped layer functions as a triplet "sensor" since CBP triplets transfer to, and localize on the lower energy phosphor triplet state. Phosphor emission thus serves to indicate the presence of CBP triplets in the doped region. Since the rate of triplet transfer depends strongly on energetic resonance between host and guest, the use of $Ir(ppy)_3$ and PQIr, which have different triplet energies (see Table 1) allows host–guest triplet transfer in the sensing layer to be isolated from that of diffusion in CBP.

A CBP spacer layer of thickness, X, varied between 100 Å and 1200 Å, is deposited on the sensing layer surface. Prior to deposition, all organics are purified at least once by train sublimation [19], and all deposition is carried out at a growth rate of approximately 3 Å/s in vacuum at a base pressure of 10^{-7} Torr. Immediately following deposition, samples are placed in a closed-cycle He cryostat, and the chamber is evacuated to roughly 50 mTorr.

We focus the output of a pulsed N_2 laser (<1 ns pulse width; wavelength $\lambda = 337$ nm; pulse energy from 0.9 to 4.1 μJ) onto a 2 mm diameter spot incident on the spacer layer surface. Each pulse generates an exponentially decaying singlet density spatial profile according to the measured CBP absorption coefficient of $\alpha = 2.0 \times 10^5\ cm^{-1}$ at the pump laser wavelength. Neither interference effects nor absorptive saturation are expected to significantly change this excited state profile. Using the above parameters at a pulse energy of 4.1 μJ, we estimate an initial singlet density of $(2.9 \pm 0.4) \times 10^{19}\ cm^{-3}$ at the film surface on which the beam is

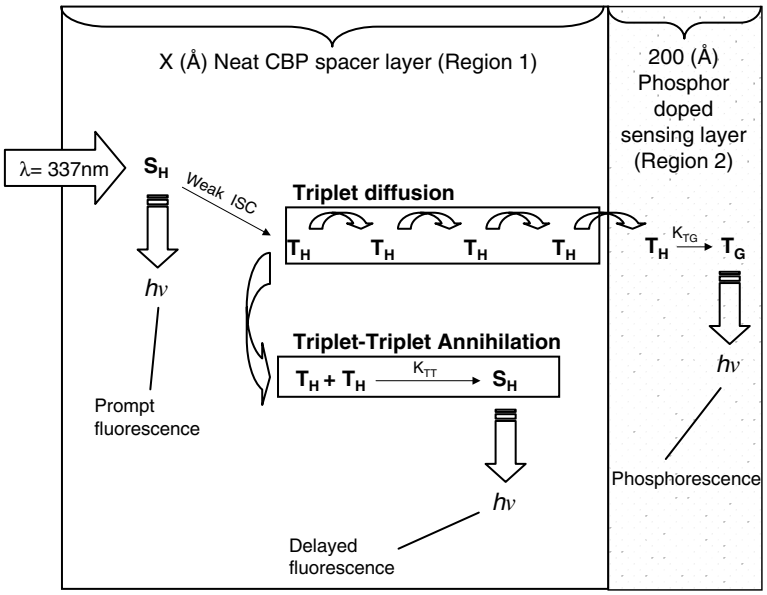

Fig. 1. Schematic illustration of the light emission process in the time-of-flight experiments. The sample structure is also defined in this diagram. A spacer layer of neat CBP with thickness X (Å) is deposited on top of a 200 Å phosphor doped (10 wt.%) triplet 'sensing' layer on a Si substrate. Pulsed laser excitation is incident on the spacer surface, generating singlets. Most singlets decay immediately (prompt fluorescence), while a small fraction intersystem cross to the triplet state. The triplets diffuse through the spacer to the sensing layer where they emit from the guest phosphors (phosphorescence). As they diffuse, they also undergo triplet–triplet annihilation, which can result in delayed fluorescence.

Table 1
Fitting results: CBP triplet dynamics

Parameter	CBP	
D (cm^2/s)	$(1.4 \pm 0.3) \times 10^{-8}$	
K_{TT} (cm^3/s)	$(1.6 \pm 0.4) \times 10^{-14}$	
T_{H0} (cm^{-3})	$(7 \pm 2) \times 10^{17}$	
τ_H (ms)	(14 ± 8)	
	CBP/Ir(ppy)$_3$ ($\Delta E_T \sim -0.2$ eV)	CBP/PQIr ($\Delta E_T \sim -0.4$ eV)
K_{TG} (s^{-1})	$(0.8 \pm 0.4) \times 10^7$	$(0.5 \pm 0.2) \times 10^7$

incident. The resulting luminescence from the samples is focused into a fiber and channeled to a Hamamatsu C4334 streak camera that monitors the time-resolved spectral decay.

The majority of singlets decay within nanoseconds following the optical pulse, while a small fraction cross into the long-lived triplet manifold [20]. The concentration gradient stemming from the large optical absorption coefficient results in net diffusion towards the sensing layer. During diffusion, triplets may annihilate to produce delayed fluorescence. Fig. 1 schematically illustrates the decay progression.

This is a pseudo-time-of-flight (TOF) experiment since varying the spacer layer thickness changes the time that it takes for the bulk of the triplet population to diffuse into the sensing layer to produce phosphorescence. We also vary the incident laser intensity by a factor of 5 to control the initial triplet excitation density. This affects the amount of T–T annihilation (and hence delayed fluorescence intensity).

4. Results

The results of the TOF transient experiments are shown in Figs. 2 and 3 for two different sets of samples employing Ir(ppy)$_3$ and PQIr as the sensing layer dopant, respectively. These plots show the decay of the delayed fluorescence and the sensing layer phosphorescence for different spacer thicknesses, X. No significant change in the shape of either the delayed fluorescence or phosphorescence transient decay occurs as X varies from 1200 Å to 600 Å, while the decay for both accelerates for $X \leqslant 300$ Å. This reflects a balance reached between the losses that occur in the spacer and the increased decay rate in the sensing layer due to the presence of the phosphor molecules.

The thickness of the spacer layer in relation to both the optical absorption and triplet diffusion lengths is one factor that determines the balance between the various decay channels. For a thick

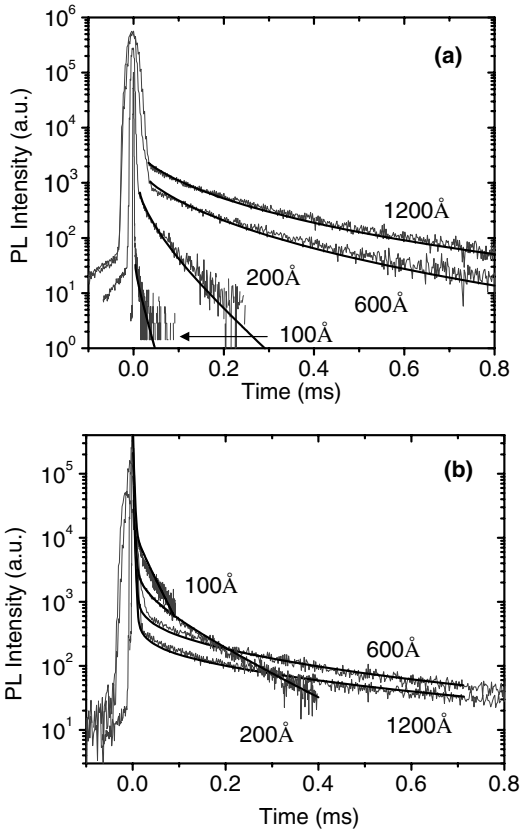

Fig. 2. Spectrally resolved photoluminescence (PL) transients for $Ir(ppy)_3$ doped in CBP as the sensing layer. The spacer layer thickness ranges from 100 Å to 1200 Å. The large peaks at the start of each transient are due to prompt fluorescence and phosphorescence. The delayed fluorescence transient from CBP ($\lambda < 400$ nm) is shown in (a), with the corresponding $Ir(ppy)_3$ phosphorescence ($\lambda > 450$ nm) in (b). Transients for all samples are fit (solid lines) using the theory in the text to give a diffusion constant of $D = (1.4 \pm 0.3) \times 10^{-8}$ cm^2/s, a triplet–triplet annihilation rate of $K_{TT} = (1.6 \pm 0.4) \times 10^{-14}$ cm^3/s, and an initial triplet density of $T_{H0} = (7 \pm 2) \times 10^{17}$ cm^{-3}.

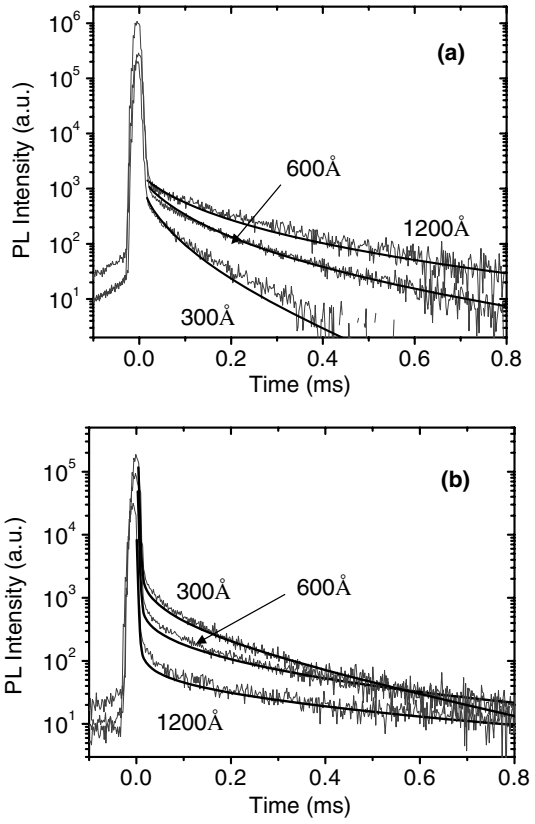

Fig. 3. Spectrally resolved photoluminescence (PL) transients for samples using a PQIr doped CBP sensing layer, as in Fig. 2. The spacer layer thickness ranges from 300 Å to 1200 Å. The delayed fluorescence transient from CBP ($\lambda < 400$ nm) is shown in (a), with the corresponding PQIr phosphorescence ($\lambda > 450$ nm) in (b). Transients for all samples are fit (solid lines) using the theory in the text to give $D = (1.4 \pm 0.3) \times 10^{-8}$ cm^2/s, $K_{TT} = (1.6 \pm 0.4) \times 10^{-14}$ cm^3/s, $T_{H0} = (7 \pm 2) \times 10^{17}$ cm^{-3}.

spacer layer, the majority of triplets are generated too far from the sensing layer to diffuse to it before they annihilate or otherwise naturally decay. In that case, the delayed fluorescence is intense while the phosphorescence is weak due to the small fraction of triplets that reach the sensor. Conversely, samples with thin spacers show increased phosphorescence intensity and fast decays for both luminescence signals, since diffusion to the sensing layer efficiently competes with annihilation and natural decay.

The intensity of the exciting optical pulse is also a factor in determining the decay transients, since the annihilation rate is proportional to the square of the triplet density. To examine this effect, we vary the pulse energy incident on a sample with a spacer thickness of $X = 300$ Å deposited on a PQIr sensing layer. The transient results are plotted in Fig. 4 for pulse energies ranging from 0.9 μJ to 4.1 μJ. Both luminescent transients decay more slowly and become less intense with decreasing pump fluence, although this trend is most evident in the delayed fluorescence signal.

Scattering or trapping of triplet excitons at defect sites in a thin film are expected to reduce the triplet diffusion coefficient as compared to a defect-free film. We demonstrate this effect by doping into CBP the wide energy gap molecule *p*-bis(triphenylsilyly)benzene (UGH2) whose triplet energy [21] is ~3.5 eV; well in excess of the 2.6 eV CBP triplet [22]. Since no energy transfer from the CBP to

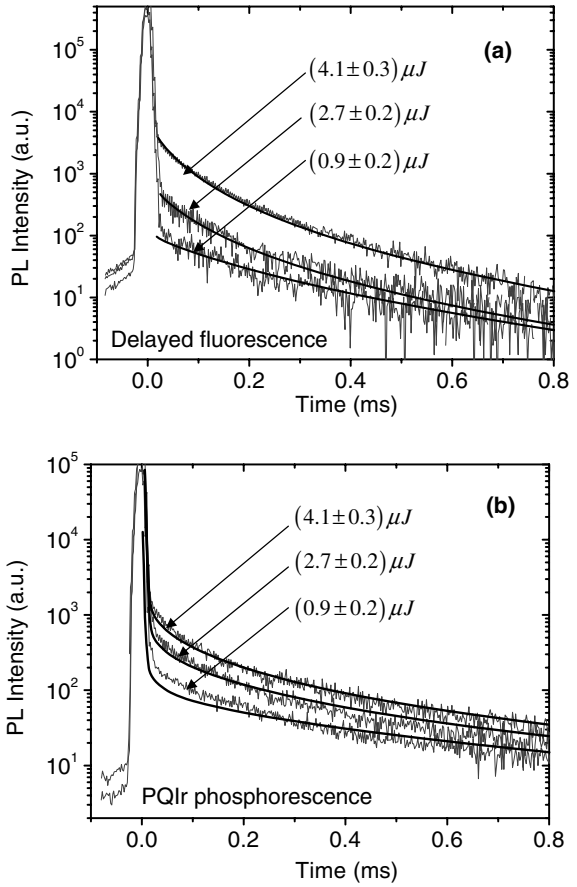

Fig. 4. Spectrally resolved photoluminescence transients obtained for several excitation pulse intensities for samples with PQIr doped into CBP as a sensing layer. Subplots (a) and (b) show the delayed fluorescence of CBP, and the phosphorescence of PQIr, respectively. Solid lines show fits calculated for different T_{H0} (listed in Table 2) while holding D and K_{TT} constant at the values given in Table 1.

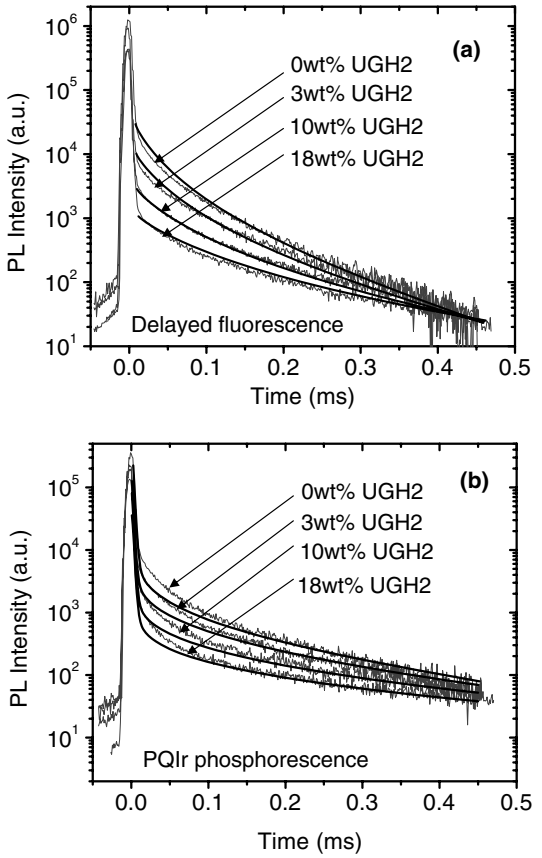

Fig. 5. Spectrally resolved delayed fluorescence (a) and PQIr phosphorescence (b) transient data obtained for samples using a PQIr sensing layer with a 300 Å thick CBP spacer layer co-doped with varying concentrations of the wide-gap molecule UGH2. Solid lines indicate fits to the theory in the text by varying D and K_{TT}, holding all other parameters constant at the values listed in Table 1.

the UGH2 triplet state is possible, the UGH2 molecules scatter triplets and frustrate their movement through the CBP matrix, decreasing the diffusion coefficient.

Transient decays are shown in Fig. 5 for samples having 0, 3, 10 and 18 wt.% UGH2 doped into a 300 Å thick CBP spacer, using a PQIr-doped sensing layer. Both delayed fluorescence and phosphorescence trend towards lower intensity and slower decays with increasing UGH2 concentration. The reduced delayed fluorescence indicates that the T–T annihilation rate decreases in the presence of UGH2, whereas the decreased and extended phosphorescence signal suggests that triplets take longer to reach the sensing layer. Both of these observations are consistent with a reduced triplet mobility in the spacer layer.

We also determined the natural CBP triplet lifetime, τ_T, at temperatures from 5 K to 170 K by optically pumping a neat, 500 Å thick film deposited on Si. The phosphorescence decay rates shown in Fig. 6 are obtained from monoexponential fits to the phosphorescence transient for times $t > 5$ ms following the N_2 laser pulse to eliminate effects from T–T annihilation. The green CBP phosphorescence with a high-energy edge at $\lambda = 480$ nm is apparent in the inset of Fig. 6, along with the delayed fluorescence signal centered at $\lambda = 410$ nm.

As shown in Fig. 6, the natural triplet decay is independent of temperature below ~50 K, and is only weakly activated at higher temperatures, with an energy, $E_a = 9 \pm 1$ meV. Since the phosphorescent decay of a single molecule is typically independent of temperature [20], the lifetime of triplets at

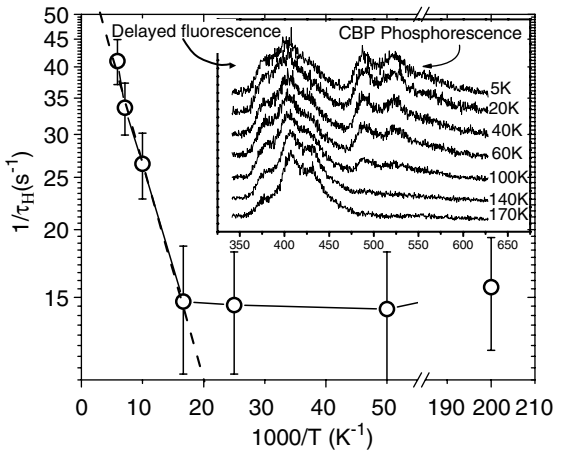

Fig. 6. Arrhenius plot of the natural CBP triplet decay rate ($1/\tau_H$) obtained for temperatures in the range from 5 K to 170 K. Inset: Spectra of CBP phosphorescence and delayed fluorescence at 1 ms following the initial optical excitation pulse.

higher temperatures is likely limited by quenching with impurities encountered in the course of migration in the film. As temperature increases, levels of higher energy in the triplet density of states (with typical Gaussian width $\sigma \sim 30$ meV [14], similar in magnitude to the value of E_a determined here) are populated. This increases the exciton mobility, and leads to more frequent encounters with quenching sites, thus decreasing the lifetime. This effect is intrinsic to the CBP films grown in these experiments, and extrapolation of the fit to room-temperature yields the natural triplet lifetime of $\tau_T = 14 \pm 8$ ms at $T = 295$ K.

5. Discussion

We analyze the TOF transient data by applying Eqs. (2) and (3) to region 1 of our samples (see Fig. 1), and Eqs. (4) and (5) to region 2. Eq. (2) describes the CBP triplet density in the spacer layer, $T_H(x,t)$, while Eq. (4) quantifies it in the sensor layer. These two equations are coupled at the spacer/sensor layer interface, with both $T_H(x,t)$ and its spatial derivative taken to be continuous across the boundary. The non-linear partial differential equations (2) and (4) are solved using finite element methods [23].

The solutions for the spacer layer singlet population, $S_H(x,t)$ (Eq. 3), and the sensing layer guest triplet population, $T_G(x,t)$ (Eq. 5), are determined once $T_H(x,t)$ is known. By spatially integrating $S_H(x,t)$ and $T_G(x,t)$ across their respective regions, we find the total luminescent populations $S'_H(t)$ and $T'_G(t)$. These functions are then least-squares fit with statistical weighting to the corresponding TOF luminescence transient data.

We fit the data in Figs. 2 and 3 for a given sensing layer using Eqs. (2)–(5) by varying the parameters D, K_{TT}, K_{TG}, and T_{H0}, (the initial triplet density). For these fits, we use the measured CBP triplet lifetime in Section 4, the CBP singlet lifetime of $\tau_s = 0.7$ ns [24], and the known triplet lifetimes of $Ir(ppy)_3$, $\tau_G = 0.8$ μs [11] and PQIr, $\tau_G = 2.0$ μs [25].

The fitting results are summarized for both $Ir(ppy)_3$ and PQIr samples in Table 1, and are shown by the solid lines in Figs. 2 and 3. Within experimental uncertainty, we obtain the same values for the parameters D, K_{TT}, and T_{H0}, for both sets of samples, as would be expected. However, K_{TG} is nearly a factor of two greater for CBP → $Ir(ppy)_3$ transfer than for CBP → PQIr, presumably due to the stronger resonance between $Ir(ppy)_3$ and CBP triplet energies resulting in more efficient and rapid transfer.

Accounting for T–T annihilation at $T_{H0} = 7 \times 10^{17}$ cm^{-3}, the effective diffusion length is $L_D \approx 250$ Å, which is considerably less than $L_D = \sqrt{D\tau_H} \approx 1400$ Å found in the absence of T–T annihilation. This is similar to the case of *tris*(8-hydroxyquinoline) (Alq_3), where [26] $L_D > 1400$ Å was found at low excitation, and reduced to 140 Å at high excitation [11]. Note that the effective diffusion length of 250 Å calculated for these TOF results is consistent with the previous observation that significant changes in the transients only occur as the spacer is thinned to 300 Å. We similarly fit the data of Fig. 4 by fixing all parameters at the values given in Table 1, and allowing only T_{H0} to vary. In Table 2, the fitted values for T_{H0} are nearly proportional to the excitation intensity, as expected.

Fitting the transient data for the UGH2 doped samples of Fig. 5 confirms that the diffusion coefficient decreases with increasing UGH2 concentration. In this case, D and K_{TT} are varied while holding all other parameters constant. Summarizing the fitting results in Fig. 7, we find that both D and K_{TT} decrease at the same rate, consistent with Eq. (1). At an UGH2 concentration of 18 wt.%, corresponding to less than two CBP molecules between each UGH2 molecule, the diffusion coefficient in the spacer layer drops by a factor of four. This effect is analogous to diffusion through porous media in that UHG2 molecules act as scattering centers for triplets diffusing in CBP [27].

Table 2
Fitting results: initial triplet density vs. pulse energy

Excitation level (% of full)	Initial triplet density $T_{H0} \times 10^{17}$ cm^{-3}
4.1 μJ (100%)	9 ± 1 (100%)
2.7 μJ (65%)	6 ± 1 (66%)
0.9 μJ (22%)	2 ± 1 (22%)

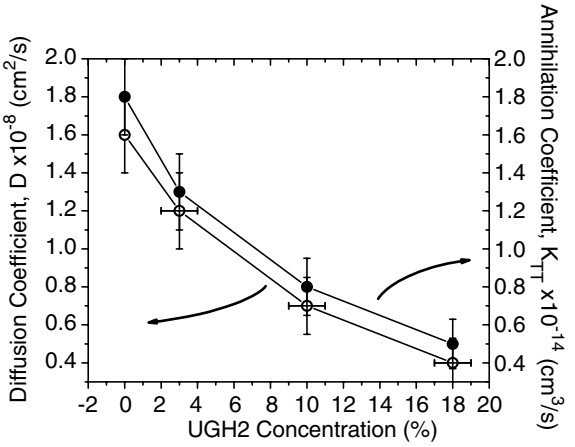

Fig. 7. Diffusion coefficient (D) and annihilation rate (K_{TT}) obtained from the data of Fig. 5. Both D and K_{TT} decrease in proportion to one another with increasing UGH2 concentration, consistent with Eq. (1) in the text. This is a result of triplet scattering by UGH2 molecules which frustrates transport through the CBP matrix.

6. Analysis of the fluorescent/phosphorescent WOLED

The concept of the fluorescent/phosphorescent white organic light emitting device (WOLED) recently introduced by Sun et al. [4], involves separating the radiative decay channels available to singlet and triplet excitons. In that device, whose structure and emission properties are shown in Fig. 8, the extended triplet diffusion length provides the exciton separation mechanism. Excitons form on CBP in a blue fluorescent-doped region within the WOLED emissive layer. The singlets rapidly Förster transfer [5] to the blue fluorophore, while the long-lived triplet excitons diffuse to a spatially separated phosphor-doped region that provides the green and red components of the white emission spectrum. Fig. 9a summarizes these energy transfer paths.

Hole transport from the indium-tin-oxide (ITO) anode to the emissive layer is facilitated by a 400 Å thick layer of 4,4′-bis[*N*-(1-naphthyl)-*N*-phenyl-amino]-biphenyl (NPD). A 200 Å thick layer of 4,7-diphenyl-1,10-phenanthroline (BPhen) followed by a 200 Å thick Li doped BPhen layer at a 1:1 molar ratio serves to transport electrons from the cathode while confining excitons within the emissive layer (EML). In the center of the EML is a 200 Å thick region consisting of Ir(ppy)$_3$ and PQIr

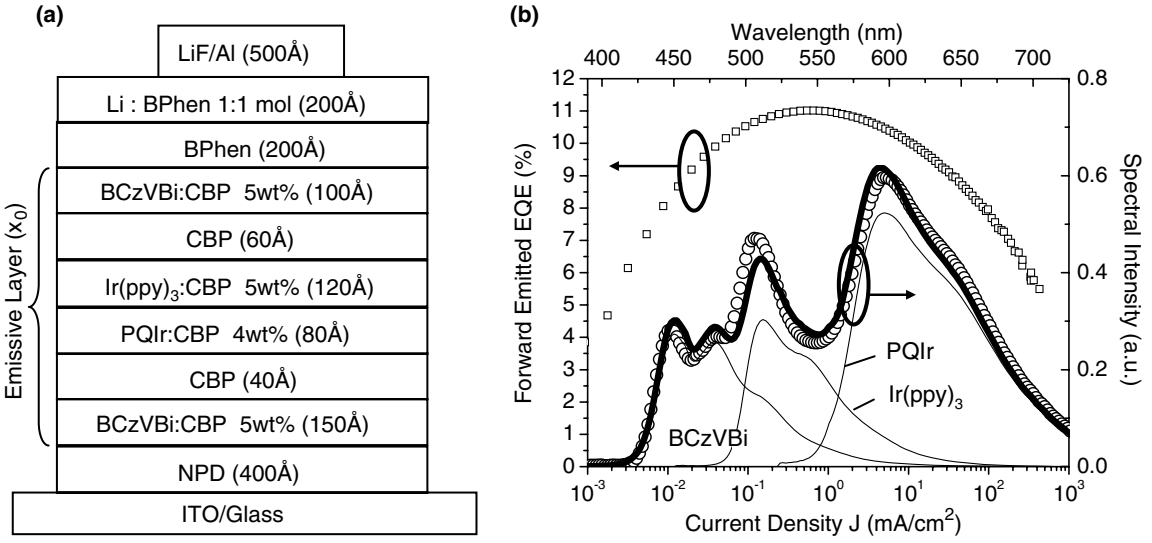

Fig. 8. (a) Schematic structure of the fluorescent/phosphorescent (F/P) WOLED of Ref. [4]. (b) The forward-emitted external quantum efficiency of the F/P WOLED (open squares) as a function of current density (J), and the emission spectrum at $J = 10$ mA/cm^2 (open circles). This spectrum is fit (solid, bold line) using the individual dopant photoluminescent spectra (solid, thin lines).

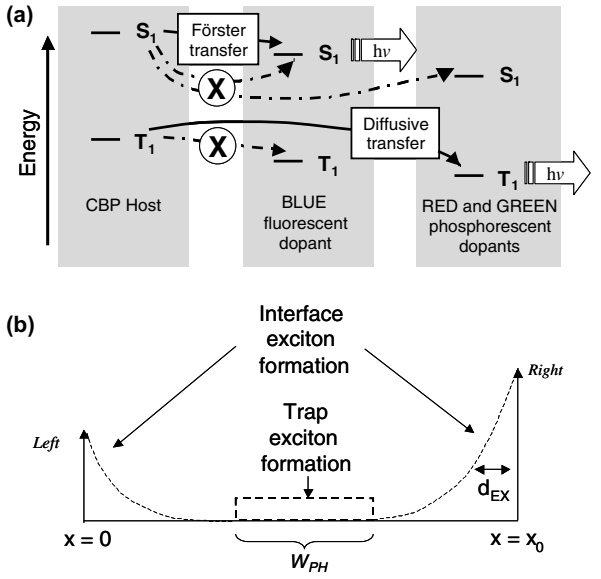

Fig. 9. (a) The energy transfer routes available to singlet and triplet excitons for the device of Fig. 8. '*X*' denotes an energy transfer route that is unlikely to occur due to the spatial separation and concentration of the fluorescent and phosphorescent dopants. (b) Exciton density within the emission layer of the device in Fig. 8 (dashed line). Trap recombination is assumed to be spatially uniform in the phosphor region, while formation on the CBP host follows an exponential profile at both edges of the emissive layer. The ratio of exciton densities at the two edges of the emission layer is $\delta_{\mathrm{Left}}/\delta_{\mathrm{Right}}$, with $\delta_{\mathrm{Left}} + \delta_{\mathrm{Right}} = 1$.

doped into CBP. This phosphorescent region is sandwiched between two undoped CBP spacers (one 40 Å and the other 60 Å thick, see Fig. 8a), which in turn are sandwiched between two layers of CBP (one 150 Å and the other 100 Å thick, see Fig. 8a) doped with 5 wt.% of the blue fluorophore, 4,4′-*bis*(9-ethyl-3-carbazovinylene)-1,1′-biphenyl (BCzVBi). Exciton formation has been shown to occur in both blue fluorophore-doped regions [4]. Roughly 75% of the resulting phosphor emission is due to triplet diffusion from the EML edges followed by Dexter transfer to the dopants [4], with the remainder due to excitons formed by direct charge trapping on the phosphors.

Here, we quantitatively analyze the operation of this device in steady-state using the values of D and K_{TT} obtained in Section 5. We assume negligible diffusion of singlets away from their fluorescent zones at both EML edges due to their comparatively shorter diffusion lengths [8]. All quenching processes are neglected except T–T annihilation since it is expected to be the dominant source of loss for the diffusing triplets. In addition, we assume that triplets do not transfer to the blue fluorescent dopant due to the poor guest–host orbital overlap that results from their different molecular conformations [28]. Finally, the exciton distribution is assumed to exponentially decrease with distance from each edge of the EML [29] with characteristic length, d_{EX} (see Fig. 9b). In this structure, nearly every injected charge results in an exciton since the transport layers (NPD and BPhen) confine charge within the emissive layer, thereby providing balanced electron and hole injection [30].

The component of the external quantum efficiency due to blue emission from BCzVBi is directly proportional to the number of singlets present in the two fluorescent zones. Using the fluorescent quantum yield of BCzVBi (ϕ_{FL}) and the optical out-coupling efficiency through the glass substrate [18,31] ($\phi_{\mathrm{OC}} = 0.2$), we can estimate the singlet density, S, as a function of injection current density, J. By equating S to the integral of the singlet exciton formation profile (see Fig. 9b) over the two distinct fluorescent zones, we can determine the total exciton density distribution, since three triplets are formed for every singlet [26]. In addition, we allow for a fraction, α_{T}, of the total exciton population to form by trapping directly on the phosphors. Using this profile, the rate equations for the singlet and triplet densities in the emissive layer are

$$\begin{aligned}\frac{\partial T}{\partial t} = {} & D_{\mathrm{T}}\frac{\partial^2 T}{\partial x^2} - \frac{T}{\tau_{\mathrm{T}}} - k_{\mathrm{TT}}T^2 \\ & + \frac{3J(1-\alpha_{\mathrm{T}})}{qd_{\mathrm{EX}}(1-\exp[-x_0/d_{\mathrm{EX}}])}\left[\frac{\eta_{\mathrm{Blue}}}{\phi_{\mathrm{FL}}\phi_{\mathrm{OC}}}\right] \\ & \times\left(\delta_{\mathrm{Left}}\exp\left[\frac{-x}{d_{\mathrm{EX}}}\right] + \delta_{\mathrm{Right}}\exp\left[\frac{x-x_0}{d_{\mathrm{EX}}}\right]\right) \\ & + \left[\frac{3J(\eta_{\mathrm{Blue}})\alpha_{\mathrm{T}}}{q\phi_{\mathrm{FL}}\phi_{\mathrm{OC}}W_{\mathrm{PH}}} - TK_{\mathrm{TG}}\right]_{\substack{\mathrm{PH}\\ \mathrm{Rgn}}}, \end{aligned} \tag{6}$$

and

$$\begin{aligned}\frac{\partial S}{\partial t} = {} & -\frac{S}{\tau_{\mathrm{S}}} + \frac{J(1-\alpha_{\mathrm{T}})}{qd_{\mathrm{EX}}(1-\exp[-x_0/d_{\mathrm{EX}}])}\left[\frac{\eta_{\mathrm{Blue}}}{\phi_{\mathrm{FL}}\phi_{\mathrm{OC}}}\right] \\ & \times\left(\delta_{\mathrm{Left}}\exp\left[\frac{-x}{d_{\mathrm{EX}}}\right] + \delta_{\mathrm{Right}}\exp\left[\frac{x-x_0}{d_{\mathrm{EX}}}\right]\right) \\ & + \frac{J(\eta_{\mathrm{Blue}})\alpha_{\mathrm{T}}}{q\phi_{\mathrm{FL}}\phi_{\mathrm{OC}}W_{\mathrm{PH}}}. \end{aligned} \tag{7}$$

Here, $\delta_{\mathrm{Left/Right}}$ are the weighting fractions for exciton formation at the left/right side of the emissive layer (see Fig. 9b), and τ_{G} and τ_{S} are the phosphor and BCzVBi lifetimes, respectively. We find that $\phi_{\mathrm{FL}} \sim 0.6$ for BCzVBi in toluene solution, using

standard procedures [32]. Also, η_{Blue} is the forward-emitted external quantum efficiency (EQE) for an optimized, purely fluorescent device using a 5 wt.% BCzVBi:CBP emissive layer, and ranges from 2.7% at $J = 1\ mA/cm^2$ to 2.3% at $100\ mA/cm^2$. Any deviation in the blue component of the F/P WOLED efficiency from η_{Blue} is a result of the fraction, α_T, of excitons formed by direct charge trapping on the phosphor molecules outside of the fluorescent zones, as described by the last term on the right-hand side of Eqs. (6) and (7).

Solving Eqs. (6) and (7) in steady-state for $S(x)$ and $T(x)$, we can express the fluorescent (η_{FL}) and phosphorescent (η_{PH}) components of the total WOLED efficiency as

$$\frac{J}{q\phi_{OC}\phi_{FL}}(\eta_{FL}) = \frac{1}{\tau_S}\int_{\substack{\text{Fluor}\\ \text{Regions}}} S(x)\,dx, \tag{8}$$

and

$$\frac{J}{q\phi_{OC}}(\eta_{PH}) = \frac{1}{\tau_G}\int_{\substack{\text{PH}\\ \text{Region}}} [T(x) + S(x)]\,dx, \tag{9}$$

where the phosphor quantum yield is taken to be unity [33]. Fig. 10 summarizes the results, showing lines of constant component efficiency (solid = fluorescent; dashed-dotted = phosphorescent) at a current density of $10\ mA/cm^2$ for the device in Fig. 8, as determined from the weighted contributions of the dopant photoluminescent spectra to the device emission (see Fig. 8). These are overlaid on contours that indicate the percentage of total excitons formed by trapping on the phosphors (dotted line). Note that the total exciton fraction formed in the phosphor-doped region, indicated by the contours, is slightly greater than the trapping fraction, α_T, since the exponential tails of the edge formation distributions also extend into the phosphor-doped region.

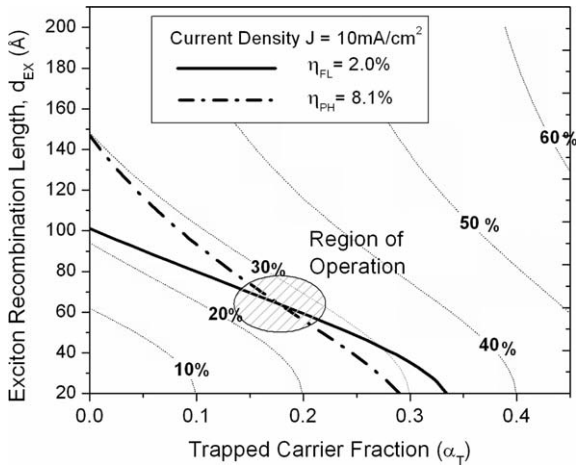

Fig. 10. Model results for the fluorescent/phosphorescent WOLED calculated using Eqs. (6)–(9) in text. The dotted contours indicate the percentage of excitons that are formed by direct charge trapping on the phosphor dopants. Superimposed on this contour plane are lines of constant component dopant efficiency at a current density of $J = 10\ mA/cm^2$ for the fluorophore (solid line) and phosphor (dashed-dotted line) that are obtained by fits to the WOLED device data of Ref. [4].

Although neither d_{EX} nor α_T are known, the device operating point must correspond to the crossing of the fluorescent and phosphorescent efficiency lines. The crossings at all current densities (1 and $100\ mA/cm^2$, not shown) lie within the shaded region of Fig. 10, indicating a characteristic exciton formation length of $d_{EX} \sim 75$ Å, and a total exciton trapping fraction of 20–30%.

In Fig. 11 we simulate the external quantum efficiency at this operating point. For the fluorescent component, we find good agreement at all current densities with the device data from Ref. [4], which has been reproduced for comparison. At low current densities, however, the model overestimates the phosphorescent emission component of the EQE. This discrepancy is attributed to losses, such

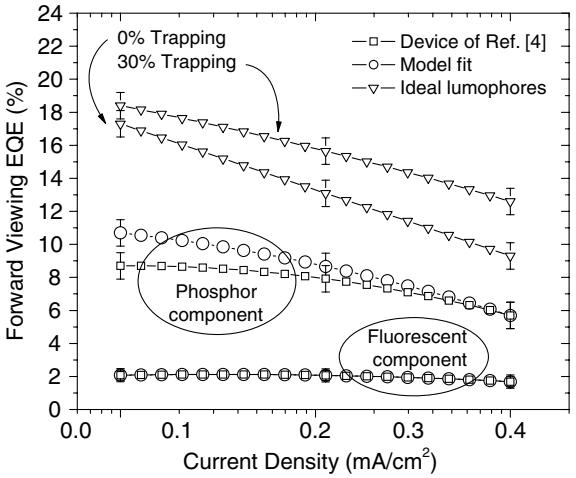

Fig. 11. Forward-emitted external quantum efficiency (EQE) vs. current density obtained from the data of Ref. [4] (squares) and the fit (circles) given by the model in the text. The separation of the device EQE data into individual fluorescent and phosphorescent contributions is obtained by weighting to the photoluminescent spectra of each lumophore in the fit to the WOLED emission spectrum as shown in Fig. 8, making sure to account for the intensity to quantum yield conversion. Inverted triangles indicate predictions for the structure in Fig. 8 using "ideal" emitters having unity quantum yield for the cases of 0% and 30% direct exciton formation on the phosphors.

as exciton–polaron and singlet–triplet quenching, not accounted for in the model. However, at higher current densities where T–T annihilation becomes the dominant source of loss, the model prediction falls close to the device data.

Balanced white emission with a high color rendering index [34] (CRI) can be achieved with a smaller blue emissive component than the singlet spin fraction ($\chi_S = 1/4$) affords. Charges that form excitons by trapping increase the phosphor emission at the expense of blue fluorescence, since they are prevented from otherwise forming BCzVBi singlets. Trap formation is thus beneficial to device performance since the trapped exciton fraction is not subject to diffusive transport losses, and the reduced triplet density at the EML edges decreases T–T quenching. From the photoluminescent spectrum of each dopant (see Fig. 8b), we calculate that CRI > 80 can be maintained for up to 35% exciton formation via direct trapping. Thus, the device of Ref. [4] operates close to the optimum point, representing a tradeoff between high efficiency and white color balance.

We can extend this model to predict the performance for this same structure using an ''ideal'' fluorescent dopant with unity luminescent quantum yield. As shown in Fig. 11, the maximum forward-emitted efficiency increases from 17% (CRI = 86) in the absence of trapping to 18.5% (CRI = 81) for an optimum trapping fraction of 30%. Accounting for all white light emitted [35] the total (integrated) external quantum efficiency for this optimized device is 31%. In addition, the roll-off in EQE with increasing current density is lessened (as compared to the device without trapping) since T–T annihilation is reduced, as discussed above.

7. Conclusions

We have studied triplet exciton diffusion in amorphous thin films of the commonly used organic semiconductor, CBP, using optically pumped time-of-flight techniques. The diffusion of triplets through a CBP spacer layer to a phosphor doped sensing layer was used to determine a diffusion coefficient of $D = (1.4 \pm 0.3) \times 10^{-8}$ cm^2/s, and a triplet–triplet annihilation rate $K_{TT} = (1.6 \pm 0.4) \times 10^{-14}$ cm^3/s. Both D and K_{TT} are similar in magnitude to corresponding results obtained for other amorphous, small-molecule films [11,36]. We also demonstrated that D can be reduced by a factor of four from its value in neat CBP by doping with the wide energy-gap molecule UGH2 at 18 wt.%, demonstrating that this dopant introduces scattering centers that frustrate exciton transport.

The model of exciton transport was extended to analyze the operation of a recently reported fluorescent/phosphorescent WOLED that depends on triplet diffusion to obtain high efficiency and a balanced white color emission. The model confirms that triplet diffusion is the dominant mechanism contributing to the total phosphor emission of this device, although charge trapping is also an important factor in obtaining optimum performance and color balance. Our analysis suggests that this particular device architecture can yield a total external quantum efficiency EQE = 31% using optimized dopants in a CBP host.

Acknowledgements

The authors thank Universal Display Corporation and the US Department of Energy for partial financial support of this work. In addition, we thank Dr. H. Kanno for sharing experimental data, as well as Prof. M. Thompson and Mr. R.J. Holmes for helpful discussions.

References

[1] B.W. D'Andrade, M.E. Thompson, S.R. Forrest, Adv. Mater. (Weinheim, Fed. Repub. Ger.) 14 (2002) 147–150.
[2] B.W. D'Andrade, S.R. Forrest, J. Appl. Phys. 94 (2003) 3101–3109.
[3] P. Peumans, A. Yakimov, S.R. Forrest, J. Appl. Phys. 93 (2003) 3693–3723.
[4] Y. Sun, N.C. Giebink, H. Kanno, B. Ma, M.E. Thompson, S.R. Forrest, Nature 440 (2006) 908–911.
[5] M. Pope, C. Swenberg, Electronic Processes in Organic Crystals and Polymers, Oxford University Press, New York, NY, 1999.
[6] M.A. Baldo, S.R. Forrest, Phys. Rev. B 66 (1999) 14422–14428.
[7] N. Matsusue, S. Ikame, Y. Suzuki, H. Naito, J. Appl. Phys. 97 (2005).
[8] C.W. Tang, S.A. Vanslyke, C.H. Chen, J. Appl. Phys. 65 (1989) 3610–3616.
[9] R.C. Powell, Z.G. Soos, J. Lumin. 11 (1975) 1–45.
[10] M.A. Baldo, C. Adachi, S.R. Forrest, Phys. Rev. B 62 (2000) 10967–10977.
[11] M.A. Baldo, S.R. Forrest, Phys. Rev. B 62 (2000) 10958–10966.
[12] D.L. Dexter, J. Chem. Phys. 21 (1953) 836–850.
[13] B. Movaghar, M. Grunewald, B. Ries, H. Bassler, D. Wurtz, Phys. Rev. B 33 (1986) 5545–5554.
[14] R. Richert, H. Bassler, J. Chem. Phys. 84 (1986) 3567–3572.
[15] D. Hertel, H. Bassler, R. Guentner, U. Scherf, J. Chem. Phys. 115 (2001) 10007–10013.

[16] S. Chandrasekhar, Rev. Modern Phys. 15 (1943) 1–84.
[17] M.A. Baldo, S. Lamansky, P.E. Burrows, M.E. Thompson, S.R. Forrest, Appl. Phys. Lett. 75 (1999) 4–6.
[18] B.W. D'Andrade, R.J. Holmes, S.R. Forrest, Adv. Mater. (Weinheim, Fed. Repub. Ger.) 16 (2004) 624–627.
[19] S.R. Forrest, Chem. Rev. 97 (1997) 1793–1896.
[20] N.J. Turro, Modern Molecular Photochemistry, University Science Books, Menlo Park, CA, 1991.
[21] X.F. Ren, J. Li, R.J. Holmes, P.I. Djurovich, S.R. Forrest, M.E. Thompson, Chem. Mater. 16 (2004) 4743–4747.
[22] R.J. Holmes, B.W. D'Andrade, S.R. Forrest, X. Ren, J. Li, M.E. Thompson, Appl. Phys. Lett. 83 (2003) 3818–3820.
[23] COMSOL_Multiphysics, Burlington, 2005.
[24] Y. Kawamura, H. Yamamoto, K. Goushi, H. Sasabe, C. Adachi, H. Yoshizaki, Appl. Phys. Lett. 84 (2004) 2724–2726.
[25] S. Lamansky, P. Djurovich, D. Murphy, F. Abdel-Razzaq, R. Kwong, I. Tsyba, M. Bortz, B. Mui, R. Bau, M.E. Thompson, Inorg. Chem. 40 (2001) 1704–1711.
[26] M.A. Baldo, D.F. O'Brien, M.E. Thompson, S.R. Forrest, Phys. Rev. B 60 (1999) 14422–14428.
[27] M.H. Abbasi, J.W. Evans, I.S. Abramson, AIChE J. 29 (1983) 617–624.
[28] C. Hosokawa, H. Higashi, H. Nakamura, T. Kusumoto, Appl. Phys. Lett. 67 (1995) 3853–3855.
[29] J. Kalinowski, N. Camaioni, P. Di Marco, V. Fattori, A. Martelli, Appl. Phys. Lett. 72 (1998) 513–515.
[30] C. Adachi, M.E. Thompson, S.R. Forrest, IEEE J. Selected Topics Quant. Electron. 8 (2002) 372–377.
[31] G. Gu, D.Z. Garbuzov, P.E. Burrows, S. Venkatesh, S.R. Forrest, M.E. Thompson, Opt. Lett. 22 (1997) 396–398.
[32] J.V. Morris, M.A. Mahaney, J.R. Huber, J. Phys. Chem. 80 (1976) 969–974.
[33] Y. Kawamura, K. Goushi, J. Brooks, J.J. Brown, H. Sasabe, C. Adachi, Appl. Phys. Lett. 86 (2005) 071104.
[34] In Method of measuring and specifying colour rendering properties of light sources, Commission Internationale de L'êclairage (CIE), 1974.
[35] B.W. D'Andrade, S.R. Forrest, Adv. Mater. 16 (2004) 1585–1595.
[36] J. Kalinowski, W. Stampor, J. Mezyk, M. Cocchi, D. Virgili, V. Fattori, P. Di Marco, Phys. Rev. B 66 (2002).

Available online at www.sciencedirect.com
ScienceDirect
Organic Electronics 7 (2006) 387–396
Organic Electronics
www.elsevier.com/locate/orgel

Spectroscopic study on sputtered PEDOT · PSS: Role of surface PSS layer

Jaehyung Hwang *, Fabrice Amy, Antoine Kahn

Department of Electrical Engineering, Princeton University, B420 Electrical Engineering, Engineering Quadrangle Olden St., Princeton, NJ 08544, USA

Received 6 January 2006; received in revised form 15 March 2006; accepted 25 April 2006
Available online 19 May 2006

Abstract

The structure of poly(3,4-ethylenedioxythiophene)–poly(styrenesulfonate) (PEDOT · PSS) consists of an insulating PSS layer surrounding doped PEDOT grains. In this study, X-ray and ultraviolet photoelectron spectroscopy (XPS and UPS) are used to investigate the composition and electronic structure of as-loaded and lightly sputtered PEDOT · PSS films. The sputtered film shows a significant increase in the PEDOT/PSS ratio (from 0.12 to 0.7) as well as a build-up of the density of filled states close to the Fermi level, consistent with the removal of the insulating PSS layer and the uncovering of the highly doped conducting PEDOT · PSS. The thickness of PSS layer is estimated at 35 ± 5 Å. The elimination of the PSS shell reduces PEDOT · PSS work function to a value equal to that of highly doped PEDOT. The effect of the PSS removal on the charge injection barrier at the interface with the hole-transport material *N*,*N*′-diphenyl-*N*,*N*′-bis(1-naphthyl)-1,1′-biphenyl-4,4′-diamine (α-NPD) is also investigated. The increase in interface dipole and hole-injection barrier suggests a stronger interaction between the two materials, and points out the key role of the PSS layer in making PEDOT · PSS an effective hole-injection material.

Keywords: PEDOT · PSS; XPS; UPS; Interfaces; Ion sputtering

1. Introduction

The structure of organic-based optoelectronic devices such as organic light emitting diodes (OLED) requires that at least one side of the device be conducting and transparent to the emitted photons. Finding high-performance conducting and transparent contacts has therefore long been one of the key issues for making OLEDs. In addition to conductivity and transparency, the work function of the contact is very important, as it affects directly carrier injection barrier and device performance.

Indium-tin-oxide (ITO) was an early favorite for hole-injection cathode, displaying good transparency and conductivity. Its average work function of 4.3 eV can be significantly increased using, for example, exposure to UV ozone, and can reach values in excess of 4.8 eV [1,2]. More recently, the search for material that would give lower hole-injection barrier focused on poly(3,4-ethylenedioxythiophene)–poly(styrenesulfonate) (PEDOT · PSS) (Fig. 1) as one of

* Corresponding author.
E-mail address: jhwang@princeton.edu (J. Hwang).

1566-1199/$ - see front matter © 2006 Elsevier B.V. All rights reserved.
doi:10.1016/j.orgel.2006.04.005

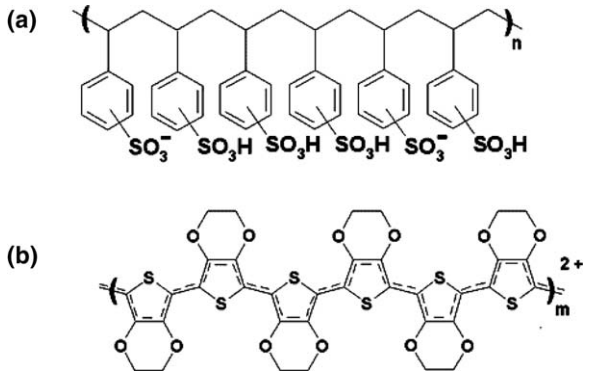

Fig. 1. Chemical structure of (a) PSS and (b) PEDOT. Dashed line in PEDOT shows the conjugation path through the backbone.

the most promising candidate for cathode in OLED. PEDOT is a derivative of polythiophene with dioxyethylene, which is stable in air in its doped oxidized form [3]. Because of its planar structure, which leads to high electron delocalization along the chain, PEDOT has relatively high conductivity (10^{-3}–10^{-5} S/cm for OLED grade) [4] and good transparency [5]. Insolubility, which was the major drawback, was solved by Bayer AG using a new polymerization of PEDOT using PSS as an electrolyte [6,7]. When mixed with PSS, PEDOT forms colloidal particles dispersed in water and becomes processible by simple spin-coating. The PSS also acts as a charge-compensating counter-ion and stabilizes the p-doped PEDOT [8]. Films of the PEDOT · PSS blend have a work function of 5.2 eV [9,10], which enables efficient hole-injection efficiency in OLEDs. PEDOT · PSS also gives longer device life time since it forms a blocking layer that prevents oxygen from ITO from diffusing into the active material (hole transport or emitting layer) [11].

In view of these advantages, many groups have worked on the electrical and chemical properties of PEDOT · PSS. One of the methods to investigate these properties is photoemission spectroscopy. Ultraviolet photoemission spectroscopy (UPS) and X-ray photoemission spectroscopy (XPS) are well-established methods to study valence states and core levels, and investigate both electronic and chemical properties of materials. Inverse photoemission spectroscopy (IPES) is equally useful, for investigating unoccupied electronic states of materials. Fig. 2 shows the combined UPS/IPES spectra of PEDOT · PSS measured in our laboratory, which demonstrate the first striking fact: the Fermi level (E_F) appears to lie near the middle of the gap, far from both bands and, in particular, from the filled states. This is in apparent contradiction with the fact that PEDOT is in a highly p-doped form. Note that this cannot be ascribed to a phenomenon of

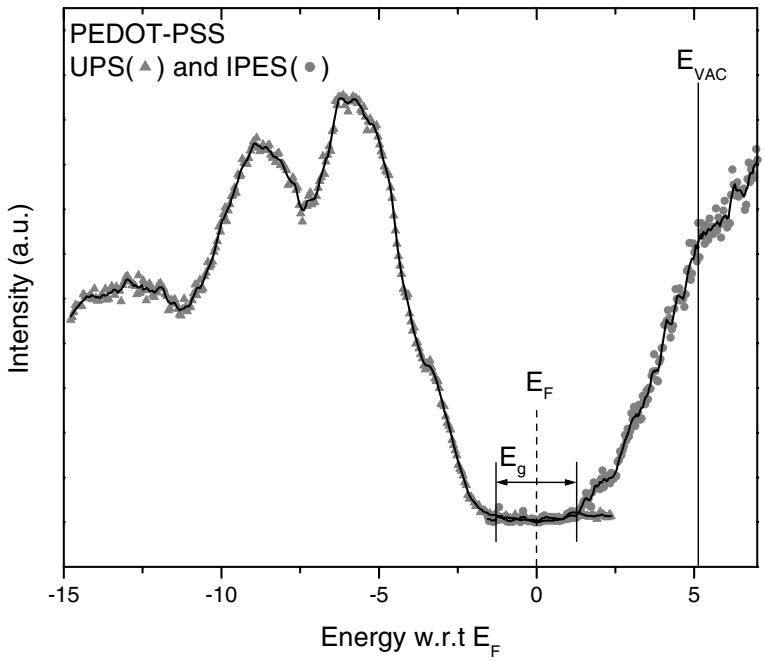

Fig. 2. Filled (▲) and empty (●) states of PEDOT · PSS measured with UPS and IPES, respectively.

''band bending'' at the surface of the polymer film, something that is frequently encountered at the surface of inorganic semiconductors and explained by surface state-induced E_F pinning deep in the gap. A second issue with PEDOT · PSS is the discrepancy between the PEDOT/PSS ratio measured by XPS and the known composition of the solution. In order to address the Fermi level and composition issues, Greczynski et al. proposed a structure of PEDOT grains enclosed in a PSS shell [12]. With this model, the lack of states near E_F is explained by the presence of the insulating PSS, which strongly attenuates the signal from the doped PEDOT grain. Similarly, the mismatch in the concentration ratio is explained by the layered structure: the top PSS attenuates the signal from the bulk PEDOT, and artificially decreases its apparent concentration.

In this study, we remove the top layer of PSS with light Argon sputtering and characterize the undamaged layer of the underlying PEDOT · PSS. Using XPS, we determine the PEDOT/PSS ratio in the bulk of the film, and estimate the thickness of the PSS shell. UPS spectra taken on the sputtered surface show a large increase in the density of filled states close to the Fermi level, consistent with the uncovering of the conductive doped PEDOT. Finally, we deposit a layer of the hole-transport material (HTM) *N*,*N*′-diphenyl-*N*,*N*′-bis(1-naphthyl)-1,1′-biphenyl-4,4′-diamine (α-NPD) to confirm that the increased density of state of the sputtered PEDOT · PSS substrate also leads to a stronger interaction with the organic semiconductor overlayer. We observe a larger interface dipole and hole-injection barrier for the interface formed on sputtered PEDOT · PSS, consistent with the presence of a larger density of induced interface states in the gap of the HTM.

2. Experimental

The PEDOT · PSS solution was obtained from Starks (Baytron® P AI 4083; OLED grade), stored at ~5 °C and brought up to room temperature before film preparation. According to Baytron®, the nominal PSS-to-PEDOT composition ratio is ~4.5:1 [4]. The ITO substrates are first cleaned chemically using sequential baths of Alconox®, acetone and iso-propanol, followed by exposure to UV-ozone for 30 min. The PEDOT · PSS solution is filtered through 0.45 μm PVDF filters and spun on the pre-cleaned ITO in nitrogen for 80 s at 3000 rpm, resulting in ~40 nm thick films. Following spin-coating, the films are annealed at 180 °C in dry nitrogen for 1 h to drive out residual water, and transferred without ambient exposure to the ultrahigh vacuum (UHV) chamber for UPS and XPS analysis (base pressure 2×10^{-10} Torr). Samples made for combined UPS/IPES analysis are transferred with short ambient exposure (2–3 min) to another chamber. Comparison via UPS of E_F position in the gap of the exposed and non-exposed films reveal no significant difference caused by the short air exposure.

UPS is done using the He I (21.22 eV) and He II (40.8 eV) photon lines of a He-discharge lamp. The photoelectrons are counted with a double-pass cylindrical mirror analyzer. The total energy resolution of the measurement is 150 meV, as determined from the width of the Fermi step measured on a clean poly-crystalline Au substrate. The ionization energy of the polymer film is defined here as the energy difference between the vacuum level, determined in a standard way from the position of the onset of photoemission, and the extrapolated leading edge of the highest occupied molecular orbital (HOMO) [13]. XPS is done with the MgK_α (1253.6 eV) line with a total energy resolution of ~0.9 eV. Sputtering of the PEDOT · PSS film is performed using 4×10^{-5} Torr of research grade purity Ar, at a very slow rate modulated by the ion energy (200–500 eV) and beam current density.

For the XPS analysis, particular attention is given to changes in the chemical state of sulfur and oxygen by following the evolution of the S 2p and O 1s core levels. Core level peak decomposition is done according to the work of Greczynski et al. [14]. When PEDOT · PSS is spun on a substrate without any acid treatment, it contains sodium residues from the $Na_2S_2O_8$ oxidizing agent used during the polymerization of PEDOT [3]. The present XPS analysis of the as-loaded PEDOT · PSS film (not shown here) clearly shows the presence of sodium with a relative Na/S concentration of ~80%. However, we are unable to correctly decompose the S 2p and O 1s core levels peaks assuming this concentration with all the Na present as PSS-Na. Our S 2p and O 1s peak decompositions suggest that only half of the Na is present as PSS-Na.

Finally, the interfaces between α-NPD and as-loaded or sputtered PEDOT · PSS are investigated by evaporating 30 Å of α-NPD for UPS interface measurements and 1000 Å of α-NPD for current–voltage (*I*–*V*) measurements. For the latter, a

300 Å top Au contact is thermally evaporated on top of α-NPD to form a PEDOT · PSS/α-NPD/Au structure (inset of Fig. 8) and study (hole-only) injection from the polymer electrode. Both Au deposition and *I–V* measurements are done in situ, without ever exposing the PEDOT · PSS/α-NPD structure to ambient atmosphere.

3. Results and discussion

The UPS spectrum of the top of the filled states and energy gap of an as-loaded PEDOT · PSS film, i.e. the UPS part of Fig. 2, is shown in Fig. 3. The enhancement of the spectrum by ×300 (inset) shows a clear density of states extending close to the Fermi level, in good agreement with the report by Greczynski et al. [14] which suggests that the density of states of the doped PEDOT film is indeed suppressed by an overlayer in this surface sensitive measurement.

Spectra (i) in Fig. 4 correspond to the S 2p and O 1s core levels of the as-loaded PEDOT · PSS film. The peak decomposition of the S 2p core level assumes a spin–orbit splitting ($2p_{3/2}$ and $2p_{1/2}$) of 1.2 eV and the statistical 1:2 branching ratio for p-levels. Following the interpretation of Greczynski et al. [12,14], the PSS peaks are decomposed into PSSH and PSS-Na only, neglecting the PSS^- component. The S 2p level shows large differences in binding energy depending on the S location (PEDOT or PSS), which makes it very suitable for composition analysis of the sample. Low binding energy peaks correspond to PEDOT and high binding energy peaks come from PSS complexes (heretofore PSS denotes PSS complexes, unless otherwise mentioned). The O 1s core level (Fig. 4(b)(i)) can also be decomposed into PEDOT, PSSH, and PSS-Na components. Unlike for the S 2p case, however, the PSSH contribution to the O 1s peak must be decomposed in two parts, i.e. two oxygen atoms corresponding to O–S bonds and one to the O–H bond. From the S 2p data, the PEDOT-to-PSS ratio of the as-loaded PEDOT · PSS is estimated at ~0.12. The same analysis using the O 1s core level leads to a ratio of ~0.16. Both values are smaller than that given by the supplier (0.22), but consistent with previously reported studies [12,14].

The evolution of the S 2p and O 1s core levels with increasing sputtering time is shown is Fig. 4(ii)–(v). The Ar^+ ion beam density is 9×10^{11} ions/cm^2 s with an energy of 0.25 kV. Note that the Na signal is eliminated after the shortest sputtering time, suggesting that Na is initially segregated at the surface of the film and is therefore easily

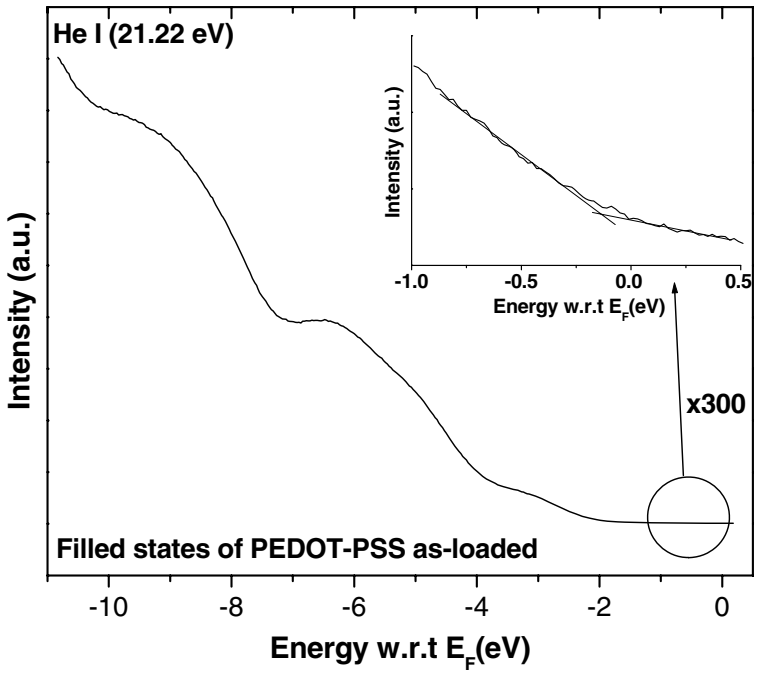

Fig. 3. UPS spectra (He I, $h\nu = 21.22$ eV) of as-loaded PEDOT · PSS. Inset shows magnified view (×300) of the DOS near E_F.

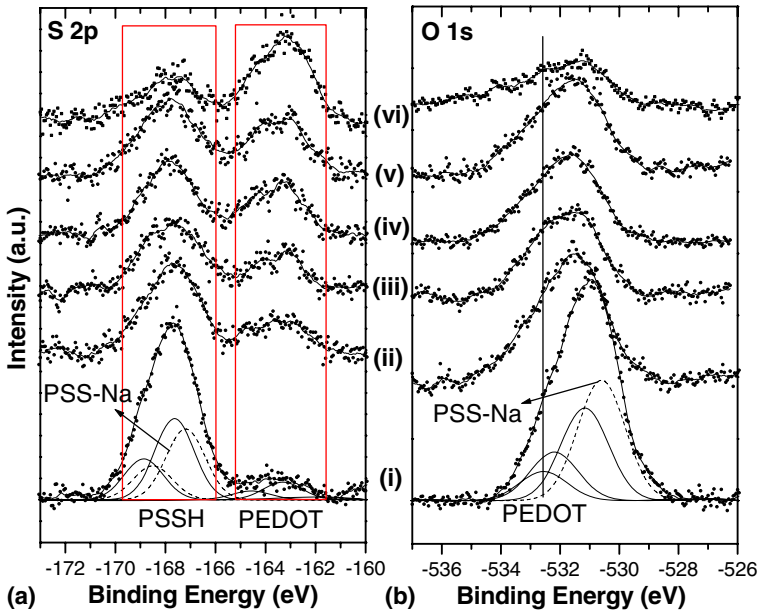

Fig. 4. XPS spectra of S 2p and O 1s with the MgK_α ($h\nu = 1253.6$ eV) for as-loaded PEDOT · PSS (with peak decomposition) (i) and PEDOT · PSS after light sputtering (9×10^{11} ions/cm^2 s, 0.25 kV) for 5 min (ii), 10 min (iii), 20 min (iv), 30 min (v) at 250 V, 5 mA. Sample (vi) was sputtered at higher rate (9×10^{12} ions/cm^2 s, 0.5 kV).

sputtered away. This is consistent with the fact that Na can be also washed out with a quick rinse in 10% HCl.

The evolution of the S 2p core level shows an increase in the PEDOT-to-PSS ratio up to 20 min of sputtering, after which the ratio remains constant at ~0.7. The same behavior is observed for the O 1s peak, though it is harder to separate the contribution from each component. The ratios extracted from the two elements (S and O) are entirely consistent (Fig. 5).

Harsher sputtering conditions (9×10^{12} ions/cm^2 s with energy of 0.5 kV, 5 min) were used to assess the damage induced by Ar ions (Fig. 4(vi)). The S 2p peak indicates that only a very small amount of PSS is left in the film. Moreover, a large decrease in O intensity is observed. These two observations suggest that the composition of the film is drastically changed by the harsher sputtering conditions: the SO_3 from the PSS as well as the dioxyethylene from the PEDOT are sputtered away, leaving only the thiophene in the film. The film also becomes less transparent, which might be an indication of de-doping (reduction due to loss of SO_3^- counter-ion) and destruction of the PEDOT · PSS film [16].

Even with the milder sputtering conditions used from steps (ii) to (v), damaging of the film surface is still expected, however it seems that the bulk of the PEDOT · PSS is well preserved. The residual peaks needed for correct decomposition of the S 2p and O 1s core levels are likely to correspond to the fraction of damaged polymers chains. However the fact that the PEDOT-to-PSS ratio remains constant and S and O maintains the same concentration regardless of sputtering time (after 20 min) suggests that sputtering has removed the PSS layer and reached the bulk of the PEDOT-PSS, and hence only the bulk of PEDOT-PSS is seen with XPS. There is no change in film transparency after 30 min of gentle sputtering, unlike what was observed when using higher sputtering rates. It is likely that lower sputtering rates can still induce some damages to the polymer film, however the damaged material is mostly sputtered away and only the very top layer is disturbed. To verify this point, conductivity measurements were performed on both sputtered and as-loaded films via 4-point probe. For this measurement, the PEDOT · PSS film was spun on a glass substrate to insure that the measured conductivity was that of PEDOT · PSS, and not of the substrate (e.g. ITO). Both as-loaded and sputtered films gave identical results, which confirms that light sputtering, as done in our study, does not destroy the conjugation path on the backbone of the polymer chain in the bulk, but only disturbs and removes

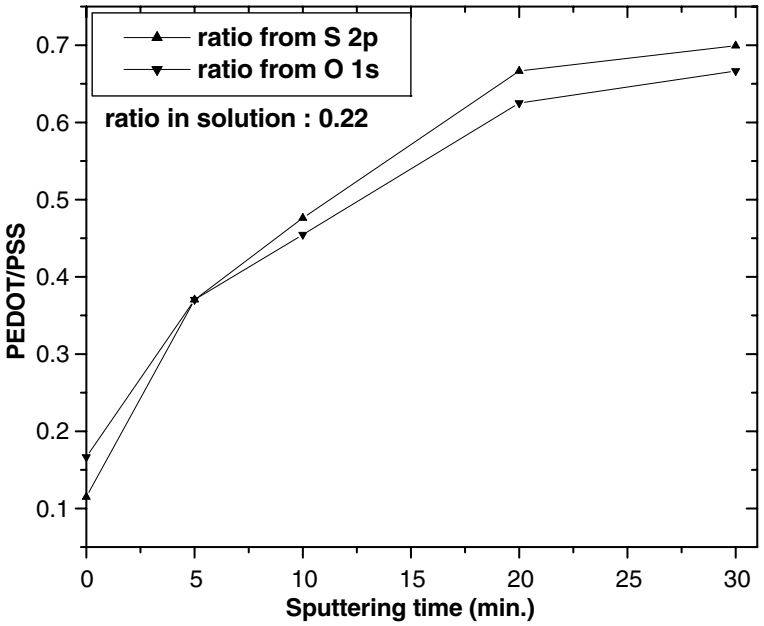

Fig. 5. Ratio of PEDOT to PSS vs. sputtering time deduced from S 2p (▲) and O 1s (▼) peak decomposition. The ratio in the original solution is 0.22.

the surface part of the film. For both S 2p and O 1s core levels, most of the XPS signal comes from a depth of about 40 Å (electron mean free path ~20–25 Å), therefore the contribution from the undamaged bulk PEDOT · PSS dominates the signal. In contrast, at higher sputtering rate, the damage goes beyond the probing depth of XPS and the destroyed part of the sample dominates the signal. The composition obtained from XPS using lower sputtering rate is therefore closer to the nominal bulk composition of PEDOT · PSS, with a PEDOT to PSS ratio of ~0.7.

The PSS layer thickness can be evaluated using the measured PEDOT-to-PSS ratio of as-loaded (0.12) and sputtered PEDOT · PSS (0.7). For the as-loaded sample, the assumed structure is that of a pure PSS layer on top of the doped PEDOT · PSS. As the XPS signal is recorded using normal emission geometry, the signal intensity from the PEDOT and the PSS of the as-loaded film can be written as

$$
\begin{aligned}
I_{\mathrm{PEDOT}} &= \frac{r}{1+r}\cdot I^{0}_{\mathrm{PEDOT}}\exp(-d/\lambda)\\
I_{\mathrm{PSS}} &= I^{0}_{\mathrm{PSS}}\left[(1-\exp(-d/\lambda)+\left(1-\frac{r}{1+r}\right)\exp(-d/\lambda)\right]\\
&= I^{0}_{\mathrm{PSS}}\left\{1-\frac{r}{1+r}\cdot\exp(-d/\lambda)\right\}
\end{aligned}
\tag{1}
$$

where r is the ratio of PEDOT-to-PSS in the bulk of the doped film, which is measured on the sputtered PEDOT · PSS sample, λ is the inelastic mean free path of electrons at the detecting kinetic energy (~1100 eV in this case) and d is the thickness of the PSS layer. I^{0}_{PEDOT} and I^{0}_{PSS} would be the intensities measured from pure PEDOT or PSS sample with infinite thickness. Since we measure S 2p for both PEDOT and PSS, these intensities cancel out in the analysis. Using the S 2p core level XPS data (Fig. 4) and an inelastic mean free path of 27 ± 3 Å [23], the thickness of the PSS layer is estimated at 35 ± 5 Å.

Fig. 6(a) and (b) compare the He I (21.22 eV) and He II (40.8 eV) UPS spectra of as-loaded and sputtered PEDOT · PSS. The as-loaded PEDOT · PSS film has a work function of 5.15 ± 0.05 eV, which is in good agreement with previously reported studies [9,10]. After sputtering, the work function is lowered by 0.4 eV. Although the surface is now a mixture of PEDOT and PSS, the work function agrees quite well with what is expected for a highly p-doped PEDOT [17]. The most striking result is the dramatic increase of the density of state close to the Fermi level. The inset of Fig. 6(a) shows the logarithmic plot of the He I UPS signal intensity between −2.5 eV and E_{F}. It shows that the intensity is nearly an order of magnitude larger for the

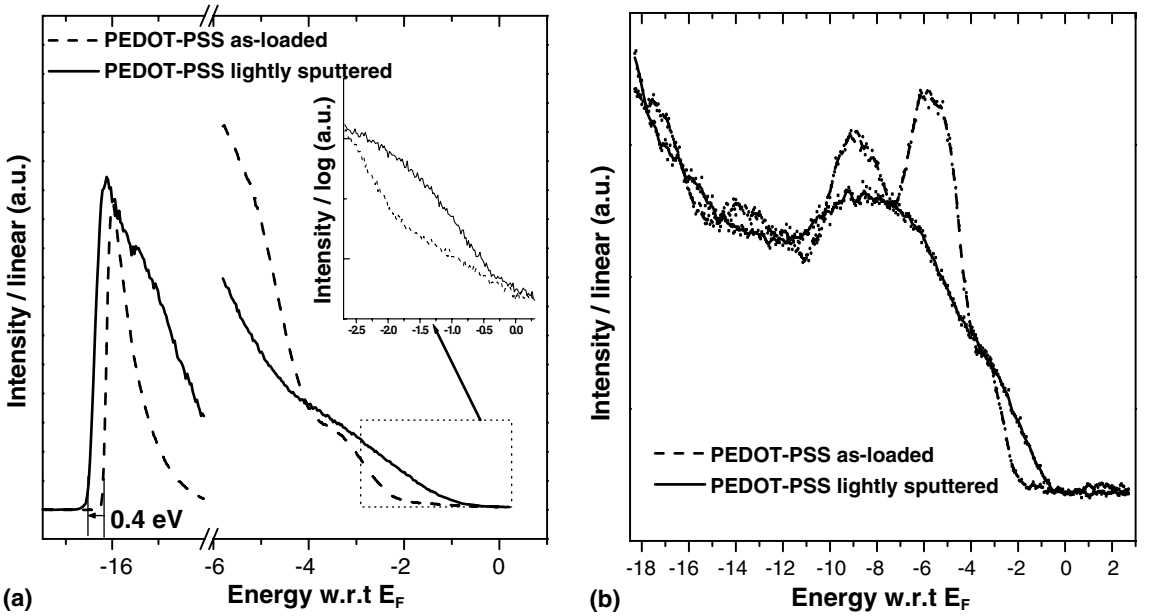

Fig. 6. UPS spectra of PEDOT · PSS before sputtering (dashed line) and after sputtering (solid line) using (a) the He I line (21.22 eV) and (b) the He II line (40.8 eV). The inset in (a) shows a logarithmic plot of the DOS near E_F.

sputtered sample than for the as-loaded one, and that the states extend up to ~250 meV below the Fermi level. The kinetic energy of the corresponding electrons is 13–15 eV, which leads to a relatively large inelastic mean free path of ~12–15 Å [15]. Such a mean free path in Eq. (1) yields a PSS thickness of about 20 Å. This is somewhat thinner than the thickness estimated from the XPS data, although a factor of two is not totally unreasonable in this type of measurement. The discrepancy is also probably due to the disruption and reduction of the highest occupied states by sputtering. In any case, the increase in intensity near Fermi level is a clear indication that, although the surface layer of insulating PSS has no states around the Fermi level, the bulk of PEDOT · PSS underneath this layer exhibits filled (valence) states up to E_F, as expected for a heavily p-doped PEDOT layer. Interestingly, the sputtering does not appear to induce a significant density of electronic states deep in the gap, as would be generally observed on inorganic semiconductor surfaces. Such a density of defect states would pin the Fermi level deep in the gap at the surface, causing significant band bending. If defect states are created by sputtering, it is therefore likely that their energy is either close to HOMO level or lower (in the filled valence state energy range).

Considering the superior performance of PEDOT · PSS as an electrode, a key question is whether the insulating PSS shell is a facilitator or impediment to the hole-injection process. To investigate this point, layers of the hole-transport material α-NPD are deposited on both sputtered and as-loaded PEDOT · PSS, and the hole-injection barrier and *I–V* characteristics are measured via UPS and tested via *I–V* measurements. The results from UPS measurements are summarized in Fig. 7. The as-loaded PEDOT · PSS film has a 0.4 eV higher work function than the sputtered film. On the as-loaded film, E_F-$HOMO_{\alpha-NPD}$ is smaller than on the sputtered film (0.47 eV vs. 0.97 eV) and so is the interface dipole (0.14 eV vs. 0.24 eV). This results in a 0.5 eV increase in the hole-injection barrier with sputtered PEDOT · PSS, which is larger than the change in substrate work function (0.4 eV).

This difference in hole-injection barrier is correlated with *I–V* measurements done on PEDOT · PSS/α-NPD(1000 Å)/Au (Fig. 8; the inset shows the structure of the measured device). The top Au layer freshly evaporated in UHV is known to form a high work function contact (~5.2 eV) on the organic material [25]. A negative voltage applied to the top Au contact results therefore in a hole-only current injected from PEDOT · PSS. The current

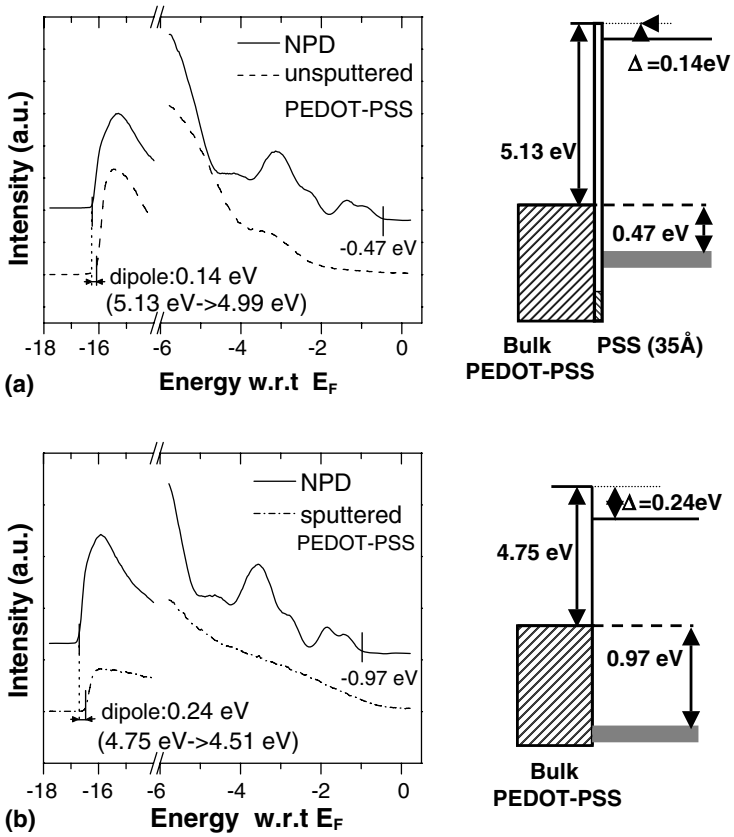

Fig. 7. UPS spectra and energy band diagram of a 30 Å α-NPD deposited on as-loaded PEDOT · PSS (a) and sputtered PEDOT · PSS (b).

through α-NPD on as-loaded PEDOT · PSS shows a sharp increase around 3 V and is thereafter higher by 2 orders of magnitude than the current injected from sputtered PEDOT · PSS, confirming the difference in hole-barrier.

The S interface parameter, used to quantify the variation of Schottky barriers as a function of metal work function or electronegativity at metal/semiconductor interfaces, describes how the metal/semiconductor interaction is screened at the interface. S is defined as $S = \frac{d\phi_n}{d\phi_M}$, where ϕ_n is the electron injection barrier and ϕ_M, the metal work function. The S parameter ranges between 0 and 1: $S = 0$ means that the Fermi level is pinned at one point in the gap regardless of the metal work function, and $S = 1$ means that the Fermi level is free to move within the gap (Schottky–Mott limit). S has been used successfully to describe a range of metal/organic interfaces, and was found to be ~0.5 for α-NPD [18–20]. Yet, the measurements presented here for α-NPD on as-loaded and sputtered PEDOT · PSS show that the injection barrier change (0.5 eV) is larger than the change in electrode work function (0.4 eV), leading to an un-physically large S.

To resolve this apparent discrepancy, the interaction between organic molecules and substrates is reconsidered in light of a recent investigation of the formation of interfaces on contaminated metal surfaces[22]. Interfaces of small-molecule organic semiconductors with clean metals have S between 0 and 0.8 [18–20], depending on the organic material, whereas polymers generally lead to S closer to 1 [21]. In a recent study, Wan et al. demonstrated that even for small molecules S gets closer to unity when using metal substrates contaminated by air exposure (mostly hydrocarbon contamination) [22] or modified by a specific treatment such as UV–ozone exposure. The interpretation is that contamination (or product of surface treatment) physically and electronically decouples the organic film from the continuum of the metallic electronic states [22,24]. This in turns, decreases the interaction between the two materials, reduces the density of interface states induced in the gap of the organic

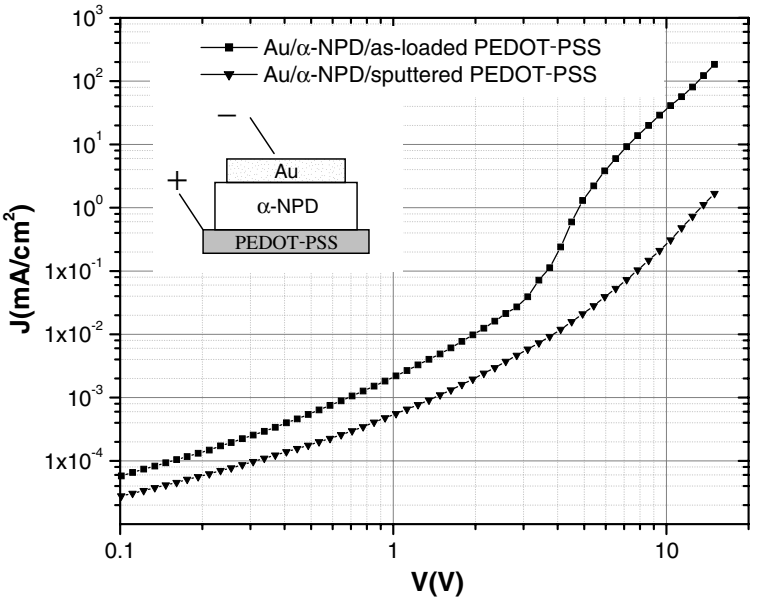

Fig. 8. *I–V* measurement of Au/α-NPD/as-loaded PEDOT · PSS (■) and Au/α-NPD/sputtered PEDOT · PSS (▼). Inset shows the structure of measured device. Bias is such that holes are injected from the PEDOT · PSS.

material, reduces the interface dipole and results in near vacuum-level alignment. The *S* parameter measured or calculated for interfaces with clean metals [18–20] cannot therefore be applied to describe contaminated interfaces, since the interaction between the organic material and the electrode is drastically changed by insertion of contaminants.

A similar argument is applied to the PEDOT · PSS/α-NPD interface. On the as-loaded PEDOT · PSS substrate, the PSS layer prevents any strong interaction between the heavily doped PEDOT and α-NPD. The α-NPD film is in contact with the large band gap insulating PSS layer, whose density of states around the Fermi level is negligible (Fig. 2). Since the PSS density of states does not overlap with the α-NPD gap and anchor energy levels, only a small interface dipole is formed. In contrast, after sputtering, the interface is formed between α-NPD and the heavily doped PEDOT. The larger density of PEDOT valence states overlaps with the gap of the α-NPD, resulting in a stronger interaction that leads to a stronger "pinning" of the Fermi level in the organic gap and a larger interface dipole. Going from as-loaded to sputtered PEDOT · PSS changes not only the work function of the electrode but also the type of interaction with the α-NPD layer. Thus the *S* parameter obtained from measurements on interfaces formed on as-loaded vs. sputtered PEDOT · PSS substrate is different than that reported for clean metals.

4. Summary

The surface electronic structure and composition of as-loaded and Ar-ion sputtered PEDOT · PSS films were investigated. The apparent discrepancy between the notion of a heavily p-doped hole-injection layer and the observation of the Fermi level near mid-gap on the as-loaded material is explained by the presence of a thin insulating PSS layer at the surface of the PEDOT · PSS grains. Gentle sputtering of the film removes this PSS-rich top layer without damaging the bulk of the film and leads to the determination of the composition of the bulk of PEDOT · PSS blend. The bulk PEDOT/PSS ratio and thickness of the PSS overlayer are estimated at 0.7 and 35 ± 5 Å, respectively. The removal of the PSS overlayer uncovers the large density of the filled states close to the Fermi level that corresponds to p-doped PEDOT. Removing the PSS layer also changes the interaction between the hole-injection layer and a hole-transport materials deposited on it. The small hole-injection barrier at the PEDOT · PSS/α-NPD interface, as seen by UPS and *I–V* measurements, increases by more than the decrease in PEDOT · PSS work function when the PSS shell is removed. This points out the very important role of the insulating PSS layer, which, not only gives its large work function to the PEDOT · PSS film large (~5.2 eV), but also reduces the interaction between the valence states

of the doped PEDOT and the HTM, leading to a smaller interface dipole and hole-injection barrier.

Acknowledgement

Funding of this work by the DOE (DE-FG02-04ER46165) is gratefully acknowledged.

References

[1] C.C. Wu, C.I. Wu, J.C. Sturm, A. Kahn, Appl. Phys. Lett. 70 (1997) 1348.
[2] S.Y. Kim, J. Lee, K. Kim, Y. Tak, J. Appl. Phys. 95 (2004) 2560.
[3] L. Groenendaal, F. Jonas, D. Freitag, H. Pielartzik, J.R. Reynolds, Adv. Mater. 7 (2000) 481.
[4] Bayer, Bayer P VP AI 4083 Product information, Bayer, 2005.
[5] H.C, Starks, Baytron® Micro symposium, 2002.
[6] F. Jonas, W. Kraft, B. Muys, Macromol. Symp. 100 (1995) 169.
[7] F. Jonas, G. Heywang, Electrochim. Acta 39 (1995) 1345.
[8] S. Ghosh, O. Inganäs, Synth. Met. 126 (2002) 311.
[9] N. Koch, A. Kahn, J. Ghijsen, J.J. Pireux, J. Schwartz, R.L. Johnson, A. Elschner, Appl. Phys. Lett. 82 (2003) 70.
[10] J. Huan, P.F. Miller, J.S. Wilson, A.J. de Mello, J.C. de Mello, D.D.C. Bradley, Adv. Funct. Mat. 15 (2005) 290.
[11] Y. Cao, G. Yu, C. Zhang, R. Menon, A.J. Heeger, Synth. Met. 87 (1997) 171.
[12] G. Greczynski, Th. Kugler, W.R. Salaneck, Thin Solids Films 354 (1999) 129.
[13] D. Cahen, A. Kahn, Adv. Mat. 15 (2003) 271.
[14] G. Greczynski, Th. Kugler, M. Keil, W. Osikowicz, M. Fahlman, W.R. Salaneck, J. Electron. Spectrosc. Relat. Phenom. 121 (2001) 1.
[15] M.P. Seah, W.A. Dench, Surf. Interf. Anal. 1 (1979) 2.
[16] J.C. Gustafsson, B. Liedberg, O. Inganäs, Polymer 10 (1994) 35.
[17] K.Z. Xing, M. Falman, X.W. Chen, O. Inganäs, W.R. Salaneck, Synth. Met. 89 (1997) 161.
[18] H. Ishii, E. Sugitama, E. Ito, K. Seki, Adv. Mater. 11 (1999) 605.
[19] A. Kahn, N. Koch, W. Gao, J. Polym. Sci., Polym. Phys. 41 (2003) 2529.
[20] H. Vázquez, W. Gao, F. Flores, A. Kahn, Phys. Rev. B 71 (2005) 041306.
[21] T. Kulger, W.R. Salaneck, H. Rost, A.B. Holmes, Chem. Phys. Lett. 310 (1999) 391.
[22] A. Wan, J. Hwang, F. Amy, A. Kahn, Org. Electron. 6 (2005) 47.
[23] P.J. Cumpson, M.P. Seah, Surf. Interf. Anal. 25 (1997) 430.
[24] H. Vazquez, R. Oszwaldowski, P. Pou, J. Ortega, R. Perez, F. Flores, A. Kahn, Europhys. Lett. 65 (6) (2004) 802.
[25] A. Kahn, N. Koch, W. Gao, J. Polym. Sci., Polym. Phys. 41 (2003) 2529–2548.

Available online at www.sciencedirect.com
ScienceDirect
Organic Electronics 7 (2006) 397–402
Organic Electronics
www.elsevier.com/locate/orgel

Polymeric electronic oscillators based on bistable conductance devices

José A. Freire [a], Guilherme A. Dal Moro [a], Rogério Toniolo [a], Ivo A. Hümmelgen [a,*], Carlos A. Ferreira [b]

[a] *Departamento de Física, Universidade Federal do Paraná, Caixa Postal 19044, 81531-990 Curitiba, PR, Brazil*
[b] *LAPOL/PPGEM, Universidade Federal do Rio Grande do Sul, Caixa Postal 15010, 91501-970 Porto Alegre, RS, Brazil*

Received 20 March 2006; received in revised form 3 May 2006; accepted 4 May 2006
Available online 5 June 2006

Abstract

We show electrical oscillatory behavior in simple circuits using poly(1,5-diaminonaphthalene)-based volatile switches and determine the analytical expression for the oscillation period, as well as the minimum allowed oscillation period as a function of oscillator capacitance, series resistance, the switch resistance in the ON- and OFF-states and switch critical voltages for the ON–OFF and OFF–ON transitions.

PACS: 84.30.Ng; 81.05.Hd; 85.30.De

Keywords: Organic switches; Organic oscillators; Bistable conductance

1. Introduction

In the last years several organic materials presenting an abrupt switching of electrical resistance [1–14] that can be controlled through the applied voltage [5–8,10] were observed. In some of these devices an OFF-state (highly resistive) remains until a voltage (V) above a critical value (V_{crit}) is applied to the device. For $V > V_{crit}$, the device resistance is reduced by up to six orders of magnitude [4,5,7,8,10]. In some of the reported devices [4,5,7] this ON-state condition remains so long as the applied voltage is maintained above a lower limit-value (V_{hold}) and for $V < V_{hold}$, the OFF value is restituted. The phenomenon is reversible, the ON–OFF transition is fast and V_{crit} and V_{hold} were observed to be proportional to the material layer thickness, so that these parameters can be controlled [5,7].

The ON–OFF transition has been attributed to different mechanisms. It was explained as originated by different conductivities presented by the organic material at different charge states [8,15] with a possible contribution of conformational changes of the molecules under high electric fields [16] (the electronic density of states is highly sensitive to molecular conformation). In some cases, the effect was attributed to charge traps in the organic layer of the device [17–19] or even to nanoparticles

* Corresponding author. Fax: +55 413613645.
E-mail address: iah@fisica.ufpr.br (I.A. Hümmelgen).

1566-1199/$ - see front matter © 2006 Elsevier B.V. All rights reserved.
doi:10.1016/j.orgel.2006.05.001

intentionally introduced [20] or accidentally precipitated inside the organic semiconductor film during metal electrode evaporation [21].

Some years ago the use of these switches for organic memories has been proposed [5]. The potential application in organic memory devices [22–28] increased the interest concerning these switches, motivated by the perception that existing technologies are inadequate in one or more memory operating parameters [20]. Apart from this major research effort, quite simple organic oscillators were also demonstrated using bistable volatile conductance switching devices [29].

In this article, we demonstrate the construction of an oscillator based on an organic switch. To exemplify it, we use poly(1,5-diaminonaphthalene), PDAN, whose electrical switching properties are essentially similar to previously reported poly(5-amino 1-naphthol) switches [4]. The molecular structure of PDAN is shown in Fig. 1. The construction of the oscillator is similar to a previously reported oscillator based on a poly(5-amino 1-naphthol) [29]. It uses, besides the organic switch, a capacitor and a resistor (see Fig. 2). In this article we obtain the theoretical expression for the frequency of the oscillator constructed in this manner and we discuss the requirements for the organic switch for successful construction of oscillators, particularly emphasizing the requirements for building high frequency oscillators.

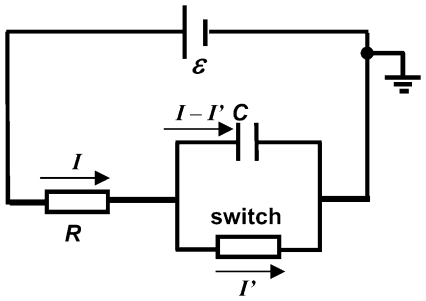

Fig. 2. Oscillator circuit composed by a PDAN-switch, a resistor R and a capacitor C. The applied voltage ε is supplied by a voltage source.

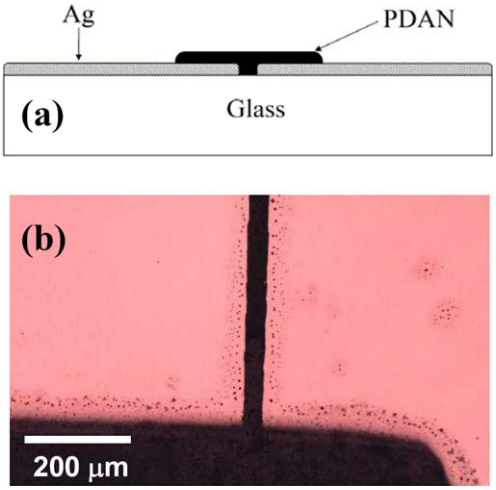

Fig. 3. (a) Schematic lateral view of the PDAN-switching devices. (b) Optical micrograph of the area of the Ag film containing the scratch, observed through the glass substrate (bottom view).

2. Experimental

The switching device was constructed by evaporating a ~200 nm thick Ag film on glass substrate. In the sequence the film was scratched using a tungsten tip with 17.15 g load. The scratch produces a well-defined ~27 μm wide gap in the Ag film, as can be seen in Fig. 3. The PDAN, whose synthesis is reported elsewhere [30,31], was deposited in the gap region by dropping a 10 mg/ml PDAN:DMF solution (DMF: *N*-*N*′-dimethylformamide). After deposition the samples were dried for 2 h at room temperature in flowing nitrogen, leading to a 1500 nm thick film. This planar geometry was chosen to minimize the capacitance of the switch, which would be higher in a sandwich structure, and to reduce shorts probability due to the high roughness of the deposited PDAN films.

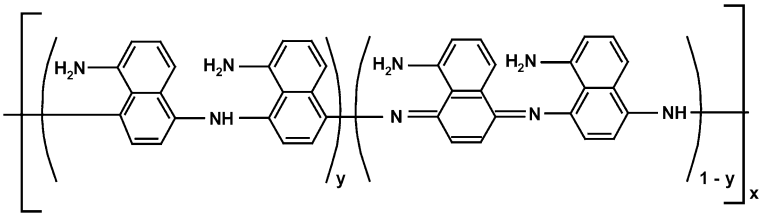

Fig. 1. Structure of poly(1,5-diaminonaphthalene). If the polymer is totally reduced $y = 1$ and if it totally oxidized $y = 0$.

The oscillator was constructed associating the switching device with a capacitor of capacitance C and a series resistance R as shown in Fig. 2. A voltage source was used to apply a voltage ε to the circuit and the voltage drop in the series resistor was recorded with an oscilloscope.

3. Results

3.1. Switch and oscillator

The electrical characteristic of switching devices presenting bistable conductivity is presented in Fig. 4(a). In these devices the OFF-state (highly resistive) remains until a voltage V above a critical value V_{crit} is applied to the device. For $V > V_{crit}$, the device resistance is rapidly reduced and this ON-state condition remains so long as the applied voltage is maintained above a lower limit-value V_{hold}. For $V < V_{hold}$, the OFF value is restituted and the cycle can be repeated. A relatively high dispersion of V_{crit} and V_{hold} values is observed in a set of devices with nominally identical characteristics. We attribute this problem, in part, to the bad film-forming properties of the material, which presents high roughness after deposition. But such a high dispersion was reported even in case of devices produced under much more refined conditions [20].

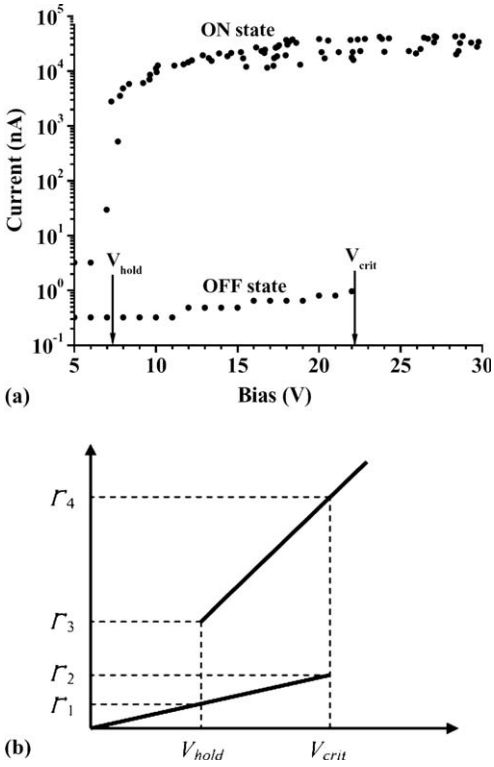

Fig. 4. (a) Electrical characteristics of a planar Ag/PDAN/Ag bistable conductance switch. (b) The electrical characteristics of the model for the switch that was used in the theoretical analysis.

The plot of the current through the series resistor versus time of an oscillator constructed using $R = 101$ MΩ, $C = 10$ nF is presented in Fig. 5, demonstrating the oscillating behavior. For this oscillator, the frequency is $f = 0.77$ Hz.

3.2. Theoretical analysis of the oscillator

Consider a switch, with characteristics like those presented in Fig. 4(b), used in a circuit like that of Fig. 2. In order to obtain an analytical solution, the switch resistance is assumed to be constant, independent of the potential applied to the switch device, both in the OFF-state (R_{off}) and in the ON-state (R_{on}). Denoting by I the current that passes through R and I' the current that passes through the switch of resistance r (which can be either R_{on} or R_{off}), one has

$$\varepsilon = RI + rI'. \tag{1}$$

The relationship between I and I' is obtained from $\frac{Q}{C} = rI'$, where $\frac{dQ}{dt} = I - I'$ and Q is the charge in the capacitor. It follows that $I - I' = rC\frac{dI'}{dt}$. This equation has as solution

$$I'(t) = I'_0 e^{-t/rC} + \int_0^t e^{-(t-t')/rC}\frac{I(t')}{rC}dt', \tag{2}$$

where I'_0 is fixed by the initial condition. The resulting integro-differential equation for $I(t)$ reads:

$$\varepsilon = RI + rI'_0 e^{-t/rC} + \frac{1}{C}\int_0^t e^{-(t-t')/rC} I(t')dt'. \tag{3}$$

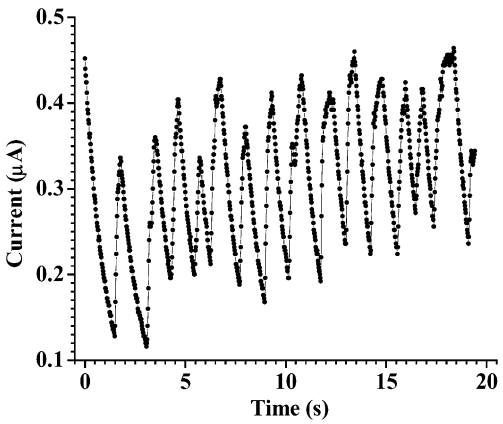

Fig. 5. Current as a function of time in a resistor $R = 101$ MΩ of an oscillator constructed with $C = 10$ nF, $\varepsilon = 100$ V.

The solution of this equation is

$$I(t) = \frac{\varepsilon}{R+r} + \frac{r}{R}\left(\frac{\varepsilon}{R+r} - I'_0\right)\exp(-t/\tau), \tag{4}$$

where $\tau = rRC/(r+R)$ is the characteristic time. The corresponding expression for $I'(t)$ is

$$I'(t) = \frac{\varepsilon}{R+r} + \left(I'_0 - \frac{\varepsilon}{R+r}\right)\exp(-t/\tau). \tag{5}$$

These expressions assume that the switch resistance r does not change in the time interval between $t = 0$ and t. In the case of a switch four currents are of relevance, see Fig. 4(b):

$$I'_1 = \frac{V_{\text{hold}}}{R_{\text{off}}} < I'_2 = \frac{V_{\text{crit}}}{R_{\text{off}}} \quad \text{and} \quad I'_3 = \frac{V_{\text{hold}}}{R_{\text{on}}} < I'_4 = \frac{V_{\text{crit}}}{R_{\text{on}}}. \tag{6}$$

Two characteristic times appear in the current expressions:

$$\tau_{\text{on}} = \left(\frac{R_{\text{on}}R}{R_{\text{on}}+R}\right)C < \tau_{\text{off}} = \left(\frac{R_{\text{off}}R}{R_{\text{off}}+R}\right)C. \tag{7}$$

If I' starts out at I'_1 (the switch operating with resistance R_{off}), it will increase its value only if

$$\frac{\varepsilon}{R+R_{\text{off}}} > \frac{V_{\text{hold}}}{R_{\text{off}}}. \tag{8}$$

Moreover, I' will reach the value I'_2 only if

$$\frac{\varepsilon}{R+R_{\text{off}}} < \frac{V_{\text{crit}}}{R_{\text{off}}}. \tag{9}$$

When I' reaches the value I'_2 the switch resistance drops to R_{on} and the current I' becomes I'_4. I' will then decrease from I'_4 only if

$$\frac{\varepsilon}{R+R_{\text{on}}} < \frac{V_{\text{crit}}}{R_{\text{on}}}. \tag{10}$$

Moreover, I' will reach the value I'_3 only if

$$\frac{\varepsilon}{R+R_{\text{on}}} < \frac{V_{\text{hold}}}{R_{\text{on}}}. \tag{11}$$

When I' reaches the value I'_3 the switch resistance changes back to R_{off} and the current I' becomes I'_1, thus completing the cycle.These four conditions can be summarized as

$$\frac{\varepsilon}{1+(R/R_{\text{on}})} < V_{\text{hold}} < V_{\text{crit}} < \frac{\varepsilon}{1+(R/R_{\text{off}})}. \tag{12}$$

The time needed for the current I' to change from I'_1 to I'_2 (the OFF part of the cycle) is

$$t_{\text{off}} = \tau_{\text{off}} \ln\left[\frac{\varepsilon - V_{\text{hold}}(1+R/R_{\text{off}})}{\varepsilon - V_{\text{crit}}(1+R/R_{\text{off}})}\right] \tag{13}$$

and the time needed for the current I' to change from I'_4 to I'_3 (the ON part of the cycle) is

$$t_{\text{on}} = \tau_{\text{on}} \ln\left[\frac{V_{\text{crit}}(1+R/R_{\text{on}}) - \varepsilon}{V_{\text{hold}}(1+R/R_{\text{on}}) - \varepsilon}\right]. \tag{14}$$

Finally, the oscillation period is given by

$$T = \left(\frac{R_{\text{on}}RC}{R_{\text{on}}+R}\right)\ln\left[\frac{V_{\text{crit}}(1+R/R_{\text{on}}) - \varepsilon}{V_{\text{hold}}(1+R/R_{\text{on}}) - \varepsilon}\right] + \left(\frac{R_{\text{off}}RC}{R_{\text{off}}+R}\right)\ln\left[\frac{\varepsilon - V_{\text{hold}}(1+R/R_{\text{off}})}{\varepsilon - V_{\text{crit}}(1+R/R_{\text{off}})}\right]. \tag{15}$$

4. Discussion

It can be seen from Eq. (12) that a proper selection of ε and R is necessary in order to obtain current oscillations. The condition involves four switch parameters, which are not necessarily dependent on each other. The condition $V_{\text{hold}} < V_{\text{crit}}$ is observed whenever conductance bistability occurs, by definition. In some cases investigated using switching devices in a sandwich structure [5,7] V_{crit} and V_{hold} were observed to be proportional to the material layer thickness, so that these parameters can, at least in these cases, be controlled. Still, from Eq. (12), it can be seen that in order to allow for a significant difference between V_{crit} and V_{hold}, which would result in a more reliable device operation, a significant difference between R_{on} and R_{off} is desirable.

The oscillator frequency is inversely proportional to the value of C, so that this is the simplest frequency control parameter. In what regards the switching device characteristics, the values R_{on} and R_{off} are the most important factors determining the frequency.

In Fig. 6 the oscillation period T is shown as a function of ε and R. For the circuit to operate as an oscillator, ε must be in the range

$$V_{\text{crit}}(1+R/R_{\text{off}}) < \varepsilon < V_{\text{hold}}(1+R/R_{\text{on}}). \tag{16}$$

This inequality has a solution only if the switch parameters are such that $(V_{\text{crit}}/R_{\text{off}}) < (V_{\text{hold}}/R_{\text{on}})$, which is equivalent to $I'_2 < I'_3$, see Fig. 4(b). This condition is easily attained since, for a representative resistance ratio $R_{\text{off}}/R_{\text{on}} \approx 10^3$ and $V_{\text{crit}}/V_{\text{hold}} \approx 2$. The contour lines shown in the figure correspond to a particular case where $R_{\text{off}}/R_{\text{on}} = 20$ and $V_{\text{crit}}/V_{\text{hold}} = 5$, although these are not typical switch parameters they make the structure of the contour lines more visible. For any parameter values, the oscillator period is infinite along the straight borders and smaller periods are found as one moves

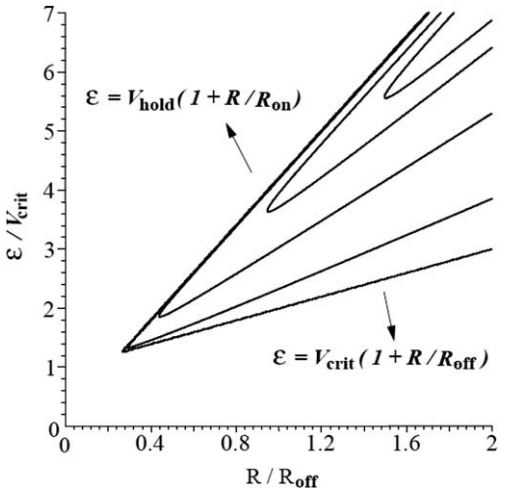

Fig. 6. The period T as a function of ε and R according to Eq. (15). The switch parameters were taken to be such that $R_{off}/R_{on} = 20$ and $V_{crit}/V_{hold} = 5$. Five contour lines are displayed. Along the borderlines, where ε is at the boundary of the range shown in Eq. (16), the period is infinite. As one moves away from the borderlines, towards larger values of R and ε, the period decreases monotonically towards the T_{min} of Eq. (18).

away from the borderlines towards larger values of R and ε.

By changing the value of ε, for a fixed R, one can obtain all periods between infinity and a minimum period, T_{min}. The minimum period expression, as a function of R, is

$$T_{min}(R) = \left(\frac{R_{on}RC}{R_{on}+R}\right) \ln\left[\frac{(V_{crit}/V_{hold})(1+R/R_{on}) - (1+R/R_{off})}{(V_{hold}/V_{crit})(1+R/R_{on}) - (1+R/R_{off})}\right] + \left(\frac{R_{off}RC}{R_{off}+R}\right) \ln\left[\frac{(1+R/R_{on}) - (V_{hold}/V_{crit})(1+R/R_{off})}{(1+R/R_{on}) - (V_{crit}/V_{hold})(1+R/R_{off})}\right]. \quad (17)$$

In the limit $R \gg R_{off}$, $T_{min}(R)$ converges to

$$T_{min} \to (R_{on}C)\ln\left[\frac{(V_{crit}/V_{hold}) - (R_{on}/R_{off})}{(V_{hold}/V_{crit}) - (R_{on}/R_{off})}\right] + (R_{off}C) \times \ln\left[\frac{(R_{off}/R_{on}) - (V_{hold}/V_{crit})}{(R_{off}/R_{on}) - (V_{crit}/V_{hold})}\right]. \quad (18)$$

This period is the smallest period that can be obtained with a given set of switch parameters, R_{on}, R_{off}, V_{crit} and V_{hold}, and a capacitance C.

If, for example, the values mentioned above after Eq. (16), are used ($R_{off}/R_{on} \approx 10^3$ and $V_{crit}/V_{hold} \approx 2$), $T_{min} \approx 3R_{on}C$, so that using capacitances of the order of a few pF, frequencies larger than radio frequency identification low frequency band (~130 kHz) should be possible. It must be pointed out, however, that this analysis assumes instantaneous switching, ignoring peculiarities of the switching process characteristic times related to, for example, modification of molecular conformation, modification of molecular charge state, charge emission and capture by traps, etc., which may also be limiting factors.

5. Conclusion

In summary, we reported the construction of oscillators using poly(1,5-diaminonaphthalene)-based switches and determined the analytical expression for the oscillation period, as well as the minimum allowed oscillation period (corresponding to a maximum frequency) as a function of oscillator components: capacitance, series resistance, switch resistance in the ON- and OFF-states and switch critical voltages for the ON–OFF and OFF–ON transition.

The theoretical results show that in principle, it is possible to produce oscillators operating at higher frequencies, provided that stable materials with appropriate characteristics can be found.

Acknowledgements

The authors thank CNPq, Renami and Instituto do Milênio IM^{2}C for research grants.

References

[1] R.S. Potember, T.O. Pehler, D.O. Cowan, Appl. Phys. Lett. 34 (1979) 405.
[2] S.G. Liu, Y.Q. Liu, D.B. Zhu, Thin Solid Films 280 (1996) 271.
[3] M. Ouyang, K.Z. Wang, H.X. Zhang, Z.Q. Xue, C.H. Huang, D. Qiang, Appl. Phys. Lett. 68 (1996) 2441.
[4] A.C. Arias, I.A. Hümmelgen, A. Meneguzzi, C.A. Ferreira, Adv. Mater. 9 (1997) 972.
[5] D. Ma, M. Aguiar, J.A. Freire, I.A. Hümmelgen, Adv. Mater. 12 (2000) 1063.
[6] L.P. Ma, J. Liu, Y. Yang, Appl. Phys. Lett. 80 (2002) 2997.
[7] R.M.Q. Mello, E.C. Azevedo, A. Meneguzzi, M. Aguiar, L. Ackcelrud, I.A. Hümmelgen, Macromol. Mater. Eng. 287 (2002) 466.
[8] A. Bandyopadhyay, A.J. Pal, J. Phys. Chem. B 107 (2003) 2531.
[9] T. Oyamada, H. Tanaka, K. Matsushige, H. Sasabe, C. Adachi, Appl. Phys. Lett. 83 (2003) 1252.
[10] A. Bandyopadhyay, A.J. Pal, Appl. Phys. Lett. 82 (2003) 1215.

[11] S.K. Majee, A. Bandyopadhyay, A.J. Pal, Chem. Phys. Lett. 399 (2004) 284.
[12] T. Ouisse, O. Stéphan, Org. Electron. 5 (2004) 251.
[13] H.S. Majumdar, C. Botta, A. Bolognesi, A.J. Pal, Synth. Met. 148 (2005) 175.
[14] H.S. Majumdar, J.K. Baral, R. Österbacka, O. Ikkala, H. Stubb, Org. Electron. 6 (2005) 188.
[15] B. Mukherjee, A.J. Pal, Synth. Met. 155 (2005) 336.
[16] A. Bandyopadhyay, A.J. Pal, Appl. Phys. Lett. 84 (2004) 999.
[17] S.H. Kang, T. Crisp, I. Kymissis, V. Bulovic, Appl. Phys. Lett. 85 (2004) 4666.
[18] D. Todelier, K. Lminouni, D. Villaume, C. Fery, G. Haas, Appl. Phys. Lett. 85 (2004) 5763.
[19] L.D. Bozano, B.W. Kean, V.R. Deline, J.R. Salem, J.C. Scott, Appl. Phys. Lett. 84 (2004) 607.
[20] L.D. Bozano, B.W. Kean, M. Beinhoff, K.R. Carter, P.M. Rice, J.C. Scott, Adv. Funct. Mater. 15 (2005) 1933.
[21] W. Tang, H. Shi, G. Xu, B.S. Ong, Z.D. Popovic, J. Deng, J. Zhao, G. Rao, Adv. Mater. 17 (2005) 2307.
[22] S. Möller, C. Perlov, W. Jackson, C. Taussig, S.R. Forrest, Nature 426 (2003) 166.
[23] S.R. Forrest, Nature 428 (2004) 911.
[24] J.C. Scott, Science 304 (2004) 62.
[25] J. Ouyang, C.W. Chu, C.R. Szmanda, L. Ma, Y. Yang, Nature Mater. 3 (2004) 918.
[26] J. Chen, D. Ma, Appl. Phys. Lett. 87 (2005) 023505.
[27] Q.D. Ling, Y. Song, S.J. Ding, C.X. Zhu, D.S.H. Chan, D.L. Kwong, E.T. Kang, K.G. Neoh, Adv. Mater. 17 (2005) 455.
[28] S. Paul, A. Kanwal, M. Chhowalla, Nanotechnology 17 (2006) 145.
[29] R. Toniolo, I.A. Hümmelgen, Electron. Lett. 40 (2004) 566.
[30] M.A. Basso, Dissertation, Universidade Federal do Rio Grande do Sul, Porto Alegre, 2001.
[31] C.A. Ferreira, Miguel A. Basso, A. Meneguzzi, Annals of the Simpósio Brasileiro de Eletroquímica e Eletroanalítica, Araraquara, Brazil, 2002, p. 568.

Available online at www.sciencedirect.com
ScienceDirect
Organic Electronics 7 (2006) 403–409
Organic Electronics
www.elsevier.com/locate/orgel

Conductivity of the thin film phase of pentacene

P. Parisse *, M. Passacantando, S. Picozzi, L. Ottaviano

CNR-INFM and Dipartimento di Fisica, Università degli Studi dell'Aquila, Via Vetoio, 10 67010 Coppito, L'Aquila, Italy

Received 19 January 2006; received in revised form 12 April 2006; accepted 8 May 2006
Available online 6 June 2006

Abstract

We investigated the morphological, structural and transport properties of pentacene thin films (20 nm) grown by high vacuum thermal evaporation on patterned substrates with different interelectrodes distances. X-ray diffraction and atomic force microscopy show a structure in the so called "thin film phase" with 1–2 μm sized grains. By means of in situ electrical measurements we found for these films a resistivity value of $\rho = 4.7 \pm 0.2 \times 10^4$ Ωm, that is an order of magnitude lower than the value reported to date in literature for single crystals of pentacene. This value is not affected by the presence of grain boundaries. The resistivity is further reduced by a factor 8.9 ± 0.7, 14 ± 1, 2.3 ± 0.3 upon exposure to oxygen, nitrogen and ambient air, respectively.

PACS: 61.66.Hq; 72.80.Le; 68.55.−a; 73.61.Ph; 68.37.Ps

Keywords: Pentacene; Organic semiconductors; AFM; Transport properties; Polycrystalline films

1. Introduction

Molecular electronics is an interesting field of research aiming at a reduction of cost and dimensions of devices. The potential applications of organic molecules in nano and microelectronics industry are the objectives of the scientific and technological research [1,2]. It is therefore very important the investigation and the understanding of the structural, electronic and transport properties of thin films of such molecules. In recent years, many molecules have been extensively studied. Among these, pentacene ($C_{22}H_{14}$) seems to be one of the best candidates for several applications (OTFTs, OLEDs, Schottky diodes, solar cells) [3–8]. This organic molecule, constituted by a linear chain of five planar benzenic rings, crystallizes in a triclinic structure with an herringbone arrangement of the molecules in the unit cell [9]. Depending on growth parameters (substrate, substrate temperature, evaporation rate, thickness of the film) pentacene appears in four polymorphs, that principally differ from one to another for the tilting of the molecules with respect to the substrates and for the (001) interplanar distance [10]. Among the various polymorphs, due to the tremendous size downscaling of state of the art electronics, obvious attention has to be devoted to the polymorph which is stable in the nanometer thickness range, namely the "thin film phase". This phase is observed in polycrystalline

* Corresponding author. Tel.: +39 0862433097; fax: +39 082433033.
E-mail address: pietro.parisse@aquila.infn.it (P. Parisse).

1566-1199/$ - see front matter © 2006 Elsevier B.V. All rights reserved.
doi:10.1016/j.orgel.2006.05.002

thin films (thickness $\leqslant$50 nm) deposited on inert substrates (passivated Si, HOPG, SiO_2, Si_3N_4, LiF) [3,12,14–17] with micrometer sized grains. Theoretical and experimental works suggest that it is very promising for OTFT applications [4,11–13]. The transport and electronic properties of this phase are presently a subject of intense investigation. As far as the transport properties are concerned, although the room temperature (RT) is quite close to the critical temperature where the transport changes from band-like to an hopping regime, nevertheless a band-like transport has been clearly demonstrated for pentacene in the thin film phase at RT [29]. The different molecular stacking produces a change in the overlap between the electronic orbitals belonging to adjacent molecules and this significantly modifies the band structure from one polymorph to another. Indeed, a theoretical work [11] shows that the HOMO bandwidth of the thin film phase is more than four times larger than the one of the single crystal phase. This increase of the HOMO bandwidth, combined with the more isotropic mobility in the *ab* plane, can very likely increase the conductivity of pentacene in the thin film phase. Moreover, beside the enlargement of the HOMO–LUMO bandwidth, recent works show that even slight changes in the orientation of molecules in the unit cell can dramatically affect also the HOMO–LUMO gap, in addition to the above mentioned increase of the HOMO and LUMO bandwidth [30,31]. Nonetheless, there is still a lack of fundamental experimental information about the resistivity of pentacene in the thin film phase. Moreover, in view of technological applications (i.e., air exposed devices), the influence of oxygen, nitrogen and ambient air on such physical property has never been quantitatively investigated.

The focus of this work is to experimentally address these issues by means of electrical measurements performed on thin films of pentacene in high vacuum and in controlled atmosphere of O_2, N_2, and ambient air, respectively. The role of grain boundaries is also investigated by using devices with different interelectrodes spacing. Ancillary atomic force microscopy (AFM) and X-ray diffraction (XRD) measurements were carried out for a morphological and structural characterization of these films.

2. Experimental details

Pentacene (Aldrich Chemicals) was deposited in a high vacuum (HV) (base pressure: 1×10^{-8} Torr) chamber by vacuum thermal evaporation. The chamber pressure during the film growth was 2×10^{-8} Torr and the evaporation rate was 1.3 Å/min (as monitored by a quartz crystal micro-balance after thickness calibration with AFM measurements). Particular attention was devoted to grow high purity films by cleaning the substrates and outgassing the starting material for 3–4 h at 100 °C before the film growth. As substrates, we used two different (hereafter A and B) interdigitated patterned devices, with gold electrodes grown onto 1000 Å SiO_2/Si(1 0 0) (device A) and Si_3N_4/Si(1 0 0) (device B). The thickness of the electrodes is 150 nm (device A) and 80 nm (device B), the interelectrodes distance is 5 μm (device A) and 30 μm (device B) and the length of electrodes is 150 μm (device A) and 3 mm (device B). Current–voltage measurements of as prepared samples were carried out in situ at RT with a Keithley source measure unit, model number 236. The I/V curves have been acquired varying every 0.5 s the voltage at steps of 0.05–0.2 V. The evaporation chamber was equipped with a leak-valve for a controlled inlet of O_2 (Air Liquid 99.99% purity), N_2 (Air Liquid 99.99% purity), and ambient air (60% partial humidity). I–V curves of the gas exposed devices have been taken as a function of time after 1 atm pressure was reached in the chamber. All the electrical measurements have been performed in fluorescent light ambient illumination. Tapping mode AFM measurements are performed ex situ in air with a Digital D5000 equipped with Nanoscope IV controller using commercial silicon nitride cantilevers (cantilever resonance frequency = 70 kHz for "soft" organic samples). The samples have been also investigated by X-ray diffraction (XRD) using a Siemens D5000 diffractometer with Cu K_α radiation in the Bragg–Brentano geometry. Photoemission valence band spectra of ambient air exposed samples have been taken at the VUV beamline (Elettra–Trieste) using synchrotron radiation light ($h\nu = 120$ eV) to investigate the increase of the HOMO bandwidth, in comparison with previously published data taken on freshly prepared samples [17].

3. Results

In Fig. 1(a) we show an AFM micrograph of a film of pentacene (20 nm nominal thickness) deposited on device A. As shown in the image, the distance between Au electrodes (brighter zones) is of 5 μm. The growth is different on the electrodes

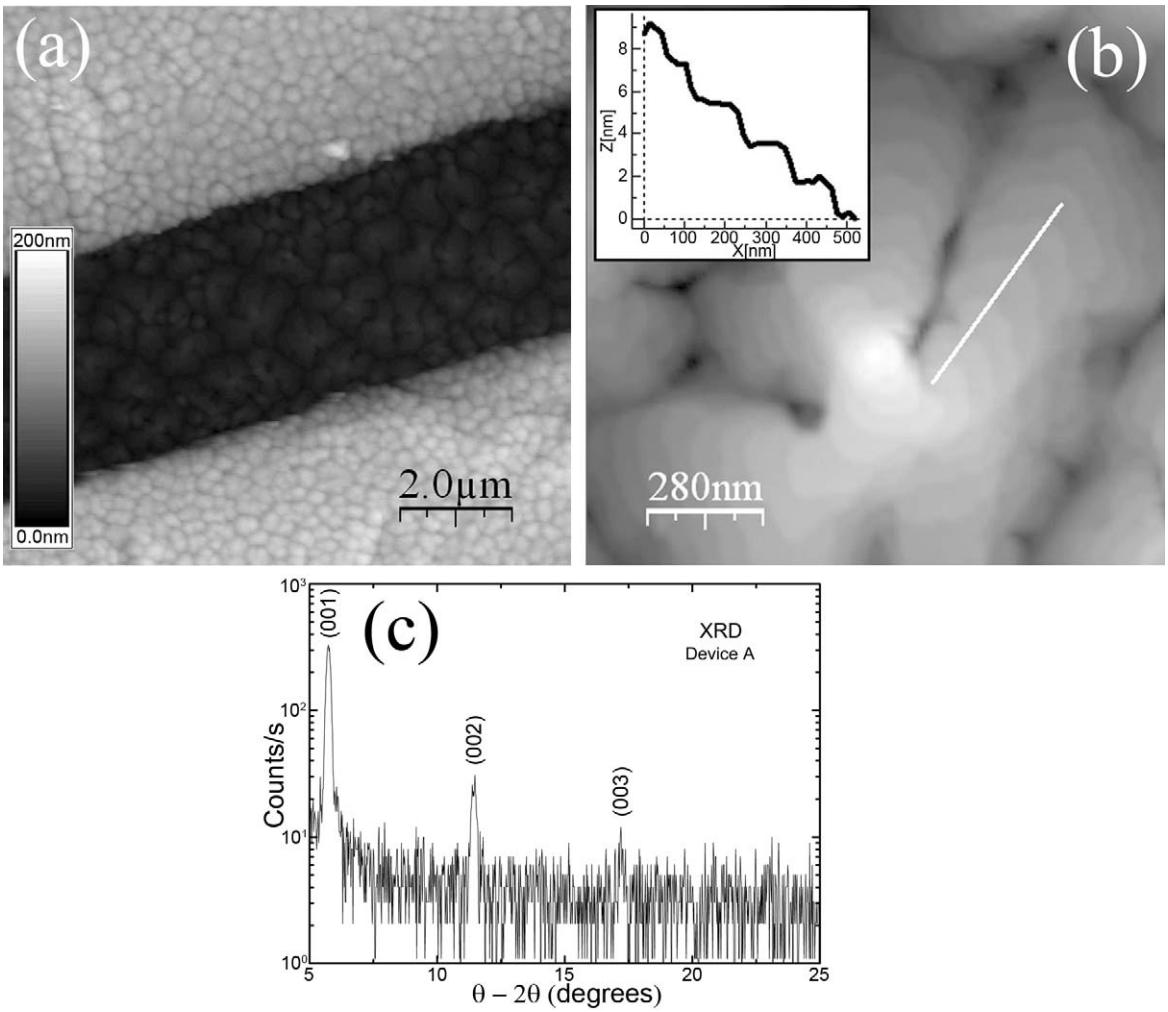

Fig. 1. (a) 10 μm × 10 μm image of a 20 nm nominal thickness film on device A. The brighter zones are the Au electrodes, the dark zone is the SiO_2 substrate. (b) High resolution AFM image of the pentacene crystallites betweeen electrodes showing a terrace structure as evidenced by the line profile shown in the inset. (c) XRD Bragg-Brentano diffraction pattern of 20 nm of pentacene deposited onto device A.

and on the SiO_2 substrate. On the oxide surface the pentacene film grows in a dendritic way with micrometer sized crystallites, showing a terrace structure (Fig. 1(b)), while on the metallic surface (gold electrodes) we can observe no particular structure with grains of submicrometric dimensions. Device B shows the same morphology and structural features, as can be seen in Fig. 2. The samples have been also studied with XRD. This investigation is reported in Fig. 1(c). The diffraction pattern shows three peaks assigned to the (00l) plane Bragg reflection and gives a (001) interplanar distance of 1.54 nm, in excellent agreement with the one of the thin film phase of pentacene [10,14]. By combining the structural and morphological data we claim that the film grows onto the oxide surface in crystallites in the thin film phase with the c axis perpendicular to the substrate surface. Onto the gold substrate the film appears to be likely amorphous. This, of course, does not affect our electrical measurements, since these latter give information about the conductivity of the polycrystalline film between the electrodes along the *ab* plane. The mobility in molecular crystals is often anisotropic, due to the typical crystalline arrangement of the molecules along stacking axes. In pentacene, the mobility is extremely anisotropic along the three axes for all the phases, except for the thin film polymorph, where it is essentially uniform in the *ab* plane, while a strong anisotropy remains along the *c* axis [11].

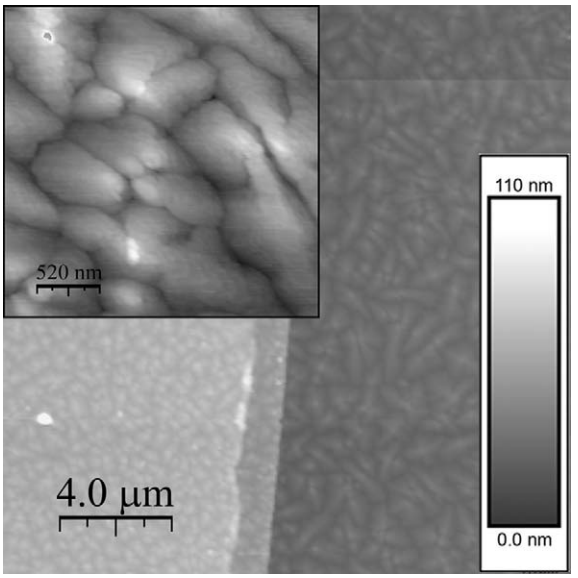

Fig. 2. 20 μm × 20 μm image of a 20 nm nominal thickness film on device B. The gold electrode is on the left side of the micrograph. The inset shows a zoomed-in image of the pentacene film onto the substrate (right part of the micrograph).

Therefore, the orientation of the *ab* plane of the crystallites with respect to the substrate is unimportant.

Transport properties have been investigated by means of current–voltage measurements. Preliminary I/V curves on the A and B devices prior to the growth of the pentacene film were carried out to evaluate the intrinsic resistance of the devices, R_s. In the final configuration the circuit can be schematized as two resistances R_s and R_f in parallel, where R_f is the film resistance (Fig. 3).

In order to estimate the effects of the grain boundaries in our film we perform measurements on differently spaced electrode devices, namely A and B. In Fig. 4 we summarize the density of current

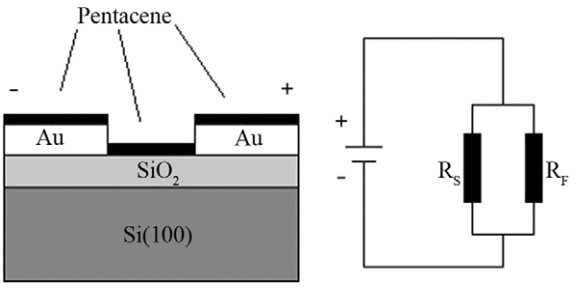

Fig. 3. Scheme of devices A and B and circuit of the final configuration of the device.

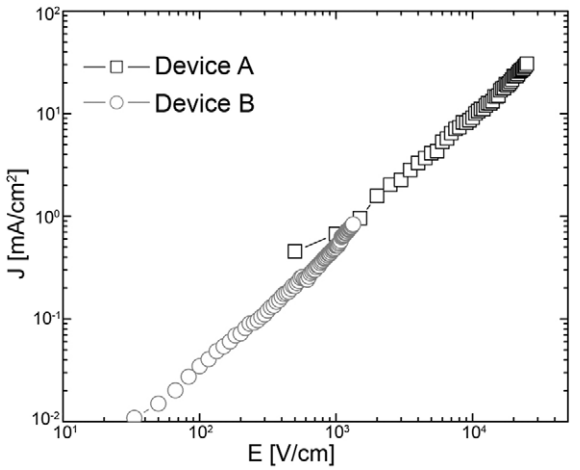

Fig. 4. Density of current (J)–electric field (E) characteristics of the thin film phase of pentacene. Measurements were performed in air and under ambient illumination.

(J)–electric field (E) results obtained for the measurements performed in ambient air and under ambient illumination for these samples. We can observe that the curves for the samples A and B lie on the same line on the log–log plot, indicating the same value of conductivity. This indicates that the change in the number of grains does not significantly affect the transport properties of our films. In a recent work Edura et al. show that the intergrain resistance is one order of magnitude larger than the intragrain resistance [19]. If this is the case, therefore, in our samples the difference in the resistance film should remarkably change as a function of the interelectrodes distance. Evidently, the pentacene grows in a Stransky–Krastanov mode with a layer by layer growth at the very initial stages of deposition. As already observed by several groups [26–28] the transport occurs principally in the first layers: charges follow percolation paths in these layers that result more ordered than the remaining islands, overcoming in this way the grain boundary effects. By analyzing the ohmic regime and considering the geometry of our devices, we can determine the value of the resistivity ρ_f for the pentacene in the thin film phase. The electrical measurements performed in air give a resistivity value of $\rho_{air} = 2.0 \pm 0.2 \times 10^4\ \Omega$m. This value is of course useful for device applications, but it can be in principle affected by chemical impurities, therefore not representing an intrinsic property of the film.

To rule out these effects, we perform current–voltage measurements in HV on freshly prepared

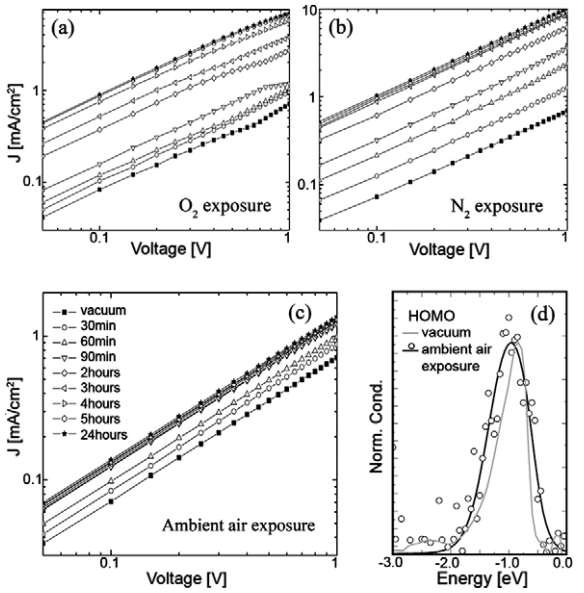

Fig. 5. (a)–(c) Evolution of the density of current (J)–voltage characteristics of the thin film phase of pentacene after exposure to pure O_2 (a), pure N_2 (b), and ambient air (c). (d) HOMO peak of the thin film phase of pentacene in vacuum (STS measurement) and after exposure to ambient air (photoemission valence band spectrum).

samples. The results of these measurements are shown in Fig. 5 (lower curves (black filled squares) in panels (a), (b) and (c)), where we report the measurements performed on sample B. The resistivity value in vacuum results to be $\rho_{\text{vacuum}} = 4.7 \pm 0.2 \times 10^4$ Ωm. This value slightly (5%) changes for the different samples analyzed and it is not affected by changes of the interelectrodes distance, since similar results are obtained for sample A. Therefore, our results provide information on the intrinsic physical properties of the pentacene in the thin film phase, rather than on trivial intergrain boundary effects (as already discussed in detail for air exposed samples). The resistivity value is one order of magnitude lower than the value reported by Jurchescu et al. [20] for the single crystal phase. We believe that this dramatic change of resistivity has to be assigned to the peculiar changes in the electronic structure of the thin film phase. In agreement with Troisi and Orlandi [11], the increase of the HOMO and LUMO bandwidth has been already demonstrated by our group by means of scanning tunneling spectroscopy (STS) measurements on freshly prepared pentacene thin films in HV [17]. In particular, the experimental STS plot of the HOMO is reported in Fig. 5 panel (d) (normalized conductance spectrum). Our estimate for the HOMO bandwidth is 0.7 eV. This value is not obviously altered by chemical impurities, although it can be increased by shallow structural defects such as vertical sliding of the pentacene molecules, as demonstrated by Kang et al. [18]. Anyway, the AFM analysis shows a mean roughness on the terraces of 1.4 ± 0.5 Å. Assuming this as the mean displacement of molecules, we obtain, according to the calculation of Kang, an increase of HOMO and LUMO bandwidth by less than 100 meV, comparable with typical thermal broadening effects.

In order to selectively investigate the effects of chemical impurities or doping due to exposure to ambient air, we performed also electrical measurements on freshly prepared samples exposed to either oxygen, or nitrogen, or ambient air. Upon exposing the samples to 1 atm of the different gases, we observe that the resistivity tends to slowly decrease reaching a saturation value in approximately 3 h, as shown in Fig. 5(a)–(c). In Table 1 we report the saturation values of the resistivity after 24 h exposure. Both nitrogen and oxygen decrease the film resistivity by one order of magnitude (namely by a factor 14 ± 1 and 8.9 ± 0.7 for N_2 and O_2, respectively). Exposure to ambient air, instead, decreases this value by only a factor 2.3 ± 0.3, as already observed for pentacene in the single crystal phase [21]. Oxygen doping likely causes a lowering of the hole injection barrier at the pentacene/Au interface and also increases the density of charge carrier and, as consequence, the conductivity [22]. We can exclude that oxygen is chemisorbed by pentacene: in this case, it would form a chemically stable compound with two carbonyl groups at opposite sides of the middle ring, namely 6,13-pentacenequinone ($C_{22}H_{12}O_2$) [23,24]. At variance with what observed after oxygen exposure, the formation of pentacenequinone should reduce the conduction properties of the film, introducing structural defects that act as centers of scattering for the charge carriers. This ''oxidized'' form of pentacene crystallizes in a monoclinic structure, that has a (0 0 1) interplanar

Table 1
Resistivity values for the thin film of pentacene after 1 day exposure to 1 atm different gases and $\rho_{\text{vacuum}}/\rho$ ratio

	ρ (Ωm)	$\rho_{\text{vacuum}}/\rho$
Vacuum	$4.7 \pm 0.2 \times 10^4$	1
Nitrogen	$3.3 \pm 0.2 \times 10^4$	14 ± 1
Oxygen	$5.3 \pm 0.2 \times 10^3$	8.9 ± 0.7
Ambient air	$2.0 \pm 0.2 \times 10^3$	2.3 ± 0.3

distance of 17.4 Å [25], 2 Å larger than the one of the pure pentacene in the thin film phase. This occurrence is quite unlikely, as it is favoured only upon exposure to UV light and it was not observed with XRD in our oxygen exposed samples. Oxygen is therefore present in the thin film as an impurity and clearly does not form stable compounds with pentacene.

As expected, the role played by nitrogen is similar to oxygen: it dopes the thin film, increasing its conductivity. On the other hand, evidently the water vapour in ambient air plays a competing effect against doping due to oxygen and nitrogen. In fact, according to literature [21,23], water tends to form trapping sites for the injected charges and, therefore, strongly reduces the conductivity of the oxygen and nitrogen doped films. The enhancement of conductivity after exposure to air can be further explained as follows: not only doping can be induced by the chemical defects, but even the HOMO bandwidth can be modified by this kind of impurities. To estimate this effect (due to the chemically different molecular environment), we report in Fig. 5 panel (d) the photoemission spectrum of the HOMO state of an ambient air exposed thin film. Compared with the HV STS measurement, we observe an increase of the HOMO bandwidth of 0.3 ± 0.1 eV. This further explains the enhancement of the conductivity under exposure to ambient air.

4. Conclusions

We performed electrical measurements to investigate the resistivity of pentacene in the thin film phase (as checked with AFM and XRD analyses). We found a resistivity value of $\rho_{\text{vacuum}} = 4.7 \pm 0.2 \times 10^4\ \Omega\text{m}$ in vacuum and of $\rho_{\text{air}} = 2.0 \pm 0.2 \times 10^4\ \Omega\text{m}$ in ambient air. These values are not trivially affected by the inter electrode distances (grain boundaries effects). Exposure to oxygen and nitrogen remarkably (by a factor 8.9 ± 0.7 and 14 ± 1, respectively) decreases the resistivity of the films with respect to the vacuum value. We rationalize our results by commenting the relevance of several distinct effects, namely: the impurities and defect states induced by chemical or structural modification of the film, the exposure to air and ambient illumination and the specific electronic properties of this polymorph. Evidently, our results confirm that pentacene in the thin film phase is an excellent candidate in view of OTFT applications.

Acknowledgements

This work was supported with grants from MIUR (Italian Ministry for the University and Research) fondo COFIN2004. We thank Alessandro Urbani for the help in the realization of the home built probe station for electrical measurements in vacuum.

References

[1] C. Reese, M. Roberts, M. Ling, Z. Bao, Materials Today, September 2004.
[2] C.D. Dimitrakopoulos, D.J. Mascaro, IBM J. Res. Dev. 45 (1) (2001) 11.
[3] Y.Y. Lin, D.J. Gundlach, T.N. Jackson, S.F. Nelson, IEEE Trans. Electron. Dev. 44 (8) (1997) 1325.
[4] M. Daraktchiev, A. von Mhlenen, F. Nesch, M. Schaer, M. Brinkmann, M-N. Bussac, L. Zuppiroli, New J. Phys. 7 (2005) 133.
[5] J. Lee, D.K. Hwang, C.H. Park, S.S. Kim, Seongil Im, Thin Solid Films 451–452 (2004) 12.
[6] M.H. Choo, W.S. Hong, Seongil Im, Thin Solid Films 420&421 (2002) 492.
[7] D. Knipp, R.A. Street, J. Non-Cryst. Solids 338–340 (2004) 595.
[8] C. Voz, J. Puigdollers, I. Martin, D. Munoz, A. Orpella, M. Vetter, R. Alcubilla, Solar Energy Mater. Solar Cells 87 (2005) 567573.
[9] R.B. Campbell, J. Monteath Robertson, J. Trotter, Acta Crystallogr. 14 (1961) 705.
[10] C.C. Mattheus, A.B. Dros, J. Baas, G.T. Oostergetel, A. Meetsma, J.L. de Boer, T.T.M. Palstra, Synth. Met. 138 (2003) 475.
[11] A. Troisi, G. Orlandi, J. Phys. Chem. B 109 (5) (2005) 1849.
[12] U. Haas, A. Haase, H. Maresch, B. Stadlober, G. Leising, in: Polytronic IEEE Conference on Polymers and Adhesives, 2004.
[13] I.P.M. Bouchoms, W.A. Schoonveld, J. Vrijmoeth, T.M. Klapwijk, Synth. Met. 104 (1999) 175.
[14] R. Ruiz, A.C. Mayer, G.G. Malliaras, B. Nickel, G. Scoles, A. Kazimirov, H. Kim, R.L. Headrick, Z. Islam, Appl. Phys. Lett. 85 (21) (2004) 4926.
[15] S. Pratontep, M. Brinkmann, F. Nuesch, L. Zuppiroli, Synth. Met. 146 (2004) 387.
[16] A.C. Mayer, R. Ruiz, R.L. Headrick, A. Kazimirov, G.G. Malliaras, Org. Electron. 5 (2004) 257.
[17] P. Parisse, M. Passacantando, L. Ottaviano, Appl. Surf. Sci., in press.
[18] J.H. Kang, D. da Silva Filho, J.L. Bredas, X.-Y. Zhu, Appl. Phys. Lett. 86 (2005) 152115.
[19] T. Edura, H. Takahashi, M. Nakata, K. Tsutsui, K. Itaka, H. Koinuma, J. Mizuno, Y. Wada, Curr. Appl. Phys. 6 (2006) 109.
[20] O.D. Jurchescu, J. Baas, T.T.M. Palstra, Appl. Phys. Lett. 84 (6) (2004) 3061.
[21] O.D. Jurchescu, J. Baas, T.T.M. Palstra, Appl. Phys. Lett. 87 (5) (2005) 052102.
[22] A. Vollmer, O.D. Jurchescu, I. Arfaoui, I. Salzmann, T.T.M. Palstra, P. Rudolf, J. Niemax, J. Pflaum, J.P. Rabe, N. Koch, Eur. Phys. J. E 17 (2005) 339.

[23] C.C. Mattheus, Ph.D. Thesis, RuG, 2002.
[24] A.V. Dzyabchenko, V.E. Zavodnik, V.K. Belsky, Acta Cryst. 35 (1979) 2250.
[25] D.K. Hwang, K. Kim, J.H. Kim, Seongil Im, D.-Y. Jung, E. Kim, Appl. Phys. Lett. 85 (23) (2004) 5568, and Ref. [11] therein.
[26] R. Ruiz, A. Papadimitratos, A.C. Mayer, G.G. Malliaras, Adv. Mater. 17 (2005) 1795.
[27] F. Dinelli, M. Murgia, P. Levy, M. Cavallini, F. Biscarini, D.M.D. Leeuw, Phys. Rev. Lett. 92 (2004) 116802.
[28] M. Kiguchi, M. Nakayama, K. Fujiwara, K. Ueno, T. Shimada, K. Saiki, J. Appl. Phys. 42 (2003) L1408.
[29] O. Ostroverkhova, D.G. Cooke, S. Shcherbyna, R.F. Egerton, F.A. Hegmann, R.R. Tykwinski, J.E. Anthony, Phys. Rev. B 71 (2005) 035204.
[30] K. Doi, K. Yoshida, H. Nakano, A. Tachibana, T. Tanabe, Y. Kojima, K. Okazaki, J. Appl. Phys. 98 (2005) 113709.
[31] P. Parisse, S. Picozzi, L. Ottaviano, B. Delley, unpublished.

Available online at www.sciencedirect.com
ScienceDirect
Organic Electronics 7 (2006) 410–422
Organic Electronics
www.elsevier.com/locate/orgel

The role of casting solvents on the phase separation and morphological behavior of model TPD/polymer charge transport composites

Ferdous Khan [1], P.R. Sundararajan *

Department of Chemistry, Carleton University, 1125 Colonel By Drive, Ottawa, Ont., Canada K1S 5B6

Received 11 April 2006; received in revised form 10 May 2006; accepted 13 May 2006
Available online 12 June 2006

Abstract

Whether a polymer in solution exhibits an extended rod-like conformation or a coiled globular form would depend on its interaction with the solvent. Model charge transport composites of polycarbonate or polystyrene with the hole transport molecule TPD were prepared with various solvents. While the T_g's of the polymers by themselves are unaffected by the choice of the solvent, a significant effect is found when films are cast with the polymer and TPD. A larger depression of the T_g of the polymer and a smaller extent of phase separation of TPD upon annealing were found with the composites prepared with 1,1,2,2-tetrachloroethane than with any other solvent used in this work. Infrared spectroscopy and viscosity measurements show that the above polymers adopt extended conformation in solution, which enhances the intercalation of TPD, when films are cast from this solvent. Whereas the previous studies were concerned with the effect of solvent on the charge transport behaviour of polymers such as polythiophenes, we show that the morphological stability is enhanced when the polymer adopts an extended conformation. This is further confirmed by the observation that the stability against phase separation is improved with the cyclohexyl polycarbonate compared to the bisphenol polycarbonate due to the restricted conformational flexibility of the former.

PACS: 61.25Hq; 64.75+g; 87.15Nn; 71.20Rv; 81.30Mh; 82.35Lr

Keywords: Charge transport; Photoreceptor; Solvent; Phase separation; TPD

1. Introduction

Xerographic photoreceptors are normally prepared in a dual layer arrangement, consisting of a charge generation layer (CGL) and a charge transport layer (CTL). The latter contains electron donor or acceptor molecules in a polymer binder. *N*,*N*′-diphenyl-*N*,*N*′-bis(3-methylphenyl)-[1,1/-biphenyl]-4,4′-diamine (TPD) is known to be electron donor and is extensively used for photocopying devices in the charge transport layer (CTL), with polycarbonate as the binder [1]. The TPD is also used for electroluminescent devices [2], color organic light

* Corresponding author. Tel.: +1 613 520 3605.
E-mail address: Sundar@Carleton.ca (P.R. Sundararajan).
[1] Present address: School of Chemistry, The University of Edinburgh, Edinburgh, Scotland EH9 3JJ, UK.

1566-1199/$ - see front matter © 2006 Elsevier B.V. All rights reserved.
doi:10.1016/j.orgel.2006.05.004

emitting diodes [3], and flat panel display [4]. A series of papers have been published [5–10] on the luminescence properties of TPD/polymer devices. The properties of CTL depend on the type and nature of the charge transport molecules and their concentration. Since the charge transport involves a hopping mechanism [11,12] it is necessary to maximize the concentration of the charge transport molecule in the polymer matrix, and it is common practice to incorporate 50-wt.% or more of TPD in polycarbonate. Although it was initially considered that the polymer binder served merely as a matrix for the charge transport molecule, Pai and coworkers showed [13–17] that the polymer does have a significant influence on the properties of the CTL. For example, the CTL based on TPD/polystyrene (TPD/PS) showed higher charge mobility as compared to the TPD/polycarbonate (TPD/PC) films [13,14] and this was attributed to the better dispersion of TPD with PS than the PC.

Due to the requirement of the rather high loading of the TPD in the polymer, the phase stability of the CTL composite is an important factor. Either thermal factors or mechanical abrasion could lead to partial phase separation and crystallization of TPD. The crystallization of TPD will also depend on the T_g of the host polymer used as a binder. In a series of papers [18–20], we discussed the influence of the polymer matrix on such phase separation of the transport molecule upon annealing. This is similar to accelerated ageing. It was found that the molecular flexibility of the polymer, and hence the glass transition temperature has an effect on the extent of phase separation [18–20]. Molecular level interactions between the charge transport molecule and the polymers were also discussed based on infrared spectra and the depression of the glass transition temperature. The differences in charge transport properties were interpreted in terms of the morphological aspects. It was also shown [19] that the enhanced charge mobility with polystyrene as the host polymer could be due to the poor miscibility of TPD in polystyrene, leading to the profuse formation of sub-micron sized crystals, and chaining of these crystals.

Solution coating of the transport layer is a common approach to fabricating devices. The CTL is usually prepared with dichloromethane (CH_2Cl_2) or chloroform ($CHCl_3$) solutions [13–17]. For photoreceptor applications, two different types of polycarbonates are used: bisphenol A-polycarbonate (BPAPC) and cyclohexyl polycarbonate (PCZ) [21,22]. The effect of casting solvent on the charge transport properties of polymers such as poly(3,4-ethylenedioxythiophene) (PEDOT) [23], poly(3-methylthiophene) [24,25], polypyrroles [26], and polyanilines [27] has been discussed by a number of authors. Phenomena such as enhanced ordering of the polymer enabled by certain types of solvents, polarity of the solvent, dielectric screening by the solvent and ion pairing have been used to account for the observed behaviour.

It is known that polymer solubility is highly selective, and properties such as the viscosity depend on the polymer–solvent pair. Intrinsic viscosity is a measure of the polymer chain dimension in a solvent, and higher viscosity would indicate rod-like stiff and elongated chain behaviour, whereas a flexible coil would lead to low viscosity. Janeczek and Turska [28] reported a helix to random coil transition in dilute solutions of BPAPC, with a binary solvent system of *n*-propyl alcohol and 1,1,2,2-tetrachloroethane ($Cl_2C_2H_2Cl_2$). The intrinsic viscosity decreased as the concentration of the alcohol increased, and a conformational transition occurred at a concentration of 30–40% (vol) of *n*-propyl alcohol. This is indicative of the chain collapse to a globular conformation. As we pointed out in previous publications, the conformational studies of polycarbonate [29,30] showed that both extended zig-zag and flat helical conformations are possible with equal probability for this polymer.

The question then arises as to the effect of such conformational variability of the polymer, brought about by the solvent, on the morphological features of charge transport composites. If we consider that the shape of the polymer in solution would persist when cast as a film (in the absence of high shear or any such perturbation), the morphology of the resulting film would depend on the solvent used. It was mentioned before [19] that it was difficult to obtain stable composite film with dichloromethane as a solvent in the case of TPD/PS composite, whereas good quality films were obtained in the case of TPD/PC system. Here we describe our studies on the morphological features and phase-separation behaviour of TPD/BPAPC, TPD/PCZ and TPD/polystyrene (TPD/PS) composite films prepared with different types of solvents: dichloromethane (CH_2Cl_2), chloroform ($CHCl_3$), toluene, tetrahydrofuran (THF) and 1,1,2,2-tetrachloroethane ($Cl_2C_2H_2Cl_2$). Techniques such as the DSC, X-ray diffraction, polarizing optical microscopy, and viscometry were used.

2. Experimental

The samples of TPD, BPAPC and PCZ are the same as used before [18,19] and were courtesy of Xerox Research Centre of Canada. Polystyrene, with an average molecular weight of 250,000 (density = 1.05 g cm^{-3}), was purchased from Across Organics. Composite films were prepared by dissolving appropriate mixtures of TPD/BPAPC, TPD/PCZ and TPD/PS in dichloromethane (CH_2Cl_2), chloroform ($CHCl_3$), tertrahydrofuran (THF), toluene and 1,1,2,2-tetrachloroethane ($Cl_2C_2H_2Cl_2$) of laboratory grade. Concentrations between 10% and 50% (wt) of TPD in the polymer were used. Films were coated on a glass substrate using an electrically driven film coater. Films prepared with CH_2Cl_2, $CHCl_3$, THF and toluene were dried at a very low rate of solvent evaporation at ambient conditions for 24 h, and then under vacuum for 48 h at 40 °C. Films prepared in $Cl_2C_2H_2Cl_2$ were initially dried at ambient condition, and these were then dried under vacuum at 80 °C for 48 h. The final thickness of the films was about 10–15 μm.

Thermal analysis was performed using a TA 2010 differential scanning calorimeter (DSC) at a heating rate of 10 °C min^{-1} under nitrogen flow (50 ml min^{-1}). The DSC instrument was calibrated for temperature and energy with indium and tin reference samples. DSC thermograms were recorded with about 8–10 mg of sample. The crystallinity of the samples was calculated as the ratio of the measured heat of fusion of the film corresponding to the melting endotherm of TPD (normalized to the weight fraction of TPD in the sample), and the heat of fusion of 100% TPD.

X-ray diffraction measurements were performed using a Philips automated powder diffractometer Model PW 1710. Nickel-filtered Cu K_α radiation ($\lambda = 1.54$ Å) was used. The MDI Data Scan 3.2 software (Materials Data Inc., Livermore, CA) was used for data collection. The results were analyzed using MDI Jade 5, to determine the crystallinity (X_c). The X_c was calculated as the ratio of the intensity under the crystalline peaks above the background and the total intensity.

Fourier transform infrared (FTIR) spectroscopic measurements were performed at ambient conditions using a Michelson M120 BOMEM FTIR spectrometer. The BOMEM GRAMS/386 software was used for data collection.

The viscosity measurements were carried out using a Gallenkamp viscometer at 30 °C, with the viscometer immersed in a thermostatic water bath with an accuracy of 0.01 °C. The reduced viscosity was determined as a function of the polymer concentration between 0.05 and 0.25 g dl^{-1} for all solvents used in this study. Each experiment was performed in triplicate. The intrinsic viscosity [η] was determined using the Huggin's relationship [31] as follows:

$$\frac{\eta_{sp}}{c} = \eta_{red} = [\eta] + k_H[\eta]_c^2 \quad (1)$$

Here, η_{sp}, and η_{red} are the specific and reduced viscosity, respectively. The concentration of the solute (c) is expressed in g/dl. The intercept corresponds to the intrinsic viscosity and the Huggin's constant (k_H) is determined from the slope of the curve.

A Zeiss Axioplan polarizing optical microscope was used to record optical micrographs. The crystal size was calculated using the Northern Eclipse version 6.0 image analysis software.

3. Results and discussion

3.1. Solubility of TPD in the host polymer with various solvents

The melting temperature of TPD is 171 °C, with a heat of fusion 17.8 cal g^{-1}. No other transition was seen in the first DSC scan. A glass transition temperature of TPD was seen at 63 °C in the second scan, which is similar to the values of 65 °C and 61 °C reported by Shirota et al. [32], and O'Brien et al. [33], respectively. The BPAPC, PCZ and polystyrene (PS) were amorphous as detected by DSC, with T_g's of 154, 184 and 103 °C, respectively.

The thermal properties of the as-prepared films with 50% TPD are listed in Table 1. The extent of depression of the glass transition temperature of the polymer is taken as an indicator of the relative solubility of TPD in the three host polymers (BPAPC, PCZ and PS). It is interesting that the depression of T_g depends on the solvent used for preparing the films. Fig. 1 shows the measured T_g as a function of TPD concentration, for the three polymers, prepared with different solvents. The BPAPC was not soluble in THF and toluene. Fig. 1a shows that the addition of 50% TPD in BPAPC lowers the glass transition temperature to 81 °C when the films were cast from CH_2Cl_2 and $CHCl_3$. This is a depression of 73 °C. The films prepared from $Cl_2C_2H_2Cl_2$ showed a significantly lower T_g of 68 °C (Table 1) for the same concentration of

Table 1
Thermal properties of 'as-prepared' composites using various solvents

Solvent	TPD/BPAPC: 50/50			TPD/PCZ: 50/50			TPD/PS: 50/50		
	T_g (°C)	T_m (°C)	ΔH (cal/g)	T_g	T_m	ΔH (cal/g)	T_g	T_m	ΔH (cal/g)
CH_2Cl_2	81			96.4	166	0.32	–	–	–
$CHCl_3$	79.4	166	1.24	86	165.4	0.25	76.9	161	0.05
THF	–	–	–	90.6	164	0.25	79.9	163	3.82
Toluene	–	–	–	92.4	165	0.15	81	167	8.42
$Cl_2C_2H_2Cl_2$	68.5	165.7	0.53	75.8	165.7	0.16	70	–	–

TPD in BPAPC. Fig. 1b shows the variation of T_g with the concentration of TPD in PCZ. Although the difference in T_g is negligible with films prepared with CH_2Cl_2, $CHCl_3$, THF and toluene, a significantly lower T_g is seen in the case of $Cl_2C_2H_2Cl_2$. With TPD/PCZ: 50/50, the depression of T_g was found to be 98 °C for CH_2Cl_2 and $CHCl_3$, 92 °C for THF and toluene, and 108 °C for $Cl_2C_2H_2Cl_2$. The difference is especially significant between $Cl_2C_2H_2Cl_2$ and the rest of the solvents, with concentrations of TPD ranging from 10% to 40%. Note that PCZ is soluble in THF and toluene whereas BPAPC was not.

The T_g determined for the films of PS and TPD/PS films prepared from $CHCl_3$, THF, toluene and $Cl_2C_2H_2Cl_2$, are shown in Fig. 1c. With TPD/PS: 50/50, the T_g is reduced to 80 °C with THF and toluene, i.e., a depression of 23 °C. A larger reduction of T_g by 26 and 33 °C occurs for the films cast from $CHCl_3$ and $Cl_2C_2H_2Cl_2$, respectively. Thus, for the three polymers with TPD, a larger reduction in T_g is seen with films cast from $Cl_2C_2H_2Cl_2$. For each of the compositions, the depression of the T_g is more pronounced in the case of TPD/PCZ than for TPD/BPAPC and TPD/PS systems. We noted before that higher the T_g of the host polymer, the larger is the depression of T_g by TPD (or TTA) [18]. In the case of TPD/PS system, it was observed that the films cast in CH_2Cl_2, $CHCl_3$ and $Cl_2C_2H_2Cl_2$ were clear and transparent up to 50% of TPD concentration, whereas the limit was 40% of TPD in the case of THF as the solvent. The phase separation begins at much lower concentration of TPD (e.g. >20%) in PS matrix in the case of toluene than the other solvents, as discussed in the next section.

A concern could be raised that these differences in the depression of T_g could be due to residual solvent in some cases. However, it was found that there was no difference in the T_g of the polymer by itself, when films were cast from these various solvents, and dried under the conditions described above. Thus, we believe that the differences in the depression are due to the differences in the conformations of the polymer in the different solvents, and the effect of these on the miscibility of TPD with the polymer. As it was mentioned in the Introduction, conformational modeling [29,30] showed that the polycarbonate chain could adopt a number of different types of conformations, ranging from extended zigzag to flat helical, with equal probability. The former would facilitate a close packing of TPD with the polymer segment. We show later, with viscosity measurements that these polymers adopt an extended conformation in $Cl_2C_2H_2Cl_2$.

3.2. Effect of annealing on T_g

Not only does the depression of glass transition temperature depends on the solvent used, but also the recovery of the T_g upon annealing these films. In previous publications, we discussed the annealing-induced phase separation behaviour of the charge transport molecule from the host matrices, and rationalized them on the basis of molecular interactions and the molecular flexibility of the polymer. Annealing was performed at a few degrees below the T_g of the host polymer. We considered this to be similar to accelerated ageing. Accelerated thermal treatment has been used by several authors to study the ageing of polymers and polymer composites [34]. While there might not be a standard testing procedure to estimate the ageing effect of charge transport layers (to include the combined effect of heat, corona charging and other device conditions) we used thermal annealing as a means to study the phase separation of the hole transport molecule from the charge transport layer.

Annealing was performed at 120, 130 and 140 °C between 0.5 h to 4.0 h for TPD/BPAPC: 50/50, and TPD/PCZ: 50/50 films. Upon annealing these films at different temperatures and times, phase

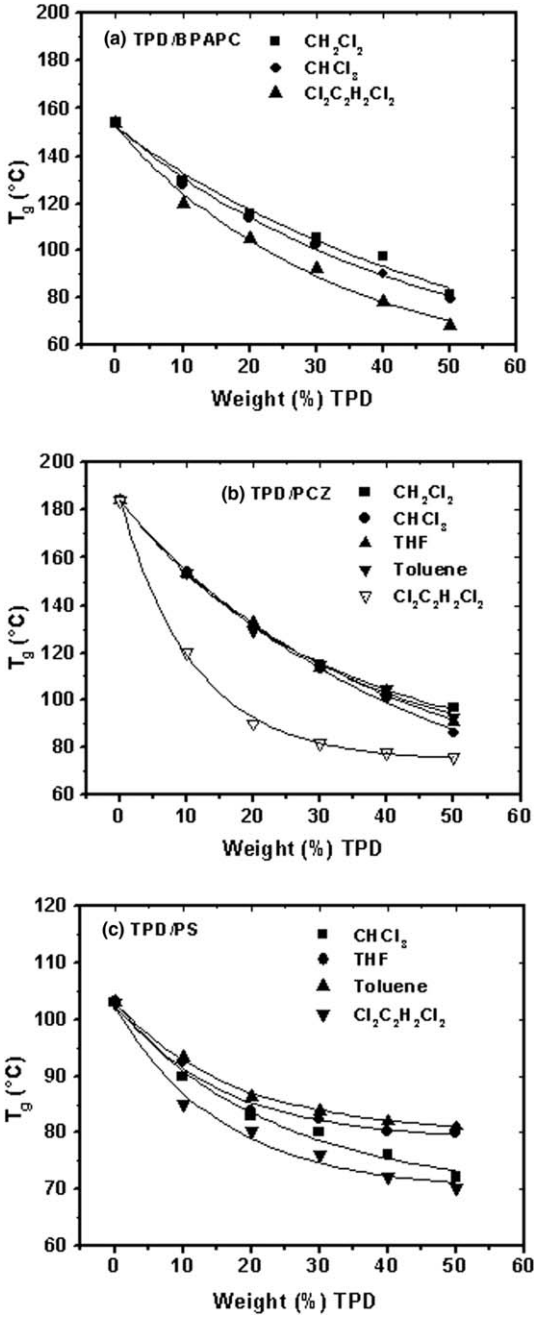

Fig. 1. The glass transition temperature is plotted as a function of TPD concentration for the TPD/polymer composite films cast in various solvents: (a) TPD/BPAPC, (b) TPD/PCZ and (c) TPD/PS.

separation of TPD occurs, leading to partial recovery of the T_g of the polymer. Fig. 2 compares the variation of T_g when TPD/BPAPC films prepared from $CHCl_3$, CH_2Cl_2, and $Cl_2C_2H_2Cl_2$ were annealed at 120 °C, as a function of annealing time.

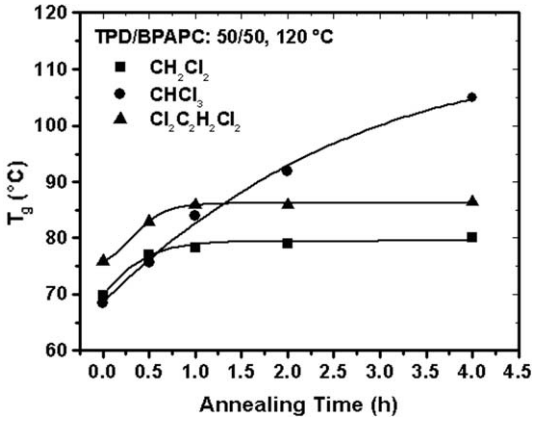

Fig. 2. The recovery of T_g with annealing time at 120 °C for TPD/BPAPC: 50/50 films cast from $CHCl_3$, CH_2Cl_2 and $Cl_2C_2H_2Cl_2$.

With the latter two solvents, there is a recovery of only about 10° during the first half hour of annealing, and no further significant increase occurs with time. However, with chloroform, the T_g continues to recover, and after 4 h of annealing, it is 105 °C. The films were not annealed beyond 4 h. Upon annealing at higher temperatures of 140 °C for 4 h, the T_g recovery was higher by about 10°. With an annealing temperature of 140 °C, after 4 h, the extent of recovery in T_g was 49 °C for $CHCl_3$ and 21 °C in the case of $Cl_2C_2H_2Cl_2$. Thus, apart from the depression of T_g of the as-prepared films, the recovery upon annealing also depends on the solvent used.

The recovery of T_g upon annealing at 120 °C with time for the PCZ/TPD: 50/50 films cast with

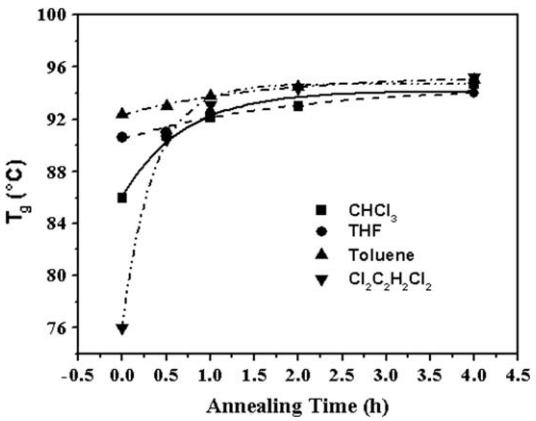

Fig. 3. The recovery of T_g with annealing time at 120 °C for TPD/PCZ: 50/50 films cast from $CHCl_3$, THF, toluene and $Cl_2C_2H_2Cl_2$.

various solvents is shown in Fig. 3. With the film cast in $CHCl_3$, the maximum recovery of T_g was less than 10°, which is a third of the maximum recovery of T_g for BPAPC/TPD with this solvent. The recovery of T_g was even lower (about 5°) for the PCZ/TPD: 50/50 films made from THF and toluene. In contrast to those solvents, a sharp increase in T_g (although only about 15°) was observed during the first hour of annealing for the film prepared from $Cl_2C_2H_2Cl_2$. Thus, although BPAPC and PCZ are homologous polymers, differing only in the substitution at the isopropyledene carbon, the T_g recovery is different for the films made with $CHCl_3$.

As mentioned earlier, the T_g of PS is 51 °C and 81 °C lower than the BPAPC and PCZ, respectively. The phase separation of TPD was observed in TPD/PS: 50/50 system with the films cast from THF and toluene. Although the composites prepared in $Cl_2C_2H_2Cl_2$ were transparent and clear, the film was brittle, and hence no annealing experiments were undertaken. Samples prepared from $CHCl_3$in the case of TPD/PS system with 50% TPD concentration was transparent, clear and less brittle, and the annealing was performed between 80 and 90 °C. There was an increase in T_g up to 1 h of annealing time, beyond which the increase in T_g was negligible. The maximum recovery of T_g was only about 8 °C for annealing at 90 °C for 4 h. This can be contrasted with the T_g recovery with films of PS/TPD made from CH_2Cl_2, which showed a recovery of 30 °C with the same annealing conditions [19].

3.3. Effect of solvents on crystallinity of phase-separated TPD

The crystallinity of phase-separated TPD was evaluated from the X-ray diffraction and the heat of fusion. The weight percent of TPD that crystallized out from the host polymer is referred to as crystallinity in this study. Fig. 4a illustrates typical changes in the X-ray diffraction profile of TPD/BPAPC: 50/50 film with annealing. No crystalline peak is observed with the as-prepared film, which suggests that the TPD is dispersed in the host polymer at molecular level and no aggregation has taken place to form crystals that could be detected by X-ray diffraction. The crystalline peaks due to the phase separated TPD in BPAPC begin to appear after annealing at 120 °C for 0.5 h. The intensity of these peaks increased with the annealing temperature and time. Fig. 4a shows the diffraction pattern

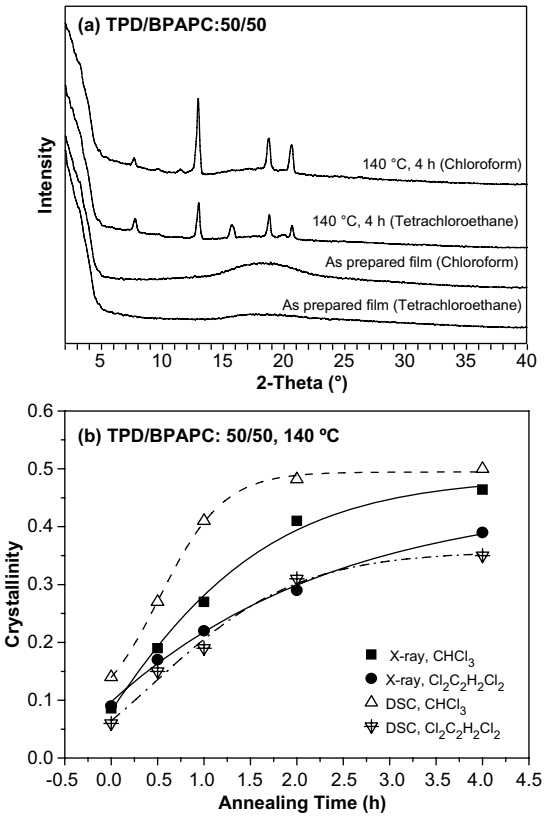

Fig. 4. X-ray and DSC crystallinity measurements for TPD/BPAPC: 50/50 composites: (a) X-ray diffraction traces, (b) X-ray and DSC crystallinities plotted as a function of annealing time for films cast from $CHCl_3$ and $Cl_2C_2H_2Cl_2$.

after annealing at 140 °C for 4 h. The crystallinity calculated from X-ray diffraction and the DSC methods are shown in Fig. 4b, for TPD/BPAPC: 50/50 films prepared from $CHCl_3$ and $Cl_2C_2H_2Cl_2$. With the films cast in $CHCl_3$ the crystallinity of phase separated TPD is about 45–50% with annealing at 140 °C for 4 h. Small differences in the crystallinities measured by the two methods is expected. The X-ray measurement is static i.e., the sample was annealed and then the diffraction was performed at room temperature. However, with the DSC method, the sample is again heated. For the films cast in $Cl_2C_2H_2Cl_2$, the crystallinity upon annealing is about 10% lower. As discussed before, the films cast in $CHCl_3$ showed a much higher T_g recovery (30 °C) upon annealing at 140 °C for 4.0 h, than that cast from $Cl_2C_2H_2Cl_2$ (Fig. 2). The extent of crystallinity of phase separated TPD in films prepared with $Cl_2C_2H_2Cl_2$ is significantly higher than the T_g recovery. The latter is only about

10°, whereas the crystallinity is about 35%. Similar was the behaviour of the films prepared from CH_2Cl_2 i.e., the recovery of the T_g was less than what could be expected from the crystallinity of the phase separated TPD [18]. This contrast was attributed previously [18] to some of the submicron crystals acting as a plasticizer, and lowering the T_g of BPAPC.

Annealing of films of TPD/PCZ cast in various solvents (e.g. $CHCl_3$, THF, toluene and $Cl_2C_2H_2Cl_2$), with 50% TPD concentration, led to crystallinity values of less than 10%. This is in accord with a small T_g as shown in Fig. 3.

Fig. 5 shows the crystallinity of phase separated TPD upon annealing the PS/TPD: 50/50 film prepared with $CHCl_3$ at 80, 85 and 90 °C. No significant crystallinity is detected by annealing at 80 °C. The crystallinity increases with time upon annealing at 85 or 90 °C, to about 16%. In contrast, our previous study [19] showed a crystallinity of about 30% with films made from CH_2Cl_2, annealed at similar temperatures.

Some comments should be made on the films prepared with polystyrene as the host matrix. It is difficult to prepare uniform films of TPD/PS with 50% TPD concentration. With films made from $CHCl_3$ and THF, no endotherm was detected up to 40% concentration of TPD. However, with toluene as the casting solvent, phase separation begins from 30% of TPD concentration and a melting endotherm (T_m) of TPD was detected at 158 °C. The

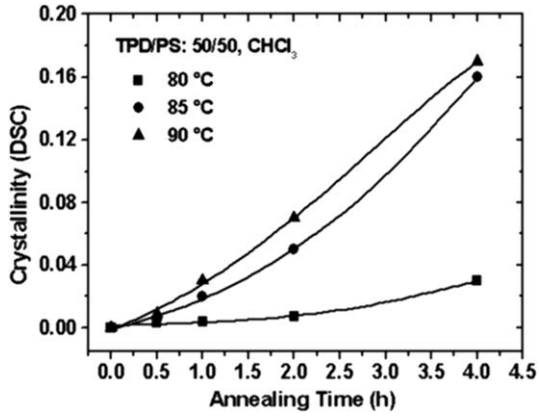

Fig. 5. Crystallinity of phase separated TPD from TPD/PS: 50/50 composite plotted as a function annealing time.

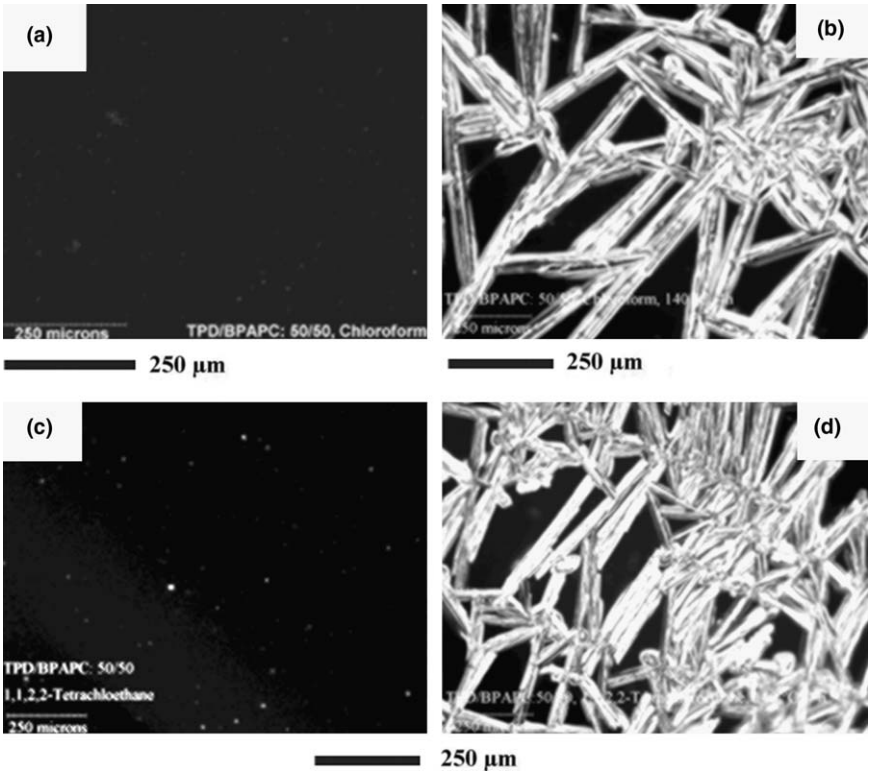

Fig. 6. Optical micrographs of TPD/BPAPC composites with 50% TPD concentration, film cast in $CHCl_3$ (a) as prepared, (b) annealed at 140 °C for 4 h; $Cl_2C_2H_2Cl_2$ (c) as prepared film and (d) annealed at 140 °C for 4 h.

T_m increases to 167 °C with a TPD concentration of 50%. The melting temperature of TPD (by itself) is 171 °C. When it is dispersed in a polymer matrix, a depression of T_m is noted. With BPAPC/TPD or PCZ/TPD films (prepared with CH_2Cl_2) in our previous study, a depression of about 5 °C was noted in the T_m of TPD. We have previously reported [35,36] similar depression of the T_m of other small molecules when dispersed in polymer matrices. As seen in Table 1, in the present study it was found that the T_m of TPD was 161, 163 and 167 °C for films of PS/TPD: 50:50, prepared with $CHCl_2$, THF and toluene, respectively. Thus, the extent of depression of T_m also depends on the solvent used in the case of polystyrene.

3.4. Effect of solvent and annealing on the morphology

As we discussed the effect of solvent used for film casting on the thermal and phase separation properties, it is also interesting that the morphology of the phase separated TPD depends on these factors. The optical micrographs of as prepared film of TPD/BPAPC prepared from $CHCl_3$ and $Cl_2C_2H_2Cl_2$, and annealed at 140 °C for 4 h are shown in Fig. 6. Certainly the crystal growth would depend on the temperature and time used for annealing. We show the morphology corresponding to the as-prepared films and those annealed at 140 °C for 4 h. Fig. 6a and c show that the as prepared films are amorphous, although a few tiny crystals (~10 μm) are observed with both solvents. Upon annealing at 140 °C for 4 h, needle-like crystals grow, with average lengths of 1200 and 800 μm, respectively (Fig. 6b and d), for films cast from $CHCl_3$ and $Cl_2C_2H_2Cl_2$ (although it is difficult to see the length clearly from these figures). These crystals seem to grow in clusters from a common center. On the other hand, the morphology is significantly different for PCZ based films, as seen in Fig. 7. In this case, the as prepared films showed an amorphous nature for all solvents similar to that of BPAPC. With annealing at 140 °C for 4 h, the crystal sizes are found to be in the range of 2–500 μm using $CHCl_3$ as the solvent, and the population of crystals is far less than that of BPAPC for the same solvent (compare Fig. 6b and 7a). The average size of crystals is significantly smaller with films of TPD/PCZ made from THF (10–100 μm), toluene

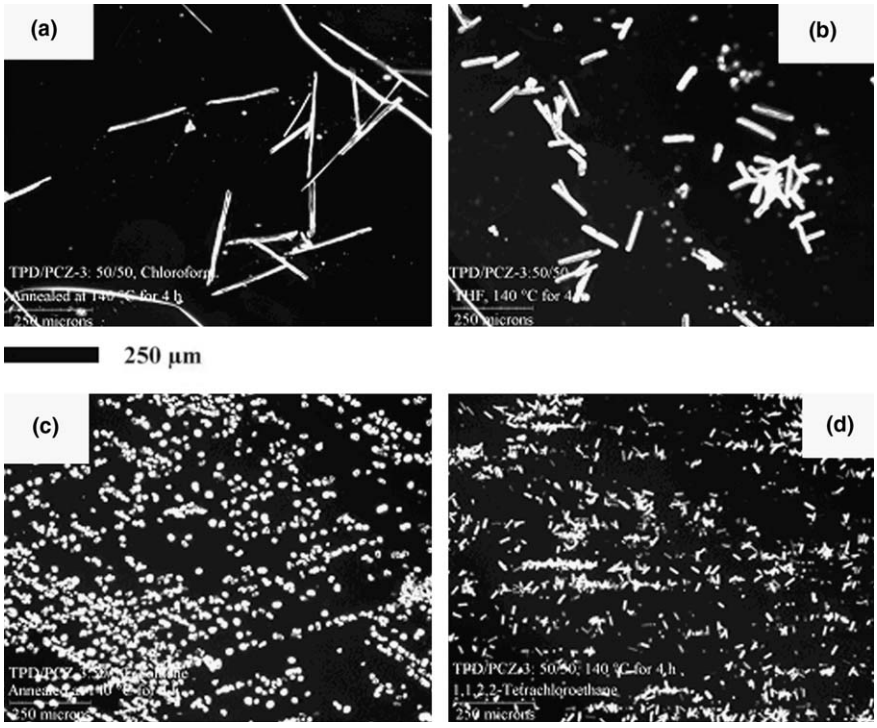

Fig. 7. Optical micrographs of TPD/PCZ composites with 50% TPD concentration, annealed at 140 °C for 4 h. Films cast in various solvents (a) $CHCl_3$, (b) THF, (c) toluene and (d) $Cl_2C_2H_2Cl_2$.

(2–50 μm) and $Cl_2C_2H_2Cl_2$ (1–20 μm). In each case except with toluene, the crystals grow with a needle shape, and the nucleation density seems to increase in the order $CHCl_3$, THF and $Cl_2CH_2CH_2Cl_2$. The crystals are prismatic in the case of toluene.

The micrographs of TPD/PS films are shown in Fig. 8. No crystals were seen up to 50% of TPD concentration in the films prepared from $CHCl_3$ (Fig. 8a) and $Cl_2C_2H_2Cl_2$. However, with the latter, the films were brittle and no further analysis was performed. Phase separation begins above 40% of TPD with THF as the solvent (Fig. 8c), and above 20% of TPD when using toluene (Fig. 8d). The average crystal sizes are 70 and 40 μm, for the morphologies shown in Fig. 8c and d, respectively. It should be noted that due to the small sizes of the crystals in these figures, the films might appear transparent. The profuse crystallization with PS/TPD: 50/50 with toluene as the solvent is shown in Fig. 8e. Although the as-prepared film in chloroform does not show any significant crystallization, whiskers of crystals develop upon annealing at 90 °C for 4 h. Thus the crystal habits are different, indicating that the kinetics of phase separation and crystal growth depend on the solvent used for casting the films.

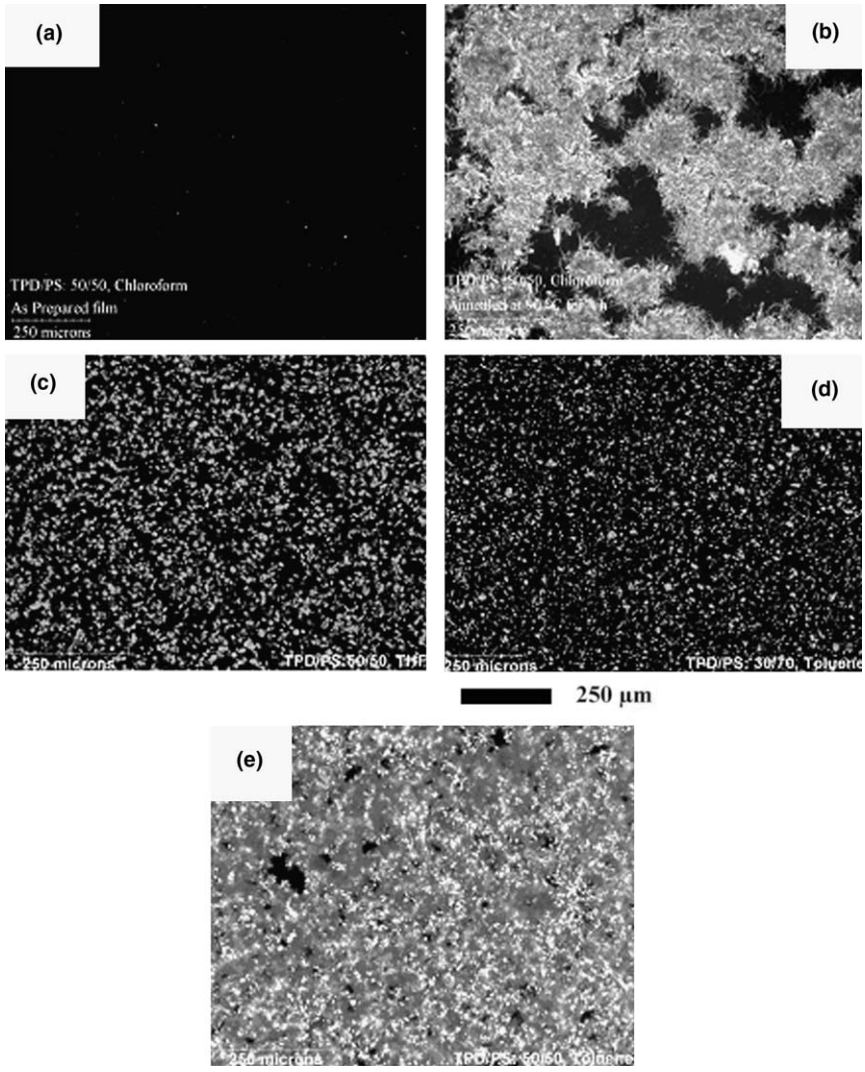

Fig. 8. Optical micrographs of TPD/PS composites; TPD/PS: 50/50 (a) as prepared film cast in $CHCl_3$, (b) annealed at 90 °C for 4 h (cast in $CHCl_3$), (c) as prepared film in THF, (e) in toluene and (d) TPD/PS 30/70 in toluene.

3.5. Infrared spectroscopy

We used IR spectra before to qualitatively infer the molecular interactions between TPD or tritolylamine (TTA) with polycarbonates in the films cast from methylene chloride [18,20]. Certainly, there would be differences in the absorption frequencies between the polycarbonate in the solid state and in solution. In the latter case, the intermolecular interaction between the polymer chains is replaced to a large extent by the polymer–solvent interaction. The absorption spectra would depend on the local conformation of the polymer. This in itself is a specialized study. However, for qualitative comparison, we recorded FTIR spectra for BPAPC, PCZ and PS in the solid state and in solution with the three different solvents (CH_2Cl_2, $CHCl_3$ and $Cl_2C_2H_2Cl_2$), at a concentration of 0.25 g/dl. The specific absorption bands are discussed for these polymers to illustrate that conformational differences could exist, depending on the solvent. Developing detailed correlations between the peak positions and the conformation of the polymer is a major study by itself, and is not attempted here. Some of the absorption frequencies are listed in Table 2 for the solid polymer, and the dilute solution in the above solvents. The peaks at 3059 and 3042 cm^{-1} in BPAPC and PCZ spectra correspond to aromatic CH stretch [37]. A single peak at 3051 cm^{-1} was observed for BPAPC in CH_2Cl_2 solution. This peak is shifted to a much lower value (e.g. 3031 and 3009 cm^{-1}), in the case of $CHCl_3$ and $Cl_2C_2H_2Cl_2$. A similar difference in the peak shift is also seen in the case of PCZ and PS in these solvents.

The band at 1775 cm^{-1} is due to the carbonate segment. Varnell et al. [38] used the position of this absorption peak to determine the conformation of polycarbonate, in its blend with poly(ε-caprolactone). They observed that the carbonyl stretching vibration at 1775 cm^{-1} corresponds to the conformation in the (disordered) amorphous state. This peak shifts to 1768 cm^{-1} in their work, when the polycarbonate adopts a conformation similar to that in the crystalline state. This is the ''preferred conformation'' which allows for stretching of the polymer chain so as to allow interactions of the carbonate group with the solvent. In the present work, this peak is shifted to a lower wave number by 9 and

Table 2
Comparison of some IR peak positions of BPAPC, PCZ and PS polymers in solid state and in different solvents

Assignments	Wave number (cm^{-1})			
	BPAPC (solid)	BPAPC + CH_2Cl_2 (0.25 g/dl)	BPAPC + $CHCl_3$ (0.25 g/dl)	BPAPC + $Cl_2C_2H_2Cl_2$ (0.25 g/dl)
Aromatic C–H stretch	3059, 3042	3051	3031	3009
C=O stretch	1775	1772	1770	1766
C–O–C antisymmetric stretch	1365, 1225	1264, 1195	1334, 1231	1339, 1280
Aromatic C–H in-plane-bend	1164, 1104 1081, 1015	1164, 1081, 1015	1164, 1081, 1046 1016	1163, 1088, 1015
Aromatic C–H out-of-plane-bend	888, 831, 769 707	894	928, 877, 850	977, 935, 910
	PCZ (solid)	PCZ + CH_2Cl_2 (0.25 g/dl)	PCZ + $CHCl_3$ (0.25 g/dl)	PCZ + Cl_2C_2 H_2Cl_2 (0.25 g/dl)
Aromatic C–H stretch	3058, 3043 2936, 2861	3060, 2981, 2863	3028, 2977 2940, 2896	3007, 2863
C=O stretch	1776	1773	1771	1765
C–O–C antisymmetric stretch	1226	1251, 1197	1231, 1164	1279, 1204
Aromatic C–H in-plane-bend	1199, 1164 1107, 1014	1197, 1164, 1014 986	1164, 1108, 1046 1015	1089, 1014, 977
Aromatic C–H out-of-plane-bend	886, 822, 769	898	929, 877, 850	933, 910
	PS (solid)	PS + CH_2Cl_2 (0.25 g/dl)	PS + $CHCl_3$ (0.25 g/dl)	PS + Cl_2C_2 H_2Cl_2 (0.25 g/dl)
Aromatic C–H stretch	3102, 3082 3060, 3025 3002	3060, 2991	3014, 2977	3006
C=C–C aromatic ring stretch	1600, 1583 1493, 1452	1602, 1551, 1422	1602, 1581, 1523, 1476, 1424	1602, 1561, 1519 1493, 1453, 1442 1417
Aromatic C–H in-plane-bend	1180, 1155 1069, 1029	1253, 1156, 1020	1222, 1046,	1279, 1156, 1089 1029
Aromatic C–H out-of-plane-bend	842, 758, 701	986, 898	929, 877, 850	977, 910

11 cm^{-1} in the solutions of BPAPC and PCZ, respectively in $Cl_2C_2H_2Cl_2$. This indicates that the conformation of the polycarbonate is stretched (or extended as in its crystalline state) in this solvent. The shift of this peak (i.e., carbonate segment) was insignificant (e.g. 2–5 cm^{-1}) with the other two solvents.

The band at 1225 cm^{-1} is attributed to the C–O–C stretch which shifted to higher wave number by 39, 6 and 55 cm^{-1} for BPAPC in CH_2Cl_2, $CHCl_3$ and $Cl_2C_2H_2Cl_2$, respectively. A similar trend is also observed in the case of PCZ in these solvents. The peaks in the region from 700 to 1200 cm^{-1} are due to the aromatic CH in-plane and out-of-plane bending vibration of polymers. The peak positions are again dependent on the solvent. Similar shifts in absorption frequencies are seen with polystyrene as well.

3.6. Viscosity

We find that when only the polymer is used for casting the films (without the TPD), the T_g's of the polymers are not affected by the solvent used. We are not aware of any reported case to the contrary with any polymer. It is also known that when a solvent is used as a diluent, it can plasticize a polymer and depress its T_g. However, in the present work, the depression of T_g with TPD concentration depends on the solvent. If the conformation of a polymer in a solvent were such that it is extended (stretched out), an efficient intercalation of the TPD with the polymer would be possible. This would then lead to a larger depression of the T_g of the polymer. We noted before that the depression of T_g with either TPD or TTA is much larger with PCZ than with BPAPC. The former is more sterically hindered than BPAPC. It is possible that the molecular conformation of polycarbonate depends on the solvent, as was found in the studies of Janeczek and Turska [28].

The effect of the solvent on the configuration of the polymer was investigated by means of viscosity measurements. The variation of reduced viscosity with the solvent is plotted in Fig. 9 as a function of polymer concentration for various solvents. The intrinsic viscosity [η] as determined from the intercepts of the curves in Fig. 9, are presented in Table 3. It is seen that the η is significantly higher in the case of $Cl_2C_2H_2Cl_2$ as compared to the other solvents for the two types of polycarbonates and PS.

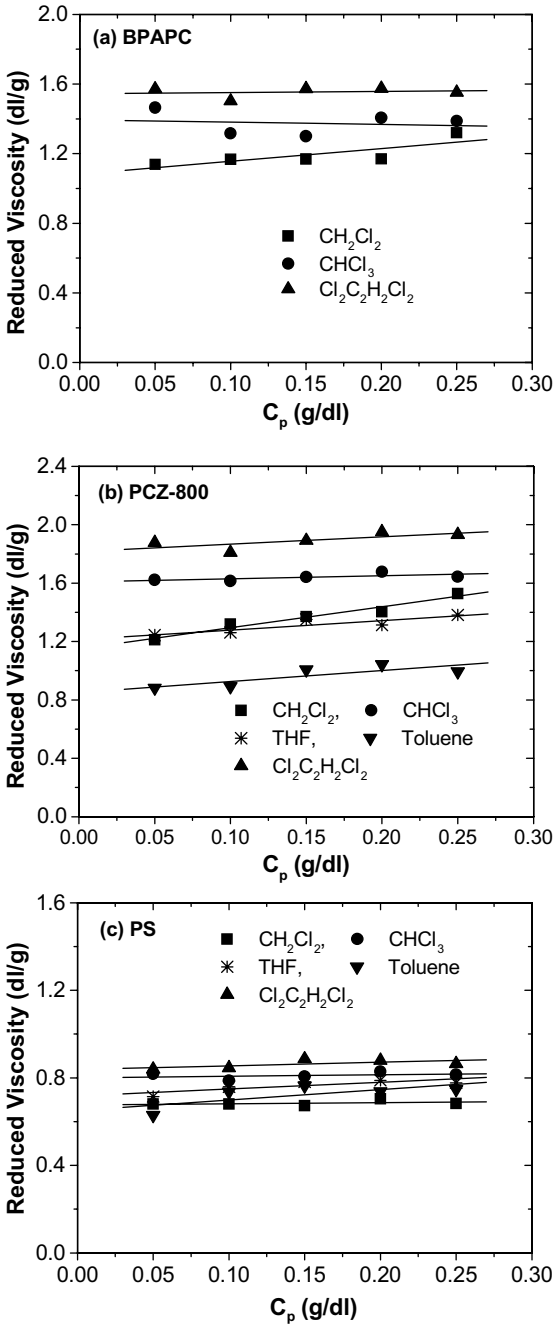

Fig. 9. The reduced viscosity plotted as a function of polymer concentration (C_p, g/dl) in various solvents.

The maximum T_g depression was observed for all composites prepared with this solvent, as seen in Fig. 1. Fig. 9a and Table 3 show that the [η] increases in the order CH_2Cl_2, $CHCl_3$ and $Cl_2C_2H_2Cl_2$. It is also seen from Table 2, that the shift of the IR peak position corresponding to

Table 3
Intrinsic viscosity of the polymers in the selected solvents

Solvent	Intrinsic viscosity (η) (dl/g)		
	BPAPC	PCZ	PS
CH_2Cl_2	1.1083	1.1821	0.6752
$CHCl_3$	1.3903	1.6016	0.8001
THF	–	1.2135	0.7358
Toluene	–	0.8584	0.6958
$Cl_2C_2H_2Cl_2$	1.5378	1.8107	0.8374

C=O stretch decreases in the same order. The same trend is seen for PCZ in Fig. 9b, and in the shift of the IR frequency. The [η] for PCZ is higher than that for BPAPC in each of these solvents. Thus the polycarbonate chain is more extended in $Cl_2C_2H_2Cl_2$. While this does not manifest itself in the T_g of the polymer by itself, it facilitates a more efficient plasticization by the small molecule in the presence of TPD. This in turn increases the stability of the composite against phase separation upon annealing. Since PCZ is conformationally more restricted compared to BPAPC, the effect is more pronounced.

4. Conclusions

We show that the conformation of polycarbonate and polystyrene is extended when $Cl_2C_2H_2Cl_2$ is used for film casting. This facilitates the intercalation of TPD, and results in larger depression of the T_g of the polymer in the composites with TPD. This in turn reduces the phase separation upon annealing. The extended conformation of the polymer in this solvent is confirmed with IR spectra as well as the viscosity measurements. As noted before, the work of Janeczek and Turska [28] also showed the extended (rod-like) conformation of polycarbonate in $Cl_2C_2H_2Cl_2$, which transitioned to a coil in mixtures of this solvent with *n*-propyl alcohol. Previous studies [23–27] were concerned with the effect of solvent on the charge transport properties of polythiophenes, polypyrroles and polyanilines. In the present study, we focused on the influence of the film-casting solvent on the stability of the polymer-charge transport molecule composite against phase separation. We show that the extended conformation of the polymer in $Cl_2C_2H_2Cl_2$ is responsible for this enhancement of the morphological stability.

Acknowledgement

Financial support from the Natural Sciences and Engineering Research Council of Canada (NSERC) and Xerox Research Centre of Canada (XRCC) is gratefully acknowledged.

References

[1] P.M. Borsenberger, D.S. Weiss, Organic Photoreceptors for Xerography, Marcel Decker Inc., New York, 1998;
A.R. Melnyk, D.M. Pai, in: Hard Copy and Printing Materials, Media and Process, SPIE vol. 1253, 1990, pp. 141–154.
[2] M. Strukelj, R.H. Jordan, A. Dodabalapur, J. Am. Chem. Soc. 118 (1996) 1213.
[3] J. Kalinowski, P. DiMarco, M. Cocchi, V. Fattori, N. Camaioni, J. Duff, Appl. Phys. Lett. 68 (1996) 2317.
[4] V. Bulovic, G. Gu, P.E. Burrows, S.R. Forrest, M.E. Thompson, Nature 380 (1996) 29.
[5] A. Yamamori, C. Adachi, T. Koyama, Y. Taniguchi, J. Appl. Phys. 86 (1999) 4369.
[6] J.D. Anderson, E.M. McDonald, P.A. Lee, M.L. Anderson, E.L. Ritchie, H.K. Hall, T. Hopkins, E.A. Mash, J. Wang, A. Padias, S. Thayumanavan, S. Barlow, S.R. Marder, G.E. Jabbour, S. Shaheen, B. Kippelen, N. Peyghambarian, R.M. Wightman, N.R. Armstrong, J. Am. Chem. Soc. 120 (1998) 9646.
[7] H. Mattoussi, H. Murata, C.D. Merritt, Y. Iizumi, J. Kido, Z.H. Kafafi, J. Appl. Phys. 86 (1999) 2642.
[8] C. Py, D. Roth, I. Lévesque, J. Stapledon, A. Donat-Bouillud, Synth. Met. 122 (2001) 225.
[9] V. Savvate'ev, J.H. Friedl, L. Zou, K. Christensen, W. Oldham, L.J. Rothberg, Z. Chen-Esterlit, R. Kopelman, J. Shinar, Synth. Met. 121 (2001) 1713.
[10] S.E. Shaheen, G.E. Jabbour, M.M. Morrell, Y. Kawabe, B. Kippelen, N. Peyghambarian, M.-F. Nabor, R. Schlaf, E.A. Mash, N.R. Armstrong, J. Appl. Phys. 84 (1998) 2324.
[11] P.M. Borsenberger, J. Appl. Phys. 68 (1990) 6263.
[12] L.-B. Lin, S.A. Jenekhe, P.M. Borsenberger, Appl. Phys. Lett. 69 (1996) 3495.
[13] H.-J. Yuh, D.M. Pai, Phil. Mag. Lett. 62 (1990) 61.
[14] H.-J. Yuh, D.M. Pai, in: Hard Copy and Printing Materials, Media and Process, SPIE vol. 1253, 1990, p. 162.
[15] H.-J. Yuh, D.M. Pai, Mol. Cryst. Liq. Cryst. 183 (1990) 217.
[16] D.M. Pai, in: P.N. Prasad, J.K. Nigam (Eds.), Frontiers of Polymer Research, Plenum Press, New York, 1991, p. 315.
[17] H.-J. Yuh, D.M. Pai, J. Imaging Sci. Tech. 36 (1992) 477.
[18] F. Khan, A.-M. Hor, P.R. Sundararajan, J. Phys. Chem. B 108 (2004) 117–126.
[19] F. Khan, A.-M. Hor, P.R. Sundararajan, Pure Appl. Chem. 76 (2004) 1467–1478.
[20] F. Khan, A.-M. Hor, P.R. Sundararajan, Synth. Metals 150 (2005) 199–211.
[21] P.D. Kemmesat, J.K. Neely, C.M. Randolph, K.R. Srinivasan, US Patent 6,001,523, 1999.
[22] L.-B. Lin, M.R. Silvestri, J.F. Yanus, R.H. Nealy, H.F. Hammond, C.C. Chen, K.-T.T. Dinh, J.M. Markovics, US Patent 6,242,144, 2000.
[23] T.Y. Kim, J.E. Kim, K.S. Suh, Polym. Int. 55 (2006) 80–86.

[24] F.J. Pern, A.J. Frank, J. Electrochem. Soc. 137 (1990) 2769–2777.
[25] H.N. Cong, C. Sene, P. Chartier, J. de Phys. Phys-Chim. Biol. 92 (1995) 979–982.
[26] J. Joo, Y.C. Chung, J.-K. Lee, J.K. Hong, W.P. Lee, S.M. Long, A.J. Epstein, H.S. Woo, K.S. Jang, E.J. Oh, Synth. Metals 84 (1997) 831–832.
[27] J. Joo, H.G. Song, Y.C. Chung, J.S. Baeck, S.K. Jeong, J.S. Suh, E.J. Oh, J. Korean Phys. Soc. 30 (1997) 230–236.
[28] H. Janeczek, E. Turska, Polymer 28 (1987) 847–851.
[29] P.R. Sundararajan, Macromolecules 22 (1989) 2149–2154.
[30] P.R. Sundararajan, Macromolecules 26 (1993) 344–348.
[31] M.L. Huggins, J. Am. Chem. Soc. 64 (1942) 2716.
[32] Y. Shirota, K. Okumoto, H. Inada, Synth. Met. 111–112 (2000) 387.
[33] D.F. O'Brien, P.E. Burrows, S.R. Forrest, B.E. Koene, D.E. Loy, M.E. Thompson, Adv. Mater. 10 (1998) 1108.
[34] D.M. Hoffman, L.E. Caley, Org. Coatings Plast. Chem. 44 (1981) 686;
S. Ciutacu, P. Budrugeac, G. Mares, I. Boconcios, Polym. Degrad. Stab. 29 (1990) 321;
T.K. Tsotsis, J. Comp. Mater. 29 (1995) 410;
R. Bernstein, D.K. Derzon, K.T. Gillen, Polym. Degrad. Stab. 88 (2005) 480.
[35] S. Drappel, P.R. Sundararajan, A. Rudin, Polymer 38 (1997) 1259.
[36] L. Alexandru, J. Zamin, P.R. Sundararajan, J. Appl. Polym. Sci. 43 (1991) 2259.
[37] T.M. Madkour, in: J.E. Mark (Ed.), Polymer Data Handbook, Oxford University Press, New York, 1999, p. 363;
I. Noda, A.E. Dowrey, C. Marcott, in: J.E. Mark (Ed.), Physical Properties of Polymers Handbook, New York, Amer. Inst. Phys., 1996, p. 291.
[38] D.F. Varnell, J.P. Runt, M.M. Coleman, Macromolecules 14 (1981) 1350.

Available online at www.sciencedirect.com
ScienceDirect
Organic Electronics 7 (2006) 423–427
Organic Electronics
www.elsevier.com/locate/orgel

Letter

Jet-printed electrodes and semiconducting oligomers for elaboration of organic thin-film transistors

S. Sanaur [a,*], A. Whalley [b], B. Alameddine [c], M. Carnes [b], C. Nuckolls [b]

[a] Departement of Packaging and Flexible Substrate, Center for Microelectronics of Provence – Georges Charpak, Ecole Nationale Supérieure des Mines de Saint-Étienne, Laboratoires Morandat, impasse de la Plaine 13120, Gardanne, France
[b] Department of Chemistry and The Nanoscience Center, Columbia University, 3000 Broadway Avenue, New York, NY 10027, USA
[c] Chemistry Department, University of Balamand, P.O. Box 100, Tripoli, Lebanon

Received 9 March 2006; received in revised form 2 May 2006; accepted 3 May 2006
Available online 9 June 2006

Abstract

A new oligomer of bithiophene and substituted fluorene has been successfully synthesized, exhibiting good FET performance. Our results show that devices can be obtained from inkjetted OTFTs and elaborated by direct writing without any particular pre-patterning or self-alignment techniques. We have also demonstrated the possibility to fabricate inexpensive OTFTs by direct writing paving the way toward using inkjet printing as the key technology for such applications in plastic electronics. The ease of this technique allows charts a clear path to flexible electronics.

PACS: 85.30.−z; 72.80.Le; 81.07.−b; 73.61.Ph; 85.30.Tv

Keywords: Inkjet printing; OTFT; Semiconductor molecular engineering; Gold nanoparticles; Direct writing

Here we describe the direct inkjet printing of transistors that utilize a semiconducting layer formed from the oligomers of bithiophene and the substituted fluorene and source and drain electrodes formed from gold nanoparticles. Organic materials are promising candidates to make organic thin-film transistors (OTFTs) active components for the fabrication of low-cost devices for applications such as radio frequency identity (RFID) tags [1], polymer electronics [2], and OTFT display backplanes [3]. However, the carrying out of OTFTs does not attain the low-cost expected. Inline mass production, where the global process is made in continuous by one machine as fast as possible, fills this requirement. That is to say the integration of processes like spin-coating, photolithography, e-beam lithography, or vacuum thermal evaporation (VTE) steps [4] will become too expensive.

Direct printing techniques are mentioned to be one of the key-technologies [5] to complete such plastic electronics devices. The first existing technique consists of a pad printing technique in continuous processing [6]. The second approach is based on flexography technique which requires, as a preceding step to processing, the fabrication of a solid master by photolithography [7]. The last approach

* Corresponding author. Tel.: +33 4 42 50 92 74; fax: +33 4 42 51 34 22.
E-mail address: sanaur@emse.fr (S. Sanaur).

1566-1199/$ - see front matter
doi:10.1016/j.orgel.2006.05.003

is based on drop on-demand inkjet printing (DOD-IJP) technique. This latter process allows the elaboration of OTFTs, even without (i) patterning through a shadow- or photo-mask, (ii) drops self-alignment thanks to a pre-patterning made by photolithography [8], (iii) etching and cleaning steps. Nonetheless, the materials used in DOD-IJP must be present in solution and potentially have high electrical properties.

Based on the work of Fréchet et al. [9], we selected well-defined oligomers rather than polymers as the subunit for the semiconducting layer. We utilized the oligomers of fluorene and bithiophene because their polymers [10] and other related oligomers [11] have been used extensively in electrical devices [10,11]. Oligomers present many advantages over polymers. For example, a higher degree of purity in oligomers should allow for a better opportunity to control the molecular arrangement. In addition the oligomers are easily processed due to their solubility and low viscosity.

Scheme 1 shows the synthesis of our target organic semiconductor (**1**). The synthesis involves two sequential Suzuki coupling reactions [12]. The first coupling differentiates the two bromine atoms of the bithiophene by reaction with phenylboronic acid, and the second coupling joins two of these pieces to the diboronic acid of 9,9-didodecylfluorene (Scheme 1).

To test **1** for its efficacy in thin film transistors, we have fabricated thermally evaporated thin films of it and used a metal mask to define the source and drain electrodes. The doped silicon wafer serves as a global back gate for the devices. We deposited 50 nm of **1** followed by the Au electrodes, again by vacuum evaporation. The channel length (L) was 75 μm and the electrode width (W) was 2 mm. Fig. 1a and b show the transconductance and transistor output for a typical device. The mobility ($8 \times 10^{-3} \pm 10^{-3}\ \mathrm{cm^2\ V^{-1}\ s^{-1}}$) and threshold voltage (below -20 V) are calculated by plotting $|I_{DS}|^{1/2}$ versus V_G, using the formula [13]: $I_{DS} = (\mu W C_i/2L) \cdot (V_G - V_{TH})^2$ with the capacitance $C = 11.3\ \mathrm{nF/cm^2}$ for the gate dielectric layer [14]. The gate dielectriccapacitance (300 nm of SiO_2 and a monolayer of HMDS) comes from measurements over a range of frequencies [13] and is what would be expected for a 300 nm thick silicon oxide layer

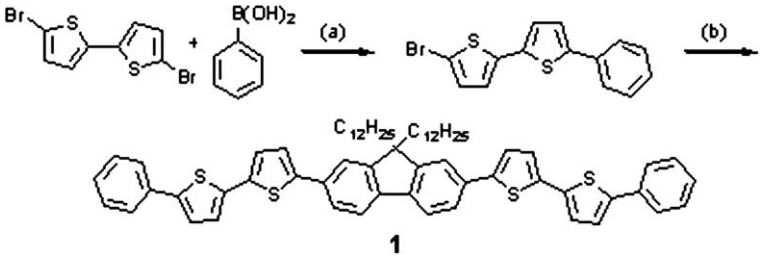

Scheme 1. Reagents and conditions: (a) K_2CO_3, $Pd(PPh_3)_4$, toluene/H_2O, reflux, (b) 9,9-didodecylfluorene-2,7-diboronic acid, K_2CO_3, $Pd(PPh_3)_4$, toluene/H_2O, reflux.

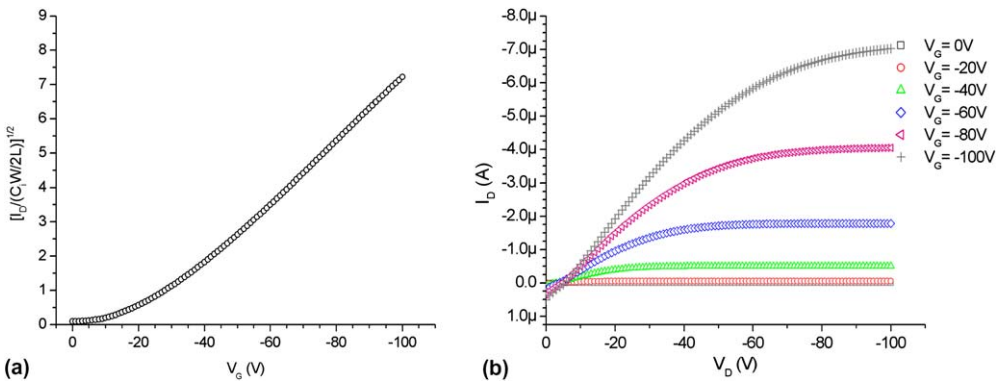

Fig. 1. (a) Transconductance at $V_{DS} = -100$ V and (b) output characteristics for OTFTs from **1** deposited by thermal vacuum evaporation (dots in each figure are experimental data).

with few defects [14]. These unoptimized result are consistent with the performance of fluorene-bithiophene based polymeric semiconductors [15,16].

Next we focus on printing the source and drain electrodes. Here we use nanoparticles of Au [18,19] and print them on clean silicon wafers coated with an HMDS self-assembled monolayer. We filtered a solution of capped gold nanoparticles (3 wt.%) diluted in toluene/α-terpineol mixing (1.5/1 v/v) and then printed them with the inkjet setup described in the experimental section. Wafers were heated at 40 °C during the deposition process and the printed lines were subsequently annealed at 130 °C for ~1 h under ambient conditions to enhance the conductivity of the gold lines. We can notice shortest anneal times can be addressed for Au nanoparticles capped with shorter alkane-thiols chains [18]. The spatial control of features goes down to 30 μm without pre-patterning the wafer or conductor self-alignment techniques [8,10,15]. The cross section of a line is not uniform in thickness due to a splash-effect. The printed lines are 1 mm long, 120 μm wide and 200 nm thick. Fig. 2 shows an optical microscopy image of inkjet printed gold lines.

Fig. 3 shows the results of simple two-probe measurements comparing the conductivity from thermally evaporated gold lines and the inkjet printed lines. The conductivity of printed lines were lower by around a factor of 3 (from 3×10^4 S/cm and 9×10^4 S/cm) and similar to the results of others who have printed gold lines from gold nanoparticles [17,18].

Using these printed lines, we next turned our attention to printing the oligomer that was synthesized and tested above. We first filter (Millipore™, 200 nm pore diameter) a solution of **1** in 1,2,4 tricholorobenzene (5 mg/mL) and print this between gold lines that define the source and drain of the transistor (Fig. 4a). The material was annealed at 140 °C for 30 min under an argon atmosphere. The printed OTFTs have a channel length (L) of 45 ±5 μm and channel width (W) of 270 μm. The device exhibits an average field effect mobility of 5.4×10^{-4} cm^2 V^{-1} s^{-1} and an on/off current ratio of 6×10^3 at $V_{DS} = -100$ V (Fig. 4b). The output characteristics show good saturation and no sign of significant contact resistance (Fig. 4c). The threshold gate voltage is below −30 V (Fig. 4b).

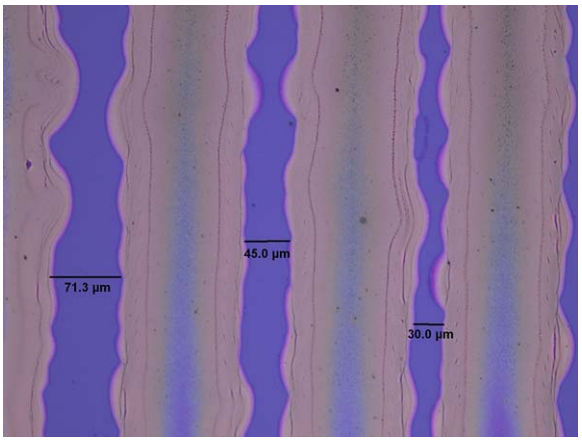

Fig. 2. Optical microscopy image of inkjet printed gold lines separated by 71.3 μm, 45 μm and 30 μm, respectively without pre-patterning or self-alignment on substrates.

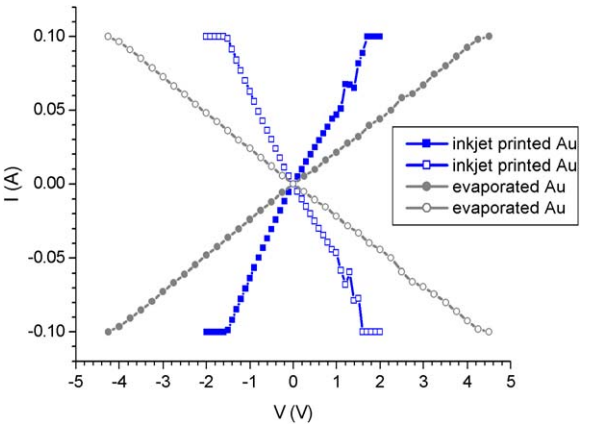

Fig. 3. Two-probe conductivity measurements of inkjetted and evaporated gold lines.

In conclusion, a new oligomer has been successfully synthesized, exhibiting good FET performance. Our results show that devices with good performance can be obtained from an all-inkjetted OTFT elaborated by direct writing without any particular pre-patterning or self-alignment techniques [8,10,15]. We have also demonstrated the possibility to fabricate inexpensive OTFTs by direct writing paving the way toward using inkjet printing as the key technology for such applications in plastic electronics. The ease of this technique and the possibility of organic semiconductor engineering with better electrical performances allow charts a clear path to flexible electronics.

Experimental section

The devices made by VTE were measured under daylight and ambient conditions using an HP4156C semiconductor analyzer, and exhibiting a field-effect mobility of 8×10^{-3} cm^2 V^{-1} s^{-1} with

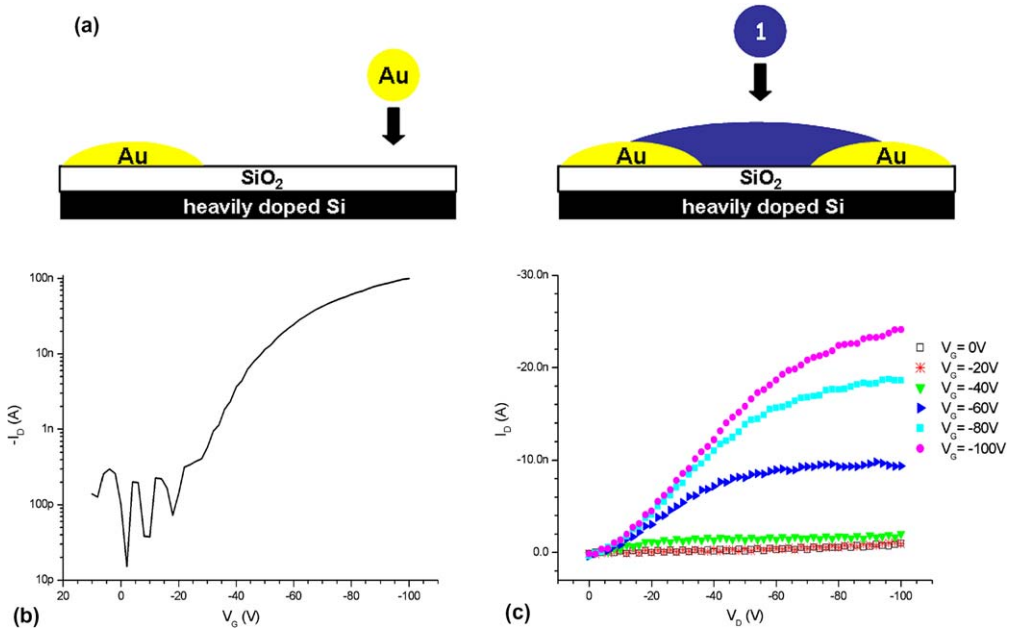

Fig. 4. (a) Schematic description of OTFT fabrication by printing (DOD-IJP): source, drain (gold nanoparticles) electrodes and **1** as semiconductor, (b) transconductance at $V_D = -100$ V and (c) output characteristics of all-inkjet printed OTFTs on insulated silicon wafer.

an on/ off current ratio of 6×10^3 at $V_{DS} = -100$ V (Fig. 1a).

The synthesis of gold nanoclusters were first reported by Murray [19]. 1.5 g of tetroactylammonium bromide was mixed with 80 mL of toluene and added to 0.31 g of $HAuCl_4{:}xH_2O$ in 25 mL of deionized water. $AuCl_4^-$ was transferred into toluene and the aqueous phase was removed.

The DOD-IJP experiment used in the present study is a custom-build setup, composed of three parts: (i) DOD-IJP assembly, (ii) X–Y translation stages, and (iii) a computing system, which commands both the DOD-IJP dispensing device and the X–Y stages, simultaneously. MicroJet™ printheads, drop-on-demand dispensing devices, provided by Microfab Inc. were employed. The Piezoelectric DOD used in this apparatus is suited for dispensing droplets with a diameter of 50 μm from a range of solvents including water and many organic solvents. Waveform dispensing controller generates bipolar pulses which avoids the formation of satellites droplets during jetting. X–Y translation stages are driven by a stepper-motor with a resolution of 1 μm over which is mounted a hotplate used to heat the predeposited droplets, and to enhance the continuity of the printed lines. The DOD-IJP experiment was undertaken in a standard laboratory environment at under ambient conditions, with no temperature or humidity control.

References

[1] T.W. Kelley, P.F. Baude, C. Gerlach, D.E. Ender, D. Muyres, M.A. Haase, D.E. Vogel, S.D. Theiss, Chem. Mater. 16 (23) (2004) 4413.
[2] 'Field of technology in which polymers and/or oligomers assume an electrical and/or electronic function': J. Ficker, A. Ullman, W. Fix, H. Rost, W. Clemens, J. Appl. Phys. 94 (2003) 2638.
[3] L. Chabinyc, W.S. Wong, K.E. Paul, R.A. Street, Adv. Mater. 15 (2003) 1903.
[4] W. Kelley, P.F. Baude, C. Gerlach, D.E. Ender, D. Muyres, M.A. Haase, D.E. Vogel, S.D. Theiss, Chem. Mater. 16 (2004) 4413.
[5] J. Mills, Printed Electronics Conference (New Orleans, USA), 2004.
[6] A. Knobloch, A. Manuelli, A. Bernds, W. Clemens, J. Appl. Phys. 96 (2004) 2286.
[7] U. Zschieschang, H. Klauk, M. Halik, G. Schmid, C. Dehm, Adv. Mater. 15 (2003) 1147.
[8] H. Sirringhaus, T. Kawase, Science 290 (2000) 2123.
[9] P.C. Chang, J. Lee, D. Huang, V. Subramanian, A.R. Murphy, J.M.J. Fréchet, Chem. Mater. 16 (23) (2004) 4783.
[10] N. Stutzmann, R.H. Friend, H. Sirringhaus, Science 299 (2003) 1881.
[11] H. Meng, Z. Bao, A.J. Lovinger, B.-C. Wang, A.M. Mujsce, J. Am. Chem. Soc. 123 (2001) 9214.
[12] N. Miyaura, A. Suzuki, Chem. Rev. 95 (1995) 2457.

[13] Q. Miao, M. Lefenfeld, T.-Q. Nguyen, T. Siegrist, C. Kloc, C. Nuckolls, Adv. Mater. 17 (2005) 407.
[14] S.M. Sze, Physics of Semiconductor Devices, Wiley-Interscience, New York, 1969.
[15] T. Kawase, T. Shimoda, C. Newsome, H. Sirringhaus, R.H. Friend, Thin Solid Films 438 (2003) 279.
[16] K.E. Paul, W.S. Ong, S.E. Ready, R.A. Street, Appl. Phys. Lett. 83 (2003) 2070.
[17] Y. Wu, Y. Li, B.S. Ong, P. Liu, S. Gardner, B. Chiang, Adv. Mater. 17 (2005) 184.
[18] D. Huang, F. Liao, S. Molesa, D. Redinger, V. Subramanian, J. Electrochem. Soc. 150 (2003) G412.
[19] M.J. Hostetler, J.E. Wingate, C.J. Zhong, J.E. Harris, R.W. Vchet, M.R. Clark, J.D. Longdono, S.J. Green, J.J. Stokes, G.D. Wignall, G.L. Glish, M.D. Porter, N.D. Evans, R.W. Murray, Langmuir 14 (1998) 17.

Available online at www.sciencedirect.com
ScienceDirect
Organic Electronics 7 (2006) 428–434
Organic Electronics
www.elsevier.com/locate/orgel

Letter

Low-temperature self-assembly of copper phthalocyanine nanofibers

Shich-Chang Suen [a], Wha-Tzong Whang [a,*], Fu-Ju Hou [b], Bau-Tong Dai [b]

[a] *Department of Materials Science and Engineering, National Chiao Tung University, 1001 Ta Hsueh Road, Hsinchu 30050, Taiwan, ROC*
[b] *National Nano Device Laboratories, No. 26, Prosperity Road I, Science-based Industrial Park, Hsinchu, Taiwan, ROC*

Received 26 April 2006; received in revised form 29 May 2006; accepted 30 May 2006
Available online 30 June 2006

Abstract

This paper describes a method for producing 1D organic nanofibers by exploiting intermolecular dispersive forces during the self-assembly of CuPc molecules. The average length of these CuPc nanofibers deposited at 100 °C, a temperature much lower than that required for the synthesis of carbon nanotubes, was ca. 500 nm, with diameters in the range 15–50 nm. XRD analysis of these nanofibers revealed that they possessed an α phase structure. HRTEM images indicated that the CuPc nanofibers formed through layered stacking of CuPc molecules. These CuPc nanofibers exhibit field emission characteristics (with a turn-on field of 13.6 V/μm) and follow Fowler–Nordheim behavior in a manner similar to that of carbon nanotubes. The stable emission current and relative simplicity of their synthesis suggest a broad range of applications for CuPc nanofibers in nanoscience and nanotechnology.

PACS: 79.70.+q; 81.07.Nb; 85.35.; 81.16.Dn; 72.80.Le

Keywords: Field emission; Self-assembly (nanofabrication); Organic semiconductors; Nanofibers; Copper Phthalocyanine

1. Introduction

One-dimensional (1D) nanostructures of inorganic materials continue to attract a great deal of interest because of their peculiar properties, relative to those of their bulk counterparts, and great potential for application [1–5]. Presently, however, the conditions employed to synthesize such inorganic nanostructures involve the use of high-temperatures and/or catalysts. Many recent studies have indicated that organic compounds can form 1D nanostructures under mild conditions when intermolecular dispersive forces are exploited in self-assembly processes [6–12]. When biased in a vacuum chamber, most of these nanostructures exhibit excellent field emission characteristics [10–12]. Copper phthalocyanine (CuPc), which has been known for almost a century, is a particularly appealing compound for a variety of applications. For example, its extreme resistance to chemical and thermal degradation and its p-type semiconducting characteristics have led to its use as a hole transport layer in organic

* Corresponding author. Tel.: +886 3 5726111x31873; fax: +886 3 5724727.
E-mail address: wtwhang@mail.NCTU.edu.tw (W.-T. Whang).

1566-1199/$ - see front matter
doi:10.1016/j.orgel.2006.05.008

light-emitting diodes (OLEDs) [13] and as an active layer in organic thin film transistors (OTFTs) [14]. In addition, the excellent photoconductive properties of CuPc enable its application in the photoconductive layers of photocopying machines and solar cells [15,16]. All of these applications are based, however, on the electrical characteristics of CuPc in the form of thin films. To our knowledge, there have been no previous reports describing the applications of CuPc as 1D structures. The planar macrocyclic structure and extended π-electron system of CuPc molecules suggested to us that they would be good candidates for forming 1D structures through intermolecular π–π stacking interactions. In this study we prepared 1D CuPc nanofibers and evaluated their field emission characteristics. We have characterized these CuPc nanofibers using scanning electron microscopy (SEM), X-ray diffraction spectroscopy (XRD), and high-resolution transmission electron microscopy (HRTEM) techniques.

2. Experimental procedure

The CuPc films were grown through vacuum sublimation in a thermal coater at a base pressure of ca. 3×10^{-6} torr. Commercial powders of CuPc were sublimed onto various substrates, including Al, Ti, TiN, Au, and SiO_2, from a heated crucible. The temperature of the crucible was ca. 100 °C; the corresponding deposition rate, determined using a quartz crystal microbalance, was 3 Å/s. To study the effect of the temperature on the film morphology, these substrates were maintained at 25, 100, 150 or 200 °C. Structural investigations were performed using a JEOL JSM-6500 F scanning electron microscope. Grazing incident X-ray diffraction was performed using a PHILIPS X'Pert Pro X-ray diffraction system equipped with a Cu-K_α radiation source. Contact angles and surface energies were determined using a KRUSS GH-100 universal surface tester. The profiles and fine structures of the nanostructures were imaged and analyzed using a JEOL JEM-2010 F high-resolution transmission electron microscope equipped with an Oxford energy dispersive spectrometer. The field emission measurements were performed in a vacuum chamber (ca. 10^{-6} torr) with a cylindrical copper electrode (diameter: 2.2 mm) positioned above the substrate surface at a distance of 75 μm. A Keithley 237 instrument was used to measure the emission current of the CuPc nanofibers as a function of the sweep bias.

3. Results and discussions

The choice of film growth method and the crystalline properties and surface energies of the substrates have profound effects on the surface morphologies of coated organic thin films [17]. In most cases, the crystallinity of the substrate strongly affects the crystallinity of the deposited film. The surface energy of the substrate, which governs the mobility of the deposited molecules on that surface, determines the wetting ability of the coated film. Therefore, to determine the growth conditions necessary to prepare 1D CuPc nanostructures, we deposited CuPc molecules onto different substrates, namely Al, Au, Ti, TiN and SiO_2, at various temperatures and used SEM to investigate their morphologies.

Fig. 1(a) and (b) present SEM images of CuPc films deposited at room temperature onto SiO_2 and Au substrates, respectively. Both images display contiguous granular crystals that possess smooth morphologies. The mean diameters of the granular crystals formed on the Au and SiO_2 substrate were both ca. 25 nm. Similar granular morphologies were exhibited for the films coated on the other substrates (Al, Ti and TiN), although with different crystallite sizes. When the substrates were heated above 100 °C, however, we observed totally different morphologies. Fig. 1(c) displays the in-plane island morphology of the CuPc layer on SiO_2. In contrast, the layer deposited onto the Au substrate possessed an out-of-plane 1D nanofiber morphology (Fig. 1(d)). The CuPc packing morphologies on TiN were similar to those on the gold surface, whereas those on the Ti and Al substrates were a mixture of both kinds. The average length of the nanofibers formed on the gold substrate was ca. 500 nm, with their diameters falling in the range 15–50 nm. At a higher deposition temperature, but with the same process time, the CuPc nanofibers that formed were longer and had larger diameters, but their density was lower. Fig. 2 displays the various morphologies of the CuPc layers deposited at (a) room temperature and at (b) 100, (c) 150 and (d) 200 °C. For the CuPc nanofibers deposited on the Au surface at 150 °C, the average length increased to 1 μm and the mean diameter expanded to 60 nm.

Contact angle measurements indicate that SiO_2 has a higher surface energy (50.7 mJ/m^2) than does gold (39.4 mJ/m^2), suggesting that the oxide substrate has a higher concentration of unsaturated surface bonds, which tend to adsorb molecules to lower the surface free energy. Therefore, it was

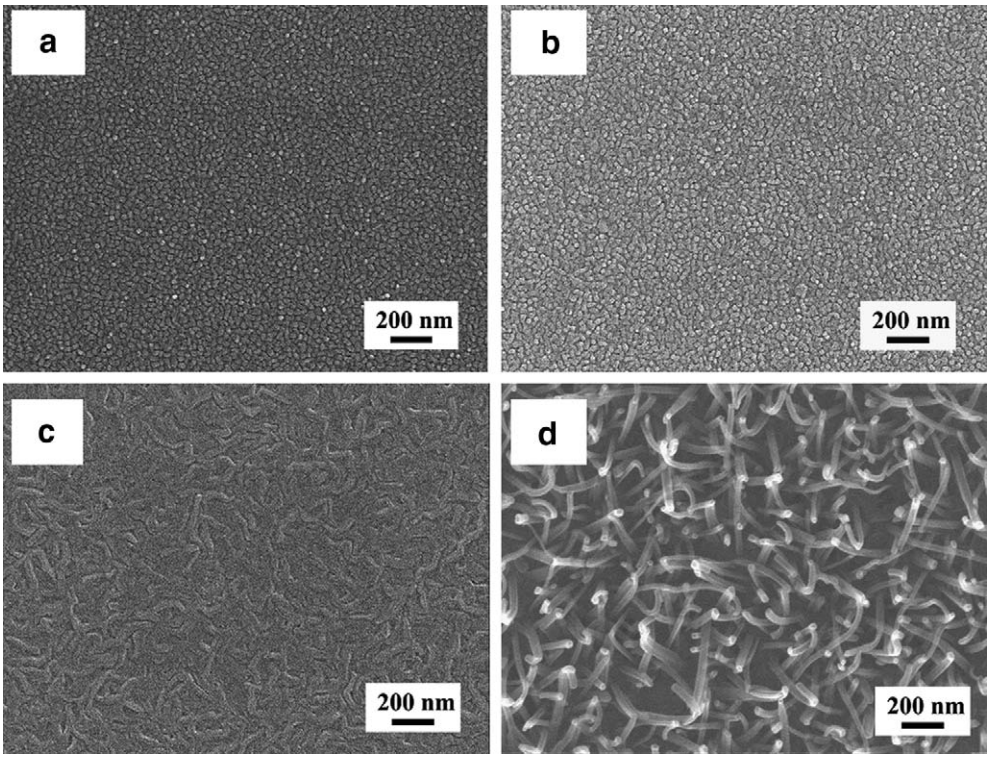

Fig. 1. Top-view SEM images of CuPc layers deposited at room temperature on (a) SiO_2 and (b) Au and at 100 °C on (c) SiO_2 and (d) Au.

not unexpected that the deposited CuPc molecules would have a stronger tendency to cover the whole SiO_2 surface, rather than stack to form out-of-plane nanofibers.

In the case of the CuPc layer formed on the gold substrate, the change in morphology that occurred upon increasing the temperature can be explained by considering the following equation [18]:

$$\gamma = \gamma^0 \left(1 - \frac{T}{T_c}\right)^n \quad (1)$$

where γ is the surface energy at temperature T and γ^0 is the surface energy at the critical temperature, T_c; the value of n may be closer to unity for metals. According to this formula, the surface energy of the gold substrate decreases as the temperature increases. This reduction in surface energy weakens the molecule–substrate interactions, resulting in the intermolecular π–π interactions becoming dominant. Meanwhile, the high substrate temperature favors surface diffusion, driving the adsorbed molecules toward growth at certain nucleation sites, which are formed owing to the lattice mismatch between CuPc and Au polycrystalline [19,20]. Therefore, the CuPc molecules prefer to stack up into nanofibers, rather than spread out to cover the gold substrate in a mesh-like film.

The surface energies for Ti, Al and TiN are 37.51, 35.14 and 36.3 mJ/m^2, respectively. These values are similar to – but lower than – the surface energy of the gold substrate. The CuPc layers on those substrates all exhibit the out-of-plane nanofiber morphology, except that a mesh-like morphology coexists on the Al and Ti substrates. Although the lower surface energies should lead to weaker interaction forces between the adsorbate and the substrates, these metal substrates are more easily oxidized than is the gold substrate. We suspect that the oxygen atoms of the resulting metal oxides react, or interact noncovalently, with the organic molecules to cause this phenomenon. For the TiN surface, its relative inertness toward oxygen and columnar crystal morphology combine to form the out-of-plane nanofiber structure.

Depending on its processing conditions, CuPc may form one, or a mixture, of many crystal phases, which are termed the α, β, γ, δ, ε, and x phases [21]. Of the various polymorphic forms, the most common structures are the α and β phases, which exhibit slightly different structural and electrical characteris-

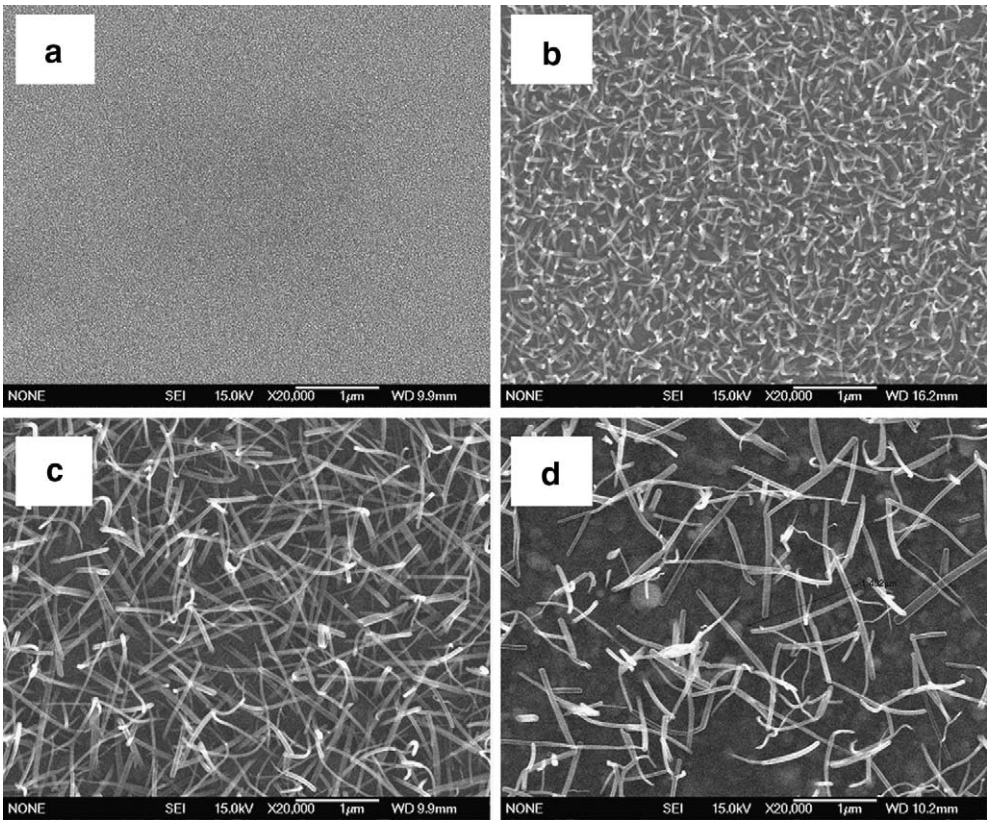

Fig. 2. Top-view SEM images of CuPc layers deposited on Au substrates at (a) room temperature and at (b) 100, (c) 150 and (d) 200 °C.

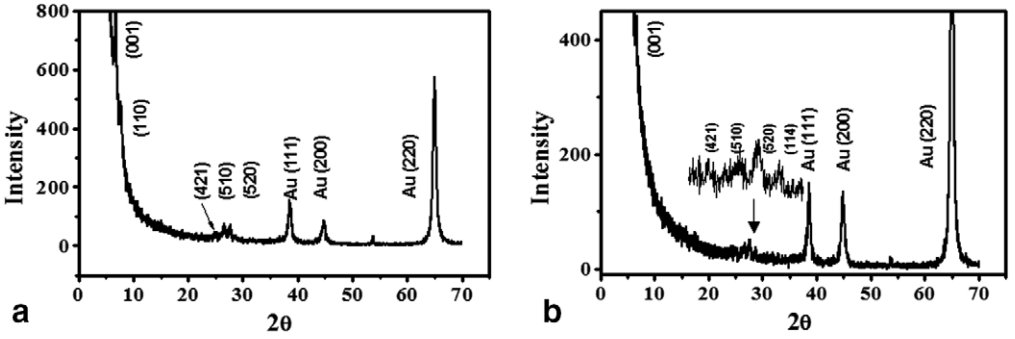

Fig. 3. XRD spectra of CuPc layers deposited on Au substrates at (a) room temperature and (b) 150 °C.

tics. Films deposited at room temperature exhibit the α phase, whereas those deposited at higher-temperatures transform into the β phase [22]. Fig. 3(a) and (b) present the grazing incident X-ray diffraction (GID) patterns of the CuPc layers deposited at room temperature and 150 °C, respectively. The incident angle and the scan step used to obtain both patterns were 0.5° and 0.02°. The 2θ peaks at 38.4°, 44.7° and 64.9° in both patterns are associated with the gold substrate. The recognizable diffraction peaks of the CuPc film at (0 0 1), (1 1 0), (4,2 1), (5 1 0), and (5 2 0) in Fig. 3(a) indicate that the CuPc film that we deposited at room temperature existed in the tetragonal α phase [23]. The diffraction peaks from the CuPc nanofibers deposited at 150 °C (Fig. 3(b)) are similar to those arising from the CuPc film, but the (1 1 0) peak is absent. Although, in theory, the crystallinity of a film should be greater after higher-temperature processing, the morphology change (from a film to fibers) at the higher deposition temperature

resulted in a rough and discontinuous CuPc layer on the gold substrate, leading to lower intensities of some of the diffraction peaks. According to the reference diffraction peak for a monoclinic β-phase structure [23], at least three intense peaks should be present at 7.0°, 9.2° and 23.8°. These peaks are absent in Fig. 3(b), suggesting that the structure of the CuPc nanofibers deposited at 150 °C was that of the α phase.

Fig. 4(a) presents an HRTEM image of a single CuPc nanofiber (diameter: 16 nm), which was synthesized on a heated gold substrate (100 °C). Unlike related carbon nanotubes (CNTs), no catalyst appears at the top of the fiber. This feature was further verified after recording the energy dispersive spectra (EDS), which exhibited no peaks arising from gold atoms at any point along the entire length of the CuPc nanofiber. Fig. 4(b) presents a magnified image of the CuPc nanofiber; it exhibits fringes, suggesting that the CuPc units were stacked in the growth direction and aligned in a parallel manner. This high-resolution image indicates that the nanofibers formed through layered stacking of CuPc molecules. Fig. 4(b) also presents the corresponding profile analyzed using Fuji Imagegauge software. The average interlayer distance (4.3 Å) slightly exceeds the value of 3.8 Å found for the spacing h between two molecular layers along the stacking direction of α-CuPc thin films [24], depicted schematically in Fig. 4(c). This difference may be caused by the high aspect ratio of the 1D nanofiber structure, which suffers more stress and has a larger inclination angle (φ') of stacking than that angle (φ) of 2D smooth thin film structures. Therefore, at a constant interlayer distance d (3.4 Å), a larger inclination angle (φ') corresponds to a greater distance h, according to the cosine relationship.

We performed field emission characterization of the CuPc nanofibers that we synthesized on a heated (100 °C) gold substrate; this analysis was performed under vacuum (5×10^{-6} torr) after placing a cylindrical Cu electrode (diameter: 2.2 mm) 75 μm above the surface of the sample. The Cu electrode was connected to the source monitor unit (SMU) of a Keithley 237 instrument; the gold substrate under the CuPc nanofibers was grounded. Fig. 5 presents a plot of the emission current density J as a function of the applied field E. The turn-on field required for the CuPc nanofibers to produce a current density of 10 μA/cm^2 was 13.6 V/μm, a value that is somewhat higher than the fields required for turning on other previously reported organic nanofibers [10–12]. The electron affinity (3.1 eV) of CuPc [25] is much lower than the work function (5.1 eV) of the gold substrate, so the energy barrier (ca. 2 eV) that exists at the metal–organic contact limits electron injection from the substrate. Consequently, the finite injected electrons require a higher electric field to reach the same level of emission current. The inset of Fig. 5 displays a plot of $\ln(J/E^2)$ as a function of $1/E$; this straight line

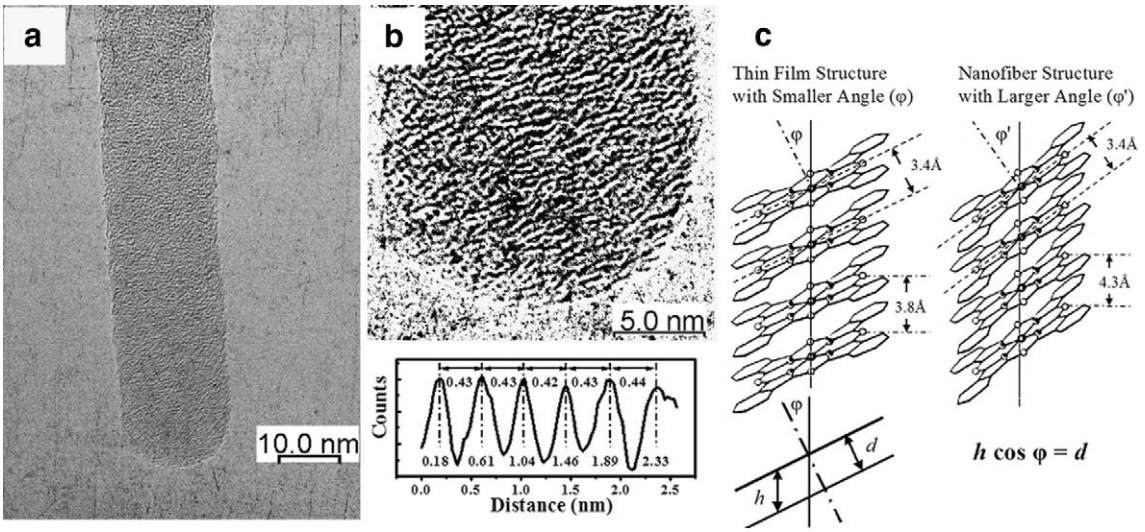

Fig. 4. (a) HRTEM image of a single CuPc nanofiber (diameter: 16 nm). (b) Magnified image of this nanofiber, which has been overcontrasted to intensify the fringes, and the corresponding profile analyzed using Fuji Imagegauge software. (c) Schematic illustration of CuPc molecules stacked at different inclination angles (φ).

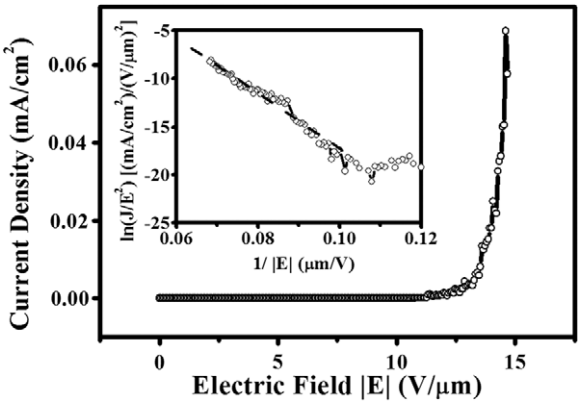

Fig. 5. Field emission J–E curve of the CuPc nanofibers. Inset: Corresponding FN plot.

implies that the field emission from these nanofibers follows the Fowler–Nordheim (FN) theory [26–28]. Taking into account the work function of bulk CuPc (3.1 eV), we deduced the field enhancement factor β of the CuPc nanofibers from the slope of the FN plot to be ca. 130. Normally, the enhancement factor is proportional to the length-to-radius ratio (L/r) of a 1D nanostructure [10]. Because the CuPc nanofibers reported herein possess shorter lengths (500 nm) and larger radii (50 nm), it is reasonable that they would exhibit a smaller enhancement factor relative to those of AlQ_3 organic nanowires [10]. Fig. 6 displays the emission current stability of the CuPc nanofibers when biased at 1000 V ($E = 13.3$ V/μm) for 1800 s. The mean current density was ca. 3 μA/cm^2, with a perturbation within one order of magnitude, which may arise from the random orientation of the CuPc nanofibers on the surface. The field emission current did not decay during the period of the stability measurement, suggesting that these CuPc organic nanofibers are suitable for use in electron emitting devices.

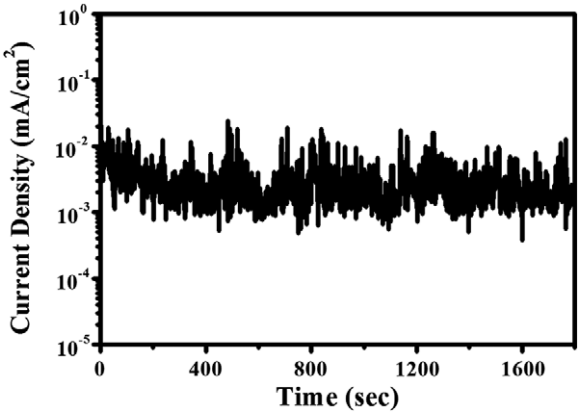

Fig. 6. Emission current stability of the CuPc nanofibers at constant voltage.

4. Conclusions

In this paper, we describe a simple method for producing CuPc organic nanofibers at low-temperature. XRD analysis of these nanofibers revealed that they possessed α-phase structures; HRTEM images indicated that they formed through layered stacking of CuPc molecules. The CuPc nanofibers exhibit field emission characteristics and follow Fowler–Nordheim behavior similar to that of CNTs. The stability of the emission current and the simplicity of the synthetic process suggest that these CuPc nanofibers may find a broad range of applications in nanoscience and nanotechnology.

Acknowledgments

We thank the National Science Council of the Republic of China for supporting this research financially under Contract No. NSC 94-2216-E-009-019. The technical support provided by the National Nano Device Laboratories is greatly appreciated. Authors also would like to thank Dr. Peter Glink for English correction.

References

[1] W.A. de Heer, A. Châtelain, D. Ugarte, Science 270 (1995) 1179.
[2] C.J. Lee, T.J. Lee, S.C. Lyu, Y. Zhang, H. Ruh, H.J. Lee, Appl. Phys. Lett. 81 (2002) 3648.
[3] Z. Pan, H.L. Lai, F.C.K. Au, X. Duan, W. Zhou, W. Shi, N. Wang, C.S. Lee, N.B. Wong, S.T. Lee, S. Xie, Adv. Mater. 12 (2000) 1186.
[4] J. Zhou, N.S. Xu, S.Z. Deng, J. Chen, J.C. She, Z.L. Wang, Adv. Mater. 21 (2003) 1835.
[5] W. Yi, T. Jeong, S. Yu, J. Heo, C. Lee, J. Lee, W. Kim, J.B. Yoo, J. Kim, Adv. Mater. 20 (2002) 1464.
[6] F.J.M. Hoeben, P. Jonkheijm, E.W. Meijer, A.P.H.J. Schenning, Chem. Rev. 105 (2005) 1491.
[7] S.I. Stupp, V. LeBonheur, K. Walker, L.S. Li, K.E. Huggins, M. Keser, A. Amstutz, Science 276 (1997) 384.
[8] H. Liu, Y. Li, S. Xiao, H. Gan, T. Jiu, H. Li, L. Jiang, D. Zhu, D. Yu, B. Xiang, Y. Chen, J. Am. Chem. Soc. 125 (2003) 10794.
[9] J.P. Hill, W. Jin, A. Kosaka, T. Fukushima, H. Ichihara, T. Shimomura, K. Ito, T. Hashizume, N. Ishii, T. Aida, Science 304 (2004) 1481.
[10] J.J. Chiu, C.C. Kei, T.P. Perng, W.S. Wang, Adv. Mater. 15 (2003) 1361.
[11] S.C. Suen, W.T. Whang, B.W. Wu, Y.F. Lai, Appl. Phys. Lett. 84 (2004) 3157.

[12] H. Liu, Q. Zhao, Y. Li, Y. Liu, F. Lu, J. Zhuang, S. Wang, L. Jiang, D. Zhu, D. Yu, L. Chi, J. Am. Chem. Soc. 127 (2005) 1120.
[13] S.T. Lee, Y.M. Wang, X.Y. Hou, C.W. Tang, Appl. Phys. Lett. 74 (1999) 670.
[14] Z. Bao, A.J. Lovinger, A. Dodabalapur, Appl. Phys. Lett. 69 (1996) 3066.
[15] I.A. Levitsky, W.B. Euler, N. Tokranova, B. Xu, J. Castracane, Appl. Phys. Lett. 85 (2004) 6245.
[16] P. Peumans, A. Yakimov, S.R. Forrest, J. Appl. Phys. 93 (2003) 3693.
[17] F. Schreiber, Phys. Status Solidi 201 (2004) 1037.
[18] A.W. Adamson, Physical Chemistry of Surfaces, John Wiley & Sons Publishers, 1990, p. 55.
[19] F. Yang, M. Shtein, S.R. Forrest, J. Appl. Phys. 98 (2005) 014906.
[20] Y.L. Lee, W.C. Tasi, J.R. Maa, Appl. Surf. Sci. 173 (2001) 352.
[21] H. Saijo, T. Kobayashi, N. Uyeda, J. Cryst. Growth 40 (1997) 118.
[22] T.V. Basova, B.A. Kolesov, Thin Solid Films 325 (1998) 140.
[23] 2001 JCPDS-International Centre for Diffraction Data; (a) PDF No. 06-0007 for α-CuPc, (b) PDF No. 37-1846 for β-CuPc.
[24] R. Hiesgen, M. Räbisch, H. Böttcher, D. Meissner, Sol. Energy Mater. Sol. Cells 61 (2000) 73.
[25] A.K. Mahapatro, S. Ghosh, Appl. Phys. Lett. 80 (2002) 4840.
[26] R.H. Fowler, L. Nordheim, Proc. R. Soc. London, Ser. A 119 (1928) 626.
[27] R.D. Young, Phys. Rev. 113 (1950) 110.
[28] A. Buldum, J.P. Lu, Phys. Rev. Lett. 91 (2003) 236801.

Available online at www.sciencedirect.com
ScienceDirect
Organic Electronics 7 (2006) 435–439
Organic Electronics
www.elsevier.com/locate/orgel

Letter

Low-voltage organic thin-film transistors with polymeric nanocomposite dielectrics

Fang-Chung Chen [a,*], Chiao-Shun Chuang [b], Yung-Sheng Lin [b], Li-Jen Kung [a], Tung-Hsien Chen [a], Han-Ping D. Shieh [a]

[a] Department of Photonics and Display Institute, National Chiao Tung University, 1001 Ta Hsueh Road, Hsinchu 300, Taiwan
[b] Department of Photonics and Institute of Electro-optical Engineering, National Chiao Tung University, Hsinchu 300, Taiwan

Received 24 February 2006; received in revised form 17 June 2006; accepted 22 June 2006
Available online 21 July 2006

Abstract

High performance organic thin-film transistors (OTFTs) incorporated with high dielectric nanoparticles in the dielectric layers have been demonstrated. The dielectric insulator consists of cross-linked poly-4-vinylphenol (PVP) and titanium dioxide (TiO_2) nanoparticles. In order to obtain highly soluble TiO_2 nanoparticles in organic solutions, the surface of nanoparticles was modified with organosiloxane. Moreover, the concern of higher leakage current, while using the high dielectric nanocomposite insulators, has been overcome by further applying another poly(α-methylstrylene) layer. As a result, we have demonstrated low-voltage OTFTs, which can be operated within 10 V.

PACS: 82.35.Np; 85.30.Tv

Keywords: Organic; Nanoparticle; Dielectrics; Thin-film transistors

Organic thin-film transistors (OTFTs) have been recognized as promising technology for next generation electronics due to their unique advantages, such as light-weight, flexibility, and low-cost fabrication [1–3]. Potential applications include flexible displays [4,5], radiofrequency identification (RFID) tags [6], "smart" cards, and other consumer electronics [7,8]. However, the major challenge to realize the commercialization of related products comes from their high threshold and operating voltages, due to the intrinsic low charge motilities of organic semiconductors. Because the field-induced current is proportional to the field-induced charge density, one feasible approach to achieve low-voltage operation in OTFTs is to use high dielectric constant (high-κ) materials as the gate insulators, which can afford greater surface charge density at the semiconductor-dielectric interface. Several works, especially those adopting inorganic high-κ materials, have demonstrated successfully the reduction of the OTFTs operating voltages using this concept [9,10]. However, these inorganic materials are usually expensive to fabricate and not compatible with

* Corresponding author. Tel.: +886 3 5131484; fax: +886 3 5737681.
E-mail address: fcchen@mail.nctu.edu.tw (F.-C. Chen).

1566-1199/$ - see front matter © 2006 Elsevier B.V. All rights reserved.
doi:10.1016/j.orgel.2006.06.009

plastic substrates due to the high-annealing-temperature processes and their fragility.

Using a solution-processable method high-κ polymers can be easily fabricated and used as dielectrics for OTFTs without the complications associated with sputtering high-κ materials and the high-temperature annealing [11]. Nanocomposite materials, consisting of titanium dioxide (TiO_2) nanoparticles and cross-linked poly-4-vinylphenol (PVP), were dispersed well in organic solvents. Upon spin-coating and thermal annealing, a composite insulator film was obtained. Due to the limited solubility of TiO_2 nanoparticles, the dielectric constant only increased from 3.5 to 5.4 after blending high-κ nanoparticles into the polymer matrix. In this work, surface modified TiO_2 nanoparticles with organosiloxane was used in order to increase the solubility in organic solvents. With the higher content of TiO_2 incorporated, a dielectric constant higher than 11 is achieved. More importantly, we will show that the current leakage problem through the gate dielectrics can be overcome by further applying another thin organic polymer insulator. As a result, we have also demonstrated low-voltage OTFTs, which can operate within 10 V.

Titanium dioxide exists naturally as three possible crystal types, namely, rutile, anatase and brookite [12]. In this study, we employed TiO_2 with rutile structure due to its higher dielectric constant ($\kappa = 114$) than that of other structures. In addition, rutile TiO_2 has much lower photocatalytic activity; possible photoreactions can be avoided. Nanocomposite dielectric layers, consisting of TiO_2 nanoparticles, whose surface was further modified with organosiloxane (Ishihara Sangyo Kaisha LTD., Japan), and cross-linked PVP were prepared for OTFT gate insulators. PVP (11 wt%) and poly (melamine-co-formaldehyde) methylated (4 wt%), as a cross-linking agent, were dissolved in propylene glycol monomethyl ether acetate (PGMEA), [13] and blended with different concentrations of TiO_2 nanoparticles. The composite solution was then spin-coated onto indium–tin-oxide (ITO) patterned glass substrates which were used as gate electrodes. The thickness of these insulators is ~700 nm. Pentacene was thermally evaporated as the semiconductor layer. Finally, gold metal was thermally evaporated through the shadow mask and used as the source and drain electrodes (top-contact). The channel length (L) and width (W) are 160 and 2000 μm, respectively. The film thickness and roughness were measured by DI 3100 series atomic force microscopy (AFM). The current–voltage (I–V) characteristics of OTFTs were measured by a HP 4156 A semiconductor parameter analyzer. The devices with metal–insulator–metal (MIM) structure, consisting of different dielectric materials sandwiched between ITO and Al electrodes, were used for capacitance measurements. The capacitance measurements were conducted with a HP 4284 A Precision LCR meter.

For a pure cross-linked PVP film, the dielectric constant is 4.3 at 1 kHz, which is close to the value reported earlier [11,14]. From Table 1, we can see that the dielectric constant increases with the amount of the TiO_2 nanoparticle embedded in the thin films. For the dielectric film with 15 wt% of TiO_2 nanoparticle, the dielectric constant increased to 10.8, due to the higher solubility of the organosiloxane surface modified TiO_2 fillers, compared to that reported earlier [11].

The drain–source current (I_D) vs. drain–source voltage (V_D) of OTFTs with different TiO_2 concentrations incorporated in the gate insulators is shown in Fig. 1. The carrier mobility was calculated in the saturation regime using the following equation:

$$I_{DS} = (WC_i/2L)\mu(V_G - V_T)^2 \quad (1)$$

where C_i is the capacitance per unit area of the insulator, and V_T is the threshold voltage. For the de-

Table 1
Electrical parameters of the OTFTs in this study

TiO_2 wt%	Dielectric constant	Mobility μ_{sat} (cm^2/Vs)	Threshold voltage V_{th} (V)	Surface roughness[a] (nm)	On/Off ratio
0	4.3	0.42	−5.2	0.30	5×10^4
1	4.8	0.39	−14.4	9.76	4×10^4
5	6.7	0.42	−10.9	16.19	9×10^3
10	8.5	0.34	−3.3	26.99	6×10^3
15	10.8	0.32	+5.9	31.43	1×10^3
15%/PαMS[b]	11.6	0.41	−3.0	13.30	3×10^4

[a] Surface roughness of the dielectric layers.
[b] PαMS: poly(α-methylstryrene).

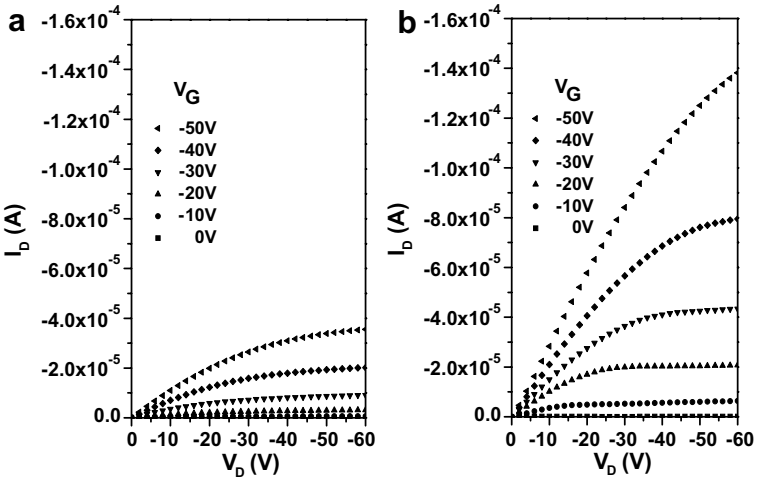

Fig. 1. The output characteristics (drain current, I_D vs. drain voltage, V_D,) of OTFTs with (a) a neat PVP insulator; (b) a composite insulator with 15 wt% TiO_2 nanocomposite insulators.

vice with a neat PVP gate insulator, (Fig. 1a) the mobility in the saturation region and the threshold voltage of the OTFT are 0.42 $cm^2 V^{-1} s^{-1}$ and −5.2 V, respectively. The on–off ratio is more than 10^4. With 15 wt% of TiO_2 nanoparticles blended into the dielectric layer, (Fig. 1b) the device exhibits more than triplet the field-induced current compared with that of the device using the pure PVP insulator which is attributed to the higher surface capacitance. Fig. 1 reveals that the drain–source current increased by increasing the content of TiO_2 nanoparticles in the gate insulators. The parameters of the dielectric materials as well as the corresponding electrical characteristics of the OTFTs with different amount of TiO_2 nanoparticles embedded in the gate insulators are summarized in Table 1.

On the other hand, we also observe that the threshold voltage (V_{th}) decreases and then increases when more nanoparticles were added (Table 1). From the surface morphology study by AFM, the insulator roughness increased with the increasing concentration of TiO_2 blended. Consequently, the shift of V_{th} to higher values may be the result of the insulators surface roughness. The interface between the organic semiconductor and the insulator is affected by the incorporation of TiO_2 nanoparticles.

Additionally, we can also find that the on–off ratio decreases while the concentration of TiO_2 increases (Table 1). Fig. 2 shows clearly that the device with 15 wt% TiO_2 has much higher leakage current than that with 1 wt% nanoparticles. The leakage problem is probably due to the low-band gap of TiO_2. In addition, structure defects induced by the present of high concentration TiO_2 might also result in the higher leakage current, which has been confirmed from the fact that the surface roughness of the insulators increased with the content of nanoparticles (Table 1).

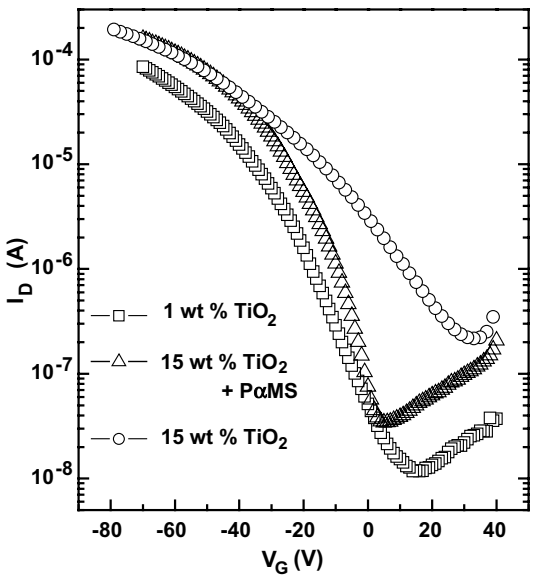

Fig. 2. The transfer characteristic (drain current, I_D vs. gate voltage, V_G) at constant $V_D = -40$ V for OTFTs with 1 wt%, 15 wt% of TiO_2 nanocomposite insulators, and nanocomposite insulators with the PαMS interfacial layer.

In order to rectify this problem, the insulator layer was covered with a poly(α-methylstrylene) (PαMS) layer. Due to the robustness of cross-linked polymers, the underlayer was not affected by this process. As shown in Fig. 2, the device off current is dramatically suppressed after spin-coating ~30 nm PαMS on the nanoparticle/cross-linked PVP insulator. The over-coating of another interfacial layer can reduce the concentration of surface defects of the dielectrics and smooth the dielectric surface. In addition the dielectric constant of the insulator modified with PαMS is higher than that without modification. This further supports the fact that PαMS can inhibit the leakage current and enhance the dielectric strength of the composite polymer.

On the other hand, the smooth dielectric surface might also induce the formation of a more orderly crystalline pentacene film, and subsequently, increase the device mobility as shown in Table 1. Table 1 apparently shows that the surface roughness of the dielectric layer affects the device mobility in the saturation regime. While the concentration of TiO_2 is more than 5 wt%, the mobility drops dramatically. The rough dielectric surface probably interferes with the formation of an ordered crystal structure. Fig. 3 shows the surface morphology of pentacene deposited on different dielectrics. In contrast to the clear crystal formation on the neat cross-linked PVP, the grain size of pentacene on the 15 wt% TiO_2 filled-PVP film is rather small. The higher concentration of grain boundary might limit the charge transport in the organic films. However, after over-coating the PαMS layer, typical lamella morphology appears again, which implies the formation of an ordered crystal structure. In summary, the PαMS layer not only suppresses the leakage current by reducing the concentration of defects in the dielectric layer, but also induces pentacene to form a more ordered molecular conformation thus maintaining the high mobility in the conducting channel.

Since the leakage problem has been overcome by incorporating an interfacial layer, thinner dielectric layers will be allowed to achieve a greater capacitance value. Fig. 4 shows the output characteristics for an OTFT with a 270 nm nanocomposite insulator, consisting of one layer of 15 wt% TiO_2 filled-PVP film and another thin PαMS. The dielectric constant of this composite is 10.5, which is slightly lower than that of previous one. The device exhibits mobility of $\sim 0.4\ cm^2\ V^{-1}\ s^{-1}$. The sub-threshold slope is 1.0 V/decade and the threshold voltage is −2.9 V. The on–off ratio is more than 3.0×10^4.

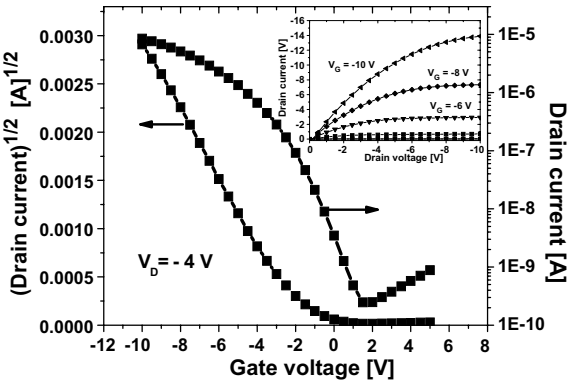

Fig. 4. The transfer characteristics of the OTFT with a thinner gate insulator. The inset shows the corresponding output characteristic from $V_G = 0$ V to −10 V.

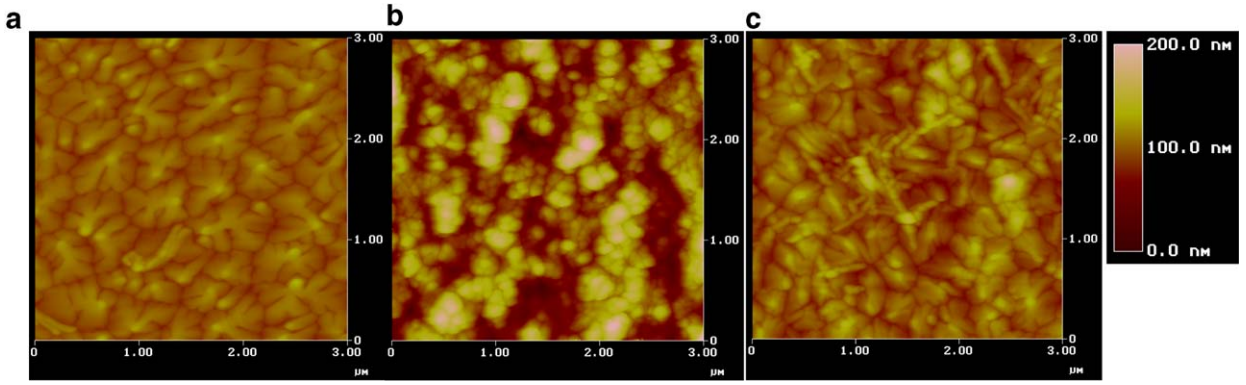

Fig. 3. AFM height-mode images of pentacene deposited on the surface of (a) neat cross-linked PVP; (b) cross-linked PVP blended with 15 wt% TiO_2 nanoparticles; (c) cross-linked PVP blended with 15 wt% TiO_2 nanoparticles and further modification with PαMS interfacial layer.

From Fig. 4, it is apparent that low-voltage OTFTs can be fabricated by using nanocomposite dielectric polymers with simple and solution-processable processes.

In conclusion, high performance organic thin-film transistors incorporated with high dielectric nanoparticles in the dielectric layers have been demonstrated successfully. Moreover, the problem of leakage current of OTFTs, while using the nanocomposite insulators, has been overcome using over-coat of another thin interfacial layer. This method offers a feasible and economic way to deposit gate insulators for OTFTs with high capacitance without the complications associated with sputtering of high dielectric materials and high-temperature annealing. Finally, one low-voltage OTFT, which can operate within 10 V, has also been achieved by this method.

Acknowledgements

This work is supported by AU Optronics Corp. (AUO), Casier, UST and MOE ATU Program. F.-C.C. would also like to thank the financial support from National Science Council, ROC.

References

[1] Y.Y. Lin, D.J. Gundlach, S.F. Nelson, T.N. Jackson, IEEE Trans. Electr. Dev. 44 (1997) 320.
[2] H.E. Katz, Z. Bao, J. Phys. Chem. B 104 (2000) 671.
[3] M. Shtein, J. Mapei, J.B. Benziger, S.R. Forrest, Appl. Phys. Lett. 81 (2002) 268.
[4] P. Mach, S.J. Rodriguez, R. Nortrup, P. Wiltzius, J.A. Rogers, Appl. Phys. Lett. 78 (2001) 3592.
[5] C.D. Sheraw, L. Zhou, J.R. Haung, D.J. Gundlach, T.N. Jackson, M.G. Kane, I.G. Hill, M.S. Hammond, J. Campi, B.K. Greening, J. Francl, J. West, Appl. Phys. Lett. 80 (2002) 1088.
[6] T.W. Kelley, P.F. Baude, C. Gerlach, D.E. Ender, D. Muyres, M.A. Haase, D.E. Vogel, S.D. Theiss, Chem. Mat. 16 (2004) 4413.
[7] A. Facchetti, M.H. Yoon, T.J. Marks, Adv. Mat. 17 (2005) 1705.
[8] H. Sirringhaus, Adv. Mat. 17 (2005) 2411.
[9] C.D. Dimitrakopoulos, S. Purushothaman, J. Kymissis, A. Callegari, J.M. Shaw, Science 283 (1999) 822.
[10] G. Velu, C. Legrand, O. Tharaud, A. Chapoton, D. Remiens, G. Horowitz, Appl. Phys. Lett. 79 (2001) 659.
[11] F.C. Chen, C.W. Chu, J. He, Y. Yang, J.L. Lin, Appl. Phys. Lett. 85 (2004) 3295.
[12] L.J. Berberich, M.E. Bell, J. Appl. Phys. 11 (1940) 681.
[13] H. Klauk, M. Halik, U. Zschieschang, G. Schmid, W. Radlik, W. Weber, J. Appl. Phys. 92 (2002) 5259.
[14] J. Veres, S. Ogier, G. Lloyd, Chem. Mater. 16 (2004) 4543.

Available online at www.sciencedirect.com
ScienceDirect
Organic Electronics 7 (2006) 440–444
Organic Electronics
www.elsevier.com/locate/orgel

Letter

Enhancement of conductivity in poly (3-hexylthiophene) films prepared by spin-coating from blended solutions with small molecules

Takuya Kambayashi [a,*], Hiroshi Wada [a], Masanao Goto [a], Takehiko Mori [a], Byoungchoo Park [b], Hideo Takezoe [a], Ken Ishikawa [a]

[a] *Department of Organic and Polymeric Materials, Tokyo Institute of Technology, 2-12-1 O-okayama, Meguro-ku, Tokyo 152-8552, Japan*
[b] *Department of Electrophysics, Kwangwoon University, Seoul 139-701, Republic of Korea*

Received 11 May 2006; received in revised form 20 July 2006; accepted 31 July 2006
Available online 24 August 2006

Abstract

Conductivity of poly (3-hexylthiophene) (P3HT) films was enhanced by blending P3HT with organic semiconducting molecule dibenzotetrathiafulvalene (DBTTF). Films were fabricated by conventional spin-coating from blended solutions of P3HT and DBTTF. Enhancement of the conductivity was achieved in the films containing 30–80% of DBTTF. In these films, large DBTTF crystalline domains of dendrite shapes were observed in atomic force micrographs. Growth mechanisms of dendritic domains are discussed on the basis of viscosity of blended solutions and degree of oversaturation.

PACS: 73.61.Ph; 81.10.Dn; 82.35.Cd

Keywords: Organic semiconductor; Wet process; Crystal growth; Conductivity

1. Introduction

Organic field-effect transistors (OFETs) have attracted growing attention for future electronic devices [1–4]. Organic crystalline films of small molecules such as pentacene have been mainly used as active materials for OFETs, because of their higher mobility than those of typical polymeric semiconductors. Commonly, highly conductive films of crystalline small molecules for OFETs have been fabricated by vacuum deposition techniques. However, these techniques have drawbacks such as high cost, fabrication processes at high temperatures, and most importantly the size limitation, preventing applications of OFETs to wide areas. On the other hand, wet process, which is generally used for polymer materials, has been believed to be difficult to apply small molecules. In this respect, if solution process could be applied to fabricating OFETs made of small molecules, technological impacts would be quite large.

* Corresponding author. Tel.: +81 3 5734 2773; fax: +81 3 5734 2876.
E-mail address: bayanshi629@mbox.op.titech.ac.jp (T. Kambayashi).

1566-1199/$ - see front matter
doi:10.1016/j.orgel.2006.07.012

Recently, Russel et al. [5] succeeded in combining the ease of fabrication process of polymer films with high performance of small molecules by spin-coating from blended solution containing polymer and small molecule. Field-effect mobility in the OFET having a polymer/small molecule blended channel was improved by a factor of 10, since the channel contained small crystals of the small molecules [5]. However, the growth of the small crystals was not uniform, so that the conductivity of the films was position dependent on the film surface. Uniform film formation is indispensable for application to channels of OFETs. Our aim in this work is to improve and optimize the wet process introduced by Russel et al. For the purpose, we used blended films of dibenzotetrathiafulvalene (DBTTF) and poly (3-hexylthiophene) (P3HT) (Fig. 1(a)) fabricated from blended solutions with various mixing ratios (Fig. 1(b)). DBTTF is known as an active material for OFETs [3,4], possessing high field-effect mobility ($1.4\ cm^2\ V^{-1}\ s^{-1}$) in single crystals grown from solution [3] and ($0.06\ cm^2\ V^{-1}\ s^{-1}$) in crystalline films fabricated by vacuum deposition [4]. Blended films possessing uniform morphology and conductivity were obtained by carefully adjusting the mixing ratio of the blended solutions. Moreover, conductivity of these P3HT/DBTTF films is enhanced by containing higher conductive DBTTF crystals than pure P3HT.

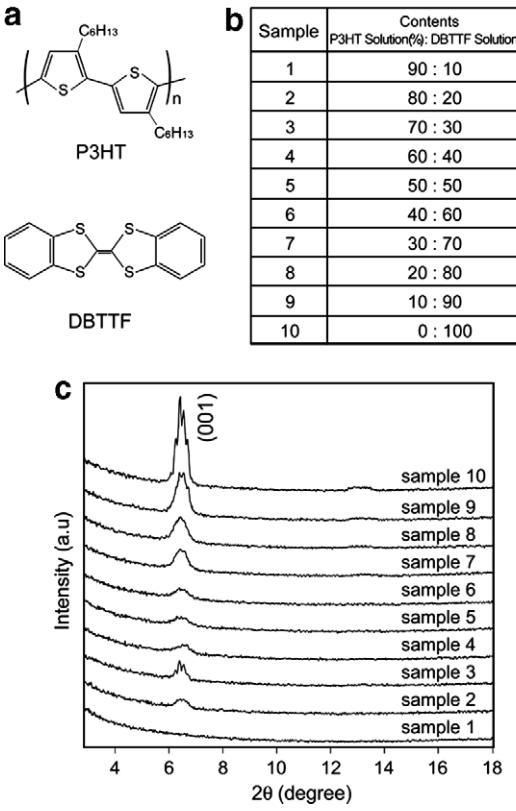

Fig. 1. (a) Molecular structures of P3HT and DBTTF. (b) List of mixed solutions of P3HT solution and DBTTF solution. (c) XRD patterns of all samples. A Bragg diffraction peak assigned to (0 0 1) of a DBTTF crystal is observed in every sample except for sample 1.

2. Experiments

In this work, P3HT [6] and DBTTF were used as source materials. Molecular structures of P3HT and DBTTF are shown in Fig. 1(a). P3HT (Mw: 9500) was purchased from Merck. DBTTF was synthesized in our laboratory and was purified by sublimation for two times. First, we prepared two chloroform solutions of P3HT and DBTTF; P3HT solution (0.25 wt.%) and DBTTF solution (0.5 wt.%). Mixing two solutions, we prepared 9 blended solutions, as listed in Fig. 1(b). From these 9 solutions and a DBTTF solution, we fabricated 10 kinds of films on glass substrates, which were cleaned by acetone and 2-propanole using ultrasonic washing equipment. Spin-coating was performed at 3000 rpm for 20 s.

Contact-mode atomic force microscopy (AFM) images were recorded using a Seiko Instruments SPA-300/SPI3800 probe system, equipped with an SiN cantilever (Olympus, OMCL-TR400PSA-1, force constant 0.09 N/m, tip curvature radius −15 nm). X-ray diffraction measurements were conducted using a thin film X-ray diffractometer (X'Pert-MPD PW3050 Philips). Four-probe *I–V* characteristics were measured by a KEITHLEY 4200 semiconductor characterization system. All experiments were performed at room temperature in air.

3. Results and discussion

First, we observed X-ray diffraction patterns from the blended films (Fig. 1(c)) spin-coated on glass substrates. In the sample 1, because of small amount of DBTTF, no peak was detected in the diffraction pattern. As the concentration of DBTTF solution increases over 20%, a Bragg reflection peak at about $2\theta = 6.6°$ (13.5 Å) appeared and grew. This peak is indexed as (0 0 1) by referring the existing data of DBTTF (monoclinic, $P2_1/c$, $a = 12.082$ Å, $b = 3.955$ Å, $c = 14.553$ Å, $\beta = 114.36°$ [7]). A series

of diffraction data suggests the increasing crystalline domains of DBTTF in the films with increasing DBTTF ratio.

In order to directly observe the formation of DBTTF crystals, surface morphologies of the blended films were observed by AFM. Fig. 2 shows AFM images (10 μm square) of each film surface. For the films with high polymer binder P3HT solution over 80%, phase-separated polygon domains were observed on homogeneous surfaces. In our previous work, no polygon domains were observed in the AFM image of pure P3HT film surfaces [8]. Based on this fact and the present observation, i.e., the number of polygon domains increases with increasing DBTTF, the polygon domains and the flat surface are assigned to DBTTF and P3HT. When the fraction of DBTTF solution exceeds 30%, the surfaces of the blended films become rough and dense, small domains begin to appear, as shown in the AFM image of sample 3. With further increasing DBTTF fraction, dendrite domains appear (sample 5) and are converted to seaweed domains, as observed in [9], i.e., branches and edges of dendrite domains become wider and blunter (samples 6, 7 and 8). Finally in the films with higher fraction of DBTTF solution over 90%, the size of domains becomes smaller and domains are sparsely observed (samples 9 and 10). These AFM observations indicate that size, shape and density of DBTTF domains depend on the fraction of DBTTF in the blended solutions. They also depend on molecular weight of P3HT, i.e., in P3HT (Mw: 20 100), size and density of DBTTF domains became smaller, and polygonal and dendrite domains were not observed. It is known that the shape of branching domains depends on the degree of oversaturation [9], i.e., when oversaturation becomes higher, the shape of domains changes from dendrite to seaweed. Thus, appropriate oversaturation condition is achieved by properly choosing the blending condition.

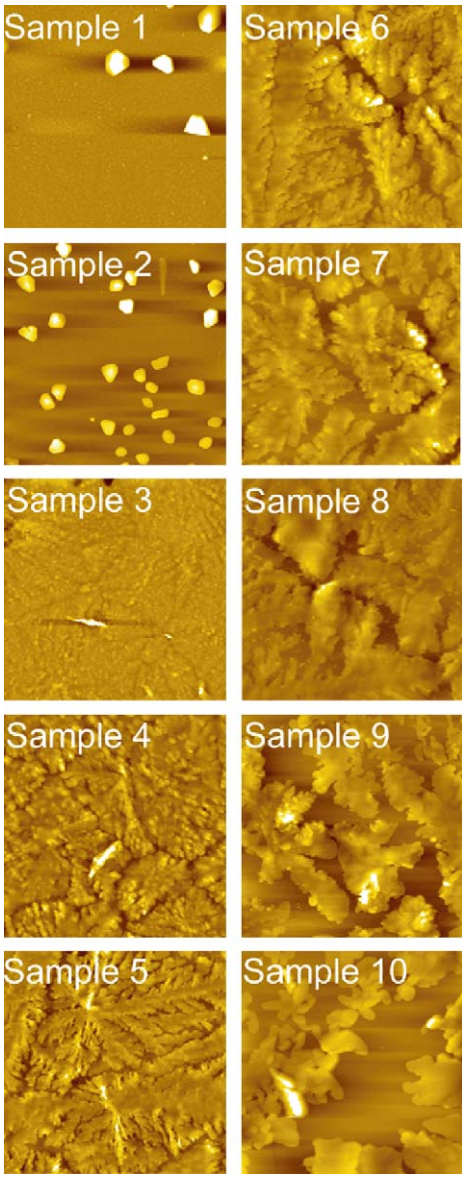

Fig. 2. AFM images of the samples 1–10 shown in Fig. 1(b). Scanning areas of all images are 10 μm square. Several kinds of domains, which have different shape and size, are observed depending on DBTTF ratio.

Branching DBTTF domains such as dendrite and seaweed are usually observed under fast growth conditions. What kinds of factors contribute to the fast growth condition in the present case? It is known that crystal growth velocity under oversaturation conditions is generally fast. This must be an important factor. The other factor is a supplying rate of reactants to crystal surfaces, which is governed by the viscosity of solution. High supplying rate due to lower viscosity gives branched crystal morphologies than that slow rate due to higher viscosity does. In spin-coating from blended solutions, viscosity of the blended solutions containing more P3HT solution is higher, and viscosity of those containing more DBTTF solution is lower. Hence, branching domains such as dendrite and seaweed are easily grown using the DBTTF-rich solutions of lower viscosity. Thus, the two both factors, oversaturation and low viscosity, lead to the formation of branching DBTTF domains.

Next, we measured *I–V* characteristics of blended films by the four-probe technique. The results are shown in Fig. 3. Conductivity was normalized by the thickness of the blended films. As shown in the figure, the conductivity of the blended films of lower fraction of DBTTF solution than 20% is small and comparable to that of the P3HT polymer film. On the other hand, when the fraction of DBTTF solution exceeds 30%, the conductivity of the blended films is enhanced. In these films, percolation paths between DBTTF crystals were realized. For films of higher fraction of DBTTF than 90%, the conductivity of the blended film decreases abruptly, although the crystallinity of the films increases, as shown in Fig. 1(c). The low conductivity is explained by the lack of percolation paths, which is clearly seen in the AFM images, i.e., island morphology is observed in the blended films 9 and 10. It is noted that the enhancement of electric conductivity also depends on the molecular weight of P3HT, i.e., the enhancement was smaller in P3HT (Mw: 20 100) than that in P3HT (Mw: 9500). We attributed this difference to the different viscosity of the two P3HTs.

For discussing the conductivity of nonuniform films, percolation threshold is important. Usually, the shape and directional distribution strongly influence the percolation threshold: smaller percolation volumes are obtained if length-to-width aspect ratio of domains is high [10]. Thus, dendrite domains of DBTTF would be more favorable than polygonal and seaweed domains for realizing percolation paths. The density of DBTTF domains in the samples is also important to realize DBTTF percolation paths because higher conductivity originates from dense DBTTF domains.

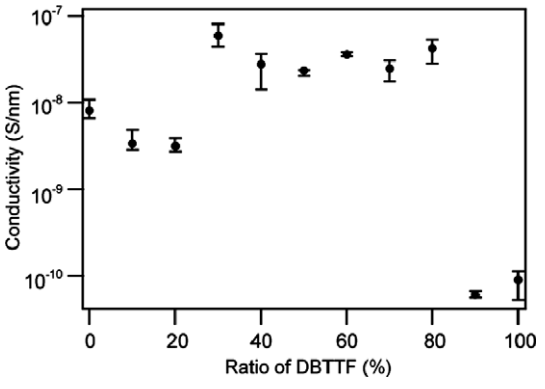

Fig. 3. Conductivity in the samples 1–10 shown in Fig. 1(b). The abscissa is the fraction of DBTTF solution in each mixed solution. All the conductivity values are normalized by each thickness.

Finally, we have to note the uniformity of the films used. The conductivity measurements were conducted in several positions on the sample surfaces. The measured conductivity of the blended films falls in almost the same error bar range as that of pure P3HT (see left point in Fig. 3). This fact ensures that the blended films are uniform enough for the conductivity measurements. Namely, for the blended films containing lower fraction of DBTTF solution (less than 20%), the typical crystal size of DBTTF is less than few μm (see Fig. 2), which is much smaller than the electrode gap of about 100 μm, and the density is relatively low. On the contrary, for the blended films containing 30–80% fraction of DBTTF, the DBTTF crystal size is large and the density is high. In both cases, the position independent conductivity results.

In conclusion, when the fraction of DBTTF solution is between 30% and 80%, blended films show higher conductivity. The conductivities are insensitive to the mixing ratio in this range and to the measuring position on the whole surface area. This higher conductivity originates from the size, shape and density of higher conductive DBTTF domains in the film, which is closely related to the percolation paths of the DBTTF domains. The morphology of the domains varies with DBTTF fraction, being explained by two factors; viscosity of blended solutions and degree of oversaturation, which can be controlled in solution process. By optimizing the fraction of DBTTF, uniform films were realized. Thus, the wet process using blended solutions has advantages in forming crystalline small molecular films, providing a useful technique for organic device fabrications.

References

[1] S.F. Nelson, Y.Y. Lin, D.J. Gundlach, T.N. Jackson, Appl. Phys. Lett. 72 (1998) 1854.
[2] S.R. Forrest, Nature 428 (2004) 911.
[3] M. Mas-Torrent, P. Hadley, S.T. Bromley, N. Crivillers, J. Veciana, C. Rovira, Appl. Phys. Lett. 860 (2005) 12110.
[4] Naraso, J. Nishida, S. Ando, J. Yamaguchi, K. Itaka, H. Koinuma, H. Tada, S. Tokito, Y. Yamashita, JACS 127 (2005) 10142.
[5] D.M. Russel, C.J. Newsome, S.P. Li, T. Kugler, M. Ishida, T. Shimoda, Appl. Phys. Lett. 87 (2005) 222109.
[6] H. Sirringhaus, P.J. Brown, R.H. Friend, M.M. Nielsen, K. Bechgaard, B.M.W. Langeveld-Voss, A.J.H. Spiering, R.A.J. Janssen, E.W. Meijer, P. Herwig, D.M. de Leeuw, Nature 401 (1999) 685.

[7] T.J. Emge, F.M. Wiygul, J.S. Chappel, A.N. Bloch, J.P. Ferraris, D.O. Cowan, T.J. Kistenmacher, Mol. Cryst. Liq. Cryst. 87 (1982) 137.
[8] T. Kambayashi, M. Goto, T. Mori, H. Takezoe, K. Ishikawa, Jpn. J. Appl. Phys. 45 (2006) 526.
[9] E. Brener, H. Muller-Krumbhaar, D. Temkin, Phys. Rev. E 54 (1996) 2714.
[10] M. Ambrozic, A. Dkskobler, M. Valant, Eur. Phys. J. Appl. Phys. 30 (2005) 23.

Available online at www.sciencedirect.com
ScienceDirect
Organic Electronics 7 (2006) 445–451
Organic Electronics
www.elsevier.com/locate/orgel

Correlation of growth of pentacene films at various gas ambience conditions to organic field-effect transistor characteristics

W.Y. Chou [a,*], Y.S. Mai [a], H.L. Cheng [a], C.Y. Yeh [a], C.W. Kuo [a], F.C. Tang [a], D.Y. Shu [b], T.R. Yew [b], T.C. Wen [c]

[a] *Institute of Electro-Optical Science and Engineering, National Cheng Kung University, Tainan 701, Taiwan*
[b] *Department of Materials Science and Engineering, National Tsing Hua University, Hsinchu 300, Taiwan*
[c] *Department of Chemical Engineering, National Cheng Kung University, Tainan 701, Taiwan*

Received 7 February 2006; received in revised form 20 May 2006; accepted 25 May 2006
Available online 28 June 2006

Abstract

Pentacene based thin-film transistors (TFTs) have been fabricated using pentacene films grown under various ambiences, such as N_2, H_2, Ar, He, and high vacuum, to define correlation of the device performance, in particular mobility properties, to molecular ordering in pentacene films. The field-effect mobility of 0.24 cm^2/Vs was obtained from TFTs fabricated under 2×10^{-5} Torr nitrogen ambience, however, the pentacene TFTs fabricated in hydrogen ambience under the same pressure yielded very poor mobility of 0.008 cm^2/Vs. Pentacene films deposited by thermal evaporation at increased pressure in nitrogen ambience have a high degree of molecular ordering with larger dendritic grains without any surface modification on silicon oxide dielectric. A clean relation between field-effect mobility and XRD estimated crystallites size was obtained.

Keywords: Organic thin film transistors; Pentacene; Deposition ambient conditions; Crystalline size; Molecular ordering; XRD

Recent technological trends draw much attention to organic thin film transistors (OTFTs). The performance of OTFTs has improved dramatically lately, and this stands true in particular in regards to conjugated oligoacenes [1,2]. Pentacene, a fused-ring polycyclic aromatic hydrocarbon, is considered as a highly promising material for application in OTFTs due to great mobility and good semiconducting behavior [1–4]. To this day, pentacene-based OTFTs have exhibited the highest field-effect mobility and have been considered to be the candidate of choice for replacement of amorphous silicon TFTs.

The electronic characteristics of a pentacene thin film depend on the film's structure such as molecular orientation and morphology [1,5,6]. Pentacene films with various polymorphisms can be fabricated by changing the deposition conditions, film structure

* Corresponding author. Tel.: +886 6 2757575x65282; fax: +886 6 2747995.
E-mail address: weiyang@mail.ncku.edu.tw (W.Y. Chou).

1566-1199/$ - see front matter © 2006 Elsevier B.V. All rights reserved.
doi:10.1016/j.orgel.2006.05.007

and polymorphism in bulk and in thin film, both of which have been an object of experimental and theoretical studies [7,8]. Many attempts have been made to improve the carrier transport properties via substrate modification, depositary conditions, purification, or functionalization of these molecular structures. Formed crystalline film usually features grain morphology; hence, it is generally believed that the carrier transport efficiency is increased due to the well-ordered crystalline structure and/or large grain size [9].

In this study, we investigated the effects of different gas ambience deposition conditions on crystalline size, and eventually on the performance of pentacene-based OTFTs. During the analysis, the morphology and crystalline size of active layer were investigated. The trap state of pentacene film deposited under various gas ambience states and dependence on the mobility of OTFTs were also included and the results were discussed.

Typical bottom-gate pentacene-based TFTs with top-contact source and drain electrodes were fabricated under the following conditions. Heavily doped *n*-type Si(1 1 1) wafers with a doping concentration of 5×10^{15} cm^{-3} were used as the substrates and served as the bottom gate electrode. A 300 nm silicon dioxide (SiO_2, root-mean-square roughness – 2.5 nm) layer, grown on the substrate by plasma enhanced chemical vapor deposition (PECVD), performed the function of the gate insulator. Next, the pentacene film was deposited from the PBN crucible onto the surface of SiO_2 layer at a rate of deposition of approximately 0.4 Å/s. The film was grown by vacuum sublimation at a pressure of 7×10^{-7} Torr and the substrate was kept at room temperature. The background pressure of the growth chamber was equal to 2×10^{-7} Torr. In order to investigate the film properties of pentacene grown at different ambience conditions, the growth chamber was filled with various gases, such as N_2, H_2, He, and Ar, while the pressure of the growth chamber was maintained at 2×10^{-5} Torr. The mean thickness of the pentacene film, ranging from 90 to 100 nm, was calibrated using an atomic force microscope (AFM, Digital Instrument Multimode SPM AS-12VMF) and monitored via the frequency shift of a quartz oscillator. Finally, the gold source–drain electrodes were deposited upon the surface of the pentacene film to form an electrode through a shadow mask in order to complete the top-contact OTFT device and create a channel with length of 140 μm and width of 640 μm. The electrical characteristics of OTFT devices were measured by Keithley 4200-SCS semiconductor parameter analyzer in a dark chamber. The structures of pentacene films were elucidated by X-ray diffraction (XRD) in a symmetric reflection, coupled ($\theta - 2\theta$) mode. X-ray diffraction patterns were obtained using Cu K_α radiation ($\lambda_{K_\alpha} = 1.5406$ Å) and a wide-angle graphite monochromator.

Fig. 1(a) shows the electrical output (drain current (I_{DS}) – drain to source voltage (V_{DS})) characteristics of an OTFT device with pentacene active layer

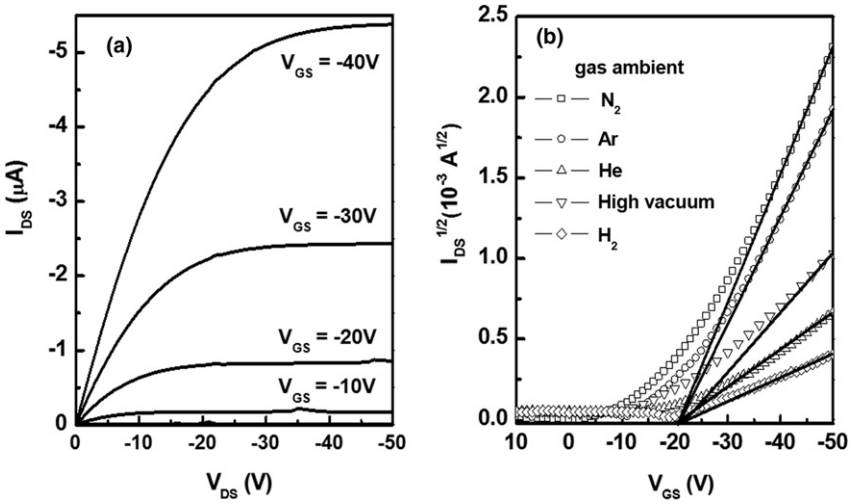

Fig. 1. (a) I_{DS} versus V_{DS} characteristics at various gate biases for a typical pentacene TFT with pentacene film deposited onto SiO_2/silicon wafer at N_2 ambience of 2×10^{-5} Torr. (b) Measured transfer curves of pentacene TFTs deposited at various ambience conditions for $V_{DS} = -40$ V.

grown in an atmosphere of 2×10^{-5} Torr nitrogen (N_2). Fig. 2(b) shows typical electrical transfer characteristics (I_{DS} – gate voltage (V_{GS})) of OTFT devices, in which pentacene thin films were deposited under different ambience conditions, operating in saturation regime ($V_{DS} = -40$ V). By fitting the data to saturation regime standard field-effect transistor equations, the extracted field-effect mobility (μ_{sat}) and threshold voltage (V_{th}) of all devices were compiled in Table 1. Typically, the field-effect hole mobility of our device fabricated under high vacuum was around 0.045 cm^2/Vs, with a variation of ± 0.02 cm^2/Vs, consistent with the fact that the polycrystalline pentacene film was grown under room temperature conditions on a SiO_2 substrate, which had not undergo any surface treatments [1]. Analyzing different conditions, we can note that the pentacene film fabricated under nitrogen ambience exhibits the maximum μ_{sat}. However, the pentacene film that was grown in hydrogen ambience displays the worst mobility. On the other hand, experimental devices exhibit similar values of V_{th} as shown in Fig. 1(b) and Table 1. Similar V_{th} behaviors among the study devices imply that trapping states within the gate dielectric, at the semiconductor/dielectric interface and/or in the semiconductor itself, all have the same level.

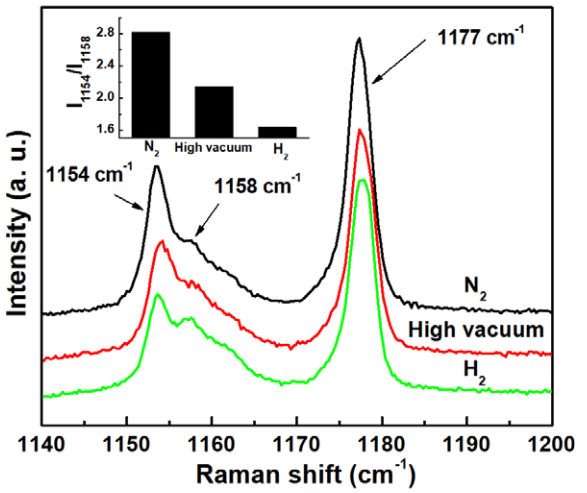

Fig. 2. MicroRaman spectra of pentacene films deposited under N_2, high vacuum, and H_2 ambiences. The inset shows the ratio of the intensity of peak 1154 cm^{-1} to that of peak 1158 cm^{-1} as function of those gases.

Table 1
Performance of OTFTs whose pentacene active layers grow at various ambiences

Sample ID	Ambient gas	V_{th} (V)	Mobility (cm^2/Vs)	I_{on}/I_{off}
A	N_2	−20.80	0.236	10^7
B	High vacuum	−18.82	0.045	10^3
C	H_2	−21.70	0.008	10^3
D	He	−23.40	0.052	10^3
E	Ar	−21.83	0.093	10^5

The modulated on/off current ratios for experimental devices, taken from log(I_{DS}) versus V_{GS} characteristics, are all included in Table 1. It is worth to note that the pentacene TFT with higher field-effect mobility has larger on/off current ratio. Interestingly, the modulated on/off current ratio for device featuring nitrogen-ambience-grown pentacene film is approximately 10^7, which is larger by a factor of 10^4 when compared to the device with hydrogen-ambience-grown pentacene film. We believe that the most significant factor allowing obtaining higher mobility and on/off ratio is the improved quality of the deposited pentacene layer achieved through application of different gas ambience conditions.

Raman spectroscopy is a powerful tool to investigate the correlation between the intermolecular couplings and the carrier transports within pentacene films [10,11]. A Jobin Yvion LABRAM-HR single grating monochromator was used to take Raman shift, whose resolution is below 0.2 cm^{-1}, referred to 633 nm laser line. Raman spectra, wavenumber ranging from 1140 to 1200 cm^{-1}, were measured on the pentacene films deposited at various ambiences, as shown in Fig. 2. The Raman peaks at 1158 cm^{-1} and 1177 cm^{-1} correspond to originate from the C–H in-plane vibration of single pentacene molecule, respectively. Additionally, the split of the vibration mode of 1158 cm^{-1} locates at 1154 cm^{-1} band as in-phase intermolecular coupling (twinning) vibrations of different pentacene molecules in a unit cell. Comparing the Raman spectra of pentacene films deposited at various gas ambiences, the pentacene film grown at nitrogen ambience shows the strongest 1154 cm^{-1} band implying strong in-phase (intralayer) intermolecular interaction between pentacene molecules, on the contrary, the minimum 1154 cm^{-1} band appears at that under hydrogen ambience, as shown in the inset of Fig. 2. The peak intensity of 1154 cm^{-1} band for the pentacene film grown at high vacuum condition lies in between those grown under nitrogen and hydrogen ambiences. Apparently the in-phase intermolecular coupling of pentacene molecules can be enhanced at the growth condition of nitrogen ambience. The improvement of the intermolecular coupling or

twinning effect is also observed by Robinson et al. for anthracene crystals grown under nitrogen at reduced pressure [12]. At the microscopic level, the carrier transport within a pentacene film was enhanced by the increment of π-orbital overlap between pentacene molecules as a result of the increase of the intermolecular coupling. These results imply that the optimal π-orbital overlap in a pentacene film can be obtained through the appropriate growth ambience.

Next, we turn our attention to study of the structure and morphology of the pentacene films grown at various gas ambience conditions. X-ray diffraction (XRD) measurements were performed to rate pentacene films freshly deposited on SiO_2 substrates under different gas ambiences and at the same growth rate, as shown in Fig. 3. The XRD spectra of the pentacene films include four major reflections, in particular, pentacene growth blended with N_2 exhibits five clear reflection peaks. The films consist of only one phase with a first-order diffraction peak at $5.72 \pm 0.05°$ corresponding to a d_{001}-spacing of 1.54 ± 0.01 nm, which can be attributed to "thin film" phase polymorph [13], also see the inset of Fig. 3. Pentacene thin films have a layered structure [16] and the calculated interlayer d-spacing is slightly lower than the length of the pentacene molecule (~1.62 nm) thus the molecules are slightly tilted to the substrate plane. According to paracrystal theory [14–16], the $\overline{L}_{hkl}$ [the mean dimension of the crystallites perpendicular to the plane (hkl)] and g_{II} (the distance fluctuation between successive planes of the family (hkl) or second kind of distortions of crystal structure) would be obtained from XRD data using the following formula:

$$(\delta s)_0^2 = (\delta s)_c^2 + (\delta s)_{II}^2 = \frac{1}{\overline{L}_{hkl}^2} + \frac{\pi^4 g_{II}^4 m^4}{\overline{d}_{hkl}^2} \quad (1)$$

where $(\delta s)_0 = 2\cos\theta\,\delta\theta/\lambda$ is the overall broadening, excluding instrumental broadening; λ represents the X-ray wavelength; θ is the diffraction angle and $\delta\theta$ is in radians; $(\delta s)_c$ specifies the broadening associated with the size of the crystalline domain; $(\delta s)_{II}$ measures the broadening due to lattice distortions of the second kind; m is the order of the diffraction, and $\overline{d}_{hkl}^2$ is the mean spacing between (hkl) planes. In a pentacene film possessing distortions of second kind or paracrystalline distortions, the long-range disorder is lost due to polycrystalline structure with at least two phases. The square of $(\delta s)_0$ is plotted versus the fourth power of the order of diffraction (m^4) of each peak $(00l)$ from the pentacene films. Consequently, $\overline{L}_{hkl}$ and g_{II} of thin-film phase are calculated from the intercept on the ordinate axis and the slope of the straight line determined by the least-squares method and fitted according to Eq. (1). A semi-logarithmic plots of μ_{sat} versus the calculated $\overline{L}_{00l}$ of pentacene films, grown at various gas ambience conditions, are shown in Fig. 4; the g_{II} value is also shown in this figure. The largest crystalline size is found in the pentacene film grown at N_2 ambience. On the contrary, the smallest domain size appears in the

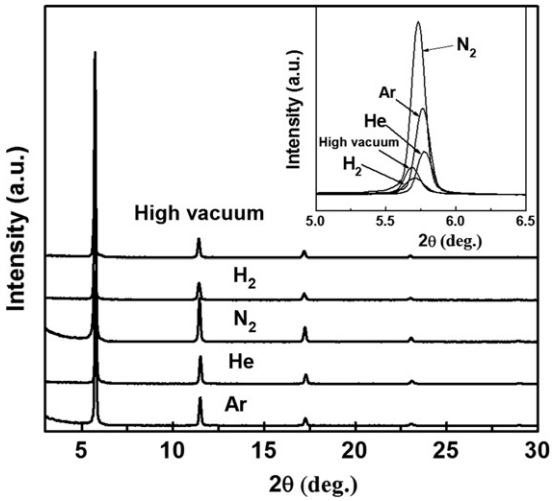

Fig. 3. XRD spectra of pentacene films grown at high vacuum, H_2, N_2, He, and Ar ambiences. The inset is the first-order reflection (001) obtained from all pentacene films.

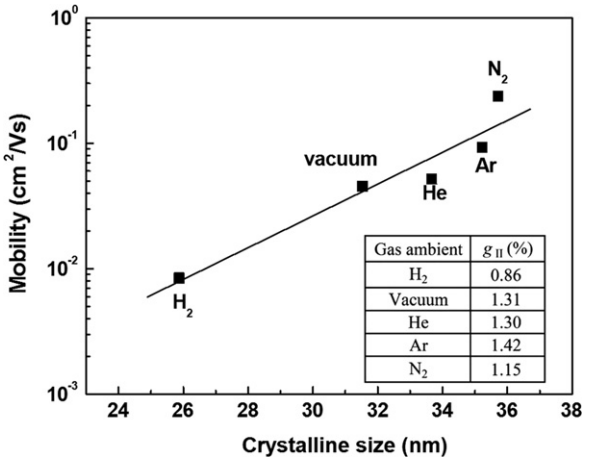

Fig. 4. Field-effect mobility of pentacene-based OTFTs as function of the crystal domain size of pentacene films (~900 Å) grown at different ambience conditions.

film grown at H_2 ambience. Our observations show a clear linear relation of $\log(\mu_{sat})$ with crystallites size $\overline{L}_{00l}$ obtained with slope of 0.0127 ± 0.0023, though its physical origin remained unclear at this stage. On the other hand, we have not observed a relationship between μ_{sat} and g_{II}, implying that the degree of structural perfection of the crystallites along the surface normal does not dominate the transport properties.

Fig. 5 displays atomic force microscope (AFM) images of pentacene films prepared on SiO_2 dielectric under the different gas ambience conditions described above. All samples show the grain morphology with slightly different grain size. The image

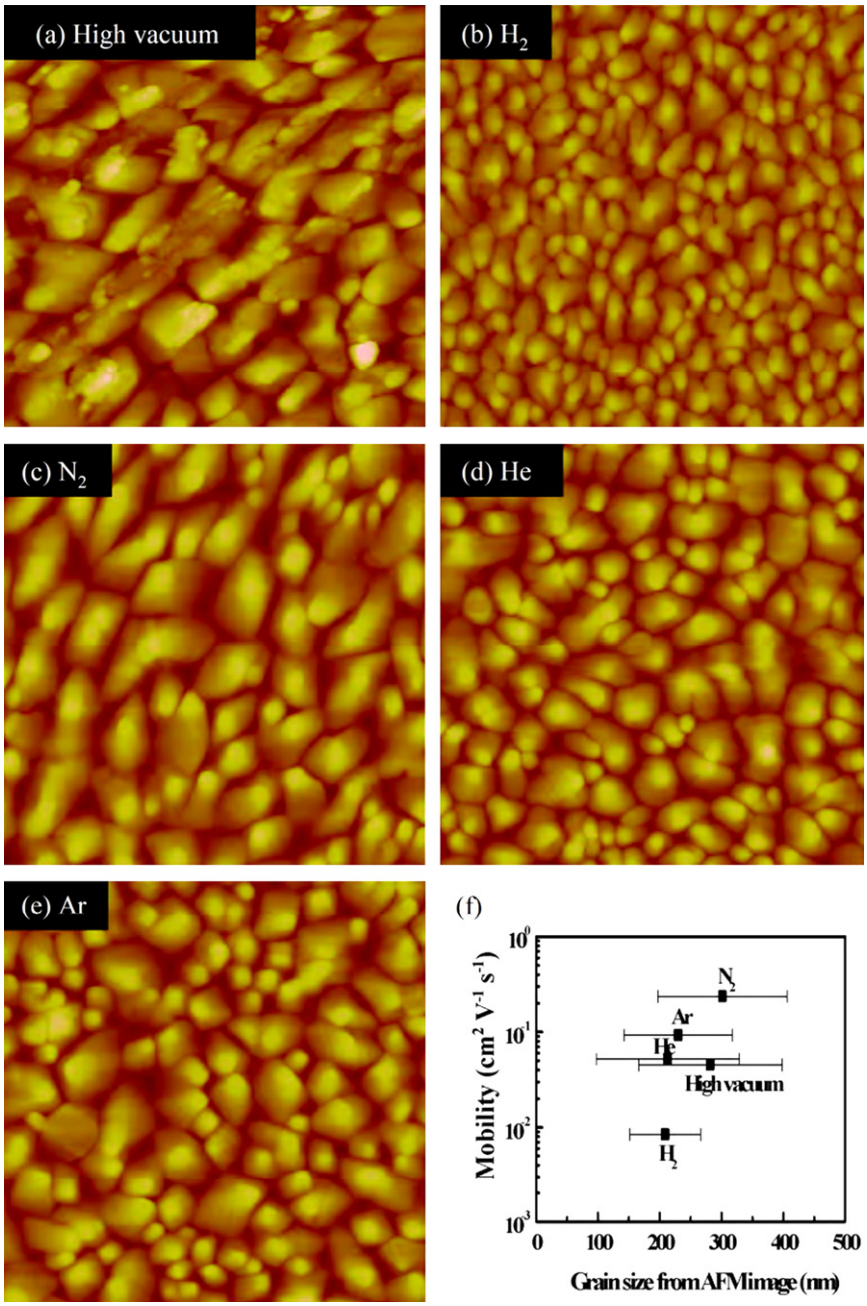

Fig. 5. AFM images (2 μm × 2 μm) of pentacene films deposited onto SiO_2 surfaces at (a) high vacuum, (b) H_2, (c) N_2, (d) He, (e) Ar ambiences and (f) field-effect mobility as function of grain size of pentacene films surface morphology.

of pentacene film grown at N_2 ambience reveals larger grains as compared to others. Small grains are observed in the pentacene film deposited onto a SiO_2 substrate at H_2 ambience. Because of the improved molecular packing at nitrogen ambience the grain morphology must be affected on the surface of the pentacene film. Formed polycrystalline film with grain morphology is generally believed to have increased carrier transport efficiency due to well-ordered crystalline structure and/or large grain size. However, we have not observed clear relation between μ_{sat} and grain size in the samples that were studied in our experiments, as shown in Fig. 5(f). Grain boundaries potentially influence mobility and device characteristics, and our research was focused on analysis of intrinsic and grain boundary-induced carrier transport and film growth mechanisms. Most researchers utilize crystal structure and grain size to interpret the performance of OTFTs [1,5,17–19]. However, some reported data is not consistent with the observations presented above. In some cases, the carrier mobility does not improve when the grain size is increased and consequently the grain boundaries significantly decrease [4,17,20]. Small grain size OTFTs sometimes provide better performance results as compared to OTFTs with large grain [17,21]. Comparing with the crystallite size obtained from the analysis of X-ray and the morphology grain size from AFM measurement, the crystallite size of the pentacene film correlated closely with the carrier mobility of OTFTs. The value of the crystallite size is an overall and average measurement for pentacene active layer involving the carrier transport path including the field-effect channel near the dielectric surface and the way from source and drain electrodes to the channel. On the contrary, the surface morphology of the active layer could not reflect directly the mechanism of carrier transport.

This research focused on the pentacene films used as an active layer of OTFTs. The films were grown upon room temperature SiO_2 surface by sublimation under different gas ambience conditions. (i.e. N_2, Ar, He, and H_2, at a high vacuum) All studied pentacene-based OTFTs show a similar threshold voltage behavior. However, pentacene grown under N_2 gas ambience conditions showed higher mobility and larger on/off ratios, which were attributed to the well-ordered crystalline structure, larger crystallites size perpendicular to the (0 0 l) planes and larger grain size. However, the corresponding grain size does not show any significant relation to the field-effect mobility. The obtained results show higher mobility of about $0.24\ cm^2\ V^{-1}\ s^{-1}$ which is close to one order of magnitude improvement when compared to film grown in normal high vacuum conditions. The result is comparable to that of thermal evaporation pentacene deposited on octadecyltrichlorosilane treated SiO_2, which shows typical values of 0.1–$1.0\ cm^2$/Vs. We found that there is an easy way to achieve high performance in OTFTs by depositing pentacene molecules in N_2 ambience. Furthermore, we obtained a clear relationship between field-effect mobility of OTFTs and crystallite sizes perpendicular to the (0 0 l) planes via XRD measurements derived from the samples.

Acknowledgements

The authors would like to thank the National Science Council of the Republic of China for financially supporting this research under Contract No. NSC 94-2112-M-006-022, NSC 94-2112-M-006-021, and the Center for Micro/Nano Technology Research, National Cheng Kung University, Taiwan, for their equipment support and cooperation.

References

[1] C.D. Dimitrakopoulos, P.R.L. Malenfant, Adv. Mater. 14 (2002) 99, and reference therein.
[2] T.W. Kelley, P.F. Baude, C. Gerlach, D.E. Ender, D. Muyres, M.A. Haase, D.E. Vogel, S.D. Theiss, Chem. Mater. 16 (2004) 4413.
[3] Y.Y. Lin, D.J. Gundlach, S.F. Nelson, T.N. Jackson, IEEE Electron. Dev. Lett. 18 (1997) 606.
[4] T.W. Kelley, D.V. Muyres, P.F. Baude, T.P. Smith, T.D. Jones, Mater. Res. Soc. Symp. Proc. L6.5.1 (2003) 771.
[5] D.J. Gundlach, Y.Y. Lin, T.N. Jackson, S.F. Nelson, D.G. Schlom, IEEE Electron. Dev. Lett. 18 (1997) 87.
[6] W.Y. Chou, H.L. Cheng, Adv. Func. Mater. 14 (2004) 811, and reference therein.
[7] R.G. Della Valle, A. Brillante, E. Venuti, L. Farina, A. Girlando, M. Masino, Org. Electron. 5 (2005) 1, and reference therein.
[8] C.C. Mattheus, G.A. de Wijs, R.A. de Groot, T.T.M. Palstra, J. Am. Chem. Soc. 125 (2003) 6323.
[9] Frank-J. Meyer zu Heringdorf, M.C. Reuter, R.M. Tromp, Nature 412 (2001) 517.
[10] H.L. Cheng, W.Y. Chou, C.W. Kou, F.C. Tang, Y.W. Wang, Appl. Phys. Lett. 88 (2006) 161918.
[11] W.Y. Chou, C.W. Kou, H.L. Cheng, Y.S. Mai, F.C. Tang, S.T. Lin, C.Y. Yeh, J.B. Horng, C.T. Chia, C.C. Liao, D.Y. Shu, J. Appl. Phys. 99 (2006) 114511.
[12] P.M. Rabinson, H.G. Scott, J. Crystal Growth 1 (1967) 187.
[13] C. Dimitrakopoulos, A.R. Brown, A. Pomp, J. Appl. Phys. 80 (1996) 2501.

[14] R. Hosemann, S.N. Bagchi, Direct Analysis of Diffraction by Matter, North-Holland, Amsterdam, 1962.
[15] R. Hosemann, A.M. Hindeleh, J. Macromol. Sci. Phys. B34 (1995) 327.
[16] L.E. Alexander, X-ray Diffraction Methods in Polymer Science, Wiley, New York, 1969. And references therein.
[17] D. Knipp, R.A. Street, A. Völkel, J. Ho, J. Appl. Phys. 93 (2003) 347.
[18] P.V. Pesavento, R.J. Chesterfield, C.R. Newman, C.D. Frisbie, J. Appl. Phys. 96 (2004) 7312.
[19] A. Di Carloa, F. Piacenza, A. Bolognesi, B. Stadlober, H. Maresch, Appl. Phys. Lett. 86 (2005) 263501.
[20] L. Torsi, A. Dodabalapur, L.J. Rothberg, A.W.P. Fung, H.E. Katz, Science 272 (1996) 1462.
[21] M. Shtein, J. Mapel, J.B. Benziger, S.R. Forrest, Appl. Phys. Lett. 81 (2002) 268.

Available online at www.sciencedirect.com
ScienceDirect
Organic Electronics 7 (2006) 452–456
Organic Electronics
www.elsevier.com/locate/orgel

Singlet exciton diffusion in MEH-PPV films studied by exciton–exciton annihilation

A.J. Lewis [a], A. Ruseckas [a], O.P.M. Gaudin [a], G.R. Webster [b], P.L. Burn [b], I.D.W. Samuel [a,*]

[a] *Organic Semiconductor Centre and Ultrafast Photonics Collaboration, School of Physics and Astronomy, University of St. Andrews, North Haugh, St. Andrews, Fife KY16 9SS, United Kingdom*

[b] *Chemistry Reasearch Laboratory, Department of Chemistry, University of Oxford, Mansfield Road, Oxford, Oxfordshire, OX1 3TA, United Kingdom*

Received 9 January 2006; received in revised form 29 May 2006; accepted 30 May 2006
Available online 30 June 2006

Abstract

We report time-resolved photoluminescence studies in MEH-PPV films for a wide range of excitation intensities. The results fit well to a diffusion-limited exciton–exciton annihilation model with an annihilation constant $\gamma = (2.8 \pm 0.5) \times 10^{-8}\,\mathrm{cm^3\,s^{-1}}$. This enables us to estimate the exciton diffusion coefficient to be $D = (3 \pm 1) \times 10^{-3}\,\mathrm{cm^2\,s^{-1}}$. This corresponds to a diffusion length between 5 and 8 nm for one-dimensional diffusion.

Keywords: Exciton; Diffusion; Solar cell; Photovoltaic; Photophysics; MEH-PPV

1. Introduction

Conjugated polymers show great potential for applications in photovoltaics because of a high absorption coefficient ($\sim 10^5\,\mathrm{cm^{-1}}$) in thin films and ability to transport charge [1–3] combined with simple processing and hence the scope for low cost manufacture. Primary photoexcitations in conjugated polymers are singlet excitons with the Coulombic binding energy generally accepted to lie between 0.3 and 1 eV [4–6], although lower values have been reported [7]. Because of this, charge separation generally occurs at an interface with another material at a planar or bulk heterojunction [8–12]. For photovoltaic devices it is essential to convert excitons into charge carriers, so the transport (by diffusion) of excitons to the heterojunction is a very important step in the operation of an organic solar cell. A widely used method to study exciton diffusion is based on interface quenching in which the reduction of fluorescence lifetime is studied by a quenching layer [13–17]. In this method the interface with a quencher should be sharp (no inter-diffusion), and short capture distance as well as high capture rate at the interface are desirable. It is not always possible to satisfy all these three conditions.

In this paper we explore an alternative way to measure exciton diffusion by studying exciton–

* Corresponding author. Tel.: +44 133 446 3114; fax: +44 133 446 3104.
E-mail address: idws@st-and.ac.uk (I.D.W. Samuel).

1566-1199/$ - see front matter © 2006 Elsevier B.V. All rights reserved.
doi:10.1016/j.orgel.2006.05.009

exciton annihilation (or exciton fusion). It occurs when two excitons in close proximity (within an annihilation or reaction radius) combine, forming a higher excited state, which relaxes quickly to the lowest excited state. As a result, one exciton is lost into heat. This process occurs when the density of excitons reaches a sufficient level, usually greater than $10^{17}\,cm^{-3}$ [18–21], although this does vary between materials. We have previously used it to determine the exciton diffusion coefficient in light emitting dendrimers [22]. The dynamics of exciton density is described as a bimolecular process, and the exciton diffusion coefficient can be calculated from the annihilation rate provided the annihilation (or reaction) radius is known.

The use of MEH-PPV in devices is quite extensive, including solar cells [3], light-emitting diodes (LEDs) [23], and optically pumped polymer lasers [24]. Consequently, it is extremely beneficial to understand the processes involved in this polymer in order to enhance devices fabricated with it. Previously reported studies have shown a one-dimensional diffusion length of the exciton in MEH-PPV films in the range of 6–14 nm [9,16,17] using interface quenching methods. This variation can be explained to some extent by different morphologies of the bulk films and interfaces used in these studies as well as by different lifetimes of the mobile intrachain excitons. Excitation intensity dependent exciton lifetime has been reported in MEH-PPV films [25], but quantitative estimates of annihilation parameters were not given.

We report here quantitative studies of exciton–exciton annihilation in MEH-PPV films using time-resolved photoluminescence (PL). PL kinetics can be described with a time independent annihilation rate, which provides information on exciton diffusion in the bulk MEH-PPV films without the complexity of surface effects.

2. Experimental

Fused silica substrates were cleaned by ultrasonication in acetone for 6 min then in propan-2-ol for 6 min. MEH-PPV films were deposited by spin-coating from solution in chlorobenzene. The weight average molecular weight of the MEH-PPV was 320,000 and the polydispersity was 12. Film thickness was calculated from the measured absorbance (see Fig. 1) using an absorption coefficient determined by spectroscopic ellipsometry. A thin film of 35 nm was used to ensure no amplified spontaneous

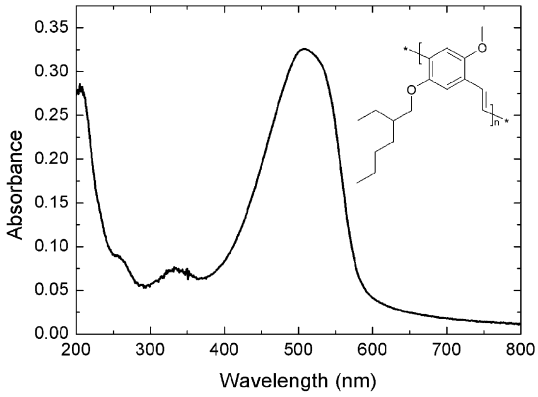

Fig. 1. Molecular structure and absorbance spectrum of MEH-PPV.

emission (ASE) was present, which could add a further decay channel for excitons [26]. Excitation was by 100 fs pulses at 400 nm with a repetition rate of 50 kHz. For comparison some experiments were performed using a 5 kHz pulse repetition rate. Time-resolved PL integrated over the spectral range of 550–680 nm was measured using a synchroscan streak camera. The instrumental response function was ~5 ps (FWHM). PL decays were measured under a vacuum of 2×10^{-5} mbar. The excitation spot size was measured to have a diameter of 0.5 mm at $1/e^2$ of the maximum intensity and the excitation pulse energy was varied using neutral density filters. The excitation density was calculated assuming one absorbed photon produces one exciton, which is justified because the chromophore density is more than two orders of magnitude higher than the highest excitation density of 1.5×10^{18} cm^{-3}, so that sequential photon absorption is negligible. The excitation density is essentially uniform through the film as the absorbance of the 35 nm thick film at 400 nm is only 0.08.

3. Results and discussion

The results of time-resolved luminescence measurements as a function of excitation density are shown in Fig. 2. The initial PL decay at low excitation density ($<10^{17}\,cm^{-3}$) is close to mono-exponential with a time constant of 140 ps. This is consistent with previous literature work [27]. As the excitation density is increased, the decays become progressively faster due to exciton–exciton annihilation. At high repetition rates, accumulated long-lived excitations, such as triplets and photogenerated charges (polarons) can potentially quench singlet excitons and

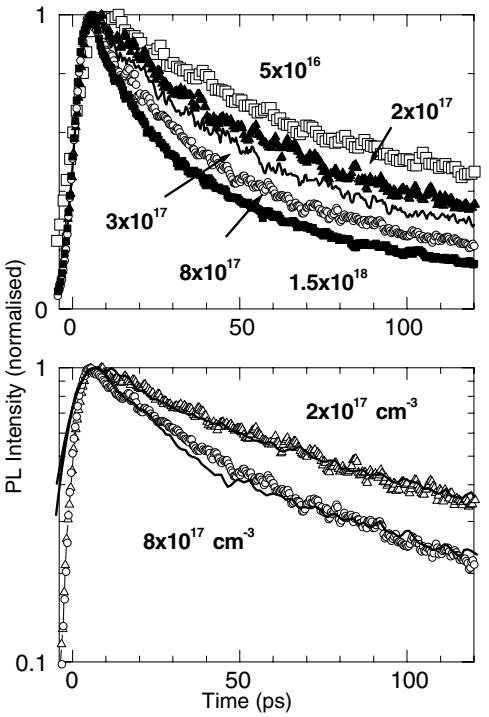

Fig. 2. A range of representative photoluminescence (PL) decays measured with a 50 kHz pulse repetition rate (top panel). Excitation densities are given in cm^{-3}. The PL lifetime decreases with increasing excitation density. The bottom panel shows a comparison of PL decays measured using the 50 kHz excitation rate (symbols) and 5 kHz (solid lines) at two different excitation densities.

contribute to faster PL decays. We would not expect this to happen at our repetition rate of 50 kHz, but to make sure we performed some time-resolved PL measurements at a lower pulse repetition rate (5 kHz) for comparison. These measurements gave similar PL decays at identical excitation densities (bottom panel in Fig. 2), allowing us to conclude that quenching by accumulated triplets and polarons is negligible at these excitation densities and repetition rates. Exciton–exciton annihilation can be modeled using the following rate equation:

$$\frac{dn(t)}{dt} = -kn - \gamma n^2 \quad (1)$$

which has the solution for time independent γ:

$$n(t) = \frac{n(0)\exp(-kt)}{1 + \frac{\gamma}{k}n(0)[1 - \exp(-kt)]} \quad (2)$$

where $n(t)$ is the exciton density at time t, $k = 1/140\ ps^{-1}$ is the decay rate with no annihilation and γ is the annihilation rate constant. Eq. (2) predicts a linear dependence of $1/n(t)$ on $\exp(kt)$, and this

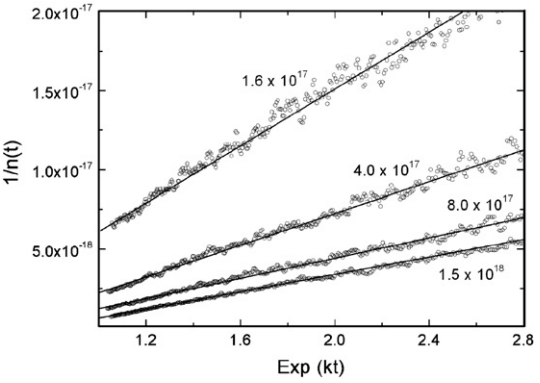

Fig. 3. A representative range of linearised results of the measured PL decays. Excitation densities are given in cm^{-3}.

is indeed observed in Fig. 3. The slope of these linearised curves gives the singlet–singlet annihilation rate constant for the MEH-PPV film. The results are shown in Fig. 4. γ was calculated to be $=(2.8 \pm 0.5) \times 10^{-8}\ cm^3\ s^{-1}$ for the three excitation densities lower than $5 \times 10^{17}\ cm^{-3}$. There is an apparent reduction of the annihilation constant at higher excitation densities, which can be explained by the non-resolved PL decay due to rapid annihilation of excitons generated within the annihilation (reaction) radius that can be much faster for non-relaxed excitons before dynamic localization [28]. Neglecting rapid annihilation at high densities overestimates the initial exciton density used to calculate the annihilation rate, which then results in lower values of γ. The fact that annihilation kinetics fit well with time independent γ agrees with annihilation data in PPV [18,19] and polythiophene films

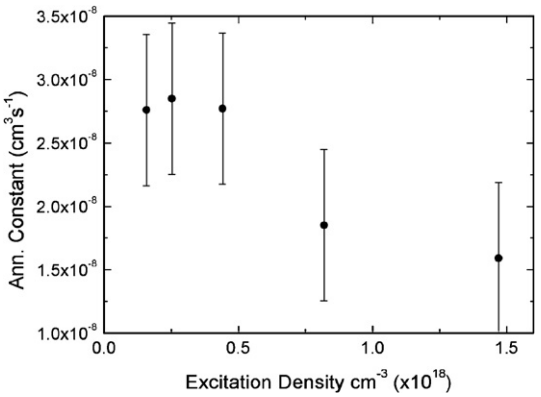

Fig. 4. Final results for the values of γ obtained for each excitation density. Densities where annihilation was not observed ($n(0) < 10^{17}\ cm^{-3}$) are not displayed.

[20] and indicates that exciton diffusion is generally three-dimensional in polymer films [29]. We also performed time-resolved PL measurements in a concentrated MEH-PPV solution in chlorobenzene (5 mg/ml), however no sign of exciton–exciton annihilation was observed for excitation densities up to 1×10^{17} cm^{-3} (calculated from the absorption depth of 1 mm in solution). The highest excitation densities showed PL line narrowing and an associated fast decay component due to ASE (data not shown). This indicates that exciton annihilation conditions are difficult to reach in solution.

It is possible to determine the exciton diffusion coefficient, D, from the measured annihilation rate using:

$$\gamma = 4\pi D R_a \tag{3}$$

where R_a is the annihilation radius of excitons, which corresponds to the distance at which annihilation is faster than diffusion. This equation is valid only for diffusion-limited annihilation, where the exciton has to diffuse a significant distance before annihilation occurs. This condition is satisfied in our case. If it were not satisfied, then γ would show strong time dependence, and the plots in Fig. 3 would be nonlinear. Singlet–singlet annihilation is likely to be dominated by dipole–dipole interaction, and so $R_a = a(R_e/R_g)^{3/2}$, where a is an average exciton hopping distance identical to a typical interchain distance in MEH-PPV films of ~ 1 nm, and R_e and R_g are Förster radii for excitation transfer onto the excited segment and onto the segment in ground state, respectively. Generally the Förster radius in organic materials is <5 nm [30], and the largest reported value of 8 nm was obtained for the perfectly overlapping PL spectrum of the glassy phase of polyfluorene with the very strong absorption of the crystalline phase [31]. Using $R_e/R_g = 4$ we get $R_a = 8$ nm as the upper estimate, which gives the lower limit of the diffusion coefficient $D_{min} = 2.8 \times 10^{-3}$ cm^2 s^{-1}. This is a factor of 21/2 larger than the reported value in MEH-PPV films from surface quenching measurements on a 30–800 ps time scale, where an infinitely large exciton quenching rate at the interface with polymerised C_{60} was assumed [16]. Given the fact that exciton diffusion slows down in time due to energetic disorder [4,20,27], the agreement is acceptable. The diffusion length of the singlet exciton can be calculated using

$$L_d = (dD\tau)^{\frac{1}{2}} \tag{4}$$

where $\tau = 140$ ps is the singlet exciton lifetime and d is the dimensionality used. An approximate value for the diffusion length in three dimensions, L_{3D} can be determined from the annihilation data using the density at which annihilation begins to occur, found here to be $n(0) \sim 10^{17}$ cm^{-3}. Assuming that exciton diffusion is isotropic the volume sampled by the exciton can be approximated as a sphere and the density of these spheres is $n(0)$, so that

$$\frac{4}{3}\pi n(0) L_{3D}^3 = 1 \tag{5}$$

This results in $L_{3D} \sim 13$ nm, which is in fact the sum of L_{3D} and R_a, so this value can be taken as an upper estimate for the three-dimensional diffusion length. It corresponds to $D_{max} = 4 \times 10^{-3}$ cm^2 s^{-1}, which gives a stronger constraint on D_{max} than the surface quenching by TiO_2 [17]. Taking this value and the estimated value of D_{min} we obtain $D = (3 \pm 1) \times 10^{-3}$ cm^{2}s^{-1}. The diffusion length, L_d, depends upon the dimensionality which needs to be appropriate to the situation being considered. For exciton diffusion across a film to a planar heterojunction or quenching interface, only diffusion in one direction matters, and so it is the one-dimensional diffusion length ($d = 1$ in Eq. (4)) which is relevant. Our range of values for the diffusion coefficient indicates that L_{1D} lies in the range 5–8 nm.

4. Conclusion

Singlet–singlet annihilation in MEH-PPV films occurs with a time independent rate and is limited by exciton diffusion. The diffusion coefficient of singlet excitons is found to be $(3 \pm 1) \times 10^{-3}$ cm^2 s^{-1}, which lies in between other reported values. Our results show that exciton–exciton annihilation measurements are a very useful way of studying exciton diffusion. For MEH-PPV, the results of the exciton diffusion measurements are consistent with those obtained by diffusion to an interface. The three-dimensional exciton diffusion length is estimated to lie in the range of 9–13 nm. For direct comparison to planar devices and interface quenching, the one dimensional diffusion length lies between 5 and 8 nm. The fact that the exciton diffusion length is much shorter than the absorption length currently constrains organic solar cell design. It provides opportunities for materials and processing development to increase the exciton diffusion length and/or nanostructured device design to accommodate it.

References

[1] J.J.M. Halls, C.A. Walsh, N.C. Greenham, E.A. Marseglia, R.H. Friend, S.C. Moratti, A.B. Holmes, Nature 376 (1995) 498.

[2] N.S. Sariciftci, L. Smilowitz, A.J. Heeger, F. Wudl, Science 258 (1992) 1474.

[3] S.E. Shaheen, C.J. Brabec, N.S. Sariciftci, F. Padinger, T. Fromherz, J.C. Hummelen, Appl. Phys. Lett. 78 (2001) 841.

[4] M. Scheidler, U. Lemmer, R. Kersting, S. Karg, W. Riess, B. Cleve, R.F. Mahrt, H. Kurz, H. Bässler, E.O. Gobel, P. Thomas, Phys. Rev. B 54 (1996) 5536.

[5] S.F. Alvarado, P.F. Seidler, D.G. Lidzey, D.D.C. Bradley, Phys. Rev. Lett. 81 (1998) 1082.

[6] V. Gulbinas, Y. Zaushitsyn, V. Sundström, D. Hertel, H. Bässler, A. Yartsev, Phys. Rev. Lett. 89 (2002) 107401.

[7] D. Moses, J. Wang, A.J. Heeger, N. Kirova, S. Brazovski, Proc. Nat. Assoc. Sci. USA 98 (2001) 13496.

[8] J.J.M. Halls, K. Pichler, R.H. Friend, S.C. Moratti, A.B. Holmes, Appl. Phys. Lett. 68 (1996) 3120.

[9] A. Haugeneder, M. Neges, C. Kallinger, W. Spirkl, U. Lemmer, J. Feldmann, U. Scherf, E. Harth, A. Gugel, K. Müllen, Phys. Rev. B 59 (1999) 15346.

[10] P. Peumans, S.R. Forrest, Appl. Phys. Lett. 79 (2001) 126.

[11] K.M. Coakley, M.D. McGehee, Appl. Phys. Lett. 83 (2003) 3380.

[12] D. Chirvase, Z. Chiguvare, M. Knipper, J. Parisi, V. Dyakonov, J.C. Hummelen, J. Appl. Phys. 93 (2003) 3376.

[13] B.A. Gregg, J. Sprague, M.W. Peterson, J. Phys. Chem. B 101 (1997) 5362.

[14] M. Theander, A. Yartsev, D. Zigmantas, V. Sundström, W. Mammo, M.R. Andersson, O. Inganäs, Phys. Rev. B 61 (2000) 12957.

[15] D.E. Markov, E. Amsterdam, P.W.M. Blom, A.B. Sieval, J.C. Hummelen, J. Phys. Chem. A 109 (2005) 5266.

[16] D.E. Markov, C. Tanase, P.W.M. Blom, J. Wildeman, Phys. Rev. B 72 (2005) 045217.

[17] V.M. Burlakov, K. Kawata, H.E. Assender, G.A.D. Briggs, A. Ruseckas, I.D.W. Samuel, Phys. Rev. B 72 (2005) 075206 (We have divided the reported value by $\sqrt{2}$ to make it consistent with our definition of diffusion length.).

[18] R.G. Kepler, V.S. Valencia, S.J. Jakobs, J.J. McNamara, Synth. Metals 78 (1996) 227.

[19] G.J. Denton, N. Tessler, N.T. Harrison, R.H. Friend, Phys. Rev. Lett. 78 (1997) 733.

[20] A. Ruseckas, M. Theander, L. Valkunas, M.R. Andersson, O. Inganäs, V. Sundström, J. Luminesc. 76&77 (1998) 474.

[21] M.A. Stevens, C. Silva, D.M. Russell, R.H. Friend, Phys. Rev. B 63 (2001) 165213.

[22] E.B. Namdas, A. Ruseckas, I.D.W. Samuel, S.C. Lo, P.L. Burn, Appl. Phys. Lett. 86 (2005) 091104.

[23] G. Gustafsson, G.M. Treacy, Y. Cao, F. Klavetter, N. Colaneri, A.J. Heeger, Synth. Metals. 57 (1993) 4123.

[24] I.D.W. Samuel, G.A. Turnbull, Mater. Today 7 (2004) 28.

[25] I.B. Martini, A.D. Smith, B.J. Schwartz, Phys. Rev. B 69 (2004) 035204.

[26] A.K. Sheridan, G.A. Turnbull, A.N. Safonov, I.D.W. Samuel, Phys. Rev. B 62 (2000) 11929.

[27] G.R. Hayes, I.D.W. Samuel, R.T. Phillips, Phys. Rev. B 52 (1995) R569.

[28] A. Ruseckas, P. Wood, I.D.W. Samuel, G.R. Webster, W.J. Mitchell, P.L. Burn, V. Sundström, Phys. Rev. B 72 (2005) 115214.

[29] V. Gulbinas, M. Chachisvilis, L. Valkunas, V. Sundström, J. Phys. Chem. 100 (1996) 2213.

[30] J.R. Lakowicz, Principles of Fluorescence Spectroscopy, Kluwer Academic/ Plenum, 1999.

[31] A.L.T. Khan, P. Sreearunothai, L.M. Hertz, M.J. Banach, A. Köhler, Phys. Rev. B 69 (2004) 085201.

Available online at www.sciencedirect.com
ScienceDirect
Organic Electronics 7 (2006) 457–464
Organic Electronics
www.elsevier.com/locate/orgel

Bottom contact ambipolar organic thin film transistor and organic inverter based on C_{60}/pentacene heterostructure

S.D. Wang [a,*], K. Kanai [b], Y. Ouchi [b], K. Seki [c]

[a] Research Center for Materials Science, Nagoya University, Furocho, Chikusa-ku, Nagoya 464-8602, Japan
[b] Department of Chemistry, Graduate School of Science, Nagoya University, Furocho, Chikusa-ku, Nagoya 464-8602, Japan
[c] Department of Chemistry, Graduate School of Science and Institute for Advanced Research, Nagoya University, Furocho, Chikusa-ku, Nagoya 464-8602, Japan

Received 14 March 2006; received in revised form 7 June 2006; accepted 9 June 2006
Available online 3 July 2006

Abstract

We report on the fabrication and characterization of the bottom contact organic thin film transistor and inverter based on a heterostructure of C_{60} on pentacene. The transistor shows ambipolar transport characteristics with high electron and hole mobilities of 0.23 $cm^2 V^{-1} s^{-1}$ and 0.14 $cm^2 V^{-1} s^{-1}$, respectively. Both the n-channel in C_{60} and the p-channel in pentacene are stable in N_2 atmosphere. After exposure to air, the n-channel is completely degraded whereas the p-channel keeps working. The inverter exhibits typical transfer characteristics, which are interpreted by the distribution of the accumulated electrons and holes depending on the bias conditions. The combination of the high performance and the bottom configuration of our devices suggests a potential way to fabricate organic complementary circuits without patterning of organic materials.

PACS: 85.30.De; 85.30.Tv; 73.61.Ph; 73.61.Wp

Keywords: Organic semiconductor; Organic thin film transistors; Organic inverter; Ambipolar; Bottom contact; Pentacene; Fullerene; Current–voltage characteristics

1. Introduction

Organic thin film transistors (OTFTs), with advantages of low-cost, flexibility and large-area capability, are attractive for numerous applications including switching devices for various displays [1] and components for organic integrated circuits [2]. Most OTFTs reported so far exhibit either n-type or p-type behavior [1,3], and electron and hole mobilities as high as 0.5 $cm^2 V^{-1} s^{-1}$ and 1.5 $cm^2 V^{-1} s^{-1}$ have been demonstrated in fullerene (C_{60})-based [4] and pentacene-based [5] transistors, respectively. However, development of organic complementary technology, where both n-type and p-type transistors are incorporated, is essential for achieving efficient organic integrated circuits with low power dissipation, good noise immunity and high operational stability. There are two approaches to this goal. One is

* Corresponding author. Fax: +81 52 789 2944.
E-mail addresses: dong@mat.chem.nagoya-u.ac.jp, trueccfs@hotmail.com (S.D. Wang).

1566-1199/$ - see front matter © 2006 Elsevier B.V. All rights reserved.
doi:10.1016/j.orgel.2006.06.001

to incorporate separate n-type and p-type transistors by electrical connection [2,6–8]; the other is to realize ambipolar charge transport in a single transistor. The latter has superiorities for device fabrication such as operation at both positive and negative voltages and simplicity of circuit design. Recently solution-processed ambipolar OTFTs and organic inverters using interpenetrating blends [9–11] or small-bandgap polymer [9] have been reported. As for organic small molecules, OTFTs based on a heterostructure, first reported by Dodabalapur et al. [12], have exhibited ambipolar transport characteristics [13–15]. The heterostructure consists of two active layers, one of which is n-type organic semiconductor and the other is p-type. Thus both electron and hole can be accumulated depending on the gate bias. Nevertheless, the carrier mobility in the ambipolar bilayer transistors is quite low (10^{-6}–10^{-3} $cm^2\ V^{-1}\ s^{-1}$) compared with those in the corresponding n-type or p-type transistors, and efforts to improve the mobility are still needed.

Recently Kuwahara, Kubozono and co-workers reported ambipolar transistors based on C_{60}/pentacene heterostructure with relatively high electron and hole mobilities (10^{-3}–10^{-2} $cm^2\ V^{-1}\ s^{-1}$) [16,17]. In their devices, however, no ambipolar behavior could be observed with the top and bottom contact configurations, and only devices with the middle contact configuration, which is equivalent to a top contact for pentacene and a bottom contact for C_{60}, have shown ambipolar transport characteristics after annealing in high vacuum (HV). The middle contact configuration requires electrode patterning after the deposition of pentacene. Since pentacene is dissolved to many solvents, photolithographic etching cannot be employed on already deposited pentacene film, making such configuration not practical in device manufacturing [18,19]. Furthermore, the vacuum annealing process also limits the practicability for real device fabrication.

In this paper we report the fabrication of transistors based on C_{60}/pentacene heterostructure with bottom contact configuration, which is very similar with that in Ref. [16], whereas the in situ measurements of our devices in HV have shown significantly different results. Clear ambipolar transport characteristics were observed in the bottom contact devices without any annealing treatment, while the electron and hole mobilities reached the order of 0.1 $cm^2\ V^{-1}\ s^{-1}$. A bottom contact inverter was also successfully fabricated by incorporating two C_{60}/pentacene ambipolar transistors. Such devices have advantages that (1) the patterning of the electrodes can be carried out before the deposition of organic materials, and (2) the simple sequential deposition of the two organic materials after electrode patterning completes the device fabrication without annealing. The devices work in N_2 atmosphere as well, demonstrating the possibility of utilizing this bottom contact configuration in practical devices.

2. Experimental

The heavily doped silicon (Si) wafers with 1 μm silicon dioxide (SiO_2) layers, purchased from Photo Precision Co., Ltd., were used as the substrates. The Si and SiO_2 act as the gate electrode and the gate dielectric, respectively. The gold (Au) electrodes, with thickness of 50 nm, were deposited by thermal evaporation through a shadow mask on the substrate pre-cleaned by the sequential ultrasonic bath of acetone and ethanol. The channel length and channel width were 0.1 mm and 2 mm, respectively. All the electrodes were connected to vacuum electrical feedthroughs before the deposition of organic films. Commercially available pentacene and C_{60} (TCI Co., Ltd.) were used as received. The organic materials were sublimated by quartz cells in a HV system, where the base pressure was about 6×10^{-5} Pa and two quartz crystal microbalances are installed. Both of the microbalances were calibrated by UV–visible absorption measurements of deposited films dissolved in solution. One of the microbalances (fixed) was used to monitor the films deposition, and the other one (movable) was used in advance for setting the tooling factor of the fixed one. The deposition rates of both materials are 0.1–0.2 Å/s. Both the transistor and the inverter were fabricated by the successive deposition of 10 nm pentacene and 20 nm C_{60} on the Au patterns, with two terminals (drain and source, see Fig. 1) for the transistor, and with three terminals (supply, output and ground, see Fig. 6) for the inverter. The in situ electrical measurements were performed at room temperature just after the fabrication.

3. Results and discussion

3.1. Bottom contact ambipolar OTFTs with C_{60}/pentacene and pentacene/C_{60} heterostructures

Fig. 2(a) and (b) shows the drain current (I_D) versus drain voltage (V_D) characteristics of a bottom contact transistor with an active layer of 20 nm C_{60}

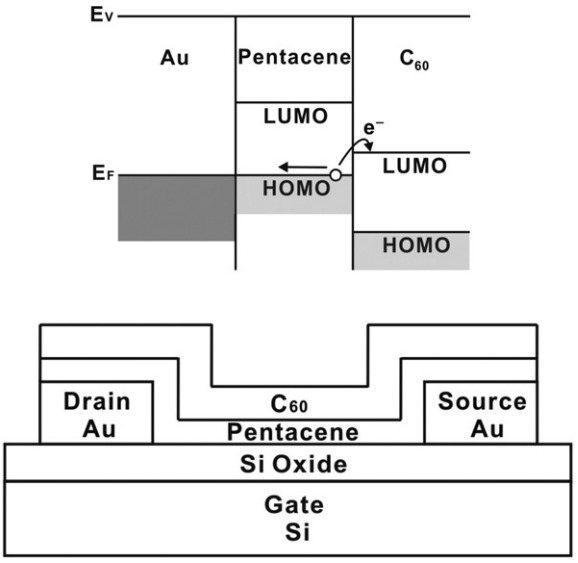

Fig. 1. Bottom: schematic device structure of a bottom contact transistor based on C_{60}/pentacene heterostructure. Top: schematic energy level diagram of C_{60}/pentacene/Au structure.

on 10 nm pentacene (C_{60}/pentacene heterostructure), whose schematic device structure is shown in Fig. 1. In the region of high positive and negative gate voltages (V_G), the transistor show typical output characteristics of an n-channel and a p-channel OTFT, respectively. I_D increases with the magnitude of V_D, with transition from a linear regime to a saturation regime, and becomes larger at higher V_G. However, in the region of low V_G and high V_D, I_D increases superlinearly with V_D, and becomes smaller at higher V_G. According to our analysis described below, this phenomenon indicates the ambipolar charge transport in the C_{60}/pentacene heterostructure.

The schematic energy level diagram of the C_{60}/pentacene/Au structure is depicted in Fig. 1, where the vacuum level (E_V) is simply assumed to be aligned at the interfaces. In this case, the hole injection barrier is determined by the energy difference between the Fermi level (E_F) of the metal and the highest occupied molecular orbital (HOMO) level of the organic material [20]. The actual barrier at the pentacene/Au interface in ultrahigh vacuum (UHV) was reported to be 0.5 eV, with the formation of an interfacial dipole layer [21]. However, most pentacene-based transistors were fabricated in HV, and both the reported [1,5] and present device data suggest that the pentacene/Au contacts are ohmic. This might be due to the difference between UHV and HV conditions. Therefore, holes can be efficiently injected into the HOMO level of pentacene and form hole accumulation layer at the pentacene/SiO_2 interface. For the electron injection, the injection barrier from Au into the lowest unoccupied molecular orbital (LUMO) level of pentacene, assuming the vacuum level alignment, is high (1.8 eV) [21]. Even when we consider the reported large interfacial dipole, there will be still a 1.2 eV injection barrier [21]. Thus the electron injection from Au into the LUMO level of C_{60} through the LUMO level of pentacene is not probable. Instead, we propose that electrons are injected from the HOMO level of pentacene into the LUMO level of C_{60} to form electron accumulation layer at the C_{60}/pentacene interface, while the holes left in the pentacene layer are transported to the contacts (see Fig. 1). The mismatch between the LUMO level of C_{60} at about 4.4 eV [22] and the HOMO level of pentacene at 5.0 eV [21] results in a 0.6 eV barrier for electron injection from pentacene into C_{60}, which is consistent with the non-linear increase of I_D at low V_D observed in Fig. 2(a).

Here we define the grounded contact as the source contact in an ambipolar transistor. For positive V_G and V_D with $V_D < V_G - V_T$, where V_T is the threshold voltage, the gate electrode is effectively positively biased with respect to both the drain and the source contacts. Accordingly, only electrons are injected and accumulated in the C_{60} layer, and holes are depleted in the pentacene layer. In this voltage range, the device works like an n-channel transistor, and I_D reaches saturation with increasing V_D. For positive V_G and V_D with $V_D > V_G - V_T$, the gate electrode is effectively negatively biased with respect to the drain contact, but still positively biased with respect to the source contact. In this case, holes start to be injected into the pentacene layer at the drain contact, while electrons are still injected in the C_{60} layer at the source contact. Thus both the electron and the hole accumulation layers are distributed in the channel depending on the bias condition. At the site with the same potential as the gate electrode, electrons and holes will recombine at the C_{60}/pentacene interface due to the coulomb attraction (see Fig. 6). As a consequence, either electrons or holes are accumulated in this voltage range, and there will be no full depletion region through the entire channel. This explains the superlinear increase of I_D with V_D shown in Fig. 2(a). For negative V_G and V_D, the current behavior shown in Fig. 2(b) can be interpreted by the same mechanism. Actually the ambipolar transistor is equivalent to an

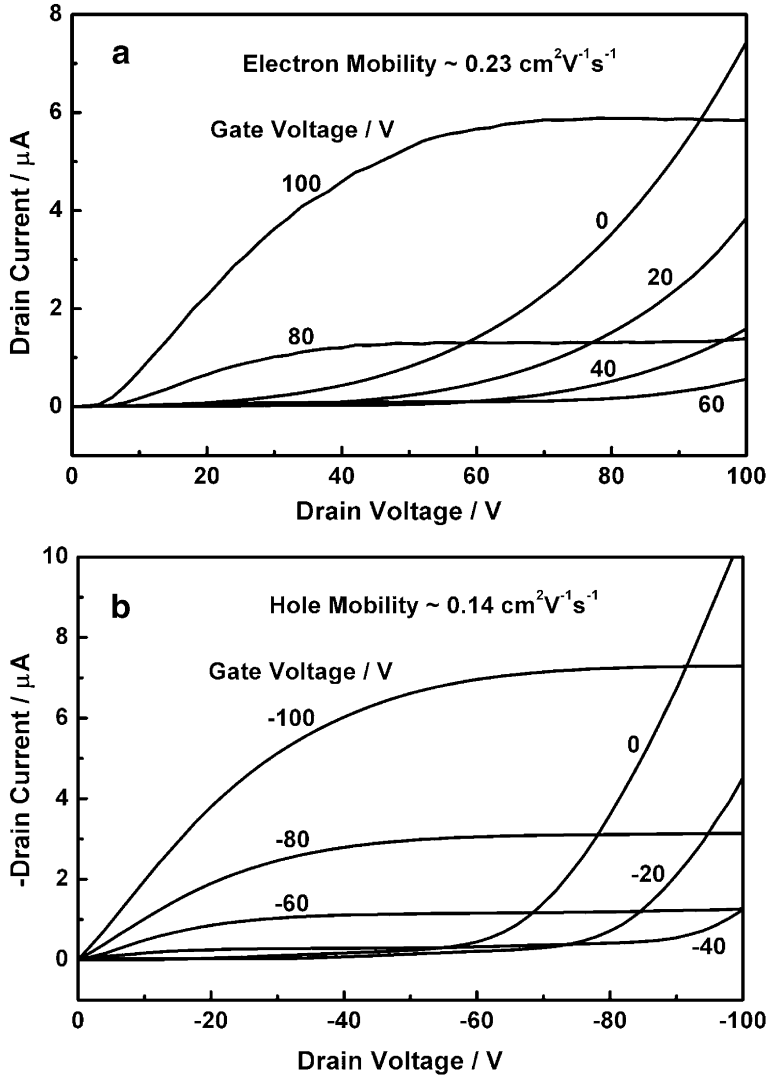

Fig. 2. I_D–V_D characteristics of a bottom contact transistor with an active layer of 20 nm C_{60} on 10 nm pentacene, (a) at positive gate voltages, (b) at negative gate voltages.

n-channel TFT and a p-channel TFT in parallel. At the locations where the n-channel is enhanced, the p-channel is depleted; and vice versa. The simultaneous operation of the parallel channels will produce the same characteristics as those in Fig. 2.

According to the transistor data in the high V_G region, the electron and hole mobilities are estimated to be 0.23 $cm^2\ V^{-1}\ s^{-1}$ and 0.14 $cm^2\ V^{-1}\ s^{-1}$, respectively. These mobilities are close to the best reported values for bottom contact C_{60}-based [4] and pentacene-based [19] transistors, suggesting that the heterostructure of C_{60} on pentacene does not degrade the charge transport properties in the C_{60} and pentacene layers. Fig. 3 shows the I_D versus V_G characteristics of our transistor under various environments. The non-monotonic change of I_D with $|V_G|$ observed in HV can be ascribed to the ambipolar charge transport discussed above. After exposure to nitrogen (N_2) at atmospheric pressure, I_D is only slightly decreased, and the ambipolar characteristics remain unchanged. The low sensitivity to N_2 implies that the circuits based on the transistor can be encapsulated in N_2 atmosphere. In contrast, the V_G dependence of I_D becomes monotonic after exposing the transistor to air, indicating the disappearance of the ambipolar characteristics. The I_D versus V_G characteristics of a pentacene-based transistor are presented in Fig. 3, and the

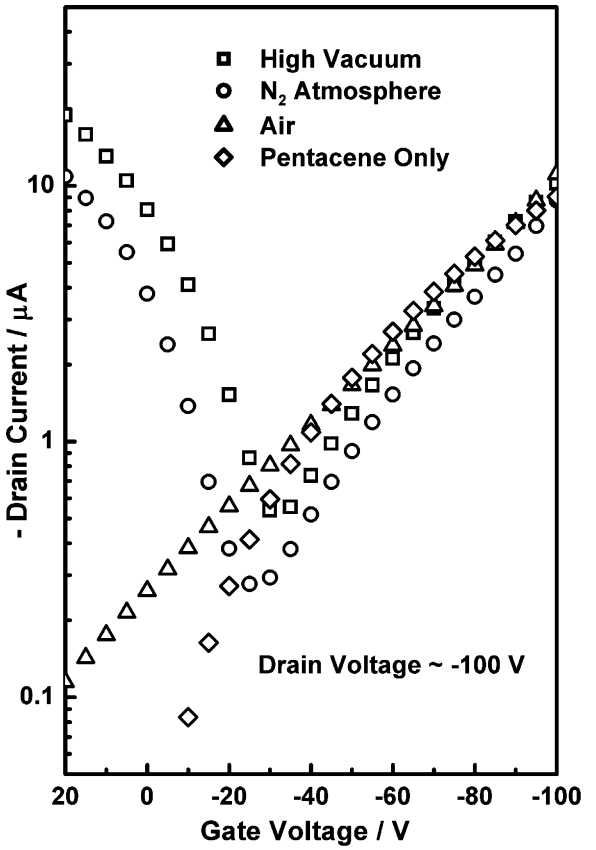

Fig. 3. I_D–V_G characteristics of the transistor depicted in Fig. 2 under various environments. Data represented by diamonds were recorded in high vacuum from a pentacene-based (30 nm) transistor.

comparison with the characteristics of the ambipolar transistor demonstrates (1) the almost complete degradation of the n-channel and (2) the maintenance of the p-channel in the ambipolar transistor after exposure to air. The phenomenon can be understood in terms of the high sensitivity of the electron injection and/or transport in C_{60} thin films to oxygen (O_2) [4,23]. Although there is no detailed statement about in situ measurements in Ref. [16], we may speculate that (1) the absence of the ambipolar characteristics in their bottom contact transistors might be due to such effect of ambient atmosphere, and (2) the annealing required for the appearance of the ambipolar behavior even for their middle contact transistors was necessary to remove the O_2 molecules in the C_{60} layer [4,23].

We also fabricated and in situ measured a transistor with an opposite heterostructure of 20 nm pentacene on 10 nm C_{60} (pentacene/C_{60} heterostructure), whose I_D versus V_G characteristics are shown in Fig. 4. Comparing with the C_{60}/pentacene transistor, the ambipolar characteristics can be still observed in this transistor, and we can consider the similar energetics of the carrier injection with that for the C_{60}/pentacene transistor. I_D in the electron enhancement mode (low negative V_G and positive V_G) is in the same order of magnitude. On the other hand, the magnitude of I_D in the hole enhancement mode (high negative V_G) is about two orders smaller, implying a much lower hole mobility in the top pentacene layer. In considering this difference from the C_{60}/pentacene transistor, we note that the film structure of C_{60} on pentacene can be isotropic owing to its symmetric molecular structure, hence the C_{60} layers on pentacene and on SiO_2 may possess similar structure, morphology, and electron mobility. On the other hand, the film growth of pentacene is known to be strongly influenced by the surface conditions of the substrate [19], and the large difference of hole mobility in the two heterostructures may be ascribed to the different film structure and/or molecular orientation of

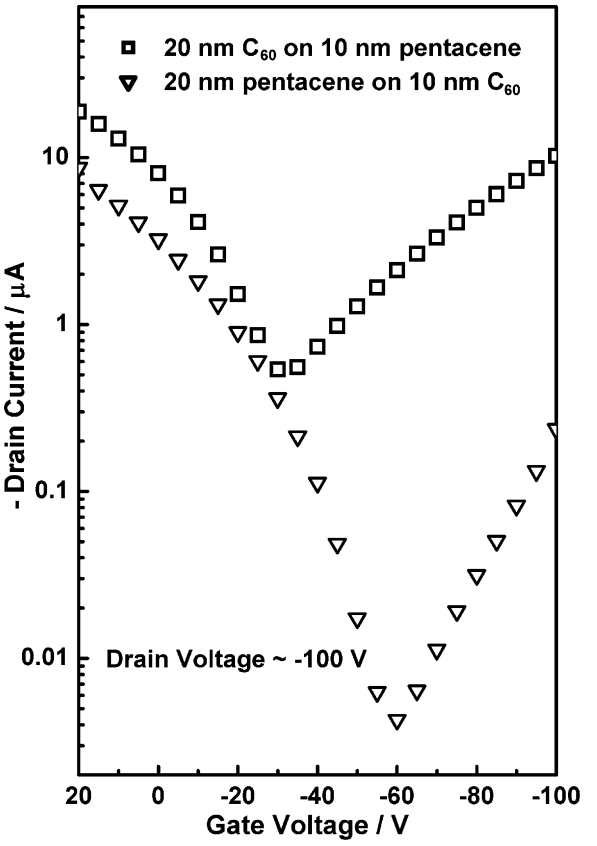

Fig. 4. I_D–V_G characteristics of bottom contact transistors with different active layers.

pentacene on C_{60} and on SiO_2. The severe n-channel degradation after exposure to air was also observed in the pentacene/C_{60} transistor, as in the case of C_{60}/pentacene, suggesting the O_2 diffusion into the bottom C_{60} layer through pentacene.

3.2. Bottom contact inverter with C_{60}/pentacene heterostructure

Using the same fabrication process, a bottom contact inverter based on the C_{60}/pentacene heterostructure could be fabricated by simply modifying the Au electrodes patterning. The transfer characteristics at positive supply voltage (V_{DD}) and the schematic device structure of the inverter are shown in Figs. 5 and 6, respectively. The circuit layout of the inverter is also presented in Fig. 5. The inverter exhibits typical voltage transfer characteristics, i.e. low/high input voltage (V_{IN}) leading to high/low output voltage (V_{OUT}), with a high gain of about 13, at both positive and negative supply voltages.

In the following, we will give an explanatory view of the operation mechanism of the inverter using Fig. 6. In Fig. 6, four different working states, marked A–D in Fig. 5, are chosen to demonstrate the realization of the transfer characteristics. The inverter consists of two identical ambipolar transistors, where the common gate electrode acts as V_{IN}, and the three Au electrodes play the roles of V_{DD} (100 V), V_{OUT}, and ground (0 V), respectively. At state *A*, V_{IN} is low so that the gate is highly negatively biased with respect to V_{DD} contact, while there is almost no gate bias with respect to the ground. Therefore, only hole accumulation occurs

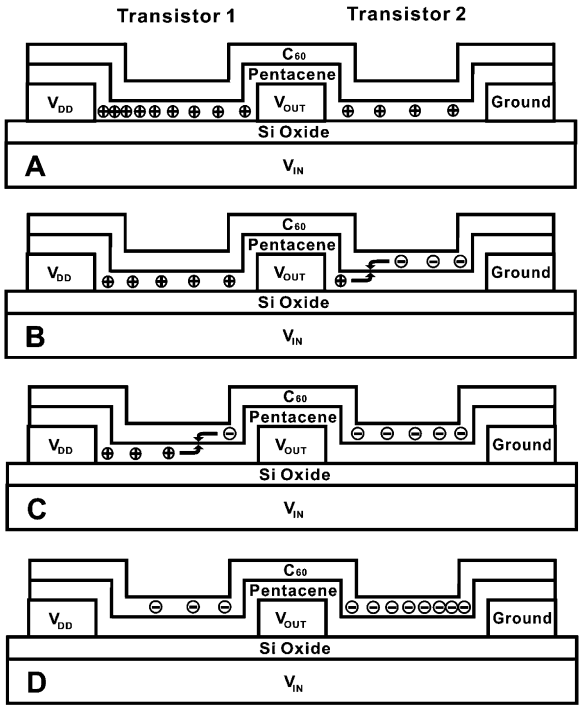

Fig. 6. Schematic illustration of the operation principle of the inverter depicted in Fig. 5. Circles with plus and subtraction signs indicate holes and electrons, respectively. Capital letters A, B, C, D represent different working states of the inverter marked in Fig. 5.

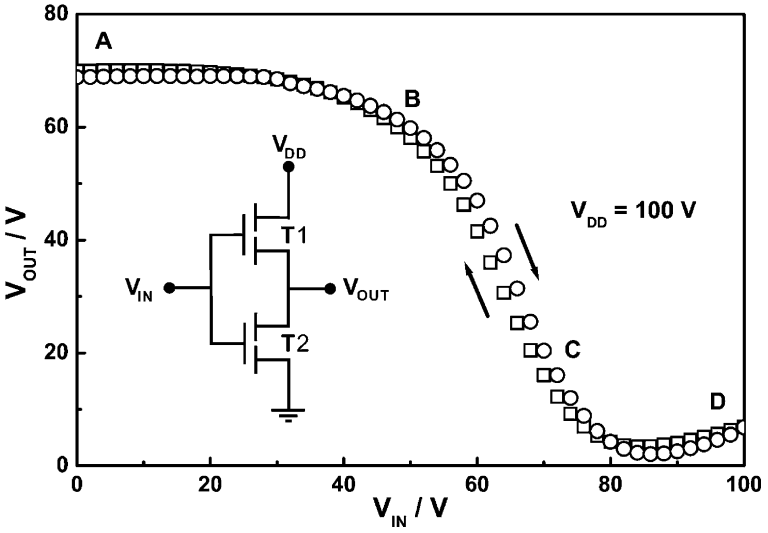

Fig. 5. Transfer characteristics of a bottom contact inverter with an active layer of 20 nm C_{60} on 10 nm pentacene at positive supply voltage. The circuit layout of the inverter is inserted, T1 and T2 represent the two ambipolar transistors.

in both of the transistors. Furthermore, the channel conductance of transistor 1 is much higher than that of transistor 2, leading to high V_{OUT} close to V_{DD}.

At state *B*, V_{IN} is increased, and the gate is negatively biased with respect to V_{DD} contact whereas positively biased with respect to the ground. The change of V_G from the state *A* reduces the hole concentration in transistor 1, and induces the electron injection at the ground which starts the ambipolar transport in transistor 2. V_{OUT} is decreased owing to the modification of the channels conductance.

At state *C*, the roles of the two transistors are exchanged with respect to those at state *B*, and accordingly V_{OUT} is decreased to a smaller value. At state *D*, opposite to the case of state *A*, high V_{IN} results in that only electrons are accumulated in the both transistors, and that the channel conductance of transistor 1 is much lower than that of transistor 2. Consequently V_{OUT} is close to 0 V.

In short, the inverter works like a gate controlled voltage divider. Depending on the voltage configuration, the distribution of the accumulated electrons and holes can modify the channels conductance of the two incorporated ambipolar transistors, and further realize the transfer characteristics.

In an ideal inverter, high and low V_{OUT} should approach V_{DD} and 0 V, respectively, and the threshold voltage (V_{Tinv}) should be equal to the half of V_{DD}. These are not achieved in Fig. 5. At states A and D in Fig. 6, it is clearly shown that no ambipolar transistors can be fully switched off during the inverter operation, and the leakage current from V_{DD} to the ground results in a relatively low gain [9,17] compared with the organic inverters incorporating separate n-type and p-type transistors [7,8]. On the other hand, the estimated carrier mobilities in our transistors are V_G dependent; the electron mobility is lower and higher than the hole mobility at low and high V_G (not shown), respectively. The variance of the electron and hole mobilities may lead to (1) a displacement of V_{Tinv} from the half of V_{DD} (see Fig. 5); and (2) a situation that the ratios of the voltage drops on the two transistors at low and high V_{OUT} are not in a reciprocal relationship, i.e. states A and D in Fig. 6 are not inversely equivalent. Similar with the ambipolar transistors, the inverter was observed to be insensitive to N_2 and highly sensitive to air.

4. Conclusions

The bottom contact transistor and inverter based on a heterostructure of C_{60} on pentacene were fabricated and in situ characterized. The ambipolar transport characteristics were observed in the transistor. It is proposed that electrons are injected from the pentacene HOMO level into the C_{60} LUMO level, and move in the C_{60} layer with electron mobility of 0.23 $cm^2 V^{-1} s^{-1}$; and that holes are injected from the Fermi level of Au into the pentacene HOMO level, and move in the pentacene layer with hole mobility of 0.14 $cm^2 V^{-1} s^{-1}$. The transistor with an opposite heterostructure of pentacene on C_{60} also showed ambipolar behavior, but with poorer performance, mainly owing to the low hole mobility in the top pentacene film. The performance of the transistors is stable in N_2 atmosphere, whereas the complete n-channel degradation was observed in air probably due to the high sensitivity of C_{60} to O_2. The typical voltage transfer characteristics for an inverter were achieved by combining two C_{60}/pentacene transistors by the analogous fabrication process, and the qualitative analysis on the accumulation and distribution of carriers is given to interpret the operation mechanism of the inverter.

We emphasize that the bottom contact configuration of the devices may simplify the design and fabrication of organic complementary circuits. The most advantageous aspect is that these devices can be fabricated by a sequence of (1) electrode patterning on a gate insulating layer, e.g. by photolithography, and (2) simple sequential deposition of two electronically functional organic layers without any patterning. The presently observed relatively high performance, together with the capability of encapsulation in inert gas, and the possible improvements by further choice of appropriate materials, demonstrate the potential usefulness of this type of devices for future applications.

Acknowledgements

This work was supported in part by the Creative Scientific Research (No. 14GS0213), the 21st century COE Project (No. 14COEB01), and the NEDO International Collaboration Project (No. 02BR1).

References

[1] C.D. Dimitrakopoulos, P.R.L. Malenfant, Adv. Mater. 14 (2002) 99.
[2] B. Crone, A. Dodabalapur, Y.Y. Lin, R.W. Filas, Z. Bao, A. LaDuca, R. Sarpeshkar, H.E. Katz, W. Li, Nature 403 (2000) 521.
[3] G. Horowitz, Adv. Mater. 10 (1998) 365.

[4] A. Tapponnier, I. Biaggio, P. Günter, Appl. Phys. Lett. 86 (2005) 112114.
[5] Y.Y. Lin, D.J. Gundlach, S.F. Nelson, T.N. Jackson, IEEE Electron. Dev. Lett. 18 (1997) 606.
[6] A. Dodabalapur, J. Laquindanum, H.E. Katz, Z. Bao, Appl. Phys. Lett. 69 (1996) 4227.
[7] T. Kanbara, K. Shibata, S. Fujiki, Y. Kubozono, S. Kashino, T. Urisu, M. Sakai, A. Fujiwara, R. Kumashiro, K. Tanigaki, Chem. Phys. Lett. 379 (2003) 223.
[8] Y. Inoue, Y. Sakamoto, T. Suzuki, M. Kobayashi, Y. Gao, S. Tokito, Jpn. J. Appl. Phys. 44 (2005) 3663.
[9] E.J. Meijer, D.M. de Leeuw, S. Setayesh, E. van Veenendaal, B.H. Huisman, P.W.M. Blom, J.C. Hummelen, U. Scherf, T.M. Klapwijk, Nat. Mater. 2 (2003) 678.
[10] A. Babel, J.D. Wind, S.A. Jenekhe, Adv. Funct. Mater. 14 (2004) 891.
[11] Y. Hayashi, H. Kanamori, I. Yamada, A. Takasu, S. Takagi, K. Kaneko, Appl. Phys. Lett. 86 (2005) 052104.
[12] A. Dodabalapur, H.E. Katz, L. Torsi, R.C. Haddon, Science 269 (1995) 1560.
[13] A. Dodabalapur, H.E. Katz, L. Torsi, R.C. Haddon, Appl. Phys. Lett. 68 (1996) 1108.
[14] C. Rost, D.J. Gundlach, S. Karg, W. Riess, J. Appl. Phys. 95 (2004) 5782.
[15] J. Wang, H.B. Wang, X.J. Yan, H.C. Huang, D.H. Yan, Chem. Phys. Lett. 407 (2005) 87.
[16] E. Kuwahara, Y. Kubozono, T. Hosokawa, T. Nagano, K. Masunari, A. Fujiwara, Appl. Phys. Lett. 85 (2004) 4765.
[17] E. Kuwahara, H. Kusai, T. Nagano, T. Takayanagi, Y. Kubozono, Chem. Phys. Lett. 413 (2005) 379.
[18] D.J. Gundlach, T.N. Jackson, D.G. Schlom, S.F. Nelson, Appl. Phys. Lett. 74 (1999) 3302.
[19] I. Kymissis, C.D. Dimitrakopoulos, S. Purushothaman, IEEE Trans. Electron. Dev. 48 (2001) 1060.
[20] H. Ishii, K. Sugiyama, E. Ito, K. Seki, Adv. Mater. 11 (1999) 605.
[21] F. Amy, C. Chan, A. Kahn, Org. Electron. 6 (2005) 85.
[22] S.C. Veenstra, A. Heeres, G. Hadziioannou, G.A. Sawatzky, H.T. Jonkman, Appl. Phys. A 75 (2002) 661.
[23] R.C. Haddon, A.S. Perel, R.C. Morris, T.T.M. Palstra, A.F. Hebard, R.M. Fleming, Appl. Phys. Lett. 67 (1995) 121.

Available online at www.sciencedirect.com
ScienceDirect
Organic Electronics 7 (2006) 465–473
Organic Electronics
www.elsevier.com/locate/orgel

Environmentally stable organic thin-films transistors: Terminal styryl *vs* central divinyl benzene building blocks for p-type oligothiophene semiconductors

C. Videlot-Ackermann [a,*], J. Ackermann [a], K. Kawamura [b], N. Yoshimoto [b], H. Brisset [a], P. Raynal [a], A. El Kassmi [a], F. Fages [a]

[a] *Laboratoire des Matériaux Moléculaires et des Biomatériaux, GCOM2 UMR CNRS 6114, Université de la Méditerranée, Faculté des Sciences de Luminy, Case 901, 13288 Marseille Cedex 9, France*
[b] *Graduate School of Engineering, Iwate University, 4-3-5 Ueda, Morioka, 020-8551, Japan*

Received 4 April 2006; received in revised form 14 June 2006; accepted 18 June 2006
Available online 20 July 2006

Abstract

A series of linear oligomers combining thiophene, phenyl and vinyl units were designed and synthesized to investigate the influence of the number and sequence of the π-conjugating groups on the stability and performance of organic thin-film transistors. The optical and electrochemical properties of oligomers in solution were investigated by UV–vis absorption and photoluminescence spectroscopies, and cyclic voltammetry. High vacuum evaporated thin films were investigated by optical absorption, X-ray diffraction and AFM, and implemented as p-type semiconducting layers into organic thin-film transistors (OTFTs). Furthermore, shelf-live tests (under ambient conditions) of the OTFTs based on the distyryl-substituted oligomer, **DS-2T**, show that the mobility was almost unchanged for 100 days, indicating a high environmental stability and the great importance of end-substitution to provide stability against air-oxidation.

PACS: 72.80.Le; 33.15.−e; 85.30.Tv; 06.30.Ft

Keywords: Organic semiconductors; Molecular structure; Field-effect transistors; Mobility; Stability

1. Introduction

In recent years much attention has been attracted by organic electronics. Organic thin-film transistors (OTFTs) are in particular a topic of intensive investigation [1]. The performance of OTFTs has been continually improving to the point of now being viable in integrated circuit applications [2]. Organic transistors will be one of the basic components of future electronic devices because of their advantages over conventional inorganic electronics, i.e., as example hydrogenated amorphous silicon thin-film transistors, such as low-cost, facile packaging, attractive appearance, reduced temperature of fabrication and compatibility with flexible substrates.

* Corresponding author. Tel.: +33 4 91 82 95 88; fax: +33 4 91 82 95 80.
E-mail address: videlot@luminy.univ-mrs.fr (C. Videlot-Ackermann).

1566-1199/$ - see front matter © 2006 Elsevier B.V. All rights reserved.
doi:10.1016/j.orgel.2006.06.005

Nevertheless for low-cost manufacturing, the processing needs to be carried out in ambient conditions, which requires the materials to be stable to ambient environmental effects (i.e., exposure to oxygen). Any precautionary methods to insulate devices from air would lead to increased cost, thus canceling the fundamental advantage of using organic materials as a low-cost alternative to their amorphous silicon counterparts. By consequence for the exploitation of OTFTs in commercial applications, it is of paramount importance that the active materials have sufficient air stability to achieve and maintain useful functional performance characteristics without protective encapsulation. Very recently, several groups reported significant enhancements of OTFTs stability under ambient conditions in the case of semiconducting small molecules [3], oligomers [4,5] and polymers [6]. Exceptional stability features were described for acene-thiophene semiconductors [4].

The oligothiophene skeleton is among the most versatile and effective molecular scaffold on which to base the rational design of organic semiconductors [7]. However oligothiophene derivatives are generally recognized to offer only poor air-stability and the fact is that their OTFTs show rapid performance degradation. In a previous work, we reported a new series of structurally simple and readily available oligothiophenes end-capped with styryl units, **DS-*n*T** ($n = 2, 3, 4$), that were used as the semiconducting layer in OTFTs [8]. The devices not only showed very high field-effect mobility (up to 0.1 cm^2/Vs) and on/off ratios (up to 10^5), but were also found to be exceptionally long-lived (more than one year of storage) and stable toward continuous operation, under atmospheric conditions. In the same conditions octithiophene 8T showed a decrease of about 70% of its initial mobility value after 100 days. To our knowledge, compound **DS-4T** is the first example of a long-chain oligothiophene derivative that allows to fabricate highly stable OTFTs with a life of more than 17 months. As yet, it remains unclear whether the unique behavior of the **DS-*n*T** ($n = 2, 3, 4$) compounds stems from the inherent electronic structure of the styryl group or its connection at the terminal oligomer positions. End-substitution has been shown to impart oligothiophene semiconductors with enhanced chemical stability [9]. In an attempt to answer this question, we decided to investigate analogous systems in which the regiochemical connectivity of phenyl, vinyl, and thiophene units is varied. To this end, oligomers **1** and **2** were synthesized (Fig. 1) and compared to **DS-2T** previously published [8,10,11]. We describe herein the optical and electrochemical properties of **1** and **2** in solution. High vacuum evaporated thin films were investigated by optical absorption, X-ray diffraction and AFM, and implemented as p-type semiconducting layers into OTFTs. The influence of substrate deposition temperature and substrate chemical treatment prior to organic deposition is described. Interestingly, comparable mobility values of $\sim$0.02 cm^2/Vs are obtained for both oligomers **2** and **DS-2 T** while only **DS-2T**-based OTFTs show high stability under ambient conditions.

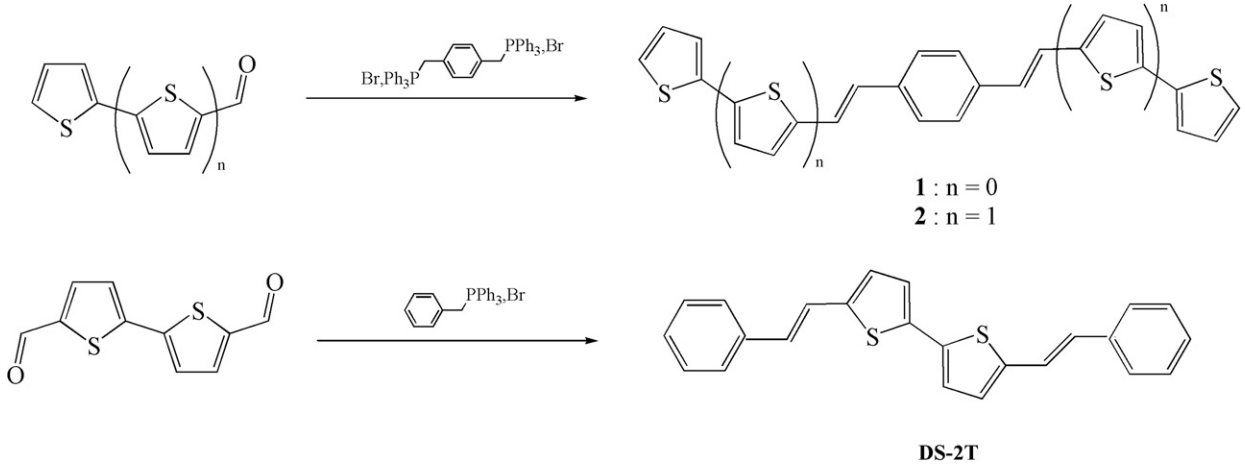

Fig. 1. Synthetic routes towards **1**, **2** and **DS-2T** oligomers.

2. Experimental details

2.1. Synthesis

Cyclohexane, methylenechloride, tetrahydrofurane (THF) were purchased from CarloErba. Tetrabutylamonium hexafluorophosphate ($TBAPF_6$) was purchased from Fluka. Benzylphosphonium bromide salt, *p*-xylylenebis(triphenylphosphoniumbromide), potassium *t*-butoxide and thiophene-2-carboxaldehyde were purchased from Aldrich. 2,2′-Bithienyl-5-carboxaldehyde and 5,5′-diformyl-2,2′ bithiophene were prepared according to literature [12]. Melting points are uncorrected and were obtained from an Electrothermal 9100 apparatus. ^{1}H NMR spectra were recorded on Bruker AC 250 at 250 MHz.

2.1.1. Typical procedure for the synthesis of 1 and 2

To a solution of thiophene-2-carboxaldehyde or 2,2′-bithiophene-5-carboxaldehyde (2.07 mmol) and *p*-xylylene-bis(phosphonium bromide) (0.9 mmol) in 60 mL of anhydrous tetrahydrofurane at 0 °C under argon, was added *t*-BuOK (4.14 mmol) portionwise. The mixture was stirred at room temperature for 10 h. After evaporation of the solvent, the crude product was dissolved in methylenechloride. The organic layer was washed with water, dried over $MgSO_4$, and evaporated to dryness. The product was purified on a silica gel column eluting with methylene chloride/cyclohexane (1:4 v/v).

2.1.2. E,E-1,4-bis(2-ethenylthienyl)-benzene (1)

Yield: 77%. Mp 267 °C; ^{1}H NMR (250 MHz, $CDCl_3$) δ: 6.93 (d, 2H, $J = 16.05$ Hz, $2 \times H_{ethylenic}$), 7.03 (dd, 2H, $J = 3.00$ Hz, $J = 3.25$ Hz, $2 \times H_{thioph}$), 7.09 (d, 2H, $J = 3.00$ Hz, $2 \times H_{thioph}$), 7.21 (d, 2H, $J = 3.75$ Hz, $2 \times H_{thioph}$), 7.27 (d, 2H, $J = 16.43$ Hz, $2 \times H_{ethylenic}$), 7.46 (s, 4H, H_{benz}). Elemental Analysis calcd for $C_{18}H_{14}S_2$: C, 73.43; H, 4.79; S, 21.78 Found: C, 72.71; H, 4.76; S, 22.53.

2.1.3. E,E-1,4-bis(5-ethenyl-2,2′-bithienyl)-benzene (2)

Yield: 67%. Mp 255 °C, ^{1}H NMR (250 MHz, $CDCl_3$) δ: 6.88 (d, 2H, $J = 15.75$ Hz, $2 \times H_{ethylenic}$), 6.98 (d, 2H, $J = 3.75$ Hz, $2 \times H_{thioph}$), 6.99 (dd, 2H, $J = 1.25$ Hz, $J = 3.50$ Hz, $2 \times H_{thioph}$), 7.08 (d, 2H, $J = 3.75$ Hz, $2 \times H_{thioph}$), 7.18 (dd, 2H, $J = 1.25$ Hz, $J = 3.75$ Hz, $2 \times H_{thioph}$), 7.30 (dd, 2H, $J = 1.25$ Hz, $J = 3.75$ Hz, $2 \times H_{thioph}$), 7.29 (d, 2H, $J = 16.00$ Hz, $2 \times H_{ethylenic}$), 7.46 (s, 4H, H_{benz}). Elemental Analysis calcd for $C_{26}H_{18}S_4 \cdot 0.5\ C_6H_{12}$: C, 69.56 H, 4.83; S, 25.61 Found: C, 69.32; H, 5.11; S, 25.56.

2.1.4. 5,5′-Distyryl-2,2′-bithiophene (DS-2T)

DS-2T was obtained according to a procedure similar to that described above for the synthesis of **1** and **2**, using benzyl(triphenylphosphonium bromide) (2 mmol) and 5,5′-diformyl-2,2′-bithiophene (0.9 mmol).

Yield: 79%. Mp 221 °C; ^{1}H NMR (250 MHz, $CDCl_3$) δ: 6.82 (d, 2H, $J = 16.11$ Hz, $2 \times H_{ethylenic}$), 6.89 (d, 2H, $J = 3.63$ Hz, $2 \times H_{thioph}$), 7.01 (d, 2H, $J = 3.63$ Hz, $2 \times H_{thioph}$), 7.11 (d, 2H, $J = 16.43$ Hz, $2 \times H_{ethylenic}$), 7.25-7.41 (m, 10H, H_{benz}). Elemental Analysis calcd for $C_{24}H_{18}S_2$: C, 77.80; H, 4.90; S, 17.31 Found: C, 77.84; H, 5.07; S, 17.81.

2.2. Solution measurements

UV–vis absorption and fluorescence emission spectra were obtained on a Varian Cary 1E spectrophotometer and a Varian Cary Eclipse spectrofluorimeter, respectively. Corrected emission spectra were obtained on diluted solution (CH_2Cl_2, conc. $<10^{-5}$ M) upon excitation at the absorption maximum wavelength. Cyclic voltammetry was performed using a BAS 100 Potentiostat (Bioanalytical Systems) operated with BAS 100W (v2.3) software. A three-electrode setup based on a Pt working electrode (diameter 1.6 mm), a Pt counter electrode, and an Ag/AgCl (filled with 3 M NaCl) were used. Tetrabutylammonium hexafluorophosphate ($TBAPF_6$) was used as received as electrolyte (0.1 M). All experiments were carried out in 1,2-dichlorobenzene at 20 °C. Ferrocene used as internal standard.

2.3. OTFTs fabrication

The "top contact" configuration (Fig. 2) was used for the OTFT devices based on **1**, **2** and **DS-2T**. Highly *n*-doped silicon wafers (gate), covered with thermally grown silicon oxide SiO_2 (3000 Å, insulator layer), were purchased from A.C.M (France) and used as device substrates. In order to change the surface property of the SiO_2 layer from hydrophilic to hydrophobic, SiO_2-covered substrates were treated with a solution of hexamethyldisilazane (HMDS). The capacitance per unit area of either untreated or HMDS-modified silicon dioxide dielectric layers was $1.2–1.3 \times 10^{-8}$ F/cm^2. The semiconductor layer was then vacuum deposited onto the substrates, using an Edwards Auto 306

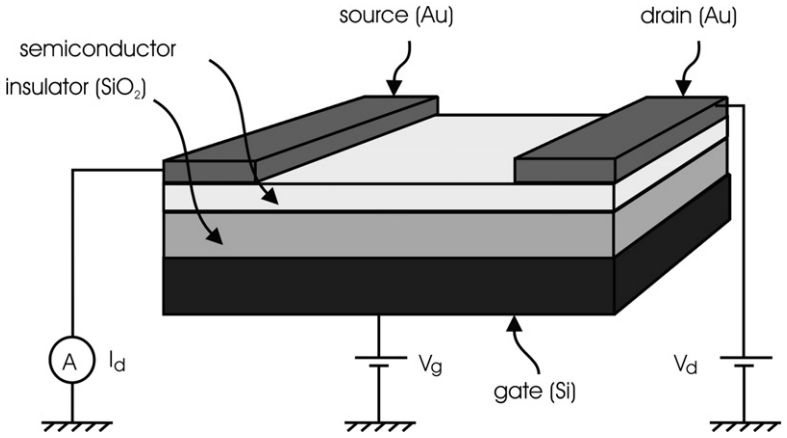

Fig. 2. Schematic "top contact" configuration used for OTFT measurements.

apparatus, at a rate of 4–7 nm/min under a pressure of $1–2 \times 10^{-6}$ mbar to a nominal thickness of 50 nm as determined with a in situ quartz crystal monitor. Substrate temperature (T_{sub}) during deposition was controlled by heating the block on which the substrates are mounted. The Au source and drain electrodes (channel length $L = 50$ μm, channel width $W = 1$ mm) were evaporated on top of the organic thin film through a shadow mask. Current–voltage characteristics were obtained at room temperature under ambient conditions with a Hewlett-Packard 4140B pico-amperemeter-DC voltage source. The source-drain current (I_D) in the saturation regime is governed by the equation:

$$(I_D)_{sat} = WC_i\mu/2L(V_G - V_t)^2 \quad (1)$$

where C_i is the capacitance per unit area of the gate insulator layer, V_G is the gate voltage, V_t is the threshold voltage, and μ is the field-effect mobility. The on/off ratio values given in Table 1 were determined from the current I_D at $V_G = -100$ V to the current I_D at $V_G = +100$ V under a constant drain-source voltage $V_D = -30$ V. All the data in Table 1 were obtained by randomly measuring 10 individual OTFTs for each substrate temperature.

2.4. Thin film measurements

UV–vis absorption spectra of thin films were obtained on a Varian Cary 1E spectrophotometer. Thin films were vacuum evaporated on glass substrate to a nominal thickness of 50 nm. Substrate temperature (T_{sub}) during deposition was the same as Si/SiO_2 substrates, i.e., $T_{sub} = 30$ °C or 80 °C. The optical absorption was measured under a normal incidence 0° (the normal of the substrate is parallel to incident light beam) and an oblique incidence 60° (an angle of 60° is induced between the normal of the substrate and the incident light beam). A dichroic ratio R is measured at absorption maxima by using $R = A_{60°}/A_{0°}$, $A_{60°}$ and $A_{0°}$ being the absorbance under an oblique incidence 60°

Table 1
Charge carrier mobility (μ), on/off ratio and threshold voltage (V_t) for OTFTs fabricated with semiconductors **2** and **DS-2T** at different substrate temperature on untreated and HMDS-treated silicon oxide substrates

Material	T_{sub} (°C)	Substrates	μ (cm^2/Vs)	On/off	V_t (V)
2	30	SiO_2/Si	$1–2 \times 10^{-2}$	$1.3–2 \times 10^5$	2.8–9.5
		HMDS-treated SiO_2/Si	$1–2 \times 10^{-2}$	$1.7–5.3 \times 10^5$	0–2.7
	80	SiO_2/Si	$1–2.1 \times 10^{-2}$	$5.2–8.2 \times 10^4$	9.2–33
		HMDS-treated SiO_2/Si	$1–2.3 \times 10^{-2}$	$1–3.2 \times 10^4$	8.3–10
DS-2T[a]	30	SiO_2/Si	$2–6 \times 10^{-3}$	$1.6–1.9 \times 10^5$	4–8
		HMDS-treated SiO_2/Si	$3–9 \times 10^{-3}$	$1.5–3.3 \times 10^5$	(−2)–(−7)
	80	SiO_2/Si	$1–2 \times 10^{-2}$	$2–2.3 \times 10^5$	0–19
		HMDS-treated SiO_2/Si	$1–2 \times 10^{-2}$	$2.1–2.8 \times 10^5$	(−1.2)–(−4)

[a] Results from [8].

and a normal incidence 0°. A dichroic ratio of 1 indicates an isotropic arrangement of molecules with no preferential orientation of molecules on the substrate. If $R > 1$, a preferential orientation occurs during the thin film formation with an upright orientation of the molecules due to their linear shape. Such optical analyses give a preliminary tendency of the molecular orientation in thin films which is confirmed by further measurement as AFM measurements. Atomic force microscopy (AFM) measurements were done on thin films in air with a Nanoscope III Multimode (Instrument, Inc.), operating in the tapping mode.

2.5. X-ray diffraction

Thin films of **2** and **DS-2T** were fabricated by vacuum deposition in a pressure of 5×10^{-5} Pa using K-cell type crucible. Si wafer (covered by SiO_2 layer 300 nm thick) was used as substrates which were kept at room temperature. The deposition rate and final film thickness were 0.1 nm/s and 100 nm, respectively. The as-deposited thin films were characterized using X-ray diffraction in air using an X-ray diffractometer (Regaku Co., ATX-G) which was specially designed for characterization of thin films. A parabolic multiplayer positioned next to the laboratory X-ray source produces high intensity parallel beam (Cu Kα) using a HOPG analyzer. The goniometer has not only usual $\omega/2\theta$ axes but also in-plane $\phi/2\theta\chi$ axes for measuring both in-plane and out of plane diffraction. The details of the diffractometer and characterization method were described elsewhere [13].

3. Results and discussion

3.1. Molecular characterization

The electronic absorption spectra of **1, 2** and **DS-2T** in methylenechloride solution are given in Fig. 3. Although they display a broad vibronic structure as a result of rotational disorder, they appear more structured than those of parent oligothiophenes, which can be due to a more planar geometry around the ethylenic bonds. The more resolved structure of the fluorescence emission spectrum of **DS-2T** is indicative of a more planar geometry in the excited relative to the ground state. The shorter oligomer **1** shows absorption and emission maxima in the near-UV region ($\lambda_{abs}/\lambda_{em}$ (nm): **1** 375/444) leading to a high optical band gap value of $E_g = 2.99$ eV. UV–

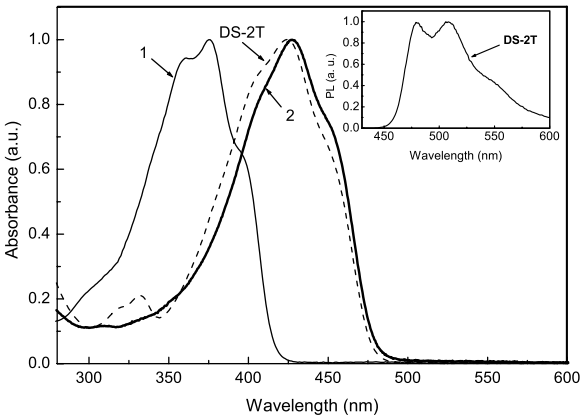

Fig. 3. Optical absorption of **1** (fine line), **2** (thick line) and **DS-2T** (dashed line) in CH_2Cl_2. Inset: Optical emission of **DS-2T** in CH_2Cl_2.

vis/fluoresence data point to comparable electron conjugation pathway in both compounds, **2** and **DS-2T**, as indicated by the similar values of the absorption and emission maxima ($\lambda_{abs}/\lambda_{em}$ (nm): **2** 427/484; **DS-2T** 425/477). Furthermore electron conjugation pathways are more extended within **2** and **DS-2T** relative to parent oligothiophenes, such as **4 T** ($\lambda_{abs}/\lambda_{em}$ (nm) = 393/451 nm) leading to significantly reduced optical band gap values (E_g (eV): **2** 2.55; **DS-2T** 2.60; **4T** 2.80). Cyclic voltammetry (CV) measurement of **1** and **2** shows an irreversible and a quasi-reversible oxidation waves peeking at 1.17 and 1.00 V *vs* Ag/AgCl, respectively. The negative shift of oxidation potential for **2** as compared to **1** correlates with the bathochromic shift of the optical absorption maxima and reflects the increase of the number of thiophene rings as classically described for thiophene oligomers [7]. The application of recurrent potential scans to **1** and **2** leads to the emergence of a new redox system with the oxidation and reduction waves corresponding to the doping/undoping process of the growing polymer at the surface electrode (Fig. 4). The CV curves of corresponding polymers were similar with an oxidation potential peak at 1.01 and 1.10 V *vs* Ag/AgCl for poly(**1**) and poly(**2**), respectively. For comparison, the CV of **DS-2T** was shown to display a reversible one-electron oxidation wave corresponding to the formation of the cation radical at $E_{1/2} = 0.96$ V *vs* Ag/AgCl at a less positive potential than that recorded for **4T** ($E_{1/2} = 1.18$ V) [8]. According to CV data, distyryl end groups provide stabilization against polymerization and oxidation. The HOMO and LUMO energy levels of **DS-2T**

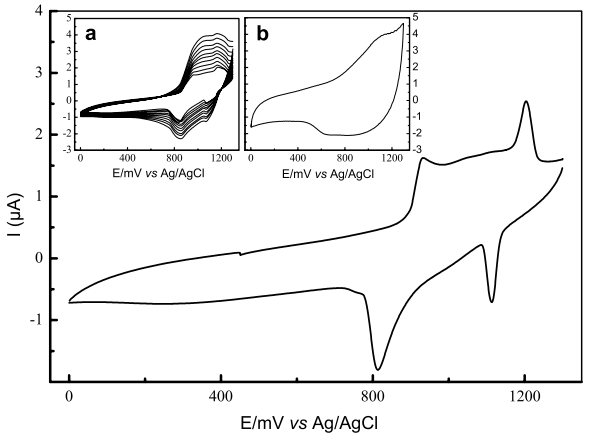

Fig. 4. Cyclic voltammogram of **2** at 1×10^{-3} in 0.1 M $TBAPF_6$/1,2-dichlorobenzene. Inset : (a) Electropolymerization in potentiodynamic condition at $v = 100$ mV/s and (b) cyclic voltammogram of poly(**2**) in 0.1 M $TBAPF_6/CH_3CN$ at $v = 100$ mV/s.

were estimated at −5.32 eV and −2.72 eV, respectively, on using electrochemical and absorption data [14].

Optical absorption spectra of **1**, **2** and **DS-2T** 50 nm-thick films are shown on Fig. 5. The absorption spectra exhibit peaks at high energy (200–280 nm) as found for all oligothiophenes and originate from the aromatic groups (thiophene and arene) [7]. The shorter oligomer **1** presents a broad absorption band (Inset of Fig. 5a) in the 280–700 nm range with peak maximum at 310 nm and a low energy shoulder at 437 nm. The shape of the $\pi \rightarrow \pi^*$ transition indicates a poor conjugated length together with an unless solid state packing in **1**-based thin films. As a contrary, spectra of **2** and **DS-2T** show almost identical features with narrow and intense maximum peaks together with fine structures at lower energy. Small ipsochromic shifts are observed for **DS-2T** (λ_{abs} (nm): **2** 278/339/438/474/510; **DS-2T** 256/331/433/463/498) with any drastic change in the shape of the $\pi \rightarrow \pi^*$ transition revealing ground state of **2** and **DS-2T** not being influence by the sequence of bithiophene and phenyl groups in the oligomer core. Furthermore the existence of organized thin films can be demonstrated by measuring the UV–vis absorption under different incidence angles [15]. In Fig. 5a and b optical absorption spectra under 0° and 60° of **2** and **DS-2T**-based thin films vacuum deposited on glass substrate at $T_{sub} = 80$ °C are shown, respectively. A dichroic ratio of ~2 and ~5 was obtained at 339 nm and 331 nm for **2** and **DS-2T**-based thin films, respectively. For **2** and **DS-2T**-based thin

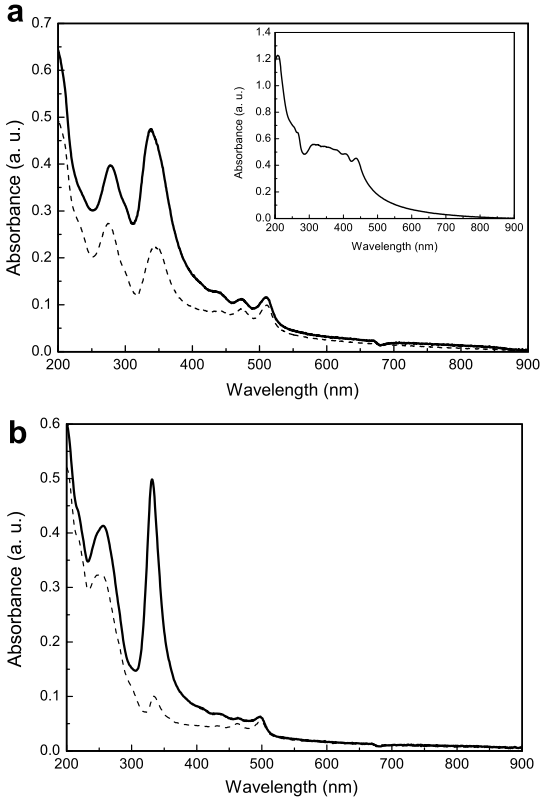

Fig. 5. Optical absorption of 50 nm-thick films fabricated at $T_{sub} = 80$ °C based on **2** (a) and **DS-2T** (b) under oblique (thick line) and normal (dashed line) incidence. Inset: Optical absorption of **1** as 50 nm-thick film fabricated at $T_{sub} = 30$ °C.

films deposited at $T_{sub} = 30$ °C lower dichroic ratio of ~1.5 and ~3 were obtained, respectively, revealing less order in films by decreasing the substrate temperature. The higher intensity arising under an oblique incidence 60° indicating that the molecules are preferentially oriented perpendicular to the substrate with a higher degree of ordering on heated substrates.

3.2. Thin film morphology

Film microstructure and morphology of vapor deposited thin films of **2** and **DS-2T** grown on SiO_2/Si were investigated by XRD and AFM. θ-2θ X-ray diffraction spectra of **2** and **DS-2T**-based thin films vacuum deposited at 30 °C with a nominal thickness of 100 nm reveal that both films are characterized by a high degree of texture (Fig. 6). Sharp and strong reflections up to the nineth order for **2** confirm the high degree of lamellar ordering even at low deposition temperature. Thin films are con-

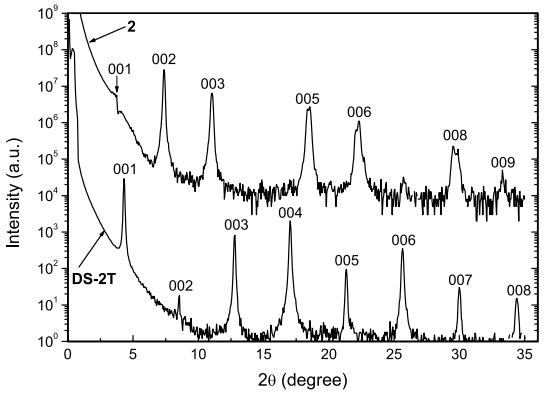

Fig. 6. X-ray diffraction pattern of $\theta/2\theta$ scan of **2** (top curve) and **DS-2T** (bottom curve) films deposited onto SiO_2/Si substrates at $T_{sub} = 30$ °C.

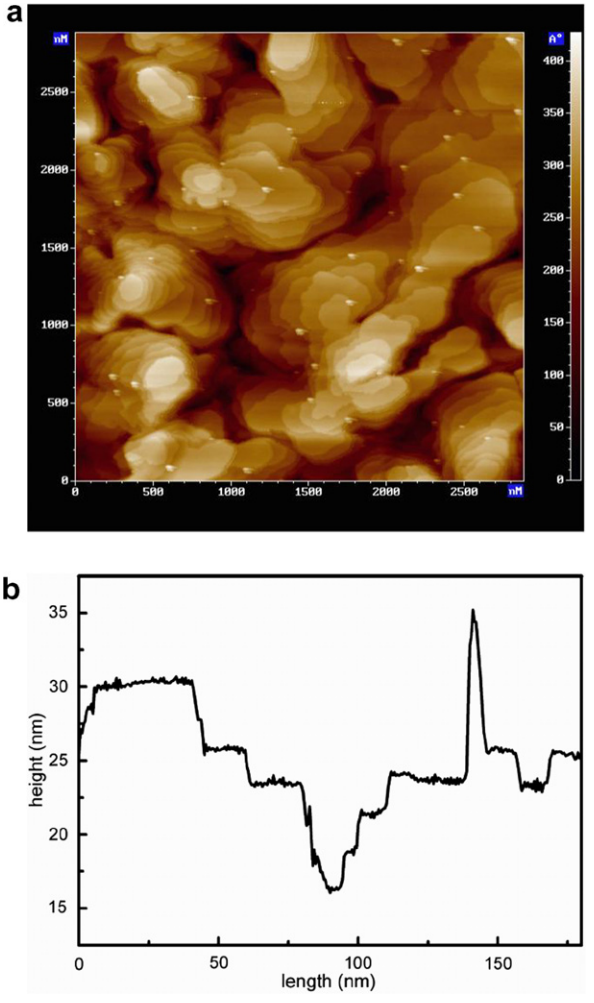

Fig. 7. AFM image, scale = 2.9 μm × 2.9 μm (a) and corresponding profile (b) of a thin film based on **2** vacuum evaporated on SiO_2/Si at $T_{sub} = 80$ °C.

sidered by highly oriented poly-crystals having an interplanar *d*-spacing of 2.38 and 2.07 nm for **2** and **DS-2T**, respectively. AFM pictures show the formation of islands whose size increases with the substrate deposition temperature. At $T_{sub} = 80$ °C, a terrace-and-step morphology is clearly observed for **2** (Fig. 7a), an average value of 2.3–2.4 nm being determined for the steps height which corresponds to the molecular length (Fig. 7b). In the case of **DS-2T**, an island growth with the formation of terraces is observed by AFM. Such rod-like molecules are mainly oriented with their long molecular axes parallel to the substrate normal as already observed in the **DS-*n*T** series [8]. Consequently, the molecular orientation in **2** and **DS-2T**-based thin films is favorable for efficient charge transport across the SiO_2-semiconductor interface.

3.3. Thin-film transistors and characterization measurements

OTFT devices were fabricated using the top contact geometry (Fig. 2). Transistor responses were obtained only for negative bias, which is indicative that compounds are p-type semiconductors (Fig. 8a). The devices work in the accumulation mode with the presence of a well-defined linear regime at $V_D < V_G$ followed by a saturation regime at $V_D > V_G$. Fig. 8b shows the plot of the square of $I_{D,sat}$ taken at $V_D = -100$ V (saturation regime), as a function of V_G. A mobility of 0.015 cm^2/Vs and a threshold voltage of 19 V are obtained from linear fitting in Fig. 8b and using Eq. (1). The field-effect mobilities are shown to increase with the substrate deposition temperature as due to the formation of better ordered thin films at elevated T_{sub} (Table 1). The highest value of the hole mobility (0.023 cm^2/Vs) was obtained for **2** at 80 °C on HMDS-treated SiO_2/Si. HMDS treatment was observed to improve the mobility and on/off ratio together with a decrease of the threshold voltage V_t relative to unmodified samples, in agreement with previous reports [16]. For the shorter oligomer **1** a low mobility up to 1.6×10^{-7} cm^2/Vs at $T_{sub} = 30$ °C on polymethyl-methacrylate (PMMA) as insulator layer was obtained in agreement with the unless electron conjugation pathway already observed by cyclic voltammetry measurement and optical absorption. In the same conditions, OTFTs based on **2** gave rise to mobility values up to $6–7 \times 10^{-3}$ cm^2/Vs [10] which are comparable with values at $T_{sub} = 30$ °C in Table 1.

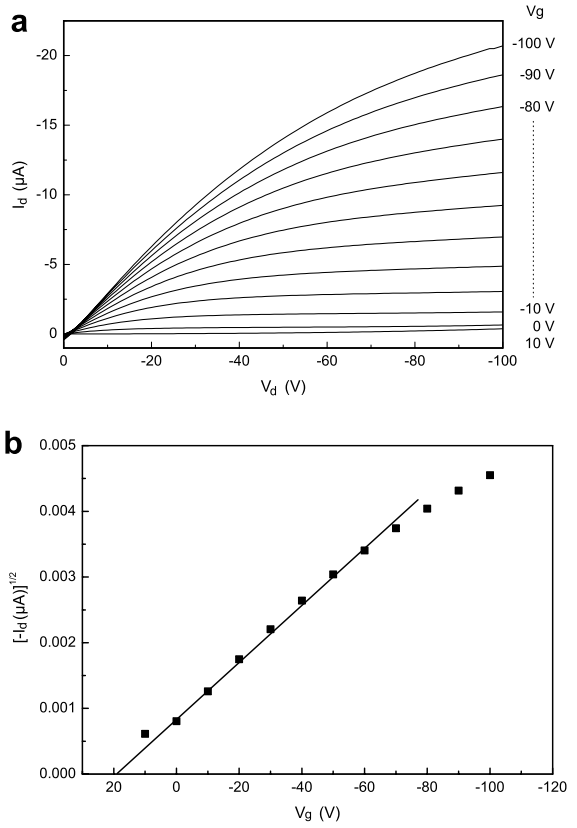

Fig. 8. (a) Plot of I_D vs V_D at various gate voltages V_G and (b) transfer characteristic, $[-I_D]^{1/2}$ vs V_D at $V_D = -100$ V, for a **DS-2T**-based OTFT device fabricated at $T_{sub} = 80$ °C on untreated SiO_2/Si.

OTFT devices based on **2** and **DS-2T** were stored over 100 days in the dark under ambient conditions and device performances were measured periodically. Fig. 9 illustrates the stability of the hole mobility values obtained for **DS-2T**-based films deposited at two temperatures onto unmodified SiO_2/Si substrates. In contrast, the mobility value determined under the same conditions for **2** showed a decrease of about 92% of its initial values after 100 days either at $T_{sub} = 30$ °C or at $T_{sub} = 80$ °C. Any p-doping process over time for **2** and **DS-2T** can be ruled out at this stage as no change, and especially no decrease, of the on/off ratio was noticed upon storage. **2** and **DS-2T** have relatively comparable optical band gaps and oxidation potential in solution leading to the same potential degradation of OTFTs by air-oxidation according to previous observations [4,5]. By consequence such decreases over time of mobility values observed for **2**-based OTFTs compare to **DS-2T** suggest that the molecular design and engineering to reach high performing

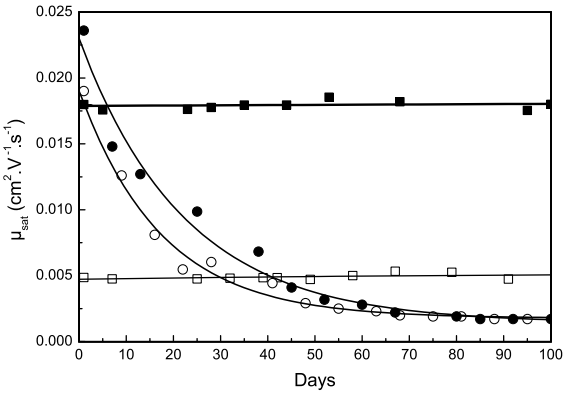

Fig. 9. Plots of hole mobilities (μ) vs storage days for OTFTs fabricated at different substrate temperatures on untreated SiO_2/Si with active layers based on: **2** at $T_{sub} = 30$ °C (open circle) and $T_{sub} = 80$ °C (full circle); **DS-2T** at $T_{sub} = 30$ °C (open square) and $T_{sub} = 80$ °C (full square).

OTFTs and long-time stability are essential criteria. Additionally in the series of α,ω-distyryl-oligothiophenes [8], the longest oligomer **DS-4T** showed the highest stability along with the best electrical characteristics and the lower oxidation potential in contrast as previous observation where compounds with low band gaps and high energy HOMO levels tend to be easily oxidized and cause degradation of the resulting devices [5a]. Furthermore, OTFTs devices based on octithiophene 8T [8] measured in the same conditions as **DS-4T**-based OTFTs were not stable over 17 months confirming the great importance of the molecular structure on OTFT stability. The present end-encapsulation of the semiconducting oligomers by distyryl groups decreases considerably the degradation by air-oxidation of the organic thin film in OTFTs. Therefore, styryl end-substitutions of oligothiophenes are properly designed end-cap substituents and offer further incorporation of solubilizing or self-assembling groups on the versatile termini benzene moieties [17].

4. Conclusion

The stability of organic electronics devices, i.e., the resistance to any atmosphere influences is a crucial point to avoid an expensive encapsulation which would render such devices non-viable for all low-cost high-volume applications. Molecular design and engineering can open the way to the syntheses of air-stable molecules. We have developed a simple

chemical synthesis to end-capped the semiconductors by less oxidable aromatic groups as styryl ones. The distyryl-end substitutions on bithiophene permits to reach high mobility values together with an air-stability over 100 days. By consequence, distyryl-oligothiophenes represent a novel class of OTFT semiconductors that combine good electrical performances and exceptional stabilities. The synthesis of soluble and n-type analogous derivatives is currently underway for applications in flexible electronics.

References

[1] (a) For a recent account on organic electronics, see the special issue of Chemistry of Materials: Chem. Mater. 16 (23) (2004);
(b) C.D. Dimitrakopoulos, P.R.L. Malefant, Adv. Mater. 14 (2002) 99.

[2] (a) H. Sirringhaus, N. Tessler, R.H. Friend, Sciences 280 (1998) 1741;
(b) H. Sirringhaus, N. Tessler, R.H. Friend, Synthetic Metals 102 (1999) 857;
(c) C.D. Sheraw, L. Zhou, J.R. Huang, D.J. Gundlach, T.N. Jackson, M.G. Kane, I.G. Hill, M.S. Hammond, J. Campi, B.K. Greening, J. Francl, J. West, Appl. Phys. Lett. 80 (2002) 1088;
(d) W. Fix, A. Ullmann, J. Ficker, W. Clemens, Appl. Phys. Lett. 81 (2002) 1735.

[3] B.A. Jones, M.J. Ahrens, M.-H. Yoon, A. Facchetti, T.J. Marks, M.R. Wasielewski, Angew. Chem. Int. Ed. 43 (2004) 6363.

[4] (a) H. Meng, F. Sun, M.B. Goldfinger, G.D. Jaycox, Z. Li, W.J. Marshall, G.S. Blackman, J. Am. Chem. Soc. 127 (2005) 2406;
(b) J.A. Merlo, C.R. Newman, C.P. Gerlach, T.W. Kelley, D.V. Muyres, S.E. Fritz, M.F. Toney, C.D. Frisbie, J. Am. Chem. Soc. 127 (2005) 3997.

[5] (a) H. Meng, Z. Bao, A.J. Lovinger, B.-C. Wang, A.M. Mujsce, J. Am. Chem. Soc. 123 (2001) 9214;
(b) H. Meng, J. Zheng, A.J. Lovinger, B.-C. Wang, P. Gregory Van Patten, Z. Bao, Chem. Matter. 15 (2003) 1778.

[6] M. Heeney, C. Bailey, K. Genevicius, M. Shkunov, D. Sparrowe, S. Tierney, I. McCulloch, J. Am. Chem. Soc. 127 (2005) 1078.

[7] D. Fichou (Ed.), Handbook of Oligo- and Poly-thiophenes, Wiley-VCH, Weinheim, 1999.

[8] C. Videlot-Ackermann, J. Ackermann, H. Brisset, K. Kawamura, N. Yoshimoto, P. Raynal, A. El Kassmi, F. Fages, J. Am. Chem. Soc. 127 (2005) 16346.

[9] S. Mohapatra, B.T. Holmes, C.R. Newman, C.F. Prendergast, C.D. Frisbie, M.D. Ward, Adv. Funct. Mater. 14 (2004) 605.

[10] C. Videlot, J. Ackermann, A. El Kassmi, P. Raynal, Thin Solid Films 403–404 (2002) 380.

[11] In the previous work [10] reported in 2002 an error occurred. While the molecular structure and the synthesis of 2 was reported, the experimental data reported in solution (absorption spectrum and oxidation potential) corresponded to compound 1.

[12] Y. Wei, B. Wang, W. Wang, J. Tian, Tetrahedron Lett. 36 (1995) 665.

[13] N. Yoshimoto, T. Sato, K. Ogawa, K. Omote, M. Yoshizawa, Mol. Cryst. Liq. Cryst. 377 (2002) 381.

[14] (a) $E_{1/2}$ (**DS-2T**) = 0.48 V *vs* Fc^{+}/Fc;
(b) M. Kawamoto, H. Mochizuki, A. Shishido, O. Tsutsumi, T. Ikeda, B. Lee, Y. Shirota, J. Phys. Chem. B (2003) 4887;
(c) A. Miura, Z. Chen, H. Uji-I, S. De Feyter, M. Zdanowska, P. Jonkheijm, A.P.H.J. Schenning, E.W. Meijer, F. Würthner, F.C. De Schryver, J. Am. Chem. Soc. 125 (2003) 14968.

[15] (a) C. Videlot, A. El Kassmi, D. Fichou, Solar Energy Materials and Solar Cells 63 (2000) 69;
(b) C. Videlot, V. Grayer, J. Ackermann, A. El Kassmi, D. Fichou, G. Hadziioannou, Synthetic Metals 139 (2003) 115;
(c) J. Ackermann, C. Videlot, P. Dumas, A. El Kassmi, R. Guglielmetti, V. Safarov, Organic Electronics 5 (2004) 213.

[16] T.C. Gojanc, I. Lévesque, M. D'Iorio, Appl. Phys. Lett. 84 (2004) 930.

[17] B.-K. An, D.-S. Lee, J.-S. Lee, Y.-S. Park, H.-S. Song, S.Y. Park, J. Am. Chem. Soc. 126 (2004) 10232.

Available online at www.sciencedirect.com
ScienceDirect
Organic Electronics 7 (2006) 474–479
Organic Electronics
www.elsevier.com/locate/orgel

PEDOT:PSS polymeric conducting anode for admittance spectroscopy

S.W. Tsang, S.C. Tse, K.L. Tong, S.K. So *

Department of Physics and Centre for Advanced Luminescence Materials, Hong Kong Baptist University, Kowloon Tong, Hong Kong, China

Received 4 March 2006; received in revised form 21 June 2006; accepted 22 June 2006
Available online 20 July 2006

Abstract

The carrier mobilities of two hole transporting organic materials were evaluated by admittance spectroscopy (AS). The materials were 4,4′,4″-tris{*N*,-(3-methylphenyl)-*N*-phenylamino}triphenylamine (*m*-MTDATA) and *N*,*N*′-diphenyl-*N*,*N*′-bis(1,1′-biphenyl)-4,4′-diamine (NPB). They were sandwiched in a configuration of anode/organic material/cathode. The anode was either indium-tin-oxide (ITO) or poly(3,4-ethylenedioxythiophene) doped with polystrenesulphonic acid (PEDOT:PSS). It is shown that PEDOT:PSS can, respectively, form Ohmic and quasi-Ohmic contact with *m*-MTDATA and NPB. Using PEDOT:PSS as the anode, the average hole mobilities of *m*-MTDATA and NPB were extracted by AS through susceptance analysis. The results are in excellent agreement with those obtained by an independent time-of-flight (TOF) technique. With PEDOT:PSS, the application of AS for characterizing carrier mobilities can be extended to hole transporting organic materials with highest occupied molecular orbital (HOMO) energy levels down to 5.4 eV.

PACS: 73.61.Ph

Keywords: Carrier transport; Injection; Admittance spectroscopy; Carrier mobility; Susceptance; Ohmic contact; PEDOT

1. Introduction

Current driven organic electronic devices, e.g., organic light emitting diodes (OLEDs), organic solar cells, and organic field-effect transistors, are gaining increasing status. The performances of these devices depend greatly on both the injection of charge carriers and their transport properties inside organic electronic materials. There are different experimental techniques for characterizing charge transport properties. Among them, optical time-of-flight (TOF) technique is, perhaps, the most well-known [1]. However, in TOF, due to the finite photon penetration depth (typically 0.1–0.3 μm) of the excitation laser, the sample thickness should exceed 1 μm. For emerging charge transporters, they are usually available in small quantities for evaluation, often because the route for high yield synthesis is being optimized. Thus TOF appears not to be a practical method for mobility evaluation in these cases. There is a clear need to look for an alternative.

An emerging technique, known as admittance spectroscopy (AS), has been shown to be very useful

* Corresponding author.
E-mail address: skso@hkbu.edu.hk (S.K. So).

1566-1199/$ - see front matter
doi:10.1016/j.orgel.2006.06.002

for carrier mobility evaluation [2–4]. Compared to TOF, AS imposes no specific requirements for the sample thickness. Furthermore, AS offers simpler experimental setup. For organic materials, AS based on small signal space-charge-limited current (SCLC) theory has been used to measure carrier mobilities. For a device with a structure of anode/organic material/cathode, with an Ohmic hole contact in the anode and an electron blocking cathode, one can subject the sample to the sum of a dc voltage V_{dc} and a small ac excitation v_{ac} with a frequency f. If organic material is trap-free, with a dielectric constant ε, then the complex admittance $Y(\Omega)$ can be written in the form [4]:

$$Y(\Omega)=\frac{\varepsilon A}{\tau_{dc}d}\left\{\frac{\Omega^3}{2i[0.75\tilde{\mu}(\Omega)]^2\left[1-\exp\left(\frac{-i4\Omega}{3\tilde{\mu}(\Omega)}\right)\right]+1.5\tilde{\mu}(\Omega)\Omega-i\Omega^2}\right\} \quad (1)$$

where d and A are the thickness and the area, of the sample, respectively. In Eq. (1) above, $i^2=-1$. τ_{dc} is the average hole transit time in the absence of the ac signal, and $\Omega=2\pi f\tau_{dc}=\omega\tau_{dc}$. The normalized mobility is defined as $\tilde{\mu}(\Omega)=\mu(\Omega)/\mu_{dc}$ where $\mu_{dc}=d^2/(V_{dc}\tau_{dc})$ is the *dc* hole mobility in the absence of the ac field. Eq. (1) can be derived by applying Poisson's and the current continuity equations to the organic material in the configuration of anode/organic material/cathode. For Eq. (1) to be applicable to describe hole transport dynamics, the sample must satisfy the following conditions: (i) the anode/organic contact must be Ohmic, (ii) the organic/cathode contact must be electron-blocking, and (iii) the material should be trap-free. When conditions (i)–(iii) are fulfilled, the current response j_{ac} of the material to v_{ac} is a measure of the charge dynamics at different frequencies. They are related to the device capacitance C by $C=\frac{|j_{ac}|}{\omega|v_{ac}|}\sin\theta$ where θ is the phase difference between j_{ac} and v_{ac}. At high frequencies, $\theta=\pi/2$. The measured capacitance is only contributed by the dipole charges and is equal to its geometric value $C_{geo}=\varepsilon_r\varepsilon_o A/d$. At lower frequency ($f\sim\tau_{dc}^{-1}$), the device capacitance is changed because j_{ac} is contributed by the responses of the dipole charges as well as the injected free carriers. Due to the resistive behavior of the injected carriers, the overall phase difference is reduced, and $\theta<\pi/2$. So, the device capacitance is reduced. The reduction of capacitance in frequency domain provides a means to evaluate the carrier mobility of an organic electronic material.

To extract the carrier mobility, one can analyze the imaginary part of the admittance in Eq. (1), i.e., the susceptance in the frequency domain [4–6]. Specifically, the negative differential susceptance of the device can be defined as $-\Delta B\equiv-2\pi f(C-C_{geo})$. By plotting $-\Delta B$ vs f, a maximum at a characteristic frequency $f=\tau_r^{-1}$ can be observed. From Eq. (1) and computer simulations, the average carrier transit time τ_{dc} is found to be related to τ_r by [4]:

$$\tau_{dc}=0.56\tau_r \quad (2)$$

From the known thickness of the organic layer d, and the electric field E, the carrier mobility $\mu_{dc}=d/(\tau_{dc}\cdot E)$ can be extracted.

In previous demonstrations, only hole transporting organic materials (polymeric PPV derivatives [1,3,5] and small molecular *m*-MTDATA [4]) with relatively small highest occupied molecular orbital (HOMO) energy levels (~5.1 eV) were reported. However, many hole transporting materials, especially those for OLED applications, have HOMO energy levels substantially larger than 5 eV. Thus, there is a clear need to investigate if AS is applicable to materials with larger HOMOs. We report below AS measurements of two phenylamine compounds: (a) *m*-MTDATA, and (b) NPB using PEDOT:PSS as the hole injecting anode. The later material, NPB, has a relative large HOMO value of ~5.4 eV. We found that when PEDOT:PSS is used as the anode, the hole mobilities extracted by AS are in excellent agreement with those from independent TOF measurements. The effect of film thickness to AS measurement will also be discussed.

2. Experimental

Hole-only devices with a general structure of anode/organic layer/cathode were prepared for this study. The small molecular *m*-MTDATA and NPB were purchased from Syntec. GmbH and E-Ray, respectively. They were used without further purification. The chemical structures are shown in the insets of Fig. 1. The thicknesses of the organic films were measured by a profilometer (Tencor Alphastep 500). For some devices, pre-patterned ITO on glass was used as the anode. For other devices, a 50 nm PEDOT:PSS (BAYRON® P VP AL 4083, H.C. Starck GmbH) was spin-coated on ITO substrate to act as the anode. The PEDOT:PSS layer was subsequently heated in air at 150 °C for 30 min before organic deposition. In all cases, the

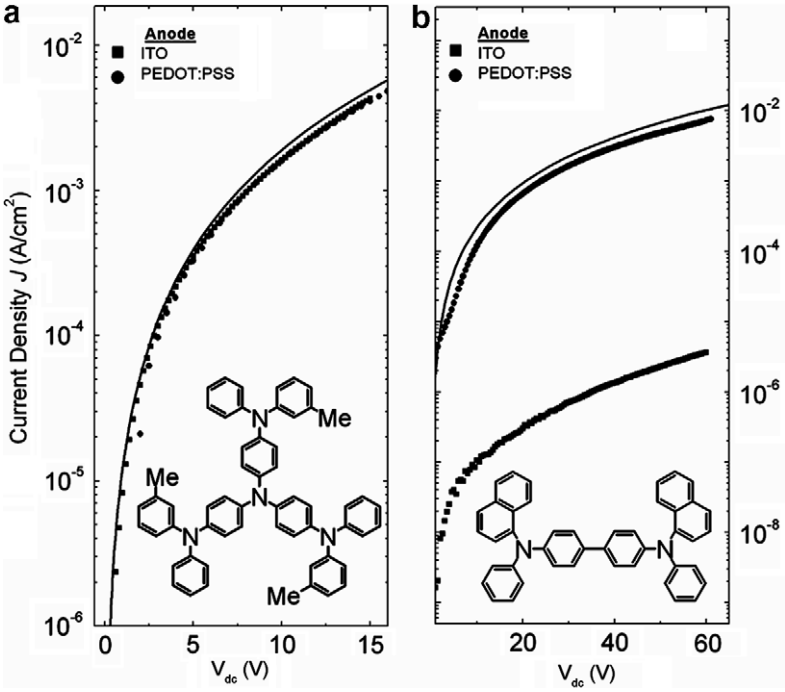

Fig. 1. *J–V* characteristics of (a) *m*-MTDATA (735 nm) and (b) NPB (3.70 μm) devices with different anodes. The symbols are experimental data. The solid lines are computed from the TFSCLC theory in Eq. (3). The chemical structures of *m*-MTDATA and NPB are shown in the insets of (a) and (b), respectively.

ITO substrate was cleaned by a sequence of ultrasonic baths and uv-ozone (UVO) treatment.

Details of TOF measurements have been reported elsewhere [7]. For the current–voltage and admittance measurements, ITO or PEDOT:PSS on ITO was used as the anode. The organic layer, *m*-MTDATA (735 nm) or NPB (3.70 μm), was coated on the anode by thermal evaporation. For all the devices, silver (Ag) was evaporated to form the cathode contact. The active area of the device was about 0.036 cm^2. The Ag cathode also acts as an electron blocking contact. Since there is a significant energy difference between the lowest unoccupied molecular orbital (LUMO) of the organic materials (2.0 eV for *m*-MTDATA and 2.5 eV for NPB) and the work function of Ag (4.3 eV), few electrons can be injected from the cathode. On the other hand, the energy barriers for hole injection at the ITO/*m*-MTDATA and PEDOT:PSS/NPB interfaces are much smaller (<0.3 eV). Therefore the overall current is dominated by the hole current. The admittances of the devices were measured by an impedance analyzer (GenRad 1639 RLC Digitbridge™) as a function of frequency. The achieve this, an ac modulation of amplitude 50 mV ($f = 10^2$–10^5 Hz) was superimposed on a dc bias voltage (0–30 V). Current–voltage measurement (*JV*) was carried out with a source-measure-unit (KEITHLEY 236). All the measurements (*J–V*, AS and TOF) were performed at 289 K inside a cryostat (Oxford) under a vacuum level better than 10^{-3} Torr.

3. Results and discussion

Fig. 1 shows the measured *J–V* characteristics (filled symbols) of hole-only organic devices with a structure of anode/organic layer/Ag. The solid lines are the calculated *J–V* characteristics from trap-free space-charge-limited current (TFSCLC) theory with field dependent carrier mobility [8]:

$$J_{\mathrm{TFSCLC}} = \frac{9}{8}\varepsilon_r\varepsilon_0\mu_0 \exp(0.89\beta\sqrt{E})\frac{V^2}{d^3} \qquad (3)$$

where $\varepsilon_r = 3$ is the relative permittivity of the organic materials, ε_0 is the absolute permittivity, E is the applied electric field, $V(=E \cdot d)$ is the applied voltage, and d is the thickness of the organic film. β and μ_0 are, respectively, the field dependent coefficient and the zero field mobility. Both parameters are

obtained independently from TOF technique. For *m*-MTDATA devices, Fig. 1(a), the experimental data for both types of anodes match very well with Eq. (3). As reported previously [4,9] and shown in this study, ITO forms an Ohmic contact with *m*-MTDATA and the conduction is limited by the bulk organic film which follows TFSCLC. Obviously, using PEDOT:PSS as the anode that has higher work function cannot further increase the current density. As a result, the *J–V* characteristics of both devices coincide with each other. On the other hand, for NPB devices [Fig. 1(b)], the device with a PEDOT:PSS anode has a current density about three orders of magnitude higher than the device with an ITO anode. The results clearly indicate that the ITO/NPB device is injection-limited and deviates substantially from TFSCLC. On the other hand, the *J–V* characteristics of PEDOT:PSS/NPB device is very close to the theoretical TFSCLC in Fig. 1(b), signifying the PEDOT:PSS/NPB contact is close to Ohmic.

Next, we demonstrate AS alone can be used to extract hole mobilities in MTDATA and NPB with an Ohmic or a quasi-Ohmic contact. Fig. 2 shows the frequency dependent capacitances of the same devices in *J–V* measurements. In order to give a fair comparison, the same voltage bias V_{dc} is used and the measured capacitance C is normalized by the geometrical capacitance $C_{geo} = \varepsilon_0\varepsilon_r A/d$. In the case of *m*-MTDATA devices, the general frequency dependent capacitances [Fig. 2(a)] are almost identical for both the ITO and the PEDOT:PSS anode. The normalized capacitances C/C_{geo} go through a minimum at an intermediate frequency; at high frequencies, the capacitances reach their geometrical values. In NPB devices as shown in Fig. 2(b), there are drastic differences between the device with PEDOT:PSS anode and the one with ITO anode. A well-defined minimum can be observed in the capacitance only when PEDOT:PSS is used as the anode. This feature cannot be found in the device with an ITO anode. In the later case, the capacitance is practically bias independent for $f > 10^4$ Hz.

The extracted average hole mobilities μ_{dc} by AS are compared to those measured by TOF. As demonstrated in Refs. [4–6], the carrier mobility can be extracted by plotting $-\Delta B$ vs f and from Eq. (2). Fig. 3(a) and (b), respectively, show the $-\Delta B$ vs f plots of ITO/*m*-MTDATA/Ag and PEDOT:PSS/NPB/Ag devices. For each V_{dc}, there exists a maximum at a well-defined frequency f_r. This maximum shifts to higher frequency as V_{dc} increases. Therefore, the location of the relaxation peak $\tau_r^{-1} \equiv f_r$ for each V_{dc} can be clearly resolved. From Eq. (2), one can compute τ_{dc} and hence the average hole mobility from $\mu_{dc} = d/(\tau_{dc} \cdot E)$. The results are summarized in Fig. 4. The filled symbols are hole mobilities derived by AS. The open symbols are hole mobilities derived by TOF at $t_{1/2}$, the time that the current has dropped to half of its value in the

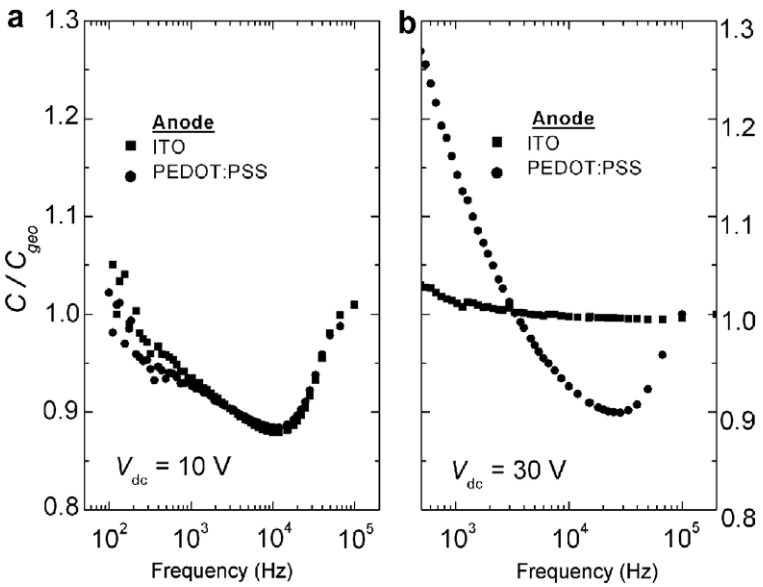

Fig. 2. Experimentally determined frequency dependent capacitances of (a) *m*-MTDATA (735 nm) and (b) NPB (3.70 μm) devices.

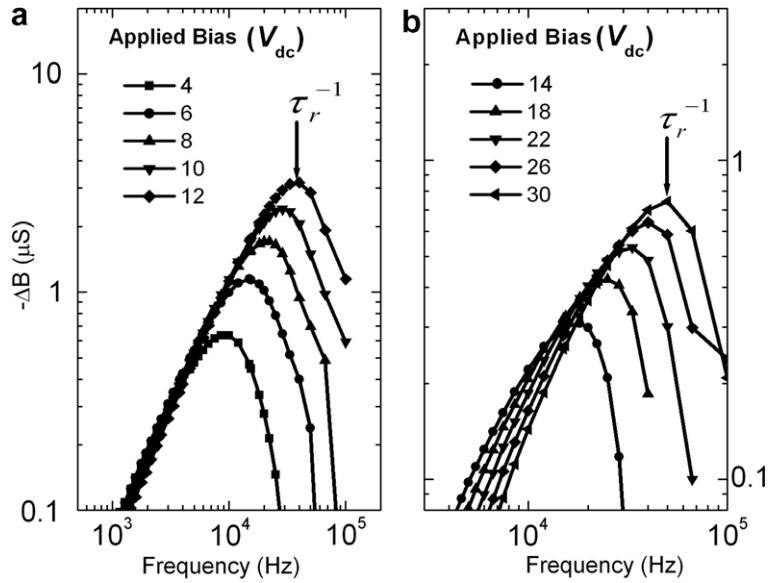

Fig. 3. Negative differential susceptances $-\Delta B = -2\pi f(C - C_{geo})$ of (a) ITO/*m*-MTDATA (735 nm)/Ag, and (b) PEDOT:PSS/NPB (3.70 μm)/Ag derived from measured frequency dependent capacitance data at different voltage biases V_{dc}. At each V_{dc}, there exists a maximum where the position is defined as τ_r^{-1} and is related to the average hole transit time by $\tau_{dc} = 0.56\ \tau_r$.

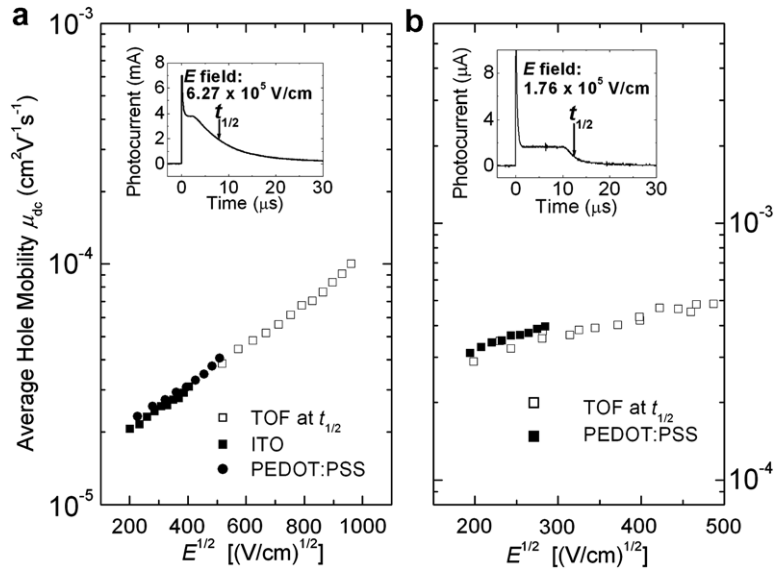

Fig. 4. Average hole mobility μ_{dc} of (a) *m*-MTDATA (735 nm) and (b) NPB (3.70 μm) devices extracted by admittance spectroscopy (filled symbols) as a function of anode and TOF at $t_{1/2}$ (open symbols). The insets show the typical TOF transients of (a) *m*-MTDATA (3.5 μm) and (b) NPB (7.6 μm). The average hole transit time τ_{dc} can be estimated from the TOF transient at $t_{1/2}$, the instant the current drops to one half of the value in the plateau region.

plateau region. In the case of *m*-MTDATA devices as shown in Fig. 4(a), the mobilities extracted by AS are in excellent agreement with those obtained from TOF. In case of PEDOT:PSS/NPB devices, as depicted in Fig. 4(b), the mobilities extracted by AS match very well with TOF mobilities.

Finally, we want to comment on the effects of film thickness on AS measurements. In principle, AS can be used to evaluate carrier mobility for any arbitrary film thickness because the location of hole injection can be defined precisely at the anode/organic interface. To inspect if there is indeed

any thickness limitation, we apply AS to measure the hole mobility of *m*-MTDATA in a configuration of ITO/*m*-MTDATA (*d* nm)/Ag. The thickness *d* varies from 735 nm to 230 nm. The results are shown in Fig. 5. For $d > 400$ nm, there is practically no difference between AS and TOF results. However, as *d* becomes smaller, the AS results begin to deviate from the TOF results. Fig. 6 shows the ratio of AS-derived hole mobility (μ_{AS}) to the TOF-derived mobility (μ_{TOF}). For $d < 400$ nm, the ratio becomes smaller than 1. At this thickness regime, there is a clear discrepancy between AS and TOF results. The origin is not clear to us. One possibility may be related to the existence of an interfacial capacitance at the ITO/*m*-MTDATA interface. This interfacial capacitance may arise from charge exchange between ITO and *m*-MTDATA. For a thick film, the bulk capacitance dominates. As the film thickness shrinks, the interface becomes more important; the experimentally determined capacitance should then be the series combination of the interfacial and bulk capacitances. A correct interpretation of AS for thin films will require the delineation of these capacitances and is beyond the scope of this investigation.

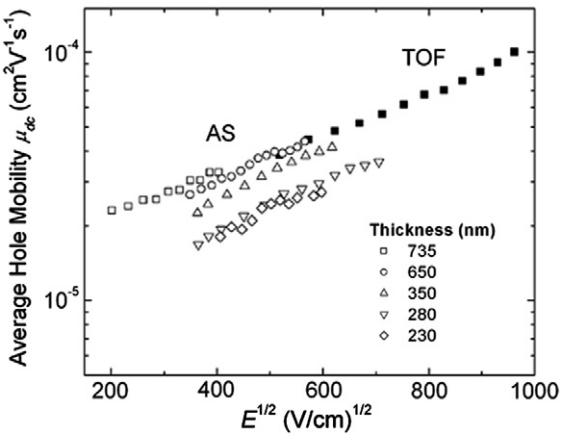

Fig. 5. The average hole mobilities μ_{dc} of *m*-MTDATA extracted by AS (filled symbols) with different film thicknesses. The open symbols are mobilities obtained by TOF.

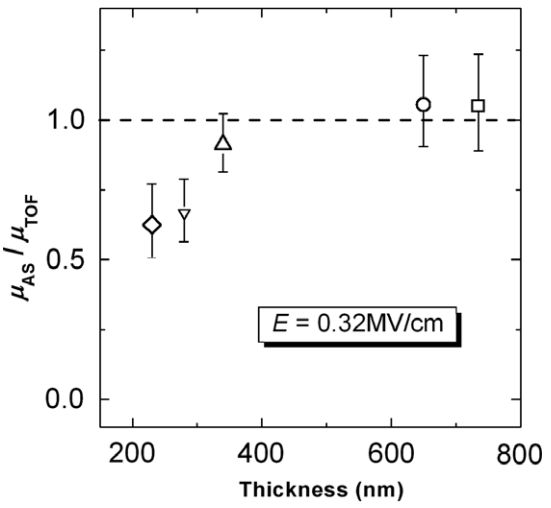

Fig. 6. Normalized mobilities of *m*-MTDATA extracted by AS for different thicknesses at $E = 0.32$ MV/cm.

4. Conclusion

We have experimentally demonstrated the validity of using PEDOT:PSS as an anode in AS to extract average hole mobilities μ_{dc}. Ohmic and quasi-Ohmic contacts are formed, respectively, at PEDOT:PSS/*m*-MTDATA and PEDOT:PSS/NPB interfaces. The extracted average hole mobilities by AS are in very good agreement with those obtained by independent TOF measurements. When PEDOT:PSS is used as the anode, it is expected that AS can be applied to evaluate carrier mobilities of hole transporting organic materials with HOMO energy levels down to 5.4 eV.

Acknowledgement

Support of this research by the Research Grant Council of Hong Kong under Grant # HKBU/211205 is gratefully acknowledged.

References

[1] P.M. Borsenberger, D.S. Weiss, in: Organic Photoreceptors for Imaging Systems, Marcel Dekker, New York, 1993 (Chapter 9).
[2] H.C.F. Martens, H.B. Brom, P.W.M. Blom, Phys. Rev. B 60 (1999) R8489.
[3] S. Berleb, W. Brütting, Phys. Rev. Lett. 89 (2002) 286601; H.H.P. Gommans, M. Kemerink, G.G. Andersson, R.M.T. Pijper, Phys. Rev. B 69 (2004) 155216.
[4] S.W. Tsang, S.K. So, J.B. Xu, J. Appl. Phys. 99 (2006) 013706.
[5] H.C.F. Martens, J.N. Huiberts, P.W.M. Blom, Appl. Phys. Lett. 77 (2000) 1852.
[6] D. Poplavskyy, F. So, Proc. SPIE 5937 (2005) 583712.
[7] H.H. Fong, S.K. So, J. Appl. Phys. 98 (2005) 023711; H.H. Fong, K.C. Lun, S.K. So, Jpn. J. Appl. Phys. 41 (2002) L1122.
[8] P.N. Murgatroyd, J. Phys. D: Appl. Phys. 3 (1970) 151.
[9] C. Giebeler, H. Antoniadis, D.D.C. Bradley, Y. Shirota, Appl. Phys. Lett. 72 (1998) 2448.

Available online at www.sciencedirect.com
ScienceDirect
Organic Electronics 7 (2006) 480–489
Organic Electronics
www.elsevier.com/locate/orgel

Soluble derivatives of perylene and naphthalene diimide for n-channel organic field-effect transistors

Th.B. Singh [a,*], S. Erten [b], S. Günes [a], C. Zafer [b], G. Turkmen [b], B. Kuban [b], Y. Teoman [b], N.S. Sariciftci [a], S. Icli [b]

[a] Linz Institute for Organic Solar Cells (LIOS), Physikalische Chemie, Johannes Kepler Universität Linz, Altenbergerstr. 69, A 4040 Linz, Austria
[b] Solar Energy Institute, Ege University, Bornova, 35100 Izmir, Turkey

Received 30 December 2005; received in revised form 15 April 2006; accepted 29 June 2006
Available online 1 August 2006

Abstract

Solution-processed n-type organic field-effect transistors (OFETs) have been fabricated using soluble derivatives of perylene diimide and naphthalene diimide. We report the synthesis of the organic semiconductors and the fabrication of bottom gate OFET devices using solution-processed organic dielectrics. Surface morphology studies reveal films with layered textures and liquid crystalline-like structure. Devices show field-effect electron mobilities of 10^{-2} cm^2/V s and 10^{-3} cm^2/V s for N,N'-bis-*n*-butyl-1,4,5,8-naphthalenediimide-NDI under inert conditions and in air, respectively. N,N'-bis-(1-pentyl)hexyl-3,4,9,10-perylene diimide-PDI-4 shows mobility of 5×10^{-4} cm^2/V s. Organic field-effect transistors based on N,N'-bis(dehydroabietyl)-3,4,9,10-perylene diimide-PDI-1 derivative exhibit ambipolar transport.

PACS: 85.30.Tv

Keywords: Organic field-effect transistors; Organic dielectrics; Naphthalene diimide; Mobility; N-type; Soluble

1. Introduction

High performance organic field-effect transistors (OFETs) have been utilized in integrated circuits [1–3], chemical and pressure sensors [4,5], displays [6], and memory elements [7,8]. The performance of these devices depends mainly on the charge carrier mobility of the organic semiconductor employed. The current benchmark material for high performance OFETs is based on vacuum-evaporated pentacene films with a field-effect hole mobility as high as ~1–3 cm^2/V s [9,10]. However, to meet the requirement for more advanced logic elements, materials with high electron mobility, as well as high hole mobility, are required. Due to technological and cost effectiveness issues, many research groups are focussing on soluble organic semiconductors with hole-only semiconducting properties (p-type). Air stable high mobility solution-processed electron transporting organic semiconductors are scarce and very few OFETs using soluble n-type organic semi-

* Corresponding author. Tel.: +43 732 2468 1767; fax: +43 732 2468 8770.
E-mail addresses: birendra.singh@jku.at (Th.B. Singh), icli@mail.ege.edu.tr (S. Icli).

1566-1199/$ - see front matter
doi:10.1016/j.orgel.2006.06.010

conductors [11–13] have been realized. The reason is mainly due to difficulty in synthesis of n-type materials with an electron affinity that allows the injection of electrons from stable electrodes in air. The majority of OFETs with high mobility n-type semiconductors are with vacuum sublimed films [14,15]; with a few exceptions [16–20]. Solution-processed NDI with a mobility of 0.1 cm^2/V s was first reported by Katz et al. [16]. Solution-processed air-stable with two core cyanated PDI derivative as a semiconductor which exhibit electron mobility of 0.1–0.64 cm^2/V s was reported by Wasielewski et al. [17]. Marks et al. [18] investigated series of perfluoroalkyl and alkyl-functionalized oligothiophene with electron mobilities as high as of 0.22 cm^2/V s [18]. Phenacyl-quaterthiophene exhibit electron mobilities as high as 0.51 cm^2/V s [19]. Carbonyl functionalized quaterthiophenes were demonstrated to be high electron mobility semiconductors with ambipolar transport [20].

In this paper, we present results on solution-processed, high electron mobility ($\sim 10^{-2}$ cm^2/V s) *N*,*N*′-bis-*n*-butyl-1,4,5,8-naphthalene diimide-NDI OFETs. In addition results of various OFETs based on soluble perylene derivatives with electron mobilities ranging from 7×10^{-5} to 5×10^{-4} cm^2/V s are obtained on various organic dielectrics. However, these moblities depend on the film formation quality. One of the perylene derivatives, *N*,*N*′-bis-(dehydroabietyl)-3,4,9,10-perylene diimide, is also able to transport both electron and holes making it ambipolar. All these compounds are solution-processed and some provide successful device operation at ambient conditions.

2. Experimental

2.1. FET fabrication and characterization

A scheme of the top contact OFET device structure along with the chemical formulas of respective gate dielectrics used is shown in Fig. 1a–d. Device fabrication procedure has been discussed previously [13]. For capacitance measurements, separate sandwich devices were prepared. The obtained dielectric functions and capacitances are presented in Table 1. Various organic dielectrics were chosen for different compounds/solvents in order to optimize film nanomorphology according to the hydrophobicity and hydrophilicity of the dielectric/semiconductor interface. Semiconducting films were deposited as follows:

For device I: 2% (20 mg/mL) NDI solution in acetonitrile was spin-coated on top of PVA; for device II: 2% PDI-4 solution in chlorobenzene was spin-coated on top of BCB; for device III: 2% PDI-2 solution in chlorobenzene was spin-coated on top of PVA; for device IV: 2% PDI-2 solution in chlorobenzene was spin-coated on top of BCB ; for device V: 2% PDI-1 solution in chlorobenzene was spin-coated on top of PVA. The surface morphology and thickness of the dielectrics and the organic semiconductor films on top of the dielectric materials were measured with a Digital Instrument 3100 atomic force microscope and a DekTak Stylus profilometer, respectively. The top source and drain electrodes, LiF/Al (0.6/60 nm), were evaporated under vacuum (2×10^{-6} mbar) through a shadow mask with channel length, *L*, of 20 μm and width, *W*, of 1.4 mm. An Agilent E5273A Source/Measure unit Unit was employed for the steady state current–voltage measurements and all measurements were performed with an integration time of 2 s in steps of 2 V. In all the devices reported here, parasitic leakage current due to the gate electrode was less than 10^{-8} A/cm^2. All the device processing and measurements were performed at room temperatures.

2.2. Synthesis

2.2.1. PDIs

The 1-pentylhexyl and 1-butylpentyl substituted perylene diimide derivatives were prepared using well-established procedures [21–23]: A mixture of 0.800 g (2.03 mmol) of 3,4,9,10-perylene tetracarboxylic dianhydride, 5.07 mmol of amine, [24] 16 g of imidazole and 0.35 g (1.89 mmol) of zinc acetate was heated at 160 °C for 4 h under argon atmosphere. The precipitate was collected by vacuum filtration and washed with a mixture of methanol and water. Further washing of the precipitate was done with 2 N hydrochloric acid. The raw product was then dried at 100 °C for 12 h and further purified by column separation (silica gel, chloroform).

2.2.2. *N*,*N*′-bis-(1-butyl)pentyl-3,4,9,10-perylene diimide-PDI-3

% Yield: 45, colour: red-IR(KBr), (cm^{-1}), *v*: 2955, 2927, 2861, 1696, 1654, 1593, 1506, 1461, 1434, 1403, 1337, 1251, 1208, 1176, 1121, 1099, 969, 851, 808, 746.

^{1}H-NMR ($CDCl_3$) δ: 8.64 (brd, 4H), 8.57 (d, 4H), 5.18 (m, 2H), 2.25 (m, 4H), 1.88 (m, 4H), 1.30 (m, 16H), 0.85 (t, 12H)

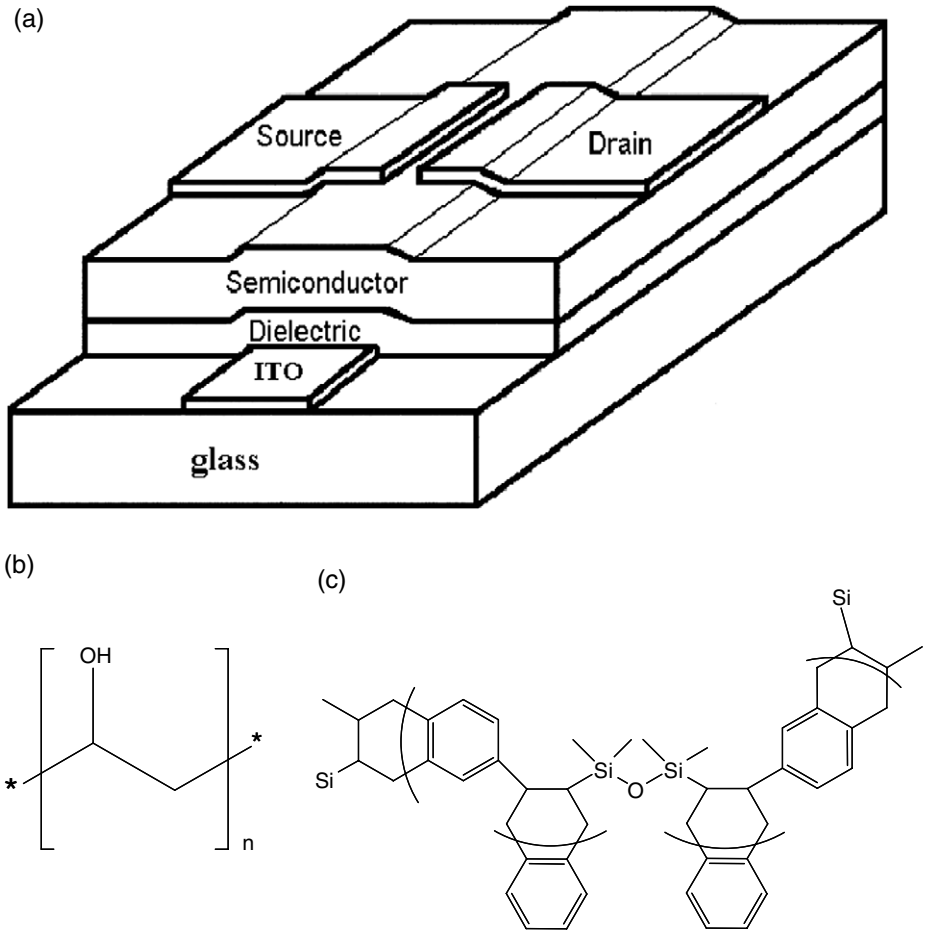

Fig. 1. (a) Scheme of the top contact OFET. Chemical structures of: (b) polyvinyl alcohol (PVA) and (c) divinyltetra-methyldisiloxane-bis(benzocyclobutene) (BCB) respectively.

Table 1
Summary of the device parameters for various Naphthalene diimide and perylene diimide OFETs with different dielectrics materials

Device	Dielectric	ε	C (nF/cm^2)	μ_e (cm^2 V^{-1} s^{-1})	μ_h (cm^2/V s)
Device-I	PVA	8	1.8	0.012	Not active
Device-I	PVA	8	1.8	0.006[a]	Not active
Device-II	BCB	2.6	1.2	5×10^{-4}	Not active
Device-III	PVA	8	1.8	8×10^{-5}	Not active
Device-IV	BCB	2.6	1.2	3×10^{-5}	Not active
Device-V	PVA	8	1.8	7×10^{-5}	8×10^{-5}

The values shown here are an average of at least 10 different devices fabricated under identical conditions and measured at room temperatures under Ar atmosphere
[a] Measured in air.

^{13}C-NMR ($CDCl_3$) δ: 164.75, 163.67 (C=O), 1.34.66, 131.94, 131.34, 129.80, 126.64, 124.05, 123.16 (aromatic), 54.91 (C–N), 32.31, 29.37, 22.84, 14.25 (aliphatic).

2.2.3. N,N′-bis(1-pentyl)hexyl-3,4,9,10-perylene diimide-PDI-4

% Yield: 30, colour: red-IR(KBr), (cm^{-1}), ν: 2952, 2926, 2859, 1699, 1657, 1594, 1460, 1435,

Table 2
Summary of the redox potential and LUMO–HOMO energy levels of Naphthalene diimide and perylene diimide calculated from cyclic voltammetry measurements

Dye	E_{ox} (eV)[a]	E_{r1} (eV)[b]	E_{r2} (eV)[c]	E_{Fc} (eV)[d]	LUMO (vs. Fc)eV	LUMO (eV)	HOMO (eV)
NDI	–	−0.58	−1.10	0.41	−0.84	−3.57	−6.67
PDI-1	1.67	−0.56	−0.76	0.41	−0.97	−3.83	−6.06
PDI-2	–	−0.56	−0.78	0.41	−0.97	−3.83	−6.01
PDI-3	1.62	−0.56	−0.78	0.41	−0.97	−3.83	−6.01
PDI-4	1.63	−0.55	−0.78	0.41	−0.96	−3.82	−6.02

$E_{LUMO} = (E_{r1} - E_{Fc}) + 4.8 E_{HOMO} = (E_{ox} - E_{Fc}) + 4.8$

[a] E_{ox} is the oxidation potential.

[b] E_{r1} is the first reduction potential.

[c] E_{r2} is second reduction potential.

[d] E_{Fc} is ferrocene internal reference electrode potential (0.39 eV).

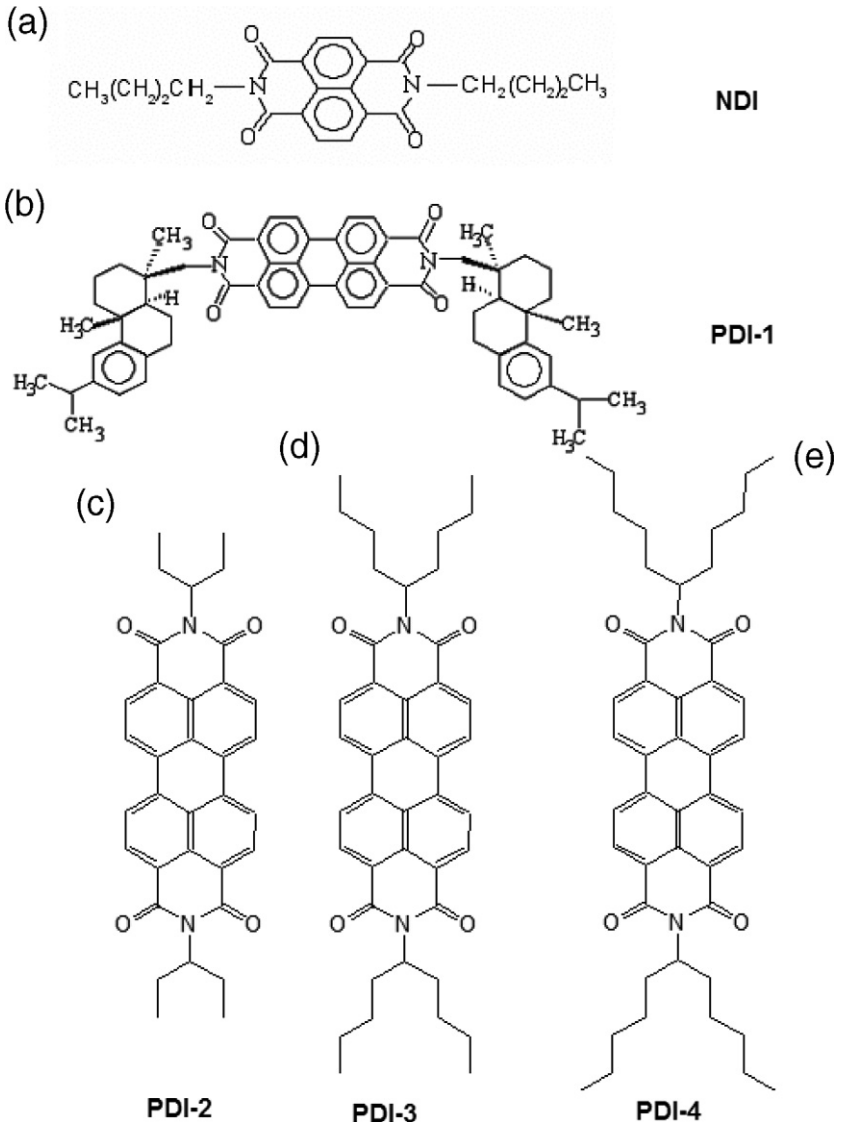

Fig. 2. Chemical structure: (a) NDI; (b) *N*,*N*′-bis-dehydroabietyl-3,4,9,10-perylenediimide-PDI-1; (c) *N*,*N*′-bis-(1-ethyl)propyl-3,4,9,10-perylene diimide-PDI-2; (d) *N*,*N*′-bis-(1-butyl)pentyl-3,4,9,10-perylene diimide-PDI-3 and (e) *N*,*N*′-bis-(1-pentyl)hexyl-3,4,9,10-perylene diimide-PDI-4.

1405, 1337, 1253, 1208, 1176, 1123, 1105, 961, 850, 809, 746.

^{1}H-NMR($CDCl_3$)δ: 8.49 (d, 4H), 8.57 (brd, 4H), 5.15 (m, 2H), 2.24 (m, 4H), 1.86 (m, 4H), 1.30 (m, 24H), 0.84 (t, 12H).

^{13}C-NMR($CDCl_3$)δ: 164.7, 163.7 (C=O), 134.59, 131.97, 131.28, 129.74, 126.57, 124.14, 123.41, 123.12 (aromatic), 54.98 (C–N), 32.55, 31.95, 26.85, 22.76, 14.22 (aliphatic).

2.2.4. *N,N′-bis(dehydroabietyl)-3,4,9,10-perylene dimide, PDI-1*

% Yield: (70), colour: red, IR (KBR); (cm^{-1}) 2950, 2900, 2850, 1707, 1666, 1580, 1495, 1380, 1315, 1445, 1245, 1160, 1050, 980, 880, 810, 765.

^{1}H NMR ($CDCL_3$): δ (ppm) 8.40 (4H, d), 8.47 (4H, d), 7.33 (2H, s), 7.19 (2H, d), 7.03 (2H, d), 4.33 (4H, q), 2.9 (2H, m), 1.4–1.5 (2H, t), 1.4–1.5 (20H, t), 2.8 (12H, s), 1.6 (12H, d).

2.2.5. *NDI*

The naphthalene *N,N′*-disubstituted imide was synthesized by condensation of naphthalene 1,4,5,8-tetracarboxylic dianhydride and alkyl primary amine in the presence of solvent (DMA and isoquinoline) [29].

The mixture of 1,4,5,8-naphthalene dianhydride (0.5 g, 1.87 mmol) and butyl amine (0.27 g, 3.73 mmol) was dissolved in 20 ml *N,N*-dimethylacetamide (DMA) and a few drops of isoqunoline was added. The temperature was gradually increased to 160 °C. The mixture was kept at this temperature for 10 h under argon atmosphere. The reaction was inspected continuously by thin layer chromatography. DMA was vaporized by rotary evaporation using an oil pump. Crude product was purified by silica gel column chromatography, using dichloromethane as the eluent.

2.2.6. *N,N′-bis(n-butyl)-1,4,5,8-naphthalene diimide, NDI*

% Yield: 80, colour: pink (needle crystals), IR (KBR); (cm^{-1}), 2950, 1700, 1650, 1580, 1452, 1381, 1250, 1180, 1080, 990, 880, 750.

^{1}H NMR ($CDCL_3$): δ (ppm) 8.76 (4H, s), 4.20 (4H, t), 1.74 (4H, m), 1.46 (4H, m), 1,1 (6H, t).

Redox potential and LUMO–HOMO energy levels of all the compounds described are summarised in Table 2 based on cyclic voltammetry measurements Fig. 2.

3. Results and discussion

3.1. Thin-film nanomorphology

Film nanostructure and morphology were examined using atomic force microscopy, crossed-polarized microscopy and X-ray diffraction as shown in Figs. 3–5. The organic dielectric layers with measured thicknesses of 3.8 μm and 2 μm for PVA and BCB film respectively were previously found a surface roughness of <5 nm [20]. OFET mobilities and other parameters are generally assessed using top contact FET geometry simply because the application of electrodes to the already deposited semiconductor films ensures intimate contact over much of the electrode area [25]. Spin coated films of NDI on PVA were found to have a layered texture. Closer inspection revealed crystallite sizes as large as ~2 μm with a rather high surface roughness of ~150 nm (Fig. 3a). X-ray diffraction studies (not shown here) revealed highly crystalline structure in the NDI system. PDI-3 films on PVA (Fig. 3b) formed lamellar-like features with a surface roughness of around 90 nm. The formation of smectic liquid crystalline phases in PDI has already been reported [26]. Spin coated films of PDI-2 on PVA show large elongated needle-like crystallites, some as long as about 2.5 μm with a surface roughness of 100 nm (Fig. 4a). PVA is known for its high surface energy, compared to BCB, due to its hydrophilic nature [25]. When PDI-2 is spin coated on the hydrophobic surface of BCB, films with even more elongated needle-like structures are observed (Fig. 4b). Modification of semiconducting film morphology due to different surface energy among the organic dielectric has been reported previously [20]. The film morphology of PDI-4 on BCB is quite surprising when compared to other derivatives of PDI (see Fig. 5a). It forms a very smooth, amorphous-like film with a surface roughness of less than 15 nm. A PDI-1 film on PVA has similar film morphology with a rather smooth surface (Fig. 5b). Crossed polarized microscope images of PDI-1 films on PVA, as shown in Fig. 5c, reveal textured, macroscopic-ordered structures.

3.2. OFET characteristics

Naphthalene diimide (NDI) with its short side groups and highly crystalline film morphology, should give rise to high electron mobility. Fig. 6a demonstrates the output characteristics of an n-

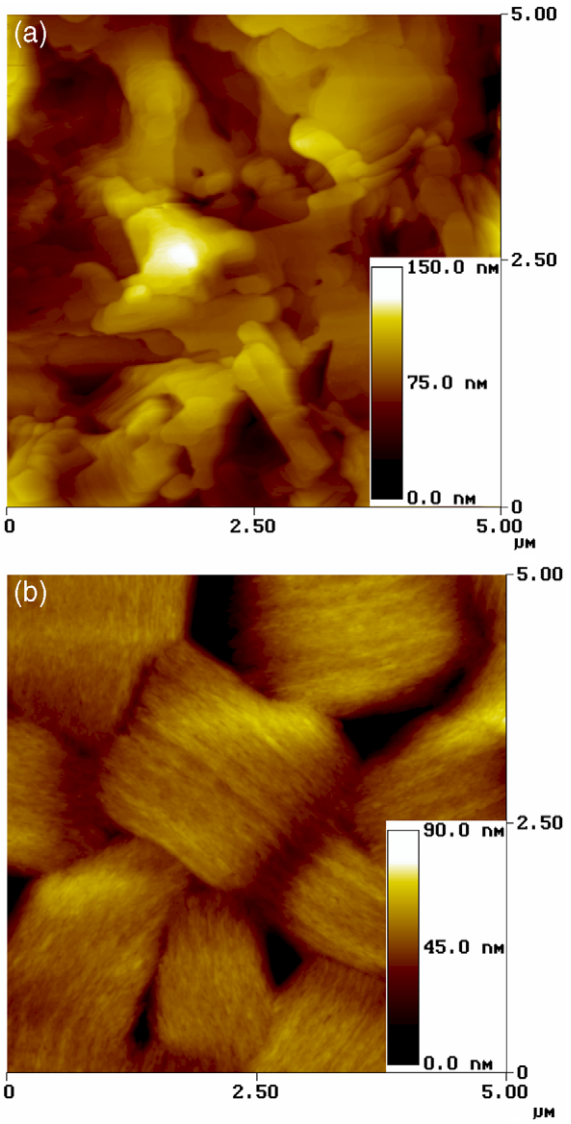

Fig. 3. Tapping mode AFM images (5 μm × 5 μm) of: (a) NDI film on PVA layer showing terraced growth of individual grains and (b) PDI-3 on PVA.

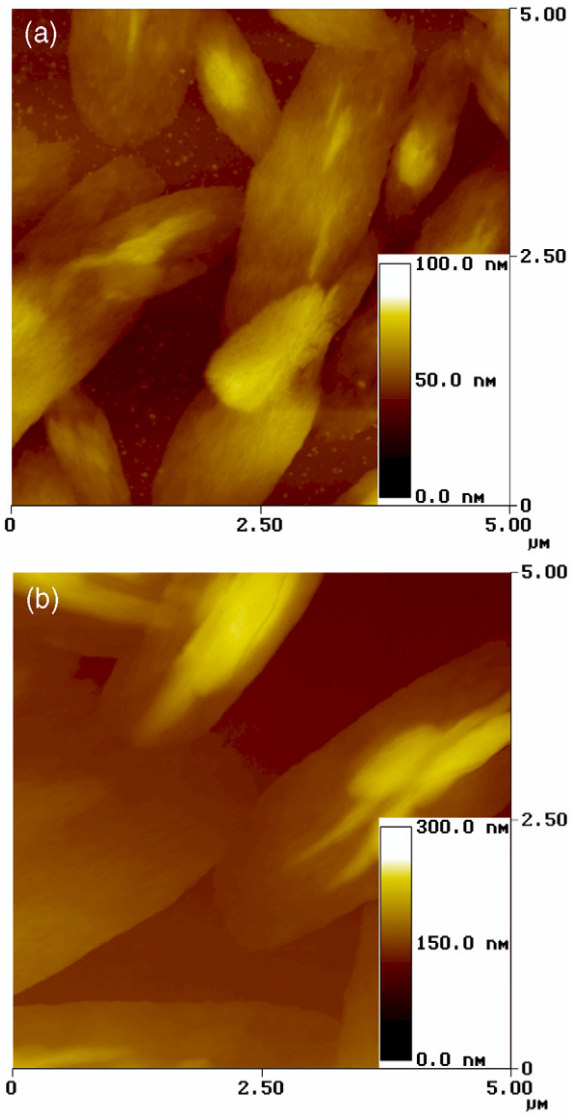

Fig. 4. Tapping mode AFM images (5 μm × 5 μm) of: (a) PDI-2 on PVA showing liquid crystalline-like structure and (b) PDI-2 film on BCB showing the elongated liquid crystalline-like structure.

channel NDI OFET (device-I). For an applied positive drain-source voltage, V_{ds}, above a positive gate voltage, V_{gs}, a saturated drain current, I_{ds}, is observed in the range of 2×10^{-6} A for applied V_{gs} of 60 V. Transfer characteristics are also shown in Fig. 6b and demonstrate a quadratic increase of the I_{ds} (V_{gs}) with significant hysteresis. The reason for such hysteresis is assumed to be due to the charge trapping at the interface of the organic semiconductor and organic insulator [13]. A plot of $\sqrt{I_{ds}}$ vs. V_{gs} is presented in the right scale of Fig. 6b. From curve (V), we extracted a saturated regime mobility of 0.012 cm^2/V s. and a threshold voltage V_{th} of 0 V for NDI using the standard transistor equation [27] in which there is no correction for contact resistances [28]. On/off ratios (+60 V/0 V) are $\sim 10^4$. The mobility and V_{th} obtained when devices are characterized in air are 0.006 cm^2/V s and 8 V, respectively. We have previously shown that NDI structures are air, thermal, and photo stable. [29]. In addition small hysteresis is observed in Fig. 6b. A possible reason for such a feature is attributed to the presence of interfacial traps. The interfacial

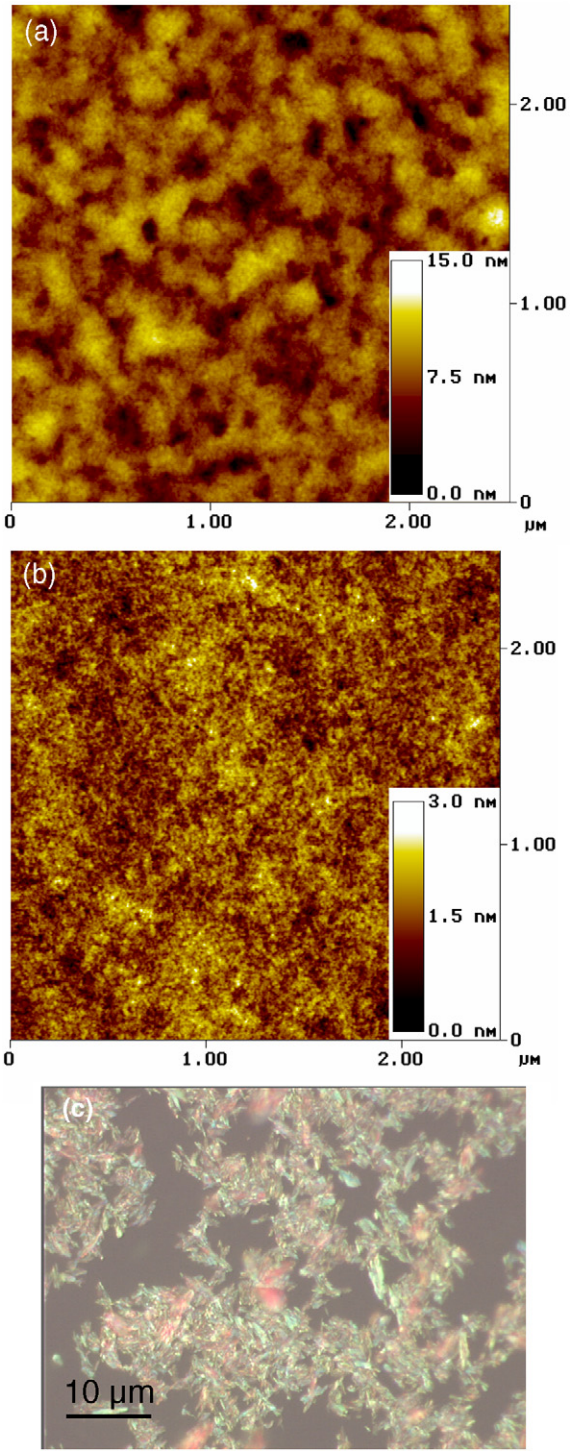

Fig. 5. Tapping mode AFM images (2.5 μm × 2.5 μm) of: (a) PDI-4 film on BCB; (b) PDI-1 film on PVA and (c) Cross polarized microscopy image of PDI-1 film on PVA at room temperature.

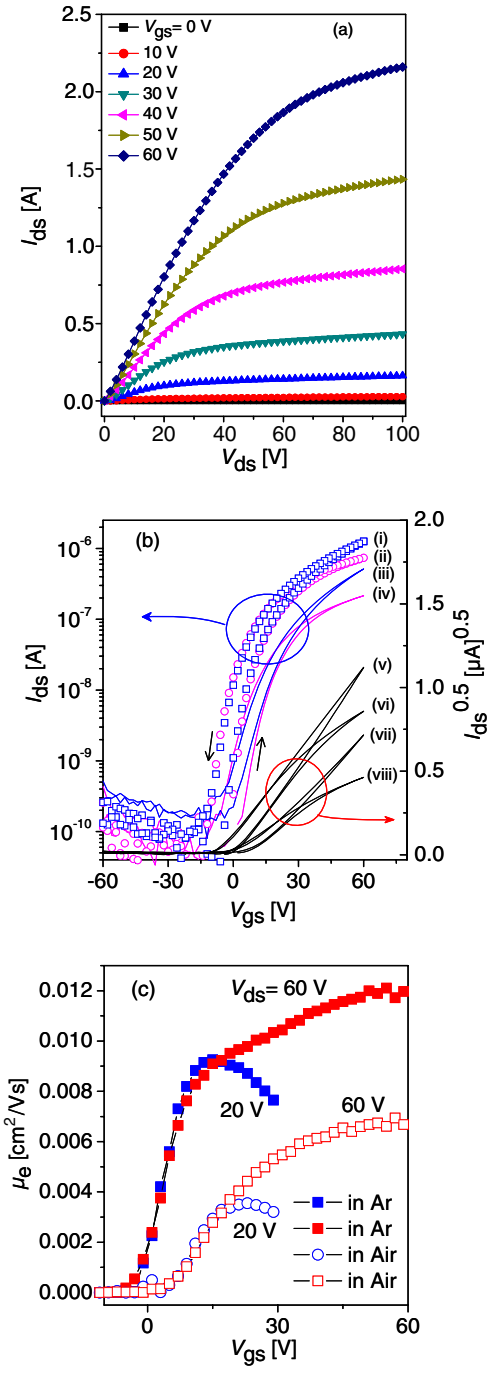

Fig. 6. (a) Transistor output characteristics of device I. (b) Transfer characteristics, left scale: I_{ds} vs. V_{gs}, $V_{ds} = 60$ V in Ar atmosphere (i); $V_{ds} = 20$ V in Ar atmosphere (ii); $V_{ds} = 60$ V in air (iii); $V_{ds} = 20$ V in air (iv); right scale: $\sqrt{I_{ds}}$ vs. V_{gs} curves of $V_{ds} = 60$ V in Ar atmosphere (v); $V_{ds} = 20$ V in Ar atmosphere (vi); $V_{ds} = 60$ V in air (vii) and $V_{ds} = 20$ V in air (viii). (c) Saturated field-effect electron mobility μ_e vs. V_{gs} plot using data taken from the forward sweeping curves of Fig. 6(b) (i–iv) using transconductance equation (1).

traps, rather than the doping of the semiconductor, are responsible for these effects. The presence of trap levels in the semiconductor lowers the conductivity of the material. The "low threshold voltage" behaviour is not related to the thickness of the dielectric. It should also be noted that these observations favour the formation of highly conductive channels at the interface between the polymeric dielectric and the organic semiconductor [13]. We also plotted the transconductance with a local approximation function of V_{gs} (Fig. 6c) to obtain (the electron mobility) μ_e, from the equation: [27]

$$\mu = \frac{2L}{WC}\left(\frac{\partial\sqrt{I_{ds}}}{\partial V_{gs}}\right)^2 \quad (1)$$

An increase of μ_e with V_{gs} can be explained using various models [27,30] and is attributed to the defect-induced charge traps in the semiconductor film. The basic assumption is that there is a distribution of localized states close to the band edge. At thermal equilibrium, these states are filled up to the Fermi level. As the absolute V_{gs} increases, the Fermi level gradually moves towards band edge as more of the empty traps become filled due to charge injection. Accordingly, the ratio of free to trapped carriers increases, so the effective mobility increases too. To account for the decrease of the mobility occurring at high $V_{gs}(\geqslant V_{ds})$, we note that when the V_{gs} increases, charges in the conducting channel tend to accumulate close to the gate/insulator interface. The μ_e obtained here is comparable to the one obtained by Katz et al. from solution-processed films of naphthalenetetracarboxylic diimide on SiO_2 dielectrics with mobilities of 0.06–0.1 $cm^2/V\,s$ depending on the W/L ratio[16]. However, the overall performance of our devices versus theirs cannot be directly compared because of the different device parameters used such as choice of dielectric, dielectric thickness, gate electrode work function, and W/L ratio. Like Katz et al. [16], we also found that a BCB dielectric is not suitable for NDI OFETs. Finally, we note that the mobilities of our films are similar to that of an NDI derivative reported by Waseilewski et al. [17].

We now consider the transistor characteristics of OFETs with films of perylene diimide derivatives. Considering the film morphology presented in Figs. 3–5, OFETs based on four compounds were selected for further testing. First, we considered device II (OFET with PDI-4 on BCB dielectric). Fig. 7a shows typical n-channel transistor output characteristics with a well defined pinch-off as a function of

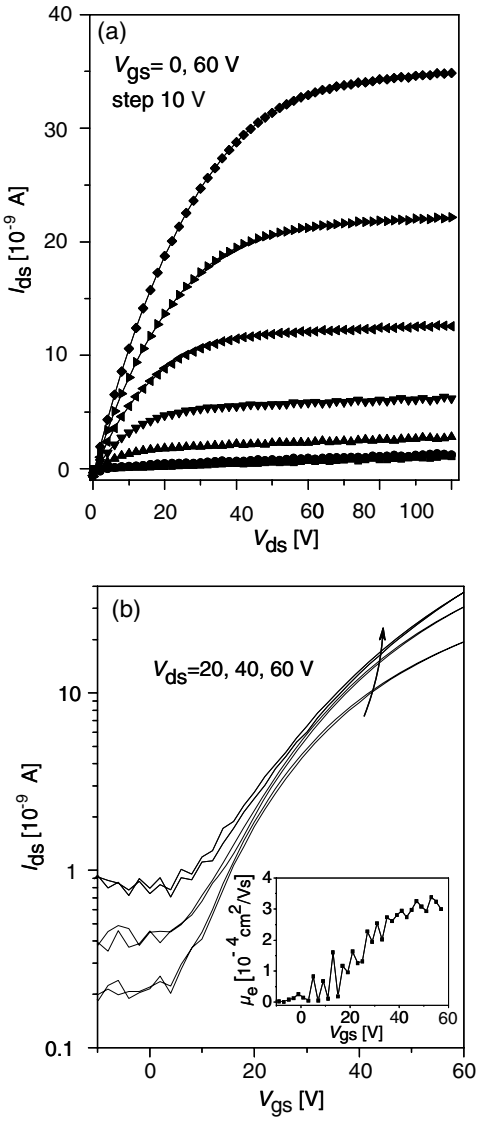

Fig. 7. (a) Transistor output characteristics of device II (b) Transfer characteristics (I_{ds} vs. V_{gs}) for different V_{ds}. Inset of (b): field-effect electron mobility μ_e vs. V_{gs} plot using data taken from return curve of transfer characteristics with $V_{ds} = 60$ V using transconductance equation (1).

V_{gs}. In Fig. 7b, a transfer characteristic is presented with virtually no hysteresis for different V_{ds}. A μ_e vs. V_{gs} plot using Eq. (1) is also presented in the inset. μ_e is observed to be increasing with V_{gs} which can be explained with the concept discussed above in the case of naphthalene diimide. μ_e of 5×10^{-4} $cm^2/V\,s$ is four orders of magnitude less than the other perylene films sublimed on SiO_2 dielectrics [15]. Furthermore, we considered the transistor characteristics of PDI-2 and PDI-4 on different organic dielectrics in Fig. 8a and b. Parameters extracted

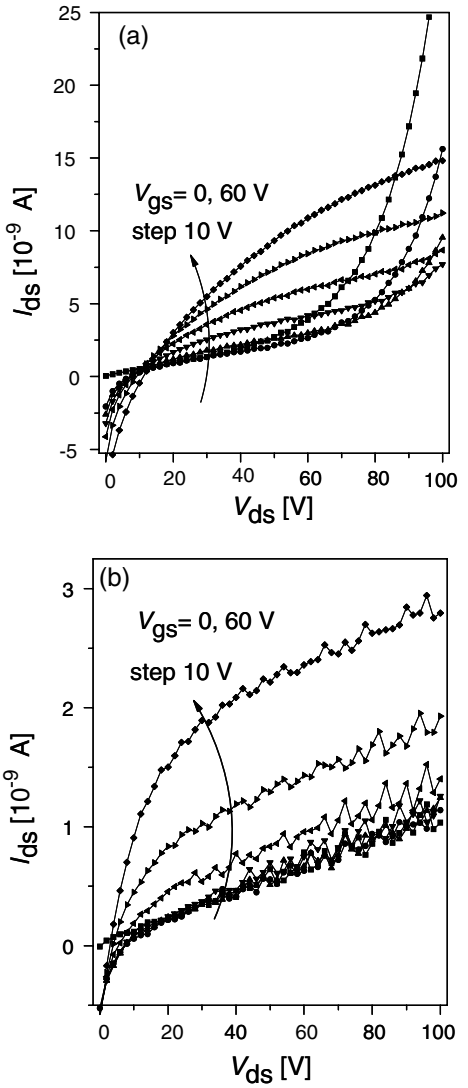

Fig. 8. Output characteristics of (a) device III and (b) device IV.

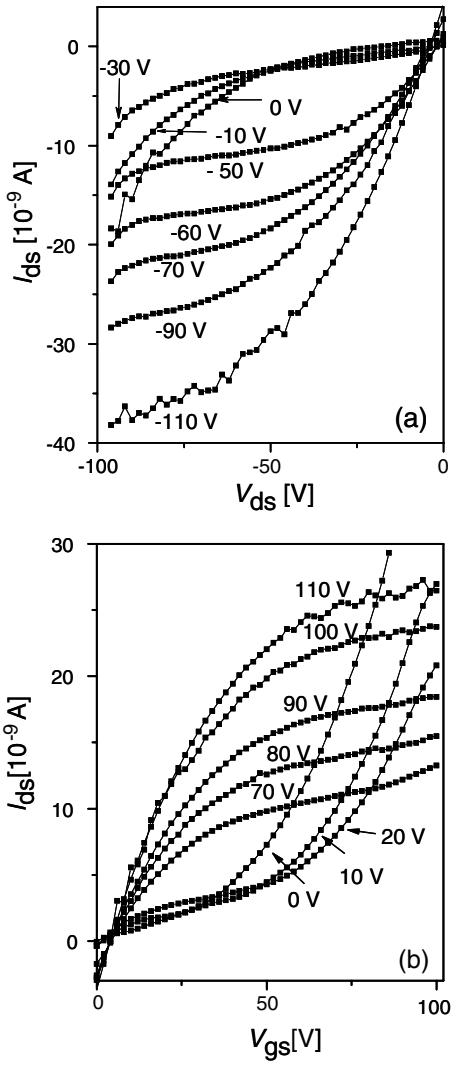

Fig. 9. Ambipolar transistor output characteristics of device V: (a) hole-enhancement-mode and (b) electron-enhancement-mode.

from these devices are presented in Table 1. It is observed that the μ_e in all of these compounds is one order of magnitude less than that of PDI-4 and this is presumably related to the smoothness of the interface (See Fig. 5b).

Perylene diimide derivative: *N*,*N*′-bis-(dehydroabietyl)-3,4,9,10-perylenediimide-PDI-1 film on PVA (device-V) shows an ambipolar transport. Fig. 9 shows output characteristics of an ambipolar transistor with a hole enhancement mode (Fig. 9a) and an electron-enhancement mode (Fig. 9b). The presence of a second aromatic ring on the side chain of PDI-1 might be the cause of ambipolar behaviour although comparison of the LUMO-HOMO energy levels shows no significant difference among the different PDI systems reported here (see Table 2). Perylene diimides are also attractive for organic light-emitting transistors [31].

Solution-processed n-type organic semiconductor devices are inferior to those grown by sophisticated hot wall epitaxy which have electron mobilities of around 3 cm^2/V s [32]. PDI systems with mobility exceeding 1 cm^2/V s are also reported after the correction of contact resistance [33]. However these devices are not stable in air. Air stable n-type semiconductors still remained to be investigated in further detail. However, introduction of fluorinated or cyanated compounds within an n-type semiconductor, as shown by Facchetti et al. [34], seems to be very promising with regard to

device stability in air. Unfortunately, the suitable choices of organic materials are limited, especially for n-type semiconductors.

4. Conclusion

The solution-processed, air-stable organic semiconductors discussed here can be useful in devices and circuits that need electron transport. Naphthalene diimide films show high electron mobility up to 10^{-2} cm^2/V s. Perylene diimide materials have ambipolar carrier characteristic which might give rise to light emitting transistors. We observed experimentally that choice of the organic dielectric materials is crucial. The structure-property relationship at the organic dielectric/organic semiconductor interface is also important.

References

[1] J.A. Rogers, Z. Bao, K. Baldwin, A. Dodabalapur, Brian Crone, V.R. Raju, V. Kuck, H. Katz, K. Amundson, J. Ewing, P. Drzaic, Proc. Natl. Acad. Sci. 98 (2001) 4835.

[2] H.E.A. Huitema, G.H. Gelinck, J.B.P.H. van der Putten, K.E. Kuijk, C.M. Hart, E. Cantatore, P.T. Herwig, A.J.J.M. van Breemen, D.M. de Leeuw, Nature 414 (2001) 599.

[3] C.D. Sheraw, L. Zhou, J.R. Huang, D.J. Gundlach, T.N. Jackson, M.G. Kane, I.G. Hill, M.S. Hammond, J. Campi, B.K. Greening, J. Francl, J. West, Appl. Phys. Lett. 80 (2002) 1088.

[4] G. Darlinski, U. Böttger, R. Wasser, H. Klauk, M. Halik, U. Zschieschang, G. Schmid, C. Dehm, J. Appl. Phys. 97 (2005) 093708.

[5] B.K. Crone, A. Dodabalapur, R. Sarpeshkar, A. Gelperin, H.E. Katz, Z. Bao, J. Appl. Phys. 91 (2001) 10140.

[6] A.R. Brown, C.P. Jarret, D.M. de Leeuw, M. Matters, Synth. Met. 88 (1997) 37.

[7] R. Schroeder, L.A. Majewski, M. Grell, Adv. Mater. 16 (2004) 633.

[8] Th. B. Singh, N. Marjanović, G.J. Matt, N.S. Sariciftci, R. Schwödiauer, S. Bauer, Appl. Phys. Lett. 85 (2004) 5409.

[9] Y.Y. Lin, D.J. Gundlach, S.F. Nelson, T.N. Jackson, IEEE Electron Devices Lett. 18 (1997) 606.

[10] H. Klauk, M. Halik, U. Zschieschang, G. Schmid, W. Radlik, J. Appl. Phys. 92 (2002) 5259.

[11] A. Babel, S.A. Jenekhe, J. Am. Chem. Soc. 125 (2003) 13656.

[12] T.D. Anthopoulos, C. Tanase, S. Setayesh, E.J. Meijer, J.C. Hummelen, P.W.M. Blom, D.M. de Leeuw, Adv. Mater. (Weinheim, Ger.) 16 (2004) 2174.

[13] Th. B. Singh, N. Marjanović, P. Stadler, M. Auinger, G.J. Matt, S. Günes, N.S. Sariciftci, R. Schwödiauer, S. Bauer, J. Appl. Phys. 97 (2005) 083714.

[14] H.E. Katz, J. Johnson, A.J. Lovinger, W. Li, J. Am. Chem. Soc. 122 (2000) 7787.

[15] P.R.L. Malenfant, C.D. Dimitrakopoulos, J.D. Gelorme, L.L. Kosbar, T.O. Graham, Appl. Phys. Lett. 80 (2002) 2517.

[16] H.E. Katz, A.J. Lovinger, J. Johnson, C. Kloc, T. Siegrist, W. Li, Y.-Y. Lin, A. Dodabalapur, Nature 404 (2000) 478.

[17] B.A. Jones, M.J. Ahrens, M.-H. Yoo, A. Facchetti, T.J. Marks, M.R. Wasielewski, Angew. Chem. Int. Ed. 43 (2004) 6363.

[18] A. Faccetti, M. Musshrush, M.-H. Yoon, G.R. Hutchison, M.A. Ratner, T.J. Marks, J. Am. Chem. Soc. 126 (2004) 13859.

[19] J.A. Letizia, A. Faccetti, C.. Stern, M.A. Ratner, T.J. Marks, J. Am. Chem. Soc. 127 (2005) 13476.

[20] M.- H. Yoon, S.A. Dibenedetto, A. Facchetti, T.J. Marks, J. Am. Chem. Soc. 127 (2005) 1348.

[21] S. Demmig, H. Langhals, Chem. Ber. 121 (1988) 225.

[22] L.D. Wescott, D.L. Mattern, J. Org. Chem. 68 (2003) 610058.

[23] H. Langhals, R. Ismael, O. Yürük, Tetrah. 5435 (2000) 56.

[24] E. Rohrmann, H.R. Shoule, J. Am. Chem. Soc. 1516 (1944) 66.

[25] Th. B. Singh, S. Günes, N. Marjanović, R. Menon, N.S. Sariciftci, J. Appl. Phys. 97 (2005) 114508.

[26] C.W. Strujick et al., J. Am. Chem. Soc. 122 (2000) 11057.

[27] S.M. Sze, Physics of Semiconductor Devices, Wiley, New York, 1981.

[28] L. Burgi, T.J. Richards, R.H. Friend, H. Sirringhaus, J. Appl. Phys. 94 (2003) 6129.

[29] (a) S. Erten, S.AlpS. Icli, J. Photochem. Photobiol: A Chem. 175 (2005) 214;
(b) H. Icil, S. Icil, C. Sayil, Spectrosc. Lett. 31 (1998) 1643.

[30] W. Kalb, Ph. Lang, M. Mottaghi, H. Aubin, G. Horowitz, M. Wutting, Synth. Met. 146 (2004) 279.

[31] C. Rost, S. Karg, W. Riess, M.A. Loi, M. Murgia, M. Muccini, Appl. Phys. Lett. 85 (2004) 1613.

[32] A.M. Ramil, B. Singh, N. Haber, N. Marjanovic, S. Guenes, A. Andreev, G. Matt, R. Resel, H. Sitter, S. Sariciftci, J. Crys. Growth 288 (2006) 123.

[33] R.J. Chesterfield, J.C. McKeen, Ch. R. Newman, C.D. Frisbie, P.C. Ewbank, K.R. Mann, L.L. Miller, J. Appl. Phys. 95 (2004) 6396.

[34] A. Facchetti, Y. Deng, A. Wang, Y. Koide, H. Sirringhaus, T.J. Marks, R.H. Friend, Angew. Chem. 112 (2000) 4721.

Available online at www.sciencedirect.com
ScienceDirect
Organic Electronics 7 (2006) 490–494
Organic Electronics
www.elsevier.com/locate/orgel

Using a low-index host layer to increase emission from organic light-emitting diode structures

L.H. Smith, W.L. Barnes *

School of Physics, University of Exeter, Exeter, EX4 4QL, UK

Received 22 March 2006; received in revised form 29 June 2006; accepted 7 July 2006
Available online 15 August 2006

Abstract

The out-coupling efficiency of organic light-emitting diodes (OLEDs) may be significantly increased by use of a low-index host material for the organic emitters. We report on modelling undertaken for substrate-emitting and top-emitting OLED structures and show that up to a 2.5 fold increase in out-coupling efficiency, over that for structures containing a standard emissive layer, may be achieved in both cases. The relationship between radiation efficiency and refractive index varies for each type of structure and this is discussed, as is the nature of the electromagnetic (EM) modes supported.

PACS: 85.60.Jb; 72.80.Le

Keywords: Organic light-emitting diode (OLED); Out-coupling efficiency; Refractive index

1. Introduction

Since their introduction in 1987 [1] much work has been undertaken concerning organic light-emitting diodes (OLEDs), with a large amount of this work centring on the efficiency of such devices. Research into improving efficiency may be split into two main branches, optical efficiency and electrical efficiency. Both of these factors must be considered if one is to construct an efficient device. Much of the work into efficiency has concentrated on the electrical aspect, with huge advances being made. These have included improvements to hole and electron injection [2–4], and the introduction of phosphorescent materials [5,6]. However, there is still much scope for further improvements particularly by way of optical out-coupling efficiency – the amount of light produced within a device which escapes as radiation. Most of the light generated within an OLED, typically about 80%, is trapped, and if this could be recovered the overall device efficiency could be significantly enhanced. To date, a number of methods have been investigated with this aim in mind [7–12]. Here we examine how reducing the refractive index of the organic host layer may improve the efficiency with which light is extracted from the device.

The refractive index of a typical organic emissive material is approximately 1.7 (dielectric permittivity, $\varepsilon = 2.89$) within the optical regime. A simple ray model can be used to demonstrate that the pro-

* Corresponding author. Tel.: +44 (0) 1392 264104; fax: +44 (0) 1392 264111.
E-mail address: w.l.barnes@ex.ac.uk (W.L. Barnes).

1566-1199/$ - see front matter
doi:10.1016/j.orgel.2006.07.001

portion of light lost to these waveguide modes may be reduced by using an emissive layer whose refractive index is less than 1.7. For example, considering a structure consisting of air and an organic layer, with a refractive index of 1.7, only light emitted within the cone of ±36° relative to a surface normal may be radiated into air. However, if the index of the organic is reduced to 1.5, the radiation cone increases to ±42°. These escape cones correspond to 40% and 47%, respectively, of the total power dissipated by the emitter.

Different materials whose refractive indices are less than 1.7 are now being used as hosts for organic emitters. A host is a non-emissive material in which emissive organic molecules may be placed. An example of such a host is polystyrene (PS) which is non-polar and produces a high quality film [13]; the ratio of host to emissive molecules used by Yang et al. [13] was 83:17% by weight. The refractive index of PS is 1.58 within the visible spectrum and thus acts to reduce the power dissipated by the emitter into waveguide modes.

Low-index materials may also be used for other OLED layers. For example, Tsutsui et al. [12] used an aerogel layer placed between the indium-tin-oxide (ITO) and silica layers of a substrate-emitting OLED. Aerogel has a very low refractive index of 1.03, and is almost transparent. Within an OLED, this layer decreases the amount of power that is lost to waveguide modes within the thick silica substrate, and as a result the fraction of the total power radiated is increased.

Here we investigate the use of low-index host materials within two types of OLED, substrate- and top-emitters. We focus on the optical out-coupling efficiency and demonstrate the dependence of this efficiency on the index of the host layer.

2. Method

The structures considered for this study are illustrated in Fig. 1. Fig. 1(a) shows a substrate-emitting OLED consisting of an aluminium (Al) cathode, a host layer containing the organic emitters, an ITO anode and a thick silica substrate. The Al cathode is considered to be optically thick for the purposes of the modelling. Fig. 1(b) displays a top-emitting structure consisting of a composite silver (Ag)/ITO anode, a host layer containing the organic emitters, and a composite Ag/ITO cathode. In this structure the Ag part of the anode is taken to be optically thick.

We have considered host materials with refractive indices in the range of $n = 1.0 \rightarrow 1.76$, which corresponds to dielectric permittivities off $\varepsilon = 1.0 \rightarrow 3.1$. By way of example, the emitters placed within the host material are taken to be the first generation *fac-tris*(2-phenylpyridine) iridium-cored dendrimer (Ir–Gl) [14]. For each of the cases studied here the emission spectrum of Ir–Gl has been accounted for, with the results weighted accordingly. The index of the host material is assumed to be dispersionless over the emission range (~450–700 nm). When Ir–Gl is used as an emissive organic material within an OLED it is often mixed with another material, for example 4,4′-bis(*N*-carbazole) biphenyl 3 (CBP). The index of Ir–Gl and CBP mixed 20:80% by weight [14] at the peak emission wavelength of 518 nm is 1.76 ($\varepsilon = 3.1$). We have chosen to represent the dielectric permittivities of Al, Ag and ITO by polynomial functions [15].

To model the structures we make use of a classical technique which calculates the power lost by an emissive dipole in a planar multilayered structure

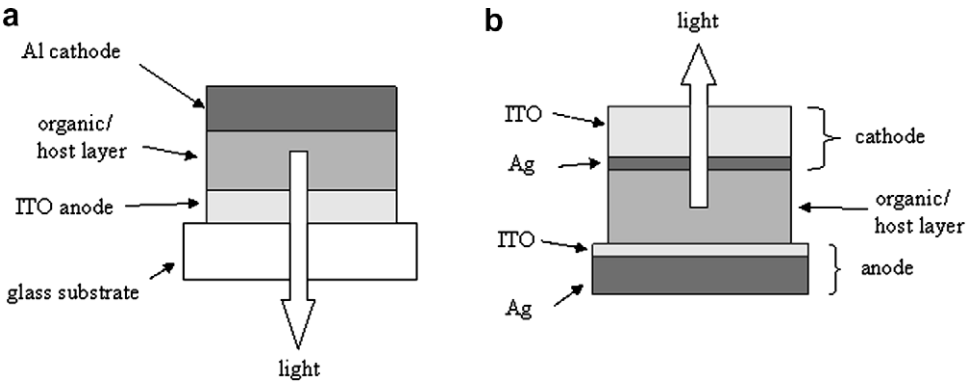

Fig. 1. Schematics of the (a) substrate-emitting and (b) top-emitting OLED structures investigated.

[16–18]. The emitters are considered as forced, damped, electric-dipole oscillators. The dipole field is represented by a sum of plane waves, each wave being characterised by a different in-plane wavevector, k_x, where k_x is the component of the wavevector parallel to the interfaces. The model allows the modes of a given structure to be identified and provides information as to the strength of coupling between the emitter and these modes [16–18]. It can also be used to calculate the percentage of the total power dissipated that may emerge from a structure as useful far-field radiation. This radiated percentage is often referred to as the out-coupling efficiency.

3. Results

For a number of host layer ε values within the range of $1.0 \rightarrow 3.1$, the maximum possible out-coupling efficiency has been calculated for the structures shown in Fig. 1. The optimum dimensions of both the organic and ITO layers, for each ε value, have been determined to the nearest 5 nm, and the radiation from this optimised structure calculated. Plots showing these results are displayed in Fig. 2.

Considering first the substrate-emitters, it may be seen that the power radiated increases significantly as the host layer ε value is reduced. It is apparent from the plot that there are two different regimes. The first, with the organic emissive host layer having $\varepsilon_{org} = 1.0 \rightarrow 2.1$, describes host layers with $\varepsilon_{air} \leqslant \varepsilon_{org} < \varepsilon_{silica}$.

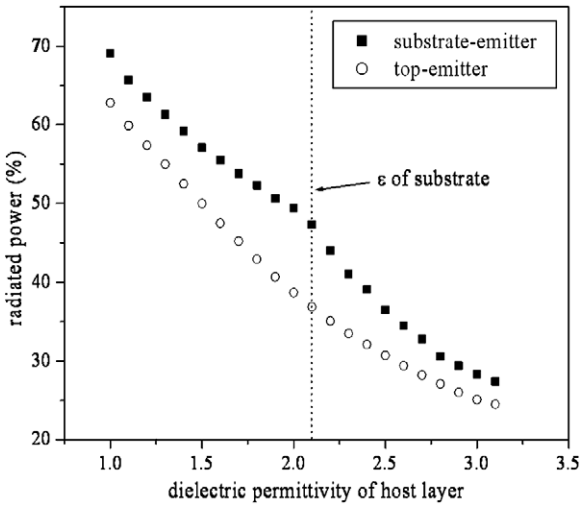

Fig. 2. A plot showing the percentage of the total power radiated (the optical out-coupling efficiency) for the substrate-emitting (■) and top-emitting (○) OLED structures.

The second regime, with $\varepsilon_{org} = 2.1 \rightarrow 3.1$, describes host layers with $\varepsilon_{org} > \varepsilon_{silica}$.

If the host material has $\varepsilon = 1.0$ then the amount of power radiated from the structure reaches 69.1%. With a value of $\varepsilon = 2.0$ this is reduced to 49.4%, and for $\varepsilon = 3.1$ only 27.4% of the power is radiated from the structure. This dramatically demonstrates the potential of lower index host layers to improve optical out-coupling.

In contrast, the data for top-emitters displays only one regime, with the radiated power decreasing as the dielectric permittivity of the host material is increased. It is the lack of a silica layer which leads to this result; the organic host layer is now always of a lower dielectric permittivity than the other structure layers above it (Ag and ITO). In this case, if the host material has $\varepsilon = 1.0$ then the power radiated form the structure may be 62.7%, falling to 38.7% for $\varepsilon = 2.0$% and 24.5% for $\varepsilon = 3.1$.

The structure dimensions required for maximum radiation for each different ε value vary greatly. As the ε value of the host material increases, the cavity thickness decreases. For example, for the substrate-emitting structure, at $\varepsilon = 1.0$ the combined organic/ITO cavity thickness is 385 nm. However, at $\varepsilon = 2.0$ this thickness is 275 nm, and at $\varepsilon = 3.0$ it is only 225 nm. This behaviour is expected as higher ε – valued materials increase the effective cavity width [19]. A cavity consisting of materials with high ε values has a lower cut-off thickness for waveguide modes than a cavity comprising low ε – valued materials. For the top-emitting structures the trend is the same. The combined organic/Ag/ITO cavity thickness for a host layer value of $\varepsilon = 1.0$ is 360 nm. For $\varepsilon = 2.0$ this is 195 nm and for $\varepsilon = 3.0$ it is 170 nm.

In order to gain an understanding of the nature of the modes supported by structures incorporating host layers with differing ε values, it is instructive to examine dispersion diagrams calculated for these structures. Such dispersion diagrams may be produced using the oscillating dipole model [16–18] and display the power dissipated by the emitter as a function of both k_x and angular frequency, ω. Figs. 3(a) and (b) show such plots for ε values of 1.06 and 3.0 respectively for the substrate-emitting structure. The value of $\varepsilon = 1.06$ is equivalent to that of aerogel, a material which might in future perhaps be used as a host. The value $\varepsilon = 3.0$ represents a typical value for organic emitters. It is evident from the plots (Figs. 3(a) and (b)) that the two substrate-emitting systems are very different in nature.

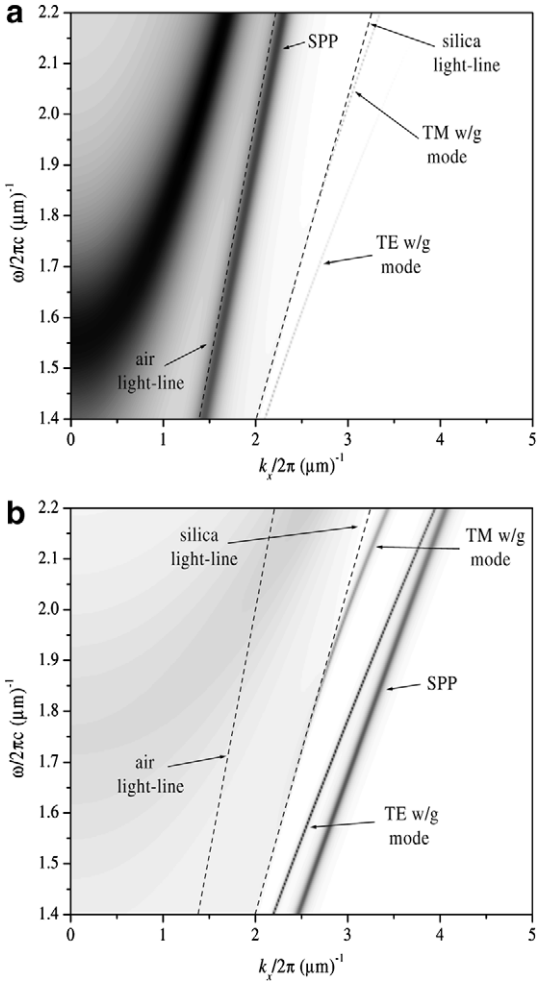

Fig. 3. Dispersion diagrams for the substrate-emitting OLED structure shown in Fig. 1(a) for ϵ values of the host material of: (a) 1.06 and (b) 3.0.

Although both structures support two waveguide modes and one surface plasmon-polariton (SPP) mode the dispersion of these modes varies, and crucially so does the strength with which the emitter couples to them. From Fig. 3(a), showing the modes for a system containing a host with $\varepsilon = 1.06$, the vast majority of the dissipated power lies within the air light-line. The strong feature within this region is a leaky waveguide mode and much of the power lost to this mode emerges from the structure as radiation. The SPP mode in this case is close to the air light-line and will lie just to the right of the host layer light-line. It is the only guided mode within the structure to which a significant amount of power is lost. The two waveguide modes, one TE- and one TM-polarised, are very weak in nature. This is because the k_x values of the photons emitted in the organic layer are low enough that they are not reflected by the silica/ITO interface, thus preventing the formation of a cavity. It may also be noted that for the same reason, a negligible amount of power is trapped within the silica layer.

The reasons for a drop in radiated power when a higher ε – valued material is used may be observed from Fig. 3(b). Using a host with $\varepsilon = 3.0$ leads to sharper, stronger guided modes which account for much of the dissipated power. This means that less power is lost to the left of the light-line than for the structure modelled in Fig. 3(a). A considerable fraction of power is also trapped within the silica substrate in this case as some light produced within the organic layer has k_x values too high to escape this layer.

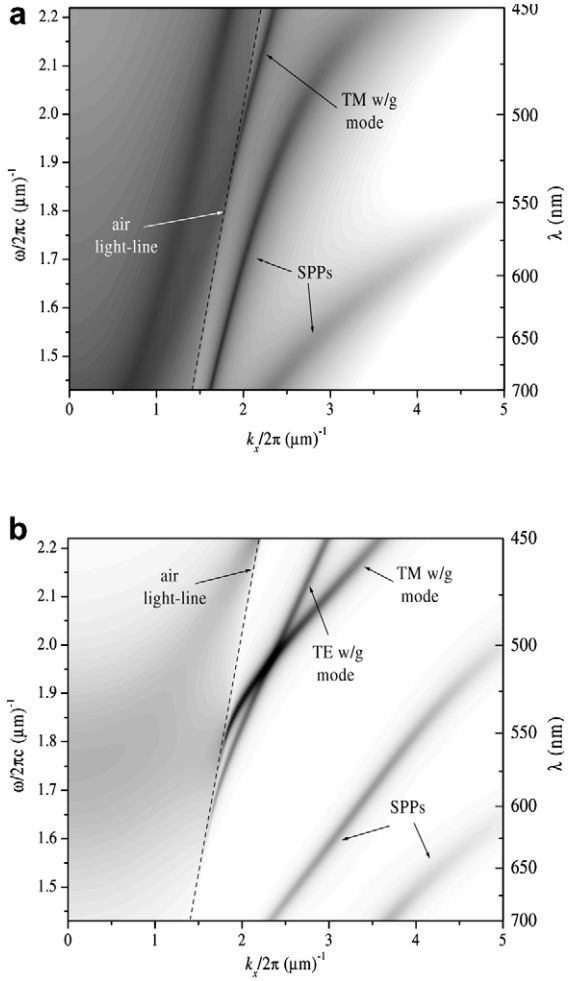

Fig. 4. Dispersion diagrams for the top-emitting OLED structure shown in Fig. 1(b) for ϵ values of the host material of: (a) 1.06 and (b) 3.0. Note that for (a) the z-axis is on a log scale to allow the highest k_x valued SPP mode to be seen.

Fig. 4 shows similar dispersion diagrams but for the top-emitting structure, with (a) and (b) corresponding to host layer ε values of 1.06 and 3.0 respectively. As for the substrate-emitting system, these plots differ greatly from one another. Both structures support two SPP modes which are coupled with respect to the thin Ag cathode layer and are both also influenced by the Ag anode interface. From Fig. 4(a), when $\varepsilon = 1.06$, it may be seen that there is one TM waveguide mode close to the air light-line and another leaky mode within the light-line. It is this leaky mode which provides most of the far-field radiation from this structure and yields the relatively high out-coupling efficiency. When $\varepsilon = 3.0$, Fig. 4(b), both of these modes lie to the right of the light-line and hence are trapped modes. This leads to a lower out-coupling efficiency for this structure.

4. Conclusions

We have investigated the effects of using a low-index material as a host for organic emitters within an OLED. We have considered two types of structure, substrate- and top-emitting OLEDs. For the substrate-emitting structure it was shown that the out-coupling efficiency may be enhanced by up to 2.5 times its value for a standard organic emissive layer by use of a lower index host material. The relationship between radiation and ε is clearly divided into two regimes. For the top-emitting structure a similar 2.6 fold increase in out-coupling efficiency may also be achieved by use of a host material.

This modelling clearly indicates the desirability of keeping the refractive index of the emissive layer as low as possible. This poses a significant materials challenge since none of the emitting materials to date have the low index required. As a result emissive molecules would probably need to be dispersed in a low index host. However, there is then the competing requirement of having a high enough loading of the emissive guest to achieve the desired electrical characteristics. If this problem could be overcome then this material has the potential to increase the efficiency of OLEDs by more than a factor of two over the efficiency of current devices.

Acknowledgements

The authors would like to thank both the EPSRC (through the DTI-link Project XTRAOLED) and CDT for financial support. This work was also supported by ‘‘Surface Plasmon Photonics’’, an EC funded STREP Project, FP6 NMP4-CT-2003-505699.

References

[1] C.W. Tang, S.A. VanSlyke, Appl. Phys. Lett. 51 (1987) 913.
[2] S.A. VanSlyke, C.H. Chen, C.W. Tang, Appl. Phys. Lett. 69 (1996) 2160.
[3] J.S. Kim, R.H. Friend, F. Cacialli, Appl. Phys. Lett. 74 (1999) 3084.
[4] N.C. Greenham, S.C. Moratti, D.D.C. Bradley, R.H. Friend, A.B. Holmes, Nature 365 (1993) 628.
[5] M.A. Baldo, D.F. O’Brien, Y. You, A. Shoustikov, S. Sibley, M.E. Thompson, S.R. Forrest, Nature 395 (1998) 151.
[6] J.P.J. Markham, S.-C. Lo, S.W. Magennis, P.L. Burn, I.D.W. Samuel, Appl. Phys. Lett. 80 (2002) 2645.
[7] I. Schnitzer, E. Yablonovitch, C. Caneau, T.J. Gmitter, A. Scherer, Appl. Phys. Lett. 63 (1993) 2174.
[8] J.M. Lupton, J. Matterson, I.D.W. Samuel, M.J. Tory, W.L. Barnes, Appl. Phys. Lett. 77 (2000) 3340.
[9] P.T. Worthing, W.L. Barnes, Appl. Phys. Lett. 79 (2001) 3035.
[10] T. Yamasaki, K. Sumioka, T. Tsutsui, Appl. Phys. Lett. 76 (2000) 1243.
[11] C.F. Madigan, M-H. Lu, J.C. Sturm, Appl. Phys. Lett. 76 (2000) 1650.
[12] T. Tsutsui, M. Yahiro, H. Yokogawa, K. Kawano, M. Yokoyama, Adv. Mater. 13 (2001) 149.
[13] J.P. Yang, Y.D. Jin, P.L. Heremans, R. Hoefhagels, P. Dieltiens, F. Blockhuys, H.J. Geise, M. Van der Auweraer, G. Borghs, Chem. Phys. Lett. 325 (2000) 251.
[14] T.D. Anthopoulous, J.P.J. Markham, E.B. Namdas, I.D.W. Samuel, S.-C. Lo, P.L. Burn, Appl. Phys. Lett. 82 (2003) 4824.
[15] L.H. Smith, J.A.E. Wasey, I.D.W. Samuel, W.L. Barnes, Adv. Func. Mat. 15 (2005) 1839.
[16] G.W. Ford, W.H. Weber, Phys. Rep. 113 (1984) 195.
[17] W.L. Barnes, J. Mod. Opt. 45 (1998) 661.
[18] J.A.E. Wasey, W.L. Barnes, J. Mod. Opt. 47 (2000) 725.
[19] H. Benisty, H. De Neve, C. Weisbuch, IEEE J. Quantum Electron. 34 (1998) 1612.

Available online at www.sciencedirect.com
ScienceDirect
Organic Electronics 7 (2006) 495–499
Organic Electronics
www.elsevier.com/locate/orgel

Charge transport properties of a metal-free phthalocyanine discotic liquid crystal

C. Deibel [a,*], D. Janssen [a], P. Heremans [a,1], V. De Cupere [b], Y. Geerts [b], M.L. Benkhedir [c], G.J. Adriaenssens [c]

[a] *IMEC, Kapeldreef 75, 3001 Leuven, Belgium*
[b] *Laboratoire de Chimie des Polymères, CP 206/1, Université Libre de Bruxelles, Boulevard du Triomphe, 1050 Bruxelles, Belgium*
[c] *Laboratorium voor Halfgeleiderfysica, University of Leuven, 3001 Leuven, Belgium*

Received 11 November 2005; received in revised form 19 June 2006; accepted 11 July 2006
Available online 7 August 2006

Abstract

Discotic liquid crystals can self-align to form one-dimensional semiconducting wires, many tens of microns long. In this letter, we describe the preparation of semiconducting films where the stacking direction of the disc-like molecules is perpendicular to the substrate surface. We present measurements of the charge carrier mobility, applying temperature-dependent time-of-flight transient photoconductivity, space-charge limited current measurements, and field-effect mobility measurements. We provide experimental verification of the highly anisotropic nature of semiconducting films of discotic liquid crystals, with charge carrier mobilities of up to 2.8×10^{-3} cm^2/V s. These properties make discotics an interesting choice for applications such as organic photovoltaics.

PACS: 73.23.−b; 81.16.Dn; 83.80.Xz

Keywords: Discotic liquid crystals; Self-assembly; Electronic transport; Mobility

1. Introduction

Discotic liquid crystals (DLC) are molecules with a disc-shape core that is conjugated, surrounded by aliphatic chains to render them liquid-crystalline [1]. The pi-orbitals of the core house delocalized electrons and extend perpendicular to the plane of the disc. Due to the natural tendency of pi-orbitals of adjacent molecules to maximally overlap, the molecules can self-align into columnar molecular stacks, resulting in the formation of one-dimensional semiconductor wires. Such a wire is surrounded by entangled aliphatic chains of all the molecules, forming an insulating sheet around the semiconducting wire. A film of ordered columns is expected to exhibit a highly anisotropic mobility: very high compared to disordered organic materials along the columns and very low perpendicular to the columns. This is an attractive feature for many

* Corresponding author.
E-mail addresses: Carsten.Deibel@physik.uni-wuerzburg.de (C. Deibel), heremans@imec.be (P. Heremans).
[1] Tel.: +32 16 281521.

1566-1199/$ - see front matter © 2006 Elsevier B.V. All rights reserved.
doi:10.1016/j.orgel.2006.07.002

applications, as in most semiconductor devices, be it transistors, solar cells or light-emitting diodes, it is the intention to provide electrical conduction in a single direction, and isolation in perpendicular directions [1–3].

The mobility of discotic liquid semiconducting materials is typically determined using time-of-flight photoconductivity measurements [4,5]. Reports on space-charge limited current mobilities of these materials [6], where also charge carrier injection has to be considered, are scarce. We were not able to find a combination of both complementary methods in literature.

In this letter, we present the realization and characterization of semiconducting devices of aligned discotic liquid crystalline columns between two planparallel electrodes. Such configuration with the columns perpendicular to the electrode surfaces corresponds to the architecture of relevant organic semiconductor devices such as organic light-emitting diodes and organic solar cells.

2. Experimental

The discotic liquid crystal material we used is the discotic 2(3), 9(10), 16(17), 23(24)-tetra(2-decyltetradecyloxy)-phthalocyanine, abbreviated $H_2Pc(OC14,10)_4$, and shown in Fig. 1(a).

The synthesis of the $H_2Pc(OC14,10)_4$ molecule is described elsewhere [7]. Differential scanning calorimetry shows two phase transitions above room temperature: a transition from the liquid crystalline columnar rectangular to columnar hexagonal phase at 333 K, and the transition to the isotropic phase in the melt at 453 K. A highly ordered liquid-crystalline columnar phase can be attained by heating the material to the isotropic melt and then slowly cooling to room temperature to induce self-alignment of molecular stacks. Further interesting properties of the selected material are that it is processable from solution, and that the peak absorption wavelength is between 600 and 700 nm, quite adequate for photovoltaic applications. In order to realize films with homeotropic alignment (i.e., with the column axes normal to the substrate), we proceeded as follows. Two glass substrates with indium-tin oxide (ITO) contacts of varying width were separated by SiO_2 beads, chosen 3 or 5 μm diameter, as shown in Fig. 1(b). The phthalocyanine discotic was applied to the edge of this sample cell. Heating to 456 K into the isotropic phase lead to capillary action, the liquid H_2Pc $(OC14,10)_4$ filled the space between the ITO substrates. The sample was usually cooled at a rate of 1 K/min to 426 K, then with approx. 20 K/min back to room temperature. Optical microscopy with crossed polarizers revealed a homeotropic alignment of the discotics between the ITO plates, as seen in Fig. 1(c). The micrograph also shows birefringent defect lines typical for homeotropic alignment [8], and SiO_2 spacers. One set of samples was prepared with ITO plates coated with an Octadecyltrichlorosilane (OTS) monolayer by deposition from vapor phase. With this pretreatment, the DLC alignment tends to be homogenous (i.e., column axes parallel to the substrate) and/or random rather than homeotropic, as indicated by optical microscopy. Measurements of conduction perpendicular to the column stacking direction were not only performed on the OTS samples: for verification, we prepared field effect transistor (FET) samples on SiO_2 (100 nm)/Si/Al substrates with Au bottom-contact. In one set of samples, the DLC was sandwiched between a glass plate and the FET substrate (both not OTS-treated), and aligned homeotropically as described above. As in FET structures the conduction channel is along the substrate, and the DLC was aligned homeotropically, conduction perpendicular to the column stacking direction is looked at, yielding ideally very low currents. We also tried to prepare FET structures for measuring the DLC mobility along the discotic columns by means of different surface treatments, but did not succeed yet. A second set of FET samples was prepared by spin coating the DLC from solution (20 mg/ml, solvent: toluene) on top of Au bottom-contact structures.

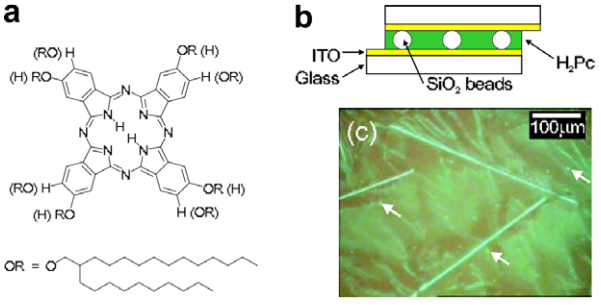

Fig. 1. (a) The molecular structure of $H_2Pc(OC14,10)_4$, (b) symmetric sample cell and (c) cross-polarized microscopy of a filled sample cell shows homeotropic alignment of the DLC. Three birefringent defect lines and the SiO_2 spacers, some of them indicated by arrows, are also visible.

On the glass/ITO/DLC/ITO/glass samples, we performed frequency-dependent capacitance measurements using an HP 4275 LCR meter, and esti-

mated the device thickness L from the capacitance C at 1 MHz frequency

$$L = \frac{\varepsilon\varepsilon_0}{C}. \quad (1)$$

Here, ε_0 is the vacuum permittivity. In Eq. (1), we assumed the equivalence of our samples to a parallel plate capacitor filled with a medium (the discotic) with a dielectric constant ε of 3. This value is a commonly used estimate for organic materials. For triphenylenes, $\varepsilon \approx 2.5$ was reported [3]. For verification of the device thickness, we checked the SiO_2 bead distribution under an optical microscope, which supplies a lower limit.

The temperature-dependent current–voltage measurements as well as the FET measurements were performed using an HP 4156 C parameter analyzer with the device on a hotstage. The DLC deposition, and the capacitance and current–voltage measurements were performed in N_2 atmosphere, optical microscopy was done in air. In the time-of-flight setup [9], pulsed light with a wavelength of 660 nm and a pulse width of 6 ns was obtained from an LSI nitrogen laser with dye cell attachment. The photocurrent signals were recorded on an Iwatsu 8132 digitizing storage oscilloscope. An HP 214B pulse generator was used as a bias voltage source. The sample was held on a temperature-controlled metal support in a vacuum chamber.

3. Results and discussion

3.1. Space-charge limited current measurements

The space-charge limited current measurements were performed on the glass/ITO/DLC/ITO/glass samples. The effect of homeotropic alignment on the charge transport is demonstrated by the current–voltage measurements shown in Fig. 2. A homeotropically aligned $H_2Pc(OC14,10)_4$ sample cell is compared to a sample with OTS treated ITO plates, the latter showing a partly homogenous, partly homeotropic alignment by optical microscopy with crossed polarizers. As in this latter sample the charges partly have to be transported perpendicular to the molecular columns, the current density is at least two orders of magnitude lower than for the case of completely homeotropic alignment, indicating a high electrical anisotropy. From the current–voltage characteristics, we determined space-charge limited current (SCLC) mobilities in cases where

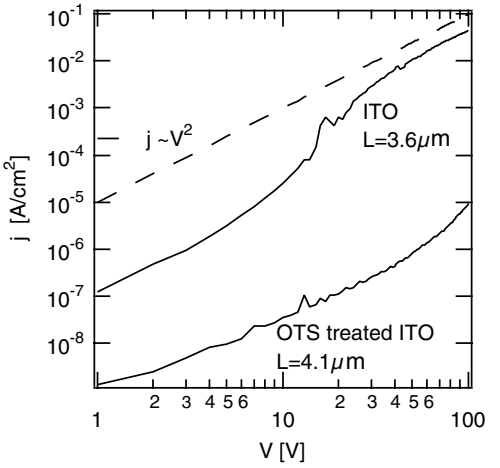

Fig. 2. Current density–voltage characteristics of a two sample cells filled with $H_2Pc(OC14,10)_4$, one of them with OTS-treated ITO.

the measurements obey the Mott–Gurney law for trap-free SCLC

$$j = \frac{9}{8}\varepsilon\varepsilon_0\mu\frac{V^2}{L^3}, \quad (2)$$

where j is the current density at the voltage V, μ denotes the drift mobility, L denotes the sample thickness, and $\varepsilon\varepsilon_0$ the electric permittivity of the DLC. The temperature-dependent current–voltage measurements of an $H_2Pc(OC14,10)_4$ sample cell (Fig. 3) show the characteristic $j \propto V^2$ behaviour. At lower temperatures and intermediate voltages,

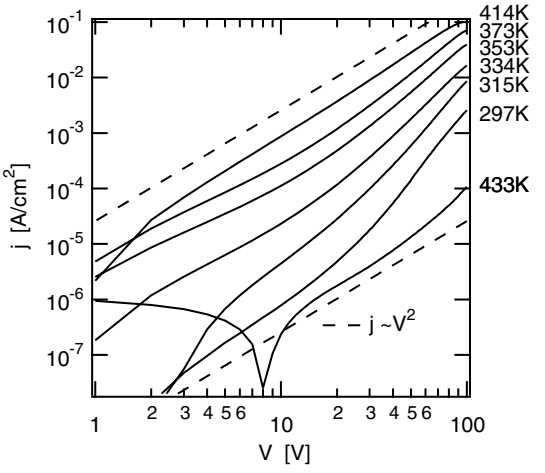

Fig. 3. Temperature-dependent current density–voltage characteristics of an $H_2Pc(OC14,10)_4$ sample cell (sample thickness 5.0 μm). The shifted zero-crossing of the curve at 433 K temperature is due to hysteresis.

a slope larger than two indicates an energy-distributed defect state. At higher temperatures, trap-free SCLC can be observed over the whole voltage range measured. The mobilities extracted from SCLC measurements range from 7×10^{-4} cm^2/V s at room temperature to about 4×10^{-3} cm^2/V s at 414 K. The difference of these two values is probably mainly due to the susceptibility of the SCLC method to injection barriers [10,11]. The higher one corresponds to the true SCLC mobilities, the values being comparable to SCLC mobilities measured on CuPc DLC Langmuir–Blodgett films [6].

3.2. Field effect transistor measurements

As we can neither exclude a possible influence of the OTS monolayer as charge injection barrier, nor possess the means to properly quantify the influence of the OTS treatment on the stacking direction of the discotic columns, we performed measurements on two different types of FET samples for verification (not shown). The first set of samples consists of a homeotropically aligned DLC sandwiched between the FET substrate and a cover glass (channels of 3 μm length and 1 mm width). As the current in FET structures flows from source to drain along the surface of the dielectric layer, we were able to investigate conduction perpendicular to the discotic columns. The resulting source-drain currents were of the order of 10^{-12} A for drain and gate voltages of up to −40 V. No clear gate voltage dependence, and thus no transistor action, could be observed. A second set of FET samples was prepared by spin-coating the DLC from solution on FET substrates, yielding amorphous films (channels of 10 μm length and 1 mm width). These structures had very low source-drain currents of the order of 10^{-10}A, but clearly exhibited typical transistor output and transfer characteristics. The latter are shown in Fig. 4. The shape of the FET characteristics indicates that contact resistances are present, but not dominant. From the saturation regime, we determined FET mobilities of about 10^{-7} cm^2/V s. This low value is mainly due to the disordered nature of the spin-coated film.

The FET measurements illustrate that charge transport perpendicular to the DLC columns is limited mainly by the anisotropic charge transport properties rather than injection barriers. On basis of these results we also feel justified to rule out a dominant contribution of ionic conduction. The space-charge limited current and FET measurements clearly demonstrate a strong anisotropy of the charge transport properties, in dependence of the stacking direction of the discotics.

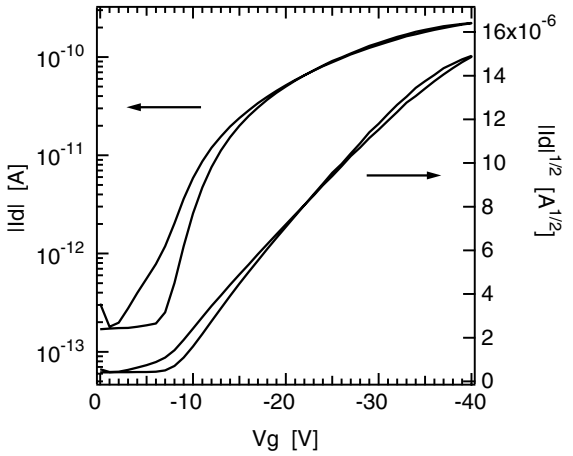

Fig. 4. Transfer characteristics in the saturated regime of a disordered $H_2Pc(OC14,10)_4$ field effect transistor, spin-coated from solution.

3.3. Transient photoconductivity

In the time-of-flight transient photoconductivity measurements, charge carriers were photogenerated by a laser pulse at one electrode of the glass/ITO/DLC/ITO/glass device, and drifted to the other electrode due to an external field. The corresponding displacement current for holes is shown in Fig. 5. From the measured photocarrier transit time τ, we determined the mobility μ using

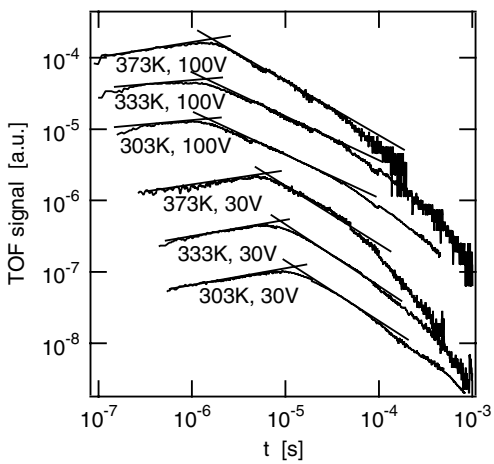

Fig. 5. Time-of-flight transient photocurrents of an $H_2Pc(OC14,10)_4$ sample cell (sample thickness 6.7 μm). The curves were y-shifted for clarity.

$$\mu = \frac{L^2}{V\tau} \quad (3)$$

where L is the device thickness. For an applied voltage V of 30 V, the hole mobilities ranged from 1.0×10^{-3} cm^2/V s at 303 K to 2.6×10^{-3} cm^2/V s at 373 K. At 100 V, the hole mobilities were between $(2.6–2.8) \times 10^{-3}$ cm^2/V s. Upon changing the polarity of the external field in order to measure electron mobilities, the transient photocurrents were too low to be detected with our setup. For the $H_2Pc(OC14,10)_4$ sample cell with OTS treated ITO electrodes, we also could not measure any photocurrents, supporting the results of the SCLC and FET methods that the mobility perpendicular to the columns is much lower than along them.

3.4. Discussion

The determined values for the hole mobility along the DLC columns using the transient photoconductivity method agree very well with the mobilities we observed using the SCLC method. As the dependence of the mobility determined by these two experimental methods is quite different with respect to voltage and sample thickness, the agreement indicates that the values for the sample thickness calculated using an estimated dielectric constant of three are approximately correct. Furthermore, the results support the suggestion that the lower apparent mobilities observed in the SCLC experiments at room-temperature are influenced by contact-limited injection. The $H_2Pc(OC14,10)_4$ hole mobilities determined by us correspond well with time-of-flight mobilities measured recently on a CuPc DLC [5]. However, in publication [5] electron mobilities of a similar order of magnitude were stated. Similarly, single-crystalline derivatives of phthalocyanines show comparable electron and hole mobilities [12]. As of yet, we were not able to explain this discrepancy.

We would like to point out that the charge carrier mobilities presented here were determined by experimental techniques in the low carrier concentration regime, such as SCLC and TOF. These measurements are more susceptible to charge trapping as, for instance, FET and pulse-radiolysis time-resolved microwave conductivity measurements [13], and can therefore yield orders of magnitude lower mobilities.

Our measurements comparing charge transport along and perpendicular to the DLC columns clearly demonstrate a strong anisotropy of the charge transport properties, in dependence of the stacking direction of the discotics.

4. Conclusions

We have fabricated devices of homeotropically aligned discotic liquid crystal material, and characterized the mobility using time-of-flight photoconductivity and space-charge limited current measurements. The mobility along the columns of discotic molecules attains up to 2.8×10^{-3} cm^2/V s in homeotropic alignment and is at least two orders of magnitude lower for transport perpendicular to the columns.

Acknowledgements

This work was performed in the framework of the Soltex project. The authors would like to thank V. Arkhipov for discussions, and S. Put and S. Schols for performing some of the current–voltage measurements.

References

[1] R. Chandrasekhar, S. Krishna Prasad, Contemp. Phys. 40 (1999) 237.
[2] L. Schmidt-Mende, A. Fechtenkötter, K. Müllen, E. Moons, R.H. Friend, J.D. MacKenzie, Science 293 (2002) 1119.
[3] N. Boden, R.J. Bushby, J. Clements, B. Movaghar, J. Mater. Chem. 9 (1999) 2081.
[4] D. Adam, F. Closs, T. Frey, D. Funhoff, D. Haarer, H. Ringsdorf, P. Schuhmacher, K. Siemensmeyer, Phys. Rev. Lett. 70 (1993) 457.
[5] H. Fujikake, T. Murashige, M. Sugibayashi, K. Ohta, Appl. Phys. Lett. 85 (2004) 3474.
[6] C.L. Donley, R.A.P. Zangmeister, W. Xia, B. Minch, A. Drager, S.K. Cherian, L. LaRussa, B. Kippelen, B. Domercq, D.L. Mathine, D.F. O'Brian, N.R. Armstrong, J. Mater. Res. 19 (2004) 2087.
[7] J. Tant, Ph.D. thesis, Université Libre de Bruxelles, 2004.
[8] J.F. van der Pol, E. Neeleman, J.W. Zwikker, R.J.M. Nolte, W. Drenth, J. Aerts, R. Visser, S.J. Picken, Liq. Cryst. 6 (1989) 577.
[9] G.F. Seynhaeve, R.P. Barclay, G.J. Adriaenssens, J.M. Marshall, Phys. Rev. B 39 (1989) 10196.
[10] R.W.I. de Boer, M. Jochemsen, T.M. Klapwijk, A.F. Morpurgo, J. Appl. Phys. 95 (2004) 1196.
[11] J. Reynaert, V.I. Arkhipov, G. Borghs, P. Heremans, Appl. Phys. Lett. 85 (2004) 603.
[12] G.A. Cox, P.C. Knight, J. Phys. C Solid State Phys. 7 (1974) 146.
[13] A.M. van de Craats, J.M. Warman, M.P. de Haas, D. Adam, J. Simmerer, D. Haarer, P. Schuhmacher, Adv. Mat. 8 (1996) 823.

Available online at www.sciencedirect.com
ScienceDirect
Organic Electronics 7 (2006) 500–507
Organic Electronics
www.elsevier.com/locate/orgel

Non-destructive patterning of conducting-polymer devices using subtractive photolithography

C. Balocco, L.A. Majewski, A.M. Song *

School of Electrical and Electronic Engineering, University of Manchester, Sackville Street Building, Room D31, Manchester M60 1QD, UK

Received 23 January 2006; received in revised form 6 July 2006; accepted 18 July 2006
Available online 22 August 2006

Abstract

We demonstrate a non-destructive, high-throughput, and high-resolution lithographic patterning method to fabricate organic-semiconductor devices based on UV lithography with the standard equipment of well-established silicon technology. The method is applied to fabricate poly(3-hexylthiophene) (P3HT)-based organic thin-film transistors (OTFTs) with high yield. Patterns with features down to 2 μm are reproducibly demonstrated. We show that a few modifications in the processing steps are necessary in order to spin-coat photoresist onto P3HT films and to completely remove P3HT residues on the substrates that have been treated with a self-assembled monolayer. Compared with OTFTs whose P3HT channels are not patterned, the on/off ratio of the patterned devices is improved by over four orders of magnitude from about 70 to 10^6, because of the dramatically reduced gate leakage current. The extracted carrier mobility is not only virtually unchanged after the lithography processes, but also as high as 0.027 cm^2/V s. Both the on/off ratio and the mobility are among the best reported values in P3HT-based OTFTs fabricated and measured in ambient conditions.

PACS: 81.05.Lg; 85.40.Hp; 73.61.Ph; 85.30.Tv; 73.40.Cg

Keywords: Conducting polymer; Lithography; P3HT; Organic thin-film transistors

1. Introduction

Since the first report of metallic conductivities in polyacetylene in 1977 [1], the industrial and academic interest in what is now known as ''plastic (opto-)electronics'' has grown rapidly. A number of distinctive advantages, particularly the potentially very low cost enabled by solution-processable conducting polymers, make organic devices real competitors for amorphous-silicon-based devices, and a huge market share has been envisioned in the future. Among the most promising applications are flexible displays and disposable radio-frequency identification tags (RFIDs). For these applications, remarkable progresses have been made in organic thin-film transistors (OTFTs) [2–8], photodiodes [9,10], and light-emitting diodes [11–15]. One of the necessary steps in the development of OTFTs is the patterning of the active semiconducting material. This is required in order to reduce leakage

* Corresponding author. Tel.: +44 161 200 4762; fax: +44 161 200 4770.
E-mail address: a.song@manchester.ac.uk (A.M. Song).

1566-1199/$ - see front matter © 2006 Elsevier B.V. All rights reserved.
doi:10.1016/j.orgel.2006.07.009

currents, crosstalk between individual devices, unwanted parasitic capacitance, and to increase the much-needed operational speed (current devices mostly operate around or below KHz frequencies). The most common patterning techniques developed so far include screen printing [16], ink-jet printing [17,18], lithographic stamping [19,20], photochemical crosslinking [21], and nanoimprint [22–24]. Despite these methods, conducting polymers in OTFTs reported to date are often not patterned, largely because of the lack of non-standard equipment and methods. Even though ink-jet printing is one of the most promising choices for future organic electronics, it is a serial process and the achievable feature dimensions are limited by the size of the droplets, which is typically around tens of micrometers [25].

Ultraviolet (UV) photolithography is a well-established technology in the silicon electronics industry, and has been used to manufacture ~100-nm-sized structures with very high yield and throughput. It is desirable to extend the technology to plastic electronics because of the availability of the standard equipment and established lithography processes in industry and university laboratories. Even though UV lithography has been used to pattern small-molecule semiconductors [26], it was reported that some common chemicals used, such as acetone, could affect the carrier mobility. However, little has been reported about applications of UV lithography for patterning conjugated polymers such as the well-studied regioregular poly(3-hexylthiophene) (rr-P3HT) [7,27]. Recently, we developed an additive lithographic technique, by coating a P3HT film on a patterned photoresist film and then performing lift-off in a mixture of one part of acetone and four parts of methanol [28]. The method can be applied generally to both small molecules and conducting polymer materials since UV exposure to the conducting polymer film was prevented throughout the lithography processes. P3HT structures as fine as 1 μm were fabricated with high yield. However, P3HT solutions had to be made using a special solvent, xylene, rather than common solvents such as chloroform, toluene, etc., in order to avoid reactions between the solvent and photoresist. This led to a rather low hole-mobility in P3HT of about 5×10^{-4} cm^2/V s, as would be expected since the carrier mobility in P3HT is sensitively dependent on the choice of solvent [29,30].

Here we develop a new method based on UV lithography, which is a subtractive approach for patterning P3HT. Since the photoresist is applied after the P3HT film has been completely dried, any P3HT solvent can be used. As a result, the extracted carrier mobility in the fabricated OTFTs reaches 0.027 cm^2/V s. An on/off ratio as high as 10^6 is also obtained. Although excellent performance was achieved earlier in unpatterned P3HT OTFTs in controlled environments [30,31], the mobility and on/off ratio reported in this work are among the best in P3HT-based OTFTs fabricated and measured in ambient conditions. Another important advantage of the subtractive process is the ability to pattern the organic film without the need to expose the substrate to any chemicals, which may be crucial if a self-assembled monolayer (SAM), e.g., hexametyldisilazane (HMDS) or *n*-octadecyltrichlorosilane (OTS), is adopted to improve the OTFT performance. The method also offers better-defined pattern edges, because the removal of unwanted P3HT areas is by etching (dissolving) rather than by mechanical tearing which typically results in edges bending upward with sharp features. A rough edge is not important for most organic devices but can become problematic for micron- or nano-sized structures. We show patterns as small as 2 μm are produced with high yield. We fabricate bottom-contact P3HT OTFTs and find over four orders of magnitude improvement in the on/off ratio and gate leakage current over the OTFTs whose P3HT channels are not patterned. The mobility in the saturated regime is found to be virtually unchanged before and after the P3HT patterning, confirming that no obvious degradation of the material quality has been induced during the processes. Our results also reveal that the poor on/off ratios of unpatterned P3HT-based OTFTs fabricated in air are mainly a result of the (vertical) gate leakage current rather than (in-plane) spurious current within the P3HT film.

2. Experiments

Conventional bottom-contact OTFTs were fabricated in order to test the field-effect carrier mobility before and after patterning, and hence identify any degradation of P3HT during the lithography. Highly-doped silicon wafers with a thermally-grown SiO_2, 61 nm thick as determined by separate capacitance measurements, were used as the substrates. Gold source and drain electrodes, 50 nm thick, were evaporated and then defined by the standard photolithography and lift-off. A self-assembled

monolayer, OTS, was employed in some of the substrates to improve the interface between SiO_2 and P3HT. The OTS deposition was carried out by immersing the substrates in 10^{-3} M of OTS in cyclohexane at a temperature of 5 °C for an hour, followed by baking at 200 °C for 10 min in order to remove water molecules and to finish the OTS polymerization. Regioregular P3HT (more than 98.5% head-to-tail coupling) was obtained from Aldrich, and reduced by hydrazine. P3HT solutions of 1% weight in p-xylene or 1,2,4-trichlorobenzene (TCB) were spun at 4000 rpm for 120 s onto the substrates, which led to films about 20 nm thick on bare SiO_2 and about 50 nm on SiO_2 treated with OTS due to different surface hydrophobicities. The OTFTs were annealed at 100 °C for 1 h in nitrogen gas flow in order to improve the degree of crystallinity of the P3HT films and hence also the carrier mobility [32]. Since we found that the high boiling-point solvent TCB led to a higher carrier mobility [33], the results made from TCB-based P3HT solutions are presented here. Xylene-based P3HT solutions yielded to a lower carrier mobility but produced very similar results in terms of the pattern definition. Apart from SiO_2 substrates, some experiments were also performed on mica, which showed very similar pattern definitions.

The patterning processes mainly consist of spin coating photoresist onto a P3HT film, development of the photoresist, and the removal of P3HT in the so-uncovered areas, as sketched in Fig. 1. The photoresist S1813 from the Microposit S1800 series, purchased from Shipley, was chosen, which is among the most commonly available photoresists and can be processed with well-established methods. However, since the photoresist was designed to coat hydrophilic surfaces, it was not possible to spin coat S1813 directly onto the P3HT film, which has a highly hydrophobic surface. We therefore warmed up the S1813 in a sealed bottle on a hotplate at 90 °C, and then immediately spun at 4000 rpm for 60 s onto the P3HT film (Fig. 1(B)). The increased temperature reduced the surface tension of the photoresist solution [34], which was evidenced by the

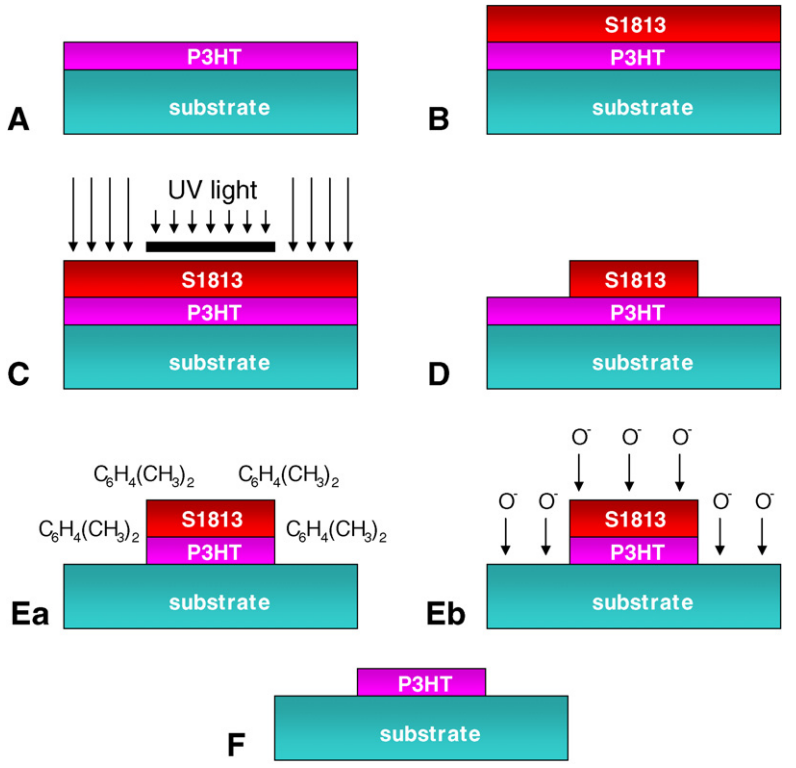

Fig. 1. Schematic diagrams of the lithographic processes to pattern a P3HT film: (A) P3HT film formed by spin coating onto the substrate; (B) photoresist S1813 spun onto the P3HT layer after being warmed at 90 °C; (C) the photoresist exposed by UV as in the conventional photolithography; (D) after the development of the photoresist; (E) the uncovered P3HT layer removed by either wet etching in xylene (Ea) or oxygen plasma ashing (Eb); (F) the photoresist stripped off with acetone and methanol.

clear improvement of the wettability and the much better coverage on the P3HT film surface. The obtained photoresist layer thickness was 1.5 μm, as measured with a Tallystep profilometer. In comparison, the photoresist thickness is about 1.3 μm if is spun onto a normal SiO_2 substrate under the same spin-coating conditions, which reflected the difference in the surface hydrophobicity.

After spin-coating photoresist the sample was soft-baked on a hotplate at 40 °C for 10 min. We found that a baking temperature higher than 90 °C normally led to the cracking of the P3HT film, when it was covered by the S1813, which could be due to a difference in the thermal expansion and/or possible relaxation of an incompletely-dried P3HT film when the remaining P3HT solvent continued to evaporate off the film. The photoresist was then exposed to UV light through a mask (Fig. 1(C)), followed by the development in a 1:1 solution of Microposit developer, also purchased by Shipley, and deionised water (Fig. 1(D)). The P3HT in the areas that were covered by the mask during the UV exposure was not damaged by the UV light. Although it has been reported that UV radiation at high doses could crosslink P3HT molecules and make the film insoluble [35], our experiments showed that P3HT in the areas that were exposed could still be removed unless an OTS surface treatment had been carried out on the substrate. This suggests that the typical exposure (about 150 mJ/cm^2) was not enough to cause serious cross-linking. Furthermore, the photoresist on top of the P3HT film might have absorbed much of the UV light. The P3HT film in the areas that photoresist was removed during the development was then etched (dissolved) in xylene for 5 s (Fig. 1(Ea)), followed by a rinse in acetone, which stopped the xylene etching and stripped off the photoresist (Fig. 1(F)). The sample was then rinsed in methanol and blow-dried with anhydrous nitrogen, leaving only the patterned P3HT structures on the substrate.

Xylene was chosen as the etching solvent because of its high boiling point. The low evaporation rate assured that not much P3HT residual was formed. We also investigated other high-boiling-point solvents, namely TCB and chlorobenzene, but they typically led to a serious undercut of the P3HT film, most likely due to the swelling of the photoresist and the diffusion of the solvents between layers, which hampered the resolution of the proposed method. These high-boiling-point solvents, however, could be used to prepare P3HT solutions, even though they were not suitable in the etching process.

It was found that the P3HT film was not completely removed by xylene if the substrate had been functionalized with OTS. In this case the P3HT film in unwanted areas was removed by a quick oxygen-plasma ashing after the development of the photoresist (Fig. 1(Eb)). The chamber pressure during the ashing process was kept at 60 mtorr with an oxygen flow of 50 sccm. The sample was ashed for 30 s at a power of 30 W. The photoresist was then stripped off with acetone and rinsed in methanol as in Fig. 1(F).

Fig. 2 shows the microphotographs of grid-like patterns that were transferred to a P3HT film. The sizes of the holes (brighter areas) are 10 μm, 5 μm, and 2 μm in Fig. 2(B)–(D), respectively. The 2 μm grid shows dots instead of squares, which was due to the limit of our lithography equipment rather than a problem during the process, since it can also be seen in the patterned photoresist S1813 in Fig. 2(A). The difference in the contrast between the patterned P3HT and patterned S1813 was due to the large difference in the film thicknesses: about 50 nm for P3HT and 1.5 μm for the photoresist.

One of our test devices, consisting of a 10 μm-wide Hall-bar structure fabricated on a mica substrate, is shown in Fig. 3. The Au ohmic contacts in Fig. 3(A) were defined by the conventionally photolithography followed by lift-off, and a 20 nm-thick P3HT active layer was patterned using the above lithographic method. Fig. 3(B) is an atomic-force microscope (AFM) image of the P3HT bar, which shows that the obtained P3HT structure had smooth edges. This is in contrast to P3HT structures produced by the lift-off (additive) lithographic method [28], which typically results in edges bending upward with sharp features because the removal of unwanted P3HT areas is by mechanical tearing rather than by etching (dissolving).

Fig. 4 shows the sketches (A and C) and the transfer characteristics (B and D) of two OTFTs, one without and the other with the P3HT patterning. As can be seen from the layouts, after patterning, the OTFT channel width was slightly reduced from 2.3 mm (A) to 2.0 mm (C), in order to simplify the mask alignment. The channel length was 75 μm in both OTFTs, as defined by the distance between the two ohmic contacts. Photos of the devices could not be taken since the OTFTs were much bigger than the largest optical field of our microscope. Without

patterning the P3HT film, the on/off ratio of the device was only about 70 as shown in the transfer characteristic in Fig. 4(B). The output characteristic of the device is plotted in Fig. 5(A), which was clearly dominated by the gate leakage current. The leakage current was in the order of μA within the ranges of the negative gate and source-drain voltages in our experiments. This means that the low on/off ratio in Fig. 4(B) was mainly due to the gate leakage current, which is understandable because it was integrated over the entire P3HT film area on the substrate. The large leakage current also means that the threshold voltage of the unpatterned OTFT was not around −7 V. Furthermore, it was observed that doped P3HT films caused the leakage current through a silicon oxide substrate to increase by a few orders of magnitude [36]. This might explain the large leakage current observed here, since the P3HT film was slightly doped during our fabrication in air as evidenced by the positive threshold in the patterned P3HT OTFT in Fig. 4(D). The leakage

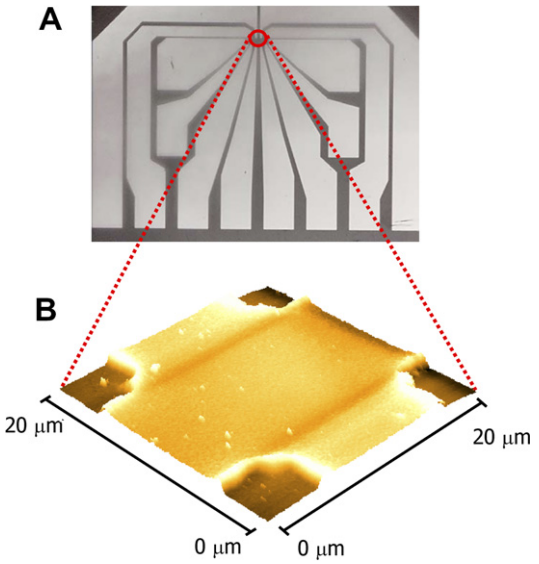

Fig. 3. (A) Microphotograph of a 10 μm P3HT Hall bar with Au ohmic contacts; (B) AFM image of the P3HT bar in the center.

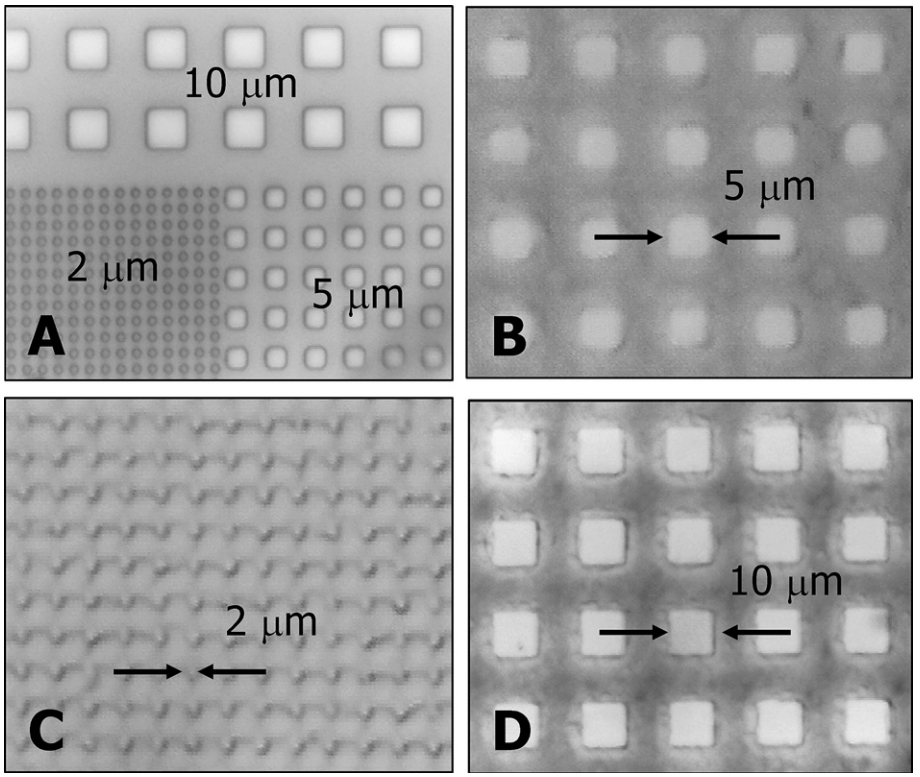

Fig. 2. Optical microscope photographs showing grid-like patterns transferred into a 50-nm-thick P3HT layer: (A) patterned photoresist on the P3HT film; (B) 5 μm P3HT grid; (C) 2 μm P3HT grid; (D) 10 μm P3HT grid. The imperfect squares of the 2 μm P3HT grid were due to the limit of the resolution of our lithography equipment rather than a problem during of P3HT patterning, because the same was seen in (A) with photoresist.

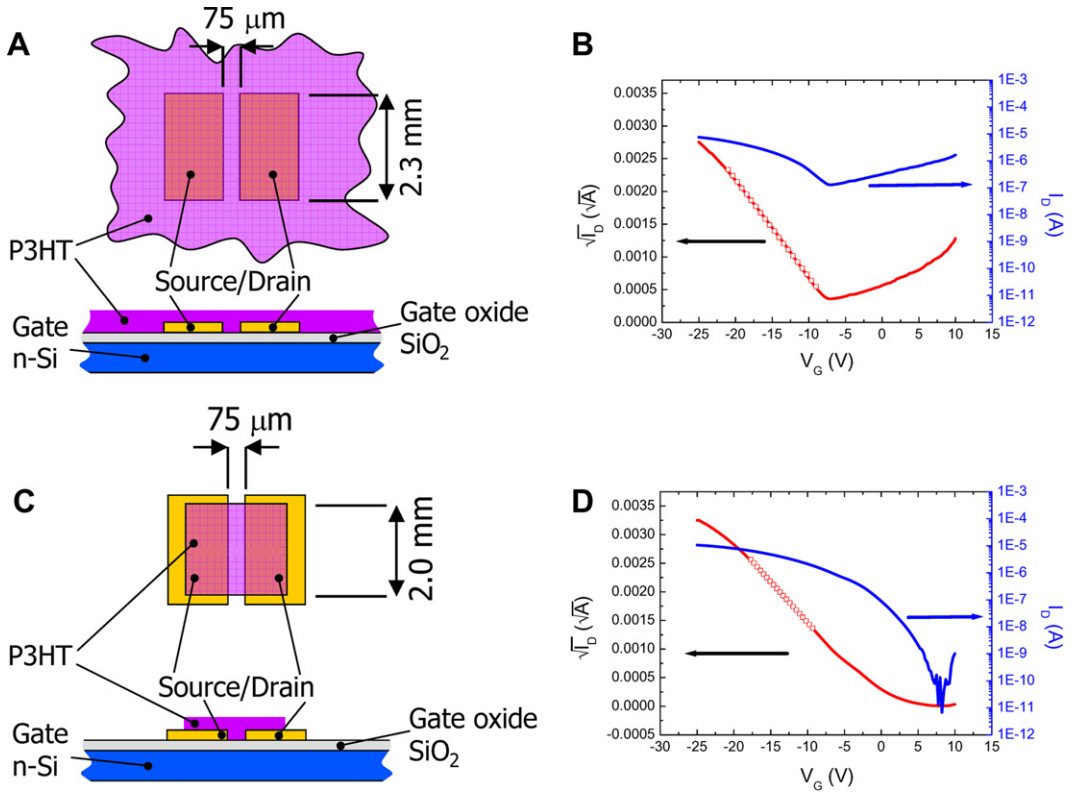

Fig. 4. Sketches and transfer characteristics of two P3HT OTFTs: (A) schematic diagram of an unpatterned OTFT (the large size of the device made it difficult to take a photo of the complete OTFT with an optical microscope); (B) Transfer characteristic of the OTFT in (A), showing a very low on/off ratio of about 70, mainly due to the gate leakage integrated all over the P3HT film; (C) sketch of a different device after UV patterning of the P3HT film; (D) the transfer characteristic of the patterned OTFT in (C) showing a significantly improved on/off ratio of over 10^6. The drain voltage was −25 V in the both measurements, in order to ensure the saturation of the OTFTs. The dotted lines are the linear fittings of the square root of the drain current as functions of the drain voltages, used to extract the carrier mobility.

may also be a result of undesired P3HT residuals at the sample edge formed during the spin coating step. Finally, our unoptimized oxide growth process might lead to a higher leakage current than industry-standard oxide. Nevertheless, the patterning technique has allowed us to reduce the leakage and obtain high on/off ratios.

The OTFT transfer characteristic after patterning is plotted in Fig. 4(D). The on/off ratio was dramatically improved from 70 to about 10^6 due to the reduction of the P3HT film coverage, which was confined only between the source and drain electrodes. The output characteristics of the OTFTs with and without patterning are shown in Fig. 5(A) and (B), respectively. In Fig. 5(A), the gate leakage current could be even larger than 80 μA at zero V_D for negative gate voltages. The measurements were carried out in ambient conditions and in dark at room temperature. The dramatic reduction in the gate leakage current in the OTFT with a patterned P3HT channel, which largely determines the off current and consequently also the on/off ratio, is hence evident. The results in Figs. 4 and 5 were reproduced in tens of devices that we fabricated and tested. The obtained mobility varied from 0.02 to 0.03 cm^2/V s because of the slight unintentional differences in the process conditions.

We note that previous unpatterned P3HT-based OTFTs that were fabricated and measured in air generally showed poor performance, similar to that in Fig. 4(B). Doping in ambient environments was often regarded as a key reason. Our results suggest that the main cause could actually be the high gate-leakage current if the device was not patterned. By using proper photolithography to define the P3HT channel, we show that high-performance OTFTs can be fabricated and measured in ambient conditions.

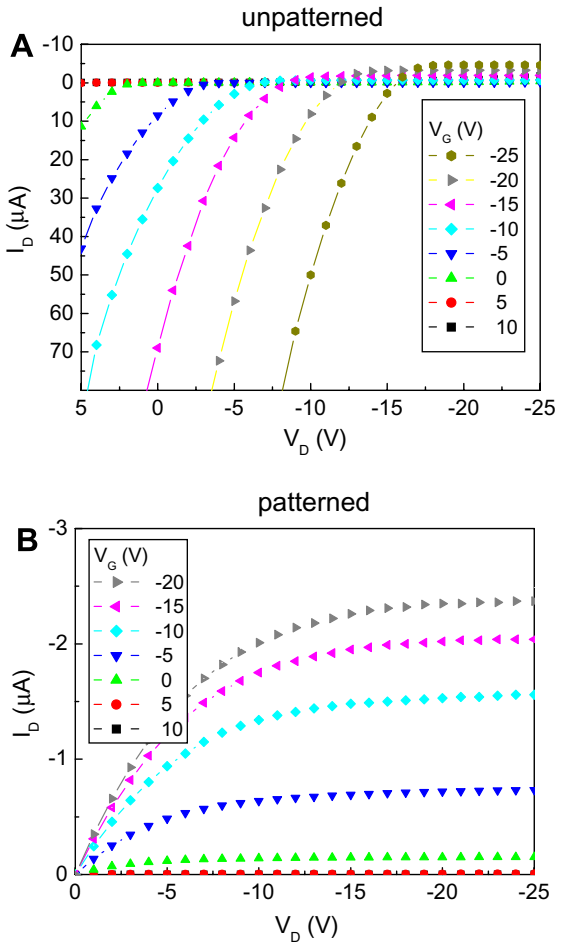

Fig. 5. Output characteristics of two P3HT OTFTs: (A) an OTFT with the P3HT film not patterned; (B) an OTFT with a patterned P3HT channel. The unpatterned device showed a very strong gate leakage much higher than the saturated drain current at low drain voltages.

To extract the hole mobility, μ_h, standard OTFT transport theory was used with the relation between the drain current, I_D, and the gate voltage, V_G, given by:

$$I_D = \frac{1}{2}\mu_h C' \frac{W}{L}(V_G - V_{TH})^2,$$

where V_{TH} is the threshold gate voltage, C' is the capacitance per unit area of the gate dielectric, and W and L are the width and length of the transistor channel, respectively. The mobility, determined by a linear fitting of the square root of the drain current versus the gate voltage curve, was virtually the same in the unpatterned OTFT ($0.025\ cm^2/V\ s$) and in the patterned device ($0.027\ cm^2/V\ s$). This demonstrates that no obvious degradation in the electrical properties of the P3HT film occurred during the entire process. The use of acetone and methanol thus does not seem to affect the carrier mobility of the conducting polymer spun from TCB onto OTS-modified substrates, which is different from the reported influence on small-molecule semiconductors such as pentacene [26]. The slight increase in the mobility in the patterned device could well be due to a small amount of doping in air, and the resulted additional carriers could screen and/or neutralize some of the charge traps in the P3HT film [37].

3. Conclusions

To conclude we have demonstrated a non-destructive method to pattern P3HT thin films based on UV lithography. The method was successfully applied to the patterning of P3HT OTFTs. Electrical measurements showed a dramatic improvement in the on/off ratio, by over four orders of magnitude, from about 70 to 10^6. The extracted mobility in the saturation regime was virtually unchanged at about $0.027\ cm^2/V\ s$, which is among the highest hole mobilities in P3HT-based OTFTs that were fabricated in ambient conditions. We also show that it was mainly the gate leakage current rather than the spurious current within the P3HT film that resulted in the poor performance of unpatterned OTFTs.

Acknowledgements

The authors would like to thank P. Coppo and M.F. McGowan for technical help. This work was supported by the Engineering and Physical Science Research Council (GR/S17741/01 and EP/E502814/1) and UMIP.

References

[1] C.K. Chiang, C.R. Fincher Jr., Y.W. Park, A.J. Heeger, H. Shirakawa, E.J. Louis, S.C. Gau, A.G. MacDiarmid, Phys. Rev. Lett. 39 (1977) 1098.
[2] F. Garnier, R. Hajlaoui, A. Yassar, P. Srivastava, Science 265 (1994) 1684.
[3] P. Ostoja, S. Guerri, S. Rossini, M. Servidori, C. Taliani, R. Zamboni, Synth. Met. 54 (1993) 447.
[4] L. Torsi, A. Dodabalapur, L.J. Rothberg, A.W.P. Fung, H.E. Katz, Science 272 (1996) 1462.
[5] Y. Yang, A.J. Heeger, Nature 372 (1994) 344.
[6] A.R. Brown, A. Pomp, C.M. Hart, D.M. de Leeuw, Science 270 (1995) 972.
[7] H. Sirringhaus, N. Tessler, R.H. Friend, Science 280 (1998) 1741.

[8] H. Sirringhaus, P.J. Brown, R.H. Friend, M.M. Nielsen, K. Berchgaard, B.M.W. Langeveld-Voss, A.J.H. Spiering, R.A.J. Janssen, E.W. Meijer, P. Herwig, D.M. de Leeuw, Nature 401 (1999) 685.
[9] G. Yu, J. Gao, J.C. Hummelen, F. Wudl, A.J. Heeger, Science 270 (1995) 1789.
[10] M. Granström, K. Petritsch, A.C. Arias, A. Lux, M.R. Andersson, R.H. Friend, Nature 395 (1998) 257.
[11] J.H. Burroughes, D.D.C. Bradley, A.R. Brown, R.N. Marks, K. Mackay, R.H. Friend, P.L. Burns, A.B. Holmes, Nature 347 (1990) 539.
[12] P.L. Burn, A.B. Holmes, A. Kraft, D.D.C. Bradley, A.R. Brown, R.H. Friend, R.W. Gymer, Nature 356 (1992) 47.
[13] N.C. Greenham, S.C. Moratti, D.D.C. Bradley, R.H. Friend, A.B. Holmes, Nature 365 (1993) 628.
[14] D. Braun, A.J. Heeger, Appl. Phys. Lett. 58 (1991) 1982.
[15] G. Gustafsson, Y. Cao, G.M. Treacy, F. Klavetter, N. Colaneri, A.J. Heeger, Nature 357 (1992) 477.
[16] Z.N. Bao, Y. Feng, A. Dodabalapur, V.R. Raju, A.J. Lovinger, Chem. Mater. 9 (1997) 1299.
[17] S.C. Chang, J. Bharathan, Y. Yang, R. Helgeson, F. Wudl, M.B. Ramey, J.R. Reynolds, Appl. Phys. Lett. 73 (1998) 2561.
[18] T.R. Hebner, C.C. Wu, D. Marcy, M.H. Lu, J.C. Sturm, Appl. Phys. Lett. 72 (1998) 519.
[19] J.A. Rogers, Z. Bao, A. Makhija, P. Braun, Adv. Mater. 11 (1999) 741.
[20] Changsoon Kim, Paul E. Burrows, Stephen R. Forrest, Science 288 (2000) 831.
[21] F.J. Touwslager, N.P. Willard, D.M. de Leeuw, Appl. Phys. Lett. 81 (2002) 4556.
[22] J. Wang, X. Sun, L. Chen, S.Y. Chou, Appl. Phys. Lett. 75 (1999) 2767.
[23] D.Y. Khang, H. Yoon, H.H. Lee, Adv. Mater. 13 (2001) 749.
[24] D. Suh, H.H. Lee, J. Vac. Sci. Technol. B 22 (2004) 1123.
[25] J.R. Sheats, J. Mater. Res. 19 (2004) 1974.
[26] J.E. Anthony, D.L. Eaton, S.R. Parkin, Org. Lett. 4 (2002) 15.
[27] A. Tsumura, H. Koezuka, T. Ando, Appl. Phys. Lett. 49 (1986) 1210.
[28] J. Chan, X.Q. Huang, A.M. Song, J. Appl. Phys. 99 (2006) 023710.
[29] Z. Bao, A. Dodabalapur, A.J. Lovinger, Appl. Phys. Lett. 69 (1996) 4108.
[30] J.F. Chang, B.Q. Sun, D.W. Breiby, M.M. Nielsen, T.I. Sölling, M. Giles, I. McCulloch, H. Sirringhaus, Chem. Mater. 16 (2004) 4772.
[31] H. Sirringhaus, T. Kawase, R.H. Friend, T. Shimoda, M. Inbasekaran, W. Wu, E.P. Woo, Science 290 (2000) 2123.
[32] A. Zen, J. Pflaum, S. Hirschmann, W. Zhuang, F. Jaiser, U. Asawapirom, J.P. Rabe, U. Scherf, D. Neher, Adv. Funct. Mater. 14 (2004) 757.
[33] L.A. Majewski, J.W. Kingsley, C. Balocco, A.M. Song, Appl. Phys. Lett. 88 (2006) 222108.
[34] A.W. Adamson, Physical Chemistry of Surfaces, third ed., John Wiley and Sons, 1976.
[35] T.K.S. Wong, S. Gao, X. Hu, H. Liu, Y.C. Chan, Y.L. Lam, Mat. Sci. Eng. B 55 (1998) 71.
[36] Giles Lloyd, Munira Raja, Ian Sellers, Naser Sedghi, Raffaella Di Lucrezia, Simon Higgins, Bill Eccleston, Microelectron. Eng. 59 (2001) 323.
[37] X. Jiang, Y. Harima, K. Yamashita, Y. Tada, J. Ohshita, A. Kunai, Chem. Phys. Lett. 364 (2002) 616.

Available online at www.sciencedirect.com
ScienceDirect
Organic Electronics 7 (2006) 508–513
Organic Electronics
www.elsevier.com/locate/orgel

Organic photovoltaic devices based on a block copolymer/fullerene blend

Richard P. Barber Jr. [1], Romel D. Gomez, Warren N. Herman, Danilo B. Romero *

Laboratory for Physical Sciences, University of Maryland, 8050 Greenmead Drive, College Park, MD 20740, USA

Received 20 March 2006; received in revised form 30 June 2006; accepted 18 July 2006
Available online 10 August 2006

Abstract

Conjugated semiconducting block copolymers are interesting organic materials for possible photovoltaic device applications because of their capability to form self-organized nanostructures and the tunability of their electronic and optical properties as a function of the relative lengths of the constituent monomers. In this work, we report the results of our investigation of polymer bulk heterojunction photovoltaic devices based on the block copolymer [MEH-PPV]-co-[biphenylene vinylene] derived from the widely used poly[2-methoxy-5-[2′-ethyl-hexyloxy]-1,4-phenylene-vinylene] (MEH-PPV) as an electron donor material in conjunction with the common electron acceptor molecule [6,6]-phenyl C61 butyric acid methyl ester, a soluble derivative of C_{60}. We find that the morphology and photovoltaic characteristics of these devices are strongly influenced by the blend concentration and thickness of the electro-active organic layer. Our initial results demonstrate that a power conversion efficiency of 2.4% is achieved with these materials.

PACS: 72.80.Le; 73.50.Pz; 83.80.Uv; 85.65.+h

Keywords: Block copolymer; Organic; Photovoltaic; Bulk heterojunction; MEH-PPV; C_{60}

1. Introduction

Organic photovoltaic devices have the potential to revolutionize the production of solar cells by offering an inexpensive and versatile alternative to inorganic semiconductors currently available [1–3]. The allure of lightweight, flexible and mechanically robust devices allows imaginative applications from photovoltaic coated building exteriors to wearable power sources printed onto clothing. However, despite the wide variety of material systems studied to date, the progress in achieving device performance comparable to those of the inorganic photovoltaic devices [4] remains elusive. Challenges such as thermal and chemical instability and the relatively low-power conversion efficiencies represent significant hurdles toward fruition.

The device physics of organic photovoltaic devices based on blends of semiconducting conjugated polymers and fullerenes results from

* Corresponding author. Tel.: +1 301 935 6475; fax: +1 301 935 6723.
E-mail address: dbromero@lps.umd.edu (D.B. Romero).
[1] Permanent address: Department of Physics, Santa Clara University, Santa Clara, CA 95053 (USA).

1566-1199/$ - see front matter
doi:10.1016/j.orgel.2006.07.004

the complex interplay of disorder-induced morphological and electronic structure modification in the blend [1–3]. The modification results from the well-established phenomenon that charge separation in these devices occurs at the interface of the heterojunction formed by the donor–acceptor molecular complex [5]. Unlike the conventional silicon-based photovoltaic device associated with a pn-junction formed by a sharply defined interface, the donor–acceptor heterojunction is randomly distributed over the entire electro-active layer of the organic photovoltaic device [1–3,6,7]. The photovoltaic characteristics of these devices will, therefore, be strongly influenced by the relative concentration of the donor and acceptor molecules. This is because the localized fluctuations in the donor–acceptor concentration can lead to variations in the electrical, optical, and structural properties of the device.

In this work, we explored the use of a block copolymer poly[2-methoxy-5-[2′-ethyl-hexyloxy]-1,4-phenylene-vinylene], derived from the widely used MEH-PPV, blended with [6,6]-phenyl C61 butyric acid methyl ester (PCBM), a soluble derivative of C_{60}, for fabricating organic polymer bulk heterojunction photovoltaic devices. Recently, semiconducting block copolymers have attracted attention for possible organic optoelectronic applications due to their ability to form self-assembled nanostructures and the tunability of their electronic and optical properties as a function of the relative lengths of the constituent monomers [8]. Furthermore, blending C_{60} with similar polymers has been shown to dramatically increase their photo-oxidative stability [9]. The steady improvement in device characteristics that has accompanied the tuning of a variety of controllable parameters in our measurements suggests that this system might represent a foundation for a viable technology. We investigate the effects of the relative concentration of the donor–acceptor molecules and film thickness on the photovoltaic characteristics of devices using blends of the MEH-PPV block copolymer and PCBM as the organic active layer.

2. Experimental

The chemical structures of the molecules investigated in this work are shown in the inset to Fig. 1. Chlorobenzene was used as a solvent for these organic materials because an earlier report [10]

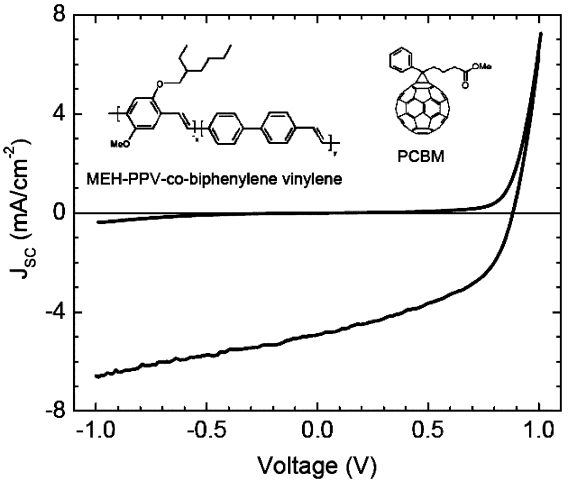

Fig. 1. Comparison of the dark and illuminated current versus voltage characteristics for a device with $x = 0.57$ C_{60} molar fraction. The photovoltaic characteristics of this device are: $V_{OC} = 0.88$ V, $J_{SC} = 4.92$ mA/cm^2, FF = 0.47, $\eta^{P}_{ext} = 2.4\%$ using AM1.5 direct solar simulator with $P_{in} = 92$ mW/cm^2. The inset shows the chemical structures of MEH-PPV-co-biphenylene vinylene and PCBM molecules investigated in this work.

showed that highly homogeneous films can be spun-cast using this solvent. Since the relative concentration of the MEH-PPV block copolymer: PCBM is a critical parameter in our investigation, we developed a simple procedure that allows for an accurate determination of the molar fraction of C_{60} in the blend. Separate solutions of the MEH-PPV copolymer and PCBM in chlorobenzene were prepared and stirred at 80 °C for a few days. The solutions were then filtered using a 1 μm filter. To determine their new concentrations, a small amount of the filtered solutions was weighed to estimate the weight of the solvent. The solvent was then allowed to evaporate and the weight of the remnant organic material was measured. This procedure yielded approximately 0.45% for the concentration of both filtered solutions. Blends with different relative concentrations of MEH-PPV copolymer: PCBM were prepared from appropriate combinations of the filtered solutions. We chose to express the relative concentration of C_{60} and copolymer as the molar fraction x of C_{60}. Film thickness variations were determined using a similar technique. In this case, a solution with molar fraction 0.69 was diluted with additional solvent to make thinner films or subjected to further solvent evaporation to make thicker films. These solutions with identical molar fraction were then weighed before and after the

chlorobenzene was evaporated, yielding weight percents between 0.4 and 2.5. We expressed the thickness in terms of concentration of the organic molecules in solution. Typical values for all of these experiments were of order 1%.

The devices were fabricated using indium-tin-oxide (ITO) coated glass substrates purchased from Delta Technologies with sheet resistance of ~2 ohms per square as the transparent conducting electrode for hole-injection. The ITO was photolithographically patterned on the glass substrate by means of wet chemical-etching techniques. A layer (~100 nm) of PLED grade Baytron poly[3,4-ethylenedioxythiophene]:poly[styrenesulfonate] (PEDOT:PSS) followed by the organic active layer (~150 nm) was spin-cast onto the ITO glass substrate in an inert nitrogen atmosphere inside a glove box. Both the PCBM and the MEH-PPV block copolymer are commercially available products from American dye source. The electron-injecting contact consisted of a patterned layer of ~2 nm thick lithium-flouride (LiF) followed by ~100 nm of aluminum (Al) deposited on top of the organic layer by shadow mask thermal evaporation. The electrically active area of the fabricated devices is 2 mm × 2 mm. In the initial experiments that included the stoichiometric data, the samples were covered with an aluminum foil to minimize photo-oxidative degradation and moved to an external evaporator for top electrode fabrication. Later samples were prepared using an evaporator contained within the glove box. This upgrade resulted in a significant improvement in the device characteristics.

The photovoltaic characteristics of the devices were extracted from the current versus voltage characteristics under illumination from an AM1.5 direct solar simulator with ~92 mW/cm^2 intensity.

3. Results and discussion

Fig. 2 shows representative atomic force microscopy scans of devices with varying blend composition. The MEH-PPV copolymer: PCBM blend exhibits a granular morphology that changes systematically with the relative concentration of the two species. The pure C_{60} device ($x = 1$) shows the appearance of amorphous large clusters (~1 μm). These clusters transform into relatively uniform fine grains (~100 nm) at intermediate values of x. This relatively ordered clustering disappears and is replaced by an inhomogeneous morphology in the pure polymer film ($x = 0$). Similarly, it is apparent that connected islands also form in the blends at intermediate molar fractions and increase in density as x is decreased. Such complex morphology is an inherent characteristic of polymer blends [11] and earlier works [10,12] have indicated improvements in the optical and electrical characteristics of organic electronic devices as a function of the morphology. We examine the effects of this morphological variation on the photovoltaic characteristics of organic photovoltaic devices fabricated from the MEH-PPV copolymer/C_{60} blends.

The spectral dependence of the incident photon to current conversion efficiency (IPCE) is shown in Fig. 3 for three representative devices. The spectra are compared to the absorbance spectrum of the pure MEH-PPV copolymer. For each device, the peaks in the IPCE spectrum are shifted to shorter wavelengths when compared to the MEH-PPV copolymer absorbance peak. The $x = 0.6$ device displays a single peak near $\lambda = 486$ nm. The peak for the $x = 0.8$ device appears to move to shorter wavelength while the $x = 0.1$ device manifests two peaks, one at shorter wavelengths and the other close to the absorbance peak of the MEH-PPV copolymer. These results suggest the formation of a donor–

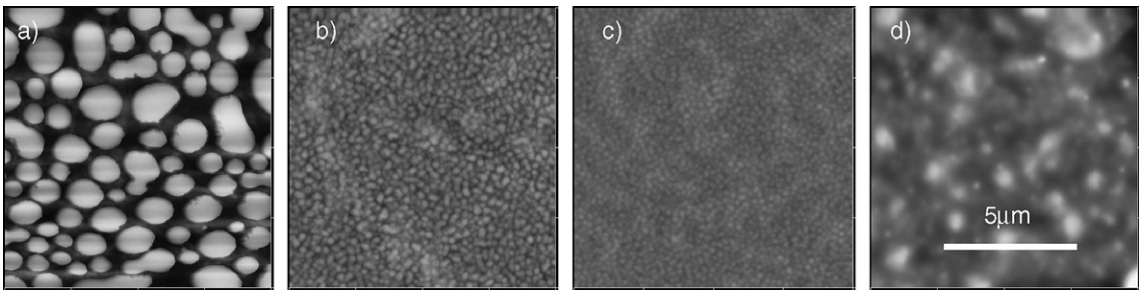

Fig. 2. Representative atomic force microscopy images as a function of C_{60} molar fraction for four different photovoltaic devices: (a) $x = 1$, (b) $x = 0.43$, (c) $x = 0.26$, (d) $x = 0$. The scale of all four images is shown in the right frame.

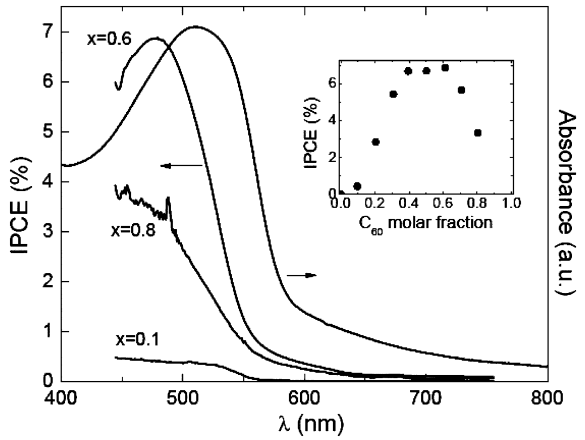

Fig. 3. Spectral dependence of the incident photon to current conversion efficiency (IPCE) for three representative devices. The absorbance for the pure MEH-PPV copolymer film is also shown for comparison. The inset plots the IPCE at $\lambda = 486$ nm as a function of the C_{60} molar fraction.

acceptor complex in the copolymer/C_{60} blend that is responsible for the IPCE maximum near $\lambda = 486$ nm. The density of this donor–acceptor complex is optimum around $x = 0.4$–0.6, the range of C_{60} molar fractions in which the IPCE is maximum as depicted in the inset to Fig. 3. We note that this range of concentration corresponds to the case of approximately one C_{60} molecule bound to the polymer repeat unit. This is highly suggestive of significant photodoping at intermediate blend concentration. The electron transfer from the polymer to the C_{60} leads to the creation of mobile hole polarons that enhances the charge transport along the polymer chain.

Fig. 1 displays the dark and illuminated current versus voltage (I–V) characteristic from a device with $x = 0.57$. From these curves, we extract the photovoltaic characteristics of the device. The open-circuit voltage, V_{OC}, is the voltage intercept at zero current. The short-circuit current density, J_{SC}, is the current intercept at zero voltage. The fill factor, FF, is calculated as $FF = (VJ)_{max}/(V_{OC}J_{SC})$ where $(VJ)_{max}$ is the maximum electrical power density that is generated by the device [2]. A practical figure of merit for photovoltaic devices is the external power conversion efficiency, η_{ext}^{P}, defined as the ratio of the maximum electrical power density generated in the device to the incident light intensity [2],

$$\eta_{ext}^{P} = \frac{(VJ)_{max}}{P_{in}} = \frac{V_{OC}J_{SC}}{P_{in}}FF.$$

Fig. 3 summarizes the values of V_{OC}, J_{SC}, FF, and η_{ext}^{P} derived from the devices with different x. The plot shows the strong dependence of η_{ext}^{P} on x. The pure MEH-PPV copolymer device ($x = 0$) manifests a weak photovoltaic effect. While there is significant V_{OC} (~0.82 V) in this device, J_{SC} (~0.1 mA/cm^2) is very small. The low value of J_{SC} is due to radiative recombination dominating over the charge separation process with much of the latter taking place near the PEDOT:PSS/MEH-PPV copolymer interface. On the other extreme, pure PCBM device ($x = 1$), similarly shows no photovoltaic effect in either V_{OC} or J_{SC}. At intermediate x, η_{ext}^{P} increases significantly with a maximum of 1% near $x = 0.6$. We note that the maximum η_{ext}^{P} does not appear at $x = 0.5$ which corresponds to the case of one C_{60} molecule for each repeat unit of the MEH-PPV copolymer in which charge separation is expected to be optimal. This suggests that a higher concentration of C_{60} molecules is necessary for better electron transport in the blend to achieve maximum η_{ext}^{P}.

In general, the open-circuit voltage is determined by the built-in voltage associated with the band-offset at the electrode/organic layer interface as well as

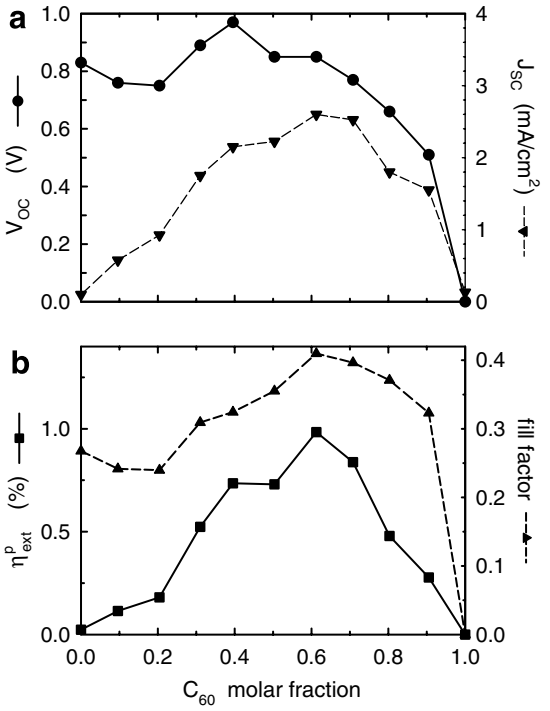

Fig. 4. Dependence of the photovoltaic device characteristics on the C_{60} molar fraction. (a) Open-circuit voltage and short-circuit current density, (b) Power conversion efficiency and fill factor.

the diffusion of the separated charge carriers in the device [13]. In Fig. 3 we find that V_{OC} is essentially constant ($V_{OC} \sim 0.85$ V) for $x < 0.7$ then decreases to $V_{OC} = 0$ V for the pure C_{60} device. The fact that V_{OC} is nearly the same for a wide-range of blend concentration indicates that the contribution of charge diffusion to the open-circuit voltage is negligible in organic photovoltaic devices. Therefore, proper engineering of the interfaces can lead to higher V_{OC} in these devices.

Fig. 3 shows that the x dependence of η_{ext}^{P} mimics that of J_{SC}. The short-circuit current is determined by a three step process: (1) exciton creation, (2) exciton diffusion towards the donor–acceptor junction for charge separation, and (3) charge transport to and collection at the electrodes [1]. These processes are expected to be strongly dependent on the thickness of the organic layer in the photovoltaic devices. Fig. 4 shows the photovoltaic device parameters for a series of films of different weight percent prepared from the same $x = 0.69$ mixture. We note the dramatic effect of varying this parameter producing devices with η_{ext}^{P} up to 1.7%. Measurements of the resultant thickness range with a Dektak stylus profiler indicated that these samples varied in thickness by nearly a factor of two from 120 nm to 210 nm over the range of weight percents from 0.4 to 2.25. Note that in polymer-based bulk heterojunction photovoltaic devices, the charge separation efficiency is close to unity since the excitons are created close to the heterojunction and the concomitant charge-transfer process is very fast [1,5]. Thus, the thickness dependence of η_{ext}^{P} that we observe is most likely a result of the competition between the exciton creation and charge collection efficiencies in the photovoltaic devices. For the devices with a thin organic layer, a larger fraction of the incident light is not absorbed, which results in a reduced production of charge carriers. On the other hand, poor transport in the devices with thick active layer inhibits the separated holes and electrons from reaching the electrodes in order to represent a measurable current. Thus, the optimum thickness seen in Fig. 4 represents a compromise between these two mechanisms to maximum power conversion efficiency in the devices (Fig. 5).

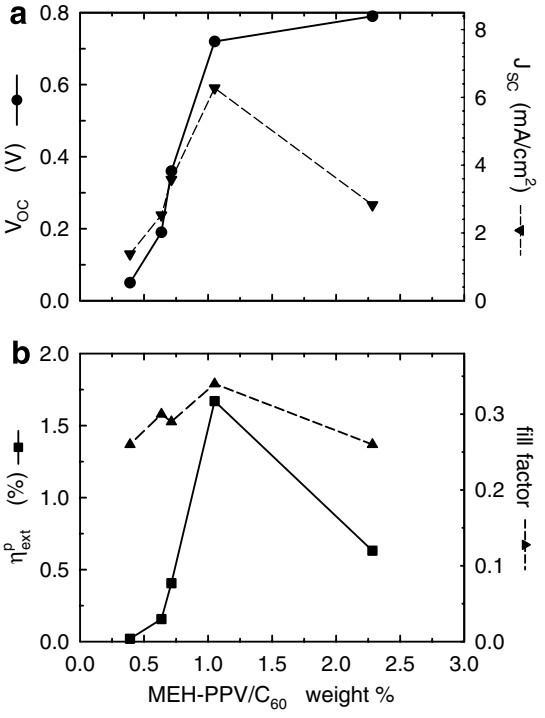

Fig. 5. Dependence of the photovoltaic device characteristics on the organic solution weight percentage. (a) Open-circuit voltage and short-circuit current density. (b) Power conversion efficiency and fill factor.

4. Conclusion

In summary, we have investigated the dependence of the photovoltaic properties of conjugated block copolymer: C_{60} based photovoltaic devices on the relative concentration of donor–acceptor heterojunctions. We find that the best performance is exhibited by devices with a C_{60} molar fraction of 0.6. This concentration is slightly higher than the ideal concentration for optimal charge separation which corresponds to one C_{60} per polymer molecular repeat unit. Furthermore, control of the active layer thickness also produced significant gains in power conversion efficiency. These results by no means represent an exhaustive investigation of a rather large phase space of controllable device parameters. The potential to "tune" the peak absorption wavelength by varying the composition of the copolymer provides an additional method for adjusting device performance. We expect that further refinement of this system will lead to continued improvement and perhaps even a technologically usable design.

Acknowledgements

This work is supported by the Polymer Program at the Laboratory for Physical Sciences under the Organic Polymer Photocell Technology project.

References

[1] C. Brabec, V. Dyakonov, J. Parisi, N.S. Sariciftici (Eds.), Organic Photovoltaics: Concepts and Realization, Springer Series in Materials Science, 2003.
[2] H. Hoppe, N.S. Sariciftci, J. Mater. Res. 19 (7) (2004) 1924.
[3] S.E. Shaheen, D.S. Ginley, G.E. Jabbour, Mater. Res. Soc. Bull. 30 (1) (2005) 10.
[4] S.F. Baldwin, Phys. Today 55 (2002) 62.
[5] N.S. Sariciftci, L. Smilowits, A.J. Heeger, F. Wudl, Science 258 (5087) (1992) 1474.
[6] G. Yu, J. Gao, J.C. Hummelen, F. Wudl, A.J. Heeger, Science 270 (5243) (1995) 1789.
[7] J.J.M. Halls, C.A. Walsh, N.C. Greenham, E.A. Marseglia, R.H. Friend, S.C. Moratti, A.B. Holmes, Nature 376 (6540) (1995) 498.
[8] G. Hadziioannou, Mater. Res. Soc. Bull. 27 (6) (2002) 456.
[9] H.W. Sarkas, W. Kwan, S.R. Flom, C.D. Merritt, Z.H. Kafafi, J. Phys. Chem. 100 (13) (1996) 5169.
[10] S.E. Shaheen, C.J. Brabec, N.S. Sariciftci, F. Padinger, T. Fromherz, J.C. Hummelen, Appl. Phys. Lett. 78 (6) (2001) 841.
[11] G. Malliaras, R. Friend, Phys. Today 58 (2005) 53.
[12] T. Nguyen, B.J. Schwartz, J. Chem. Phys. 116 (18) (2002) 8198.
[13] G.G. Malliaras, J.R. Salem, P.J. Brock, J.C. Scott, J. Appl. Phys. 84 (3) (1998) 1583.

Available online at www.sciencedirect.com
ScienceDirect
Organic Electronics 7 (2006) 514–520
Organic Electronics
www.elsevier.com/locate/orgel

Effect of side chain length on molecular ordering and field-effect mobility in poly(3-alkylthiophene) transistors

Yeong Don Park, Do Hwan Kim, Yunseok Jang, Jeong Ho Cho, Minkyu Hwang, Hwa Sung Lee, Jung Ah Lim, Kilwon Cho *

Department of Chemical Engineering, Polymer Research Institute, Pohang University of Science and Technology, San 31 Hyoja-dong, Nam-gu, Pohang, Gyungbuk 790-784, Republic of Korea

Received 21 February 2006; received in revised form 21 July 2006; accepted 24 July 2006
Available online 14 August 2006

Abstract

The effect of alkyl side chain length on the molecular ordering and electrical properties of regioregular poly(3-alkylthiophene) (P3AT)-based field-effect transistors (FETs) was investigated using P3ATs with various alkyl side chain lengths ($-(CH_2)_nCH_3$, $n = 3$, 5, and 7) as active materials. The inner structures and surface morphologies of the P3ATs thin films fabricated on an insulator substrate were characterized, and the electrical properties of FETs based on these films were correlated with the structure and alkyl chain length of the P3ATs. The FET based on poly(3-butylthiophene), which has the shortest alkyl side chains among the three P3ATs considered, showed the highest field-effect mobility, possibly because the film formed from molecules with short butyl side chains had a higher density of π-stacked ordered structures in the charge transport region.

Keywords: Side chain length; Field-effect transistors; Poly(3-alkylthiophene)

1. Introduction

The high field-effect mobility, stability and solution processability of regioregular poly(3-alkylthiophene)s (P3ATs) has stimulated considerable interest in the utilization of these fascinating polymers as the active materials in organic field-effect transistors (OFETs) [1–15]. In particular, previous studies have shown that a preferential supramolecular two-dimensional ordering of the P3AT chains with high regioregularity gives rise to a high field-effect mobility [10] of up to $0.3\,cm^2V^{-1}s^{-1}$, a value approaching that of single crystalline oligothiophenes.

Many factors affect the structures of P3AT films and the electric properties of FETs based on these films: molecular parameters such as regioregularity [3], molecular weight [16] and side chain length [17–25], and processing conditions such as solvent power [6], film thickness [26], doping level [27] and the method used to form the film [28]. For P3ATs, one of the key factors is the alkyl side chain length which greatly affects the solubility of these polymers in organic solvents. P3ATs with long alkyl side

* Corresponding author. Tel.: +82 54 279 2270; fax: +82 54 279 8269.
E-mail address: kwcho@postech.ac.kr (K. Cho).

1566-1199/$ - see front matter
doi:10.1016/j.orgel.2006.07.007

chains are highly soluble, which facilitates the fabrication of transistor devices by solution processing. However, for linear alkyl chains, the field-effect mobility is expected to decrease with increasing chain length due to the isolated nature of the alkyl substituents. Several groups have examined the effect of side chain length on the thin film structures and electrical properties of P3AT thin films in TFTs [20–24]. Despite this previous work, the role of the alkyl side chains is poorly understood and the correlation between the film structure and FET electrical properties has not been systematically studied. In the present study, we systematically characterized the inner structures and surface morphologies of thin films of P3ATs with three side chain lengths (alkyl = butyl [P3BT], hexyl [P3HT], octyl [P3OT]), and evaluated the electrical performances of FET devices based on these P3ATs. In addition, we determined the correlation between the thin film structure and electrical properties of the FETs according to the side chain length of the P3AT.

2. Experiments

The regioregular P3ATs used in this study, P3BT, P3HT, and P3OT, were obtained from the Rieke Metals Incorporation. The molecular weights of the alkylthiophenes had almost same values ($M_n = 45$–50 kg/mol). The coupling ratio of head–tail to head–head and tail–tail was estimated to be about 93% by NMR integration.

A highly doped Si substrate was used as the transistor substrate as well as the gate electrode. A thermally grown silicon dioxide (SiO_2) layer of thickness 300 nm acted as the gate dielectric. A simple spin-coating method was used to fabricate regioregular P3AT thin films of thickness 100–110 nm. Films of P3BT, P3HT, and P3OT were spin-coated from a 1 wt% solution in chloroform ($CHCl_3$) onto SiO_2/Si substrates and then subsequently annealed for 20 min at 250 °C, 235 °C, and 205 °C, respectively, after which they were cooled at a rate of 3 °C/min. All solutions were filtered through a 0.45 μm pore size poly(tetrafluoro ethylene) membrane syringe filter before use. Au electrodes of thickness 170 nm, functioning as source and drain electrodes (channel length 40 μm and channel width 800 μm), were deposited on top of the P3AT films by evaporation.

An atomic force microscope (Digital Instruments Multimode) operating in tapping mode using a silicon cantilever was employed to characterize the surface morphologies of the samples. FT-IR spectra with a resolution of 1 cm^{-1} were recorded using a Bruker IFS 66v/S model spectrometer. Film thickness was determined using an ellipsometer (M-2000 V, H.A.Woollam Co., Inc.). Grazing-incidence X-ray diffraction (GIXD) and X-ray reflectivity measurements were performed at the 3C2, 4C2 and 8C1 beamlines, respectively, at the Pohang Accelerator Laboratory (PAL), Korea.

3. Results and discussion

Fig. 1 shows AFM topographic and phase images of P3AT thin films on insulator substrates (Si/SiO_2) [29,30]. Before annealing, the spin-coated film shows featureless characteristics (Fig. 1(a)). However, after annealing by slow heating to the melting temperature above the order–disorder transition temperature of the P3AT backbone chain, followed by slow cooling, peculiar morphologies indicative of nanoribbon structures with the width of 20–40 nm are observed in the phase images (Fig. 1(b)–(d)). These randomly oriented rodlike nanoribbons are formed spontaneously during the crystallization process after heating the film to above the order–disorder transition temperature (P3BT: 250 °C, P3HT:

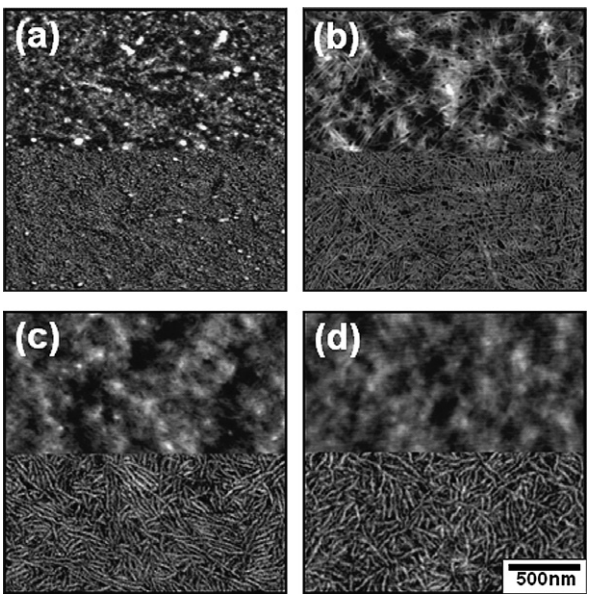

Fig. 1. Tapping mode atomic force microscope (AFM) topography and phase images of (a) P3HT thin film without annealing; (b) P3BT thin film annealed at 250 °C for 20 min, domain size: 15–20 nm; (c) P3HT thin film annealed at 235 °C for 20 min, domain size: 20–25 nm; and (d) P3OT thin film annealed at 205 °C for 20 min, domain size: 25–30 nm. Upper half represents topograph images and lower half represents phase images for each samples.

235 °C, P3OT: 205 °C). The width and shape of the nanoribbons vary depending on the alkyl chain length because the alkyl side chains have a crucial effect on the structures formed during crystallization. For the P3BT thin film, the nanoribbons are narrow and straight. For the P3HT and P3OT thin films, by contrast, the nanoribbons are broader and denser than those observed for the P3BT thin film. To elucidate the inner structures of the nanoribbons, we analyzed the P3BT, P3HT and P3OT thin films using grazing incidence X-ray diffraction (GIXD), X-ray reflectivity, and FT-IR.

In the present study, the morphology of the top surface of the P3AT thin films was studied by AFM and the molecular ordering that prevails throughout the films was determined from X-ray measurements [31,32]. The reflectivity data, presented in Fig. 2, were obtained at room temperature after annealing above the order–disorder transition temperature for 20 min. The reflectivity patterns of the thin films all show both Kiessig fringes and Bragg peaks. Kiessig fringes are caused by interferences between beams reflected at the air-polymer and polymer-substrate interfaces, respectively. Because the locations of the Kiessig fringes depend on the film thickness, the total thickness of the film can be derived from the distance between adjacent maxima of the fringes [33]. All of the polymer films deposited on insulator substrates were found to have thicknesses in the range 100–110 nm. For each film, the film thickness determined by X-ray reflectivity was approximately the same as that measured by ellipsometry.

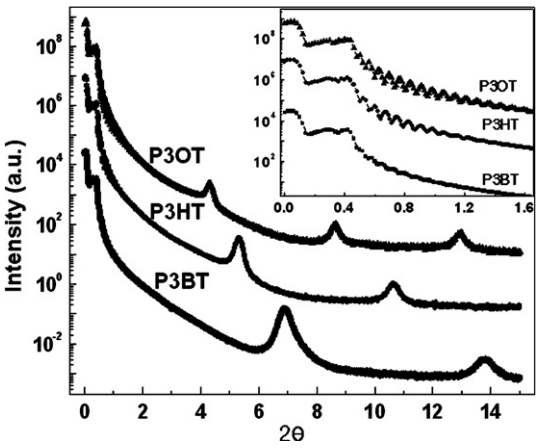

Fig. 2. X-ray reflectograms for P3AT thin films on a silicon substrate. The inset shows Kiessig fringes peaks for P3AT thin films as a function of the angle of incidence, θ.

For the P3BT, P3HT, and P3OT thin films, the second Bragg peak is observed in addition to the first Bragg peak. These peaks are caused by a periodic density modulation perpendicular to the surface and are indicative of the formation of an ordered phase. The correlation lengths of the ordered phases of P3BT, P3HT and P3OT, as determined from the position of the Bragg peak, were 12.5 Å, 16.1 Å, 19.8 Å, respectively. In the case of the P3OT thin film, however, the intensities of the Bragg peaks dramatically decrease. Since the P3BT, P3HT and P3OT films have almost the same thickness (i.e., 100–110 nm), but different side chain lengths, the films will have different numbers of layers in their ordered structures. In other words, the P3AT with the shortest alkyl side chains, P3BT, will have a greater number of ordered domains than the other P3AT thin films. As a result, the intensities of the Bragg peaks decrease as the alkyl side chain length increases.

To examine the molecular orientation as a function of side chain length, we studied the microstructure of the annealed P3AT films using grazing-incidence X-ray diffraction (GIXD) [19]. The orientations of the P3AT chains with respect to the insulator substrate were studied for the in-plane and out-of-plane modes. Similar orientations of the ordered domains with respect to insulator substrate were identified for all three films (Fig. 3), specifically, the preferential

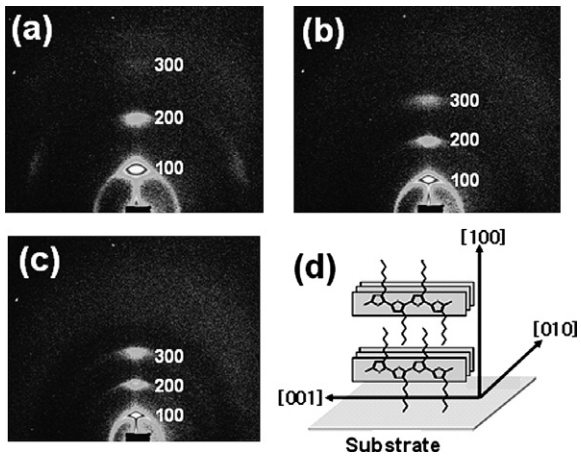

Fig. 3. Grazing incidence wide-angle X-ray scattering images representing the two-dimensional distribution of scattered CuKα X-rays from spin-coated, 100–110 nm thick P3AT films on a SiO_2/Si substrate. The vertical (horizontal) axes correspond to scattering out of (in) the plane of the film. (a) P3BT, (b) P3HT, (c) P3OT, and (d) schematic representation of the edge-on structure in P3AT.

orientation of the ordered domains was with the (1 0 0)-axis normal to the substrate. The interlayer spacing of the ordered phases of P3BT, P3HT and P3OT, as determined from the position of the Bragg peak, were 12.5 Å, 16.1 Å, 19.8 Å, respectively. The interlayer spacing increased linearly with the alkyl chain length. The (0 1 0) reflection was not observed in the pseudo-out-of-plane direction (Fig. 3), indicating that the preferred orientation of the π-stack is in the plane of the sample (the edge-on structure) as shown schematically in Fig. 3(d) [10].

To investigate the conformation of the alkyl side chains as a function of side chain length, we measured infrared vibrational spectra of the P3AT thin films [34]. Fig. 4 shows typical FT-IR absorption spectra in the CH stretching region as a function of the alkyl chain length. When the hydrocarbon chains are predominantly in the all-trans conformation, which represents a centrosymmetric arrangement of the methylene groups, the dominant features of the FT-IR spectra are the symmetric and asymmetric methylene vibrations at 2851 and 2919 cm^{-1}, respectively. These characteristic peaks exhibit an upward shift as the ordered, mainly trans-conformation chain structures transform into disordered structures with increasing gauche defects. The Fig. 4 indicates that the alkyl chains of the P3AT thin films are not all-trans conformation, but they are distinguished from band positions.

In the FT-IR spectrum of the P3BT thin film in Fig. 4, four sharp and intense bands are observed at 2861, 2870, 2932, and 2956 cm^{-1}, which are assigned to the CH_2 symmetric, CH_3 symmetric, CH_2 asymmetric, and CH_3 asymmetric stretching bands, respectively. These band positions and the spectral profiles are known to be sensitive to the change in the packing of the alkyl chains. Inspection of the positions of these four peak, $v_s(CH_2)$, $v_s(CH_3)$, $v_{as}(CH_2)$, and $v_{as}(CH_3)$, as a function of alkyl chain length reveals that $v_s(CH_2)$ and $v_{as}(CH_2)$ shift to lower wavenumber with increasing alkyl side chain length. These results suggest that the packing of the alkyl chains attached to the P3AT backbone change from a less ordered configuration to a trans zigzag conformation as the alkyl side chain increase in length. We can speculate that the increase of the alkyl side chain length at the 3-position in P3ATs leads to enhanced side chain ordering. The intensities of $v_s(CH_3)$ and $v_{as}(CH_3)$ decreases as the alkyl side chain length increases. This decrease in the intensities of $v_s(CH_3)$ and $v_{as}(CH_3)$ implies the relative number of $-CH_3$ functional group which is directly related to the number of ordered layers which form with the perpendicular orientation of the P3AT chains. The layers in the ordered P3OT thin film are thicker than those in the P3BT film, because the latter polymer has shorter side chains. Thus, for the three P3AT thin films studied here, all of which have similar film thickness, the number of layers in the thin film will increase with decreasing side chain length.

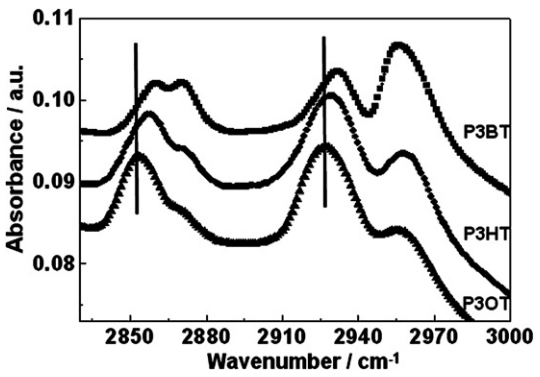

Fig. 4. Infrared absorption spectra of P3BT, P3HT, and P3OT films. The vertical bars mean two sharp and intense bands observed at 2855, and 2929 cm^{-1}, which are assigned to the CH_2 symmetric and CH_2 asymmetric stretching bands of P3OT thin film, respectively.

To determine the relationship between alkyl side chain length and field-effect mobility, the field-effect mobilities of the regioregular P3ATs were measured using a top-contact thin-film FET geometry. Heavily doped Si wafer was used as a gate electrode, and SiO_2 (thickness 300 nm) was used as the gate insulator (capacitance = 10.8 $nFcm^{-2}$). Thin films of P3BT, P3HT, and P3OT were then spin-coated from 1 wt% P3AT solutions in chloroform at 3000 rpm, and annealed at 250 °C, 235 °C and 205 °C for 20 min, respectively. Gold was deposited as a source and drain electrode on the P3AT thin film. No additional energy barriers are introduced with this method, as the conducting polythiophene layer forms ohmic contacts with the gold layers.

Fig. 5 shows typical source-drain current (I_{DS}) vs source-drain voltage (V_{DS}) plots at various gate voltages for the regioregular P3AT FETs operating in accumulation mode. The average field-effect mobility of each transistor was calculated in the saturation regime ($V_{DS} = -80$ V) by plotting the square root of the drain current versus the gate voltage (Fig. 6) and fitting the data to the following equation [7–9].

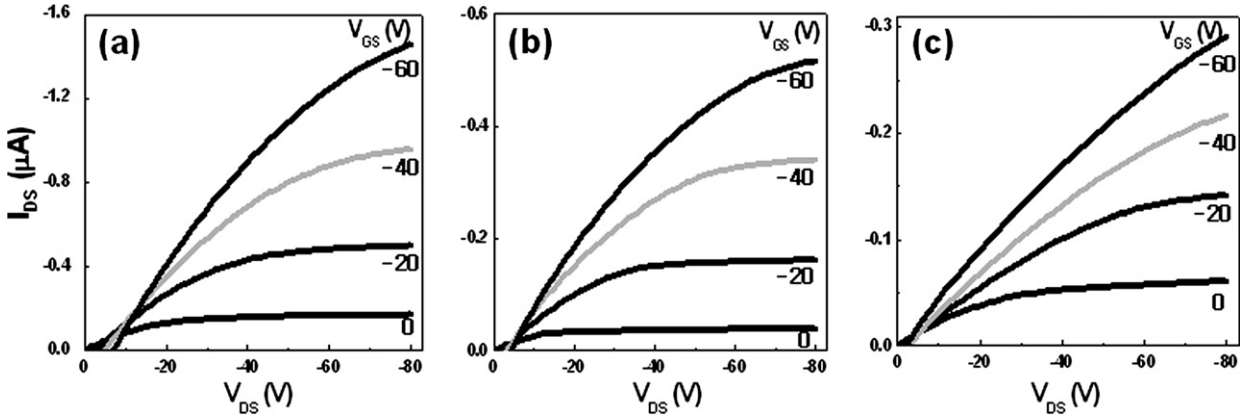

Fig. 5. Electrical characteristics of P3AT FETs: Current–voltage output characteristics of a 40 μm (length) by 800 μm (width) transistor. (a) P3BT, (b) P3HT and (c) P3OT.

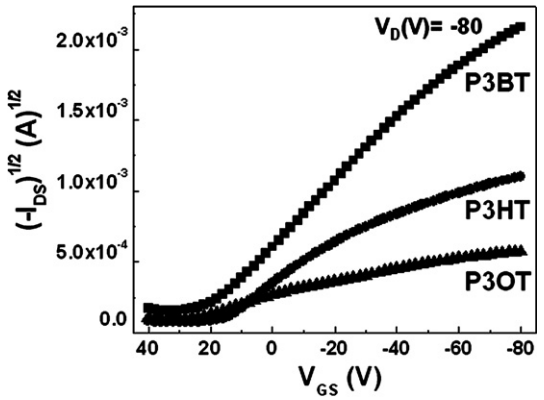

Fig. 6. Transfer characteristics $[(-I_{DS})^{1/2}$ vs. V_G at $V_{DS} = -80$ V] with respect to alkyl side chain length.

Table 1
Average mobility values obtained from the transfer curve of the P3BT, P3HT, and P3OT FETs

	P3BT	P3HT	P3OT
Mobility ($\times 10^{-3}$) $cm^2 V^{-1} s^{-1}$	10	5.4	0.52
On/off ratio	200	250	150

$$I_{DS} = \frac{WC_i}{2L}\mu(V_{GS} - V_T)^2$$

where $C_i = 10.8 \times 10^{-9}\,Fcm^{-2}$, $W = 800$ μm, and $L = 40$ μm.

Table 1 shows the the field-effect mobilities for the systems with different side chain lengths. The field-effect mobility of the P3BT system ($0.010\,cm^2 V^{-1} s^{-1}$) is about 20 times greater than that of the P3OT system ($5.2 \times 10^{-4}\,cm^2 V^{-1} s^{-1}$). This difference may be due to the different number of perpendicularly oriented layers with respect to the insulator substrate in the P3BT and P3OT thin films. Specifically, the perpendicularly oriented layers enable the charge carrier to transport in the two-dimensional conjugation direction [3], resulting in a higher field-effect mobility for P3AT films with more layers in the charge transport region. As previously noted, the P3BT thin film contains more layers in its ordered structure compared to the other P3ATs thin films in a few nanometers of the semiconductor near the interface between the semiconductor and insulator (Fig. 7), and hence

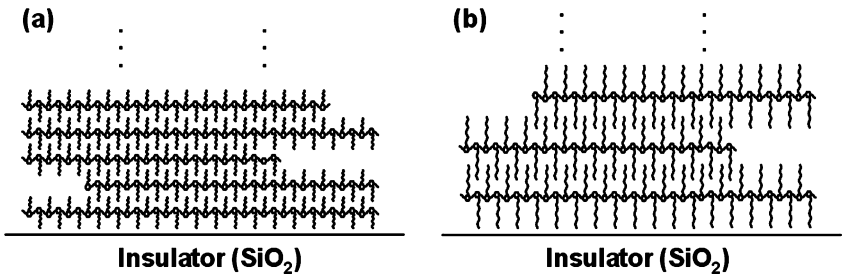

Fig. 7. Schematic representation of the internal structures of (a) P3BT and (b) P3OT at the interface between the semiconductor and insulator.

the P3BT thin film will have more opportunities to transport the charge carrier at the interface between the semiconductor and insulator. Previous work has shown that the alkyl side chains in unannealed P3AT films act as insulators, which interferes with inter-chain hopping [21]. The insulating portion has a large impact on the way the P3AT chains pack, which in turn has a significant effect on the field-effect mobility. And Jenekhe et al. has shown hexyl side chain is optimum for charge transport because of better self-organization in poly(3-heylthiophene) compared to other polymers [24]. Therefore the hole mobility as a function of alkyl chain length showed the highest value for poly(3-hexylthiophene). However, we have shown here that in the annealed P3AT film, the side chain ordering is improved as the increasing alkyl side chain length.

4. Summary

The inner structure and surface morphologies of a P3BT, P3HT, and P3OT thin films on insulator substrates were characterized, and the electrical properties of FETs based on these polymers were correlated with the structure and alkyl side chain length of the P3ATs. Thermal annealing of the thin films above the order–disorder transition temperature of the P3AT allowed the P3AT molecules to rearrange into an ordered structure. X-ray reflectivity and GIXD studies of the P3BT, P3HT, and P3OT thin films indicated that the inner part of each thin film had a well-ordered, multilayered structure with an edge-on orientation. Furthermore, analysis of FT-IR spectra revealed that the side chains in the thin films became more ordered as the length of the alkyl side chain increased, indicating that the alkyl side chain assists in the ordering of the P3AT backbones.

The charge carrier transport behavior in P3BT, P3HT and P3OT was investigated by fabricating thin film transistors based on the P3ATs and characterizing their properties. The hole mobility was found to decrease with increasing alkyl chain length, with the hole mobility for P3BT ($0.010\ cm^2/(Vs)$) being 20 times greater than that for P3OT. This result suggests that the side chain length greatly affects the electrical properties of P3AT-based devices. As the alkyl side chain length was decreased, the P3AT thin film showed an increased number of ordered structures in channel region.

Acknowledgements

This work was supported by the National Research Laboratory Program and ERC Program (R11-2003-006-03 005-0) of the MOST/KOSEF, a grant (F0 004 022) from the Information Display R&D Center under the 21st Century Frontier R&D Program and the Regional Technology Innovation Program (RTI04-01-04) of the MOCIE, and the BK21 Program of the Ministry of Education and Human Resources Development of Korea. The authors are grateful to the Pohang Accelerator Laboratory for access to synchrotron radiation at the 3C2, 4C2, and 8C1 beamlines.

References

[1] H. Sirringhaus, N. Tessler, R.H. Friend, Science 280 (1998) 1741.
[2] R. Österbacka, C.P. An, X.M. Jiang, Z.V. Vardeny, Science 287 (2000) 839.
[3] H. Sirringhaus, P.J. Brown, R.H. Friend, M.M. Nielsen, K. Bechgaard, B.M.W. Langeveld-Voss, A.J.H. Spiering, R.A.J. Janssen, E.W. Meijer, P. Herwig, D.M. de Leeuw, Nature 401 (1999) 685.
[4] A. Facchetti, M.H. Yoon, T.J. Marks, Adv. Mater. 17 (2005) 1705.
[5] C.J. Drury, C.M.J. Mutsaers, C.M. Hart, M. Matters, D.M. deLeeuw, Appl. Phys. Lett. 73 (1998) 108.
[6] Z. Bao, A. Dodabalapur, A.J. Lovinger, Appl. Phys. Lett. 69 (1996) 4108.
[7] C.D. Dimitrakopoulos, P.R.L. Malenfant, Adv. Mater. 14 (2002) 99.
[8] G. Horowitz, Adv. Mater. 10 (1998) 365.
[9] H. Sirringhaus, Adv. Mater. 17 (2005) 2411.
[10] D.H. Kim, Y.D. Park, Y. Jang, H.C. Yang, Y.H. Kim, D.G. Moon, S. Park, T. Chang, C. Chang, M. Joo, C.Y. Ryu, K. Cho, Adv. Funct. Mater. 15 (2005) 77.
[11] D.H. Kim, Y. Jang, Y.D. Park, K. Cho, Langmuir 21 (2005) 3203.
[12] D.H. Kim, Y.D. Park, Y. Jang, K. Cho, Macromol. Rapid Comm. 26 (2005) 834.
[13] T.A. Chen, X. Wu, R.D. Rieke, J. Am. Chem. Soc. 117 (1995) 233.
[14] T.J. Prosa, M.J. Winokur, R.D. McCullough, Macromolecules 29 (1996) 3654.
[15] R.D. McCullough, Adv. Mater. 10 (1998) 93.
[16] R.J. Kline, M.D. McGehee, E.N. Kadnikova, J. Liu, J.M. Fréchet, J. Adv. Mater. 15 (2003) 1519.
[17] S. Pal, A.J. Nandi, Phys. Chem. B 109 (2005) 2493.
[18] S. Pal, A. Nandi, Macromolecules 36 (2003) 8426.
[19] V. Causin, C. Marega, A. Marigo, L. Valentini, J. Kenny, Macromolecules 38 (2005) 409.
[20] A. Zen, M. Saphiannikova, D. Neher, U. Asawapirom, U. Scherf, Chem. Mater. 17 (2005) 781.
[21] K. Kaneto, W. Lim, W. Takashima, T. Endo, M. Rikukawa, Jpn. J. Appl. Phys. 39 (2000) L872.
[22] H. Tachibana, N. Hosaka, Y. Tokura, Macromolecules 34 (2001) 1823.

[23] A. Babel, S. Jenekhe, J. Phys. Chem. B 107 (2003) 1749.
[24] A. Babel, S. Jenekhe, Synth. Met. 148 (2005) 169.
[25] H. Xie, S. O'Dwyer, J. Corish, D. Morton-Blake, Synth. Met. 122 (2001) 287.
[26] H.G.O. Sandberg, G.L. Frey, M.N. Shkunov, H. Sirringhaus, R.H. Friend, Langmuir 18 (2002) 10176.
[27] J.J. Apperloo, R.A.J. Janssen, M. Nielsen, K. Bechgaard, Adv. Mater. 12 (2000) 1594.
[28] J. Liu, E. Sheina, T. Kowalewski, R. McCullough, Angew. Chem. Int. Ed. 41 (2002) 329.
[29] S. Hugger, R. Thomann, T. Heinzel, T. Thurn-Albrecht, Colloid Polym. Sci. 282 (2004) 932.
[30] H. Yang, T.J. Shin, L. Yang, K. Cho, C.Y. Ryu, Z. Bao, Adv. Funct. Mater. 15 (2005) 671.
[31] T. Yamamoto, D. Komarudin, M. Arai, B. Lee, H. Suganuma, N. Asakawa, Y. Inoue, K. Kubota, S. Sasaki, T. Fukuda, H. Matsuda, J. Am. Chem. Soc. 120 (1998) 2047.
[32] K.E. Aasmundtveit, E.J. Samuelsen, M. Guldstein, C. Steinsland, O. Flornes, C. Fagermo, T.M. Seeberg, L.A.A. Pettersson, O. Inganäs, R. Feidenhans'l, S. Ferrer, Macromolecules 33 (2000) 3120.
[33] K. Cho, J.H. Cho, S. Yoon, C.E. Park, J.C. Lee, S.H. Han, K.B. Lee, J. Koo, Macromolecules 36 (2003) 2009.
[34] D.H. Lee, D. Kim, T. Oh, K. Cho, Langmuir 20 (2004) 8124.

Available online at www.sciencedirect.com
ScienceDirect
Organic Electronics 7 (2006) 521–527
Organic Electronics
www.elsevier.com/locate/orgel

Ellipsometric study of an organic template effect: H_2Pc/PTCDA

O.D. Gordan [a,*], T. Sakurai [b], M. Friedrich [a], K. Akimoto [b], D.R.T. Zahn [a]

[a] *Institut für Physik, Technische Universität Chemnitz, Reichenhainer Str. 70/457, D-09107 Chemnitz, Germany*
[b] *Institute of Applied Physics, University of Tsukuba, 1-1-1 Tennodai, Tsukuba, Ibaraki 305-8573, Japan*

Received 22 March 2006; received in revised form 24 July 2006; accepted 24 July 2006
Available online 18 August 2006

Abstract

A key prerequisite for fabricating opto-electronic devices with organic molecules is to control the molecular growth mode. In this work we present an ellipsometric study of the templating effect of 3,4,9,10-perylene tetracarboxylic dianhydride (PTCDA) on the growth mode of metal free phthalocyanine (H_2Pc). The difference in the anisotropic dielectric function between the H_2Pc films grown on bare glass or silicon substrates compared to the anisotropic dielectric function of H_2Pc films grown on PTCDA indicates a drastic change in molecular orientation. From the strong in-plane/out-of-plane anisotropy the average molecular tilt angle of H_2Pc was found to be around 52° for the films grown on bare substrates and around 25° for H_2Pc films grown on PTCDA. A splitting in the H_2Pc Q-band was observed for the H_2Pc films grown on PTCDA which indicates a deviation from the perfect H_2Pc α-phase crystal.

PACS: 81.15.Ef; 68.55.Jk

Keywords: Ellipsometry; Anisotropy; Dieletric function

1. Introduction

The development of organic electronics progressed rapidly in this decade and organic photovoltaic cells are regarded as one of the future high potential molecular electronic applications with the advantage of low cost production of printable and flexible devices [1]. Among novel research subjects for improving photovoltaic cell efficiencies, such as the development of low band-gap materials and device structures, especially controlling the molecular orientation has a great potential for improving the electrical and optical properties of organic films because the anisotropic molecular orbitals contribute to carrier transport and visible light absorption [2]. Nevertheless, only few attempts to control the molecular orientation have been made for the application of photovoltaic cells because most organic semiconductors are difficult to be controlled in their molecular orientation on substrate surfaces of glass and metal oxides due to a weak adsorbate-substrate interaction [3].

It was recently reported using X-ray studies [4] and a combination of X-ray and infrared (IR) [5] that 3,4,9,10-perylene tetracarboxylic dianhydride

* Corresponding author. Tel.: +49 371 531 3548; fax: +49 371 531 3060.
E-mail address: ovidiu.gordan@physik.tu-chemnitz.de (O.D. Gordan).

1566-1199/$ - see front matter © 2006 Elsevier B.V. All rights reserved.
doi:10.1016/j.orgel.2006.07.008

(PTCDA) template layers can control the stacking direction of H_2Pc and phthalocyanine derivative films parallel to the surface of a glass substrate. Such a molecular templating technique is one of the easiest methods for fabricating device structures. Moreover, the orientation of the H_2Pc molecular plane formed on PTCDA is beneficial for photovoltaic cell applications because the stacking direction of the π orbitals predominantly contributes to carrier transport and optical absorption [2]. Especially for this specific device application it is very important to know the optical properties (or the dielectric function) of the active organic layers. In this work these properties were determined using spectroscopic ellipsometry, which is a non-destructive and very surface sensitive technique. The structural as well as the orientational changes within the H_2Pc layers can be detected from the magnitude of the optical anisotropy.

2. Experiment

H_2Pc and PTCDA layers were deposited on glass (Corning 7059) and SiO_2/Si (0 0 1) substrates by organic molecular beam deposition (OMBD) at a base pressure of 1.5×10^{-9} mbar. The organic source materials were purified three times by gradient sublimation and were charged into Knudsen cells. The glass substrates were cleaned in ultrasonic baths of acetone and ethanol and then dried in nitrogen flow before being loaded into the OMBD chamber. The SiO_2/Si structure was fabricated depositing SiO_2 on Si(0 0 1) wafers by electron beam evaporation. After a PTCDA template layer was grown, thick H_2Pc layers were deposited on it. The sample holder was held at room temperature during all deposition processes. The deposition rate was measured using a quartz oscillator close to the substrate holder and was maintained below 0.1 Å/s.

Ellipsometric measurements were performed using a variable angle spectrometric ellipsometer (VASE, J.A. Woollam Co. Inc.). In order to determine the thickness and optical properties of the samples, the measurements were carried out in a large spectral range, from 0.73 to 5 eV, with a 0.02 eV energy step. Measuring the samples at incidence angles around the Brewster angle of the substrate increases the sensitivity of this technique. The samples on glass substrates were measured at several angles of incidence, between 55° and 70° with a step of 5°. The measurements for the SiO_2/Si substrates were performed between 65° and 75° with the same step. In addition, the transmittance of the organic layers on glass substrates was also measured.

In ellipsometry the change in the polarisation state of light is measured after reflection on a sample. The relation between the amplitudes of the reflected E_r and incident E_i electric field can be written in the Jones matrix formalism as

$$\begin{pmatrix} E_{rp} \\ E_{rs} \end{pmatrix} = \begin{pmatrix} r_{pp} & r_{sp} \\ r_{ps} & r_{ss} \end{pmatrix} \begin{pmatrix} E_{ip} \\ E_{is} \end{pmatrix}$$

The diagonal elements of the Jones matrix represent the change of amplitude and phase of the p- and s-components, while the off-diagonal elements describe the transfer of energy from the p-component to the s-component and vice versa. For isotropic samples or anisotropic uniaxial samples with in-plane isotropy the off-diagonal elements of the Jones matrix are zero. In this case the change in the polarization state can be described in terms of the ellipsometric parameters Ψ and Δ. The ellipsometric parameters are related to the ratio of Fresnel reflection coefficients r_{pp} and r_{ss} by

$$\rho = \frac{r_{pp}}{r_{ss}} = \tan \Psi \exp(i\Delta).$$

For the evaluation of the ellipsometry spectra a model which describes the interaction of light with a specific sample structure has to be taken into consideration. A detailed description of the ellipsometry principles and theory can be found in Ref. [6].

3. Results

3.1. Single layers

In order to assess the in-plane anisotropy, all samples were measured at different azimuthal angles. The measurement revealed that the ellipsometric spectra are independent of the azimuthal angle. This indicates that all samples have in-plane isotropy. However, due to their intrinsic molecular anisotropy and their crystalline growth it is known that H_2Pc [7,8] and PTCDA form anisotropic layers [9,10]. Therefore, an out-of-plane optical anisotropy was considered when modeling the optical response of the organic layers. In this case the in-plane contributions are equal, i.e. $\varepsilon_x = \varepsilon_y = \varepsilon_{\parallel}$, while the out-of-plane one, perpendicular to the substrate surface, $\varepsilon_z = \varepsilon_{\perp} \neq \varepsilon_{\parallel}$ is different. As the transmission measurements were performed at normal incidence, these data can be used to determine $\varepsilon_{\parallel}$ for the films deposited on transparent substrates.

The first step in data evaluation is thickness determination. For an accurate determination of the thickness the optical properties of the substrates are taken into account. The optical response of the silicon reference substrate was simulated using the existent dielectric function in the data base for silicon [11] and for the silicon oxide [12]. The thickness of the silicon oxide was found to be 31 (±0.02) nm.

The dielectric function of the glass substrate was determined from a reference ellipsometric measurement. During the fit the data from both ellipsometry and transmission measurements are considered. Especially for anisotropic samples this procedure is particularly useful in lowering the correlation factor between the floating parameters used to simulate the in-plane and out-of-plane contributions.

The film thicknesses of the organic layers were determined in the transparent range of the material where the optical properties are described by the Cauchy dispersion relation:

$$n(\lambda) = A + \frac{B}{\lambda^2} + \frac{C}{\lambda^4},$$

where n is the film refractive index and λ is the wavelength. In the numerical fitting procedure A, B, C and the film thickness are floating parameters. Usually A and B are enough to describe the optical dispersion in the transparent range and C is set to zero. For uniaxial anisotropic films two sets of Cauchy relations are used to describe the optical properties in a direction parallel with the film surface and perpendicular to it, respectively. The thicknesses obtained from the ellipsometric data evaluation are presented for the layers on glass in the transmittance plots and in Table 1 for the layers on SiO_2/Si.

After the thickness determination the transmission spectra can be used to determine $\varepsilon_{||}$. Considering an isotropic model the simulation of the ellipsometric spectra using the extinction coefficient determined from the absorption together with the Kramers–Kronig consistent refractive index does not provide satisfactory agreement with the experimental data. Therefore an uniaxial model has to be considered for the ellipsometric data. In this model two sets of dielectric functions are used to model the sample properties in the directions parallel and perpendicular to the sample surface. In order to have a Kramers–Kronig (KK) consistent solution, the imaginary part of the dielectric function is simulated using Gaussian oscillators while the real part is solved employing the KK relation. In order to reduce the correlation between parameters during the fitting procedure, three samples with different thicknesses are considered in the model together with their transmission data. The validity of this evaluation holds as long as the organic films have the same optical properties regardless of the film thickness. In Fig. 1 the simulated and experimental transmittance data of the H_2Pc films on glass substrates are plotted. The reference glass transmittance is also shown.

Table 1
The thicknesses of the single layers determined from ellipsometry in the transparent range of the H_2Pc and PTCDA films on SiO_2/Si substrates

Substrate	Material	Thickness/nm
SiO_2/Si	H_2Pc	36.7 ± 3.4
		18.3 ± 1.7
		11.2 ± 1.1
SiO_2/Si	PTCDA	10 ± 1
		0.5 ± 0.4

The anisotropic dielectric function of H_2Pc is presented in Fig. 2. As all transmission measurements were performed at normal incidence, the simulation of the transmittance spectra is done using the in-plane components. The shape of the absorption bands is in agreement with previous reports [9,13] and indicates that the films consist of α-phase H_2Pc with its well known herringbone structure [7,8]. Taking into account that the absorption features in the presented spectral range are induced by π–π* transitions, which are polarized in the

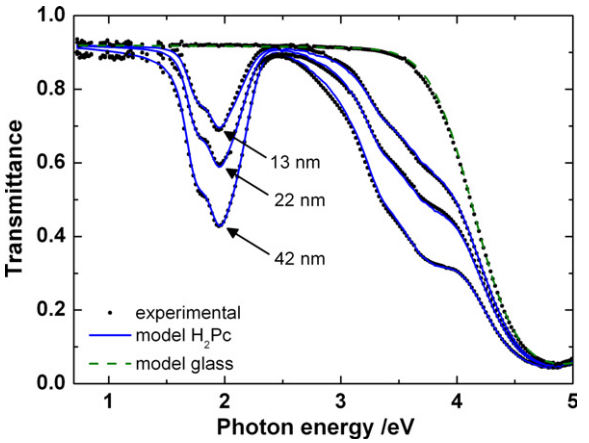

Fig. 1. Transmittance spectra of H_2Pc layers on glass substrates. For comparison the transmittance of the glass substrate is also plotted. The continuous lines represent the model simulation of the transmittance using the in-plane component of the dielectric function.

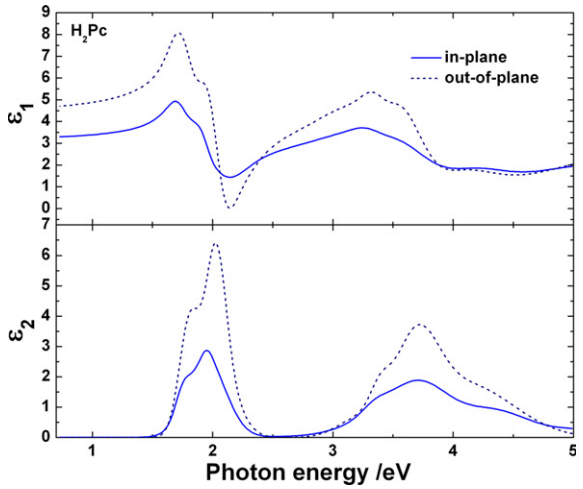

Fig. 2. The real and imaginary parts of the dielectric function of the H_2Pc films deposited on glass and SiO_2/Si.

molecular plane, an average molecular orientation can be deduced from the differences in the extinction coefficient between the *xy* (in-plane) and the *z* (perpendicular) contribution [9]. Considering in a first approximation that the H_2Pc is planar and the overall absorption intensity is the result of a scalar product between the electric field vector and the transition dipole, the average orientation of the molecules with respect to the substrate was found to be ~52°. This indicates that the growth mode of H_2Pc is α-phase with the molecular stacking axis oriented parallel with the substrate surface. Due to the reduced ellipsometric sensitivity for the out-of-plane component [14] we estimate a possible error in the tilt angle determination of ±4°. While we consider that we detect the right anisotropy magnitude, the error is estimated from the slightly different solutions that can be obtained for the out-of-plane component.

A similar analysis procedure was applied for the H_2Pc films grown on the silicon oxide/silicon substrates. The in-plane dielectric function was found to be identical with the one presented in Fig. 2. The out-of-plane component was slightly different leading to a tilt angle of ~53°. As the in-plane component of the dielectric function is identical for the H_2Pc films grown on glass with the one of H_2Pc films grown on silicon substrates and the difference in the out-of-plane component is within the error limits we consider that these films exhibit similar growth modes.

These findings are in agreement with recent studies of H_2Pc orientation studied by infra-red reflection absorption spectroscopy (IRRAS) [5], X-ray diffraction [15] and consistent with previous results derived from ellipsometry for CuPc [10].

A similar analysis was performed for PTCDA molecules grown on glass and silicon oxide/silicon substrates. Fig. 3 shows the anisotropic dielectric function of PTCDA. In Fig. 4 the corresponding experimental transmittance spectra of PTCDA on glass and the corresponding model simulation are presented. The difference in the imaginary part of the dielectric function between the in-plane component and the out-of-plane one indicates that the molecules lie flat on these substrates [5]. The shape of the in-plane dielectric function is in agreement with previous reports [16,17].

3.2. Heterostructures

In the ellipsometric data evaluation of the heterostructures H_2Pc/PTCDA/substrate, the previously determined dielectric function was used for the PTCDA layer. The thicknesses of the PTCDA layers were estimated from transmission measurements, in the range where PTCDA has its strong absorption feature and H_2Pc has a very low absorption. With the PTCDA thickness fixed, the previously described ellipsometric procedure was applied to find the H_2Pc thickness. Compared to H_2Pc single layers a good data simulation was obtained only if surface roughness was considered in the model. Again the thicknesses obtained for the layers on the glass substrates are presented in

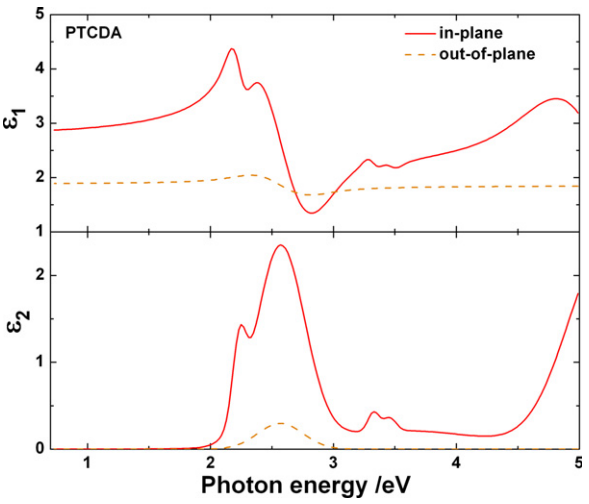

Fig. 3. The real and imaginary parts of the dielectric function of the PTCDA films deposited on glass and SiO_2/Si.

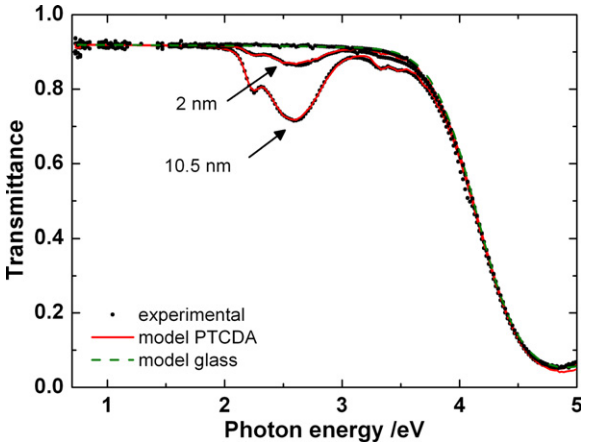

Fig. 4. Transmittance spectra of PTCDA layers on glass substrates. For comparison the transmittance of the glass substrate is also plotted. The continuous lines represent the model simulation of the transmittance using the in-plane component of the dielectric function.

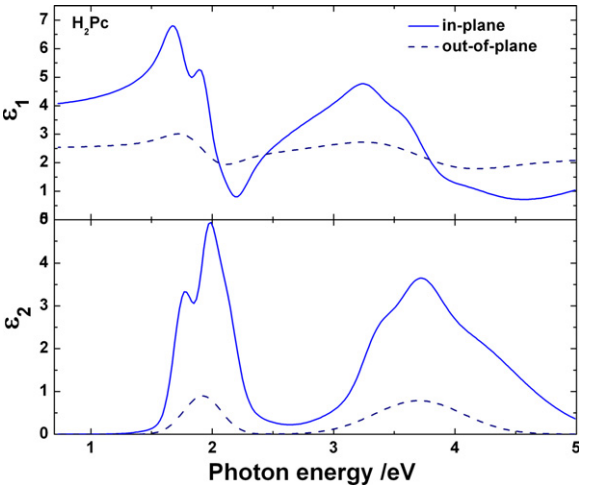

Fig. 5. The real and imaginary parts of the dielectric function of the H_2Pc films deposited on PTCDA.

the transmittance figures, while the thicknesses for the layers on SiO_2/Si are summarized in Table 2.

Fig. 5 shows the anisotropic dielectric function of the H_2Pc layer deposited on PTCDA. As can be seen the in-plane component now is stronger than the out-of-plane one suggesting that the H_2Pc molecules have a considerably lower tilt angle with respect to the substrate. This is most likely due to the strong interaction of the PTCDA π orbitals with the π orbitals of the first monolayer of H_2Pc, which leads to a templating effect [4,5,15]. Applying the procedure described above, a ~25° average tilt angle was calculated for the molecular orientation. This value is very close to the 27° value deduced from IRRAS [5] and in agreement with a crystalline growth of H_2Pc with the stacking axis perpendicular with the substrate surface, since the angle between the normal to the molecular plane and *b*-axis is 26.5°.

Fig. 6 shows the transmittance data of the H_2Pc films on PTCDA layers thicker than 6 nm and the model simulation. The total thickness of the H_2Pc layers is indicated. In ellipsometry the surface roughness is modelled using an effective medium approximation with 50% voids. The total thickness thus is calculated by adding the surface roughness divided by 2. As can be seen in Fig. 6 the model

Table 2
The thicknesses of the organic layers in the heterostructures: H_2Pc/PCTDA/Substrate determined from the simulation of the ellipsometry spectra using the dielectric functions from figs. 3 (PTCDA) and 5 (H_2Pc)

Substrate	PTCDA Thickness/nm	H_2Pc	
		Thickness/nm	Surface roughness/nm
SiO_2/Si	7.5	19.6	7.9
	13.3	16.5	2.5
	10.4	5	1.2
SiO_2/Si	5.1	25.3	12.5
	5.9	9.5	8.3
	3.8	5.5	7.8

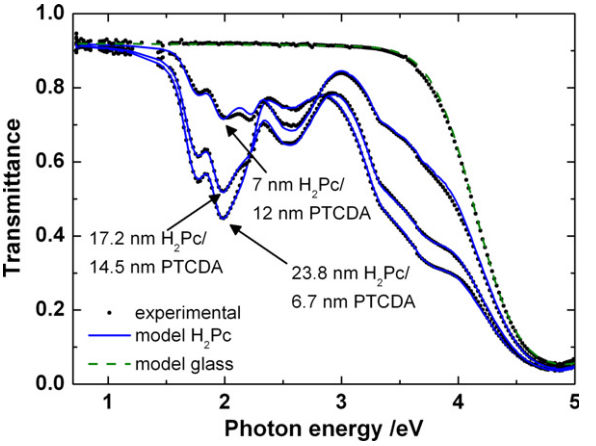

Fig. 6. Transmittance spectra of H_2Pc layers on PTCDA/glass substrates with PTCDA thickness higher than 7 nm. For comparison the transmittance of the glass substrate is also plotted. The continuous lines represent the model simulation of the transmittance using the in-plane component of the dielectric function.

simulation matches perfectly for the thick H_2Pc layers, but a small deviation in the transmission data can be noticed for the 7 nm H_2Pc layer. This deviation was also observed in the ellipsometric spectra. This is an indication that the thin H_2Pc layer has a small deviation in the optical constants, when compared to thicker layers. The difference is probably due to a small difference in the molecular packing [15], as the structure of the first H_2Pc monolayers have a deviation from the α-phase H_2Pc due to the templating effect of the PTCDA.

The same model was applied successfully to H_2Pc layers grown on PTCDA layers with thicknesses lower than 1.4 nm. This proves that even a very small thickness of PTCDA is sufficient to induce the template effect. Fig. 7 shows the transmittance data for these layers grown on the glass substrate. Also in this case a small deviation from the experimental data was noticed for the 34 nm H_2Pc layer. As this layer is the thickest, it seems to support a small molecular reorientation with the increasing thickness. However, for this layer a higher uncertainty in calculating the PTCDA layer thickness was noticed due to the small value, probably less than 0.3 nm.

The data evaluation for the SiO_2/Si substrate was more difficult because it was hard to estimate the thickness of the PTCDA layer beneath H_2Pc. The previous determined dielectric functions of the H_2Pc on PTCDA and of PTCDA on glass were used to determine the thickness. This evaluation gave a

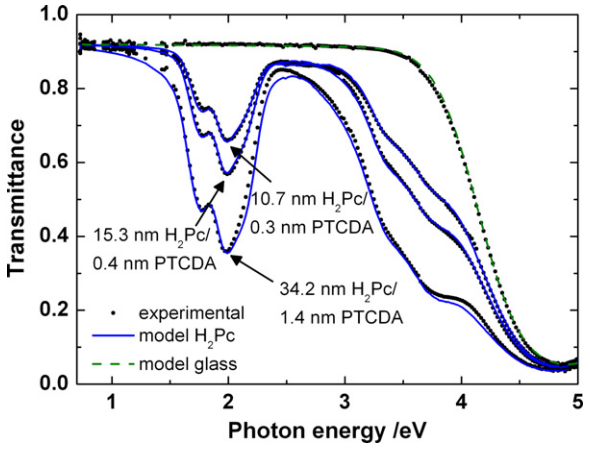

Fig. 7. Transmittance spectra of H_2Pc layers on PTCDA/glass substrates with PTCDA thickness less than 2 nm. For comparison the transmittance of the glass substrate is also plotted. The continuous lines represent the model simulation of the transmittance using the in-plane component of the dielectric function.

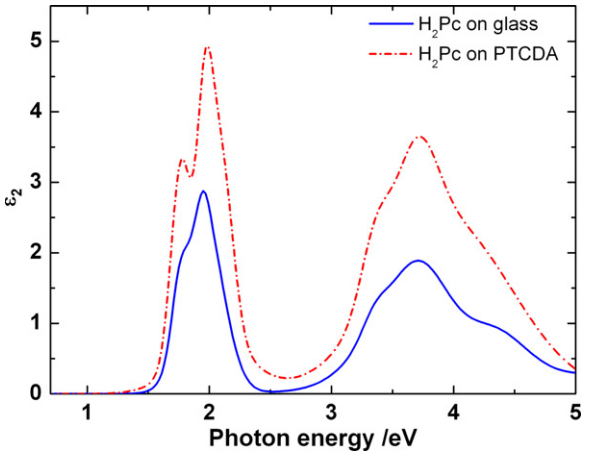

Fig. 8. Comparison between the in-plane imaginary dielectric function of H_2Pc on glass and SiO_2/Si and the in-plane imaginary dielectric function of H_2Pc on PTCDA.

very good simulation of the ellipsometric spectra in the measured spectral range, indicating that the films on SiO_2/Si substrates have the same optical properties like the ones on glass substrates.

Fig. 8 shows the imaginary part of the in-plane dielectric function for the H_2Pc layers grown on glass and SiO_2/Si substrates, compared with the one of the films grown on PTCDA. Besides the higher values for H_2Pc grown on PTCDA due to the lower tilt angle with respect to the substrate, which demonstrate the template effect induced by PTCDA, a splitting of the Q-band can be observed. The splitting is also visible in the transmission measurements. While the difference can be attributed to the observation of the optical properties of the α-phase H_2Pc in different crystal direction, the splitting can also be a sign of a small deviation from the perfect H_2Pc α-phase crystal. As the degree of overlapping of the H_2Pc π orbitals changes the shape of the Q-band thus making it possible to distinguish between the different crystalline forms of H_2Pc [7,8], the possibility that PTCDA induces a deviation from the perfect α-phase crystal has to be taken into consideration [15,18].

4. Summary

The optical response of H_2Pc layers grown on SiO_2/Si and glass substrates and on PTCDA were determined using spectroscopic ellipsometry. Due to the intrinsic anisotropy of the H_2Pc and PTCDA, the optical anisotropy was considered when modeling the optical response of organic layers. For a

H_2Pc layer grown on a glass substrate, the tilt angle of H_2Pc molecule with respect to the substrate surface was found to be 52° while its angle for H_2Pc deposited on PTCDA layer was estimated to be approximately 25°. Such variation of the H_2Pc molecular orientation is consistent with IR-RAS and XRD results reported previously [5] and is caused by the van der Waals intermolecular interaction between PTCDA and H_2Pc at the heterointerface. The simulated results of transmittance spectra, which were calculated from the in-plane components of the dielectric functions, match perfectly with the experimental results. While the lower orientation angle of the H_2Pc on PTCDA increases the light absorption efficiency, the overlapping of the π orbitals in a direction perpendicular to the film surface should also decrease the electrical resistance in this direction. This effect could thus be useful for the organic solar cells construction.

The splitting of the Q-band that was observed in both transmission and the imaginary part of the in-plane dielectric function for H_2Pc/PTCDA heterostructure might be caused by a small deviation from the perfect α-H_2Pc crystal. Therefore, the reliable optical parameters of H_2Pc films grown on glass and PTCDA can be determined from the simulation of ellipsometric spectra proving that this technique can be a useful tool for improving the structural and optical properties of the organic films.

Acknowledgement

We gratefully acknowledge the financial support of the Deutsche Forschungsgemeinschaft, Graduiertenkolleg 829 ‘‘Akkumulation von einzelnen Molekülen zu Nanostrukturen‘‘.

References

[1] C.J. Brabec, N.S. Sariciftci, J.C. Hummelen, Adv. Funct. Mater. 11 (2001) 15.
[2] M. Pope, C. Swenberg, Electronic Processes in Organic Crystals and Polymers, second ed., Oxford University Press, New York, 1999.
[3] S. Tokito, J. Sakata, Y. Taga, Thin Solid Films 256 (1995) 182.
[4] S. Heutz, R. Cloots, T.S. Jones, Appl. Phys. Lett. 77 (2000) 3938.
[5] T. Sakurai, S. Kawai, J. Shibata, R. Fukasawa, K. Akimoto, Jpn. J. Appl. Phys. 44 (2005) 1982.
[6] R.M.A. Azzam, N.M. Bashara, Ellipsometry and Polarized Light, Elsevier, Amsterdam, 1992.
[7] N.B. McKeown, Phthalocyanine Materials, Cambrige University Press, 1998.
[8] C.C. Leznoff, A.B.P. Lever, Phthalocyanines, Properties and Applications, VCH, New York, 1996.
[9] O. Gordan, M. Friedrich, D.R.T. Zahn, Thin Solid Films 455–456 (2004) 551.
[10] O. Gordan, M. Friedrich, D.R.T. Zahn, Org. Electron. 5 (2004) 291.
[11] G.E. Jellison, Opt. Mater. 1 (1992) 41.
[12] E. Palik (Ed.), Handbook of Optical Constants of Solids, vol. 1. Academic Press, p. 759.
[13] H. Arwin, D.E. Aspnes, Thin Solid Films 138 (1986) 195.
[14] D.E. Aspnes, J. Opt. Soc. Am. 70 (10) (1980) 1275.
[15] T. Sakurai, R. Fukasawa, K. Akimoto, Jpn. J. Appl. Phys. 45 (2006) 255.
[16] O. Gordan, S. Hermann, M. Friedrich, D.R.T. Zahn, J. Appl. Phys. 97 (2005) 63518.
[17] M. Friedrich, Th. Wagner, G. Salvan, S. Park, T.U. Kampen, D.R.T. Zahn, Appl. Phys. A 75 (2002) 501.
[18] S. Heutz, G. Salvan, S.D. Silaghi, T.S. Jones, D.R.T. Zahn, J. Phys. Chem. B 107 (2003) 3782.

Available online at www.sciencedirect.com
ScienceDirect
Organic Electronics 7 (2006) 528–536
Organic Electronics
www.elsevier.com/locate/orgel

Field-induced mobility degradation in pentacene thin-film transistors

Mohammad Mottaghi, Gilles Horowitz *

ITODYS, CNRS-UMR 7086, University Denis-Diderot, 1 rue Guy de la Brosse, 75005 Paris, France

Received 15 June 2006; received in revised form 21 July 2006; accepted 26 July 2006
Available online 22 August 2006

Abstract

Pentacene-based organic thin-field transistors (OTFTs) with bottom-gate, top-contact architecture were fabricated on alumina substrates. The devices were divided into two sets, depending on whether pentacene was deposited on bare alumina or on alumina modified with a fatty acid self-assembled monolayer (SAM). Previous analysis have shown that the modification of alumina with SAMs result in a substantial decrease of the size of the grains in hte polycrystalline films. Careful parameters extraction, including an original determination of the threshold voltage, and contact resistance extraction through the transfer line method (TLM), allowed us to estimate the gate-voltage dependent mobility in both series. The mobility is found to first increase at low bias, and then decrease at higher gate voltage (mobility degradation). The latter behavior is explained through an estimation of the distribution of charges across the accumulation layer, in which the pentacene film is modeled as a stack of dielectric layers, the distribution being calculated using basic equations of electrostatics and thermodynamics. A good agreement was found when the mobility in the layer next to the insulator was assumed to be negligible as compared to that in the bulk of the film. The initial rise of the mobility is interpreted in terms of multiple trap and release (MTR) with a distribution of traps located in the grain boundaries. Interestingly, the mobility corrected for both contact resistance and mobility degradation is found around 3 cm^2/V s for pentacene deposited on bare alumina, and 5 cm^2/V s when pentacene is deposited on SAM modified alumina. We conclude that the smaller grains grown on modified alumina are more regular, and hence less defective, than the larger grains deposited on bare alumina.

PACS: 72.20.Jv; 73.40.−c; 73.61.Ph; 85.30.Tv; 68.55.Ln

Keywords: Organic field-effect transistors; Self-assembled monolayers; Mobility extraction; Transfer line method; Multiple trapping and release

1. Introduction

Gate-voltage dependent mobility is now a well-recognized feature in organic thin-film transistors (OTFTs) [1–4]. Most usually, mobility is found to increase with gate voltage. Two useful models for accounting for this are the multiple trapping and release (MTR) and variable range hopping (VRH). The basic assumption of MTR [3,4] is a distribution of states localized in the energy gap close to the transport band edge. These states are liable to trap

* Corresponding author.
E-mail address: horowitz@paris7.jussieu.fr (G. Horowitz).

1566-1199/$ - see front matter
doi:10.1016/j.orgel.2006.07.011

the charge carriers injected into the channel of the transistor, thus reducing the current. When increasing the gate voltage, the Fermi level moves towards band edge as more of the empty traps are filled by injected charge. Accordingly, the ratio of free to trapped carriers increases, and so does the channel conductivity, which is interpreted in term of an increase of the effective mobility. The VRH model [2] also assumes a distribution of localized levels; it proposes that transport occurs via hopping in that distribution. Like with the MTR model, the gate-voltage dependent mobility is explained through the filling of the lower energy states, so additional carriers occupy higher energy states, which demand lower activation energy to hop to the next site.

More recently, a reverse behavior has been reported, where the mobility *decreases* with gate voltage [5–7]. It is worth pointing out that a similar trend has been identified for long in conventional silicon-based metal-oxide-semiconductor field-effect transistors (MOSFETs) [8], where it is attributed to various scattering agents in the vicinity of the insulator interface, namely charged centers, surface phonons and surface roughness. A usual way to describe this behavior is to introduce the so-called "mobility degradation factor" θ, which in its simplest formulation leads to a mobility that looks like

$$\mu = \frac{\mu_0}{1 + \theta(V_G - V_T)}, \quad (1)$$

where V_G is the gate voltage and V_T the threshold voltage.

We have previously shown [5] that the structure of pentacene films vapor deposited on alumina (Al_2O_3) is drastically changed by modifying the surface of the oxide with a self-assembled monolayer (SAM). On bare alumina, we observed a two-dimensional growth of the first monolayer followed by a three-dimensional process with larger grains, while films on SAM-modified alumina were made of grains of smaller dimension. In this paper, we report on new gate-voltage dependent measurements that bring evidence for field-induced mobility degradation on pentacene deposited on both substrates. A model for charge distribution in the channel, based on the layered structure of the pentacene film, is developed to account for this feature. It is found that the mobility in the molecular layer close to the insulator–semiconductor interface is substantially lower than that in the bulk of the pentacene film. For the latter, the mobility is interpreted in terms of the MTR model. The respective trap-free mobility and trap distribution in bare and SAM-modified devices are discussed under the perspective of the corresponding structure of the films.

2. Experimental

The OTFTs where fabricated on highly doped p-type silicon wafers that acted as the gate electrode of the device. The insulator (Al_2O_3) was grown in a homemade vacuum chamber by bombarding an aluminum target with oxygen ions under reduced pressure (~1 Pa). The growth rate in this unusual deposition technique is very low, thus resulting in highly dense and smooth films, with a root-mean square (RMS) roughness, as measure by atomic force microscopy (AFM) profiling, comparable to that of the underneath silicon substrate (0.2 nm). The thickness of the Al_2O_3 layer was 100 nm and its capacitance 75 nF/cm^2. Before pentacene deposition or modification, the alumina substrates were cleaned in pure sulfuric acid, rinsed in deionized water and blown dry in a flux of argon. Self-assembled monolayers of eicosanoic acid $CH_3(CH_2)_{18}COOH$ were deposited by dipping the substrate during 45 min. into a solution in benzene. Silanes (e.g., octadecyltrichlorosilane OTS) are commonly used on silicon oxides. However, a fatty acid (in our case, eicosanoic acid) was preferred to silanes because it more readily assembles on alumina. We note that, because the length of the alkyl chain is comparable in OTS and eicosanoic acid (18 and 19 carbon atoms, respectively), the robustness of the corresponding SAMs is equivalent, as was checked by contact angle measurement and surface IR spectroscopy [5]. 30 nm of pentacene (Aldrich, used as received) was vapor deposited at a base pressure of 10^{-5} Pa at a rate of 0.01 nm/s on substrates kept at room temperature. Source and drain electrodes were made of 20 nm thick gold evaporated through a shadow mask with channel lengths ranging between 5 and 40 μm. The current–voltage characteristics were recorded under ambient condition with a Karl Suss manual probe station and a Keithley 4200 semiconductor characterization system.

3. Multi-layer model

The multi-layer model takes advantage of the layer structure of vapor deposited molecular films with rigid molecules like pentacene or the oligothiophenes. A first version of the model has been published recently [9]. However, we discovered that this

first version contained an inappropriate formulation of Gauss's law (see Eq. (A.2)), which is corrected here. Note that this initial mistake only resulted in quantitative changes, while the general conclusions of the model were preserved.

Pentacene molecules can be viewed as rigid rods, which in the solid state assemble parallel to each other, thus forming parallel layers, the thickness of which equals the length of the molecule (minus a small correction to account for a tilt angle). Because

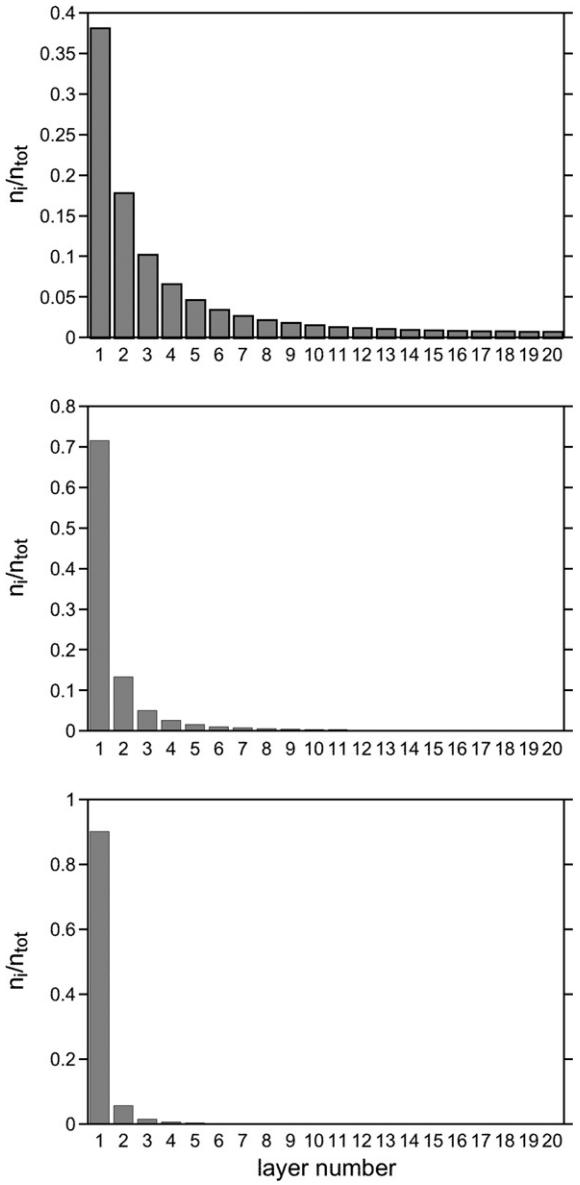

Fig. 1. Distribution of charge carriers in a 30 nm (20 ML) thick pentacene film with an insulator capacitance of 75 nF/cm^2. From top down: $V_G = 1$ V, 5 V and 25 V.

(1) each molecule cannot bear more than one elemental charge carrier and (2) the charge practically extends all over the molecule [10], we assimilate the pentacene film to a stack of n dielectric layers of thickness d, each layer carrying a uniform density of carriers n_i. The layers are numbered starting from the insulator side. The calculation of the charge distribution is detailed in the Appendix. It does not lead to an analytical expression, but rather to Eq. (A.10) that relates the charge in layer i to that in layers $(i+1)$ to n.

Two additional equations were used to perform the numerical calculation. The first one derives from a product of Eq. (A.9) and gives the potential at the insulator–semiconductor interface

$$V_0 = \frac{kT}{q} \ln \frac{n_1}{n_n}, \tag{2}$$

while the second one gives the total charge in the film.

$$qn_{\text{tot}} = q \sum_1^n n_i = C_i(V_G - V_0). \tag{3}$$

Here, we have assumed $V_T = 0$. In pentacene, the thickness of a monolayer, as determined by X-ray diffraction, is 1.54 nm [11], so a 30 nm thick layer roughly contains 20 monolayers. Fig. 1 shows the distribution of charge carriers at three different gate voltages: 1, 5 and 25 V. It clearly appears that as V_G increases, the charge concentrates in the first layer.

At this stage, it is worth pointing out that our calculation only refers to the distribution of the total (free and trapped) charge in the semiconductor. No assumption was made on how these charge moves; in particular, we stress that the presence in the insulator of charges (fixed and mobile) and dipoles only acts on the mobility and threshold voltage, not on the charge distribution.

4. Results

4.1. Structure of the evaporated films

The effect of the eicosanoic acid SAM on the structure of the pentacene layer has been extensively studied in our previous works [5]. It appeared that on bare Al_2O_3, the growth starts two dimensional and then turns to three-dimensional with larger, though loosely connected grains, while on SAM modified substrates, the growth is three-dimensional all along, with much smaller grains. The situation is schematically depicted in Fig. 2. Note that the

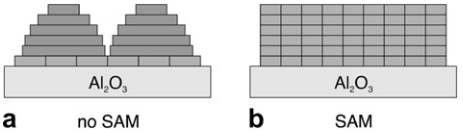

Fig. 2. These cartoons are schematic view of the structure of vapor deposited pentacene on (a) bare and (b) eicosanoic acid SAM modified Al_2O_3. In (a), a two-dimensional layer of medium-sized (~200 nm) grains is topped by larger three-dimensional islands (average diameter 1 μm). In (b) the size of the grains is reduced to 50 to 100 nm, while the growth process is three-dimensional all along.

actual number of layers in our films is significantly higher than what drawn in the figure, so that the disruption between grains only occurs far from the insulator–semiconductor interface.

4.2. Parameters extraction

Extracting the mobility and threshold voltage of an OTFT from its current–voltage characteristics is a crucial step for any modeling of the device operation. The most widespread technique uses the saturation current, which is predicted by simple models to be proportional to $(V_G - V_T)^2$, so that plotting the square root of the current as a function of the gate voltage would give a straight line from which both parameters can be estimated. However, this method presents two major drawback: It cannot be corrected for contact resistance, and it is blind to gate-voltage dependence.

Another common method uses the first derivative of the linear-regime current Eq. (4) as a function of gate voltage (the so-called linear-regime transconductance.)

$$I_D = \frac{W}{L}\mu C_i (V_G - V_T) V_D. \tag{4}$$

However, for a gate-voltage dependent mobility the exact expression of the linear-regime transconductance is

$$\frac{\partial I_D}{\partial V_G} = \frac{W}{L} C_i V_D \left(\mu + (V_G - V_T)\frac{\partial \mu}{\partial V_G}\right), \tag{5}$$

so that the method is only valid when the second term in brackets can be neglected, that is, for a slowly varying mobility (which seems to be only the case with single crystals [12].) Be this condition not fulfilled, the resulting mobility would be overestimated when mobility increases with gate voltage, and underestimated when it decreases. The problem is illustrated in the middle panel in Fig. 3, where it

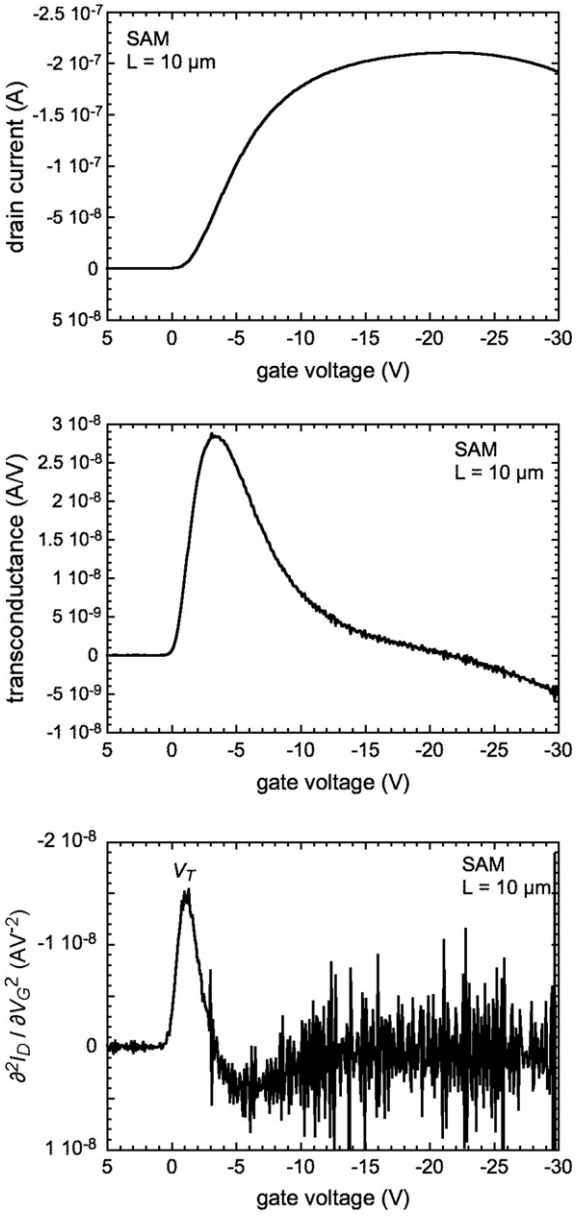

Fig. 3. These curves are representative of the linear-regime in our devices. Top panel: drain current vs. gate voltage at a drain voltage of −0.2 V. Middle panel: first derivative (linear transconductance); this curve is often claimed to be proportional to the mobility. The lower panel illustrates the method used to estimate the threshold voltage. It shows the second derivative of the drain current. The threshold voltage corresponds to the first peak ($V_T = -1.0$ V).

can be seen that the linear transconductance presents strong variations, and eventually becomes negative at high gate bias.

Our method includes a separate extraction of the threshold voltage from the linear regime, which then

allows for estimating the mobility without any derivation step. The sequential steps of the method are detailed as follows.

4.2.1. Threshold voltage

The threshold voltage is defined as the point above which significant drain current flows. In conventional MOSFETs, it is understood as the transition point between weak and strong inversion. In the OTFT, which operates in the accumulation regime, the change is between depletion and accumulation. As the threshold voltage is of fundamental importance for circuit modeling, numerous methods have been developed to extract its value in conventional MOSFETs [13]. Interestingly, extraction is mostly done at low drain voltages, where the device operates in the linear regime. The technique we have selected for this work determines V_T from a double derivation of the drain current at low drain voltage with respect to the gate voltage [14]. This method was preferred because it was claimed to be insensitive to both mobility degradation and contact resistance. A representative example is given in Fig. 3 for a SAM modified device.

With this method, V_T could be extracted for each device. Of the 12 devices without SAM and 13 devices with SAM used in this work, we obtained a threshold voltage of (1.2 ± 0.4) V in the former series and (-1.2 ± 0.1) V in the latter one. We note that V_T is shifted by around -2.4 V by the presence of the SAM, and that the dispersion of the data is less pronounced in SAM modified devices, which can be explained by stating that, owing to its reduced surface energy, SAM-modified alumina is less liable to contamination than bare alumina.

Once V_T is known, the gate-voltage dependent mobility is directly calculated from Eq. (4), which does not requires any derivation. The result is shown in Fig. 4. for the same sample as in Fig. 3.

4.2.2. Contact resistance

Contact resistance R_s is becoming a major issue as the performance of OTFTs improves. There are two main methods for extracting R_s: Four-point measurements [6,15,7] and the transfer line method (TLM) [16–19]. Although the latter is less reliable because it requires measurements on different devices, the contact resistance of which may vary from sample to sample, we used this second method because it is less technologically demanding. We used four channel lengths L (5, 10, 25, and 40 μm), and two to four devices for each channel length. The width normalized resistance in the linear regime is given by

$$RW = R_s W + \frac{L}{\mu C_i (V_G - V_T)}. \quad (6)$$

Because the threshold voltage was independently known for each device, Eq. (6) could give both the contact resistance and gate-voltage dependent mobility. In practice, we measured the transfer characteristic of each sample at low drain voltage ($V_D = -0.2$ V) and then used a linear regression method to estimate the gate-voltage dependent R_s and μ. Data are shown in Fig. 5; we recall that they result of 12 different devices for the bare alumina series and 13 devices for the SAM-modified series. Note that the contact resistance is very similar for both series, which is consistent with the fact that we used a top-contact geometry, so that the contacts are little affected by the nature of the insulator–semiconductor interface.

It is worth pointing out that, while the data of the SAM-modified devices are in good agreement with our earlier report [5], there is some discrepancy as for the devices made on bare alumina. In our earlier work, we reported a significantly lower mobility that tended to increase all along with the gate voltage. The discrepancy was identified as coming from a defective surface cleaning, as was checked by comparing devices prepared according to the old cleaning process to the new one. In the latter case, the alumina substrates were introduced in the evaporation chamber immediately after etching with pure sulfuric acid; waiting for roughly one hour (as was the case in the old process) resulted in a substantial degradation of the characteristics.

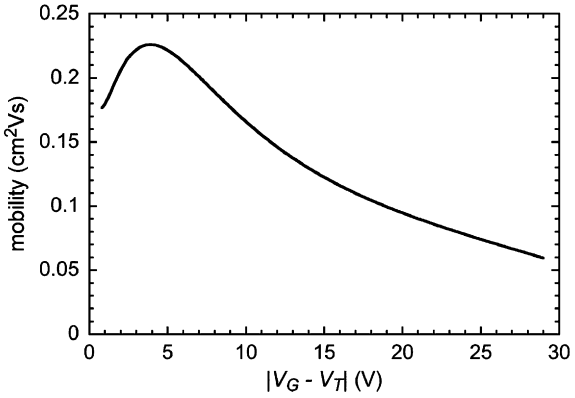

Fig. 4. Gate voltage dependent mobility of the same device as in Fig. 3. The mobility is calculated form Eq. (4) where V_T is estimated with the second derivative method illustrated in the bottom panel of Fig. 3.

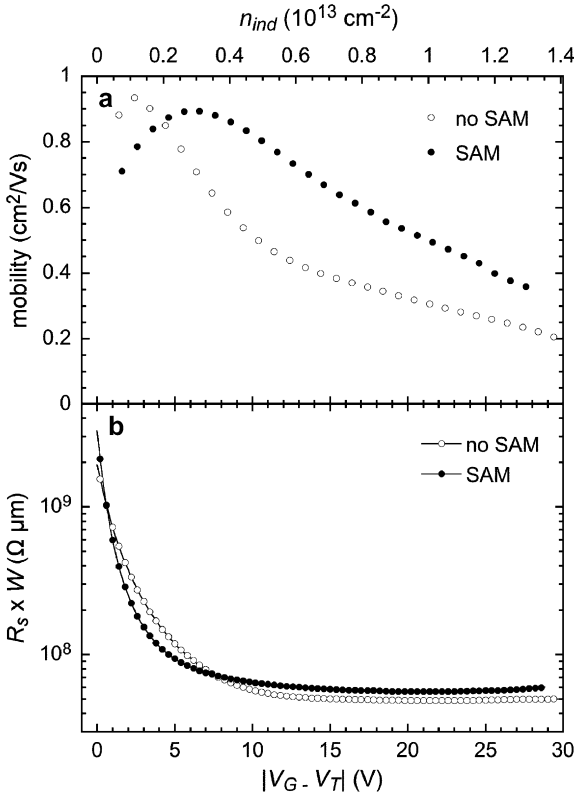

Fig. 5. Gate-voltage dependent mobility (a) and contact resistance (b) as deduced from the transfer line method on pentacene films deposited on bare and SAM-modified alumina. The upper x axis in (a) shows the surface density of injected charge.

4.3. Estimation of the bulk mobility

In all cases, the gate-voltage dependent mobility shows a decrease at high gate voltage. To account for this effect, we assume that the mobility is substantially lower in the region close to the insulator–semiconductor interface than in the bulk of the film. The above developed multi-layer model was used to account for this degradation of the mobility. The effective mobility of the semiconductor is derived by identifying the film to parallels layers of mobility μ_i:

$$\mu_{\text{eff}} = \sum_{1}^{n} \mu_i \frac{n_i}{n_{\text{tot}}}. \tag{7}$$

If the mobility in the first layer can be neglected in front of that in the bulk of the film, we have

$$\mu_{\text{eff}} \simeq \mu_{\text{b}} \left(1 - \frac{n_1}{n_{\text{tot}}}\right), \tag{8}$$

where μ_{b} is the bulk mobility.

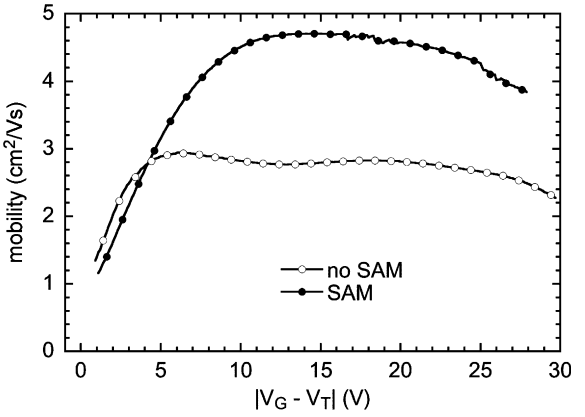

Fig. 6. Variation of the bulk mobility as a function of gate voltage.

In practice, the steps of the calculation were as follows: (1) from Eqs. (A.10), (2) and (3), the density of charges n_i in each layer of a 20 layer-thick pentacene film (permittivity: $\varepsilon = 3\varepsilon_0$, room temperature, thickness of a layer $d = 1.5$ nm, insulator capacitance $C_i = 75$ nF/cm^2) was numerically calculated as a function of gate voltage; (2) The variation of $(1 - n_1/n_{\text{tot}})$ as a function of gate voltage was found to be nicely fitted to an empirical function of the form $(1 + V_{\text{G}})^{-C}$ where $C = 0.71$; (3) The resulting gate-voltage dependent bulk mobility is shown in Fig. 6. These curves will be discussed in the next section.

5. Discussion

The most prominent finding of our modeling is that the mobility in the layer next to the insulator is significantly lower than that in the bulk of the film. We note that this is in agreement with what found by measuring the mobility as a function of the thickness of the film; it was reported that the mobility steadily increases with film thickness, with bulk mobility only occurring above six layers [20].

The first point to discuss is: Why is mobility degradation so rarely observed in organic transistors [6,5]? The answer is in the amount of charge induced in the channel. Most OTFTs use gate dielectrics with a typical capacitance of 10 nF/cm^2, and gate voltages up to a few tens of volts, which represents a maximum density of charge carriers of a few 10^{12} cm^{-2}; this is almost one order of magnitude lower than the magnitude used in this work (up to 1.3×10^{13} cm^2, see upper x-axis in Fig. 4). Devices with high gate dielectric capacitance are usually designed to work at low voltage, so that here too the density of charge in the channel remains moderate [21–23]. The reason

why mobility degradation is only observed in few occasions is thus simply that the gate voltage is not (or cannot be, because of, e.g., limitation due to dielectric strength) pushed up to values where the phenomenon occurs.

A second important question is the origin of low mobility in the first layer. A likely explanation stems from the nature of our gate dielectric, namely, alumina. There is now strong evidence for that mobility in OTFTs depends on the material used as gate dielectric. In particular, mobility decreases when the dielectric constant increases [24,12], so alumina (dielectric constant ~8–9) is not favorable in that respect. What our result suggests is that the decrease of the mobility is the more important as one gets closer to the insulator–semiconductor interface; this seems in good agreement with the model of Veres and coworkers that invokes the role of dipole moments in the insulator [24], the effect of which decreases when getting farther from the insulator. It is worth pointing out that the thickness of a SAM does not appear sufficient to weaken mobility degradation, in contrast to what reported with ultra-thin polymer layers [25]. Accordingly, it can be expected that mobility degradation will be of lesser extent in devices involving low dielectric constant insulators.

As for the bulk mobility, Fig. 6, we note that it first increases with gate voltage, and then levels off at a magnitude that can be viewed as the grain (single crystalline) mobility. According to the MTR model, the initial increase corresponds to the filling of the traps in the grain boundaries. The fact that it takes longer to fill the traps in the SAM modified devices is consistent with smaller grains (average diameter ranging between 50 and 100 nm, as compared to around 1 μm on bare alumina). That is, grain boundaries occupy a larger part of the film. On the other hand, the grain mobility is higher in smaller grains (ca. 5 $cm^2/V\,s$) than in larger ones (ca. 3 $cm^2/V\,s$), meaning that large grains are more defective than small ones. Such a conclusion could account for the now well-documented fact that the mobility of pentacene decreases when grain size increases [26,27], which is at variance with what usually found in polycrystalline semiconductors.

6. Conclusion

We have determined the gate-voltage dependent mobility in pentacene films vapor deposited on bare and SAM-modified alumina. Raw data were corrected for contact resistance and mobility degradation. This was done with the help of an original parameter extraction method, and the use of a model to estimate the distribution of charge in the conducting channel, in which the pentacene film is depicted as a stack of dielectric layers. The thus extracted bulk mobility was found to first increase, then level off at a value that is interpreted as the grain mobility. Following the MTR model, the initial increase is attributed to the filling of traps located in grain boundaries. In films deposited on SAMs, made of small grains, the density of traps associated to grain boundaries is higher, while the mobility within the grains is larger than in the large grains found in films grown on bare alumina. In other words, large grains present more defects than small ones, which is in agreement with the well-documented fact that high mobility in pentacene is associated with small grains.

Acknowledgements

We thank Dr. Hervé Aubin and Mr. Hatem Diaf for the deposition of alumina, and Dr. Philippe Lang for the elaboration of the self-assembled monolayers. The multi-layer model was initiated with Prof. Libero Zuppiroli and Prof. Marie-Noëlle Bussac, and developed during a stay at Bologne, Italy, under the invitation of Dr. Fabio Biscarini. Financial support for this stay by the Italian CNR is acknowledged.

Appendix A. The multi-layer model

The organic semiconductor film is modeled as a stack of n dielectric layers of thickness d, where the density of charge n_i is assumed to be uniform. This is valid in the low injection regime because (1) no more than one charge per molecule is injected and (2) the injected charge practically extends all over the molecule [10]. Let F_i and V_i be the value of the electric field and potential at the borderline between the ith and $(i+1)$th layers. Because n_i is constant, F varies linearly with distance:

$$F = a_i \frac{x}{d} + b_i, \quad i \leqslant \frac{x}{d} \leqslant i+1. \tag{A.1}$$

Applying Gauss's law to the ith layer gives

$$F_{i-1} - F_i = \frac{qn_i}{\varepsilon}. \tag{A.2}$$

where q is the elemental charge and ε the permittivity of the semiconductor. Summing up Eq. (A.2) from $i+1$ to n and setting $F_n = 0$ leads to

$$F_i = \frac{q}{\varepsilon}\sum_{i+1}^{n} n_j. \tag{A.3}$$

The electric field at both sides of the ith layer writes

$$F_{i-1} = a_i(i-1) + b_i \tag{A.4}$$

and

$$F_i = a_i i + b_i. \tag{A.5}$$

From Eqs. ((A.3)–(A.5)), a_i and b_i are calculated as

$$a_i = F_i - F_{i-1} = -\frac{qn_i}{\varepsilon} \tag{A.6}$$

and

$$b_i = F_i - a_i i = \frac{q}{\varepsilon}\left(in_i + \sum_{i+1}^{n} n_j\right). \tag{A.7}$$

In turn, the electrical potential V is obtained by integrating $F = -\mathrm{d}V/\mathrm{d}x$ between $\frac{x}{d} = i-1$ and $\frac{x}{d} = i$.

$$-\int_{i-1}^{i} \mathrm{d}V = d\int_{i-1}^{i} F\left(\frac{x}{d}\right)\mathrm{d}\left(\frac{x}{d}\right),$$

$$V_{i-1} - V_i = \frac{qd}{\varepsilon}\left[-\frac{n_i}{2}\left(\frac{x}{d}\right)^2 + \left(in_i + \sum_{i+1}^{n} n_j\right)\frac{x}{d}\right]_{\frac{x}{d}=i-1}^{\frac{x}{d}=i}$$

$$= \frac{qd}{\varepsilon}\left(\frac{n_i}{2} + \sum_{i+1}^{n} n_j\right). \tag{A.8}$$

Thermal equilibrium between the layers gives us the following additional relation between the densities of charge:

$$\frac{n_i}{n_{i+1}} = \exp\left[\frac{q}{kT}(V_i - V_{i+1})\right]. \tag{A.9}$$

Inserting Eq. (A.8) in Eq. (A.9), we finally obtain

$$n_i = n_{i+1}\exp\left[\frac{q^2 d}{\varepsilon kT}\left(\frac{n_{i+1}}{2} + \sum_{i+2}^{n} n_j\right)\right]. \tag{A.10}$$

References

[1] A. Brown, D. de Leeuw, E. Havinga, A. Pomp, A universal relation between conductivity and field-effect mobility in doped amorphous organic semiconductors, Synth. Metal. 68 (1) (1994) 65–70.

[2] M. Vissenberg, M. Matters, Theory of the field-effect mobility in amorphous organic transistors, Phys. Rev. B 57 (20) (1998) 12964–12967.

[3] G. Horowitz, R. Hajlaoui, D. Fichou, A. El Kassmi, Gate-voltage dependent mobility of oligothiophene field-effect transistors, J. Appl. Phys. 85 (6) (1999) 3202–3206.

[4] G. Horowitz, M. Hajlaoui, R. Hajlaoui, Temperature and gate voltage dependence of hole mobility in polycrystalline oligothiophene thin-film transistors, J. Appl. Phys. 87 (9, Pt. 1) (2000) 4456–4463.

[5] W. Kalb, P. Lang, M. Mottaghi, H. Aubin, G. Horowitz, M. Wuttig, Structure-performance relationship in pentacene/Al2O3 thin-film transistors, Synth. Metal. 146 (3) (2004) 279–282.

[6] R.J. Chesterfield, J.C. McKeen, C.R. Newman, C.D. Frisbie, P.C. Ewbank, K.R. Mann, L.L. Miller, Variable temperature film and contact resistance measurements on operating n-channel organic thin-film transistors, J. Appl. Phys. 95 (11, Pt. 1) (2004) 6396–6405.

[7] J.A. Merlo, C.R. Newman, C.P. Gerlach, T.W. Kelley, D.V. Muyres, S.E. Fritz, M.F. Toney, C.D. Frisbie, p-channel organic semiconductors based on hybrid acene–thiophene molecules for thin-film transistor applications, J. Am. Chem. Soc. 127 (11) (2005) 3997–4009.

[8] R. van Langevelde, F.M. Klaassen, Effect of gate-field dependent mobility degradation on distortion analysis in MOSFET's, IEEE Tans. Electron Dev. 44 (11) (1997) 2044–2052.

[9] G. Horowitz, Organic thin-film transistors: from theory to real devices, J. Mater. Res. 19 (7) (2004) 1946–1962.

[10] J.C. Sancho-Garcia, G. Horowitz, J.L. Brédas, J. Cornil, Effect of an external electric field on the charge transport parameters in organic molecular semiconductors, J. Chem. Phys. 119 (23) (2003) 12563–12568.

[11] S.E. Fritz, S.M. Martin, C.D. Frisbie, M.D. Ward, M.F. Toney, Structural characterization of a pentacene monolayer on an amorphous SiO_2 substrate with grazing incidence X-ray diffraction, J. Am. Chem. Soc. 126 (13) (2004) 4084–4085.

[12] A.F. Stassen, R.W.I. de Boer, N.N. Iosad, A.F. Morpurgo, Influence of the gate dielectric on the mobility of rubrene single-crystal field-effect transistors, Appl. Phys. Lett. 85 (17) (2004) 3899–3901.

[13] A. Ortiz-Conde, F.J. Garcia Sanchez, J.J. Liou, A. Cerdeira, M. Estrada, Y. Yue, A review of recent MOSFET threshold voltage extraction methods, Microelectron. Reliab. 42 (4–5) (2002) 583–596.

[14] H.-S. Wong, M.H. White, T.J. Krutsick, R.V. Booth, Modeling of transconductance degradation and extraction of threshold voltage in thin oxide MOSFET's, Solid-State Electron. 30 (9) (1987) 953–968.

[15] I. Yagi, K. Tsukagoshi, Y. Aoyagi, Direct observation of contact and channel resistance in pentacene four-terminal thin-film transistor patterned by laser ablation method, Appl. Phys. Lett. 84 (5) (2004) 813–815.

[16] P.V. Necliudov, M.S. Shur, D.J. Gundlach, T.N. Jackson, Contact resistance extraction in pentacene thin-film transistors, Solid-State Electron. 47 (2) (2003) 259–262.

[17] H. Klauk, G. Schmid, W. Radlik, W. Weber, L. Zhou, C.D. Sheraw, J.A. Nichols, T.N. Jackson, Contact resistance in organic thin-film transistors, Solid-State Electron. 47 (2) (2003) 297–301.

[18] J. Zaumseil, K. Baldwin, J. Rogers, Contact resistance in organic transistors that use source and drain electrodes formed by soft contact lamination, J. Appl. Phys. 93 (10) (2003) 6117–6124.

[19] E. Meijer, G. Gelinck, E. van Veenendaal, B. Huisman, D. de Leeuw, T. Klapwijk, Scaling behavior and parasitic series resistance in disordered organic field-effect transistors, Appl. Phys. Lett. 82 (25) (2003) 4576–4578.

[20] R. Ruiz, A. Papadimitratos, A.C. Mayer, G.G. Malliaras, Thickness dependence of mobility in pentacene thin-film transistors., Adv. Mater. 17 (14) (2005) 1795–1798.

[21] C. Dimitrakopoulos, I. Kymissis, S. Purushothaman, D. Neumayer, P. Duncombe, R. Laibowitz, Low-voltage, high-mobility pentacene transistors with solution-processed high dielectric constant insulators, Adv. Mater. 11 (16) (1999) 1372–1375.
[22] M. Halik, H. Klauk, U. Zschieschang, G. Schmid, C. Dehm, M. Schuetz, S. Maisch, F. Effenberger, M. Brunnbauer, F. Stellacci, Low-voltage organic transistors with an amorphous molecular gate dielectric., Nature 431 (7011) (2004) 963–966.
[23] L.A. Majewski, R. Schroeder, M. Grell, Low-voltage, high-performance organic field-effect transistors with an ultra-thin TiO_2 layer as gate insulator, Adv. Funct. Mater. 15 (6) (2005) 1017–1022.
[24] J. Veres, S. Ogier, S. Leeming, D. Cupertino, S. Khaffaf, Low-k insulators as the choice of dielectrics in organic field-effect transistors, Adv. Funct. Mater. 13 (3) (2003) 199–204.
[25] T.W. Kelley, L.D. Boardman, T.D. Dunbar, D.V. Muyres, M.J. Pellerite, T.P. Smith, High-performance OTFTs using surface-modified alumina dielectrics, J. Phys. Chem. B 107 (24) (2003) 5877–5881.
[26] D. Knipp, R.A. Street, A. Völkel, J. Ho, Pentacene thin-film transistors on inorganic dielectrics: Morphology, structural properties, and electronic transport, J. Appl. Phys. 93 (1) (2003) 347–355.
[27] S.Y. Yang, K. Shin, C.E. Park, The effect of gate-dielectric surface energy on pentacene morphology and organic field-effect transistor characteristics, Adv. Funct. Mater. 15 (11) (2005) 1806–1814.

Available online at www.sciencedirect.com
ScienceDirect
Organic Electronics 7 (2006) 537–545
Organic Electronics
www.elsevier.com/locate/orgel

Molecular orientation dependent energy levels at interfaces with pentacene and pentacenequinone

N. Koch [a,*], I. Salzmann [a], R.L. Johnson [b], J. Pflaum [c], R. Friedlein [d], J.P. Rabe [a]

[a] Humboldt-Universität zu Berlin, Institut für Physik, Newtonstrasse 15, 12489 Berlin, Germany
[b] Universität Hamburg, Institut für Experimentalphysik, 22761 Hamburg, Germany
[c] Universität Stuttgart, 3. Physikalisches Institut, 70550 Stuttgart, Germany
[d] Department of Physics, Chemistry and Biology (IFM), Linköping University, 581 83 Linköping, Sweden

Received 4 May 2006; received in revised form 26 July 2006; accepted 27 July 2006
Available online 22 August 2006

Abstract

We used ultraviolet photoelectron spectroscopy (UPS) to investigate the energy level alignment at contacts between pentacene and Ag(1 1 1) in the presence of interfacial 6,13-pentacenequinone (PQ). Depending on the metal pre-coverage with PQ, we found evidence for three distinctly different interface morphologies and molecular orientations, accompanied by significant changes of the energy level alignment. Consequently, the hole injection barrier between pentacene and Ag(1 1 1) varied between 1.1 eV (pristine Ag) and 0.45 eV (5.4 nm PQ pre-coverage on Ag). In addition, our UPS results suggest that PQ can act as deep trap for electrons in a pentacene matrix. Depending on the exact mutual orientation of PQ and pentacene, the depth of these traps can be in the range of 0.2–0.75 eV.

PACS: 73.61.Ph; 73.40.Lq; 79.60.−i

Keywords: Organic semiconductor; Interface; Photoelectron spectroscopy; Electronic structure

1. Introduction

Conjugated organic materials receive considerable attention due to their huge potential for the use as active layers in novel (opto-)electronic applications, such as thin film field effect transistors (FETs) [1–3] or light emitting diodes (LEDs) [4–8]. In addition to application-oriented studies, significant efforts are directed towards an understanding of fundamental physical properties of organic molecular crystals and thin films, particularly with regard to the nature of charge transport and charge carrier mobility. In order to assess the intrinsic mobility of charge carriers, samples of exceptional high purity are needed [9]. Besides structural defects, chemical impurities can significantly complicate the evaluation of intrinsic material properties [10]. Particularly, chemical defects can act as deep charge carrier traps. Pentacene (PEN) is one of the most intensively studied molecular materials, since it holds great potential for application in FETs (due to its higher sublimation

* Corresponding author. Tel.: +49 30 2093 7819; fax: +49 30 2093 7632.
E-mail address: norbert.koch@physik.hu-berlin.de (N. Koch).

1566-1199/$ - see front matter © 2006 Elsevier B.V. All rights reserved.
doi:10.1016/j.orgel.2006.07.010

temperature compared to smaller oligoacenes), and high charge carrier mobilities have been reported for thin film [11,12] and single crystal samples [13]. In this context, the presence of 6,13-pentacenequinone (PQ) in a pentacene matrix has been identified as a "key" chemical defect lowering carrier mobility [13]. Moreover, in order to measure charge carrier mobilities, or to fabricate FETs, contacts between the organic material and metal electrodes are ubiquitous. The importance of the energy level alignment at organic/metal interfaces has been pointed out in many studies [14,15]. One may speculate that some PQ is formed on the surface of PEN crystals due to photo-oxidation, as, e.g., was shown for tetracene single crystals [10]. If that were the case, the energy level alignment at interfaces between PEN and metals may be altered significantly by the presence of interfacial PQ.

The aim of the present work was to investigate the energy level alignment between pentacene and pentacenequinone, and the effects of PQ presence on the interface energetics between an electrode material (Ag) and PEN. Using photoemission spectroscopy, we show that PQ can act as deep trap (up to ca. 0.75 eV) for electrons in PEN, and that interfacial PQ can significantly influence the hole injection barrier between PEN and Ag. Furthermore, we highlight the importance of mutual molecular orientation at organic/organic hetero-interfaces. We find evidence for a molecular orientation dependent energy level alignment, which may be generally the case at organic/organic heterojunctions. Only few interfaces of this type have been studied until now [16–20], despite their obvious importance.

2. Experimental

Ultraviolet photoelectron spectroscopy (UPS) experiments were performed at the end-station of the Flipper II beamline at Hasylab (Hamburg, Germany) [21]. Sample transfer between the preparation and analysis chambers (base pressure: 4×10^{-9} and 2×10^{-10} mbar, respectively) proceeded without breaking ultrahigh vacuum (UHV) conditions. Prior to the deposition of the organic materials, the Ag(1 1 1) single crystal substrate was cleaned by repeated Ar-ion sputtering and annealing cycles until a clear low-energy electron diffraction pattern could be observed. The SiO_2 substrate (native oxide) was cleaned by sonication in methanol and acetone before placement in the UHV system, and heated to 300 °C *in vacuo* prior to the deposition of organic materials. Pentacene (Aldrich) and pentacenequinone (Aldrich) (both purified by vacuum sublimation once before use) were evaporated from resistively heated pin-hole sources. The chemical structures of both molecules are shown in Fig. 1. The mass-thickness was monitored with a quartz crystal microbalance. No correction was made for possible differences in sticking coefficients on quartz and Ag. UPS spectra were recorded with a double-pass cylindrical mirror analyzer, set to an energy resolution of 150 meV (80–20% intensity drop at the Ag Fermi-edge). The photon energy was set to 22 eV. The secondary electron cutoff (for determination of sample work function and molecular ionization energy) was measured with −3 V sample bias.

3. Results and discussion

The energy level alignment of pentacene (PEN) on polycrystalline Ag has been reported before [22,23]. In Fig. 1a we briefly summarize our results obtained for PEN on Ag(1 1 1). For a nominal coverage (θ_P) of 15 nm, the peak derived from the PEN highest occupied molecular orbital (HOMO) is centered at a binding energy (BE) of 1.5 eV. The HOMO low-BE onset is found 1.1 eV below the Ag Fermi energy (E_F); this value corresponds to the hole injection barrier (HIB) at the interface. At lower θ_P, this value for the barrier approaches 1.0 eV, which is attributed to more efficient photohole screening close to the metal surface, observed for essentially all metal/organic interfaces without strong chemical interactions [14,15]. The sample work function (ϕ) changed from 4.45 eV for pristine Ag(1 1 1) to 3.95 eV for 15 nm PEN, inferred from the change in kinetic energy of the secondary electron cutoff (SECO) shown in the inset of Fig. 1a. Due to the weak interaction between Ag and PEN, this interface dipole is attributed to the "push-back" effect of electrons spilling out into vacuum for the clean Ag surface [14,24,25]. The ionization energy (IE) of PEN was determined to be 5.0 eV for this sample. A physisorption-like interaction between Ag and PEN can be assumed since no charge-transfer (e.g., from Ag to the PEN lowest unoccupied molecular orbital) induced new spectral intensity can be seen below the HOMO-derived peak. The first few layers of PEN are most likely oriented with their long molecular axes parallel to the Ag surface [26], however, a change to an almost

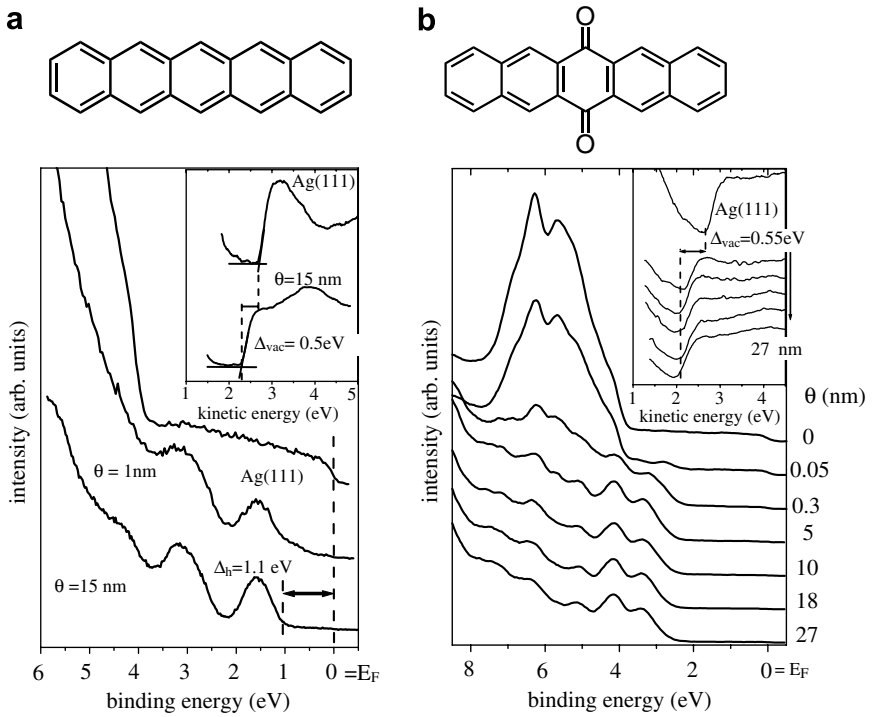

Fig. 1. (a) Molecular structure and UPS spectra for increasing coverage (θ) of (a) pentacene on Ag(1 1 1), and (b) 6,13-pentacenequinone on Ag(1 1 1). Insets: secondary electron cutoffs.

vertical orientation of PEN molecules at higher θ_P can be expected [27].

The evolution of photoemission spectra for PQ deposited on Ag(1 1 1) is shown in Fig. 1b. For a PQ coverage (θ_{PQ}) of 27 nm we attribute the emission feature centered at 3.4 eV to be derived from the PQ HOMO. The onset is found 2.6 eV below E_F; this value also corresponds to the HIB. As expected, spectra at lower θ_{PQ} are shifted towards lower BE (due to better screening efficiency, see above), such that the HIB equals 2.4 eV for $\theta_{PQ} = 0.3$ nm. The sample work function changed from 4.45 eV for pristine Ag(1 1 1) to 3.9 eV, very similar to PEN/Ag(1 1 1). This points towards a similarly weak interaction between PQ and Ag, which is further supported by the lack of photoemission features in the energy gap of PQ throughout the deposition sequence. The IE for PQ in the 27 nm thick film is 6.5 eV.

It is reasonable to assume that also the first few layers of PQ are oriented with their long molecular axes parallel to the Ag surface, supported by the fact that the photoemission (PE) intensity of the substrate (close to E_F) is already substantially quenched at $\theta_{PQ} = 0.3$ nm. For higher θ_{PQ}, a transition towards vertically inclined PQ molecular is possible. Furthermore, island growth of PQ after monolayer formation can be proposed, since close inspection reveals that the reduction of the photoemission signal from the substrate is less efficient for coverages beyond 0.3 nm. Even for $\theta_{PQ} = 27$ nm a low PE intensity can be seen at E_F.

In order to investigate the influence of the presence of PQ on the energy level alignment at interfaces between Ag and PEN, Ag(1 1 1) surfaces were pre-covered with PQ layers of three different thicknesses before the deposition of PEN.

The lowest PQ pre-coverage of only 0.05 nm (denoted as "*case 1*" in the following) has negligible influence on the observed energy levels of PEN films on Ag(1 1 1) (see Fig. 2a). The HOMO-onset for the PQ sub-monolayer is found at 2.35 eV below E_F. For *case 1*, the sequence of spectra for different film thicknesses of PEN is virtually identical to that obtained for PEN deposited on clean Ag(1 1 1). Already at low θ_P, a clear PE signature of the PEN HOMO is visible, with the center at 1.45 eV BE and the low BE-onset at 1.0 eV. Increasing θ_P leads to the expected screening-related shift towards higher BE, and the position of the HOMO-onset reaches 1.15 eV for $\theta_P = 7.5$ nm. Consequently, the offset between the HOMOs of PQ and PEN is

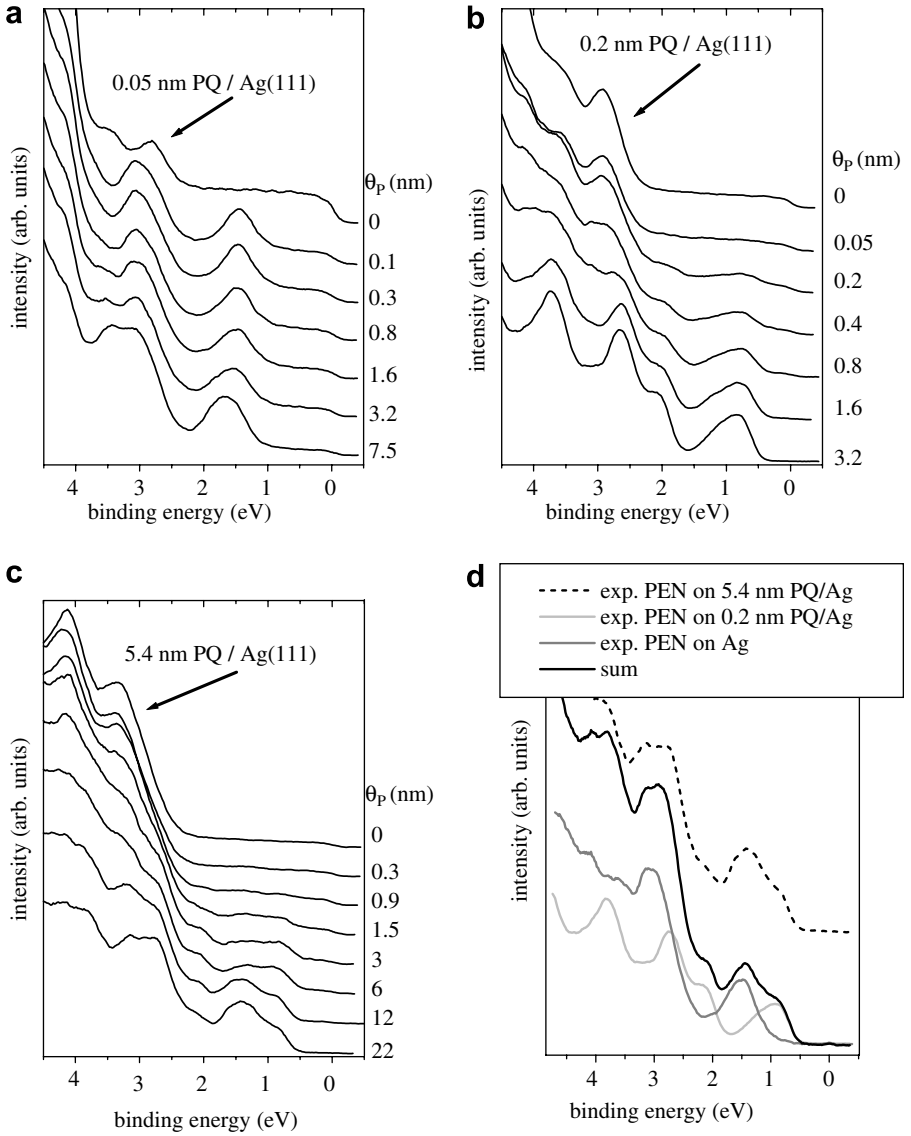

Fig. 2. UPS spectra for increasing PEN coverage (θ_P) on Ag(1 1 1) pre-covered with (a) *case 1*: 0.05 nm PQ, (b) *case 2*: 0.2 nm PQ, and (c) *case 3*: 5.4 nm PQ. (d) Experimental (dashed) and simulated (thick solid) UPS spectra of PEN on 5.4 nm PQ/Ag(1 1 1). For details see text.

1.35 eV at low θ_P and 1.2 eV at high θ_P. Note that the lineshape of the HOMO-derived peak at monolayer-range coverage (ca. 0.3 nm) is rather symmetric, and becomes only slightly asymmetric for higher coverages. The lineshape of monolayer PEN/Ag(1 1 1) resembles that reported for PEN on highly oriented graphite [28,29], indicating flat-lying PEN molecules. Since a finite PE intensity at E_F is still observed for $\theta_P = 7.5$ nm, we conclude that PEN growth results in the formation of multilayer islands, with a few uncovered patches of Ag being present. The overall lineshape and peak intensity ratios of the high coverage PEN film corresponds well to PE spectra obtained for PEN samples where the long molecular axis of PEN is oriented parallel to the substrate surface [28,29]. The total change in the SECO position for this sequence is 0.55 eV, i.e., a final ϕ of 3.9 eV is obtained.

Increasing the PQ pre-coverage of Ag(1 1 1) to 0.2 nm (ca. one monolayer, denoted as "*case 2*") leads to a remarkable change in the energy level position and morphology of subsequently deposited PEN films (Fig. 2b). The HOMO-onset for PQ is found at 2.4 eV BE. In contrast to *case 1*, the intensity of PEN-derived spectral features is lower at comparable nominal θ_P. In addition, the lineshape

of the HOMO-derived PE feature is highly asymmetric, and the intensity ratios of individual features from PEN are rather different in comparison to Fig. 2a. PE spectra of this kind have been reported for PEN samples, where the long molecular axis is almost perpendicular to the substrate surface, e.g., pentacene films on SiO_2 [28,29]. For these two reasons, we conclude that the same molecular orientation of PEN prevails in the present sample. Virtually no PE intensity at E_F is observed for $\theta_P = 3.2$ nm, suggesting a close-packed molecular film. Most strikingly, the HOMO-onset of PEN is now found at 0.45 eV BE ($\theta_P = 3.2$ nm, corresponding to ca. two upright standing molecular layers of PEN), i.e., ca. 0.7 eV lower than for PEN/Ag(1 1 1) and PEN/0.05 nm PQ/Ag(1 1 1) (*case 1*). Consequently, the HOMO-offset (Δ_{HOMO}) between PQ and PEN for this sample is 1.95 eV. The total change in the SECO position for this sequence is 0.5 eV, i.e., a final ϕ of 3.95 eV is obtained, resulting in an IE of 4.4 eV.

In the third set of experiments, Ag(1 1 1) was precovered with 5.4 nm PQ prior to the deposition of PEN Fig. 2c, "*case 3*". Since at this PQ coverage multilayers are present, the HOMO-onset for PQ is found at 2.45 eV BE. The spectra obtained for PEN on top of this PQ layer do not resemble any of the two former cases. Rather than just a single new spectral feature between the PQ HOMO and E_F, we now observe two features, centered at ca. 0.85 eV and 1.35 eV BE. The low BE onset of these features is 0.45 eV below E_F at low coverage, and at 0.55 eV for $\theta_P = 22$ nm. It is unreasonable to assume that a chemical reaction between PEN and PQ leads to the splitting of the PEN HOMO-derived feature at low BE. Rather, a more complex organic/organic heterolayer morphology, in conjunction with the molecular orientation dependent energy level alignment shown for the two previous cases, *case 1* and *case 2*, can be invoked to explain the spectra of Fig. 2c. In fact, these spectra can be reproduced by a superposition of spectra obtained for *case 1* [PEN on 0.05 nm PQ/Ag(1 1 1); which is virtually identical to PEN on pristine Ag(1 1 1)] and *case 2* [PEN on 0.2 nm PQ/Ag(1 1 1)]. This is demonstrated in Fig. 2d, where the experimentally obtained PE spectrum for PEN on 5.4 nm PQ/Ag(1 1 1) is compared to the sum of appropriately scaled bottom-most spectra from Fig. 2a (contribution from Ag substrate subtracted) and Fig. 2b. From this we conclude that the nominally 5.4 nm thick PQ film on Ag(1 1 1) must be discontinuous, exposing some bare Ag areas. Interestingly, this was not the case for the 0.2 nm PQ film on Ag(1 1 1), where only one type of PEN energy levels was seen. A possible explanation for this could be a morphology change for PQ on Ag(1 1 1) after the completion of a monolayer. Details shall be investigated in future studies. We note that a similar wetting-dewetting transition at about monolayer coverage was observed for another molecular system: coronene on ZnO [30].

Schematics of the three sample morphologies proposed above, including deduced relative molecular orientation, are depicted in Fig. 3a–c.

In order to further investigate the impact of relative molecular orientation at organic/organic heterojunctions on the interface energetics, PQ was

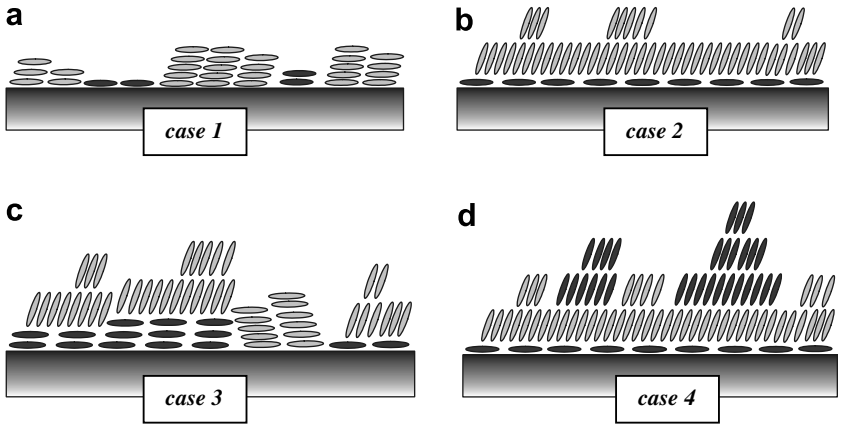

Fig. 3. Schematic morphology and molecular orientation for (a) PEN on 0.05 nm PQ/Ag(1 1 1), (b) PEN on 0.2 nm PQ/Ag(1 1 1), (c) PEN on 5.4 nm PQ/Ag(1 1 1), and (d) for PQ on 3.2 nm PEN/0.2 nm PQ/Ag(1 1 1). Dark: PQ, light: PEN.

deposited onto the closed PEN layer existing on 0.2 nm PQ pre-covered Ag(1 1 1) (denoted as "*case 4*"). The starting point thus was the sample whose PE spectrum is shown as bottom-most in Fig. 2b, i.e., *case 2*. Increasing the PQ coverage (θ_{PQ}) on this sample leads to an attenuation of PEN features (most notably seen for the PEN HOMO in Fig. 4), and at $\theta_{PQ} = 16$ nm the spectrum resembles mostly that of PQ, except for a still weak emission originating from the PEN HOMO (centered at ca. 0.8 eV BE). This obvious PE signature of PQ (to be compared with Fig. 1b) becomes clearer after subtraction of an appropriately scaled PEN spectrum. The resulting spectrum is indicated by PQ* in Fig. 4. Notably, the HOMO-onset of this PQ layer grown on PEN is at 1.95 eV BE, in contrast to the 2.6 eV obtained for PQ of comparable thickness on pristine Ag(1 1 1). This energy difference of 0.65 eV parallels that obtained for the PEN on pristine and differently PQ pre-covered Ag surfaces of ca. 0.7 eV, as recognized by comparing Fig. 2a–b. Δ_{HOMO} (between PQ and PEN) for PQ on 3.2 nm PEN/0.2 nm PQ/Ag(1 1 1) is thus 1.95 eV – 0.45 eV = 1.5 eV. Interestingly, within the error-bar due to screening effects (± 0.1 eV), this value is very similar to those found for PEN and PQ grown separately on Ag(1 1 1) (ca. 1.5 eV; Fig. 1a and b) and PEN grown on 0.05 nm PQ/Ag(1 1 1) (1.35 eV; Fig. 2a; *case 1*). All these values are markedly smaller than the Δ_{HOMO} values measured for *case 2* (PEN on 0.2 nm PQ/Ag(1 1 1)) and one of the components of *case 3* (PEN on 5.4 nm PQ/Ag(1 1 1)), which were 1.95 eV (Fig. 2b) and 2.00 eV (Fig. 2c), respectively.

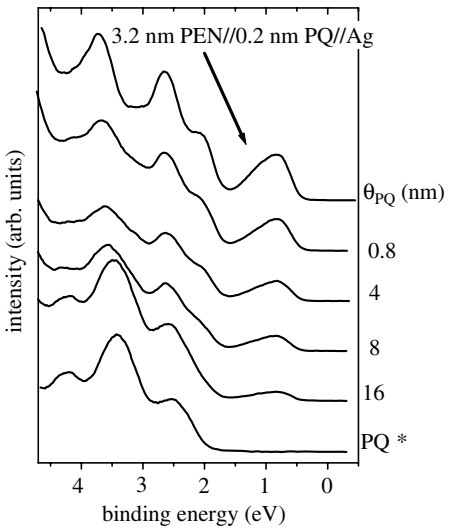

Fig. 4. UPS spectra for increasing PQ coverage (θ_{PQ}) on 3.2 nm PEN/0.2 nm PQ/Ag(1 1 1); *case 4*.

A summary of all energy level alignment scenarios observed in the study of PEN/PQ hetero-interfaces on Ag(1 1 1) is shown in Fig. 5. In this figure, the ionization energies and binding energy values for the HOMO levels have been measured. The position of the pentacene LUMO level (i.e., electron transport level) was estimated by using the transport gap of 2.2 eV [31,32] instead of the optical gap. However, these values posses a large error bar, since changes in molecular polarization cannot readily be assessed for these level (see detailed discussion below). For PQ, only the optical gap is known (ca. 2.94 eV [33]). The position of the electron transport level was estimated by assuming a similar difference between optical and charge transport gap, i.e., 0.4 eV, as reported for pentacene [31,32]. Fig. 5 displays clearly that PQ incorporated into a PEN matrix can act as deep trap for electrons, with trap depths ranging from 0.2 to 0.75 eV in our

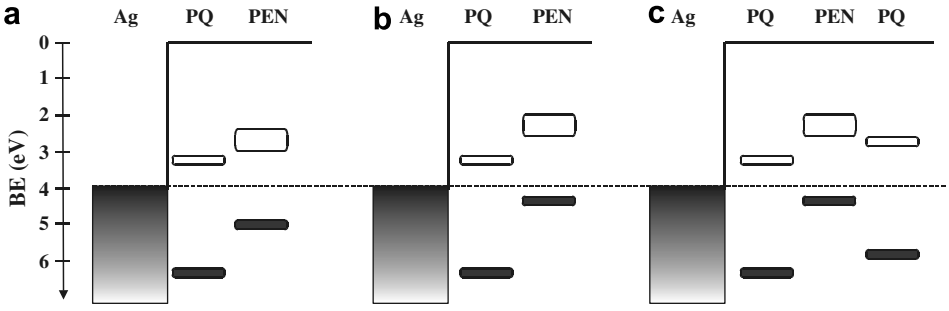

Fig. 5. Summary of experimentally observed energy level diagrams of PEN and PQ hetero-layers on Ag(1 1 1). (a) *case 1*, (b) *case 2*, and (c) *case 4*. *Case 3* is a mixture of (a) and (b). The open symbols for the LUMO levels were chosen broader than the HOMO levels to reflect a larger uncertainty because possible quadrupole terms in the charge polarization energy are not known (see text).

simple model, depending on mutual orientation (compare according morphologies from Fig. 3).

While molecular orientation behavior can be rather complicated on metal surfaces, as pointed out above, we have also chosen a substrate, where molecular orientation is the same for mono- and multilayers, i.e., silicon oxide. An almost standing orientation of PEN and PQ on SiO_2 is well documented [33–35]. In a first step, 20 nm PQ were deposited onto SiO_2 (bottom curve in Fig. 6a). Then 1.5 nm PEN were deposited on top (top curve in Fig. 6a), and photoemission features of both materials can be distinguished. The HOMO-offset was 1.4 eV, again very close to the value obtained for *case 1* (PEN on 0.05 nm PQ/Ag(1 1 1)). No change in the position of the secondary electron cutoff was observed (inset of Fig. 6a). Fig. 6b shows a schematic representation of the sample morphology and molecular orientation. We propose that non-interacting PEN and PQ (residing side-by-side like in Fig. 3a), as well as PEN/PQ heterostructures where molecules are growing on each other as depicted in Fig. 6b, exhibit Δ_{HOMO} of ca. 1.4 eV. Thus, only for the case where PEN molecules grow in an almost perpendicular orientation relative to PQ (Fig. 3b and c) a larger Δ_{HOMO} of 1.95 eV (Fig. 2b) is found.

As evident from Fig. 5, the IE of pentacene depends dramatically on molecular orientation, i.e., this value changed from ca. 5.0 eV (lying configuration) to ca. 4.4 eV (almost standing), for both monolayer and multilayer range. A similar trend of IE has been observed before for pentacene on highly oriented graphite [36] and α,ω-dihexylsexithiophene on Ag(1 1 1) [37]. The strong and in this magnitude unexpected changes in IE may be related to the intermolecular screening of a hole expressed as the charge polarization energy P [32]. This screening is known to depend on the local state of aggregation and therefore also on the crystal structure as for instance seen in a rigid shift of all spectral features by 0.3 eV between the structural modifications of α- and β-perylene [38].

In order to explain the IEs of the pentacene films, we performed calculations of the charge polarization energy (P) for a number of different pentacene cluster model systems, consisting of N molecules. We included the principal term for the interaction between an excess localized charge on one molecule with electrical dipoles induced on surrounding molecules (P_{id}) [32] and a correction term for the interaction between the induced dipoles (P_{dd}) [39]:

$$P_{id} = \sum_{k=1}^{N-1} \frac{e^2}{2r_k^6} \sum_{i,j} b_i(\beta_{ij} r_{jk})^2 \quad (i,j = 1, 2, 3) \tag{1}$$

$$P_{dd} = \sum_{k<l} \frac{e^2 \bar{\alpha}^2}{r_k^3 r_l^3 r_{kl}^3} \left[\vec{r}_k \vec{r}_l \frac{3}{r_{kl}^2} (\vec{r}_k \vec{r}_{kl})(\vec{r}_l \vec{r}_{kl}) \right] \tag{2}$$

where e is the elementary charge, $\vec{r}_k$ and $\vec{r}_l$ are the vectors between neutral molecules k and l and the molecular ion, and $\vec{r}_{kl}$ is the distance between two neutral molecules. b_i are the main components of the tensor of molecular polarizability α along the main axes of the molecule (values for pentacene

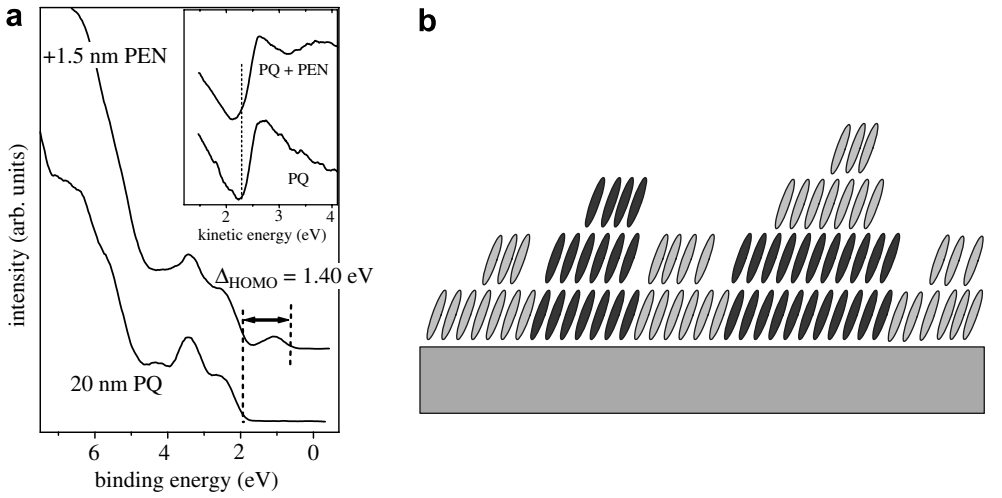

Fig. 6. (a) UPS spectra for 20 nm PQ on SiO_2 prior (bottom) and after deposition of 1.5 nm of PEN (top). Inset: secondary electron cutoff. (b) Schematic morphology and molecular orientation for PEN/PQ/SiO_2. Dark: PQ, light: PEN.

taken from Ref. [40]), and β_{ij} are the respective cosines of angles of inclination between the b_i and the axes of the pentacene molecular crystal. While P_{id} was thus evaluated taking into account the anisotropy of α, P_{dd} was obtained using the average isotropic molecular polarizability $\bar{\alpha}$.

An almost square cluster of 25 molecules arranged in a planar conformation (in the following referred to as *model 1*) was used to approximate P for the experimental *case 1*. Since an ordered monolayer structure of pentacene/Ag(1 1 1) is not known, we used a close-packed structure proposed for pentacene/Au(1 1 1) [41], where $a = 5.76$ Å, $b = 15.3$ Å, $\gamma = 79.1°$. Another simple model cluster was composed of a single molecular sheet consisting of 23 pentacene molecules in the *ab*-plane of a pentacene polymorph obtained by vapor transport ($a = 6.266$ Å, $b = 7.775$ Å, $c = 14.53$ Å, $\alpha = 76.47°$, $\beta = 87.68°$, $\gamma = 84.68°$) [42]. This cluster (*model 2*) was used to evaluate P for an almost standing pentacene layer (corresponding to the experimental *case 2*). In both models, the excess charge was placed at the center of the cluster, thus including somewhat more than next-nearest neighbor interactions.

As expected, P_{id} for *model 1* (0.64 eV) was smaller than that of *model 2* (2.54 eV). Accordingly, P_{dd} showed the same trend, yielding values of 0.01 eV for *model 1* and 1.79 eV for *model 2*. Since P_{dd} acts opposite to P_{id}, resulting values for P for the two models are rather similar, i.e., $P_{\parallel} = 0.63$ eV for *model 1* and $P_{\perp} = 0.75$ eV for *model 2*. Taking into account the different distance of the lying and standing monolayer from the metal surface in the experiments one should add up to 0.2 eV to the value of $P_{\parallel}$ [40,43]. Additional calculations for other model lying monolayer geometries yielded similar results. Consequently, the sum of molecular ion polarization by induced dipoles and dipole–dipole interactions is inadequate to explain our experimental observations regarding the change in IE. Higher-order correction terms may be needed, e.g., the interaction between the charge and permanent quadrupole moments [32], which can amount to several tenths of an eV for pentacene [44]. However, without an exact knowledge of the true structure of our pentacene thin films this term cannot be evaluated reliably. Regarding, the position of the LUMO in Fig. 5, substantial quadrupole terms in the expression for the polarization energy [32] would not lead to a change in the width of the transport gap. Rather, these contributions would simply shift the energy levels rigidly with respect to the vacuum level. Moreover, the existence of substantial energy band dispersion in pentacene thin films [29,36] may preclude the applicability of the above simple model for P [40].

As an alternative explanation for the observed differences in IE, pentacene in *case 1* may not exhibit any far-range structural order, resulting in significantly smaller polarization than for any highly ordered system (like *case 2*) [36].

4. Conclusion

We have investigated the influence of pentacene-quinone at interfaces between pentacene and Ag(1 1 1) on the energy level alignment. Three different pre-coverages of PQ on Ag(1 1 1) led to three markedly different interface energetics scenarios. (i) Submonolayer θ_{PQ} did not change the energy level alignment between PEN and Ag(1 1 1) compared to the case of PEN on the pristine metal surface. (ii) ca. one monolayer coverage of PQ on Ag lowered the hole injection barrier between PEN and Ag(1 1 1) by 0.7 eV. (iii) Multilayer θ_{PQ} resulted in a mixture of the two former cases. These differences were explained by different mutual molecular orientations at the investigated organic/organic heterojunctions, accompanied by changed intermolecular coupling, and possibly different charge polarization energies for the two different pentacene polymorphs. Furthermore, our photoemission results show that PQ can form deep traps for electrons in a PEN matrix, with depths ranging from 0.2 eV to 0.75 eV, depending on molecular orientation.

Acknowledgements

This work was supported by the Sfb448 (DFG), the OFET focus program (DFG, project no. PF385/2), and the Swedish Science Research Council (VR, project nos. 12252003 and 12252020). NK acknowledges financial support by the Emmy Noether-Program (DFG).

References

[1] D.J. Gundlach, Y.Y. Lin, T.N. Jackson, D.G. Schlom, Appl. Phys. Lett. 71 (1997) 3853.
[2] M. Halik, H. Klauk, U. Zschieschang, T. Kriem, G. Schmid, W. Radlik, K. Wussow, Appl. Phys. Lett. 81 (2002) 289.
[3] C.D. Dimitrakopoulos, P.R.L. Malenfant, Adv. Mater. 14 (2002) 99.
[4] C.W. Tang, S.A.V. Slyke, Appl. Phys. Lett. 51 (1987) 913.

[5] J.H. Burroughes, D.D.C. Bradley, A.R. Brown, R.N. Marks, K. Mackey, R.H. Friend, P.L. Burns, A.B. Holmes, Nature 347 (1990) 539.
[6] V. Ohmori, M. Uchida, K. Muro, K. Yoshino, Jpn. J. Appl. Phys. 30 (1991) L1941.
[7] G. Grem, G. Leditzky, B. Ullrich, G. Leising, Adv. Mater. 4 (1992) 36.
[8] V. Bulovic, G. Gu, P.E. Burrows, S.R. Forrest, M.E. Thompson, Nature 380 (1996) 29.
[9] K.H. Probst, N. Karl, Phys. Stat. Sol. A 27 (1975) 499.
[10] J. Pflaum, J. Niemax, A.K. Tripathi, Chem. Phys. 325 (2006) 152.
[11] N. Karl, Synth. Met. 133 (2003) 649.
[12] T.W. Kelley, P.F. Baude, C. Gerlach, D.E. Ender, D. Muyres, M.A. Haase, D.E. Vogel, S.D. Theiss, Chem. Mater. 16 (2004) 4413.
[13] O.D. Jurchescu, J. Baas, T.T.M. Palstra, Appl. Phys. Lett. 84 (2004) 3061.
[14] H. Ishii, K. Sugiyama, E. Ito, K. Seki, Adv. Mater. 11 (1999) 605.
[15] A. Kahn, N. Koch, W.Y. Gao, J. Polymer Sci. B 41 (2003) 2529.
[16] W.Y. Gao, A. Kahn, Appl. Phys. Lett. 82 (2003) 4815.
[17] I.G. Hill, A. Kahn, J. Appl. Phys. 84 (1998) 5583.
[18] I.G. Hill, A. Kahn, J. Appl. Phys. 86 (1999) 4515.
[19] A. Rajagopal, C.I. Wu, A. Kahn, J. Appl. Phys. 83 (1998) 2649.
[20] A. Rajagopal, A. Kahn, Adv. Mater. 10 (1998) 140.
[21] R.L. Johnson, J. Reichardt, Nucl. Instr. Methods 208 (1983) 791.
[22] N.J. Watkins, L. Yan, Y.L. Gao, Appl. Phys. Lett. 80 (2002) 4384.
[23] N. Koch, A. Elschner, J.P. Rabe, R.L. Johnson, Adv. Mater. 17 (2005) 330.
[24] P.S. Bagus, V. Staemmler, C. Wöll, Phys. Rev. Lett. 89 (2002) 096104.
[25] N. Koch, J. Ghijsen, J.-J. Pireaux, J. Schwartz, R.L. Johnson, A. Elschner, A. Kahn, Appl. Phys. Lett. 82 (2003) 70.
[26] M. Eremtchenko, R. Temirov, D. Bauer, J.A. Schaefer, F.S. Tautz, Phys. Rev. B 72 (2005) 115430.
[27] G. Witte, C. Wöll, J. Mater. Res. 19 (2004) 1889.
[28] A. Vollmer, O.D. Jurchescu, I. Arfaoui, I. Salzmann, T.T.M. Palstra, P. Rudolf, J. Niemax, J. Pflaum, J.P. Rabe, N. Koch, Eur. Phys. J. E 17 (2005) 339.
[29] N. Koch, A. Vollmer, I. Salzmann, B. Nickel, H. Weiss, J.P. Rabe, Phys. Rev. Lett. 96 (2006) 156803.
[30] H. Glowatzki, S. Blumstengel, J.P. Rabe, N. Koch, unpublished.
[31] N. Koch, J. Ghijsen, R.L. Johnson, J. Schwartz, J.-J. Pireaux, A. Kahn, J. Phys. Chem. B 106 (2002) 4192.
[32] E.A. Silinsh, Organic Molecular Crystals, Springer, Berlin, 1980.
[33] D.K. Hwang, K. Kim, J.H. Kim, S. Im, D.-Y. Jung, E. Kim, Appl. Phys. Lett. 85 (2004) 5568.
[34] C.D. Dimitrakopoulos, D.J. Mascaro, IBM J. Res. Dev. 45 (2001) 11.
[35] R. Ruiz, B. Nickel, N. Koch, L.C. Feldman, R.F. Haglund, A. Kahn, G. Scoles, Phys. Rev. B 67 (2003) 125406.
[36] H. Fukagawa, H. Yamane, T. Kataoka, S. Kera, M. Nakamura, K. Kudo, N. Ueno, Phys. Rev. B 73 (2006) 245310.
[37] S. Duhm, H. Glowatzki, R.L. Johnson, J.P. Rabe, N. Koch, Appl. Phys. Lett. 88 (2006) 203109.
[38] R. Friedlein, X. Crispin, M. Pickholz, M. Keil, S. Stafström, W.R. Salaneck, Chem. Phys. Lett. 354 (2002) 398.
[39] F. Gutmann, L.E. Lyons, Organic Semiconductors, John Wiley & Sons, New York, 1967.
[40] E.V. Tsiper, Z.G. Soos, Phys. Rev. B 68 (2003) 085301.
[41] C.B. France, P.G. Schroeder, J.C. Forsythe, B.A. Parkinson, Langmuir 19 (2003) 1274.
[42] C.C. Mattheus, A.B. Dros, J. Baas, A. Meetsma, J.L. de Boer, T.T.M. Palstra, Acta Cryst. C 57 (2001) 939.
[43] N. Koch, G. Heimel, J. Wu, E. Zojer, R.L. Johnson, J.-L. Brédas, K. Müllen, J.P. Rabe, Chem. Phys. Lett. 413 (2005) 390.
[44] N. Sato, H. Inokuchi, E.A. Silinsh, Chem. Phys. 115 (1987) 269.

Available online at www.sciencedirect.com
ScienceDirect
Organic Electronics 7 (2006) 546–550
Organic Electronics
www.elsevier.com/locate/orgel

In situ polymerization of amphiphilic diacetylene for hole transport in solid state dye-sensitized solar cells

Yanping Wang [a], Ke Yang [a], Xiaoyu Wang [a], Ramaswamy Nagarajan [a], Lynne A. Samuelson [b], Jayant Kumar [a,*]

[a] *Center for Advanced Materials, University of Massachusetts Lowell, Lowell, MA 01854, United States*
[b] *Nanomaterials Science Team, US Army Natick Soldier Center, RDECOM, Natick, MA 01760, United States*

Received 9 January 2006; received in revised form 11 July 2006; accepted 12 July 2006
Available online 8 September 2006

Abstract

Solid state dye-sensitized solar cells were fabricated using polydiacetylene as the hole transport material. The polydiacetylene was incorporated into the nanoporous TiO_2 film by solution casting of an amphiphilic diacetylene and subsequent in situ polymerization. Polydiacetylenes as prepared via solid state polymerization are crystalline, exhibiting high charge carrier mobility. Our preliminary experiments demonstrated a short-circuit current density of 3.73 mA/cm^2 and an overall power conversion efficiency of 0.62% under AM 1.5 illumination (100 mW/cm^2).

PACS: 73.61.Ph; 73.63.Bd; 82.47.Jk

Keywords: Polydiacetylene; Hole transport; Dye-sensitized solar cell

1. Introduction

Dye-sensitized nanocrystalline (nc) TiO_2 solar cells (DSSCs) have attracted significant attention due to their potential as a high-efficiency and low-cost alternative to conventional inorganic solar cells [1]. The prototype devices using liquid electrolytes achieved power conversion efficiencies up to 10% under AM 1.5 illumination (100 mA/cm^2) [2]. Their practical applications, however, are limited by the problems associated with corrosion due to a reactive electrolyte and leakage of the liquid electrolyte. Therefore, numerous efforts have been attempted to replace the liquid electrolyte with a solid state hole transport material (HTM) [3–10].

Semiconducting polymers are regarded as promising HTMs due to their low-cost, tailorability and processability [8]. However, the efficiencies of solid state DSSCs using polymeric HTMs have been quite low compared to those devices using nonpolymeric HTMs. There are two main reasons for their poor performance: (1) poor electronic contact between the dye molecules and polymeric HTMs due to interface dewetting and incomplete integration of the bulky polymer molecules with the TiO_2 nanopores; (2) low hole mobility for polymeric HTMs

* Corresponding author. Tel.: +1 978 934 3788; fax: +1 978 458 9571.
E-mail address: Jayant_Kumar@uml.edu (J. Kumar).

1566-1199/$ - see front matter © 2006 Elsevier B.V. All rights reserved.
doi:10.1016/j.orgel.2006.07.013

due to the disordered arrangement of their molecule chains. In order to introduce the conjugated polymer into the void of the nanoporous TiO_2 film, Saito et al. employed in situ chemical and photoelectrochemical polymerizations [9]. Their devices using in situ prepared poly(3,4-ethylenedioxythiophene) (PEDOT) as the HTM performed the best with a reported short-circuit current density (J_{sc}) of 2.3 mA/cm^2 and overall power conversion efficiency (η) of 0.53% [10].

In the present work, in situ solid state polymerized polydiacetylene (PDA) was used as the HTM. PDA/silica nanocomposite films have been prepared by self-assembly, using polymerizable diacetylenic surfactants as both structure-directing agents and monomers [11]. It was expected that the amphiphilic diacetylene (DA) monomers would form a highly ordered, crystalline structure in the nanoporous TiO_2 film. Such a dense packing of the monomers is essential for the topochemical solid state polymerization [12]. There are a number of advantages in this case. Firstly, this method improves the incorporation of the bulky polymer molecules into the TiO_2 nanopores. Secondly, PDAs as prepared via solid state polymerization are highly crystalline, exhibiting high charge carrier mobility about 10^3 larger than those of partially crystalline or amorphous conjugated polymers [13]. Thirdly, the desired intimate contact of the HTM with the dye may be provided by the formation of hydrogen bonding between them. Finally, this approach is simple and incorporates minimum impurities compared to chemical or photoelectrochemical polymerizations.

Regardless of the HTMs used, the efficiencies of solid state DSSCs are still low in comparison to the liquid electrolyte-based DSSCs. Interfacial charge recombination is suggested to be the main loss mechanism [14].

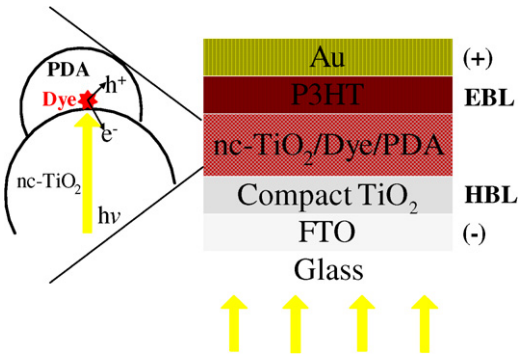

Fig. 1. Device structure.

2. Experimental

The structure of our photovoltaic devices is shown in Fig. 1.

A compact TiO_2 layer was deposited onto a Fluorine-doped Tin oxide (FTO) coated glass substrate (Hartford Glass, TEC-15, sheet resistance 15 Ω/sq) by a sol–gel process [15]. The dense TiO_2 layer acts as a hole-blocking layer (HBL) between the FTO and HTM, preventing electron–hole recombination. A nanoporous TiO_2 film (Degussa, P25) approximately 3 μm thick was then spin coated onto the compact TiO_2 layer. The P25 nc-TiO_2 paste was prepared in a manner similar to "Method B" described by Nazeeruddin et al. [2]. After sintering at 450 °C for 30 min, the TiO_2 electrode was sensitized with *cis*-dithiocyanato-*N*,*N*-bis(2,2′-bipyridyl-4,4′-dicarboxylic acid)-ruthenium(II) (Ru–N3, EIC Laboratories) by soaking overnight in a 0.3 mM solution of mixed acetonitrile/*tert*-butanol (50:50/V%) at room temperature. The resulting colored films were typically rinsed with absolute ethanol and dried under flowing nitrogen. A 0.05 M amphiphilic diacetylene (DA) solution of 10,12-pentacosadiynoic acid (PCDA, Alfa Aesar), was prepared in mixed acetonitrile/tetrahydrofuran (50:50/V%). A small amount of 4-*tert*-butyl pyridine (*t*BP) was added into the DA solution with the concentration of about 0.07 M. The DA-PCDA monomer solution was then drop cast onto the dye-coated TiO_2surface. The polymerization was carried out via ultraviolet irradiation (254 nm) for 10 min. Since the top surface of the nc-TiO_2 layer may not be fully covered by the PDA, a thin but continuous film of regioregular poly(3-hexyl-thiophene) (P3HT, Aldrich) was spin coated from chloroform as the electron-blocking layer (EBL). Finally, a gold layer of approximately 40 nm thick was deposited as the hole-collecting electrode by thermal evaporation under vacuum. The whole device was annealed at 80 °C for 10 min under Argon before testing.

The PDA morphology characterization was performed via an optical microscope (Unitron ME-2097) in combination with a color video camera (Sony SSC-C350). The photocurrent–voltage (*J*–*V*) characteristics were measured using a source meter (Keithley SMU 2400) in conjunction with a computer. The AM 1.5 illumination (100 mW/cm^2) was simulated by the use of a xenon lamp (Oriel 1000 W) and appropriate filters. The photocurrent action spectrum was obtained with a 150 W xenon lamp (Photon Technology) coupled to a

monochromator (Digikrom 240). Incident light intensity was measured with an optical power meter (Newport 835) coupled to a photodiode. The photocurrent was collected on a digital multimeter (Keithley 169 DMM). The active area of all devices was set as 0.25 cm by 0.25 cm with a window.

3. Results and discussion

As shown in Fig. 2(a), upon polymerization, the DA-PCDA monomer results in a PDA with a carboxylic acid side group. Fig. 2(b) is the UV–vis absorption spectrum of a PDA-PCDA film on a glass slide. This polymerized film shows the characteristic absorption in the visible region, whereas the unpolymerized film has no absorption in the visible region. The optical anisotropy of this PDA-PCDA film was also observed via polarizing microscopy. Upon drop casting onto the N3-coated nc-TiO_2, the DA-PCDA molecules penetrated into the nanopores, and their carboxylic acid groups may hydrogen bond with the remaining two carboxylic acid groups on the Ru–N3 molecule [16]. (We expect that hydrogen bonding is occurring between the DA and dye, although we have no spectroscopic evidence at this time.) As the solvent evaporated, the DA-PCDA molecules organized into an ordered and densely packed structure inside the TiO_2 nanopores. After ultraviolet irradiation, the film became visually darker. This can be attributed to the formation of the PDA-PCDA, which is blue in the absence of Ru–N3. This color change also confirmed that the DA-PCDA molecules were sufficiently ordered and packed to permit polymerization. The micrograph

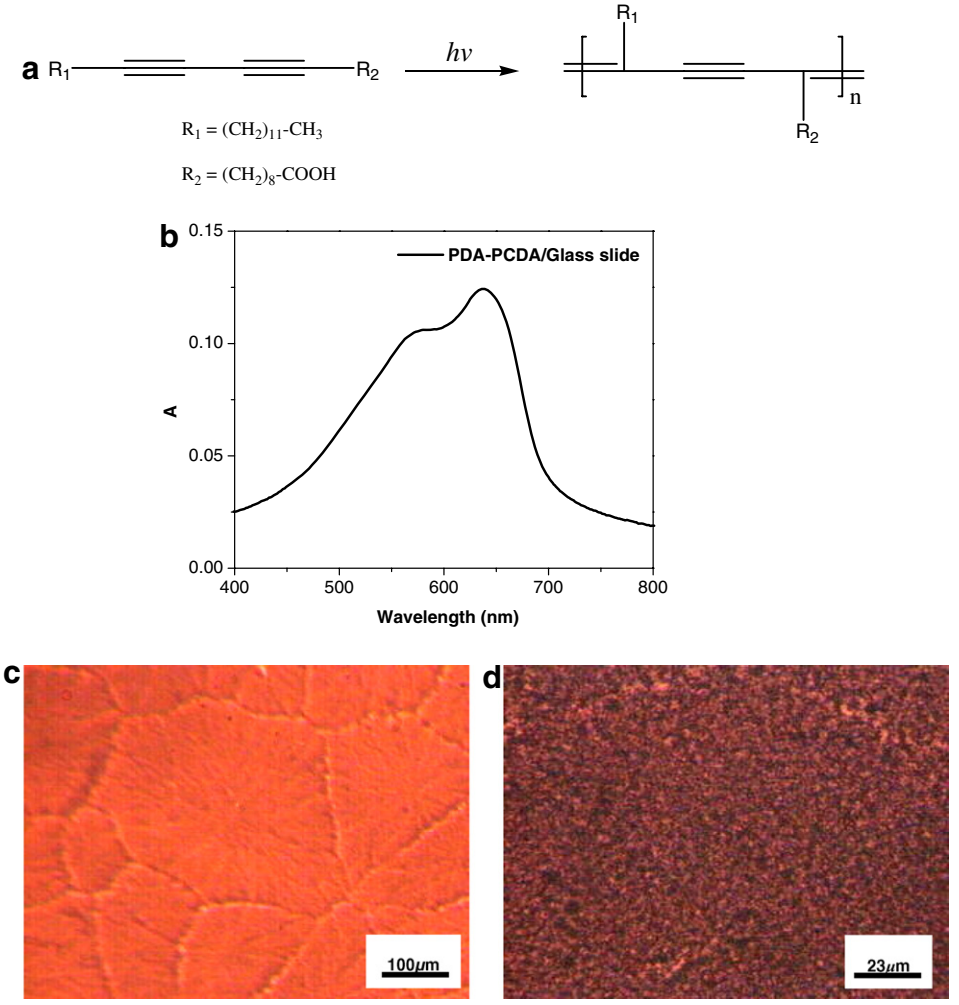

Fig. 2. (a) Solid state polymerization of DA-PCDA. (b) UV–vis absorption spectrum of PDA-PCDA on a glass slide. (c) and (d) Micrographs of PDA-PCDA in a dye/nc-TiO_2 film.

in Fig. 2(c) shows the PDA-PCDA domains inside the N3/nc-TiO_2 film. At the higher magnification, shown in Fig. 2(d), it can be seen that the large domains in Fig. 2(c) are composed of disoriented microstructures, which could be due to the combination of the TiO_2 nanoparticles with the surrounding PDA-PCDA. However, the disordered arrangement of these microstructures may result in a reduction of the charge transport properties of the PDA. Further morphology studies are in progress. In addition, it should be noted that the PDA-PCDA underwent a solvatochromic blue to red transformation when applying the P3HT from chloroform. This could also cause an undesired absorption overlap of PDA-PCDA with Ru–N3.

The schematic energy level alignment of the components of this device is illustrated in Fig. 3. The components have been chosen to reduce the energy barrier to charge transfer, transport and collection. The HOMO level of the PDAs is approximately −5.5 eV [17], slightly higher than the HOMO level of Ru–N3 (−5.6 eV [16] or −5.7 eV [18]) and lower than the HOMO level of regioregular P3HT (−5.1 eV [19]). Therefore holes can be transported without a potential barrier. Due to the presence of the HBL, the holes cannot reach the FTO electrode from the HTM. Similarly, due to the presence of the EBL, the electrons cannot reach the gold electrode from the nc-TiO_2, either. In addition, an ohmic contact is formed at the Au–P3HT interface.

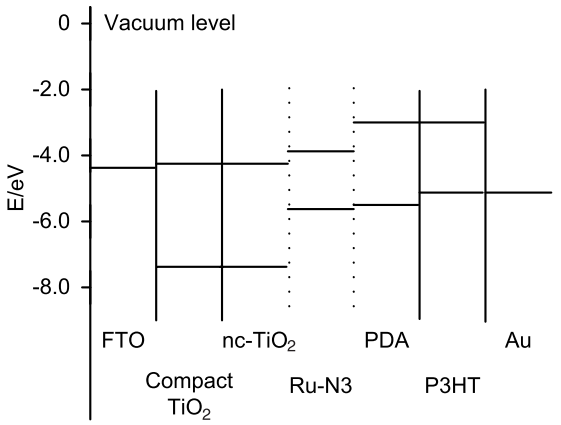

Fig. 3. Schematic illustration of energy level alignment.

Fig. 4(a) shows the photocurrent–voltage characteristics of a typical cell. Under AM 1.5 illumination (100 mW/cm^2), the cell achieved a J_{sc} of 3.73 mA/cm^2, open-circuit voltage (V_{oc}) of 0.51 V, fill factor (FF) of 0.31 and η of 0.62%. The photocurrent action spectrum (IPCE) is shown in Fig. 4(b). The given values are not corrected for the reflection and absorption losses caused by the FTO-coated glass substrate and the glass slide for mounting the cell. The IPCE curve resembles the absorption spectrum of the Ru–N3 dye, but exhibits relatively small values in the range of 500–550 nm. It can be preliminarily concluded that the observed photocurrent arises from the photoinduced electron transfer from the dye. Part of the incident light is absorbed and/or scattered by the PDA and does not contribute to the photocurrent. In addition, the low FF of 0.31 indicates that the photovoltaic performance of this cell is limited by the increased series resistance, which can be partly attributed to the disoriented arrangement of the PDA microstructures in the nanoporous TiO_2 film.

Regioregular P3HT exhibits hole mobilities between 10^{-4} and 0.1 $cm^2\,V\,s^{-1}$, depending on the regioregularity of the polymer and the degree of order within the film [19]. It can also work as a HTM in solid state DSSCs. For the purpose of comparison, some cells were fabricated with no PDA-PCDA and just

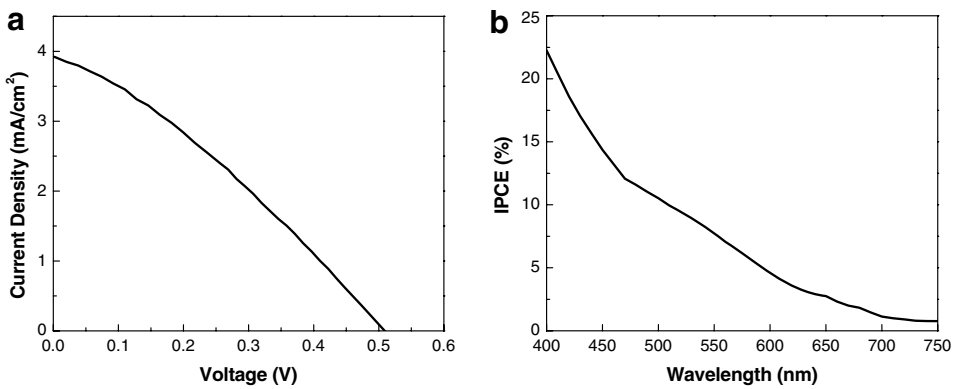

Fig. 4. (a) Current–voltage characteristics. (b) Photocurrent action spectrum.

P3HT spincoated on top. The test results show that their photovoltaic performance is poor, extremely unstable, and significantly dependant on the thickness of the nc-TiO_2 film. Their efficiencies decayed quickly during the test. For a thin nc-TiO_2 film (1.5 μm), the steady-state efficiency was 0.22%; for a thick nc-TiO_2 film (2.9 μm), the steady-state efficiency was only 0.10%. Both are much lower than the efficiency of 0.62% for a cell with both PDA and P3HT (nc-TiO_2 film: 2.9 μm thick).

In principle, semiconducting polymers can function as a sensitizer and HTM at the same time. A cell was constructed using PDA-PCDA in place of Ru–N3. Here the photovoltaic performance was extremely poor and the negligible photocurrent arises from the band-gap excitation of TiO_2 at 400 nm, indicating that the PDA-PCDA cannot function as a light sensitizer. This observation agrees with the literature [17], where Sariciftci et al. reported the absence of photoinduced electron transfer from PDA to C_{60} and attributed the reason to the relatively large exciton binding energy of PDAs, up to 0.5 eV. In this case, the short PDA exciton lifetime should be taken into account as well.

4. Conclusions

Our preliminary results show that in situ solid state polymerized PDA-PCDA can serve as a hole transport material, but not a light sensitizer, for solid state DSSCs. Since many parameters of the cell assembly have not yet been optimized, further improvement of the photovoltaic performance is expected. In particular, future work will focus on improving the PDA-PCDA microstructure orientation, inhibiting interfacial charge recombination and reducing the parasitic PDA absorption.

Acknowledgements

We would like to acknowledge the financial support of the US Army Natick Soldier Center (#DAAD16-01-C-0011) and the supply of Ru–N3 by EIC Laboratories. We also thank Prof. Daniel J. Sandman for his helpful discussions about polydiacetylenes. Y.W. thanks Dr. Seong-Cheol Kim for his advice on writing this contribution.

References

[1] B. O'Regan, M. Gratzel, Nature 353 (1991) 737.
[2] M.K. Nazeeruddin, A. Kay, I. Rodicio, R. Humphry-Baker, E. Muller, P. Liska, N. Vlachopoulos, M. Gratzel, J. Am. Chem. Soc. 115 (1993) 6382.
[3] K. Tennakone, G.R.R.A. Kumara, I.R.M. Kottegoda, K.G.U. Wijayantha, V.P.S. Perera, J. Phys. D: Appl. Phys. 31 (1998) 1492.
[4] U. Bach, D. Lupo, P. Comte, J.E. Moser, F. Weissortel, J. Salbeck, H. Spreitzer, M. Gratzel, Nature 395 (1998) 538.
[5] J. Kruger, R. Plass, L. Cevey, M. Piccirelli, M. Gratzel, Appl. Phys. Lett. 79 (2001) 2085.
[6] J. Kruger, R. Plass, M. Gratzel, H. Matthieu, Appl. Phys. Lett. 81 (2002) 367.
[7] L. Schmidt-Mende, S.M. Zakeeruddin, M. Gratzel, Appl. Phys. Lett. 86 (2005) 013504.
[8] D. Gebeyehu, C.J. Brabec, N.S. Sariciftci, D. Vangeneugden, R. Kiebooms, D. Vanderzande, F. Kienberger, H. Schindler, Synth. Met. 125 (2002) 279.
[9] Y. Saito, T. Azechi, T. Kitamura, Y. Hasegawa, Y. Wada, S. Yanagida, Coord. Chem. Rev. 248 (2004) 1469.
[10] Y. Saito, N. Fukuri, R. Senadeera, T. Kitamura, Yuji Wade, S. Yanagida, Electrochem. Commun. 6 (2004) 71.
[11] Y. Lu, Y. Yang, A. Sellinger, M. Lu, J. Huang, H. Fan, R. Haddad, G. Lopez, A.R. Burns, D.Y. Sasaki, J. Shelnutt, C.J. Brinker, Nature 410 (2001) 913.
[12] T. Aida, K. Tajima, Angew. Chem., Int. Ed. 40 (2001) 3803.
[13] D.J. Sandman, I. Kim, J.M. Njus, D. Lee, A.L. Cholli, S. Sahoo, Macromol. Symp. 192 (2003) 99.
[14] U. Bach, J. Kruger, M. Gratzel, Organic Photovoltaics, SPIE-the International Society for Optical Engineering, San Diego, CA, 2000.
[15] M.S. Lee, I.C. Cheon, Y.I. Kim, Bull. Korean Chem. Soc. 24 (2003) 1155.
[16] A. Hagfeldt, M. Gratzel, Acc. Chem. Res. 33 (2000) 269.
[17] N.S. Sariciftci, B. Kraabel, C.H. Lee, K. Pakbaz, A.J. Heeger, D.J. Sandman, Phys. Rev. B 50 (1994) 12044.
[18] R. Mosurkal, J. He, K. Yang, L.A. Samuelson, J. Kumar, J. Photochem. Photobiol. A: Chem. 168 (2004) 191.
[19] W.U. Huynh, J.J. Dittmer, N. Teclemariam, A.P. Alivisatos, Phys. Rev. B 67 (2003) 115326.

Available online at www.sciencedirect.com
ScienceDirect
Organic Electronics 7 (2006) 551–560
Organic Electronics
www.elsevier.com/locate/orgel

Polariton effects in electroabsorption of molecular crystals with several molecules in the unit cell – Sexithiophene

Anna Stradomska, Piotr Petelenz *

K. Gumiński Department of Theoretical Chemistry, Jagiellonian University, Ingardena 3, 30-060 Cracow, Poland

Received 31 January 2006; accepted 15 August 2006
Available online 11 October 2006

Abstract

Polariton effects in a model molecular crystal with several molecules in the unit cell are described within a semiclassical formalism taking complete account of the strong electrodynamic coupling between excitons and the photon field. Explicit formulas are derived for the specific cases of two and four molecules in the unit cell, and applied to calculate numerically the absorption spectrum of the sexithiophene crystal. The input data are almost entirely non-empirical, based on the results of previous calculations. The electroabsorption (EA) signal of the crystal is calculated as the difference between the absorption spectra at non-zero and at zero electric field, without any a priori assumptions regarding the shape of the individual EA fingerprints. The results confirm the previous conclusion that an isolated Frenkel exciton always yields a first-derivative EA signal, regardless of its intensity, and that this conclusion is not affected by polaritonic effects. For the specific case of sexithiophene, the experimental absorption spectrum is well reproduced, but the EA signal of the Frenkel states, in spite of full inclusion of polariton couplings, is underestimated by orders of magnitude. The results demonstrate that a satisfactory theoretical reproduction of the sexithiohene EA spectrum is possible only when low-energy charge-transfer states are included, as was done in a recent paper.

PACS: 71.35.Cc; 71.36.+c; 78.20.Ci; 78.20.Jq

Keywords: Sexithiophene; Polaritons; CT states; Electroabsorption

1. Introduction

Theoretical description of intramolecular (Frenkel) excitons in molecular crystals was comprehensively addressed in the sixties and seventies of the past century [1,2]. The fundamental characteristics of the excitons, such as the Davydov splitting, bandwidth and absorption spectrum, were derived and amply discussed.

The results obtained then are nowadays considered classic and are widely used for interpretation of experimental data. However, for a long time the main thrust of experimental research was focused on optical transitions of moderate or low-oscillator strength. As a consequence, one of the classic conclusions went to oblivion: namely, the orientational dispersion of exciton energies at the centre of the Brillouin zone, resulting from the

* Corresponding author. Tel.: +48 12 6632212; fax: +48 12 6340515.
E-mail address: petelenz@chemia.uj.edu.pl (P. Petelenz).

1566-1199/$ - see front matter © 2006 Elsevier B.V. All rights reserved.
doi:10.1016/j.orgel.2006.08.004

long range of the dipolar interaction and giving rise to the directional dependence of the transition energies. In fact, the effect is marginal for weak transitions, since its size depends on the square of the transition dipole moment.

As the transition dipole moment governs also the interaction of the excitons with photons, its large value gives rise to another peculiar effect, sometimes confused with the former one because of their concomitant occurrence. When the coupling with photons is strong enough, quasiparticles of a new kind are formed [1,2]. These quasiparticles, called polaritons, are coherent superpositions of excitons and photons, and are characterized by a forbidden gap in the energy spectrum, observed as a ''stopping band'' of metallic reflection. The appearance of the stopping band is often accompanied by dramatic intensity redistribution between different vibronic transitions [2].

The recent extensive experimental studies [3–6] have prompted some questions concerning the fingerprint of intense electronic transitions in electroabsorption (EA) spectroscopy. According to the standard interpretational paradigm [7,8], any isolated non-degenerate Frenkel exciton (regardless of its intensity) gives rise to the EA signal proportional to the first derivative of the corresponding absorption band. Contradicting this view, a new paradigm was later proposed [3–6], based on the *ad hoc* assumption that for a strong electronic transition the transition dipole moment (i.e., an off-diagonal matrix element of the dipole moment operator) behaves much in the same way as the permanent dipole moment (a diagonal matrix element of the dipole moment operator), which motivated the claim that the corresponding EA signal should have second-derivative shape. This postulated behaviour was presented as a consequence of electrodynamic coupling, peculiar to polariton states [3].

Specifically, this latter approach led to the conclusion that the electroabsorption spectrum of crystalline sexithiophene (T6) is dominated by Frenkel transitions [3–6], contrary to the results of quantitative calculations based on a microscopic Hamiltonian, which attributed a major part of the observed EA spectrum of T6 to charge-transfer (CT) states [9]. In view of the presumably crucial role of CT states in the context of (opto)electronics, the interpretational problem that has ensued, in addition to its fundamental impact, has also potential ramifications for applied research.

In order to resolve this controversy, the classic approach developed in the sixties of the past century [1,2] has recently been employed to study the consequences of electrodynamic polariton effects for electroabsorption spectroscopy, without invoking any arbitrary assumptions regarding the shape of exciton EA fingerprints [10]. The results have confirmed the standard paradigm, assigning to any non-degenerate Frenkel transition a first-derivative electroabsorption signal.

However, this conclusion was derived for a model crystal with only one molecule in the unit cell. Although the validity of the derivation is general, for the sexithiophene crystal confrontation of the results with experimental spectra and with the results of the treatment based on the *ad hoc* postulate mentioned above is impeded by the specific circumstances due to the fact that this crystal contains several molecules in the unit cell. The objective of the present paper is to bridge this gap by extending the derivation of Ref. [10] for a crystal with four molecules in the unit cell. The approach is illustrated by numerical calculations for the sexithiophene crystal.

2. Sexithiophene crystal and its spectra

The α-sexithiophene crystal is known to have two polymorphic forms [11,12]. The high-temperature polymorph is monoclinic (space group $P2_{1/a}$) and contains two molecules in the unit cell. Its herringbone structure largely resembles the archetypal anthracene crystal [13,14]. This form of T6 is of lesser interest in the present context, since the most reliable experimental spectra [3,4,15,16] which are addressed in our numerical calculations, have been measured for the low-temperature polymorph. However, for the sake of completeness the main formulas will be derived also for the high-temperature phase with two molecules in the unit cell.

The structure of low-temperature α-sexithiophene polymorph is also monoclinic (space group $P2_{1/n}$) with four molecules in the unit cell, arranged in two pairs. The distance between the centres of mass of the molecules within each pair is smaller than 5 Å, while the distance between the molecules from different pairs exceeds 20 Å. The intense lowest molecular excited state, polarized along the long molecular axis ($1B_u$) is split into four components, of which two, a_g and b_g, are dipole-forbidden. The upper Davydov component (b_u state) carries almost all the oscillator strength of the molecular excita-

tion; as the long axes of sexithiophene molecules are almost perpendicular to the crystallographic b-axis, the lower Davydov component (a_u state) is very weak and can be detected only at low-temperatures. These two components can be selectively probed by light polarized parallel to c' and b crystallographic direction, respectively.

For light polarized along the b crystallographic axis both absorption and electroabsorption spectra are available [3,4,17]. In the low-energy range, i.e., below about 2.5 eV, the absorption spectrum exhibits a set of sharp and well resolved features starting at about 2.27 eV. The electroabsorption spectrum in this energy range follows very closely the first derivative of the absorption spectrum. These features were attributed to the a_u and a_g Davydov components and to their vibronic replicas borrowing intensity from the intense upper Davydov component [18].

Starting from about 2.5 eV the absorption spectrum exhibits broad and intense bands at about 2.6 eV and 2.76 eV. The electroabsorption signal is a series of overlapping features, readily recognizable as second-derivative shapes, but not directly attributable to the bands observed in the absorption spectrum. The provenance of these features is subject of the controversy described in the introduction. Calculations based on a microscopic Hamiltonian [9] assigned these features to CT states. In the papers of Weiser and collaborators [3,4,17] a new postulate was invoked, stating that because of polaritonic effects electroabsorption signal of a strong Frenkel transitions follows the second derivative of the absorption spectrum. It allowed the authors to ascribe the signal above 2.5 eV to Frenkel states. This new postulate was based only on intuitive arguments and no derivation was presented to support it.

In fact, the classical theory of the coupling of photons to excitons for molecular crystals containing one molecule per unit cell and one molecular transition [10] shows that although polaritonic effects play some role in the absorption spectra of strongly absorbing crystals, the electroabsorption spectra follow the first derivative of the absorption, irrespective of the oscillator strength of the transition under consideration. In the present paper the treatment is generalized for crystals containing several molecules in the unit cell (2 and 4), and the constituent molecules may have multiple molecular transitions polarized along the same molecular axis. This generalization allows us to calculate the absorption and electroabsorption spectra of the α-sexithiophene crystal.

3. Excitons in crystals with several centrosymmetric molecules per unit cell

In the classical consideration of the coupling between a molecular exciton of frequency ω_{0u} and oscillator strength f_u, located at site s, and the radiation field [2], the transition dipole moment $\vec{d}_{su} = \langle 0|\vec{d}_s|u\rangle$ is represented by a classical oscillating point dipole $\vec{d}_{su}(t)$. Its equation of motion in the electric field $\vec{E}'(\vec{r}_s, t)$:

$$\left[\frac{\partial^2}{\partial t^2} + \omega_{0u}^2(\vec{F})\right]\vec{d}_{su}(t) = \frac{e^2 f_u(\vec{F})}{m_e}\hat{d}_{su}\hat{d}_{su}\cdot\vec{E}'(\vec{r}_s, t), \quad (1)$$

is solved in conjunction with Maxwell's equations which describe the driving fields. $\hat{d}_{su}$ stands for a unit vector pointing along $\vec{d}_{su}$.

In our previous paper [10], we solved the Eq. (1) for the molecular crystal containing one centrosymmetric molecule per unit cell, subjected to static electric field $\vec{F}$ and interacting at the same time with the monochromatic field of the light wave of frequency ω. The same general approach will be adopted here, and some results will be used directly.

After the Fourier transformation from time to frequency domain the equations corresponding to zero frequency and optical frequency decouple from each other (Eqs. (22)–(25) of Ref. [10]). Therefore, at the level of classical electrodynamics, the static electric field does not contribute at the frequency of optical fields. However, it does affect the optical phenomena by modifying the molecular excitation frequencies and oscillator strengths, which is readily accounted for by quantum-mechanical perturbation theory (Eqs. (3) and (9) of Ref. [10]), reconstituting the familiar square dependence of the energies on electric field strength, governed by static polarizability.

We presently rewrite the results concerning the part of the field that is relevant to optical phenomena (Eqs. (24) and (25) of Ref. [10]) with two small changes. As we are dealing with crystals with several molecules in the unit cell it is now convenient to split the site index into two parts $s = (n, \beta)$, where n labels the unit cells and β denotes the site within the unit cell. We also omit the index D, which was previously used to denote the optical Fourier component of all dynamical quantities, since static quantities do not appear in this paper. Then, the relevant equations read:

$$\sum_{m\gamma}\left[\mathbf{1}\delta_{nm}\delta_{\beta\gamma}+4\pi\boldsymbol{\alpha}_{\beta}(\omega)\cdot\boldsymbol{T}_{n\beta,m\gamma}\right]\cdot\vec{P}_{m\gamma}=\frac{\mathrm{i}\omega}{c}\boldsymbol{\alpha}_{\beta}(\omega)\cdot\vec{A}(\vec{r}_{n\beta}),\tag{2}$$

$$\left(\nabla^2+\frac{\omega^2}{c^2}\right)\vec{A}(\vec{r})=\mathrm{i}\frac{4\pi}{c}\omega\vec{P}^{\perp}(\vec{r}),\tag{3}$$

where $\vec{A}(\vec{r})$ is the vector potential, $\boldsymbol{\alpha}_{\beta}(\omega)$ is a polarizability tensor of the molecule located at site $n\beta$:

$$4\pi\boldsymbol{\alpha}_{\beta}(\omega)=\frac{e^2}{m_e v_0}\sum_{u}\frac{f_u(\vec{F})}{\omega_{0u}^2(\vec{F})-\omega^2}\hat{d}_{\beta u}\hat{d}_{\beta u},\tag{4}$$

the dipole tensor $\boldsymbol{T}_{n\beta,m\gamma}$ describes the interaction of two point dipoles located at the distance $\vec{R}_{n\beta,m\gamma}=\vec{r}_{n\beta}-\vec{r}_{m\gamma}$ from each other

$$\boldsymbol{T}_{n\beta,m\gamma}=\frac{v_0}{4\pi}\left|\vec{R}_{n\beta,m\gamma}\right|^{-3}\left(\mathbf{1}-3\widehat{R}_{n\beta,m\gamma}\widehat{R}_{n\beta,m\gamma}\right)\left(1-\delta_{nm}\delta_{\beta\gamma}\right),\tag{5}$$

and site-polarization (divided by unit cell volume v_0) is given by

$$\vec{P}_{n\beta}=\frac{1}{v_0}\sum_{u}\vec{d}_{n\beta u}.\tag{6}$$

Following the classic monograph [2], Eqs. (2) and (3) are first solved in the limit $\vec{A}(\vec{r},t)=0$, i.e., in the absence of light waves. This yields the frequencies of Coulombic excitons as the roots of the equation:

$$\det\left|\mathbf{1}\delta_{\beta\gamma}+4\pi\boldsymbol{\alpha}_{\beta}(\omega)\cdot\boldsymbol{T}_{\beta\gamma}(\vec{k})\right|=0,\tag{7}$$

where

$$\boldsymbol{T}_{\beta\gamma}(\vec{k})=\sum_{m}\boldsymbol{T}_{n\beta,m\gamma}\exp\left[\mathrm{i}\vec{k}\cdot\left(\vec{r}_{n\beta}-\vec{r}_{m\gamma}\right)\right]\tag{8}$$

is the Fourier transform of the dipole tensor.

For a crystal consisting of molecules with all transitions polarized along the same molecular axis ($\hat{d}_{\beta}$ for molecule on βth position in unit cell) the secular determinant assumes the simpler form

$$\det\left|\delta_{\beta\gamma}+4\pi\alpha(\omega)T_{\beta\gamma}(\vec{k})\right|=0\tag{9}$$

where

$$\alpha(\omega)=\hat{d}_{\beta}\cdot\boldsymbol{\alpha}_{\beta}(\omega)\cdot\hat{d}_{\beta}\tag{10}$$

and

$$T_{\beta\gamma}(\vec{k})=\hat{d}_{\beta}\cdot\boldsymbol{T}_{\beta\gamma}(\vec{k})\cdot\hat{d}_{\gamma}.\tag{11}$$

The secular Eq. (9) can be further simplified for certain special directions in $\vec{k}$-space by using the symmetry group of the wave vector. This will be done in Sections 5 and 6 for a monoclinic crystal with two and four molecules per unit cell.

4. Polaritons in crystals with several centrosymmetric molecules per unit cell

For an infinite crystal and finite driving transverse electric field, the vector potential $\vec{A}(\vec{r},t)$ is assumed in the form of a plane wave:

$$\vec{A}(\vec{r})=\vec{A}_0\exp\left(\mathrm{i}\vec{k}\cdot\vec{r}\right),\tag{12}$$

where $\vec{k}$ is a vector from the first Brillouin zone and $\vec{A}_0$ is perpendicular to $\vec{k}$. Following Philpott [2], we disregard the coupling of excitons with wave vector $\vec{k}$ to photons with wave vector $\vec{k}+\vec{K}$, where $\vec{K}$ is any reciprocal lattice vector (different from the null vector). This approximation holds well in the visible and ultraviolet range.

After the Fourier transformation to $\vec{k}$-space, Eq. (3) is solved for $\vec{A}_0$; subsequently the result is substituted into (Fourier transformed) Eq. (2). This yields the following secular equation as the condition for the existence of non-trivial solutions for polarization:

$$\det\left|(n^2-1)\left[\mathbf{1}\delta_{\beta\gamma}+4\pi\boldsymbol{\alpha}_{\beta}(\omega)\cdot\boldsymbol{T}_{\beta\gamma}(\vec{k})\right]-4\pi\boldsymbol{\alpha}_{\beta}(\omega)\cdot(\mathbf{1}-\hat{k}\hat{k})\right|=0.\tag{13}$$

Again, the secular determinant assumes a simpler form for molecules with all transitions polarized along the same direction:

$$\det\left|(n^2-1)\left[\delta_{\beta\gamma}+4\pi\alpha(\omega)T_{\beta\gamma}(\vec{k})\right]-4\pi\alpha(\omega)\sum_{i=1}^{2}(\hat{d}_{\beta}\hat{e}_i)(\hat{d}_{\gamma}\hat{e}_i)\right|=0,\tag{14}$$

where $\hat{e}_1$, $\hat{e}_2$ are two orthogonal light polarization versors; $n=c|\vec{k}|/\omega$ is the (unknown) refractive index, which may be found by solving Eq. (14).

After adding some phenomenological damping (γ_u), the polarizability becomes complex:

$$\alpha(\omega)=\frac{e^2}{m_e v_0}\sum_{u}\frac{f_u(\vec{F})}{\omega_{0u}^2(\vec{F})-\omega^2-\mathrm{i}\omega\gamma_u},\tag{15}$$

and so does the refractive index. Its imaginary part can then be related to the extinction coefficient,

$$\varepsilon(\omega,\vec{k})=\frac{2\omega\mathrm{Im}\left[n(\omega,\vec{k})\right]}{c}\tag{16}$$

which yields the (observable) absorption spectrum of the crystal. The electroabsorption spectrum is

then readily calculated as the difference between the absorption spectra for non-zero and zero electric field.

5. Crystal with two molecules per unit cell

As has been mentioned above, the excitonic (9) and polaritonic (14) secular equations can be further simplified for certain directions of $\vec{k}$. Let us consider a monoclinic crystal with two molecules in the unit cell, such as the high-temperature T6 polymorph, taking into account only the transitions polarized along the long molecular axis. The two molecules in the unit cell are related to each other by a screw axis parallel to the crystallographic b direction. The symmetry implies the following relations for dipole sums (the $\vec{k}$-dependence of the dipole sums is omitted for clarity):

$$T_{11} = T_{22} \tag{17}$$

$$T_{12} = T_{21}. \tag{18}$$

For the states with $\vec{k}$ parallel to the b axis or lying in the ac plane, the exciton dispersion relation (9) splits into two separate equations – one for the states polarized along the b axis (i.e., states of symmetry A, plus sign in the following equations) and another for the states polarized in the ac plane (states of B symmetry, minus sign in the following equations):

$$1 + 4\pi\alpha(\omega)T_{\pm}(\vec{k}) = 0, \tag{19}$$

where the lattice sums are given by

$$T_{\pm}(\vec{k}) = T_{11}(\vec{k}) \pm T_{12}(\vec{k}). \tag{20}$$

The polariton dispersion relation (14) can be simplified in a similar way, giving rise to two separate equations for the states of A and B symmetry, which can be easily solved to yield the refractive indices:

$$n_{\pm}^2(\omega, \vec{k}) = 1 + \frac{2\pi\alpha(\omega)(\hat{e}_\lambda \cdot \vec{d}_{\pm})^2}{1 + 4\pi\alpha(\omega)T_{\pm}(\vec{k})}, \tag{21}$$

where

$$\vec{d}_{\pm} = \hat{d}_1 \pm \hat{d}_2 \tag{22}$$

and $\hat{e}_\lambda$ is the light polarization versor. $\vec{d}_-$ lies in the ac plane and $\vec{d}_+$ is parallel to the b axis.

The dipole sums T_{1i} can be split into the analytic and non-analytic part [2,19]:

$$T_{1i}(\vec{k}) = t_{1i}(0) + (\hat{k} \cdot \hat{d}_i)^2. \tag{23}$$

which gives rise to a similar $\vec{k}$-dependence of the symmetry-adapted dipole sums $T_{\pm}$, and ultimately to the orientational dependence of the exciton energies and of the refraction index.

6. Crystal with four molecules per unit cell

The focus of this paper is on the low-temperature polymorph of the α- sexithiophene crystal, which is monoclinic and contains four molecules in the unit cell. The treatment is again restricted to the transitions polarized along the long molecular axis of the molecule. The molecules within the unit cell are labelled in the following way: assuming that the c' axis is directed vertically, molecules 1 and 2 are located in the upper half of the unit cell, and are related to each other by the two-fold screw axis parallel to the b crystallographic direction. The pair of molecules 3 and 4, located in the lower part of the unit cell, is related to pair 1–2 by inversion. Owing to symmetry, only 4 out of 16 products of the form (11) are independent (for clarity the explicit $\vec{k}$ dependence of dipole sums is now omitted):

$$T_{11} = T_{22} = T_{33} = T_{44}, \tag{24}$$

$$T_{12} = T_{21} = T_{34} = T_{43}, \tag{25}$$

$$T_{13} = T_{31} = T_{24} = T_{42}, \tag{26}$$

$$T_{14} = T_{41} = T_{23} = T_{32}. \tag{27}$$

The exciton dispersion relation may be derived from the equation:

$$\begin{vmatrix} 1 + 4\pi\alpha(\omega)T_{11}(\vec{k}) & 4\pi\alpha(\omega)T_{12}(\vec{k}) & 4\pi\alpha(\omega)T_{13}(\vec{k}) & 4\pi\alpha(\omega)T_{14}(\vec{k}) \\ 4\pi\alpha(\omega)T_{12}(\vec{k}) & 1 + 4\pi\alpha(\omega)T_{11}(\vec{k}) & 4\pi\alpha(\omega)T_{14}(\vec{k}) & 4\pi\alpha(\omega)T_{13}(\vec{k}) \\ 4\pi\alpha(\omega)T_{13}(\vec{k}) & 4\pi\alpha(\omega)T_{14}(\vec{k}) & 1 + 4\pi\alpha(\omega)T_{11}(\vec{k}) & 4\pi\alpha(\omega)T_{12}(\vec{k}) \\ 4\pi\alpha(\omega)T_{14}(\vec{k}) & 4\pi\alpha(\omega)T_{13}(\vec{k}) & 4\pi\alpha(\omega)T_{12}(\vec{k}) & 1 + 4\pi\alpha(\omega)T_{11}(\vec{k}) \end{vmatrix} = 0. \tag{28}$$

The matrix on the left-hand-side of Eq. (28) is readily diagonalized by the similarity transformation with the matrix:

$$\mathbf{U} = \begin{pmatrix} 1 & 1 & 1 & 1 \\ 1 & 1 & -1 & -1 \\ 1 & -1 & -1 & 1 \\ 1 & -1 & 1 & -1 \end{pmatrix}, \tag{29}$$

leading to four independent exciton dispersion relations:

$$1 + 4\pi\alpha(\omega)T_i(\vec{k}) = 0 \tag{30}$$

where $i = 0\pm, \pm$ and

$$T_{0\pm}(\vec{k}) = T_{11}(\vec{k}) \mp T_{12}(\vec{k}) + T_{13}(\vec{k}) \mp T_{14}(\vec{k}), \tag{31}$$

$$T_{\pm}(\vec{k}) = T_{11}(\vec{k}) \pm T_{12}(\vec{k}) - T_{13}(\vec{k}) \mp T_{14}(\vec{k}). \tag{32}$$

For the states with wave vector $\vec{k}$ lying in the *ac* plane or parallel to the *b* direction, the polaritonic dispersion relation (14) can be simplified in the same way as the excitonic dispersion relation. The resultant transition dipoles are:

$$\vec{d}_{0\pm} = \hat{d}_1 \mp \hat{d}_2 + \hat{d}_3 \mp \hat{d}_4 = 0, \tag{33}$$

$$\vec{d}_{\pm} = \hat{d}_1 \pm \hat{d}_2 - \hat{d}_3 \mp \hat{d}_4. \tag{34}$$

$\vec{d}_-$ is contained in the *ac* plane and $\vec{d}_+$ is parallel to the *b* axis. The $\vec{d}_{0\pm}$ states are mute in optical spectra as they carry no net transition dipole moment. As in the case of two molecules per unit cell, for $\vec{k}$ lying in the *ac* plane both $\vec{d}_+$ and $\vec{d}_-$ states are observable and for $\vec{k}$ parallel to the *b* direction only the $\vec{d}_-$ state is observable.

For the light polarization versor lying in the *ac* plane or parallel to the *b* axis, also the polariton dispersion relation splits into four independent equations, which can be solved for the refractive indices.

For obvious reasons, the first two equations, for the states with vanishing transition moment $\vec{d}_{0\pm}$, produce the refraction coefficient $n = 1$ (no refraction). The second pair of equations, for states with transition dipoles along $\vec{d}_{\pm}$ yields:

$$n_{\pm}^2(\omega, \vec{k}) = 1 + \frac{\pi\alpha(\omega)(\hat{e}_\lambda \cdot \vec{d}_{\pm})^2}{1 + 4\pi\alpha(\omega)T_{\pm}(\vec{k})}. \tag{35}$$

Like in the case of two molecules per unit cell, due to non-analyticity of the dipole sums, the energies of Coulombic excitons and the polaritonic effects depend on the direction of wave vector $\vec{k}$.

It is readily seen that Eqs. (35) and (21) are formally identical. Therefore one can use the simpler model of the crystal with two molecules per unit cell to simulate the absorption and electroabsorption spectra of the more complex crystal with four molecules per unit cell, provided that the transition moments and the lattice sums are properly recalculated according to Eqs. (31)–(34). In effect, the formalism developed in this paper affords a unified description of both sexithiophene polymorphs and, if needed, may in the future be applied for the high-temperature phase.

7. Numerical calculations for α-sexithiophene single crystal

All the input data necessary for calculations of absorption and electroabsorption spectra of the sexithiophene single crystal are available in the literature. The geometry of the simulated experiment is identical with the one described by Weiser and collaborators [3,4,17] and so is the static electric field of 23 kV/cm. Dipole tensors for α-sexithiophene crystals were calculated by Munn et al. [20]. Other parameters are essentially the same as those used previously in the interpretation of the experimental electroabsorption spectrum of the α-sexithiophene single crystal [9]. For the sake of simplicity, we take into account only one low-lying electronic transition of the sexithiophene molecule, polarized along the long molecular axis, located at 2.50 eV, and endowed with the transition dipole moment of 2.1 eÅ. The exciton transition is accompanied by a vibronic progression in the most prominent sexithiophene normal mode of frequency 0.18 eV, with the assumed Franck–Condon displacement parameter of 1.2 (corresponding to the Huang–Rhys factor of about 0.7). The polarizability change upon excitation is 80 $Å^3$ for both states and the damping parameter (γ) is tentatively set to 0.25 eV.

With these input parameters, the absorption spectrum was calculated using Eqs. (16) and (35). Then the field-modified values of transition energies and oscillator strengths were evaluated using Eqs. (3) and (9) of Ref. [10], and applied to calculate the absorption spectrum at the electric field of 23 kV/cm. Subsequently the electroabsorption signal was calculated as the difference between the absorption spectra at non-zero and at zero electric field.

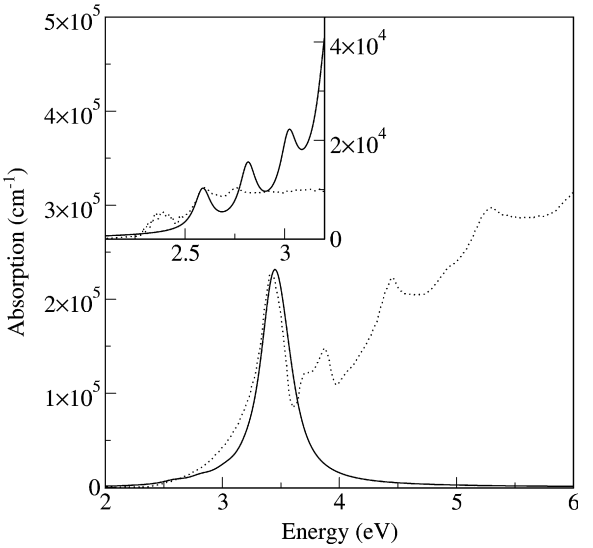

Fig. 1. c'-polarized absorption spectra of the α-sexithiophene single crystal. Solid line – calculated, dotted line – experimental (main panel – Ref. [15], inset – Ref. [16]).

The calculated c'-polarized absorption spectrum is shown in Fig. 1 and compared with the experimental spectrum of Ref. [15], obtained from the crystal reflection spectrum by the Kramers–Kronig transformation. The agreement is very satisfactory. Especially noteworthy is the (correctly reproduced) accumulation of absorption intensity in the high-energy region, just below the position of the longitudinal exciton; this feature is a manifestation of polariton effects.

In the crucial energy range between 3 eV and 3.5 eV, the above experimental spectrum differs from that measured directly in absorption experiment, published by the same authors [3,4] and later confirmed by Loi et al. [16]. In the following, we use as reference the spectrum of Loi et al., since it exhibits no effects of crystal misalignment or imperfection, perceptible in the low-energy part of the Möller and Weiser spectrum, where some intensity leak from c' to b polarization is rather obvious. In contrast, no such effect is observable in the results of Ref. [16], where the spectra in the two polarizations are clearly distinct.

The difference between the spectrum measured directly [3,4,16] and that obtained from the reflection spectrum [15] should probably be attributed to the different experimental technique. At the very least, the resolution of the applied equipment was probably different; also the Kramers–Kronig transformation might smear out some fine structure.

We tentatively mimic the difference in resolution by changing the width of absorption resonances in our calculations from 0.25 eV to 0.10 eV. The inset in Fig. 1 compares the calculated c'-polarized spectrum with that of Ref. [16]. It is readily seen that, apart from the weak low-energy onset, the salient features of the absorption spectrum are well reproduced. The anomalously high-intensity at high-energies is correctly accounted for. The approximate position of the calculated 0–0 band agrees reasonably well with the absorption maximum observed at about 2.6 eV. The vibronic progression that follows is a bit too pronounced, but this was to be expected since the broadening of the resonances with increasing energy has been disregarded in the model; its inclusion would blur the vibronic structure at higher energies. The neglected part of vibronic interactions would also contribute to the overall diffuse shape. In addition, the interaction with charge-transfer (CT) states is bound to modify the transition energies and probably also the intensities, although these effects, governed by (rather small) CT integrals are unlikely to show up prominently in c'-polarization, dominated by intense, strongly interacting transitions. Assuming that, ultimately, the peak just above 3 eV would be turned into diffuse background, the anomalously high-intensity at high-energies qualitatively agrees with the trend observed in the experimental spectrum; quantitatively, the calculations somewhat exaggerate this general tendency. However, one can hardly attach quantitative significance to this discrepancy in view of the striking difference between the published experimental spectra [15,16] in that energy range (Cf. the main panel and the inset of Fig. 2).

Although the spacing between the peaks at 2.6 eV and about 2.78 eV is evidently overestimated, in view of the overall simplifications of the model this discrepancy seems to be a minor one: in order to avoid direct fitting of the spectrum, a generic value of 0.18 eV is taken for the effective vibrational frequency, the dipole tensor is calculated [20], not adjusted to fit the experimental data, and only one electronic state per molecule is explicitly included.

Absence of the low-energy features (starting at about 2.3 eV) is no surprise either: as has been demonstrated by detailed calculations [18], the corresponding transitions are vibronically induced satellites deriving from the (extremely weak) b-polarized a_u Davydov component and from the a_g Davydov component which, according to Eq. (33),

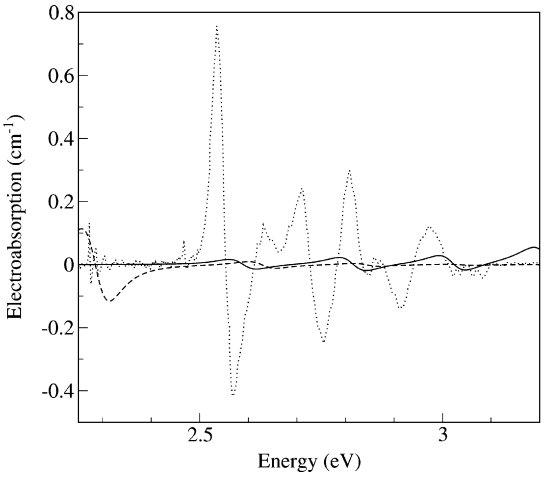

Fig. 2. Electroabsorption spectra of the α-sexithiophene single crystal. Solid line – calculated (c'-polarized), broken line – calculated (b-polarized, magnified by 10^4), dotted line – experimental (b-polarized).

carries no intrinsic transition dipole moment. As vibronic coupling is not included in our present model (the low-frequency vibrations that mediate this coupling are completely ignored), these states are predicted to be mute.

The calculated position of the 0–0 line in polarization b is reasonably well reproduced. Confrontation of the shape of the b-polarized absorption spectrum with experiment is pointless; owing to the very small transition dipole of the corresponding Davydov component, it exhibits no polariton effects, while the structure of the corresponding transition is determined by low-frequency vibrations, which are out of our present scope. Altogether, within the inherent limitations of the applied model the agreement between the calculated and experimental absorption spectra is pretty satisfactory, which is readily seen in the intense c' polarization.

Unfortunately, direct comparison is not possible for electroabsorption, since for this polarization and energy range no experimental EA spectrum is available in the literature. However, the same crystal misalignment and/or imperfections that gave rise to the intensity leak from the c'-polarized to the b-polarized absorption spectrum in Refs. [3,4] should have affected the EA spectrum in an analogous way. This allows one to use the b-polarized electroabsorption spectrum [3,4] to look for potential manifestations of polaritonic effects. The same methodology was implicitly adopted in the original papers [3,4], where the features detected in the b-polarized EA spectrum were assigned to the strong c'-polarized b_u exciton.

It should be noted marginally that interpretation of the weak EA signal observed in polarization b at about 2.3–2.4 eV [3] is beyond the scope of the present paper. For this signal, deriving from the weak vibronically induced bands mentioned above, polariton effects have never been suggested and the original explanation of Ref. [3] is indubitably valid. The present paper is focused on the signal starting at about 2.5 eV, because of its controversial provenance.

Fig. 2 shows the calculated c'-polarized EA signal of the T6 crystal (solid line), compared with the experimental b-polarized electroabsorption spectrum (dotted line). The amplitude of the calculated signal is evidently about an order of magnitude smaller than that actually measured. One should bear in mind that the former is strictly c'-polarized, while the latter represents only the fraction of c'-polarized intensity which is spilt into polarization b. Assuming the "leak" of as much as 10% (which would imply pretty strong crystal misalignment or imperfection), the simulated b-polarized spectrum would have to be reduced by another factor of ten. As the scale of the calculated absorption spectrum agrees quite well with that actually observed (*vide supra*), in order to reconcile the disparate amplitudes of the EA signal the polarizability change between the ground and excited state of the molecule would have to be increased by about two orders of magnitude with respect to the value assumed in our calculations. The applied value of 80 Å^3 is typical for molecules of comparable size; a value ten times larger would be difficult to justify, and larger by a factor of 100 would be inconceivable. Hence, the signal of the transitions observed in c'-polarized absorption is far too low to rationalize the experimental b-polarized EA spectrum of sexithiophene.

Moreover, the predicted signal shape is also in dramatic conflict with the observed one. Obviously, it consists of a sequence of first-derivative curves located at the positions of the resonances observed in absorption. Contrary to the recently invoked hypothesis [3], there is no indication of any second-derivative contributions. It should be emphasized that the present model completely accounts for the polariton effects of exciton–photon coupling; their manifestation in the predicted absorption spectrum is evident. The EA signal of Fig. 2 has been directly calculated as the difference between the

absorption spectra at zero and non-zero electric field; its shape is a *result*, not an *assumption* – in contrast to the second-derivative shape, postulated in Ref. [3]. As demonstrated by Fig. 2, this postulate was physically invalid.

The extremely weak *b*-polarized absorption of the almost forbidden a_u Davydov component gives rise to the signal shown in Fig. 2 as the broken line (magnified by 10^4). It is again much weaker than the experimentally observed features, has a different shape and a different location.

This clearly demonstrates that in order to rationalize the observed electroabsorption spectrum of the sexithiophene crystal it is necessary to invoke another set of states, which need not be very intense in absorption but must exhibit a strong EA signal of approximately second-derivative shape. These are the nearest-neighbour charge transfer (CT) states. As has already been shown [9], the absorption bands due to the eigenstates of CT parentage appear in polarization *b*, practically coinciding with the position (2.6 eV) of the Frenkel transition observable in polarization c' (the corresponding vibronic replicas also coincide, as the vibrational frequency is the same). Tentative data available for quaterthiophene (T4) suggest that in that crystal the coincidence is not nearly as perfect as it is for T6, although in other respects the two systems are quite similar. A more detailed study of the T4 case will be undertaken in a forthcoming paper.

For T6, the *b*-polarized absorption spectrum in the relevant energy range has already been theoretically reproduced in considerable detail, along with the corresponding EA signal [9]. The calculations were based on a microscopic Hamiltonian, derivable from the total many-electron Hamiltonian of the crystal. The input data were mostly estimated from independent calculations, with a minimum set of adjustable parameters. The achieved agreement with experiment was very good. Until now, the interpretation proposed at that time coexisted with the alternative one, invoking polariton effects as the possible source of the observed second-derivative EA signals [3]. In the present paper we have demonstrated that polariton effects, although clearly operative in T6 and rather spectacular in its absorption spectrum, do not explain the features observed in electroabsorption. This leaves the quantitative interpretation of Ref. [9] as the only one that is compatible with experimental data, and further confirms the crucial role of CT states in spectroscopy of the sexithiophene crystal.

8. Conclusions

This work confirms our recent result [10] that polariton effects in Frenkel exciton spectra *do not* give rise to second derivative shapes of the electroabsorption signal, contrary to the *ad hoc* postulate of Ref. [3]. For the specific case of sexithiophene, it is demonstrated here that the EA spectrum of the low-energy Frenkel states, calculated with complete inclusion of polariton effects, dramatically differs from the experimental one. Even if one makes liberal allowance for (possibly) inaccurate parametrization, the resultant electroabsorption amplitude is much lower than observed; moreover, the shape of the calculated spectrum bears no visual resemblance to the experimental spectrum. This rules out the possibility that the polariton effects alone could explain the *b*-polarized absorption and electroabsorption spectra of the T6 crystal.

The sexithiophene EA spectrum is plausibly rationalized if charge transfer excitations are taken into account. In that case, quantitative reproduction of the experimental spectrum was achieved based on a well founded model Hamiltonian and parametrization [9]. The present results supplement those of Ref. [9] by suggesting that in this particular crystal the coincidence of some absorption features observed for different light polarizations may be accidental and misleading, with the c'-polarized spectrum dominated by Frenkel excitons strongly coupled to the radiation field and the CT states contributing in the *b* polarization practically at the same energy. It cannot be ruled out that some c'-polarized states of CT parentage, which only marginally contribute to the absorption spectrum since their weak absorption is masked by the intense Frenkel contribution, may be crucial for c'-polarized electroabsorption signal in the energy range between 2.5 eV and 3.2 eV. This would resemble the situation encountered, e.g., for polyacenes, where the sensitivity of the CT states to electric field compensates their weak optical absorption. At the present moment this issue cannot be finally settled, since for the relevant energy range no experimental c'-polarized EA spectrum of a sexithiophene single crystal is available in the literature; we hope that it will be measured in the future. Likewise, a comparative study of the spectra of other oligothiophenes might be instrumental in unraveling the coincidences mentioned above. Further theoretical work in this direction is underway and new experimental findings would be invaluable.

References

[1] V.M. Agranovich, Theory of Excitons, Nauka, Moscow, 1968 (in Russian).

[2] M.R. Philpott, Advances in chemical physics, Some modern aspects of exciton theory, 23, John-Wiley and Sons, 1973, pp. 227–339.

[3] S. Möller, G. Weiser, F. Garnier, Electric field effects on the Davydov components of a strong intramolecular transition: α-sexithiophene single crystals, Physical Review B 61 (23) (2000) 15749–15755.

[4] S. Möller, G. Weiser, Comparison of the optical spectra of single crystal and crystalline films of α-sexithiophene, Synthetic Metals 122 (1) (2001) 41–43.

[5] S. Möller, G. Weiser, C. Taliani, The role of electrodynamics in the spectra of organic crystals with mesoscopic order: nanocrystalline α-sexithiophene, Chemical Physics 295 (1) (2003) 11–20.

[6] G. Weiser, Polariton effects in π-conjugated molecular solids: single crystal and nanocrystaline films of sexithiophene, Synthetic Metals 139 (3) (2003) 719–722.

[7] L. Sebastian, G. Weiser, H. Bässler, Charge transfer transitions in solid tetracene and pentacene studied by electroabsorption, Chemical Physics 61 (1981) 125–135.

[8] L. Sebastian, G. Weiser, G. Peter, H. Bässler, Charge transfer transitions in crystalline anthracene and their role in photoconductivity, Chemical Physics 75 (1983) 103–114.

[9] M. Andrzejak, P. Petelenz, M. Slawik, R.W. Munn, Theoretical calculation of the electro-absorption spectrum of the α-sexithiophene single crystal, Journal of Chemical Physics 117 (3) (2002) 1328–1335.

[10] P. Petelenz, A. Stradomska, Theoretical interpretation of electro-absorption spectra for intense optical transitions, Physical Review B 71 (23) (2005) 235205.

[11] G. Horowitz, B. Bachet, A. Yassar, P. Lang, F. Demanze, J.-L. Fave, F. Garnier, Growth and characterization of sexithiophene single crystals, Chemistry of Materials 7 (1995) 1337–1341.

[12] T. Siegrist, R.M. Fleming, R.C. Haddon, R.A. Laudise, A.J. Lovinger, H.E. Katz, P. Bridenbaugh, D.D. Davis, The crystal structure of the high-temperature polymporph of α-sexithienyl (α–6T/HT), Journal of Materials Research 10 (9) (1995) 2170–2173.

[13] D.W.J. Cruickshank, A detailed refinement of the crystal and molecular structure of anthracene, Acta Crystallographica 9 (1956) 915–923.

[14] D.W.J. Cruickshank, A detailed refinement of the crystal and molecular structure of anthracene, Acta Crystallographica 10 (1957) 470–503.

[15] G. Weiser, S. Möller, Directional dispersion of the optical resonance of π–π^* transitions of α-sexithiophene single crystals, Physical Review B 65 (2002) 045203.

[16] M.A. Loi, C. Martin, H.R. Chandrasekhar, M. Chandrasekhar, W. Graupner, F. Garnier, A. Mura, G. Bongiovanni, Primary optical excitations and excited-state interaction energies in sexithiophene, Physical Review B 66 (2002) 113102.

[17] S. Möller, G. Weiser, F. Garnier, Absorption and electroabsorption spectra of an α-sexithiophene single crystal at 20 K, Synthetic Metals 116 (1–3) (2001) 305–309.

[18] P. Petelenz, M. Andrzejak, Vibronic interpretation of the low-energy absorption spectrum of the sexithiophene single crystal, Journal of Chemical Physics 113 (24) (2000) 11306–11314.

[19] M. Born, K. Huang, Dynamical Theory of Crystal Lattices, Clarendon Press, Oxford, 1954.

[20] R.W. Munn, M. Andrzejak, P. Petelenz, A. Degli Esposti, C. Taliani, Calculation of refractive indices and local electric field tensors in α-sexitiophene crystal, Chemical Physics Letters 336 (2001) 357–363.

Available online at www.sciencedirect.com
ScienceDirect
Organic Electronics 7 (2006) 561–567
Organic Electronics
www.elsevier.com/locate/orgel

Propagation properties and self-waveguided fluorescence emission in conjugated molecular solids

S. Tavazzi [a,*], P. Spearman [a,b], L. Silvestri [c], L. Raimondo [a], A. Camposeo [d], D. Pisignano [d]

[a] CNR-INFM and Dipartimento di Scienza dei Materiali, Università degli Studi di Milano Bicocca, Via Cozzi 53, I-20125 Milano, Italy
[b] School of Chemical and Pharmaceutical Sciences, Kingston University, Kingston upon Thames, KT1 2EE, United Kingdom
[c] Scuola Normale Superiore, Piazza dei Cavalieri 7, I-56100 Pisa, Italy
[d] National Nanotechnology Laboratory of CNR-INFM, Distretto Tecnologico ISUFI, Università di Lecce, via Arnesano, I-73100 Lecce, Italy

Received 1 February 2006; received in revised form 17 July 2006; accepted 15 August 2006
Available online 20 September 2006

Abstract

The propagation properties of the emitted light from oligothiophene crystals are discussed. The internal reflectivity at the interface between the crystal and an isotropic ambient medium has been derived, allowing to discuss the effect of self-waveguiding of the emission on the basis of the components of the material dielectric tensor.

PACS: 42.25.−p; 78.40.−q; 78.55−m

Keywords: Molecular solids; Internal reflection; Fluorescence; Self-waveguiding

1. Introduction

Over recent years, organic semiconductors have been studied as possible substitutes to inorganic materials for the wide range of applications in micro- and opto-electronic devices. The abundant choice of starting organic materials and possible chemical substitutions allow tuning of their properties in the solid state. By such means, organic light emitting diodes [1] and organic solid-state lasers [2,3] have the potential to provide light over a broad range of wavelengths throughout the visible and the near infrared range and to replace inorganic ones for a wide variety of uses, such as illumination [4], memories [5], and excitation sources for bio-diagnostics [6]. Both amorphous and crystalline organic semiconductors can be effectively employed for realizing devices with relatively low cost on a variety of substrates, including flexible plastic sheets [5] by soft processing and lithography methods [7]. In particular, the feedback effect, which is required for achieving lasing action from compounds providing stimulated emission, could be accomplished by several different geometries [8–15].

Among conjugated molecules in their crystalline phase, amplified spontaneous emission and stimulated

* Corresponding author. Tel.: +39 02 64485012; fax: +39 02 64485400.
E-mail address: silvia.tavazzi@mater.unimib.it (S. Tavazzi).

1566-1199/$ - see front matter
doi:10.1016/j.orgel.2006.08.003

emission have been reported for octithiophene [16] and sexithiophene [17] crystals with the relevant result that emitted radiation has been observed in a cone oriented normal to the main molecular transition dipole in the crystal plane itself. Other authors recently observed stimulated emission at the edge of the crystal without emission from inside at all in polycrystalline phases of other conjugated molecules [18], similarly as reported for needle-shaped crystals of sexiphenyl grown on top of potassium chloride substrates [19,20]. The relevance of the crystal and molecular structures and crystal quality is chiefly responsible for these peculiar observations. In fact, these systems exploit the natural packing of the molecules that provoke collective excitonic emission to predominate rather than utilising and optimising the isolated molecular emission in a non-interacting system. In such interacting aggregates, the emission can be concentrated into only one or two replicas, which in some cases can even lead to super-radiant emission [21,22], and counters against any destructive interference between one and two-particle emissions that leads to a reduction of their intensities compared to the corresponding isolated molecular emissions [23]. However, the advantages of organic materials are not yet fully exploited. The following experimental results and the requirement of an interpretation based on a comparison with theoretical modelling indicate the importance of studying single crystals and films with controlled structural and morphological properties.

In this paper, we discuss the propagation of the emitted light in quaterthiophene single crystals and the effect of self-waveguiding after deriving and simulating the internal reflectivity at the interface with an isotropic medium. Quaterthiophene is taken as a prototype system with molecules aligned parallel to each other in a direction almost perpendicular to the crystal face.

2. Experimental

Oligothiophenes (nT) were synthesized according to standard procedures. Single crystals were grown as thin flakes with monoclinic crystallographic structure following the procedure reported in Ref. [24]. Since different names can be found in the literature for the axes of the unit cell, for the sake of clarity we denote the monoclinic axis as *b* axis and the longest axis as *c* axis for all the crystals of the oligothiophene family. The accessible face for optical measurements is along the *ab* plane. The sample thickness ranges from few hundreds of nm to few μm as measured by a Digital Instruments Nanoscope IIIa MMAFM equipped with a J-type scanner and a Digital Instrument Dektak 8 profiler. Prior to optical measurements, single crystals were selected by homogeneously extinguishing light under crossed polariser and analyser. Indeed, when light is impinging at normal incidence and is either *a* or *b* linearly polarized, the transmitted light by a single crystal maintains its polarization since *b* is a principal axis of the dielectric tensor and *a* lies in the *ac* principal plane [25].

Images of the sample have been taken with an optical microscope Olympus SZX12. In addition, fluorescence micrographs of the printed patterns were collected by a Leica fluorescence inverted microscope fitted with a monochrome camera AxioCam MR (Zeiss). Fig. 1 shows an image of a 4T crystal under the optical microscope either in fron-

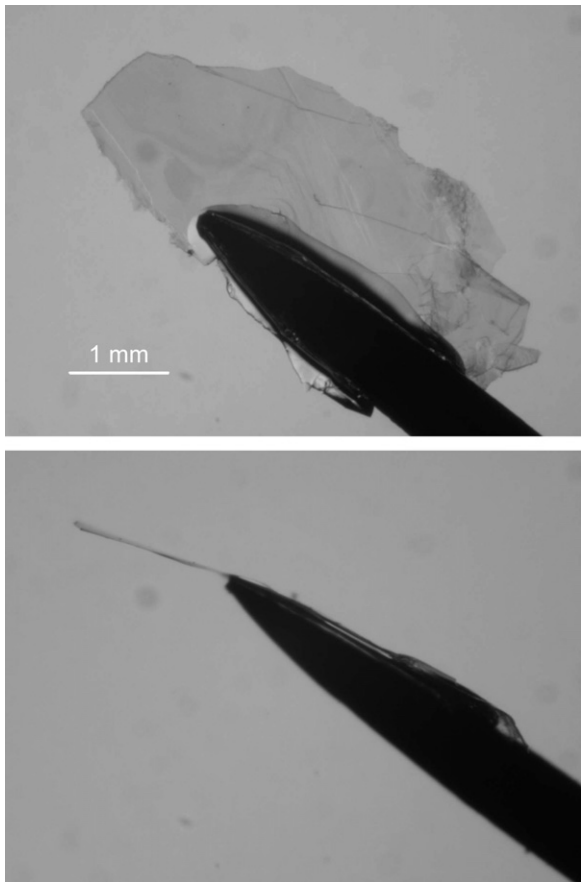

Fig. 1. Images of 4T single crystal (a few hundred nanometers thick) under the optical microscope.

tal (a) or lateral (b) view. This image shows the typical growth mode as thin flakes of olighothiophene crystals.

Photoluminescence emission (PL) measurements were performed at room temperature with a home made apparatus equipped with a nitrogen cooled charge-coupled-device detector and a Xe lamp as excitation source. The spectra were corrected for the instrument spectral response.

3. Results and discussion

Resonance interactions in oligothiophene solids are known to split the lowest singlet molecular transition into two optically accessible transitions of a_u and b_u symmetry with dipole moments parallel and perpendicular to the monoclinic b axis, respectively [26]. The direction L of the stronger transition moment to the b_u state lies in the ac plane at an angle α to the normal c^* axis to the ab face and in the case of 4T α is about 27°. As far as the emission at temperature $T = 0$ K is concerned, a model has been proposed recently [21] for oligothiophenes which considers the origin of the luminescence from the bottom of the a_u band. The resulting emission is b polarised and can be clearly detected at low temperature [22]. The 0–0 line is predominantly b polarised and is very sensitive to structural defects since they interrupt the coherence, which scales with the number of molecules contributing to the exciton. On the contrary, the room temperature spectrum is mainly ac polarized and dominated by broad vibronic replicas and only a very weak 0–0 line strength as shown in Fig. 2 for single crystals of several members of the oligothiophene family.

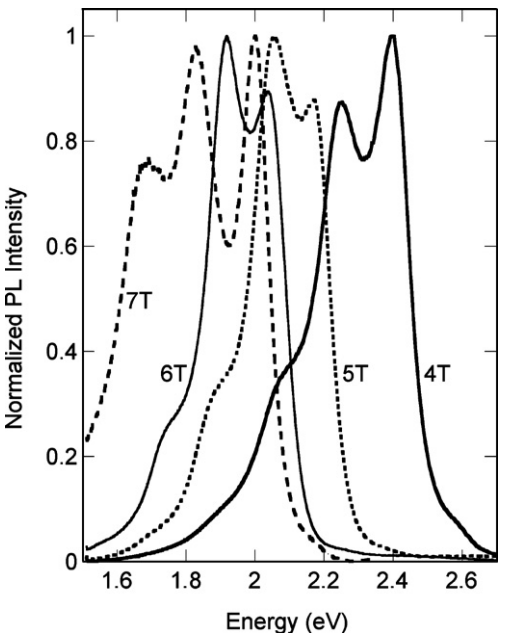

Fig. 2. Photoluminescence spectra of 4T, 5T, 6T, and 7T single crystals as measured at room temperature with 3.5 eV excitation energy.

The observation of the emitted light at room temperature at the edge of the crystal without emission from inside at all, as reported by several authors in the literature [16,17], confirms its ac polarization. By contrast, b polarized light propagates inside the crystal in the ac plane (i.e., perpendicularly to the corresponding transition moment). The propagation of light is transverse since b is a principal axis of the dielectric tensor [25] and it is described by the ordinary refractive index $\hat{n}_b(\omega) = \sqrt{\hat{\varepsilon}_{bb}(\omega)}$ where $\hat{\varepsilon}_{bb}(\omega)$ is one of the components of the dielectric tensor. For 4T, the complex dielectric tensor has recently been reported [27]. In the coordinate system given by the a, b, and c^* axes of 4T, it can be written as

$$\varepsilon(\omega) = \begin{bmatrix} \hat{\varepsilon}_{aa}(\omega) & 0 & \hat{\varepsilon}_{ac^*}(\omega) \\ 0 & \hat{\varepsilon}_{bb}(\omega) & 0 \\ \hat{\varepsilon}_{ac^*}(\omega) & 0 & \hat{\varepsilon}_{c^*c^*}(\omega) \end{bmatrix}, \quad (1)$$

and its components are reported in Fig. 3. The real part of $\hat{n}_b(\omega)$ varies between about 1.5 and 1.6 for energies below 2.5 eV where the room temperature emission of 4T is found. From Snell's law, the limit angle θ_{lim} for total internal reflection at the crystal/air interface is about 40°, which implies that b polarized light emitted at an angle to the surface normal lower than θ_{lim} is expected to be transmitted through the crystal/air interface and hence it should be observed emitting from the surface of the 4T crystal plate. This can be calculated considering that the wave vector is obtained by solving Fresnel's equation [28]:

$$\hat{k}^2 = (\omega/c)^2 \hat{n}_b^2, \quad (2)$$

with the assumption that the projection k_a of the wave-normal vector $\hat{k}$ along the a 4T axis on the surface is real. Transmitted and reflected waves are found by imposing standard boundary conditions at the surface and the reflectivity calculated as the ratio of the time averaged reflected energy flux to the incident flux. Each flux is given by the averaged component normal to the surface (i.e., along the c^* axis of 4T) of the corresponding Poynting vector, i.e., by $S_{c^*} = \text{Re}\left[\frac{c}{4\pi} E \times H^*\right]_{c^*}$ [29]. We note that

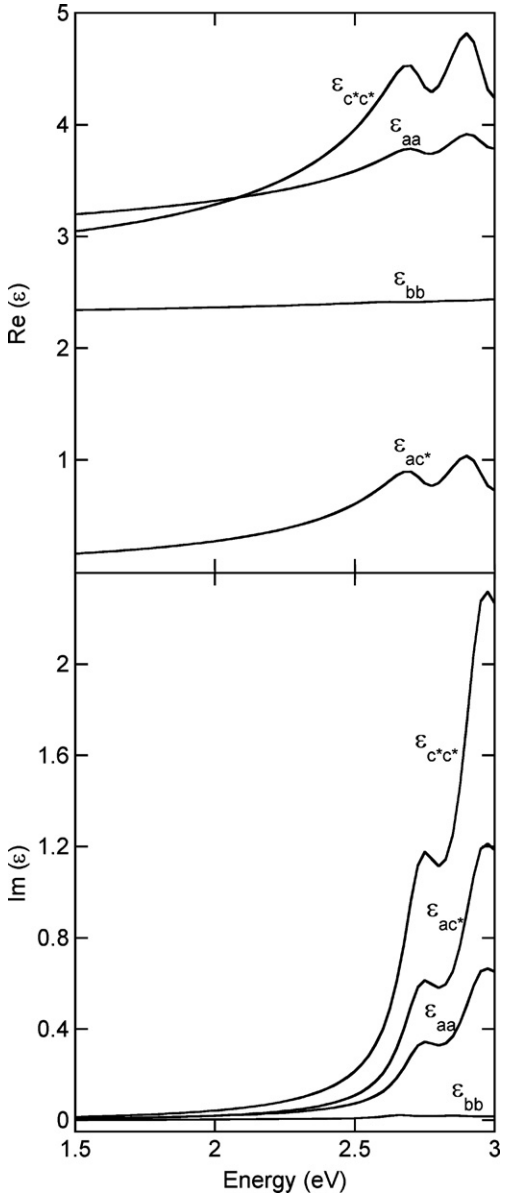

Fig. 3. Real (a) and imaginary (b) parts of the components of the 4T complex dielectric tensor (1) with respect to the coordinate system given by the a, b, and c^* axes of 4T, as reported in Ref. [27].

since the plane of incidence is a principal plane for the b polarization, there is a single reflected wave, which is ordinary and b polarised [25].

We now consider the emitted light polarized in the ac plane along L. The perpendicular to the planes of constant phase of the emitted light is along the real part of the wave-normal vector $\hat{k}$ and represents the direction of light propagation [28,30]. It lies in a plane perpendicular to the direction L of the transition moment L as sketched in Fig. 4: α is the inclination of the transition moment L to the surface normal, β is the dihedral angle between the plane ac and the plane of incidence, the latter being formed by the surface normal and the direction of propagation of the emitted light inside the crystal ($\beta = 0°$ corresponds to ac as plane of incidence). The angle of incidence on the crystal/air interface (angle between $\mathrm{Re}(\hat{k})$ and the surface normal) can be deduced from geometrical considerations; it is given by

$$\eta(\beta) = \arccos\left[-\frac{\sin(\alpha)\cdot\cos(\beta)}{\sqrt{\cos^2(\alpha)+\cos^2(\beta)\sin^2(\alpha)}}\right], \quad (3)$$

and its value is reported in Fig. 5 as a function of β.

In this context, we only consider $\hat{k}$ in the ac principal plane ($\beta = 0°$) and we demonstrate that emitted light is totally internally reflected at the crystal surface. Even if a complete description would require the calculation of the reflectivity for all the angles β, we underline that $\beta = 0°$ is a particularly relevant case since for increasing β the angle η of incidence on the interface increases, thus making the total internal reflection more probable. A definitive analysis of the light propagation for other directions of propagation becomes more complex since the plane of incidence onto the crystal/air interface is no longer a principal plane and a mixing

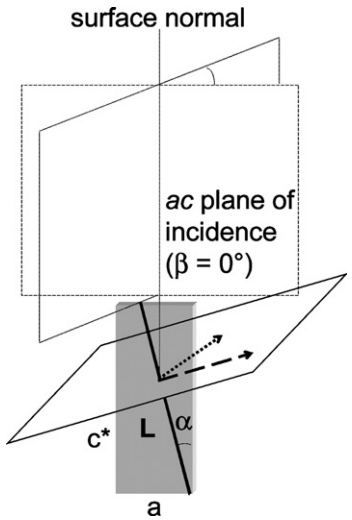

Fig. 4. Sketch of the oligothiophene unit cell, of the direction L of the transition moment, and of the wave-normal vector k of the emitted light impinging on the crystal/air interface.

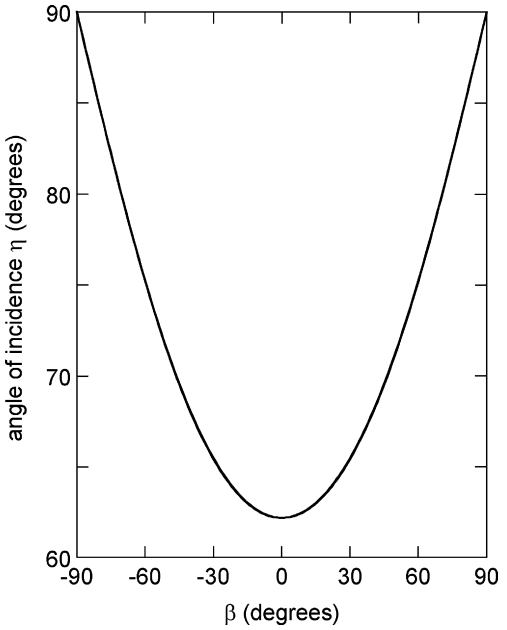

Fig. 5. Angle of incidence on the crystal/air interface calculated using Eq. (3) for the L polarized emitted light and for the different planes of incidence indicated by β.

of the p and s polarized waves occurs after internal reflection.

The procedure we use is similar to the one described previously for b polarised waves: we assume that k_a is real and find the corresponding $\hat{k}_{c^*}$ by solving Fresnel's equation, which for ac polarisation reads

$$\varepsilon_{c^*c^*}\hat{k}_{c^*}^2 + 2\varepsilon_{ac^*}k_a\hat{k}_{c^*} + \varepsilon_{aa}k_a^2 + (\omega/c)^2\varepsilon_{ac^*}^2 - (\omega/c)^2\varepsilon_{aa}\varepsilon_{c^*c^*} = 0, \quad (4)$$

where ε_{aa}, $\varepsilon_{c^*c^*}$, ε_{ac^*} are the components of the dielectric tensor reported in Fig. 3 in the coordinate system given by the a, b, c^* axes of 4T [28]. By choosing an appropriate value of k_a we are able to obtain the desired direction of propagation. Considering that we are far from the region of absorption and that the direction of propagation of the incident wave lies in the corresponding principal plane orthogonal to L, the incident wave can be considered as an ordinary wave, even if we have assumed a real k_a. Once the incident wave vector and polarisation are known, we can compute the reflectivity. As with the b polarised wave case, there is only one ac polarised reflected wave since there is no mixing between s and p polarized waves after reflection. However, the reflected wave does not propagate in the principal plane for the ac polarization and it is therefore extraordinary. Fig. 6 shows the calculated reflectivity as a function of energy at the 4T interface. For $n_{amb} = 1$, the emitted light propagating in the ac plane is totally reflected at the crystal/air interface in the whole energy range and self-waveguided along the plates.

This result has to be compared with the conclusions of a previous work where we discussed the directional dispersion observed in p polarized absorption spectra of 4T taken with ac as plane of incidence for incident light travelling in air [28,31]. We found that by varying the angle of incidence a fraction of the directional dispersion can be probed between the transverse ω_T and longitudinal ω_L angular frequencies of the L polarized transition. In the limiting case of purely transverse excitation of the optical transitions, a band centred at the transverse frequency ω_T in absorption and the typical stopping band between ω_T and ω_L is expected. However, transverse propagation of the light inside the crystal cannot be achieved due to intrinsic limits of the refraction at the air/4T interface. Also for energies below $\hbar\omega_T$, the spectral range of interest for the emission, the transverse propagation of light (with the electric field along L) is not achievable as a consequence of refraction at the air/crystal

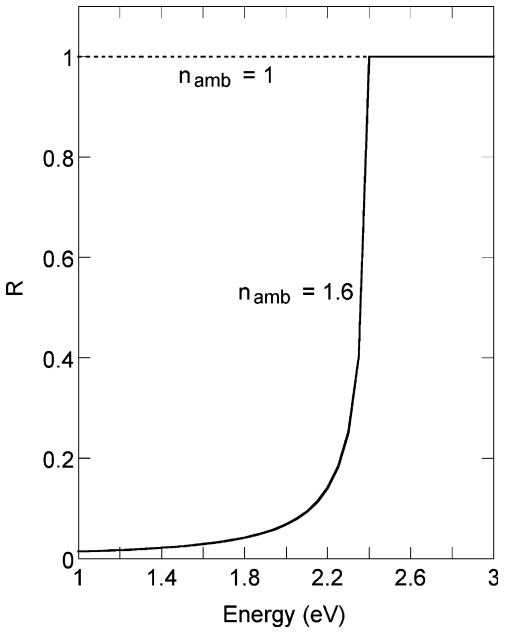

Fig. 6. Reflectivity of the crystal interface with an isotropic medium with refractive index n_{amb} calculated as described in the text for L polarized emitted light and considering ac as plane of incidence.

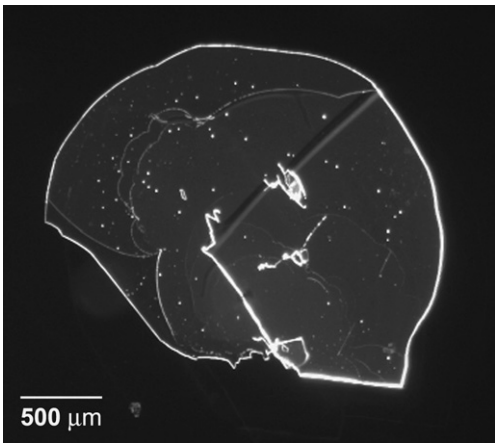

Fig. 7. Image of a few hundreds nm thick 4T crystal taken with a fluorescence microscope.

interface. In a complementary way, total internal reflection at the 4T/air interface of the emitted light which is polarized along L is another aspect of the same phenomenon, namely the light is unable to escape across the crystal/air interface. If the transverse component was accessible then due to the reversibility of the light path across an interface the emission would also be able to escape.

Similarly as for $n_{amb} = 1$, we have also calculated the internal reflectivity at the crystal interface with an isotropic medium with refractive index $n_{amb} = 1.6$, shown in Fig. 6. In this case, a fraction of the emitted light is transmitted through the interface and light is expected to emerge from the top of the crystal plate.

Finally, in our crystals another outcoupling path can occur, as light is expected to be transmitted through the surface when defects (such as stacking faults) are present, which can influence the light propagation. These can be seen as the bright points or striations in Fig. 7 which shows the image of a few hundreds nm thick 4T crystal taken with a fluorescence microscope.

4. Conclusions

The propagation of the emitted light in quaterthiophene crystals has been described on the basis of the material dielectric tensor. Fluorescence polarized in the *ac* plane has been found to be self-waveguided along the plates. In the framework of organic lasers, and especially distributed feedback devices, combining both stimulated emission and waveguiding along the crystal slab is crucial for achieving an effective laser action. The line-narrowing, resulting from amplified spontaneous emission assisted by the waveguiding effect, is indeed an important prerequisite for lasing.

The effect is strongly affected when the crystal is in contact with high refractive index media. In particular, the outcoupling of guided modes providing laser emission can be accomplished by the subsequent engraving of periodic gratings by means of lithographic processes. The resulting periodic variation of the effective refractive index can induce Bragg scattering along the crystal slab. The variation of the external refractive index or the lithographically-induced tuning of the effective refractive index along the slab directly affect the waveguiding/outcoupling relative efficiency. We believe therefore that structuring optical gain organic crystals is a promising candidate route for the realization of efficient organic semiconductor lasers.

Since the waveguiding effect is also strongly affected when defects are present, the analysis of the emitted light from the crystal can be also exploited in a sensor to reveal substances with high enough refractive index, as a probe to study the contact between the crystal and another medium, independently of the excitation process, which may be by electrical or optical pumping, in the latter case independent of the energy, polarization, and direction of the excitation source.

Acknowledgements

We are pleased to thank S. Trabattoni and A. Papagni for the 4T synthesis and purification, M. Campione and M. Moret for the crystal growth, and A. Borghesi for assistance.

References

[1] R.H. Friend, R.W. Gymer, A.B. Holmes, J.H. Burroughes, R.N. Marks, C. Taliani, D.D.C. Bradley, D.A. Dos Santos, J.L. Brédas, M. Lögdlund, W.R. Salaneck, Nature 397 (2000) 121.
[2] N. Tessler, Adv. Mater. 11 (1999) 363.
[3] M.D. McGehee, A.J. Heeger, Adv. Mater. 12 (2000) 1655.
[4] Organic Light Emitting Diodes (OLEDs) for General Illumination Update 2002, ed. by M. Stolka, An OIDA Technological Roadmap, 2002. Available from: <http://www.netl.doe.gov/ssl/publications.html>.
[5] L.P. Ma, J. Liu, Y. Yang, Appl. Phys. Lett. 80 (2002) 2997.
[6] D. Schneider, T. Rabe, T. Riedl, T. Dobbertin, M. Kröger, E. Becker, H.-H. Johannes, W. Kowalsky, T. Weimann, J.

Wang, P. Hinze, A. Gerhard, P. Stössel, H. Vestweber, Adv. Mater. 17 (2005) 31.
[7] E. Mele, F. Di Benedetto, L. Persano, R. Cingolani, D. Pisignano, Nano Lett. 5 (2005) 1915.
[8] D. Pisignano, M. Anni, G. Gigli, R. Cingolani, M. Zavelani-Rossi, G. Lanzani, G. Barbarella, L. Favaretto, Appl. Phys. Lett. 81 (2002) 3534.
[9] T. Virgili, D.G. Lidzey, D.D.C. Bradley, G. Cerullo, S. Stagira, S. De Silvestri, Appl. Phys. Lett. 74 (1999) 2767.
[10] T. Granlund, M. Theander, M. Berggren, M. Andersson, A. Ruzeckas, V. Sundstrom, G. Björk, M. Granström, O. Inganäs, Chem. Phys. Lett. 288 (2000) 879.
[11] M. Bergreen, A. Dodabalapur, R.E. Slusher, Appl. Phys. Lett. 71 (1997) 2230.
[12] J.M. Lupton, B.J. Matterson, I.D.W. Samuel, M.J. Jory, W.L. Barnes, Appl. Phys. Lett. 77 (2000) 3340.
[13] M. Bergreen, A. Dodabalapur, R.E. Slusher, A. Timko, O. Nalamasu, Appl. Phys. Lett. 72 (1998) 410.
[14] S. Riechel, C. Kallinger, U. Lemmer, J. Feldmann, A. Gombert, V. Wittwer, U. Scherf, Appl. Phys. Lett. 77 (2000) 2310.
[15] B.J. Scott, G. Wirnsberger, M.D. McGehee, B.F. Chmelka, G.D. Stucky, Adv. Mater. 13 (2001) 1231.
[16] D. Fichou, S. Delysse, J.M. Nunzi, Adv. Mat. 9 (1997) 1179.
[17] G. Horowitz, Opt. Mater. 9 (1998) 46.
[18] M. Ichikawa, R. Hibino, M. Inoue, T. Haritani, S. Hotta, T. Koyama, Y. Taniguchi, Adv. Mat. 15 (2003) 213.
[19] H. Yanagi, T. Morikawa, Appl. Phys. Lett. 75 (1999) 187.
[20] H. Yanagi, T. Ohara, T. Morikawa, Adv. Mat. 13 (2001) 1452.
[21] F.C. Spano, J. Chem. Phys. 118 (2003) 981.
[22] F. Meinardi, M. Cerminara, A. Sassella, A. Borghesi, P. Spearman, G. Bongiovanni, A. Mura, R. Tubino, Phys. Rev. Lett. 89 (2002) 157403.
[23] F.C. Spano, J. Chem. Phys. 120 (2004) 7643.
[24] M. Campione, R. Ruggerone, S. Tavazzi, M. Moret, J. Mater. Chem. 15 (2005) 2437.
[25] S. Tavazzi, A. Borghesi, M. Laicini, P. Spearman, J. Chem. Phys. 121 (2004) 8542.
[26] A.S. Davydov, Theory of Molecular Excitons, Plenum Press (1971).
[27] M. Laicini, P. Spearman, S. Tavazzi, A. Borghesi, Phys. Rev. B 71 (2005) 045212.
[28] P. Spearman, A. Borghesi, M. Campione, M. Laicini, M. Moret, S. Tavazzi, J. Chem. Phys. 122 (2005) 014706.
[29] M. Born, E. Wolf, Principles of Optics, Pergamon Press, 1965.
[30] L.P. Mosteller, F. Wooten, J. Opt. Soc. Am. 58 (1968) 511.
[31] L. Raimondo, A. Borghesi, M. Laicini, S. Tavazzi, P. Spearman, J. Chem. Phys. 122 (2005) 064706.

Available online at www.sciencedirect.com
ScienceDirect
Organic Electronics 7 (2006) 568–575
Organic Electronics
www.elsevier.com/locate/orgel

Copper hexafluorophthalocyanine field-effect transistors with enhanced mobility by soft contact lamination

Mang-Mang Ling, Zhenan Bao *

Department of Chemical Engineering, 381 North-south Mall, Stanford University, Stanford, CA 94305, United States

Received 7 July 2006; received in revised form 30 August 2006; accepted 21 September 2006
Available online 18 October 2006

Abstract

We report enhanced field-effect mobility of hexafluoro-copper phthalocyanine (F_{16}CuPc) transistors made by soft contact lamination. In this way, the damage to organic semiconductor during conventional vacuum deposition of metal electrodes can be avoided. The injection of charge carrier from metal electrodes into semiconductor layer can be improved. Combined with surface chemical treatment of the dielectric layer, an enhanced charge carrier mobility, ca. 0.08 cm^2/Vs for F_{16}CuPc devices is achieved, higher than the typical value of 0.03 cm^2/Vs for devices made by direct metal deposition methods.

Keywords: Organic transistor; Soft lamination; n-Channel; Mobility

1. Introduction

Driven by the need of organic complementary metal-oxide (CMOS), much progress has been made to obtain high performance n-channel organic semiconductors, including C_{60} and its derivatives [1–5], copper hexafluoro phthalocyanine (F_{16}CuPc), [6,7] perylene and its derivatives [8–12], oligothiophene and its derivatives [13,14]. By far F_{16}CuPc is among the most widely used n-channel materials due to its relatively high mobility (i.e., 0.03 cm^2/Vs), superb air stability, and readily commercially available. A top-contact device configuration is typically used to fabricate thin film transistors, in which the source/drain metal electrodes are deposited by vacuum evaporation through a shadow mask. However, the evaporated metal could diffuse into the organic semiconductor as well as cause chemical degradation to the organic material resulting in a higher contact resistance [15–21]. Therefore, the overall device performance may be compromised, hindering the potential for high operating speed for organic CMOS circuitry. Although bottom contact configuration may avoid the above problems, such devices generally have inferior performance than top contact devices due to poor morphology of organic semiconductors grown on the rough surface of electrodes [22,23]. Soft contact lamination technique thus becomes the best choice [24–30]. In this approach, source and drain metal electrodes are first formed on an elastomeric substrate, such as polydimethylsiloxane (PDMS). The devices were completed by the conformal contact of such

* Corresponding author. Tel.: +1 650 723 2419.
E-mail address: zbao@stanford.edu (Z. Bao).

1566-1199/$ - see front matter
doi:10.1016/j.orgel.2006.09.003

electrodes with the substrate which already has a gate electrode, a dielectric layer and a semiconductor layer. Combined with other device improvement procedures such as multiple purifications of the organic semiconductor and surface chemical treatment of the substrates, we demonstrated that the device performance for the n-channel $F_{16}CuPc$ transistor can be further improved.

2. Experimental

$F_{16}CuPc$ was purchased from Aldrich Inc. The purification was carried out by three consecutive vacuum sublimations using a three-temperature-zone furnace (Lindberg/Blue Thermo Electron Corporation). The three temperature zones were set to be 320 °C, 295 °C and 200 °C and the vacuum level during sublimation was 10^{-6} Torr or less while the starting material was placed in the first temperature zone. Highly doped n-type Si (100) wafers (<0.004 Ω-cm) with a thermally grown dry oxide layer (capacitance per unit area $C_i = 10$ nF/cm^2) as gate dielectric were used as substrates. After the substrates were cleaned with acetone and followed by isopropyl alcohol (IPA), they were further treated with *n*-octadecyl triethoxysilane [$C_{18}H_{37}Si(OC_2H_5)_3$, OTS, obtained from Aldrich Chem. Co.]. Details for the OTS treatment are as follows: a drop of pure OTS was loaded on top of a preheated glass plate (~100 °C) inside a reactor. The reactor was immediately evacuated for 1 min (~25 mmHg) then the valve to vacuum was closed. The SiO_2/Si substrates were left in the reactor heated to 110 °C for at least five hours to give a hydrophobic surface. Finally, the substrates were baked at 110 °C for 15 min, rinsed with isopropanol and dried with a stream of air. As shown in Fig. 1a, $F_{16}CuPc$ thin films (45 nm thickness) were vacuum-deposited on Si/SiO_2 substrates through a shadow mask (7 mm × 20 mm) at elevated temperature of 125 °C with a deposition rate of 1.0 Å/s at 10^{-6} Torr.

Top-contact devices with soft contact laminated electrodes were fabricated as follows: first, gold

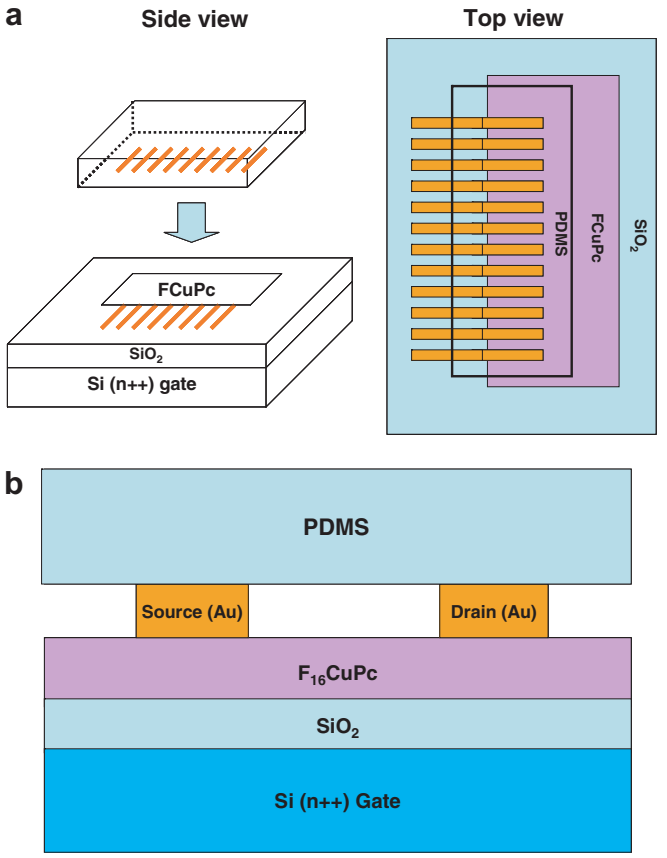

Fig. 1. (a) Soft contact lamination for $F_{16}CuPc$ TFTs and (b) top-contact configuration for the laminated $F_{16}CuPc$ TFTs.

contact electrodes (40 nm thickness) were deposited onto the substrate besides the organic semiconductor films through a shadow mask (channel width/length = 4000 μm/200 μm) to match the drain and source electrodes on PDMS stamp. Separately, source and drain gold electrodes (40 nm thickness) were deposited on a PDMS elastomeric substrate using the same drain/source shadow mask. Secondly, the devices were completed by placing such electrodes on PDMS onto a substrate with a gate electrode, a dielectric layer and the semiconductor layer as shown in Fig. 1a. Note that portions of the source/drain electrodes were intentionally left uncovered by the PDMS stamp in order to leave enough room for probing during the electrical tests. The top contact configuration is thus achieved, as shown in Fig. 1b. In addition to gold, other metals such as silver, aluminum and ruthenium are also tested as the soft contact electrodes. Both silver and aluminum electrodes were deposited by thermal evaporation while ruthenium was deposited by sputtering.

3. Results and discussion

The electrical characteristics of OTFT devices were measured using a Keithley 4200-SCS semiconductor parameter analyzer. Key device parameters, such as charge carrier mobility (μ), on/off current ratio (I_{on}/I_{off}) and the threshold voltage (V_{th}), were extracted from the drain–source current (I_{ds})–gate voltage (V_g) characteristics. Typical current–voltage characteristics of $F_{16}CuPc$ TFTs with Au electrodes made by both soft contact lamination and

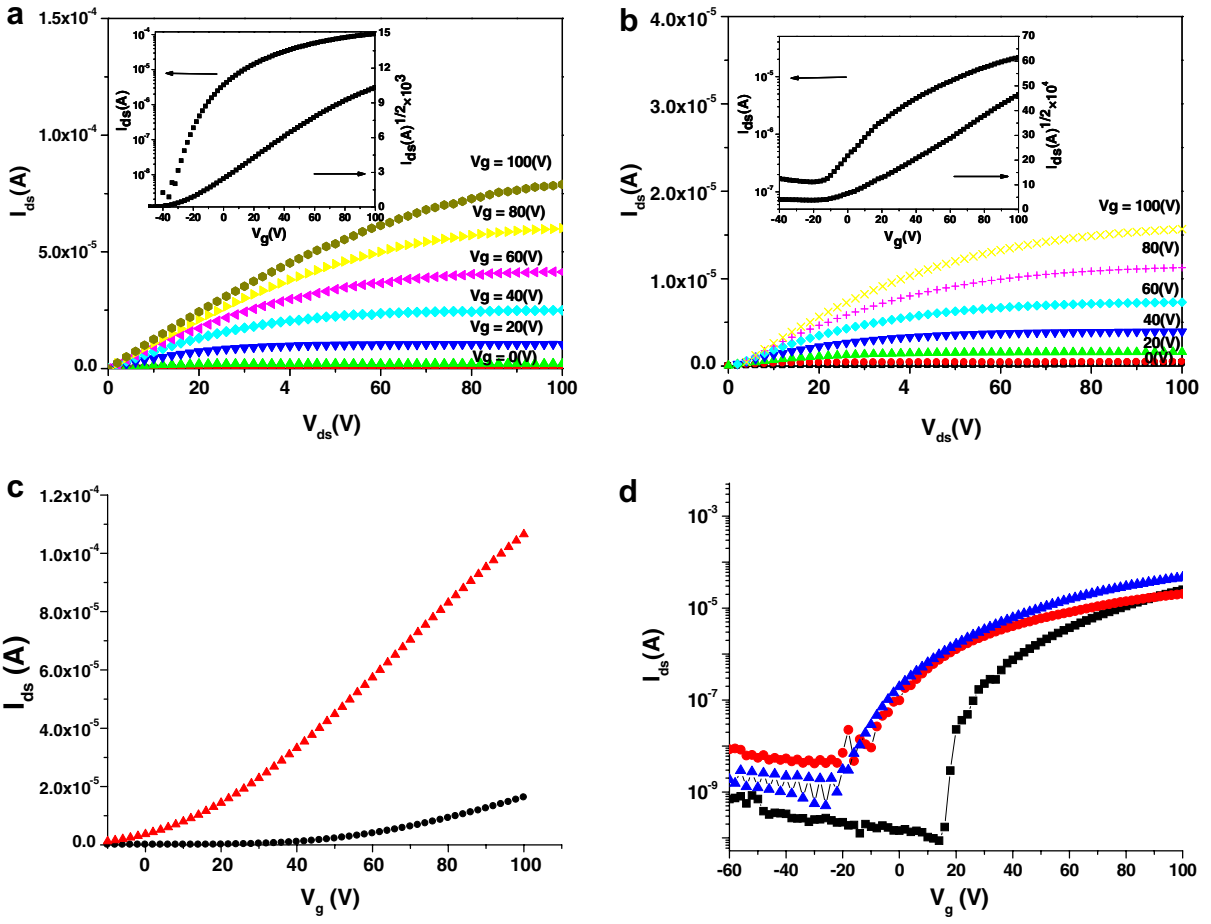

Fig. 2. Current–voltage characteristics ($I_{ds} - V_{ds}$ for various V_g) of $F_{16}CuPc$ (deposited at substrate temperature of 125 °C) TFT devices with Au electrodes made by (a) soft contact lamination and (b) conventional evaporation methods. Inset: $I_{ds} - V_g$ for $V_{ds} = 100$ V. (c) Comparison of the current–voltage characteristics of $F_{16}CuPc$ TFTs made by both soft contact lamination (triangle) and conventional way (solid dot). (d) Comparison of the current–voltage characteristics of $F_{16}CuPc$ TFTs made by soft contact lamination using various metal electrodes : aluminum (square), silver (circle) and ruthenium (triangle).

conventional methods are shown in Fig. 2a and b, respectively. It can be seen that the general features of IV curves for devices made by both lamination and conventional methods are similar. After averaging over forty devices, the averaged mobility achieved is 0.08 cm^2/Vs (standard deviation of 0.0046 cm^2/Vs), the on/off ratio is about 10^5, and the threshold voltage is about −23 V. The mobility obtained this way is close to three times that of the typical value of F_{16}CuPc TFTs (i.e., 0.03 cm^2/Vs averaged over forty devices, standard deviation of 0.0036 cm^2/Vs) made by conventional top-contact method. It is also higher than the previously reported results for soft contact lamination [26].

The device statistics can be seen in Fig. 3a and b. For comparison, as shown in Fig. 2(c), the source and drain current I_{ds} is plotted as a function of the gate voltage (V_g) for both the laminated device and the device made by conventional top-contact method. Mobility, on/off ratio and threshold voltage for different substrate temperatures during thin film deposition are summarized in Table 1a for soft contact lamination using gold electrodes. It can be seen that, for F_{16}CuPc films deposited at room temperature, the improvement of charge carrier mobility is only marginal: mobility increased from 0.0045 cm^2/Vs to 0.0056 cm^2/Vs. The on/off ratios are 4.4×10^4 and 1.2×10^5 for lamination and conventional methods, respectively. The corresponding threshold voltages are 29.4 V and 34.2 V, respectively. For elevated substrate temperature of 125 °C, the mobility increased from about 0.03 cm^2/Vs to 0.08 cm^2/Vs. The on/off ratios are 3.5×10^5 and 3.3×10^5 for lamination and conventional methods, respectively. The corresponding threshold voltages are −23 V and 21 V, respectively. It is unclear why the threshold voltages of the laminated devices prepared with F_{16}CuPc deposited at this temperature were much more negative than the others. The value quoted here is averaged over forty devices with a standard deviation of 5.21 V. It has been reported that electron traps of hydroxyl OH groups can cause the shift of threshold voltage V_{th} [31]. Also structural and chemical imperfections in the semiconductor can produce deep traps and therefore shift V_{th} [32]. Organic thin film morphology and dipole from self-assembled monolayer (SAM) can also affect V_{th} [33]. In our case, it is unclear exactly what mechanism plays a major role. It could be possible that lamination procedure itself would somehow introduce charge traps at the metal/organic interface and therefore cause the shift of V_{th}. For example, the different degree of diffusion of metal into organic layer for both lamination and conventional lamination methods might cause different interface barrier [34] and therefore different threshold voltage for the devices.

It was also suggested by Horowitz et al. that the conventional method of calculating threshold voltage may not be accurate for devices with significant contact resistance, which is typically the case for organic transistors. They suggested extracting threshold voltage using the transconductance change (TC) method [35] by plotting the second derivative of the drain current as a function of gate voltage V_g in the linear region at low applied source/drain voltage V_{ds} [36]. V_{th} is then given by the corresponding V_g for the peak position of the curve. Since TC method is insensitive to contact resistance, the threshold voltages obtained this way are more reliable. We also calculated V_{th} using this method. In most cases, V_{th} obtained by TC method are smaller compared to previous results. The averaged threshold voltage for laminated and evaporated Au electrode are about 14 V and 18 V, respectively, comparing to −23 V and 21 V using extrapolation method. This indicates that the difference in threshold voltage calculated using previous method may be a result of the large difference in the contact resistance, which is indeed the case as discussed below.

In soft contact lamination process, the bonding between the metal electrodes and organic semiconductor is in the form of van der Waals forces [24]. Therefore, damages to the semiconductor due to pressure and heat can be avoided. The improved quality of the devices made by soft contact lamination can be directly seen in the lower contact resistance. In our case, the estimated contact resistance is about $3.68 \times 10^5\ \Omega$ for laminated devices, less than devices made by conventional method (ca. $1.091 \times 10^6\ \Omega$), indicating improved contact between metal electrodes and organic semiconductor layer using soft contact lamination method. The contact resistance was extrapolated from the plot of resistance versus channel length (see Fig. 3c) [37].

Various other metals were also used as soft contacts in order to investigate the effect of metal work function. Metals such as silver, aluminum and calcium have lower work functions (4.7 eV, 4.1 eV and 2.9 eV, respectively) compared to gold, which should lead to better alignment against the LUMO level (4.4 eV) of F_{16}CuPc [38,39]. Thus, one would potentially be able to achieve better

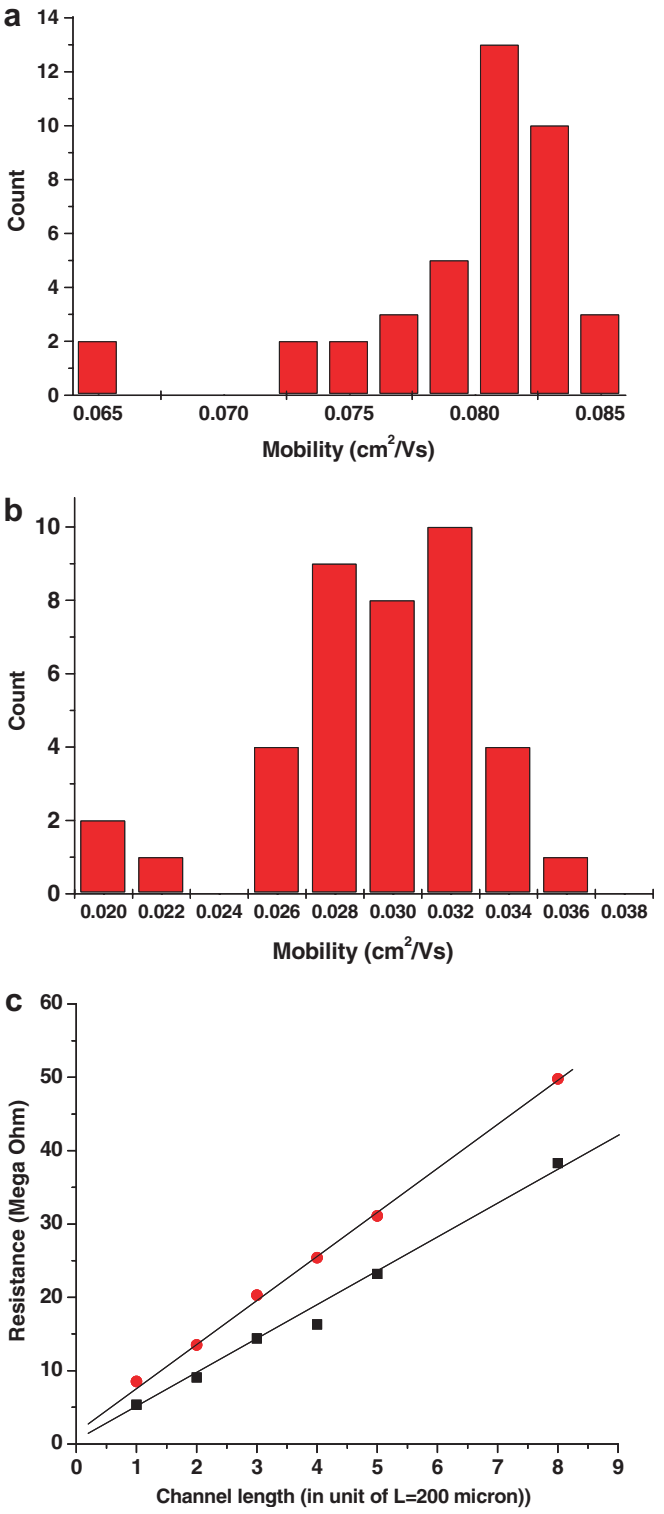

Fig. 3. The mobility distributions of $F_{16}CuPc$ (deposited at substrate temperature of 125 °C) devices gold electrodes by: (a) soft contact lamination; (b) conventional evaporation method; and (c) the extrapolation of contact resistance for both lamination method (square) and conventional evaporation method (circle).

Table 1a
Mobility, on/off ratio and threshold voltage for laminated $F_{16}CuPc$ TFTs using gold electrodes for different substrate temperatures during thin film deposition

S/D electrode	25 °C		125 °C	
	Laminated	Direct evaporation	Laminated	Direct evaporation
Au				
Mobility (cm^2/Vs)	4.5×10^{-3}	5.6×10^{-3}	0.082	0.030
On/off ratio	4.4×10^{4}	1.2×10^{5}	3.5×10^{5}	3.3×10^{5}
V_{th} (V)	29	34	−23 (14)	21 (18)

N/A, not measured.
Note: Threshold voltages obtained by transconductance change (TC) method are listed in parenthesis.

device performance using these metals as source/drain electrodes for the transistors. However, these low work function metals are reactive and prone to oxidation, the overall device performance is thus compromised. The top-contact devices with direct evaporation of aluminum onto $F_{16}CuPc$ results in very low mobilities of 8×10^{-4} cm^2/Vs due to reaction between Al and F atoms [21]. The corresponding mobility using silver as top-contact electrodes is 3.5×10^{-4} cm^2/Vs. The mobility, on/off ratio and threshold voltage results for laminated $F_{16}CuPc$ TFTs using aluminum, silver and ruthenium electrodes are summarized in Table 1b. The laminated devices always had better performance than the ones with direct metal evaporation onto $F_{16}CuPc$, but are still not as good as with higher work function and more inert gold electrodes. For example, using aluminum as soft contact electrodes, for substrate temperature of 50 °C and a slow deposition rate of 0.1 Å/s for $F_{16}CuPc$, the laminated devices show carrier mobility of about 0.0037 cm^2/Vs, lower than the gold electrode counterpart. The on/off ratio and threshold voltage are in the same order as the devices laminated using gold electrodes. For substrate temperature of 125 °C and a deposition rate of 1.0 Å/s for $F_{16}CuPc$, the laminated devices show carrier mobility of about 0.06 cm^2/Vs, still lower than the gold electrode counterpart. The on/off ratio and threshold voltage are 1.26×10^{6} and 30 V, respectively. Partial oxidation of the aluminum electrodes may prevent them from having good contacts with semiconducting layer. When using silver soft contact electrodes, for substrate temperature of 125 °C and a deposition rate of 1.0 Å/s for $F_{16}CuPc$, the laminated devices show carrier mobility of about 0.021 cm^2/Vs. The on/off ratio and

Table 1b
Device parameters for laminated $F_{16}CuPc$ TFTs using aluminum, silver and ruthenium electrodes for various substrate temperatures and deposition rates during thin film deposition

Electrodes	Substrate temperature					
	50 °C		80 °C		125 °C	
	Deposition rate (Å/s) of $F_{16}CuPc$					
	0.1		0.2		1.0	
	Laminated	Direct evaporation	Laminated	Direct evaporation	Laminated	Direct evaporation
Al						
Mobility (cm^2/Vs)	3.7×10^{-3}	N/A	4.9×10^{-3}	N/A	0.061	8.0×10^{-4}
On/off	1.4×10^{4}		8.3×10^{3}		1.3×10^{6}	5.9×10^{4}
V_{th} (V)	20		18		30 (21)	28 (25)
Ag						
Mobility (cm^2/Vs)	N/A		N/A		0.021	3.5×10^{-4}
On/off	N/A		N/A		8.7×10^{3}	1.7×10^{3}
V_{th} (V)	N/A		N/A		7 (9)	25 (21)
Ru						
Mobility (cm^2/Vs)	N/A		N/A		0.066	0.019
On/off	N/A		N/A		3.0×10^{4}	3.8×10^{3}
V_{th} (V)	N/A		N/A		7 (6)	18 (21)

Note: Threshold voltages obtained by transconductance change (TC) method are listed in parenthesis.

threshold voltage are 8.7×10^3 and 7.12 V, respectively.

We also used another high work function metal ruthenium (5.5 eV). Its work function is slightly higher than that of gold (i.e., 5.1 eV). The best obtained charge carrier mobility for soft contact Ru electrodes is about 0.066 cm^2/Vs, while for direct evaporation the mobility is 0.019 cm^2/Vs. The on/off ratio is 3×10^4, and the threshold voltage is 7 V. Comparison of the current–voltage characteristics for $F_{16}CuPc$ TFTs made by soft contact lamination using aluminum, silver and ruthenium can be seen in Fig. 2d.

As shown in Fig. 4, $F_{16}CuPc$ TFTs with Au electrodes made by both soft contact lamination and evaporation methods show good air stability. Both charge carrier mobility and on/off ratio do not decrease very much after the devices being stored in ambient lab environment for 1 month.

4. Summary and conclusions

We obtained electron mobility as high as 0.08 cm^2/Vs for $F_{16}CuPc$ TFTs made by soft contact lamination using gold electrodes. The dielectric layer was treated with OTS so as to reduce charge trapping before depositing the purified organic semiconductor. Interface engineering such as soft contact lamination used in our case can further enhance device performance by improving the charge carrier injection from metal electrodes into semiconductor layer. This approach makes it possible for high speed operating of organic CMOS circuitry.

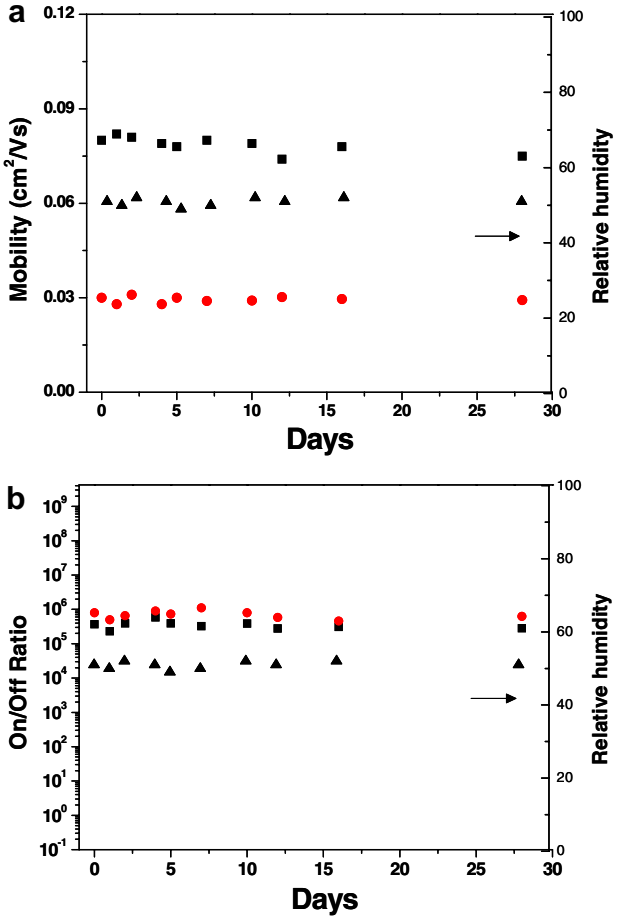

Fig. 4. Air-stability measurements of $F_{16}CuPc$ TFTs with Au electrodes: (a) charge carrier mobility as a function of time and (b) on/off ratio as a function of time. Square: Au electrodes made by lamination method; circle: Au electrodes made by evaporation method; and triangle: the relative humidity of the ambient lab environment.

Acknowledgements

Z.B. acknowledges financial support from 3M Faculty Award, Du Pont Science and Technology Grant and Stanford Center for Integrated Systems. The authors thank Dr. Jason Locklin, Dr. Stefan Mannsfeld, Mark Roberts and Colin Reese for helpful discussions.

References

[1] E.J. Meijer, D.M. De Leeuw, S. Setayesh, E. van Veenendaal, B.H. Huisman, P.W.M. Blom, J.C. Hummelen, U. Scherf, T.M. Klapwijk, Nat. Mater. 2 (2003) 678.
[2] R.C. Haddon, A.S. Perel, R.C. Morris, T.T. Palstra, A.F. Hebard, R.M. Fleming, Appl. Phys. Lett. 67 (1995) 121.
[3] S. Kobayashi, T. Takenobu, S. Mori, A. Fujiwara, Y. Iwasa, Appl. Phys. Lett. 82 (2003) 4581.
[4] T. Shimada, A. Koma, Jpn. J. Appl. Phys. Part 1 41 (2002) 2724.
[5] T.W. Lee, Y. Byun, B.W. Koo, I.N. Kang, Y.Y. Lyu, C.H. Lee, S.Y. Lee, Adv. Mater. 17 (2005) 2180.
[6] Z. Bao, A. Lovinger, J. Brown, J. Am. Chem. Soc. 120 (1998) 207.
[7] E. Kol'tsov, T. Basova, P. Semyannikov, I. Igumenov, Mater. Chem. Phys. 86 (2004) 222.
[8] B.A. Jones, M.J. Ahrens, M.H. Yoon, A. Facchetti, T.J. Marks, M.R. Wasielewski, Angew. Chem., Int. Ed. 43 (2004) 6363.
[9] H.E.H.E. Katz, A.J. Lovinger, J. Johnson, C. Kloc, T. Siegrist, W. Li, Y.Y. Lin, A. Dodabalapur, Nature 404 (2000) 478.
[10] P. Ranke, I. Bleyl, J. Simmerer, D. Haarer, A. Bacher, H.W. Schmidt, Appl. Phys. Lett. 71 (1997) 1332.
[11] P.R.L. Malenfant, C.D. Dimitrakopoulos, J.D. Gelorme, L.L. Kosbar, T.O. Graham, A. Curioni, W. Andreoni, Appl. Phys. Lett. 80 (2002) 2517.
[12] R.J. Chesterfield, J. McKeen, C.R. Newman, C.D. Frisbie, P.C. Ewbank, K.R. Mann, L.L. Miller, J. Appl. Phys. 95 (2004) 6396.
[13] A. Facchetti, M. Mushrush, H.E. Katz, T.J. Marks, Adv. Mater. 15 (2003) 33.
[14] A. Facchetti, M. Mushrush, M.H. Yoon, G.R. Hutchison, M.A. Ratner, T.J. Marks, J. Am. Chem. Soc. 126 (2004) 13,859.
[15] M. Abkowitz, J.S. Facci, J. Rehm, J. Appl. Phys. 83 (1998) 2670.
[16] A. Ionnidis, J.S. Facci, M.A. Abkowitz, J. Appl. Phys. 84 (1998) 1439.
[17] T. Suzuki, M. Kurahashi, X. Ju, Y. Yamauchi, Appl. Phys. Lett. 83 (2003) 4342.
[18] M.H. Choo, J.H. Kim, S. Im, Appl. Phys. Lett. 83 (2003) 4342.
[19] N. Koch, A. Elschner, J. Schwartz, A. Khan, Appl. Phys. Lett. 83 (2003) 2281.
[20] C.F. Shen, A. Kahn, Appl. Phys. Lett. 90 (2001) 4549.
[21] C.F. Shen, A. Khan, J. Appl. Phys. 90 (2001) 6236.
[22] Y. Roichman, N. Tessler, Apply. Phys. Lett. 80 (2001) 151.
[23] I. Kymissis, C.D. Dimitrakopoulos, S. Purushothaman, IEEE Trans. Electron. Dev. 48 (2001) 1060.
[24] J. Zaumseil, T. Someya, Z. Bao, Y.L. Loo, R. Cirelli, J.A. Rogers, Appl. Phys. Lett. 82 (2003) 793.
[25] Y.L. Loo, T. Someya, K. Baldwin, Z. Bao, P. Ho, A. Dodabalapur, H.E. Katz, J.A. Rogers, Appl. Phys. Lett. 81 (2002) 562.
[26] Y.L. Loo, R.W. Willett, K. Baldwin, J.A. Rogers, Proc. Nat. Acad. Sci. 99 (2002) 10252.
[27] J. Zaumseil, K.W. Baldwin, J.A. Roger, J. Appl. Phys. 93 (2003) 6117.
[28] D.A. Bernards, T. Biegala, Z.A. Samuels, J.D. Slinker, G.G. Malliaras, S.F. Torres, H.D. Abruna, J.A. Rogers, Appl. Phys. Lett. 84 (2004) 3675.
[29] Y.L. Loo, J.W.P. Hsu, R.L. Willett, K.W. Baldwin, K.W. West, J.A. Rogers, J. Vac. Sci. Technol. B 20 (6) (2002) 2853.
[30] I.M. Rutenburg, O.A. Scherman, R.H. Grubbs, W.R. Jiang, E. Garfunkel, Z. Bao, J. Am. Chem. Soc. Commun. 126 (2004) 4062.
[31] L.L. Chua, J. Zaumseil, J.F. Chang, E.C.W. Ou, P.K.H. Ho, H. Sirringhaus, R.H. Friend, Nature 434 (2005) 194.
[32] A.R. Volkel, R.A. Street, D. Knipp, Phys. Rev. B 66 (2002) 195336.
[33] K.P. Pernstich, S. Hass, D. Oberhoff, C. Goldmann, D.J. Gundlach, B. Batlogg, J. Appl. Phys. 96 (2004) 6431.
[34] N.J. Watkins, L. Yan, Y. Gao, Appl. Phys. Lett. 80 (2002) 4384.
[35] H.S. Wong, M.H. White, T.J. Krutsick, R.V. Booth, Solid State Electron. 30 (1987) 953.
[36] M. Mottaghi, G. Horowitz, Org. Electron. 7 (2006) 528.
[37] J. Zaumseil, K.W. Baldwin, J.A. Rogers, Appl. Phys. Lett. 93 (2003) 6117.
[38] P.A. Tipler, R.A. Llewellyn, Modern Physics, third ed., W.H. Freeman, 1999.
[39] A. Kahn, N. Koch, W.Y. Gao, J. Polym. Sci.: Part B: Polym. Phys. 41 (2003) 2529.

Available online at www.sciencedirect.com
ScienceDirect
Organic Electronics 7 (2006) 576–585
Organic Electronics
www.elsevier.com/locate/orgel

Novel EDOT and fluorene-based electroluminescent "bricks" as materials for OLEDs

Anne de Cuendias [a], Mathieu Urien [b], Sébastien Lecommandoux [a], Guillaume Wantz [b], Eric Cloutet [a,*], Henri Cramail [a]

[a] Laboratoire de Chimie des Polymères Organiques (UMR 5629), ENSCPB, 16 avenue Pey Berland, 33607 PESSAC, France
[b] Laboratoire de Physique des Interactions Ondes-Matière (UMR 5501), ENSCPB, 16 avenue Pey Berland, 33607 PESSAC, France

Received 18 July 2006; received in revised form 5 September 2006; accepted 25 September 2006
Available online 24 October 2006

Abstract

Luminescent materials based on 3,4-ethylenedioxythiophene (EDOT) and dihexylfluorene were designed. EDOT–fluorene–EDOT molecule, **C3**, was synthesized in high yields by a Stille cross-coupling reaction. The formylation of EDOT units yielded **C4** molecule and a subsequent coupling reaction of **C4** with a Wittig reagent produced **C5**. Electrochemical and optical experiments allowed us to accurately determine the energy level diagram corresponding to these three new molecules. Finally, in order to compare the electroluminescent behaviour of the bricks **C3**, **C4** and **C5**, a simple monolayer OLED structure [ITO/PEDOT-PSS(50 nm)/**Cx**(50 nm)/Ca(100 nm)/Al(100 nm)] was designed. In the case of **C5**, energetic barriers at both interfaces were significantly reduced. For these reasons, devices based on **C5** exhibit very high luminance values of approximately 1000 Cd/m^2 at low applied voltage (below 10 V) with a turn-on voltage of 4.5 V. Maximum quantum and luminous efficiencies of 0.3 Cd/A and 0.1 lm/W are reported. According to the basic single layer structure, such values are very promising if **C5** is used as emissive material in a multilayer-device.

PACS: 78.60.Fi; 78.40.Me; 71.20.Rv; 82.45.Wx

Keywords: Fluorene; 3,4-Ethylenedioxythiophene; Electroluminescence; OLED

1. Introduction

Since the mid-80s, considerable research efforts have been carried out in the field of organic light-emitting devices to obtain brightness and operating voltages suitable for commercial applications [1–4]. Nowadays, the highly efficient organic light-emitting diodes (OLEDs) represent an attractive alternative to conventional inorganic LEDs in the field of flat panel displays manufacturing as well as lighting [5–9]. Recently, much attention has been focused on thiophene derivatives-based linear π-conjugated oligomers and particularly on 3,4-ethylenedioxythiophene (EDOT), the latter monomer being used as a building block in several multi-ring systems due to its unique properties such as electrochromism

* Corresponding author. Tel.: +33 5 40 00 84 88; fax: +33 5 40 00 84 87.
E-mail address: cloutet@enscpb.fr (E. Cloutet).

1566-1199/$ - see front matter © 2006 Elsevier B.V. All rights reserved.
doi:10.1016/j.orgel.2006.09.004

[10,11] and photoluminescence [12]. Moreover, PEDOT derivatives have interestingly been described as low band gap polymers easing positive charge injection and transport [13,14]. Besides, among the other conjugated polymers, polyfluorenes (PFs) have emerged as the most promising candidates for OLEDs [15]. PFs present numerous advantages such as high luminescence quantum efficiencies, high hole mobility and thermal stability. They are also widely investigated for the development of blue light-emitting materials. Furthermore, the 9,9-dialkylfluorene class of oligomers and polymers has shown enhanced solubility and processability of π-conjugated segments. However, PFs have a poor spectral stability because they are known to form fluorenone [16] and excimers [17] in the solid state, implying a quenching of fluorescence and giving an irreversible color emission change from blue to green. Many groups have associated the EDOT and fluorene molecules in a same heteroaromatic structure in order to improve the injection of holes in the resultant material. Some syntheses of association-based copolymers through palladium-catalyzed Suzuki reaction [18] or by dehalogenative polycondensation involving zero-valent metal coupling [19] have already been described.

Reynolds and coll. have reported the synthesis of such copolymers by electropolymerization [20] and Stille coupling [21], from a molecule composed of a central didecylfluorene and EDOT-based heterocycles symmetrically placed on each side. Polymer light-emitting diodes were prepared with these polymers (ITO/polymer/LiF/Ag/Al device) showing luminance around 2.1 cd/m^2 [18b] and band gap close to 2.15 eV [21]. These electroluminescent results showed these polymers as promising candidates in PLEDs.

With a similar strategy, we designed a series of rigid molecular bricks combining a central dihexylfluorene blocked on each side by one functionalized (or not) EDOT unit. It is noteworthy that such functional bricks are aimed to be subsequently used in coupling reactions with functionalized coil polymers in order to synthesize rod–coil systems and to investigate the propensity of the latter to form self-assemblies with original optoelectronic properties. Similarly to the approach developed by Larmat et al. [20] we have synthesized the molecule bis-(3,4-(ethylenedioxy)thien-2-yl)-9,9′-dihexylfluorene (BEDOT-HF) (**C3**) by Stille coupling from 2,7-dibromo-9,9-dihexylfluorene and 2-(trimethylstannyl) EDOT (see Scheme 1). This molecule was then functionalized in incorporating carboxaldehyde (**C4**) and vinyl-ester (**C5**) moieties. The synthesis and the characterizations of BEDOT-HF and its derivatives are reported hereafter. Optical, electrochemical and electroluminescence properties of each molecule were studied. OLEDs based on these 3 ''bricks'' were also investigated. We especially demonstrated that the optical properties and electronic stability of these molecules are very sensitive to the function attached to the ''bricks''.

2. Results and discussion

2.1. Synthesis and characterization of conjugated ''bricks''

The syntheses of a series of conjugated molecular ''bricks'' **C3**, **C4** and **C5** bearing fluorene and EDOT moieties are described hereafter (see Scheme 1). First, starting materials **C1** and **C2** were obtained as follows. 2-Trimethyltin-3,4-ethylenedioxythiophene **C1** was synthesized by stannylation of EDOT with trimethyltin chloride in the presence of *n*-Buli. In order to avoid the formation of distannyl-EDOT, the reaction was performed under dilute conditions ($[EDOT] = 8.8 \times 10^{-2}$ M). Besides, 2,7-dibromo-9,9-di-*n*-hexylfluorene **C2** was easily obtained by alkylation of 2,7-dibromofluorene with 1-bromohexane using a NaOH aqueous solution as reductive agent and tetrabutylammonium chloride as a catalyst. Then, the synthesis of **C3** was first achieved via a nickel(II) chloride catalyzed Grignard cross-coupling between **C1** and **C2** using an entrainment procedure with Mg^0 turnings and 1,2-dibromoethane. Yields obtained by this way were not enough satisfactory and one decided to use preferentially the Stille coupling method. This reaction has been efficiently used to design a whole class of original and tunable electro-active conjugated molecules, oligomers or polymers [22–25]. Compounds **C1** and **C2** were thus allowed to react through a Stille cross-coupling using $Pd(PPh_3)_4$ as a catalyst to give **C3**. The latter was then purified by silica gel chromatography and crystallized in hexane to get final product with a good yield (70%). The structure of the molecule **C3** was confirmed by electrospray ionization. A value of $m/Z = 614.4$ was obtained, in good agreement with the theoretical value. Afterwards, the formylation of the compound **C3** was readily realized in the presence of *n*-BuLi and DMF, leading (BEDOT-HF)-di(CHO)

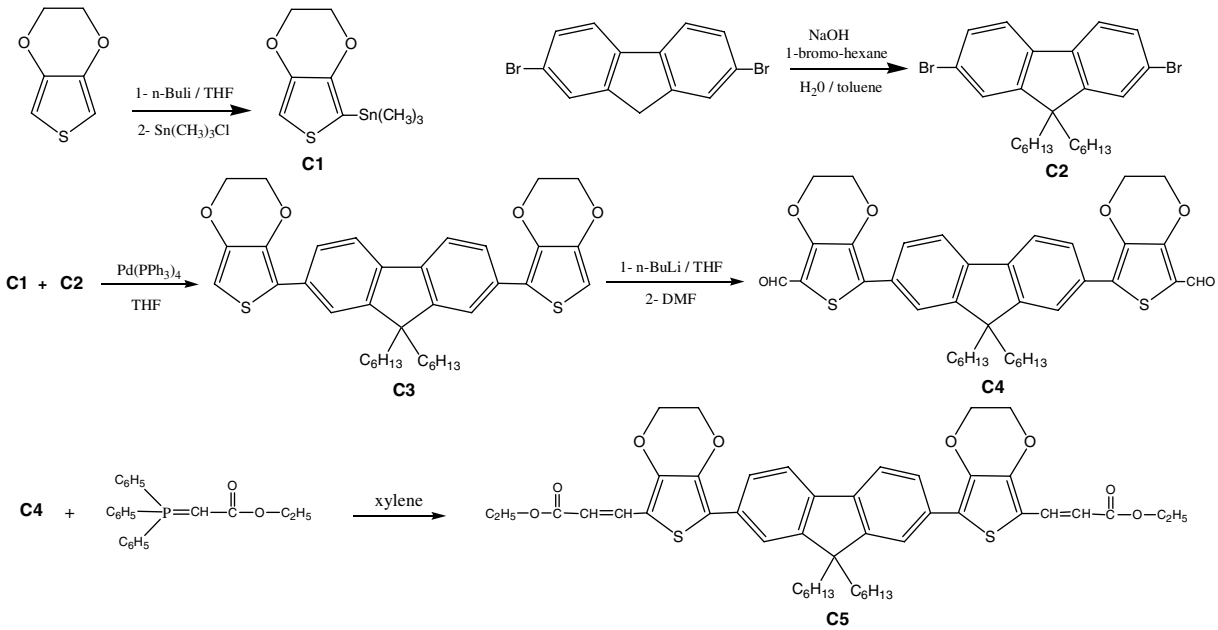

Scheme 1. Synthetic strategy towards EDOT and fluorene-based molecular "bricks" **C3**, **C4** and **C5**.

(**C4**) in 80% yield after purification by chromatography on silica gel (eluent = dichloromethane). Finally, the aldehyde functions of **C4** were allowed to react at 140 °C with (ethoxycarbonylmethylen)-triphenylphosphoran (Wittig compound) to quantitatively yield the product **C5**. After purification by chromatography on silica gel (eluent = toluene/ethyl acetate (50/50) (v/v)), **C5** was characterized by ^{1}H NMR (see Fig. 1) showing a majority of the *cis*-form isomer.

2.2. Optical properties of the "bricks" *C3, C4 and C5*

The absorption spectra of molecules **C3** to **C5** in dilute $CHCl_3$ solution (10^{-5} M) are shown in Fig. 2a. Results are summarized in Table 1. In solution, **C3**, **C4** and **C5** exhibit comparable absorption spectra. Indeed, they show a relatively broad absorption peak with an absorption maximum attributed to π–π^* transition and a shoulder to the higher wavelength. A noticeable red shift in the absorption maximum (from 359 nm to 430 nm) is observed after each functionalization step. This result can be due to two phenomena: the extension of the conjugation length and the changes of the HOMO–LUMO levels as electron withdrawing groups are attached to **C3** (i.e. aldehyde and vinyl ester).

Regarding the fluorescence analysis (Fig. 2b), the spectrum of **C3** shows a wide peak with an emission maximum at 418 nm and three shoulders at higher wavelengths. The stronger peak at 418 nm and the first shoulder at 442 nm can be assigned to vibronic side bands and precisely to 0–0 band and 0–1 band respectively [26]. The two other shoulders (489 and 521 nm) seem to correspond to other species, likely formed due to the instability of **C3** towards oxygen. It is noteworthy that EDOT-base derivatives are very sensitive to light and give rise to photooxidation [27]. The large spectral covering of **C3** leads to a pale blue emission. The other "bricks" exhibit similar behaviours with well-defined structure indicating a precise backbone in the excited state and offer a blue–green emission. The maximum emission of **C4** and **C5** were found respectively at 462 nm and 486 nm.

Solid films on glass were prepared by thermal evaporation under vacuum (10^{-6} mbar). UV–vis spectra are shown in Fig. 3. Compared to the corresponding solution absorption spectra, the film absorption spectra were nearly the same for the compound **C4** and **C5**. No additional peak can be observed. It is believed that the adopted conformation prevents the arrangement of molecules under aggregate forms. Concerning **C3**, the absorption spectrum was red-shifted of about 21 nm and the absorption maximum was shifted of about 10 nm. Such a bathochromic shift can be explained by a parallel alignment of the conjugated backbone (J-

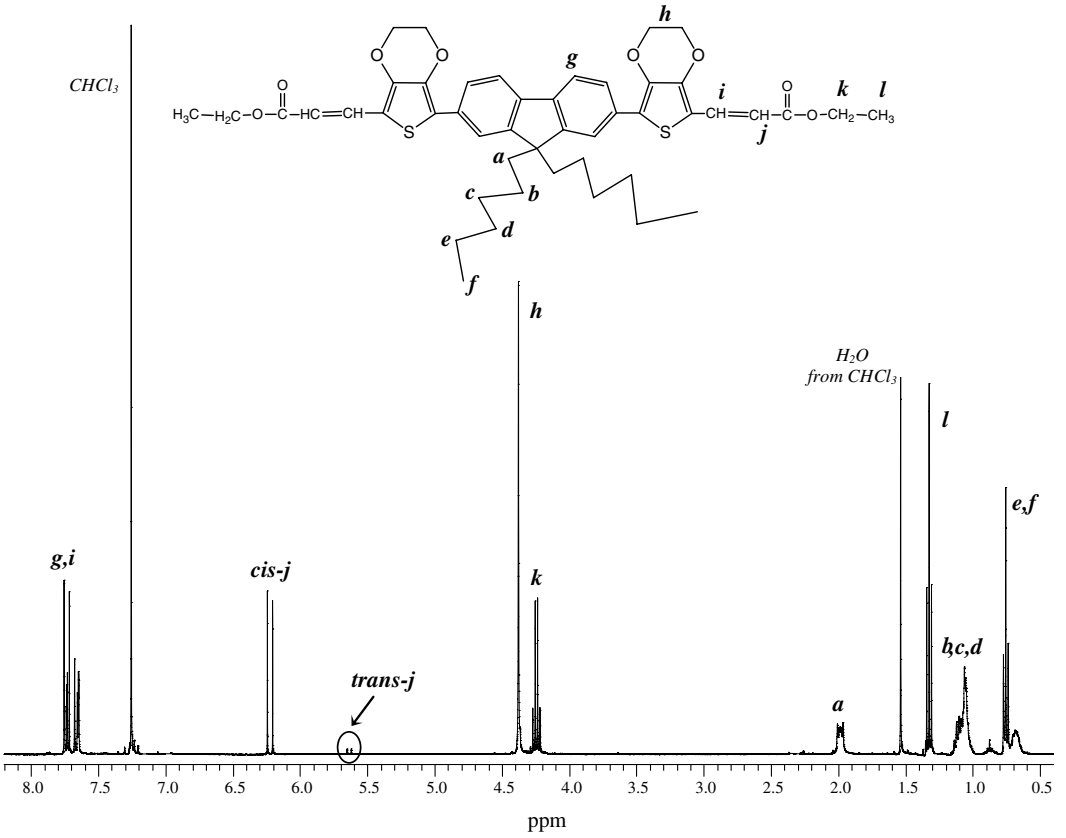

Fig. 1. ^{1}H NMR spectrum of **C5** in $CDCl_3$ (400 MHz).

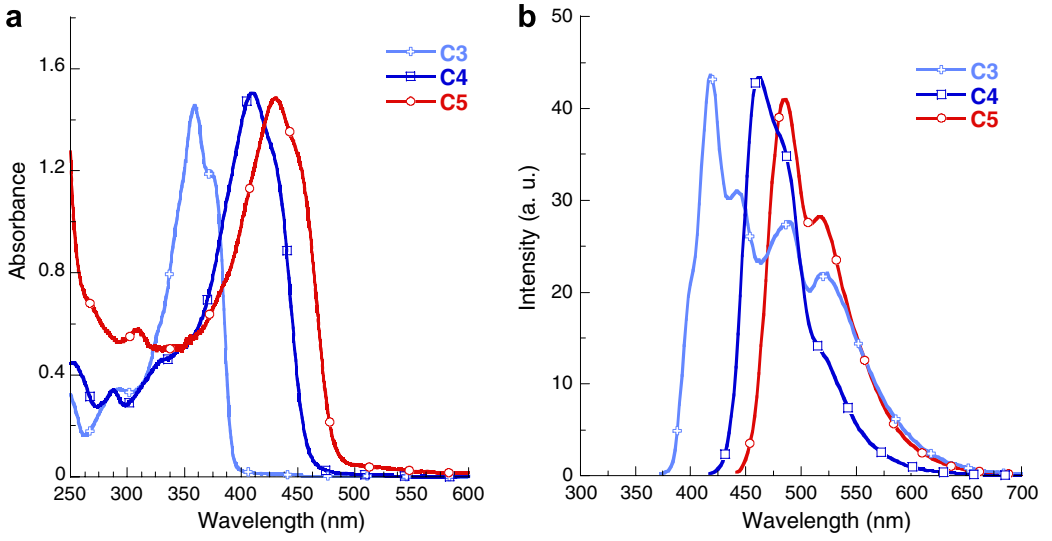

Fig. 2. UV–vis absorption (a) and fluorescence emission (b) spectra of compounds **C3**, **C4** and **C5** in $CHCl_3$ (10^{-5} M).

aggregates). **C3** may have a higher ability to crystallize and thus create more important intermolecular interactions in the solid state favoring coplanar arrangements of the aromatic rings. From the onset wavelength of absorptions, optical gaps of each molecule have been calculated (Table 1). These

Table 1
UV–vis absorptions and electrochemical properties

Sample	Absorption in $CHCl_3$	Absorption film	Oxidation onset	Reduction onset	Energy levels (eV)		E_g[a] (eV)	E_g[b] (eV)
	λ_{max} (nm)	λ_{max} (nm)	(V vs Ag)	(V vs Ag)	HOMO	LUMO		
C3	359	369	0.81	–	−5.14	−2.11[a]	3.03	–
C4	410	411	1.16	−1.52	−5.49	−2.81	2.66	2.68
C5	430	431	0.94	−1.47	−5.27	−2.86	2.54	2.41

[a] Estimated from the onset wavelength of optical absorption of the thin solid film.
[b] Calculated according to the equation: $E_{LUMO} = E_{HOMO} + E_g$.

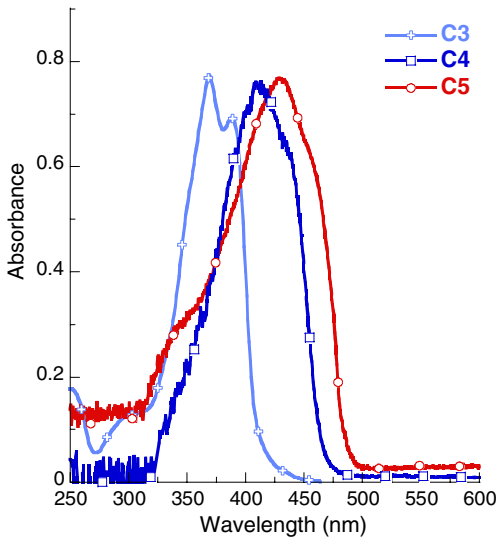

Fig. 3. Normalized UV–vis absorption of compounds **C3**, **C4** and **C5** in film.

values will be compared afterwards with electrochemical data.

2.3. Electrochemical investigations of the "bricks" *C3, C4 and C5*

Cyclic voltammetry (CV) studies of compounds **C3** to **C5** in solution, have been carried out in CH_2Cl_2 solution containing tetrabutylammonium hexafluorophosphate (nBu$_4$NPF$_6$) (0.1 M) as electrolyte (see Fig. 4).

All the molecules exhibit non-reversible processes. For molecule **C3**, the onset of oxidation starts at 0.81 V with a peak at 0.98 V (E_p^a vs Ag). The oxidation waves for **C5** and **C4** are successively shifted to positive potentials for **C5** (onset: 0.94 *V*, $E_p^a = 1.08$ V vs Ag) and **C4** (onset: 1.16 V, $E_p^a = 1.33$ V vs Ag) due to the presence of electron withdrawing groups (i.e. vinyl-ester or aldehyde respectively). Besides, as it could be expected from electron rich molecule, the reduction was not observed for **C3** within the solvent limit, indicating that its reduction occurred at very low potentials. The onset of the reduction starts at −1.47 V ($E_p^c = -1.65$ V vs Ag) and at −1.52 V ($E_p^c = -1.58$ V vs Ag) for **C5** and **C4** respectively which results in band gaps of ΔE_{CV}(**C5**) = 2.41 eV and ΔE_{CV}(**C4**) = 2.68 eV relatively well matching the optical band gaps ($\Delta E_{opt.}$(**C5**) = 2.54 eV and $\Delta E_{opt.}$(**C4**) = 2.66 eV) determined on thin solid films. According to these redox data, the incorporation of electron withdrawing moieties onto molecule **C3** has a predominant influence on the electronic properties of **C5** and **C4**, whereby both, oxidation and reduction are positively shifted. It has to be noted that the functionalization of **C3** not only affects the HOMO–LUMO levels but also increases its stability towards its oxidative polymerization. In fact, as already described by Reynolds and coll. [20], an electropolymerization of **C3** at the electrode with the formation of a dark blue film has been observed.

The energy levels (vs vacuum) of the frontier orbitals HOMO and LUMO of the three molecules **C3**, **C4** and **C5** directly correlate to the redox processes. They are calculated from the onset of oxidation (Φ_p) and reduction (Φ_n) according to the following equations reported by de Leeuw, E_{HOMO} (eV) = $-(\Phi_p + 4.4 + E_{(Ag+/Ag)}/SCE)$ and E_{LUMO} (eV) = $-(\Phi_n + 4.4 + E_{(Ag+/Ag)}/SCE)$ [28]. For that purpose, $E_{(Ag+/Ag)}/SCE$ was determined with respect to the ferrocene/ferricinium couple and found equal to −0.07 V. HOMO and LUMO values are reported in Table 1. A corresponding energy level diagram is depicted in Fig. 5a. To evaluate the performance of the molecules **C3** to **C5** in light-emitting diodes, the HOMO and LUMO levels are compared to the electrode work functions commonly used for the fabrication of such devices.

The substitution of molecule **C3** by electron withdrawing groups lowers the HOMO and LUMO levels. This effect is more pronounced for **C5** which

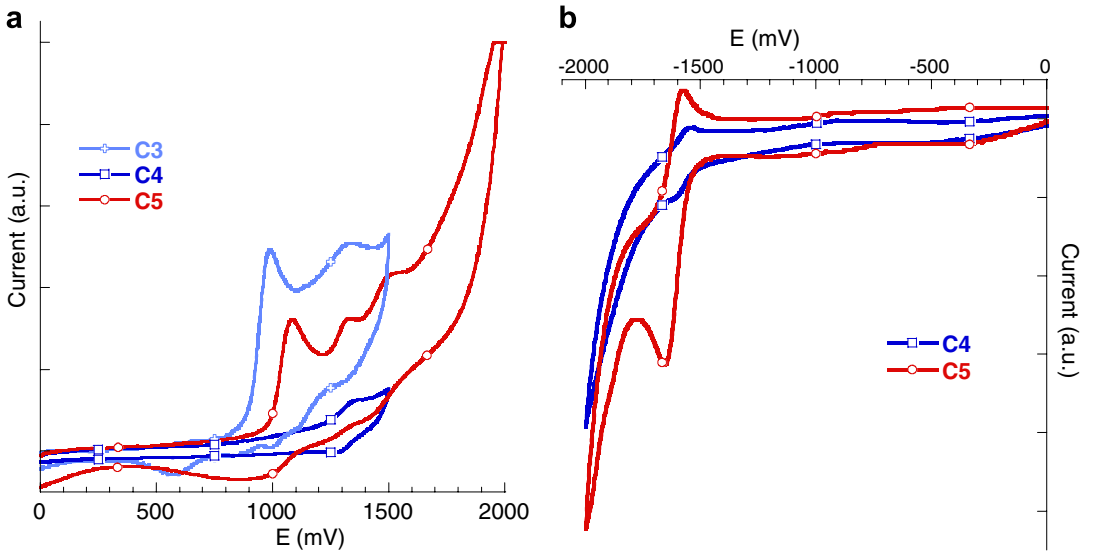

Fig. 4. Cyclic voltammograms (100 V/s) of compounds **C3**, **C4** and **C5** in dichloromethane/nBu$_4$NPF$_6$ (0.1 M) at scanning rate of 100 mV/s.

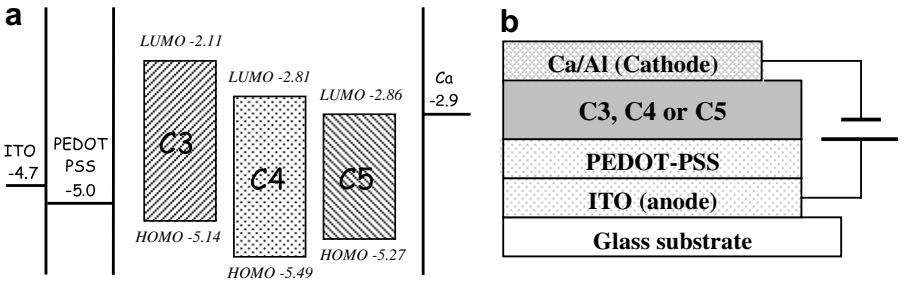

Fig. 5. (a) Energy levels (eV) of **C3**, **C4** and **C5** in comparison to work functions of common electrode materials used in EL devices; (b) structure of the electroluminescent devices.

seems to be the most in adequacy with the electrodes. In this case, the increase in conjugation has to be taken into account. The LUMO level has been lowered down to −2.86 eV to ease the injection of electrons and the HOMO level has been raised up to −5.27 eV to maximize the injection of holes.

2.4. OLEDs characterizations

In order to compare the electroluminescent behaviour of the bricks **C3**, **C4** and **C5**, a simple monolayer OLED structure was designed (see Fig. 5b).

The device structure was ITO/PEDOT-PSS(50 nm)/**Cx**(50 nm)/Ca(100 nm)/Al(100 nm). Indium tin oxide, commonly used as a transparent electrode, was covered with a layer of poly(3,4-ethylenedioxythiophene) doped with poly(styrene sulfonate), known as PEDOT-PSS. This buffer layer is commonly used in OLEDs to improve the injection of holes from the ITO to the HOMO level of the organic material and increases device performances [29]. Calcium has been chosen as cathode material to achieve a good injection of electrons in the LUMO levels of the organic material because of its very low work function (−2.9 eV). The calcium layer was capped with an aluminum layer and such devices are made and characterized under inert nitrogen atmosphere (O_2 and $H_2O < 0.1$ ppm). The characteristics of the OLEDs are listed in Table 2 and the luminance–voltage curves (L–V) are shown in Fig. 6.

C3-based OLEDs exhibit low luminance values, i.e. 6 Cd/m^2 at 11.3 V. A low voltage threshold of 6 V was observed, indicating a good injection of charge carriers in **C3**. According to the band diagram (Fig. 5a), holes injection from PEDOT-PSS (−5 eV) to the HOMO of **C3** (−5.14 eV) is more facilitated than the injection of electrons from Ca

Table 2
Characteristics of OLEDs from **C3**, **C4** and **C5**

OLED	Luminance max (Cd/m^2)	Quantum efficiency max (Cd/A)	Luminous efficiency max (Lm/W)
C3	6.1	9.7×10^{-4}	2.8×10^{-4}
C4	2.2	4.3×10^{-4}	4.1×10^{-4}
C5	1013	0.3	0.1

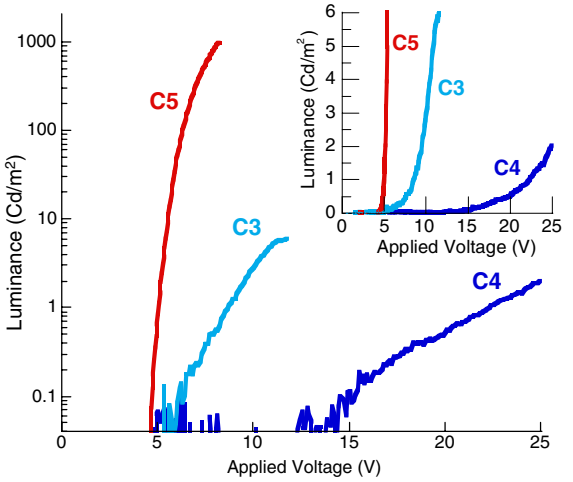

Fig. 6. Luminance–voltage characteristics of OLEDs based on **C3**, **C4** and **C5** on a semilogarithmic scale; inset shows the same curves on a linear scale.

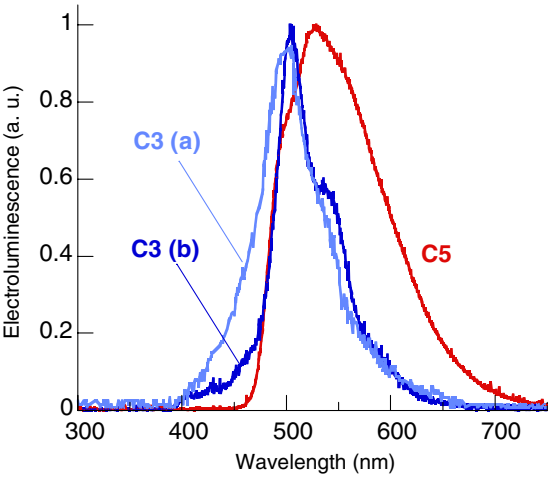

Fig. 7. Normalized electroluminescence spectra of OLEDs based on **C5** and **C3**: (a) measured right after the device is turned on for the very first time, (b) spectrum measured after 1 min of operation.

(−2.9 eV) to its LUMO (−2.11 eV) because of a huge energetic barrier at the **C3**/Ca interface. The electroluminescence (EL) spectra have been recorded right after the OLED was turned on for the very first time (Fig. 7). A pale blue–green emission with chromaticity coordinates (CIE 1964) $X = 0.18$ and $Y = 0.45$ was observed. In fact, the EL spectrum showed a major green peak at 500 nm with a tiny blue shoulder located at 426 nm. The latter is consistent with the band-gap value of **C3**. While EL spectra were recorded after 10 s of operation, the color shifted from blue–green to greenish emission with $X = 0.24$ and $Y = 0.53$. The blue peak has been reduced during operation and the major green contribution was emphasized with a more pronounced vibronic structure. Such a vibronic structure with a typical Huang–Rhys behaviour is commonly observed in polymer-based OLEDs [30]. It is believed that a current flow in the device can induce a polymerization from EDOT groups of **C3** to form dimers and/or trimers that emit a green light due to the enhancement of the conjugation length. The EL spectra measured one minute right after the device was turned on, also shows a green component. It is believed this peak appeared faster than the time needed to perform the EL measurement (below 2 s).

C4-based devices present poor performances. Very low luminance values are obtained (maximum 2 Cd/m^2 at 25 V), with a high voltage threshold, i.e. 15 V (Table 2). The EL spectrum was not recorded considering the weakness of the signal and the very fast degradation of the device (only few seconds). The behaviour of **C4** is due to the detrimental effect of the electron withdrawing aldehyde groups that lower the HOMO level down to −5.49 eV and thus make difficult the injection of holes. In addition, aldehyde groups can act as electron traps.

In the case of **C5**, energetic barriers at both interfaces were significantly reduced. For these reasons, devices based on **C5** exhibit very high luminance values of approximately 1000 Cd/m^2 at low applied voltage (below 10 V) with a turn-on voltage of 4.5 V. Maximum quantum and luminous efficiencies are reported in Table 2. 0.3 Cd/A and 0.1 lm/W have been respectively recorded. According to the basic single layer structure, such values are very promising if **C5** is used as emissive material in a multilayer-device. As shown in the EL spectrum of

C5 (Fig. 7), a green emission with chromaticity coordinates $X = 0.38$ and $Y = 0.55$ is observed with a maximum at 530 nm. Contrary to devices based on **C3** and **C4**, this OLED was found very stable and did not degrade while operating for hours. Both the EL spectrum and the emitted color were unchanged under the charge carrier flow.

3. Conclusion

A series of conjugated bricks **C3**, **C4** and **C5** composed of a central dihexylfluorene blocked on each side by one functionalized (or not) EDOT unit were synthesized efficiently by coupling reactions. These molecules show specific electronic and optic characteristics. It is noteworthy that the incorporation of electron withdrawing moieties (i.e. aldehyde or vinyl-ester groups respectively for **C4** and **C5**) not only prevents the polymerization of the brick **C3** but also affects the redox processes and therefore the HOMO–LUMO levels. We have demonstrated that the incorporation of vinyl-ester groups on **C3** giving rise to compound **C5** improves markedly the OLED device performance with a high EL efficiency and low driving voltage. Intensive studies on the electroluminescent, holes and electrons-transport properties of these materials in multilayer OLED devices are in progress for getting higher performance. Moreover, the bricks **C4** and **C5** have been reacted to coil polymers and the optoelectronic characteristics of the resulting coil–rod–coil block copolymers are currently under investigation.

4. Experimental

4.1. General

^{1}H NMR spectra were recorded on a Bruker AC400 spectrometer operating at 400 MHz and the samples were dissolved in $CDCl_3$. UV–vis spectra were measured in the spectral range of 200–700 nm in chloroform solutions, and recorded on a Varian Cary 3E UV–visible Spectrophotometer. UV–vis spectra of the films were measured in the spectral range of 200–700 nm, and recorded on a Varian Cary 3E UV–visible. Fluorescence spectra were recorded on a SAFAS Spectrofluorometer flux spectrometer. The cyclic voltammetry measurements were performed with a Tacussel apparatus (PGSTAT10) at room temperature with a scanning rate of 100 mV/s. The analysis of the sample solutions were carried out in CH_2Cl_2 (HPLC grade, Fisher Scientific) containing 0.1 M of tetrabutylammonium hexafluorophosphate (nBu$_4$NPF$_6$) as supporting electrolyte in a one-compartment cell equipped with three electrodes. The working anode was platinum, the counter-electrode a platinum wire and an $Ag/AgNO_3$ reference electrode were used. ESI (electrospray ionization) analysis was performed with an ions trap thermo LCQ type spectrometer. The reactions were carried out by the procedures described below.

4.2. Materials

Trimethyltin chloride (1 M in hexane), 3,4-ethylenedioxythiophene (EDOT), *n*-butyllithium (*n*-BuLi), *N*-pivaloyl-*o*-toluidine, 2,7-dibromofluorene, 1-bromohexane, sodium hydroxide, tetrabutylammonium chloride hydrate, tetrakis-(triphenylphosphin)-palladium(0) [Pd(PPh$_3$)$_4$] and (ethoxycarbonylmethylen)-triphenylphosphoran were purchased from Aldrich. EDOT and DMF were stirred with CaH_2 overnight, and distilled prior to use. *n*-BuLi was filtrated and titrated prior to use, with *N*-pivaloyl-*o*-toluidine by the method described by Suffert [31]. The other products were used as received without further purification. THF was dried and distilled over CaH_2 and sodium/benzophenone respectively. Toluene and xylene were used as received without further purification. All reactions were carried out under a dry nitrogen atmosphere, using flame-dried glassware.

2-Trimethyltin-3,4-ethylenedioxythiophene (**C1**). EDOT (3 g, 21.1 mmol) was dissolved in THF (240 mL), and the solution was cooled to −78 °C. *n*-Butyllithium (13.2 mL, 21.1 mmol) was slowly added drop-wise, and the mixture was kept under stirring at −78 °C during 1 h. Then, trimethyltin chloride (21.1 mL, 21.1 mmol) was added at −78 °C via a syringe and the yellow mixture was allowed to warm to ambient temperature with stirring for 24 h. At the end of the reaction, water (100 mL) was added to the mixture which became orange. The phases were separated, and organic layer was extracted from the aqueous layer with ether. All the organic layers were then washed with water, subsequently dried over Na_2SO_4 and concentrated to give a brown viscous liquid. After, the product was crystallized in hexane in order to remove the residual EDOT and to give a brown solid (4.6 g, yield = 71%). ^{1}H NMR ($CDCl_3$): $\delta = 6.57$ (s, 1H, CH), $\delta = 4.17$ (s, 4H, OCH_2-CH_2OH), $\delta = 0.35$ (s, 9H, $Sn(CH_3)_3$).

2,7-Dibromo-9,9-di-*n*-hexylfluorene (C2). 2,7-Dibromofluorene (3 g, 9.26 mmol), 1-bromohexane (13 mL, 92.6 mmol), tetrabutylammonium chloride (300 mg), toluene (17 mL) and aqueous NaOH solution (14,81 g, 0.37 mol in 31 mL of distilled water) were stirred vigorously under reflux overnight. The purple reaction mixture was allowed to cool to room temperature and was extracted with toluene. The extracted organic layer was washed with water, dried over Na_2SO_4 and concentrated to give a yellow liquid. The product was purified by distillation in order to remove 1-bromohexane in excess and then by column chromatography on silica gel using hexane as eluent, to obtain yellow crystallized solid (4.3 g, yield = 94%). ^{1}H NMR ($CDCl_3$): $\delta = 7.55$–7.46 (6H, Ar), $\delta = 1.93$ (4H, CH_2), $\delta = 1.16$–1.07 (12H, CH_2), $\delta = 0.81$ (6H, CH_3), $\delta = 0.61$ (4H, CH_2).

Bis(3,4-ethylenedioxythiophene)-9,9-di-*n*-hexylfluorene (C3). Compound **C2** (1 g, 2.03 mmol), compound **C1** (1.363 g, 4.47 mmol) and [$Pd(PPh_3)_4$] (0.1 g, 0.089 mmol) were introduced in a flask, purged with nitrogen and kept under vacuum for 1 h. After, the products were dissolved in THF (60 mL) and the mixture was stirred under reflux for 30 h. Then, the reaction mixture was allowed to cool at room temperature and THF was removed by evaporation. Purification by chromatography on silica gel (hexane/ethyl acetate = 90/10 (v/v)) afforded the molecule as a brown liquid. Then, the product was precipitated from hexane as a yellow powder (0.87 g, 70%). ^{1}H NMR ($CDCl_3$): $\delta = 7.72$–7.62 (6H, Ar (**2**)), $\delta = 6.31$ (s, 1H, CH **1**), $\delta = 4.35$–4.29 (d, 4H, OCH_2CH_2OH), $\delta = 1.98$ (4H, CH_2(**2**)), $\delta = 1.13$–1.05 (12H, CH_2 (**2**)), $\delta = 0.76$ (6H, CH_3 (**2**)), $\delta = 0.68$ (4H, CH_2 (**2**)). ESI (high resolution): $m/Z = 614.4$.

(Bis(3,4-ethylenedioxythiophene)-9,9-di-*n*-hexylfluorene) – dicarboxaldehyde (C4). Compound **C3** (1 g, 1.63 mmol) was dissolved in THF (40 mL), and the solution was cooled to −78 °C. *n*-Butyllithium (6.7 mL, 10.7 mmol) was slowly added drop-wise, and the mixture turning under a red–brown color, was kept under stirring at −78 °C during 1 h. Then, DMF (0.62 mL, 8.13 mmol) was added at −78 °C via a burette and the mixture was allowed to warm to ambient temperature with stirring for 24 h. At the end of the reaction, water (30 mL) was added to the mixture. After, the phases were separated and the yellow organic layer was extracted from the aqueous layer with ether. All the organic layers were then washed several times with water, subsequently dried over Na_2SO_4 and concentrated. The product was then purified by chromatography on silica gel using CH_2Cl_2 as eluent, leading to a yellow solid (0.87 g, yield = 80%). ^{1}H NMR ($CDCl_3$): $\delta = 9.96$ (2H, CHO), $\delta = 7.84$–7.71 (6H, Ar (**2**)), $\delta = 4.46$–4.43 (4H, OCH_2CH_2O), $\delta = 1.99$ (4H, CH_2(**2**)), $\delta = 1.14$–1.05 (12H, CH_2 (**2**)), $\delta = 0.76$ (6H, CH_3 (**2**)), $\delta = 0.69$ (4H, CH_2 (**2**)).

Divinyl(bis(3,4-ethylenedioxythiophene)-9,9-di-*n*-hexylfluorene)-diester (C5). To a solution of the above aldehyde **C4** (1 g, 1.49 mmol) dissolved in 50 mL of xylene, was added (ethoxycarbonylmethylen)-triphenylphosphoran (1.55 g, 4.47 mmol). The whole mixture was stirred under "reflux" (at 140 °C) during 7 h. Then, the reaction mixture which became dark orange, was allowed to cool at room temperature and xylene was removed by cryodistillation. Purification by chromatography on silica gel (toluene/ethyl acetate = 50/50 (v/v)) afforded the molecule as a yellow solid (1.15 g, yield = 95%). ^{1}H NMR ($CDCl_3$): $\delta = 7.75$–7.65 (6H, Ar (**2**); d, 2H, CH), $\delta = 6.22$ (d, 2H, *cis*-CH), $\delta = 5.63$ (d, 2H, *trans*-CH), $\delta = 4.38$ (4H, OCH_2CH_2O), $\delta = 4.24$ (q, 4H, CH_2O), $\delta = 1.99$ (4H, CH_2(**2**)), $\delta = 1.32$ (t, 6H, CH_3), $\delta = 1.14$–1.05 (12H, CH_2 (**2**)), $\delta = 0.76$ (6H, CH_3 (**2**)), $\delta = 0.69$ (4H, CH_2 (**2**)).

4.3. Device fabrication and characterization

Organic light-emitting diodes were fabricated on ITO (indium–tin oxide) substrates on glass covered with a 50 nm-thick layer of poly(3,4-ethylenedioxythiophene) doped with poly(styrenesulfonate) (PEDOT-PSS) deposited by spin coating at 5000 rpm. This conducting polymer layer was annealed at 80 °C under rotary pump vacuum for 1 h. Then, the active layer (**C3**, **C4** or **C5**) was thermally evaporated under secondary vacuum (10^{-6} mbar). The deposited thickness (50 nm) was monitored using a piezoelectric balance set-up inside the vacuum chamber close to the substrate holder. Bi-layer cathodes of calcium (100 nm-thick) and aluminium (100 nm-thick) were then sublimed through a shadow mask. All investigated devices have an active area of 10 mm^2. Samples were then stored and characterized under inert atmosphere in a nitrogen glove box (O_2 and $H_2O < 1$ ppm). Contacts were taken using a prober (*Karl Suss PM5*). Current–voltage–luminance (I–V–L) curves were recorded using a *Keithley 4200 SCS* coupled with a photodiode calibrated with a *Minolta CS-100* luminancemeter. Electroluminescence (EL) spectra

were investigated using an *Ocean Optics HR2000* Spectrometer.

References

[1] C.W. Tang, S.A. Van Slyke, Appl. Phys. Lett. 51 (1987) 913.
[2] C. Adachi, S. Tokito, T. Tsutsui, S. Saito, Jpn. J. Appl. Phys. 27 (1988) L269.
[3] R.F. Service, Science 273 (1996) 878.
[4] H. Nakada, T. Tohma, Inorganic and Organic Electroluminescence, Wissenschaft-und-Technik-Verlag, Berlin, 1996, p. 385.
[5] M.A. Baldo, M.E. Thompson, S.R. Forrest, Nature 403 (2000) 750.
[6] M.A. Baldo, D.F. O'Brien, Y. You, A. Shoustikov, S. Sibley, M.E. Thompson, S.R. Forrest, Nature 385 (1998) 151.
[7] C. Adachi, M.A. Baldo, M.E. Thompson, S.R. Forrest, J. Appl. Phys. 90 (2001) 5048.
[8] R.H. Friend, R.W. Gymer, A.B. Holmes, J.H. Burroughes, R.N. Marks, C. Taliani, D.D.C. Bradley, D.A. dos Santos, J.L. Brédas, M. Lögdlund, W.R. Salaneck, Nature 387 (1999) 121.
[9] B. Geffroy, P. le Roy, C. Prat, Polym. Int. 55 (2006) 572.
[10] G.A. Sotzing, J.R. Reynolds, P.J. Steel, Chem. Mater. 8 (1996) 882.
[11] M.F. Pepitone, S.S. Hardaker, R.V. Gregory, Chem. Mater. 15 (2003) 557.
[12] H.W. Heuer, R. Wehrmann, S. Kirchmeyer, Adv. Func. Mater. 12 (2002) 89.
[13] G.A. Sotzing, T.A. Thomas, J.R. Reynolds, P.J. Steel, Macromolecules 31 (1998) 3750.
[14] Y. Fu, H. Cheng, R.L. Elsenbaumer, Chem. Mater. 9 (1997) 1720.
[15] A.W. Grice, D.D.C. Bradley, M.T. Bernius, M. Inbasekaran, W.W. Wu, E.P. Woo, Appl. Phys. Lett. 73 (1998) 629.
[16] (a) E.J.W. List, U. Scherf, Adv. Mater. 14 (2002) 477;
(b) X.O. Gong, P.K. Iyer, D. Moses, G.C. Bazan, A.J. Heeger, S.S. Xiao, Adv. Funct. Mater. 13 (2003) 325.
[17] (a) K.-H. Weinfurtner, H. Fujikawa, S. Tokito, Y. Taga, Appl. Phys. Lett. 76 (2000) 2502;
(b) M. Grell, D.D.C. Bradley, G. Ungar, J. Hill, K.S. Whitehead, Macromolecules 32 (1999) 5810;
(c) G. Zeng, W.-L. Yu, S.-J. Chua, W. Huang, Macromolecules 35 (2002) 6907.
[18] (a) P. Blondin, J. Bouchard, S. Beaupré, M. Belletête, G. Durocher, M. Leclerc, Macromolecules 33 (2000) 5874;
(b) A. Donat-Bouillud, I. Lévesques, Y. Tao, M. D'Iorio, S. Beaupré, P. Blondin, M. Ranger, J. Bouchard, M. Leclerc, Chem. Mater. 12 (2000) 1931;
(c) P.-H. Aubert, M. Knipper, L. Groenendaal, L. Lutsen, J. Manca, D. Vanderzande, Macromolecules 37 (2004) 4087.
[19] O. Stephan, F. Tran-Van, C. Chevrot, Synth. Met. 131 (2002) 31.
[20] F. Larmat, J.R. Reynolds, B.A. Reinhardt, L.L. Brott, S.J. Clarson, J. Polym. Sci. A: Polym. Chem. 35 (1997) 3627.
[21] B. Tsuie, J.L. Reddinger, G.A. Sotzing, J. Soloducho, A.R. Katritzky, J.R. Reynolds, J. Mater. Chem. 9 (1999) 2189.
[22] A. Berlin, G. Zotti, S. Zecchin, G. Schiavon, B. Vercelli, A. Zanelli, Chem. Mater. 16 (2004) 3667.
[23] H. Goto, Y.S. Jeong, K. Akagi, Macromol. Rapid Commun. 26 (2005) 164.
[24] J. Casado, R. Ponce Ortiz, M.C. Ruiz Delgado, V. Hernández, J.T. Lopez Navarrete, J.-M. Raimundo, P. Blanchard, M. Allain, J. Roncali, J. Phys. Chem. B 109 (2005) 16616.
[25] M.B. Ramey, J. Hiller, M.F. Rubner, C. Tan, K.S. Schanze, J.R. Reynolds, Macromolecules 38 (2005) 234.
[26] M.C. Hung, J.L. Liao, S.A. Chen, S.H. Chen, A.C. Su, J. Am. Chem. Soc. 127 (2005) 14576.
[27] K. Jeuris, L. Groenendaal, H. Verheyen, F. Louwet, F.C. De Schryver, Synth. Met. 132 (2003) 289.
[28] D.M. de Leeuw, M.M.J. Simenon, A.R. Brown, R.E.F. Einerhand, Synth. Met. 87 (1997) 53.
[29] A. van Dijken, A. Perro, E.A. Meulenkamp, K. Brunner, Org. Elec. 4 (2003) 131.
[30] G. Wantz, L. Hirsch, N. Huby, L. Vignau, A.S. Barrière, J.P. Parneix, J. Appl. Phys. 97 (2005) 034505.
[31] J. Suffert, J. Org. Chem. 54 (1989) 509.

Available online at www.sciencedirect.com
ScienceDirect
Organic Electronics 7 (2006) 586–591
Organic Electronics
www.elsevier.com/locate/orgel

Bottom gate organic field effect transistors made by laser structuring

Ronald M. Meixner [a,*], Rocco Wille [a], Peter Schertling [a], Holger Goebel [a], H. Harde [b], K.-H. Steglich [b], F.A. Yildirim [c], W. Bauhofer [c], W. Krautschneider [d]

[a] *Helmut–Schmidt-University/University of the Federal Armed Forces Hamburg, Department of Electronics, Holstenhofweg 85, 22043 Hamburg, Germany*
[b] *Helmut–Schmidt-University/University of the Federal Armed Forces Hamburg, Laser Engineering and Materials Science, Holstenhofweg 85, 22043 Hamburg, Germany*
[c] *Institute of Optical and Electronic Materials, Hamburg University of Technology, Eissendorfer Strasse 38, D-21073 Hamburg, Germany*
[d] *Institute of Nanoelectronics, Hamburg University of Technology, Eissendorfer Strasse 38, D-21073 Hamburg, Germany*

Received 8 June 2006; received in revised form 21 September 2006; accepted 26 September 2006
Available online 26 October 2006

Abstract

This paper presents a process to manufacture all-polymer field effect transistors in a bottom gate configuration where all electrodes – including the gate electrode – are patterned using an excimer laser in combination with a scanning unit. This technique yields channel lengths of 10 μm between the source and the drain electrodes. Being a combination of a scanning and a single shot patterning process it is a promising candidate for an industrial process with a resolution of 10 μm and an operational throughput of at least 6 cm^2/s.

Keywords: Laser patterning; P3HT; Thin-film transistors; Bottom gate

1. Introduction

One of the most interesting features of organic electronics is the possibility to realize disposable electronics due to its low-cost potential. In order to fully enjoy the low-cost feature, simple and cost-effective process technologies are key requirements for the fabrication of organic electronic devices.

Since the first papers describing completely organic field effect transistors (FETs) [1] appeared in 1994, several all-organic thin-film transistors have been reported during the past decade. Based on these devices, interesting applications like ring-oscillators [2,3], a four-bit parallel-to-serial converter [4] or RFID-tags [5] were presented. Most of these organic field effect transistors (OFETs) are realized with simple and cheap patterning techniques, for example screen-printing [6], ink-jet printing [7], micro-contact printing [8], laser-induced thermal imaging [9] or direct laser patterning [10], representing the required simple and cheap key technologies

* Corresponding author. Tel.: +49 40 6541 2228/2456; fax: +49 40 6541 3518.
E-mail address: meixner@unibwh.de (R.M. Meixner).

1566-1199/$ - see front matter
doi:10.1016/j.orgel.2006.09.005

for a plastic electronics industry. These examples illustrate that, apart from the simplicity and hence low-cost attributes of these technologies, other factors such as high throughput, small device dimensions and compatibility to current fabrication processes have to be taken into account.

Direct laser patterning offers the potential for inexpensive and flexible patterning. The concepts incorporating laser based patterning techniques range from direct patterning of organic semi-conductors [11] over assistance in printing processes [12] to structuring of source and drain electrodes in a top gate configuration [10] or opening a trench for vertical-channel transistors [13].

In this paper, we present a process that was developed to manufacture all-polymer field effect transistors in a bottom gate configuration. By employing an excimer laser system that uses a combination of a scanning and a shot patterning process the possible degrees of freedom in fabrication are increased so that all electrodes – including the gate electrode – are patterned by this laser system.

2. Laser structuring unit

The patterning of the electrode structures was accomplished with a laser system that was originally designed and employed for surface cleaning purposes. This prototype – called Scanning Excimer Laser Cleaning Unit (SELCU) – consists of the Excimer Laser Lumonics PM 848 followed by an variable attenuator, a beam homogenizer, a field-

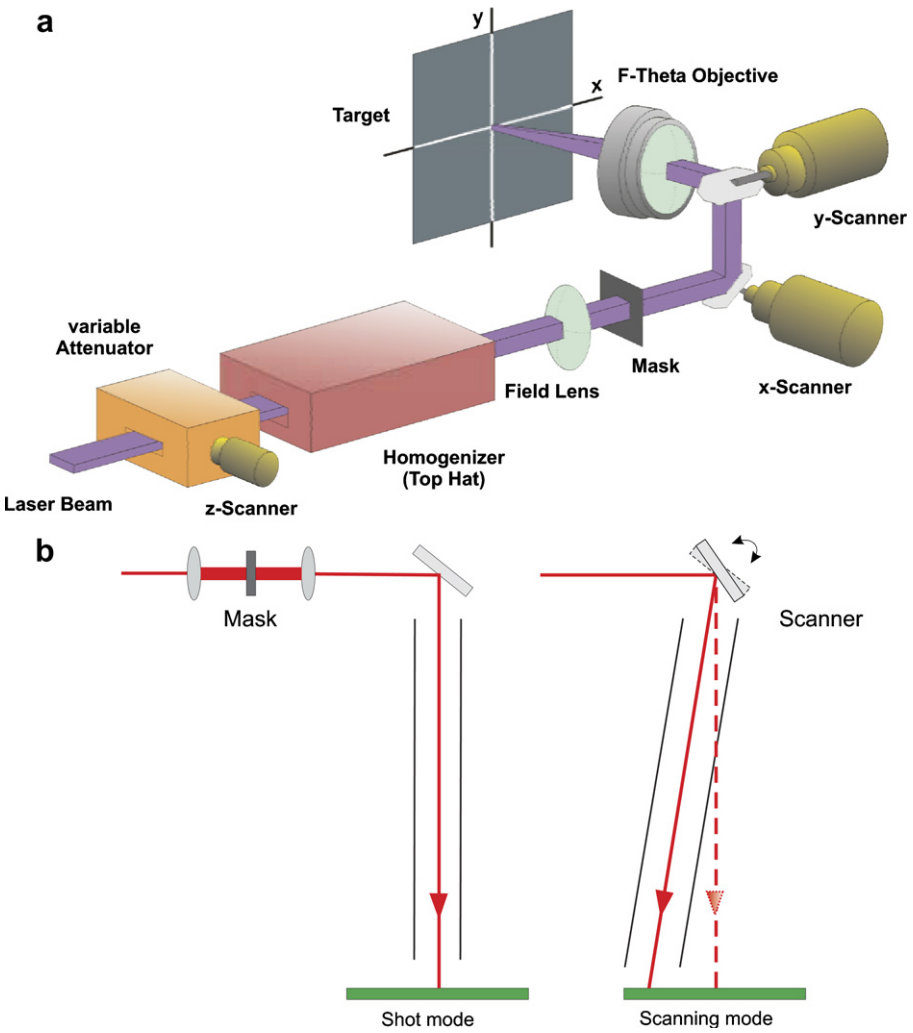

Fig. 1. (a) Setup of the Scanning Excimer Laser Cleaning Unit (SELCU) used to pattern both the source/drain electrodes and the gate electrode. (b) Principle of the shot and the scanning mode.

lens, two galvo scanners and finally an *F*-Theta lens (80 mm in diameter, front lens is 66 mm in diameter at a length of 40 mm) [14]. The setup of the actual cleaning unit is depicted in Fig. 1a. The key element is a beam forming and scanning unit. To improve the laser beam quality for homogenous irradiation of samples, a beam homogenizer was developed, which forms a rectangular cross section with a top-hat profile. This system can operate in a shot and a scanning mode (Fig. 1b). The scanning area is defined by the maximal cross section dimension of the beam ($\approx$8 mm $\times$ 24 mm, hence 24 mm), the maximal angular travel ($\pm$10°), the diameter of the input and output of the *F*-Theta lens (lens diameter input 50 mm, output 66 m), the focus of the *F*-Theta lens ($F = 200$ mm, 3:1 zoom factor) and the distance between *F*-Theta lens and surface to scan ($\approx$300 mm). These parameters would allow for a scanning area of up to 150 mm $\times$ 150 mm using an ideal axis formed round beam. Due to the rectangular shape and its dimensions the effective area will be reduced down to 70 mm $\times$ 70 mm. In scanning mode the beam is focused down to 2×2 mm^2 and directed across the surface by a beam scanner, which uses two galvano mirrors. The scanning rate and consequently the deflection of the beam is adapted to the pulse repetition rate (up to 1 kHz) and therefore allows for extremely fast automated processing. An accurately controlled beam positioning together with the top-hat profile ensures a very homogenous, uniform and reliable irradiation of each surface element with almost identical laser fluence.

In order to process large areas, the beam moves step by step to adjacent sites of action where the scanning speed is adapted to the pulse frequency of the excimer laser. The whole setup is computer controlled so that exact and highly reproducible positioning is possible. For structuring the poly(ethylenedioxythiophene)/polystyrenesulfonate (PEDOT/PSS) layer of the gate electrode the laser is routed over the layer and thus ablates material leaving a thin gate structure on the glass substrate.

3. Fabrication of all polymer FETs

Fabrication of all polymer FETs starts with the formation of the gate electrode on a glass substrate. This is done by spin-coating filtered (PVDF 0.45 μm pore size) PEDOT/PSS in the formulation CPP 105D from H.C. Starck with 2000 rpm for 10 s. This formulation of PEDOT/PSS was chosen due to its high conductivity in comparison to other PEDOT/PSS formulations and its good adhesion, especially on glass. After spin-coating, the sample undergoes

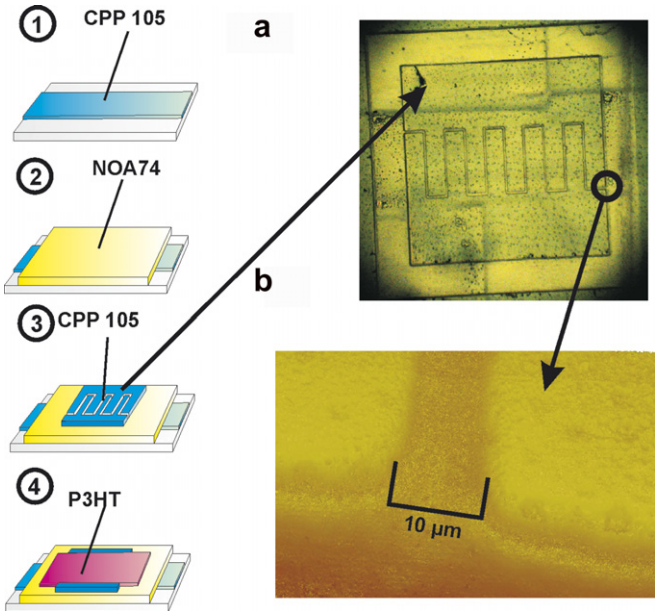

Fig. 2. Simplified process flow: (1) glass substrate with CPP 105D – patterned in the scanning mode (2) followed by the gate dielectric NOA74 and (3) source and drain electrode from laser patterned CPP 105 in the shot mode. (4) The last layer consists of the semiconductor P3HT. Additionally to the process flow two magnified images ((a) optical, (b) AFM) of the 10 μm channel are displayed.

a hot-plate annealing for about 10 min at 80 °C. For the formation of the gate electrode, the SELCU is set to a fluence of 1500 mJ/cm^2 since lower values left remains of CPP105D on the glass substrate. Subsequently, the laser beam is moved across the surface by the *x*- and *y*-scanner so that large areas are ablated and only one small stripe of CPP 105D with a length of 2.6 cm and a width of 0.35 mm remains. The next process step is the deposition of the insulating layer of NOA74 (filtered PTFE 0.2 μm pore size) diluted in *n*-methylpyrrolidone (NMP) – ratio-one-to-one. This material is spin-coated for 60 s at 6000 rpm resulting in a 1.2 μm layer. NOA74 is then cured under an UV-lamp (253.7 nm) for approximately 1 h. The resulting film has a dielectric constant of 5.46 at 10 MHz and an average roughness of 15 nm. The next layer – as a preparation for the source and drain electrodes – is again spin-coated from filtered CPP 105D and structured in shot mode. As mentioned before, a positive chromium mask is inserted into the first focal point and the pattern on the mask is projected onto the CPP 105D layer on the insulating NOA74 layer. This patterning technique is being

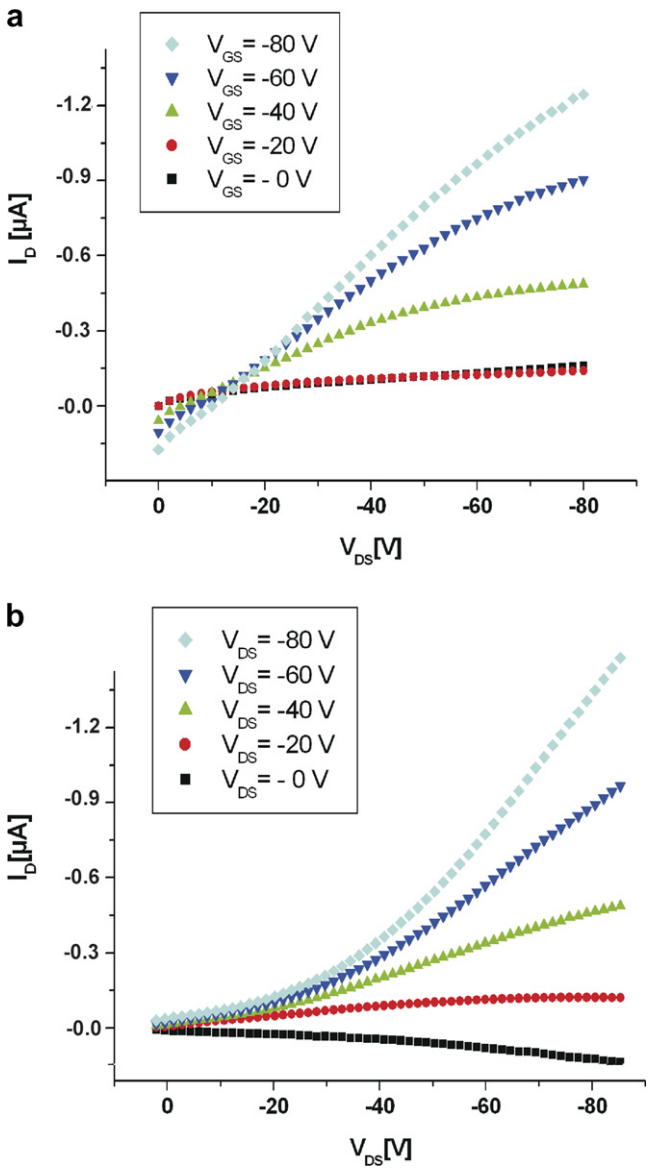

Fig. 3. (a) Output and (b) transfer characteristics of an all polymer transistor with an NOA-NMP gate dielectric.

strongly supported by the ductile surface properties of the optical adhesive. The image projection of 1:3 reduces the actual size of the square mask and results in a channel length of 10 μm. The best results are obtained using 200 shots at a repetition rate of 200 Hz and with fluences between 150 and 200 mJ/cm^2. For the semi-conducting layer poly(3-hexylthiphene) (P3HT) – 0.5 weight percent in $CHCl_3$ (99.9%+ purity, <0.01% H_2O) – is filtered (0.2 PTFE μm pore size) and spin-coated (3 s at 800 rpm, 10 s at 2000 rpm) on the electrode structure. Residues of the solvent are removed with a temperature treatment at 120 °C for 60 min in vacuum. The resulting thickness of the P3HT layer is 50 nm on average, determined by profilometry on a flat glass surface. After preparation the devices were characterized in a glove box using an Agilent parameter analyzer 4156C. Fig. 2 shows a simplified process flow.

Evaluation of measured transistor characteristics in the saturation regime yields mobilities around 4.2×10^{-4} cm^2/Vs, on–off-ratios of 1.82×10^2 and threshold voltages of approximately 33 V. Fig. 3 depicts the exemplary output and transfer characteristics of one of the fabricated transistors. The well known phenomena in full-organic thin-film transistors – lacking adequate saturation at high drain currents and non quadratic increase of the saturation drain current with the gate bias – are also observed along with these devices. The latter can be explained by a gate voltage dependence of the mobility, whereas the lacking saturation at high drain voltages is attributed to a parallel resistance. Both effects have also been observed in inorganic transistors with organic semi-conductors and in hybrid transistors from earlier studies [15].

4. Summary and conclusion

All polymer FETs employing a laser system were presented. The laser system allows for precise and quick structuring of gate source and drain electrodes in a bottom gate configuration. With a throughput of 6 cm^2/s, this method certainly enables a route towards a roll-to-roll process – especially in connection with ink-jet printing or doctor blading. The FETs – with a mobility of 4.2×10^{-4} cm^2/Vs – were produced at a minimum feature size of 10 μm.

In order to take a closer look at a possible of a practical application in a reel-to-reel process the given setup has to be compared with commercially available systems such a dry printing system [9]. These direct write systems employ an infra-red diode laser and require one tenth of the laser fluence. They are suitable to write over 1 m^2 area. On the other hand, due to the conversion of light to heat, which enables the dry printing process, only certain materials can be processed [9]. In contrast, taking one of the most prominent features of the ablation process into account – namely fact that the energy transfer from the ablation site to the adjacent material is negligible – a precise shaping (see AFM image in Fig. 2b) of almost any kind of material is possible even metal films can be shaped at a reasonable laser fluence, e.g. 50 nm gold on NOA74 at 120 mJ/cm^2. In doing so, no influence of the process parameters for example on the conductivity of polymers can be observed. Moreover, this precise material processing allows not only for the removal of material but also for certain process steps, such as the cross linking of functional polymers [16].

The fact that an *F*-Theta lens is used renders it possible to set aside the employment of movable target. The financial expenditure of an *F*-Theta lens is less than for *x*–*y* planar motors at a comparable precision.

References

[1] F. Garnier, R. Hajlaoui, A. Yassar, P. Srivastava, All-polymer field-effect transistor realized by printing techniques, Science 265 (1994) 1684–1686.
[2] H. Klauk, D.J. Gundlach, T.N. Jackson, Fast organic thin-film transistor circuits, Device Lett. IEEE Electron. 20 (June) (1999) 289–291.
[3] M.G. Kane, J. Campi, M.S. Hammond, F.P. Cuomo, B. Greening, C.D. Sheraw, J.A. Nichols, D.J. Gundlach, J.R. Huang, C.C. Kuo, L. Jia, H. Klauk, T.N. Jackson, Analog and digital circuits using organic thin-film transistors on polyester substrates, IEEE Electron. Device Lett. 21 (November) (2000) 534–536.
[4] J. Krumm, E. Eckert, W.H. Glauert, A. Ullmann, W. Fix, W. Clemens, A polymer transistor circuit using PDHTT, IEEE Electron. Device Lett. 25 (June) (2004) 399–401.
[5] P.F. Baude, D.A. Ender, M.A. Haase, T.W. Kelley, D.V. Muyres, S.D. Theiss, Pentacene-based radio-frequency identification circuitry, Appl. Phys. Lett. 82 (2003) 3964–3966.
[6] Z. Bao, Y. Feng, A. Dodabalapur, V.R. Raju, A. Lovinger, High performance organic transistors fabricated by printing techniques, Chem. Mater. 9 (1997) 1299–1301.
[7] H. Sirringhaus, T. Kawase, R.H. Friend, T. Schimoda, M. Inbasekaran, W. Wu, E.P. Woo, High-resolution inkjet printing of all-polymer transistor circuits, Science 290 (2000) 2123–2126.

[8] J.A. Rogers, Z. Bao, A. Makhija, P. Braun, Printing process suitable for reel-to-reel production of high-performance organic transistors and circuits, Adv. Mater. 11 (1999) 741–744.
[9] G.B. Blanchet, Y.-L. Loo, J.A. Rogers, F. Gao, C.R. Fincher, Large area, high resolution, dry printing of conducting polymers for organic electronics, Appl. Phys. Lett. 82 (2003) 463–465.
[10] M. Schrödner, R.-I. Stohn, K. Schultheis, S. Sensfuss, H.-K. Roth, Polymer field effect transistors made by laser patterning, Org. Elec. 6 (2005) 161–167.
[11] T.K.S. Wong, S. Gao, X. Hu, H. Liu, Y.C. Chan, Y.L. Lam, Patterning of poly(3-alkylthiophene) thin films by direct-write ultraviolet laser lithography, Mater. Sci. Eng. B (1998).
[12] H. Sirringhaus, S.E. Burns, C. Kuhn, K. Jacobs, J.D. MacKenzie, M. Etchells, K. Chalmers, P. Devine, N. Murton, N. Stone, D. Wilson, P. Cain, T. Brown, A.C. Asais, J. Mills, R.H. Friend, Active matrix displays made with printed polymer thin film transistors, SID Int. Sym. Dig. Tech. Papers 34 (2003) 1084–1087.
[13] R. Parashkov, E. Becker, G. Ginev, T. Riedl, H.-H. Johannes, W. Kowalsky, Organic vertical channel transistors structured using excimer laser, Appl. Phys. Lett. 85 (2004) 5751–5753.
[14] K.-H. Steglich, H. Harde, Sensitive surface cleaning using an excimer laser in scanner conference on lasers and electro-optics (CLEO 2001), Technical Digest, 2001, p. 233.
[15] R. M. Meixner, H. Goebel, F.A. Yildirim, R.R. Schliewe, W. Bauhofer, W. Krautschneider, Low-temperature process for manufacturing all polymer thin-film transistors, in: Proc. Polytronic 2005, 2005, pp. 197 –199.
[16] T.K.S. Wong, S. Gao, X. Hu, H. Liu, Y.C. Chan, Y.L. Lam, Patterning of poly(3-alkylthiophene) thin films by direct write ultraviolet laser lithography, Mater. Sci. Eng. B 55 (1998) 71–78.

Available online at www.sciencedirect.com
ScienceDirect
Organic Electronics 7 (2006) 592–599
Organic Electronics
www.elsevier.com/locate/orgel

Thin-film field-effect transistors: The effects of traps on the bias and temperature dependence of field-effect mobility, including the Meyer–Neldel rule

P. Stallinga *, H.L. Gomes

Universidade do Algarve, Facudade de Ciencias e Tecnologia, Campus de Gambelas, 8005-139 Faro, Portugal

Received 16 May 2006; received in revised form 29 September 2006; accepted 4 October 2006

Abstract

Based on the model of thin-film transistors in which the active layer is treated as two-dimensional, the effects of traps are studied. It is shown that when abundant discrete trap states are present, the field-effect mobility becomes temperature dependent. In case the traps are distributed exponentially in energy, a Meyer–Neldel rule for the temperature dependence of mobility and current results. When also the mobile states are distributed in energy, in the so-called band-tail states, the mobility is no longer thermally activated.

PACS: 85.30.De; 85.30.Tv

Keywords: Thin-film transistors; Traps; Meyer–Neldel rule; Temperature dependence

1. Introduction

Organic materials for electronic components are beginning to find commercial applications in consumer electronics where they serve as low cost alternatives for traditional materials. The description of the electronic behavior is still under debate while the products are already for sale. However, for increased control over the behavior, it is important to determine what are causing the properties and limitations of the final devices. An important organic electronic device is the thin-film field effect transistor (TFT), used in, for instance, switching elements in active matrix displays. Note that recently it has been shown that organic TFTs, because of the improved quality and accompanying ambipolar character of conduction, can also be the light emitting element [1,2]. Traditionally, these devices have been described by the metal-oxide-semiconductor field-effect-transistor (MOS-FET) model [3], including those devices made of organic materials [4], since this type of device is well established and described and the behavior at first glance is very similar to that of TFTs. There are however some features that are difficult to explain in the MOS-FET framework. One of the things that

* Corresponding author. Tel.: +351 969541198; fax: +351 289800030.
E-mail address: pjotr@ualg.pt (P. Stallinga).

1566-1199/$ - see front matter
doi:10.1016/j.orgel.2006.10.003

deserve extra attention is the temperature dependence. Currents and charge-carrier mobilities of MOS-FET devices based on silicon are basically independent of temperature. On the other hand, TFTs based on organic materials do normally not show this characteristic; complicated temperature dependencies are often observed and reported.

Probably, the most remarkable feature of TFTs is the fact that, normally, the active layer is non-compatible with the substrate in terms of crystallographic properties. Often, the thin active layer has a different lattice parameter compared to the underlying insulating material (see Fig. 1 for a cross-section of a TFT). Take as an example a TFT made of silicon grown on top of silicon oxide. Especially the first mono-layers of silicon are impossible to grow with a well-defined crystallographic structure. Inevitably, many defects are created. In fact, the silicon becomes amorphous. Generally speaking, since the material of the active layer has a lattice mismatch compared to the insulating layer, defects are unavoidable. These defects can be electrically active and can, for instance, trap free charges that would otherwise contribute to external currents. Thus, these traps, normally distributed over the entire bandgap of the semiconductor, can cause severe modifications of the electronic properties of the device. In the current work, we will show how traps change the temperature dependence of the parameters of TFTs. Moreover, as we will show, the temperature dependence can shed light on the density of states involved in electronic conduction.

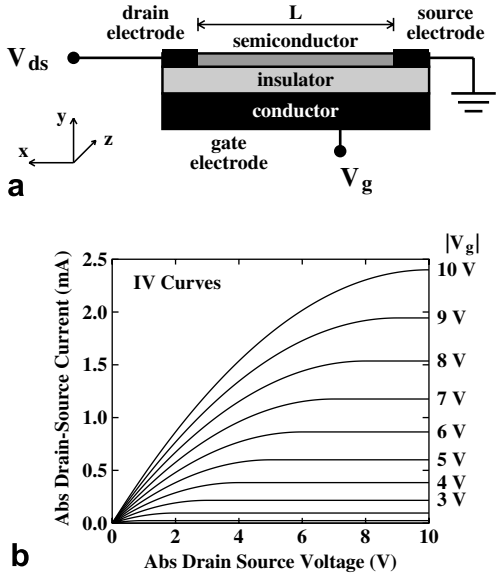

Fig. 1. (a) Cross-section of a TFT device with the names of parameters and variables used in the current work. (b) Representations of Eq. (3) with parameters as in Table 1 and $L = 10\ \mu m$ and $W = 1$ cm.

One special case of temperature dependence is the Meyer–Neldel Rule (MNR) [5]. The MNR is an observation which states that the magnitude of a process is dependent on a certain parameter, but that the dependence disappears at the iso-kinetic temperature. This behavior is truly cross-disciplinary as it is found back in many processes in nature, such as diffusion and conduction. Although not limited to the process of electronic conduction, we focus here on this field. As an example there is the observation of the MNR for ionic conductivity [6], glassy [7], poly-crystalline [8] and organic [9] materials. We will show that the current and carrier-mobility of TFTs depend on the bias conditions in a way following the Meyer–Neldel Rule when the material has abundant traps that are distributed in energy. This finding may be relevant in understanding such observations reported in electronic devices (organic and inorganic alike [10,11]). The Meyer–Neldel Rule applied to the process of electronic conduction in TFTs can best be described by the following two points: (i) The activation energy of drain–source current, I_{ds}, or as-measured carrier mobility, μ_{FET}, depends on the gate bias. (ii) There exists a temperature, known as the iso-kinetic temperature T_{MN}, where the dependence of current or mobility on bias disappears. In other words, when presented in an Arrhenius plot (logarithm of the measured quantity vs. reciprocal temperature), the curves of current or mobility are straight lines that pass through or converge to a common point. For amorphous silicon transistors, based on the model of Shur and Hack [13], we determined the immediate consequence of the presence of abundant trap states to the observation of the MNR [15]. In the current work, we show how the two-dimensional model for TFTs results in similar results. However, the results are not identical to the ones obtained with the MOS-FET model. The results and the differences will be discussed.

2. Results and discussion

Where a MOS-FET is basically a three-dimensional device, *i.e.*, has finite thickness, a TFT is best described by a in a two-dimensional way. Apart from this, it is convention to use the *inversion*-channel model to analyze the TFTs, whereas most organic TFTs are operating in *accumulation* mode.

When these two things are taken into account, a direct result is that there are no band bendings in the active layer. In other words, all voltage drop is absorbed by the insulator. The local density of charge in the active layer is directly proportional to the voltage drop across the insulator

$$\rho(x) = C_{\mathrm{ox}}[V(x) - V_{\mathrm{g}}]. \tag{1}$$

This charge can be either free holes p (for the current work we consider a p-type accumulation channel TFT), or trapped charge N_{T}^{+}. At any given point in the device, the current is proportional to the local free charge density, the free-charge (band) mobility μ_0 and the local electric field, $\mathrm{d}V(x)/\mathrm{d}x$:

$$I_{\mathrm{x}}(x) = qWp(x)\mu_0 \frac{\mathrm{d}V}{\mathrm{d}x}, \tag{2}$$

with q the elementary charge, and W the channel width (the current density has been integrated over the width of the channel to get the total current passing a line at position x). In the absence of any current sources or sinks, the current $I_{\mathrm{x}}(x)$ has to be constant over the entire channel length ($0 \leqslant x \leqslant L$) and equal to the externally observable current I_{ds} (see Fig. 1a for a cross-section of a device). In the absence of any traps the charge is only free charge, $\rho = p$, and it can easily be shown that in this case [14]

$$I_{\mathrm{ds}} = -\frac{W}{L} C_{\mathrm{ox}}\mu_0 \left(V_{\mathrm{g}} V_{\mathrm{ds}} - \frac{1}{2} V_{\mathrm{ds}}^2 \right). \tag{3}$$

(See Fig. 1b for the IV curves). This result is very similar to the current–voltage equations of MOS-FETs [3]. For small drain–source biases, the quadratic term V_{ds} disappears from the above equation and this is then called the linear regime.

Conventionally, for MOS-FETs, the field-effect mobility μ_{FET} is defined via the derivative of the transfer curve (I_{ds} vs. V_{g}) in the linear regime:

$$\mu_{\mathrm{FET}} \equiv -\frac{L}{W} \frac{1}{C_{\mathrm{ox}} V_{\mathrm{ds}}} \frac{\partial I_{\mathrm{ds}}}{\partial V_{\mathrm{g}}}. \tag{4}$$

Equally standard is applying this definition of μ_{FET} to TFTs, which then sometimes becomes bias or temperature dependent. Furthermore, it can be stated that at low drain–source bias, in the so-called linear regime, the charge density and electric field can be considered homogeneous along the channel. In this case, the current is proportional to the free charge density, holes (p) in the case of p-channel FETs. The mobility in the linear regime is thus proportional to the derivative of the function of the hole-density as a function of gate bias:

$$\mu_{\mathrm{FET}} = -\frac{q\mu_0}{C_{\mathrm{ox}}} \frac{\partial p(V_{\mathrm{g}})}{\partial V_{\mathrm{g}}}. \tag{5}$$

For intrinsic TFTs this relation is linear. The as-measured mobility is therefore bias independent. (For this analysis we consider the intrinsic (band) mobility μ_0 to be temperature independent; effects of optical-phonon scattering, etc., are not included. In any case, these are slowly varying functions of temperature, such as $T^{1/2}$ [3]). The function becomes non-linear and the transfer curves with it, when – and only then – the material is full of traps. As a first attempt we try a discreet trap. In this case, the mobility is lowered significantly by the reduced ratio of free-to-total charge, and becomes temperature dependent, but remains independent of bias. This result is similar to the model of Poole and Frenkel [3] and the reasoning is as follows: Free holes (p) in the conduction band, originally induced by the gate bias, can be captured by the traps, turning these positively charged. At thermal equilibrium, the ratio of densities of holes and charged traps N_{T}^{+} is determined by the energetic distance $E_{\mathrm{T}} - E_{\mathrm{V}}$ between them, the relative abundance of the levels, N_{V} and N_{T}, respectively, and the temperature T (*Note*: since the active layer is treated as purely two-dimensional, all densities have units "per square meter"):

$$\frac{p}{N_{\mathrm{T}}^{+}} = \frac{N_{\mathrm{V}}}{N_{\mathrm{T}}} \exp\left(\frac{E_{\mathrm{V}} - E_{\mathrm{T}}}{kT} \right), \tag{6}$$

where the Boltzmann statistics function was used presupposing that the Fermi level is far away from both the conductive as well as the trap state levels (for the simulations, however, the full Fermi–Dirac distribution was used). The total charge induced in the channel is proportional to the gate bias (Eq. (1)):

$$p + N_{\mathrm{T}}^{+} - n = -C_{\mathrm{ox}} V_{\mathrm{g}}/q. \tag{7}$$

The current is only proportional to the free hole density because the trapped states, by definition, do not contribute to current and the density of electrons is insignificant. The solution of the above equations is that the current is linearly proportional to the gate bias and that the effective, as-measured mobility of Eqs. (4) and (5), defined via the derivative of the transfer curve, is therefore depending on temperature, but not on bias

$$\mu_{\mathrm{FET}} \approx \mu_0 \frac{N_{\mathrm{V}}}{N_{\mathrm{T}}} \exp\left(-\frac{E_{\mathrm{T}} - E_{\mathrm{V}}}{kT} \right). \tag{8}$$

In other words, the Arrhenius plots of mobility are straight lines; independent of bias, the slope of the

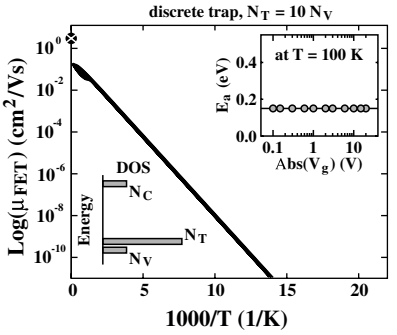

Fig. 2. Arrhenius plot of mobility for the case of an abundant discrete trap. In this particular case, $N_T = 10N_V$. The mobility is strongly temperature dependent and the plot reveals the trap depth of 150 meV, independent of bias. The insets show the schematic DOS and the activation energy of mobility (and current) as a function of gate bias. The symbol $\otimes$ at the mobility axis indicates the free-hole mobility μ_0.

plot reveals the activation energy of mobility, which is then equal to the depth of the trap level, $E_a = E_T - E_V$, see Fig. 2. This result is similar to the Poole–Frenkel model [3], or the variable-range hopping model of Horowitz [4]. Note that extrapolation of the curves to $T = \infty$ gives an effective prefactor in the mobility equal to $\mu_\infty = \mu_0 N_V/N_T$, which can be well below the free-hole band value μ_0 when the traps are abundant. For the figure, $N_T = 10N_V$ was used.

The assumption was made here that the trap states are truly abundant, effectively unlimited: $N_T \gg N_V$. When this is not the case, the trap states can be exhausted and, once all filled, the induced charge is necessarily free charge (holes) and the mobility returns to the band value μ_0. In the above calculations, it involves replacing the Boltzmann distribution approximation by the full Fermi-Dirac distribution function. The traps become depleted when the induced charge density is comparable to the trap density. This defines the trap-free-limit voltage for the gate bias

$$V_{tfl} = -qN_T/C_{ox}. \tag{9}$$

In Fig. 3, a transition case is shown with the trap density equal to the effective density of valence band states, $N_T = N_V$. For this specific case, $V_{tfl} = -10.4$ V. For gate biases below this voltage, the activation energy is equal to the trap depth (150 meV), while above it, the mobility rapidly becomes independent of temperature and settles at the free-hole value μ_0, as can be seen in the figure. In this case, it is not easy to give an algebraic solution. Fig. 3b shows the bias dependence of the mobility for different temperatures, which is based on numerical simulations: For a certain bias V_g, the Fermi level that zeros the total charge minus induced charge is found by a numerical algorithm as described by Ref. [12]. Once the Fermi level is found, the free charge is determined by substituting this energy in the free hole distribution $p(E_F)$. The voltage is stepped by a tiny amount and the free charge is calculated again. The mobility is then the derivative according to Eq. (5). (*Remark*: this technique was also used for Fig. 2). As can be seen, for $-V_g > -V_{tfl}$ the mobility is equal to the free-hole value indicated by $\otimes$ at the mobility axis. In fact, Eq. (9) gives a fast way of determining the trap density, provided the rapid transition in the transfer curves is observed that allows for a determination of V_{tfl}.

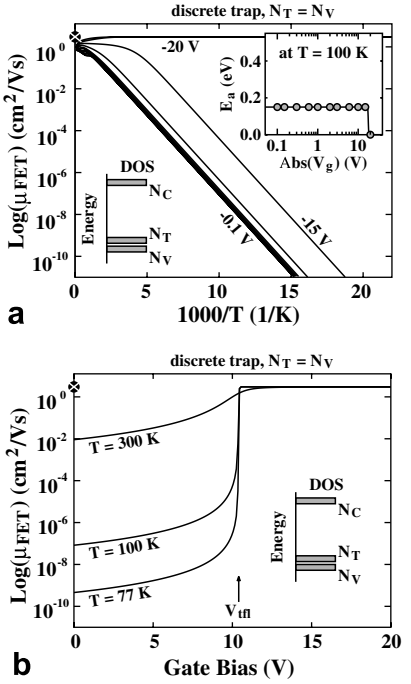

Fig. 3. (a) Arrhenius plot of mobility for a discrete trap with density equal to the effective density of valence band states, $N_T = N_V$. The activation energy is equal to the trap depth for biases below the trap-free-limit voltages $V_g < V_{tfl}$. For larger biases, the mobility is no longer thermally activated and the plots resemble those of trap-free devices. The insets show the schematic DOS and the activation energy of mobility (and current). The symbol $\otimes$ at the mobility axis indicates the free-hole mobility μ_0. (b) The bias dependence of mobility at three different temperatures. The trap-free limit voltage, V_{tfl} of Eq. (9) is indicated.

Inspired by the model of Shur and Hack [13] we then tried a model in which the trap states are distributed in energy. This, as we determined, can give rise to a bias- and temperature-dependent mobility.

Using a normal valence band and trap states N_T exponentially distributed in energy,

$$N_T(E) = g_{T0} \exp\left(\frac{E_V - E}{kT_2}\right) \tag{10}$$

with E the energy of an electron, g_{T0} the density of states (DOS) of traps at the valence band E_V, k Boltzmann's constant, and T_2 a parameter describing the distribution (the slope of a logarithmic plot of the DOS, see Fig. 4). When following the same reasoning as followed for the discrete trap, but with a convolution over trap states in Eqs. (6) and (7), it can be shown that the drain–source current is (see Appendix)

$$I_{ds} = q\mu_0 \frac{W}{L} V_{ds} N_V \left(\frac{-C_{ox} V_g}{qN_{T0}(T)}\right)^{T_2/T} \tag{11}$$

with

$$N_{T0}(T) = \alpha(T) g_{T0} \frac{k^2 T_2^2}{kT_2 - kT} \tag{12}$$

with $\alpha(T)$ a slowly varying function of temperature (and therefore irrelevant for the discussion), oscillating between 1 and 0.8 in the temperature range 0–T_2, with a minimum halfway. The as-measured mobility is proportional to the gate-bias derivative of this function (see Eq. (4)):

$$\mu_{FET} = \frac{T_2}{T} \mu_0 \frac{N_V}{N_{T0}(T)} \left(\frac{-C_{ox} V_g}{qN_{T0}(T)}\right)^{T_2/T-1}. \tag{13}$$

It is immediately clear that (i) the mobility depends on gate bias and (ii) the dependence disappears at a temperature $T = T_2$, thus following the Meyer–Neldel Rule, with $T_{MN} = T_2$. Fig. 5 shows simulations of the above equation with parameters as in Table 1. From this figure it can be seen that, because of the effects of the factor T in the denominator of the above equation, as well as the temperature dependence of α, the iso-kinetic temperature falls slightly below T_2 and the curves do not exactly extrapolate to a single point. However, in most cases will the instrumental resolution be too low to accurately determine this small deviation. Note also the sharp drop in current when the temperature approaches T_2. This is due to the factor $1/(kT_2 - kT)$ in Eq. (12), which diverges for $T \to T_2$. To our knowledge, no reports in literature exist for measurements at or in the vicinity of the iso-kinetic temperature; in all cases, T_{MN} is found by extrapolation.

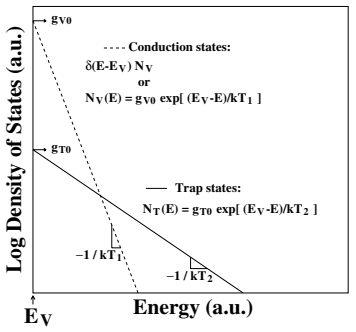

Fig. 4. Density of states used for the last calculations (Figs. 5 and 6). The trap states (solid line) are exponentially distributed in energy. For the conduction states, two distributions are tried: A discreet band at $E = E_V$ and an exponentially decaying function (dashed line). The former results in the observation of the MNR with bias and temperature dependent current and mobility, see Fig. 5. For the latter, only the bias dependence remains and the temperature dependence nearly vanishes, see Fig. 6.

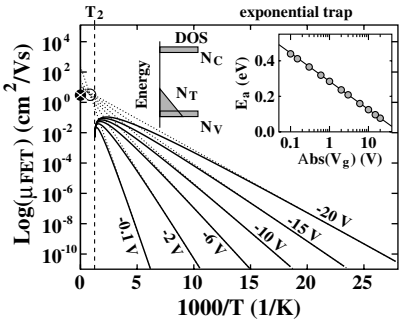

Fig. 5. Graphical representation of temperature-dependent as-measured mobility of Eq. (13) of a system with a DOS as in Fig. 4, namely an exponential distribution of trap states and discrete conduction states. Parameters as in Table 1, with gate biases from −0.1 V to −20 V as indicated. The open circle (○) represents the Meyer–Neldel point (T_{MN}, μ_{MN}). The inset shows the effective activation energy as a function of bias.

Table 1
Parameters used to generate figures

Parameter	Value	Unit
N_V	1.04×10^{16}	m^{-2}
N_T	1.04×10^{17}	m^{-2}
C_{ox}	160	$\mu F/m^2$
g_{T0}	10^{18}	$m^{-2}\,eV^{-1}$
g_{V0}	10^{17}	$m^{-2}\,eV^{-1}$
T_2	800	K
T_1	300	K
μ_0	3	$cm^2\,V^{-1}\,s^{-1}$

Analyzing Eqs. (11) and (13) it is easily shown that the activation energy of the field mobility (and current alike), as measured via the slope of an Arrhenius plot, depends on the bias in the following way

$$E_a \equiv -\frac{d\ln(\mu_{FET})}{d(1/kT)} = kT_2\ln(N_{T0}) - kT_2\ln(-C_{ox}V_g/q). \quad (14)$$

This is shown in the inset of Fig. 5. Thus, the activation energy of mobility or current does not reveal the depth of an energetic level. Rather, it depends on the parameters of the distribution (T_2 and g_{T0}) and the bias.

At this moment it is interesting to point out the difference between our model and the model of Shur and Hack [13]. Where they have a factor of $2T_2/T-1$ in the exponent in the current, we have T_2/T (Eq. (11)). This results, in our case, in an infinite iso-kinetic temperature for the current, whereas they have $T_{MN} = 2T_2$ [15]. For mobility, both models arrive at $T_{MN} = T_2$; the dependence of mobility on bias disappears at this temperature, as shown by Eq. (13).

A more fundamental difference is that Shur and Hack use exponential distribution for both the traps states as well as the valence band states (the so-called "tail states"), where we use only a distributed trap state, while we maintain a Dirac-delta function for the DOS of the valence band. When we include exponentially distributed tail states,

$$N_V(E) = g_{V0}\exp\left(\frac{E_V - E}{kT_1}\right), \quad (15)$$

with similar reasoning we arrive at a strongly bias dependent, but temperature independent mobility (see Appendix),

$$\mu_{FET} = \frac{T_2}{T_1}\mu_0\frac{N_{V0}(T)}{N_{T0}(T)}\left(\frac{-C_{ox}V_g}{qN_{T0}(T)}\right)^{T_2/T_1-1} \quad (16)$$

with

$$N_{V0}(T) = \beta(T)g_{V0}\frac{k^2T_1^2}{kT_1 - kT} \quad (17)$$

with T_1 the parameter describing the distribution of band-tail states, see Fig. 4, and β a function equal to α but scaled with T_1 instead of T_2. Fig. 6 shows a simulation of the mobility as a function of temperature and bias. Interesting in this respect is the observation by us of exactly such a behavior [16], something that is inexplicable in the theory of Shur and Hack.

Fig. 7 compares the various models described in this work and the model of Shur and Hack [13]. For the latter we used a value of 0.484 eV for their parameter E_{F0} and the value for their parameter g_{F0} (defining the density of states at E_{F0}) can then be found by extrapolating our g_{T0} to $E = E_{F0}$ in Eq. (10) and dividing it by 1 nm. This gives $g_{F0} = 8.93\times10^{23}/m^3$ eV. As can be seen, the model of Shur and Hack with conduction and donor states

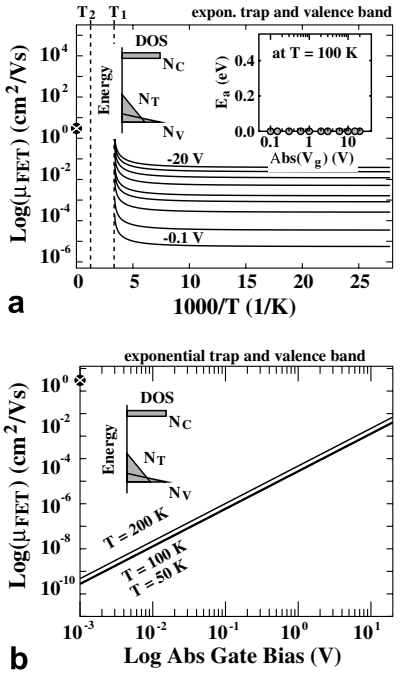

Fig. 6. Graphical representation of temperature-dependent as-measured mobility of Eq. (16) of (a) system with a DOS as in Fig. 4, namely an exponential distribution for both the trap states as well as the conduction states. Parameters as in Table 1, with gate biases from −0.1 V to −20 V as indicated. The mobility is strongly bias dependent, but independent of temperature; the inset shows the effective activation energy as a function of bias. (b) Shows the bias dependence of mobility for three different temperatures, which clearly follow a power law.

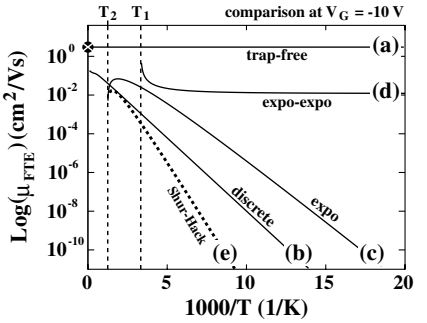

Fig. 7. Comparison of the various models: (a) trap-free model, (b) abundant discrete trap, (c) exponentially distributed trap, (d) exponentially distributed trap and conduction band, (e) model of Shur and Hack (with $E_{F0} = 0.484$ eV, $g_{F0} = 8.93\times10^{23}/m^3$ eV, $N_V = 1.04\times10^{25}/m^3$, $\varepsilon = 11.9\varepsilon_0$ and other parameters as in Table 1).

exponentially distributed in energy behaves much like our model with only the trap states distributed exponentially in energy. Noteworthy, the model of Shur and Hack was developed for amorphous silicon devices based on the MOS-FET model with a three-dimensional active layer, while our model is based on the two-dimensional accumulation-channel TFT model.

In conclusion, we have shown that a material that is full of traps (electronic states that can capture the free charge), when used in the active layer of TFTs, results in a strongly temperature dependent current and mobility. When the trap states are distributed in energy the mobility also becomes bias dependent, resulting in the observation of the so-called Meyer–Neldel Rule. The iso-kinetic temperature, the temperature where the as-measured mobility is independent of bias, is equal to T_2, the parameter describing the DOS of the traps. When also the conduction states are distributed in energy, the mobility loses its temperature dependence. As such, a set of Arrhenius plots for different biases may serve as a rapid evaluation tool of the quality of the material. More specifically, they give direct insight into the density-of-states governing the conduction. In cases, where a sharp transition in mobility is observed in the transfer curves the density of (discrete) traps can directly be determined via the trap-free-limit voltage V_{tfl}, see Eq. (9) and Fig. 3b.

As a final remark, it has to be pointed out that in this analysis at all times thermal equilibrium is assumed. Especially, for deep traps this equilibrium can take very long time to establish, in which case the electrical characteristics will depend on things such as the scanning speed and even the history of the device in case of extremely deep electronic levels.

Acknowledgements

This work was financed by the Portuguese Foundation for Science and Technology (FCT), Project POCTI/FAT/47956/2002 and the Programa Operacional Sociedade do Conhecimento, Research Unit No. 631, CEOT.

Appendix. Derivation of Eqs. (11) and (16)

To arrive at Eq. (11) a density of states (DOS) exponentially decaying in energy is used,

$$N_{\mathrm{T}}(E) = g_{\mathrm{T0}} \exp\left(\frac{E_{\mathrm{V}} - E}{kT_2}\right) \tag{18}$$

with g_{T0} the density of states at $E = E_{\mathrm{V}}$ and T_2 the decay rate, parameters that describe the distribution. The dependence of N_{T}^{+} on the position of the Fermi level thus becomes

$$N_{\mathrm{T}}^{+}(E_{\mathrm{F}}) = \int_{-\infty}^{\infty} N_{\mathrm{T}}(E)[1 - f(E - E_{\mathrm{F}})]\,\mathrm{d}E \tag{19}$$

with f the Fermi–Dirac distribution function,

$$f(E - E_{\mathrm{F}}) = \frac{1}{1 + \exp[(E - E_{\mathrm{F}})/kT]}. \tag{20}$$

The integral of Eq. (19) converges when $T < T_2$. To a good approximation, the solution can be found by dividing the integral into two parts, see Fig. 8. In the first part, below E_{F}, the slope is $1/kT - 1/kT_2$ as a result of the difference of slopes in N_{T} and the exponential approximation for $1 - f$. Above E_{F}, $1 - f$ is considered unity and the resulting slope is $1/kT_2$. With this help, it can easily be shown that the integral is equal to

$$N_{\mathrm{T}}^{+}(E_{\mathrm{F}}) = N_{\mathrm{T0}}(T) \exp\left(\frac{E_{\mathrm{V}} - E_{\mathrm{F}}}{kT_2}\right), \tag{21}$$

where N_{T0} is as in Eq. (12) in which $\alpha(T)$ an ad hoc correction factor that compensates for the error of integration; compare the rounded distribution of N_{T}^{+} of Fig. 8 and the triangular integration described above. Numerical simulations show that $\alpha(T)$ oscillates between 1 and 0.8 in the temperature range 0–T_2 (see Fig. 9). This makes N_{T0} essentially temperature independent for T not very close to T_2. For $T \geqslant T_2$ the integral diverges.

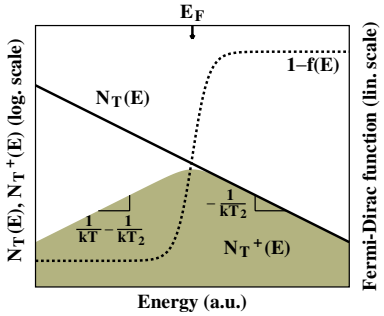

Fig. 8. Graphical schematic of the distribution in energy of trap states $N_T(E)$ (solid line) and charged trap states N_{T}^{+} (shaded area). The latter is a result of a multiplication of the former by the Fermi–Dirac function $1 - f(E)$ (dashed line). This shows that the total trapped charge N_{T}^{+} as a function of Fermi level, see the integral of Eq. (21), can easily be approximated by dividing the integral into two parts.

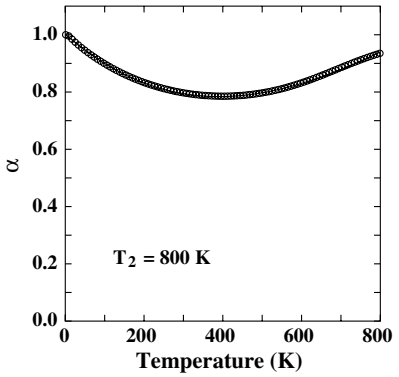

Fig. 9. The ad hoc correction factor α as a function of temperature, calculated numerically. α is a slowly varying function of T and its contribution to the calculation is minimal. For the calculations, α is approximated by a third-order polynomial (solid line).

If the conduction states are assumed to be discrete in energy, a standard valence band with N_V states at E_V, the density of holes follows

$$p = N_V \exp\left(-\frac{E_F - E_V}{kT}\right). \tag{22}$$

These two densities of p and N_T^+ can be introduced into the induced charge equation (Eq. (7)), ignoring the tiny contribution of the free electron density n

$$p + p^{T/T_2}\left(\frac{N_{T0}(T)}{N_V^{T/T_2}}\right) = \frac{-C_{ox}V_g}{q}. \tag{23}$$

For high densities of traps, the first term is negligible and the free hole density can then easily be determined as

$$p(V_g) = N_V\left(\frac{-C_{ox}V_g}{qN_{T0}(T)}\right)^{T_2/T}. \tag{24}$$

The current can then be found by Eq. (2), where in the linear regime, p is homogeneous in space and $dV/dx = V_{ds}/L$. This results in Eq. (11).

Next, conduction states exponentially distributed in energy are tried

$$N_V(E) = g_{V0}\exp\left(\frac{E_V - E}{kT_1}\right) \tag{25}$$

with g_{V0} the density-of-states at $E = E_V$, and T_1 a parameter describing the distribution (see Fig. 4). Similar integration techniques result in

$$p(E_F) = N_{V0}(T)\exp\left(\frac{E_V - E_F}{kT_1}\right) \tag{26}$$

with N_{V0} as in Eq. (17), in which β is a function similar to α, but scaled with T_1 instead of T_2. Again, this can be substituted in the induced-charge equation (Eq. (7)) and for high trap densities, the free charge density follows

$$p(V_g) = N_{V0}(T)\left(\frac{-C_{ox}V_g}{qN_{T0}(T)}\right)^{T_2/T_1} \tag{27}$$

substitution into Eq. (2) and using the field-mobility definition of Eq. (4) yields Eq. (16).

References

[1] C. Santato, R. Capelli, M.A. Loi, M. Murgia, F. Cicoira, V.A.L. Roy, P. Stallinga, R. Zamboni, S.F. Karg, M. Muccini, Synth. Met. 146 (2004) 329.
[2] S. Setayesh, D. de Leeuw, M. Büchel, T. Anthopoulos, E. Smits, P. Blom, in: Proceedings of the ECME 8 Abstract book, 2005, p. 15.
[3] S.M. Sze, Physics of semiconductor devices, second ed., Wiley Interscience, 1981.
[4] G. Horowitz, Adv. Mater. 10 (1998) 365.
[5] W. Meyer, H. Neldel, Z. Tech. 18 (1937) 588.
[6] K.L. Ngai, Solid State Ionics 105 (1998) 231.
[7] K. Shimakawa, F. Abdel-Wahab, Appl. Phys. Lett. 70 (1997) 652.
[8] S.K. Ram, S. Kumar, R. Vanderhaghen, P. Roca i Cabarrocas, J. Non-Crystalline Solids 299–302 (2002) 411.
[9] E.J. Meijer, M. Matters, P.T. Herwig, D.M. de Leeuw, T.M. Klapwijk, Appl. Phys. Lett. 76 (2000) 3433.
[10] Y. Lubianiker, I. Balberg, J. Non-Crystalline Solids 227–230 (1998) 180.
[11] M. Kondo, Y. Chida, A. Matsuda, J. Non-Crystalline Solids 198–200 (1996) 178.
[12] W.H. Press, S.A. Teukolsky, W.T. Vetterling, B.P. Flannery, Numerical Recipes in C, 2nd ed., Cambridge University Press, 1992. Available online at http://www.nr.com .
[13] M. Shur, M. Hack, J. Appl. Phys. 55 (1984) 3831.
[14] P. Stallinga, H.L. Gomes, Opt. Appl. 36 (2006).
[15] P. Stallinga, H.L. Gomes, Org. Electr. 6 (2005) 137.
[16] P. Stallinga, H.L. Gomes, F. Biscarini, M. Murgia, D.M. de Leeuw, J. Appl. Phys. 96 (2004) 5277.

Available online at www.sciencedirect.com
ScienceDirect
Organic Electronics 7 (2006) 600–606
Organic Electronics
www.elsevier.com/locate/orgel

Letter

Electronically controlled nonvolatile memory device using PAMAM dendrimer

Won-Jae Joo [a,*], Tae-Lim Choi [b,*], Sang Kyun Lee [a], Youngsu Chung [c], Myung-Sup Jung [a], Jong Min Kim [a]

[a] Display Device and Material Lab, Samsung Advanced Institute of Technology, P.O. Box 111, Suwon 440-600, Republic of Korea
[b] Electronic Chemical Materials Division, Cheil Industries Inc., 332-2 Gocheon-dong, Uiwang-si, Gyeonggi-do, Republic of Korea
[c] AE Center, Samsung Advanced Institute of Technology, P.O. Box 111, Suwon 440-600, Republic of Korea

Received 7 July 2006; received in revised form 18 September 2006; accepted 2 October 2006
Available online 25 October 2006

Abstract

The nonvolatile memory behavior, using novel material, PAMAM dendrimer was investigated. Although PAMAM dendrimers are intrinsically insulating materials, the metal coordinating functionality in the dendrimers can provide the PAMAM device the electronically controllable conductivity. In order to realize the bistable memory behavior in the PAMAM device, an external circuit consisting of two diodes and one resistor plays an important role in maintaining the resistance of the higher conductive state within a desired narrow range. Consequently, the PAMAM device shows good memory performance, such as relatively long retention time of at least 30 h, low operation voltage below 5 V and the on-off ratio which can be controlled from 10 to 10^3.

PACS: 73.61.Ph

Keywords: Nonvolatile memory; PAMAM dendrimer; Copper ion coordination

Dendrimers are a new class of macromolecules with uniform branching repeat unit [1]. They are unique materials due to potential advantages such as monodispersity in size, three-dimensional structure, and various functionalities [1]. Since the first discovery in 1985 [2], lots of efforts have been focused on the synthesis and the characterization of new dendrimers [3,4]. Especially, polyamidoamine (PAMAM) dendrimers were successfully commercialized by Dendritech Inc. [5] and owing to their availability, various applications using them were intensively demonstrated in the fields of the gene therapy, the environmental science, and the material science [1,6–8]. Among them, PAMAM dendrimers have received the most attention from the biomedical researchers due to possibility for selective modification at their cores, branches, and peripheries [1,6]. For example, PAMAMs have been considered as promising materials for the safe, non-

* Corresponding authors. Tel.: +82 31 280 6731; fax: +82 31 280 9349 (W.-J. Joo).
E-mail addresses: wj.joo@samsung.com (W.-J. Joo), tl.choi@samsung.com (T.-L. Choi).

1566-1199/$ - see front matter
doi:10.1016/j.orgel.2006.10.001

imunogenic, and highly efficient synthetic vector for the gene delivery through the complexation between amino surface group of PAMAM and DNA [1]. Moreover, when functionalized with fluorescent markers or chelated paramagnetic metals, they can be used as contrast agents for magnetic resonance imaging (MRI) [1,9]. Using a highly efficient metal chelating ability of PAMAM dendrimer, where up to approximately 150 Cu(II) ions can be bound in a generation eight dendrimer, the polymer supported ultrafiltration for copper ions was demonstrated in the field of environmental science [7]. Still the needs for new applications are desired in spite of the great development in dendrimer technology.

In this paper, as a new application of PAMAM dendrimer, we focus on the nonvolatile organic resistive memory. Up to the present, lots of organic memory systems have been studied for write-once-read-many-times memory and reversible one [10–12]. However the memory performances achieved in these organic system still remains in the early stage and breakthrough in materials is required. For the reversible memory application, the device should have two different states, which are controllable with voltage application as well as thermally stable for nonvolatile data storage. The bistability would be realized in the PAMAM device by electronically controlling the density of the copper ions within the dendrimer layer. The mechanism of memory behavior would be investigated with the time-of-flight secondary ion mass spectrometry (TOF-SIMS) and the feasibility was tested for memory application.

Experimentally, methanol solution of fourth-generation hydroxyl-terminated polyamidoamine (PAMAM-OH) dendrimers was commercially obtained from Aldrich and was used for device fabrication without further purification. Fig. 1 shows the third generation PAMAM-OH dendrimer. For electronic measurement, the test device was prepared with the structure of Cu/PAMAM-OH/Au. Bottom electrode (gold) was thermally evaporated on Si wafer coated with 200 nm-thick silicon oxide layer. Then 2 wt.% of PAMAM-OH dendrimer in methanol solution was spin coated to form

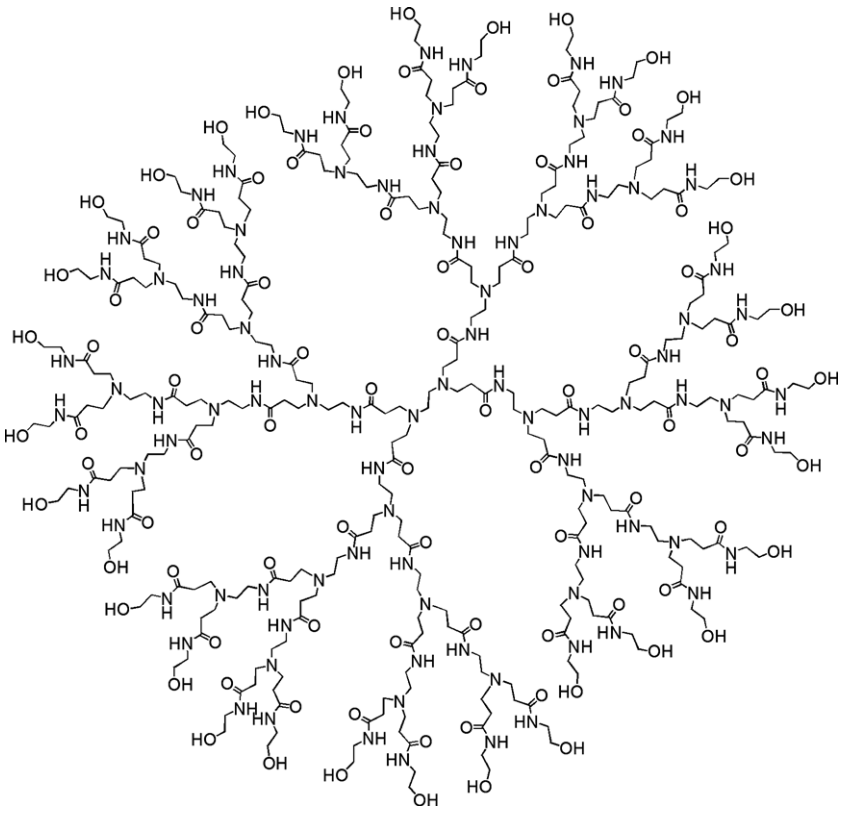

Fig. 1. Chemical structure of PAMAM-OH dendrimer (third generation).

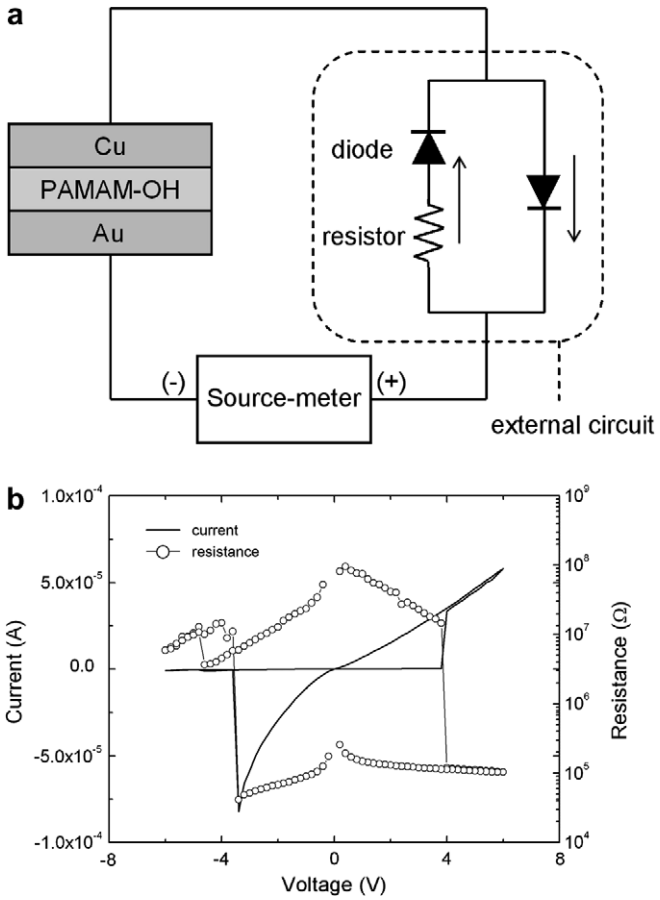

Fig. 2. (a) Schematic circuit diagram for measuring the memory behavior of PAMAM device. The external circuit shown in dotted box allows dendrimer device to have bistability. (b) Typical voltage-current-resistance curves of bistable memory behavior in PAMAM dendrimer device.

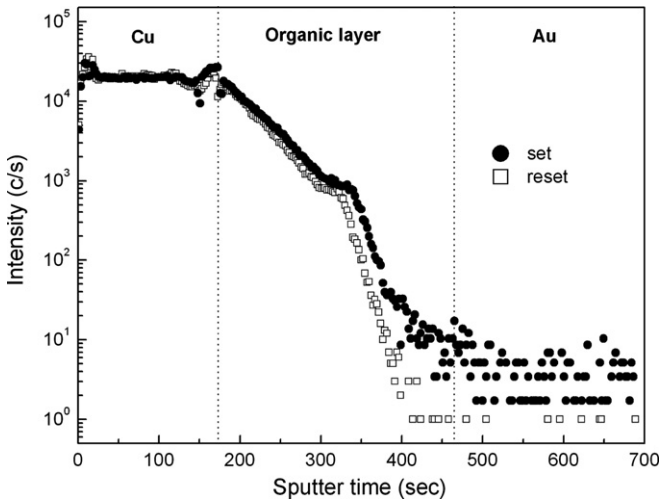

Fig. 3. Cu profiles in PAMAM dendrimer device at the set and reset states using TOF-SIMS.

30–50 nm thick organic layer, followed by heating the device on hot plate at 60 °C for removing the remnant solvent. Finally, top electrode (Cu) was deposited using thermal evaporator to make the active area of 0.25 mm^2. For the electronic measurement of the test device, programmable sourcemeter (model Keithley 2400) was used with computer interface and a unique external circuit was used together with the sourcemeter as shown in Fig. 2a. The circuit is consisted of two schottkey diodes (model RB521S-30) and one ceramic resistor. The purposes of the circuit are to provide the bistability to the device and to adjust the resistance value of the higher conductive state. The operation principle of the external circuit will be discussed in detail later. Cu density within dendrimer was investigated using TOF-SIMS (ION-TOF IV). Cu depth profiles were acquired in the dual beam interlaced mode using 500 eV Cs primary ion and 25 keV Bi analysis gun.

Memory behavior of PAMAM-OH device was observed in the voltage sweep mode (Fig. 2b). The resistance at the right axis is defined as a sum of the device resistance and the external resistance; in this case 50 kΩ. Before applying a voltage, resistance of the device has high resistance between 10 M and 100 MΩ. Then the total resistance suddenly drops to 110 kΩ at 4 V and the reduced resistance is maintained even in the absent of the bias voltage. Considering the external resistance of 50 kΩ, the resistance of the device is decreased to 60 kΩ. During the negative voltage sweep, the resistance returns to the original value at −3.5 V. Here, the higher and lower conductive states are called "the set" and "the reset" states, respectively. In the set switching, the response time obtained from an exponential fitting of the rising current curve was 3.1 ms. This memory behavior is reproducibly observed only with the external circuit, and the device without it shows no memory behavior implying that the circuit plays an important role in the memory operation.

Prior to describing the role of the circuit, the mechanism of the memory behavior should be understood in the PAMAM-OH device. PAMAM-OH dendrimers are electronically insulating material because they do not have any conductive path, such as pi-conjugated main chains and carrier hopping moiety (e.g. triphenylamine and carbarzole). Nevertheless, such a highly conductive state was achieved by voltage application which means that electronically conductive media was introduced by the electric stress and was contributed to the change in the resistance of device. We conjecture that copper ions act as the conductive media because copper is highly diffusive materials [13] and it can be injected into organic layer containing coordination sites under electric field [14,15]. The injected copper ions can be captured at the binding sites such as amine of PAMAM groups leading to the decrease of the device resistance [7]. In addition, when a less diffusive metal, aluminum, was used as top electrode instead of copper, the devices did not show a memory behavior.

To validate our assumption, the copper density within the dendrimer layer was measured at both

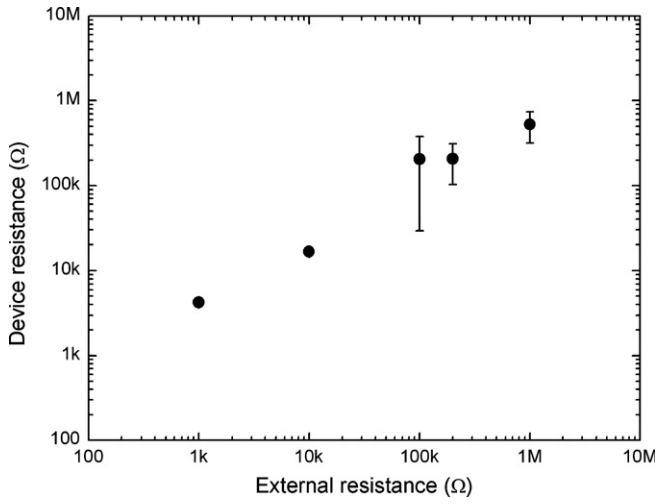

Fig. 4. The resistance of the higher conductive (set) state as a function of the resistance of the external resistance.

set and reset states using the TOF-SIMS as shown in Fig. 3. Cu profile is not abrupt at the interface of Cu and organic layers but shows a gentle slope to about a half thickness of organic layer, due to the penetration of Cu to organic layer during thermal evaporation of Cu. In addition, ion beam mixing during SIMS measurements also widen the trailing tail although low energy primary ion was used to reduce that. In spite of these, we can see the clear difference of Cu profiles at the tail. The difference in the tail seems to be caused by the drift of copper ions under electric field, which, as result, creates the difference in the resistance between the two states. Conclusively, the application of positive voltage injects the copper ions to decrease the resistance of device and the application of negative one retrieves the injected ions to increase the resistance.

However, since the conductivity of the device is very sensitive to the density and distribution, unfortunately, it was impossible to keep the higher conductive state within the desired narrow range by controlling the parameters of voltage pulse such as duration time and amplitude.

To overcome this problem, the external circuit is designed for giving the lower limitation of the decreasing resistance in the set switching operation. According to the Ohm's law, when two resistors are connected in series, the applied total voltage is divided onto the resistors with the ratio of two resistance values. Originally, the memory device has much higher resistance than that of the external resistor, so most of the applied total voltage is loaded to the memory device. On the other hand, during the set switching, the voltage loaded on the memory device decreases with decreasing the resistance of the device, and it becomes the half of the total voltage when the resistance of the device is identical to that of the external resistor. The decrease in the voltage loaded to the device results in the decrease of the driving force for the set switching. Consequently, during the application of the voltage pulse, once the resistance of the memory device reaches to that of the external resistor, the voltage loaded on the device is sufficiently lowered not to change the resistance any more. Therefore, the resistance of the set state could be controlled near the resistance of the external circuit. On the other hand, since the resistance of the reset state is not much sensitive to the voltage application in the reset switching process, the external circuit makes total voltage load on the device in the negative bias.

Memory device should have large enough sensing margin between two different states to fault-

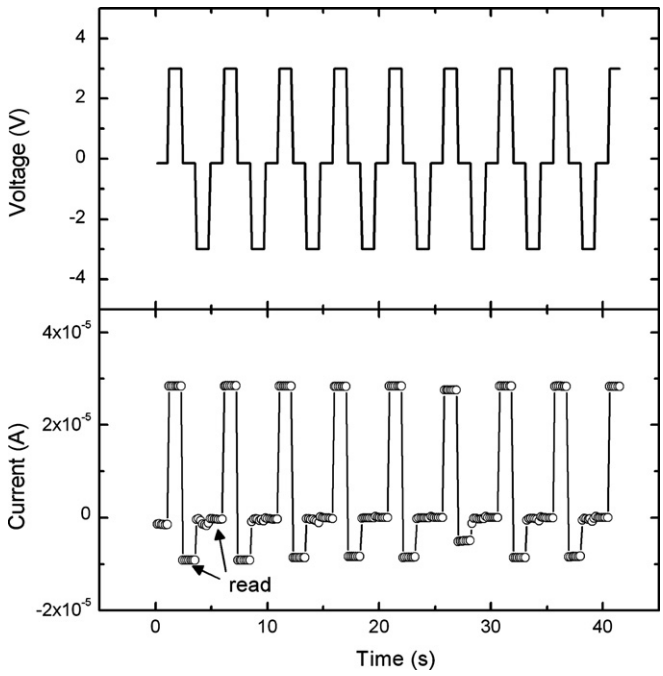

Fig. 5. Write-read-erase-read cycles of PAMAM dendrimer device. The write, erase and read voltages are applied to the device with +3, −3, and −0.15 V, respectively.

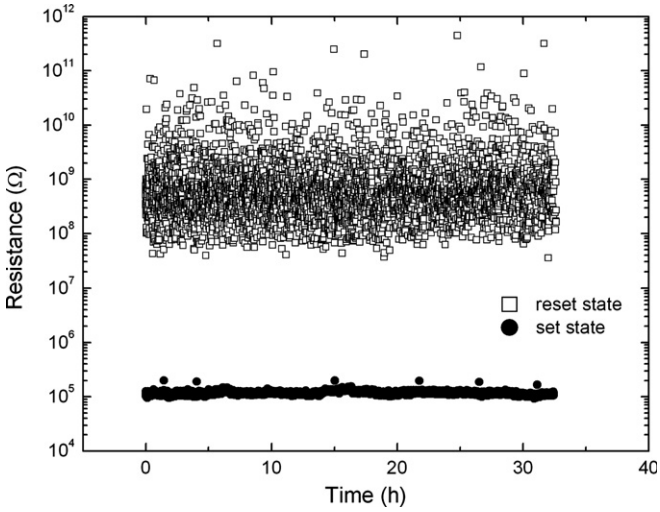

Fig. 6. Retention time of PAMAM device measured at −0.15 V in air.

lessly read the assignment (“0” or “1”) of the addressed cell. As mentioned before, by changing the resistance of the external resistor, the sensing margin can also be controlled. The resistance values of the set state were measured several times at the different resistance of the external circuit as shown in Fig. 4. The set resistance tends to increase linearly with the external resistance. This becomes more important as the two states have larger variations in resistance.

The memory device was operated with the write-read-erase-read pulse voltages in Fig. 5. The operation voltages for the set and reset switching were 3 and −3 V, respectively, and reading voltage was −0.15 V. Reproducible switching data was obtained with the external resistance of 10 kΩ and the resistances of the set and reset states were found to be 16 kΩ and 500 kΩ, respectively. In order to evaluate the nonvolatile ability of the PAMAM-OH dendrimer device, retention time of the same device was measured at continuous bias of −0.15 V in air. As shown in Fig. 6, the set state was maintained for 30 h without significant change which is a relatively good result compared to that of other organic memory devices.

In conclusion, we demonstrated the nonvolatile memory behavior as a new application of PAMAM-OH dendrimers. In order to provide the bistability to the PAMAM-OH device, an external circuit consisting of two diodes and one resistor was newly designed. In the absent of the circuit, the higher conductive state is so unstable that memory behavior was not observed. The two-terminal structured PAMAM-OH device shows nonvolatile memory behavior with retention time over 30 h. Further, the resistance value of the higher conductive state was controlled simply by changing the resistance of the circuit which enlarges the sensing margin in read operation. For a future study, the dependence of the binding energy of the metal-organic complex on the retention time will be investigated further to improve the retention time.

References

[1] M. Fischer, F. Vogtle, Angew. Chem. Int. Ed. 38 (1999) 884.
[2] D.A. Tomalia, H. Baker, J. Dewald, M. Hall, G. Kallos, S. Martin, J. Roeck, J. Ryder, P. Smith, Polym. J. 17 (1985) 117.
[3] C.J. Hawker, J.M.J. Fréchet, J. Am. Chem. Soc. 112 (1990) 7638.
[4] M. Slany, M. Bardaji, M.-J. Casanove, A.-M. Caminade, J.-P. Majoral, B. Chaudret, J. Am. Chem. Soc. 117 (1995) 9764.
[5] P.R. Dvornic, J. Polym. Sci.: Part A 44 (2006) 2755.
[6] M.X. Tang, C.T. Redemann, F.C. Szoka Jr., Bioconjugate Chem. 7 (1999) 703.
[7] M.S. Diallo, L. Balogh, A. Shafagati, J.H. Johnson Jr., W.A. Goddard III, D.A. Tomalia, Environ. Sci. Technol. 33 (1999) 820.
[8] J.-W. Kim, W.-A. Choi, S.-M. Park, J. Electrochem. Soc. 150 (2003) E202.
[9] G. Francese, F.A. Dunand, C. Loosli, A.E. Merbach, S. Decurtins, Magn. Reson. Chem. 41 (2003) 81.
[10] S. Moller, C. Perlov, W. Jackson, C. Taussing, S.R. Forrest, Nature 426 (2003) 166.
[11] H.S. Majumdar, A. Bandyopadhyay, A.J. Pal, Org. Electron. 4 (2003) 39.

[12] J. Ouyang, C. Chu, C.R. Szmanda, L. Ma, Y. Yang, Nature Mater. 3 (2004) 918.
[13] C.L. Platt, K.W. Wierman, E.B. Svedberg, R. van de Veerdonk, J.K. Howard, A.G. Roy, D.E. Laughlin, J. Appl. Phys. 92 (2002) 6104.
[14] A.L.S. Loke, J.T. Wetzel, O.H. Townsend, T. Tanabe, R.N. Vrtis, M.P. Zussman, D. Kumar, C. Ryu, S.S. Wong, IEEE Trans. Electron Dev. 46 (1999) 2178.
[15] A. Mallikarjunan, C. Wiegand, J.J. Senkevich, G.-R. Yang, E. Williams, T.-M. Lu, Electrochem. Solid-State Lett. 6 (2003) F28.